

Electrification

2020 Annual Progress Report

Vehicle Technologies Office

(This page intentionally left blank)

Disclaimer

This report was prepared as an account of work sponsored by an agency of the United States government. Neither the United States government nor any agency thereof, nor any of their employees, makes any warranty, express or implied, or assumes any legal liability or responsibility for the accuracy, completeness, or usefulness of any information, apparatus, product, or process disclosed or represents that its use would not infringe privately owned rights. Reference herein to any specific commercial product, process, or service by trade name, trademark, manufacturer, or otherwise does not necessarily constitute or imply its endorsement, recommendation, or favoring by the United States government or any agency thereof. The views and opinions of authors expressed herein do not necessarily state or reflect those of the United States government or any agency thereof.

Acronyms

A

AC	Alternating Current
ACC	Adaptive Cruise Control
accel	Acceleration
ACS	Advanced Combustion Systems
ACSforEVER	Advanced Climate Systems for EV Extended Range
AER	All-electric range
AFV	Alternative Fuel Vehicle
AMI	Advanced Metering Infrastructure
AMT	Automated Mechanical Transmission
ANL	Argonne National Laboratory
ANN	Artificial Neural Network
AOI	Areas of Interest
APEC	Asia Pacific Economic Council
APRF	Advanced Powertrain Research Facility
APT	Pressure Sensor
ASD	Aftermarket Safety Device
AVTA	Advanced Vehicle Testing Activity
AVTE	Advanced Vehicle Testing and Evaluation

B

BaSce	Baseline and Scenario
Batt	Battery
BEB	Battery Next-Generation Electric Transit Bus
BEC	Bussed Electrical Center
BEMS	Building Energy Management System
BET	Battery Electric Truck
BEV	Battery Electric Vehicle
BMW	Bayerische Motoren Werke AG
BSFC	Brake Specific Fuel Consumption
BTE	Brake Thermal Efficiency

C

CAC	Charge Air Cooler
CACC	Cooperative Adaptive Cruise Control
CAE	Computer-Aided Engineering
CAFE	Corporate Average Fuel Economy
CAN	Controller Area Network
CAV	Connected and automated vehicles
CARB	California Air Resources Board
CBD	Central Business District
CCS	Combined Charging System
CW, CCW	Clockwise, Counterclockwise

CD	Charge-Depleting
CERV	Conference on Electric Roads and Vehicles
CFD	Computational Fluid Dynamics
CFDC	Commercial Fleet Data Center
CFL	Combined Fluid Loop
CH ₄	Methane
CHTS	California Household Travel Survey
CIP	Common Integration Platform
Cm ³	Cubic
CNG	Compressed Natural Gas
CO	Carbon monoxide
CO ₂	Carbon Dioxide
COMM	Commuter
Conv	Conventional Vehicle
COP	Coefficient of Performance
CRADA	Cooperative Research and Development Agreement
CS	Charge Sustaining
Cs	Cold start
CV	Conventional vehicle

D

D3	Downloadable Dynamometer Database
DC	Direct current
DCFC	Direct Current Fast Charge
DCT	Dual-clutch transmission
decel	Deceleration
DER	Distributed energy resource
DFGM	Digital Flux Gate Magnetometer
DFMEA	Design of Failure Modes Analysis
DGE	Diesel Gallon Equivalent
DOE	U.S. Department of Energy
DOHC	Dual overhead cam
DS	Down speeding
DSM	Distributed Security Module
DSM	Diagnostic Security Module
DSP	Digital Signal Processor
DSRC	Dedicated Short Range Communications
dt	Change in time
dv	Change in velocity
Dyno	Dynamometer

E

EAVS	Electrically Assisted Variable Speed Supercharger
EC	European Commission
EDV	Electric Drive Vehicle
EDT	Electric Drive Technologies

EDX	Energy dispersive x-ray spectroscopy
EERE	Energy Efficiency and Renewable Energy
EGR	Exhaust Gas Recirculation
EG/W	Ethylene glycol/water
EOL	End of life
EPA	Environmental Protection Agency
ePATHS	Electrical PCM Assisted Thermal Heating System
EREV	Extended-Range Electric Vehicles
ESIF	Energy Systems Integration Facility
ESS	Energy Storage System
ETT	Electric Transportation Technologies
E-TREE	Electric Truck with Range Extending Engine
EUMD	End-Use Measurement Device
EV	Electric Vehicle
EV2G	Electric Vehicle-to-Grid
EVSE	Electric Vehicle Service Equipment
EXV	Electronic Expansion Valve

F

F	Force
FASTSim	Future Automotive Systems Technology Simulator
FC	Fuel cell
FC	Fast charge
FCons	Fuel consumption
FCTO	Fuel Cell Technologies Office
FE	Fuel Economy
FEA	Finite Element Analysis
FEX	Front-end Heat Exchanger
FHWA	Federal Highway Administration
FLNA	Frito-Lay North America
FM	Friction Modifier
FMEP	Friction Mean Effective Pressure
FOA	Funding Opportunity Announcement
FTIR	Fourier transform infrared spectroscopy
FTP	Federal Test Procedure
FWD	Four-wheel drive
FY	Fiscal year

G

g	gram
GB	Gigabyte
GCEDV	Grid Connected Electrical Drive Vehicles
GEM	Gas Emissions Model
GHG	Greenhouse Gas
GITT	Grid Interaction Tech Team
GMLC	Grid Modernization Lab Consortium

GnPs	graphene nanoplatelets
GO	Graphene Oxide
GPRA	Government Performance and Results Act
GPS	Global Positioning System
GREET	Greenhouse gases, Regulated Emissions, and Energy use in Transportation
GSF1	Generic Speed Form 1
GSU	Grid side unit
GUI	Graphic User Interface
GVW	Gross Vehicle Weight

H

h-APU	hybrid Auxiliary Power Unit
HATCI	Hyundai America Technical Center, Inc.
HC	Unburned hydrocarbons
HD	Heavy Duty
HEV	Hybrid-Electric Vehicle
H-GAC	Houston-Galveston Area Council
HHDDT	Heavy Heavy-Duty Diesel Truck
HHV	Hydraulic Hybrid Vehicle
HIL	Hardware-In-the-Loop
HP	Heat Pump
Hp	Horsepower
HTML	HyperText Markup Language
HV	High Voltage
HVAC	Heating Ventilating and Air Conditioning
HWFET	Highway Fuel Economy Test
HPMS	Highway Performance Monitoring System
HVTB	High Voltage Traction Battery
HWY	Highway Program or Highway Fuel Economy Test Cycle
HPC	High Performance Computing
HTR	Heater
Hz	Hertz

I

I	Inertia
IC	Internal Combustion
ICD	Interim Component Durability
ICDV	Internal Combustion Drive Vehicles
ICE	Internal Combustion Engine
ICTF	Intermodal Container Transfer Facility
ICU	Inverter-Charger Unit
IEB	Information Exchange Bus
IEC	International Electrotechnical Commission
IGBT	Insulated Gate Bipolar Transistors
IHX	Internal Heat Exchanger
INL	Idaho National Laboratory

INTEGRATE	Integrated Network Testbed for Energy Grid Research and Technology
IOT	Internet of Things
IR	Infrared Radiation
ISO	International Organization for Standardization
ITS	Intelligent Transportation Systems

J

JIT	Just-in-Time
-----	--------------

K

kg	Kilogram
km	Kilometer
kW	Kilowatt
kWh	Kilowatt hour

L

L	litre
L1	Level 1 benchmark
L2	Level 2 benchmark
Lbf	Pounds force
LCC	Liquid-Cooled Condenser
LD	Light duty
LH	line haul
Li	Lithium
LIB	Lithium-ion battery
LLNL	Lawrence Livermore National Laboratory
LNG	Liquefied natural gas
LTC	Lockport Technical Center
LV	Leading Vehicle

M

M	Mass
MBSE	Model Based System Engineering
MD	Medium Duty
mpg	Miles per gallon
MMTCE	Million Metric Tons of Carbon Equivalent
MIIT	Ministry of Industry and Information Technology
mi	Mile
MJ	Megajoules
MOSFET	Metal-Oxide Semiconductor Field-Effect Transistor
mph	Miles per hour
MPGe,	Miles per gallon equivalent, Miles per gallon gasoline equivalent
MTDC	Medium Truck Duty Cycle
MOVES	Motor Vehicle Emission Simulator
MRF	Moving Reference Frame
MURECP	Medium-Duty Urban Range Extended Connected Powertrain
MY	Model year

M2 Meters squared

N

NACFE North American Council for Freight Efficiency
 NDA Non-Disclosure Agreement
 NETL National Energy Technology Laboratory
 NHTS National Household Travel Survey
 NHTSA National Highway Transportation Safety Administration
 NM Newton meters
 NOx Nitrogen oxides
 NR Natural Rubber
 NRE Non-Recurring Engineering
 NREL National Renewable Energy Laboratory
 NRT National Retail Trucking
 NVH Noise, vibration, and harshness
 NVUSD Napa Valley Unified School District
 NYSERDA New York State Energy Research Development Authority

O

OBC On-board charger
 OCBC Orange County Bus Cycle
 OEM Original Equipment Manufacturer
 OneSAF One Semi-Automated Forces
 ORNL Oak Ridge National Laboratories

P

P Active Power
 PC Polycarbonate
 PCM Phase-Change Material
 PCU Power Control Unit
 PCU Powertrain Control Unit
 PEEM Power Electronics and Electric Motor
 PFC Power factor correction
 PFI Port fuel injection
 PGW Pittsburgh Glass Works
 PHEV Plug-in Hybrid Electric Vehicle
 PHEV## Plug-in hybrid electric vehicle with ## miles of all-electric range
 PI Principal Investigator
 PM Permanent Magnet
 PM Particulate Matter
 ppm Parts per Million
 PTC Positive Temperature Coefficient (Electric Heater)
 PTO Power Take-Off
 PVP Polyvinylpyrrolidone
 PWWMD Public Works and Waste Management Department
 λ Power Factor

ϕ	Power Angle
Q	
Q	Reactive power
QA	Quality assurance
QC	Quality control
R	
R2	Coefficient of Determination
R/D	Receiver / Dryer
REV	New York State's Reforming the Energy Vision Initiative
REx	Range Extending Engine
rGO	reduced graphene oxide
RH	Relative Humidity
RMS	Root Mean Square
ROL	Ring-On-Liner
rpm	Revolutions Per Minute
RSU	Road Side Unit
RWDC	Real-World Drive-Cycle
S	
S	Apparent power
SAE	Society of Automotive Engineers
SBR	Styrene-Butadiene Rubber
SC03	SC03 Supplemental Federal Test Procedure
SCAG	Southern California Association of Governments
SCAQMD	South Coast Air Quality Management District
SCIG	Southern California International Gateway
SCR	Silicon Controlled Rectifier
SCR	Selective Catalytic Reduction
SDO	Standards Definition Organizations
SI	<u>Systeme International d'Unités</u>
SI	Gasoline Spark Ignition
SNR	Sensor
SOC	State of Charge
SPL	Sound Pressure Level
SR	Speed Ratio
SS	Steady State
SPaT	Signal Phase and Timing
StAR	Storage-Assisted Recharging
T	
T	Torque
TA	Technical Area
TA	Torque Assist
TC	Thermocouple
TE	Thermoelectric

TE	Transmission Error
TES	Thermal Energy Storage
TGA	thermogravimetric analysis
THC	Total hydrocarbon emissions
TIM	Thermal Interface Materials
TLRP	Thermal Load Reduction Package
TN	Testing Network
TOU	Time-Of-Use
TSDC	Transportation Secure Data Center
TSI	Turbocharged stratified injection
TUSD	Torrance Unified School District
TXVs	Thermal Expansion Valves

U

U.S. DRIVE	U.S. Driving Research and Innovation for Vehicle Efficiency and Energy Sustainability
UA	Transfer Coefficient
UC	Ultra-capacitor
UCR	University of California, Riverside
UDDS	Urban Dynamometer Driving Schedule
UN ECE	United Nations Economic Council for Europe
UPS	United Parcel Service
URL	Uniform Resource Locator
US06	Environmental Protection Agency US06 or Supplemental Federal Test Procedure
USABC	United States Advanced Battery Consortium
USCAR	U.S. Council for Automotive Research
Util	Battery capacity utilization

V

V	Voltage
V2G	Vehicle-to-Grid
VAr	Volt-Amp-reactive
VGI	Vehicle-Grid Integration
VGT	Variable Geometry Turbocharger
VIP	Vacuum Insulated Panels
VMT	Vehicle Miles Traveled
VS	Vehicle Systems
VSATT	Vehicle Systems Analysis Technical Team
VSI	Vehicle Systems Integration
VSST	Vehicle Systems Simulation and Testing
VTCab	Vehicle Thermal Cab Simulator
VTIF	Vehicle Testing and Integration Facility
VTO	Vehicle Technologies Office

W

dw	Change in Angle W
WCC	Water Cooled Condenser

WEC World Endurance Championship
WEG Water/Ethylene Glycol
Wh Watt hour
WHR Waste Heat Recovery
WPT Wireless Power Transfer
WTW Well-to-Wheels

X

XFC Extreme Fast Charging
XPS x-ray photoelectron spectroscopy

Z

ZECT Zero-emissions cargo transport

Executive Summary

During fiscal year 2020 (FY 2020), the U.S. Department of Energy (DOE) Vehicle Technologies Office (VTO) funded early-stage research & development (R&D) projects that address Batteries and Electrification of the U.S. transportation sector. The VTO Electrification Sub-Program is composed of Electric Drive Technologies, and Grid Integration activities. The Electric Drive Technologies group conducts R&D projects that advance electric motors and power electronics technologies. The Grid and Charging Infrastructure group conducts R&D projects that advance grid modernization and electric vehicle charging technologies. This document presents a brief overview of the Electrification Sub-Program and progress reports for its R&D projects. Each of the progress reports provide a project overview and highlights of the technical results that were accomplished in FY 2020.

Table of Contents

Acronyms	ii
Executive Summary	xi
Vehicle Technologies Office Overview	1
Electric Drive Technologies Program Overview	3
Grid and Infrastructure Program Overview	5
I Electric Drive Technologies	23
I.1 Electric Drive Technologies Research	23
I.1.1 Highly Integrated Power Module (Oak Ridge National Laboratory).....	23
I.1.2 High-Voltage, High-Power Density Traction Drive Inverter (Oak Ridge National Laboratory).....	30
I.1.3 High-Fidelity Multiphysics Material Models for Electric Motors (Oak Ridge National Laboratory).....	37
I.1.4 Non-Heavy Rare-Earth High-Speed Motors (Oak Ridge National Laboratory).....	41
I.1.5 Integrated Electric Drive System (Oak Ridge National Laboratory)	50
I.1.6 Advanced Packaging Designs – Reliability and Prognostics (NREL).....	57
I.1.7 Electric Motor Thermal Management (National Renewable Energy Laboratory).....	65
I.1.8 Integrated Traction Drive Thermal Management (NREL).....	72
I.1.9 Power Electronics Materials and Bonded Interfaces – Reliability and Lifetime (NREL)	81
I.1.10 Power Electronics Thermal Management (NREL)	89
I.1.11 Power Electronics: Vertical GaN Device Development (Sandia National Laboratories)	98
I.1.12 Power Electronics: Active Device and Passive Component Evaluation (Sandia National Laboratories)	107
I.1.13 Bottom-Up Soft Magnetic Composites (Sandia National Laboratories).....	114
I.1.14 Component Modeling, Co-Optimization, and Trade-Space Evaluation (Sandia National Laboratories)	122
I.1.15 Magnetics for Ultra-High Speed Transformative Electric Motor (MUST-EM)	129
I.1.16 Integrated Motor and Drive for Traction Application (University of Wisconsin-Madison).....	135
I.1.17 Rugged WBG Devices and Advanced Electric Machines for High Power Density Automotive Electric Drives (North Carolina State University)	144
I.1.18 Design, Optimization, and Control of a 100-kW Electric Traction Motor Meeting or Exceeding DOE 2025 Targets (Illinois Institute of Technology)	154
I.1.19 Multi-Objective Design Optimization of 100 -W Non-Rare-Earth or Reduced-Rare Earth Machines (Purdue University).....	163
I.1.20 Integration Methods for High-Density Integrated Electric Drives (University of Arkansas)	171
I.1.21 Ultra-High-Speed, High-Temperature Motor (University of Illinois, Urbana-Champaign)	179
I.1.22 Cost competitive, high-Performance, highly Reliable (CPR) Power Devices on SiC and GaN	184
I.1.23 Cost competitive, high-Performance, highly Reliable (CPR) Power Devices on GaN.....	190

I.1.24	Next-Generation, High-temperature, High-frequency, High-efficiency, High-power-density Traction System (University of California, Berkeley)	193
I.1.25	Device- and System-Level Thermal Packaging for Electric-Drive Technologies	201
I.1.26	Heterogeneous Integration Technologies for High-temperature, High-density, Low-profile Power Modules of Wide Bandgap Devices in Electric Drive Applications	209
I.1.27	Implementation of WBG devices in circuits, circuit topology, system integration as well as SiC devices (The Ohio State University)	218
I.2	Electric Drive Technologies Development	226
I.2.1	Amorphous Metal Ribbon (AMR) and Metal Amorphous Nanocomposite (MANC) Materials Enabled High Power Density Vehicle Motor Applications (Carnegie Mellon University)	226
I.2.2	Wound Field and Hybrid Synchronous Machines for EV Traction with Brushless Capacitive Rotor Field Excitation (Illinois Institute of Technology).....	231
I.2.3	Cost Effective Rare-Earth-Free Flux Doubling, Torque Doubling, 8X Power Density Traction Motor with Near-Zero Open-Circuit Back- Electromotive Force (EMF) and No Cogging Torque (University of North Carolina at Charlotte)	239
I.2.4	Motor with Advanced Concepts for High power density and INtegrated cooling for Efficiency (MACHINE) – Raytheon Technologies Research Center	245
I.2.5	Cost Effective 6.5% Silicon Steel Laminate for Electric Machines (Iowa State University)	251
I.2.6	High Speed Hybrid Reluctance Motor Utilizing Anisotropic Materials (General Motors LLC)....	261
I.2.7	Highly Integrated Wide Bandgap Power Module for Next Generation Plug-In Vehicles (General Motors).....	271
I.2.8	Mapping the North American Rare Earth Magnets Supply Chain: Assessment of Suppliers, Technology Developments and Gaps. (Synthesis Partners, LLC)	277
I.2.9	Wound Field Synchronous Machine System Integration towards 8x Power Density and Commercialization (Magna Services of America, Inc.).....	285
II	Grid and Infrastructure	291
II.1	Industry Awards	291
II.1.1	SCAQMD ZECT-SanPedro FCCEV and HEV Demo (South Coast Air Quality Management District)	291
II.1.2	Cummins Electric Truck with Range-Extending Engine (ETREE) (Cummins, Inc.).....	301
II.1.3	Development and Commercialization of Heavy-Duty Battery Electric Trucks Under Diverse Climate Conditions (DTNA).....	307
II.1.4	Development and Demonstration of Medium-Heavy Duty PHEV Work Trucks (Odyne Systems).....	311
II.1.5	Medium-Duty Urban Range Extended Connected Powertrain (MURECP), Robert Bosch LLC ...	317
II.1.6	Long-Range, Heavy-Duty Battery-Electric Vehicle with Megawatt Wireless Charging.....	323
II.1.7	Medium-Duty Vehicle Powertrain Electrification and Demonstration (McLaren Engineering)	330
II.1.8	Improving the Freight Productivity of a Heavy-Duty, Battery Electric Truck by Intelligent Energy Management.....	333
II.1.9	Intelligent, Grid-Friendly, Modular Extreme Fast Charging System with Solid-State DC Protection (North Carolina State University)	339

II.1.10	Enabling Extreme Fast Charging with Energy Storage (Missouri S&T)	348
II.1.11	High-Efficiency, Medium-Voltage-Input, Solid-State-Transformer-Based 400-kW/1000-V/400-A Extreme Fast Charger for Electric Vehicles (Delta Electronics (Americas) Ltd)	362
II.1.12	High Efficiency Powertrain for Heavy Duty Trucks using Silicon Carbide (SiC) Inverter - DE-EE0008806 (Ricardo)]	372
II.1.13	Enabling Secure and Resilient XFC: A Software/Hardware Security Co-Design Approach (Virginia Tech)	379
II.1.14	Cybersecurity for Grid Connected eXtreme Fast Charging (XFC) Station (ABB)	389
II.1.15	Bidirectional Wireless Power Flow for Medium-Duty Vehicle-to-Grid Connectivity	397
II.1.16	Wireless Extreme Fast Charging for Electric Trucks	405
II.1.17	High-Power Inductive Charging System Development and Integration for Mobility (ORNL)	419
II.1.18	Direct Current Conversion Equipment Connected to the Medium-Voltage Grid for XFC Utilizing a Modular and Interoperable Architecture (EPRI) [DE-EE0008448]	431
II.1.19	Comprehensive Assessment of On-and Off-Board Vehicle-to-Grid Technology Performance and Impacts on Battery and the Grid (EPRI)	438
II.1.20	Cybersecurity Platform and Certification Framework Development for eXtreme Fast Charging (XFC): (EPRI)	452
II.2	Grid Interoperability and Control	465
II.2.1	Smart Vehicle-Grid Integration (Argonne National Laboratory)	465
II.2.2	Demand Charge Mitigation Technologies (NREL)	472
II.2.3	Adapter for Smart EV Charging to Improve Grid Integration and Interoperability (Argonne National Laboratory)	479
II.2.4	Scalable Electric Vehicle Smart Charging Using Collaborative Autonomy (LLNL)	485
II.3	High Power Charging (HPC) Enabling Technologies	492
II.3.1	Fast Charging: Interoperability and Integration Technologies (Argonne National Laboratory)	492
II.3.2	High Power and Dynamic Wireless Charging of EVs (ORNL, INL, NREL)	498
II.3.3	Fast Charging Grid Impacts and Cybersecurity 1.3.2.111 (INL)	515
II.3.4	Development of a Multiport 1+Megawatt Charging System for Medium and Heavy-Duty Electric Vehicles (NREL)	523
II.3.5	Smart Electric Vehicle Charging for a Reliable and Resilient Grid (Recharge)	536
II.3.6	Directed Electric Charging of Transportation using xFC (DirectXFC)	549
II.3.7	Grid-Enhanced Mobility-Integrated Network Infrastructures for Extreme Fast Charging [GEMINI-xFC] (NREL, LBNL)	561
II.4	Cybersecurity	573
II.4.1	Consequence-Driven Cybersecurity for High Power EV Charging Infrastructure (Idaho National Lab, Oak Ridge National Lab, National Renewable Energy Lab)	573
II.4.2	Securing Vehicle Charging Infrastructure	583

List of Figures

Figure 1 Key technologies and challenges addressed by the Grid and Infrastructure Program.....	5
Figure 2 Examples of EV Charging Stations and Connector Standards Sources: CEC 8	8
Figure 3 Strategic areas of the Grid and Infrastructure Program. 10	10
Figure 4 Key elements of Smart Charge Management. 11	11
Figure 5 Conceptual configuration of an HPC station. 13	13
Figure I.1.1.1 Thermal measurement setup for DBC and IMSwTPG evaluation: (left) isometric view, (middle) right cross-section, and (right) front cross-section.....	24
Figure I.1.1.2 (left) Comparison of average thermal resistance of paralleled SiC MOSFETs with DBC and IMSwTPG substrates at 25°C coolant temperature, (middle) transient impedance of SiC MOSFET dies on DBC and IMSwTPG substrates, and (right) current density comparison for M ₅ under different coolant performances.....	25
Figure I.1.1.3 (left) Output characteristics of the switches M ₁₋₃ and M ₄₋₆ on the IMSwTPG substrate at 25°C junction temperature and different gate-source voltage conditions, (middle) on-state resistance of M ₁₋₃ and M ₄₋₆ with 15 V gate-source voltage at three different junction temperatures, and (top right) turn-on and (bottom right) turn-off switching waveforms at 400 V DC link, 90 A load current, and 125°C junction temperature....	25
Figure I.1.1.4 (top left) Steady-state thermal performance and (bottom left) pressure drop across coolant fluid for the pin-fin heat sink. (top right) Steady-state thermal performance and (bottom right) pressure drop across coolant fluid for the optimized heat sink.	27
Figure I.1.1.5 (left) Cross-sectional concept view of the integrated multilayer power module, and (right) CAD model of the module with power devices, integrated gate drivers, and terminals. DC = direct current; HEMT = high-electron-mobility transistor; and ODBC = Organic Direct Bonded Copper.	27
Figure I.1.1.6 (left) Design space and Pareto-front for the optimized module design, and (right) temperature profile of the module with an integrated heat sink under steady-state conditions.	28
Figure I.1.2.1 (left) Block diagram of the segmented inverter and (right) photo of a prototype using SiC MOSFETs.	31
Figure I.1.2.2 Operating waveforms; left to right: non-segmented, traditional segmented, and DREAM method.	31
Figure I.1.2.3 Block diagram of open stator winding drives with (a) a single DC source and (b) two separate DC sources.....	32
Figure I.1.2.4 Comparison of DC bus ripple currents in the open-winding (OW) (dashed lines) and segmented drives (solid lines) at various power factors with the following PWM methods for the open-winding drive: (a) bipolar switching with a 180° phase shift, (b) bipolar switching with a 120° phase shift, (c) unipolar switching, (d) bipolar switching with a 120° phase shift, (e) symmetrical SV, and (f) bus clamp SV.	33
Figure I.1.2.5 Block diagram for frequency domain analysis of capacitor ESR loss and temperature. FFT = fast Fourier transform.	34
Figure I.1.2.6 Difference in (left) capacitor ESR loss and (right) temperature vs. modulation index between the traditional and frequency domain methods.....	34
Figure I.1.2.7 Bus bar design with embedded cooling channels.....	35
Figure I.1.2.8 Comparison of capacitor temperature with and without bus bar cooling for the US06 driving cycle.....	35

Figure I.1.3.1 System diagram for PWM loss testing using a standard ring core inductor that emulates standard three-phase voltage source inverter outputs using a single H-bridge inverter and DC-blocking components. ...	38
Figure I.1.3.2 Example three-level voltage source inverter voltage and current waveforms seen by a single electric motor phase that can be emulated using the single-phase approach with DC-blocking capability.....	38
Figure I.1.3.3 Variation of PWM losses with duty ratio for a simple test case.....	39
Figure I.1.3.4 Plot of amplitude permeability and differential permeability of a typical non-oriented silicon steel.	39
Figure I.1.3.5 Complex amplitude and differential permeabilities for a typical 0.25 mm thick non-oriented electrical steel excited at 5 kHz.	40
Figure I.1.4.1 Summary of specifications.	42
Figure I.1.4.2 Heavy rare-earth-free outer rotor PM traction motor.	42
Figure I.1.4.3 Segmented drive of a dual three-phase channel motor enabling reduction of the DC bus capacitor ripple current [4].....	43
Figure I.1.4.4 Peak torque waveform with 12% design margin and line-to-line back electromotive force (EMF) waveform at 20,000 rpm.	43
Figure I.1.4.5 Demagnetization resistance under transient three-phase short-circuit at 20,000 rpm with a PM temperature of 150°C: (a) effect of purely negative d-axis peak current versus three-phase short circuit and (b) effect of subsequent faults.	43
Figure I.1.4.6 AC loss calculation.	44
Figure I.1.4.7 Calculation of PM eddy current loss.	44
Figure I.1.4.8 Performance under 55 kW continuous operation and electromagnetic loss components for 0.2 mm lamination thickness.	45
Figure I.1.4.9 B-H curves and iron loss and efficiency for various silicon lamination thicknesses.	45
Figure I.1.4.10 Mechanical assembly.	46
Figure I.1.4.11 Mechanical stress analysis at 20,000 rpm: (a) equivalent stress and (b) deformation.	46
Figure I.1.4.12 Cooling strategy: (a) stator support and rotor cooling and (b) slot heat exchanger (refer to project elt214 “Electric Motor Thermal Management” by Kevin Bennion [NREL]).....	47
Figure I.1.4.13 Effect of lamination thickness on maximum temperatures and temperature distribution for 55 kW, 20,000 rpm operation (refer to project elt214 “Electric Motor Thermal Management” by Kevin Bennion [NREL]).....	47
Figure I.1.5.1 (a) Outer rotor motor structure and (b) internal stator mount integration technique for the outer rotor motor.	51
Figure I.1.5.2 The volume of the selected capacitor technologies compared with a 2016 BMW-i3 450 V 475 uF film capacitor.	52
Figure I.1.5.3 Ceramic capacitor packaging: (a) traditional flat capacitor package and (b) proposed circular capacitor package.	52
Figure I.1.5.4 Designed capacitor packaging: (a) proposed circular package and (b) a traditional flat capacitor package.	52
Figure I.1.5.5 (a) Surface current density of all three designed capacitor packaging showing symmetrical current distribution using circular packaging and (b) circular capacitor package showing lower layout inductance.	53

Figure I.1.5.6 Designed printed circuit board–based capacitor pancaking for experimental validation: (a) flat capacitor packaging and (b) circular capacitor packaging.....	53
Figure I.1.5.7 Designed power module with heat sink: (a) CFD showing maximum die temperature and (b) pressure drop through the heat sink.	54
Figure I.1.5.8 Integration of inverter components.....	54
Figure I.1.6.1 ODBC thermal modeling geometry.....	58
Figure I.1.6.2 Thermal modeling results of a double-layer ODBC substrate with 0.01-mm device spacing (left) and 4-mm spacing (right).....	59
Figure I.1.6.3 ODBC thermomechanical modeling results.....	59
Figure I.1.6.4 Evaluation sample.....	60
Figure I.1.6.5 Microscope images of nodules from samples 1, 5, 6, and 11.....	61
Figure I.1.6.6 Electrical resistance measurements of samples during accelerated tests.....	62
Figure I.1.6.7 Microscope images of sample 5 at 0 cycles (above) and 400 cycles (below).....	62
Figure I.1.6.8 Microscope 3D image of sample 5 at 400 cycles.....	63
Figure I.1.7.1 ORNL and NREL motor analysis approach.....	67
Figure I.1.7.2 Constructed experimental hardware inside environmental chamber (Source: Emily Cousineau, NREL).....	67
Figure I.1.7.3 ORNL-led motor development focused on illustrated outer rotor motor configuration (Source: Emily Cousineau, NREL).....	68
Figure I.1.7.4 Example iterations of the ORNL-led motor development that NREL used for thermal design analysis (Source: Emily Cousineau, NREL).....	68
Figure I.1.7.5 Example motor cooling approaches. (Left) Yellow highlighted regions show cooling within the stator winding slot (A), stator inner diameter surface (B), and rotor (C). (Right) Illustration of down-selected concept for placing cooling channels within the stator slot between the coil windings and stator tooth tips. (Source: Emily Cousineau, NREL).....	69
Figure I.1.7.6 Preliminary results of the V6 motor geometry with revised slot cooling heat exchanger with 0.2-mm-thick laminations at 20,000 rpm (Source: Emily Cousineau, NREL).....	69
Figure I.1.7.7 SNL material sample MRH2-47-1 undergoing testing in ambient conditions (Source: Emily Cousineau, NREL).....	70
Figure I.1.8.1 Identified integration concepts: (a) separate power electronics enclosure attached to motor case, (b) power electronics mounted/distributed radially on the motor casing, and (c) power electronics integrated axially in the motor front/back plate (Figures by Bidzina Kekelia, NREL).....	73
Figure I.1.8.2 Radially (a) and axially (b) integrated CAD model based on the BMW i3 traction motor and SiC power devices (shared cooling) (Figures by Bidzina Kekelia, NREL).....	73
Figure I.1.8.3 HTC applied to the internal surfaces of the cooling jacket and the back of the power module copper base plate. Radially (a) and axially (b) integrated solutions shown (Figures by Bidzina Kekelia, NREL).....	74
Figure I.1.8.4 Temperature distribution from the FEA thermal model for the radially integrated BMW i3 motor and power module based on SiC devices (applied HTC of $h = 10,000 \text{ W/m}^2\cdot\text{K}$). The top image is showing a location and temperatures of the integrated power module in the motor case (maximum temperature is pointing to winding end turns hidden under the motor case). The lower image is showing temperature distribution in the key motor components (Figures by Bidzina Kekelia, NREL).....	75

Figure I.1.8.5 Temperature distribution from the FEA thermal model for the axially integrated BMW i3 motor and power module based on SiC devices (applied HTC of $h = 10,000 \text{ W/m}^2\cdot\text{K}$). The top image is showing a location and temperatures of the integrated power module in the motor case. The lower image is showing temperature distribution in the key motor components (Figures by Bidzina Kekelia, NREL).....	75
Figure I.1.8.6 ATF fan jet impingement configurations: (a) centerline of fan nozzle is aligned with the center of copper target, (b) centerline of fan nozzle is aligned with the edge of copper target, and (c) centerline of fan nozzle is tilted with regards to copper target (Figures by Xuhui Feng, NREL).....	76
Figure I.1.8.7 ATF circular (left) and fan (right) jet impingement isotherms on the target surface at 1 liter per minute (LPM) flow rate and 70°C fluid temperature (Figures by Xuhui Feng, NREL).....	76
Figure I.1.8.8 Model-predicted HTC results of the flat fan jet compared with the experimental results of circular jet impingement, with 10-mm nozzle-to-target distance. Studied flow velocities are 3, 5, and 10 m/s and fluid temperatures are 50°C, 70°C, and 90°C. (Figure by Xuhui Feng, NREL).....	77
Figure I.1.8.9 ORNL’s outer-rotor motor with integrated inverter in the central cavity (Figure by Bidzina Kekelia, NREL)	77
Figure I.1.8.10 Half-cylinder inverter housing with cooling fluid channels (Figure by Bidzina Kekelia, NREL).....	78
Figure I.1.8.11 Initial design of cooling system components: cylindrical housing with cooling fluid channels for an inverter, fluid distribution manifold-disk, and phase separator heat exchangers embedded between windings (Figure by Bidzina Kekelia, NREL).....	78
Figure I.1.8.12 The second iteration of the design of cooling system components: fluid distribution manifold-disk is thinner and modified with cutouts for winding end-turns (Figure by Bidzina Kekelia, NREL)	79
Figure I.1.9.1 Circular coupons ($\Phi 25.4\text{mm}$) for reliability evaluation; Cu (bottom) bonded to Invar (top) using sintered silver or high-lead solder (95Pb5Sn).....	82
Figure I.1.9.2 Schematic of design configurations selected for thermomechanical modeling. Circular- and square-shaped samples were considered.....	83
Figure I.1.9.3 2D model crack propagation model setup.....	84
Figure I.1.9.4 C-SAM images of 95Pb5Sn solder joints before cycling (left) and after 50 thermal cycles (right); Cu-side images (top) and Invar-side images (bottom).....	84
Figure I.1.9.5 Comparison of sintered silver samples with 95Pb5Sn solder (left) and SAC305 solder (right). Pressureless sintered silver samples were used for the comparison with SAC305 solder joints.	85
Figure I.1.9.6 C-SAM images of 95Pb5Sn solder joints before cycling (left) and after 30 thermal cycles (right); Cu-side images (top) and Invar-side images (bottom).....	85
Figure I.1.9.7 C-SAM images of Cu-Al transient liquid-phase alloys between AlSiC and Cu coupons. The thickness of the Cu coupons was 1 mm (left) and 2 mm (right).	86
Figure I.1.9.8 Strain energy density comparison between square and circular samples (left); strain energy density variation within the bond region of a square sample (right).....	86
Figure I.1.9.9 Propagation of the initially defined crack within the bonded joint under a temperature ramp loading from 25°C to 200°C.....	87
Figure I.1.10.1 Finned heat spreader as modeled (top left) and fabricated/actual (bottom left). Right image shows the 12 finned surfaces.	91
Figure I.1.10.2 Cross-section view of the copper block and finned heat spreader	91
Figure I.1.10.3 Pictures of the dielectric fluid heat exchanger and conceptual module (left) and dielectric fluid loop (right).	92

Figure I.1.10.4 CFD-predicted and experimental thermal resistance versus pumping power results for Alpha 6 fluid. Model results are in good agreement with experiments. 92

Figure I.1.10.5 Thermal resistance versus pumping power curves for Alpha 6, AC-100, and ATF at -40°C and 70°C 93

Figure I.1.10.6 CAD of double-side-cooled modules—conceptual dielectric fluid-cooled module (left) and 2013 WEG-cooled Camry module (right) 94

Figure I.1.10.7 FEA-computed temperature contours for the double-side-cooled module at $716\text{-W}/\text{cm}^2$ heat dissipation. Maximum temperatures are predicted to be $<175^{\circ}\text{C}$ 94

Figure I.1.10.8 CFD-computed pressure drop versus flow rate for the double-side-cooled heat exchanger. Series- and parallel-flow configurations results are provided..... 95

Figure I.1.11.1 (a) Schematic drawing of JBS diode, (b) schematic drawing of Trench MOSFET, and (c) schematic drawing of a Double-well MOSFET..... 99

Figure I.1.11.2 The growth and fabrication process of etched and regrown JBS diodes formed by MOCVD. The structure is homoepitaxially grown on (0001) bulk GaN substrates. Dry etching is performed to form wells for regrowth, followed by surface treatments. Regrowth of p-GaN planarizes, and undergoes a blanket etch back to reveal the alternating p- and n-type regions for the anode contact. The full fabrication process includes metal deposition, passivation, mesa isolation, and edge termination..... 100

Figure I.1.11.3 Process flow diagram for Sandia vertical GaN trench MOSFETs. 100

Figure I.1.11.4 Current-voltage characteristics of a fabricated etched-and-regrown GaN JBS diode. 101

Figure I.1.11.5 (a) SEM image showing a corrugated n-type drift pattern prior to regrowth and (b) SEM image showing a regrown pattern with the light region on top as the planarized p-type GaN and the dark region underneath as the n-type drift. 102

Figure I.1.11.6 (a) Forward IV characteristics for Schottky diode test structures on the JBS wafer, (b) reverse IV characteristics for the same devices, and (c) schematic drawing of the Schottky test structure. 102

Figure I.1.11.7 (a) Microscope image showing the contacts on the PN diode test structure for the ion-implanted sample. (b) Microscope image showing light emission under forward bias, demonstrating electron-hole recombination. (c) CTLM results of n-Ohmic contact to Si ion implanted region after 1000°C anneal. (d) CTLM results of n-Ohmic contact to Si ion implanted region after 1100°C anneal showing Ohmic behavior. 103

Figure I.1.11.8 Results from a single-finger MOSFET on the ALD- Al_2O_3 quarter with a low temperature ohmic anneal showing (a) IDVD characteristics for $V_G = 0:30\text{ V}$ in steps of 5 V , (b) transfer characteristics (IDVG) and transconductance curves demonstrating a positive threshold voltage, and (c) and optical microscope image of the fabricated device..... 104

Figure I.1.11.9 Breakdown results for single-finger MOSFETs on the ALD- Al_2O_3 quarter with the low temperature ohmic anneal showing (a) blocking voltage at a gate bias of 0 V , and (b) an optical microscope image of a device after a destructive breakdown test. 105

Figure I.1.12.1 Oxygen vacancy migration under applied bias can lead to degradation of ceramic capacitors. 108

Figure I.1.12.2 The evaluation of prototype devices in a custom testbed can inform both device designers on the strengths/weaknesses of their prototypes, as well as validate device models for simulation..... 109

Figure I.1.12.3 Schematic for WBG device testbed with embedded motor control. 109

Figure I.1.12.4 The lifetime of DC capacitors can be increased through the implementation of a bipolar switching scheme..... 110

Figure I.1.12.5 In-process fabrication for capacitor test setup which allows for stress and evaluation of a population of 40 capacitors under bipolar switching.	111
Figure I.1.12.6 (left) PCB of power stage and daughter card under test. (right) PCB of motor controller board.	112
Figure I.1.12.7 (left) Thermal image of one leg of the power stage showing the temperature of power switches at 400 V and 11 A. (right) Gate drive signaling at 400 V and 11 A showing stable operation.....	112
Figure I.1.13.1 XRD pattern of nearly phase pure Fe ₄ N produced from mixed phase commercial powders consisting of both Fe ₄ N and Fe ₃ N.....	115
Figure I.1.13.2 1,6-hexanediamine.	116
Figure I.1.13.3 4-aminophenyl sulfone.....	116
Figure I.1.13.4 trimethylpropane triglycidyl ether (TTE).....	116
Figure I.1.13.5 <i>N,N</i> -diglycidyl-4-glycidyl-oxyaniline (NND).	116
Figure I.1.13.6 Differential scanning calorimetry (DSC) data for a sample of NND based epoxy originally cured at a temperature of 180°C. The final cure temperature of 255°C is confirmed by the overlapping upper portion of the DSC curves, indicating no additional curing occurring above 255°C.....	117
Figure I.1.13.7 Zoomed-in differential scanning calorimetry (DSC) data for a sample of NND based epoxy cured at temperature of 290°C. The inflection point visible in all three curves indicates that the T _g of NND based epoxy is approximately 249°C.....	117
Figure I.1.13.8 Neat 2” x 2” epoxy sample for thermal characterization.	118
Figure I.1.13.9 2” x 2” 65 vol.% Fe ₄ N/epoxy composite sample for thermal characterization.	118
Figure I.1.13.10 Relative permeability (μ_r) as a function frequency for a set of toroidal cores with varying vol.% of Fe ₄ N in epoxy. The inset shows that the values of μ_r are increasing exponentially with the vol.% loading of Fe ₄ N.....	120
Figure I.1.14.1 Passive Component Models are Carefully Developed using Latest Design Information	123
Figure I.1.14.2 Comparison of R _{on} in MOSFETs made in Silicon, SiC, and GaN showing (left) the device structure and (right) the predicted results.	124
Figure I.1.14.3 Schematic of the synchronous boost converter with the passive and active elements to be optimized highlighted.	124
Figure I.1.14.4 Shown (left) Pareto solution evaluating Kool M μ , High Flux, and MPP and the prototypes with different inductors denoted as P1, P2, and P3 and (right) Pareto optimization solution sets with MLCC capacitors and film capacitors for input and output capacitors.....	125
Figure I.1.14.5 Shown (left) Picture of hardware prototype with the High Flux core design, P3 and (right) example of measured waveforms of the 5-kW boost converter operation with input of 400 V and output of 500 V for candidate P1 boost converter design	125
Figure I.1.14.6 Circuit topology (top) used in inverter optimization studies and (bottom) candidate flat form factor design shown from the side	126
Figure I.1.14.7 Comparison between Pareto optimal frontiers for SiC and GaN	127
Figure I.1.15.1 Demagnetization curves of the fine grain magnet fabricated by Ames Lab overlaid on Arnold’s commercial magnet using similar feedstock materials.	131
Figure I.1.15.2 MH demag curves of the bulk magnet prepared using powders blended with CuPr and sintered at different temperatures.	132

Figure I.1.15.3 a) High speed footage of melt-spinning process; b) 20 mm wide 0.05 mm thick melt-spun ribbon; c) a jar full of melting spun ribbon of 6.5%Si steel.....	133
Figure I.1.15.4 Processing steps for near-net-shape-molding of stator block.....	133
Figure I.1.16.1 Example of an integrated motor drive configuration with inverter axially mounted in the machine housing	136
Figure I.1.16.2 Torque-speed and power-speed curves of the desired traction motor that meets the project requirements with a CPSR of 3.....	139
Figure I.1.16.3 Optimized motor design points plotting the motor L-N rms voltage vs. active power density, both at 100 kW, with the data point color indicating I_{ch}/I_r for each design.....	139
Figure I.1.16.4 Cross-section view of optimized SPM machine showing all major stator and rotor design features.....	140
Figure I.1.16.5 FEA-calculated rotor stress distribution assuming that the magnets are frictionless with the sleeve and rotor.....	140
Figure I.1.16.6 FEA-calculated magnetic flux density distribution for 55 kW output power @ 6,667 rpm. ...	141
Figure I.1.16.7 Calculated torque-speed and power-speed curve of the CSI-driven SPM machine with a CPSR of 3.....	141
Figure I.1.16.8 Simulation results for the CSI drive system showing the predicted machine line-line voltage (left) and phase current (right) @ 55 kW and 6,667 rpm.....	141
Figure I.1.16.9 Calculated curves showing the effect of modulation index m on CSI drive loss components and total drive system loss for operation at 55 kW, 20,000 rpm.	142
Figure I.1.16.10 Calculated curves showing the effect of modulation index m on the machine power factor and terminal line-neutral rms voltage for operation at 55 kW, 20,000 rpm.	142
Figure I.1.17.1 Drive cycle-based loss analysis methodology.....	145
Figure I.1.17.2 Drive cycles used for loss analysis – (a) EPA UDDS (urban) and (b) EPA HWFET (highway).....	145
Figure I.1.17.3 Operating points of traction motor for EPA UDDS (urban) and EPA HWFET (highway) drive cycle.....	145
Figure I.1.17.4 FOM of commercially available devices.....	145
Figure I.1.17.5 Loss map plots in torque-speed range of traction motor for (a) SiC 2L and (b) GaN 3L-NPC inverter at $f_{sw} = 50\text{kHz}$	146
Figure I.1.17.6 Efficiency variation vs switching frequency for SiC 2L and GaN 3L-NPC inverter in (a) urban and (b) highway driving conditions.	146
Figure I.1.17.7 Turn on of device A3 at 400V, 40A. $E_{on}=65.7\mu\text{J}$	147
Figure I.1.17.8 Short circuit test of A3. $T_{sc} = 640\text{nS}$	147
Figure I.1.17.9 Test setup for short circuit test	147
Figure I.1.17.10 SOA of A3.....	148
Figure I.1.17.11 SOA of B1.....	148
Figure I.1.17.12 SOA of C1.....	148
Figure I.1.17.13 Output characteristics variation.....	148
Figure I.1.17.14 Transfer characteristics variation	148

Figure I.1.17.15 Threshold voltage variation.....	148
Figure I.1.17.16 Full current turn-off of 4 parallel GaN devices.....	149
Figure I.1.17.17 Full current turn-on of 4 parallel GaN devices.....	149
Figure I.1.17.18 Traction motor design.....	150
Figure I.1.17.19 Structure of the IPMSM in Design II.....	151
Figure I.1.17.20 Asymmetrical Dual Three Phase Inverter.....	151
Figure I.1.17.21 Structure of the Slotless-Halbach PMSM.....	151
Figure I.1.17.22 Stator Structure of the Slotless Halbach PMSM with Winding – Embedded Liquid Cooling (WELC).....	151
Figure I.1.17.23 Torque & Power-Speed Characteristics of Design II.....	152
Figure I.1.17.24 Efficiency Map of Design II.....	152
Figure I.1.17.25 Temperature Distribution of Design II at Steady-state.....	152
Figure I.1.17.26 Flux Density Plot of Magnets under SC fault at 120°C.....	153
Figure I.1.17.27 Torque Profile of the Slotless Halbach PMSM in Design III.....	153
Figure I.1.17.28 Temperature Distribution of Design III at continuous Condition.....	153
Figure I.1.18.1 Multi-material magneto-structural IPMSM rotor topology optimization (a) electrical steel distribution (red), (b) permanent magnet distribution (red).....	157
Figure I.1.18.2 Mesh deformation and distortion as the PM is displaced radially towards the airgap (a) only using Laplace smoothing, (b) using virtual connection lines to divide the topology optimization areas into sub-domains.....	157
Figure I.1.18.3 Virtual connection lines (red) to divide the region into sub-domains (numbered regions), and fixed (black) or variable (light blue) size PM, and fixed nodes (dashed lines) rotor entities.....	158
Figure I.1.18.4 Electrical steel distribution (red) of the example mesh deformation combined dimensional and topology optimization cases.....	158
Figure I.1.18.5 Von Mises stresses of the example mesh deformation combined dimensional and topology optimization cases.....	159
Figure I.1.18.6 Displacement of the example mesh deformation combined dimensional and topology optimization cases.....	159
Figure I.1.18.7 Field interpolation approach material distribution in the rotor design domain at 12,000 RPM. (a) Material distribution only where red represents electrical steel, light green represents the PM, and blue represents air. (b) In addition to the material distribution the equivalent centripetal force of the PM is calculated and assigned as a pressure on the boundary elements adjacent to the PM indicated by the orange color.....	160
Figure I.1.18.8 The (a) Von Mises stress and (b) displacement of the rotor designed using the field interpolation approach with a rotor speed of 12,000 RPM.....	160
Figure I.1.18.9 Candidate prototype IPMSM designs with different rotors: (a) three-layer rotor and (b) two-layer rotor.....	161
Figure I.1.19.1 Comparison of inverter losses against capacitor mass for the modulation strategies and switching frequency solutions evaluated in this example. Figure by Sudhoff/Pekarek research team.....	167
Figure I.1.19.2 MoM toolbox graphical user interface. Figure by Sudhoff/Pekarek research team.....	168

Figure I.1.19.3 Comparison of the results obtained from the proposed analytical model (a) vs FEA (b). Figure by Sudhoff/Pekarek research team.....	169
Figure I.1.19.4 Inert core machine. Figure by Sudhoff/Pekarek research team.....	169
Figure I.1.19.5 MoM generated flux lines of inert core machine. Figure by Sudhoff/Pekarek research team.	170
Figure I.1.20.1 A comparison between three different die electroless gold plating procedures.	173
Figure I.1.20.2 (a) Preliminary power module with a single device and copper substrate, (b) Preliminary power module with a single device and metal encapsulated TPG substrate.	174
Figure I.1.20.3 (a) Thermal image for a single power device with a copper substrate, (b) Thermal image for a single power device with a TPG embedded substrate, (c) Thermal image for two power devices with copper substrates, (d) Thermal image for two power devices with TPG embedded substrates.....	175
Figure I.1.20.4 Threshold voltage variation over temperature for NFET (left) and PFET (right) from wafers# 3, 4 and 6.....	175
Figure I.1.20.5 Die micrograph of fabricated SiC gate driver variant#1 (left), variant#3 (middle) and variant#4 (right). Die area 4.94 mm X 4.94mm.....	176
Figure I.1.20.6 Current sensing test setup (left), test results (right).....	177
Figure I.1.20.7 (a) Die image, (b) PCB designed for testing the sensor interface circuit.	177
Figure I.1.21.1 X-ray micrograph of copper wire coated with high-temperature silox insulation.....	180
Figure I.1.21.2 Dielectric breakdown voltage of Kapton and silox magnet wire at different temperatures.	180
Figure I.1.21.3 A) Design, B) polyurethane prototype, and C) ceramawire prototype of the solenoid motor..	180
Figure I.1.21.4 Force vs. temperature curves for solenoid prototypes with different insulation materials.	181
Figure I.1.21.5 A) Isometric and B) side view of the model rotor with the accompanying mesh for critical speed analysis.	181
Figure I.1.21.6 Campbell diagrams for the model rotor consisting of solid A) iron and B) mullite.....	182
Figure I.1.21.7 A) Isometric view and torque-speed curves for the model motor.	182
Figure I.1.22.1 Image of (a) the fabricated wafer and (b) packaged devices from Lot 1.....	185
Figure I.1.22.2 Output characteristics for half JFET width of 0.6 μm and channel length of 0.5 μm of (a) JFET doping of $3\text{e}16\text{ cm}^{-3}$ (Wf1), (b) JFET doping of $5\text{e}16\text{ cm}^{-3}$ (Wf2) (c) JFET doping of $7\text{e}16\text{ cm}^{-3}$ (Wf4), and (d) JFET doping of $9\text{e}16\text{ cm}^{-3}$ (Wf6).....	186
Figure I.1.22.3 Summary of specific on resistance as function of half JFET width with different JFET doping concentration.....	186
Figure I.1.22.4 BV for W_{JFET} of 0.6 μm and L_{ch} of 0.5 μm with different JFET doping (a) under $V_{\text{gs}}=0\text{V}$ and (b) $V_{\text{gs}}=-10\text{V}$	187
Figure I.1.22.5 Specific on resistance as function of channel length with different JFET doping concentration.....	187
Figure I.1.22.6 BV for W_{JFET} of 0.6 μm of JFET doping of (a) $3\text{e}16\text{ cm}^{-3}$, (b) $5\text{e}16\text{ cm}^{-3}$, (c) $7\text{e}16\text{ cm}^{-3}$, and (d) $9\text{e}16\text{ cm}^{-3}$	187
Figure I.1.22.7 Top view for p-well of (a)MOSFET, (b) HEXFET with bridge, and (c) HEXFET without bridge.	188
Figure I.1.22.8 Breakdown voltage for half JFET width of 0.6 μm of JFET doping concentration of (a) $3\text{e}16$ and (b) $9\text{e}16\text{ cm}^{-3}$	188

Figure I.1.22.9 Cross-sectional view of (a) conventional 1.2kV 4H-SiC MOSFETs and (b) novel 1.2kV 4H-SiC MOSFETs.	189
Figure I.1.23.1 Calculated D_{it} plotted as a function of energy relative to the conduction band for each annealing condition.	191
Figure I.1.24.1 Comparison in output waveforms of a conventional two-level design (left), and a 9-level, dual-interleaved FCML design (right). The latter are from results in [8], and illustrate reduced dv/dt , interleaving and high effective frequency.....	194
Figure I.1.24.2 Top: schematic and current waveforms for a dual-interleaved, 10-level FCML inverter. Bottom: hierarchical control strategy and system diagram of paralleled converters of the modular (i.e., segmented) approach.....	195
Figure I.1.24.3 Data collection and parameter control set points shown in the left image. The right image shows an output voltage waveform being plotted in real time.....	196
Figure I.1.24.4 CFD analysis of forced air flow shown in the left image. The right image shows a new modular heatsink mounting system.	197
Figure I.1.24.5 EMI spectra for various converter configurations shown in the left image. The right image shows wiring connections for the experimental test setup verifying these simulations.....	197
Figure I.1.24.6 Experimental printed circuit board (PCB) with various commutation loops and calibration structures shown in the left image. The right image shows comparative simulation and measured results for inductance across frequency.	198
Figure I.1.25.1 Bonding stack for Cu – AlSiC layers	202
Figure I.1.25.2 Mesh for the FEA model (average size of 2.7 mm).	203
Figure I.1.25.3 EDX Images of Constituent Materials in Sample	204
Figure I.1.25.4 SEM Image Showing crack in AlSiC.....	204
Figure I.1.25.5 (a) Computational geometry for baseline straight microchannel (b) Diverging microchannel geometry (case 3) with $\theta = 0.5^\circ$ showing inlet, outlet, and side profile	205
Figure I.1.25.6 Volume fraction of the vapor at different time steps.....	205
Figure I.1.25.7 Measured temperatures compared to LPTN output temperatures at 5 different points of the stator.	206
Figure I.1.25.8 Temperature profile paths: (a) path (1) (slot) and path (2) (tooth) (b) path (3) (end-winding).....	206
Figure I.1.25.9 Temperature profiles along path (1) (top-left), path (2) (top-right) and path (3) (bottom).	207
Figure I.1.25.10 Sensitivity analysis of the LPTN thermal resistances for 20 % and 50 % value reductions. .	207
Figure I.1.26.1 Schematic of the hardware to be developed in this project.	210
Figure I.1.26.2 Die-shear strength vs. sintering temperature of sintered-silver joints on a bare copper DBC substrate.	211
Figure I.1.26.3 Each double-side cooled phase-leg module consists of two 1.2 kV, 149 A SiC MOSFETs. (a) Layout #1 having both devices mounted on the bottom substrate; (b) Layout #2 having one MOSFET on the bottom substrate and the other on the top substrate; and (c) thermal simulation results of die heat-flux versus required convection coefficient for Layout #1 and Layout #2. Single-side cooling = convection applied on the bottom side; double-side cooling = convections applied on both sides).....	212
Figure I.1.26.4 (a) The prototype of module layout #1, (b) zero-gate-voltage drain current, (c) drain-source on-state resistance, and (d) transfer characteristics.	213

Figure I.1.26.5 Manufactured PCB of gate driver board with gate driver from Cissoid.	213
Figure I.1.26.6 (a) Zoomed-in waveforms at turn-on transient, and (b) zoomed-in waveforms at turn-off transient.....	213
Figure I.1.26.7 Topology of the power supply.	213
Figure I.1.26.8 (a) PCB drawing of the air-core transformer (windings are placed in the middle layers), and (b) class-E dc-dc converter with the integrated air-core transformer.	214
Figure I.1.26.9 Output performance of the power supply: (a) gate and V_{ds} waveforms of the switch showing that ZVS is achieved, and (b) output voltage increases almost linearly with the load resistance. Constant-current output characteristics are verified.	214
Figure I.1.26.10 (a) Proposed current sensor scheme 1, and (b) experimental setup of the current sensor scheme 1.	215
Figure I.1.26.11 Measurement current under different configurations.	215
Figure I.1.26.12 (a) Proposed current sensor scheme 2, and (b) experimental setup of the current sensor scheme 2.	216
Figure I.1.26.13 Proposed class-D amplifier based active filter and FFT analysis of V_{XY} with and without the active filter.	216
Figure I.1.27.1 SiC MOSFET Reliability Issues.	218
Figure I.1.27.2 Key Partnerships.	218
Figure I.1.27.3 Threshold voltage variations and gate leakage currents during stresses at $V_G=38, 33$ V.....	220
Figure I.1.27.4 63% failure times as a function of applied gate voltage for vendor H at 150°C	220
Figure I.1.27.5 Weibull distributions for vendor C at 28°C with gate biases of 45, 46, and 47 V.....	220
Figure I.1.27.6 Time-dependent threshold voltage shifts for (a) positive bias-stress of +20 V, (b) +30 V, and (c) negative bias-stress of -10 V for 50 hours. The error bars represent the spread of 5 devices measured for each vendor.	221
Figure I.1.27.7 SC sustaining time with different gate voltages with $V_{ds} = 800$ V. Devices D' to F' are SiC MOSFETs and device B is a Si IGBT.	221
Figure I.1.27.8 Degradation of I-V curves for built-in body diode of Gen-1 DMOSFETs implanted at RT. ..	222
Figure I.1.27.9 Block diagram of gate drive circuit.....	223
Figure I.1.27.10 Pin fins design liquid cooling system 3D model and TO-247 packaged power device board.	223
Figure I.1.27.11 Double pulse test waveforms using the gate driver.....	224
Figure I.1.27.12 Test Waveforms under 800 Vdc input.	224
Figure I.1.27.13 Inverter test data.....	224
Figure I.2.1.1 (a) 2.5 kW dual stator FSWPM rare earth free permanent magnet HSM constructed as part of the DOE AMO Program DE-EE0007867; (b) 20 kW Dy-lean rare earth permanent magnet/MANC FSWPM design presented as Milestone 1 in our DOE VTO Project DE-EE0008870.	229
Figure I.2.2.1 Full load dynamometer testing of the CPC with an older WFSM prototype.	233
Figure I.2.2.2 WFSM generator mode with CPC field excitation load power and CPC tank current as a function of speed.....	234

Figure I.2.2.3 Potential CPC related signals for rotor position sensorless control. (a) Stator back-emf voltages induced by switching of the buck regulator in the CPC. (b) CPC PLL resonant frequency estimate as a function of rotor position with 3 phase back-emf signals superimposed.	235
Figure I.2.2.4 Die components to produce non-rectangular profile rotor field coil.	235
Figure I.2.2.5 Machine for orthocyclic winding of multiple wires simultaneously (a) tensioner, (b) wire guides.	236
Figure I.2.2.6 Multistrand orthocyclic winding (a) and (b) end turn ramp guides and (c) example winding. ..	236
Figure I.2.2.7 Positive and negative stacked lamination dovetail (a) samples with varying nominal gaps and (b) example shrink fitting.	237
Figure I.2.2.8 Square wire (a) base layer winding guides, (b) wound bobbin, and (c) zoomed view of wound bobbin.	237
Figure I.2.3.1 QMag topology illustration, (a) type-C (all magnets are magnetized in the same direction), (b) type-A (adjacent magnets are magnetized in opposite directions to concentrate flux).	240
Figure I.2.3.2 One implementation of the QMag technology, (a) assembled view, (b) exploded view.	241
Figure I.2.3.3 Large-scale design optimization of one implementation of the QMag technology. (a) Designs evaluated by FEA, (b) Torque-speed envelopes of all the Pareto front designs in (a).	241
Figure I.2.3.4 Systematic comparison of two QMag motors with 10-P and 14-P, respectively. (a) 3D view of Pareto fronts, (b) projection in the power density-power factor plane, (c) projection in the total loss-power density plane, (d) projection in the total loss-power factor plane.	242
Figure I.2.3.5 Results of simulation analysis of motor drive inverter powering mathematical inductance model of the QMag motor	243
Figure I.2.3.6 Design of 125 kW motor drive inverter visualized, including semiconductor modules, gate drives and signal conditioning, DC bus capacitors and thermal management.	244
Figure I.2.4.1 Power density distribution in the design space for both topologies: (a) concentrated winding designs at 24000 rpm, (b) distributed winding designs at 30000 rpm.	246
Figure I.2.4.2 Selected concentrated winding designs (Design 3 and Design 4) out of many designs considered.	247
Figure I.2.4.3 Thermal model domain showing ground insulation and thermal interface material placement.	248
Figure I.2.4.4 Peak temperatures and contours in °C at: (a) max continuous load just before peak load applied; (b) after 15 s at peak load.	248
Figure I.2.4.5 Peak temperatures and contours in °C at: (a) max continuous load just before peak load applied; (b) after 15 s at peak load.	248
Figure I.2.4.6 Topology optimization: problem setup	249
Figure I.2.4.7 Topology optimized flow header design.	249
Figure I.2.4.8 Detailed features of topology optimized flow header	249
Figure I.2.4.9 Velocity distribution of optimized manifold	249
Figure I.2.4.10 Velocity streamlines of the design space compared with the optimized design.	249
Figure I.2.4.11 COMSOL vibratory response analysis: (a) 2D COMSOL model (b) Stress response spectra (with excitation swept from 0 to 5000 Hz) with vibratory deformation shapes at two prominent resonant frequencies	249
Figure I.2.5.1 Drawing motor assembly and picture of the actual motor built by Leppert-Nutmeg. This motor topology includes a Fractional Slot Concentrated Winding (FSCW) Surface Permanent Magnet (SPM)	

machine with a 10 poles and 12 slots combination using the equivalent MnBi magnets (SmCo) and the high silicon JFE steels (10JNEX900).	252
Figure I.2.5.2 Three phase back EMF at rated speed: (a) measurements, (b) predicted back EMF, (c) Measured and predicted back EMF versus different speeds.....	253
Figure I.2.5.3 Losses associated with the test motor at no-load.	254
Figure I.2.5.4 Torque versus current loading test.	254
Figure I.2.5.5 Power versus current loading test.....	254
Figure I.2.5.6 Efficiency versus current loading.....	254
Figure I.2.5.7 Predicted and measured efficiency at different speeds and different field weakening conditions under rated load.	255
Figure I.2.5.8 Temperature measurements in end coils and coil center: (a) Rising temperature condition (b) Steady temperature and (c) Falling temperature.	256
Figure I.2.5.9 (a) Temperature variation in different coil end turns for 2000 RPM, 6 kW and 28.5 Nm operation. (b) Temperature variation in end coil during transient testing at 2000 RPM cycling between 6 kW and 10 kW.....	256
Figure I.2.5.10 BPM motor cost as a function of production volume.....	257
Figure I.2.5.11 Variation in motor cost (\$/kW) as a function of MnBi magnet and 6.5 % Si Steel cost for the manufacturing of 200000 units/yr for a 55 kW BPM motor.....	259
Figure I.2.6.1 Performance of Variant 1 motor, tested at 350V.....	264
Figure I.2.6.2 Performance of Variant 2 motor, tested at 350V.....	265
Figure I.2.6.3 Variant 2 rotor after rotor endurance failure.	265
Figure I.2.6.4 Performance of Variant 3 motor.....	266
Figure I.2.6.5 Variant 3 rotor after rotor endurance failure	266
Figure I.2.6.6 Custom test fixture made for testing rotor bars.....	267
Figure I.2.6.7 Rotor bar tensile test results, Batch #1 (left) and Batch #2 (right).	268
Figure I.2.6.8 SEM SEI image showing Sample A1 measurement sets 1-3 at 200X magnification.	268
Figure I.2.6.9 Epstein test frame.....	269
Figure I.2.6.10 SST Frame.....	269
Figure I.2.7.1 Open frame 1200V SiC power module	273
Figure I.2.7.2 (a) (b) Output characteristics and on-state resistance of the power module at 25 C, (C) output characteristics of the power module at 150°C	274
Figure I.2.7.3 (a) (b) Curve tracer characterization results for on-state resistance at different temperatures (C) detailed characterization of third quadrant operation.....	275
Figure I.2.7.4 (a) Test setup to measure voltage waveform at the motor terminals along with SiC inverter, (b) waveforms measured at the motor terminals, (C) partial discharge-measuring pressure chamber inside Faraday cage (left); stator assembly inside pressure chamber (right).....	275
Figure I.2.8.1 NA RE Mine-to-Magnet Supply Chain Overview	278
Figure I.2.8.2 Distribution of Rare Earth Element Production, by Country: 2018	280
Figure I.2.8.3 Total Rare Earth Oxide Production and Demand (incl. Nd & Pr), Excluding China.....	281

Figure I.2.8.4 Priority Gap Areas, by Frequency of Gap Statements	282
Figure I.2.9.1 Sample representative WFSM designs from large-scale optimization study	287
Figure I.2.9.2 Summary of optimization pareto fronts.....	287
Figure I.2.9.3 Capacitive power coupling stack on WFSM Shaft.....	288
Figure I.2.9.4 Initial rendering of 6.78 MHz Rotor Inverter.....	288
Figure I.2.9.5 Temperature and velocity analyzed on a sample design of the stator jacket for the WFSM.....	289
Figure I.2.9.6 Sample temperature and pressure drop profiles for various jacket designs investigated for the WFSM.....	289
Figure II.1.1.1 CTE/Kenworth Fuel Cell Truck.....	292
Figure II.1.1.2 TransPower Fuel Cell Truck in Foreground & CNG Truck in Background.....	292
Figure II.1.1.3 U.S. Hybrid Truck: Design to Fabrication.....	292
Figure II.1.1.4 Kenworth/BAE - CNG Hybrid System Architecture.....	293
Figure II.1.2.1 ETREE powertrain test cell located at Cummins Technical Center, Columbus, Indiana	303
Figure II.1.2.2 ETREE alternate battery -- drivers side enclosure (shown without cover).....	303
Figure II.1.2.3 ETREE vehicle at fleet site charging	304
Figure II.1.2.4 ETREE vehicle at IMS for SAE COMVEC Technology Demo.....	305
Figure II.1.3.1 Technology Development Level Progression of the Work.....	309
Figure II.1.4.1 Odyne powertrain configuration	312
Figure II.1.4.2 Odyne hybrid architecture.....	313
Figure II.1.4.3 Odyne / Oak Ridge HIL powertrain test stand.....	314
Figure II.1.4.4 Odyne Current Production Layout.....	315
Figure II.1.4.5 Odyne Project System Layout	315
Figure II.1.5.1 New rule-based strategy shows close alignment with system optimal strategy.....	318
Figure II.1.5.2 SCR Inlet & Engine Out.....	319
Figure II.1.5.3 Simulated Underfloor & Close	319
Figure II.1.5.4 SCR Inlet & Engine Out.....	319
Figure II.1.5.5 Simulated Underfloor & Close	319
Figure II.1.5.6 Operation summary during NYCC.....	320
Figure II.1.5.7 Operation summary during UDDS	320
Figure II.1.5.8 Operation summary during HTUF4.....	320
Figure II.1.5.9 Operation summary during HHDDT	320
Figure II.1.5.10 Operation summary during CHSVC starting with full battery charge.....	321
Figure II.1.5.11 Operation summary during CHSVC with High-Medium battery charge	321
Figure II.1.5.12 Operation summary during CSHVC with Medium battery charge.....	322
Figure II.1.5.13 Operation summary during CSHVC with Medium-Low battery charge	322
Figure II.1.6.1 System block diagram.....	324

Figure II.1.6.2 Chassis Layout.....	326
Figure II.1.6.3 Configuration of the designed WPT system	327
Figure II.1.6.4 Circuit diagram of an AC-AC conversion system	328
Figure II.1.7.1 Gen 2.0 single speed/single motor system in early build and bench test configuration.....	331
Figure II.1.7.2 Gen 2.0 single speed/single motor system in early build and bench test configuration.....	331
Figure II.1.8.1 FNN model trip predictions with (a) NLL loss function (b) LUBE loss function. Both models predict the amount of energy needed to complete a given route. The prediction uncertainty decreases at the end of trips as the vehicle data used to train the model has a consistent return trip energy usage pattern when vehicles return to a depot.	335
Figure II.1.8.2 A trip of the vehicle from which collected data.	336
Figure II.1.8.3 Remaining energy of the vehicle along trips	336
Figure II.1.8.4 The velocity profile of the first round trip	337
Figure II.1.8.5 The velocity profile of the second round trip.....	337
Figure II.1.8.6 Example optimal charger station placement output from genetic algorithm optimization. Locations and number of chargers were chosen along three common trucking corridors: (1) San Antonio, TX to/from New Orleans, LA, (2) Minneapolis, MN to/from Chicago, IL, (3) Boston, MA to/from Harrisburg, PA. The objective function considered local property costs, inter-charger distance, corridor trucking traffic, and expected charging wait times.....	337
Figure II.1.9.1 System Layout showing the key components: MV SST, DC distribution network, and DC node that contains the DC/DC converter and vehicle interface.....	340
Figure II.1.9.2 MV SST Converter topology. The SST is made up of 6 Levels connected in input-series output-parallel configuration. The figure on the left shows the design of a single module with the active front end, followed by the dual active bridge topology. The figure on the right shows the details of the control approach. Each DAB is controlled using a fully decentralized controller that acts as a “DC transformer” mirroring the voltage measured on the low voltage side onto the high voltage bus. A central controller coordinates all 18 front ends to maintain a stable DC bus on the output.....	342
Figure II.1.9.3 Design and implementation of a single module of the solid-state transformer.....	343
Figure II.1.9.4 (Left) Dual active bridge under test in the lab (middle) waveforms captured showing the MV and LV side voltages and currents. The waveforms show a small voltage overshoot on device drain-to-source voltage (Right) Thermal image of the setup while in operation. The peak temperature measured on the setup was below 70 degrees Celsius.....	344
Figure II.1.9.5 Fault scenarios under investigation.....	345
Figure II.1.9.6 (Left) Assembled prototype of 1500 A SS DCCB B1 (inside view); (Right) Assembled prototype of unidirectional 500 A SS DCCB B2 (inside view).	346
Figure II.1.10.1 Block-diagram schematic of the XFC station.	349
Figure II.1.10.2 Case study results: (a) EVs SOC variation, (b) EVs load, (c) measured active power at PCC (d) measured reactive power at PCC (e) PCC voltage, (f) ESS power, (g) ESS SOC variation, (h) DC link voltage.....	350
Figure II.1.10.3 (a) Charging station demand and electricity price. (b) Energy from distribution grid, ESS charging and discharging energy, and ESS SoC.....	351
Figure II.1.10.4 Sensitivity analyses on ESS energy sizing and the savings in total cost; (a) Impact of varying the allowed No. of ESS cycles; (b) Impact of varying electricity price; (c) Impact of varying the ESS	

investment cost; (d-e) impact of both electricity price and investment cost on ESS energy sizing and the savings in total cost respectively.....	352
Figure II.1.10.5 Overall structure of the system.	353
Figure II.1.10.6 Low-power hardware prototype.....	354
Figure II.1.10.7 PCB board of the low-side controller.	354
Figure II.1.10.8 Overall connection of the system.....	355
Figure II.1.10.9 Block diagram of the proposed MDHDP for VSG.	356
Figure II.1.10.10 Injected active and reactive power from a three-phase grid connected synchronverter facing active power reference changes (a) traditional VSG, (b) magnified response for traditional VSG, (c) HDP-based VSG (d) magnified output waveform of HDP-based VSG.....	356
Figure II.1.10.11 Li plating current as a function of time in CCCV and CQtCV in charging process.	357
Figure II.1.10.12 (a) Input current C-rate profile (b) cell voltage of CCCV and CQtCV.....	358
Figure II.1.10.13 (a) Charge time vs. charge specific capacity (b) discharge specific capacity of 3C CCCV and CQtCV cycling test, (c) charge specific capacity (d) charge time of 4C and 5C CCCV cycling test.....	358
Figure II.1.10.14 (a) C-rate, (b) normalized capacity, (c) anode state of charge, and (d) terminal voltage for CQO and 3CCCV.	359
Figure II.1.10.15 (a) C-rate, (b) normalized capacity, (c) anode state of charge, and (d) terminal voltage for CTO and 3CCCV charging.	359
Figure II.1.11.1 XFC System Architecture.....	363
Figure II.1.11.2 Circuit Diagram of Power Module.....	363
Figure II.1.11.3 Picture of an SST Module at left, and Charging Controller (Buck) Module at right.....	364
Figure II.1.11.4 Front View of 13.2kV/400kW SST Design.....	364
Figure II.1.11.5 3-D View of the 400-kW Charger Power Cabinet.....	365
Figure II.1.11.6 3-D View of the Charging Dispenser.....	365
Figure II.1.11.7 400kW XFC Setup Front View (SST, Charger Power Cabinet, Dispenser, and DCE from left to right).....	366
Figure II.1.11.8 400kW XFC Setup Rear View (DCE Cooling System, Buck charger, SST from Left to Right).....	366
Figure II.1.11.9 Retrofit Vehicle with Partially Assembled RESS Tray Loaded.....	367
Figure II.1.11.10 13.2-kV 400-kW XFC System Efficiency Curves.....	368
Figure II.1.11.11 13.2-kV 400-kW SST Efficiency Curves.....	368
Figure II.1.11.12 400-kW Buck Charger Efficiency Curves.....	369
Figure II.1.11.13 Temperature Rise in the RESS Components during Current Profile.....	370
Figure II.1.11.14 Subpack 4 Component Cool-Down after End of High Current Event.....	370
Figure II.1.12.1 Hardware architecture system diagram.....	377
Figure II.1.12.2 Control board and Gate Driver board.....	377
Figure II.1.12.3 Inverter design.....	378
Figure II.1.13.1 BMS Model; Feedback Susceptible: FDI or Jamming; Controller Output Susceptible: FDA381	

Figure II.1.13.2 Jamming effectiveness: perturbation leading to violation of small signal approximation. Sensor List: 2 - Current (Output perturbation > 5%, violation), 3 - Voltage sensor (Output perturbation > 5% if FDI is used in combination) 4–5 - SOC sensors (other converters).....	381
Figure II.1.13.3 A 350 kW XFC acquired from Tritium for project use.	382
Figure II.1.13.4 ComEd’s Integration and Technology lab	382
Figure II.1.13.5 Variation of bus voltage with time for varying number of EVs during charging.	383
Figure II.1.13.6 The components of a moving target defense.	383
Figure II.1.13.7 DC-DC Converter topology enabling MTD.	383
Figure II.1.13.8 A data-driven framework for detection of replay attacks is able to detect attacks more accurately than traditional model-based detectors.	384
Figure II.1.13.9 A linear scaling of voltage sensor output from an intentional electromagnetic interference attack leads to an exponential increase in output current in a prototype AC-DC converter.	385
Figure II.1.13.10 Intentional electromagnetic interference forces a switch closed in an AC-DC converter, resulting in a short circuit.	385
Figure II.1.13.11 (left) 350 kW AC-DC System Architecture and (right) 5 kW BMS System Architecture ..	386
Figure II.1.13.12 Efficiency of reverse and forward power output of BMS design.	386
Figure II.1.13.13 Transmitter and receiver components for inductive-loop fingerprinting of vehicles.....	387
Figure II.1.13.14 (left) Update architecture and (right) formally verified update procedure for input data correctness/parsing.....	387
Figure II.1.14.1 Single line diagram of the modeled power distribution system with XFC Station.....	390
Figure II.1.14.2 Real-time model developed in Opal-RT with communications and simulated BESS	391
Figure II.1.14.3 Actual EV load and optimized BESS results (top left); optimized BESS SOC (top right); net station load (bottom left); and input energy price profile (bottom right).....	392
Figure II.1.14.4 Figure Physical and abstracted measurements for Coordinated Anomaly Detection System.	393
Figure II.1.14.5 Prediction results for normalized charging site current based on Long-Short Term Memory	394
Figure II.1.14.6 Extreme Fast Charger Management System (XMS) Incorporated in HIL Testbed.....	395
Figure II.1.15.1 System level diagram of the proposed architecture for the bidirectional wireless charging system.	399
Figure II.1.15.2 System level diagram of the proposed architecture for the bidirectional wireless charging system.	399
Figure II.1.15.3 Primary-side (a) and the secondary-side hardware of the system.	400
Figure II.1.15.4 Vehicle-side coil mount assembly (a) and the primary and secondary couplers with 11 inches magnetic airgap (b).	401
Figure II.1.15.5 Resonant voltage gain of the system using the analytical model (a) and the experimental validation (b).....	401
Figure II.1.15.6 Instrumentation setup for the project demonstration.	402
Figure II.1.15.7 G2V operation test results.....	403
Figure II.1.15.8 V2G operation test results.....	403
Figure II.1.16.1 WXFC project activities.	406

Figure II.1.16.2 Project design and implementation approach.	406
Figure II.1.16.3 System block diagram.....	407
Figure II.1.16.4 250kW Secondary Pad Model Provided to Cummins.....	410
Figure II.1.16.5 250kW Rectifier Assembly.....	411
Figure II.1.16.6 500kW Rectifier Assembly.....	411
Figure II.1.16.7 Prototype Full Power Pad Set	412
Figure II.1.16.8 EMI Test Setup	413
Figure II.1.16.9 TABSRC Schematic	414
Figure II.1.16.10 Kenworth T680 Class 8 Truck with Day Cab.....	416
Figure II.1.16.11 Single String Battery Testing Results	417
Figure II.1.17.1 System level diagram of the proposed XFC inductive charging system.....	421
Figure II.1.17.2 3D engineering CAD design of the 300-kW primary-side open-ended dual-winding high-frequency, high-power inverter (a) and physical hardware development of the inverter.	422
Figure II.1.17.3 Engineering CAD designs of the 100/300 kW transmitter and the 100- and 300-kW receiver pads.	423
Figure II.1.17.4 Engineering CAD designs of the 100/300 kW transmitter and the 100- and 300-kW receiver pads.	424
Figure II.1.17.5 Engineering CAD designs of the 100/300 kW transmitter and the 100- and 300-kW receiver pads.	424
Figure II.1.17.6 Hyundai KONA EV research vehicle at the parking lot (a) and on the vehicle lift (b).	425
Figure II.1.17.7 100-kW receiver coil and the shielding system mounting platform designed for Hyundai KONA EV research vehicle integration.....	425
Figure II.1.17.8 Laboratory prototypes of the 50 kW rectifier blocks assembled using the GeneSiC SiC diode modules (a) and MicroSemi Si diode modules (b).....	426
Figure II.1.17.9 100-kW receiver coil and the shielding system mounting platform designed for Hyundai KONA EV research vehicle integration.....	428
Figure II.1.17.10 Experimental voltage overshoot analysis of the inverter for turning of 221 A in 50 ns.	428
Figure II.1.17.11 Experimental results of the inverter and rectifier operating at 85 kHz with 85.22 kW output.	429
Figure II.1.18.1 Architecture and Core Components.....	432
Figure II.1.18.2 Collaboration and Coordination.....	433
Figure II.1.18.3 System Overview.....	436
Figure II.1.18.4 DC Load Center Specification Design.....	436
Figure II.1.18.5 Medium Voltage Converter Module performance simulations.....	436
Figure II.1.19.1 Project Footprint for Concurrent Engineering	441
Figure II.1.19.2 SPIN Product Concept 3D-Layout including DC CCM and Charging Cable	443
Figure II.1.19.3 SPIN System Component Subassemblies	443
Figure II.1.19.4 First-Ever SPIN Design Intent System, Open Lid, with CCS Cable and DC Charge Interface	444

Figure II.1.19.5 SPIN System with DC Fast Charge Module and CCS Interface, with Closed Lid.....	444
Figure II.1.19.6 SPIN Application Scenarios being Designed for Verification.....	445
Figure II.1.19.7 SPIN Integrated Ecosystem Software Architecture: In-Cloud, On-Vehicle and On-SPIN.....	445
Figure II.1.19.8 Combined IEEE2030.5 and DIN 70121 Communications Sequence Diagram	447
Figure II.1.19.9 NREL ESIF Battery Packs in the Insulated Enclosure for Performance Testing.....	449
Figure II.1.19.10 Reference Performance Test Data for 9-month Effective Period	449
Figure II.1.19.11 RPT for V2G and Baseline Packs showing SOC, Power, Current and Voltages vs. time	450
Figure II.1.19.12 High Power Performance Characterization (HPPC) Test Profiles, Baseline vs. V2G Packs	450
Figure II.1.20.1 Research scope of Cybersecurity Platform and Certification Framework Development for XFC-Integrated Charging Infrastructure Ecosystem (Secure Grid-XEV)	453
Figure II.1.20.2 Project Approach and Activities for Phase 1 Research.....	455
Figure II.1.20.3 Participants & Other Collaborating Organizations	456
Figure II.1.20.4 Secure Network Interface Card Role in the XFC Infrastructure	459
Figure II.1.20.5 Secure Network Interface Card prototype board	460
Figure II.1.20.6 Conceptual Representation of the IGSRM Tool.....	461
Figure II.1.20.7 CSRL Testing Hardware.....	462
Figure II.1.20.8 Simplified EV Systems Architecture	463
Figure II.2.1.1 Structure of the distribution network model	469
Figure II.2.1.2 DEVA prototype in use and refined design for production	470
Figure II.2.1.3 SpEC module 2.0 alpha board	470
Figure II.2.2.1 Structure of distributed control with hierarchy	473
Figure II.2.2.2 Electric Vehicle Research Infrastructure (EVRI) on right with four vehicle parking bays each with both DC and AC charging and Commercial Building Research Infrastructure (CBRI) on the left with building loads and emulation.....	474
Figure II.2.2.3 Completed CCB cabinet	475
Figure II.2.2.4 Control hardware structure	476
Figure II.2.2.5 OP-5707 software diagram	476
Figure II.2.2.6 Tritium fast charger (on left) and Samsung energy storage system with OPAL 5707 server rack (on right).....	477
Figure II.2.3.1 The SCA is an in-line adapter for SAE J1772™ PEV charging.....	479
Figure II.2.3.2 Commercial Alpha Smart Charge Adapter: Portable, Robust and Easy to Use.....	481
Figure II.2.3.3 Exploded View of Commercial Alpha Smart Charge Adapter.....	482
Figure II.2.3.4 SCA Control Options: (L) Manual Control, (M) EV Mileage Control, (R) Timer Control.....	483
Figure II.2.3.5 Screenshot of setting up charge schedule through the web app.....	483
Figure II.2.3.6 Principal Investigator's charging data overview since Q2 FY20.....	484
Figure II.2.4.1 Example topology of the charging infrastructure considered in this work. Here $S(m_1) = \{s_1, s_2\}$, $S(f_1) = \{s_1, s_2, s_3, s_4\}$, $S(g_1) = \{s_1, s_2, s_5, s_6\}$. Stations in different feeders can be part of the same reserve group.	488

Figure II.2.4.2 Whiskers plot for solution times (wall clock) of our algorithm on all synthetic instances. Dots indicate median times over 10 instances for every charging station count.	490
Figure II.2.4.3 Whiskers plot for parallel overhead of our algorithm on all synthetic instances. Dots indicate median overheads over 10 instances for every charging station count.	490
Figure II.2.4.4 Primal and dual residuals at each iteration for 288 stations, while simulating random failures with different failure rates (FR). Residuals scaled by $p S \times (2T + T \text{ spin})$. Tolerances indicated with a dashed red line.	490
Figure II.3.1.1 Keysight Charge Discovery System (CDS) Hardware	493
Figure II.3.1.2 Keysight CDS connected to BMW i3	494
Figure II.3.1.3 BTCP 200kW - Keysight CDS Control Pilot Noise	495
Figure II.3.1.4 BTCP 200kW - Keysight CDS PLC SLAC Attenuation	495
Figure II.3.2.1 Proposed optimized architecture to enable 200 kW+ dynamic wireless EV charging.	500
Figure II.3.2.2 Weight and volume of secondary side DC-DC converter including the power electronics and the filter components as a function of number of phases and Junction temperature as a function of switching frequency and number of phases for secondary side dc-dc converter.....	500
Figure II.3.2.3 CAD model of the vehicle side high frequency rectifier and secondary side dc-dc converter.	501
Figure II.3.2.4 Prototypes of optimized primary side SiC based high frequency (85 kHz) inverter and optimized vehicle side high frequency rectifier and dc-dc converter.	501
Figure II.3.2.5 Top view of the ground coupler (top left) and vehicle coupler (top right); images are to scale. Side view of the ground coupler showing the surrounding concrete and vehicle ground clearance (bottom)..	502
Figure II.3.2.6 Thermal analysis of DWPT system embedded in concrete with ambient temperature of 55C for half lane of 6' width (left), Map of critical electromagnetic field emission regions on the surface of the roadway; Green – below 15uTrms, Yellow – between 15uTrms and 27uTrms; Red – Above 27uTrms (right).	502
Figure II.3.2.7 Cross section of the DWPT system model with four transmitters, one receiver, and vehicle chassis and wheel model. The vehicle chassis and wheels are assumed to be a standard structural steel. A thin aluminum strip runs down the center of the vehicle frame to reduce the losses in the most prone regions.	503
Figure II.3.2.8 (Left) Ground and vehicle coil self-inductances, (right) ground and vehicle coupler parasitic resistances.	503
Figure II.3.2.9 CAD model of designed 200 kW ground-side and vehicle-side couplers with 11' separation (top view).	503
Figure II.3.2.10 Block diagram of test platform for large-scale deployment of DWPT system on roadways..	504
Figure II.3.2.11 Assembled power electronics building block of 200 kW+ dynamic wireless charging system.	505
Figure II.3.2.12 Standard double pulse test setup wherein the device under test is the bottom MOSFET.	505
Figure II.3.2.13 Standard double pulse test setup wherein the device under test is the bottom MOSFET.	506
Figure II.3.2.14 Experimentally obtained input voltage, output voltage, output current, and MOSFET terminal voltage (drain-to-source) at 80 kW continuous operation.....	506
Figure II.3.2.15 Measured input and output voltage, current, power, and overall efficiency of HF power electronics resonant inverter-rectifier assembly at 85.2 kW output power.	506
Figure II.3.2.16 FEA Simulation model of 200 kW+ dynamic wireless EV charging system.	506

Figure II.3.2.17 Mutual inductance obtained by FEA simulation, input power and output power of the dynamic wireless EV charging system obtained by circuit simulation. 507

Figure II.3.2.18 Experimental setup for characterization of 200 kW+ dynamic charging transmitter and receiver coils with 11-inch spacers. 507

Figure II.3.2.19 Distribution of driving range of light vehicle model with and without DWPT2. 508

Figure II.3.2.20 Distribution of driving range of heavy vehicle model with and without DWPT2. 508

Figure II.3.2.21 RER for light vehicle model with all designs 509

Figure II.3.2.22 RER for heavy vehicle model with all designs 509

Figure II.3.2.23 24-h average power and energy profiles for the entire DWPT system for all designs with 40 DWPT/300-mi, and light vehicle model 509

Figure II.3.2.24 24-h average power and energy profiles for the entire DWPT system for all designs with 40 DWPT/300-mi, and heavy vehicle model 509

Figure II.3.2.25 Baseline WPT System and Final WPT System and Proposed shielding design for High-Power WPT applications..... 509

Figure II.3.2.26 dWPT Roadway Segment and Two Scenarios for dWPT EM Safety Design and Evaluation 510

Figure II.3.2.27 dWPT Finite-element Model of (a) Scenario #1 and (b) Scenario #2 for EM Field Safety Design 510

Figure II.3.2.28 Designed dimension of passive EM shield for dWPT. 510

Figure II.3.2.29 Dynamic Response Verification of Non-contact Position Sensor for dWPT Y-alignment Measurement..... 511

Figure II.3.2.30 Position of Measurement Probes (EM-field and Y-alignment) with Respect to Vehicle Chassis 511

Figure II.3.3.1 Overview of high-power CCS charging emulator w/ 350kW XFC and grid emulator for variable input supply 516

Figure II.3.3.2 Design objective and capability goal of the high-power CCS charging emulator with the ABB XFC..... 517

Figure II.3.3.3 High power electric vehicle CCS charging emulator in INL’s Electric Vehicle Infrastructure Lab 517

Figure II.3.3.4 ABB TerraHP (350 kW) XFC charging the CCS vehicle charging emulator in INL’s EVIL.. 518

Figure II.3.3.5 Efficiency versus power of the 350-kW ABB TerraHP XFC 518

Figure II.3.3.6 Efficiency versus DC output voltage of the 350-kW ABB TerraHP XFC 519

Figure II.3.3.7 Power Factor versus power of the 350-kW ABB TerraHP XFC 519

Figure II.3.3.8 Overview schematic of complete high-power charging lab research capability 520

Figure II.3.3.9 Electrical connection between grid emulator and XFC in ESL 521

Figure II.3.3.10 350-kW ABB TerraHP XFC operation with grid emulator 480V variable input 522

Figure II.3.4.1 Flowchart of the BMS algorithm and its input/output and feedback signals 526

Figure II.3.4.2 Communication interface between the BMS, the EV battery model, and the Energy Management System (a part of the Site Controller)..... 526

Figure II.3.4.3 Block diagram of the site controller (EMO and RT-EMS)..... 527

Figure II.3.4.4 Industry Engagement Use Cases and Interactions 527

Figure II.3.4.5 Proposed xFC Topology	528
Figure II.3.4.6 Power electronics CAD design (a) Source CHB-DAB Module Pack, (b) Load DAB Converter, and System comparison to 480V charging equipment.....	529
Figure II.3.4.7 Simulation Setup with Grid, 1 Source DAB, 1 Load DAB, ESS and PV	530
Figure II.3.4.8 Intermediate CHIL Architecture	530
Figure II.3.4.9 Charging station hosting capacity analysis results.....	531
Figure II.3.4.10 Charging of four vehicles using the MPC-based BMS algorithm	532
Figure II.3.4.11 Interaction among RT-EMS and EMO over 2 minutes	532
Figure II.3.4.12 EMO over 24 h operating period.	533
Figure II.3.4.13 Fit and ergonomics evaluation of the MCS connector and inlet at NREL.....	533
Figure II.3.5.1 Increase in model complexity from adding secondary networks for grid analysis	538
Figure II.3.5.2 Process for developing secondary distribution networks.....	539
Figure II.3.5.3 Architecture of NREL charge management system.....	540
Figure II.3.5.4 Feeder power for test system that demonstrates the functionality of the control strategies implemented in Caldera	541
Figure II.3.5.5 Feeder Total Power for three scenarios: No PEV (baseline), Uncontrolled (Home), Uncontrolled (Work) for Residential (Feeder 5), Industrial (Feeder 7) and Commercial (Feeder 10) feeders.....	542
Figure II.3.5.6 EV Charging Load for four control scenarios: Uncontrolled (baseline), Time of Use - random start, Time of Use - Immediate and Random Dwell without TOU for Residential (Feeder 5), Industrial (Feeder 7) and Commercial (Feeder 10) feeders.....	542
Figure II.3.5.7 Load profiles with and without the Electric Vehicle charging results varied depending on the feeder type. Feeders with a significant number of residential loads (Feeders 1 and 8) experienced an increase in the original peak under both home and work dominant integration strategies. The commercial feeder's peak changed under the work dominant case but remained the same with the home dominant charging.	543
Figure II.3.5.8 The Electric Vehicle (EV) profiles varied depending on the control type and the integration scenario (i.e., home or work dominant). Feeder 1's uncontrolled and controlled profiles had similar results for the home and work dominant scenarios. Feeders 8 and 9, that had considerable commercial loads, exhibited different outcomes depending on the integration strategy. Under each integration scenario the controls shifted the peak from the late evening to the middle of the day with the exception of one. The immediate Time of Use control caused an extreme surge in power demand at hour 19 for all of the cases.	544
Figure II.3.5.9 EV impacts on distribution grid for 2030 High adoption scenario for four different control scenarios (top table) without secondary networks (bottom table) with secondary networks.....	545
Figure II.3.5.10 Five of the six feeders experienced minimum voltage violations on the primary system in the uncontrolled case.	545
Figure II.3.5.11 The voltage response for the six feeders ended up in three groups and corresponded with the principal component analysis results that used the X/R ratio from each of the feeders.....	546
Figure II.3.5.12 (a) Campus net load forecast compared to actual load for December 2019, (b) Test results of charge management performed for the NREL parking garage EVSE's	547
Figure II.3.6.1 xFC Station Management Implementation for PHIL Evaluation.....	553
Figure II.3.6.2 BTCP 400kW Dispenser unit.....	554
Figure II.3.6.3 Y.Cube Battery Energy Storage System by Aggreko	554

Figure II.3.6.4 (Left)XFC Site Power (Right)XFC Station Power	555
Figure II.3.6.5 ZEP Generated Vehicle VMT.....	556
Figure II.3.6.6 PEV Stock by Model (US Total)	556
Figure II.3.6.7 Net Change in PEV Stock by Model	557
Figure II.3.6.8 BTC Power 350 kW charger connected to Nissan LEAF (left) and ABB Terra HP 350 kW charger connected to vehicle emulation hardware (right).....	558
Figure II.3.6.9 Site Layout Plan for eXtreme Fast Charging Station on the Smart Energy Plaza	559
Figure II.3.7.1 HELICS Co-Simulation Framework Overview	563
Figure II.3.7.2 Example of Charging Infrastructure Planning Integration with BEAM	564
Figure II.3.7.3 Hourly EV Charging Load by Charger Type and Location for the Central Scenario.....	568
Figure II.3.7.4 Percentage Breakdown of Projected EV Charging Demands by Charger Type and Location.	568
Figure II.3.7.5 Hourly EV Charging Load by Charging Location Type and Peak Site Power.....	569
Figure II.3.7.6 Forecast of Temporal and Spatial Variation in EV Charging Loads	569
Figure II.3.7.7 Overview of GEMINI-XFC Project High-Level Modeling Structure	570
Figure II.3.7.8 Grid Modeling at High Resolution and With Base and High DER Cases for SF Bay Area	571
Figure II.4.1.1 Project tasks flow chart.....	574
Figure II.4.1.2 Laboratory Network Diagram.....	575
Figure II.4.1.3 EV Ecosystem Interconnectivity and Cybersecurity Landscape.....	578
Figure II.4.1.4 EV Fueling Station Power and Network Representation in Cyber Energy Emulation Platform	579
Figure II.4.1.5 Architecture of a Representative WPT System.....	580
Figure II.4.1.6 Abstracted Architectural Diagram	580
Figure II.4.2.1 Project tasking.....	584
Figure II.4.2.2 EVSE Best Practices [1].	585
Figure II.4.2.3 EVSE vendor recommendations based on penetration tests of EVSE equipment and networks [1].	586
Figure II.4.2.4 Complete graph. Details presented in [2].....	587
Figure II.4.2.5 The vehicle system model (left) depicts the components of the vehicle and their relationship to the charger. The charger system model (right) illustrates the relationship of the components and information flows.	588

List of Tables

Table 1 Light Duty Conventional and Electric Vehicle Refueling Characteristics	7
Table I.1.2.1 Comparison of the Segmented and Open Winding Drives.....	32
Table I.1.6.1 Quilt Packaging Accelerated Testing Summary.....	60
Table I.1.13.1 Summary of DSC data for NND and TTE epoxies. Cure times for both epoxies were 2 hrs....	117
Table I.1.13.2 Preliminary thermal conductivity results obtained by NREL.....	119
Table I.1.15.1 Average particle size, grain size and magnetic properties of the AMES sintered magnet samples.....	132
Table I.1.16.1 Power Electronics and Motor Requirements	135
Table I.1.16.2 Pugh Analysis of Different Motors for Integrated Motor Drives	137
Table I.1.16.3 Pugh Analysis of Different Inverters for Integrated Motor Drives.....	137
Table I.1.16.4 Pugh Analysis of Different Motor and Inverter Combinations for Integrated Motor Drives	139
Table I.1.17.1 Power semiconductor devices selected for loss analysis	145
Table I.1.17.2 IPMSM parameters and inverter constraints selected for determination of inverter operating points.....	145
Table I.1.17.3 Selected GaN devices	145
Table I.1.17.4 Inverter loss details for urban and highway drive cycles at fsw = 50kHz.....	146
Table I.1.17.5: Loss comparisons	147
Table I.1.17.6: SC test results	147
Table I.1.17.7 GaN device degradation after 8.5K power cycle.....	148
Table I.1.17.8 Result comparison of the three design choices.....	152
Table I.1.18.1 EDT Consortium Electric Motor Targets	154
Table I.1.18.2 Predicted Two-Layer Rotor Prototype Performance at Base Speed of 6,600 RPM with Stator Winding Temperature of 120°C and Rotor Magnet Temperature of 100°C	161
Table I.1.20.1 Power Electronics Requirements.....	171
Table I.1.20.2 A comparison between LTCC-based and 3D printed interposers	173
Table I.1.20.3 Gate driver performance figure at room temperature and elevated temperature	176
Table I.1.20.4 Measurement results of CHS circuit.....	177
Table I.1.22.1 Summary of wafer split and static characteristics (Lot 1)	185
Table I.1.22.2 Summary of wafer split for Lot 2.....	186
Table I.1.22.3 Specific on-resistance for MOSFET and HEXFET.....	188
Table I.1.23.1 MISHEMT samples fabricated.....	191
Table I.1.26.2 Parameters of the Simulated Air-core Transformer.....	214
Table I.1.27.1 Key parameters	223
Table I.2.1.1 DOE/VTO – DE-EE0008870 Program Milestones.....	227
Table I.2.1.2 DOE/VTO – DE-EE0008870 Benchmarking Enhancing Specific Power in a FSWPM axial motor design.....	229

Table I.2.2.1 Prototype Wound Field and Hybrid Excitation Synchronous Machine Target Metrics	232
Table I.2.4.1 Performance metric comparison against FOA.....	247
Table I.2.5.1 Per-phase resistance and inductance measurements.....	253
Table I.2.5.2. Different test conditions used for assessing motor thermal performance.....	255
Table I.2.5.3 Thermal performance test summary.....	257
Table I.2.5.4 Active material cost distribution for a 55 kW BPM motor using MnBi magnets.	258
Table I.2.5.5 Cost estimates for MnBi Magnet based BPM motor for various production volumes.....	258
Table I.2.6.1 Summary of measured motor performance results for all three variants.....	263
Table I.2.6.2 Performance to requirements of Variant 1 motor	264
Table I.2.6.3 Performance to requirements of Variant 2 motor	266
Table I.2.6.4 Performance to requirements of Variant 3 motor	267
Table II.1.1.1 Hydrogenics Vehicle Systems Specifications	293
Table II.1.2.1: Summary of ETREE Powertrain Components.....	302
Table II.1.2.2: Summary J1526 Testing Results.....	304
Table II.1.3.1 Project Milestones.....	309
Table II.1.4.2 NREL ReFUEL Chassis Dynamometer Fuel Economy Improvement	315
Table II.1.6.1 Parameters of the 1 MW wireless charging system given in Figure II.1.6.4.....	328
Table II.1.6.2 Charging characteristics with varying number of modules.....	328
Table II.1.10.1 Simulation parameters for ESS optimization.	351
Table II.1.10.2 Low-power hardware parameters.....	353
Table II.1.16.1 Budget Period 1 (BP1) – Project Plan Summary.....	407
Table II.1.16.2 Budget Period 2 (BP2) – Project Plan Summary.....	409
Table II.1.16.3 Battery Requirements Summary	417
Table II.1.17.1 Comparisons of High-frequency Power Inverter Architectures.....	421
Table II.1.17.2 Primary and Secondary Side Coupler Specifications.....	423
Table II.1.17.3 Component Stress Analysis Results for Secondary-Side Series and LCC Tuning Options.....	425
Table II.1.17.4 Vehicle-side Rectifier Design Considerations for 300-kW Receiver.....	426
Table II.1.19.1 Revised BP3 Milestones Factoring in COVID19 Delays.....	442
Table II.1.19.2 Pacifica PHEV Battery Impact Energy Consumption for Test Protocol (Source: FCA, NREL).....	448
Table II.1.19.3 Battery Test Cycle for Grid Services Impact Evaluation	448
Table II.1.20.1 2020 Activities	456
Table II.1.20.2 Summary of the Test Cases by Partner Laboratories and Relation to Phase 1 Activities.	457
Table II.3.2.1 Summary of loss analysis of power semiconductor modules for 200 kW+ operation at 85 kHz.	500
Table II.3.2.2 DWPT system designs under test based on FY19 feasibility analysis.	504

Table II.3.2.3 Coupler parameters obtained by FEA simulation and laboratory characterization for the centrally aligned case.....	507
Table II.3.2.4 Driving range evaluation for different designs with 40 DWPT/300-mi.....	508
Table II.3.4.1 Feeder Requirement	531
Table II.3.4.2 Onsite PV-ES-Inverter Solutions	531
Table II.3.5.1 Minneapolis Summary of EV Charge Control Impacts on Feeder Performance	543
Table II.3.5.2 Atlanta Summary of EV Charge Control Impacts on Feeder Performance.....	544
Table II.3.6.1 Fleet Adoption Trends as a Share of PEV.....	550
Table II.3.6.2 Electric Vehicle Adoption Scenarios as a Share of PEV	553
Table II.3.7.1 Summary Capabilities of TEMPO and BEAM	565
Table II.3.7.2 Summary of the Scenarios Explored – Fleet and Charger Composition.....	567
Table II.3.7.3 Summary of the Scenarios Explored – Fleet Composition	567
Table II.4.1.1 Top Fifteen Prioritized High Consequence Events	576
Table II.4.1.2 Definition of Cybersecurity Complexity Multiplier for High Consequence Events	577

Vehicle Technologies Office Overview

Vehicles move our national economy. Annually, vehicles transport 11 billion tons of freight—about \$35 billion worth of goods each day¹—and move people more than 3 trillion vehicle-miles.² Growing our economy requires transportation, and transportation requires energy. The transportation sector accounts for about 30% of total U.S. energy needs³ and the average U.S. household spends over 15% of its total family expenditures on transportation, making it the most expensive spending category after housing.⁴

The Vehicle Technologies Office (VTO) funds a broad portfolio of research, development, demonstration, and deployment (RDD&D) projects to develop affordable, efficient, and clean transportation options to tackle the climate crisis and accelerate the development and widespread use of a variety of innovative transportation technologies. The research pathways focus on electrification, fuel diversification, vehicle efficiency, energy storage, lightweight materials, and new mobility technologies to improve the overall energy efficiency and affordability of the transportation or mobility system. VTO leverages the unique capabilities and world-class expertise of the National Laboratory system to develop innovations in electrification, including advanced battery technologies; advanced combustion engines and fuels, including co-optimized systems; advanced materials for lighter-weight vehicle structures; and energy efficient mobility systems.

VTO is uniquely positioned to accelerate sustainable transportation technologies due to strategic public-private research partnerships with industry (e.g., U.S. DRIVE, 21st Century Truck Partnership) that leverage relevant expertise. These partnerships prevent duplication of effort, focus DOE research on critical RDD&D barriers, and accelerate progress. VTO focuses on research that supports DOE's goals of building a 100% clean energy economy, addressing climate change, and achieving net-zero emissions no later than 2050 to the benefit of all Americans.

Annual Progress Report

As shown in the organization chart (below), VTO is organized by technology area: Batteries & Electrification R&D, Materials Technology R&D, Advanced Engine & Fuel R&D, Energy Efficient Mobility Systems, and Technology Integration. Each year, VTO's technology areas prepare an Annual Progress Report (APR) that details progress and accomplishments during the fiscal year. VTO is pleased to submit this APR for Fiscal Year (FY) 2020. In this APR, each project active during FY 2020 describes work conducted in support of VTO's mission. Individual project descriptions in this APR detail funding, objectives, approach, results, and conclusions during FY 2020.

¹ Bureau of Transportation Statistics, Department of Transportation, Transportation Statistics Annual Report 2018, Table 4-1. <https://www.bts.gov/tsar>.

² Transportation Energy Data Book 37th Edition, Oak Ridge National Laboratory (ORNL), 2019. Table 3.8 Shares of Highway Vehicle-Miles Traveled by Vehicle Type, 1970-2017.

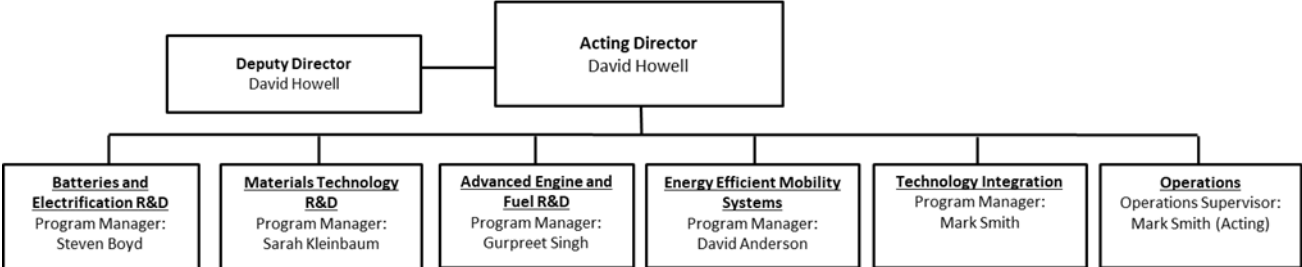
³ Ibid. Table 2.1 U.S. Consumption of Total Energy by End-use Sector, 1950-2018.

⁴ Ibid. Table 10.1 Average Annual Expenditures of Households by Income, 2016.

Organization Chart

Vehicle Technologies Office

March 2021



Electric Drive Technologies Program Overview

Introduction

The Electric Drive Technologies (EDT) program's mission is to conduct early-stage research and development on transportation electrification technologies that accelerate the development of cost-effective and compact electric traction drive systems that meet or exceed performance and reliability requirements of internal combustion engine (ICE)-based vehicles, thereby enabling electrification across all light-duty vehicle types.

Goals and Objectives

The goal of the EDT program is to develop an electric traction drive system at a cost of \$6/kW for a 100-kW peak system by 2025. In addition, the program has a 2025 power density target of 33 kW/L for a 100-kW peak system. While achieving these targets will require transformational technology changes to current materials and processes, it is essential for enabling widespread electrification across all light-duty vehicle platforms.

Program Design and Execution

The EDT program provides support and guidance for many cutting-edge automotive technologies now under development. Researchers focus on developing revolutionary new power electronics (PE), electric motor (EM), and traction drive system (TDS) technologies that will leapfrog current on-the-road technologies. This will lead to lower cost and better efficiency in transforming battery energy to useful work. Research and development (R&D) is also aimed at achieving greater understanding of, and improvements in how the various components of tomorrow's automobiles will function as a unified system.

In supporting the development of advanced vehicle propulsion systems, the EDT program fosters the development of technologies that will significantly improve efficiency, costs, and fuel economy.

The EDT program directs early-stage research through a three-phase approach intended to

- Identify overall propulsion- and vehicle-related needs by analyzing programmatic goals and reviewing industry recommendations and requirements, and then develop and deliver the appropriate technical targets for systems, subsystems, and component R&D activities.
- Develop, test, and validate individual subsystems and components, including EMs and PE
- Estimate how well the components and subsystems work together in a vehicle environment or as a complete propulsion system and whether the efficiency and performance targets at the vehicle level have been achieved.

The research performed under this program addresses the technical and cost barriers that currently inhibit the introduction of advanced propulsion technologies into hybrid electric vehicles (HEVs), plug-in HEVs, battery electric vehicles (BEVs), and fuel cell powered automobiles that meet the DOE goals.

A key element in making these advanced vehicles practical is providing an affordable electric TDS. This will require attaining weight, volume, efficiency, and cost targets for the PE and EM subsystems of the TDS. Areas of development include:

- Novel traction motor designs that result in increased power density and lower cost

- Inverter technologies that incorporate advanced wide bandgap (WBG) semiconductor devices to achieve higher efficiency while accommodating higher-temperature environments and delivering higher reliability.
- Converter concepts that leverage higher-switching-frequency semiconductors, nanocomposite magnetics, higher-temperature capacitors, and novel packaging techniques that integrate more functionality into applications offering reduced size, weight, and cost.
- New onboard battery charging electronics that build from advances in converter architectures for decreased cost and size
- More compact and higher-performing thermal controls achieved through novel thermal materials and innovative packaging technologies
- Integrated motor-inverter TDS architectures that optimize the technical strengths of the underlying PE and electric machine subsystems.

VTO competitively awards funding through funding opportunity announcement (FOA) selections, and projects are fully funded through the duration of the project in the year that the funding is awarded. The future direction for direct-funded work at the National Laboratories is subject to change based on annual appropriations.

Electric Drive Technologies Lab Consortium

The multi-lab EDT Consortium will leverage U.S. research expertise and facilities at the national labs and universities to improve the power density of electric drives by 10X compared with the 2015 numbers while reducing the cost by 50% and doubling the lifetime miles within the next 5 years. The final objective of the consortium is to develop a 100-kW traction drive system that achieves a power density of 33 kW/L, has an operational life of 300,000 miles, and a cost of \$6/kW. The system will be composed of a 100 kW/L inverter and a >20,000 rpm, 50 kW/L electric motor.

Research will be performed within the framework of a new research consortium consisting of a multi-disciplinary team that will plan, establish, conduct, and manage a portfolio of multi-lab and multi-university research efforts to advance the state-of-the-art in electric drive technologies.

The consortium is organized around three Keystone projects: (1) Power Electronics; (2) Electric Motors; and (3) Traction Drive System. The consortium will focus on early-stage research projects on advanced materials, high-density integration of dissimilar layers/materials, multifunctional subcomponents, and optimized and new thermal/electrical/magnetic architectures. New materials such as WBG semiconductors, soft magnetic materials, and ceramic dielectrics, merged using multi-objective co-optimization design techniques, will be utilized to achieve the program goals. Moreover, integration of components and subcomponents will further propel the research toward the goals of the consortium.

Consortium National Laboratory members include Ames Laboratory, The National Renewable Energy Laboratory (NREL), Oak Ridge National Laboratory (ORNL), and Sandia National Laboratories (SNL). University consortium partners include: North Carolina State University, The University of Arkansas, Virginia Polytechnic Institute, University of Wisconsin-Madison, Georgia Institute of Technology, University of California-Berkeley, Illinois Institute of Technology (IIT), Purdue University, The State University of New York (SUNY), and The Ohio State University.

Grid and Infrastructure Program Overview

Introduction

The Grid and Charging Infrastructure (G&I) program's mission is to conduct early-stage research and development on transportation electrification technologies that enable reduced petroleum consumption by light, medium, and heavy-duty vehicles. The program identifies and enables the role of vehicles in the future electrical grid.

Charging of EVs@Scale creates an unpredictable and stochastic load demand on the electric grid. Newer EVs being introduced in the market can charge at low and high rates based on the need and availability of charging infrastructure. Additionally, charging profiles for EVs manufactured by different Original Equipment Manufacturers (OEMs) vary significantly which complicates meeting the aggregated charging loads. This creates difficulty in the prediction of magnitude, location, and timing of charging loads and could potentially have a detrimental grid impact.

To enable successful deployment of EVs@Scale, a holistic approach is required across the vehicle, charging infrastructure, and electric grid. Figure 1 presents the key components of charging ecosystems that create challenges to be addressed. This includes controls, high voltage power electronics, interoperability, wireless and other advanced HPC technologies, and integration and optimization with the grid and Distributed Energy Resources (DERs) such as stationary storage and photovoltaics.

Hence, the effective control and optimization of the charging ecosystem is essential and is otherwise known as Smart Charge Management (SCM). SCM emphasizes the identification of pathways to reduce the potential grid impacts of EVs@Scale, while providing enhanced value for EV/charging/grid systems including reduced costs and increased opportunities for grid services. If unmanaged, EVs@Scale connecting to the grid would create numerous challenges for utilities, particularly at the distribution level, such as feeder voltage violations, system imbalances, flickers, equipment overloading, and large increases in daily peak loads. Interoperability and scalability, and high-speed communications and control are critical challenges facing SCM. Effective SCM will enable response to inappropriate energy management, malfunctioning equipment, and Cyber-Physical Security (CPS) breaches. SCM can also facilitate the provision of grid services from EV charging, including, but not limited to, peak load shaving, demand charge mitigation, voltage support, frequency regulation, and integration of renewable energy generation.

HPC of up to 400kW for light-duty (LD) EVs, and 1+ MW for medium-duty (MD) and heavy-duty (HD) EVs, can enable greater vehicle utilization, extended range, and reduce recharging times. Technical advances are steadily being made with regards to HPC, but further progress is needed to facilitate the mass market adoption of EVs. Specific technical challenges include the requirement for intelligent design and integration with the

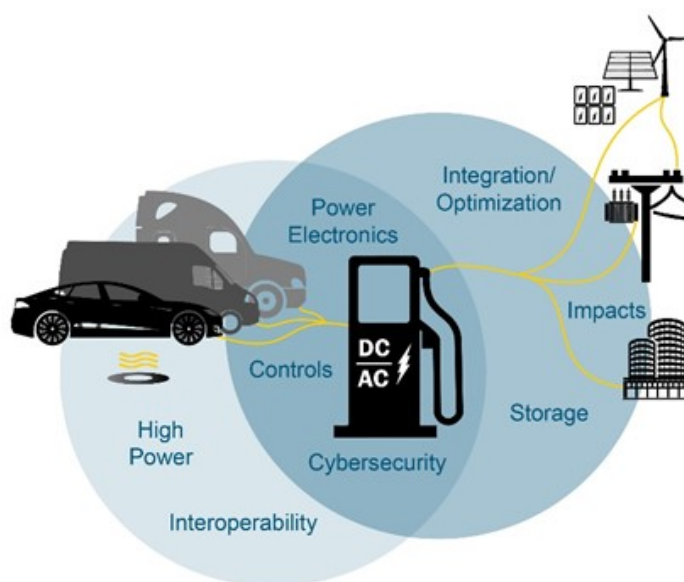


Figure 1 Key technologies and challenges addressed by the Grid and Infrastructure Program.

grid and DERs, to mitigate ramp rates and surge power demands, lower system cost of ownership, and interoperability of HPC infrastructure with MD and HD EVs. Additionally, as the charging power levels steadily increase, new challenges are manifested in ensuring HPC is effectively integrated with the grid in an efficient, flexible, and secure manner. High voltage power electronics and materials with better thermal and electrical properties are key enabling technologies for advancing HPC. Furthermore, improvements in wireless charging are required including the development of novel coils, advanced field shaping techniques, and control strategies.

Rapidly increasing numbers of EVs with advanced communication functionalities and networked chargers, as well as the trend towards HPC, dramatically increase cyber related risks and consequences. Coordinated cyber-attacks on chargers/charging stations can lead to serious local and potentially broader grid disruptions such as wide-scale blackouts and/or brownouts. A comprehensive understanding of the threat environment, including risks and consequences therein, is needed to identify, minimize, and/or eliminate critical cyber-physical vulnerabilities. Advances are required in strategies, systems, and tools, including hardware/software for intrusion detection, threat mitigation and isolation, and charging system recovery. Typically, the most promising countermeasures are targeted based on overall risk formulations with regards to the EV charging ecosystem.

Addressing the barriers above can only be done by conducting high risk projects that are beyond the suitable scope and developmental timeframes of industry. Furthermore, the transportation and utility sectors historically have not worked together, which complicates collaboration. A significant level of pre-competitive and vendor-neutral Research and Development (R&D) effort is needed to address the challenges associated with a safe and secure charging ecosystem for EVs@Scale.

State of the Art

Electric Vehicle Charging

It is desirable to reduce EV refueling times to be competitive with conventional vehicle refueling times (e.g., 5-10 minutes for 400 miles of LD vehicle driving range). The table below lists the refueling characteristics of several types of installed commercial chargers and a conventional gasoline fueling pump. The technologies employed in the EV charging stations are shown in the figure below. It is important to note that the rate of energy transfer peaks early in the charging cycle and decreases as the battery pack approaches 100% state of charge (SOC). While the energy transfer rate is not constant during charging, given two chargers with different peak power ratings the charger with the higher peak power rating is potentially capable of minimizing EV charging times when compared to the EVSE with a lower maximum power rating. It is notable that the EV must be capable of accepting the higher power provided by the EVSE with the higher maximum power rating. To accomplish this capability some vehicle OEMs are increasing the operating voltage of the on-board battery pack and the maximum C-rate for charging battery cells. Currently Electrify America offers commercial charger solutions with peak power rating of 350KW DC¹. However, currently the maximum charge rate that is accepted by a LD vehicle is 262 KW DC (800V Porsche Taycan 2020). This LD vehicle can recharge from 0-80% SOC (~207 real-world miles of range) in 22 minutes using a 350KW DC Fast Charger (CCS Charging Standard)⁵.

Charging Standards

The two open fast charging standards on the market today CCS and CHAdeMO were both originally designed to work at 400V and have evolved to increase their peak charging power ratings.

The Combined Charging System (CCS) is an open, universal, and international charging system for electric vehicles based on international standards. It provides the solution for all charging requirements. The Combined

⁵ Source: <https://www.zap-map.com/charge-points/porsche-taycan-charging-guide/>. June 2021

Charging System is therefore ONE system for ALL. The CCS combines single-phase with fast 3-phase AC charging using alternating current of maximum of 43 kW. It also provides very fast high-power DC charging (up to 450 kW) within a single system. Members are presently also working on a High-Power charging connector for commercial vehicles that can take multiple MW charging power. This extended High-Power charging will be used for specialty EV like busses, truck, etc. The CCS system includes the connector, the managing of control functions and the charging communication between electric vehicle and infrastructureⁱⁱ. The standard is backed by major European and US OEMs and is positioned as the preferred option for a European network.

CHAdEMO was an initiative of Japanese car companies and was originally designed to charge at up to 50KW at 400V.

The mid-term objective of XFC is to reduce LD charging time to approximately 10 minutes via a charge rate of approximately 350 to 400 KW. The long-term objective is to achieve charge rates of greater than 1 MW that will enable fast charging of both LD and Heavy Duty (HD) vehicles. The CHARIN connector standard is dedicated to achieving charge rates of up to 4 MW.

In addition to the conductive charging standards discussed above the wireless power transfer standard J2954 addresses charging of LD vehicles at peak rates of 22KW and MD/HD vehicle charge rates of approximately 200 KW.

Currently Installed Charging Systems in the U.S

The characteristics of charging stations that are currently installed in the U.S. are provided in Table 1 and are shown in Figure 2.

Table 1 Light Duty Conventional and Electric Vehicle Refueling Characteristics

Type of Refueling	Gasoline	Level 1 110V (~1.4kW)	Level 2 220V (~7.2kW)	DC Fast Charger (50kW, 150kW, 350kW)	Tesla V2 & V3 SuperChargers (145kW,250kW)
Range per Charge Time	400 miles /5 mins	3-5 miles /60 mins	25 miles /60 mins	50KW: 150 miles /90 mins	250KW:~360 miles ⁶ /60 mins
Time to Charge for 200 miles	<5 mins	37 hours	8 hours	50KW: 2 hours	250KW: 24 mins
Number of U.S. stations/connectors circa 2021 ⁷	153,000	42/312	39,915/85,615	4246/8430	1077/10,628

The summary of charge connector standards provided in the figure below includes the connector diagram, maximum output power, and applications for each of the connector standards.

⁶ Source: Tesla Model 3 range, battery & charging, June 2021. <https://www.drivingelectric.com/tesla/model-3/range>

⁷ Source: Alternative Fuels Data Center, National Renewable Energy Laboratory, June 2021. <https://afdc.energy.gov>


	Level 1	Level 2	DC Fast Charger	Tesla Supercharger
Examples of Charging Stations	 	 		
Diagram	Connector Standard	Maximum Output Power	Application Notes	
	SAE J1772	19.2 kW AC	Used for Level 1 and Level 2 charging in North America. Commonly found on home, workplace, and public chargers.	
	CCS	450 kW DC	Used for DC fast charging most vehicle models in North America. Generally installed at public chargers.	
	ChAdemo	400 kW DC	Used for DC fast charging select vehicles models in North America. Generally installed at public chargers.	
	Tesla	22 kW AC 250 kW DC	Used for both AC and DC fast charging for Tesla models only.	
	SAE J2954	22 kW light-duty, 200 kW heavy duty	Wireless power transfer. Standard for MD/HD vehicles is under development.	
	SAE J3105	>1 MW	Automated connection device to charge MD/HD vehicles. Variants include pantograph up or down and pin-and-socket.	
	CharIN Megawatt Charging System	4 MW	Conductive MW-level charging for MD/HD vehicles. Standard is under development.	

Figure 2 Examples of EV Charging Stations and Connector Standards Sources: CEC 8,9,10,11,12,13,14

⁸ U.S. Department of Energy Alternative Fuels Data Center. “Developing Infrastructure to Charge Plug-In Electric Vehicles.” https://afdc.energy.gov/fuels/electricity_infrastructure.html

⁹ CharIn. 2020 “Mapping Standards for Low- and Zero-Emission Electric Heavy-Duty Vehicles,” presentation. International Transportation Forum February 18-20, 2020 Workshop. <https://www.itf-oecd.org/sites/default/files/docs/charging-infrastructure-standardisation-developments-bracklo.pdf>.

¹⁰ ChAdemo. “Technology Overview.” <https://www.chademo.com/technology/technology-overview/>.

¹¹ Tesla Motors. 2015. Form 10-K. Edgar Online. <http://large.stanford.edu/courses/2015/ph240/romanowicz2/docs/tesla-annual.pdf>

¹² Tesla Motors. 2019. “Introducing V3 Supercharging.” <https://www.tesla.com/blog/introducing-v3-supercharging>.

¹³ SAE. 2013. “Wireless Power Transfer of Heavy-Duty Plug-In Electric Vehicles and Positioning Communication J2954/2 Standard”. <https://www.sae.org/standards/content/j2954/2/>.

¹⁴ CharIn. 2020. “Mapping Standards for Low- and Zero-Emission Electric Heavy-Duty Vehicles,” presentation. International Transportation Forum February 18-20, 2020 Workshop. <https://www.itf-oecd.org/sites/default/files/docs/charging-infrastructure-standardisation-developments-bracklo.pdf>.

Prototype Charging Systems

The research community has developed prototypes that charge at rates greater than 350KW.

Light Duty Charging Station Prototype

Initiated in July 2016, the “Fast Charge” research project has received €7.8 million in funding from the German Federal Ministry of Transport and Digital Infrastructure. The implementation of the funding guidelines is being coordinated by the German National Organization Hydrogen and Fuel Cell Technology (NOW). The industrial consortium includes automotive manufacturers the BMW Group and Dr. Ing. h. c. F. Porsche AG, as well as operators Allego GmbH, Phoenix Contact E-Mobility GmbH (charging technology) and Siemens AG (electrical engineering)

The research consortium presented a prototype for a charging station with an output of up to 450 kW in Jettingen-Scheppach, located near the A8 motorway between Ulm and Augsburg. The new charging station is suitable for electric models of all brands with the European standard Type 2 variant of the widely used Combined Charging System (CCS) and is now available for use free of charge. A Porsche research vehicle with a net battery capacity of approximately 90 kWh achieved a charging capacity of over 400 kW on the new charging station, allowing for charging times of less than 3 minutes for the first 100 km range

Medium and Heavy-Duty Charging Station Prototype

Portland General Electric and Daimler Trucks North America are co-developing “Electric Island,” a large public charging site for medium- and heavy-duty electric commercial vehicles expected to be the first of its kind in the United States. It is designed to support up to nine vehicle charging stations with charging levels of up to greater than one megawattⁱⁱⁱ.

Charging at Scale

The largest EV fast charging station in the U.S. opened in February 2020 in Pasadena, California. The station is comprised of 24 Tesla Superchargers and 20 of Tritium’s DC fast chargers^{iv}.

There are several charging networks that have been initiated in the U.S.

- The Electrify America charging network currently has 635 installed charging stations and 125 charging stations that are ‘coming soon’. The network currently has 2097 CCS, 635 CCS-CHAdEMO, and 118 Level 2 chargers¹⁵.
- The FordPass network will include more than 12,000 charging stations with a total of 35,000 plugs in the United States and some parts of Canada^v.
- Tesla has 1077 public charging stations with about 10,628 plugs in the United States, according to the Alternative Fuels Data Center.

General Motors Co. is working with electric-vehicle charging operator EVgo Services to build a nationwide fast-charging infrastructure as the automaker prepares a major push into battery-powered models. The two companies will jointly invest in 2,750 fast chargers in cities and suburbs across the U.S. as GM moves to solve a chicken-and-egg problem that comes with selling EVs: A sparse network of chargers has turned off some potential buyers, but utilities and charging companies have been loath to expand the infrastructure until more plug-ins are on the road.^{vi}

¹⁵ Source: <https://www.electrifyamerica.com/locate-charger/>

Goals and Objectives

Program Goal

The goal of the Grid and Infrastructure Program is to identify system pathways and conduct research to facilitate the development and harmonization of robust, interoperable, and cyber-secure electric vehicle charging and grid infrastructure that supports EVs@Scale and incorporates advanced charging technologies, Distributed Energy Resources, and grid services

The G&I Program is focused on EVs, Electric Vehicle Supply Equipment (EVSE or chargers), and integration with the grid. The emphasis is upon foundational systems analyses; exploratory Research, Development, and Deployment (RD&D); and CPS; especially in critical areas that other stakeholders are not able to address. The three strategic areas addressed by the program are SCM, HPC, and CPS of charging infrastructure, as shown in Figure 3.

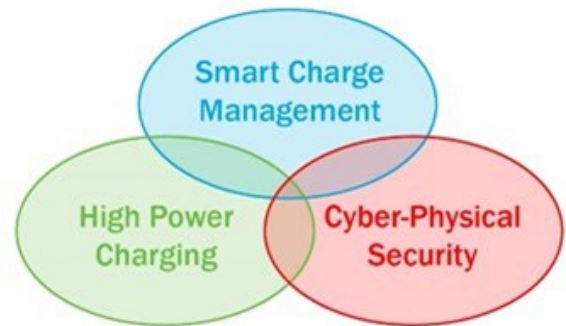


Figure 3 Strategic areas of the Grid and Infrastructure Program.

Each strategic area informs the others, providing a feedback mechanism to continuously refine and adjust program direction and focus. R&D activities span electrification of the LD, MD, and HD sectors of transportation. Additionally, given the cross-sectoral nature (vehicle, charging infrastructure, and the electric grid) of these activities, the program emphasizes close communication and coordination with other governmental and industry stakeholders, including Federal agencies, charger and vehicle OEMs, utilities, and charging network providers.

The G&I Program has established two targets for each of these strategic areas (SCM, HPC, and CPS) for the years 2023 and 2026. The strategic area targets directly support the long-term 2030 G&I Program targets, which are focused on resolving barriers and operationalizing solutions, in concert with transportation electrification stakeholders. All targets for 2023, 2026, and 2030 are listed below.

Year 2023

- SCM: Develop at least two viable smart charge management strategies and relevant tools to reduce the potential grid impacts of EVs@Scale and enhance the value of EV charging systems by enabling grid services.
- HPC: Develop strategies and technologies for high power dynamic wireless charging and multi-port 1+ MW charging stations that enable vehicle charging through direct connection to medium voltage (≥ 12.47 kV) distribution.
- CPS: Develop a comprehensive threat model, prioritize high consequence events, and identify appropriate defense, detection, and mitigation strategies and tools for the EV charging ecosystem.

Year 2026

- SCM: Demonstrate and validate smart charge management strategies and relevant tools capable of controlling wide-scale utilization of high-power charging at 400 kW and above, while incorporating robust cyber-physical security methodologies.
- HPC: Demonstrate and validate viable high power dynamic wireless charging, and multi-port 1+ MW charging stations with direct connection to medium voltage distribution.

- CPS: Conduct wide-scale demonstrations to validate viable and robust cyber-physical security for the charging ecosystem in support of EVs@Scale.

Year 2030

- Address technical barriers to the development and harmonization of a grid-integrated, robust, interoperable, and cyber-secure electric vehicle charging ecosystem that supports EVs@Scale.
- Operationalize two technologies, tools or platforms that will enable interoperable, secure charging solutions that reduce costs for EV owners and fleets.

Program Design and Execution

The G&I Program carries out its mission by focusing its R&D investments on early stage, medium and long-term technology projects that are unlikely to be pursued by industry alone but have significant potential public benefit.

G&I R&D Functions

Smart Charge Management

Importance

The focus of SCM is to identify pathways to reduce the potential grid impacts of EVs@Scale, while providing enhanced value for EV/charging/grid systems, including reduced costs and increased opportunities for grid services. If unmanaged, EVs@Scale connecting to the grid would create numerous challenges for utilities, particularly at the distribution level. SCM techniques can be employed to intelligently control, and shift charging loads to mitigate this problem and facilitate the provision of advanced grid services from EV charging.

Specific challenges and barriers to SCM include determining the impact of controlled charging versus uncontrolled charging, identifying critical strategies, and enabling technologies, developing, and demonstrating SCM in integrated networks of building systems and DERs including stationary storage, and facilitating bi-directional power flow. Interoperability and scalability of SCM systems are needed to allow EVs from all OEMs to charge at EVSEs from multiple vendors to enable EVs@Scale. High speed communication and controls with compatible device protocols and test tools for verification are required. SCM research is also needed to develop strategies and technologies for charging all EVs to enhance station resilience and mitigate potentially negative grid impacts. Finally, costs should be factored into the design of SCM hardware and grid upgrades so that they are minimized, while still providing the necessary charging service.

VTO's current SCM R&D efforts

The G&I Program's SCM activities include systems analyses; research, development, and validation of critical enabling strategies and technologies; and demonstrations. Current projects have created tools and methodologies that form the building blocks for effective

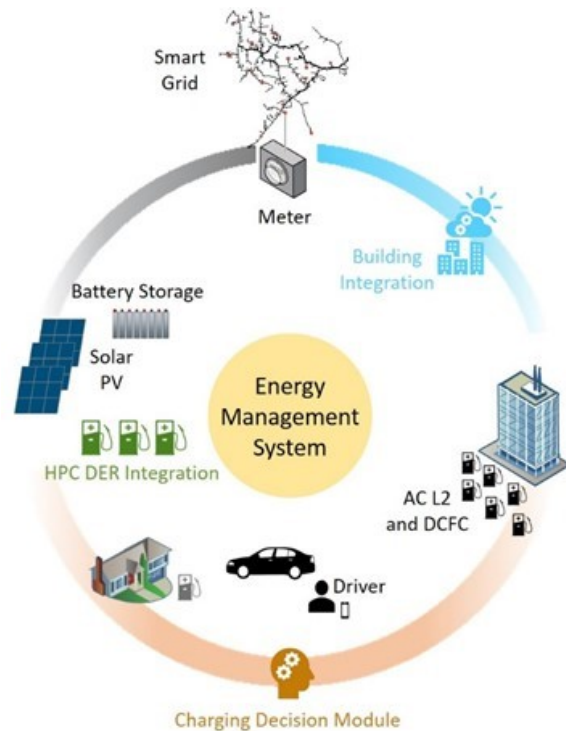


Figure 4 Key elements of Smart Charge Management.

SCM. The DOE National Laboratories are focused on quantifying the effects of uncontrolled charging versus controlled charging, developing and evaluating the effectiveness of smart charge control strategies, and identifying required constraints and mechanisms to implement high-value charge control strategies.

In the fall of 2020, VTO launched utility-managed SCM projects that include research, development, and execution of a wide-scale demonstration that enables grid services from EVs and provides benefits to electricity grid operators, energy services providers, charging network operators, and EV owners. Figure 3 illustrates key elements of SCM including predictive charge decision making, controls, and integration of vehicle charging and distributed energy resources with buildings and the grid.

VTO R&D Outlook for Key Focus Areas

Building on the advances from current R&D efforts, future SCM activities target LD, MD, and HD EVs and fleets at charging stations, fleet depots, and travel centers. R&D is needed for real time detection and implementation of mitigation procedures when an EV charging station is acting out of the norm or has suffered a cyber breach. Likewise, for MD/HD EV fleet charging at depots and travel centers, the focus is to develop and demonstrate SCM strategies, systems, and tools to provide benefit to MD/HD fleets and owners, and to reduce potential grid impacts. To achieve effective SCM, a thorough understanding of HPC charge profiles, both conductive and inductive, is required for optimal integration of charging stations and the utility distribution grid. Another future thrust is to identify viable vehicle-to-everything (V2X) applications and requirements, and to subsequently develop and demonstrate technologies (on and off board) for low cost, interoperable, controllable, and bi-directional power flow. The following identifies specific targets for SCM for the years 2023 and 2026.

YEAR 2023

- Develop at least two viable smart charge management strategies and relevant tools to reduce the potential grid impacts of EVs@Scale and enhance the value of EV charging systems by enabling grid services.

YEAR 2026

- Demonstrate and validate smart charge management strategies and relevant tools capable of controlling wide-scale utilization of high-power charging at 400 kW and above, while incorporating robust cyber-physical security methodologies.

High Power Charging

Importance

Successful deployment of HPC for LD (up to 400 kW) and MD/HD (1+ MW) EVs offers numerous benefits, including greater vehicle utilization, extended range, and recharging times comparable to refueling for conventional vehicles. However, HPC systems face multiple technical challenges and must be intelligently designed and integrated with the grid and DERs to mitigate ramp rates and surge power demands, lower system total cost of ownership, maximize the potential for grid services, and enable interoperability of HPC infrastructure with MD and HD EVs.

HPC exploratory R&D and analyses are needed to address issues associated with materials, power electronics, thermal management, and overall costs. Specific barriers exist with thermal loading of equipment and cables that enable service from the medium voltage grid and power transfer to the vehicle. Investigations are also needed into automated EVSE for HPC, especially above 400 kW charging levels. Advances in wireless charging are required, including the development of novel coils, advanced field shaping technologies, and mitigation of stray electric and magnetic fields.

Likewise, assessment and research are needed to understand the impacts of HPC on the grid, and unexpected grid events on HPC-enabled vehicles, and to help determine the appropriate response from EVs and EVSE. Clear understanding of both the impact of large numbers of HPC systems on distribution feeders and of methods to integrate and control stationary storage and other DERs, in support of HPC, are needed. Furthermore, identification and development of control strategies will be required to enable HPC stations to provide grid and building services.

VTO's current HPC R&D efforts

The G&I Program supports RD&D of HPC in three areas: charging stations with multiple 400 kW EVSE for LD EVs, multi-MW charging stations for MD/HD EVs, and high-power static and dynamic wireless charging. For LD EVs, the focus is on developing and demonstrating charging stations with charging ports rated up to 400 kW and a total combined power rating that exceeds 1 MW. These stations will connect directly to medium voltage distribution networks and utilize stationary storage systems to minimize negative impacts on the grid. For MD/HD EVs, efforts are focused on developing strategies and technologies for 1+ MW multi-port chargers at fast charging travel plazas/truck stops and/or fleet depots. The G&I Program will conduct charging station utilization and load analysis, grid impacts and interconnection analysis, detailed power electronics component design, site and battery charge control, and charging connector design. Figure 5 provides a conceptual configuration of an HPC station for MD/HD EVs. High power static and dynamic wireless charging activities target establishing feasibility, overcoming technology gaps, and validating high power wireless charging with vehicle-level demonstrations. Efforts will analyze, design, build, and validate integrated high-power static and dynamic wireless charging systems that are viable for real world traffic conditions in the U.S.

VTO R&D Outlook for Key HPC Focus Areas

Future HPC activities target several areas including integration of dynamic wireless power transfer (dWPT) into roadways and development of innovative means to provide service to charging facilities. Deployment of dWPT into the roadway will require researching performance, field emissions, and power and control requirements, and addressing integration of the charging system. DC-as-a-Service (DCaaS) is an approach to provide direct current (DC) to charging stations that seamlessly integrates facility and EVSE loads, and DER. Research is needed to address DC isolation, metering, measurement, and protection. The following identifies specific HPC targets for 2023 and 2026.

YEAR 2023

- Develop strategies and technologies for high power dynamic wireless charging and multi-port 1+ MW charging stations that enable vehicle charging through direct connection to medium voltage (≥ 12.47 kV) distribution.

YEAR 2026

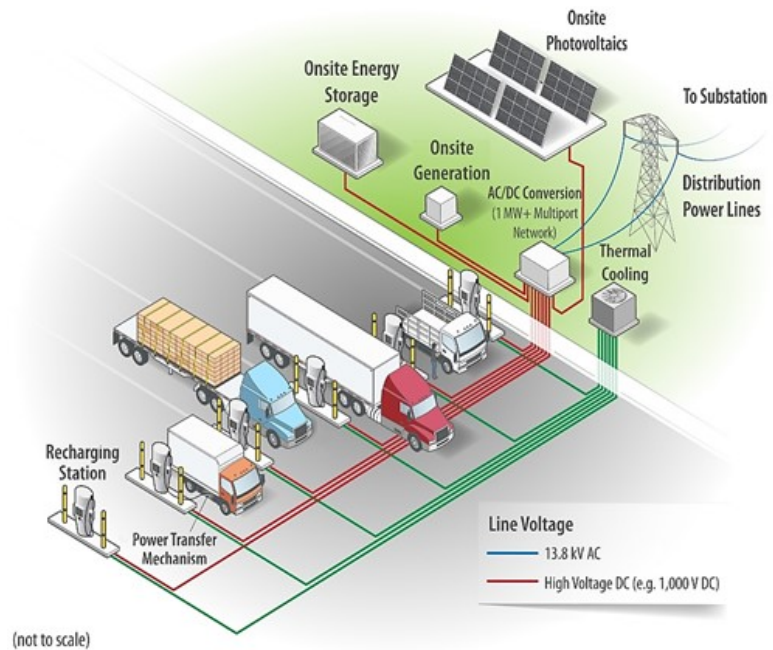


Figure 5 Conceptual configuration of an HPC station.

- Demonstrate and validate viable high power dynamic wireless charging, and multi-port 1+ MW charging stations with direct connection to medium voltage distribution.

Cyber-Physical Security

Importance

EVs and their connectivity with external systems have become increasingly complex. Apart from AC Level 1 chargers, EVSE have evolved rapidly to be networked and maintain a wide variety of communication functions. As communication networks for EVs, EVSE, and external systems increase, attack vectors and cyber-physical risks also increase for the charging infrastructure. Since EVSE at workplaces and public charging stations connect with many different EVs to provide charging services, it makes assuring CPS extremely difficult.

A major challenge posed by compromised charging infrastructure is the threat it poses to the electric grid. A localized cyber-physical attack on a set of EVSE/charging stations can lead to a sudden addition or reduction of loads that can cause local disruptions, brownouts, voltage imbalances, and undesirable power quality impacts. Large-scale, coordinated cyber-physical attacks on charging infrastructure supporting EVs@Scale can also lead to wider grid disruptions, such as blackouts over large geographical areas. The lack of a comprehensive understanding of threats; disjointed implementation approaches; and limited best practices are major barriers to ensuring overall security of EVs, charging infrastructure, and the grid.

VTO's current CPS R&D efforts

Current CPS activities include research, development, and validation of technologies for real-time threat detection, mitigation, isolation, and restoration of charging infrastructure based on its physical signatures and performance. Activities at the National Laboratories include developing a comprehensive threat model, attack graphs, and technical risk assessment of the EV charging ecosystem, and prioritizing charging infrastructure high consequence events and mitigation strategies. Additional activities include penetration testing of 50 kW DC fast chargers and 400 kW HPC and developing recommendations for secure communications. VTO-funded projects led by industry, academia, and non-profit organizations are developing real-time detection, defense, and mitigation systems to protect EVs, charging infrastructure, and the grid. This includes hardened controllers, converters, and monitoring systems; a retrofittable and scalable open-source cybersecurity architecture; and game theory-based hardware and software to provide secure charging.

VTO R&D Outlook for Key CPS Focus Areas

Based on the assessments of risk and high consequence events, future activities will implement the best approaches to mitigate vulnerabilities and threats associated with the EV charging ecosystem. This effort will incorporate strategies, systems, and tools for secure charging, including hardware/software for cyber-physical intrusion detection, threat mitigation and isolation, and recovery. The most promising CPS countermeasures will be identified based on risk formulation (e.g., public key infrastructure, blockchain, moving target defense, and redundancy). Identified countermeasures that address the highest consequence events will be demonstrated and validated. The following identifies specific CPS targets for 2023 and 2026.

YEAR 2023

- Develop a comprehensive threat model, prioritize high consequence events, and identify appropriate defense, detection, and mitigation strategies and tools for the EV charging ecosystem.

YEAR 2026

- Conduct wide-scale demonstrations to validate viable and robust cyber-physical security for the charging ecosystem in support of EVs@Scale.

The G&I program was established in January 2017. The program inherited a few of its FY 2019 projects from VTO's Vehicle Systems program. These inherited G&I projects have been assigned to Grid Modernization,

Industry Awards, or Fast Charging Enabling Technologies sections of this Electrification Annual Progress Report (APR). The Grid Modernization section contains project reports that were awarded to members of the Grid Modernization Laboratory Consortium (GMLC). The Industry section describes projects that were awarded to commercial industry performers via DOE’s Funding Opportunities Announcement (FOA) solicitation process. The Fast Charging Enabling Technologies projects were awarded to National Laboratories via direct funding agreements.

Grid and Infrastructure Research Highlights

Accomplishments	Organization	Focus Area	Project Title
<u>Designed a Novel High Power WPT device:</u> The team worked on modeling, simulations, analysis, and design of the system power conversion stages and control systems and completed the design and simulations of the 300 kW inductive charging system. Since proposed concept is new, a relatively low-power, scaled-down version of the couplers were developed and tested to validate the concept and the operation. The prototype was tested with ~95% dc-to-dc efficiency with ~50 kW output.	ORNL	High Power Wireless Charging	High-Power Inductive Charging System Development and Integration for Mobility
<u>Built and demonstrated zero emission capable electric truck technologies for drayage operations:</u> As of 2019, all eleven electric trucks funded under this project were constructed with two trucks continuing demonstration efforts until March 2020. Overall, the trucks that have completed demonstration have proven successful in demonstrating their feasibility in various drayage operations and handling daily loads and many routine schedules. The trucks have generated significant interest from trucking companies, which helps to promote and to accelerate market adoption of electric truck technologies in cargo transport operations.	South Coast Air Quality Management District	Industry Awards	Zero Emission Drayage Trucks Demonstration (ZECT I)
<u>65% Reduction in Fuel Consumption via Electrification:</u> The Electric Truck with Range Extending Engine (ETREE) project team has developed an EV powertrain and related systems and completed J1526 fuel consumption testing that demonstrated 65% reduction in fuel consumption on a modified NREL80 cycle over a baseline vehicle. The test exceeded the project goal of 50% reduction in fuel consumption.	Cummins	Industry Awards	Cummins Electric Truck with Range-Extending Engine (ETREE)
<u>McLaren built and tested a novel eAxle system, energy storage & range extender systems for installation and final calibration in four MD demonstration vehicles.</u> There have been continued challenges to achieve the desired reliability for demonstration routes. The current system with the two-speed transmission feature will continue to be developed for demonstration in FY20.	McLaren Engineering	Industry Awards	Medium Duty Vehicle Powertrain Electrification and Demonstration

Accomplishments	Organization	Focus Area	Project Title
<p><u>Delta designed and tested a high-efficiency, medium-voltage-input, solid-state-transformer-based 400-kW XFC for EVs achieving better than 96.5 percent efficiency.</u> The XFC system consists of a Solid-State Transformer (SST), a Charge Controller (in power cabinet), a Charge Dispenser (A.K.A. User Unit) and an optional Energy Storage System (ESS). The test result shows that the SST module and the Buck module meet the specification. The integration of the series SST and Buck module is successful. The program objectives of FY19 were completely met.</p>	Delta Electronics (Americas) Ltd)	Industry Awards – Fast Charging Enabling Technologies	High-Efficiency, Medium-Voltage-Input, Solid-State-Transformer-Based 400-kW/1000-V/400-A Extreme Fast Charger for Electric Vehicles
<p><u>Bosch progressed development of a commercially viable PHEV powertrain for MD vehicles that reduces fuel consumption by 50% on a real-world drive cycle</u> by utilizing an advanced dual-planetary gear transmission with multiple clutches, coupled with cost-optimized electric machines. The integration phase of the PHEV powertrain continued throughout the year. A dual 24V power pack was installed for electro-hydraulic power steering and braking while the ICE is not running. Thermal management is accomplished using an integrated fluids box from VOSS including new thermally controlled valves. Fluids box installed on the chassis, filled and commissioned for initial chassis dyno testing. E/E Architecture was frozen and the 12V 24V and HVIL (High Voltage InterLock) systems were integrated into a single Power Distribution Unit for convenient access and space considerations. In parallel, engine dyno test results with a downsized diesel engine assembled to a hybrid transmission successfully demonstrated mode switches between one and two motor EV as well as Powersplit during transient cycles.</p>	Robert Bosch LLC	Industry Awards	Medium-Duty Urban Range Extended Connected Powertrain (MURECP), ()
<p><u>High Power Wireless System Development:</u> The CALSTART project made significant progress in developing systems for high power and high-efficiency wireless charging of an electric medium duty delivery trucks. Team developed the resonant stage components and verified the resonant voltage gains that would optimize the power transfer between the ~750-800V primary dc bus voltage and the nominal 420V secondary. As of September 2019 the team was working on vehicle integrations and preparations to demonstrate the operation of the technology on the UPS research truck.</p>	CALSTART, ORNL, UPS	Industry Awards- High Power Wireless Charging	Bidirectional Wireless Power Flow for Medium Duty Vehicle Grid Connectivity
<p><u>Odyne progressed the development of a new class of PHEV Work Truck which will be modularized and customized to provide optimal ROI across multiple customers and applications.</u> The work initially focused to demonstrate this technology as a Utility Work Truck variant. The project completed the final analytical drive optimization, selection of the primary path battery system. The project also built the prototype test chassis and ORNL Hardware-in-Loop (HIL)</p>	Odyne Systems	Industry Awards	Development and Demonstration of Medium-Heavy Duty PHEV Work Trucks

Accomplishments	Organization	Focus Area	Project Title
powertrain dynamometer test system fixturing and assembly.			
<p><u>NREL developed technology to mitigate demand charges via a charge management system integrating many different types of controllable loads for demand charge mitigation. The central controller only needs to add a list of MQTT message topics that are required for the new controllable loads and aggregate the forecasted energy needs of them into the optimization.</u></p>	NREL	Fast Charging Enabling Technologies	Demand Charge Mitigation Technologies
<p><u>WAVE developed a HP WPT System Requirements to develop and integrate a new 500kW WXFC system into a Class 8 electric drayage truck developed by Cummins so that it can automatically and wirelessly charge at a high charging rate (c-rate) during their dwell times. The proposed wireless charger features a direct connection to the Medium Voltage (MV) 3-phase grid developed by Utah State University and Schneider Electric and the final prototype will be deployed at Total Transportation Services Inc. (TTSI), which is a truck operator at the Port of Los Angeles (POLA).</u></p>	WAVE, Utah State University, Schneider Electric, Total Transportation Services	Industry Awards-High Power Wireless Charging	High-Power Inductive Charging System Development and Integration for Mobility
<p><u>EPRI progressed V2G technology to improve the value of owning a Plug-in Electric Vehicle (PEV) in the form of an off-vehicle Smart Power Integrated Node (SPIN) system. SPIN enables increased renewable generation on the grid and providing Vehicle to Home type services in conjunction with on-vehicle and off-vehicle storage. A fully functional SPIN unit was delivered to NREL NTRC for acceptance testing of its operational modes. The project defined DC DER software and communications strategy—an industry first, that will inform both the IEC/ISO and SAE standards. The project defined a control and communications architecture for information exchange between the grid and SPIN as well as the SPIN and PEV. The project developed the SPIN master controller and integrated the IoTecha EVCC and SECC cards on Pacifica PHEV and SPIN. Setup of an End to end communications bench to verify system-level communications and control functions began.</u></p> <p>Off-board V2G functionality of the Pacifica PHEVs have been accomplished by refreshing the on-board V2G program. from the on-board V2G program have been refreshed to</p> <p>A battery test cycle has been defined and the battery has been provided by FCA to NREL where the test set up has been completed and the battery testing has commenced.</p>	EPRI	Industry Awards-	Comprehensive Assessment of On- and Off-Board Vehicle-To-Grid Technology Performance and Impacts On Battery and The Grid (EPRI SPIN)
<p><u>MUST began advancing the state of the art in EV charging by addressing the three key challenges of 1) battery charging algorithms for minimal damage during extreme fast charging, 2) medium-voltage</u></p>	Missouri University of Science and	Industry Awards – Fast Charging	Enabling Extreme Fast Charging with Energy Storage

Accomplishments	Organization	Focus Area	Project Title
power conversion for rapid, inexpensive deployment, and 3) grid compatibility to mitigate the impact of charging transients on the grid. The project produced preliminary results on sub-scale analysis, design, and construction that are to be completed in FY20 and scaled up in future years.	Technology (MUST)	Enabling Technologies	
<u>NCSU has made significant progress in all key aspects of the XFC station design.</u> The team has selected the MV SST topology; completed the system-level control simulations, and has constructed a small proof-of-concept prototype to validate the system control. In addition, the team has made significant progress in designing the full-scale SST module and has identified a vendor for the DC/DC stage that will make up the DC node for the system. The team has made significant progress in developing the DC solid-state breaker and has completed a number of system-level protection coordination studies, which will drive the design of the DC distribution system. Finally, the team has selected the deployment site for the system and is making progress on completing the detailed engineering drawings for the system site.	North Carolina State University (NCSU)	Industry Awards – Fast Charging Enabling Technologies	Intelligent, Grid-Friendly, Modular Extreme Fast Charging System with Solid-State DC Protection
<u>The EPRI led project team initiated development and validation of a system of PEV XFC equipment with a direct connection to the medium-voltage utility grid with a novel, modular, and interoperable approach.</u> The objective of the project is to develop and demonstrate medium voltage SiC-based AC-DC conversion equipment and the DC-to-DC head unit for use in XFC equipment capable of simultaneously charging multiple light duty PEVs at rates of ≥ 350 kW and a combined power level of ≥ 1 MW while minimizing the impact on the grid and operational costs.	Electric Power Research Institute (EPRI), Eaton Corporation, NREL, Tritium, ANL	Industry Awards – Fast Charging Enabling Technologies	Direct Current Conversion Equipment Connected to the Medium-Voltage Grid for XFC Utilizing a Modular and Interoperable Architecture
<u>Argonne collaborated with the European Union’s JRC to uncover ‘childhood diseases’ in new XFC technology and inform the manufacturers accordingly.</u> The project addressed identification and resolution of issues associated with a 200 kW XFC system. had a few technical issues early on, but when these issues were addressed by the manufacturer it was found to communicate according to the standards using an industry-standard interoperability test tool. The results showed the EVSE to be backward compatible with EVs below 50 kW charge levels. The DC communication analysis showed consistent messaging and timing. The results imply that integration of higher power charging stations in communication networks via OCPP should be accomplished with no more effort than lower power EVSE that communicate using OCPP.	ANL	Fast Charging Enabling Technologies	Fast Charging: Interoperability and Integration Technologies

Accomplishments	Organization	Focus Area	Project Title
<p><u>INL developed XFC Technology Requirements:</u> This project completed important preliminary research that is necessary for understanding the impact of fast charging on grid stability and identifying and mitigating cybersecurity vulnerabilities. A transient characteristic of a prototype commercial 350KW XFC was discovered – namely ramp-down rate at the end of charge events – that has the potential to impact grid stability.</p>	<p>INL</p>	<p>Fast Charging Enabling Technologies</p>	<p>Fast Charging: Grid Impacts and Cyber Security</p>
<p><u>ORNL identified technology targets to achieve an economically feasible dynamic wireless EV charging system applicable to LD vehicles and primary roadways.</u> The performance targets are:</p> <ol style="list-style-type: none"> 1) Power transfer level for range extension: 150 kW – 235 kW 2) Efficiency: 90 % 3) Surface power density (SPD): 400 kW/m² <p>The project also analyzed</p> <ol style="list-style-type: none"> a) Minimum roadway coverage solution for primary roadways for a LD vehicle, b) Current capabilities of SOA dynamic wireless systems, c) Performance of two candidate coil reference design as applied to 200KW systems, and d) Derived a control-to-coil-current transfer function for a DWPT controller. <p><u>INL WPT EM-field Shaping and Shielding Solutions</u></p> <p>Advanced magnetics 3-D finite element modeling tools were used to develop and analyze the EM field surrounding a 200-kW light-duty WPT system. The new EM-field shaping design uses innovated geometry of ferrite placement around the WPT to effectively shape the EM field therefore reducing the stray EM field surrounding the WPT system.</p>	<p>ORNL, INL, NREL</p>	<p>High Power Wireless Charging</p>	<p>High Power and Dynamic Wireless Charging for EVs</p>
<p>The GMLC 1.4.2 Grid Services from Devices project has <u>completed the specification of the general battery-equivalent interface for eight device models</u> and is preparing to publish the models in the form of an open-source Python-based software library. The project is in the final stages of completing the grid services software that will be used for exercising the models and provide insights into devices’ abilities to respond to a range of prototypical grid services. The project has analyzed how existing appliance standards test procedures could be leveraged to provide equipment parameters useful for characterizing how well devices can supply grid services, and has developed plans for testing example devices from three device classes—electric vehicles, commercial</p>	<p>GMLC - PNNL, with ANL, INL, LBNL, LANL, NREL, ORNL, SNL</p>	<p>Grid Modernization</p>	<p>GMLC 1.4.2 – Definitions, Standards and Test Procedures for Grid Services from Devices</p>

Accomplishments	Organization	Focus Area	Project Title
refrigeration, and water heaters—to validate their device models.			
<p><u>Developed Grid-XFC Requirements to promote a reliable and resilient electric grid:</u></p> <p>NREL quantified the effects of uncontrolled charging to understand how increased PEV adoption may negatively impact the grid. Progress considered the limitations of the grid and the impacts of PEV adoption. After acquiring distribution feeder data, the hosting capacity analysis displayed the grid’s ability to serve larger loads, such as xFC. This analysis leads into uncontrolled charging simulations in which high levels of PEV adoption begin to create voltage and line loading violations throughout the feeder. These challenges make the case for controlled charging as a way to mitigate these problems.</p> <p>INL quantified the effects of uncontrolled charging to understand how increased PEV adoption may negatively impact the grid, and to analyzed the effectiveness of multiple control strategies in mitigating negative grid impacts introduced by PEVs at scale. High-fidelity charging models were integrated into Caldera to supplement existing control strategies developed in past projects. INL began work to develop new PEV charging control strategies.</p>	NREL, INL, SNL	Fast Charging Enabling Technologies	Smart Electric Vehicle Charging for a Reliable and Resilient Grid (RECHARGE)
<p><u>NREL Developed MultiPort 1+MW Charging Requirements -:</u> The first year work of the project included -1) considered various use cases and travel patterns to develop / quantify expected vehicle loads at a multi-MW station, 2) analyzed and optimized charge port control and battery requirements in a multi-MW station, 3) developed a framework to analyze grid impacts of various multi-MW stations at the distribution level, 4) Analyzed and quantified connector and charging system electrical and thermal requirements.</p> <p><u>ANL Developed MultiPort 1+MW Charging Requirements:</u> The work-in-progress CharIN HPCCV coupler specification covers MD/HD electric truck charging connections, with similar remaining requirements gaps in communication reliability, safety interlocks, cooling, and cord handling including robotic insertion/removal processes.</p> <p>A draft MW+ multiport charging requirements document was compiled. A concise digest was created to highlight the state of readiness of stake holders to plan deployment of MW+ multiport EV charging systems, including gaps in standards or data.</p> <p><u>ORNL assessed candidate 1+MW charging architectures:</u> The three candidate architectures listed below were selected for in-depth study:</p>	NREL, ANL, ORNL	Fast Charging Enabling Technologies	Development of a Multiport 1+Megawatt Charging System for Medium- and Heavy-Duty Electric Vehicles

Accomplishments	Organization	Focus Area	Project Title
<p>1) DC Coupled architecture: components are interconnected through a common 2kV DC bus</p> <p>2) AC-Coupled architecture: components are interconnected through a common 480V, 60Hz AC bus</p> <p>3) Medium Voltage(MV) Architecture: connects directly to the medium voltage distribution grid using a cascaded H-Bridge (CHB) converter</p> <p>Each of these approaches were investigated from the grid conversion and impact as well as the interaction with DERs and EV load converters. The MV topology using the CHB converter was selected as the most suitable.</p>			
<p><u>Developed charging infrastructure cyber threat prioritization system:</u> Research efforts for this project were focused on trying to prevent high consequence manipulation and misuse of EV charging infrastructure. In order to effectively do so, researchers first conceptualized events that could be brought about by cyber manipulation to create a physically adverse effect on high-powered charging infrastructure, EVs, and/or the electric grid. Researchers then quantitatively scored the events using an impact severity scoring matrix and complexity multiplier. The high consequence events (HCEs) were scored and prioritized based upon this quantitative method. This prioritization ranking allows researchers to focus their efforts on identifying and securing attack pathways enabling the most severe HCEs, then working to develop mitigation solutions to prevent and identify the cyber threats potentially leading to those HCEs.</p>	INL	Cyber Security	Consequence-Driven Cybersecurity for High-Power Charging Infrastructure
<p><u>Began Developing EVSE Cyber Security Threat Models:</u> There is no comprehensive EVSE cybersecurity approach and limited best practices have been adopted by the EV/EVSE industry. For this reason, there is an incomplete industry understanding of the attack surface, interconnected assets, and unsecured interfaces. Thus, comprehensive cybersecurity recommendations founded on sound research are necessary to secure EV charging infrastructure. This project is providing the automotive industry with a strong technical basis for securing this infrastructure by developing threat models, prioritizing technology gaps, and developing effective countermeasures. Specifically, the team is creating a cybersecurity threat model and performing a technical risk assessment of EVSE assets, so that automotive, charging, and utility stakeholders can better protect customers, vehicles, and power systems in the face of new cyber threats.</p>	SNL, PNNL, ANL	Cyber Security	Securing Vehicle Charging Infrastructure
<p><u>ANL progressed incorporating EVs and EVSE with 'smart' communication capabilities in the network at the Smart Energy Plaza;</u> use cases have been demonstrated for controlled and emulated smart charging, EVs and EVSE have been acquired with high</p>	ANL, INL	Fast Charging Enabling Technologies	Smart Vehicle-Grid Integration (Smart-VGI)

Accomplishments	Organization	Focus Area	Project Title
level language (i.e., smart) capability and the common integration platform, CIP.io, has been enhanced to enable charge scheduling using ISO 15118. However the GMLC use cases that depend on smart charging have not been demonstrated on schedule due to delays in overcoming the proprietary interfaces of the EVSE, The beta version of the Diagnostic Electric Vehicle Adapter (DEVA) was demonstrated on schedule.			
<u>LLNL progressed development of a decentralized, collaborative algorithm that will enable local groups of charging station controllers to coordinate the load reduction responses required by the centralized grid command center,</u> while meeting technological, policy, and contractual constraints imposed at the level of the smart charging stations and possibly at the level of the individual electric vehicles. The work developed charge management algorithms.	LLNL	Grid and Infrastructure Grid Interoperability and Control	Scalable Electric Vehicle Smart Charging Using Collaborative Autonomy
<u>The EPRI team developed the IGSRM tool.</u> The EA tool and database provided a scalable architecture to develop new sub-systems, components, and cybersecurity risks and recommendations. The tool shall be used to develop a web-based IGSRM tool that reflect the reference cybersecurity architecture of a connected XFC ecosystem, recommended controls and their associated risk profiles. For the cybersecurity testing at the laboratories, The EPRI CSRL team focused on the EVSE charging infrastructure in fulfillment of its evaluation objectives. The NREL team completed laboratory testing of several cybersecurity aspects of the EV charging ecosystem using hardware, software emulation, and cloud interfaces.	EPRI	Cyber Security	Cybersecurity Platform and Certification Framework Development for eXtreme Fast Charging (XFC)

In this report the Grid and Infrastructure project reports have been grouped into the chapter categories of Industry Awards, Grid Modernization, and Fast Charging Enabling Technologies. Many of the projects address multiple programs objectives.

Questions regarding the Grid and Infrastructure Program can be directed to the Technology Development Manager, Lee Slezak via email: Lee.Slezak@ee.doe.gov or telephone: (202) 586-2335

ⁱ <https://electrify-commercial.com/1/25/2021>

ⁱⁱ <https://www.charinev.org/faq/1/25/2021>.

ⁱⁱⁱ https://www.greenfleetmagazine.com/10131365/daimler-announces-electric-island-commercial-vehicle-charging-showcase?utm_source=feedburner&utm_medium=feed&utm_campaign=Feed%3A+GreenFleetMagazine-All+%28Green+Fleet+Magazine%29. December 1, 2020.

^{iv} <https://cleantechnica.com/2020/02/17/largest-ev-fast-charging-station-in-the-us-opens-in-pasadena-california/>

^v <https://www.cnn.com/2019/10/17/cars/ford-electric-vehicle-charging-network/index.html>

^{vi} <https://www.ttnews.com/articles/gm-build-nationwide-ev-charging-network>. July 31, 2020.

I Electric Drive Technologies

I.1 Electric Drive Technologies Research

I.1.1 Highly Integrated Power Module (Oak Ridge National Laboratory)

Emre Gurpinar, Principal Investigator

Oak Ridge National Laboratory
1 Bethel Valley Road
Oak Ridge, TN 37830
Email: gurpinare@ornl.gov

Susan Rogers, DOE Technology Development Manager

U.S. Department of Energy
Email: susan.rogers@ee.doe.gov

Start Date: October 1, 2019

End Date: September 30, 2020

Project Funding: \$880,000

DOE share: \$880,000

Non-DOE share: \$0

Project Introduction

This project covers the design and development of next-generation wide-bandgap power modules and associated components within the system. Various component challenges in the system tackled such as substrates, integrated heat sinks and automated design tools for power electronics to advance the power density, reduce the footprint of the system and increase level of integration.

Objectives

The overall objective of the project is to develop technologies for next-generation advanced integrated power electronic systems enabling high power density and reliability to achieve the US Department of Energy (DOE) Electrification Technologies (ELT) 2025 technical targets: 100 kW/L, \$2.70/kW, and a 300,000-mile lifetime. Under the overall objective, two main streamlines have been identified: (1) power module design and (2) automated design of power electronics.

Approach

The main approach is to increase the power density and reliability of power electronics to meet DOE ELT 2025 targets (100 kW/L, \$2.70/kW, and a 300,000-mile lifetime) by focusing on power module design and automated design of power electronics.

Under the power module design streamline, investigations were conducted on substrates for power electronic modules that allowed increased power density and high reliability for wide-bandgap device-based power modules via better coefficient of thermal expansion matching between wide-bandgap devices and power module materials, improved heat extraction, and enhanced thermal and power cycling capability. Furthermore, multilayer substrates for enhanced electrical and thermal performance were evaluated. These solutions enabled reduced parasitic inductance in the system for optimum switching performance, reduced power module size, and enabled direct attachment of high-performance heat sinks.

Two evaluations were conducted under the power module design streamline: the feasibility of thermally annealed pyrolytic graphite in insulated metal substrates (IMs), and the development of an integrated multilayer substrate using advanced materials, integrated cooling, and gate driver solutions. For the automated design of power electronics, a new algorithm to develop advanced liquid-cooled heat sinks using artificial intelligence and Fourier series was developed and validated using finite element analysis.

Results

Experimental Validation of Graphite-Embedded Substrate

The substrates based on an insulated metal substrate with embedded thermally-annealed pyrolytic graphite-IMS (IMSwTPG) and an aluminum nitride-based direct-bonded copper (DBC) substrate were compared for use in power modules with SiC MOSFETs. The experimental analysis was divided into two sections: (1) comparison of DBC and IMSwTPG based on steady-state and transient-based thermal characterization, and (2) static and dynamic electrical characterization of a SiC MOSFET-based IMSwTPG power module at rated operating conditions. Half-bridge SiC MOSFET-based test samples were fabricated on DBC and IMSwTPG substrates as shown in Figure I.1.1.1. The SiC MOSFETs were soldered onto the substrate with 50 μm thick 63Sn/37Pb solder, and the 250 μm aluminum wire bonds were used for power and gate interconnects. A high-temperature 3D printed structure was used for housing and assembly of the sample to the test setup.

For the thermal analysis, the substrate under evaluation was mounted on a liquid-cooled cold plate, with pre-calibrated thermocouples located at different locations on the base of the substrate as shown in Figure I.1.1.1. High-performance thermal interface material with 13 $\text{W}/(\text{m}^2\text{K})$ was used with 1 mm thickness between the substrate and the cold plate. The substrate surface and SiC MOSFET die surface temperatures were measured using an infrared thermal camera. For this purpose, the top surface of the sample was painted with black flat spray paint to achieve constant emissivity. The temperature measurement at the base of the substrate decoupled the thermal impedance measurement for DBC- and IMSwTPG-based samples, so the temperature difference between the SiC MOSFET die surface and the substrate base temperature could be directly measured.

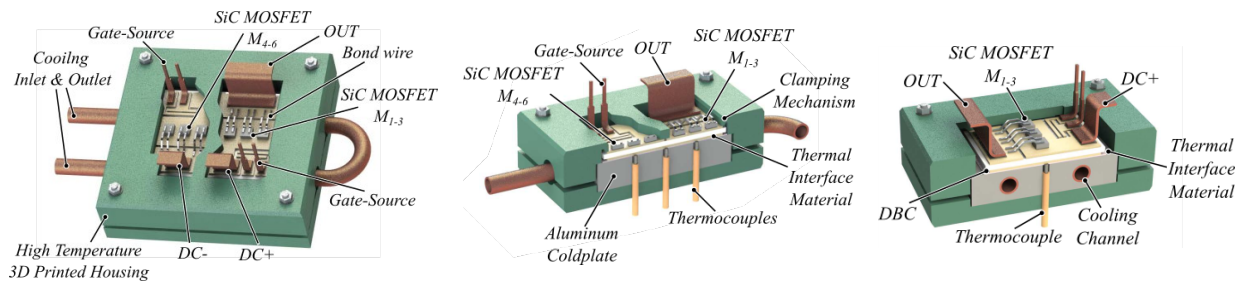


Figure I.1.1.1 Thermal measurement setup for DBC and IMSwTPG evaluation: (left) isometric view, (middle) right cross-section, and (right) front cross-section.

The summary of thermal analysis and comparison of DBC and IMSwTPG in terms of steady-state thermal resistance, transient thermal impedance, and current density of SiC MOSFETs with different substrates is presented in Figure I.1.1.2. IMSwTPG provides up to 17% reduction in steady-state thermal resistance compared with DBC because of improved heat spreading provided by the embedded graphite. Furthermore, the IMSwTPG provides up to 40% improvement in transient thermal impedance because of the increased heat capacity underneath the MOSFET dies. These two thermal improvements with IMSwTPG provide a 10% increase in current density for SiC MOSFET dies regardless of thermal management strategy employed to cool the substrates as presented in Figure I.1.1.2.

The static characterization of the switches was conducted with a high-power curve tracer with up to 250 A drain current per switch. The SiC MOSFET dies used in this study were rated at 66 A at 25°C junction temperature with 30 $\text{m}\Omega$ typical, and 39 $\text{m}\Omega$ maximum on-state resistance. The output characteristics for M_{1-3} and M_{4-6} at a 25°C junction temperature and different gate-source voltages are presented in Figure I.1.1.3. The output characteristics of both switches were matched well at different gate voltages. Based on the output characteristics extracted at different junction temperature and gate-source biases, the on-state resistance for each switch was calculated as a function of drain current as presented in Figure I.1.1.3. According to the data

sheet of the die, the on-state resistance of three paralleled dies should be between 10 and 13 mΩ at a 105 A drain current and a 25°C junction temperature. At 125°C, this on-state resistance range should increase by factor of approximately 1.2, to 12 and 15.6 mΩ. Considering only die conduction performance, when these theoretical values are compared with the experimental results shown in Figure I.1.1.3, which include the contribution of wire bond, terminal, and substrate performance to on-state resistance, it is clear that the IMSwTPG substrate—including the TPG tiles, the copper core underneath the dies, and the interconnects used in the module design—minimally affected conduction performance. The measured on-state resistance presented in Figure I.1.1.3 is very close to the theoretical value.

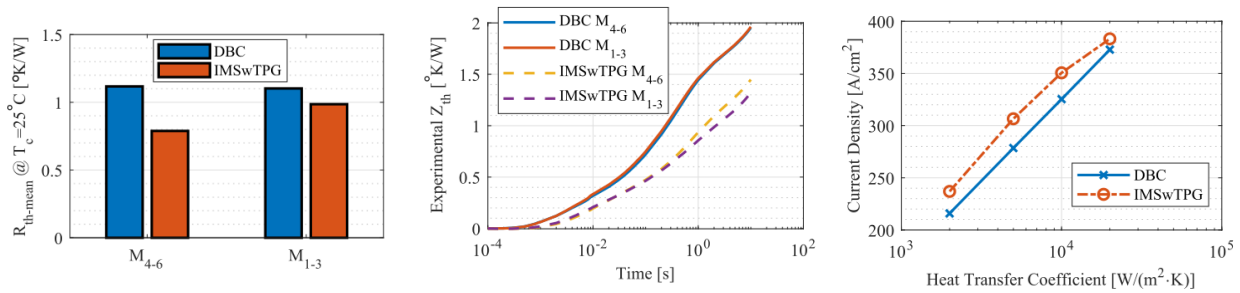


Figure I.1.1.2 (left) Comparison of average thermal resistance of paralleled SiC MOSFETs with DBC and IMSwTPG substrates at 25 °C coolant temperature, (middle) transient impedance of SiC MOSFET dies on DBC and IMSwTPG substrates, and (right) current density comparison for M_5 under different coolant performances.

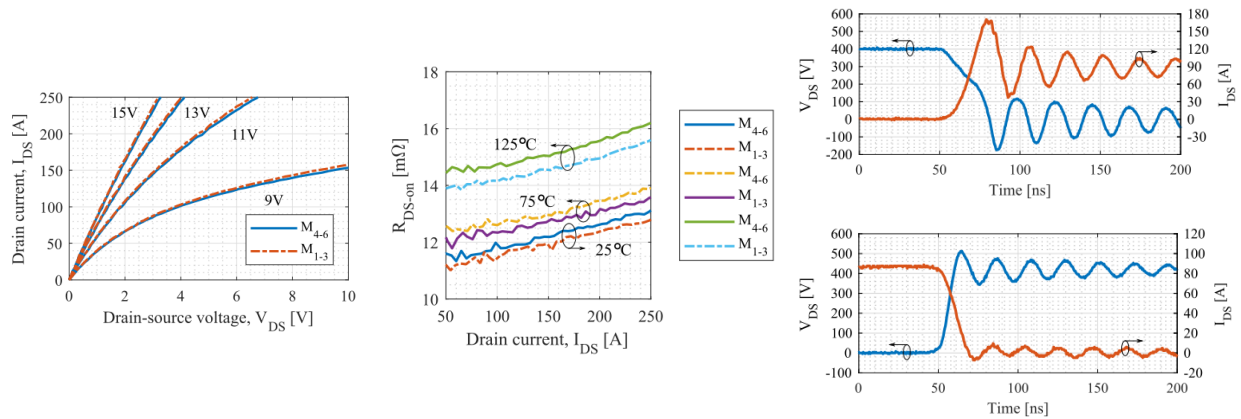


Figure I.1.1.3 (left) Output characteristics of the switches M_{1-3} and M_{4-6} on the IMSwTPG substrate at 25 °C junction temperature and different gate-source voltage conditions, (middle) on-state resistance of M_{1-3} and M_{4-6} with 15 V gate-source voltage at three different junction temperatures, and (top right) turn-on and (bottom right) turn-off switching waveforms at 400 V DC link, 90 A load current, and 125 °C junction temperature.

Advanced Heat Sink Designs Using Artificial Intelligence and Fourier Series

Optimal heat dissipation in power modules can significantly increase their power density. Removing the generated heat is critical for capturing the benefits of advanced semiconductor materials and improving the reliability of the device operation. Under this task, a design optimization method was proposed for liquid-cooled heat sinks that uses a Fourier analysis-based tool and an evolutionary optimization algorithm to optimize the heat sink geometry for specified objectives. The optimized heat sink geometry was then compared with state-of-the-art solutions in literature based on finite element analysis of different designs. The proposed methodology can develop complex geometries that outperform the conventional heat sink geometries.

To this end, consider a 2D surface H confined in an area spanned by $0 \leq x \leq L_x$, $0 \leq y \leq L_y$ in a Cartesian coordinate system where L_x and L_y are the maximum allowed horizontal and vertical dimensions, respectively. The 2D structure is created starting from its base at $y = 0$. For simplicity, the structure is assumed to have no holes and can be mathematically defined using a single-dimensional function with each point representing the height of the material added to the structure. By using the:

$$F_{am}(x) = F_0 + \sum_{n=1}^{N_{hs}} \left(F_h[n] \cos \left(\frac{2\pi}{\lambda_x} h[n]x + \phi_h[n] \right) \right)$$

$$F_{am}(x) = F_0 + \sum_{n=1}^{N_{hs}} \left(F_h[n] \cos \left(\frac{2\pi}{\lambda_x} h[n]x + \phi_h[n] \right) \right)$$

mathematical representation of a stationary wave, the surface of the manufactured structure $F_{am}(x)$ —considering the assumptions—can be expressed using the summation of sinusoidal harmonics as

where x varies between 0 and L_x , F_0 is a constant shift; λ_x is the wavelength, which is also equal to L_x ; $h[n]$ is the harmonic order; $F_h[n]$ and $\phi_h[n]$ are its amplitude and phase shift, respectively; and N_{hs} is the total number of harmonics considered.

A design optimization case study was undertaken with an IMS-based wide-bandgap semiconductor module layout presented in the previous section. To reduce the modeling complexity of the finite element analysis setup, thin power module material layers were not modeled in the heat sink design optimization, and the heat sources were directly applied to the heat sink surface. To contain the coolant, 0.5 mm thick plates were assumed to be attached to the two sides and the bottom side of the heat sink. Aluminum was selected as the heat sink material, which is commonly used for power electronics thermal management. Water was used as the input coolant and was supplied at 10/6 L/min flow rate at 65°C. In the design domain, $N_{hs} = 10$ and each harmonic order $h[n]$ were a variable between 1 and 100. The maximum allowed heat sink height was 12.5 mm. Hence, minimum and maximum amplitudes of each harmonic were set as 0 and 12 mm, respectively. The phase angle for each harmonic was allowed to vary between 0 and 2π . Constraints were imposed so that the total height of the heat sink was greater than 1 mm and less than 12.5 mm, and the Reynolds number was $<2,000$.

For comparison, a pin-fin-based heat sink was taken from a 2016 BMW i3 FS800R07A2E3 power module and one-third of the heat sink structure was simulated to match the dimensions of the power module. The pin-fin heat sink height was 12.5 mm, and it was used with the module layout for its performance comparison with optimized designs. Results from the simulations are shown in Figure I.1.1.4. As shown in the figure, the maximum device steady-state temperature was 110.29°C with an average pressure drop at 106 Pa. The total volume of the heat sink was 24 cm³. With this as the baseline, an additional constraint was imposed on the design optimization so that the optimal designs have a maximum semiconductor junction temperature of less than or equal to 110°C. This will ensure that the optimal designs have better thermal performance than the baseline pin-fin heat sink.

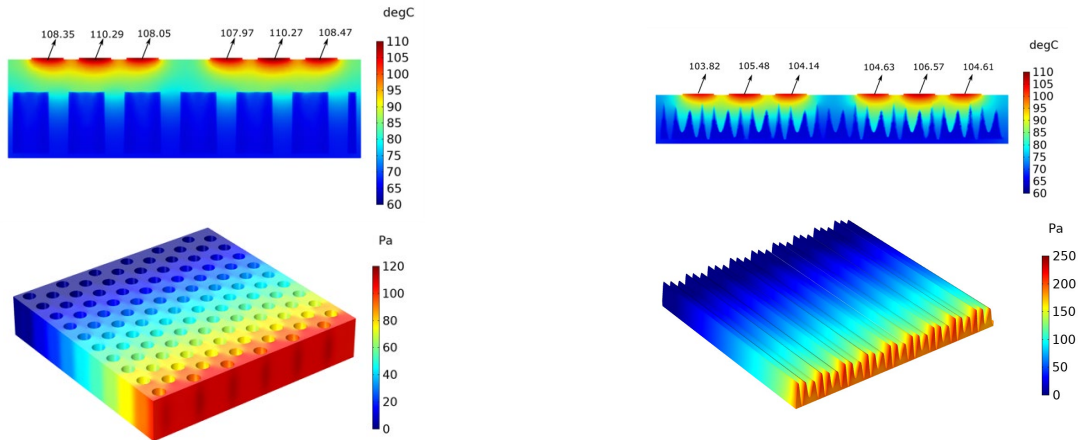


Figure I.1.1.4 (top left) Steady-state thermal performance and (bottom left) pressure drop across coolant fluid for the pin-fin heat sink. (top right) Steady-state thermal performance and (bottom right) pressure drop across coolant fluid for the optimized heat sink.

The steady-state performance of the selected heat sink is shown in Figure I.1.1.4. The optimized heat sink clearly achieved a better thermal performance in half the volume of pin-fin heat sink, doubling the power density with temperature reduction between 3°C and 4°C. Figure I.1.1.4 also shows that the steady-state pressure drop of the selected optimized heat sink nearly doubled from 106 Pa for a pin-fin heat sink to 216 Pa for an optimized heat sink. The additional pressure drop of 110 Pa adds 20 W/m² or less than 5 mW extra pump power requirement for the heat sink. Therefore, the additional pumping power requirement is justified, leading to two times increase in power density.

Integrated Power Module for Gallium Nitride High-Electron-Mobility Transistors Based on Advanced Substrates and Heat Sinks

Taking advantage of the flexible manufacturing process of the IMSs, the packaging concept presented in Figure I.1.1.5 can provide a multilayer layout with an integrated heat sink and auxiliaries for optimum electrical and thermal performance. In the proposed structure, a vertical power loop for the half-bridge circuit was employed for low-commutation loop inductance and common-mode shielding. The inner conductive layer was connected to the direct current negative terminal, which provides flux cancellation for the commutation loop inductance and inherent shielding between the switch node (output terminal) and the heat sink (ground). The high common-mode capacitance between the switch node and the ground was a well-known problem for IMSs and containing the common-mode interference within the module is crucial for successful operation of the system. The thickness of the conductive layers and module width can be varied for optimum heat spreading and mitigating the effect of using two dielectric layers in the transfer path. The area outside of the power loop can be used for integration of gate driver circuitry and power terminals as presented in Figure I.1.1.1. The multilayer layout also provides the opportunity to place the gate drivers for each power device as close as possible to ensure reduced gate loop inductance and increased high switching speed.

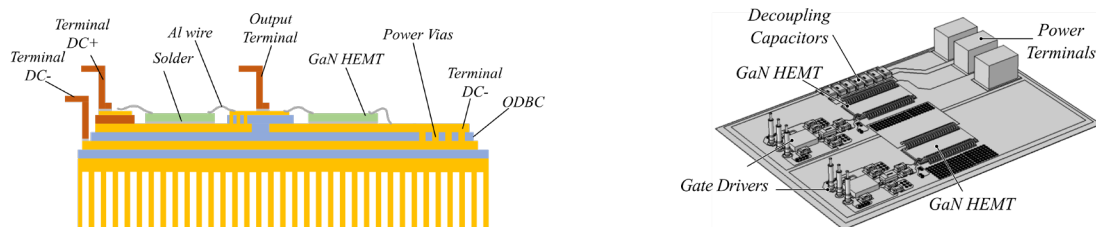


Figure I.1.1.5 (left) Cross-sectional concept view of the integrated multilayer power module, and (right) CAD model of the module with power devices, integrated gate drivers, and terminals. DC = direct current; HEMT = high-electron-mobility transistor; and ODBC = Organic Direct Bonded Copper.

In this optimization, the gallium nitride high-electron-mobility transistor (HEMT) current density, top copper thickness, module width, and integrated heat sink parameters were considered as unknowns while the rest of the module parameters, such as middle copper thickness and coolant flow rate, were provided as fixed quantities. Middle copper thickness was taken equal to 1 mm. An input water ethylene glycol 50%/50% mixture coolant temperature was set to 65°C with a 10 L/min flow rate. Copper was selected as the heat sink material. The maximum junction temperature was limited to 150°C and the maximum coolant pressure drop was limited to 2 kPa as design constraints. Current density was allowed to vary between 10 and 200 A/cm². Top copper thickness was a variable between 1 and 5 mm, and module width could vary between 45- and 60-mm. Limits on Fourier terms for the heat sink structures were taken from the previous work mentioned above. For the optimization, the power module was assumed to operate in a steady-state condition at the peak current density. Each design was evaluated based on thermal and flow finite element simulations to search for the highest current density with the lowest volume while satisfying the steady-state temperature and pressure drop constraints.

From the optimization results, the design space and Pareto-front for the optimized power module design in terms of device current density and power module volume are presented in Figure I.1.1.6. The selected design, as presented in Figure I.1.1.6, achieved more than 125 A/cm² current density for the gallium nitride HEMTs with 23 cm³ power module volume. The steady-state temperature profile of the selected module design along with the dimensions is presented in Figure I.1.1.6, as well. The maximum temperature was 147.7°C and there was a 3.6°C temperature difference between the top and the bottom switch due to the flow direction in the cooling structure.

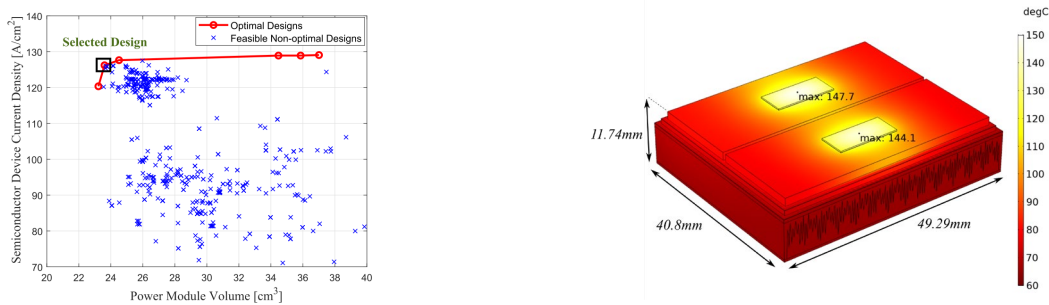


Figure I.1.1.6 (left) Design space and Pareto-front for the optimized module design, and (right) temperature profile of the module with an integrated heat sink under steady-state conditions.

Conclusions

This report introduces a new substrate, a heat sink, and integrated technologies for next-generation advanced integrated power electronic systems enabling high power density and reliability to achieve DOE ELT 2025 technical targets (100 kW/L, \$2.7/kW, and 300,000-mile lifetime). Conventional aluminum nitride-based DBC was compared with copper core-based and TPG core-based IMSs in experimental steady-state and transient thermal analyses. The IMSwTPG provided a lower junction temperature under transient and steady-state operating conditions for SiC MOSFET switches compared with IMS- and DBC-based solutions. The IMSwTPG provided reduced junction temperatures for SiC MOSFETs at rated power loss and coolant temperatures. A new heat sink design algorithm was developed using artificial intelligence and Fourier series along a multiphysics finite element analysis simulation. The develop algorithm can provide heat sink designs that are two times more compact than conventional pin-fin-based liquid-cooled heat sink solutions. Based on the multilayer IMS and compact heat sink solutions, an integrated power module for gallium nitride HEMTs was develop that provides high electrical and thermal performance.

Key Publications

1. E. Gurpinar, S. Chowdhury, B. Ozpineci, and W. Fan, “Graphite Embedded High Performance Insulated Metal Substrate for Wide-bandgap Power Modules,” *IEEE Transactions on Power Electronics*, vol. 36, no. 1, pp. 114-128, 2020. doi: 10.1109/TPEL.2020.3001528.
2. E. Gurpinar, B. Ozpineci, and S. Chowdhury, “Design, Analysis, Comparison, and Experimental Validation of Insulated Metal Substrates for High-Power Wide-Bandgap Power Modules,” *Journal of Electronic Packaging*, vol. 142, no. 4, 041107, 2020. doi: 10.1115/1.4047409.
3. E. Gurpinar, B. Ozpineci, and S. Chowdhury, “Design, Analysis and Comparison of Insulated Metal Substrates for High Power Wide-Bandgap Power Modules,” *2019 ASME International Technical Conference and Exhibition on Packaging and Integration of Electronic and Photonic Microsystems (IPACK 2019)*, Anaheim, California, USA, 2019.
4. E. Gurpinar, B. Ozpineci, J. P. Spires, and W. Fan, “Analysis and Evaluation of Thermally Annealed Pyrolytic Graphite Heat Spreader for Power Modules,” *2020 IEEE Applied Power Electronics Conference and Exposition (APEC)*, New Orleans, Louisiana, USA, pp. 2741–2747, 2020.
5. E. Gurpinar, R. Sahu, B. Ozpineci, and D. Devoto, “Analysis and Optimization of a Multi-Layer Integrated Organic Substrate for High Current GaN HEMT Based Power Module,” (lecture) *2020 IEEE Workshop on Wide Bandgap Power Devices and Applications in Asia (WiPDA Asia)*, Kyoto, Japan, 2020.

Acknowledgements

The principal investigator wishes to thank the following project team members: Randy Wiles and Jon Wilkins for mechanical design support, Starra Gribble for thermal camera setup and imaging, Shajjad Chowdhury and Larry Seiber for printed circuit board design and assembly, and Raj Sahu for heat sink design and optimization algorithms. The principal investigator wishes to thank Wei Fan from Momentive for the thermally annealed pyrolytic graphite TPG samples, Garry Wrexler for insulated metal substrate manufacturing.

I.1.2 High-Voltage, High-Power Density Traction Drive Inverter (Oak Ridge National Laboratory)

Gui-Jia Su, Principal Investigator

Oak Ridge National Laboratory
1 Bethel Valley Road
Oak Ridge, TN 37830
Email: sugj@ornl.gov

Susan Rogers, DOE Technology Development Manager

U.S. Department of Energy
Email: susan.rogers@ee.doe.gov

Start Date: October 1, 2019

End Date: September 30, 2020

Project Funding: \$400,000

DOE share: \$400,000

Non-DOE share: \$0

Project Introduction

One of the barriers to meeting the US Department of Energy (DOE) ELT 2025 power electronics targets [1] is the direct current (DC) bus capacitor in the inverter. The DC bus capacitor is needed for maintaining a stable DC bus voltage and ripple-free battery current for the voltage source inverter in electric vehicle traction drive systems. The widely used three-phase voltage source inverter is controlled with a pulse-width modulation (PWM) scheme to produce a desired set of three-phase alternating current voltages to regulate the motor current and control the motor torque and thereby generate large ripple components in the DC link current with root mean square (RMS) values over 60% of the motor currents. The DC bus filter capacitor must absorb the ripple currents and suppress voltage transients, which are detrimental to the battery life and reliability of the semiconductor switches in the inverter. Currently available capacitors that can meet the demanding requirements are costly and bulky, making up one-fifth of the volume and cost. Therefore, an urgent need exists to minimize this bulky component by significantly reducing the inverter ripple current. Unlike in DC-DC converter applications, increasing the switching frequency afforded with wide-bandgap-based switches has little impact on the RMS value of the bus capacitor ripple currents, although increasing the switching frequency does reduce the DC bus voltage and motor current ripples. The goal for this project is to increase the power density of the traction drive power electronics system to meet DOE ELT 2025 targets (100 kW/L) by focusing on power inverter architecture research and bus bar designs to reduce the requirements for passive components.

Objectives

The overall objective of this project is to develop technologies for next-generation traction drive power electronics systems with an 8× increase in power density to achieve the DOE ELT 2025 target of 100 kW/L through novel traction drive inverter architecture, optimization of bus bar design, and minimization of passive components.

The two objectives for FY 2020 were (1) to evaluate and select traction drive inverter architectures and (2) to design direct-cooled DC bus bars including embedding cooling channels and using cold plates and evaluate the effect of direct-cooled bus bars on the DC bus capacitors in various inverter configurations.

Approach

The following technical approaches were considered in this project. The first approach was selecting inverter architectures that can reduce the DC bus capacitor requirements. Multiphase inverters, segmented inverters, and open stator winding inverter drive configurations were evaluated. The second approach was increasing the inverter DC bus voltage to 800 V or higher. Doing so would better use the inherently higher voltage ratings of SiC switching devices, reduce the size of SiC dies (thus lowering the cost), and reduce phase and DC bus

currents. The third approach was optimizing designs for the inverter DC bus bars by employing embedded and distributed capacitors and direct cooling of the bus bars.

Results

A DC-ripple-energy adaptive-minimization (DREAM) modulation scheme was devised for the segmented inverter and experimentally verified with a SiC MOSFET inverter prototype (Figure I.1.2.1) in which it can further reduce the inverter DC bus ripple current over the traditional segmented PWM schemes. Figure I.1.2.2 shows inverter operating waveforms for non-segmented, traditional segmented, DREAM PWM modulation methods. Measured RMS currents of the capacitors C1 and C4 are 8.73 A for the non-segmented, 4.6 A for the traditional segmented, and 3.13 A for DREAM method. This translates to a reduction of 41.3% with the traditional segmented method and 64.3% with the DREAM method over the non-segmented inverter.

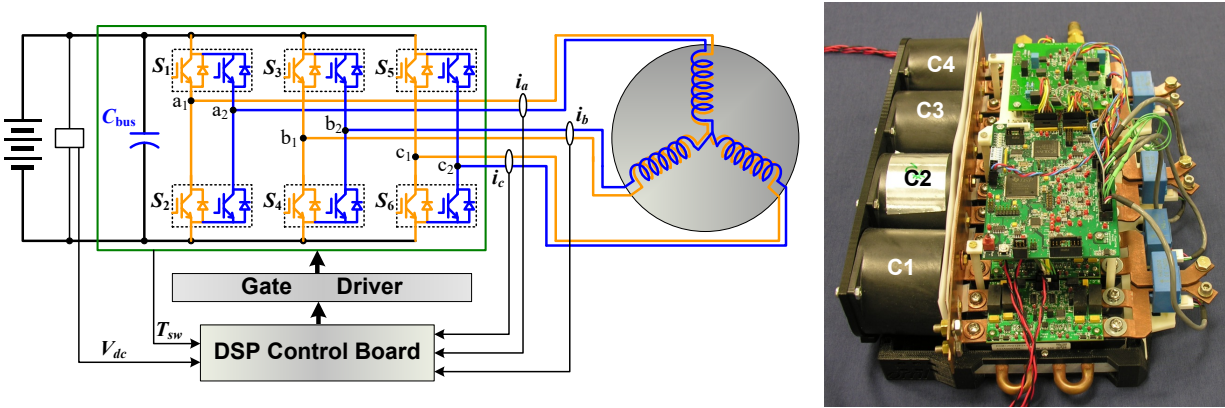


Figure I.1.2.1 (left) Block diagram of the segmented inverter and (right) photo of a prototype using SiC MOSFETs.

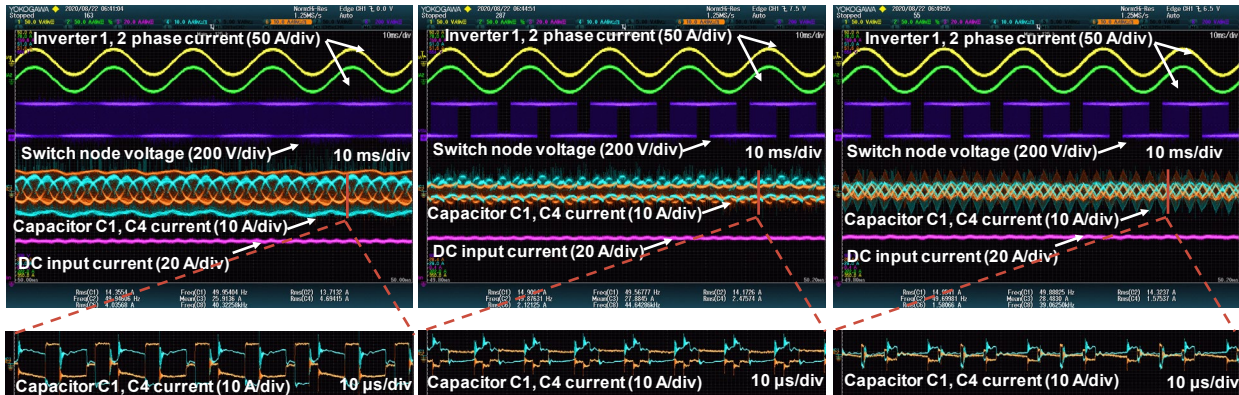


Figure I.1.2.2 Operating waveforms; left to right: non-segmented, traditional segmented, and DREAM method.

A comparison study of the segmented and open stator winding drives was carried out. Figure I.1.2.3 shows block diagrams of open stator winding drives with a single DC source in Figure I.1.2.3(a) and two separate DC sources in Figure I.1.2.3(b). The single DC source configuration is preferred for electric vehicle traction drives and was chosen for comparison in this project. Table I.1.2.1 provides a comparison of the segmented and open winding drives in terms of maximum inverter phase voltage, device current rating, and inverter rating for the linear and over-modulation ranges. For the same inverter rating, the device current rating for the segmented inverter was 86.6% of that for the open-winding drive. Additionally, over-modulation schemes cannot be applied in the open-winding drive because of the resultant zero sequence currents in the stator windings.

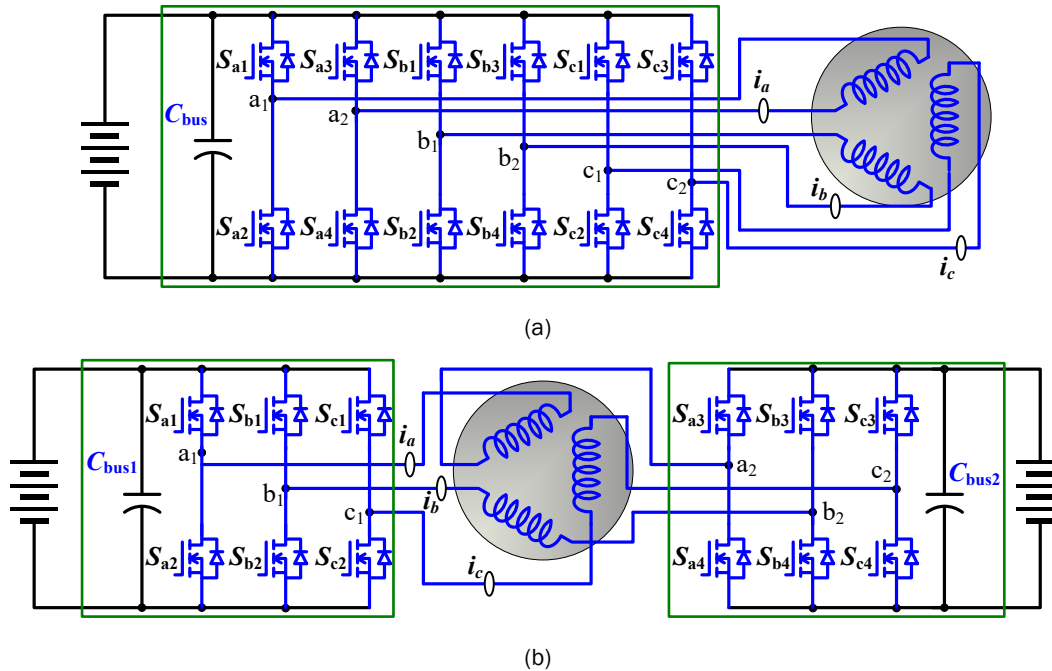


Figure I.1.2.3 Block diagram of open stator winding drives with (a) a single DC source and (b) two separate DC sources.

Table I.1.2.1 Comparison of the Segmented and Open Winding Drives

PWM modulation	Segmented drive		Open winding drive	
	Linear	Over-modulation	Linear	Over-modulation
Max. inverter phase voltage	$\frac{V_{dc}}{\sqrt{3}}$	$\frac{2V_{dc}}{\pi}$	V_{dc}	$\frac{4V_{dc}}{\pi}$
Device current rating	$\frac{I_m}{2}$		$\frac{I_m}{\sqrt{3}}$	
Inverter rating	$\sqrt{3}V_{dc}I_m$	$\frac{6V_{dc}I_m}{\pi}$	$\sqrt{3}V_{dc}I_m$	$\frac{6V_{dc}I_m}{\pi}$

A circuit model for the open-winding drive was constructed and simulated in PLECS, a commercial software package for power electronics simulations, with the following PWM schemes: (1) bipolar switching with a 120° phase shift, which can reduce the common mode voltage; (2) unipolar switching, which can reduce the switching losses; (3) symmetrical space vector (SV) PWM; (4) bus-clamp SV PWM; and (5) interleaving the carriers for the aforementioned PWM methods to reduce ripple current. Figure I.1.2.4 plots charts for comparison of DC bus ripple current in the open-winding inverter with the interleaved PWMs in dashed lines and segmented drives in solid lines at power factors of 0.7, 0.8, 0.9 and 1. The simulation results show that the segmented drive has lower DC bus ripple currents than the open-winding drives for all the cases, and the bus-clamp SV PWM produces the lowest ripple currents for the open-winding drive over the other PWM methods.

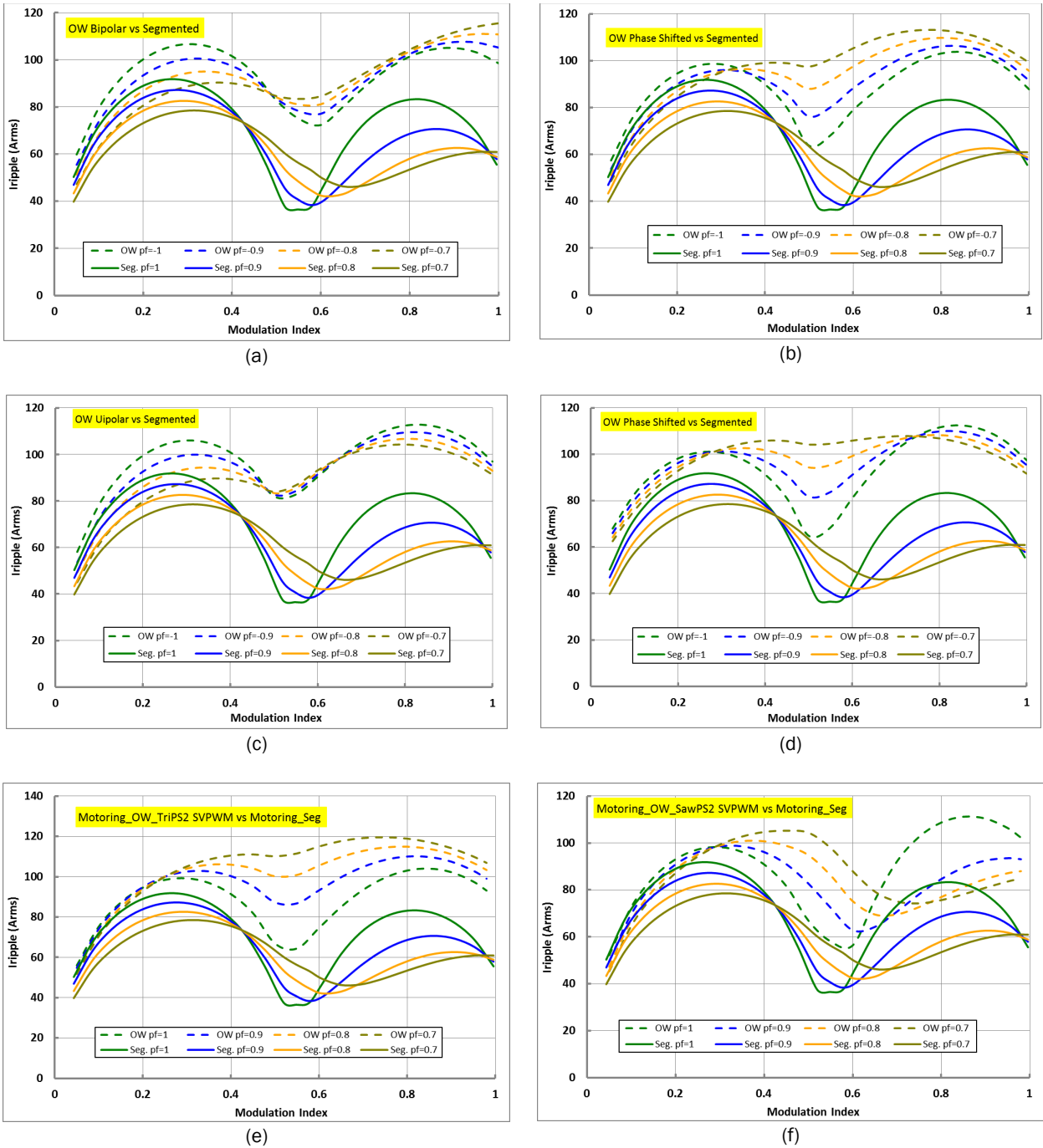


Figure I.1.2.4 Comparison of DC bus ripple currents in the open-winding (OW) (dashed lines) and segmented drives (solid lines) at various power factors with the following PWM methods for the open-winding drive: (a) bipolar switching with a 180° phase shift, (b) bipolar switching with a 120° phase shift, (c) unipolar switching, (d) bipolar switching with a 120° phase shift, (e) symmetrical SV, and (f) bus clamp SV.

A frequency domain analysis tool for the DC bus capacitor loss and temperature was developed to account for the frequency dependency of the capacitor equivalent series resistance (ESR). Figure I.1.2.5 shows a block diagram for the tool, in which the capacitor current obtained in inverter circuit simulations was fed to a fast Fourier transform block to compute the harmonic components. The capacitor loss was calculated by summing the loss of each current component on the correspond ESR interpreted using a lookup table as a function of frequency and

temperature. Figure I.1.2.6 provides results for a case study. The charts in the figure show a comparison of the frequency domain analysis results against the traditional design method in which a single typical ESR value is used as the difference in capacitor ESR loss (left) and temperature (right) vs. modulation index for the segmented PWM, non-segmented SV PWM, and non-segmented triangle carrier PWM. The results indicate the traditional method underestimated the losses by more than 18% for all three PWM schemes and capacitor temperature around 1°C for the segmented inverter but 1.5°C to 4.6°C for the other PWM methods. The narrow differences in the capacitor temperature for the segmented inverter resulted from the significantly lower ripple current.

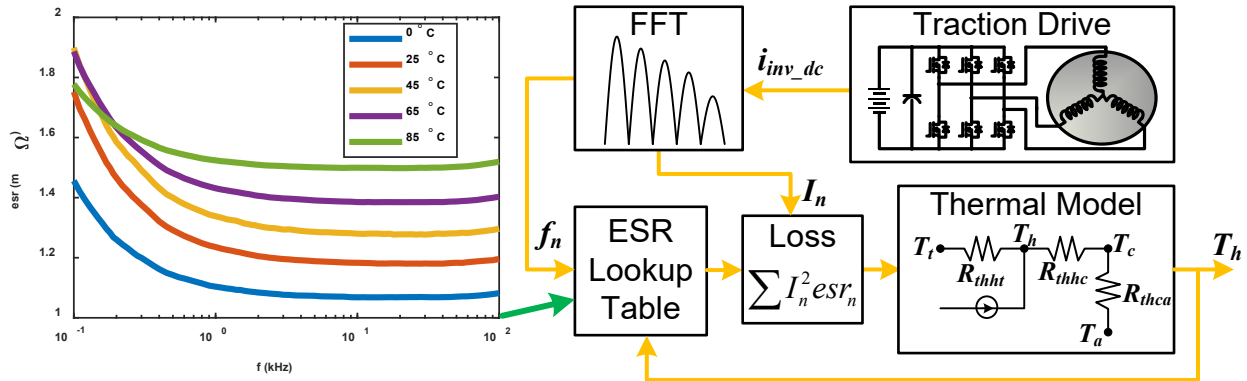


Figure I.1.2.5 Block diagram for frequency domain analysis of capacitor ESR loss and temperature. FFT = fast Fourier transform.

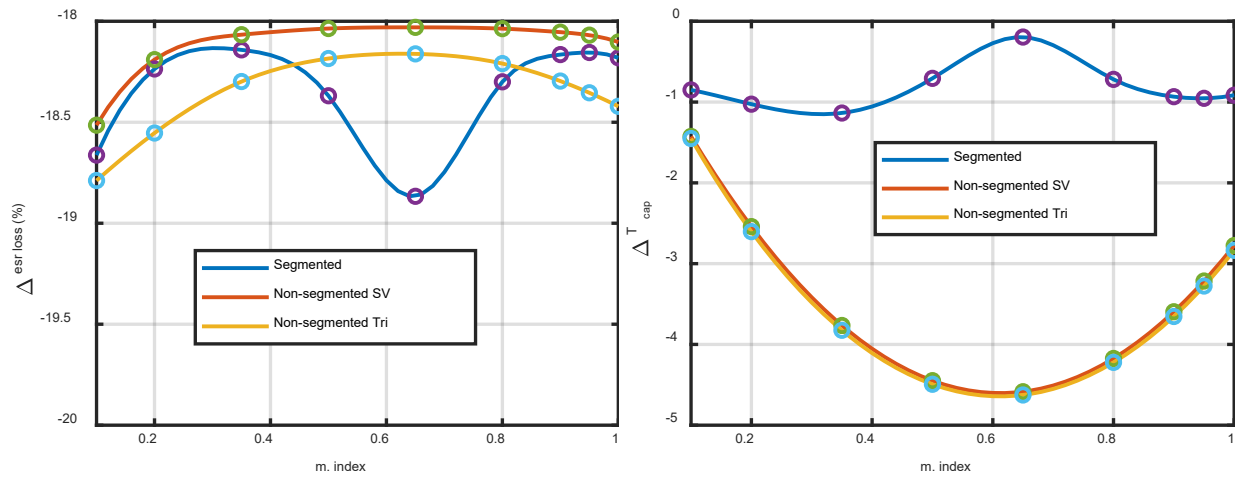


Figure I.1.2.6 Difference in (left) capacitor ESR loss and (right) temperature vs. modulation index between the traditional and frequency domain methods.

A bus bar with embedded cooling channels was designed to keep the heat losses from the inverter switches from heating the DC bus capacitors (Figure I.1.2.7). The thermal impedance of the cooling path was extracted using finite element analysis in COMSOL and used in the DC bus capacitor thermal analysis in US Environmental Protection Agency driving cycles. Figure I.1.2.8 provides the results for a case study for the US06 driving cycle. The chart shows the vehicle speed profile and the DC bus capacitor core temperatures for the non-segmented and segmented inverters with and without the direct-cooled bus bars. With direct cooling the bus bars, the capacitor temperatures reduced by 2°C to 19°C for both the inverters. Additionally, despite the segmented inverter having half the DC bus capacitors of the non-segmented inverter, its capacitor core temperatures lowered by up to 14°C compared with the non-segmented inverter under both cooling conditions.

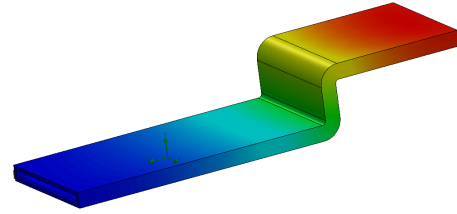


Figure I.1.2.7 Bus bar design with embedded cooling channels.

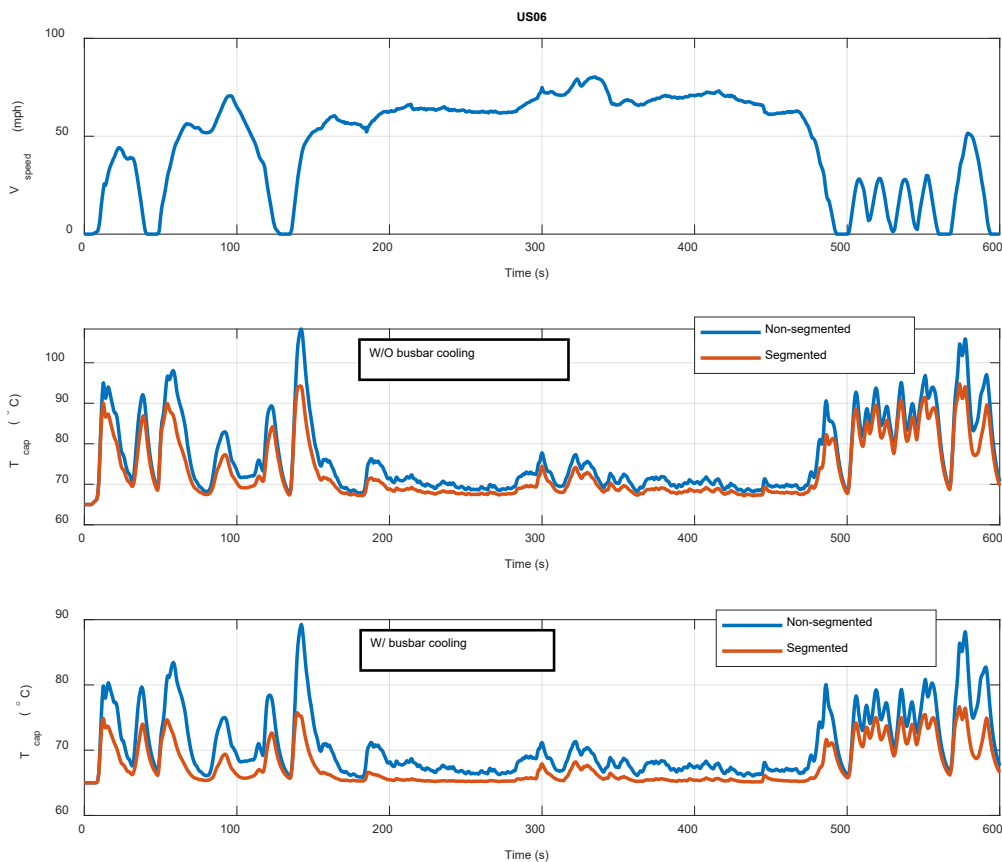


Figure I.1.2.8 Comparison of capacitor temperature with and without bus bar cooling for the US06 driving cycle.

Conclusions

A new PWM method for the segmented inverter was experimentally validated to show that it can reduce the capacitor ripple current by 23% over the conventional method.

Simulation results for the open winding drive indicate that (1) it better used the DC bus voltage but worse used the semiconductors; (2) the inverter rating reduced by 13% for the same amount of semiconductor; (3) interleaving significantly reduced the DC bus ripple current, still 15% to 100% higher than in the

segmented inverter; and (4) 3rd harmonics from the inverter and/or the motor back electromagnetic forces produce unwanted zero sequence currents.

Frequency domain analysis results indicate that the traditional design method underestimated the capacitor losses by more than 18% and the capacitor temperature around 1°C for segmented inverters but 1.5°C to 4.6°C for non-segmented inverters. Simulation results also show that with direct-cooled bus bars, the capacitor temperatures reduced by 2°C to 19°C. Additionally, despite the segmented inverter has half the DC bus capacitors of the non-segmented inverter, its capacitor core temperatures lowered by up to 14°C compared with the non-segmented inverter.

References

1. *Electrical and Electronics Technical Team Roadmap*, U.S. DRIVE, US Department of Energy, October 2017.

Acknowledgements

The PI would like to acknowledge Lincoln Xue and Randy Wiles of ORNL for their help with the experimental set up.

I.1.3 High-Fidelity Multiphysics Material Models for Electric Motors (Oak Ridge National Laboratory)

Jason Pries, Principal Investigator

Oak Ridge National Laboratory
1 Bethel Valley Road
Oak Ridge, TN 37830
Email: priesjl@ornl.gov

Susan Rogers, DOE Technology Development Manager

U.S. Department of Energy
Email: susan.rogers@ee.doe.gov

Start Date: October 1, 2019

End Date: September 30, 2020

Project Funding: \$350,000

DOE share: \$350,000

Non-DOE share: \$0

Project Introduction

The push for improved power density of electric motors and operating those motors with drives that switch at higher frequencies necessitates scrutiny of standard modeling assumptions during their design. Power-dense motors are more difficult to cool, so accurately modeling loss distributions to predict hot spots is critical for assessing the overall design of the cooling system. Furthermore, power-dense motors tend to have smaller inductances, which can result in increased pulse width modulation (PWM)–induced current ripple and can exacerbate control and efficiency challenges. The order of magnitude change in switching frequency—from about 5 to more than 50 kHz—represents an extreme challenge for PWM loss modeling. Magnetic hysteresis and eddy current losses must be accurately captured to predict losses. Additionally, how these dynamic effects are reflected in the terminal behavior of the electric machine in terms of ripple current is important for understanding the controllability of the overall drive system.

Objectives

The overall object of this project is to develop a robust methodology for analyzing the PWM-induced core losses in electric motors operating with switching frequencies of 50 kHz or greater. To accomplish this, the high-frequency PWM losses must be measured on a test sample. Additionally, a method for estimating the PWM harmonic fields in an electric machine needs to be developed that considers the effect of eddy currents on the overall field distribution and the effective high-frequency winding inductance.

Approach

A system-level diagram of the experimental test setup is depicted in Figure I.1.3.1. It uses a standard two-winding ring-core test article in which the primary current is measured to determine the magnetic field intensity and the secondary alternating current (AC) voltage is measured to determine the magnetic flux density. By adding a direct current (DC) current-blocking capacitor on the primary side and a DC voltage-blocking inductor on the secondary side, standard three-level voltage source inverter PWM waveforms seen across a single motor phase can be applied using only a standard H-bridge inverter. Example waveforms are given in Figure I.1.3.2. This approach eliminates the need to create a more complex three-phase magnetic testing apparatus.

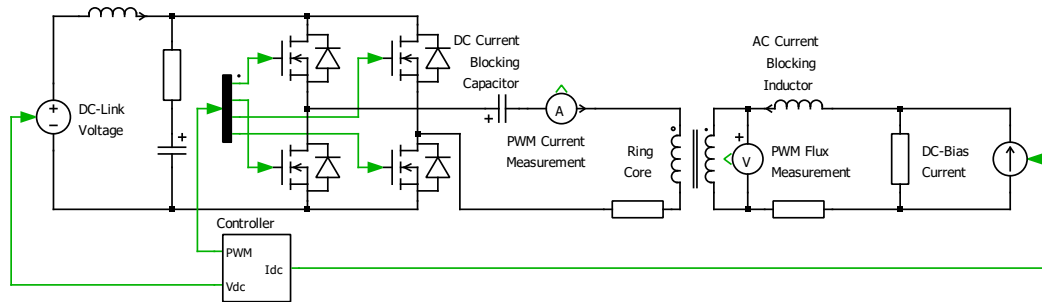


Figure I.1.3.1 System diagram for PWM loss testing using a standard ring core inductor that emulates standard three-phase voltage source inverter outputs using a single H-bridge inverter and DC-blocking components.

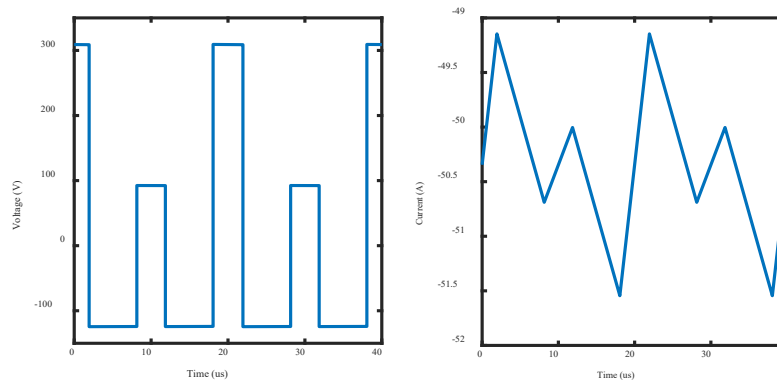


Figure I.1.3.2 Example three-level voltage source inverter voltage and current waveforms seen by a single electric motor phase that can be emulated using the single-phase approach with DC-blocking capability.

Finally, an analytical approach was taken to analyze the effect of eddy currents on the development of PWM losses. Even if the electrical steel under investigation is a perfectly isotropic magnetic material, magnetic saturation will cause any small signal excitation (such as the PWM harmonics) superimposed on the torque-producing magnetic fields to see an anisotropic permeability. Mathematically, the small-signal (differential) permeability tensor u_{ss} can be written as:

$$u_{ss} = \begin{bmatrix} u_{xx} & u_{xy} \\ u_{xy} & u_{yy} \end{bmatrix}$$

where u_{xx} , u_{xy} , and u_{yy} are the individual components of the permeability tensor. The team set out to prove some properties of this differential permeability tensor for standard isotropic nonlinear magnetic steels for low- and high-frequency excitation signals.

Results

LABView software was written to perform automatic PWM loss testing. To the greatest extent possible, this software was developed and tested at the signal level. Unfortunately, at the time of writing, limited laboratory access due to the impacts of the COVID-19 pandemic have prevented the team from fully characterizing the test samples high-frequency loss characteristics. Before the COVID-19 pandemic, the team verified the principles of operation of the system as depicted in Figure I.1.3.1. Figure I.1.3.3 shows the variation-measured PWM core losses as a function of duty ratio, which successfully demonstrates the measurement of AC losses in the presence of DC bias.

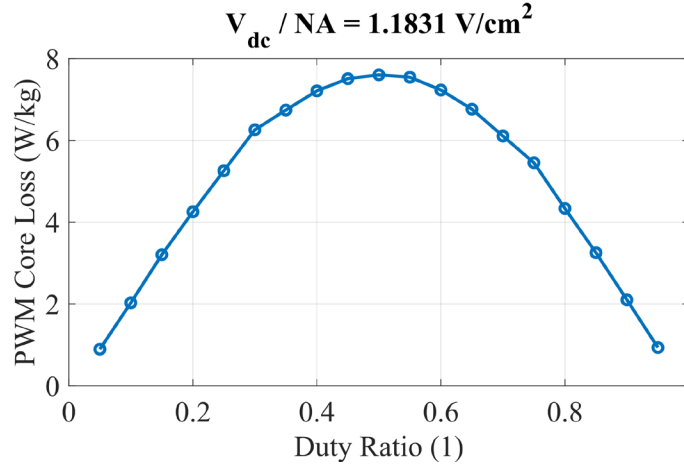


Figure I.1.3.3 Variation of PWM losses with duty ratio for a simple test case.

This analysis of the differential permeability tensor in isotropic, nonlinear sheet steels demonstrated that the permeability tensor can be decomposed into the following form,

$$u_{rot} = \begin{bmatrix} u_d & 0 \\ 0 & u_a \end{bmatrix}$$

by rotating the local coordinate system to align with the torque-producing bias field. Here, u_{rot} is the permeability tensor u_{ss} expressed in the coordinate system aligned with the bias field, u_d is the nonlinear material’s differential permeability at the bias point, and u_a is the nonlinear material’s amplitude permeability. Figure I.1.3.4 shows the difference between the amplitude permeability and differential permeability for a typical non-oriented electrical steel as a function of bias field magnitude.

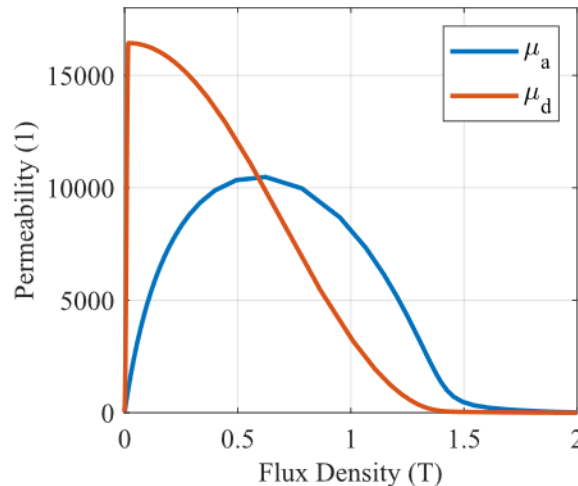


Figure I.1.3.4 Plot of amplitude permeability and differential permeability of a typical non-oriented silicon steel.

The axis of the u_{rot} associated with u_d is aligned with bias field, and the axis associated with u_a is perpendicular to the bias field. These results show that the magnetic fields see two different permeabilities, depending on their alignment with the bias field. Figure I.1.3.4 shows that at low bias field levels, the fields resulting from PWM harmonics are likely to align with the bias field. As the bias fields become higher, the amplitude permeability eventually exceeds the differential permeability and the PWM harmonic fields are likely to change direction. The important conclusion to draw from this is that because of the complex ways the PWM fields can develop, some connection between the 2D field model and bulk PWM loss characterization must be made to accurately predicted PWM losses in electric machines.

Finally, at high frequencies, the complex permeability (both amplitude and differential) of the permeability tensor μ_{rot} are given by

$$\tilde{\mu} = \mu \frac{\delta}{t(1+j)} \tanh\left(\frac{t(1+j)}{\delta}\right)$$

Here, μ is the permeability (either amplitude or differential), δ is the skin depth associated with that permeability, and t is half of the lamination thickness. The real part of the complex permeability represents the energy storage (inductive) part of the material, whereas the imaginary part represents the lossy part of the material due to eddy currents. Figure I.1.3.5 provides examples of the complex amplitude and differential permeability for the sample material assuming a 0.25 mm lamination thickness and excitation at 5 kHz. The values for 5 kHz rather than 50 kHz are shown to allow a greater distinction between the real and imaginary parts of the permeabilities. At 50 kHz, the curves are nearly indistinguishable over a very large range of bias fields.

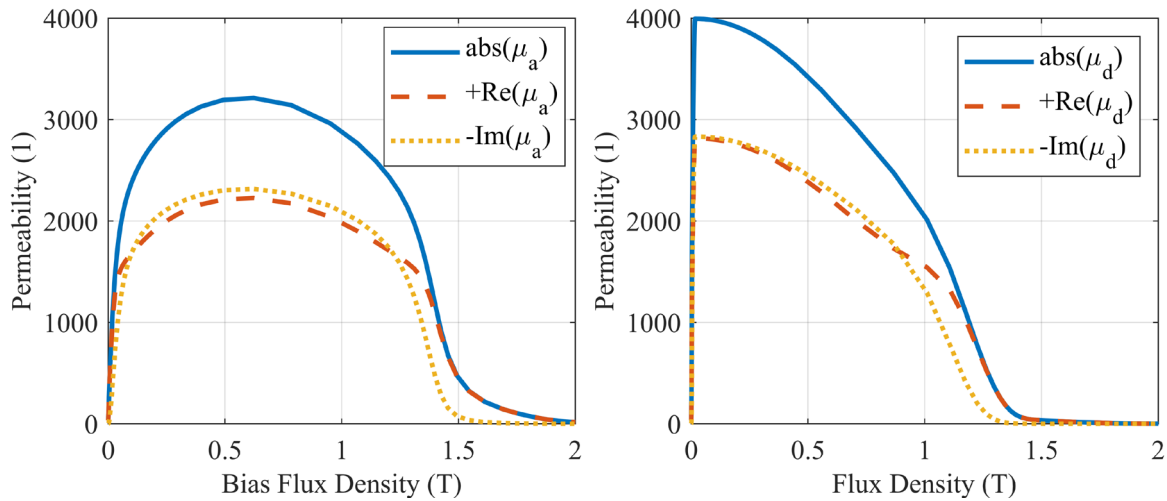


Figure I.1.3.5 Complex amplitude and differential permeabilities for a typical 0.25 mm thick non-oriented electrical steel excited at 5 kHz.

At just 5 kHz, the permeability magnitudes are about one-third to one-fourth of the low frequency permeabilities. At 50 kHz, the magnitudes are likely to drop by another one-third. This can greatly affect the high frequency inductance of the electric motor that is seen by the inverter. In turn, this can increase the PWM-induced current ripple and further increase PWM losses. Fortunately, this frequency-dependent permeability tensor is easily implemented in existing finite element analysis software such as COMSOL for analyzing frequency-dependent losses and inductances.

Conclusions

It is possible to develop a single-phase system to test PWM losses under similar waveforms and bias conditions that are experienced by phase windings in electric motors. The PWM excitation interacts in complex ways with the nonlinearity of the material, and nominal isotropic materials present a complex anisotropic material property to the PWM excitation, which depends on bias field, sample geometry, and excitation frequency. For the best predictions on the effect of PWM losses, empirical testing data should be coupled with finite element analysis to take into account the 2D field effects on the core losses.

Acknowledgements

The principal investigator would like to especially thank Tsarafidy Raminosa for providing some of the motor models that were used in the some of the finite element modeling efforts.

I.1.4 Non-Heavy Rare-Earth High-Speed Motors (Oak Ridge National Laboratory)

Tsarafidy Raminosoa, Principal Investigator

Oak Ridge National Laboratory
1 Bethel Valley Road
Oak Ridge, TN 37831
Email: raminosoat@ornl.gov

Susan Rogers, DOE Technology Development Manager

U.S. Department of Energy
Email: susan.rogers@ee.doe.gov

Start Date: October 1, 2019
Project Funding: \$470,000

End Date: September 30, 2020
DOE share: \$470,000

Non-DOE share: \$0

Project Introduction

A push for higher torque density and lower cost traction motors is happening globally. The use of non-heavy rare-earth permanent magnet (PM) materials in traction motors is being investigated for the sustainability, profitability, and affordability of electric vehicles and to broaden their adoption. A 20,000 rpm PM traction motor using non-heavy rare-earth magnet materials is proposed. A dual three-phase winding configuration driven by a segmented dual three-phase drive is proposed to reduce the current ripple and thereby reduce the direct current (DC) link capacitor, as well as ease the voltage constraint at high speed and eliminate any risk of uncontrolled regeneration. Furthermore, the dual winding configuration enables a fault-tolerant design, which is useful for reliability. This report presents comprehensive electromagnetic, thermal, and mechanical designs and analyses using an integrated approach. The results have shown that the design is robust against demagnetization and confirmed its thermal and mechanical viability.

Objectives

The overall objectives of this project are to enable the adoption of high-speed and high-power density non-heavy rare-earth traction motors and analyze the effect of new advanced materials for non-heavy rare-earth electric motors. More specifically, the objectives for FY 2020 are to:

- Design a dual three-phase non-heavy rare-earth PM high-speed traction motor to meet the US Department of Energy's Electrification Technologies 2025 specifications.
- Design the thermal management system and the mechanical assembly of the motor.

Approach

For battery electric vehicles, research and development efforts on traction motors are currently pushed toward high-power density to maximize passenger comfort and cargo space while keeping high efficiency to maximize the vehicle's range [1]. To this end, a high-speed (up to 20,000 rpm) non-heavy rare-earth PM traction motor with a peak power of 100 kW was designed to target the U.S. DRIVE specifications presented in Figure I.1.4.1. The motor uses a PM material free of dysprosium [2]. An outer rotor Halbach surface PM with concentrated tooth winding (Figure I.1.4.2) was selected for the following reasons:

1. It offers the opportunity to integrate the power electronics within the inner hollow volume of the stator.
2. Magnet retention against centrifugal force is naturally provided by the rotor yoke and the rotor support structure. Additionally, the rotor has a robust continuous construction as opposed to a spoke PM rotor, which has a segmented rotor construction, or an interior PM rotor, which relies on thin lamination bridges and posts for structural integrity.

- The air-gap radius is at the outermost possible location, which helps maximize the torque density. A previous study showed that this topology has the highest power density among several potential candidates [3].
- Tooth winding is chosen for the associated high direct inductance that improves flux weakening capability. Such winding also enables low torque ripple.

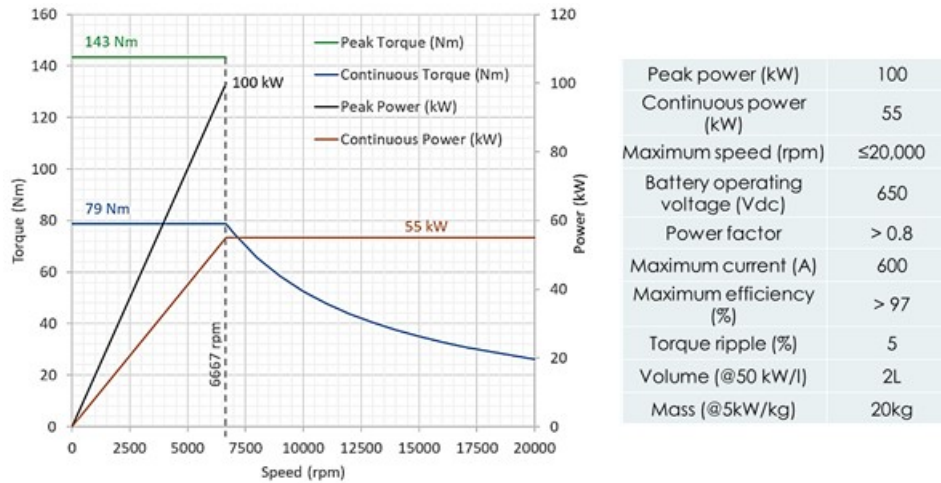


Figure I.1.4.1 Summary of specifications.

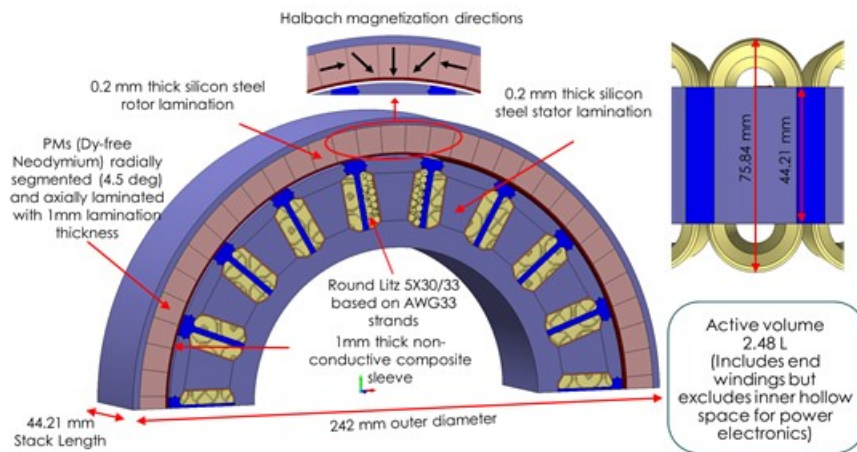


Figure I.1.4.2 Heavy rare-earth-free outer rotor PM traction motor.

A dual three-phase winding configuration is proposed so the motor can be powered by a dual three-phase segmented drive featuring interleaved switching to reduce the current ripple and thereby reduce the DC link capacitor (Figure I.1.4.3) [4]. This winding configuration also halves the back electromotive force on each set of windings and therefore eases the voltage constraint at high speeds and eliminates uncontrolled regeneration. Moreover, the dual winding configuration enables fault tolerance, which, although not required, is useful for operating at reduced performance to allow the vehicle to continue to move.

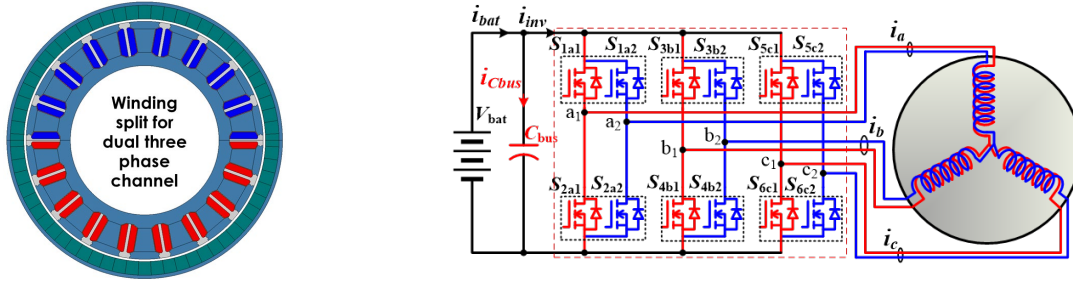


Figure I.1.4.3 Segmented drive of a dual three-phase channel motor enabling reduction of the DC bus capacitor ripple current [4].

Results

Electromagnetic characterization of the design

The designed 18 slot/20 pole motor with the dimensions and the different materials used is shown in Figure I.1.4.2. Since non-heavy rare-earth PMs are more prone to demagnetization than their conventional counterparts with heavy rare earth, special attention must be paid to the demagnetization risk. Therefore, a Halbach magnetization arrangement was chosen to maximize the air-gap flux density and reinforce the resistance to demagnetization. The torque waveform was calculated and is presented in Figure I.1.4.4. With an average torque of 163 Nm and only 1.3% ripple, the design meets the peak power and torque quality requirements. The line-to-line open-circuit voltage waveform at 20,000 rpm is also shown in Figure I.1.4.4. It is very close to the sinusoidal shape and its peak value is below the 650 V DC-link voltage. This confirms that there is no risk of uncontrolled regeneration.

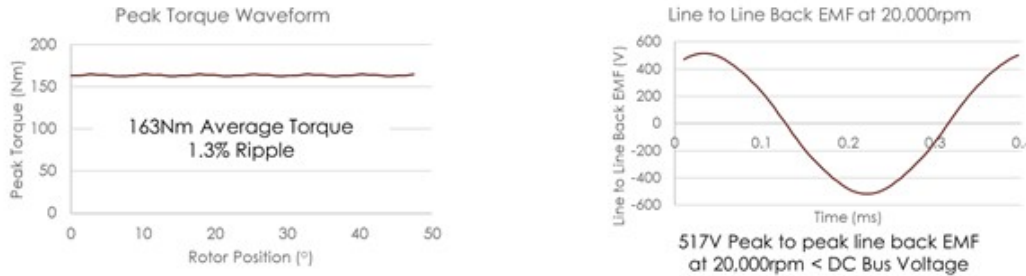


Figure I.1.4.4 Peak torque waveform with 12% design margin and line-to-line back electromotive force (EMF) waveform at 20,000 rpm.

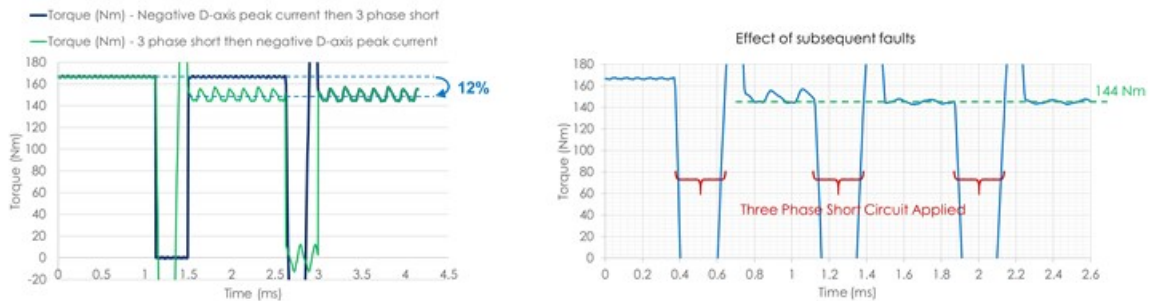


Figure I.1.4.5 Demagnetization resistance under transient three-phase short-circuit at 20,000 rpm with a PM temperature of 150 °C: (a) effect of purely negative d-axis peak current versus three-phase short circuit and (b) effect of subsequent faults.

To evaluate the risk of demagnetization, extreme scenarios of transient three-phase short-circuit fault and purely negative peak current were simulated at 20,000 rpm using finite element analysis featuring dynamic

nonlinear demagnetization modeling. The assumed temperature of the PMs was 150°C. The resulting reduction of the torque capability is shown in Figure I.1.4.5. Figure I.1.4.5(a) compares the effects of a three-phase short-circuit fault and purely negative d-axis current. The three-phase short circuit fault is more severe and causes 12% torque reduction. The order of occurrence of the two types of faults does not affect the torque reduction. Moreover, if several subsequent faults are applied, the torque stabilizes at 144 Nm and still meets the peak torque requirement (Figure I.1.4.5(b)). This confirms that the design is resistant to demagnetization and a 12% design margin was introduced to compensate for the worst-case demagnetization as shown in Figure I.1.4.4 [3]. Finally, the calculated active volume is 2.48 L. This includes the end windings assumed as arc-shaped (Figure I.1.4.2) but excludes the stator inner hollow space where the power electronics will be integrated.

Given the high operating frequency, especially at high speeds, 5×30/33 round Litz wire based on AWG33 strands was necessary for the stator winding [5]. The induced eddy current loss was evaluated on a sample of strands for all the positions of the Litz wire bundles on a tooth-wound coil as shown in Figure I.1.4.6 [6], [7]. Two-dimensional finite element analyses were carried out for a given current at 20,000 rpm. The average of the AC loss factors calculated on the bundles was used as the overall AC loss factor. For other speeds, the AC loss factor was calculated by scaling the AC component of the loss with the speed squared. The calculated AC loss factors for a range of speeds are presented in Figure I.1.4.6: the fraction of AC loss is less than 5% of the DC copper loss because of the choice of a Litz wire based on AWG33 strands.

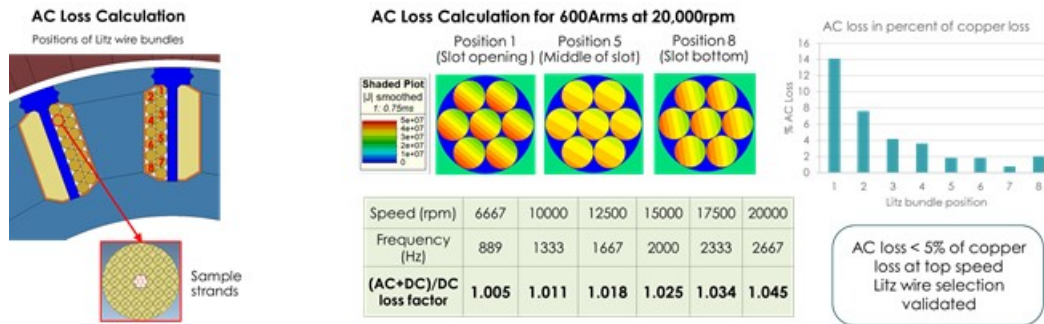


Figure I.1.4.6 AC loss calculation.

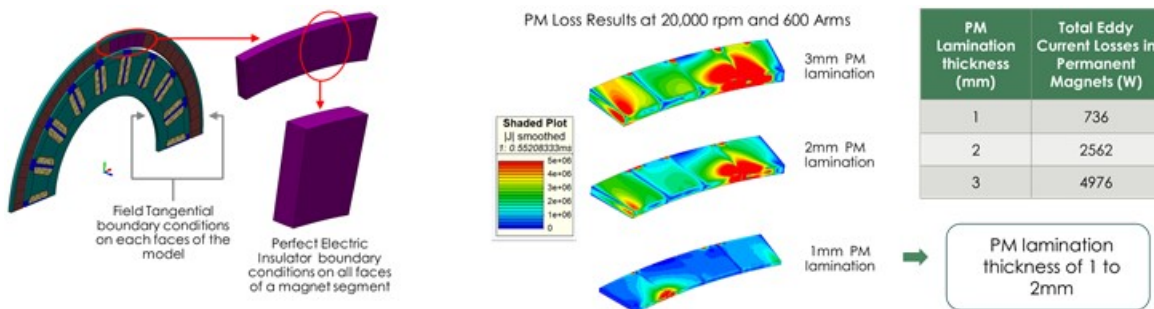


Figure I.1.4.7 Calculation of PM eddy current loss.

The rotor uses a four-segment Halbach arrangement per pole with laminated PMs (Figure I.1.4.2). Therefore, the magnets are segmented both circumferentially and axially and the eddy current flow is three-dimensional. To accurately calculate the eddy current loss, a 3D finite element model was created with an axial length equal to the thickness of a PM lamination as described in Figure I.1.4.7. PM lamination thicknesses of 1, 2, and 3 mm were analyzed. The eddy current losses in PMs were evaluated for one operating point (600 Arms at 20,000 rpm). For other operating points, the losses were scaled with the current squared and speed squared. The calculated total eddy current loss is presented in Figure I.1.4.7. A PM lamination thickness of 1 mm was chosen to minimize the eddy current loss while ensuring manufacturability [8].

The calculated torque, power, efficiency, and power factor of the design are presented in Figure I.1.4.8. The figure shows that the design can provide the required continuous 55 kW power with a 12% design margin for the whole speed range while staying within the current and voltage limits. Furthermore, the efficiency specification is met, and the motor has a very good efficiency across the whole speed range (98% at base speed and 94.7% at top speed).

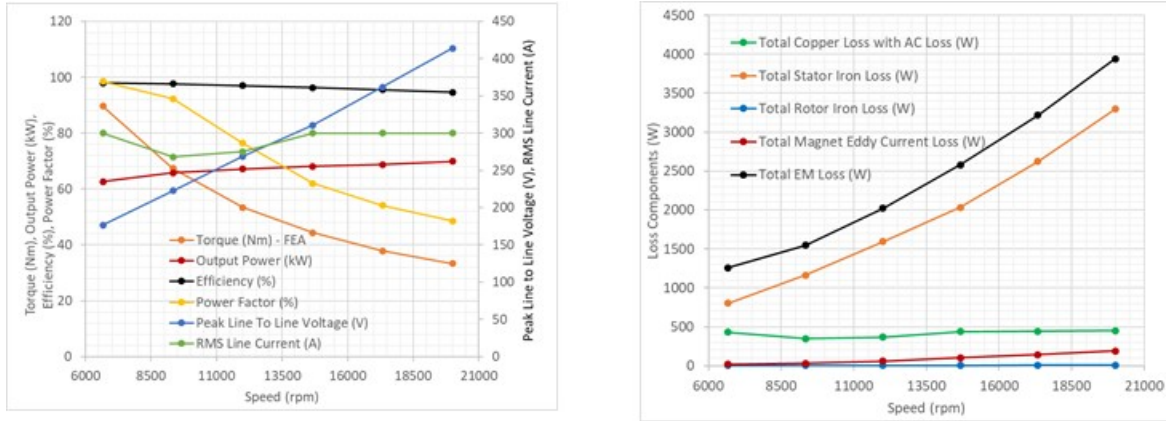


Figure I.1.4.8 Performance under 55 kW continuous operation and electromagnetic loss components for 0.2 mm lamination thickness.

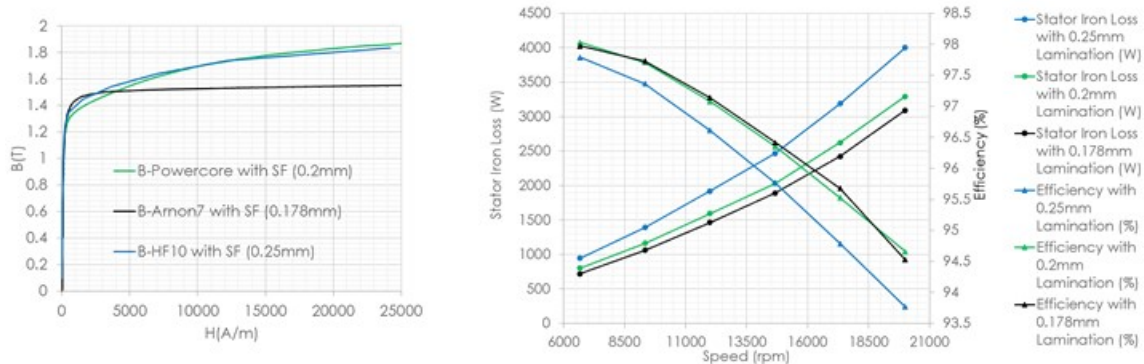


Figure I.1.4.9 B-H curves and iron loss and efficiency for various silicon lamination thicknesses.

Given the high operating frequency, commercially available thin-gauge silicon steel laminations were considered [9]–[12]. The various electromagnetic loss components are presented in Figure I.1.4.8 for a 0.2 mm thick stator and rotor laminations [10]. The stator iron loss is the predominant loss component across the whole speed range. The magnet eddy current losses are kept low even at high speed because of the segmentation and lamination of the PMs. Furthermore, all the loss components are the highest at 20,000 rpm operation, resulting in the highest heat losses and temperatures at this operating condition. Finally, analyses indicated that the tooth shoes and tooth shanks have the highest loss density, and therefore, they are potential hot spots. Figure I.1.4.9 shows the iron loss and efficiency for various commercially available thin-gauge silicon steel lamination thicknesses: 0.25 mm Di-Max HF-10 from AK Steel [9], 0.2 mm powercore 020-150Y320 from Thyssenkrupp [10], and 0.178 mm Arnon 7 from Arnold Magnetics [11],[12]. Figure I.1.4.9 suggests that the 0.2 mm thick silicon steel is the best compromise between iron loss and cost.

Mechanical viability

The overall mechanical assembly is presented in Figure I.1.4.10. Mechanical stress analyses were conducted at the maximum speed of 20,000 rpm to verify the mechanical integrity of the assembly. The results are shown in Figure I.1.4.11. According to Figure I.1.4.11(a), the stresses are below 860 MPa. Commercially available high-

strength stainless steel with a tensile strength of 1,300 MPa and yield strength of 1,000 MPa can be used for the rotor support [13]. Figure I.1.4.11(b) shows a maximum displacement of 0.22 mm. It should be noted that the displacement is radially outward and increases the designed 1 mm mechanical air gap. Hence, there is no risk of rubbing between the rotor and stator. Further improvement of the rotor support is being carried out to reduce the deformation. The above results support the viability of the proposed rotor assembly concept.

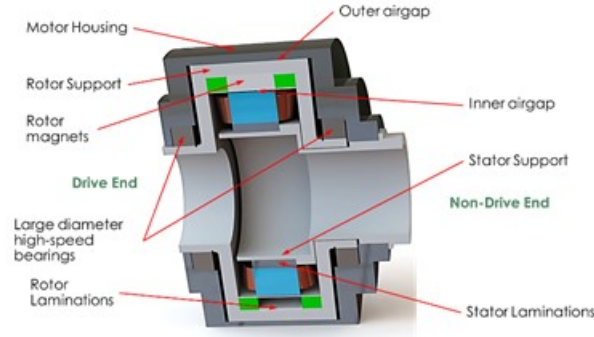


Figure I.1.4.10 Mechanical assembly.

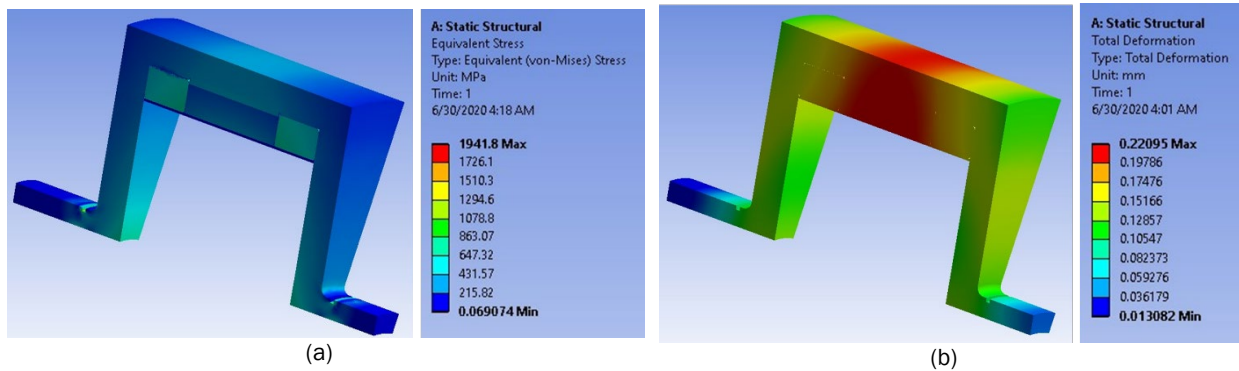


Figure I.1.4.11 Mechanical stress analysis at 20,000 rpm: (a) equivalent stress and (b) deformation.

Thermal viability (refer to project elt214 “Electric Motor Thermal Management” by Kevin Bennion [NREL])

The thermal analysis and cooling system design were conducted in collaboration with the National Renewable Energy Laboratory (NREL). The calculation of the loss distribution in the motor, including the AC losses in the winding and the eddy current losses in the magnets, and the design of the mechanical assembly were carried out at the US Department of Energy’s Oak Ridge National Laboratory. NREL performed the thermal modeling and analysis focused on 3D finite element analysis to evaluate effects and interactions between passive thermal design elements and the active cooling design. The thermal model was developed using material properties from literature [5],[14],[15]. This included evaluating the thermal impacts of alternative materials (such as lamination materials), active cooling locations, and active cooling heat transfer coefficients to identify cooling performance metrics. The thermal approach looked at applying cooling as close as possible to the heat generation sources in the windings and the magnets. The windings were cooled by a 3D printed ceramic heat exchanger similar to the one used by Sixel et al. [16]. The phase separators are converted into heat exchangers. The magnets were cooled using an oil flow through the rotor. The combined approach is very well-suited to cooling the magnets, windings, stator yoke, and tooth tips as illustrated in Figure I.1.4.12. The preliminary results presented in Figure I.1.4.13 show that, with the combined cooling approach, the maximum temperature reaches about 163°C. With additional refinement of the cooling design, further temperature reductions are expected.

Figure I.1.4.13 also compares the maximum temperatures in the motor resulting from the different losses due to varying lamination materials. Although thinner laminations reduce the stator iron loss, they tend to be more expensive, and their saturation flux density was lower. The lower saturation flux density results in the need for higher current and consequently more losses in the in the windings. A case in which the boundary condition representing the rotor cooling was removed is also highlighted in Figure I.1.4.13. Although the magnet temperature increases dramatically compared to a rotor with active cooling, the temperature is below the temperature limit of 150°C. Removing the requirement for rotor cooling benefits the motor in terms of reduced complexity and cost.

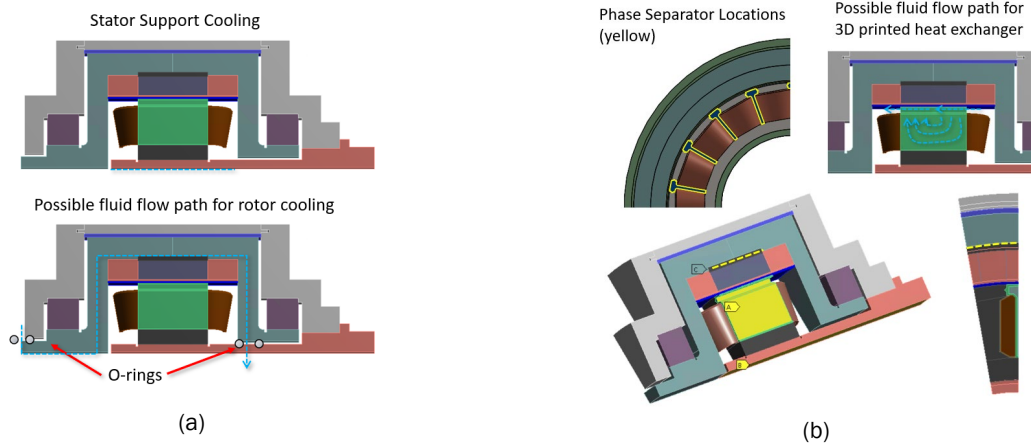


Figure I.1.4.12 Cooling strategy: (a) stator support and rotor cooling and (b) slot heat exchanger (refer to project elt214 “Electric Motor Thermal Management” by Kevin Bennion [NREL]).

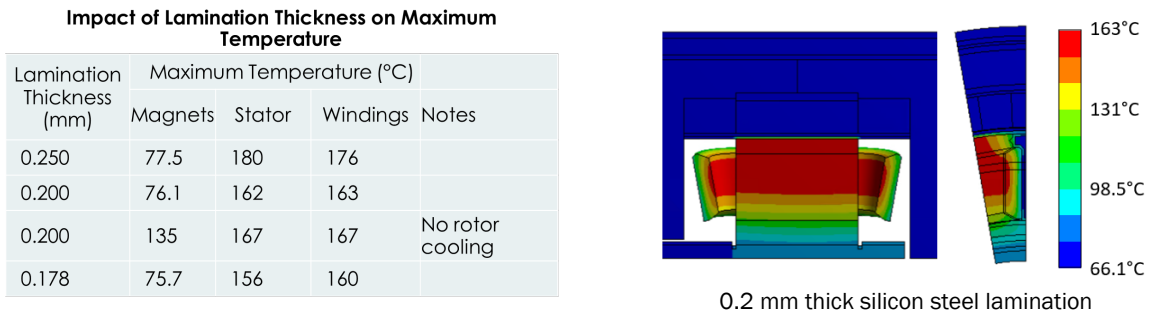


Figure I.1.4.13 Effect of lamination thickness on maximum temperatures and temperature distribution for 55 kW, 20,000 rpm operation (refer to project elt214 “Electric Motor Thermal Management” by Kevin Bennion [NREL]).

Conclusions

A high-speed non-heavy rare-earth outer rotor Halbach surface PM traction motor was designed with an integrated approach considering the electromagnetic, thermal, and mechanical aspects to meet an aggressive set of specifications. The design meets the 100-kW peak and 55 kW continuous power, torque ripple, current, voltage, and efficiency requirements. Furthermore, the design is robust against demagnetization even under the worst-case scenarios. Given the high operating frequency, elaborate winding AC loss and PM eddy current loss models were developed to accurately predict these critical loss components and ensure a reliable input to the thermal analyses. Although the very aggressive volume specification is not met, the calculated hot-spot temperature is close to the specification, and mechanical stress analyses have confirmed the viability of the design. Moreover, the possibility of avoiding active cooling of the rotor greatly simplifies the integration of the cooling system. Further refinement of the mechanical design to reduce the deformation at high speed, the cooling system design to reduce the hot-spot temperature down to 150°C, and the integration of the cooling system to the assembly are currently being carried out.

Key Publications

1. T. Raminosoa, R. Wiles, J. E. Cousineau, K. Bennion, and J. Wilkins, “A High-Speed High-Power-Density Non-Heavy Rare-Earth Permanent Magnet Traction Motor,” *2020 IEEE Energy Conversion Congress and Exposition (ECCE 2020)*, October 11, 2020.

References

1. *Electrical and Electronics Technical Team Roadmap*, U.S. DRIVE, October 2017, [Online] available at <https://www.energy.gov/sites/prod/files/2017/11/f39/EETT%20Roadmap%2010-27-17.pdf>
2. *TDK Dysprosium free Neodymium Magnet*, TDK, [Online] available at https://product.tdk.com/info/en/catalog/datasheets/magnet_neo_neorec45mhf_en.pdf
3. T. Raminosoa and T. Aytug, “Impact of Ultra-Conducting Winding on the Power Density and Performance of Non-Heavy Rare Earth Traction Motors,” *2019 IEEE International Electric Machines & Drives Conference (IEMDC)*, San Diego, California, USA, pp. 2107–2114, 2019, doi: 10.1109/IEMDC.2019.8785295.
4. G. Su and L. Tang, “A segmented traction drive system with a small dc bus capacitor,” *2012 IEEE Energy Conversion Congress and Exposition (ECCE)*, Raleigh, North Carolina, USA, pp. 2847–2853, 2012, doi: 10.1109/ECCE.2012.6342375.
5. *Litz Wire Technical Information*, New England Wire Technologies, 2003, [Online] available at http://www.litzwire.com/nepdfs/Litz_Technical.pdf
6. T. Raminosoa, A. M. El-Refai, D. Pan, K.-K. Huh, J. P. Alexander, K. Grace, S. Grubic, S. Galioto, P. B. Reddy, and X. Shen, “Reduced Rare-Earth Flux-Switching Machines for Traction Applications,” *IEEE Transactions on Industry Applications*, vol. 51, no. 4, pp. 2959–2971, 2015, doi: 10.1109/TIA.2015.2397173.
7. T. Raminosoa, D. A. Torrey, A. M. El-Refai, K. Grace, D. Pan, S. Grubic, K. Bodla, and K.-K. Huh, “Sinusoidal Reluctance Machine with DC Winding: An Attractive Non-Permanent-Magnet Option,” *IEEE Transactions on Industry Applications*, vol. 52, no. 3, pp. 2129–2137, 2016, doi: 10.1109/TIA.2015.2512521.
8. “L Type Laminated Magnets,” Arnold Magnetic Technologies, [Online] available at <https://www.arnoldmagnetics.com/products/l-type-laminated-magnets/>
9. *DI-MAX HF-10 Cold Rolled Fully Processed Non-Oriented Electrical Steel*, AK Steel, [Online] available at <https://www.aksteel.com/sites/default/files/2019-10/di-max-hf-10.pdf>
10. *powercore 020-150Y320*, ThyssenKrupp, [Online] available at https://www.thyssenkrupp-steel.com/media/content_1/publikationen/produktinformationen/powercore_no/thyssenkrupp_powercore_020-150y320_product_information_steel_en.pdf
11. Arnold Magnetic’s Arnon 7 Non-Grain Oriented Electrical Silicon Steel Magnetization Chart, [Online] available at <https://www.arnoldmagnetics.com/wp-content/uploads/2017/10/Arnon-7-NGOES-Magnetization-Curve-1.pdf>
12. *Arnon 7 Non-Grain Oriented Electrical Silicon Steel Core Loss Chart*, Arnold Magnetic Technologies, [Online] available at <https://www.arnoldmagnetics.com/wp-content/uploads/2017/10/Arnon-7-NGOES-Core-Loss-Curve-1.pdf>

13. *410 Grade Data Sheet*, Atlas Steels, [Online] available at <http://www.atlassteels.com.au/documents/Atlas%20Grade%20datasheet%20410%20rev%20May%202008.pdf>
14. J. E. Cousineau, K. Bennion, D. DeVoto, and S. Narumanchi, “Experimental characterization and modeling of thermal resistance of electric machine lamination stacks,” *International Journal of Heat and Mass Transfer*, vol. 129, pp. 152–159, 2019.
15. A. A. Wereszczak, J. E. Cousineau, K. Bennion, H. Wang, R. H. Wiles, T. B. Burrell, T. Wu, “Anisotropic Thermal Response of Packed Copper Wire,” *Journal of Thermal Science and Engineering Applications*, vol. 9, no. 4, art. no. 041006, 2017, doi: 10.1115/1.4035972.
16. W. Sixel, M. Liu, G. Nellis, and B. Sarlioglu, “Cooling of Windings in Electric Machines via 3D Printed Heat Exchanger,” *2018 IEEE Energy Conversion Congress and Exposition (ECCE)*, Portland, Oregon, USA, pp. 229–235, 2018, doi: 10.1109/ECCE.2018.8557845.

Acknowledgements

The principal investigator would like to thank Oak Ridge National Laboratory’s Randy Wiles and Jon Wilkins for the design of the mechanical assembly of the outer rotor surface permanent magnet motor and the mechanical stress analysis, and NREL’s Emily Cousineau and Kevin Bennion for the thermal analysis and design (refer to project elt214 “Electric Motor Thermal Management” by Kevin Bennion [NREL]).

I.1.5 Integrated Electric Drive System (Oak Ridge National Laboratory)

Shajjad Chowdhury, Principal Investigator

Oak Ridge National Laboratory
1 Bethel Valley Road
Oak Ridge, TN 37932
Email: chowdhuryms@ornl.gov

Susan Rogers, DOE Technology Development Manager

U.S. Department of Energy
Email: susan.rogers@ee.doe.gov

Start Date: October 1, 2019
Project Funding: \$400,000

End Date: September 30, 2020
DOE share: \$400,000

Non-DOE share: \$0

Project Introduction

In recent years, the US Department of Energy (DOE) announced technical targets for light-duty electric vehicles. DOE targets a power density of 33 kW/L for a 100 kW traction drive system by 2025 [1], which is an increment by a factor of 5.5 compared to the 2020 target. This project focuses on the tight integration of motor and inverter components to improve power density to achieve the target. In addition to optimizing integration technique, this project optimizes the bulky DC link capacitor's volume and improves electrical performance and lifetime by identifying high-energy density capacitor technologies and their packaging techniques.

Objectives

This project's overall objective is to research technologies that will allow tight integration of the inverter with the motor resulting in a high-power density-integrated traction drive. Specific objectives for FY 2020 include

- Identifying integration solutions for outer rotor motor to achieve the 2025 DOE Electrification targets
- Evaluating emerging capacitor technologies and identifying packaging techniques to optimize volume and electrical performance
- Designing a heat sink for the power module developed in DOE Electrification 208 (Keystone #1) to integrate within the outer rotor motor.

Approach

The approach to achieving the objectives is to

- Find possible integration methods for the outer rotor motor
- Identify and evaluate emerging capacitor technologies and down-select one for volume optimization
- Identify ways to package capacitors to complement wide bandgap devices
- Optimize the heat sink for the identified inverter geometry to be integrated into the outer rotor motor.

Results

Integration of Motor and Inverter

An integrated motor drive involves integrating all the components of an electric drive unit into a single casing, thus reducing volume, cost, and installation complexity. A tightly integrated drive can increase power density by 10%–20% with a concomitant reduction of manufacturing and installation costs by 30%–40% [2]. According to the literature, there are four different types of integration techniques, listed by Chowdhury et al.

[3]. These integration techniques are introduced considering a traditional motor design in which the rotor is placed inside the stator. In the electric motor development project (Keystone #2), an outer rotor motor is designed to achieve high power density, as shown in Figure I.1.5.1(a). The designed outer rotor motor has a rotating part outside the motor and has a complex mechanical structure; thus, not all the traditional integration techniques can be used. The only two options are an axial endplate mount and a radial housing mount, but they may not be suitable for tight integration. Thus, a novel integration technique was identified in which the inverter can be integrated inside the stator named “internal stator mount integration” as shown in Figure I.1.5.1(b).

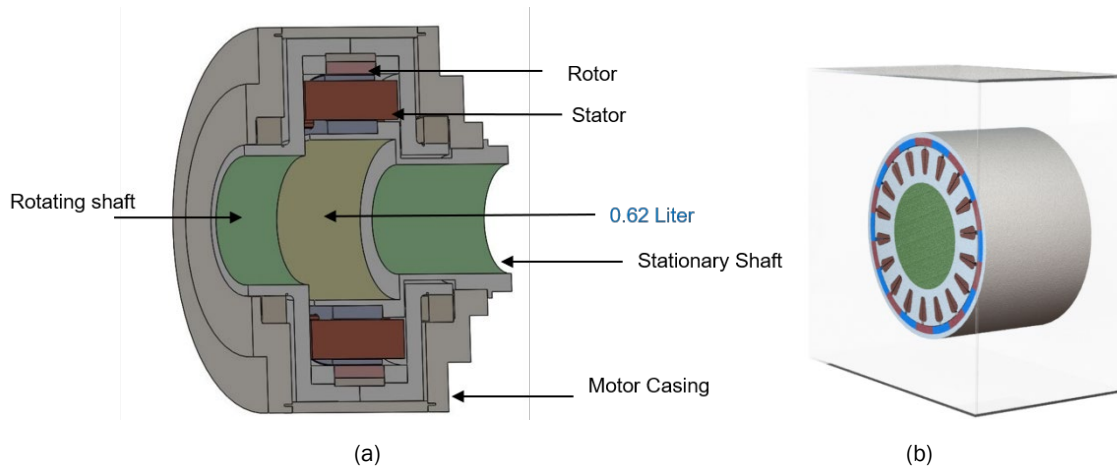


Figure I.1.5.1 (a) Outer rotor motor structure and (b) internal stator mount integration technique for the outer rotor motor.

The figure shows that the hollow space within the motor has 0.62 L of usable volume for inverter integration, which is much lower than the targeted volume of 1 L. A large bore diameter bearing can increase the volume of usable space within the motor; thus, a new 120 mm bore diameter bearing was selected for this application. This new bearing will increase the usable volume inside the motor, allowing tight integration of motor and inverter to meet the DOE 2025 electric drive power density target.

Capacitor Characterization

Direct current (DC) bus capacitors impose an obstruction to meet high power density demand in voltage source inverters employed in the electric traction drives. The DC bus capacitor’s purpose is to decouple the load from the DC supply unit, thus absorbing a large ripple current and retaining the voltage transients resulting from the inverter switching action. These capacitors use substantial space, about 20%–30% of an inverter [4], requiring better capacitor technology for optimizing power density.

Several capacitor technologies are available in the market. The most commonly used ones are electrolytic, ceramic, and film capacitors. In 2019, one sample from each capacitor was selected and evaluated to understand these capacitors’ behavior under various temperatures, excitation frequency, and DC bias voltage. The results concluded that the PLZT-based ceramic capacitors have advantages over the film- and class 2 MLCC-based capacitors and thus could be used to develop a high-power density traction drive [5]. The volume comparison of different capacitor technologies is shown in Figure I.1.5.2.

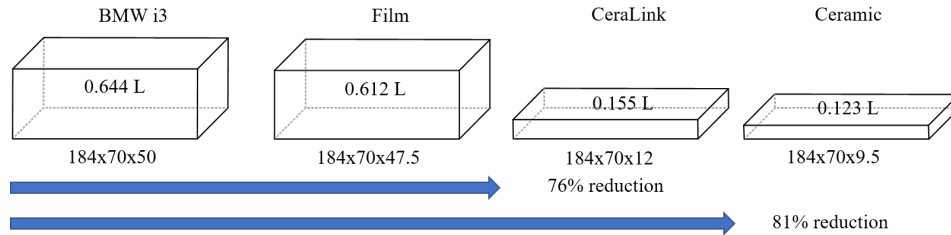


Figure I.1.5.2 The volume of the selected capacitor technologies compared with a 2016 BMW-i3 450 V 475 uF film capacitor.

The PLZT-based capacitors use antiferroelectric ceramic dielectric material and are produced in a small package; thus, several hundred capacitors will be required to handle root mean square current and keep the voltage ripple within an acceptable limit. Packaging this large number of capacitors is challenging because it will introduce additional layout inductance, which will adversely affect the power module switching performance. Traditional ceramic capacitor packaging uses a flat printed circuit board where the layout introduces asymmetry from the capacitor to the termination. The layout asymmetry will lead to asymmetrical current distribution among the parallel capacitor branches. Moreover, the top and bottom conductor's flux cancellation will be poor because of the asymmetrical current path; a traditional flat design is shown in Figure I.1.5.3(a).

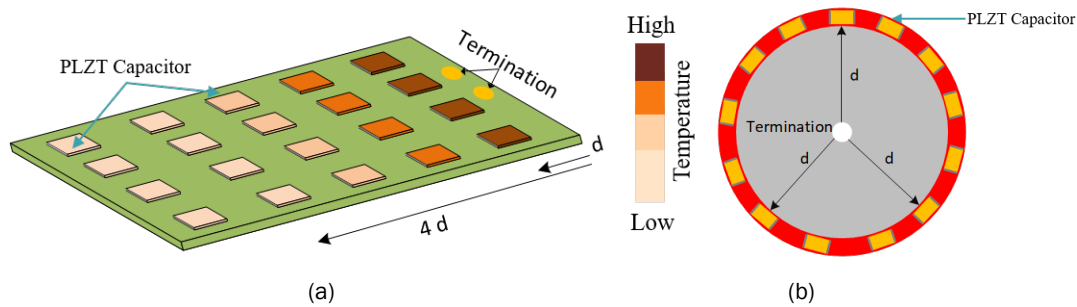


Figure I.1.5.3 Ceramic capacitor packaging: (a) traditional flat capacitor package and (b) proposed circular capacitor package.

A circular capacitor board was designed to overcome this challenge considering each capacitor distance is equal from the termination point, as shown in Figure I.1.5.3(b). This symmetry will ensure equal current distribution among the parallel capacitors and will reduce layout inductance due to overlapping current path. A CAD model of a flat capacitor board and a circular board were designed to validate the hypothesis, considering 30 capacitors for a circular design and 36 capacitors for the flat board, as shown in Figure I.1.5.4.

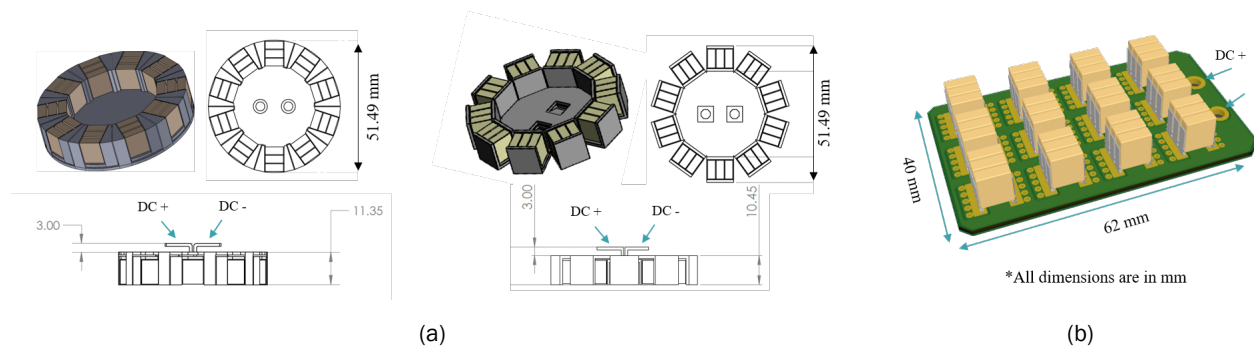


Figure I.1.5.4 Designed capacitor packaging: (a) proposed circular package and (b) a traditional flat capacitor package.

The CAD designs were then imported to a finite element analysis tool to identify surface current density and the designed capacitor packaging layout inductances. The surface current density showed the current distribution among the capacitors as shown in Figure I.1.5.5(a). Current was concentrated near the first row of the flat design, which suggests the capacitors in the first row will experience more thermal loading than the rest and will be prone to failure.

The circular design shows much better current distribution; thus, the capacitor bank's lifetime will increase compared with the flat design. The layout inductance of these capacitors was also estimated using the finite element simulation platform as shown in Figure I.1.5.5(b). Both circular designs had much lower layout inductance than the flat design.

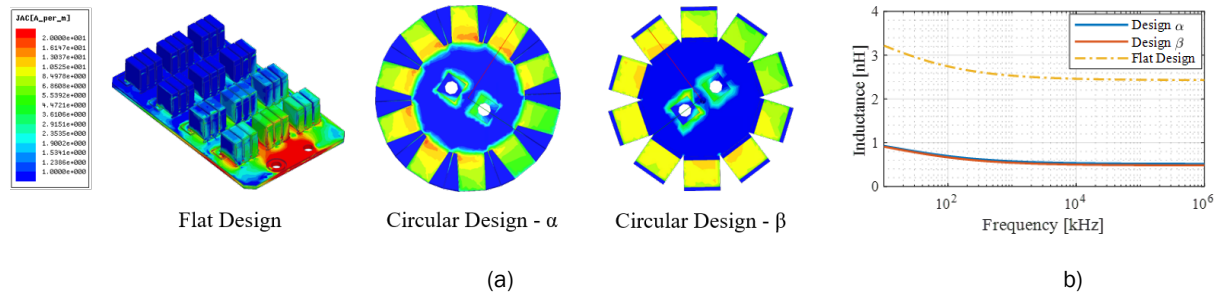


Figure I.1.5.5 (a) Surface current density of all three designed capacitor packaging showing symmetrical current distribution using circular packaging and (b) circular capacitor package showing lower layout inductance.

A printed circuit board-based circular capacitor board was designed along with the flat capacitor board for comparison as shown in Figure I.1.5.6(a). The designed capacitor board performances were determined using a frequency response analyzer at 0 V DC bias at room temperature; the experimental setup is shown in Figure I.1.5.6(b). The results showed that the flat capacitor board had 4 nH inductance, whereas the circular capacitor showed a 30% lower layout inductance than the flat design (2.38 nH).

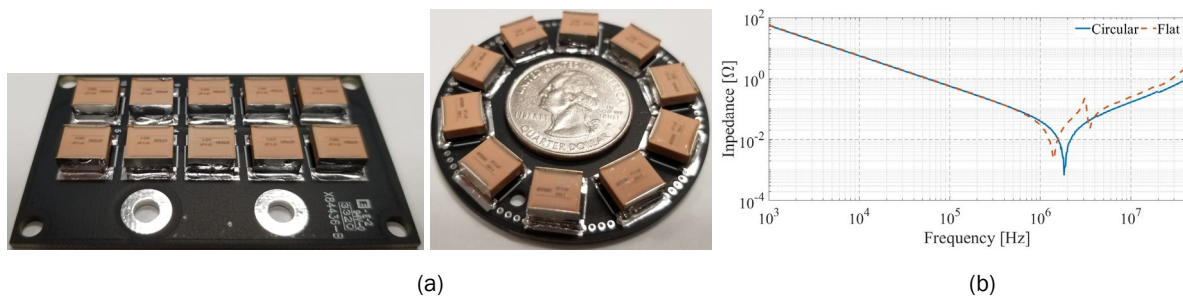


Figure I.1.5.6 Designed printed circuit board-based capacitor pancaking for experimental validation: (a) flat capacitor packaging and (b) circular capacitor packaging.

The results suggest that the circular capacitor packaging will reduce layout inductance compared with the flat capacitor board, thereby improving the inverter's dynamic performance. Moreover, it will ensure current symmetry among the parallel capacitors, which will enhance the capacitor lifetime.

Components integration

A heat sink was also designed to estimate the inverter volume for internal stator mount integration. This task used the Keystone 1 projects in which a single-phase leg module was designed considering segmented inverter topology using thermally-annealed pyrolytic graphite core insulated metal substrate. The design parameters are as follows:

- The module incorporates 1.2 kV SiC MOSFETs with two die in parallel to handle 200 A current.

- The heat sink is designed considering 100 A current is flowing through each semiconductor device.
- The coolant flow rate is considered 10/6 l/min as the segmented inverter is chosen (six-phase legs).
- The coolant inlet temperature is kept at 65°C.
- Volume and pressure drop are minimized using the genetic algorithm–based tool.

The heat sink design results are shown in Figure I.1.5.7; the device temperature was around 100°C and the designed heat sink had a maximum pressure drop of 160 Pa, which is minimal. All the designed components (power module, heat sink, traditional gate driver, and circular capacitor package) were then integrated to estimate the inverter volume as shown in Figure I.1.5.8. The estimated volume was around 0.11 L for a single-phase leg. The total inverter components volume will be six times the developed module volume as a six-phase inverter (segmented inverter) considered for this design. Thus, the inverter (module, heat sink, capacitors, and gate driver) will occupy a volume of 0.6 L, giving room to integrate the rest of the inverter components such as the sensors, controllers, busbars, and cooling manifold.

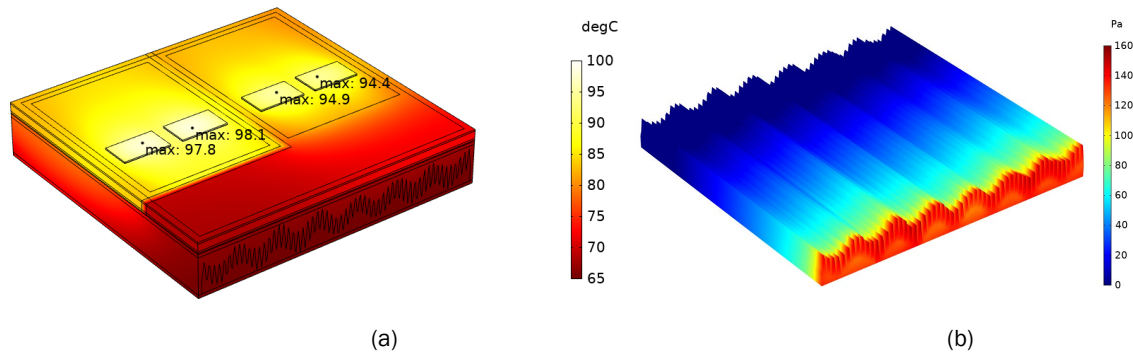


Figure I.1.5.7 Designed power module with heat sink: (a) CFD showing maximum die temperature and (b) pressure drop through the heat sink.

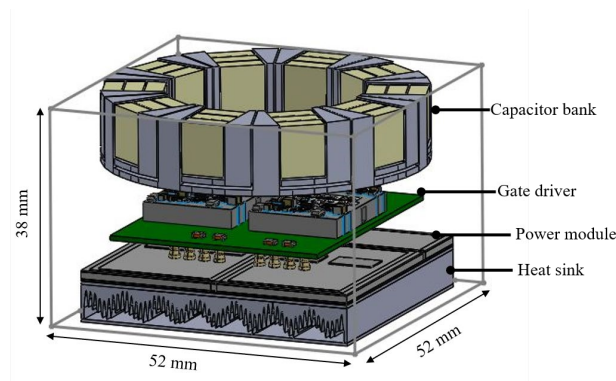


Figure I.1.5.8 Integration of inverter components.

Conclusions

This report identifies a new integration method for the outer rotor motor designed in Keystone 2. The key challenges of the proposed integration technique have been identified. The proposed integration technique will allow tight integration to achieve DOE 2025 electric drive power density target.

To improve the power density and electrical performance, capacitor technologies and their packaging techniques were analyzed. A new circular capacitor package for the DC link capacitor bank was proposed to improve electrical performance using PLZT-based capacitors. The performance of the proposed packaging

technique was validated using simulation and experimental results. The results indicate that the circular capacitor board will improve the inverter electrical performance and the capacitor bank lifetime compared with a traditional flat design.

Moreover, a six-phase inverter phase leg was designed to leverage the Keystone 1 projects and a genetic algorithm-based optimization method to develop a compact heat sink. All the components were then integrated to estimate the inverter volume. The inverter took a total of 0.6 L of volume, giving room to incorporate the rest of the inverter components.

Key Publications

1. S. Chowdhury, E. Gurpinar, and B. Ozpineci, “High-Energy Density Capacitors for Electric Vehicle Traction Inverters,” *2020 IEEE Transportation Electrification Conference & Expo (ITEC)*, Chicago, Illinois, USA, pp. 644–650, 2020, doi: 10.1109/ITEC48692.2020.9161588.
2. S. Chowdhury, E. Gurpinar, and B. Ozpineci, “Performance Evaluation of Insulated Metal Substrate Based Power Module for High Power EV Traction Inverter,” *2020 IEEE Energy Conversion Congress & Expo*, Detroit, Michigan, USA, 2020.
3. B. Kekelia, J. E. Cousineau, K. Bennion, S. Narumanchi, and S. Chowdhury, “Comparison of Thermal Management Approaches for Integrated Traction Drives in Electric Vehicles,” accepted at *InterPACK 2020* (in collaboration with the National Renewable Energy Laboratory).
4. E. Gurpinar, S. Chowdhury, B. Ozpineci, and W. Fan, “Graphite-Embedded High-Performance Insulated Metal Substrate for Wide-Bandgap Power Modules,” *IEEE Transactions on Power Electronics*, vol. 36, no. 1, pp. 114–128, 2020, doi: 10.1109/TPEL.2020.3001528.
5. E. Gurpinar, S. Chowdhury, B. Ozpineci, and W. Fan, “Design, Analysis, Comparison and Experimental Validation of Insulated Metal Substrates for High Power Wide-Bandgap Power Modules,” *Journal of Electronic Packaging*, vol. 142, no. 4, art. no. 041107, 2020, doi: 10.1115/1.4047409.

References

1. Electrical and Electronics Technical Team Roadmap, U.S. DRIVE, [Online] available at <https://www.energy.gov/sites/prod/files/2017/11/f39/EETT%20Roadmap%2010-27-17.pdf>, 2017.
2. D. Throne, F. Martinez, R. Marguire, and D. Arens, Integrated Motor/Drive technology with Rockwell connectivity, Rexroth Bosch Group, [Online] available at <http://www.cmaf.com/enewsletter/PDFs/IntegratedMotorDrives.pdf>.
3. S. Chowdhury, E. Gurpinar, G. Su, T. Raminosa, T. A. Burress, and B. Ozpineci, “Enabling Technologies for Compact Integrated Electric Drives for Automotive Traction Applications,” 2019 IEEE Transportation Electrification Conference and Expo (ITEC), Detroit, Michigan, USA, pp. 1–8, 2019, doi: 10.1109/ITEC.2019.8790594.
4. G. Su and L. Tang, “A segmented traction drive system with a small dc bus capacitor,” 2012 IEEE Energy Conversion Congress and Exposition (ECCE), Raleigh, North Carolina, USA, pp. 2847–2853, 2012, doi: 10.1109/ECCE.2012.6342375.
5. S. Chowdhury, E. Gurpinar, and B. Ozpineci, “High-Energy Density Capacitors for Electric Vehicle Traction Inverters,” 2020 IEEE Transportation Electrification Conference & Expo (ITEC), Chicago, Illinois, USA, pp. 644–650, 2020, doi: 10.1109/ITEC48692.2020.9161588.

Acknowledgments

The principal investigator wishes to thank project team members Emre Gurpinar, Raj Sahu, Gui-Jia Su, Tsarafidy Raminosoa, and Jon Wilkins of Oak Ridge National Laboratory for their contributions, and Bidzina Kekelia of the National Renewable Energy Laboratory for collaboration.

I.1.6 Advanced Packaging Designs – Reliability and Prognostics (NREL)

Douglas DeVoto, Principal Investigator

National Renewable Energy Laboratory (NREL)
15013 Denver West Parkway
Golden, CO 80401
Email: douglas.devoto@nrel.gov

Susan Rogers, DOE Technology Development Manager

U.S. Department of Energy
Email: susan.rogers@ee.doe.gov

Start Date: October 1, 2018	End Date: September 31, 2023	
Project Funding: \$175,000/year	DOE share: \$175,000/year	Non-DOE share: \$0

Project Introduction

The U.S. Department of Energy's Office of Energy Efficiency and Renewable Energy Vehicle Technologies Office and the Electrical and Electronics Technical Team have proposed aggressive research and development targets [1] aimed at improving power electronics technology to enable the mass-market penetration of electric-drive vehicles. Achieving these aggressive power electronics targets will require a decrease in cost (year 2025 cost target: \$2.70/kW) and an increase in power density (year 2025 power density target: 100 kW/L) as compared with current, on-road technology. Replacing traditional silicon device-based components with more efficient and higher-temperature wide-bandgap semiconductor device-based components will enable increasing the power density. However, meeting the power density target will also require innovative packaging and thermal management solutions to increase the heat fluxes dissipated, and allow for compact electronics packaging.

Decreasing the thermal resistance pathway in power electronics packages is a primary objective for maximizing the performance of wide-bandgap devices. This can be accomplished by either replacing package layers with new materials that enable greater thermal, electrical, and reliability performance, or eliminating layers and components through new packaging designs. Safe and robust operation of the power electronics requires electrical isolation of the high-voltage circuitry within the power electronics module. For example, typical power electronics modules use a ceramic material within the package for electrical isolation and wire bonds for electrical connections.

Objectives

The primary deliverable for this project will be to construct a power electronics package utilizing an organic, electrically insulating substrate material with a direct chip-to-chip interconnect technology and demonstrate superior thermal performance and greater reliability under thermal cycling, thermal aging, vibration, power cycling, and electrical high-potential evaluation over traditional packages. This will be accomplished through the following tasks:

- *Design optimization of a power electronics package.* A multiphysics optimization process will incorporate the electrically insulating substrate alternative into a novel power electronics package. Electrical, thermal, and mechanical constraints will be balanced through this optimization.
- *Prototype construction and evaluation.* Example power electronics packages based on an electrically insulating substrate alternative with devices joined by quilt packaging (QP) will be developed. A multiphysics modeling evaluation of the sample geometries will determine thermal and thermomechanical performance while a reliability assessment will measure electrical performance during accelerated tests.

Approach

The project aim is to develop a power-dense, reliable, and cost-effective 3D power electronics package enabled by an alternative electrical isolation material: an organic direct bond copper (ODBC) substrate. This material provides equivalent electrical isolation to current technologies while providing high thermomechanical reliability at high device junction temperatures, as well as enabling higher power densities. In addition, elimination of design constraints associated with traditional ceramic substrates reduces device-to-coolant thermal resistance, simplifies package design, and offers more design flexibility. This package design will eliminate component layers in a new, low-cost, simplified manufacturing process for a packaging design that will allow for higher power densities and reliability. Additionally, the new circuit board structure will transport heat out of encapsulated component areas within a 3D structure. This work is being performed in collaboration with Oak Ridge National Laboratory (ORNL) and DuPont.

QP is a chip-to-chip interconnect technology that incorporates conductive metal “nodules” on the sides of the chips. The technology has been commercialized by Indiana Integrated Circuits, LLC (IIC) from research originating at the University of Notre Dame [2](#). IIC designed QP test chips for NREL in FY 2019 to evaluate the electrical and reliability characteristics of the interconnect technology as a replacement for traditional wire bond interconnects. Design work with IIC also involved collaboration with ORNL.

Results

Power Electronics Module Design with Organic Insulating Substrate

Previous work has outlined the thermal performance and reliability of the ODBC substrate [3](#). Additional thermal modeling was conducted to optimize the thicknesses of the ODBC’s metallization layers, as well as to understand the impact of device placement on top of the substrate. Thermal modeling also evaluated the design concept of adding additional metallization and electrical insulation layers to allow for stacked electrical pathways below the switching devices within a power module.

Two silicon carbide (SiC) devices were attached to an ODBC substrate with SAC 305 solder for a representative thermal model. The spacing between devices was varied between 0.01 mm and 4 mm, and the thicknesses of metallization layers were varied between 0.1 mm and 4 mm. In addition to the standard metallization-insulator-metallization construction of the ODBC substrate, an additional insulation and metallization layer were each added. The device spacing and substrate construction parameters are shown in Figure I.1.6.1.

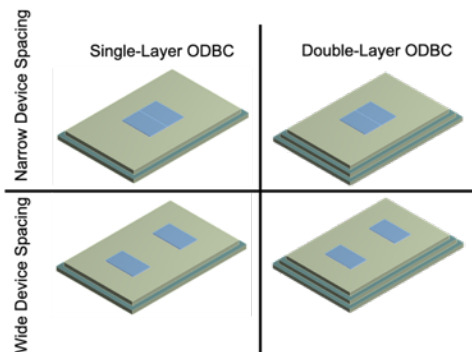


Figure I.1.6.1 ODBC thermal modeling geometry

Devices were modeled with a heat generation of 80 W per die, and a uniform heat transfer coefficient of 10,000 W/m²K was applied to the bottom metallization layer. Thermal parametric modeling results, shown in Figure I.1.6.2, indicate that device temperatures can be maintained under 160°C when devices are spaced 0.01 mm apart as long as the top metallization layer is sufficiently thick, approximately 1–1.5 mm. This confirms thermal best practices that spreading heat directly below the die to the larger footprint of the substrate is an

effective design approach for minimizing die temperatures. The bottom/middle metallization layer thicknesses had little impact on die temperatures and could be held as thin as 0.5 mm with no thermal penalty.

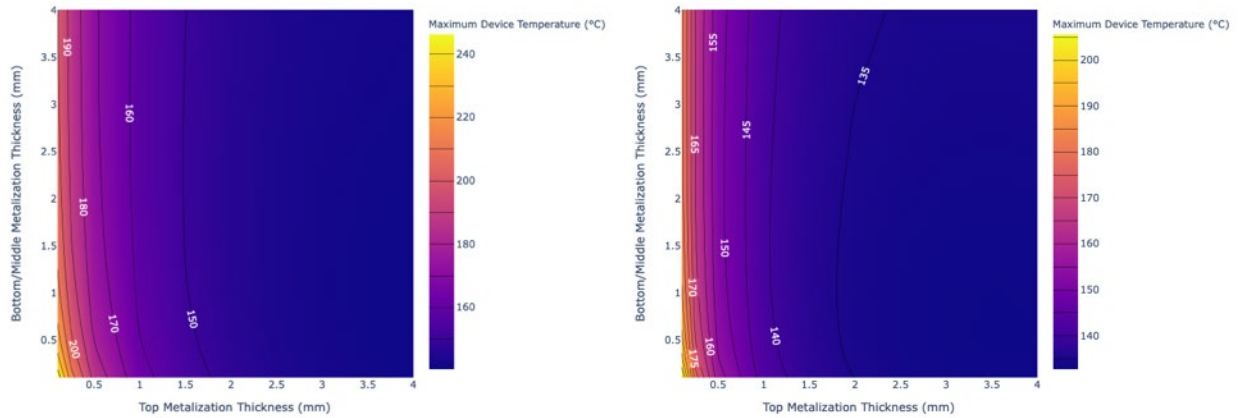


Figure I.1.6.2 Thermal modeling results of a double-layer ODBC substrate with 0.01-mm device spacing (left) and 4-mm spacing (right)

The ODBC substrate’s increased top metallization layer thickness could potentially cause premature failure within the die-attach layer due to coefficient of thermal expansion mismatch and higher strain levels. To alleviate this concern, a thermomechanical analysis of the device-attach solder layer was completed. Using the same package geometry as the thermal model, the top metallization thickness was varied from 0.5 mm to 4 mm and the package was thermally cycled between -40°C and 150°C . Temperature-dependent material properties were applied to the package layers while the solder layer’s total cumulative inelastic strain, comprising the time-dependent creep strain and the time-independent plastic deformation, was calculated by utilizing Anand’s viscoplastic constitutive model. The strain energy density values of the solder layer are plotted in Figure I.1.6.3.

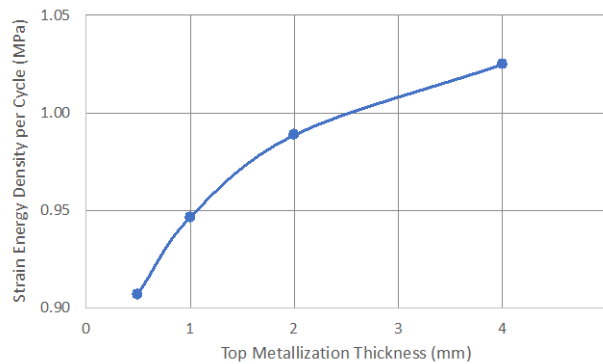


Figure I.1.6.3 ODBC thermomechanical modeling results

As the top metallization thickness increases, strain energy density values of the solder slightly increase. This indicates a reduction in the solder’s lifetime, but this analysis alone cannot directly quantify the amount of this reduction. These modeling results will be experimentally validated in FY 2021 by attaching devices to both traditional substrates and thick-metallization ODBC substrates. Both sets of samples will be thermally cycled to evaluate device-attach reliability.

Direct Chip-to-Chip Electrical Connection within a Power Electronics Module

Experimental samples were previously designed in collaboration with IIC and ORNL in FY 2019, and a design of experiments was established based on previous QP experience to optimize the size and shape of the connecting nodules. Nodules were fabricated for NREL in two different widths (100 μm and 300 μm) in both rectangular and triangular shapes. The length of the nodules extending into the chips was also varied to two

lengths, 30 μm and 70 μm . The nodule dimensions are summarized in Table I.1.6.1. Six samples were delivered to NREL and three separate accelerated tests were planned.

Table I.1.6.1 Quilt Packaging Accelerated Testing Summary

Sample	Nodule Shape	Nodule Length (μm)	Nodule Width (μm)	Accelerated Condition
1	Triangle	30	100	Thermal Cycling
5	Triangle	70	300	Thermal Cycling
6	Rectangle	30	100	Thermal Cycling
8	Triangle	30	300	Initial Failure
11	Rectangle	70	100	Mechanical Shock
12	Rectangle	30	100	Sinusoidal Vibration

The QP assemblies were mounted to DuPont ODBC substrates with a die-attach solder for ease of handling during evaluation. The complete sample package of two die joined by QP and mounted on the ODBC substrate is shown in Figure I.1.6.4.



Figure I.1.6.4 Evaluation sample

The nodule interfaces for each evaluation sample were inspected for initial quality under a digital microscope. This was qualitatively determined by ensuring that no cracks were visible and that the nodules were adequately joined by a layer of solder. Images of the samples are shown in Figure I.1.6.5.

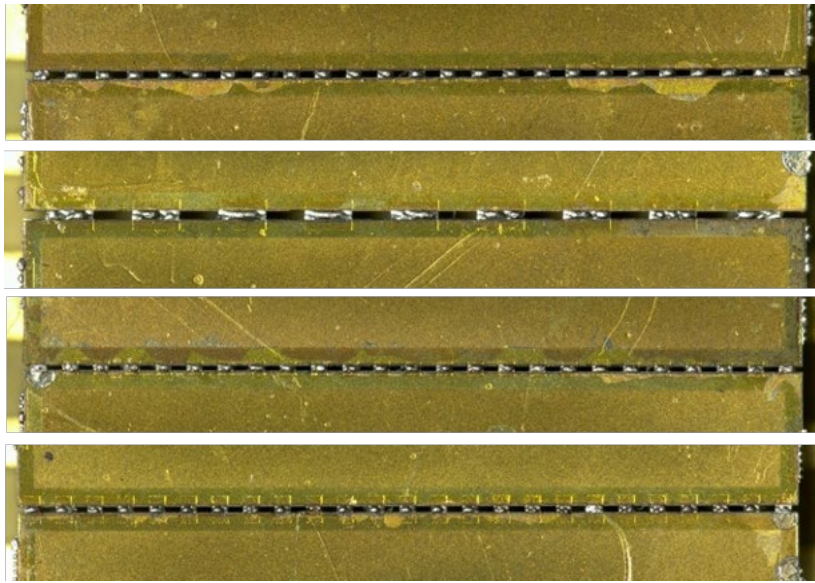


Figure I.1.6.5 Microscope images of nodules from samples 1, 5, 6, and 11

Degradation of the QP nodules can be directly monitored by electrical resistance measurements across the nodule connections. A Hioki RM3544 Resistance Meter with four-terminal direct-current probes was used to measure the resistance of nodule connections before and during accelerated tests. Samples were assigned to one of three separate accelerated tests, with parameters of each test outlined below:

- *Sinusoidal Vibration*: 20-Hz to 1,000-Hz sweep, 5-g acceleration, 2-hour duration, repeated for x, y, and z axes (IEC 60068-2-6 [4])
- *Mechanical Shock*: half-sine pulse, 30-g acceleration, 18-ms duration, 3 pulses repeated for x, y, and z axes (IEC 60068-2-27 [5])
- *Thermal Cycling*: -40°C to 150°C , $10^{\circ}\text{C}/\text{min}$ ramp rate, 15-min soak, 1,000 cycles (JESD22-A104D [6]).

For sinusoidal vibration and mechanical shock accelerated tests, microscope inspection and electrical resistance measurements were conducted after vibration excitation in each axis. Thermal cycling samples were inspected every 100 cycles. Samples were removed from accelerated test plans after resistance measurements exceeded $1\ \Omega$, an approximately 50-times increase in resistance from initial measurements. A summary of electrical resistance measurements for each accelerated test is shown in Figure I.1.6.6.

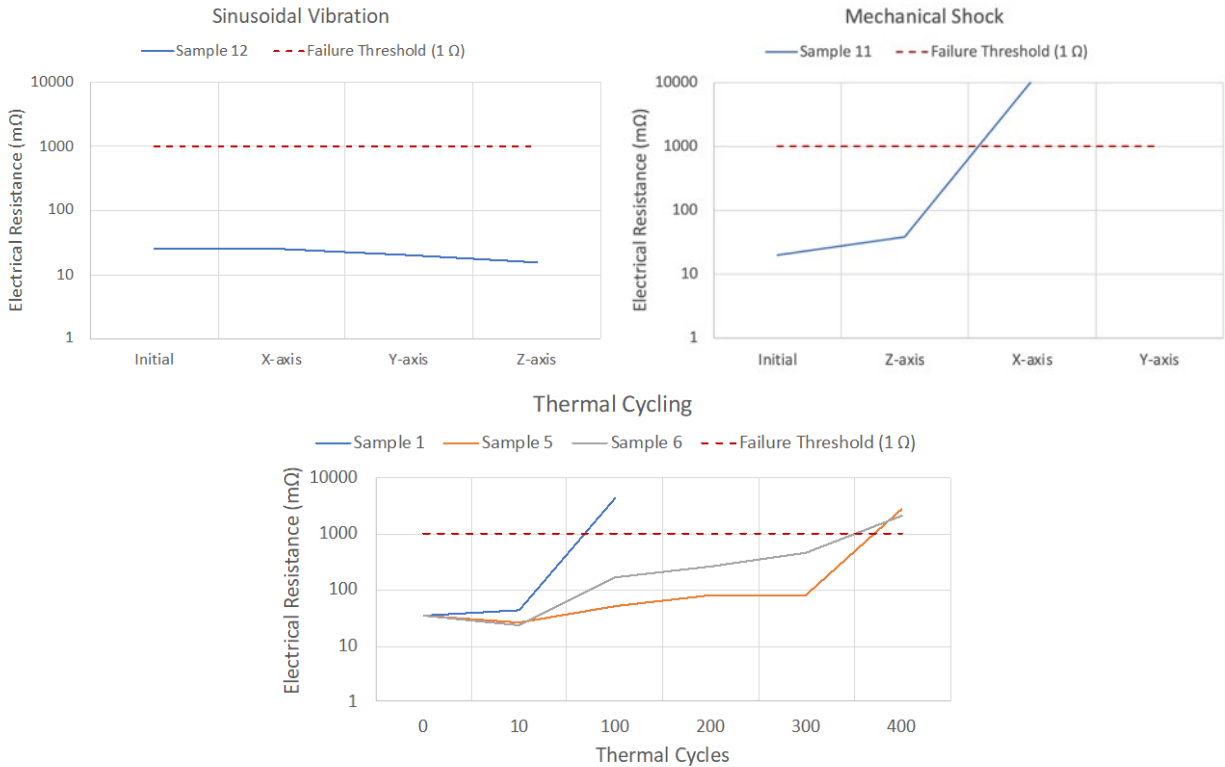


Figure I.1.6.6 Electrical resistance measurements of samples during accelerated tests

Despite acknowledging the small sample size for these experiments, some conclusions can be reached. Sinusoidal vibration at an acceleration of 5 g did not have any impact on the mechanical stability of the QP nodules. Mechanical shock testing, conducted at an acceleration of 30 g, did result in an increase in electrical resistance across the QP nodules above the failure threshold. Thermal cycling also proved to be a severe stressor to the samples, with failures occurring after 100 and 400 cycles. In addition to monitoring the steadily increasing electrical resistance values, microscope images confirmed cracking within the QP structure. In Figure I.1.6.7, it can be observed that after 400 thermal cycles, separation in the nodules developed and the overlaying solder material fractured. One particularly severe failure location can be observed in the third nodule from the left, where complete separation between the two nodule halves is visible.

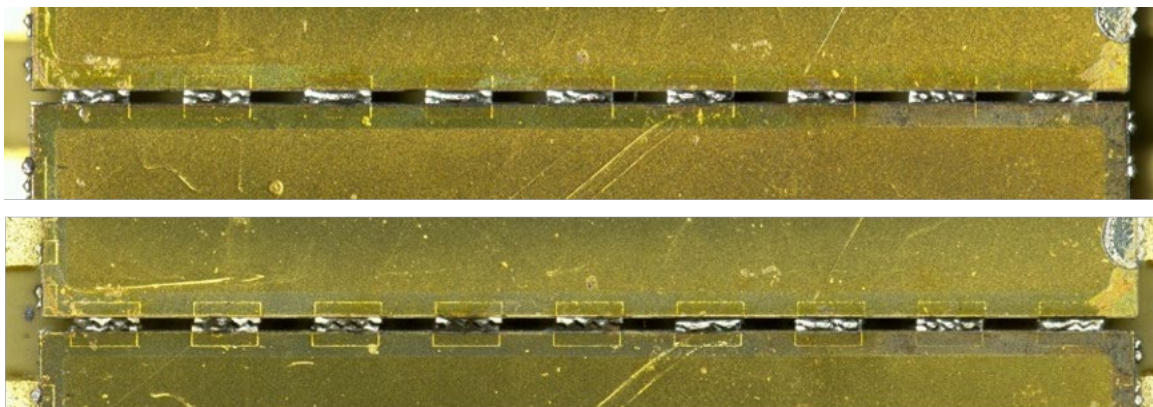


Figure I.1.6.7 Microscope images of sample 5 at 0 cycles (above) and 400 cycles (below)

The microscope used for imaging the QP samples captured a stack of images at different heights from a sample's surface. The level of focus in the resulting images varies as the distance between the microscope's lens and the sample's features changes. Using the Depth from Defocus method, the microscope can reconstruct a 3D topology of the sample being measured. The captured 2D image can then be projected over the 3D information. A 3D image of sample 5 was captured after 400 cycles and is shown in Figure I.1.6.8. Similar observations for samples 1, 6, and 11 were captured.

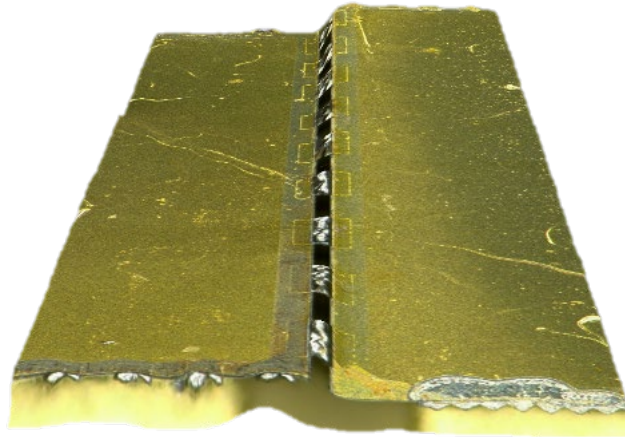


Figure I.1.6.8 Microscope 3D image of sample 5 at 400 cycles

It can be observed from this image that cracking of the QP nodules is not the only change to the mechanical structure of the sample. Cracking was initiated by a torsional stress caused by the tilting of one of the dies. Further analysis attributes this to a weak die-attach solder layer that allows movement of the die after several hundred thermal cycles. Attention will be given to improving the strength of the die attach in future samples to avoid movement of the dies under thermal cycling conditions. In FY 2021, a thermomechanical model of the quilt packaging geometry will also be developed to quantify the impact of nodule shapes and sizes under thermal cycling conditions. After these additional experimental and modeling milestones are met, the goal of an assembled half-bridge module in collaboration with ORNL, IIC, and DuPont will be pursued.

Conclusions

The project aim is to develop a power-dense, reliable, and cost-effective 3D power electronics package enabled by an alternative electrical isolation material and electrical interconnect method. The project accomplishments for FY 2020 are summarized below:

- Thermal and thermomechanical impact of polyimide-based substrate designs were modeled in representative power module structures. Device temperatures can be maintained under 160°C as long as the top metallization layer is sufficiently thick, approximately 1–1.5 mm. As the top metallization thickness increases, strain energy density values of the solder slightly increase, but future work is required to quantify the reduction in device-attach lifetime.
- Experimental sinusoidal vibration, mechanical shock, and thermal cycling experiments enable the reliability evaluation of samples, comprising devices electrically joined by QP and mounted to ODBC substrates. Sinusoidal vibration at an acceleration of 5 g did not have any impact on the mechanical stability of the QP nodules while mechanical shock and thermal cycling testing did weaken device-attach interfaces, and ultimately the QP nodules. The die attach layer will be strengthened in future samples.

Key Publications

1. DeVoto, D. 2020. “Advanced Power Electronics Designs – Reliability and Prognostics.” *2020 DOE VTO Annual Merit Review*, Washington, D.C., June 2020.
2. Gurpinar, E., R. Sahu, B. Ozpineci, and D. DeVoto. 2020. “Analysis and Optimization of a Multi-Layer Integrated Organic Substrate for High Current GaN HEMT-Based Power Module.” *2020 IEEE Workshop on Wide Bandgap Power Devices and Applications in Asia (WiPDA Asia)*, Japan, September 2020.

References

1. U.S. DRIVE. 2017. *Electrical and Electronics Technical Team Roadmap*. Washington, D.C.: USDRIIVE. <https://www.energy.gov/eere/vehicles/downloads/us-drive-electrical-and-electronics-technical-team-roadmap>.
2. Lu, T., C. Ortega, J. Kulick, G. H. Bernstein, S. Ardisson, and R. Engelhardt. 2016. “Rapid SOC prototyping utilizing quilt packaging technology for modular functional IC partitioning.” *2016 International Symposium on Rapid System Prototyping (RSP)*, Pittsburgh, PA, 2016, 1–7. doi: 10.1145/2990299.2990313.
3. DeVoto, D. 2020. “Advanced Packaging Designs – Reliability and Prognostics (NREL).” In *Electrification: 2019 Annual Progress Report*, Washington, D.C.: U.S. DOE EERE VTO, 95–101. doi:10.2172/1637435.
4. International Electrotechnical Commission. 2007. *IEC 60068-2-6:2007: Environmental Testing – Part 2–6: Tests – Test Fc: Vibration (Sinusoidal)*. Geneva, Switzerland: International Electrotechnical Commission.
5. International Electrotechnical Commission. 2008. *IEC 60068-2-27:2008: Environmental Testing – Part 2–27: Tests – Test Ea and guidance: Shock*. Geneva, Switzerland: International Electrotechnical Commission.
6. JEDEC Solid State Technology Association. 2009. *JESD22-A104D: Temperature Cycling*. Arlington, VA: JEDEC Solid State Technology Association.

Acknowledgements

The significant contributions of Joshua Major, Paul Paret, and Gilbert Moreno are acknowledged.

I.1.7 Electric Motor Thermal Management (National Renewable Energy Laboratory)

Kevin Bennion, Principal Investigator

National Renewable Energy Laboratory
15013 Denver West Parkway
Golden, CO 80401
Email: kevin.bennion@nrel.gov

Susan Rogers, DOE Technology Development Manager

U.S. Department of Energy
Email: susan.rogers@ee.doe.gov

Start Date: October 1, 2018
Project Funding: \$250,000

End Date: September 30, 2023
DOE share: \$250,000

Non-DOE share: \$0

Project Introduction

This project is part of a multi-lab consortium including multiple universities, the National Renewable Energy Laboratory (NREL), Oak Ridge National Laboratory (ORNL), Sandia National Laboratories (SNL), and Ames Laboratory. The project and the consortium leverages research expertise and facilities at the national labs, universities, and industry to significantly increase electric drive power density and reliability while simultaneously reducing cost. The consortium is organized around three Keystone projects: (1) Power Electronics, (2) Electric Motors, and (3) Traction Drive System. The Electric Motors Keystone project at NREL focuses primarily on improvements (reductions) in the passive thermal resistance of the electric motor and improved active fluid-based cooling technologies to increase power density, in line with the most recent research priorities outlined in the U.S. DRIVE Electrical and Electronics Technical Team (EETT) Roadmap [1].

In the area of electric drive motors, the EETT Roadmap highlights the importance of reducing the thermal resistance of the motor packaging stack-up to increase power density. The Roadmap also mentions that the thermal conductivity of the materials within the motor influence the amount of material necessary to generate the required mechanical power. The Roadmap emphasizes research areas with a focus on material physics-based models, improved materials, and thermally conductive epoxy and fillers. In addition, the Roadmap highlights a research gap in that the material performance characterization techniques are not well known or identified in the literature.

Heat transfer and thermal management are critical to electric motors because—as mentioned in the EETT Roadmap—thermal constraints place limitations on how electric motors ultimately perform, and “an optimized thermal design can help increase machine rated power substantially” [2]. The thermal management of electric motors for vehicles is complex because of the multiple heat transfer paths within the motor, the variation in heat due to motor operating conditions, and the multiple material interfaces through which heat must pass through to be removed. For these reasons, “heat transfer is as important as electromagnetic and mechanical design” [3] for solving research challenges to improve the electric motor power density, cost, and reliability, as outlined by the EETT Roadmap.

Objectives

Research under this project will be performed within the framework of a research consortium consisting of a multidisciplinary team that will plan, establish, conduct, and manage a portfolio of multi-lab and multi-university research efforts to advance the state of the art in electric drive technologies. The final objective of the consortium is to develop a 100-kW traction drive system that achieves a power density of 33 kW/L, has an operational life of 300,000 miles, and a cost of \$6/kW. The system will be composed of a 100-kW/L inverter and a >20,000-rpm, 50-kW/L electric motor. Building on the research experience and capabilities within each

laboratory, the multi-lab consortium will focus on achieving research objectives within three Keystone projects: (1) Power Electronics, (2) Electric Motors, and (3) Traction Drive System.

For the Electric Motors Keystone project, key consortium objectives will focus on research on motor technology gaps to enable increased power density and reliability, supporting research pathways in power electronics technologies. As power electronics technologies develop to enable higher operating temperatures, higher system voltages, and higher switching frequencies, motor technologies will also be necessary to realize the electric drive system benefits. Key consortium motor research pathways include motor material improvements (electrical, magnetic, and thermal), higher motor operating speeds, and higher system voltages. NREL research will provide motor researchers—within and outside the consortium—with the data and models to enable motor innovations and the use of novel materials and designs. The work supports broad demand for data, analytical methods, and experimental techniques to improve and better understand motor thermal management. It also combines unique capabilities, facilities, and expertise in addition to the data, analysis methods, and experimental techniques to improve and better understand heat transfer within electric motors to meet the demands of electric drive vehicles. NREL’s focus in FY 2020 included:

- Developing models and simulation tools in support of consortium team members in quantifying thermal performance and heat transfer technologies to support motor development efforts.
- Utilizing new thermal characterization setup for measuring thermal resistance of high-thermal-resistance materials and interfaces in support of the consortium team members.

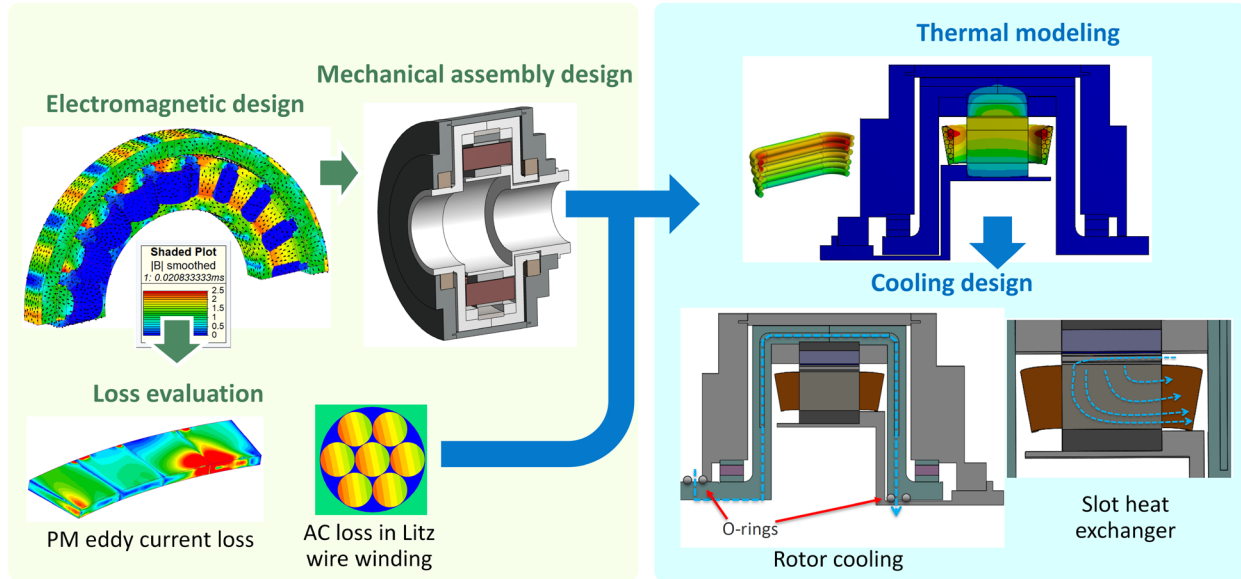
Approach

The ability to remove heat from an electric motor depends on the passive-stack heat transfer within the motor and the convective cooling heat transfer of the selected cooling technology. In addition, as new materials are developed, it is important to characterize temperature-dependent material properties and thermal interface properties. Characterization of new materials enables motor designers to evaluate the potential performance trade-offs of new materials for motor applications. For this reason, the approach for the research project splits the efforts between two primary areas. The first focus area for NREL during FY 2020 involved motor system thermal analysis support for electric motor research efforts performed within the consortium. The second focus area utilized newly developed experimental methods to measure high-thermal-resistance materials at elevated temperatures in collaboration with consortium members.

Motor System Thermal Analysis Support

The research performed in motor system thermal analysis focused on supporting two consortium collaborators involving Georgia Institute of Technology and ORNL. Collaborations with Georgia Institute of Technology supported research efforts for advanced convective heat-transfer technologies for electric machines at Georgia Institute of Technology. NREL provided technical support, motor geometry information, thermal modeling results, and experimental data to support evaluations of advanced cooling impacts. NREL also provided access to NREL laboratories to a Georgia Institute of Technology student to perform experimental work. A portion of the collaborative work led by Georgia Institute of Technology was summarized in a paper submitted to the 2020 International Technical Conference and Exhibition on Packaging and Integration of Electronic and Photonic Microsystems (InterPACK 2020).

The collaboration with ORNL supported motor thermal analysis and thermal design of advanced machine designs led by ORNL. The collaboration between NREL and ORNL is summarized in Figure I.1.7.1. ORNL led the overall iterative electric machine design process with an emphasis on the electromagnetic and mechanical assembly design. NREL, in collaboration with ORNL, supported the thermal analysis and cooling design. This report focuses on the collaboration with ORNL. A summary of the initial work is summarized in an ORNL-led paper submitted to the 2020 IEEE Energy Conversion Congress and Exposition (ECCE).

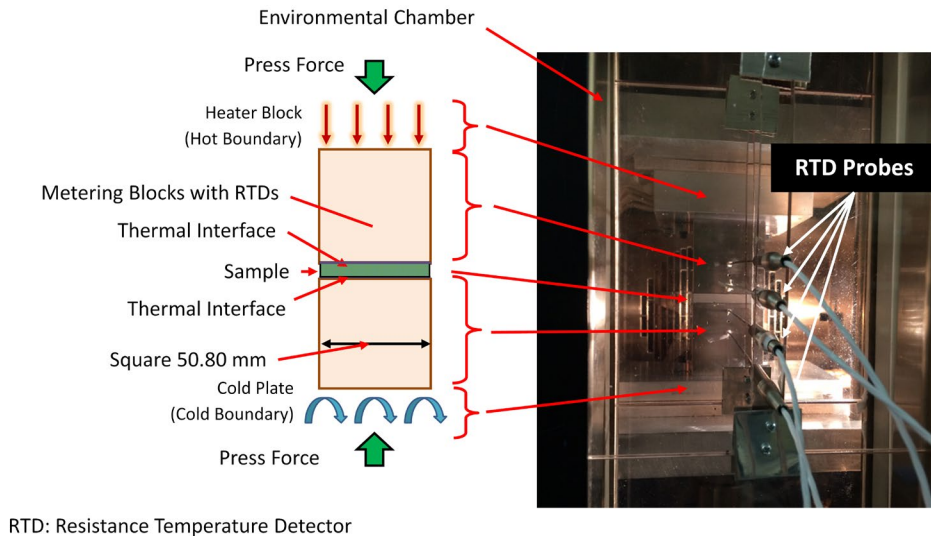


PM: Permanent Magnet, AC: Alternating Current

Figure I.1.7.1 ORNL and NREL motor analysis approach

Material and Interface Thermal and Mechanical Characterization

NREL also utilized newly developed experimental methods to measure high-thermal-resistance materials at elevated temperatures in collaboration with SNL. The experimental setup was described in the FY 2019 annual report, and the hardware is illustrated in Figure I.1.7.2. The work during FY 2020 with SNL focused on supporting mechanical and thermal measurements of new motor materials, led by SNL.



RTD: Resistance Temperature Detector

Figure I.1.7.2 Constructed experimental hardware inside environmental chamber (Source: Emily Cousineau, NREL)

Results

The following sections summarize the results for both the thermal resistance experimental work for material thermal characterization and the consortium team member motor system thermal analysis collaborations.

Motor System Thermal Analysis Support

The work supporting the ORNL-led motor research efforts focused on an outer rotor motor configuration as shown in Figure I.1.7.4. Key sections of the motor are highlighted with the dotted lines where the blue, yellow, and red dotted lines represent the case, rotor, and stator respectively. The motor design went through multiple design iterations (a few examples are illustrated in Figure I.1.7.3). The iterative design approach investigated multiple design configurations incorporating items such as alternate materials, bearing sizes, stator slot-winding configurations, and cooling approaches. Because NREL led the thermal analysis aspects of the motor design, this report summarizes some of the analysis performed by NREL in collaboration with ORNL.

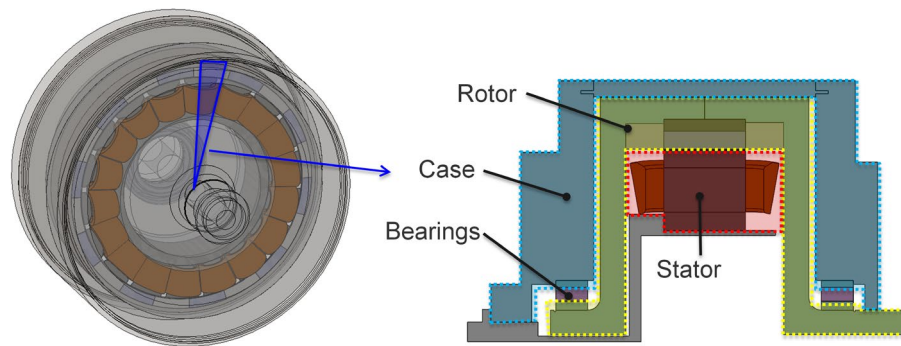


Figure I.1.7.3 ORNL-led motor development focused on illustrated outer rotor motor configuration (Source: Emily Cousineau, NREL)

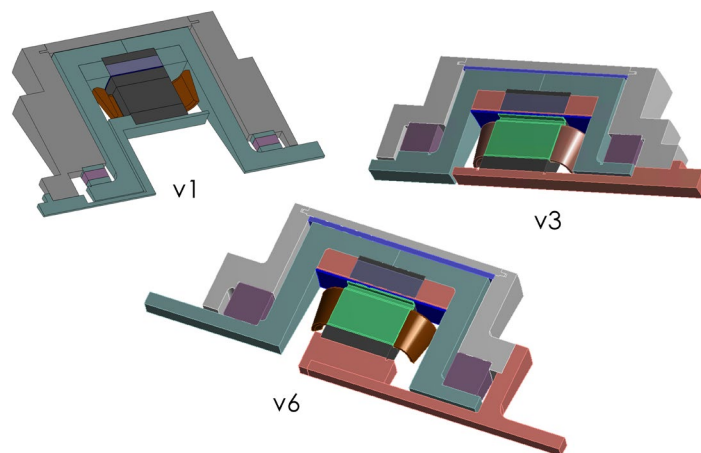


Figure I.1.7.4 Example iterations of the ORNL-led motor development that NREL used for thermal design analysis (Source: Emily Cousineau, NREL)

Thermal modeling and analysis focused on three-dimensional finite element analysis to evaluate impacts and interactions between passive thermal design elements and the active cooling design. The thermal model was developed using material properties from literature [4],[5],[6]. This included evaluating the thermal impacts of alternative materials such as lamination materials [7]–[10], active cooling locations, and active cooling heat-transfer coefficients to identify cooling performance metrics. Several alternative cooling approaches were investigated for the motor thermal management. Examples of approaches included options shown in Figure I.1.7.5. Cooling options included a combination of active cooling within the stator slots between the winding coils (similar to [11]), cooling the inner diameter of the stator, and active cooling of the rotor and magnets. Besides investigating active cooling technologies, the NREL thermal analysis also supported ORNL in evaluating the impacts of alternative lamination materials. A key accomplishment as described in the submitted ECCE conference paper (referenced in the Key Publications) was the ability to maintain the magnet

temperature while operating at 20,000 rpm without active cooling of the rotor. Removing the requirement for active cooling of the rotor benefits the motor in terms of reduced complexity and cost.

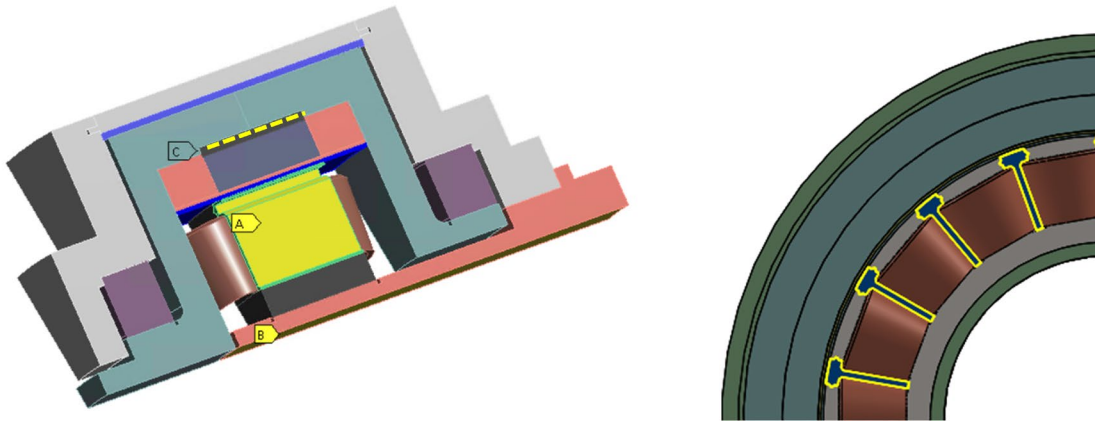


Figure I.1.7.5 Example motor cooling approaches. (Left) Yellow highlighted regions show cooling within the stator winding slot (A), stator inner diameter surface (B), and rotor (C). (Right) Illustration of down-selected concept for placing cooling channels within the stator slot between the coil windings and stator tooth tips. (Source: Emily Cousineau, NREL)

The thermal analysis was performed at multiple operating conditions and speeds. The target peak speed for the motor design is 20,000 rpm, and the most challenging thermal conditions were encountered at the peak speed operating condition. Figure I.1.7.6 highlights preliminary temperature distribution results with 0.2-mm-thick powercore® [10] laminations with a revised design for the slot heat exchanger. The peak magnet temperature reaches approximately 122°C, and the peak winding temperature reaches approximately 151°C. The peak temperature of the motor occurs within the stator with a maximum temperature of 162°C. The results are based on a 65°C coolant temperature to the motor.

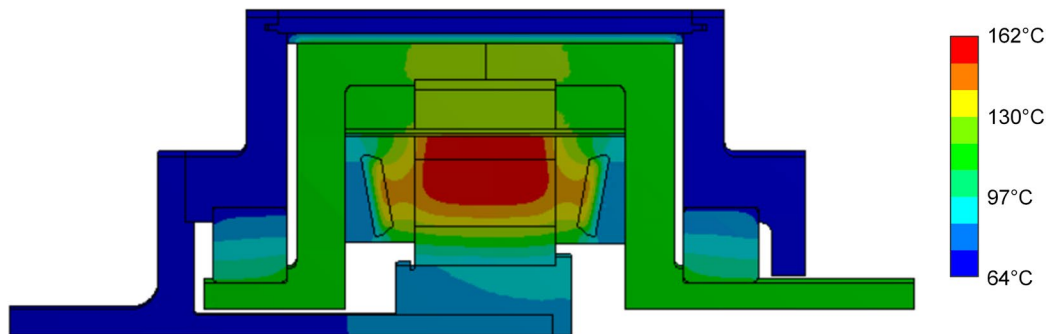


Figure I.1.7.6 Preliminary results of the V6 motor geometry with revised slot cooling heat exchanger with 0.2-mm-thick laminations at 20,000 rpm (Source: Emily Cousineau, NREL)

Material and Interface Thermal and Mechanical Characterization

The material characterization efforts focused on collaboration with SNL to measure the thermal properties of new materials being developed and researched at SNL. NREL utilized a newly developed experimental apparatus to measure high-thermal-resistance materials at elevated temperatures. An image of the experimental setup with one of the SNL-provided samples is shown in Figure I.1.7.7. Initial measurement results show the baseline neat epoxy samples average thermal conductivity of approximately 0.24 W/m·K, whereas the SNL-developed filled epoxy samples had an average thermal conductivity of 1.8 W/m·K. Additional details on the SNL materials and development can be found in the research and report led by SNL as part of the research consortium.

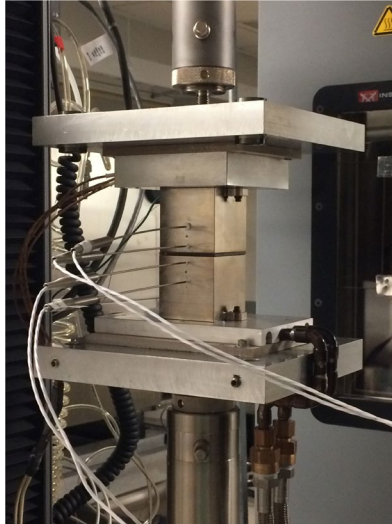


Figure I.1.7.7 SNL material sample MRH2-47-1 undergoing testing in ambient conditions (Source: Emily Cousineau, NREL)

Conclusions

During FY 2020, NREL efforts focused on supporting collaborations with external research partners within the Electric Drive Technologies research consortium. The primary collaborations described in this report include Georgia Institute of Technology, ORNL, and SNL. Efforts with Georgia Institute of Technology supported research led by Georgia Institute of Technology for advanced convective heat-transfer technologies for electric machines. The work led to a submitted conference publication (InterPACK 2020), highlighted in the Key Publications. The work also led to NREL providing access to the NREL laboratory for a student to perform experimental work related to motor cooling concepts developed by Georgia Institute of Technology. The collaboration with ORNL supported efforts led by ORNL to develop a high-speed non-heavy-rare-earth outer-rotor motor. NREL supported the ORNL effort by leading the thermal analysis and design of advanced machines. The work resulted in identifying a thermal management approach to meet the aggressive motor performance objectives. A summary of the motor research was submitted for publication to the 2020 ECCE conference. Finally, collaborations with SNL utilized a newly developed experimental apparatus at NREL to measure high-thermal-resistance materials at elevated temperatures. The work was initiated in FY 2020, and the measurements are scheduled to continue into FY 2021.

Key Publications

1. Bennion, K. 2020. “Electric Motor Thermal Management R&D.” 2020 DOE VTO Annual Merit Review, Washington D.C., June 2020.
2. Raminosoa, T., R. Wiles, J.E. Cousineau, K. Bennion, and J. Wilkins. 2020. “A High-Speed High-Power-Density Non-Heavy Rare-Earth Permanent Magnet Traction Motor.” *2020 IEEE Energy Conversion Congress and Expo (ECCE)*, Detroit, MI, October 11–15, 2020.
3. Sequeira, S., K. Bennion, J.E. Cousineau, S. Narumanchi, G. Moreno, S. Kumar, and Y. Joshi. 2020. “Validation and Parametric Investigations Using Lumped Thermal Parameter Model of an Internal Permanent Magnet Motor.” Accepted for publication for the *2020 International Technical Conference and Exhibition on Packaging and Integration of Electronic and Photonic Microsystems (InterPACK)*, October 27–29, 2020.

References

1. U.S. DRIVE. 2017. Electrical and Electronics Technical Team Roadmap: October 2017. Washington, D.C.: U.S. Department of Energy Office of Energy Efficiency and Renewable Energy Vehicle

Technologies Office.

<https://www.energy.gov/sites/prod/files/2017/11/f39/EETT%20Roadmap%2010-27-17.pdf>.

2. T.A. Lipo, Introduction to AC Machine Design, 3rd Ed. (Madison, WI: Wisconsin Power Electronics Research Center, University of Wisconsin).
3. J.R. Hendershot and T.J.E. Miller. 1994. Design of Brushless Permanent-Magnet Motors. (Oxford, UK: Magna Physics Publishing).
4. New England Wire Technologies. 2003. "Litz Wire Technical Information." http://www.litzwire.com/nepdfs/Litz_Technical.pdf.
5. J.E. Cousineau, K. Bennion, D. DeVoto, and S. Narumanchi. 2019. "Experimental Characterization and Modeling of Thermal Resistance of Electric Machine Lamination Stacks." Int. J. Heat Mass Transf. 129: 152–159. doi: 10.1016/j.ijheatmasstransfer.2018.09.051.
6. A.A. Wereszczak, J.E. Cousineau, K. Bennion, H. Wang, R.H. Wiles, T.B. Burrell, and T. Wu. 2017. "Anisotropic Thermal Response of Packed Copper Wire." J. Therm. Sci. Eng. Appl. 9 (4): 041006–041006–9. doi: 10.1115/1.4035972.
7. Arnold Magnetic Technologies. 2017. "Arnon 7 DC Magnetizing Properties." <https://www.arnoldmagnetics.com/wp-content/uploads/2017/10/Arnon-7-NGOES-Magnetization-Curve-1.pdf>.
8. Arnold Magnetic Technologies. 2017. "Arnon 7 Core Loss Properties." <https://www.arnoldmagnetics.com/wp-content/uploads/2017/10/Arnon-7-NGOES-Core-Loss-Curve-1.pdf>.
9. AK Steel. 2019. "DI-MAX® HF-10 Cold Rolled Fully Processed Non-Oriented Electrical Steel." <https://www.aksteel.com/sites/default/files/2019-10/di-max-hf-10.pdf>.
10. Thyssenkrupp. 2017. "Powercore® 020-150Y320 - Product information for electrical steel for e-mobility." https://www.thyssenkrupp-steel.com/media/content_1/publikationen/produktinformationen/powercore_no/thyssenkrupp_powercore_020-150y320_product_information_steel_en.pdf.
11. W. Sixel, M. Liu, G. Nellis, and B. Sarlioglu. 2019. "Ceramic 3D Printed Direct Winding Heat Exchangers for Improving Electric Machine Thermal Management." In 2019 IEEE Energy Conversion Congress and Exposition (ECCE), Baltimore, MD, September 29–October 3, 2019, 769–776. doi: 10.1109/ECCE.2019.8913234.

Acknowledgements

The significant contributions from Emily Cousineau, Doug DeVoto, Xuhui Feng, Bidzina Kekelia, Joshua Major, Gilbert Moreno, Sreekant Narumanchi, and Jeff Tomerlin (NREL) to the project are acknowledged. The following support and collaborations are also acknowledged: Tsarafidy Raminosoa and Randy Wiles (ORNL), Todd Monson (SNL), and Sebastien Sequeira, Yogendra Joshi, and Satish Kumar (Georgia Institute of Technology).

I.1.8 Integrated Traction Drive Thermal Management (NREL)

Bidzina Kekelia, Principal Investigator

National Renewable Energy Laboratory
15013 Denver West Parkway
Golden, CO 80401
Email: bidzina.kekelia@nrel.gov

Susan Rogers, DOE Technology Development Manager

U.S. Department of Energy
Email: susan.rogers@ee.doe.gov

Start Date: October 1, 2018
Project Funding: \$250,000

End Date: September 30, 2023
DOE share: \$250,000

Non-DOE share: \$0

Project Introduction

To enable the mass-market penetration of electric-drive vehicles and meet consumer electric vehicle performance expectations, the U.S. DRIVE 2017 *Electrical and Electronics Technical Team Roadmap* [1] proposes aggressive research and development targets aimed at reducing cost and increasing electric traction drive system power density to 33 kW/L by 2025. The target includes high-voltage power electronics and a single traction-drive electric motor. Achieving this level of system power density would most likely require integration of the inverter and the electric motor into a single traction module. However, this approach will also require innovative thermal management solutions to provide adequate cooling to more densely packed electrical components and keep their operating temperatures within optimal range.

Objectives

The main objectives of this project are to:

- Research and evaluate motor-integrated power electronics topologies and thermal management solutions for electric traction drives
- Identify candidate driveline fluids suitable for direct cooling of traction drive components and high-voltage power electronics
- Characterize selected driveline fluids by measuring convective cooling and, if appropriate and feasible, electrical properties
- Provide support to other collaborating researcher teams of the Electric Drive Technologies Consortium in thermal management aspects for their integrated drive concepts.

Approach

Based on previous literature review, three main concepts of power electronics integration into electric motors were identified (Figure I.1.8.1), and respective simplified computer-aided design (CAD) models were developed. For the electric motor geometry, the 2016 BMW i3 electric traction motor was used. The selection was based on access to its geometry/materials due to the previous teardown/evaluation by Oak Ridge National Laboratory (ORNL) and National Renewable Energy Laboratory (NREL), and availability of its detailed benchmarking/losses data [2,3]. The motor losses were used as thermal loads for thermal simulations. The power electronics CAD model was based on newer silicon-carbide (SiC) metal-oxide-semiconductor field-effect transistor (MOSFET) dies from Wolfspeed/Cree (CPM3-0900-0010A). These SiC power devices were previously used by ORNL for modeling a simulated control of the BMW i3 motor with a six-phase power module. Thus, their estimated losses/thermal loads were also available and applied during thermal simulations.

Finite element analysis (FEA) thermal simulations of the identified integration concepts were carried out and results are presented in the next section. Detailed results will also be presented and published at the ASME InterPACK 2020 conference (see Key Publications).

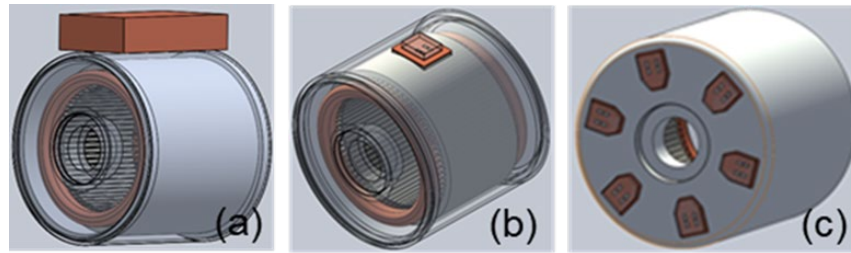


Figure I.1.8.1 Identified integration concepts: (a) separate power electronics enclosure attached to motor case, (b) power electronics mounted/distributed radially on the motor casing, and (c) power electronics integrated axially in the motor front/back plate (Figures by Bidzina Kekelia, NREL)

Support activities in thermal management component design and thermal modeling for integrated traction drives of ORNL and University of Wisconsin research teams were initiated. Preliminary cooling concepts for ORNL's outer-rotor motor is presented in the Results section. Collaboration with the University of Wisconsin team is at an early stage and results will be presented in an FY21 progress report.

Results

Modeling Integration Concepts

Based on CAD models discussed in the previous section, thermal models were developed for FEA simulations in ANSYS. For the integration approach with separate enclosures and cooling loops for the power electronics and the electric motor (Figure I.1.8.1a), simulations in ANSYS were carried out separately for the power electronics and the electric motor. For the radially (Figure I.1.8.1b) and axially (Figure I.1.8.1c) integrated power electronics concepts, thermal models were based on the CAD models shown in Figure I.1.8.2a and Figure I.1.8.2b, respectively.

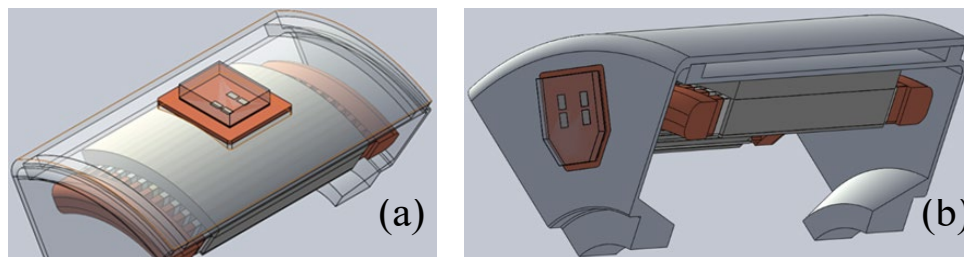


Figure I.1.8.2 Radially (a) and axially (b) integrated CAD model based on the BMW i3 traction motor and SiC power devices (shared cooling) (Figures by Bidzina Kekelia, NREL)

FEA thermal simulations were performed for a set of heat transfer coefficients (HTCs), and results for the three integration configurations were compared. Coolant temperature was assumed at $T_{fluid} = 65^{\circ}\text{C}$ and the convective HTC was applied to the internal surfaces of the cooling jacket and the back surface of the power module copper base plate (see Figure I.1.8.3), which is exposed to the coolant flow or impinging jets through the openings in the case enclosure. HTC was varied from $h = 20\text{--}75,000\text{ W/m}^2\cdot\text{K}$ for each configuration. The HTC range spans from the upper end of air natural convection ($20\text{--}25\text{ W/m}^2\cdot\text{K}$), to forced air convection ($50\text{--}500\text{ W/m}^2\cdot\text{K}$), to forced liquid (WEG) convection with jet impingement towards the higher end ($500\text{--}50,000\text{+ W/m}^2\cdot\text{K}$) and phase-change ($10,000\text{--}75,000\text{+ W/m}^2\cdot\text{K}$) cooling techniques.

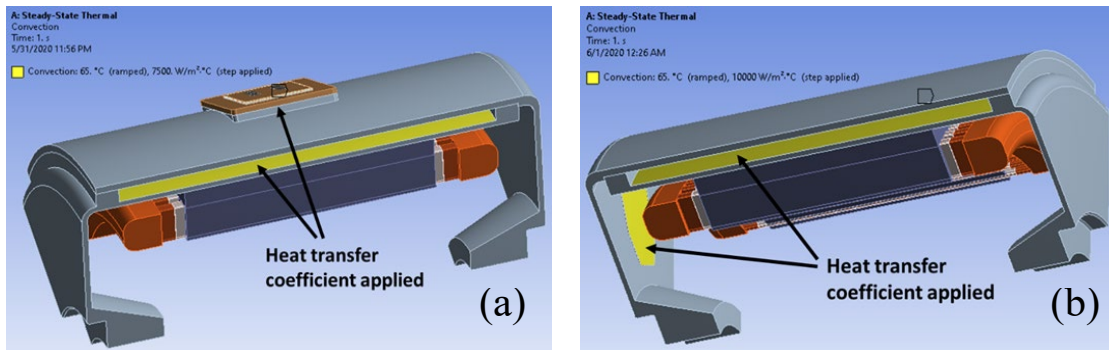


Figure I.1.8.3 HTC applied to the internal surfaces of the cooling jacket and the back of the power module copper base plate. Radially (a) and axially (b) integrated solutions shown (Figures by Bidzina Kekelia, NREL)

Temperature distributions in key components for each configuration were similar. The integrated power electronics cooling approach for both the radial and axial integration configurations seem reasonable, as the SiC power device temperatures were below key motor component temperatures. For illustration, one set of results is provided in Figure I.1.8.5 and Figure I.1.8.4. As can be seen from these figures, the highest temperatures can be observed in the winding end-turns, where a large amount of heat is generated and the thermal path resistance to the cooling fluid is the highest. From a thermal management perspective, the application of automatic transmission fluid (ATF) jet impingement cooling technique to winding end-turns may benefit overall temperature distributions within the traction drive. In the radial integration configuration, due to limited space in the cooling jacket channels, it may be difficult to substitute water–ethylene glycol (WEG) coolant with ATF jet impingement for power module cooling, but the axial integration provides an excellent opportunity for cooling the back side of the power module with ATF jets. With a single delivery channel, nozzles could be positioned with jets on one side impinging on the winding end-turns, and jets in the opposite direction cooling the back side of a power module.

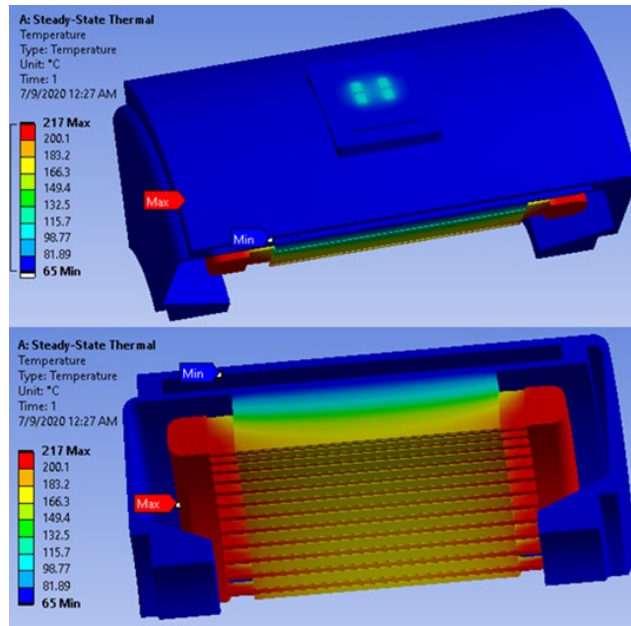


Figure I.1.8.4 Temperature distribution from the FEA thermal model for the radially integrated BMW i3 motor and power module based on SiC devices (applied HTC of $h = 10,000 \text{ W/m}^2\text{K}$). The top image is showing a location and temperatures of the integrated power module in the motor case (maximum temperature is pointing to winding end turns hidden under the motor case). The lower image is showing temperature distribution in the key motor components (Figures by Bidzina Kekelia, NREL).

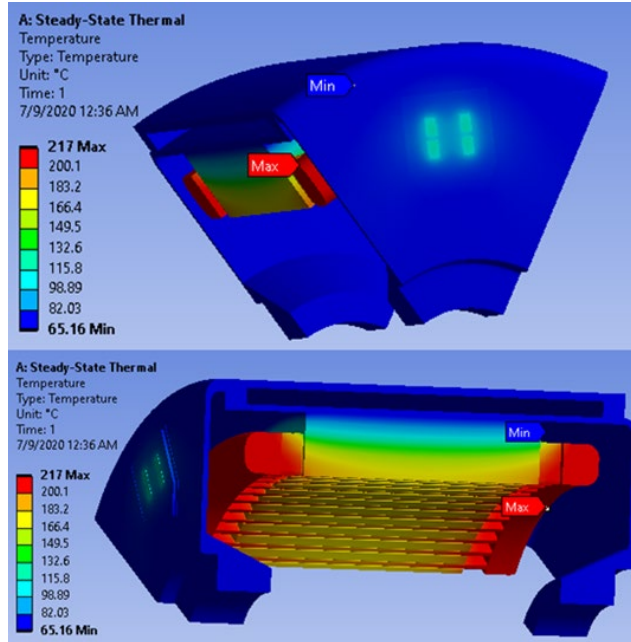


Figure I.1.8.5 Temperature distribution from the FEA thermal model for the axially integrated BMW i3 motor and power module based on SiC devices (applied HTC of $h = 10,000 \text{ W/m}^2\text{K}$). The top image is showing a location and temperatures of the integrated power module in the motor case. The lower image is showing temperature distribution in the key motor components (Figures by Bidzina Kekelia, NREL).

CFD Modeling of ATF Fan Jet Impingement

In case of cooling motor windings, a fan jet provides much larger surface coverage and may have a better overall cooling effect compared to a circular jet. A computational fluid dynamics (CFD) modeling study was carried out for different configurations of ATF fan jet impingement cooling technique (Figure I.1.8.6).

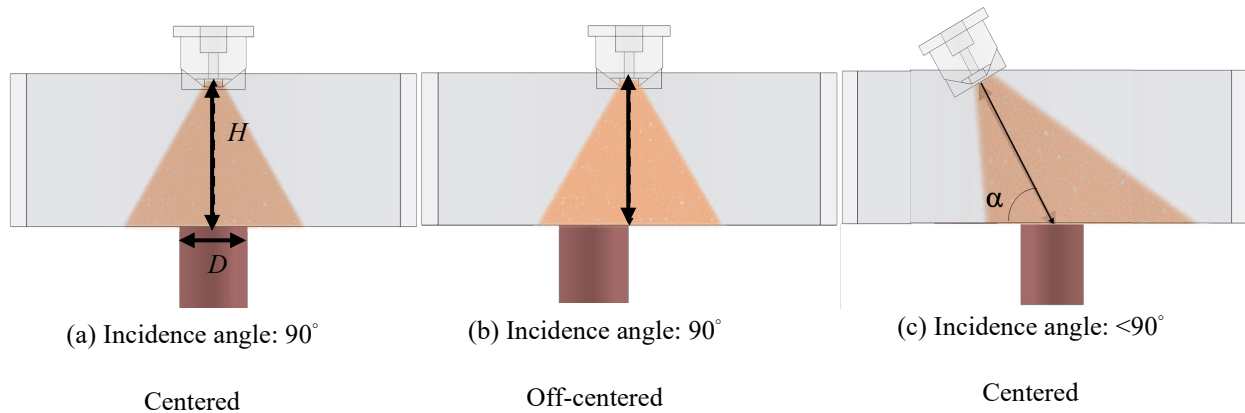


Figure I.1.8.6 ATF fan jet impingement configurations: (a) centerline of fan nozzle is aligned with the center of copper target, (b) centerline of fan nozzle is aligned with the edge of copper target, and (c) centerline of fan nozzle is tilted with regards to copper target (Figures by Xuhui Feng, NREL)

As part of the study, fan and circular jets were also compared with the same nozzle-to-target distance of 10 mm and the same flow rates and temperatures (Figure I.1.8.7). The selection of nozzle depends on the area to be cooled. Circular jets are more capable for point-like hot spots or localized thermal management, whereas fan jets work more efficiently for more spread-out heat dissipation by providing liquid with high-aspect-ratio distribution.

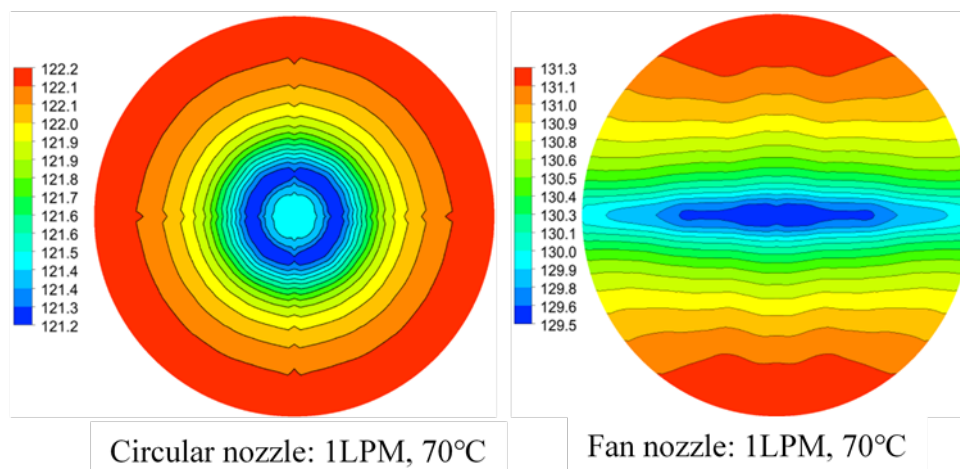


Figure I.1.8.7 ATF circular (left) and fan (right) jet impingement isotherms on the target surface at 1 liter per minute (LPM) flow rate and 70°C fluid temperature (Figures by Xuhui Feng, NREL)

In all examined cases, the circular jet resulted in higher HTC and more even temperature distribution on the impinged surface than the fan jet. Over the flow velocities studied in this work, the orifice jet provides average HTCs about 20%–25% higher as compared to the fan jet (Figure I.1.8.8). The possible reason is that whereas the circular jet impinges on the center of a target, the fan jet spreads beyond the target surface, with a considerable amount of fluid missing the target surface. The detailed manuscript of the study will be published in a high-impact journal.

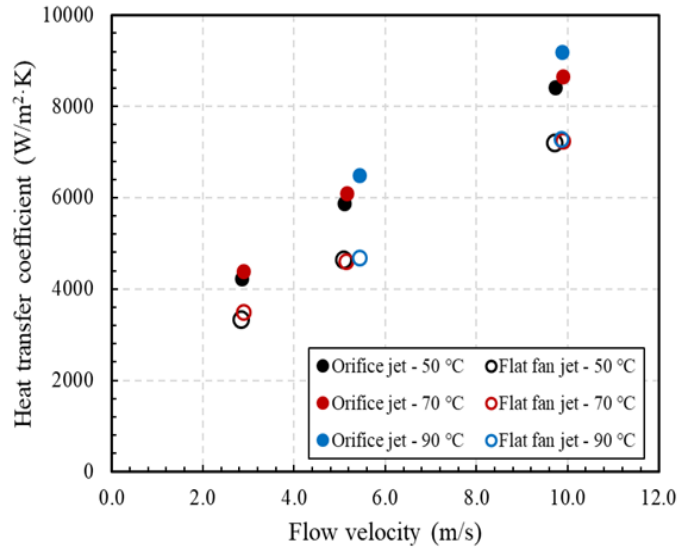


Figure I.1.8.8 Model-predicted HTC results of the flat fan jet compared with the experimental results of circular jet impingement, with 10-mm nozzle-to-target distance. Studied flow velocities are 3, 5, and 10 m/s and fluid temperatures are 50 °C, 70 °C, and 90 °C. (Figure by Xuhui Feng, NREL)

Experimental convective heat transfer characterization of jet impingement cooling with automatic transmission fluid (ATF) was not carried out during FY20. The plan is to modify the existing experimental fluid loop for characterization of additional parameters and continue planned work in FY21.

Supporting ORNL’s Outer-Rotor Integrated Motor Design

A novel packaging concept for housing and cooling an inverter, which will be integrated in the central cavity of a stator of ORNL’s outer-rotor motor (Figure I.1.8.9), was proposed. Six power modules (for a six-phase inverter) are packed into a cylindrical enclosure consisting of two half-cylinders with cooling fluid channels (see Figure I.1.8.10 and Figure I.1.8.11).

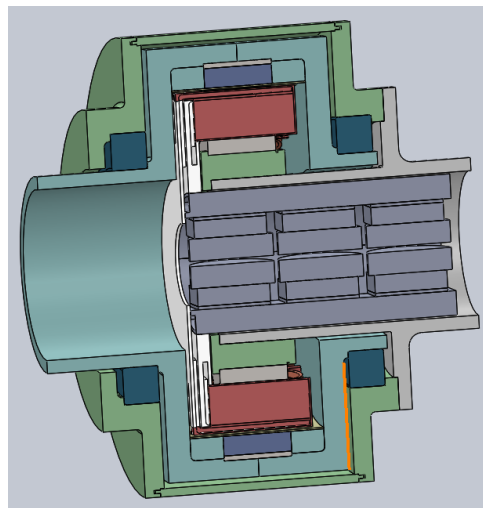


Figure I.1.8.9 ORNL’s outer-rotor motor with integrated inverter in the central cavity (Figure by Bidzina Kekelia, NREL)

Cooling fluid is pushed through the channels in half-cylinder walls (Figure I.1.8.10) and distributed via a distribution manifold-disk to phase-separator heat exchangers embedded between stator windings of the motor (Figure I.1.8.11). The fluid is supplied and removed from only one side of the phase-separator heat exchangers, which allows electrical connections from windings to inverter to be made from the opposite side. Initial design of the distribution manifold-disk is shown in Figure I.1.8.11.

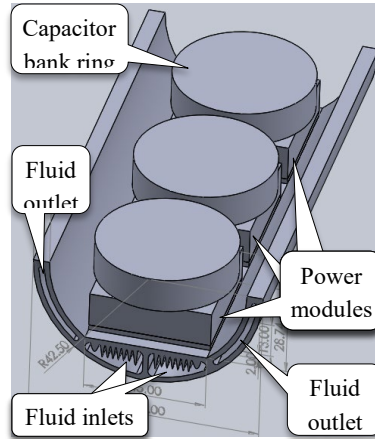


Figure I.1.8.10 Half-cylinder inverter housing with cooling fluid channels (Figure by Bidzina Kekelia, NREL)

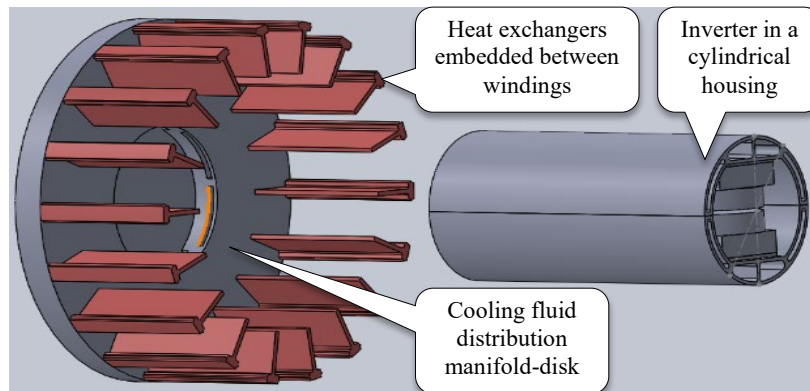


Figure I.1.8.11 Initial design of cooling system components: cylindrical housing with cooling fluid channels for an inverter, fluid distribution manifold-disk, and phase separator heat exchangers embedded between windings (Figure by Bidzina Kekelia, NREL)

As it became apparent during design and discussions with the ORNL team, the thickness of the distribution manifold-disk had to be reduced and sunk between winding end-turns to keep the motor size within targeted dimensions. The second iteration of the distribution manifold-disk with attached phase-separator heat exchangers and cylindrical inverter enclosure is shown in Figure I.1.8.12. The manifold-disk thickness was reduced from 15 mm to 13 mm, and internal channel routings were modified to allow winding end-turn cutouts. Further thermal system design and analysis is planned in FY21 by the NREL team, including FEA and CFD modeling.

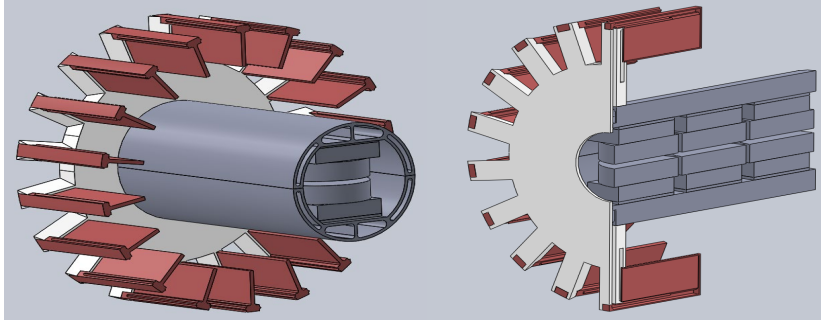


Figure 1.1.8.12 The second iteration of the design of cooling system components: fluid distribution manifold-disk is thinner and modified with cutouts for winding end-turns (Figure by Bidzina Kekelia, NREL)

Conclusions

The project accomplishments and conclusions for FY20 are summarized as follows:

- Thermal steady-state FEA simulations for three different integration configurations were carried out in ANSYS and results were compared. The integrated power electronics cooling approach for both the radial and axial integration configurations seem reasonable, as the SiC power device temperatures were below key motor component temperatures.
- A CFD modeling study was carried out for different configurations of the ATF fan jet impingement cooling technique. Fan and circular jets were also compared as part of the study. At all examined flow velocities, circular jets provide heat transfer coefficients 20%–25% higher than those obtained from the fan jet impingement. On the other hand, fan jets could provide more coverage and better temperature uniformity when cooling winding end turns.
- A novel, cylindrical packaging concept for housing and cooling an inverter was proposed, which will be integrated in the central cavity of a stator of ORNL’s outer-rotor motor. Cooling system components for ORNL’s outer-rotor motor are being designed, including a cooling fluid distribution manifold-disk supplying fluid to phase-separator heat exchangers embedded between stator windings. Further design and modeling of these components is planned by the NREL team in FY21.

Key Publications

1. Kekelia, B., J.E. Cousineau, K. Bennion, S. Narumanchi, and S. Chowdhury. 2020. “Comparison of Thermal Management Approaches for Integrated Traction Drives in Electric Vehicles.” Presented at the *ASME 2020 International Technical Conference and Exhibition on Packaging and Integration of Electronic and Photonic Microsystems (InterPACK)*, Anaheim, CA, Oct. 27–29, 2020.

References

1. U.S. DRIVE. 2017. *Electrical and Electronics Technical Team Roadmap*: U.S. Department of Energy Office of Energy Efficiency and Renewable Energy Vehicle Technologies Office. <https://www.energy.gov/sites/prod/files/2017/11/f39/EETT%20Roadmap%2010-27-17.pdf>.
2. Burress, T. 2016. “Benchmarking EV and HEV Technologies.” U.S. DOE Vehicle Technologies Office 2015 Annual Merit Review and Peer Evaluation Meeting, Washington, D.C., June 7, 2016. https://www.energy.gov/sites/prod/files/2016/06/f32/edt006_burress_2016_o_web.pdf.
3. Burress, T. 2017. “Electrical Performance, Reliability Analysis, and Characterization.” 2017 U.S. DOE Vehicle Technologies Office Annual Merit Review, Washington, D.C., June 6, 2017. https://www.energy.gov/sites/prod/files/2017/06/f34/edt087_burress_2017_o.pdf.

Acknowledgements

The author would like to acknowledge the significant contributions of Kevin Bennion, Emily Cousineau, Xuhui Feng, and Gilbert Moreno from NREL. Valuable input and technical data from Shajjad Chowdhury and Tsarafidy Raminosa from ORNL are also appreciated.

I.1.9 Power Electronics Materials and Bonded Interfaces – Reliability and Lifetime (NREL)

Paul Paret, Principal Investigator

National Renewable Energy Laboratory
15013 Denver West Parkway
Golden, CO 80401
Email: paul.paret@nrel.gov

Susan Rogers, DOE Technology Development Manager

U.S. Department of Energy
Email: susan.rogers@ee.doe.gov

Start Date: October 1, 2018
Project Funding: \$175,000

End Date: September 30, 2023
DOE share: \$175,000

Non-DOE share: \$0

Project Introduction

Robust and reliable power electronics packaging technologies are critical for the safe operation of wide-bandgap devices such as silicon carbide and gallium nitride, particularly at high temperatures. The unique characteristics of wide-bandgap devices that prove to be challenging for their packaging are high switching speed (dV/dt and di/dt), high operation temperature, and high electric field. The cost, weight, and power-density targets for these packages or modules only increase the challenges associated with their design and development. Material selection and component design within a package play a key role in determining its reliability and lifetime under high-temperature operating conditions. Advanced packaging layouts, such as 3D packaging, planar interconnects, and direct-lead bonding, are considered by researchers and engineers to minimize loop parasitics and reduce the junction-to-coolant thermal resistance. Materials in the right combination need to be properly integrated to address the inherent coefficient of thermal expansion and stiffness mismatch issues within packaging.

For a traditional silicon device-based power electronics package, bonded interfaces (i.e., die-attach and substrate-attach) are prone to failure under environmental loading conditions such as thermal cycling and power cycling. The reliability of the package is dictated—to a significant extent—by the ability of these interface materials to withstand the stress imposed on them under long-term exposure to high temperatures and thermal gradients. While the maximum operating temperature of Si devices is around 150°C, the 200°C–250°C desired operating temperature range of wide-bandgap devices places a more stringent requirement on the reliability and lifetime of the bonded interfaces. Solders such as SAC305 and 63Sn37Pb are not suitable for operation at these extreme temperatures. Among the high-temperature-compatible bonded interfaces, sintered silver and transient liquid-phase bonded materials are regarded as strong candidates; however, their reliability and failure mechanisms at high temperatures need to be investigated.

This report describes research at the National Renewable Energy Laboratory (NREL) in assessing the reliability and lifetime prediction model development of sintered silver and the copper-aluminum (Cu-Al) transient-bonded interface material. In collaboration with Virginia Tech (VT), samples with sintered silver as the bonded material were fabricated and subjected to accelerated thermal cycling. High-lead solder samples were also fabricated at NREL for comparison with sintered silver results. In addition, efforts to develop a preliminary crack propagation model for these materials are reported. Along with sintered silver, collaborative efforts between NREL and Georgia Tech on the fabrication of Cu-Al bonded interface samples are discussed.

Objectives

The major objectives of this project are to:

- Evaluate the reliability of sintered silver by subjecting coefficient of thermal expansion (CTE)-mismatched coupons—with sintered silver as the bonded interface material—to accelerated thermal

cycling. Crack propagation or any other failure mechanisms that originate and evolve under thermal cycling will be periodically monitored through scanning acoustic microscopy imaging.

- Develop thermomechanical models to obtain theoretical parameters such as von Mises stress, strain-energy density, and J-integral, and formulate a lifetime prediction model based on these modeling outputs and experimental data.
- Synthesize Cu-Al bond samples with less than 5% void fraction and subject these samples to accelerated thermal cycling.

Approach

Sintered Silver

In previous years of this project, sintered silver samples were fabricated at VT using two different synthesis profiles. One was purely a pressureless sintering approach, while a small amount of sintering pressure in the range of 3–10 MPa was attempted in the other profile. The pressureless sintering profile never resulted in good quality joints, whereas joints with less than 3% void fraction were obtained in almost all the pressure-sintered samples. In all cases, the sample configuration consisted of a Cu disk bonded to an Invar disk with sintered silver as the bonded material, as shown in Figure I.1.9.1. The diameter and thickness of these disks are 25.4 mm (1 inch) and 2 mm, respectively. With this configuration, samples with three different bond diameters (22 mm, 16 mm, and 10 mm) were fabricated and then subjected to a thermal cycle from -40°C to 200°C . Scanning acoustic microscope (C-SAM) images of the samples obtained after 50 cycles revealed a large amount of degradation in the sintered silver joint layer. A combination of adhesive and cohesive crack propagation was observed in the cross-sectional images of these samples. Thermomechanical modeling to study the degradation behavior of sintered silver joints under thermal cycling was also developed.



Figure I.1.9.1 Circular coupons ($\Phi 25.4\text{mm}$) for reliability evaluation; Cu (bottom) bonded to Invar (top) using sintered silver or high-lead solder (95Pb5Sn)

In FY 2020, samples of the same configuration but with high-lead solder (95Pb5Sn) as the bonded material were fabricated at NREL and subjected to thermal cycling for obtaining reference data. The joint diameter was kept at 10 mm for a direct comparison with the corresponding sintered silver samples. A few extra samples in which the 95Pb5Sn solder was flush with the outer disks were also synthesized. In general, it was more challenging to maintain a certain diameter for the solder joints than sintered silver because the soldering process involves the material entering a liquid phase, whereas sintering is a purely solid diffusion process. Additionally, both sintered silver and solder samples with 1-mm-thick Cu and Invar disks were fabricated to study the impact of sample thickness on the reliability of the bonded material.

While all the samples mentioned previously were subjected to a thermal cycle from -40°C to 200°C , sintered silver samples were also synthesized for cycling between -40°C and 150°C . These samples were fabricated at NREL and the material paste was purchased from an industry partner. A purely pressureless sintering approach was employed for the synthesis of these samples [1]. For reliability comparison, SAC305 solder was selected due to its maturity in commercial use and well-established synthesis procedures in the literature. In summary, the reliability of sintered silver joints was compared with 95Pb5Sn solder for high-temperature cycling, and with SAC305 solder for a standard thermal cycling range.

Cu–Al transient liquid-phase bond

A transient liquid-phase bond was developed at Georgia Tech using a Cu–Al eutectic [2], which can be used as a bonded material in high-temperature power electronics applications. To create this bond, Cu and Al foils are joined in a specific bulk ratio and heated above their eutectic point, but below the melting temperature of the constituent metals. Although this material has demonstrated potential for high reliability under certain specific configurations in other projects, its reliability—when used for bonding in CTE-mismatched samples under a thermal cycle of -40°C to 200°C —needs to be evaluated. To this end, attempts were made at Georgia Tech in FY 2019 to bond Cu–Al alloy between Cu and Invar disks; however, the weak diffusion between the Invar and Cu–Al alloy resulted in poor samples that delaminated even prior to thermal cycling. In FY2020, synthesis of a few trial samples was attempted in which the Cu–Al alloy was bonded between Cu and AlSiC coupons.

Thermomechanical modeling

In the previous year, nonlinear finite element analyses were conducted on the circular sintered silver samples to compute various theoretical parameters such as stress, strain, and strain energy density and how these vary as the stiffness of the overall sample is altered. The sample stiffness was changed by varying the thickness of the Cu and Invar coupons. These output parameters offer insight into the reliability of the sintered silver material and combining them with the cycles-to-failure experimental results would result in the formulation of lifetime prediction models. In FY 2020, the modeling was extended to samples of square footprint and a comparative analysis was conducted to study how the circular or square coupons affect the degradation behavior of the bonded material. Figure I.1.9.2 shows a schematic that represents the scope of this thermomechanical modeling.

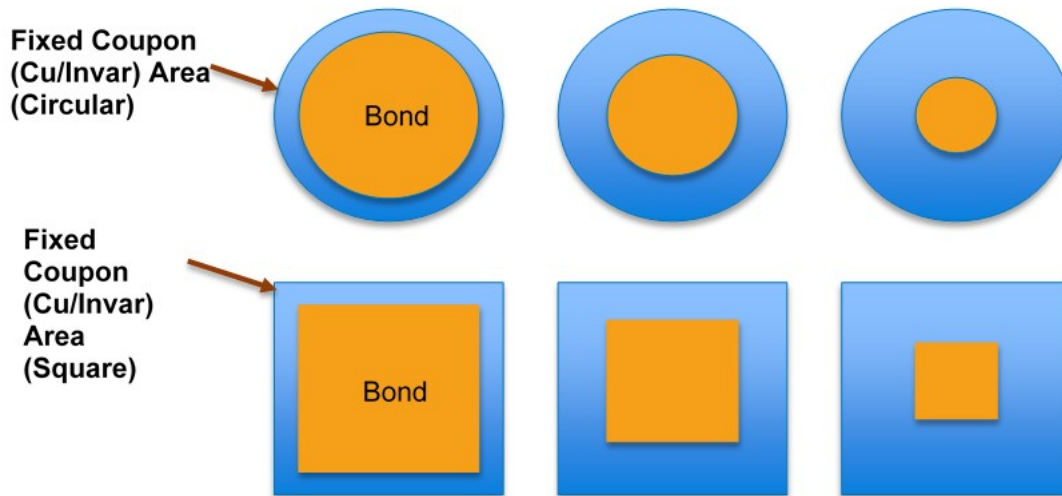


Figure I.1.9.2 Schematic of design configurations selected for thermomechanical modeling. Circular- and square-shaped samples were considered.

Additionally, a 2D crack propagation model to simulate the growth of cracks within sintered silver under a mechanical or a temperature varying load was developed. The model is based on the extended finite element method [3], which allows for crack propagation without remeshing the geometry. In this model, the potential crack growth region within the geometric domain is initially identified based on user inputs and a crack is manually defined within this region. The objective of this model is to compute outputs such as stress intensity factor or J-integral around the crack tip as the crack propagates and use those outputs to estimate the cycles-to-failure result based on an empirical equation such as the Paris law. The model is currently rudimentary in nature and is limited to just linear elastic material models. The geometric domain used to implement the crack propagation model is shown in Figure I.1.9.3.

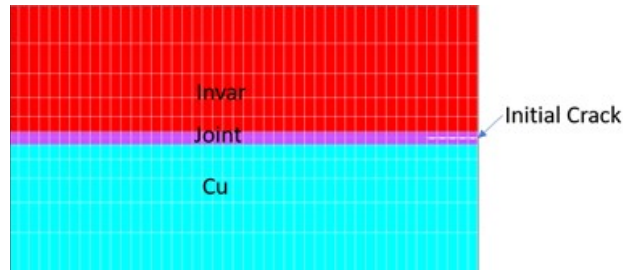


Figure I.1.9.3 2D model crack propagation model setup

Results

Comparison of solder joints with sintered silver

Case A: 2-mm-thick samples

Figure I.1.9.4 shows the C-SAM images of 95Pb5Sn solder joints as these samples were subjected to thermal cycling from -40°C to 200°C . The white dots on the images before cycling indicate the presence of voids, which are common with solder joints. Crack formation started to occur in these joints after around 40–50 thermal cycles and are revealed by the white patches in the C-SAM images. A careful observation of this figure shows that the Cu-side and Invar-side images are somewhat mirror images of each other, which leads to the plausible conclusion that unlike sintered silver, only one failure mechanism occurred in the solder joints. Based on the reported failure mechanisms of solder joints in the literature, it is likely that this failure mechanism is cohesive cracking; however, this hypothesis can be proved only with an analysis of the cross-sectional images of samples after the completion of thermal cycling. A comparison of the crack growth rate in solder and sintered silver samples is presented in Figure I.1.9.5. In both events of thermal cycling, solder joints outperformed sintered silver samples with significantly lower crack growth rates, especially in the case of SAC305 solder. The measured crack growth area for SAC305 solder samples was around 15%, even after 125 thermal cycles, whereas sintered silver samples can be considered failed in just 10 thermal cycles, following the failure criterion of 20% crack growth by area.

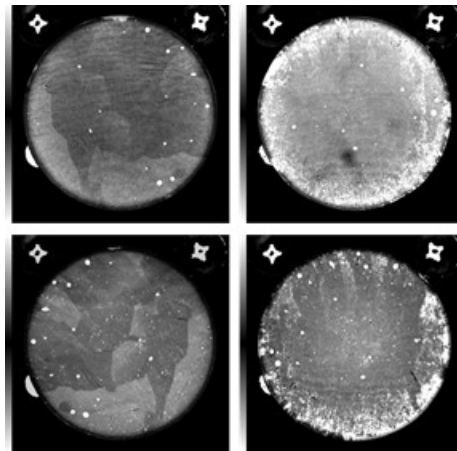


Figure I.1.9.4 C-SAM images of 95Pb5Sn solder joints before cycling (left) and after 50 thermal cycles (right); Cu-side images (top) and Invar-side images (bottom)

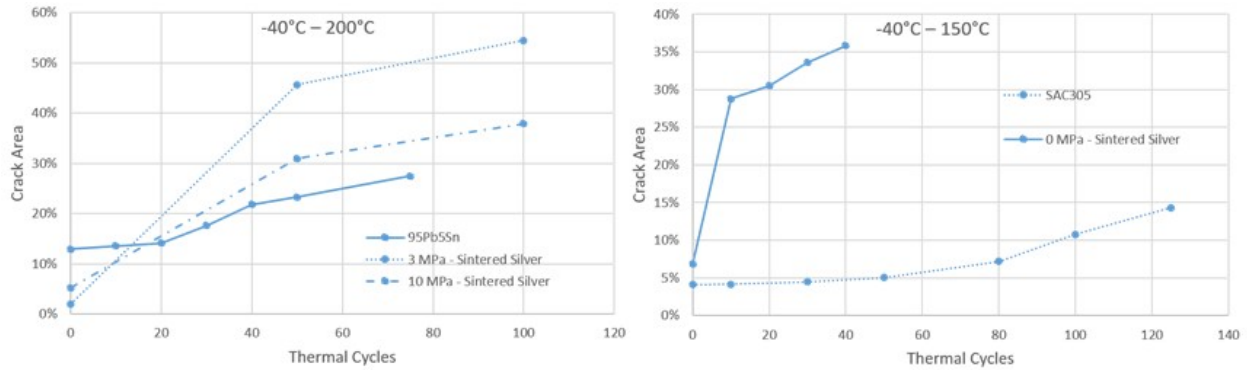


Figure I.1.9.5 Comparison of sintered silver samples with 95Pb5Sn solder (left) and SAC305 solder (right). Pressureless sintered silver samples were used for the comparison with SAC305 solder joints.

Case B: 1-mm-thick samples

Samples of the same configuration as shown in Figure I.1.9.1 but with 1-mm-thick Cu and Invar coupons were fabricated using both pressure-assisted sintered silver and 95Pb5Sn solder joints. Under a thermal cycling of -40°C to 200°C , most of the sintered silver samples delaminated just after 10 cycles, whereas no cracks or any defects were visible in the 95Pb5Sn solder joints even after 50 cycles. Figure I.1.9.6 shows the C-SAM images of 95Pb5Sn solder joints. Similar to the 2-mm-thick samples, solder joints in this modified sample configuration proved to have a higher reliability than the sintered silver joints. In general, as the thickness of the adjacent disks decreases, the reliability of the joint should increase as lower stresses are imparted onto it. While the CTE-mismatch remains the same, the sample stiffness, which plays an important role, is reduced with thinner disks, thus leading to a joint with higher reliability. Based on this argument, sintered silver samples with 1-mm-thick Cu and Invar coupons were expected to perform better than 2-mm-thick samples. The complete delamination of these samples just after 10 cycles could likely be due to the weak bonding between sintered silver and the adjacent disks, even though C-SAM images did not reveal any major cracks or voids before cycling.

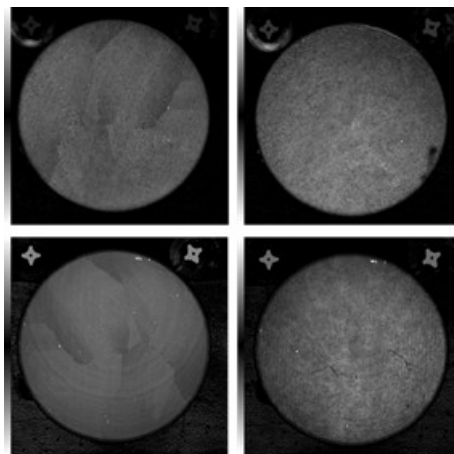


Figure I.1.9.6 C-SAM images of 95Pb5Sn solder joints before cycling (left) and after 30 thermal cycles (right); Cu-side images (top) and Invar-side images (bottom)

Cu-Al transient liquid-phase bond

Due to the weak diffusion between Cu-Al alloy and Invar disks, which resulted in delamination of the samples even prior to thermal cycling, attempts were made to create Cu-Al joints between Cu and AlSiC coupons. The footprint of these coupons was 1×1 inch (25.4×25.4 mm). While the thickness of the AlSiC coupons was fixed at 5 mm, thicknesses of 1 mm and 2 mm were used for the Cu coupons. After the samples were fabricated at Georgia Tech, the joint evaluation was performed at NREL through C-SAM images. Figure

I.1.9.7 shows the C-SAM images of the Cu-Al joint between Cu and AlSiC samples. Large patches of white regions can be observed in one of these images which denote the presence of voids. Although no such voids can be seen in the other image (the white band is an artifact of the C-SAM imaging process), the fabrication process should consistently produce such samples before finalizing the synthesis profile. Additional iterations and refinements to the synthesis process are currently ongoing at Georgia Tech to improve the bond quality of these samples.

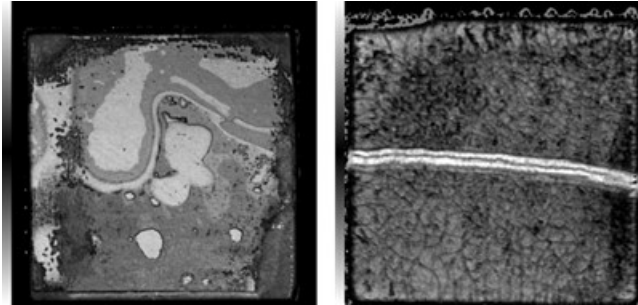


Figure I.1.9.7 C-SAM images of Cu-Al transient liquid-phase alloys between AlSiC and Cu coupons. The thickness of the Cu coupons was 1 mm (left) and 2 mm (right).

Thermomechanical modeling

Simulations were performed in the ANSYS Workbench platform to compare the impact of the sample shape on the reliability of the sintered silver joint. A thermal cycle load of -40°C to 200°C was applied on the model four times in succession to obtain convergence in results. After solution, the volume-averaged strain energy density of the entire bond pad region was computed for the different cases and are presented in Figure I.1.9.8.

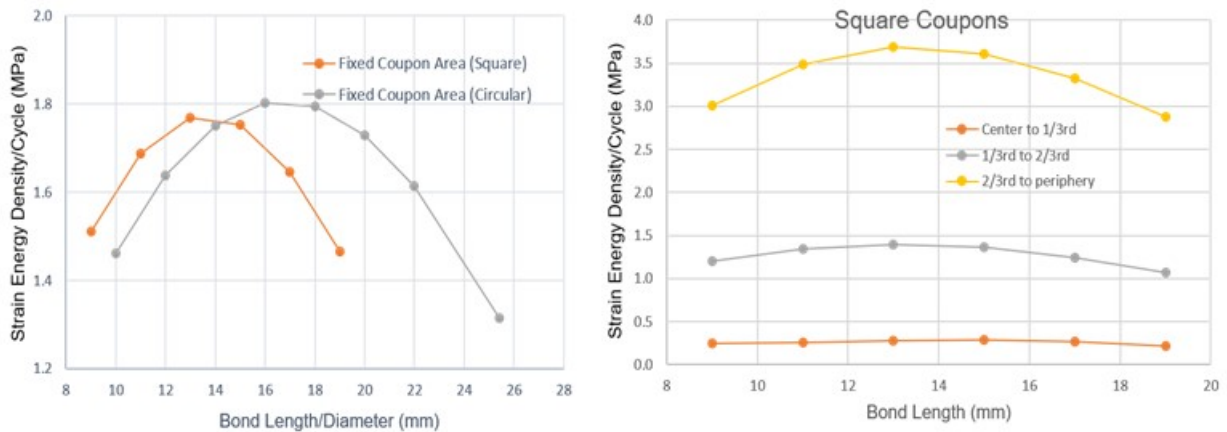


Figure I.1.9.8 Strain energy density comparison between square and circular samples (left); strain energy density variation within the bond region of a square sample (right).

Both square- and circular-shaped samples exhibit a similar trend in the variation of strain energy density values as the bond diameter/length changes. The area of the outer coupons was fixed in all cases. To understand this trend in greater detail, values of strain energy density per cycle were extracted over various regions of the sintered silver bond in square-shaped samples and plotted in Figure I.1.9.8. These results show that the highest values of strain energy density occur in the outermost regions of the bond and is where failure is likely to occur. For a fixed outer coupon area, a bond that is approximately 50% in size compared to the outer coupons would be the least-reliable joint under a thermal cycling condition. Further reductions in bond size would, in fact, increase the reliability of the joint, as the smaller bond size likely excludes the outer regions of the outer coupons in imparting any stresses onto the joint.

It should be noted that the trends observed for sintered silver joints in modeling were not actually replicated in the experimental samples. This disagreement between modeling and experimental results points to the limitations of constitutive material models that are macroscopic in nature to study the failure mechanisms of sintered silver under thermal cycling. To capture the failure mechanisms more accurately, microstructural models that simulate the initiation and propagation of cracks within these joints are required. Crack propagation models are also based on certain assumptions, but the intent here is to bridge the gap between modeling and experimental results. To this end, a preliminary 2D crack propagation model based on the extended finite element method was developed in ANSYS. After the model setup, loading was applied in the form of a temperature ramp from 25°C to 200°C. Under these conditions, the initially defined crack was observed to be propagating through the sintered silver joint. Additional post-processing work will be conducted on this model to compute relevant outputs such as stress intensity factor and J-integral values at the crack tip. Figure I.1.9.9 shows the crack extending to adjacent elements under the temperature loading.

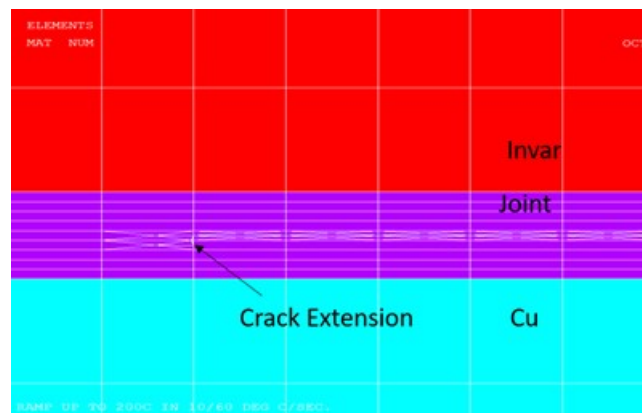


Figure I.1.9.9 Propagation of the initially defined crack within the bonded joint under a temperature ramp loading from 25°C to 200°C

Conclusions

Power electronics packaging for safe operation of wide-bandgap devices at high temperatures is a challenging research goal. This project focuses on the reliability evaluation and lifetime prediction of bonded materials to determine their applicability in high-temperature packaging. The bonded materials of interest are sintered silver and a transient liquid-phase Cu-Al bond.

Experimental evaluation of the reliability of sintered silver, 95Pb5Sn solder, and SAC305 solder bonded between CTE-mismatched coupons were conducted through accelerated thermal cycling. Two different cycling profiles were considered, and in both cases the reliability of the solder joints was found to be higher than sintered silver. The conclusion remained the same with these materials, even when the sample configuration was altered. In certain cases, complete delamination of the sintered silver samples occurred in just 10 thermal cycles. Overall, these results point to the limitations in thermomechanical performance of the sintered silver joints and challenges of high-temperature power electronics packaging. In addition to sintered silver, a transient liquid-phase Cu-Al bond and sintered copper are currently being explored for their reliability in high-temperature packaging.

Thermomechanical modeling study explored the impact of the shape of sample configuration and concluded that the degradation behavior of the bonded materials in both square- and circular-shaped samples are similar in nature. A preliminary 2D crack propagation model to simulate the failure mechanisms in these high-temperature materials was also developed. Future work will focus on extending the crack simulation model to 3D, as well as refining the geometric domain to include microstructural features of the material.

Key Publications

1. Paret, P. 2019. “Performance and Reliability of Bonded Interfaces for High-Temperature Packaging.” In *Electrification: 2018 Annual Progress Report*, Washington, D.C.: U.S. Department of Energy Office of Energy Efficiency and Renewable Energy Vehicle Technologies Office.
2. Paret, P. 2020. “Power Electronics Materials and Bonded Interfaces – Reliability and Lifetime.” *DOE VTO Annual Merit Review*, Washington, D.C., June 2020.
3. Paret, P., DeVoto, D., Major J., and Narumanchi, S. “Parametric Design Study of a Power Electronics Package for Improving Solder Joint Reliability.” *2020 19th IEEE Intersociety Conference on Thermal and Thermomechanical Phenomena in Electronic Systems (ITherm)*, Orlando, FL, July 21–23, 2020, 1065–1072, doi: 10.1109/ITherm45881.2020.9190318.

References

1. P. Paret, J. Major, D. DeVoto, S. Narumanchi, Y. Tan, and G.-Q. Lu. 2018. “Mechanical Characterization Study of Sintered Silver Pastes Bonded in a Double-Lap Configuration.” *ASME 2018 International Technical Conference and Exhibition on Packaging and Integration of Electronic and Photonic Microsystems*, August 2018, doi: 10.1115/IPACK2018-8276.
2. D. G. Pahinkar, W. Puckett, S. Graham, L. Boteler, D. Ibitayo, S. Narumanchi, P. Paret, D. DeVoto, and J. Major. 2018. “Transient Liquid Phase Bonding of AlN to AlSiC for Durable Power Electronic Packages.” *Adv. Eng. Mater.* 20, no. 10: 1800039.
3. M. Stolarska, D. L. Chopp, N. Moës, and T. Belytschko. 2001. “Modelling crack growth by level sets in the extended finite element method.” *International Journal for Numerical Methods in Engineering*, 51, no. 8: 943–960, doi: 10.1002/nme.201.

Acknowledgements

The contributions of Joshua Major and Douglas DeVoto in conducting several reliability evaluation experiments are acknowledged. The author also would like to thank Chao Ding and G.-Q. Lu at VT and Chidinma Imediegwu and Samuel Graham at Georgia Tech for their valuable technical inputs and help with sample synthesis.

I.1.10 Power Electronics Thermal Management (NREL)

Gilbert Moreno, Principal Investigator

National Renewable Energy Laboratory
15013 Denver West Parkway
Golden, CO 80401
Email: gilbert.moreno@nrel.gov

Susan Rogers, DOE Technology Development Manager

U.S. Department of Energy
Email: susan.rogers@ee.doe.gov

Start Date: October 1, 2018

End Date: September 30, 2023

Project Funding: \$350,000

DOE share: \$350,000

Non-DOE share: \$0

Project Introduction

The 2017 *Electrical and Electronics Technical Team Roadmap* [1] proposes aggressive research and development targets aimed at improving power electronics technology to enable the mass-market penetration of electric-drive vehicles. Achieving these aggressive targets will require a decrease in cost (year 2025 cost target: \$2.70/kW) and an increase in power density (year 2025 power density target: 100 kW/L) as compared with current on-road technology. Replacing traditional silicon device-based components with more efficient and higher-temperature wide-bandgap (WBG) semiconductor device-based components will enable increased power density. However, meeting the power density target will also require innovative thermal management solutions to increase the heat fluxes dissipated and allow for compact electronics packaging.

This project conducts research to develop new power electronics thermal management technologies to increase power density, enable high WBG temperature operation, and decrease cost. One of the main challenges to achieving high power densities is associated with packaging of high-temperature (up to 250°C) WBG devices near lower-temperature-rated components (e.g., electrical boards and capacitors). Additionally, the high junction temperatures of the WBG devices will result in large temperature gradients through the power module layers, which will present reliability challenges and require higher-temperature substrates and bonding materials.

Objectives

The primary project objective is to develop novel thermal management technologies to enable achieving the 100-kW/L power density target. Additional project objectives are to:

- Develop cooling solutions that enable high-temperature WBG operation and low-temperature, low-cost capacitors.
- Decrease cost by proposing low-cost cooling technologies that enable decreasing the number of semiconductor devices and use automotive-qualified fluids (e.g., water-ethylene glycol [WEG], automatic transmission fluid [ATF])

Approach

A power electronics thermal metric that is predicted to enable reaching a power density of 100 kW/L was first computed and used as a design target for the power electronics heat exchanger. The thermal target was defined in terms of a volumetric thermal resistance metric where the junction-to-coolant thermal resistance was scaled by the cold plate and power module volume requirements. The volumetric thermal resistance target value was computed to be 21 cm³·K/W, and the predicted heat load for a 100-kW WBG inverter was estimated to be 2,150 W [2]. Modeling analyses were then conducted to evaluate different cooling technologies and identify the best-performing cooling strategy. The analyses identified dielectric fluid-based cooling strategies as a

promising option due to the ability to redesign the power module and eliminate thermal bottlenecks (e.g., ceramics, thermal greases) within the package.

The dielectric fluid cooling concepts were designed and optimized to meet the thermal target using detailed computational fluid dynamics (CFD) and finite element analysis (FEA) simulations. Single- and double-side concepts were developed to dissipate heat to the dielectric fluid via single-phase heat transfer. The optimized single-side-cooled design was then fabricated via 3D printing for experimental validation. Future work is planned to validate the double-side cooling concept.

Results

In prior work, a single-side-cooled dielectric fluid cooling system was designed through CFD modeling using Alpha 6 as the coolant [3]. The dielectric fluid system uses dielectric fluid slot jets impinging on finned surfaces and is predicted to provide a high thermal performance (specific thermal resistance [$R''_{th} = 22 \text{ mm}^2 \cdot \text{K/W}$]), require a low pumping power (0.2 W), and outperform the thermal target (volumetric resistance = $9 \text{ cm}^3 \cdot \text{K/W}$). The dielectric fluid concept model-predicted thermal resistance and pumping power values are about 50% and 80% lower, respectively, as compared with the 2015 BMWi3 cooling system.

This year, experiments were conducted to validate the model results and a double-side-cooled, dielectric fluid concept was designed via modeling. Experiments were conducted using Alpha 6 fluid at various flow rates and fluid temperatures and results were compared to model-predicted values. The experimental results agreed well with model-predicted results for Alpha 6 fluid, which provided confidence in the model's predictive capabilities. The model then was used to simulate using different dielectric fluids (AC-100 and ATF) at various fluid temperatures (-40°C to 70°C). FEA and CFD were then used to design a double-side-cooled variant of the dielectric fluid cooling system. The experimental and modeling results are reported in the following sections of this report.

Experimental Validation (Single-Side-Cooled Concept)

The dielectric fluid, single-side-cooled module and heat exchanger system was fabricated to measure its performance and validate modeling results. The finned heat spreaders were fabricated by Weiland MicroCool. Figure I.1.10.1 shows images with dimensions of the model-designed and fabricated finned heat spreaders. The fabricated finned heat spreader has fins that are slightly curved and has 15 fins compared with the 16-fin design used in the CFD modeling. Aside from those differences, the dimensions of the fabricated fins are very similar to the model. Figure I.1.10.1 also shows the 12 finned areas that are cooled with dielectric fluid jets. Twelve resistive heaters were used to simulate heat from the silicon carbide (SiC) metal-oxide-silicon field-effect transistors (MOSFETs). Figure I.1.10.2 shows a cross-section view of the resistive heating system that consists of 12 cartridge heaters embedded within copper blocks. The resistive heating system design was described in the FY 2019 Annual Progress Report [3]. The fluid distribution system that generates the dielectric fluid jets consists of two parts—a polycarbonate 3D-printed fluid manifold (lower white part in Figure I.1.10.3) and a polyether ether ketone (PEEK) enclosure (top brown part in Figure I.1.10.3). Figure I.1.10.3 shows a picture of the dielectric fluid heat exchanger and module concept piped into the dielectric fluid loop. The dielectric fluid loop allows for conducting experiments with different dielectric fluids and for adjusting the fluid flow rates and temperatures.

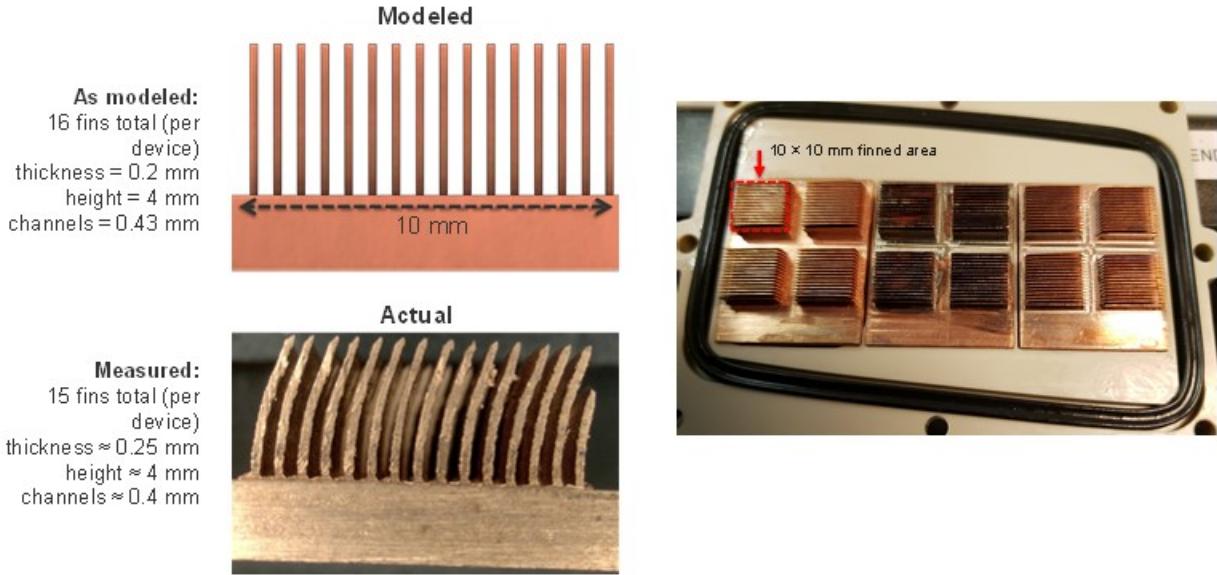


Figure I.1.10.1 Finned heat spreader as modeled (top left) and fabricated/actual (bottom left). Right image shows the 12 finned surfaces.

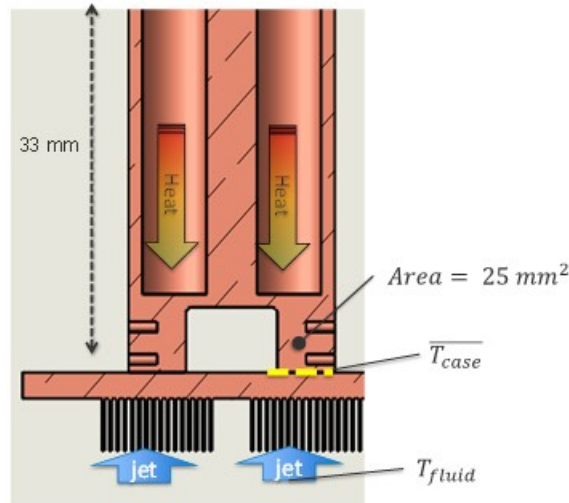


Figure I.1.10.2 Cross-section view of the copper block and finned heat spreader

Experiments were conducted to measure the case-to-fluid thermal resistance ($R''_{th, case-fluid}$) defined per Equation 1:

$$R''_{th, case-fluid} = \frac{Area (\overline{T_{case}} - T_{fluid})}{Heat_{per\ device}} \quad (1)$$

where $Area$ is the 5×5-mm area of the heat source (equal to the SiC devices being simulated), $\overline{T_{case}}$ is the average temperature at the heat spreader base (see Figure I.1.10.2), T_{fluid} is the fluid inlet temperature, and $Heat_{per\ device}$ is the heat dissipated per heater. These experiments measured the thermal performance of the heat exchanger (heat exchanger base to fluid) and not the junction-to-fluid resistance because actual devices were not used in these experiments. Experiments were conducted using Alpha 6 at 30°C and 70°C inlet temperatures and the experimental data were compared with CFD-predicted results. The flow rates were varied from 1 L/min up to 4.1 L/min.

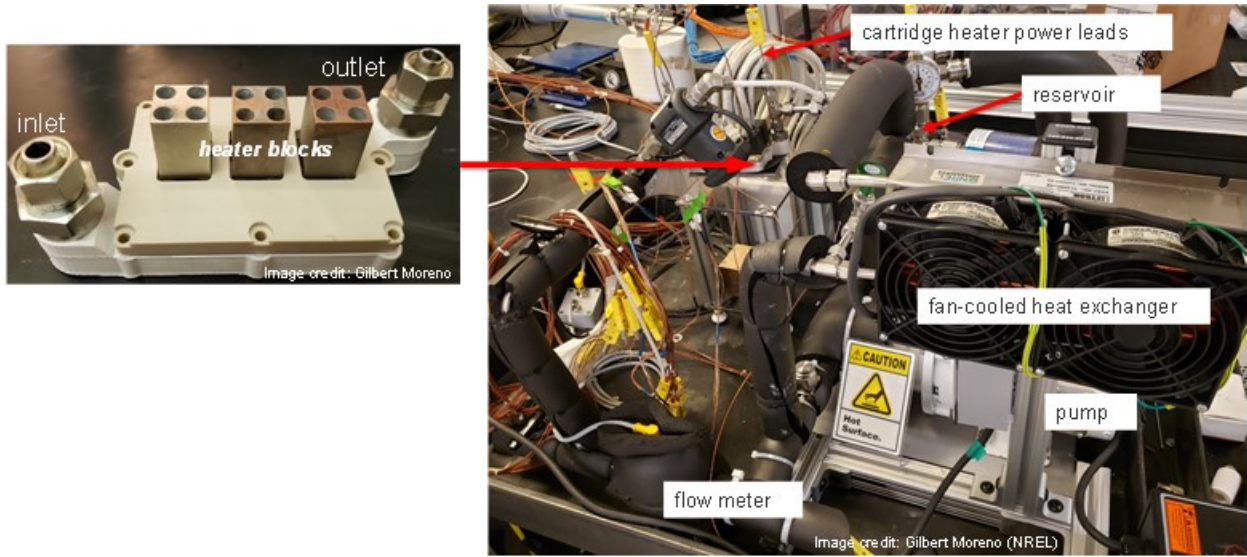


Figure I.1.10.3 Pictures of the dielectric fluid heat exchanger and conceptual module (left) and dielectric fluid loop (right).

Figure I.1.10.4 compares thermal resistance (heat exchanger case-to-fluid) versus pumping power results for the experiments and model. The modeling results are found to be in good agreement with the experimental data. The maximum difference between model and experiment thermal resistance is approximately 6%. The results show that there is initially a steep decrease in the thermal resistance at low pumping power values. The thermal resistance levels off at about 0.2 W of pumping power, or 4.1 L/min, which is the flow rate that this system was designed for [3].

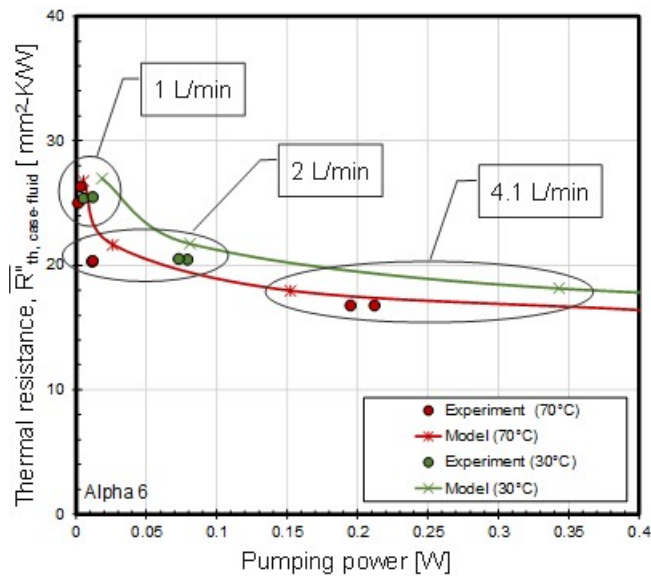


Figure I.1.10.4 CFD-predicted and experimental thermal resistance versus pumping power results for Alpha 6 fluid. Model results are in good agreement with experiments.

Modeling Different Dielectric Fluids (Single-Side-Cooled Concept)

The agreement between experimental and modeling results (for Alpha 6) provided confidence in the CFD model's predictive capabilities and was used to simulate different fluids (AC-100 and ATF) at various fluid flow rates (1 L/min up to 6 L/min) and temperatures (−40°C up to 70°C). AC-100 was evaluated as a possible coolant because it is designed for electric vehicle motor and battery cooling applications. ATF was evaluated

because it is a fluid that is qualified for automotive use and may enable integrating the power electronics with the motor. The -40°C fluid temperature is of interest because the viscosity of these fluids significantly increases at lower temperatures, and there is concern about high pumping power requirements at low temperatures. The heat exchanger was modeled via CFD simulations, which included SiC MOSFETs soldered to the copper heat spreader, and thus allowed for predicting the junction-to-fluid thermal resistance.

Figure I.1.10.5 shows the model-predicted junction-to-fluid thermal resistance versus pumping power for Alpha 6, AC-100, and ATF at different fluid temperatures. Varying the fluid temperature is predicted to have a minor effect on thermal resistance but a big influence on pumping power when compared at the same flow rate. All three fluids are predicted to provide similar performance at 70°C , with AC-100 showing slightly lower pumping power requirements. Alpha 6 and ATF are predicted to provide similar performance for both -40°C and 70°C temperature conditions and is the result of similar properties (between the two fluids). AC-100 is predicted to require significantly lower pumping power compared to the other fluids at -40°C —a result of its lower viscosity.

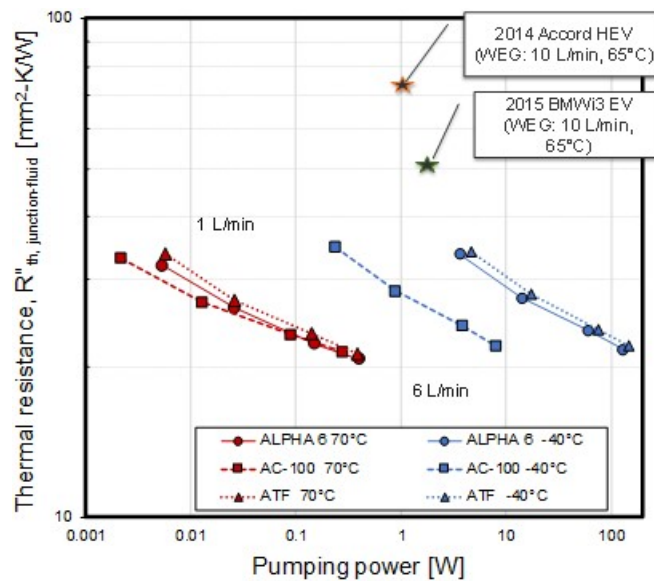


Figure I.1.10.5 Thermal resistance versus pumping power curves for Alpha 6, AC-100, and ATF at -40°C and 70°C

The performance of the 2014 Honda Accord and 2015 BMW i3 are provided in Figure I.1.10.5 and taken from [4]. All dielectric fluids are predicted to provide lower thermal resistance values compared to the automotive systems, even at the lowest flow rate of 1 L/min. Surprisingly, AC-100 is predicted to provide a lower thermal resistance and require lower pumping power at -40°C compared with both the 2014 Accord and 2015 BMW i3 at 65°C . AC-100's low pumping power requirements are associated with its lower viscosity and the low-pressure-drop design of the cooling system. This result suggests that dielectric fluid high viscosity concerns at low temperatures may not be an issue if the correct (low-viscosity) fluid is selected and combined with a low-pressure-drop heat exchanger.

Design of a Double-Side-Cooled Concept

A double-side-cooled version of the dielectric fluid heat exchanger was developed to increase thermal performance. Figure I.1.10.6 shows computer-aided design (CAD) drawings with dimensions of the conceptual double-side-cooled, dielectric fluid module and the 2013 Toyota Camry double-side (WEG-cooled) module. The dielectric fluid module configuration was intentionally designed to be like the 2013 Camry module to base the concept on an existing, reliable module concept. In the 2013 Camry module, copper heat spreaders are bonded on both sides of the insulated gate bipolar transistor (IGBT) and diode. The copper heat spreaders also provide the electrical connections to the devices [5]. Two silicon nitride ceramic sheets are placed on both

sides of the module to provide electrical insulation between the module and the aluminum WEG-cooled heat exchanger. The dielectric fluid module used smaller (5×5-mm) SiC devices instead of the larger IGBT and diode pair used in the 2013 Camry, and the copper heat spreaders are directly cooled using a dielectric fluid.

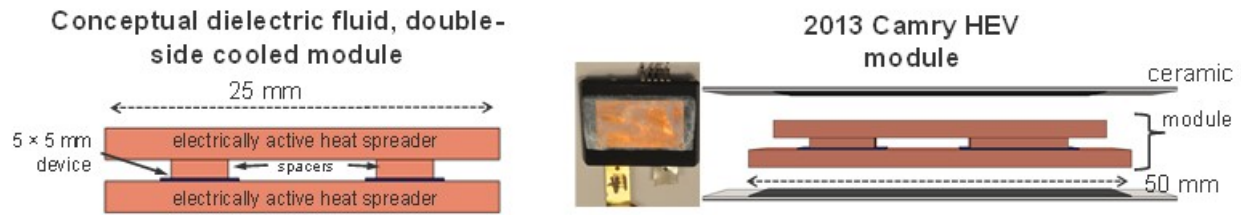


Figure I.1.10.6 CAD of double-side-cooled modules—conceptual dielectric fluid-cooled module (left) and 2013 WEG-cooled Camry module (right)

Thermal modeling (steady-state FEA) was conducted to predict the junction temperatures for the double-side-cooled module under the 716-W/cm² heat flux operating condition (same heat load used for the single-side concept). A 17,300-W/m²·K heat transfer coefficient with a 70°C fluid temperature was applied to both sides of the module to replicate the cooling magnitude that was applied and confirmed for the single-side module (see prior sections and [3]). Figure I.1.10.7 shows the computed temperature contours for the double-side-cooled module. The FEA predicts a 163°C maximum junction temperature for the 716-W/cm² heat flux condition. This junction temperature is less than 175°C (typical temperature limit of some power modules) and thus the double-side dielectric concept can use existing, low-temperature device attach materials (e.g., solder). Moreover, the double-side design is predicted to have maximum junction temperatures that are ~59°C lower than the single-side concept—a result of increased surface area.

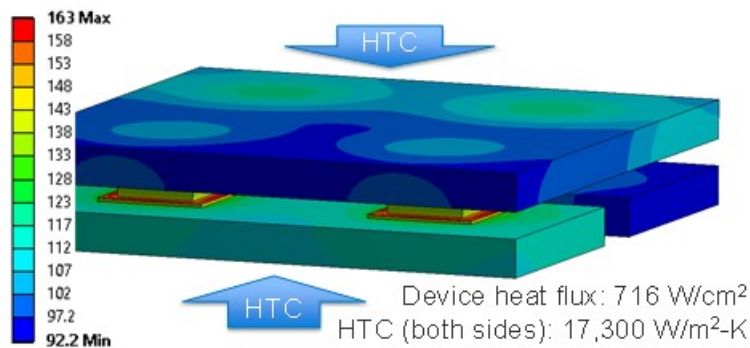


Figure I.1.10.7 FEA-computed temperature contours for the double-side-cooled module at 716-W/cm² heat dissipation. Maximum temperatures are predicted to be <175°C.

Series- and parallel-flow configuration dielectric fluid distribution manifold and enclosure/fluid containment systems were designed for the double-side-cooled module. The series-flow configuration impinged fluid jets on one side and then the other, and thus the second side received fluid at a higher temperature (associated with the temperature rise from cooling the first side). The parallel flow configuration impinged jets on both sides at the same time and at the same fluid temperature. CFD modeling was used to predict the pressure drop versus flow rate characteristics of the series and parallel flow concepts (Figure I.1.10.8). As shown, the pressure drop of the series-flow configuration is about two times higher as compared with the parallel-flow configuration—a result of the sequential flow circuit where the pressure drop across the two sides adds up. It should be noted that the parallel-flow configuration requires double the flow rate of the series confirmation to achieve the same jet velocity. Flow rates of 4.1 L/min (series) and 8.2 L/min (parallel) are required to achieve the 0.35-m/s jet velocity used for the single-side concept. As shown in Figure I.1.10.8, the series flow configuration at 4.1 L/min flow rate may be the better option due to its lower pumping power requirements compared with the

parallel flow configuration at 8.2 L/min. The 0.35-m/s jet velocity provided the $17,300\text{-W/m}^2\cdot\text{K}$ heat transfer coefficient performance that was confirmed through the experiments. A provisional patent application was submitted describing the compact fluid manifold concepts [6].

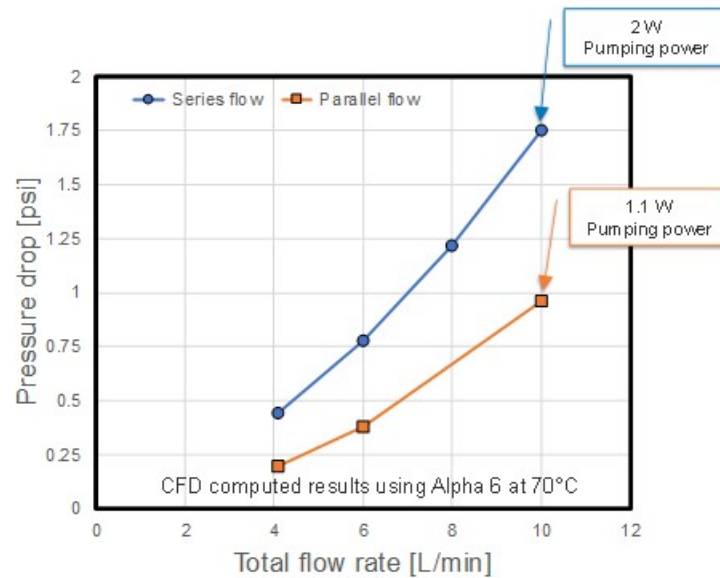


Figure I.1.10.8 CFD-computed pressure drop versus flow rate for the double-side-cooled heat exchanger. Series- and parallel-flow configurations results are provided.

Conclusions

Dielectric fluid thermal management concepts were developed for power electronics cooling. The concepts are predicted to enable reaching 100-kW/L power density (2025 DOE power density target). The project's major conclusions are summarized below:

- Experiments were conducted to measure the heat exchanger thermal resistance and pressure drop of the single-side-cooled, dielectric fluid concept. Experiments were conducted using Alpha 6 fluid at 30°C and 70°C inlet fluid temperatures and 1-L/min up to 4.1-L/min flow rates. The experimental results were found to agree with the model-predicted results at the different fluid temperatures and flow rates. The experiments confirmed the high thermal performance and low pumping power requirements of the dielectric fluid concept and provided confidence in the model's predictive abilities.
- CFD modeling was used to evaluate the effect of various dielectric fluids (Alpha 6, AC-100, and ATF) at different fluid flow rates (1 L/min up to 6 L/min) and temperatures (−40°C to 70°C). All fluids are predicted to provide the similar junction-to-fluid thermal resistance values when compared at the same flow rate—a results of similar thermal properties. However, AC-100 is predicted to require pumping power values that can be an order of magnitude lower than those of the other two fluids—a result of AC-100's lower viscosity.
- All fluids are predicted to provide a lower specific thermal resistance compared to the 2014 Honda Accord and 2015 BMW i3, even at the lowest flow rate of 1 L/min. The thermal resistance and pumping power computed for Alpha 6 at 4.1 L/min are predicted to be 50% and 80% lower, respectively, compared with the 2015 BMW i3. AC-100 is predicted to provide both lower junction-to-fluid thermal resistance and require a lower pumping power at −40°C compared with the 2014 Honda Accord and 2015 BMW i3 at 65°C. These results suggest that dielectric fluid high-viscosity

concerns at low temperatures may not be an issue if the correct (low-viscosity) fluid is selected and combined with a low-pressure-drop heat exchanger.

- FEA modeling was conducted to estimate the junction temperatures for the double-side-cooled, dielectric fluid concept. The double-side concept is predicted to have junction temperatures $<175^{\circ}\text{C}$ at the $716\text{-W}/\text{cm}^2$ heat flux condition. This performance exceeds that of the single-side design and allows for the use of conventional device attach materials. Two fluid manifold concepts have been created for the double-side-cooled, dielectric fluid module.

Future Work

- We will conduct experiments to measure the thermal performance of the single-side concept using various dielectric fluids (AC-100 and ATF) at various fluid flow rates and temperatures.
- We will complete the design of the double-side-cooled, dielectric fluid concept and fabricate prototypes for an experimental demonstration. The thermomechanical stresses of the module will be computed via modeling to evaluate concept durability.

Key Publications and Patent Applications

1. Moreno, G. 2019. “Power Electronics Thermal Management Research.” presentation to the DOE VTO Electrical and Electronics Technical Team, July 2019.
2. Moreno, G. 2019. “Power Electronics Thermal Management.” In *Electrification: 2019 Annual Progress Report*, U.S. Department of Energy Office of Energy Efficiency and Renewable Energy Vehicle Technologies Office, Washington, D.C.
3. Moreno, G., S. Narumanchi, X. Feng, R. Kotecha, and K. Bennion. 2020. “Dielectric Fluid Manifold for Double-Sided Cooling.” Provisional Patent Application No. 63/062,791, filed August 7, 2020.

References

1. U.S. DRIVE. 2017. *Electrical and Electronics Technical Team Roadmap: October 2017*. U.S. Department of Energy Office of Energy Efficiency and Renewable Energy Vehicle Technologies Office, Washington, D.C.
2. Moreno, G. 2018. “Power Electronics Thermal Management.” In *Electrification: 2018 Annual Progress Report*, U.S. Department of Energy Office of Energy Efficiency and Renewable Energy Vehicle Technologies Office, Washington, D.C.
<https://www.energy.gov/eere/vehicles/downloads/electrification-fy2018-annual-progress-report>.
3. Moreno, G. 2019. “Power Electronics Thermal Management.” In *Electrification: 2019 Annual Progress Report*, U.S. Department of Energy Office of Energy Efficiency and Renewable Energy Vehicle Technologies Office, Washington, D.C. https://www.energy.gov/sites/prod/files/2020/06/f76/VTO_2019_APR_ELECTRIFICATION_FINAL_compliant_.pdf.
4. Moreno, G., K. Bennion, C. King, and S. Narumanchi. 2016. “Evaluation of Performance and Opportunities for Improvements in Automotive Power Electronics Systems.” *2016 15th IEEE Intersociety Conference on Thermal and Thermomechanical Phenomena in Electronic Systems (ITherm)*, Las Vegas, Nevada, May 31–June 3, 2016, 185–192.
5. Burress, T. 2013. “Benchmarking EV and HEV Technologies.” EETT presentation, Southfield, Michigan.
6. Moreno, G., S. Narumanchi, X. Feng, R. Kotecha, and K. Bennion. 2020. “Dielectric Fluid Manifold for Double-Sided Cooling.” Provisional Patent Application No. 63/062,791, filed August 7, 2020.

Acknowledgements

The significant contributions of Kevin Bennion, Xuhui Feng, Ramchandra Kotecha, and Sreekant Narumanchi are acknowledged. A portion of the research was performed using computational resources - sponsored by the U.S. Department of Energy's Office of Energy Efficiency and Renewable Energy - located at the National Renewable Energy Laboratory.

I.1.11 Power Electronics: Vertical GaN Device Development (Sandia National Laboratories)

Andrew Binder, Principal Investigator

Sandia National Laboratories
P.O. Box 5800, MS 1086
Albuquerque, NM 87185
Email: abinder@sandia.gov

Susan Rogers, DOE Technology Development Manager

U.S. Department of Energy
Email: susan.rogers@ee.doe.gov

Start Date: October 1, 2018
Project Funding: \$800,000

End Date: September 30, 2023
DOE share: \$800,000

Non-DOE share: \$0

Project Introduction

This project is part of a multi-lab consortium that leverages U.S. research expertise and facilities at national labs and universities to significantly advance electric drive power density and reliability, while simultaneously reducing cost. The final objective of the consortium is to develop a 100-kW traction drive system that achieves 33 kW/L, has an operational life of 300,000 miles, and a cost of less than \$6/kW. One element of the system is a 100-kW inverter with a power density of 100 kW/L and a cost of \$2.7/kW. New materials such as wide-bandgap semiconductors, soft magnetic materials, and ceramic dielectrics, integrated using multi-objective co-optimization design techniques, will be utilized to achieve these program goals. This project focuses on a subset of the power electronics work within the consortium, specifically the design, fabrication, and evaluation of vertical GaN power devices suitable for automotive applications.

Objectives

Gallium Nitride (GaN) is a promising wide-bandgap (WBG) semiconductor material that could enable higher-performance power electronic devices than traditional Silicon (Si) or even its WBG counterpart, Silicon Carbide (SiC). This is based on the increased critical electric field of GaN, which would enable lower-resistance devices with the same hold-off voltage as devices fabricated from the other materials. This is a key performance metric for power devices. Laterally-oriented, High Electron Mobility Transistors (HEMTs) based on AlGaN and GaN materials are common in high-frequency applications and are being established in lower-voltage power switching applications (approximately 600 V and below). However, with the emerging commercial maturation of GaN substrates, traditional vertically-oriented device structures (such as are common in Si and SiC) can now be realized in GaN, with several promising demonstrations of high-voltage PN diodes and vertical transistors appearing in the literature [1], [2], [3]. While GaN PN diodes may be of interest, the ~3 V turn-on voltage, determined mainly by the bandgap of the material, discourages their use in some power-switching circuits due to the loss of power conversion efficiency resulting from this high turn-on voltage. Instead, more promising candidates for these power conversion systems, including automotive inverters, are GaN Schottky barrier diodes (SBDs) and Junction Barrier Schottky (JBS) diodes, shown in Figure I.1.11.1 (a), which have turn on voltages of ~1 V as determined by the Schottky barrier height of the metal to the semiconductor material, rather than the semiconductor bandgap.

Similarly, vertically-oriented GaN transistors promise high-performance as power electronic devices if several key growth and fabrication challenges are overcome for the GaN material system. Interestingly, several different types of vertical GaN transistors have been demonstrated including Metal Oxide Semiconductor Field-Effect Transistors (MOSFETs) in the trench configuration (T-MOSFET, shown in Figure I.1.11.1 b), the double-well (D-MOSFET) configuration (shown in Figure I.1.11.1 c), and the Current Aperture Vertical Electron Transistor (CAVET) configuration [4], [5], [6]. Each of these device topologies has benefits and challenges associated with fabrication and performance, but the MOSFET designs show the most promise for

power switching applications and are being investigated during this effort. With the MOSFET device designs, challenges exist in making the semiconductor/insulator (or oxide) interface due to the lack of a good native oxide for GaN (Si and SiC both have native oxides). In addition, selective-area doping control, which is needed to form lateral PN junctions, cannot be easily achieved in GaN. Current state-of-the-art GaN devices use techniques such as ion implantation with special anneal processes (high-pressure and high-temperature) [7] or epitaxial regrowth [8] to realize selective-area doping control. Both techniques are relatively immature in GaN, and their behavior needs to be studied and techniques need to be developed to control these processes for eventual use in power systems for electric vehicles.

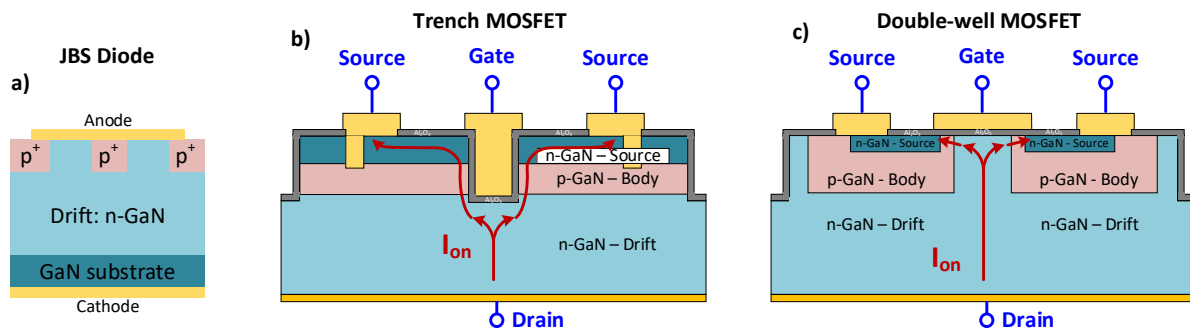


Figure I.1.11.1 (a) Schematic drawing of JBS diode, (b) schematic drawing of Trench MOSFET, and (c) schematic drawing of a Double-well MOSFET.

The first year of this effort focused on the development of simulation and modeling capabilities to help drive the designs of future GaN diodes and transistors. In parallel, epitaxial growth and fabrication processes were initiated toward realizing and demonstrating these devices. The second year of this effort has focused on fabrication and demonstration of these devices. The JBS diode and trench MOSFET were the primary focus during the past year, however some effort has gone into characterizing processes that would be necessary for a double-well MOSFET. In the future, once devices of sufficient performance are achieved these will be further characterized in a performance and reliability test-bed (created under a different project within the consortium) to evaluate their suitability for electric drive applications, especially regarding their ability to meet the DOE consortium targets. Also, with increasing maturity, the devices can be shared with the consortium partners, who will evaluate them in electric drive systems and provide feedback to us for further improvement in their performance for power electronics.

Approach

As mentioned, this work is primarily divided into two thrusts focusing on vertical GaN diode and MOSFET development. The focus this past year has been on demonstrating the JBS diode and developing trench MOSFET processing capabilities.

Vertical GaN Diodes

The JBS diode provides a combination of SBD and PN diode performance to give low turn-on voltage with a low reverse leakage current. However, while the JBS diode builds on the principles of a SBD+PN diode combination, in actuality the structure is more complex than just the sum of the two parts. Last year's effort demonstrated SBD performance with great forward IV characteristics, and previously Sandia has shown how to make PN diodes on an etched and regrown surface [9] with low reverse leakage. These are the two separate pieces necessary to begin the process of creating a JBS diode. Building on this foundation, Sandia has developed a process for etched-and-regrown JBS diodes which is briefly detailed in Figure I.1.11.2.

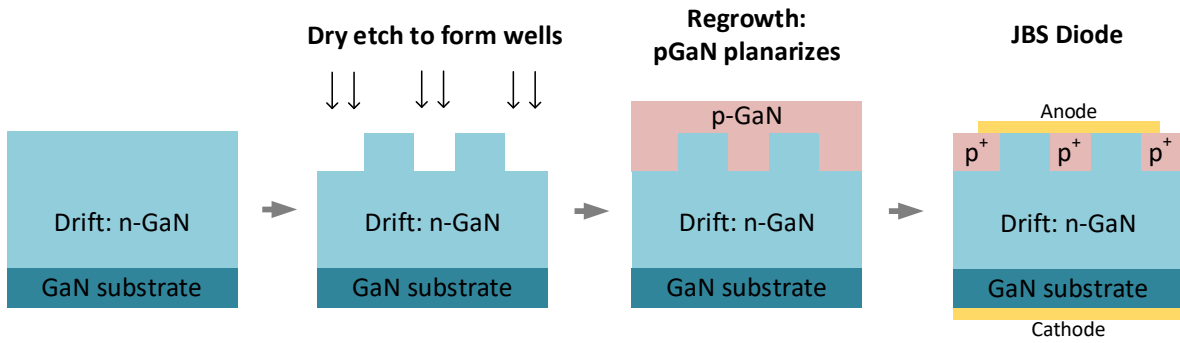


Figure I.1.11.2 The growth and fabrication process of etched and regrown JBS diodes formed by MOCVD. The structure is homoepitaxially grown on (0001) bulk GaN substrates. Dry etching is performed to form wells for regrowth, followed by surface treatments. Regrowth of p-GaN planarizes, and undergoes a blanket etch back to reveal the alternating p- and n-type regions for the anode contact. The full fabrication process includes metal deposition, passivation, mesa isolation, and edge termination.

The principal processing challenges with making this structure stem from the etch damage caused when patterning the drift region, and issues with the semiconductor surface and regrowth interface. For this reason, we planned to study various approaches to removing etch damage and methods for improving the regrowth interface. The results of this effort are detailed in the next section.

Vertical GaN Transistors

For the vertical GaN transistor, modeling conducted in year one suggested that both the D-MOSFET and T-MOSFET structures were viable from a design perspective. However, as the D-MOSFET requires a more complex dopant profile (the double-well), the primary focus on the fabrication front was to demonstrate the trench MOSFET device. Towards this end, Sandia has developed a process for trench MOSFETs which is briefly detailed in Figure I.1.11.3. As the trench MOSFET is a significantly complex process, the first goal was to demonstrate gate action for these MOSFETs. Many of the processing challenges for the trench MOSFET center around the gate and gate dielectric, primarily in creating a good interface between the semiconductor and dielectric, protecting the gate dielectric from high fields in the off-state, and depositing a high-quality dielectric film with few interface traps.

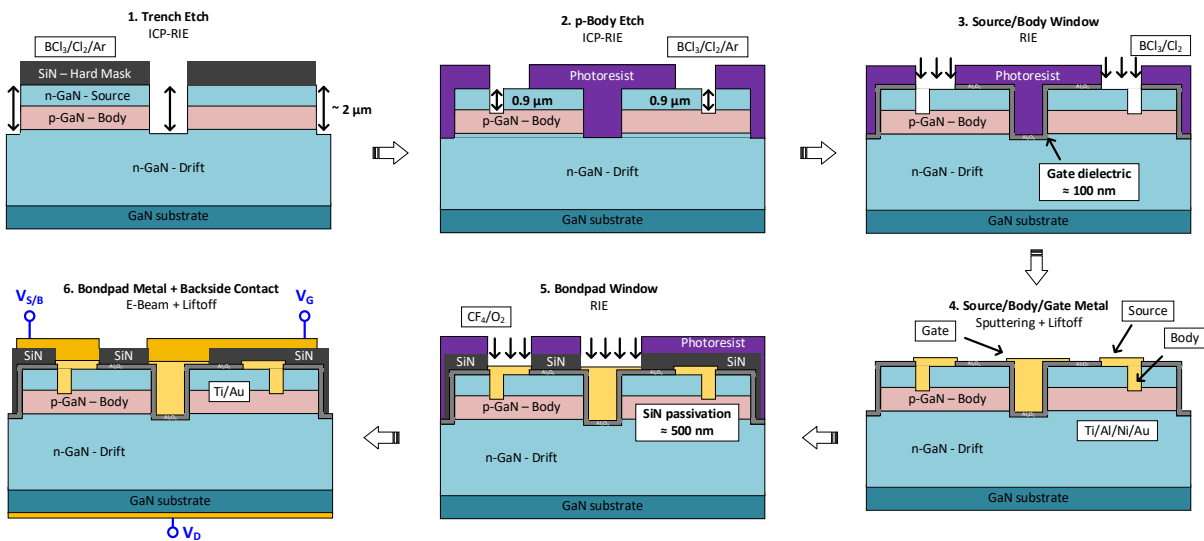


Figure I.1.11.3 Process flow diagram for Sandia vertical GaN trench MOSFETs.

As both the D-MOSFET and T-MOSFET were demonstrated to be viable in simulations, some work was also done on the D-MOS platform. This work involved studying Si ion-implantation into a p-well (necessary to create the double-well structure) and investigating activation conditions for the implant species. The trench and double-well MOSFET efforts are detailed in the following section.

Results

Vertical GaN Diodes

For the JBS process the focus was to study the etched-and-regrown interface and the effects of various surface preparations prior to regrowth. In planar etched-and-regrown PN diodes various wet chemical treatments have been shown to be successful in lowering reverse leakage caused by etch damage [9]. For the JBS diode we attempted three surface cleans prior to regrowth. The first surface treatment was to follow the drift-patterning ICP etch with a reactive ion etch (RIE) using an SF₆+CHF₄ based plasma which has been shown to be a lower damage and slower etching process. The second treatment was to follow the RIE treatment with a hot AZ400K (dilute KOH) wet etch which has been shown in PN diodes to reduce leakage in etched-and-regrown diodes. Lastly, the third treatment was to perform an RIE+AZ400K+UV-Ozone treatment where the RIE and AZ400K treatments were followed with a 30-min UV-Ozone exposure to oxidize the surface and an HF clean to remove the contaminants and oxide.

In this experiment all three surface preparations resulted in high leakage in reverse bias for both the PN diodes and JBS diodes on the wafer, although an improvement could be seen for the sample with the UV-Ozone treatment compared to the two without. The JBS devices showed Schottky-like forward characteristics with PN-like reverse characteristics, albeit both the JBS and PN diodes had high leakages attributed to the regrown junction. An example of a JBS current-voltage characteristic is shown in Figure I.1.11.4 demonstrating near 1500 V reverse voltage before breakdown.

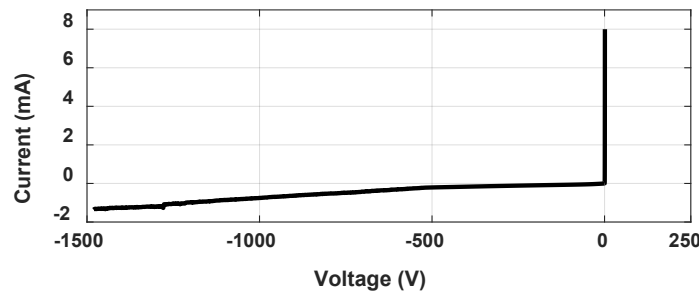


Figure I.1.11.4 Current-voltage characteristics of a fabricated etched-and-regrown GaN JBS diode.

SEM images showing the etch (Figure I.1.11.5 a) and regrowth (Figure I.1.11.5 b) for the JBS process demonstrate the planarization of the regrowth. It should be noted that planarization is a function of the feature size, where different patterns planarize to a different degree and some will grow thicker than others. Additionally, the slope of the sidewall after patterning the drift can be somewhat controlled through a crystallographic etch following the dry etch. These topics are the subject of a future study at Sandia.

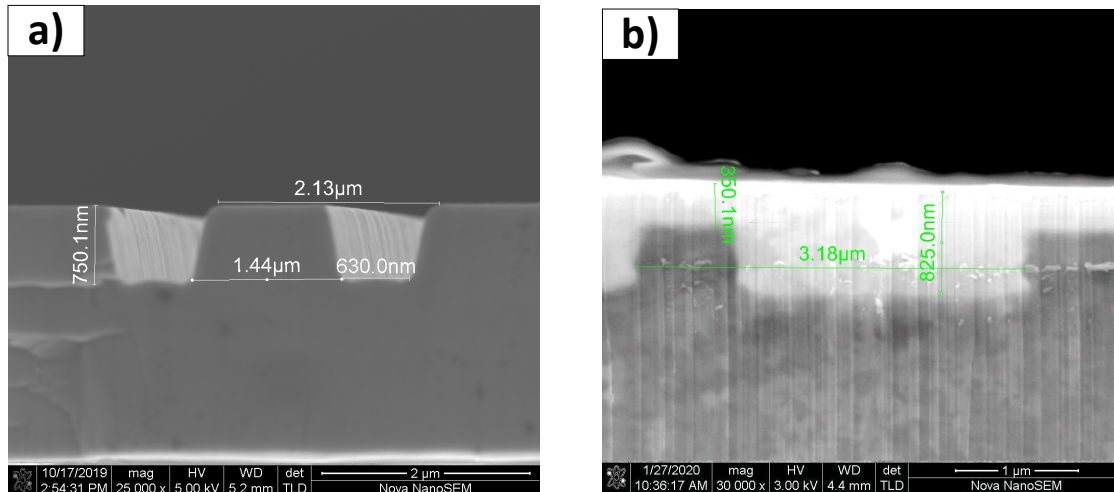


Figure I.1.11.5 (a) SEM image showing a corrugated n-type drift pattern prior to regrowth and (b) SEM image showing a regrown pattern with the light region on top as the planarized p-type GaN and the dark region underneath as the n-type drift.

It should be noted that the Schottky diode test structures on the JBS wafer showed excellent forward characteristics with an ideality factor of 1.11. Schottky diode performance is shown in Figure I.1.11.6.

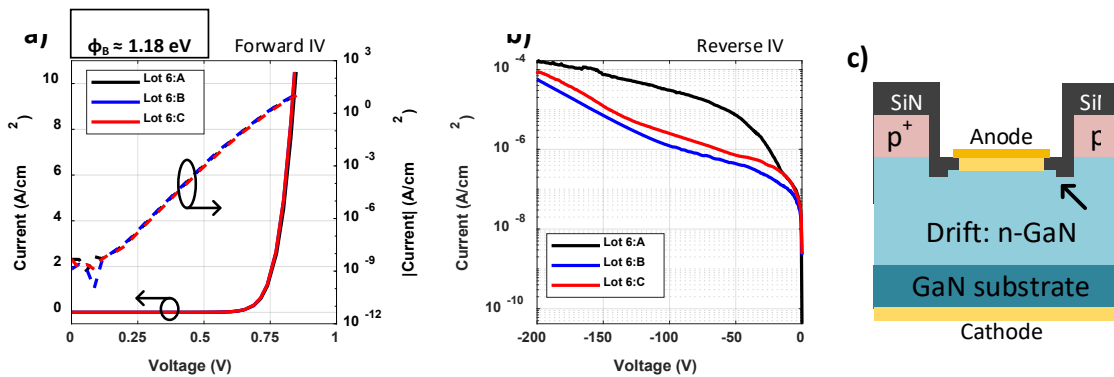


Figure I.1.11.6 (a) Forward IV characteristics for Schottky diode test structures on the JBS wafer, (b) reverse IV characteristics for the same devices, and (c) schematic drawing of the Schottky test structure.

The reverse leakage current at low bias for both the PN and JBS diodes is the next challenge to tackle for these devices. Since both the PN and JBS diodes show this behavior, it suggests that the issue exists on the C-plane regrown surface, not on the regrown sidewalls. Cleaning up the C-plane surface prior to regrowth is the next topic of study for these devices.

Vertical GaN Transistors: D-MOSFET

The study on vertical GaN transistors was divided into two focus areas: double-well MOSFETs and trench MOSFETs. The trench MOSFET process is more mature at Sandia as last year's effort focused on developing certain aspects of the trench MOSFET, while the D-MOS remained undeveloped except in simulation studies. One of the principal challenges in fabricating a D-MOS device in GaN is in forming the double well structure. Considering our extensive background in etch-and-regrowth, we are considering a D-MOS process where the p-well is formed by etch-and-regrowth and the n-source region is formed by Si ion implantation. To demonstrate the feasibility of this approach, the Si ion implantation step was studied to gauge the success of type inverting a p-type region to n-type by Si ion implantation. A custom mask was made to create PN diodes

and circular transmission line measurement (CTLM) test structures to evaluate the ion implantation process. The Si ion implantation was done with three different energy and dose specifications and implanted into a p-type region. Shown in Figure I.1.11.7 (b) the PN diode test structure on the wafer showed light emission, demonstrating electron-hole recombination under forward bias. Additionally, with an 1100°C anneal the contact to the n-type region showed Ohmic behavior with low contact resistivity. This is the first step towards demonstrating the feasibility of a D-MOS structure in vertical GaN. The next step is to demonstrate the etch-and-regrowth process for a D-MOS structure. Given that the feature size will be vastly different than for the JBS process, the regrowth planarization could be a concern.

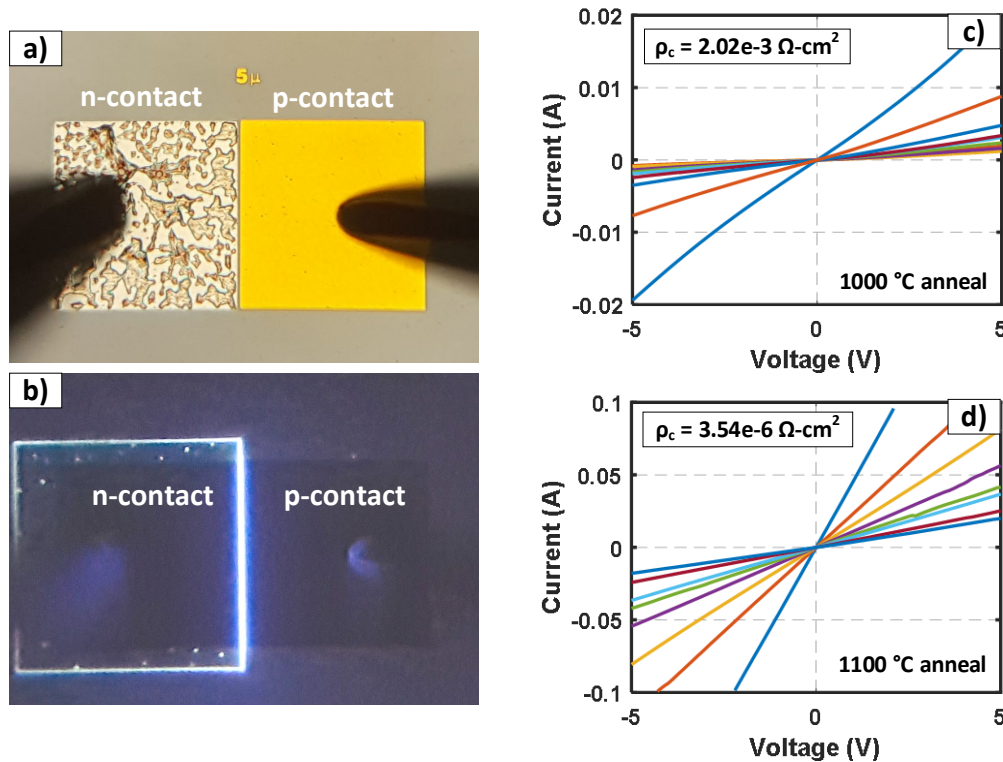


Figure I.1.11.7 (a) Microscope image showing the contacts on the PN diode test structure for the ion-implanted sample. (b) Microscope image showing light emission under forward bias, demonstrating electron-hole recombination. (c) CTLM results of n-Ohmic contact to Si ion implanted region after 1000°C anneal. (d) CTLM results of n-Ohmic contact to Si ion implanted region after 1100°C anneal showing Ohmic behavior.

Vertical GaN Transistors: T-MOSFET

Following the general process flow outlined in the approach section, trench MOSFETs were fabricated at Sandia with two types of gate dielectrics: a SiN PECVD film or an Al₂O₃ ALD film. In last year's effort atomic layer deposition (ALD) capabilities for vertical GaN devices was brought online, and both Al₂O₃ and SiO₂ films were studied. For the first fabrication lot implementing an ALD gate film the Al₂O₃ film was selected, and future lots will also study the SiO₂ ALD film. The PECVD film was used as a reference sample representing our previous process of record dielectric.

The electrical characterization results of a single-finger MOSFET on the ALD-Al₂O₃ quarter with a low temperature ohmic anneal are shown in Figure I.1.11.8. The I_DV_G curve shows an on-off ratio of >10⁷ and a threshold voltage of 6.5 V with a maximum transconductance of 0.9 mS/mm at V_D = 1 V bias. The I_DV_D curves show the current reaching 0.2 A/mm and excellent behavior depicting a clear transition between the linear and saturation regions, albeit with a slightly resistive low voltage behavior under 2 V bias. This is the first successful demonstration of a vertical GaN MOSFET at Sandia.

The breakdown characteristics are shown in

MOSFET Breakdown Result

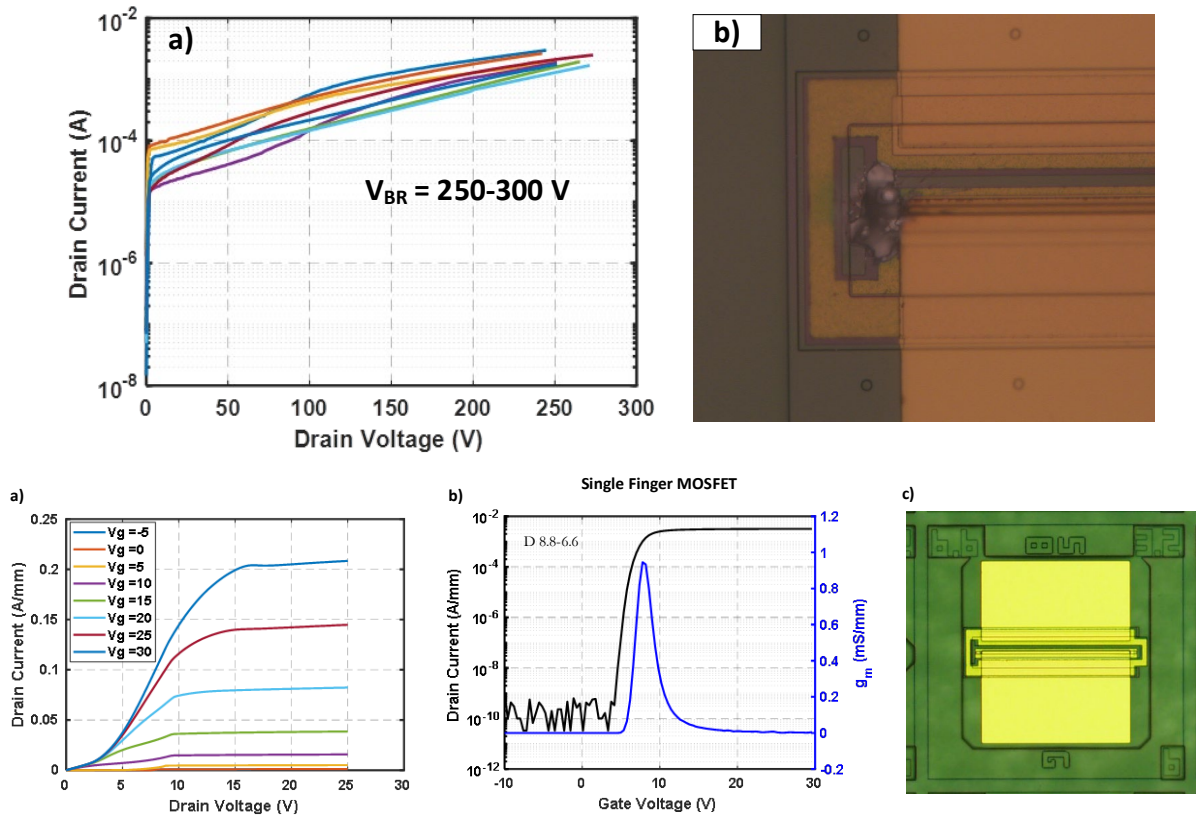


Figure I.1.11.8 Results from a single-finger MOSFET on the ALD-Al₂O₃ quarter with a low temperature ohmic anneal showing (a) IDVD characteristics for $V_G = 0:30$ V in steps of 5 V, (b) transfer characteristics (IDVG) and transconductance curves demonstrating a positive threshold voltage, and (c) and optical microscope image of the fabricated device.

Figure I.1.11.9, demonstrating a low-voltage breakdown near 250-300 V with high leakage at a low bias voltage. The low voltage breakdown is a result of a leakage path from source-to-drain and not leakage through the gate, indicating a lack of gate control in the blocking state, or leakage through the body contact. The partial lack of gate control in the blocking state is likely due to a sub-par gate dielectric and semiconductor interface, which can be improved in future lots to reduce the interface trap density and potentially reduce any effects from etch damage on the gate sidewall.

MOSFET Breakdown Result

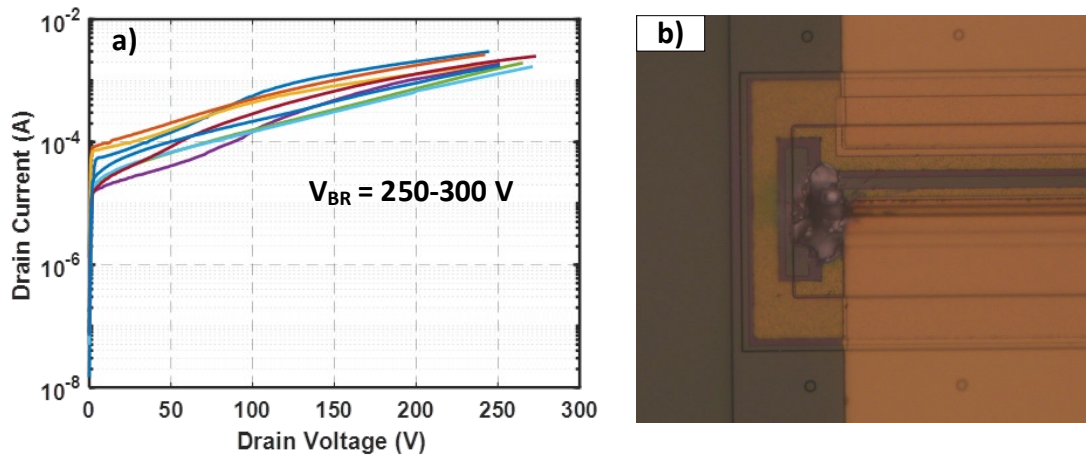


Figure I.1.11.9 Breakdown results for single-finger MOSFETs on the ALD-Al₂O₃ quarter with the low temperature ohmic anneal showing (a) blocking voltage at a gate bias of 0 V, and (b) an optical microscope image of a device after a destructive breakdown test.

The next step for the trench MOSFET is to perform more experiments to study the gate dielectric process by ALD to further improve the film quality and dielectric to semiconductor interface. The MOSFET results showed a significant hysteresis on the gate threshold indicating the presence of interface traps. Additionally, there was a leakage path formed from source-to-drain that prevented high voltage breakdown; this leakage path may be related to the gate dielectric, traps at the interface, and etch damage on the sidewall of the trench. These issues will be studied going forward.

Conclusions

GaN offers the promise of power electronic devices with performance that exceeds conventional Si and even SiC-based devices. This is due to its advantageous material properties, chiefly its higher breakdown electric field. Due to the increased maturity of GaN substrates, vertical GaN devices showing promising performance are being demonstrated and are being considered for insertion into power conversion applications. This project has focused on the design, simulation, and fabrication processes needed to build vertical GaN diodes and transistors for use in electric drive traction systems. This year's effort has yielded tremendous progress towards the end goal and has successfully demonstrated a ~1500 V JBS diode as well as the first demonstration of vertical GaN MOSFETs at Sandia. For the JBS process more work remains to solve the issue of high reverse bias leakage which appears to result from the PN junction and etched-and-regrown interface. More studies are underway to investigate alternative methods to remove etch damage and produce a better interface for regrowth. The D-MOS device remains a potential alternative MOSFET candidate and demonstration of n-type Si ion implantation into a p-type region with low resistance ohmic contacts was the first step towards realizing this structure. Trench MOSFETs remain the primary choice for the vertical GaN transistor process at Sandia with the first successful demonstration of trench MOSFETs at Sandia showing positive gate voltage and excellent on/off ratios. Future T-MOSFET work will focus on improving the gate dielectric interface and increasing the breakdown voltage.

Key Publications

1. L. Yates, A. Binder, J. Dickerson, G. Pickrell, and R. Kaplar, "Electro-thermal Simulation and Performance Comparison of 1.2 kV, 10 A Vertical GaN MOSFETs," Rio Grande Symposium on Advanced Materials, Albuquerque, NM (September 2019).

References

1. I. C. Kizilyalli, A. P. Edwards, O. Aktas, T. Prunty, and D. J. I. T. o. E. D. Bour, "Vertical power pn diodes based on bulk GaN," vol. 62, no. 2, pp. 414-422, 2014.
2. A. Armstrong *et al.*, "High voltage and high current density vertical GaN power diodes," vol. 52, no. 13, pp. 1170-1171, 2016.
3. H. Ohta, K. Hayashi, F. Horikiri, M. Yoshino, T. Nakamura, and T. J. J. J. o. A. P. Mishima, "5.0 kV breakdown-voltage vertical GaN p-n junction diodes," vol. 57, no. 4S, p. 04FG09, 2018.
4. T. Oka, Y. Ueno, T. Ina, and K. J. A. P. E. Hasegawa, "Vertical GaN-based trench metal oxide semiconductor field-effect transistors on a free-standing GaN substrate with blocking voltage of 1.6 kV," vol. 7, no. 2, p. 021002, 2014.
5. H. Otake, S. Egami, H. Ohta, Y. Nanishi, and H. Takasu, "GaN-Based Trench Gate Metal Oxide Semiconductor Field Effect Transistors with Over 100 cm²/(V s) Channel Mobility," *Japanese Journal of Applied Physics*, vol. 46, no. 25-28, p. L599, 2007.
6. S. Chowdhury, M. H. Wong, B. L. Swenson, and U. K. J. I. E. D. L. Mishra, "CAVET on bulk GaN substrates achieved with MBE-regrown AlGaIn/GaN layers to suppress dispersion," vol. 33, no. 1, pp. 41-43, 2011.
7. T. Anderson *et al.*, "Activation of Mg implanted in GaN by multicycle rapid thermal annealing," vol. 50, no. 3, pp. 197-198, 2014.
8. G. Pickrell *et al.*, "Regrown Vertical GaN p-n Diodes with Low Reverse Leakage Current," vol. 48, no. 5, pp. 3311-3316, 2019.
9. G. W. Pickrell *et al.*, "Investigation of dry-etch-induced defects in >600 V regrown, vertical, GaN, p-n diodes using deep-level optical spectroscopy," *J. Appl. Phys.*, vol. 126, no. 14, p. 145703, Oct. 2019.

Acknowledgements

This work is supported by the DOE Office of Energy Efficiency and Renewable Energy, Vehicle Technologies Office. Sandia National Laboratories is a multi-mission laboratory managed and operated by National Technology and Engineering Solutions of Sandia, LLC., a wholly owned subsidiary of Honeywell International, Inc., for the U.S. Department of Energy's National Nuclear Security Administration under contract DE-NA0003525. The views expressed in the article do not necessarily represent the views of the U.S. Department of Energy or the United States Government.

I.1.12 Power Electronics: Active Device and Passive Component Evaluation (Sandia National Laboratories)

Jack Flicker, Principal Investigator

Sandia National Laboratories
 P.O. Box 5800, MS 1033
 Albuquerque, NM 87123
 Email: jdflick@sandia.gov

Susan Rogers, DOE Technology Development Manager

U.S. Department of Energy
 Email: susan.rogers@ee.doe.gov

Start Date October 1, 2018

End Date: September 30, 2023

Project Funding: \$300,000

DOE share: \$300,000

Non-DOE share: \$0

Project Introduction

This project is part of a multi-lab consortium that leverages U.S. research expertise and facilities at national labs and universities to significantly advance electric drive power density and reliability, while simultaneously reducing cost. The final objective of the consortium is to develop a 100-kW traction drive system that achieves 33 kW/L, has an operational life of 300,000 miles, and a cost of less than \$6/kW. One element of the system is a 100-kW inverter with a power density of 100 kW/L and a cost of \$2.7/kW. New materials such as wide-bandgap semiconductors, soft magnetic materials, and ceramic dielectrics, integrated using multi-objective co-optimization design techniques, will be utilized to achieve these program goals. This project focuses on a subset of the power electronics work within the consortium, specifically the evaluation of wide-bandgap power semiconductor devices (primarily SiC) as well as passive elements (primarily ceramic capacitors).

Objectives

Silicon Carbide (SiC) is a wide-bandgap (WBG) semiconductor that has matured to the point where power electronic devices are now commercially available. However, it remains to be seen whether such devices can be used to construct a power converter (inverter) that meets the consortium's goals for performance and reliability. As such, in collaboration with consortium partners (other national labs as well as universities), this project is focused on the performance and reliability evaluation of these devices. Additionally, the passive elements within power electronic converters must be concurrently developed and evaluated to ensure that the performance promised by SiC can be realized in a real converter, and this project addresses that need as well. Note that another WBG semiconductor, Gallium Nitride (GaN), is addressed under a different project under the consortium. Similarly, magnetic materials, which are likewise critical to the performance of WBG-based power converters as well as electric motors, are addressed under a different project. Details regarding SiC device and capacitor testing, as well as the test circuit developed to perform this work, are described below.

SiC Testing

WBG semiconductors will be necessary to achieve the performance targets of the inverter, and the most mature WBG semiconductor (SiC) will be used extensively in the near future to achieve advances in electric drive technology. In conjunction with university partners, state-of-the-art SiC devices (switches and diodes) will be evaluated. Further, a strong focus will be placed on design for reliability, which to date has often been traded for high performance and low cost. While the latter two attributes are necessary for automotive applications, reliability is also of paramount importance. Thus, designs that meet all three criteria specific to the traction drive inverter of interest will be created, and devices based on these designs will be fabricated. In conjunction with NREL and ORNL, these devices will then be incorporated into power modules featuring advanced thermal management and minimized electrical parasitics to meet the performance goals of the program.

Capacitor Testing

Passive components (inductors and capacitors) are also of high importance to the overall consortium metrics. Ceramic dielectric capacitors are preferred because of their high energy density and reliability. However, achieving high performance and long lifetime at elevated temperatures has proven elusive for ceramic dielectrics. Instead of addressing this deficiency through alterations in material composition (which have not yet proven fruitful), an innovative bipolar switching strategy to periodically clear a build-up of oxygen vacancies at electrode surfaces has been implemented. This allows for ceramic dielectrics to exhibit long lifetime at high temperature. The dynamics of this strategy will be explored and optimized through the design and fabrication of a large-scale testbed for capacitor degradation evaluation.

WBG Device Test Circuit

In order to evaluate fabricated devices within the consortium (including the SiC active devices and ceramic capacitors described herein, and also GaN devices and inductors), Sandia has designed an advanced component test-bed that reproduces the functionality of an end-use vehicle inverter that is consistent with the consortium's targets. This allows for analysis of device performance and reliability under realistic scenarios. Once fabricated devices are available, the realistic evaluation of the operation of devices in the test-bed will be used by device designers to identify performance or reliability issues before incorporation into a high-power, high-density consortium exemplar inverter. Additionally, the test-bed provides validation opportunities for the development of realistic device models under varied usage scenarios for incorporation into system topology optimization.

Approach

SiC Testing

Sandia has been consulting with consortium university partners (primarily OSU and SUNY) and providing feedback on device designs and testing. Design criteria have focused on field-shaping within SiC devices through the design of the junction termination extension (JTE), as well as evaluating current commercial SiC devices for reliability. Pending the completion of the test circuit and receipt of devices from the university partners, evaluation of SiC devices will be carried out in the testbed.

Capacitor Testing

In order to reduce costs, ceramic capacitors are typically fabricated using base-metal electrodes such as Ni [1]. During the fabrication process, these require a reducing environment during sintering to avoid oxidation. An unintended side-effect of this reducing environment is that oxygen vacancies are created in the ceramic material [2]. As with any charged species, these vacancies will migrate under an applied voltage and preferentially collect at the electrode/dielectric interface (see Figure I.1.12.1). This gettering of defects results in a loss of insulation resistance and an increase in the DC leakage of the capacitor, which negatively affects the performance of the power electronics [3]. Furthermore, this leakage will increase operational temperature, resulting in quicker diffusion of vacancies. This process is a positive feedback loop that leads to an accelerating failure mechanism.

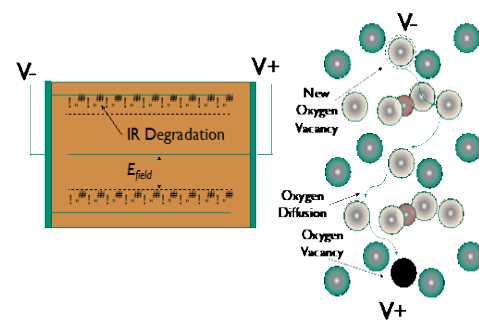


Figure I.1.12.1 Oxygen vacancy migration under applied bias can lead to degradation of ceramic capacitors.

The conventional wisdom for increasing capacitor reliability is to alter the fabrication process or materials properties of the capacitor. This is a long, complicated process that requires significant cost and effort to achieve. Instead of altering the capacitor properties, we are investigating the ability to heal capacitors periodically via reverse biasing. This reverse biasing should allow for re-distribution of oxygen vacancies to lengthen the lifetime of the component. To evaluate this mechanism, we propose a method of altering the

typical DC-field highly accelerated lifetime tests on the capacitor to an AC field variety. This reversing electric field can limit the transport of oxygen vacancies.

Test Circuit

Fabrication of new laboratory-scale devices can be beset with many reliability and performance challenges that are not present in commercialized devices. In order to move forward to a next generation of prototype device, it is necessary to understand its strengths and weaknesses in an appropriate end-use testbed. This testbed must deliver realistic stresses on the device that it will see in field use, but at a lower stress level than would be experienced in the field. By having realistic usage data available to device designers and fabricators, the process of developing a device can be accelerated and weaknesses of past devices can be addressed quickly in future generations (Figure I.1.12.2).

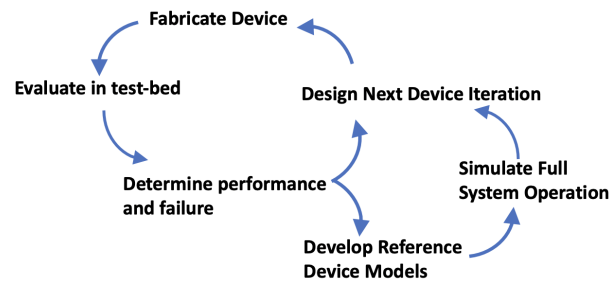


Figure I.1.12.2 The evaluation of prototype devices in a custom testbed can inform both device designers on the strengths/weaknesses of their prototypes, as well as validate device models for simulation.

In order to evaluate fabricated devices in the consortium, SNL is developing a scaled motor drive test-bed that can be tailored to prototype devices (both in voltage and current stress delivered) while still applying realistic end-use stress profiles that the device will see when mature. In order to carry this out, a 3-phase DC motor drive was designed (Figure I.1.12.3). This design is split into two sections, a control section and a power stage section. The control section applies a realistic PWM profile to the device using an embedded microcontroller specifically for motor drive applications. The three-phase power stage contains a single stage that is daughter-carded. This daughter card can be quickly removed and replaced with a card containing new device types. By daughter-carding the entire stage, parasitic inductance is kept commensurate with the other two stages to minimize asymmetric operation and get a better view of the device performance.

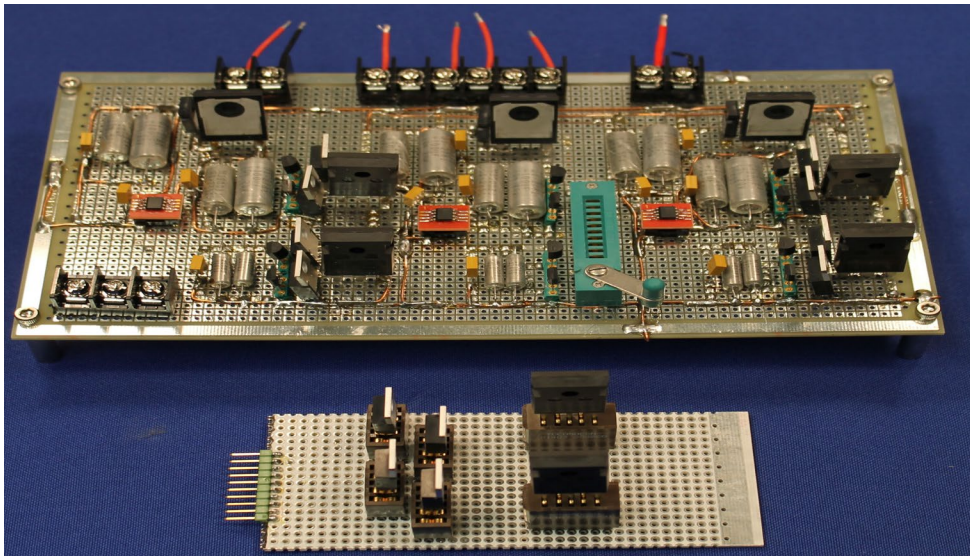


Figure I.1.12.3 Schematic for WBG device testbed with embedded motor control.

Results

SiC Testing

As discussed above, testing of SiC power devices is awaiting the receipt of consortium-fabricated devices to evaluate their performance in the motor-drive testbed.

Capacitor Testing

In FY19, SNL carried out preliminary bipolar switching testing on commercially available X7R capacitors. A DC bias of 10x the rated voltage was applied at a temperature 125°C above the rated temperature. These voltage and temperature levels are characteristic of highly-accelerated DC life tests for capacitors. The leakage current of the devices was monitored at DC bias (no switching) and bipolar operation with switching frequencies of 0.1 and 2.5 Hz. These preliminary results (subset shown in Figure I.1.12.4) show that bipolar switching can result in significantly increased time-to-failure for ceramic capacitors. The 2.5 Hz bipolar switching scheme (blue trace) demonstrated a ~4x lifetime increase compared to the DC voltage stress (black trace).

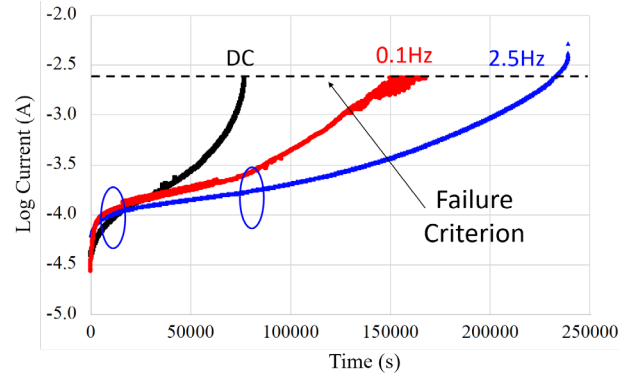


Figure I.1.12.4 The lifetime of DC capacitors can be increased through the implementation of a bipolar switching scheme.

While this initial testing shows promise, further work is needed both to elucidate the exact mechanisms for this bipolar switching and to evaluate if the effect is large enough for real-world practical application. The necessary frequency of healing procedures should decrease significantly at less accelerated conditions, but more testing is needed for a detailed understanding of the tradeoffs between frequency, voltage, and temperature and to understand if it is tractable to use very low frequencies (for example in the microhertz regime) to reverse damage.

Ultra-low frequency AC to reverse damage would enable a healing scheme to reverse bias at night to remediate damage incurred during the day while driving. In certain circumstances, it could be possible to reverse the damage every few days. However, much more testing is necessary to determine what sort of schedule might be possible for this scheme. To really understand the trade-offs and possible solution space, full-scale Highly Accelerated Lifetime Testing (HALT) of the AC degradation is needed for lifetime estimates. This would yield an adequate understanding of what the mean time-to-failure vs. frequency of reverse bias is at various temperatures, voltages, and applied frequencies. Such detailed studies will answer many of the open questions that exist, such as whether the voltage or temperature acceleration factors are also affected by frequencies and whether there is a physical model that can adequately describe the testing data.

One of the primary challenges with testing of ceramic capacitors is that large sample sizes are necessary for two reasons. The first is that ceramic capacitors often exhibit both significant infant mortality and early wear-out failures. As these are extrinsic failure mechanism which are not of interest, larger sample sizes are necessary to accommodate them. Secondly, the acceleration factors for ceramic capacitors vary significantly from manufacturer to manufacturer due to difference in materials processing. So, to achieve an encompassing overview of the industry, it is necessary to average out these differences with larger sample sizes.

For both these reasons large testing batches capable of high acceleration are needed for high-quality studies of ceramic capacitor lifetime. Work is currently ongoing to scale-up the single device test setup to be able to evaluate large statistically significant sample sizes. A new test-and-measure system that can evaluate 40 devices under test has been designed and is currently being fabricated. This test setup will be able to carry out a stress-and-measure protocol for a population of 40 capacitors. The system is divided into two buses, one for

stressing and one for measurement. Each of the DUT types is divided into 5–10 groups and one group may be measured while the rest can be stressed. Failed DUTs will be detected by a combination of voltage/current monitoring and power supply compliance monitoring. Upon a DUT failure, the DUT will be identified during the measurement sequence, then isolated. All cycle times between stress and measure are user-controllable with a maximum temperature of 300°C (with 25°C/min ramp rate) and a voltage stress of 600 V (2.6 A/1.5 kW).

Figure I.1.12.5 shows a more detailed view of the test setup that is currently being assembled. The setup is composed of an H-bridge power bus that can be used to either apply stressing voltage or allow for device measurement. Each of the 40 samples can be isolated by relays so that if a single device fails in a shorted mode, the test will not be required to stop. The 40 devices under test will be held in a steel sample fixture with integrated heater. The large thermal mass of the sample holder will be able to maintain temperature stability over the entire time run of the test.

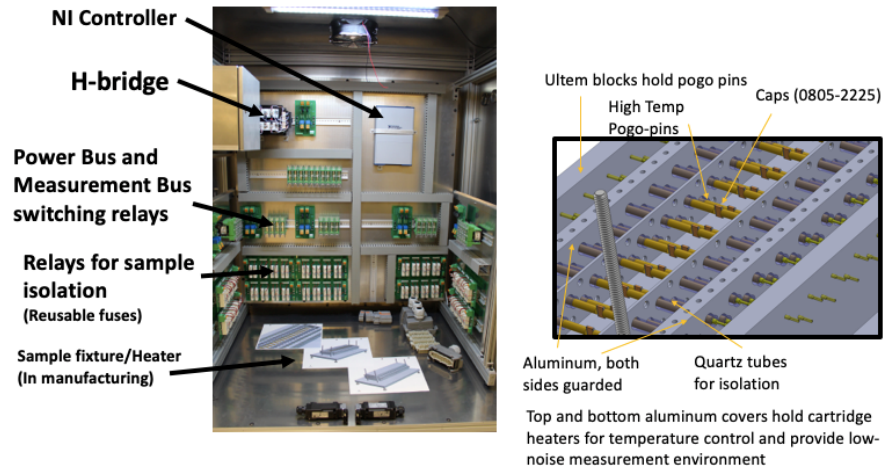


Figure I.1.12.5 In-process fabrication for capacitor test setup which allows for stress and evaluation of a population of 40 capacitors under bipolar switching.

Full commissioning of this test setup was originally slated for June, but that schedule has slipped slightly due to Coronavirus precautions in the laboratory. Fabrication of the sample setup is currently being finalized and is expected to be completed shortly.

In the next FY, in addition to continuing the experiment with larger sample sizes, capacitor sizes, and sample stress, a variety of different capacitor materials will also be evaluated. While the main focus has been on evaluating standard X7R capacitors, the system will allow for acceleration factor measurement of other interesting ceramic dielectrics, including Ceralink and KC-Link capacitors. These new ceramic capacitor dielectrics may exhibit different acceleration factors and frequency effects and may be more applicable to the drive train application area. Finally, future work will focus on how to implement such a reverse bias scheme in an actual drivetrain with different drive cycles and will evaluate the trade-offs between cost, performance, and reliability. This will allow the formulation of a healing step for these capacitors that can be implemented as easily as possible into an operational drivetrain system.

Test Circuit

The motor drive test circuit (power stage, daughter card, and motor controller) has been fully fabricated and assembled on a PCB (Figure I.1.12.6).

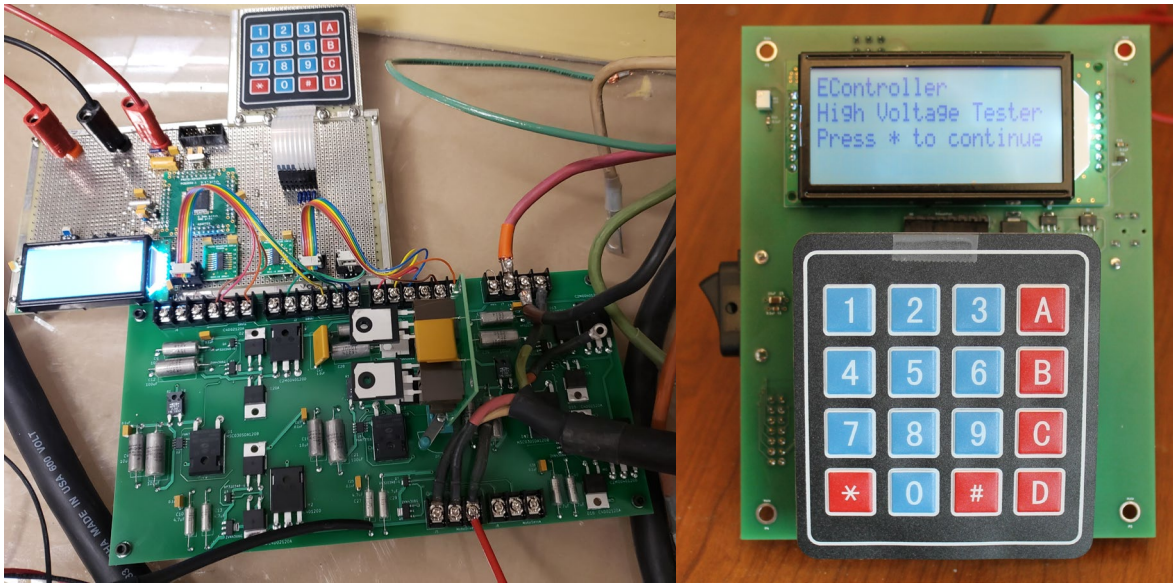


Figure I.1.12.6 (left) PCB of power stage and daughter card under test. (right) PCB of motor controller board.

The PCBs have been commissioned to ensure correct functionality. Power was supplied by a 1000 V, 10 A DC power supply and a three-phase controllable load was placed on the drive output. The board functioned correctly up to a level of 400 V (see Figure I.1.12.7). At this level, the temperature of the power stage switches (without heat-sinking) rose to only 37°C. In a full PCB-fabricated setup with surface-mount parts and proper heat-sinking, there should be no issues with higher power operation.

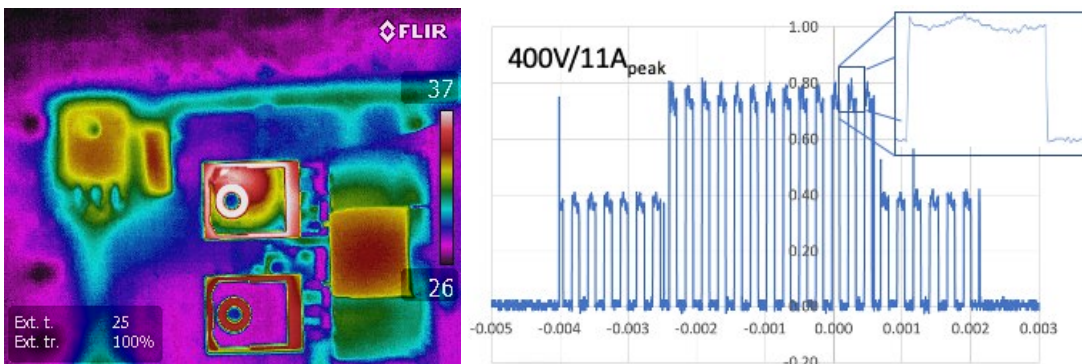


Figure I.1.12.7 (left) Thermal image of one leg of the power stage showing the temperature of power switches at 400 V and 11 A. (right) Gate drive signaling at 400 V and 11 A showing stable operation.

During commissioning of the test circuit above 400 V, the circuit failed catastrophically. After failure analysis, it was determined that three of six C2M0040120D SiC MOSFETS and 2 C4D02120A protection diodes (all 1200V) failed by short ($V_{in} = 550$ V). As there were no signs of overheating in any of the parts, it was determined that, most likely, a transient in excess of 1200 V appeared at the high voltage input. This voltage transient propagated over to controller board and caused multiple component failures.

After analysis, the failed parts were replaced. However, it was determined that the circuit driver (low-voltage) portion of the circuit was susceptible to overvoltage transients and a re-design with 1200 V rated parts was

necessary to mitigate this failure mechanism. Two potential replacement driver components were identified (both rated at 1200V). Both potential components were breadboarded and evaluated. The two designs were down-selected to one design that could replace the gate driver circuitry.

The power-stage breadboard developed in FY19 was modified to take these new parts. The gate drive circuitry is working as expected, although more functional testing is ongoing. If these parts pass the functional tests, a new circuit board will be fabricated and assembled to incorporate the 1200 V rated gate drive circuitry.

Conclusions

We have demonstrated the ability of a bipolar switching scheme to improve ceramic capacitor lifetime. This proof-of-concept result is being expanded to large-scale HALT testing through the fabrication of a test setup that will allow for testing of a large population of capacitors (40) under a variety of temperature and voltage stresses and bipolar switching profiles. This will allow for full characterization of the activation energy for oxygen vacancy migration as a function of voltage/temperature as well as the efficacy of different bipolar switching profiles. Such information will allow for incorporation of ceramic capacitors with bipolar switching into an electric traction drive.

Additionally, in FY20 a three-phase motor drive component test-bed was fabricated, assembled, and commissioned. This test-bed allows for the application of realistic operational stress to prototype devices fabricated within the consortium. A full PCB of the test circuit has been fabricated and commissioned to ensure operation. Upgrades to high voltage gate driver circuitry have been designed and tested. This improved version is being constructed and will be used to test both SiC and GaN devices fabricated by Sandia as well as consortium partners.

References

1. D Donahoe and C Hillman. Failures in base metal electrode (bme) capacitors. In 23rd Capacitor and Resistor Technology Symposium, pages 129–138, 2003.
2. T Nomura, Y Nakano, and A Satoh. Multilayer ceramic chip capacitor. US Patent 5,319,517, 1994.
3. X Zhang, T Hashimoto, and DC Joy. Electron holographic study of ferroelectric domain-walls. *Applied Physics Letters*, 60(6):784–786, 1992.

Acknowledgements

This work is supported by the DOE Office of Energy Efficiency and Renewable Energy, Vehicle Technologies Office. Sandia National Laboratories is a multi-mission laboratory managed and operated by National Technology and Engineering Solutions of Sandia, LLC., a wholly owned subsidiary of Honeywell International, Inc., for the U.S. Department of Energy's National Nuclear Security Administration under contract DE-NA0003525. The views expressed in the article do not necessarily represent the views of the U.S. Department of Energy or the United States Government.

I.1.13 Bottom-Up Soft Magnetic Composites (Sandia National Laboratories)

Todd Monson, Principal Investigator

Sandia National Laboratories
P.O. Box 5800, MS 1415
Albuquerque, NM 87185
Email: tmonson@sandia.gov

Susan Rogers, DOE Technology Development Manager

U.S. Department of Energy
Email: susan.rogers@ee.doe.gov

Start Date: October 1, 2018
Project Funding: \$150,000

End Date: September 30, 2023
DOE share: \$150,000

Non-DOE share: \$0

Project Introduction

Improved soft magnetic materials must be developed to meet 2025 goals for enhanced peak power (100 kW), specific power (50kW/L), and reduced cost (3.3 \$/kW) in a motor that operates at > 20,000 rpm. Improved soft magnetic materials will also enable high performance motors that do not rely on rare earth elements. In fact, replacement of permanent magnets with soft magnetic materials was highlighted in the Electrical and Electronics Technical Team (EETT) Roadmap [1] as a potential R&D pathway for meeting 2025 targets. Eddy current losses in conventional soft magnetic materials, such as silicon steel, will begin to significantly impact motor efficiency as motor rotational speed is increased. Soft magnetic composites (SMCs), which combine magnetic particles with an insulating matrix to increase electrical resistivity (ρ) and decrease eddy current losses, even at higher operating frequencies (or rotational speeds), are one possible solution. Today, SMCs are being fabricated with values of ρ ranging between 10^{-3} to 10^{-1} $\mu\text{ohm}\cdot\text{m}$ [2], which is significantly higher than 3% silicon steel (~ 0.5 $\mu\text{ohm}\cdot\text{m}$) [3]. The isotropic nature of SMCs is ideally suited for motors with 3D flux paths, such as axial flux motors. Additionally, the manufacturing cost of SMCs is low, and they are highly amenable to advanced manufacturing and net-shaping into complex geometries, which will further reduce manufacturing costs. There is still significant room for advancement in SMCs, and therefore additional improvements in electrical machine performance. For example, despite the inclusion of non-magnetic insulating material, their electrical resistivities are still far below that of soft ferrites ($10 - 10^8$ $\mu\text{ohm}\cdot\text{m}$).

We are developing SMCs from the bottom up, with a final objective of creating composites with high volume loading (and therefore high saturation magnetization) while increasing the value of ρ several orders of magnitude over the current state-of-the-art in SMCs. In order to accomplish our goals, we are starting with particles of γ' -Fe₄N, which has a saturation magnetic polarization (J_s) of 1.89 T, which is slightly greater than Si steel [4] and a ρ of ~ 2 $\mu\text{ohm}\cdot\text{m}$ [5]. In our bottom-up approach we begin by coating the magnetic particles with a diamine, which chemically reacts directly with epoxide terminated monomers to form a cross-linked epoxy composite. This “matrix-free” approach to composite formation will not suffer from the same nanoparticle aggregation and phase separation effects commonly observed in conventional nanocomposites [6]. Furthermore, it should ensure better separation between magnetic particles and significantly reduce or eliminate inter-particle eddy currents. A precedent already exists for the use of epoxies in electrical machine construction [7],[8]. Additionally, it is possible to design epoxy systems with glass transition temperatures (T_g) well in excess of the target maximum motor operating temperature of 150°C [9]. Furthermore, composites have been successfully demonstrated in high-speed motors [10] and even flywheels rotating at speeds up to 60,000 rpm [11].

Objectives

The project objective is to develop high-magnetization, low-loss iron-nitride-based soft magnetic composites for electrical machines. These new SMCs will enable low eddy current losses and therefore efficient motor

operation at rotational speeds up to 20,000 rpm. Additionally, iron nitride and epoxy composites will be capable of operating at temperatures of 150°C or higher over a lifetime of 300,000 miles or 15 years.

Approach

A high-level overview of our approach is:

1. Convert commercially available mixed-phase iron nitride powder to nearly phase-pure γ' -Fe₄N
2. Coat iron nitride particles with diamine molecules (part A of epoxy chemistry)
3. Combine surface functionalized particles with epoxide terminated monomers (part B of epoxy chemistry)
4. Fabricate SMC part by pouring mixture from #3 into a mold or hot-pressing die
5. Evaluate and test the fabricated SMC part

Each of these steps involves many possible optimization steps such as raw material processing conditions, epoxy monomer selection, composite curing conditions, and hot-pressing conditions.

Results

1. Confirmation of phase-pure γ' -Fe₄N

The conversion of mixed-phase commercially available iron nitride powder to nearly phase-pure γ' -Fe₄N has been confirmed. The starting material was commercially available iron nitride powder, acquired from Alfa Aesar, which is a mixture of both Fe₃N and Fe₄N. We developed a straightforward heat treatment to convert almost all of the Fe₃N phase to the higher J_s Fe₄N. X-ray diffraction (XRD) data of a purified sample that started off as a mixture of Fe₄N and Fe₃N powder is displayed in Figure I.1.13.1. This data, collected after heating to 542°C under flowing nitrogen, shows that the sample now consists of 96.2% Fe₄N, 2.3% Fe₃N, and 1.5% Fe. Since both Fe₃N and Fe are magnetic compounds, their presence in trace amounts should not present an issue.

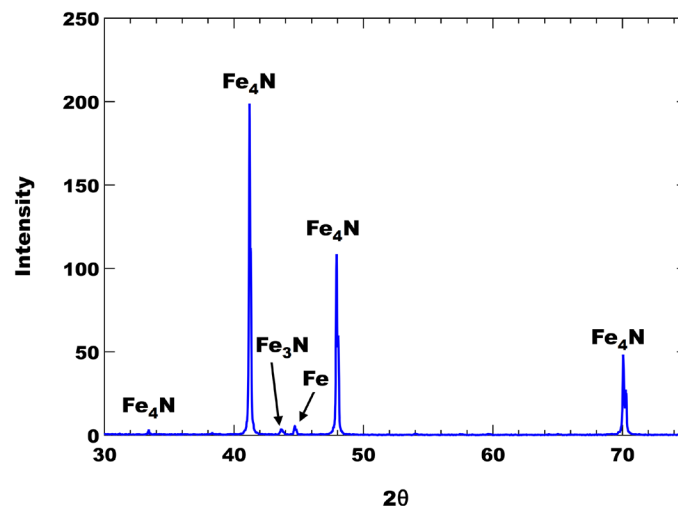


Figure I.1.13.1 XRD pattern of nearly phase pure Fe₄N produced from mixed phase commercial powders consisting of both Fe₄N and Fe₃N.

2. Development of High Operating Temperature Iron Nitride/Epoxy Composites

This year, we transitioned completely to using 4-aminophenyl sulfone (vs. 1,6-hexanediamine) as the diamine molecule used to coat the iron nitride powder and form part A of our epoxy composite. When curing larger

epoxy-based parts 1,6-hexanediamine (see Figure I.1.13.2) reacted too vigorously with the epoxide monomers and led to a very exothermic cure, resulting in excessive heating of the composite. In contrast, when 4-aminophenyl sulfone (see Figure I.1.13.3) is used as the diamine, the uncured epoxy mixture must be heated to a temperature of 130°C to initiate the curing process. However, heating beyond 130°C to complete the epoxy cure must still be conducted slowly and incrementally to prevent the reaction from becoming too exothermic.

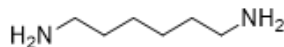


Figure I.1.13.2 1,6-hexanediamine.

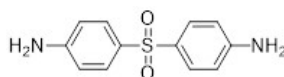


Figure I.1.13.3 4-aminophenyl sulfone.

To fabricate iron-nitride-based magnetic composites, iron nitride powder and 4-aminophenyl sulfone were milled in a SPEX high-energy ball mill until the particles were coated by 4-aminophenyl sulfone, as confirmed by infrared (IR) spectroscopy. Next, the diamine coated particles were mixed with one of two different epoxides: trimethylpropane triglycidyl ether (three epoxide groups); or *N,N*-diglycidyl-4-glycidylxyaniline (also with 3 epoxide groups). An image of trimethylpropane triglycidyl ether (TTE) is displayed in Figure I.1.13.4 and an image of *N,N*-diglycidyl-4-glycidylxyaniline (NND) is displayed in Figure I.1.13.5. After mixing the amine functionalized particles with one of the epoxide-terminated monomers listed above, the mixture was poured into a mold and cured. We fabricated an array of 3D-printed molds for this project, varying the size and shape according to the application or testing method.

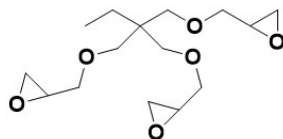


Figure I.1.13.4 trimethylpropane triglycidyl ether (TTE).

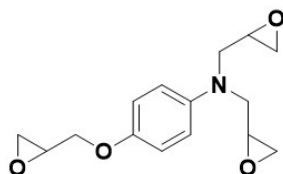


Figure I.1.13.5 *N,N*-diglycidyl-4-glycidylxyaniline (NND).

Differential scanning calorimetry (DSC) was used to evaluate the thermally dependent properties of both TTE and NND epoxies. In particular, the final cure temperature and glass transition temperature (T_g) of these epoxies were measured. Figure I.1.13.6 displays DSC data collected from an NND epoxy sample. This sample was originally cured at a temperature of 135°C but the cure was still incomplete. Even after subsequent heating to 180°C the NND sample was not cured fully. In fact, we discovered that the final cure temperature for NND based epoxy is 255°C. The cure temperature can be confirmed by the overlapping upper portion of the DSC curves (which are numbered sequentially) in Figure I.1.13.6 when the NND sample is taken to a temperature above 255°C. In curve 3 the onset of thermal decomposition is visible as the sample approaches 350°C, indicating a very thermally robust epoxy composition.

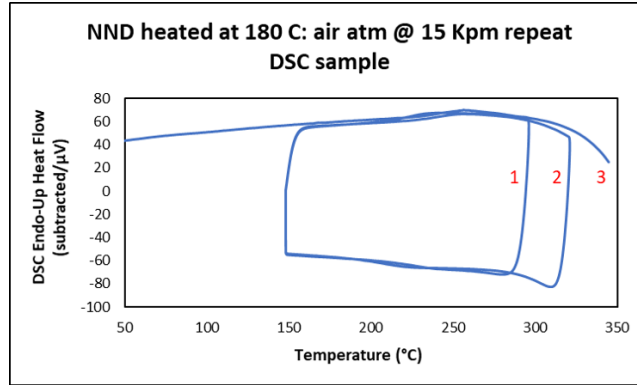


Figure I.1.13.6 Differential scanning calorimetry (DSC) data for a sample of NND based epoxy originally cured at a temperature of 180 °C. The final cure temperature of 255 °C is confirmed by the overlapping upper portion of the DSC curves, indicating no additional curing occurring above 255 °C.

A second zoomed-in set of DSC curves for a sample of NND based epoxy, this time fully cured at a temperature of 290°C prior to data collection, is displayed in Figure I.1.13.7. The inflection point visible in all three curves indicates that the T_g of NND based epoxy is approximately 249°C, well above the 150°C target maximum operating temperature for electric motors. Table I.1.13.1 summarizes the DSC results for both NND and TTE epoxies. For the sake of brevity, the DSC curves for the TTE epoxy were not displayed. In summary, the TTE epoxy had a T_g of 127°C, a little below the 150°C target maximum operating temperature for electric motors. For this reason, TTE epoxy will not be pursued further for use in high rotational speed electric motors. On the other hand, the NND based epoxy has a T_g that provides a very generous margin for operation up to and considerably above 150°C. Additionally, its negligible mass loss during curing will make fabrication of net-shaped parts straightforward as little to no shrinkage will occur as parts are cured.

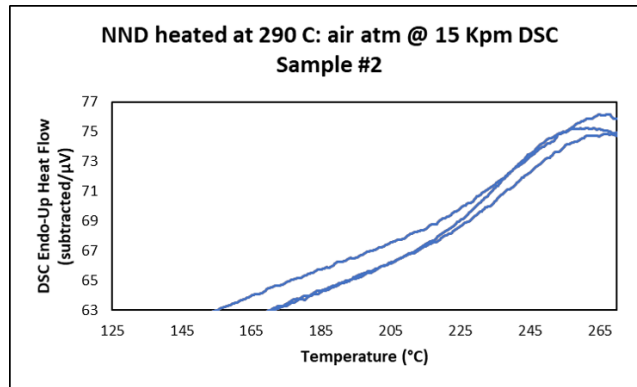


Figure I.1.13.7 Zoomed-in differential scanning calorimetry (DSC) data for a sample of NND based epoxy cured at temperature of 290 °C. The inflection point visible in all three curves indicates that the T_g of NND based epoxy is approximately 249 °C.

Table I.1.13.1 Summary of DSC data for NND and TTE epoxies. Cure times for both epoxies were 2 hrs.

Epoxly Formulation	T_g	Final Cure Temp.	Mass Loss
TTE	127 °C	180 °C	≤1%
NND	249 °C	250 °C	≤2%

3. Fabrication of Samples for Thermal Characterization

To ensure our magnetic composites are well designed for electric motor operation, it is also important to characterize, and perhaps even tune, the thermal conductivity of the samples. Understanding the thermal conductivity of our composite samples will also be important for the consortium members attempting to

integrate our bottom-up SMCs into their motor designs. Sandia has partnered with EDTC consortium member NREL to complete thermal conductivity measurements of our epoxy-based composites. NREL's thermal characterization setup requires 2" x 2" square samples no more than 2 mm thick. There is also a requirement that the square faces be flat and co-planar for high quality data to be collected.

Time was devoted to developing a process to fabricate these larger epoxy-based samples and ensure that they met the requirements of NREL's thermal characterization setup. First, a new mold was 3D printed. Next, curing profiles which included incremental increases in temperature were required for these larger samples. This way, excess heat generated during curing was minimized. Finally, the cured samples needed to be polished to ensure the square faces were both smooth and co-planar with one another. Figure I.1.13.8 displays a 2" x 2" neat epoxy sample prepared for thermal characterization and Figure I.1.13.9 displays an identically shaped sample containing 65 vol.% Fe₄N.

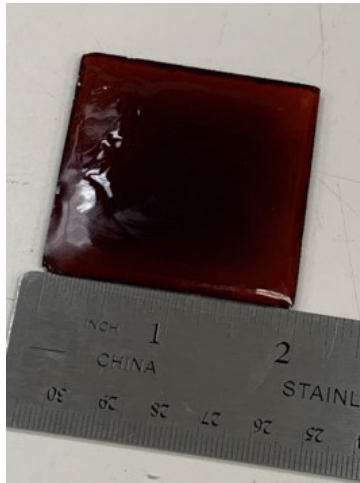


Figure I.1.13.8 Neat 2" x 2" epoxy sample for thermal characterization.

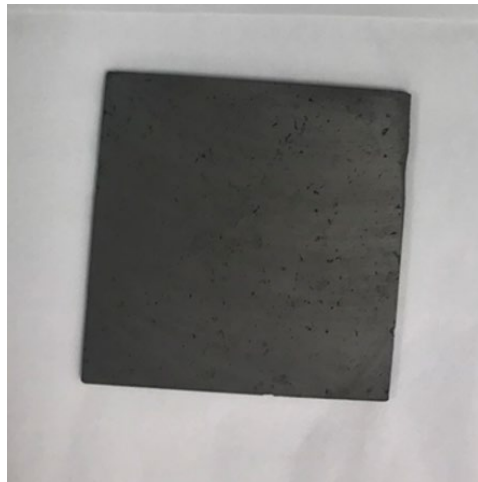


Figure I.1.13.9 2" x 2" 65 vol.% Fe₄N/epoxy composite sample for thermal characterization.

Table I.1.13.2 summarizes the initial set of results obtained by our collaborators at NREL. Both neat epoxy and Fe₄N filled epoxy samples were shipped to NREL and characterized. As some of the samples were prepared earlier in the fiscal year, TTE based samples were prepared along with NND based epoxy samples. In the future, all samples will transition to NND based epoxy. Neat epoxy samples averaged a thermal conductivity of 0.24 W/m·K and filled epoxy samples averaged a value of 1.8 W/m·K. Since the thermal

conductivity of the filled epoxy samples is higher than initially expected, this set of measurements will be repeated by NREL at a higher average temperature to see if both accuracy and precision can be improved. Iron nitride filled NND samples are also under preparation for measurement at NREL in the upcoming fiscal year.

Table I.1.13.2 Preliminary thermal conductivity results obtained by NREL.

Sample	Description	Avg. Temp. (°C)	Thermal Conductivity [W/m-K]
MRH2-40-1	NND neat epoxy	44.6	0.25
MRH2-43-1	NND neat epoxy	45.4	0.26
MRH2-47-1	TTE epoxy w/ 60 vol.% Fe ₄ N	44.1	1.87
MRH2-49-1	TTE epoxy w/ 60 vol.% Fe ₄ N	43.9	1.78
MRH2-3-1	TTE epoxy w/ 65 vol.% Fe ₄ N	44.8	1.72
MRH1-54-1	TTE neat epoxy	45.9	0.24
MRH1-84-1	TTE neat epoxy	46.7	0.23

4. Initial characterization of toroids

In addition to the samples fabricated for DSC and thermal conductivity characterization, 9 mm O.D. toroids were fabricated for magnetic characterization as a function of frequency in a B-H analyzer. An array of toroids was fabricated, and the vol.% of Fe₄N was increased up to almost 65 vol.% Fe₄N (the upper volume fraction of iron nitride that can be obtained without hot pressing). B-H loops were collected out to 1 MHz (our magnetic composite materials are relevant not only as soft magnetic materials in electric motors but could also serve as inductor core materials in power electronics). A variety of parameters can be extracted from the raw B-H data, but one of the most important metrics is relative permeability (μ_r). See Figure I.1.13.10 for a plot of μ_r as a function frequency for a set of toroidal cores with varying vol.% of Fe₄N in epoxy. At the lower volume loadings of iron nitride, the μ_r remains in the single digits but then jumps above 12 as 60 vol.% Fe₄N is reached. Perhaps more important than the initial values of μ_r themselves is the trend in the data. The inset of Figure I.1.13.10 shows that the values of μ_r are increasing exponentially with the vol.% loading of Fe₄N. This trend should allow us to reach values of μ_r in the 100s (where these materials will become relevant as low-cost soft magnets for axial flux machines) as hot pressing is introduced and the volume loading of Fe₄N is increased beyond 65 vol.%. Other strategies to increase μ_r will be implemented, including the use of a range of Fe₄N particle sizes and annealing protocols to relieve stress within samples. The nearly flat frequency response of the toroids' μ_r is also very noteworthy. This will not have as significant an impact on electric motor operation (EETT Keystone 2) where soft magnetic materials will experience an equivalent switching frequency on the order of a few kHz. However, inductors within inverters and motor drives (Keystone 1) could potentially operate with switching frequencies as high as several hundred kHz. The SMCs being developed here could certainly also be adopted as low loss inductor cores in power electronics applications.

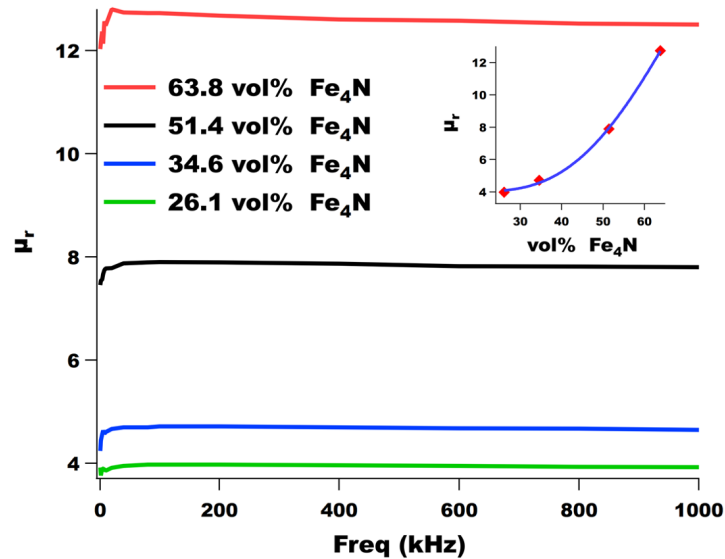


Figure I.1.13.10 Relative permeability (μ_r) as a function frequency for a set of toroidal cores with varying vol.% of Fe_4N in epoxy. The inset shows that the values of μ_r are increasing exponentially with the vol.% loading of Fe_4N .

Conclusions

During FY20, a number of important developments were made in the fabrication and characterization of iron nitride ($\gamma\text{-Fe}_4\text{N}$) based magnetic composite parts for electric motors, despite the ongoing Coronavirus outbreak. It is important to note that these materials also show substantial promise as inductor cores for electric drive power electronics. The NND based epoxy demonstrated a T_g of 249°C , well above the anticipated maximum motor operating temperature of 150°C . Samples were fabricated for thermal conductivity measurements by consortium member NREL and initial measurements obtained. Finally, we demonstrated an exponential trend in μ_r as a function of Fe_4N volume loading in epoxy-based composites. In the near future, values of μ_r relevant for axial flux electric motors should be obtained. Future work will focus on hot pressing to increase magnetic material volume loading and enhance magnetic performance in both electric motor and motor drive applications.

Key Publications

1. G. Ouyang, B. Jensen, W. Tang, J. Schlagel, C. Pan, B. Cui, K. Dennis, D. Jiles, T.C. Monson, I. Anderson, M.J. Kramer, and J. Cui, Near Net Shape Fabrication of Anisotropic Fe-6.5%Si Soft Magnetic Materials. *Acta Materialia* **201**, 209-216 (2020).
2. E. Langlois, J. Watt, D. Huber, M. McDonough, T. C. Monson, J. Neely, Design and Evaluation of Nano-Composite Core Inductors for Efficiency Improvement in High-Frequency Power Converters. *2020 IEEE Applied Power Electronics Conference and Exposition (APEC)*, 2676-2679 (2020).
3. Z. Fu, B. E. MacDonald, A. D. Dupuy, X. Wang, T. C. Monson, R. E. Delaney, C. J. Pearce, K. Hu, Z. Jiang, J. M. Schoenung, W. Chen, E. J. Lavernia, Exceptional combination of soft magnetic and mechanical properties in a heterostructured high-entropy composite. *Applied Materials Today* **15**, 590-598 (2019).

References

1. US Drive, "Electrical and Electronics Technical Team Roadmap," Partnership Plan, Roadmaps, and Other Documents 2017.
2. H. Shokrollahi and K. Janghorban, "Soft magnetic composite materials (SMCs)," *Journal of Materials Processing Technology*, vol. 189, no. 1-3, pp. 1-12, 2007, doi: 10.1016/j.jmatprotec.2007.02.034.

3. J. S. Corporation. Super Core™ Electrical steel sheets for high-frequency application. (2017). JFE Steel Corporation. [Online]. Available: <http://www.jfe-steel.co.jp/en/products/electrical/catalog/fle-002.pdf>
4. J. M. D. Coey, Magnetism and Magnetic Materials. New York: Cambridge University Press, 2010.
5. T. C. Monson et al., "Soft Magnetic Multilayered FeSiCrB–Fe₄N Metallic Glass Composites Fabricated by Spark Plasma Sintering," IEEE Magnetics Letters, vol. 10, pp. 1-5, 2019, doi: 10.1109/LMAG.2019.2906832.
6. M. Qu et al., "Magneto-photo-acoustic imaging," Biomed. Opt. Express, vol. 2, no. 2, pp. 385-396, 2011/02/01 2011, doi: 10.1364/BOE.2.000385.
7. M. Magazine. <https://magneticsmag.com/new-structural-adhesive-from-delo-for-magnet-bonding-has-high-temperature-stability/> (accessed).
8. Crosslinktech. <http://www.crosslinktech.com/products-by-application/featured-electric-motor-products.html> (accessed).
9. M. Bond. <https://www.masterbond.com/techtips/how-optimizing-glass-transition-temperature-tg> (accessed).
10. A. Schoppa and P. Delarbre, "Soft Magnetic Powder Composites and Potential Applications in Modern Electric Machines and Devices," IEEE Transactions on Magnetics, vol. 50, no. 4, pp. 1-4, 2014, doi: 10.1109/TMAG.2013.2290135.
11. P. Mason, K. Atallah, and D. Howe, Hard and soft magnetic composites in high speed flywheels. 1999.

Acknowledgements

This work is supported by the DOE Office of Energy Efficiency and Renewable Energy, Vehicle Technologies Office. Sandia National Laboratories is a multi-mission laboratory managed and operated by National Technology and Engineering Solutions of Sandia, LLC., a wholly owned subsidiary of Honeywell International, Inc., for the U.S. Department of Energy's National Nuclear Security Administration under contract DE-NA0003525. The views expressed in the article do not necessarily represent the views of the U.S. Department of Energy or the United States Government. We wish to thank Tyler Stevens, Melinda Hoyt, and Charles Pearce for their fabrication of magnetic composites, Robert Delaney and Charles Pearce for their assistance with magnetic characterization, and Mark Rodriguez for his help with X-ray diffraction data collection and analysis. We would also like to acknowledge key collaborators within the electric drive systems consortium: Kevin Bennion (NREL), Emily Cousineau (NREL), Iver Anderson (Ames Lab), Jun Cui (Ames Lab), and Matt Kramer (Ames Lab).

I.1.14 Component Modeling, Co-Optimization, and Trade-Space Evaluation (Sandia National Laboratories)

Jason Neely, Principal Investigator

Sandia National Laboratories
P.O. Box 5800, MS 1152
Albuquerque, NM 87185
Email: jneely@sandia.gov

Susan Rogers, DOE Technology Development Manager

U.S. Department of Energy
Email: susan.rogers@ee.doe.gov

Start Date: October 1, 2018
Project Funding: \$250,000

End Date: September 30, 2023
DOE share: \$250,000

Non-DOE share: 0

Project Introduction

This project is intended to support the development of new traction drive systems that meet the targets of 100 kW/L for power electronics and 50 kW/L for electric machines with reliable operation to 300,000 miles. To meet these goals, new designs must be identified that make use of state-of-the-art and next-generation electronic materials and design methods. Designs must exploit synergies between components, for example converters designed for high-frequency switching using wide band gap devices and ceramic capacitors. This project includes: (1) a survey of available technologies, (2) the development of design tools that consider the converter volume and performance, and (3) exercising the design software to evaluate performance gaps and predict the impact of certain technologies and design approaches, i.e., GaN semiconductors, ceramic capacitors, and select topologies. Early instantiations of the design tools enable co-optimization of the power module and passive elements and provide some design guidance; later instantiations will enable the co-optimization of inverter and machine.

Objectives

For FY20, these included

- Generate high-fidelity dimensional and electrical models for principal power electronic components within a novel inverter design
- Co-Optimize inverter and machine designs for power density, reliability, and efficiency
- Demonstrate and evaluate relevant converter prototypes

Approach

The approach includes four strategies for generating design guidance and optimal designs, listed in order of increased fidelity and resources:

1. **Empirical and First-Principles Analysis:** This uses first-principles knowledge, such as physical models, as well as comparative designs to inform the design.
2. **High-Fidelity Modeling and Analysis:** This uses higher-order models that consider the component equivalent circuits, dimensions, reliability calculations, etc.
3. **Global Co-Optimization:** With the definition of one or more performance metrics, components are simulated together, and their performance is measured and compared.

4. **Hardware Iteration:** Using optimal designs identified in software, hardware exemplars are built and evaluated; 3 and 4 are iterated to create the best results.

In FY20, the project focused on strategies 2 and 3, improving the fidelity of component models, developing the optimization software into a tool to identify designs in the Power Density-MTBF trade-space, using this software also to predict converter performance for SiC vs GaN and film vs ceramic capacitors, and building a power converter prototype to validate models. Hardware iteration will continue with inverter fabrication and test in FY21.

For optimization, the team used the Genetic Optimization System Engineering Tool (GOSET) developed by Purdue University [1]. This MATLAB®-based software package consists of several scripts for implementing and solving a genetic algorithm optimization problem. The genetic algorithm is a probabilistic method for optimizing multi-input systems with non-convex solution spaces using the principles of genetics and a user-defined fitness function. GOSET allows for multiple fitness functions to be co-optimized into a Pareto front. To set up the optimization, the circuit schematic and physical layout were partially defined, and the dimensions of and between components, thicknesses of insulators, lengths of conductors, choice of SiC or GaN, number of phases, etc. were formulated and linked to the schematic definition in order to compute a volume and evaluate the circuit/system performance using a dynamic simulation.

In FY20, detailed component models were developed for inductors, capacitors, switches, and heatsinks. Figure I.1.14.1 illustrates the step-by-step process to capture the electrical behavior of a power inductor. As described in the previous report, component mean time between failure (MTBF) quantities were also computed for SiC MOSFETS and capacitors using MIL-HDBK-217F calculations [2].

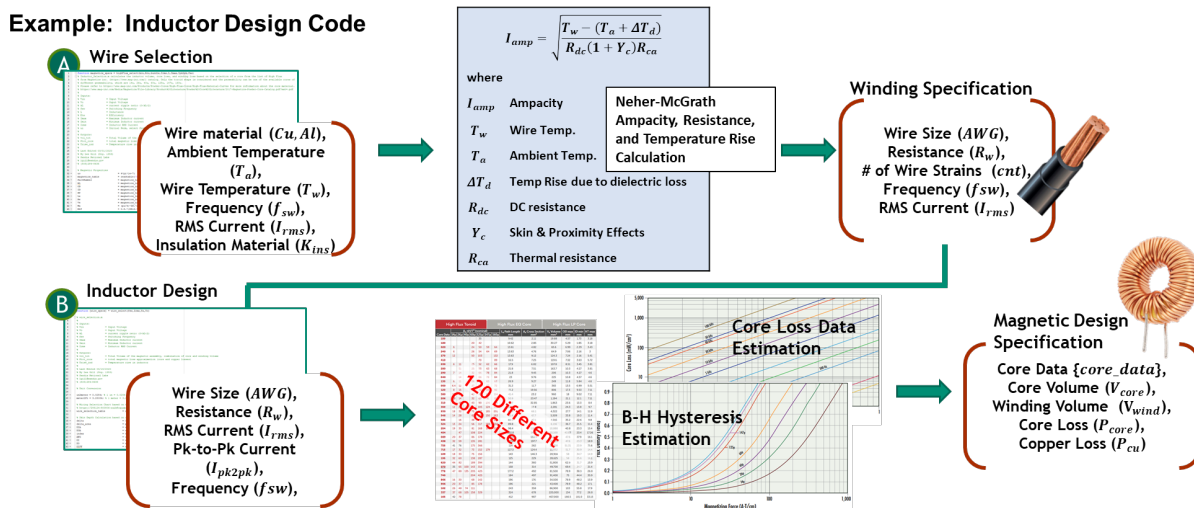


Figure I.1.14.1 Passive Component Models are Carefully Developed using Latest Design Information

A detailed model was generated to predict electrical performance and MTBF and used to co-optimize power density and MTBF for a synchronous boost converter. The boost converter optimization enabled the team to validate codes containing the MTBF calculation for a simple half-bridge converter before scaling the approach up to a multi-phase inverter.

To predict the impact of vertical GaN Junction Barrier Schottky (JBS) diodes (in development within the consortium), a comparative analysis presented in [3] was applied to compare optimally-designed GaN PiN, GaN JBS and SiC Merged PiN Schottky (MPS) diodes under operating conditions for the vehicle environment. Likewise, for a vertical FET device, assuming a fixed device structure (for comparison), the predicted R_{on} was computed as a function of breakdown voltage for devices based on Silicon, SiC, and GaN (see Figure I.1.14.2).

Therein, R_{on} for the GaN device is approximately $\frac{1}{2}$ that of the SiC device. In FY20, based on these results, component models were generated to predict the switching performance of vertical GaN MOSFETs. These switches were then used to predict the impact on multi-phase inverter power density and conversion efficiency.

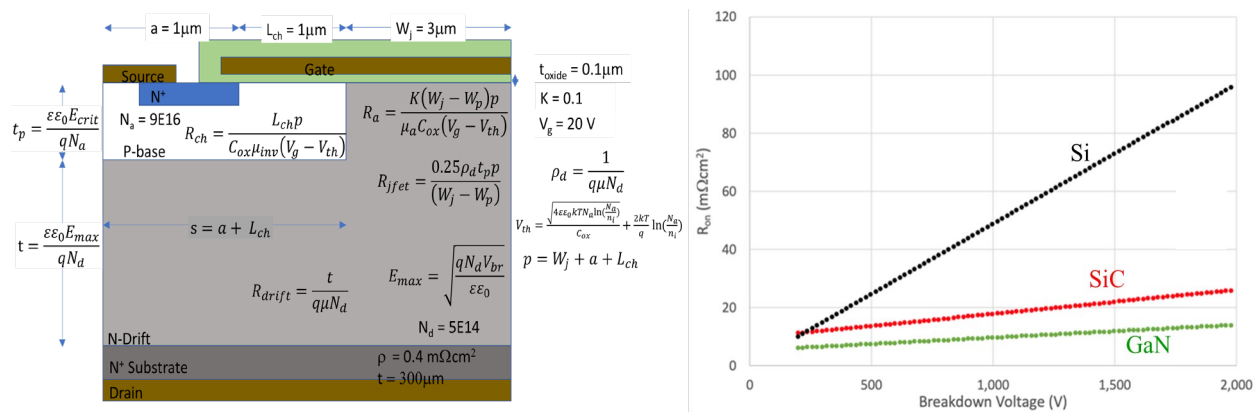


Figure I.1.14.2 Comparison of R_{on} in MOSFETs made in Silicon, SiC, and GaN showing (left) the device structure and (right) the predicted results.

Results

Optimization of Boost Converter Reliability and Volumetric Power Density

In this portion of the research effort, the team sought to provide insight in maximizing circuit MTBF while maximizing volumetric power density of a 5-kW synchronous boost converter. Due to the characteristics of a multi-variant trade space, the evolutionary algorithm within GOSET was implemented to obtain a set of optimal solutions based on the reliability of the boost inductor, transistors, capacitors, and heatsinks. Figure I.1.14.3 shows a schematic of the target circuit with key components emphasized.

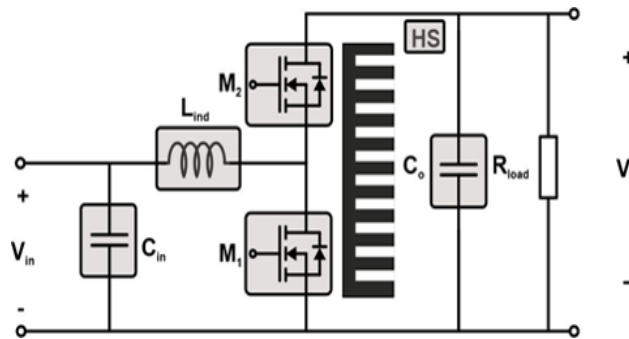


Figure I.1.14.3 Schematic of the synchronous boost converter with the passive and active elements to be optimized highlighted.

The pareto optimal solutions were observed for different component selections, identifying optimal designs and also providing insight into component selection. Figure I.1.14.4 (left) depicts the pareto optimal solutions for the 5-kW boost converter based on Film capacitors and on three magnetic materials: Kool M μ , High Flux, and MPP magnetic core materials, indicating modest difference. The general trend is similar between the three core types; higher power density designs can be realized at the expense of decreased MTBF.

For the highest power density designs, MPP and High Flux are preferred. Compared to Kool M μ , using MPP can bring about a potential gain of 10 kW/L for the boost converter. High Flux cores allow high power density designs for high power and high DC bias applications because of their high saturation flux density (1.5 T). However, when such a design is necessary, high switching frequency is required; hence, switching losses

through the devices along with the core loss can have a significant impact on the reliability factor. The differences, however, are comparatively small.

Figure I.1.14.4 (right) illustrates the disparity between circuits that use multi-layer ceramic capacitors (MLCCs) and those that use Film capacitors for C_{in} and C_o , with a clear and substantive trade-off between MTBF and power density. A 50 kW/L power density can be realized when MLCC capacitors are selected. Though MLCC performs superior in increasing power density over the film capacitor solution, however, large numbers of capacitors for achieving the required capacitance result in lowered circuit MTBF. It can be deduced from the graph that there is a theoretical limit to 5,000 hours when MLCC capacitors are used in this electronic system.

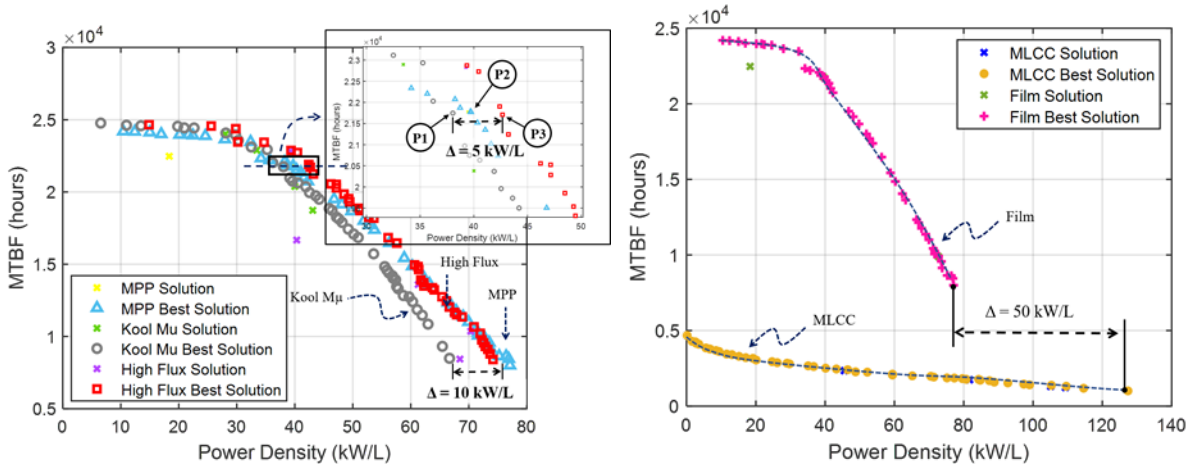


Figure I.1.14.4 Shown (left) Pareto solution evaluating Kool μ , High Flux, and MPP and the prototypes with different inductors denoted as P1, P2, and P3 and (right) Pareto optimization solution sets with MLCC capacitors and film capacitors for input and output capacitors.

The prototypes for test were selected from among the designs in Figure I.1.14.4 (left), denoted as P1, P2 and P3. These each had the same film-based input and output capacitance but different magnetic cores. These were tested, and their operating conditions were demonstrated to verify the model predictions. Figure I.1.14.5 (left) shows an image of the prototype, P3, with the High Flux solution and Figure I.1.14.5 (right) illustrate example experimental results which include the input voltage, output voltage, input current, and output current waveforms in comparison with the theoretical or simulated data from the SPICE model for the P1 design.

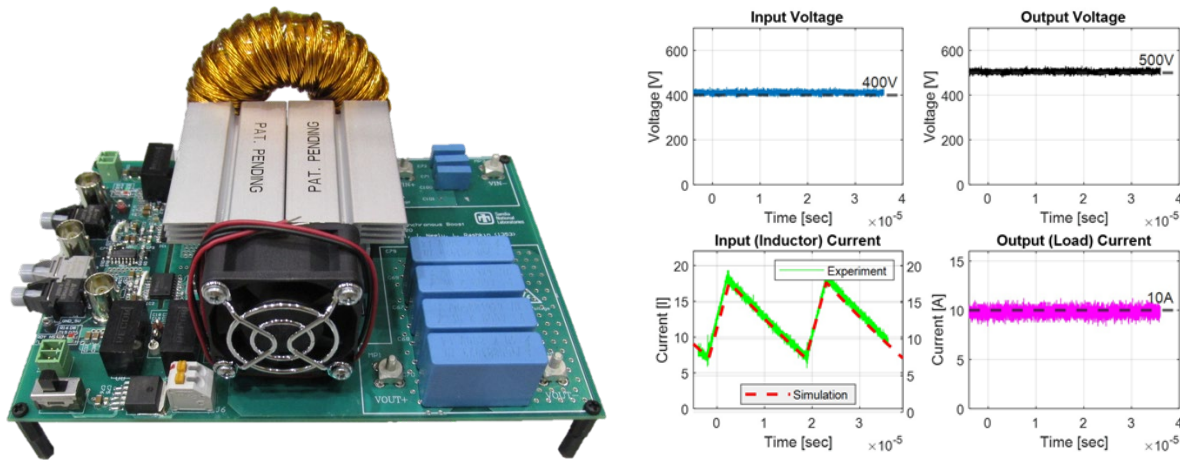


Figure I.1.14.5 Shown (left) Picture of hardware prototype with the High Flux core design, P3 and (right) example of measured waveforms of the 5-kW boost converter operation with input of 400 V and output of 500 V for candidate P1 boost converter design

The full account of this work was published at the IEEE Energy Conversion Congress & Expo, ECCE2020 [4].

Optimization of Inverter Drive Efficiency and Volumetric Power Density for SiC and GaN Switches

The team also developed inverter drive designs that utilize wide band gap devices (SiC or GaN) and ceramic capacitors to enable high-frequency switching and a compact integrated design. As with the boost converter, the multi-objective optimization was employed to select key parameters for the design. In this effort, however, the focus was on efficiency and power density disparities given the use of SiC or GaN power devices.

Figure I.1.14.6 shows the selected circuit topology used in the co-optimization problem consisting of a multiphase inverter, DC link capacitor, input inductor, and multiple parasitic terms which vary with component selection and layout. In addition, the form factor selected for the principal converter elements is also shown in Figure I.1.14.6. Therein, the module with devices, conductors, and flat capacitor assembly are packaged together. This approach has several advantages for thermal management and reduction of parasitics, as discussed in [5]. This form factor was used as a basis for the dimensional analysis.

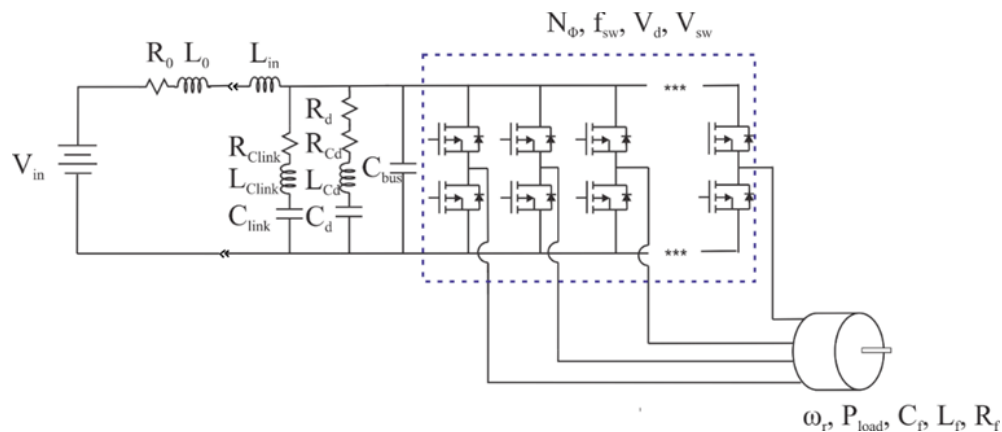


Figure I.1.14.6 Circuit topology (top) used in inverter optimization studies and (bottom) candidate flat form factor design shown from the side

The genetic optimization was run on 99 individuals over 100 generations for systems using SiC devices and GaN devices. The resulting Pareto fronts are shown in Figure I.1.14.7. These results show that GaN solutions are closer to the 100 kW/L power density target, with a solution that has a 74.949 kW/L at 89.27% efficiency. This solution is for a three-phase inverter with an input voltage of 915.42 V and a switching frequency of 343 kHz. The capacitor board uses 320 ceramic capacitors to achieve the required capacitance. This is still below the targeted power density and efficiency for the application, so it is useful to look at the component volumes and losses. In particular, it was clear that most of the volume and loss was in the filter inductors. This work was published at the IEEE Transportation Electrification Conference & Expo (ITEC2020); the full details of the work are included in [6].

Next steps in this work will be to (1) design, build, and test an inverter prototype to validate the models and demonstrated power density improvements, and (2) to investigate new methods to reduce the loss and size of the filters at the AC interface of the drive.

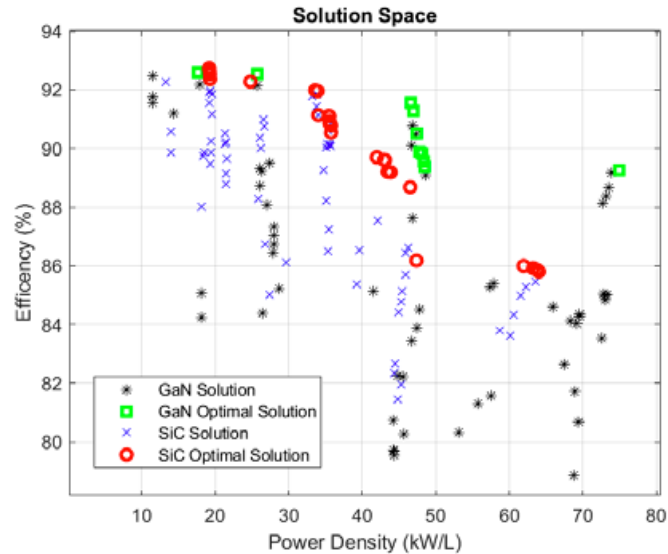


Figure I.1.14.7 Comparison between Pareto optimal frontiers for SiC and GaN

Conclusions

This project is focused on developing improved designs for future traction drive systems through the combined use of GaN devices, ceramic capacitors, high-frequency switching, and multi-phase designs that enable considerable improvements in power density. Designs are developed with the help of tools developed to perform multi-objective optimizations on electric drive designs. Unlike previous work, these include optimizations that consider component reliability. In FY20, the project team developed an optimization tool based on GOSET [1] to co-optimize converter power density and mean time between failures (MTBF) in a synchronous boost converter. A pareto optimal front was generated, converter designs were selected, built, and tested to validate time-domain performance predictions. In addition, the project team co-optimized efficiency and power density for a multi-phased inverter. Candidate designs were identified for inverters based on SiC and GaN devices. Future work will refine these tools and extend their use to co-optimize the inverter and machine designs. The team will merge the capabilities of these tools and identify prototype inverter designs with improved reliability and power density.

Key Publications / Presentations

1. J. Neely, G. Pickrell, J. Flicker, L. Rashkin, R. Kaplar, "The Case for Vertical Gallium Nitride Devices in Electric Vehicle Drives," *2020 IEEE Applied Power Electronics Conference (APEC2020)*, Industry Session: Vehicle Electrification II.
2. L. Gill, J. C. Neely, L. J. Rashkin, J. D. Flicker and R. J. Kaplar, "Co-Optimization of Boost Converter Reliability and Volumetric Power Density Using Genetic Algorithm," *2020 IEEE Energy Conversion Congress and Exposition (ECCE)*, Detroit, MI, USA, 2020, pp. 5302-5309, doi: 10.1109/ECCE44975.2020.9235716.
3. L. Rashkin, J. Neely, L. Gill, J. Flicker and R. Darbali-Zamora, "Optimal Power Module Design for High Power Density Traction Drive System," *2020 IEEE Transportation Electrification Conference & Expo (ITEC)*, Chicago, IL, USA, 2020, pp. 134-138, doi: 10.1109/ITEC48692.2020.9161703.

References

1. S. D. Sudhoff, GOSET: Genetic Optimization System Engineering Tool: For Use with MATLAB®, version 2.6, January 1, 2014.

2. *Military Handbook: Reliability prediction of electronic equipment*, 1991. Available: <https://snebulos.mit.edu/projects/reference/MIL-STD/MIL-HDBK-217F-Notice2.pdf>
3. J. Flicker and R. Kaplar, "Design optimization of GaN vertical power diodes and comparison to Si and SiC," 2017 IEEE 5th Workshop on Wide Bandgap Power Devices and Applications (WiPDA), Albuquerque, NM, 2017, pp. 31-38.
4. L. Gill, J. C. Neely, L. J. Rashkin, J. D. Flicker and R. J. Kaplar, "Co-Optimization of Boost Converter Reliability and Volumetric Power Density Using Genetic Algorithm," *2020 IEEE Energy Conversion Congress and Exposition (ECCE)*, Detroit, MI, USA, 2020, pp. 5302-5309, doi: 10.1109/ECCE44975.2020.9235716.
5. J. Stewart, J. Neely, J. Delhotal and J. Flicker, "DC link bus design for high frequency, high temperature converters," 2017 IEEE Applied Power Electronics Conference and Exposition (APEC), Tampa, FL, 2017, pp. 809-815.
6. L. Rashkin, J. Neely, L. Gill, J. Flicker and R. Darbali-Zamora, "Optimal Power Module Design for High Power Density Traction Drive System," *2020 IEEE Transportation Electrification Conference & Expo (ITEC)*, Chicago, IL, USA, 2020, pp. 134-138, doi: 10.1109/ITEC48692.2020.9161703.

Acknowledgements

This work is supported by the DOE Office of Energy Efficiency and Renewable Energy, Vehicle Technologies Office. Sandia National Laboratories is a multi-mission laboratory managed and operated by National Technology and Engineering Solutions of Sandia, LLC., a wholly owned subsidiary of Honeywell International, Inc., for the U.S. Department of Energy's National Nuclear Security Administration under contract DE-NA0003525. The views expressed in the article do not necessarily represent the views of the U.S. Department of Energy or the United States Government.

I.1.15 Magnetics for Ultra-High Speed Transformative Electric Motor (MUST-EM)

Iver Anderson, Principal Investigator

Ames Laboratory (USDOE), Iowa State University
222 Metals Development, Iowa State University
Ames, IA 50011
Email: andersoni@ameslab.gov

Matthew Kramer, Principal Investigator

Ames Laboratory (USDOE), Iowa State University
125 Metals Development, Iowa State University
Ames, IA 50011
Email: mjkramer@ameslab.gov

Jun Cui, Principal Investigator

Ames Laboratory (USDOE), Iowa State University
106 Wilhelm, Iowa State University
Ames, IA 50011
Email: cuijun@ameslab.gov

Susan Rogers, DOE Technology Development Manager

U.S. Department of Energy
Email: susan.rogers@ee.doe.gov

Start Date: October 1, 2018
Project Funding: \$250,000

End Date: September 30, 2023
DOE share: \$250,000

Non-DOE share: \$0

Project Introduction

This project is part of the multi-lab Electric Drive Systems Consortium that will leverage U.S. research expertise and facilities at the national labs and universities to improve the power density of electric drives by 10x compared with the 2015 numbers while reducing the cost by 50% and doubling the lifetime miles within the next 5 years. The project is organized around three Keystones: (1) Power Electronics; (2) Electric Motors; and (3) Traction Drive System. The research activities at Ames support the Electric Motors Keystone 2 project.

The DOE 2025 target on electric motor power density is 50 kW/L. Such an aggressive target limits the choices for permanent magnets (PM) to the most powerful Nd-Fe-B based magnets, whose magnetic properties are strongly temperature dependent, unfortunately. Better thermal stability is achieved currently by adding significant amounts of Co and Dy [1], both with increased cost. Unfortunately, Dy is extremely scarce and highly localized in supply, unlike Co that has is variable in cost and not localized in supply. The U.S. Department of Energy (DOE) highlighted Dy as the single most critical strategic metal not only in the U.S., but world-wide. According to the 2014 and 2019 USGS Minerals Commodities Summaries, the average price of Dy₂O₃ jumped from \$295/kg in 2010 to \$1410/kg in 2011, then retreated to \$180/kg in 2018. Its price and availability remain volatile, with the price back to \$247 in 2019 and expected to reach \$290 in 2022 [2]. Currently, over 70% of rare earth (RE) metals are produced in China. In 2017, some European countries and China announced that internal combustion engines will be phased out in one to two decades. With foreseeable large increase in the number of electrical vehicles and their dependence on permanent magnet traction motors, the supply risk for Nd, Pr and Dy is expected to remain at high level with their projected demand to more than double by 2030 [3]. Strategies to mitigate the RE materials criticality issues include increasing and diversifying the supply and reducing demand. While several mines outside of China-- in Australia, Vietnam and the US-- have opened and have begun production of RE elements, the most desired “heavy” RE (HRE) elements, in particular, Dy and Tb, remain low in supply because none of these newly opened mines are rich in

heavy RE reserves. To reduce the demand for heavy RE elements, alternative magnet technologies that eliminate or use much less Dy have to be developed, where Dy is used now for maintaining Nd-Fe-B's coercivity at high temperature [4]. Evidence shows that significantly reducing the grain size of a Nd-Fe-B magnet may improve its coercivity, making it possible to use a microstructure engineering grain-refinement approach to replace the chemistry approach, i.e., a Dy addition. We plan to take advantage of the inverse relationship between grain size and coercivity and develop a new type of Nd-Fe-B permanent magnet with ultrafine grain size by scalable manufacturing methods.

One viable approach to drastically increase motor power density is to increase motor speed. Although not specified by the DOE 2025 target, 90% efficiency is a key operational limit for electric motors because less efficient motors consume more power (including power for extra motor cooling), impose extra load on the vehicle battery, and diminish the impact of increasing power density. To maintain such high efficiency at high speed, the magnetic materials, especially soft magnetic cores, need to exhibit exceptionally high electrical resistivity in order to minimize otherwise substantially higher loss caused by increased eddy current heating. These tight constraints on materials are further tightened by the 2025 cost target of \$3.3/kW, which disqualifies most of the existing advanced soft magnetic materials (e.g., amorphous and nanocrystalline) from meeting these requirements. It appears that one of the barriers for meeting the DOE 2025 targets of 50 kW/L power density is the lack of cost-effective soft magnetic materials that can run at high frequency without excessive eddy current heating. We plan to address these materials challenges by developing the soft magnetic (SM) materials suitable for high-speed application. Clearly, a collective effort with the CADET consortium partners on innovative advanced materials and complex system design is needed to meet the aggressive target.

Objectives

This project will develop the PM and SM materials and their processes for high-speed traction drive motors. For PM materials, the objective is to develop fine-grain RE permanent magnet with high coercivity at high temperature and free of heavy rare earth elements. For SM materials, the objective is to develop a processing method that can be scaled to mass production of ductile 6.5% Si steel sheet for stator and rotor applications.

Approach

Grain size reduction is a viable approach for eliminating or reducing critical heavy RE (HRE) elements usage in the magnets for PM motors while maintaining their high temperature performance. It is a well-known experimental fact that the coercive field of permanent magnets increases with decreasing grain size. Micromagnetic simulations show that the increase of coercive field results from the logarithmic decrease in the demagnetizing field near the edges of a grain. At this very location, the torque exerted by an external local field onto the internal magnetization direction initiates the formation of a reversed domain. In a PM motor, the external electromagnetic force of the SM core attempts to reverse the magnetization of the PM induced rotor. With decreasing PM grain size, the external torque that can be applied to rotate the magnetization out of the anisotropy direction becomes smaller and domain rotation can happen only at higher external fields [5]. It is possible to push the coercivity to beyond 20 kOe with ultrafine grains. With such high coercivity at room temperature, even with the typical rate of coercivity decay with increasing temperature (-0.6%/K) [1], there will still be enough coercivity at the 450 K, where the high-speed motor may operate. The challenge for the ultrafine grain approach is to develop feedstock powders with particle size near 1 μm ; and more importantly, to keep the grain size near 2 μm during sintering to full density. This also requires development of alternative particle surface passivation methods and extreme care in handling powders to restrict oxidation. In FY20, Ames Lab carried out investigations of industrially-viable processing methods for synthesizing feedstock powders with ultrafine particle size (< 4 μm), and methods for sintering the powder into bulk magnets without significant grain growth, maintaining grain size of < 5 μm , showing the pathway to further improvements in FY21.

Melt-spinning is a viable approach for enabling 6.5% Si steel for high power density motor applications, in spite of its higher cost than traditional methods for producing common 3.2% Si steel. It has been established that the electromagnetic properties of 6.5% Si steel are superior to that of commonly-used 3.2% Si steel [6], except that the 6.5% Si steel is brittle and cannot be readily mass-produced using the cost-effective slab-casting and cold-rolling method. Our research shows that 6.5% Si steel becomes ductile after rapid quenching from high temperature. We found that the high Si embrittling intermetallic phases (B2 and D03) can be reduced when the material is rapidly solidified from the high temperature A2 phase [7]. Melt-spinning is traditionally used for manufacturing amorphous and nanocrystalline materials where rapid cooling rate is essential for preventing grain growth. For the 6.5% Si steel, a final microstructure with large grain size is preferred. The rapid cooling rate is for controlling phase formation, not for final grain size. As such, the principles and parameters for the traditional planar flow casting needed to be modified for casting wide 6.5% Si steel sheet and in FY20 these developments were performed sufficiently to enable offering of this technology to a company that is equipped for commercialization of it. In FY20, Ames lab also carried out initial investigations of melt-spinning related process parameters and began development of near-net-shape fabrication concepts for stator core designs, developed by ORNL, using melt-spun wires. It is further work on melt spinning of thin ribbon/wires forms and fabrication methods for highly-loaded stator cores with near-net shape that will be pursued in FY21.

Permanent magnet traction motors are the most compact and efficient electric drive motors. Their optimization is a fine balance between the properties and topology of SM and PM components and the demagnetization fields. Clearly, a new motor topology with complex flux patterns that can take full advantage of new PM and SM materials is needed. The Ames team will continue to work with ORNL, NREL, and SNL to demonstrate the newly developed magnetics in an electric motor.

Results

Task 1: Develop fine-grain RE permanent magnet with high coercivity at high temperature

In FY20, Ames Lab fabricated several Dy-free Nd-Fe-B sintered magnets via the powder metallurgical route. The starting material was hydrogen-decrepitated (HD) coarse Nd-Fe-B powder. The coarse powders were ball-milled for different hours using a low energy roller machine to obtain different particle sizes. These fine powders were magnetically aligned using a pulse-field of 9 T, then cold isostatic pressed (CIP) into the green compact under a pressure of 500 MPa. The compacts are sintered at 1080°C for 1 h, post-annealed at 900°C for 1 h and at 580°C for 1h. After final pulse magnetization, the magnets were measured for their coercivity and magnetization using a closed-loop hysteresis-graph.

To compare the quality of AMES magnet with commercial magnets, the temperature dependent demagnetization curves of the AMES magnet with $4.0 \pm 0.2 \mu\text{m}$ average grain size are plotted on top of the Arnold Magnetics N45 magnet with $4.5 \pm 0.2 \mu\text{m}$ average grain size (Figure I.1.15.1). This result qualifies the capabilities and the processes developed at Ames lab as the state-of-the-art.

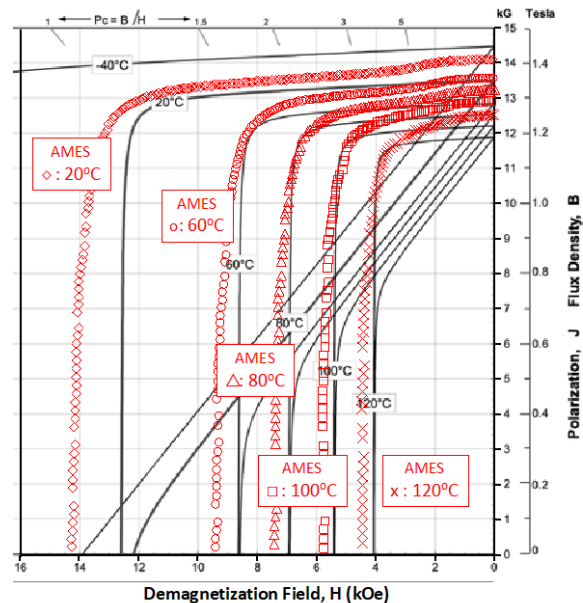


Figure I.1.15.1 Demagnetization curves of the fine grain magnet fabricated by Ames Lab overlaid on Arnold's commercial magnet using similar feedstock materials.

The magnetic properties of magnets with three different grain sizes are summarized in Table I.1.15.1. The dependence of coercivity (H_{cj}) on grain size is clearly demonstrated. Although starting feedstock particle size may be ultrafine, sintering temperature and time can affect the grain size of magnet, resulting in excess grain growth (and decreased coercivity). The Ames team has been working on optimizing the sintering process for ultrafine grain sizes and protocols for handling these powders with minimum oxidation. As an example of external liquid phase sintering additives, 5% Pr-Cu powders was blended with the feedstock powders during milling and used to reduce sintering temperatures, minimize grain growth, and raise coercivity (Figure I.1.15.2).

Table I.1.15.1 Average particle size, grain size and magnetic properties of the AMES sintered magnet samples

	Ball mill hr	7	9	11
Feedstock powders	Particle size, μm	3.6 ± 0.2	2.2 ± 0.2	2.1 ± 0.2
	Grain size, μm	5.0 ± 0.2	4.6 ± 0.2	4.0 ± 0.2
Sintered Magnets	Ms@9T, kG	14.6	14.8	14.6
	Br, kG	13.5	13.7	13.7
	Hcj, kOe	11.6	12.6	13.7
	$(BH)_{\text{max}}$, MGOe	41.6	43.1	43.6
	$-\alpha_{25-125^\circ\text{C}}$ (%/°C)	0.15	0.14	0.14
	$-\beta_{25-125^\circ\text{C}}$ (%/°C)	0.74	0.72	0.71

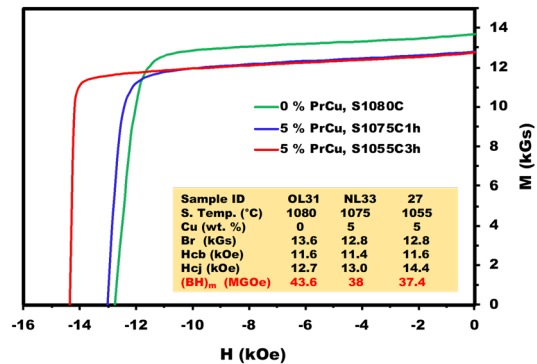


Figure I.1.15.2 MH demag curves of the bulk magnet prepared using powders blended with CuPr and sintered at different temperatures.

Task 2: Development of cost-effective manufacturing process for high performance soft magnetic materials in thin sheet form

Previous research showed that the planar flow casting method is the most promising manufacturing method for mass production of soft magnetic 6.5% Si steel in thin sheets for PM motor cores. Such methods have been used for producing amorphous and nanocrystalline materials, but these advanced SM materials have excessive cost to be pursued for the 2025 cost target of \$3.3/kW. However, these materials have relatively low melting point, typically <1400 K, compared to the melting point of low-cost 6.5% Si steel of 1750 K. Such high processing temperatures put excessive thermal load on a melt spinning system, especially an expanded capacity system for producing wide ribbon. In FY19, Ames team carried out extensive modification to the existing melt-spinning system for kilogram level ribbon production. In FY20, Ames team successfully produced 20 mm wide 6.5%Si steel ribbon. Figure I.1.15.3a shows the picture of a stable melt-pool on the copper wheel rotating at 20 m/s. This is one of the challenges for making high quality melt-spun ribbon. Figure I.1.15.3b shows the picture of 20 mm wide melt-spun ribbon of 6.5%Si steel and Figure I.1.15.3c a jar of ribbon.

In FY20, the Ames team started an effort on developing molding for near-net-shape stator cores. Different from the conventional stacking laminate approach to build the stator, the new concept uses narrow ribbons as feedstock and directly consolidates the ribbon bundles into a stator block. Each ribbon is coated with polymer or oxides to reduce eddy current losses. The texture of the ribbon bundle matches the magnetic flux lines,

allowing effective use of SM materials and copper windings. Compared to wide ribbons, narrow ribbons are much easier to manufacture and require much less complex crucible orifice designs.

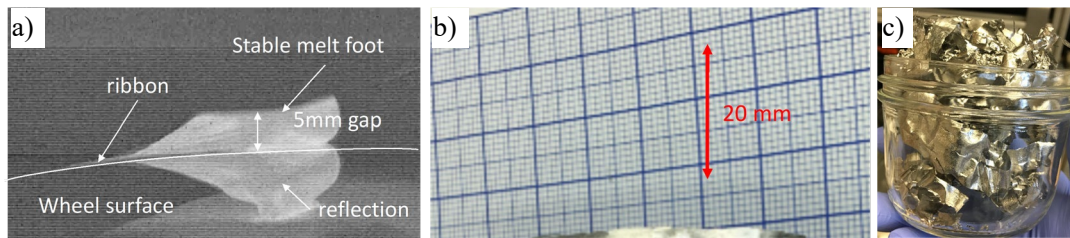


Figure I.1.15.3 a) High speed footage of melt-spinning process; b) 20 mm wide 0.05 mm thick melt-spun ribbon; c) a jar full of melting spun ribbon of 6.5%Si steel.

To demonstrate the concept, the Ames team has prepared narrow ribbons of 6.5%Si steel, cold-rolled the curly ribbon into straight and uniform flat thin wires. These wires were coated with epoxy, then bundled and consolidated into a bar with square cross section. Magnetic property measurements of the resulting bars samples will be carried out once the fixture for testing bar-shape sample arrives in November 2020. Figure I.1.15.4 shows the steps carried out to demonstrate the near-net-shape molding concept.

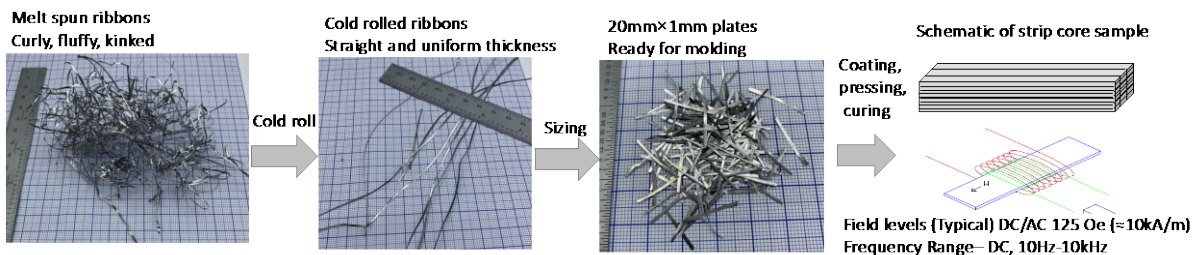


Figure I.1.15.4 Processing steps for near-net-shape-molding of stator block.

Conclusions

In FY20, the Ames team has been working on development of permanent and soft magnetic materials for the next generation of high-power density drive motors. These two efforts were aimed at improving coercivity of PM for motor rotors through grain size refinement and at reducing eddy current losses in motor cores by enabling highly resistive 6.5% Si steel to be produced, both with methods that can be scaled for manufacturing. Capability for fabricating high-performance Nd-Fe-B magnets was established; ultrafine grain magnets with improved coercivity were demonstrated. Melt-spun ribbon with 20 mm width was produced and the effort on developing near-net-shape SM materials processing and molding for stator cores was initiated.

Key Publications

1. Ouyang, G., Jensen, B., Tang, W., Schlagel, J., Hilliard, B., Pan, C., Cui, B., Dennis, K., Jiles, D., Monson, T. and Anderson, I., 2020. Near Net Shape Fabrication of Anisotropic Fe-6.5% Si Soft Magnetic Materials. *Acta Materialia*. 201, p.209-216.
2. Ouyang, G., Jensen, B., Macziewski, C.R., Ma, T., Meng, F., Lin, Q., Zhou, L., Kramer, M. and Cui, J., 2019. Characterization of ordering in Fe-6.5% Si alloy using X-ray, TEM, and magnetic TGA methods. *Materials Characterization*, 158, p.109973.

References

1. Liu, S., and G. E. Kuhl. *Development of New High Temperature and High-Performance Permanent Magnet Materials*. No. UDR-TR-2000-00092. DAYTON UNIV OH RESEARCH INST, 2000.
2. M. Garside, Global price forecast of rare earth oxides 2019-2025, Statista, 2020.

3. Castilloux, R., Shaping the Outlook for the Rare Earth Market, Adamas Intelligence.
4. Nothnagel, P., K-H. Müller, D. Eckert, and A. Handstein. "The influence of particle size on the coercivity of sintered NdFeB magnets." *Journal of magnetism and magnetic materials* 101, no. 1-3 (1991): 379-381.
5. Bance, Simon, et al. "Grain-size dependent demagnetizing factors in permanent magnets." *Journal of Applied Physics* 116.23 (2014): 233903.
6. Ouyang, Gaoyuan, et al. "Review of Fe-6.5 wt% Si high silicon steel—A promising soft magnetic material for sub-kHz application." *Journal of Magnetism and Magnetic Materials* 481 (2019): 234-250.
7. Ouyang, Gaoyuan, et al. "Characterization of ordering in Fe-6.5% Si alloy using X-ray, TEM, and magnetic TGA methods." *Materials Characterization* 158 (2019): 109973.

I.1.16 Integrated Motor and Drive for Traction Application (University of Wisconsin-Madison)

Bulent Sarlioglu

University of Wisconsin – Madison
 1415 Engineering Drive
 Madison, WI 53706
 Email: sarlioglu@wisc.edu

Susan Rogers, DOE Technology Development Manager

U.S. Department of Energy
 Email: susan.rogers@ee.doe.gov

Start Date: April 1, 2019	End Date: April 1, 2024	
Project Funding: \$300,000	DOE share: \$300,000	Non-DOE share: \$0

Project Introduction

The objective of the project is to research, design, develop, and test a high-performance traction motor and a high-efficiency traction inverter, and then to combine them into a state-of-the-art integrated motor drive (IMD) that requires only a single housing for use in vehicle applications.

The new IMD system will significantly increase the motor and inverter power density values to meet the aggressive DOE targets while simultaneously reducing their cost. The high-power-density, reduced-cost prototype IMD will become a valuable source of technical data that can be used by automakers and their suppliers to improve the performance of future EV traction drive systems.

Objectives

This project has two separate sets of performance targets for the power electronics and motor presented together in Table I.1.16.1.

Table I.1.16.1 Power Electronics and Motor Requirements

Power Electronics Requirement	
Parameter	Measure
Cost (\$/kW)	≤ 2.7
Peak Power Density (kW/L)	≥ 100
System Peak Power Rating (kW)	100
Electric Motor Requirement	
Parameter	Measure
Cost (\$/kW)	≤ 3.3
Peak Power Density (kW/L)	≥ 50
System Peak Power Rating (kW)	100

Approach

This project began with an evaluation of several types of electric motors and inverters that are candidates for future land-based vehicle traction applications. The evaluation results led to selection of the most desirable

machine plus inverter topology that is in the process of being developed into a working state-of-the-art prototype integrated motor drive (IMD) during the remainder of the project.

During Budget Period #1, a literature review was carried out that set the stage for trade-off studies to evaluate several alternative motors and inverters that are candidates for adoption in the target integrated motor drive system. The motor configurations as well as the power inverter topologies were compared, leading to selection of the most promising motor and power electronic inverter candidates for further development.

During Budget Period #2 (still under way at the time of this writing), a preliminary motor electromagnetic design and power electronics electrical design has been carried out for the selected motor and power inverter topologies. A bench-top inverter is in the process of being designed, fabricated, and tested to verify key IMD concepts and reduce technical risks. In addition, we are carrying out thermal and mechanical designs of the motor and inverter, including their physical integration into an IMD.

During Budget Period #3, the IMD design will be finalized in preparation for prototype component construction. The final design of the IMD will be carried out, leading to a final design review. The prototype machine and inverter will be fabricated and tested individually. A dynamometer test-stand will be designed and assembled, including instrumentation for testing the motor and power inverter.

During Budget Period #4, the motor and power inverter will be integrated into the same IMD enclosure and made operational. Initial tests will then be carried out to demonstrate the functionality of the prototype IMD.

During Budget Period #5, the combined prototype IMD system will be tested. The IMD performance will be measured to verify the ability of the prototype IMD to meet its performance targets.

Results

1. Pugh Analysis of Different Motor and Inverter Topologies for Integrated Motor Drives

A motor and an inverter with the controller are the key elements of an IMD, as shown in Figure I.1.16.1. By eliminating the bulky high voltage ac cables and terminals used to connect the inverter to a motor, the total volume and cost of the motor drive system can be significantly reduced [1], [2], [3]. Therefore, the IMD configuration is favored in the traction motor drive system, where minimizing volume and cost are paramount. However, it is a challenge to determine which motor and inverter topology best suits the IMD for traction applications. Numerous topologies in both machines and inverters have been compared, and topologies with the highest potential have been chosen. Further analysis has been performed using different motor and inverter topologies to find the optimal motor and inverter combination for the integrated motor drive.

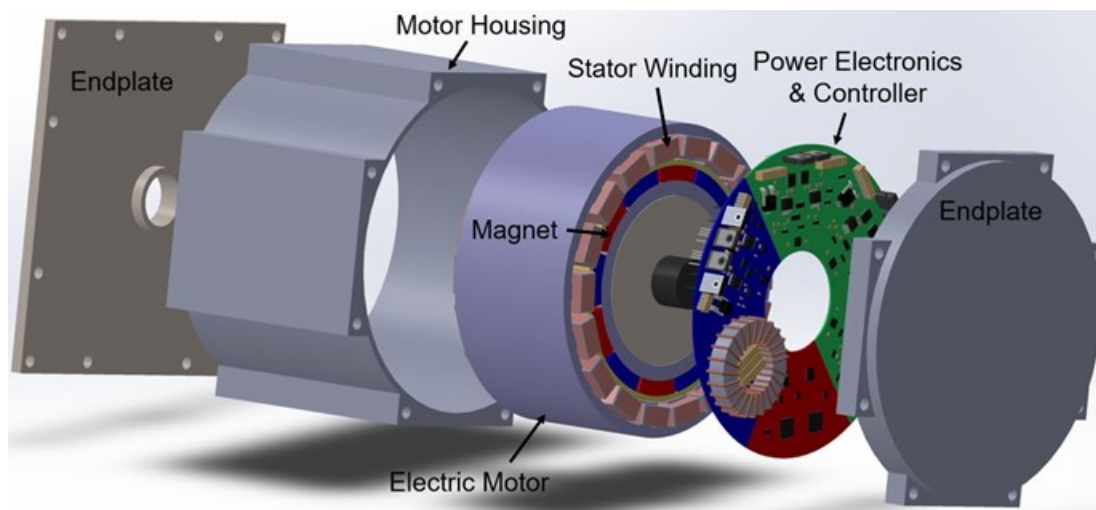


Figure I.1.16.1 Example of an integrated motor drive configuration with inverter axially mounted in the machine housing.

Pugh Analysis of Different Motor Topologies for Integrated Motor Drives

Three different permanent magnet (PM) machines (surface PM machine, spoke interior PM machine, and V-shape interior PM machine) are considered in the Pugh analysis, as shown in Table I.1.16.2. The volume, cost, field weakening capability, and efficiency of the motor are chosen as primary metrics in the Pugh analysis since they are directly relevant to the project requirements (motor peak power density ≥ 100 kW/L) and the traction drive performance. Other metrics such as high-temperature capability, mass, short circuit (SC) fault vulnerability, modularity, and noise are also considered for completeness. The surface PM machine has the highest score in the volume and efficiency metric leading to the highest score among three machines, as shown in Table I.1.16.2. Therefore, the surface PM machine has been selected as the best traction motor candidate for this project.

Table I.1.16.2 Pugh Analysis of Different Motors for Integrated Motor Drives

Criteria	Weight factor	SPM Machine		Spoke IPM		V-shape IPM	
		Rating	Weighted	Rating	Weighted	Rating	Weighted
Volume	5	5	25	4	20	4	20
Cost	5	3	15	3	15	4	20
Field weakening capability	5	5	25	5	25	5	25
Efficiency	5	5	25	4	20	4	20
High temperature capability	3	3	9	4	12	4	12
Mass	3	5	15	3	9	4	12
SC fault vulnerability	2	3	6	4	8	4	8
Modularity	2	5	10	5	10	5	10
Noise	4	5	20	5	20	5	20
Score			150		139		147

Pugh Analysis of Different Inverter Topologies for Integrated Motor Drives

Comparisons between the 2-level current source inverter (CSI) with a dc/dc converter, 2-level voltage source inverter (VSI) with sine filter, and 2-level VSI with sine filter and dc/dc converter has been carried out. Since a simple 2-level VSI using wide-bandgap switches delivers pulsed voltage waveforms to the machine with unacceptably high values of dv/dt , additional sine filters have been designed for the two VSI cases to deliver similar voltage and current waveforms to the machine that a CSI produces naturally.

Table I.1.16.3 Pugh Analysis of Different Inverters for Integrated Motor Drives

Criteria	Weight factor	2-level CSI with dc/dc converter		2-level VSI with sine filter		2-level VSI with sine filter and dc/dc converter	
		Rating	Weighted	Rating	Weighted	Rating	Weighted
Volume	5	5	25	5	25	4	20
Cost	5	4	20	5	25	4	20
Field weakening capability	5	5	25	3	15	5	25
WBG capability	5	4	20	4	20	4	20
Efficiency	5	5	25	5	25	4	20
High temperature capability	3	5	15	4	12	4	12
Score			130		122		117

The inverter system's volume and cost are the primary metrics that are explicitly stated in the project requirements, while the field weakening capability, WBG capabilities, and efficiency of the inverter system are included as essential criteria for traction drives. The high-temperature capability has been added as a secondary metric because of its importance for IMD configurations that embed the inverter inside the machine housing. The Pugh analysis results for inverter systems are shown in Table I.1.16.3.

The 2-level CSI with dc/dc converter and the 2-level VSI with filter scored the same for the volume metric, and the latter is rated higher than the former for the cost metric. However, the 2-level CSI with dc/dc converter excelled in the field weakening metric comparison due to its inherent voltage boost capability [4]. In addition, the higher thermal rating of the dc-link inductor in the CSI compared to that of dc-link capacitors in the VSI topologies caused the CSI with dc/dc converter to score higher than any other topologies for the high-temperature capability metric. Therefore, the 2-level CSI with dc/dc converter achieved the highest total score among these three different inverter topologies, as shown in Table I.1.16.3.

Pugh Analysis of Different Motor and Inverter Combinations for Integrated Motor Drives

The final Pugh analysis was performed for different motor and inverter combinations to ensure that the combination of the individually selected motor (surface PM machine) and inverter (2-level CSI with dc/dc converter) yields the optimal IMD system. Since the volume, cost, flux weakening capability, and efficiency have been fully considered when each motor and inverter candidate was analyzed, other metrics were used to evaluate the IMD system's performance, as shown in Table I.1.16.4. It is worth noting that high-temperature capability, fault tolerance, and modularity have been incorporated into the Pugh analysis for the IMD because these metrics are essential for successful development of the IMD. EMI, parts count, and total weight have also been included as evaluation metrics for comprehensive system-level analysis.

Three different motor plus inverter combinations are considered in the Pugh analysis, as shown in Table I.1.16.4. For high-temperature capability, total weight, and fault tolerance metrics, the 2-level CSI with dc/dc converter plus PM machines case outperformed the other two motor/inverter combinations (2-level VSI with sine filter plus PM machine, 2-level VSI with sine filter and dc/dc converter plus PM machine), as shown in Table I.1.16.4. This analysis has confirmed that the 2-level CSI with dc/dc converter plus PM machine is the best choice for the IMD configuration that is being developed during this project.

Table I.1.16.4 Pugh Analysis of Different Motor and Inverter Combinations for Integrated Motor Drives

Criteria	Weight factor	2-level CSI with dc/dc converter + PM machine		2-level VSI with sine filter + PM machine		2-level VSI with sine filter and dc/dc converter + PM machine	
		Rating	Weighted	Rating	Weighted	Rating	Weighted
High temperature capability	3	5	15	4	12	4	12
EMI	4	3	12	3	12	3	12
Parts count	4	4	16	5	20	4	16
Weight	3	5	15	4	12	3	9
Fault tolerance	2	4	8	2	4	2	4
Modularity	2	1	2	1	2	1	2
Score			68		62		56

2. Design of a CSI-based SPM machine with a CPSR of 3

The maximum speed of the CSI-based motor is set to 20,000 rpm, while the constant-power speed ratio (CPSR) requirement was set to a value of 3. As shown in the torque-speed curve presented in Figure I.1.16.2, the choice of 20,000 rpm maximum speed with a selected CPSR value of 3 results in a corner speed value of 6,667 rpm. Since a peak power value of 100 kW is required at the corner speed, the peak torque for this peak power condition is 143.2 Nm, while the maximum continuous torque needed to deliver 55 kW at the corner speed is 78.8 Nm.

The motor specification in Figure I.1.16.2 shows that peak torque is required from zero until the corner speed, but not beyond the corner speed. The flux weakening capability of the machine is required to deliver the specified continuous power (55 kW) between the corner speed and maximum speed. The rated continuous power operating point of the motor is achieved at the corner speed shown in Figure I.1.16.2, where 78.8 Nm is delivered at 6,667 rpm, resulting in 55 kW output power as required. In addition, the motor line-to-line voltage needs to be less than the device voltage limit in the inverter with a safety margin. The voltage limit has been set to be 800 V_{pk} maximum line-to-line voltage considering the 1.2 kV voltage limit of the SiC MOSFETs with a 50% safety factor.

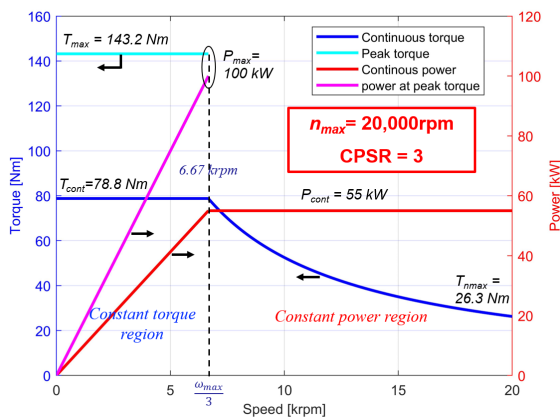


Figure I.1.16.2 Torque-speed and power-speed curves of the desired traction motor that meets the project requirements with a CPSR of 3.

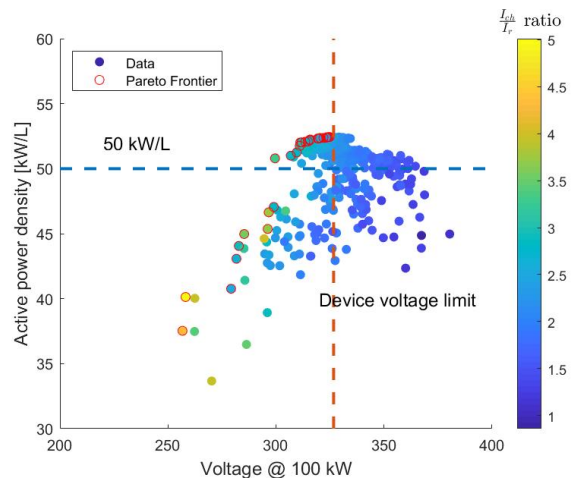


Figure I.1.16.3 Optimized motor design points plotting the motor L-N rms voltage vs. active power density, both at 100 kW, with the data point color indicating I_{ch}/I_r ratio for each design.

Based on this combined set of motor performance requirements, a genetic algorithm has been used to find an optimized SPM machine design to meet these specifications, which is shown in Figure I.1.16.3. Figure I.1.16.3 shows many candidate machine design data points that plots their active power density and motor terminal L-N voltage at 100 kW on the two axes, with the ratio of each design’s characteristic current (I_{ch}) to the rated current (I_r) at 55 kW indicated by the color of each data point. Reducing this current ratio to values less than 2 is desirable for traction applications.

The dashed lines in this figure identify the minimum machine power density target and the maximum machine line-to-neutral voltage based on the device voltage limit requirements. This means that the optimized designs meet both of these requirements, like in the upper left (2nd) quadrant defined by the two dashed lines. It is also desirable to constrain the value of the I_{ch}/I_r to be as low as possible. Therefore, in Figure I.1.16.3, the optimized machine design is selected to be the design with the smallest I_{ch}/I_r value that exceeds the 50 kW/L active power density threshold from the Pareto front in the second quadrant identified with red-circled dots. As a result, the chosen optimized design achieves the highest active power density while meeting the device voltage limits at both the 55-kW continuous power and 100 kW peak power conditions.

The configuration of the proposed design is shown in Figure I.1.16.4. Fractional-slot concentrated windings (FSCW) have been selected for the winding configuration. A composite carbon-fiber sleeve is used to retain the magnets at high rotational speeds. The minimum thickness of the carbon fiber sleeve has been calculated based on the rotor tip speed and magnet size, considering the stress in the sleeves. The thickness of the carbon fiber sleeve has also been verified using mechanical finite element analysis (FEA). Figure I.1.16.5 shows the stress distribution on the rotor under the assumed worst-case condition that the magnets are frictionless with the sleeve and rotor core. Under such conditions, the maximum von-Mise stress in the carbon fiber sleeve is much lower than the tensile strength of the carbon fiber. Figure I.1.16.6 shows the flux density distribution at 55 kW output power. Figure I.1.16.7 shows the torque-speed curve and power-speed curve of the CSI-driven SPM machine with a CPSR of 3 calculated by FEA. The proposed machine is capable of delivering 55 kW output power continuously during flux weakening operation.

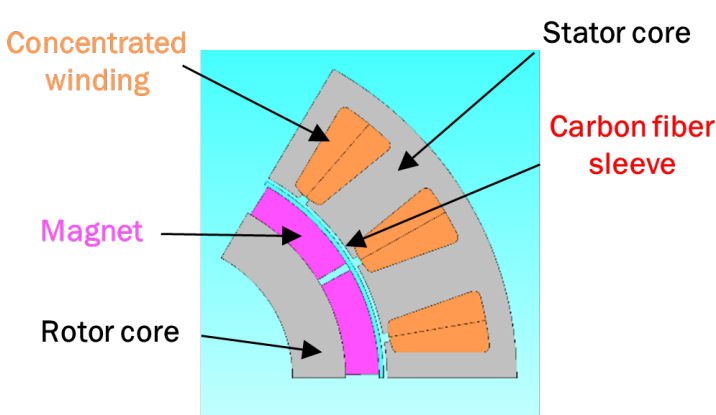


Figure I.1.16.4 Cross-section view of optimized SPM machine showing all major stator and rotor design features.

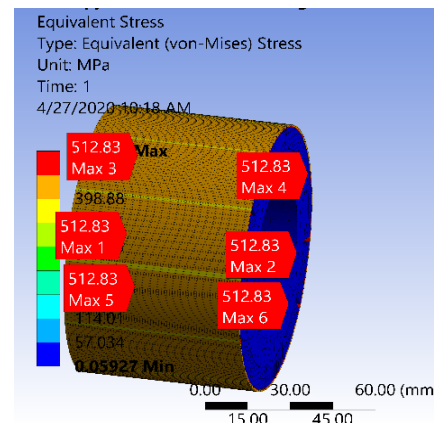


Figure I.1.16.5 FEA-calculated rotor stress distribution assuming that the magnets are frictionless with the sleeve and rotor.

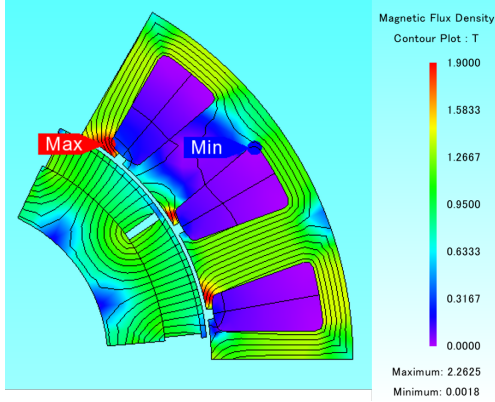


Figure I.1.16.6 FEA-calculated magnetic flux density distribution for 55 kW output power @ 6,667 rpm.

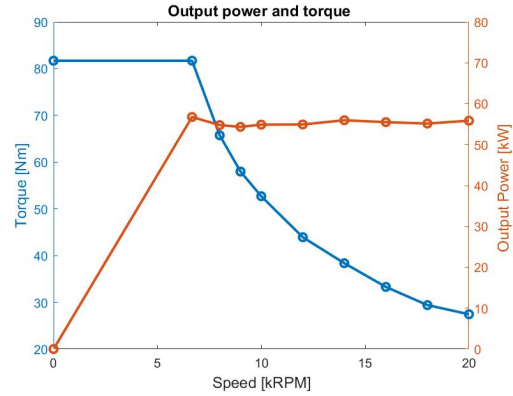


Figure I.1.16.7 Calculated torque-speed and power-speed curve of the CSI-driven SPM machine with a CPSR of 3.

3. Comprehensive Efficiency Analysis of CSI Based SPM Machine Drive System

The WBG-based CSI topology overcomes many of the VSI topology limitations by significantly lowering the output dv/dt stress, common-mode (CM) EMI emissions, bearing current risks, and temperature limitations. The predicted machine line-to-line voltage and phase current from the simulation are shown in Figure I.1.16.8. The CSI delivers much more desirable sinusoidal output voltage waveforms compared to the VSI without sine filter, which is beneficial for lowering the output dv/dt stress and common-mode EMI emission levels.

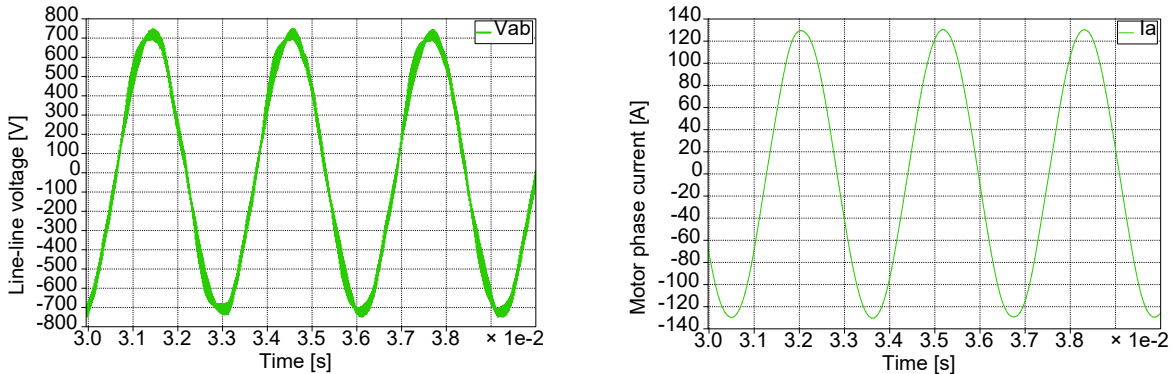


Figure I.1.16.8 Simulation results for the CSI drive system showing the predicted machine line-line voltage (left) and phase current (right) @ 55 kW and 6,667 rpm.

A notable advantage of the CSI over VSI in traction drive applications is the CSI’s natural output voltage boost function. This voltage-boost feature of the CSI offers several advantages for a traction drive application: (a) when the battery voltage drops, the CSI can boost the output voltage to maintain the same output power; (b) the voltage boost function of the CSI can be used to extend the constant power operation region to achieve a higher CPSR than the VSI; and (c) voltage boosting can be used to improve the system efficiency while reducing the CSI’s output current rating and improving the power factor at high speed.

The total loss of the IMD system including the dc/dc converter, CSI, and SPM machine can be calculated as

$$P_{total} = P_{motor} + P_{CSI} + P_{conv} \tag{1}$$

The operating condition chosen for this optimization exercise is 55 kW output power at the maximum machine speed of 20,000 rpm with 50 kHz switching frequency and 125°C junction temperature for the CSI and dc/dc converter. Based on the power loss model of the dc/dc converter, CSI, and machine, the impact of the CSI

modulation index m on these three drive loss components and the total drive system loss are plotted in Figure I.1.16.9. The modulation index m is defined as

$$m = I_{pk}/I_{dc} \quad (2)$$

where I_{pk} is the peak motor phase current and I_{dc} is the dc-link current.

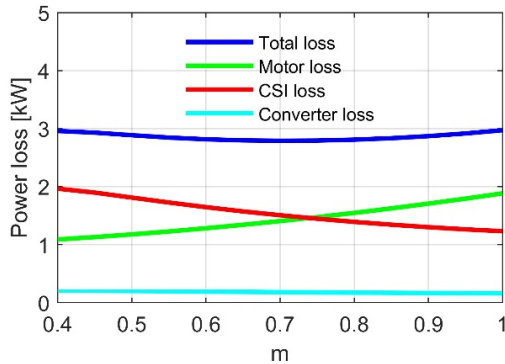


Figure I.1.16.9 Calculated curves showing the effect of modulation index m on CSI drive loss components and total drive system loss for operation at 55 kW, 20,000 rpm.

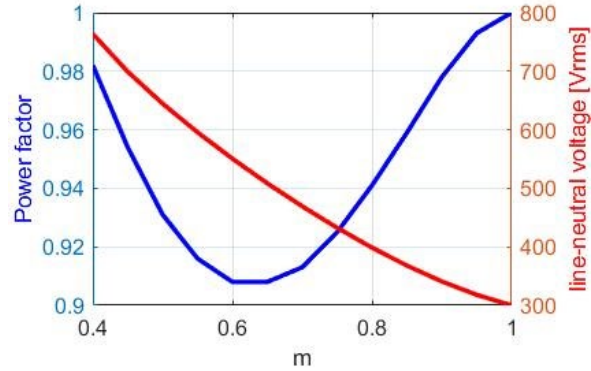


Figure I.1.16.10 Calculated curves showing the effect of modulation index m on the machine power factor and terminal line-neutral rms voltage for operation at 55 kW, 20,000 rpm.

The corresponding impact of the modulation index m on the machine power factor and the machine phase voltage is plotted in Figure I.1.16.10. It should be noted that Figure I.1.16.9 and Figure I.1.16.10 show the predicted effect of the modulation index while ignoring the voltage ratings of the power devices. To maintain the output power, the current angle between the current and back-EMF is also controlled as m changes. As shown in Figure I.1.16.9, decreasing m increases the CSI losses due to the direct impact of the boosted line-to-line voltage on the device switching loss. In contrast, the total machine loss is reduced as the modulation index m decreases because the machine phase current falls as the machine terminal voltage increases. As a result, the total machine drive power loss initially reduces as the modulation index m drops from 1 to 0.7, but then increases again as m is decreased below 0.7. Figure I.1.16.10 shows the effect of modulation index m on the power factor, which exhibits the same tendency as the system loss, dipping to a minimum value in the vicinity of $m = 0.6$ and then rising again when m is reduced below that value. The line-to-neutral voltage increases monotonically as m is reduced. For the 1,200 V SiC MOSFET and Schottky diodes that are used for this analysis, the modulation index could not be reduced below approx. 0.75 for operation at 55 kW, 20,000 rpm without exceeding the voltage limit (including 50% safety factor) set by the voltage capability of the devices. Even though the power factor is reduced as the modulation index m decreases, the system efficiency is significantly boosted which is a high priority for traction drive applications.

Conclusions

This report has provided a summary of key findings developed to date during the second year of the project. Pugh analyses of different kinds of motors, inverters, and IMD have been evaluated. The final score indicates that the 2-level CSI with dc/dc converter + SPM machine is the best option for the integrated motor drive.

A CSI-driven SPM machine with a CPSR of 3 has been designed and evaluated. The maximum speed of this machine is 20,000 rpm, and the corner speed is 6,667 rpm with a CPSR of 3. The proposed machine is capable of delivering 100 kW peak power and 55 kW continuous power. Genetic optimization has been used to optimize the machine's power density while meeting all of the machine's torque-speed requirements and operating within the voltage limits set by the power switch devices used in the inverter. Structural analysis has been performed to calculate the thickness of the carbon fiber sleeve to safely retain the magnets at all speeds

up to 20,000 rpm. The proposed CSI-driven SPM machine provides benefits by reducing the required current at higher output voltages compared with the VSI-driven SPM machines, thereby helping to reduce the IMD cost and increase the overall drive system efficiency.

The voltage boost function of the CSI has been investigated. The effects of the boost function on the total system losses, including the machine copper loss, core loss, and magnet loss, as well as the device conduction and switching loss in the CSI and dc/dc converter, have been investigated using analytical models. By properly taking advantage of this voltage-boost capability, the CSI opens valuable opportunities to improve the traction drive system efficiency during high-speed operation.

Key Publications

1. F. Chen, H. Ding, S. Lee, W. Feng, T. M. Jahns, and B. Sarlioglu, "Current source inverter based large constant power speed ratio SPM machine drive for traction applications," in *Proc. IEEE Transportation Electrification Conf. and Expo.*, Chicago, IL, USA, 2020, pp. 216-221.
2. W. Feng, H. Ding, S. Lee, F. Chen, T. Jahns, and B. Sarlioglu, "Design of a 100-kW surface permanent magnet machine with wide constant power speed ratio for traction applications," in *Proc. IEEE Transportation Electrification Conf. and Expo.*, Chicago, IL, USA, 2020, pp. 456-461.
3. F. Chen, W. Feng, H. Ding, S. Lee, T. M. Jahns, and B. Sarlioglu, "Comprehensive efficiency analysis of the current source inverter-based SPM machine drive system for traction applications," in *Proc. IEEE Energy Conversion Congr. and Expo.*, Detroit, MI, USA, 2020.

References

1. T. M. Jahns and H. Dai, "The past, present, and future of power electronics integration technology in motor drives," in *CPSS Transactions on Power Electronics and Applications*, vol. 2, no. 3, pp. 197-216, Sept. 2017.
2. J. Wang, Y. Li, and Y. Han, "Integrated modular motor drive design with GaN power FETs," in *IEEE Transactions on Industry Applications*, vol. 51, no. 4, pp. 3198-3207, July-Aug. 2015.
3. G. Su, L. Tang, C. Ayers, and R. Wiles, "An inverter packaging scheme for an integrated segmented traction drive system," in *Proc. IEEE Energy Conversion Congress and Exposition*, Denver, CO, 2013, pp. 2799-2804.
4. F. Chen, H. Ding, S. Lee, W. Feng, T. M. Jahns, and B. Sarlioglu, "Current source inverter based large constant power speed ratio SPM machine drive for traction applications," in *Proc. IEEE Transportation Electrification Conf. and Expo.*, Chicago, IL, USA, 2020, pp. 216-221.

I.1.17 Rugged WBG Devices and Advanced Electric Machines for High Power Density Automotive Electric Drives (North Carolina State University)

Victor Velladis, Subhashish Bhattacharya, Iqbal Husain, Principal Investigators

North Carolina State University
930 Main Campus Drive, Suite 200
Raleigh, NC 27606
Email: jvveliad@ncsu.edu

Susan Rogers, DOE Technology Development Manager

U.S. Department of Energy
Email: susan.rogers@ee.doe.gov

Start Date: April 1, 2019

End Date: March 30, 2024

Project Funding: \$1,500,000

DOE share: \$1,500,000

Non-DOE share: \$0

Project Introduction: WBG Devices, Prof. Subhashish Bhattacharya

The research trends for automotive electric drives are focused on achieving long-range all-electric vehicles with high fuel economy. This has led to increasing interest in the adoption of wide bandgap (WBG) devices and high voltage DC bus architectures for traction inverters. This work investigates the benefits and challenges associated with a GaN-based traction inverter. The limited voltage and current rating of commercially available GaN devices is a major roadblock in high-power traction inverter widespread adoption. Considering this, a three-level inverter operation with paralleled GaN devices is investigated as an alternate topology for electric drives. The efficiency benefits over SiC-based two-level inverters are determined by comprehensive loss analysis using standardized drive cycle models. Commercially available GaN devices are then evaluated based on their figure of merit (FOM), experimentally determined switching losses, and short circuit time to identify a suitable device for the traction inverter. The selected device is evaluated under thermo-mechanical stress by a power cycling test. A prototype test board with four parallel GaN devices is established to investigate the design challenges of the basic power building block.

Objectives

1. Comprehensive Loss Analysis of EV inverters using Drive Cycle Models
2. Evaluation of commercially available GaN devices
3. Parallel operation of discrete GaN devices.

Approach

1. Comprehensive Loss Analysis of EV inverters using Drive Cycle Models

Loss maps of inverters in the torque-speed range of an EV allow for a more comprehensive evaluation of inverters [1].

This work establishes an analytical model that produces inverter loss based on inputs in terms of inverter topology, power semiconductor devices selected, motor parameters and operating driving schedule.

The proposed model is used to assess the efficiency benefits of a GaN based three-level neutral point clamped (3L-NPC) inverter topology against that of a state-of-art SiC based two-level (2L) inverter topology for a 75kW traction inverter operating with 800V DC bus. The selection of an 800V DC bus brings benefits like faster charging, thinner and lighter cable, and higher motor efficiency for a high voltage DC bus architecture [2].

The loss analysis methodology is summarized in Figure I.1.17.1. An interior permanent magnet synchronous motor (IPMSM) with parameters given Table I.1.17.1 is selected. The wide band gap (WBG) devices used for

the realization of the inverter are shown in Table I.1.17.2. The turn-on and turn-off losses of the devices are determined using the Spice models supplied by the device manufacturers. The operating points of the inverter are determined from standard drive cycle profiles shown in Figure I.1.17.2. For this work, two kinds of drive cycles have been selected – EPA Urban Dynamometer Driving Schedule (UDDS) and EPA Highway fuel Economy Test (HWFET) [3]. The respective torque-speed operating points are shown in Figure I.1.17.3.

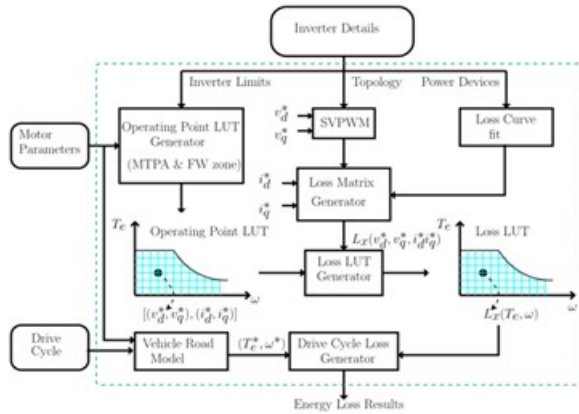


Figure I.1.17.1 Drive cycle-based loss analysis methodology

Table I.1.17.1 IPMSM parameters and inverter constraints selected for determination of inverter operating points

Parameter	Value	Description
P_{max}	75 kW	Maximum output power
V_{dc}	800 V	DC bus voltage
Pf_{min}	0.8	Minimum power factor
P	8	Number of poles
R_s	20 mΩ	Stator resistance
L_d	491 mH	d-axis inductance
L_q	678 mH	q-axis inductance
λ_f	0.122 Wb	PM flux linkage

Table I.1.17.2 Power semiconductor devices selected for loss analysis

Topology	Device	Details	Parallel units
3L-NPC	S_{A1}	GaN HEMT 650 V, 60 A	3
	D_{A1}	SiC Schottky Diode 650 V, 100 A	2
2L	S_1	SiC MOSFET 1200 V, 60 A	3

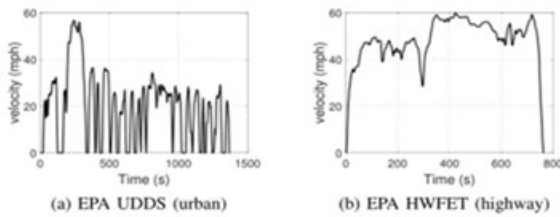


Figure I.1.17.2 Drive cycles used for loss analysis – (a) EPA UDDS (urban) and (b) EPA HWFET (highway).

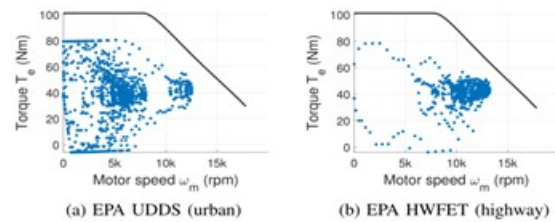


Figure I.1.17.3 Operating points of traction motor for EPA UDDS (urban) and EPA HWFET (highway) drive cycle.

2. GaN Device Selection and Characterization

Based on the discussion above, three commercially available GaN devices are selected for detailed characterization. The details of the devices are listed in Table I.1.17.3. The devices are selected based on their Figures of Merits (FOM). FOMs are calculated from the datasheet values using (1). The FOM of commercially available devices are plotted in Figure I.1.17.4.

Table I.1.17.3 Selected GaN devices

Manufacturer (Part number)	V_{dsmax}	$I_{dmax}(25^{\circ}C)$
A (A3)	650V	60A
B (B1)	600V	30A
C (C1)	650V	46.5A

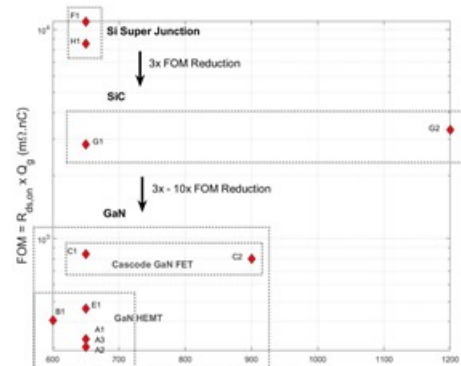


Figure I.1.17.4 FOM of commercially available devices.

$$FOM = R_{ds_on} \times Q_g \text{ (m}\Omega.nC) \quad (1)$$

Detailed characterizations of the three GaN devices are performed, including the four tests below:

- A. Double pulse test (DPT)
- B. Short circuit test (SC test)
- C. Safe operating area (SOA) determination
- D. Power cycling test (PCT)

The characterization results are presented in the results section.

3. Parallel Operation of Discrete GaN Devices

A prototype design with four parallel GaN devices (A3) in a half-bridge test configuration is made. Best PCB design practices are followed to ensure the symmetry of the power and gate loop, and to minimize the parasitic inductances. The experimental results of the prototype design are presented later.

Results

1. Comprehensive Loss Analysis of EV inverters using Drive Cycle Models

Based on the analytical results shown in Figure I.1.17.5, Table I.1.17.4 and Figure I.1.17.6 it is inferred that the GaN 3L-NPC results in significant efficiency improvement over the SiC 2L inverter for urban and highway riding conditions.

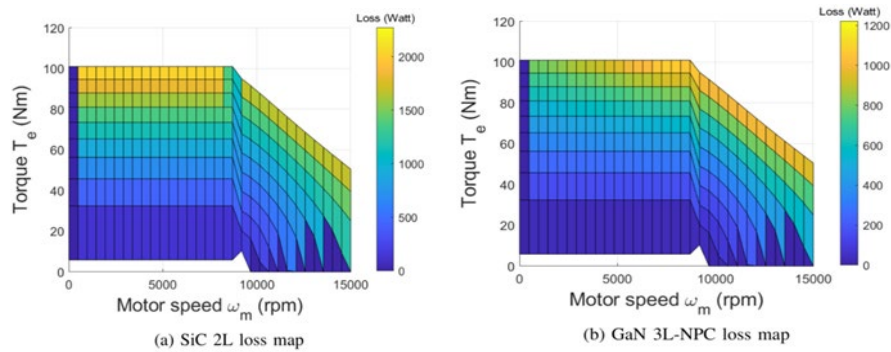


Figure I.1.17.5 Loss map plots in torque-speed range of traction motor for (a) SiC 2L and (b) GaN 3L-NPC inverter at fsw = 50kHz.

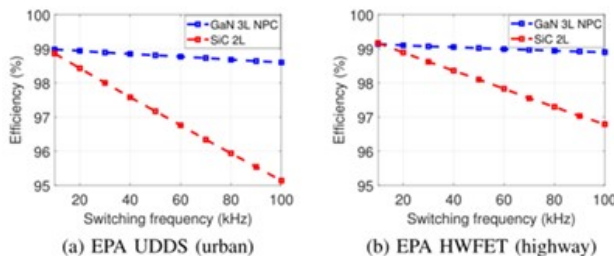


Table I.1.17.4 Inverter loss details for urban and highway drive cycles at fsw = 50kHz.

Parameter	EPA UDDS		EPA HWFET	
	2L (SiC)	3L NPC (GaN)	2L (SiC)	3L NPC (GaN)
Energy out	6.66 kWh	6.66 kWh	9.89 kWh	9.89 kWh
Energy loss	0.194 kWh	0.08 kWh	0.191 kWh	0.098 kWh
Efficiency	97.17 %	98.81 %	98.09 %	99.01 %

Figure I.1.17.6 Efficiency variation vs switching frequency for SiC 2L and GaN 3L-NPC inverter in (a) urban and (b) highway driving conditions.

2. Device Characterization Results

A. Double Pulse Test

DPTs are done to calculate the switching losses of the selected devices. A sample turn-on waveform of A3 is given in Figure I.1.17.7. The switching losses of three devices are provided in Table I.1.17.5. For “equal current” comparisons, they are multiplied by N. From Table I.1.17.5, it can be observed that A3 has the lowest loss for the same current.

Table I.1.17.5: Loss comparisons

Device	Operating point	E_{on} (uJ)	E_{off} (uJ)	$E_{on} + E_{off}$ (uJ)	No of device (N)	$(E_{on} + E_{off}) \times N$
A3	400V,40A	65.7	39.1	104.8	3	314.4
B1	400V,20A	30.3	41.2	71.5	6	429
C1	400V,30A	133.1	74.5	207.6	4	830.4

B. Short Circuit (SC) Test

The three selected devices are subjected to SC testing to measure short circuit time and energy. A sample SC measurement for A3 is shown in Figure I.1.17.8. The SC test results of the three devices are provided in Table I.1.17.6. Among the three devices, A3 has the highest short circuit time. The test setup is shown in Figure I.1.17.9

Table I.1.17.6: SC test results

Device	SC current Rating (A)	PU SC current	SC time (nS)	SC energy (mJ)
A3	300	5	640	61.5
B1	140	4.52	60	2.83
C1	533	11.5	74	8.525

C. Safe Operating Area (SOA) Determination

The SOA is required for determining safe inverter operating points and designing protection circuits. The SOA is calculated using three values. They are, measured R_{dson} , pulse current rating from the datasheet, and junction to case thermal resistance from the datasheet. The calculated SOAs of the 3 selected devices are shown in Figure I.1.17.10 – Figure I.1.17.12.

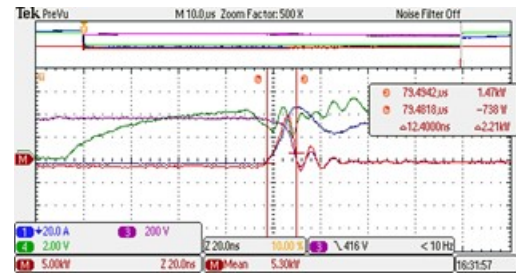


Figure I.1.17.7 Turn on of device A3 at 400V, 40A. $E_{on}=65.7\mu J$

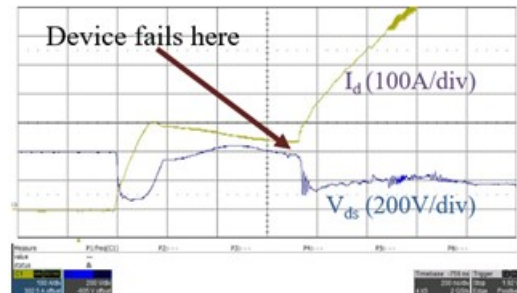


Figure I.1.17.8 Short circuit test of A3. $T_{sc}=640nS$

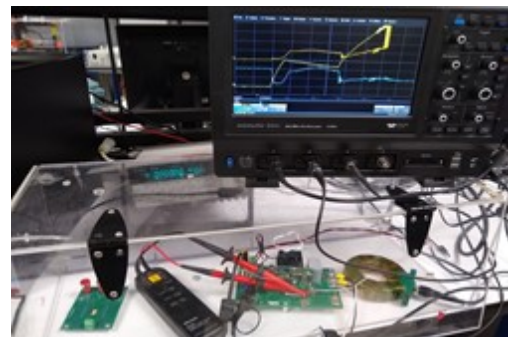


Figure I.1.17.9 Test setup for short circuit test

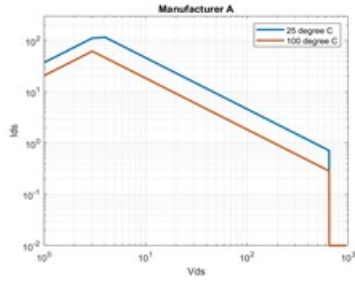


Figure I.1.17.10 SOA of A3

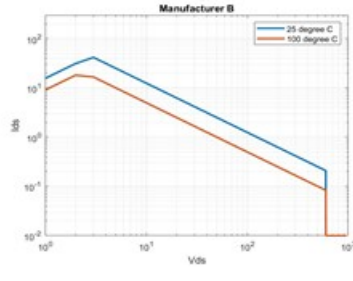


Figure I.1.17.11 SOA of B1

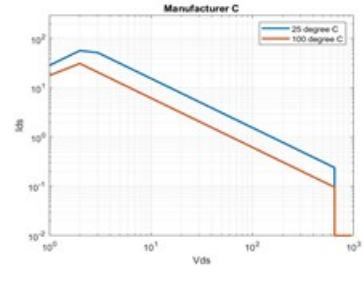


Figure I.1.17.12 SOA of C1

From the testing outlined above, A3 exhibits better performance in terms of loss, short circuit time, and SOA. Thus, device A3 is selected for further analysis.

D. Device Degradation measurement with Power cycling

The power-cycling test assesses the degradation of the GaN device under thermomechanical stress. To quantify the degradation, the output characteristic, threshold voltage, and transfer characteristics are measured prior to testing. The device is then subjected to 8.5k cycles of thermomechanical stress by passing a test current through the device and letting it cool down naturally. Device characterization is done again at this point to determine any degradation. The results are shown in Table I.1.17.7. There is 9.69% reduction in threshold voltage and 5.81% reduction in R_{dson} after 8.5k cycles. The test results of output characteristics, transfer characteristics, and threshold voltage before and after 8.5k power cycles are shown in Figure I.1.17.13 – Figure I.1.17.15.

Table I.1.17.7 GaN device degradation after 8.5K power cycle

Parameter	Initial Value	After 8.5k cycles	% variation
Vth (V) : (for Id = 15mA)	1.65V	1.49V	-9.69%
Rds,on (mΩ) : FWD	29.57mΩ	27.85mΩ	-5.81%
Rds,on (mΩ) : REV	26.86mΩ	26.86mΩ	0.00%
gm (S) : (for Vgs = 1.7V to 2.6V)	17.69S	17.22S	-2.66%
IDSS (μA) : (for Vds = 650V)	2.08μA	2.11μA	+1.44%

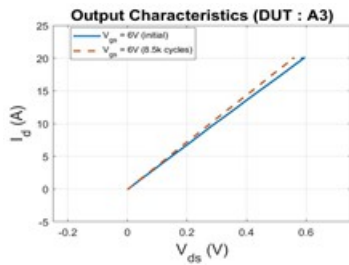


Figure I.1.17.13 Output characteristics variation

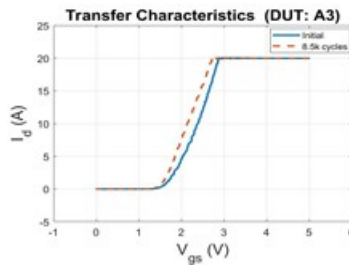


Figure I.1.17.14 Transfer characteristics variation

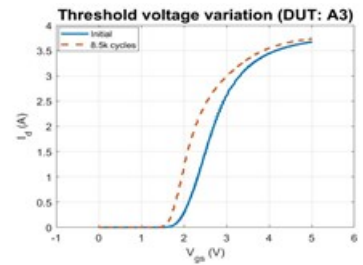


Figure I.1.17.15 Threshold voltage variation

3. Parallel Operation of Discrete GaN Devices

A half-bridge test circuit is designed to evaluate paralleling of A3 GaN devices. The half-bridge test circuit consists of 4 parallel A3 devices and has a maximum current capability of 160A. The current sharing of each device at turn-off and turn-on is shown in Figure I.1.17.16 and Figure I.1.17.17, respectively. Figure I.1.17.15 and Figure I.1.17.16 show that the steady-state current mismatch is less than 10%.

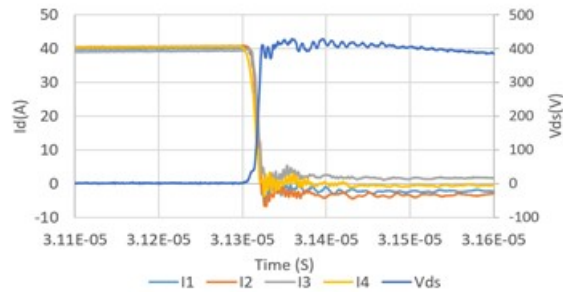


Figure I.1.17.16 Full current turn-off of 4 parallel GaN devices

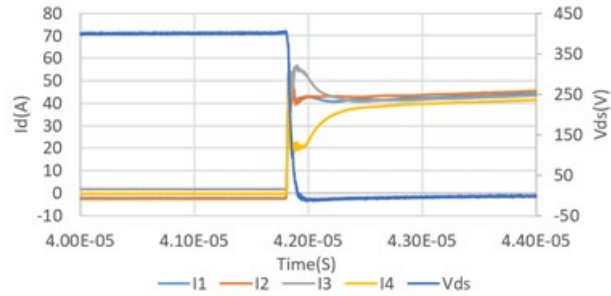


Figure I.1.17.17 Full current turn-on of 4 parallel GaN devices

Conclusions

Three commercially available GaN devices with low FOMs are characterized in terms of DPT, SC, and SOA. From the characterization data, device A3 is selected for further testing. Comprehensive loss analysis of EV inverters shows an efficiency improvement of +1.64% in urban and +0.92% in highway driving for the GaN-based 3L-NPC vs. the SiC-based 2L inverter. A prototype test board with four parallel GaN devices in a half-bridge configuration is designed and tested to establish the basic power building block. The current sharing mismatch for the prototype design is experimentally verified to be less than 10%.

Key Publications

1. S. Satpathy, S. Bhattacharya and V. Veliadis, “Comprehensive Loss Analysis of Two-level and Three-Level Inverter for Electric Vehicle Using Drive Cycle Models” Accepted in IECON 2020.
2. P. P. Das, S. Bhattacharya and V. Veliadis, “Control of Parallel Connected Interleaved Neutral Point Clamped Inverters for Electric Vehicle Drives” Accepted in IECON 2020.

References

1. A. Merkert, T. Krone and A. Mertens, “Characterization and Scalable Modeling of Power Semiconductors for Optimized Design of Traction Inverters with Si- and SiC-Devices,” in IEEE Transactions on Power Electronics, vol. 29, no. 5, pp. 2238-2245, May 2014.
2. “Fisker Inc. chooses Ricardo to support integration of state-of-the-art 800V electric powertrain,” Oct. 2017. [Online]. Available: <https://d1v9sz08rbysvx.cloudfront.net/ricardo/media/media/other%20download%20files/fisker-ricardo-release-final-draft.pdf>
3. “EPA Vehicle and Fuel Emissions Testing - Dynamometer Drive Schedules,” [Online].
4. Available: <https://www.epa.gov/vehicle-and-fuel-emissions-testing/dynamometer-drive-schedules>

Project Introduction: Advanced Electric Machines, Prof. Iqbal Husain

DOE EDT 2025 has set ambitious targets for traction electric motors. The targets are to increase power density (kW/L), and to reduce cost (\$/kW) using Heavy Rare Earth (HRE) free permanent magnets. The targets for power density, efficiency, and cost are 50 kW/L, 97%, and 3.3 \$/kW, respectively. The target peak power for the traction motor is 100 kW at 6670 rpm, producing a peak torque of 143.2 Nm with a constant power speed ratio of 3. The electric drive consortium came to an agreement on the secondary targets of peak torque and constant power speed ratio based on the primary targets of power density, efficiency and cost set forth by the program requirements. The torque speed envelope, based on the design specifications, is shown in Figure I.1.17.18. North Carolina State University aims to meet or exceed the EDT program targets by 2025 through design innovations, new manufacturing processes, and innovations in materials and thermal management.

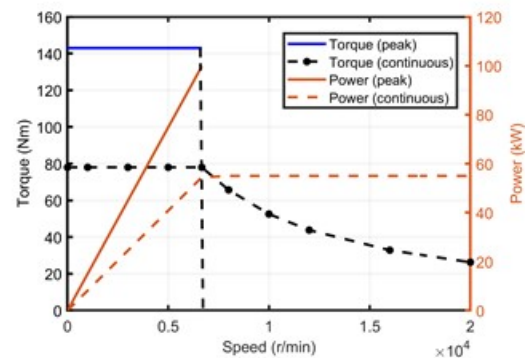


Figure I.1.17.18 Traction motor design

Objectives

The overall objective of this project portion is to design, evaluate and verify the performance of a high-speed electric machine optimized for high power density (kW/L) and ultra-high efficiency with HRE-free permanent magnet materials. The practical constraints of manufacturability and material cost and availability will be kept in context throughout the design and analysis stages while addressing the DOE EDT 2025 targets.

In the past year, the electric machines research team has been investigating alternative permanent magnet synchronous motor (PMSM) designs that can meet these set goals. This led to three initial design choices:

- Design I: Interior PMSM (IPMSM) with distributed winding and V-shaped magnets in the rotor.
- Design II: IPMSM with dual three-phase fractional-slot concentrated windings (FSCW) and V-shaped magnets.
- Design III: Slotless-Halbach outer rotor PMSM with winding embedded liquid cooling (WELC).

The V-shaped IPMSM was chosen for its high power density, high efficiency and established industry acceptance amongst electric traction motors in commercial electric vehicles. With the manufacturing pipeline for IPMSM's already established, the cost target can be met if we focus on replacements for the more expensive materials while maintaining, to the extent possible, all other low-cost manufacturing processes. Meanwhile, the choice of the Slotless-Halbach design as a viable option due to its lightweight structure and high efficiency; these machines are extremely compact, completely HRE-free, and can be operated at very high speeds and under high temperature conditions. Innovations in the winding design, rotor structure, magnet shape and materials are required to address several electromagnetic, thermal, and structural issues.

The difference in Design I and Design II is only in stator winding; the overall geometry and rotor designs are the same. However, Design II requires a dual inverter. The IPMSM structure and inverter layout for Design II are shown in Figure I.1.17.19 and Figure I.1.17.20, respectively. Design III is radically different with an outer rotor configuration; the machine structure and WELC concept are shown in Figure I.1.17.21 and Figure I.1.17.22, respectively.

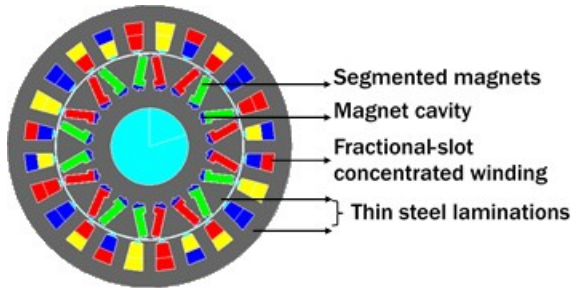


Figure I.1.17.19 Structure of the IPMSM in Design II

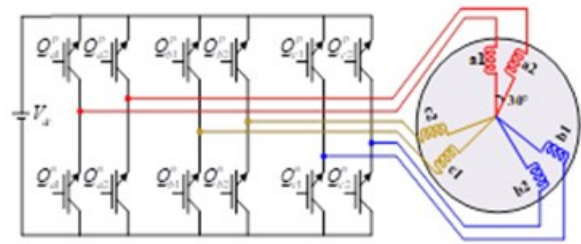


Figure I.1.17.20 Asymmetrical Dual Three Phase Inverter

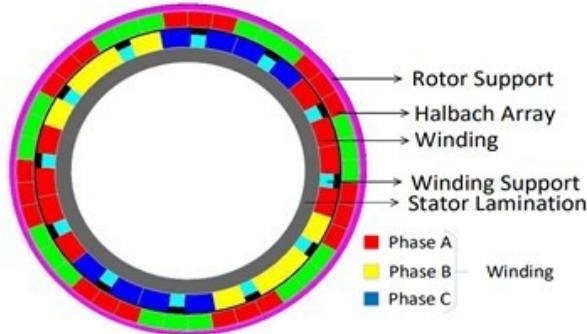


Figure I.1.17.21 Structure of the Slotless-Halbach PMSM

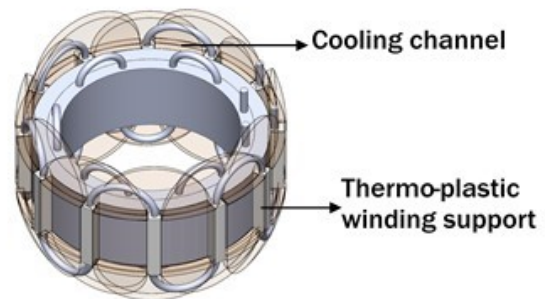


Figure I.1.17.22 Stator Structure of the Slotless Halbach PMSM with Winding - Embedded Liquid Cooling (WELC)

Approach

The performance of the three initial designs was analyzed through an extensive electromagnetic FEA to evaluate their potential to meet the DOE EDT targets. In conjunction with the exclusive use of HRE-free magnets (NEOREC45MHF), significant improvements in power density, efficiency and overall performance were facilitated by the following innovations:

Design I and Design II

- An optimal slot/pole configuration to reduce hysteresis and eddy current losses in magnets.
- Thin steel laminations to reduce core loss at high operating frequency.
- A segmented magnet structure with novel cavity design in the IPMSMs to address the issues of demagnetization at high temperature and extreme fault conditions [1].
- Double layer distributed winding for Design I and dual three-phase FSCW configuration with optimal spatial displacement for harmonic minimization and power density improvement for Design II.
- End winding cooling technology in the IPMSMs for increased electrical loading and power density.

Design III

- Double-layer slotless stator made from non-magnetic plastics for reduced core loss at high frequency.
- Halbach magnet configuration for high magnetic loading and improved torque density.
- Winding embedded liquid cooling (WELC) for thermal management and high power density [2].

The main features and electromagnetic performance of the optimized designs of the three initial choices are summarized in Table I.1.17.8.

Table I.1.17.8 Result comparison of the three design choices

Parameters	Design-I	Design-II	Design-III
Stator outer diameter (mm)	190	185	195
Length (With end-turns) (mm)	83	75	92
Peak Torque for 15s (Nm)	150	145	144
Peak Power for 15s (kW)	100	100	100
Max. speed (rpm)	20000	20000	20000
CPSR	≥ 3	≥ 3	≥ 3
Power density (kW/L)	43	50	50
Total magnet pieces	64	60	90

The results in Table I.1.17.8 show that Design I is unable to meet the target power density of 50 kW/L. Therefore, Designs II and III are selected for further analysis. These machines will be further optimized to meet the power density target taking into consideration thermal, structural and demagnetization factors.

Results

The performance and optimization of the machines were carried out in commercial simulation packages from Altair, Solidworks, Ansys and Motorcad. Some of the preliminary results of electromagnetic and thermal analysis of the selected designs are shown below:

Design II

Figure I.1.17.23 shows the torque-speed and power speed characteristic of the V-type IPMSM in both continuous and peak operating points. The designed machine is able deliver the 55kW of continuous power and 100kW peak power for 15 seconds. Figure I.1.17.24 shows its efficiency map over the entire region. It is visible that the efficiency is mostly above 97% in the continuous region. Figure I.1.17.25 shows the results of using the end-winding potting material (CoolTherm SC-320) to reduce the overall temperature rise in the machine. At steady-state, the highest temperature recorded on the stator and rotor are 150°C and 120°C, respectively. The risk of demagnetization for the proposed segmented HRE-free magnets [3] were investigated through an imposed three-phase short-circuit fault condition at 20,000 r/min and magnet temperature of 120°C. The results in Figure I.1.17.26 show the magnet flux density to be above the knee point of the HRE-free magnet. The results verify that the magnets are safe from demagnetization under such conditions.

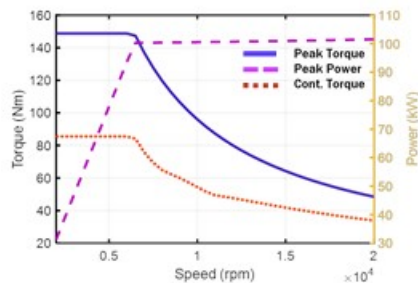


Figure I.1.17.23 Torque & Power-Speed Characteristics of Design II

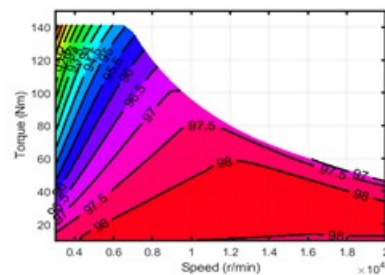


Figure I.1.17.24 Efficiency Map of Design II

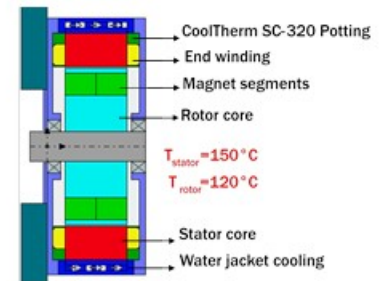


Figure I.1.17.25 Temperature Distribution of Design II at Steady-state

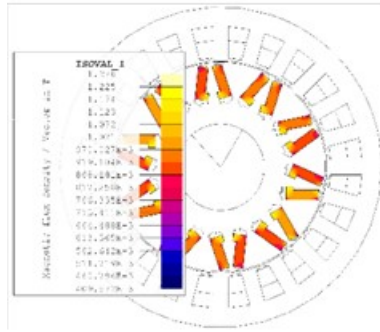


Figure I.1.17.26 Flux Density Plot of Magnets under SC fault at 120°C

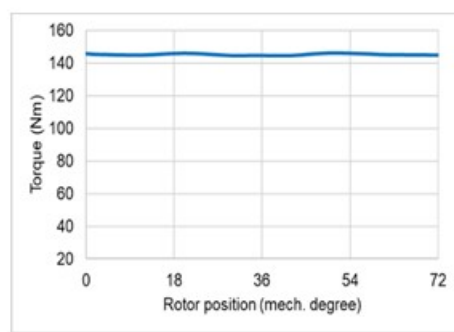


Figure I.1.17.27 Torque Profile of the Slotless Halbach PMSM in Design III

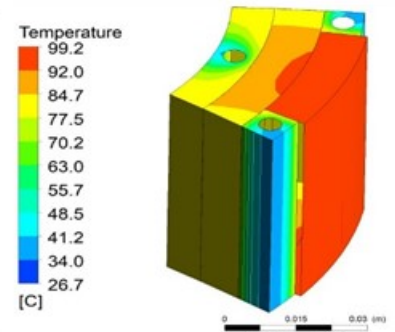


Figure I.1.17.28 Temperature Distribution of Design III at continuous Condition

Design III

This design features an outer-rotor machine with surface-mounted HRE-free magnets arranged in a Halbach array to maximize the torque density. As shown in Table I.1.17.8 and Figure I.1.17.27, this topology is capable of meeting the 50kW/L power density target with very smooth torque output ($\leq 1\%$ ripple). However, due to its very low thermal mass, a novel winding embedded liquid cooling strategy (WELC) has been developed to enhance thermal management and increase the electric loading of the machine [2]. This strategy involves passing Ethylene-glycol (50%-50%) through the cooling channels embedded in the winding support (CoolPoly D5506) as shown Figure I.1.17.28. The steady state result of a CFD analysis on 1/12th of the stator structure suggests that this arrangement is capable of handling a maximum current density of ~ 33 A(rms)/mm² (Temperature rise of 75^o C) which corresponds to peak power of 100kW for 18s. A continuous current density ~ 23 A(rms)/mm² can be achieved using the proposed WELC method which corresponds to ≥ 55 kW.

Conclusions

In this project, three HRE free PMSM designs have been investigated, optimized, and evaluated using the DOE EDT 2025 targets as a benchmark. A segmented V-shaped magnet rotor design with FSCW stator IPMSM (Design II) and an outer rotor slotless-Halbach rotor PMSM (Design III) have been shown to be viable topologies and promising options due the several innovations in topology, design, and thermal management. The HRE-free magnets in Design II have also been shown to be safe from demagnetization under a simulated SC fault condition. Simulations are currently ongoing to completely characterize the slotless Halbach PMSM and to further investigate the demagnetization performance of both designs. Furthermore, a multi-physics analysis and optimization will be carried out on both designs to address other important structural issues.

Key Publications

1. Iqbal Husain and Md Sariful Islam, "Machines Utilizing Heavy Rare Earth Free Permanent Magnets", US 63/004,951.
2. Ritvik Chattopadhyay, Md Sariful Islam, Rajib Mikail and Iqbal Husain, "Winding Embedded Liquid Cooling for High Power Density Slotless Motor," 2020 IEEE Energy Conversion Congress and Exposition.
3. Md Sariful Islam, Rajib Mikail and Iqbal Husain, "Demagnetization Performance Enhancement of Heavy Rare Earth Free Permanent Magnet Machines," 2020 IEEE Energy Conversion Congress and Exposition.

I.1.18 Design, Optimization, and Control of a 100-kW Electric Traction Motor Meeting or Exceeding DOE 2025 Targets (Illinois Institute of Technology)

Ian P. Brown, Principal Investigator

Illinois Institute of Technology
3301 South Dearborn Street
Chicago, IL 60616
Email: ibrown1@iit.edu

Susan Rogers, DOE Technology Development Manager

U.S. Department of Energy
Email: susan.Rogers@ee.doe.gov

Start Date: October 1, 2019
Project Funding: \$300,000

End Date: September 30, 2020
DOE share: \$300,000

Non-DOE share: \$42,962

Project Introduction

The Illinois Institute of Technology (IIT) is a member of the Department of Energy Electric Drives Technologies (EDT) Consortium. IIT's role in the consortium focuses on developing electric traction motors for electric vehicles with 8x the power density and half the cost of state-of-the-art traction motors.

Objectives

The overall objective of the electric motor portion of the Electric Drives Technology consortium is to research, develop, and test electric motors for use in electric vehicle applications capable of the specifications in Table I.1.18.1. Reduced scale physical prototypes and full-scale design studies are planned at regular intervals to ensure progress towards the targets.

Table I.1.18.1 EDT Consortium Electric Motor Targets

Parameter	Target Value
Peak Power Rating (kW)	100
Power Density (kW/l)	≥ 50
Cost	≤ 3.3

Approach

To meet the electric traction motor power density and cost targets, a number of approaches are being pursued simultaneously throughout the course of this project which address all of the major volumetric power density influences. Many of the approaches are synergistic and complementary with the approaches being taken by partner Electric Drive Technology Consortium member national laboratories and universities.

- Multiphysics design for increased power density through maximum utilization of active materials.
 - Improved dimensional or shape optimization techniques which simultaneously address electromagnetic, thermal, and structural design in a computationally efficient manner.
 - Topological optimization techniques to distribute materials in an optimal manner without a geometric template subject to magnetic and structural objectives and constraints.
- Synthesis of electric machine windings and PM flux barriers with controlled space harmonics.

- Develop windings and PM flux barrier optimization tools which eliminate or reduce unwanted space harmonics while maximizing the working winding factor. Ideally synthesize a feasible winding or flux barrier from a target harmonic spectrum.
- Develop high slot fill windings for increased current loadings or efficiency. Potential options that will be investigated include low proximity loss bar/hairpin windings, cast windings, and die compressed windings.
- Investigate aggressive cooling strategies and support the thermal management research of other national laboratories and universities in the Electric Drives Technology Consortium.
 - Research high slot fill windings with through conductor cooling with the optimum trade-off of copper area to heat extraction.
- Explore multiple motor topologies for increased power density.
 - Initial machine topologies targeted include high speed interior permanent magnet synchronous machines (IPMSMs) and a transverse flux machine using a low core loss material.
- Apply new technologies, concepts, materials, and learnings from the Illinois Institute of Technology research group and other Electric Drives Technology Consortium members in reduced scale electric traction motors.
 - Design, construct, and dynamometer test a reduced scale motor prototypes in budget period 2 and subsequent budget periods to calibrate progress towards motor targets.
 - Design studies of a 100-kW machine, including electromagnetic and structural finite element simulations, and lumped parameter thermal modeling to calibrate progress towards motor targets.

Results

Combined Dimensional and Topology Optimization Introduction

In the previous budget period, a magneto-structural topology optimization approach for the distribution of electric steel or air in the rotor of a synchronous reluctance or interior permanent magnet synchronous machine (IPMSM) was developed. In this approach the permanent magnets (PMs) in the IPMSM were required to be a fixed size and location. Using only topology optimization to design IPMSM rotors for maximum performance and minimum cost is attractive because the entire rotor design domain is available as the design space to distribute PM, electrical steel, or air without the restrictions of a geometric template. A multi-material magneto-structural topology optimization problem can be setup and solved without a pre-defined permanent magnet size or location. Representative topology only optimization results to maximize the average torque, subject to torque ripple, Von Mises stress, and compliance constraints are shown in Figure I.1.18.1. The PM would be very difficult and expensive to manufacture because of its complex shape, Figure I.1.18.1(b). Additionally, there is an implicit assumption that the electrical steel is bonded to the permanent magnet. In reality this is not the case.

Ideally, for the cost-effective manufacturing of IPMSM rotors, the permanent magnets would retain a rectangular or bar shape of variable size and location while the electrical steel would be free to distribute in a free form manner. In other words, we would like to combine dimensional optimization of the PM(s) and topology optimization of the electrical steel. Two combined dimensional and topology approaches have been developed in this budget period. In the first, the mesh in the non-PM regions, i.e., the magneto-structural topology optimization design domain, is deformed to account for movements or changes in size of the PM. In the second approach, the PM containing region is interpolated onto the mesh as a density variable using an external functional space. This avoids having to deform the mesh but makes the application of mechanical boundary conditions more difficult. In both approaches, the topology optimization method used is the Solid

Isotropic Material with Penalization (SIMP) method. Element material properties are parameterized continuous functions of the normalized element material densities. The element material properties are also penalized to force the convergence of the densities to solid electrical steel or air.

Mesh Deformation Combined Dimensional and Topology Optimization

For the proposed mesh morphing combined dimensional and topology optimization, the location or size of the PM will vary, and if the rotor domain was re-meshed, the number of elements and their locations would likely change. As each element outside the PM represents a control variable, the number of inputs to the optimization algorithm would also change with remeshing and potentially represent a different location or element. In order to keep the same total number of elements in the design domain, while varying the PM's location and/or size, a Laplace smoothing mesh deformation technique is utilized.

The Laplace smoothing technique solves Laplace's equations in a 2-D design domain as

$$\frac{\partial^2 x}{\partial X^2} + \frac{\partial^2 x}{\partial Y^2} = 0, \quad \frac{\partial^2 y}{\partial X^2} + \frac{\partial^2 y}{\partial Y^2} = 0$$

where x, y are the coordinates of deformed element nodal positions, and X, Y are the coordinates of the element nodal positions of the original geometry and mesh. While this approach allows the mesh to deform while keeping the same overall mesh size and number, there is a limit to the displacement or size change of the PM before the distortion becomes too great. As an example, the mesh distorts as the PM is displaced towards the in airgap, Figure I.1.18.2. As the PM is further displaced towards the airgap, the distortion becomes more severe and eventually the meshing tool will fail, Figure I.1.18.2(a). To avoid this, the displacement of the PM would need to be severely limited, defeating the purpose of the combined dimensional and topology optimization. Mesh distortions caused by the deformations of the mesh calculated by the Laplace equations, while calculated as a set for all mesh elements, are mostly influenced by neighboring elements and the deformation is mostly localized. To allow larger mesh deformations, without distortion the rotor design domain can be further sub-divided into sub-domains by virtual connection lines. Element nodal positions along the connection lines are distributed linearly by solving the Laplace equation only along the line as a function of the element displacements on the connection lines, $u_{line,x}$ and $u_{line,y}$ in the x or y direction.

$$\frac{\partial^2 u_{line,x}}{\partial X^2} + \frac{\partial^2 u_{line,y}}{\partial Y^2} = 0$$

The connection lines and sub-domains for three example scenarios are shown in Figure I.1.18.3. The greater range of PM displacement and changes in size, without severe mesh distortion or failure of the meshing tool, with the addition of the connection lines, are shown in Figure I.1.18.2(b). Using the proposed mesh deformation technique, the total number of element density control variables remains the same as the original mesh before displacements or size changes. To combine both dimensional and topology optimization into one optimization problem, both dimensional and normalized element density variables are cascaded into one vector to be compatible with a Method of Moving Asymptotes (MMA) solver [1], or its globally convergent version, GCMMA [2].

The results of three example mesh deformation combined dimensional and topology rotor optimizations are shown in Figure I.1.18.4. There are two flat bar PM configurations (left and center) and one v-bar PM configuration (right), Figure I.1.18.4. In the first flat bar PM configuration the PM size is fixed but the PM can move in the radial direction. In the second flat bar PM configuration the PM size, PM radial position, and rotor inner radius are the dimensional optimization variables. In the v-bar configuration the angle between the PMs is an optimization variable. The Von Mises stresses and displacement for the three design examples are shown in Figure I.1.18.5 and Figure I.1.18.6.

The particular optimization problem formulation used for the example IPMSM rotor design problems has an overall objective to maximize the average torque subject to a constraint on the torque ripple to be less than 10% of the average torque. To ensure the rotor's structural integrity, additional constraints on p-norm

aggregated Von Mises stress [3] and total compliance are also included. A yield strength of 275 MPa is taken in these cases. The body load centripetal force is calculated based on a rotor speed of 12,000 RPM. A magnetic only optimization is first run using the MMA algorithm [1] to serve as a seed or initial condition for the overall magneto-structural optimization using the GCMMA algorithm [2]. The reason for this is because the GCMMA calculation is much slower due to its inner iterative loop.

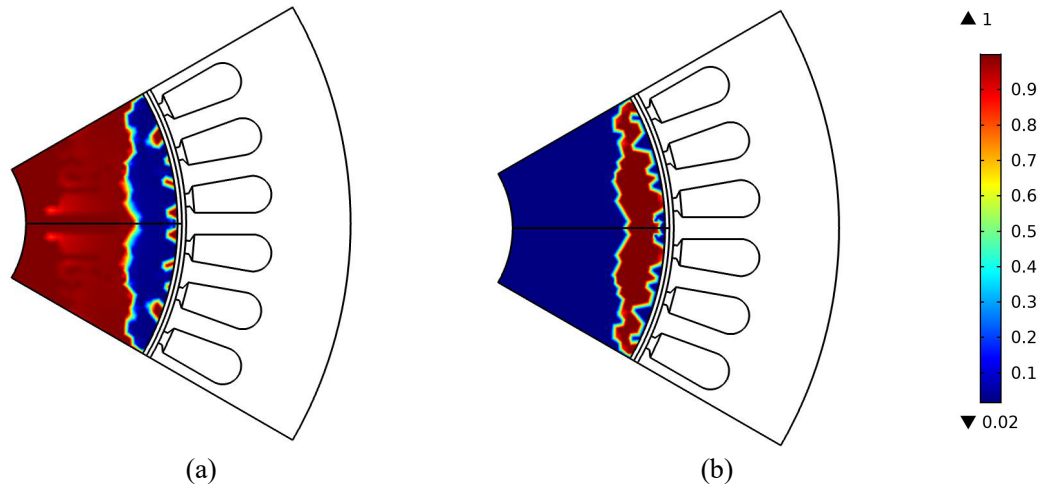


Figure I.1.18.1 Multi-material magneto-structural IPMSM rotor topology optimization (a) electrical steel distribution (red), (b) permanent magnet distribution (red).

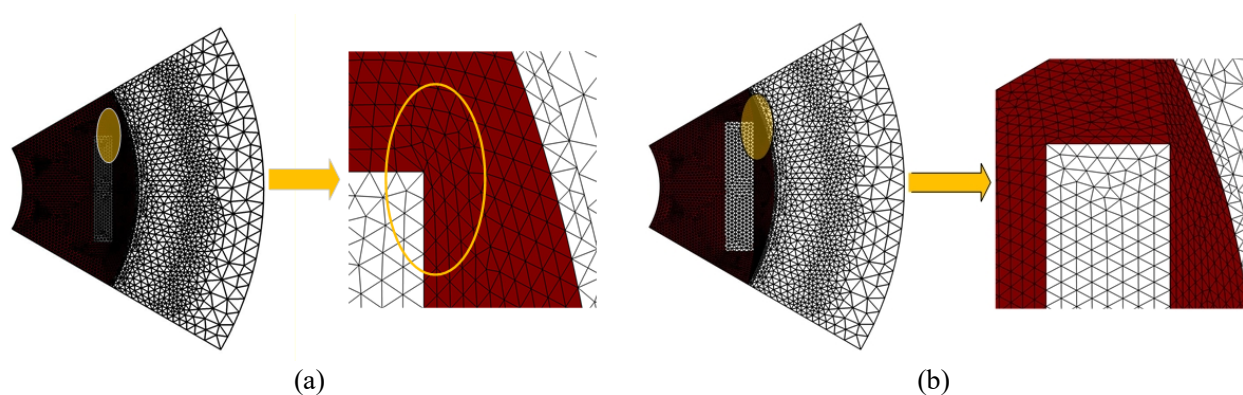


Figure I.1.18.2 Mesh deformation and distortion as the PM is displaced radially towards the airgap (a) only using Laplace smoothing, (b) using virtual connection lines to divide the topology optimization areas into sub-domains.

Field Interpolation Combined Dimensional and Topology Optimization

An alternative approach to mesh deformation has been developed for combined dimensional and topology optimization. This approach is referred to as field interpolation, as the PM material properties are interpolated or projected onto the mesh from an external functional space. In the field interpolation approach, the mesh is not deformed so that the greater PM movement or size change can be achieved in the rotor design domain. The projection of the PM permeability onto the mesh causes a sharp transition between the PM and the electrical steel design domain region reducing issues with intermediate density materials. However, the boundary between the PM and the rest of the rotor design domain is not a true geometric boundary and the mesh does not necessarily have nodes along the boundary. The lack of a true geometric boundary makes it difficult to assign realistic mechanical boundary conditions between the PM and the iron region. Instead, the equivalent

pressure as would be caused by the PM is applied to the first set of elements next to the PM in the radial outward direction. An example flat bar IPMSM was magneto-structurally optimized using the field interpolation approach at a rotor speed of 12,000 RPM Figure I.1.18.7. The elements with the pressure applied are indicated in orange. In the optimization, the fixed size PM position varies in the x-axis radial outward direction. The Von Mises stress and displacement of the optimized rotor is shown in Figure I.1.18.8.

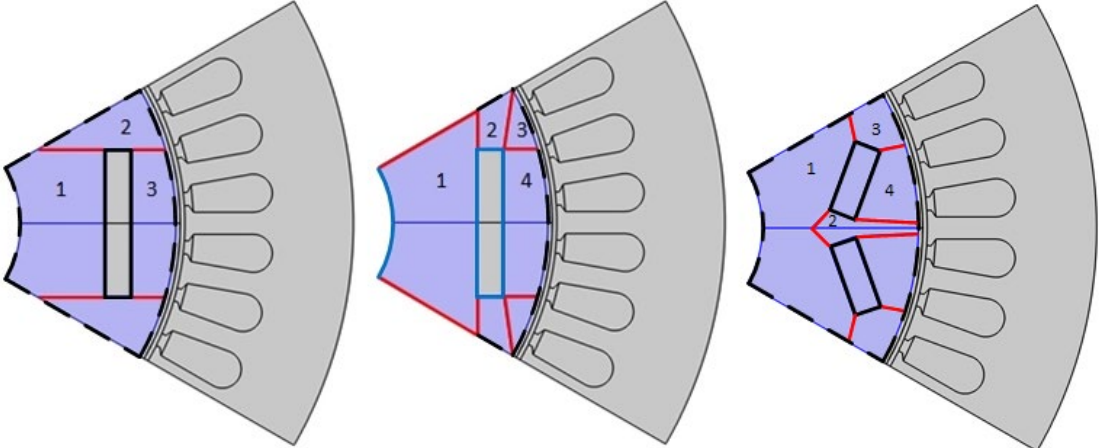


Figure I.1.18.3 Virtual connection lines (red) to divide the region into sub-domains (numbered regions), and fixed (black) or variable (light blue) size PM, and fixed nodes (dashed lines) rotor entities.

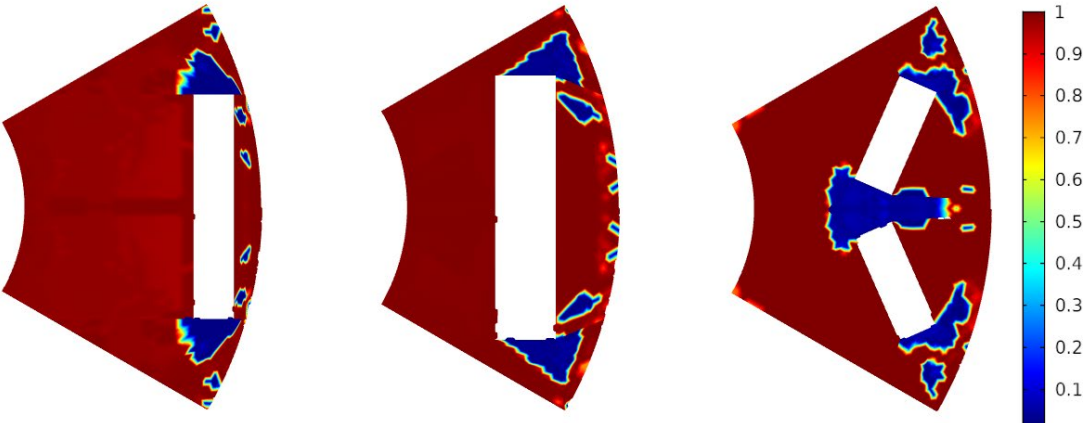


Figure I.1.18.4 Electrical steel distribution (red) of the example mesh deformation combined dimensional and topology optimization cases.

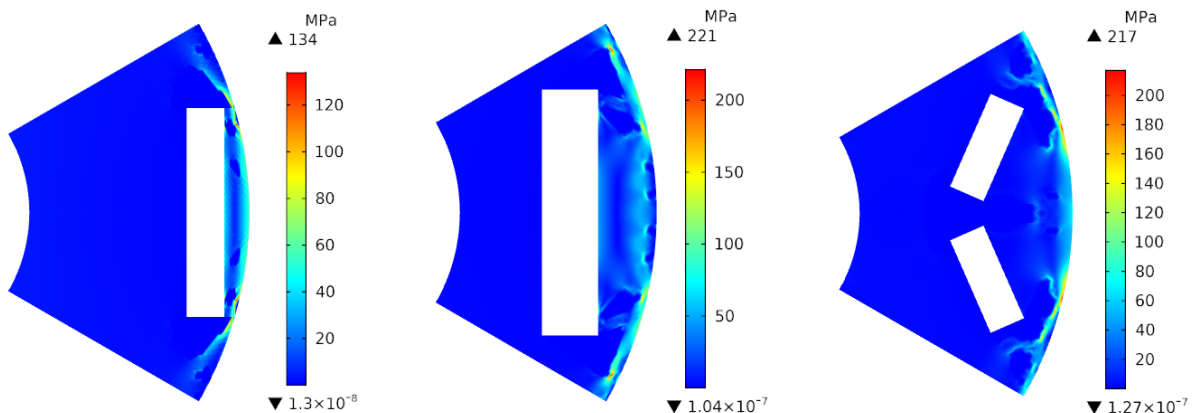


Figure I.1.18.5 Von Mises stresses of the example mesh deformation combined dimensional and topology optimization cases.

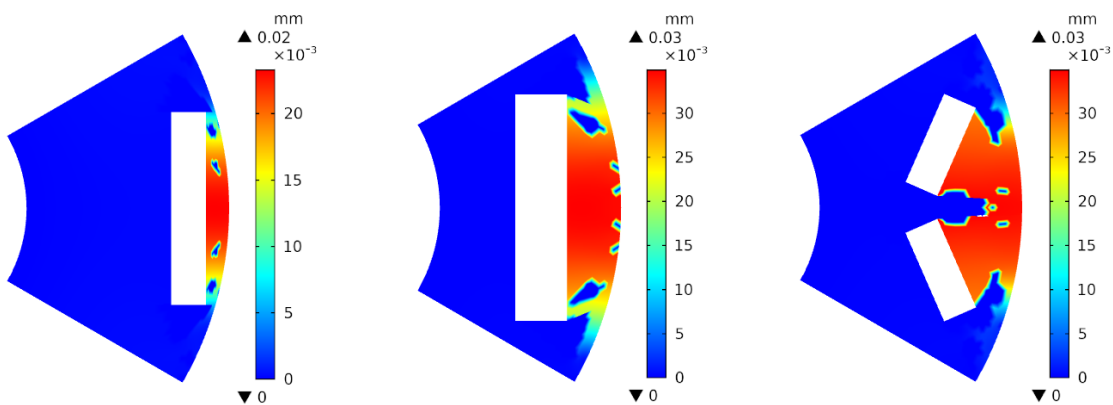


Figure I.1.18.6 Displacement of the example mesh deformation combined dimensional and topology optimization cases.

Design Toolkit for Multi-Layer IPMSM Rotor with Profiled Airgap Flux Density Distribution

Multi-layer IPM rotors are deemed as highly favorable for the fulfillment of the Project's challenging targets. With a multi-layer IPM rotor, the designer has greater flexibility to profile the airgap magnetic field distribution, which makes it possible to design the rotor in coordination with the stator winding to minimize unwanted harmonic interactions. By keeping undesired harmonic interactions to a minimal, performance improvements include reduced power losses, better power efficiency, less torque ripple, and a smoother power output. Also, a multi-layer IPM rotor can produce a higher airgap flux density while having better resistance to demagnetization, which are essential for the Project's high power density and elevated operating speeds. A design toolkit featuring a flexible geometry template has been developed for multi-layer IPM rotors that can incorporate nine dimensional parameters for each layer independently. This enables the direct design of an IPM rotor that will deliver a target power output with high quality torque waveform while minimizing the unwanted harmonic interactions with the selected stator winding.

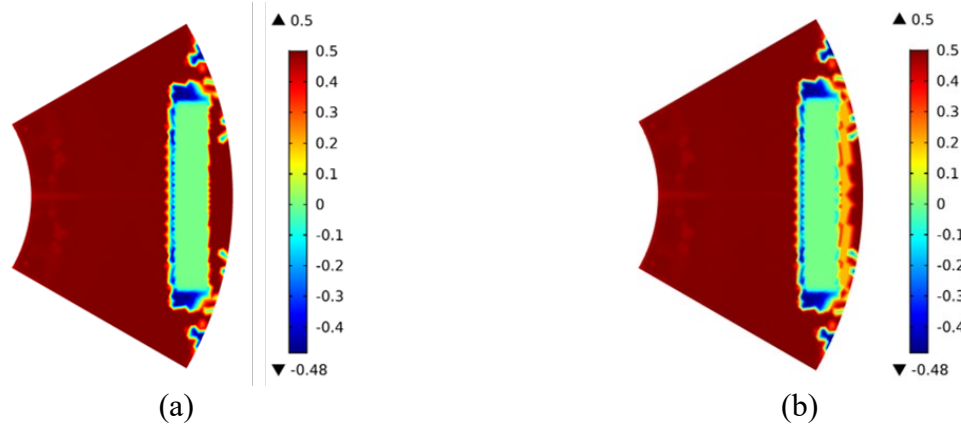


Figure I.1.18.7 Field interpolation approach material distribution in the rotor design domain at 12,000 RPM. (a) Material distribution only where red represents electrical steel, light green represents the PM, and blue represents air. (b) In addition to the material distribution the equivalent centripetal force of the PM is calculated and assigned as a pressure on the boundary elements adjacent to the PM indicated by the orange color.

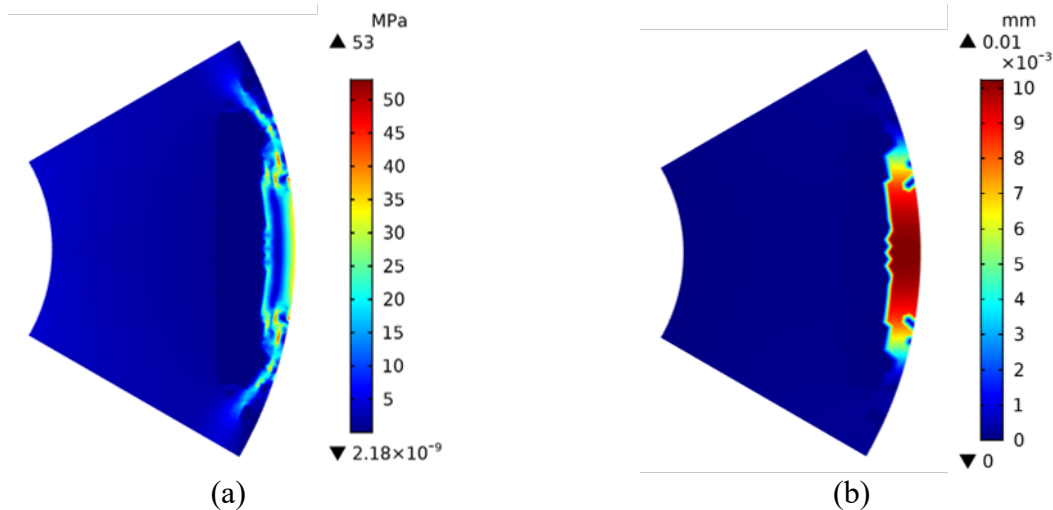


Figure I.1.18.8 The (a) Von Mises stress and (b) displacement of the rotor designed using the field interpolation approach with a rotor speed of 12,000 RPM.

Prototype Interior Permanent Magnet Synchronous Machine Design

An IPMSM targeting the Project's specifications was designed using the multi-layer PM rotor design tool and a multiphysics meta-model-based optimization process. A 12 slot, 10 pole fractional slot concentrated winding (FSCW) was selected because of the potential for high slot fills and compact end turns that can be prototyped relatively easily in an academic setting. The aspect ratio was selected to achieve an 80% active volume utilization ratio of the total volume of 2 liters. Two rotors were designed with three and two layers respectively. The three-layer rotor design allows for higher airgap flux densities and reduced harmonic content but is more difficult to prototype. The base speed of the motor is chosen to be 6600 rpm, while the maximum operating speed is 20,000 rpm. The continuous output power is 55 kW at and above the base speed, whereas the peak output power is 100 kW. The cross-sections of the prototype designs are shown below in Figure I.1.18.9.

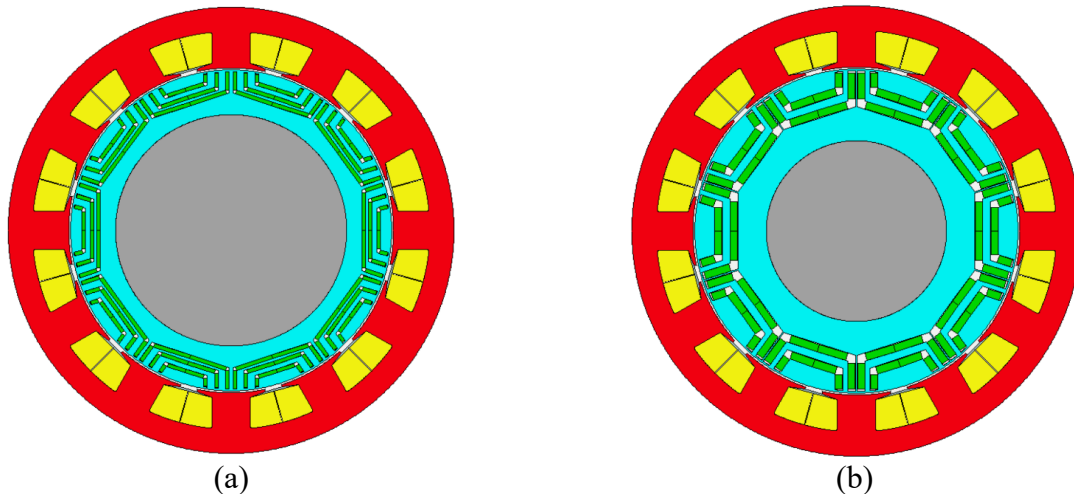


Figure I.1.18.9 Candidate prototype IPMSM designs with different rotors: (a) three-layer rotor and (b) two-layer rotor.

Table I.1.18.2 Predicted Two-Layer Rotor Prototype Performance at Base Speed of 6,600 RPM with Stator Winding Temperature of 120°C and Rotor Magnet Temperature of 100°C

Quantity	FEA Results
Current Density (A_{rms}/mm^2)	36.23
Torque Ripple (%)	3.11
Power Factor (at 100 kW)	0.8968
Output Power (kW)	102.3
Efficiency (%)	94.64

Conclusions

In this budget period, two new combined dimensional and topology methods have been developed to design high performance IPMSM rotors. The first method, using mesh deformation, allows the PM to change position and size by using Laplace smoothing. The second projects the PM onto the mesh from an external functional space. Example results for three IPMSM examples were provided. A rotor flux barrier design synthesis tool and meta-model optimization technique was used to design a 2-layer, 100 kW IPMSM with high power density and efficiency.

Key Publications

1. F. Guo, I.P. Brown, "Simultaneous Magnetic and Structural Topology Optimization of Synchronous Reluctance Machine Rotors," IEEE Transactions on Magnetics, Vol 56, No. 10, Oct. 2020, DOI: 10.1109/TMAG.2020.3014289.
2. F. Guo, I.P. Brown, "Magneto-Structural Combined Dimensional and Topology Optimization of Interior Permanent Magnet Synchronous Machine Rotors," 2020 Energy Conversion Congress and Exposition (ECCE), Oct. 11-15, 2020.

References

1. K. Svanberg, "The method of moving asymptotes a new method for structural optimization," International Journal for Numerical Methods in Engineering, Vol. 24, No. 2, pp. 359-373, Feb. 1987.

2. K. Svanberg, "A Class of Globally Convergent Optimization Methods Based on Conservative Convex Separable Approximations," *SIAM Journal on Optimization*, Vol. 12, pp. 555-573, 2002.
3. D.M. De Leon, J. Alexandersen, O. Fonseca, S. Jun, and S. Ole, "Stress-constrained topology optimization for compliant mechanism design," *Structural and Multidisciplinary Optimization*, Vol. 52, No. 5. pp. 929-943, 2015.

I.1.19 Multi-Objective Design Optimization of 100 -W Non-Rare-Earth or Reduced-Rare Earth Machines (Purdue University)

Scott Sudhoff, Principal Investigator

Purdue University
465 Northwestern Avenue
West Lafayette, IN 47907
Email: sudhoff@purdue.edu

Steve Pekarek, Co-Principal Investigator

Purdue University
465 Northwestern Avenue
West Lafayette, IN 47907
Email: spekarek@purdue.edu

Susan Rogers, DOE Technology Development Manager

U.S. Department of Energy
Email: susan.rogers@ee.doe.gov

Start Date: May 15, 2020
Project Funding: \$300,000

End Date: May 14, 2021
DOE share: \$300,000

Non-DOE share: \$0

Project Introduction

The goal of this project is to reduce the size, weight, cost, and losses associated with rotating electric machinery and its associated power electronics for electric and hybrid vehicle applications. In particular, the goal of this effort is to facilitate electric machinery that will meet the requirements set forth in the U.S. DRIVE *Electrical and Electronics Technical Team Roadmap* of October 2017. This document calls for an electric machine with a peak power of 100 kW, a continuous rated power of 55 kW, a peak speed of less than 20,000 rpm, a volume of no more than 2 liters, a mass of less than 20 kg, and a useful life of 15 years or 300,000 miles of vehicle service. This will be achieved through a combination of (i) new materials, (ii) new electric machine topologies, (iii) advances in power electronics, and (iv) superior design through the use of formal and rigorous multi-objective optimization-based design built on advanced analysis techniques. This effort is being conducted by a large consortium comprised of National Laboratories (Sandia National Laboratories, Oak Ridge National Laboratories, Ames Laboratory, and the National Renewable Energy Laboratory) and universities (Virginia Tech, Georgia Tech, SUNY, Arkansas, Ohio State, IIT, Purdue, University of Wisconsin – Madison, University of California Berkeley, and North Carolina State). Purdue’s role focuses on (ii) and (iv).

Objectives

The objective of this effort is to explore the use of new materials and develop new design paradigms to enable unprecedented propulsion motor power densities at a reduced cost. In order to achieve this objective, Purdue’s goals will be to investigate new machine topologies such as the homopolar ac machine, and to develop new improved design codes which (i) incorporate high switching frequency performance analysis, (ii) thermal performance, (iii) high-speed rotor structural analysis, and (iv) advanced magnetic analysis techniques into its existing design paradigm based on rigorous multi-objective optimization. An additional objective will be to build and test a prototype machine whose design is based on the enhanced design paradigm developed under this effort.

Approach

To achieve the objectives described in the previous section, Task 1.1 described below was completed during the second year of the program. These tasks were continued during the third and fourth quarters of budget

period 1 (BP1-Q3, BP1-Q4). In addition, Task 2.1 also described below was started during the first and second quarters of budget period 2 (BP2-Q1, BP2-Q2). These listed quarters comprise FY20.

Task 1.1 – Electric Machinery Design Paradigm Enhancements

Subtask 1.1.1 – Homopolar machines have long been considered for high-speed applications. Their attributes include a simple rotor structure well-suited for high-speeds and is ideally electrically lossless, no permanent magnet materials, has suitability to high-temperature operation, and the ability to operate over a very wide speed range. Purdue has developed a new type of homopolar machine that has advantages over its traditional counterpart and may prove to be ideal for traction applications. A basic design code is being developed under this task to see if this arrangement is in fact competitive.

Subtask 1.1.2 – High Frequency Switching Losses. Presently, the design code formulation developed at Purdue includes dc resistive, skin effect, and proximity effect losses at the fundamental frequency. Core losses are determined using an enhanced version of the Modified Steinmetz Approach. Semiconductor conduction and switching losses are also included in existing design codes. In this task, this aspect of the code development is being improved. Of particular interest will be including switching frequency losses in the machine and permanent magnet losses at both the switching frequency and the slot passing frequency. The goal is to support the co-optimization of the machine with the power electronic converter so that the impact of switching frequency on the machine is captured.

Subtask 1.1.3 – In the multi-objective optimization-based design of electric machines, one of the key analyses is the magnetic performance. While analytical magnetic equivalent circuit methods have been used with considerable success, they can require significant insight on the part of the user.

As an alternative, numerical methods of field analysis have been used, with Finite Element Analysis (FEA) being particularly common. Commercial FEA packages often include optimization capability. However, these are restricted to ‘small’ problems in the sense that there are only a few degrees of freedom. The optimization is restricted to the machine itself and does not include the converter, system, and other factors which can take the number of unknowns into the twenties, thirties, or more, whereupon the FEA approach becomes intractable. This is particularly the case when the speed/torque required by the machine is in the set of unknowns.

The Method of Moments (MoM) is a numerical method used to solve fields-based integral equations. In contrast to FEA that is based upon solving differential equations, MoM has an advantage that only the active material is meshed. In modeling electric machinery, this means there is no mesh in the airgap nor outside the machine. As a result, the number of unknowns can be greatly reduced.

In the past, a disadvantage of MoM is that numerical integration had to be used to populate the corresponding MoM matrices. Recently, Purdue developed analytical expressions for the MoM matrices that eliminates the numerical integration step. As a result, there is a strong likelihood that MoM can be much more computationally efficient compared to FEA for low frequency magnetic modeling. Thus, it is likely MoM can be used within rigorous multi-objective design of electric machinery (and passives) in which potentially millions of candidates are evaluated. In this effort, Purdue is developing an open-source MoM toolbox intended for electric machine optimization. At first the toolbox is formulated to solve magneto-static 2D problems. The toolbox will then be applied to PMSM and WRSM machines and the computational performance compared to FEA.

Task 2.1 – Electric Machinery Design Paradigm Enhancements

Subtask 2.1.1 – Integration of retention sleeve constraints into multi-physics multi-objective design framework. Centrifugal forces from the rotating components increase with the square of the angular speed. Thus, high rotor speeds create new challenges with respect to the structural integrity of the machine. Introducing a rotor retention sleeve addresses these issues and enables extreme speed design topologies. This proposal advances the current state of the art by setting forth an analytical solution (more computationally efficient than numerical models) that accounts for surface and body centrifugal forces, as well as stresses

induced by differential thermal expansion of rotor parts. This model is well suited for non-axisymmetric machine topologies with anisotropic materials. Furthermore, rather than optimizing a retention sleeve for a given motor, this task proposes to optimize the sleeve along with the electric machine.

Subtask 2.1.2 – This task originally focused on thermal model validation. However, because of some developments on the homopolar ac machine (see [Subtask 1.1.1](#)), it was decided to explore new homopolar ac machine variants instead. Toward the end of BP1, a new homopolar ac machine topology was conceived, as will be described in the results section. The machine exhibits an infinite constant power speed range, features modular construction, and enables the use of cooled and stationary magnets. Because of these exciting properties, it was decided to explore this new topology.

Subtask 2.1.3 – With a desire to reduce the cost and increase the rotational frequency of the electric machine, it is possible that inert-core PM machines (ICPM) may hold promise. Specifically, in an ICPM much of the space is occupied by air or a magnetically inert material such as plastic. There will likely be steel for the shaft and as an outer shield to limit far-field magnetic flux, but little (or none) elsewhere. The potential of such a machine is there is no core loss or cogging torque. In addition, it is possible that manufacturing costs could be significantly reduced, since materials such as plastics (i.e., Delrin) are often easier to machine than steel. Since the likelihood of ICPM success is unknown, the initial optimizations will only consider the electromagnetic behavior without detailed structural or thermal models. Proxy thermal (and structural) constraints will be included via techniques such as limiting the current density of the windings. If an ICPM is shown to hold promise, the thermal and structural aspects will be considered in more detail in Year 3.

Subtask 2.1.4 – This task originally focused on incorporating eddy currents into the MoM formulation to enable design optimization of induction machines. However, in consultation with DOE, the focus of this task changed to using the MoM to explore the asymmetrical reluctance machine (ARM). This was decided since much research from industry has gone toward the induction machine. The ARM is simpler in that it does not have windings on the rotor. Thus, it is likely to be more cost-effective and more reliable compared to induction machines. Moreover, the ARM takes advantage of asymmetry to enhance torque density in one rotor rotational direction, while sacrificing torque density in the opposite direction of rotation. The fact that in the EV application, one typically requires more torque in one rotor direction sets up perfectly for applying this potential torque density enhancement.

Results

Subtask 1.1.1 and 2.1.1 – Homopolar Machines. During BP1, an investigation into a class of homopolar ac machines was made, culminating in a Pareto-optimal front of designs in which the efficiency versus torque density of this class of machine was compared to that of a surface mounted permanent magnet ac machine, as described in last year's annual report. The topology seemed problematic in that the machine exhibited considerable torque ripple and the excitation was non-standard. This led to the consideration of another variation of this class of machine topology. Again, it was found that there were significant issues. However, at the end of BP1, a significant new topology was developed – the Dual Rotor Homopolar AC Machine. The investigators have filed a patent disclosure on this new device with Purdue.

There are several interesting aspects of the new machine. First, the voltage and current waveforms are sinusoidal, and, unlike other homopolar machines, the flux in the stator steel associated with the main windings is sinusoidal. The machine can be used with a traditional inverter. Secondly, the machine exhibits an infinite constant power speed range (limited by mechanical considerations). This is obviously very attractive. Third, there are several options for establishing the field. These include (1) the use of stationary field windings (a distinct advantage over rotating field windings), (2) the use of a stationary permanent magnet (eliminating mechanical stresses and enabling active cooling of the magnet), (3) the use of a rotating permanent magnet with an axial flux orientation which puts the magnet at a location of small radius at the inside of the rotor, or (4) the use of a stationary superconducting puck based field (this is useful in very high power applications such as ship propulsion).

Work during the last two quarters has focused on the concept of operation of this machine, which is just as important to successful operation as the topology, as well as the formulation of a plan for a pragmatic design model. Here, there is difficulty in modeling the machine since this is inherently a 3D machine which cannot be designed with 2D based models.

Subtask 1.1.2 – High Frequency Switching Losses. During Budget Period 1 of the project, high frequency loss models were proposed in satisfaction of the BP1: Q2 project milestone and have since been implemented and improved upon during BP1: Q3 through BP2: Q2.

The switched operation of the inverter creates a modulated AC voltage excitation from the DC source that is dependent on the control and modulation strategy. The non-ideal voltage waveforms produce stator currents with a corresponding harmonic content which effects machine performance. Switching effects also drive inverter loss and required capacitance.

A time domain simulation can capture the switching events in the inverter at each instantaneous current value. This is valuable to the electric drive optimization process because it enables the evaluation of different modulation strategies, and their implications in the overall system level design. However, due to the large number of candidate solution evaluations in an evolutionary optimization, computational efficiency is imperative to enable comprehensive system design over a wide search space. The incorporation of a time domain simulation in the fitness function of the electric drive needs to be efficiently implemented, while maintaining model accuracy to lead the algorithm to a true optimal. With that in mind, a high-speed time domain simulation algorithm suitable for integration with the machine design optimization was developed. This algorithm utilized an analytical solution to those differential equations. This model enables a roughly ten times faster simulation without compromising accuracy.

Using the proposed algorithm, a robust time domain simulation function can be called for each operating point in the electric drive optimization fitness function. Since it has been implemented for continuous and discontinuous modulation strategies, different variations of these can be compared in a system level context. An example of the use of this in a system optimization context is shown in Figure I.1.19.1. Therein, a study is conducted in which the DC bus voltage ripple is bound to 0.5%, and the impact of modulation strategy and switching frequency are studied on loss and on the required inverter bus capacitance (a major component of the inverter size). Interestingly, discontinuous strategies which are commonly used to reduce switching losses do not look nearly as attractive when one considers the impact of capacitor mass.

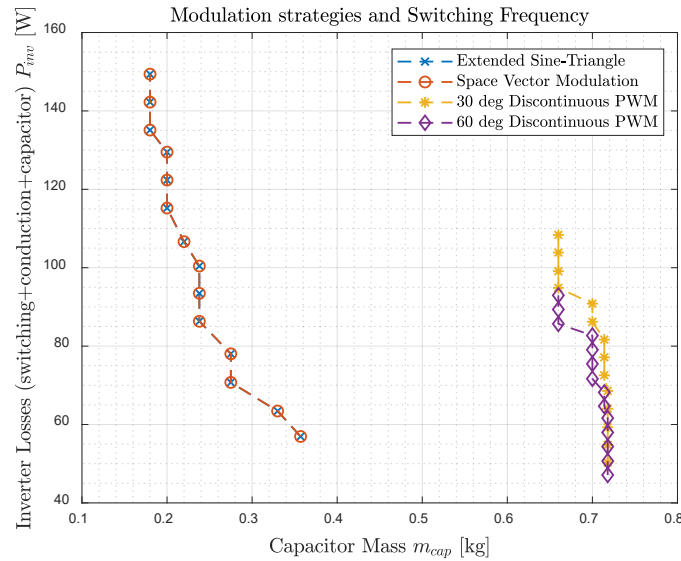


Figure I.1.19.1 Comparison of inverter losses against capacitor mass for the modulation strategies and switching frequency solutions evaluated in this example. Figure by Sudhoff/Pekarek research team.

Subtask 1.1.3 – Method of Moments. The Method of Moments (MoM) is a numerical method that can be used for solving fields-based integral equations. In contrast to methods used to solve differential equations, such as Finite Element Analysis (FEA), MoM has an advantage that only the active material is meshed. As a result, the number of unknowns can be greatly reduced compared to FEA. Additional advantages include that any combination of polygons can be used to establish the mesh, and the nodes are not required to be coincident. Thus, for machine design one can use pre-meshed building blocks and readily assemble them to generate candidate designs. Furthermore, only a surface mesh is required when the materials are magnetically linear. Over the initial year, a 2D MoM formulation has been adopted to model electric machinery.

Within this research, it has been found that the axial periodicity inherent in the geometry of electric machinery can be exploited to decrease the computational complexity of the MoM formulation. Specifically, the primary computational bottleneck in MoM field analyses is the population of the dense system matrix, thus it is desired to avoid computing it in its entirety. A method to limit the number of components that need to be computed has been derived and implemented for the case in which linear materials or nonlinear materials are used.

Finally, as part of this research, a method of efficiently computing the torque based upon a Lorentz formulation has been derived and implemented. In FEA formulations, torque is often computed using a Maxwell stress tensor approach. Such an approach can be applied in the MoM formulation. However, since the airgap is not meshed, this requires one to place additional elements within the airgap and numerically integrate the corresponding force densities to calculate torque. In the method that has been derived, one uses the bound currents at the edge of all meshed materials to calculate the flux density present at all bound and free currents on the rotor. The cross product of the vector from the center of the machine to the element then provides torque. It has been found that the approach derived is much more efficient numerically compared to a Maxwell stress tensor approach.

A goal of the MoM is to utilize it within population-based design (PBD) of electric machinery and indeed have it adopted within the consortium. Toward this goal, the approach has been tested for the PBD of surface mount PM machines operated in the linear magnetic region. Within the optimization Purdue's MATLAB-based toolbox for multi-objective optimization, GOSET, was utilized for a population size of 500 individuals applied over 500 generations. Each machine was evaluated at 4 rotor positions, over which the mean torque was evaluated. The computation time required to complete the design study was 11.4 hours on a simulation

workstation with an Intel Xeon E5-2687W v2 3.4 GHz processor and 32 GB of RAM. The computed flux density in the tooth and back-iron calculated using the MoM was found to be identical to that obtained using FEA. The FEA was performed using the commercial package ANSYS Electronics Desktop, which required more than 10,000 elements per pole on average, whereas the MoM required only 190 unknowns per pole. An approximate FEA unknown count is given since the geometry is re-meshed at each rotor position. While it is not precise to compare computation times for codes written by different authors, it is informative of the potential offered by the MoM. Specifically, the commercial FEA solver required several minutes to perform the same machine evaluation on the same workstation used to perform a 0.164 s MoM solve. Finally, a MoM toolbox was established with a graphical user interface (GUI) that enables researchers to upload a PM machine geometry, select the mesh density desired, compute quantities including torque, loss, flux density, etc., and perform multi-objective optimization. The GUI is shown in Figure I.1.19.2.

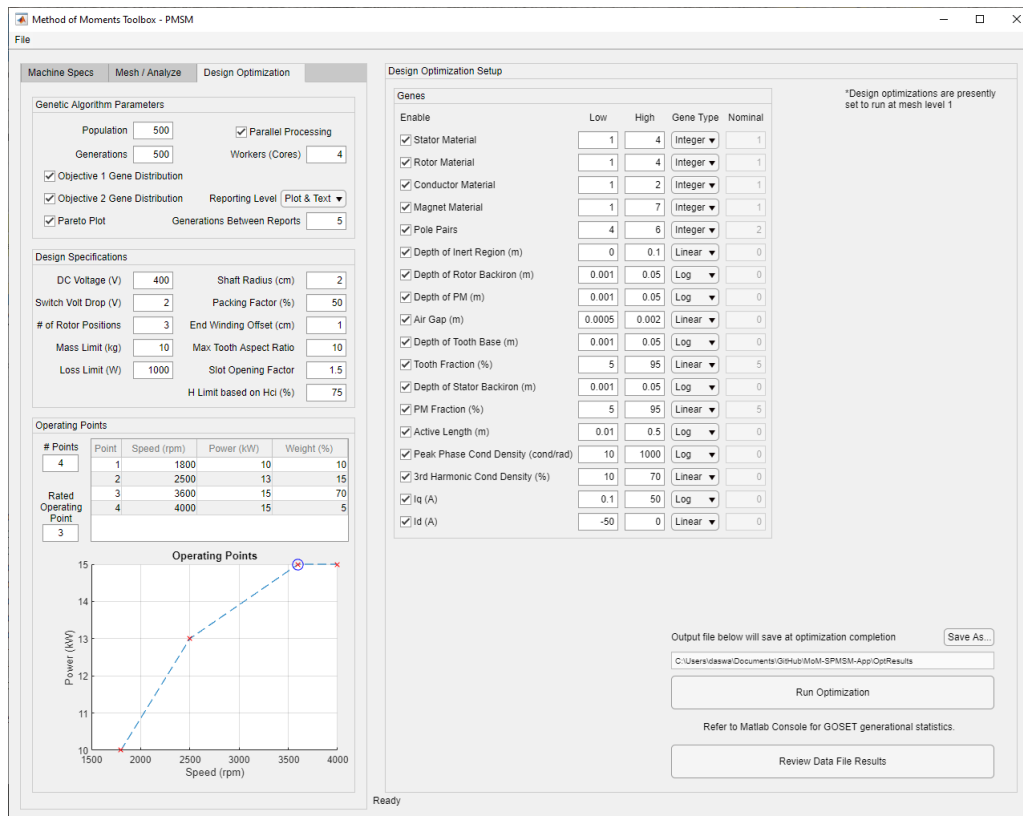


Figure I.1.19.2 MoM toolbox graphical user interface. Figure by Sudhoff/Pekarek research team.

Subtask 2.1.1 – Retention Sleeve Analysis. Perhaps the most straightforward way of increasing the power density of a drive system is by increasing the angular speed. However, centrifugal forces from the rotating components are increased with the square of the angular speed. Thus, although increasing the rotor speed does have benefits, it creates further challenges for the structural integrity of the machine. Introducing a rotor retention sleeve addresses these issues and enables extreme speed design topologies, but it creates concerns otherwise absent. Therefore, an analytical model capable of efficiently computing the existing stresses in the presence of a retention sleeve enables the enforcement of structural integrity in design optimization. Here, the importance of having an analytical model is that it facilitates a time-efficient multi-physics simulation of the machine, which includes structure. A report reviewing elasticity and failure theory of isotropic and anisotropic materials, and their implications in rotor structural analysis has been prepared as a BP2: Q2 milestone. Note that unlike the work in the literature, the model developed under this effort is valid for non-axisymmetric geometries. A validation result of this model for anisotropic sleeves is shown in Figure I.1.19.3. Therein, the

Von Mises stress field as predicted by the developed model and that predicted by FEA are shown and can be seen to agree well.

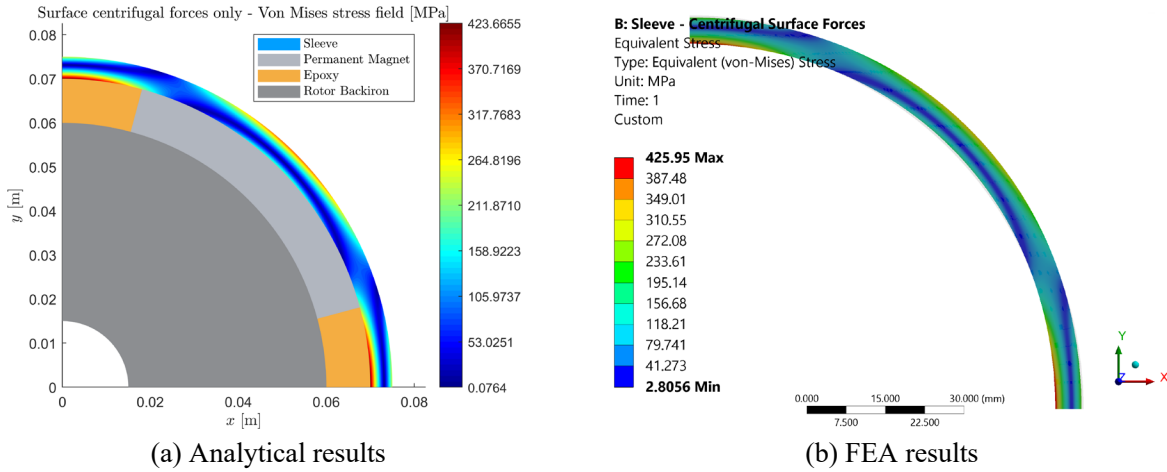


Figure I.1.19.3 Comparison of the results obtained from the proposed analytical model (a) vs FEA (b). Figure by Sudhoff/Pekarek research team.

Subtask 2.1.3 – ICPM Evaluation. The team has developed the topology of an inert core machine (ICM) that will be evaluated using the MoM toolbox. The ICM is shown in Figure I.1.19.4. As shown, the stator consists of conductors placed within a traditional laminated steel structure. The rotor has poles that are positioned within and outside of the stator. The inner and outer rotor sections each contain permanent-magnet-based poles that are configured as Halbach arrays and are arranged to establish flux in a radial direction across the airgaps. These arrays are arranged so that no rotor steel is needed to establish the flux path within the rotor. Although there is PM material in this topology, a goal will be to utilize non-rare-earth magnets in much of the array segments. Indeed, within the optimization, the height, depth, and material for each section will be included as design variables. Further evaluation of the rotor reveals that the magnets are placed upon aluminum structures that are selected over steel due to their relatively low mass and high strength. The promising aspects of this topology are the potential to reduce magnet and steel cost by using Al and non-rare-earth magnets. In BP2-Q2, a MoM model of the machine has been derived. A single pole of the machine with the flux lines over the pole that is meshed, and an adjacent pole is depicted in Figure I.1.19.5. This model will be utilized in optimization studies in BP2-Q3.

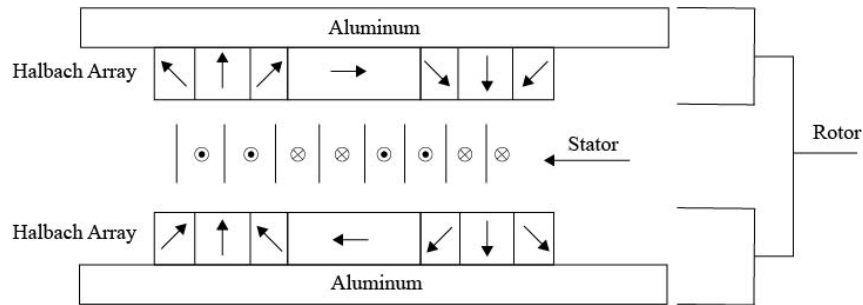


Figure I.1.19.4 Inert core machine. Figure by Sudhoff/Pekarek research team.

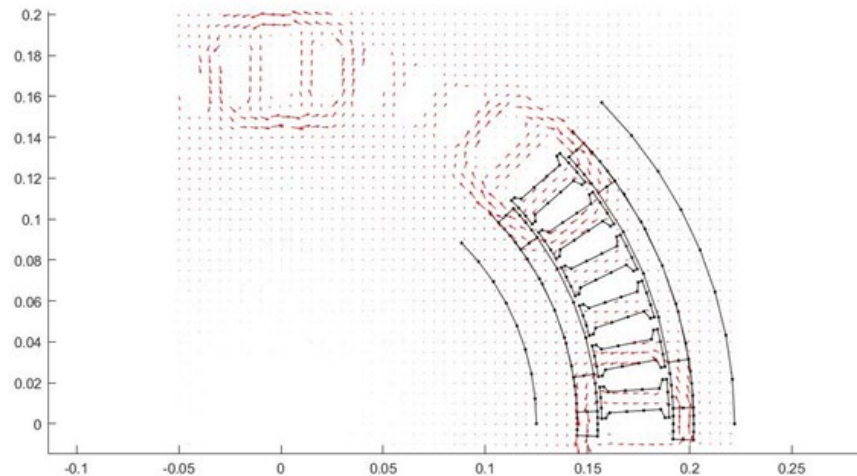


Figure 1.1.19.5 MoM generated flux lines of inert core machine. Figure by Sudhoff/Pekarek research team.

Conclusions

Progress in this effort have been in two general areas: (i) novel machine designs, and (ii) improvements in design methods; both will lead to superior drive systems and meeting roadmap goals. Under (i), the most exciting development is the Dual Rotor Homopolar AC Machine. As discussed, this machine features an infinite constant power speed range in addition to other attributes. Achievements with regard to (ii) include (a) a new and powerful method for high-speed rotor structural analysis facilitating sleeve design, (b) a new and computationally favorable method of including a time-domain inverter-machine simulation integral into the design process, and most excitingly (c) an alternative to computationally intensive FEA based design built on the Method of Moments.

Key Publications

1. Horvath, Daniel, Ross Howard, and Steven Pekarek. "Lorentz Force/Torque Calculation in 2-D Method of Moments." *IEEE Transactions on Magnetics* 56, no. 8 (June 17, 2020): 1–8.
<https://doi.org/10.1109/tmag.2020.3002982>.

Acknowledgements

Although Purdue is collaborating with the entire consortium, the relationship with Sandia National Laboratories has been particularly helpful. Thus, the help and contributions by Jason Neely, Lee Rashkin, Todd Monson, and Vipin Gupta are particularly recognized.

I.1.20 Integration Methods for High-Density Integrated Electric Drives (University of Arkansas)

H. Alan Mantooth, Principal Investigator

Department of Electrical Engineering
University of Arkansas
1475 West Cato Springs Road, Room 211
Fayetteville, AR 72701
Email: mantooth@uark.edu

Fang Luo, Principal Investigator

Department of Electrical and Computer Engineering,
Stony Brook University (SUNY at Stony Brook),
259 Light Engineering Building, Stony Brook, NY 11794-2350
Email: fang.luo@stonybrook.edu

Susan Rogers, DOE Technology Development Manager

U.S. Department of Energy
Email: susan.rogers@ee.doe.gov

Start Date: October 1, 2019

End Date: September 30, 2020

Project Funding: \$300,000

DOE share: \$300,000

Non-DOE share: \$0

Project Introduction

This project focuses on two key aspects of advancing electric drive technologies: integrated circuits and power electronic packaging. As part of the team's electronics portion, this project seeks to provide technologies that enable new power density advances. The first technology effort is integrating gate driving, sensing, and protection functions into the various packaging platforms that will be pursued by the team. Several technologies are possible, but the most advanced is silicon carbide (SiC) based integrated circuitry that can be co-packaged with the SiC power devices. The team will pursue designs that serve the target electric drive train's specifications but can survive at junction temperatures expected to enhance power density while maintaining robustness and resiliency. The second technology effort is in advancing electronic packaging for electric drive train applications. Getting the most out of the advances in wide-bandgap power semiconductor devices requires attention to careful packaging to minimize parasitic electrical influences on circuit performance and generated electromagnetic interference. Thermal management of the power devices and the surrounding circuit components must also be carefully managed. This leads to tradeoffs in the layout, arrangement, and interconnection of electronic components to balance these items. This effort will be performed in collaboration with several other organizations to achieve power density improvements for electric drives.

Objectives

The objective of the project is to research, develop, and test a heterogeneously integrated power module platform that will insert into a traction inverter system for power electronics modules capable of the following:

Table I.1.20.1 Power Electronics Requirements

Power Electronics Requirements	
Parameter	Measure
Cost (\$/kW)	≤ 2.7
Power Density (kW/L)	≥ 100
System Peak Power Rating (kW)	100

During the second budget period, the project focused on designing and fabricating a Gen 1 Stacked SiC module and a flip-chip SiC module along with high-temperature IC fabrication and testing. Activities to support them include:

- In-house Gen 1 SiC module fabrication and testing
- Reliability analysis and evaluation of Gen 1
- Integrated module validation with silicon gate driver and decoupling capacitors
- High-temperature SiC IC fabrication and unit test and evaluation
- Motor drive system EMI analysis/modeling and EMI filter design
- Integrated EMI filter design
- System/converter level packaging design and system integration concepts
- High-density current and voltage (and other) sensing.

Approach

The packaging research approach was to develop a detailed power module fabrication procedure and to fabricate the necessary parts of the power module, such as interposers, housing, and direct bond copper (DBC) substrates. Later parts came as assembly and testing of the integrated components such as a gate driver board and an isolated power supply board integrated with the differential board. For the IC design group, the focus was to test and evaluate the performance of the fabricated gate driver circuits on the SiC process and propose necessary modifications to the processing module and the circuit architectures. The focus was to continue reviewing possible integration solutions for the sensors and testing and evaluating the fabricated sensor interface circuits mainly designed for a GaN hall sensor for the integration of power electronic components. The UA team broke down its activities into the following tasks and subtasks across these three areas (taken from the Statement of Project Objectives or SOPO). The tasking begins with 2.x being budget period 2. And it is important to note that the project's budget period 2 runs from April 1, 2020 – March 31, 2021. Some tasking below is in progress.

Task 2.1 – Stacked and flip-chip module fabrication and testing:

Subtask 2.1.1 – Module layout, 3D modeling, and parasitic extraction

Subtask 2.1.2 – Module layout, circuit-level simulation, and design iteration

Subtask 2.1.3 – Process and material system validation

Subtask 2.1.4 – Dummy module fabrication and parasitic measurement (after 9/30/2020)

Task 2.2 – High-temperature SiC integrated circuit fabrication:

Subtask 2.2.1 – IC final verifications and tape out

Subtask 2.2.2 – IC fabrication

Subtask 2.2.3 – IC test and evaluation (gate driver, protection, power supply, interface, sensors, devices, and passives)

Task 2.3 – Motor drive system integration considerations (all in progress and not being reported here):

Subtask 2.3.1 – EMI modeling

Subtask 2.3.2 – EMI filter design

Subtask 2.3.3 – EMI filter integration plan for converter assembly in BP3

Results

On the packaging side of the project, a stacked half-bridge (HB) power module was designed with integrated gate driver boards. The power module was validated through ANSYS™ and SolidWorks simulations. The proposed power modules' fabrication procedure is planned in detail, and necessary modifications were applied to the fixtures and housings. Different fabrication settings were developed and tested for comparison purposes. Then, the most preferred approaches were selected for fabricating each part of the power module. Gold-plated AlN DBC substrates are used. AlN has better thermal performance in comparison with Al₂O₃. The gold layer on the DBC eases the attachment processes. These substrates are etched and diced in-house. The pressure-less silver sintering approach was tested successfully using a few dummy die and DBC pieces. An electroless gold plating procedure was developed for in-house die plating. Other nickel and gold plating thicknesses are tested to achieve consistent plating quality on the die for electroless gold plating. Figure I.1.20.1 shows a comparison between the plating thicknesses and their resultant plating quality. The electroless plated die is also characterized under a probe station. Two interposers are fabricated, one with a ceramic resin using a Formlabs 3D printer and the other using laminated Dupont 9k7 low-temperature co-fired ceramic (LTCC) sheets. The two parts were fabricated and compared in terms of weight, warpage, cost, and fabrication time in Table I.1.20.2.

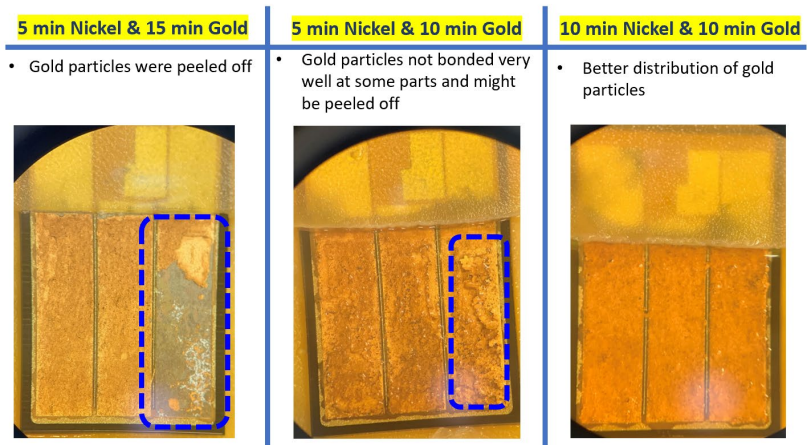


Figure I.1.20.1 A comparison between three different die electroless gold plating procedures.

Table I.1.20.2 A comparison between LTCC-based and 3D printed interposers

	LTCC Interposer	Ceramic 3D Printed interposer
Weight (g)	10.5	6.3
Warpage (µm)	46	112
Material Cost	\$\$\$	\$
Fabrication Time	++	++

The housing was 3D printed using high-temperature resin. The 3D print settings are important to successfully achieve a non-distorted object. Thus, several approaches, such as thin high-density 3D printing supports versus thick low-density supports, were tested and compared. The slope of the part and the height of supports from the 3D printer platform are also as effective as the supports' thickness and density. The post-curing process also has a high impact on the thermal characteristics of the 3D printed part. The best approach is to dry the pieces for more than two days, cure the parts with LED light for two hours at 80°C, and then use a programmable oven to heat the part to 160°C for two to three hours. It was determined that the order of the

curing process is as important as the process itself. For instance, a vice versa curing approach, i.e., heat treatment in 160°C for two hours first and LED curing at 80°C for two hours next, result in immediate fractures in the part. High-temperature material was also investigated to machine the same housing parts and compare them to the 3D printed parts. The approaches above are used to fabricate different parts of the power module.

A dummy power module is going to be assembled using the dummy parts to evaluate the fabrication process. Changes will be applied to the method if necessary, and then the power module with the functional die will be fabricated and electrically characterized. A SiC-based stacked power module was designed to enable integrating the gate driver PCBs in the power module. The power module's thermal performance was improved, and a process was developed for fabricating this power module architecture. Several methods were compared in the fabrication of each part of this power module, such as the electroless plating process, housing, and interposer. The best solution was selected to be utilized in the final power module assembly according to the comparison results.

Thermal pyrolytic graphite or TPG material can be implemented to improve a power module's thermal performance. TPG is highly crystalline graphite with well-aligned graphene planes. It is an anisotropic material where the in-plane thermal conductivity is 1700 W/m-K, and the through-plane thermal conductivity is very low (~ 10 W/m-K). This property of TPG can be extracted to provide a high heat dissipation path for the excess heat generated in a high-power electronics module through the high conductivity plane. TPG then blocks the heat flow through the low conductivity plane to avoid heat coupling from the various adjacent devices placed in the same plane. The team has proposed embedded thermal management structures, as shown in Figure I.1.20.2 (b), compared to a traditional design, as shown in Figure I.1.20.2 (a). The team has conducted both FEA simulations and experiments.



Figure I.1.20.2 (a) Preliminary power module with a single device and copper substrate, (b) Preliminary power module with a single device and metal encapsulated TPG substrate.

FEA thermal simulation indicated a junction temperature drop of up to 10°C with a metal encapsulated TPG substrate compared to a traditional DBC substrate and aluminum heatsink for a high-density power electronics module. It is found from the experiments conducted that the junction temperature for two modules with identical materials and conditions (10 W heat power loss and forced air cooling) give $\sim 6.7^\circ\text{C}$ less junction temperature for the module with WCu encapsulated TPG as a substrate [Figure I.1.20.3 (b)] as compared to a copper substrate, which verified the FEA results (temperature reduction with TPG embedded substrate for single power device = 4.5°C). The pictures shown below were taken using a thermal IR camera. When two devices are heated up, the junction temperature drop increases from 6.7°C to 10°C in the case of the metal encapsulated TPG substrate [Figure I.1.20.3 (d)] as compared to copper [Figure I.1.20.3 (c)], which demonstrates the power coupling reduction effect. It also verifies the FEA simulations (temperature reduction with TPG embedded substrate for two power devices = 9°C) for the same cases for TPG embedded substrate

and copper substrate. Hence, the use of TPG as a substrate or baseplate can dissipate more heat from the module and reduce power coupling among the devices and thus reduce the junction temperature of the module, leading to a more reliable power module.

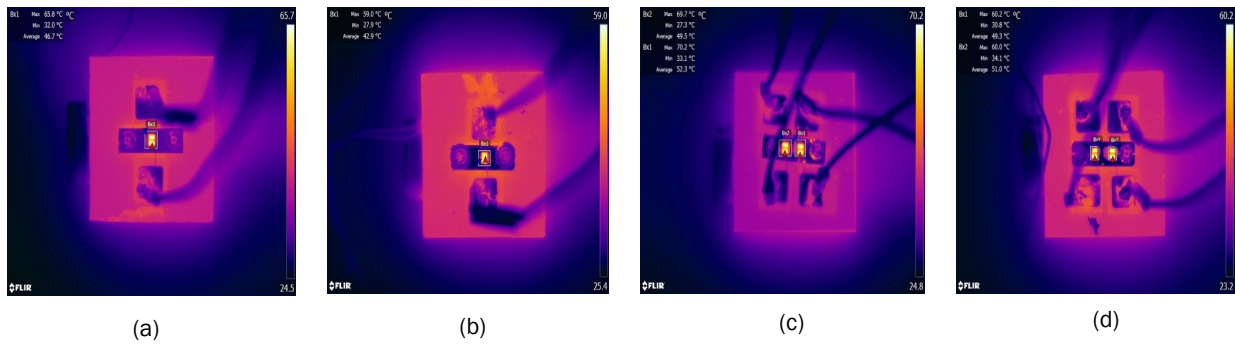


Figure I.1.20.3 (a) Thermal image for a single power device with a copper substrate, (b) Thermal image for a single power device with a TPG embedded substrate, (c) Thermal image for two power devices with copper substrates, (d) Thermal image for two power devices with TPG embedded substrates.

The UA IC design team has been actively designing gate drivers and protection circuits on the Fraunhofer 1 μm SiC CMOS process. The team received two wafers in March 2020 and the remaining four wafers in May 2020. Since then, the team tested the discrete devices along with the circuits fabricated on those wafers. The process is still in its development phase, and each of those wafers has gone through a unique fabrication process module. The idea was to examine each process module's effect on the fabricated SiC NMOS and PMOS device characteristics. For example, wafer#3 had received P-type polysilicon with poly silicidation having Pt as routing metal. Wafer#4 also has P-type polysilicon, but without any poly silicidation and has Al as routing metal. On the other hand, wafer#6 has N-type polysilicon with Al metallization. Figure I.1.20.4 shows the threshold voltage for 20 μm / 2 μm NFETs and PFETs over the temperature range of 25°C to 500°C on those three different wafers. The IC design team is carefully observing those variations and proposing possible modifications for the process modules to the fabrication facilities to achieve the best possible discrete devices.

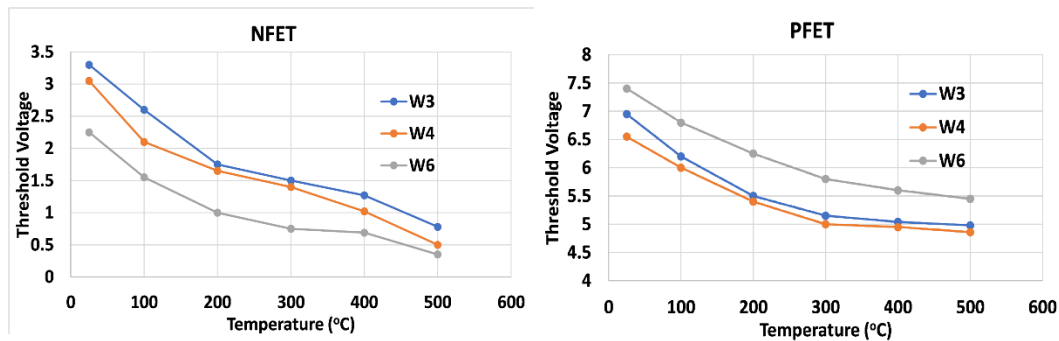


Figure I.1.20.4 Threshold voltage variation over temperature for NFET (left) and PFET (right) from wafers# 3, 4 and 6.

The team also tested four different gate driver variants fabricated on those wafers. Each of those gate drivers is unique in terms of architecture and device length. Among them, variant #2 is all NMOS based, preliminarily designed to counter the poor PFET performance revealed during the first characterization run. However, as PFET performance became relatively better during this run, the team is not considering this variant any further. Figure I.1.20.5 shows the die micrographs of three other variants, while Table I.1.20.3 summarizes the measured performance of those variants with 10 nF external loading.

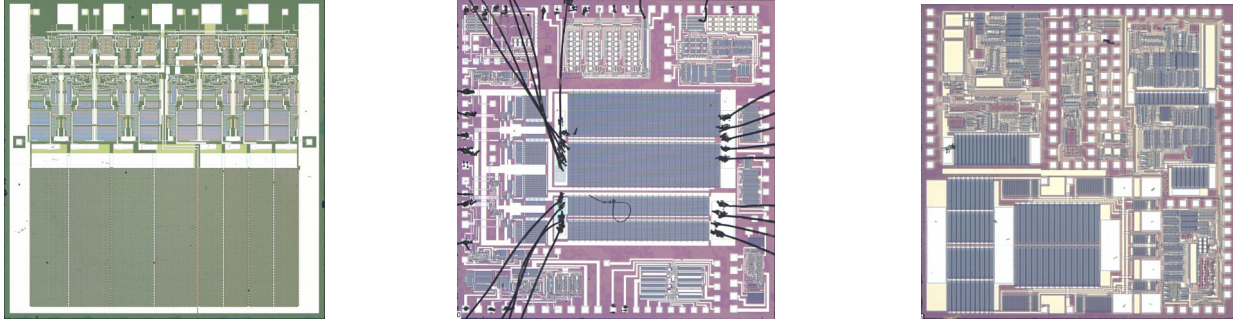


Figure I.1.20.5 Die micrograph of fabricated SiC gate driver variant#1 (left), variant#3 (middle) and variant#4 (right). Die area 4.94 mm X 4.94mm.

Table I.1.20.3 Gate driver performance figure at room temperature and elevated temperature

Gate Driver Variant	Parameters	Measured Result (25°C) @ CL=10 nF	Measured Result (200°C) @ CL=10 nF
Variant #1	Rise time	867 ns	687 ns
	Fall time	485 ns	294 ns
Variant #3	Rise time	446 ns	402 ns
	Fall time	555 ns	280 ns
Variant #4	Rise time	582 ns	429 ns
	Fall time	366 ns	172 ns

The measured results verified the functionality of the gate driver both at room temperature and at elevated temperature. A few modifications to the fabrication flow are currently being considered to improve the driver performance, such as Ti-Al silicidation, to reduce p-type contact resistance for sourcing more current and local poly-silicidation to reduce parasitic poly trace resistance. Also, careful optimization in the sizing of the output drive slices and buffer chains can push the gate driver performance figures towards further improvements in the subsequent runs.

For extracting current information out of the power devices, different current measurement methods such as Shunt resistors [1], Hall current sensors [2], GMR current sensors [3], GMI current sensors [4], Rogowski coils [5]-[7], and hybrid current sensors (combinations of two different types) [8]-[9] have been studied. Comparing various current measuring approaches shows features like small size, linearity, DC current measuring capability, and sensitivity of Hall, GMR, and GMI current sensors make them appropriate for integrating them inside the power modules. On the other hand, the GMI sensors' response to high-frequency AC current characteristics, such as frequency, amplitude, and mean value, are the main disadvantages of GMI sensors [4]. To have a clear insight into different sensors' performance, a double pulse test (DPT) on a half-bridge insulated gate bipolar transistor (IGBT) module has been implemented, as shown in Figure I.1.20.6. A current probe with a bandwidth of 120 MHz, a Rogowski coil sensor with 20 kHz, and a hall effect sensor, ACS770, from Allegro with a 120 kHz bandwidth are used to measure the inductor current in the test. As shown in Figure I.1.20.6, the green waveform is the current measured by the hall sensor, the red curve is the measured current with the Rogowski coil sensor, and the orange waveform is related to the current probe. It can be observed that all three current measurement methods result in similar values. Furthermore, comparing waveforms of the Rogowski coil and current probe with the Hall effect sensor, the mismatch amongst the waveforms because of the rise time of the Hall sensor is clear. The datasheet of ACS770 determines this time to be around 4.1 μ s [10]. While working at high frequencies, factors like skin effect can change the magnetic field distribution and decrease the accuracy of the current sensors. For this reason, placing the sensors in locations with less deviation in their magnetic field at high frequencies is essential. Different methods like folding the current-

carrying trace [11], magnetic field compensators [12], and using an image current-carrying trace have been proposed to compensate for the magnetic field deviation.

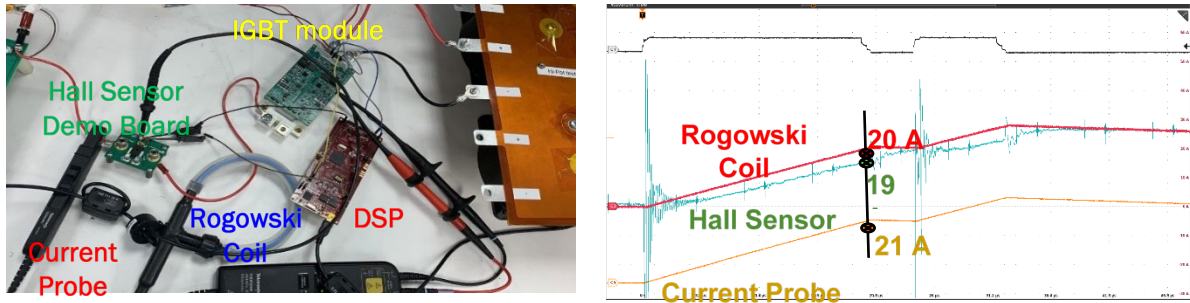


Figure I.1.20.6 Current sensing test setup (left), test results (right).

Interface circuits for the Hall sensors have been fabricated using 180 nm technology from the XFAB foundry. The die image is shown in Figure I.1.20.7 (a). The on-chip area occupied by the interface circuits is 1200 μm x 340 μm. The chip is packaged using a QFN, 40 pin, 6 mm x 6 mm package. The circuit is comprised of an offset-cancellation technique called chopper stabilization (CHS). It is combined with the Hall sensor's current spinning to separate the sensor offset and the Hall voltage. The Hall voltage is modulated while the offset remains DC and gets filtered out. Some residual offset may remain due to structural mismatches. The Hall voltage is then amplified and demodulated. Finally, an instrumentation amplifier converts the differential signal to a single-ended output. The PCB designed for the testing of the interface circuit is shown in Figure I.1.20.7 (b). It includes testability options to test the CHS technique independent of the sensor. The CHS circuit results show that the interface circuit provide a gain of ~120 V/V (Table I.1.20.4).

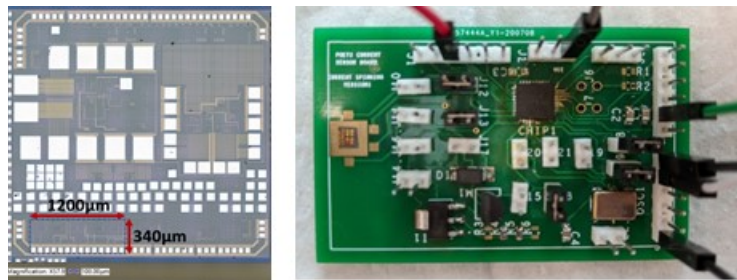


Figure I.1.20.7 (a) Die image, (b) PCB designed for testing the sensor interface circuit.

Table I.1.20.4 Measurement results of CHS circuit

VIN	VOUT
$\Delta V_{DC} = 1 \text{ mV}$	$\Delta V_{DC} = 119 \text{ mV}$
2 mV_{pk-pk}	240 mV_{pk-pk}
5 mV_{pk-pk}	610 mV_{pk-pk}
7 mV_{pk-pk}	840 mV_{pk-pk}
10 mV_{pk-pk}	1.2 V_{pk-pk}

The function of CHS is that it rejects the offset of the op amp as well as any externally applied offset. To test this functionality, a DC offset was externally applied after the modulation step. It did not affect the output, which means it got rejected by the filter, as required. This shows that the circuit can reject the offset of the Hall sensor after it is separated using the current spinning technique. The GaN Hall sensor designed by the UA team is also attached to the PCB, as shown in Figure I.1.20.7 (b) (device on far left). Amplification of the Hall voltage and reduction in the offset can be observed in the sensor's preliminary tests with the interface circuit. The characterization of the sensor with the readout circuit is currently being carried out.

Conclusions

UA research is underway, with both packaging and IC design levels in full swing. Biweekly meetings are being held with the broader team, and UA-only meetings are being held in the intermediate weeks such that a project meeting is held each week. At present, the overall project is on track in terms of its schedule, and no significant risks to the schedule in BP2 have arisen.

Key Publications

1. A. Abbasi, A. Faruque, S. Roy, R. C. Murphree, T. Erlbacher, H. A. Mantooh, "Gate Driver Design in a 1um SiC CMOS Process for Heterogeneous Integration Inside SiC Power Module", *53rd International Symposium on Microelectronics: A Global Virtual Event* [accepted].

References

1. C. Xiao, L. Zhao, T. Asada, W. G. Odendaal and J. D. van Wyk, "An overview of integratable current sensor technologies," 38th IAS Annual Meeting on Conference Record of the Industry Applications Conference, 2003., Salt Lake City, UT, USA, 2003, pp. 1251-1258 vol.2.
2. <https://patents.google.com/patent/US6819095B1/en>
3. N. Shah et al., "Power electronics modules for inverter applications using flip-chip on flex- circuit technology," Conference Record of the 2004 IEEE Industry Applications Conference, 2004. 39th IAS Annual Meeting., Seattle, WA, USA, 2004, pp. 1526-1533 vol.3.
4. Asfour, A., Zidi, M., & Yonnet, J. (2014). High frequency amplitude detector for GMI magnetic sensors. *Sensors (Basel, Switzerland)*, 14(12), 24502-24522. doi:10.3390/s141224502
5. Zhao, L., van Wyk, J. D., & Odendaal, W. G. (2004). Planar embedded pick-up coil sensor for power electronic modules. Paper presented at the, 2 945-951 vol.2. doi:10.1109/APEC.2004.1295936
6. Tukuda, M., Koga, M., Nakashima, K., & Omura, I. (2016). Micro PCB rogowski coil for current monitoring and protection of high voltage power modules. *Microelectronics Reliability*, 64, 479-483. doi:10.1016/j.microrel.2016.07.011
7. Verlag, V. (2016). Application-specific micro rogowski coil for power modules - design tool, novel coil pattern and demonstration. (pp. 1-1) VDE Verlag
8. Nibir, S. J., Hauer, S., Biglarbegan, M., & Parkhideh, B. (2018). Wideband contactless current sensing using hybrid magnetoresistor-rogowski sensor in high frequency power electronic converters. Paper presented at the 904-908. doi:10.1109/APEC.2018.8341121
9. Troster, N., Eisenhardt, T., Zehelein, M., Wolfle, J., Ruthardt, J., & Roth-Stielow, J. (2018). Improvements of a coaxial current sensor with a wide bandwidth based on the HOKA principle. Paper presented at the 1-P.9.
10. Allegro, "Thermally Enhanced, Fully Integrated, Hall-Effect-Based High-Precision Linear Current Sensor I.C. with 100 $\mu\Omega$ Current Conductor," ACS770xCB datasheet, May. 2019
11. Nibir, S. J., Hurwitz, E., Karami, M., & Parkhideh, B. (2016). A technique to enhance the frequency bandwidth of contactless magnetoresistive current sensors. *IEEE Transactions on Industrial Electronics*, 63(9), 5682-5686. doi:10.1109/TIE.2016.2561264
12. Nibir, S. J., & Parkhideh, B. (2018). Magnetoresistor with planar magnetic concentrator as wideband contactless current sensor for power electronics applications. *IEEE Transactions on Industrial Electronics*, 65(3),

I.1.21 Ultra-High-Speed, High-Temperature Motor (University of Illinois, Urbana-Champaign)

Joseph Lyding, Principal Investigator

University of Illinois, Urbana-Champaign
306 North Wright Street
Urbana, IL 61801
Email: lyding@illinois.edu

Lauren White, Principal Investigator

John Deere Electronic Solutions
4101 19th Avenue North
Fargo, ND 58102
Email: whitelauraem@johndeere.com

Susan Rogers, DOE Technology Development Manager

U.S. Department of Energy
Email: susan.rogers@ee.doe.gov

Start Date: October 2019

End Date: March 2022

Project Funding: \$875,000

DOE share: \$700,000

Non-DOE share: \$175,000

Project Introduction

This project addresses two key targets from the U.S. Drive Roadmap by developing advanced thermal management techniques along with new materials to lower cost, reduce size, and improve reliability of electric powertrains. The project is specifically a response to the Advanced Vehicle Technology Office's call for an electric motor rated for 50 kW/L – 8X the power density compared to the 2015 baseline. The target motor is rated for 125 kW with an operating speed higher than 20,000 RPM, reliability up to 300,000 miles, and a production cost of \$6/kW. To strengthen U.S. manufacturing, supply chain, and distribution sectors, this motor is being developed without rare-Earth elements and with strategic small business partners who are growing and creating domestic jobs.

Objectives

This project will achieve AVTO's performance targets by developing three key technologies: high-temperature stator insulation materials capable of operating up to 650°C, soft magnetic composites rated for operation at 60,000 RPM, and wide-bandgap silicon carbide power electronics rated for 100 kHz switching frequency and 1000V DC bus voltage.

Approach

The project team is leveraging in-house expertise and strategic small business partnerships to reach these objectives. High-temperature insulation materials are being developed by combining advances in ceramic adhesive formulations with industrial expertise in high-volume coating production to enable higher power density and increased reliability against transient thermal loads. Soft magnetic composites are being developed by combining the merits of sol-gel nanoparticles with industrial-grade 3D-printing to increase motor efficiency during high-frequency and high-flux operation. These composite materials are manufactured without energy-intensive melt-processing and welding operations used in current state-of-the-art production facilities and the monolithic design increases reliability compared to traditional spot-welded laminations. The silicon carbide inverter is being commissioned through a joint development agreement between University of Illinois and John Deere Electronic Solutions. The 100 kHz and 1000V switching capability enable high-speed operation and reduction in the volume of passive components to increase power density.

Results

To date, the project team has successfully produced and validated high-temperature insulation for 650°C operation.

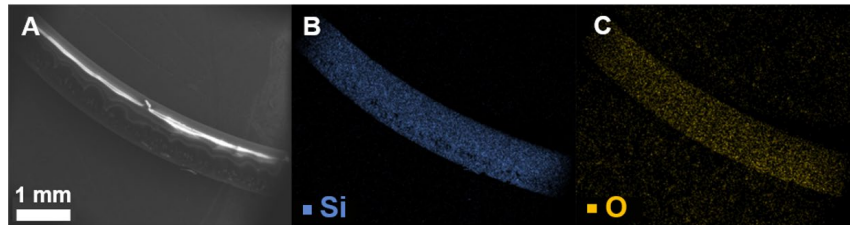


Figure I.1.21.1 X-ray micrograph of copper wire coated with high-temperature silox insulation.¹⁶

Figure I.1.21.1A shows a copper wire conformally coated in a layer of high-temperature silox insulation, with Figure I.1.21.1B and Figure I.1.21.1C confirming the uniform distribution of a silicon-oxygen layer on the wire surface. These samples were tested against state-of-the-art insulation materials to benchmark their dielectric and thermal performance.

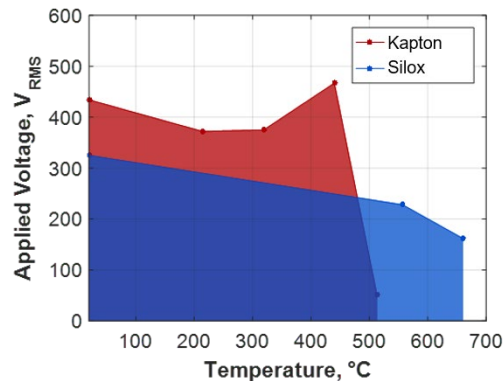


Figure I.1.21.2 Dielectric breakdown voltage of Kapton and silox magnet wire at different temperatures.¹⁷

Figure I.1.21.2 compares the dielectric performance of Kapton and silox magnet wire, showing that silox insulation enables performance up to 650°C – nearly 150°C higher than Kapton. To visualize the benefits of high-temperature operation in a motor prototype, a commercial solenoid design was selected to compare the force-generation of different dielectric insulation materials. To date, two prototypes have been built and tested with polyurethane and ceramawire insulations, with Kapton and silox prototypes currently in development and testing.



Figure I.1.21.3 A) Design, B) polyurethane prototype, and C) ceramawire prototype of the solenoid motor.

¹⁶ Arastu et al., “Magnet Wire for Venus Exploration.”

¹⁷ Arastu et al.

The solenoid prototypes shown in Figure I.1.21.3 have been experimentally tested until failure to determine their force and temperature performance as a function of applied current under fixed cooling conditions.

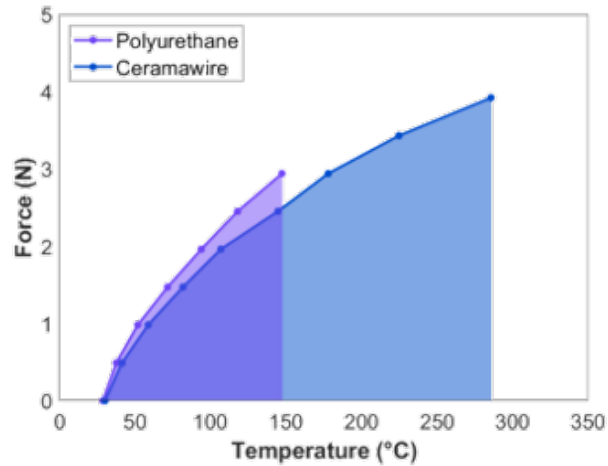


Figure I.1.21.4 Force vs. temperature curves for solenoid prototypes with different insulation materials.

The correlation curve between force and temperature for the polyurethane and ceramawire prototypes in Figure I.1.21.4 shows that increasing the temperature rating by 137°C leads to a 34% increase in force generation. This trend will continue to develop as we build and test Kapton and silox prototypes.

In a parallel effort, the project team is investigating the mechanical integrity of soft magnetic composites under high-speed operation to determine critical speeds up to 60,000 RPM.

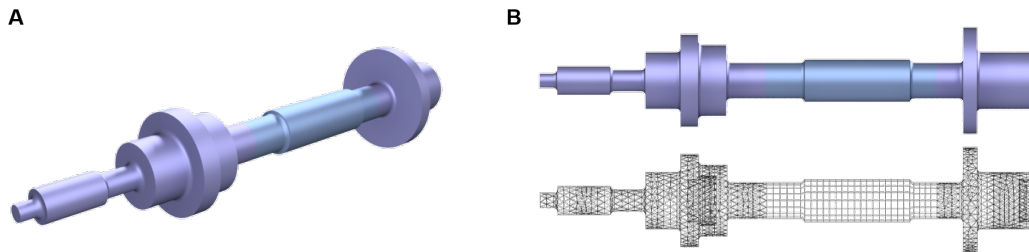


Figure I.1.21.5 A) Isometric and B) side view of the model rotor with the accompanying mesh for critical speed analysis.

Figure I.1.21.5 shows the rotor design chosen to develop a modeling method for calculating the critical speeds of an isotropic magnetic composite. This design has been used to determine the critical speeds of two rotors – one composed of iron and the other composed of mullite.

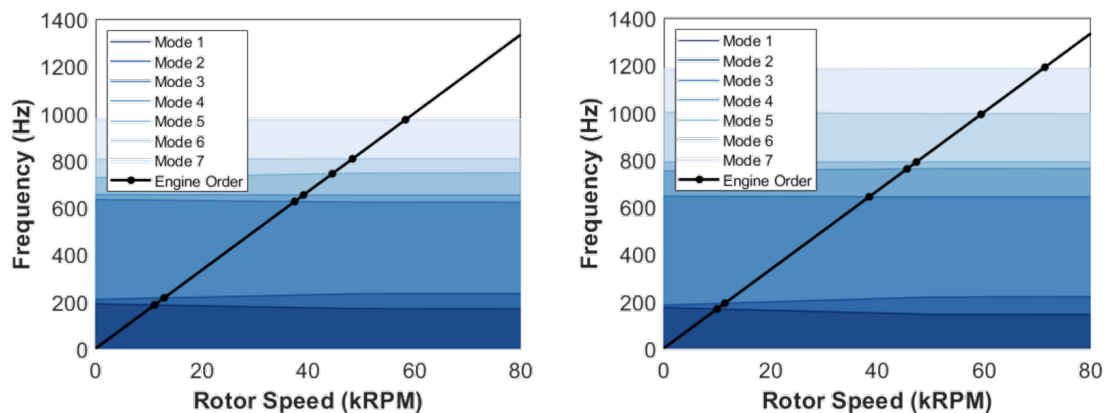


Figure I.1.21.6 Campbell diagrams for the model rotor consisting of solid A) iron and B) mullite.

Figure I.1.21.6 shows the results of the critical speed analysis for the iron and mullite rotors, setting a baseline for the number and dispersion of critical speeds for the constituent materials of the magnetic composite – in this case, 7 critical speeds for iron and 6 critical speeds for mullite. As this investigation continues, these rotor models will be combined using a composite analysis framework that takes into account the volume fraction of each material and their composite mechanical properties. The composite analysis tool will then be applied to analyze the critical speeds and amplitudes of the proposed 125 kW electric motor.

A related effort is focused on commissioning our existing silicon carbide inverter to drive the prototype electric motor. To this end, a commercial rotating motor has been experimentally tested and modeled to validate the accuracy of the simulated torque-speed analysis when the motor is driven by the silicon carbide inverter.

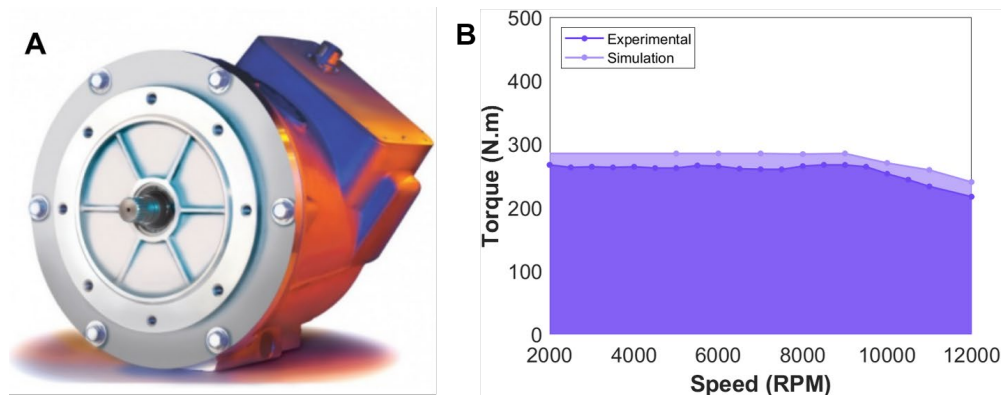


Figure I.1.21.7 A) Isometric view and torque-speed curves for the model motor.¹⁸

The results in Figure I.1.21.7B show strong agreement between the torque-speed values from the finite-elements-based simulation and the experimental dynamometer test. This marks a significant step in showing the capability of our silicon carbide inverter to drive a high-speed motor as well as the ability of our simulation tools to predict torque-speed performance before conducting an experimental test.

Conclusions

To date, we have demonstrated that high-temperature silox insulation can be manufactured to outperform the thermal stability of current state-of-the-art materials. The benefits of this increase in thermal stability have

¹⁸ BorgWarner Inc., “HVH250 -115 Electric Motor.”

been demonstrated in solenoid motors built using different insulation materials, where higher-temperature materials lead to 34% higher force generation under the same operating conditions. In parallel, we have developed simulation methods to determine the critical speeds of soft magnetic composite rotors and predict the torque-speed curves of rotating motors driven by our existing silicon carbide inverter architecture. Using this foundation in validated computational and experimental techniques, we are continuing to progress towards our objectives to develop high-temperature coils, high-speed magnetic cores, and high-frequency power electronics to achieve the AVTO's performance targets for electric powertrains.

Key Publications

Publications are currently in preparation for this work.

References

1. Arastu, Faraz, Xuan Yi, Mayank Garg, Kiruba Haran, and Joseph Lyding. "Magnet Wire for Venus Exploration." In *SciTech Forum*, 1–7. AIAA, 2019.
2. BorgWarner Inc. "HVH250 -115 Electric Motor," 2016.

I.1.22 Cost competitive, high-Performance, highly Reliable (CPR) Power Devices on SiC and GaN

Woongie Sung, Principal Investigator

Research Foundation for SUNY Polytechnic Institute
257 Fuller Road
Albany, NY 12203
Email: wsung@sunypoly.edu

Susan Rogers, DOE Technology Development Manager

U.S. Department of Energy
Email: susan.rogers@ee.doe.gov

Start Date: April 16, 2019
Project Funding: \$333,000

End Date: April 15, 2024
DOE share: \$300,000

Non-DOE share: \$33,000

Project Introduction

The primary objective of this project is to ensure that the next-generation of wide-bandgap devices have sufficient performance, reliability, and price to achieve the system-level DOE goals. In this project, we will develop 1200V SiC MOSFETs that are superior to Silicon counterpart (IGBT) in all aspects, such as cost, performance, and reliability. To accomplish the goal, many different variations in device/process design will be pursued and the proposed device will be fabricated at a production-grade cleanroom facility.

Objectives (BP1)

- Cost competitive
- High-performance ($BV=1500$ V, $R_{on,sp}=6$ m Ω -cm², $V_{th}=2$ V)
- High reliability

Approaches

Over the 5 years of the entire project span, this project aims to develop cost competitive, high performance, and highly reliable SiC MOSFETs to assist the team to achieve system level DOE goal.

Cost

A dramatic reduction in chip price can be achieved by conducting ion implantations at room temperature. Process flow will be significantly simplified by RT implants. Appropriate analyses due to RT implants will be conducted. An innovative approach for the gate oxide formation will further reduce the chip size, and thus, chip price. Unipolar diode integration within the MOSFET structure will be demonstrated.

Performance

Cell optimization will be carried out using 2-D simulation, such as reducing cell pitch and optimization of JFET region. Various edge termination structures, such as FFRs, RA-JTE, and Hybrid-JTE will be designed.

Process split, such as gate oxide using ALD, self-alignment channel, and channeling implant to form deep junction will be conducted.

Reliability

Short-circuit and avalanche characteristics will be evaluated by mixed-mode device simulations. Process split such as p-well implant and thin gate oxide will be carried out.

Results

In the first year of this project, SUNY Polytechnic Institute has fabricated SiC MOSFETs with many different design variations. As reported in the Annual Merit Review, the first group of fabricated devices (Lot 1, 1st lot in BP1) satisfies all the static performance targets.

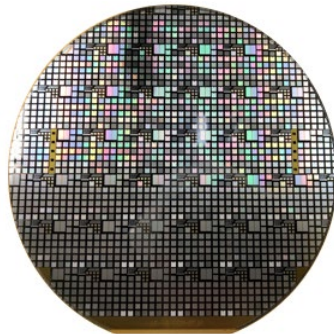
1. Lot 1 Characterization

Table I.1.22.1 summarizes wafer split and static characteristics of the nominal device from Lot 1. The nominal MOSFET has half JFET width of 0.8 μm and channel length of 0.5 μm. Different gate oxide, depth of JFET and p-well implant, and implant temperatures were investigated. Wf2 has the lowest $R_{on,sp}$ due to current spreading layer (CSL) effect. Deep p-well implant of wf3 results in the increase of $R_{on,sp}$, but the leakage current was significantly suppressed under forward blocking mode. Although all implants for wf4 were conducted at room temperature, no noticeable difference in static performances was observed. The thin gate oxide of wf5 shows higher channel mobility due to high transconductance, which allows sufficient channel conduction at lower V_{gs} . Higher channel mobility and good gate-source breakdown were achieved using thermal gate oxide (wf6). Based on results from Lot 1, it is concluded that the baseline process for the 1200V SiC MOSFET.

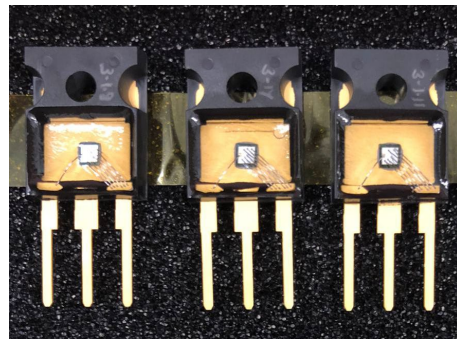
Table I.1.22.1 Summary of wafer split and static characteristics (Lot 1)

	Gate oxide (Thickness)	JFET implant depth (Implant temp.)	P-well implant depth (Implant temp.)	$R_{on,sp}$ (mohm-cm ²) ($V_{gs}=20V$)	BV (V)	Channel mobility (cm ² /Vs)
Wf1	Deposited (50nm)	0.7 μm (HT)	0.7 μm (HT)	N/A	N/A	N/A
Wf2	Deposited (50nm)	0.9 μm (HT)	0.7 μm (HT)	4.12	1559	17.3
Wf3	Deposited (50nm)	0.7 μm (HT)	0.9 μm (HT)	5.45	1555	17.6
Wf4	Deposited (50nm)	0.7 μm (RT)	0.7 μm (RT)	4.68	1559	17.5
Wf5	Deposited (25nm)	0.7 μm (HT)	0.7 μm (HT)	4.46 ($V_{gs}=12V$)	1559	26
Wf6	Thermal (50nm)	0.7 μm (HT)	0.7 μm (HT)	4.54	1558	18.7

Figure I.1.22.1 (a) shows an image of the fabricated wafer including 42 different types of devices such as MOSFET with different JFET widths, channel lengths, and cell pitches. Approximately 200 devices (Figure I.1.22.1 (b)) from Lot 1 were packaged to investigate further into reliability and ruggedness. In order to investigate into the effect of process split such as deep JFET and p-well implant, RT implant, thin gate oxide, and thermal gate oxide, MOSFETs from wf2,3,4,5, and 6 were packaged. The Ohio state university (OSU) is presently measuring reliability and ruggedness tests such as body diode degradation, short-circuit capability, and avalanche ruggedness. Furthermore, OSU is currently fabricating inverter using nominal devices of wf2.



(a)



(b)

Figure I.1.22.1 Image of (a) the fabricated wafer and (b) packaged devices from Lot 1.

2. Lot 2 Characterization

Table I.1.22.2 shows wafer split for 2nd lot. 4- different JFET doping concentrations were used to optimize JFET region in terms of specific on-resistance ($R_{on,sp}$), breakdown voltage (BV), and short-circuit (SC) capability. In previous literatures, a reduced doping concentration in the n+source, lower channel density, and use of lower gate bias have been proposed to enhance SC capability. However, these approaches result in the increase in $R_{on,sp}$. On the other hand, narrow JFET width with enhanced JFET doping concentration can improve SC capability with no major impact to $R_{on,sp}$ by reducing saturation current [1].

Table I.1.22.2 Summary of wafer split for Lot 2.

	Doping in JFET region
Wafer1	$3 \times 10^{16} \text{ cm}^{-3}$
Wafer2, 3	$5 \times 10^{16} \text{ cm}^{-3}$
Wafer4, 5	$7 \times 10^{16} \text{ cm}^{-3}$
Wafer6	$9 \times 10^{16} \text{ cm}^{-3}$

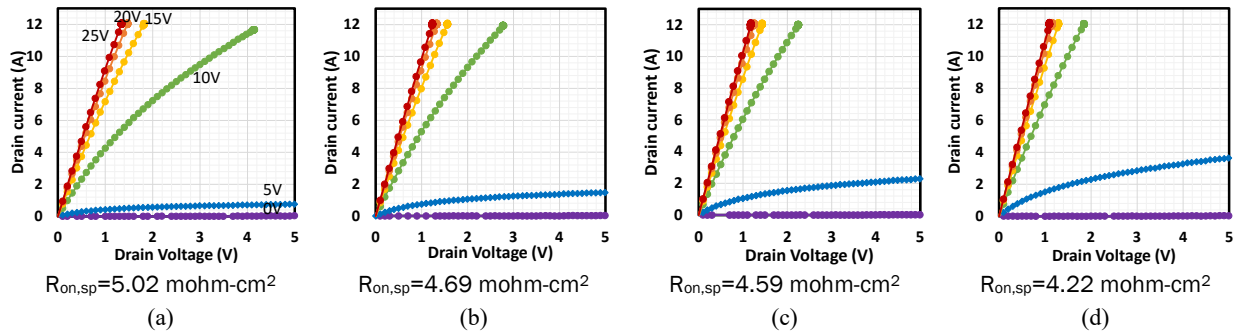


Figure I.1.22.2 Output characteristics for half JFET width of $0.6 \mu\text{m}$ and channel length of $0.5 \mu\text{m}$ of (a) JFET doping of $3 \times 10^{16} \text{ cm}^{-3}$ (Wf1), (b) JFET doping of $5 \times 10^{16} \text{ cm}^{-3}$ (Wf2) (c) JFET doping of $7 \times 10^{16} \text{ cm}^{-3}$ (Wf4), and (d) JFET doping of $9 \times 10^{16} \text{ cm}^{-3}$ (Wf6).

Figure I.1.22.2 shows output characteristics of fabricated MOSFETs with the half JFET width (W_{JFET}) of $0.6 \mu\text{m}$ and channel length (L_{ch}) of $0.5 \mu\text{m}$ for each wafer. Gate voltage is applied from 0V to 25V in increments of 5V . The enhanced JFET doping concentration provides higher conduction characteristics, which results in lower specific on-resistance. Summary of $R_{on,sp}$ as function of half JFET width with different JFET doping concentrations are shown in Figure I.1.22.3. MOSFETs with wider JFET width have lower $R_{on,sp}$ for all JFET doping concentrations. In general, narrow JFET width is preferable due to high breakdown voltage, good reliability, and good ruggedness. In order to use narrow JFET width, high JFET doping concentration should be implemented for lower $R_{on,sp}$.

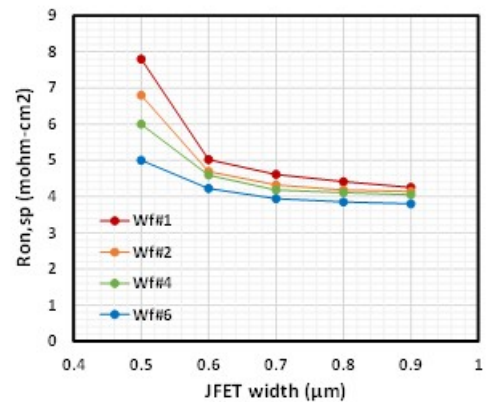


Figure I.1.22.3 Summary of specific on resistance as function of half JFET width with different JFET doping concentration.

Figure I.1.22.4 shows breakdown voltage for half JFET width for $0.6 \mu\text{m}$ and channel length of $0.5 \mu\text{m}$ with different JFET doping concentration under $V_{gs} = 0\text{V}$ and -10V . Depending on JFET doping concentration, MOSFETs have different leakage current level under forward blocking mode ($V_{gs} = 0\text{V}$); Figure I.1.22.4a. However, at $V_{gs} = -10\text{V}$, which completely closes the channel, devices with different JFET doping concentration have same breakdown voltage and leakage current; Figure I.1.22.4b. In other words, leakage current stems from the channel because high JFET doping concentration results in the reduction in channel potential within the channel region and causes a decrease in shielding effect in p-well region. Although JFET doping concentration increases, there is no negative effect on avalanche breakdown voltage under $V_{gs} = -10\text{V}$. This is because JFET

implants are shallower than P-well implants. Usually, avalanche breakdown for MOSFETs occurs in the edge of the p-well.

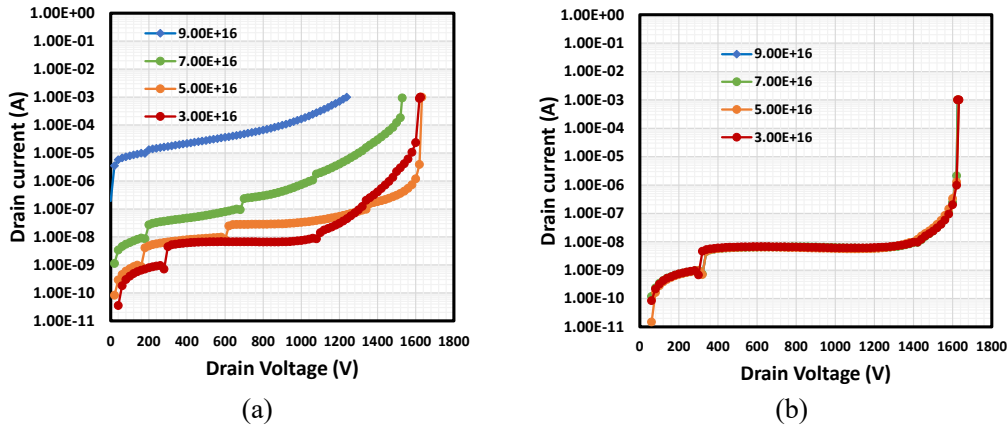


Figure I.1.22.4 BV for W_{JFET} of $0.6 \mu\text{m}$ and L_{ch} of $0.5 \mu\text{m}$ with different JFET doping (a) under $V_{gs}=0\text{V}$ and (b) $V_{gs}=-10\text{V}$

Figure I.1.22.5 shows specific on-resistance as a function of the channel length with different JFET doping concentrations. Shorter channel results in lower channel resistance, providing lower overall specific on-resistance. However, shorter channel length causes lower channel potential under forward blocking mode of operation, resulting in higher leakage current. Channel length of 0.4 and $0.5 \mu\text{m}$ has high leakage current when compared with channel length of $0.6 \mu\text{m}$, as shown in Figure I.1.22.6. The breakdown voltage of the MOSFET with channel length of $0.6 \mu\text{m}$ remains the same even when the JFET doping is $9 \times 10^{16} \text{cm}^{-3}$ with a little higher leakage current. It will be interesting to compare short circuit withstand time for MOSFETs with different JFET widths, doping, and channel lengths. Selected devices will be packaged and delivered to OSU for further evaluations with respect to body diode degradation, short circuit capability, avalanche behavior, and etc.

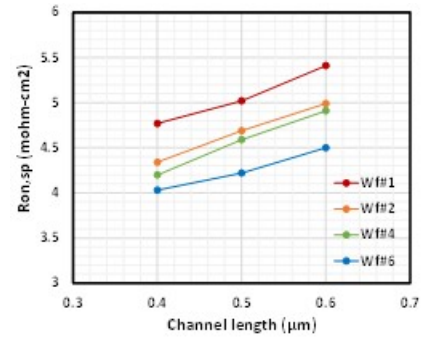


Figure I.1.22.5 Specific on resistance as function of channel length with different JFET doping concentration.

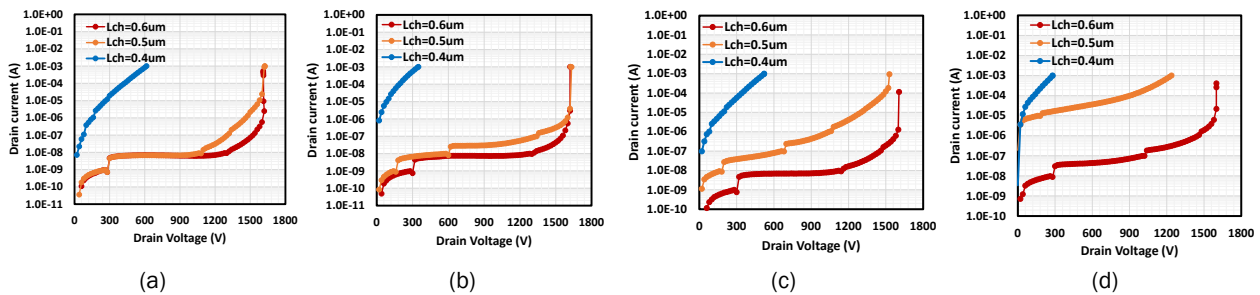


Figure I.1.22.6 BV for W_{JFET} of $0.6 \mu\text{m}$ of JFET doping of (a) $3e16 \text{cm}^{-3}$, (b) $5e16 \text{cm}^{-3}$, (c) $7e16 \text{cm}^{-3}$, and (d) $9e16 \text{cm}^{-3}$.

Layout approaches for MOSFET were also examined in Lot 2. Table I.1.22.3 summarizes specific on-resistances for the conventional stripe pattern MOSFET and hexagonal MOSFET (HEXFET). Design of the stripe pattern MOSFET, and HEXFETs are shown in Figure I.1.22.7. HEXFET with ‘bridge’ between Pwells were proposed to remove sharp edge of hexagonal pattern in the Pwell as shown in Figure I.1.22.7 (b). HEXFET w/o bridge has lower specific on-resistance due to higher channel density when compared with MOSFET. However, HEXFET with bridge has higher $R_{on,sp}$ in spite of higher channel density because bridge forms the JFET region, which interrupts movement for electrons.

Table I.1.22.3 Specific on-resistance for MOSFET and HEXFET.

	MOSFET (mohm-cm ²)	HEXFET with bridge (mohm-cm ²)	HEXFET without bridge (mohm-cm ²)
Wf1 (3e16)	5.02	6.25	4.55
Wf2 (5e16)	4.69	5.53	4.14
Wf4 (7e16)	4.59	5.22	4.09
Wf6 (9e16)	4.22	5.02	3.88

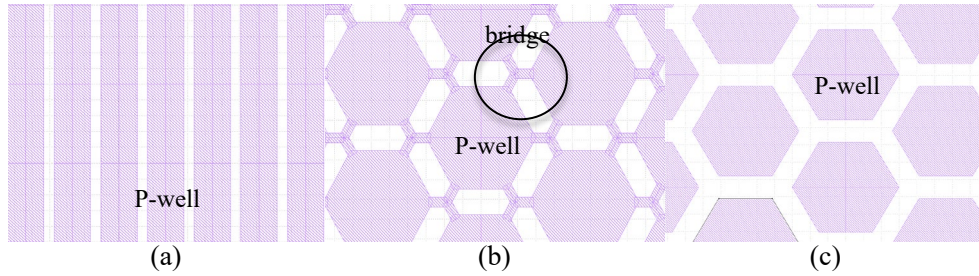


Figure I.1.22.7 Top view for p-well of (a) MOSFET, (b) HEXFET with bridge, and (c) HEXFET without bridge.

Figure I.1.22.8 shows breakdown voltage for MOSFET and HEXFET with half JFET width of 0.6 μm and channel length of 0.5 μm . Regardless of bridge, HEXFET has lower leakage current due to the channel being surrounded by P-well, which provides more depletion region and shielding effect. Especially, HEXFET with bridge has lower leakage current and higher breakdown voltage due to bridge, resulting in the increase of JFET region.

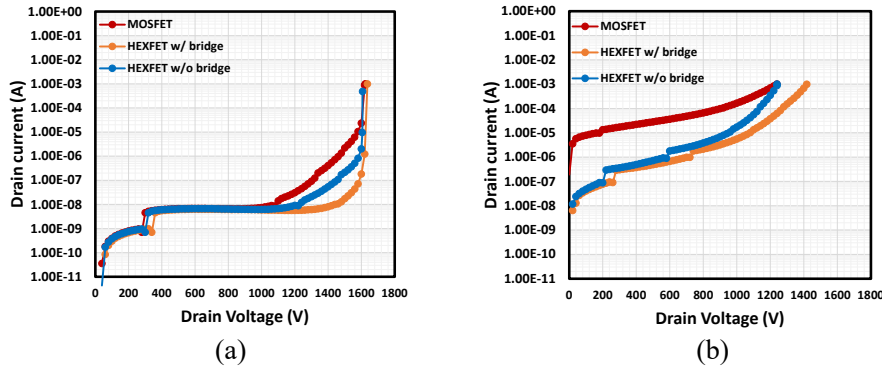


Figure I.1.22.8 Breakdown voltage for half JFET width of 0.6 μm of JFET doping concentration of (a) 3e16 and (b) 9e16 cm^{-3} .

3. Device design and fabrication of Lot 3

Figure I.1.22.9 (a) shows conventional structure of 1200V MOSFET. Drift layer was designed to be $8 \times 10^{15} \text{ cm}^{-3}$ doped and 10 μm thick to achieve about 1700V with a parallel-plane PN junction. On-resistance can be reduced through reduced cell pitch, higher channel mobility, and optimization of JFET region. The cell pitch was largely reduced by putting P+ source in orthogonal direction, intermittently. An accumulation channel was designed for higher channel mobility. For lower $R_{\text{on,sp}}$ and higher BV, JFET width and doping concentration were optimized using 2-D device simulations [2], [3]. Figure I.1.22.9 (b) shows novel structure of 1200V MOSFET. Extended p-well are formed by using channeling implant, which is novel implantation technique to implement a deep junction. Deep p-well structure can result in the improvement in static characteristics and reliability. MOSFETs with conventional and extended p-well were included in the mask design for Lot 3. Mask for Lot 3 includes 21 different devices such as PiN diodes, JBS diodes, MOSFETs, JBSFETs, and HEXFETs. Reduced cell pitches and channel lengths were designed to reduce the on-resistance of MOSFETs and JBSFETs. In addition, from Lot3, SiC MOSFETs with a solderable front-side metal stack will be

fabricated and delivered to the team for the evaluation. This will enable low inductance and efficient cooling of SiC packages. There are 13 photolithography process steps, including 6 implant processes. Lot 3 fabrication is in progress and currently at P-well implant step. The scheduled fab-out date is December 2020.

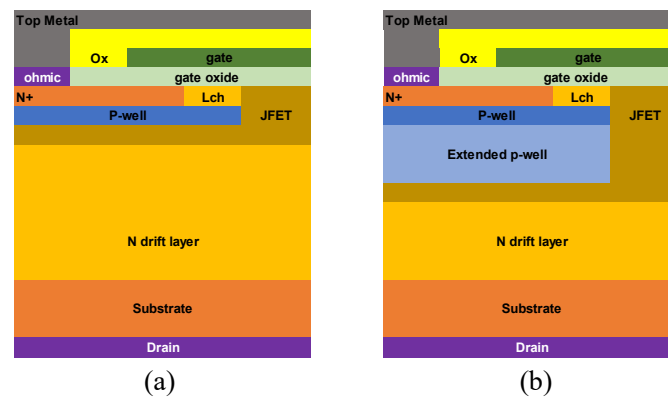


Figure I.1.22.9 Cross-sectional view of (a) conventional 1.2kV 4H-SiC MOSFETs and (b) novel 1.2kV 4H-SiC MOSFETs.

4. Device design and fabrication of Lot 4

One very efficient way to increase the power density of the power inverter is to operate the device at higher temperatures. Some devices from Lot1 will be packaged for high temperature operations and then will be evaluated at OSU. Issues identified in this evaluation will be discussed with SUNY, which will provide the basis of the design and process for Lot 4. Mask for Lot 4 includes 17 different devices, which are PiN diode, JBS diode, MOSFETs, JBSFETs, and HEXFETs. For high-temperature operation (~250 °C), MOSFETs with long channel length and narrow JFET width were included. There are 13 photolithography process steps, including 6 implant processes. Fabrication for Lot 4 will start in early December 2020.

Conclusions

This year, SUNY Poly has focused on establishing a process baseline for the 1200V SiC MOSFET. Lot 1 and Lot 2 have been successfully completed showing promising on-wafer static performances. Many different variations in both device designs and process conditions were examined through Lot 1 and Lot 2. Selected devices were packaged and are being investigated at OSU in regard to gate oxide reliability, short circuit behavior, 3rd quadrant behavior, dynamic performances, and avalanche capability. Lessons learned from Lot 1 and Lot 2 have been reflected to the design of Lot 3 and Lot 4 (1st and 2nd lots for BP2), which are currently being fabricated.

References

1. Dongyoung Kim, Adam J Morgan, Nick Yun, Woongje Sung, Anant Agarwal, and Robert Kaplar “Non-Isothermal Simulations to Optimize SiC MOSFETs for Enhanced Short-Circuit Ruggedness,” 2020 IEEE International Reliability Physics Symposium (IRPS)
2. Woongje Sung, Kijeong Han, B. J. Baliga, “Optimization of the JFET region of 1.2kV SiC MOSFETs for improved high frequency figure of merit (HF-FOM),” 2017 IEEE 5th Workshop on Wide Bandgap Power Devices and Applications (WiPDA)
3. Synopsis Inc., Sentaurus™ Device User Guide, ver. K-2015.06, June 2015

Key Publications

1. Dongyoung Kim, Adam J Morgan, Nick Yun, Woongje Sung, Anant Agarwal, and Robert Kaplar “Non-Isothermal Simulations to Optimize SiC MOSFETs for Enhanced Short-Circuit Ruggedness,” 2020 IEEE International Reliability Physics Symposium (IRPS)

I.1.23 Cost competitive, high-Performance, highly Reliable (CPR) Power Devices on GaN

Shadi Shahedipour-Sandvik, Principal Investigator

SUNY Polytechnic Institute
257 Fuller Road
Albany, NY 12203
Email: sshahedipour-sandvik@sunypoly.edu

Susan Rogers, DOE Technology Development Manager

U.S. Department of Energy
Email: susan.rogers@ee.doe.gov

Start Date: April 16, 2019	End Date: April 15, 2024	
Project Funding: \$333,000	DOE share: \$300,000	Non-DOE share: \$33,000

Project Introduction

The primary objective of this project is to demonstrate highly reliable wide bandgap AlGaIn/GaN HEMT power devices. In this project, we will demonstrate AlGaIn/GaN HEMT power devices with superior performance and reliability. To accomplish this goal, growth conditions and processing will be optimized for HEMT devices on bulk GaN to reduce the effect of defects and impurities in the bulk and at interfaces. Additionally, we investigate the quality and processing of multiple gate dielectric materials to enhance the performance and reliability of HEMT devices.

Objectives

- AlGaIn/GaN HEMT growth on foreign substrates (sapphire, Si)
- AlGaIn/GaN growth on bulk GaN substrate
- Fabrication and characterization of AlGaIn/GaN HEMT devices
- Investigation of gate dielectrics and their impact on device reliability.

Approach

Investigation of Gate Dielectrics and their Impact on HEMT Reliability

Further investigation was performed to quantify the density of interface states (D_{it}) of Al_2O_3 /GaN. GaN MIS capacitors were formed using 20 nm ALD Al_2O_3 as the dielectric layer. After deposition, the samples were annealed in forming gas, ranging in temperature from 350°C to 600°C for times ranging between 1 min and 20 min. The impact of the annealing condition on the density of charge traps at the interface of GaN and Al_2O_3 is studied through capacitance-voltage (C-V) and conductance-frequency (G-f) measurements.

Al_2O_3 is a promising gate dielectric, but poor thermal stability at temperatures $>800^\circ C$ used for ohmic contact processing does not allow for the Al_2O_3 to be deposited before ohmic metallization. By depositing the Al_2O_3 after the high temperature ohmic processing, the as-deposited oxide is preserved, but there is a high density of interface states. In an attempt to preserve the AlGaIn surface to maintain a high-quality interface, a thin (~ 3 nm) *in situ* SiN_x cap was grown by metalorganic chemical vapor deposition (MOCVD) directly after the AlGaIn/GaN heterostructure. MISHEMTs with and without this SiN_x cap were fabricated.

Results

Investigation of Gate Dielectric and its impact on HEMT Reliability

In order to evaluate the effect of the different annealing conditions on the dielectric/semiconductor interface, the conductance method [1] was used to calculate the density of interface trap states. The trap energy levels

were calculated and plots of the resulting density of interface traps as a function of energy relative to the conduction band edge for each annealing condition is shown in Figure I.1.23.1.

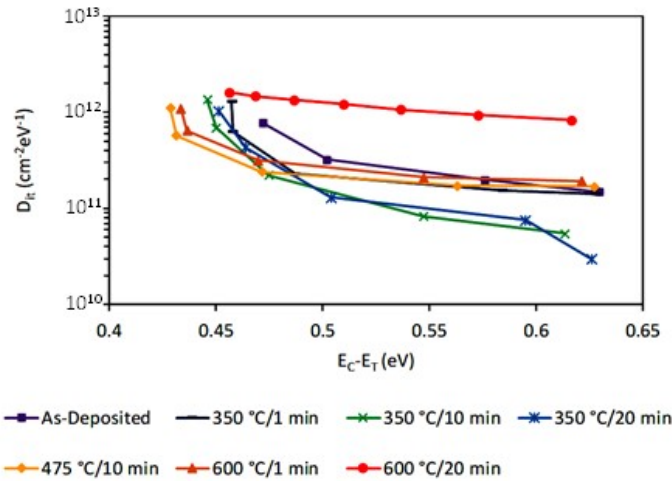


Figure I.1.23.1 Calculated D_{it} plotted as a function of energy relative to the conduction band for each annealing condition.

The density of shallow traps in all devices trends toward $1 - 2 \times 10^{12} \text{ cm}^{-2} \text{ eV}^{-1}$ regardless of annealing condition. At deeper energy levels, the lowest D_{it} was calculated for samples annealed at 350°C for 10 and 20 min. These results suggest that in order to obtain a low density of interface defects, annealing at lower temperature for longer period of time is more optimal than rapid high temperature annealing.

Considering the finding from the above, give MISHEMT wafers were designed to optimize processing methods for dielectrics with relatively low thermal budget such as Al_2O_3 . The samples are described in Table I.1.23.1 and are currently being fabricated.

A measurement of wafer quality using secondary ion mass spectroscopy (SIMS) shows expected level of unintentional impurity.

Table I.1.23.1 MISHEMT samples fabricated

Dielectric	HEMT with <i>in situ</i> MOCVD SiN_x cap	HEMT without <i>in situ</i> MOCVD SiN_x cap
Al_2O_3 before ohmic	Sample 1	Sample 2
Al_2O_3 after ohmic	Sample 3	Sample 4
Si_3N_4 before ohmic	Sample 5	

Key Publications

1. B. McEwen, I. Mahaboob, E. Rocco, K.Hogan, V. Meyers, R. Green, F. Nouketcha, T. Murray, V. Kaushik, A. Lelis, F. Shahedipour-Sandvik, “Investigation of the Effects of Forming Gas Annealing on $\text{Al}_2\text{O}_3/\text{GaN}$ Interface,” *J. Electron. Mater.* Accepted 26 September 2020.

References

1. E. H. Nicollian and J. R. Brews, MOS (Metal Oxide Semiconductor) Physics and Technology. (John Wiley & Sons, New York, 1982) pp. 196–199.

Acknowledgements

B. McEwen, I. Mahaboob, E. Rocco, K. Hogan, V. Meyers, R. Green, F. Nouketcha, T. Murray, V. Kaushik, A. Lelis, and M. Yakimov substantially contributed to the work presented here. This work was in part

supported by an award from Army Research Lab under Award#W911NF-18-2-0019. This work was performed in part at the Cornell NanoScale Facility, a member of the National Nanotechnology Coordinated Infrastructure (NNCI), which is supported by the National Science Foundation (Grant NNCI-1542081).

I.1.24 Next-Generation, High-temperature, High-frequency, High-efficiency, High-power-density Traction System (University of California, Berkeley)

Prof. Robert Pilawa-Podgurski, Principal Investigator

University of California, Berkeley
253 Cory Hall
Berkeley, CA 94720-1770
Email: pilawa@berkeley.edu

Susan Rogers, DOE Technology Development Manager

U.S. Department of Energy
Email: susan.rogers@ee.doe.gov

Start Date: October 1, 2019

End Date: September 30, 2020

Project Funding: \$302,342

DOE share: \$302,342

Non-DOE share: \$0

Project Introduction

To meet performance and reliability requirements necessary for broader adoption of electric drive vehicles, the Electrical and Electronics Technical Team of the U.S. Drive partnership has established aggressive design goals for next-generation electric vehicle drivetrains. Specifically, the 2025 roadmap stipulates a 100 kW/L power density target and a \$2.7/kW cost target for power electronics, in addition to high-voltage operation (i.e., greater than 800 VDC). The additional targets for traction motor and the overall system performance impose further challenges on the power electronics design. For example, many high specific power machines have reduced iron content, and therefore reduced intrinsic filtering, thus requiring the inverter to supply a low-distortion drive current. These machines also typically have a high pole count, thus requiring drive current at a higher electrical frequency. Other motors, such as brush-less dc and switch reluctance machines, require a carefully-shaped, non-sinusoidal drive current [1], [2], [3].

Two- and three-level inverter topologies are the conventional framework for the power electronics design of the drivetrain, and some demonstrations have shown recent progress towards addressing cost, power density and efficiency goals [4], [5], [6], [7]. However, an unconventional approach may be necessary to take the dramatic leap in power density necessitated by the roadmap—while simultaneously addressing the other system needs. Therefore, this project leverages the flying capacitor multilevel (FCML) topology, together with a scalable, modular approach, to address these needs. This type of hybrid converter has several advantages: lower voltage (i.e., less than 300 V) transistors can be used, energy-dense capacitors process most of the power, and the output current waveform is multilevel and exhibits a frequency multiplying effect—in other words, the output has reduced dv/dt and filtering requirements for the same high voltage dc bus. For example, in an electric vehicle with an 800 V bus, a 10-level FCML could leverage 100 V, commercially available GaN devices switching at 115 kHz to produce a ~1 MHz switching waveform (modulated according to the motor drive requirements) with one ninth of the dv/dt of a two-level converter.

Prior work has already demonstrated promising performance and gravimetric power density figures for more electric aircraft applications [8]. This project leverages lessons learned to achieve the volumetric power density of 100 kW/L by employing advanced liquid cooling, address the 300,000-mile reliability challenge with redundant design, topology failure studies and online health monitoring, and reduce costs to \$2.7/kW through the use of low-cost GaN devices, modular converter assemblies, and modest modifications to traditional manufacturing methods.

Objectives

The main objective of this project is to develop a 100 kW/L traction power inverter, compatible with next-generation, low-weight (and low inductance) electric machines. The efficiency, size, and cost targets will be

demonstrated through the development of several hardware prototypes, including electrical and thermal systems. This overall goal is comprised of several key tasks, including:

- Establishing the high-level traction inverter specifications
- Evaluating state-of-the-art semiconductor and passive components (e.g., inductors and capacitors)
- Performing a multi-objective optimization to establish circuit topology and operating conditions
- Prototyping designs to verify performance and implement digital control and online health monitoring
- Codesigning a liquid-cooled hardware revision
- Validating the cooling approach with finite-element analysis
- Manufacturing, assembling and experimentally validating the full hardware prototype.

Additionally, this work will address several key barriers in the 2025 roadmap:

- WBG device power and voltage levels and availability
- WBG multi-physics integration designs to enable optimal use
- Component optimization for miniaturization and cost reduction.
- Low inductance requirements for WBG multi-physics integration.

Approach

The fundamental approach for achieving the power density and performance requirements is to develop new circuit topologies and control method to enable FCML inverters in harsh automotive environments and under dynamic loads. The key benefits of this type of converter design illustrated in comparison to the conventional two-level design in Figure I.1.24.2., with relevant considerations as follows:

- Energy-dense capacitors process most of the converter energy
- Multilevel operation and high effective frequency reduce the output dv/dt and filter requirements
- High-switching frequency facilitated by GaN transistors reduces the required flying capacitance
- Dual-interleaved design to further mitigate switching ripple at the input and output.

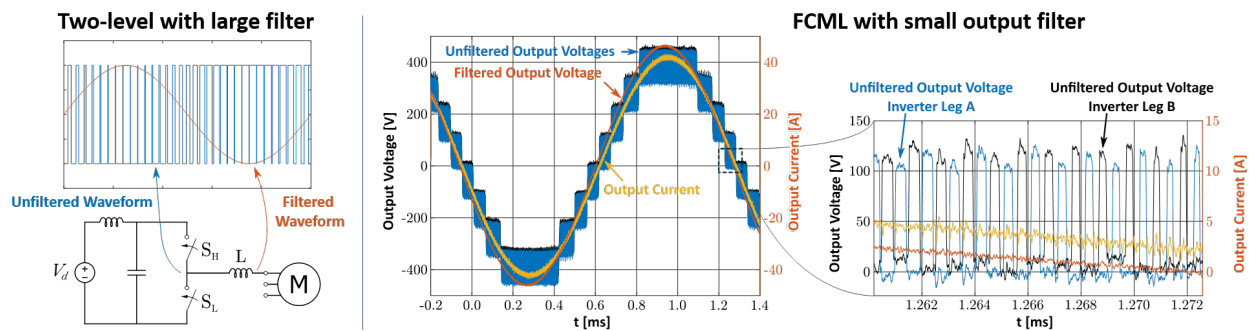


Figure I.1.24.1 Comparison in output waveforms of a conventional two-level design (left), and a 9-level, dual-interleaved FCML design (right). The latter are from results in [8], and illustrate reduced dv/dt , interleaving and high effective frequency.

Designs are informed through both theoretically and empirically derived loss modelling, wherein an optimal solution is chosen from the design space using Monte-Carlo [9] simulations and possibly informed by topology agnostic theoretical analysis [10]. This aspect of the approach provides:

- Large-signal loss models, derived from calorimetric testing of passive components, that are of higher value to the broader power electronics community than small-signal datasheet parameters [11]
- Experience in a common design toolbox, allowing for faster iterations when adding new design considerations (e.g., dynamic $R_{ds,on}$ [12], coupled inductances), or newly available components.

Furthermore, to support output power beyond the 2025 roadmap—while also providing converter redundancy—this project leverages a scalable and modular (or segmented [4]) architecture; a lower power module design is first optimized, and multiple of the resulting design are paralleled in and across phases and coil sets to achieve the full system target power. This strategy, exemplified in Figure I.1.24.2, both simplifies the scope of initial design, manufacturing and experimental testing. Additional benefits of this approach include:

- Shedding redundant modules when operating at low power to achieve higher light-load efficiency
- Supporting continued system operation at a reduced rating in the event of a module or winding failure
- Reducing filter requirements on the dc bus if switching signals across modules are also interleaved.

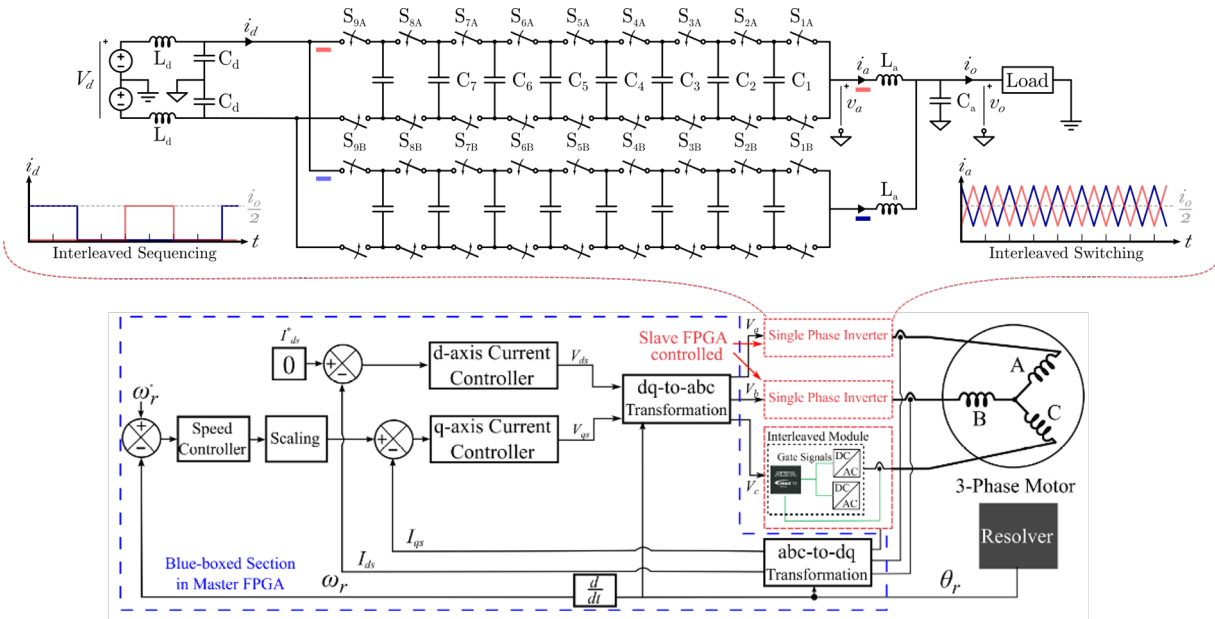


Figure I.1.24.2 Top: schematic and current waveforms for a dual-interleaved, 10-level FCML inverter. Bottom: hierarchical control strategy and system diagram of paralleled converters of the modular (i.e., segmented) approach.

Additionally, to address high-voltage module packaging challenges outlined in the 2025 roadmap, the approach of this project will often differ from conventional two- and three-level designs in that it will:

- Allow for the use lower-cost, low-voltage GaN devices, in addition to higher-voltage, wide-bandgap semiconductor modules in custom, specialized packaging
- Manufacture with conventional assembly and printed circuit board technologies to facilitate extreme cost reductions compared to high power semiconductor modules.

This plan is, however, is complemented by including some advanced manufacturing techniques, such as:

- Blind and buried vias and internal layers in circuit board fabrication to reduce parasitics [13]
- Additive manufacturing for rapid prototyping of thermal management and mechanical assemblies [14].

Results

Several aspects of the project have yielded experimental or simulated results demonstrating progress towards the ambitious goals set forth in the introduction. These are broken down into four categories:

- An expanded codebase and graphical user interface (GUI) that not only allows for readability and logging of all key lab equipment on the converter test bench, but also for debug of analog and digital signals, and sending and receiving of data over a high bandwidth link
- Improvements in the modelling and design of thermal management solution including CFD analysis of air flow through the converter, assessment of expected temperature variance between devices, and a new modular mounting mechanism
- Converter modelling and assessment of reliability in the context of short-circuit fault dynamics as well as parameter variation in the components used for the design. Dynamic model of converter developed to enable improved transient modelling and characterization of capacitor voltage balancing
- Development of mathematical framework and corresponding MATLAB script which computes loop inductance for arbitrary PCB geometries. This method is faster than finite-element analysis and amenable to use within our multi-objective optimization routines which already run in MATLAB.

Significant progress has been made in the testing and verification process of the experimental setup through the development and integration of code across local and global power converter controllers as well as with a host computer and GUI. This allows real-time monitoring and control of operating parameters including control of modulation index, frequency, and debug registers, as well as receipt of analog measurements, both in streaming and single-triggered bursts. An FPGA-based flying-capacitor voltage estimator was programmed on the FPGA local-controller, allowing for autonomous monitoring of capacitor balance on the local controller, as well as supervisory monitoring on the host PC.

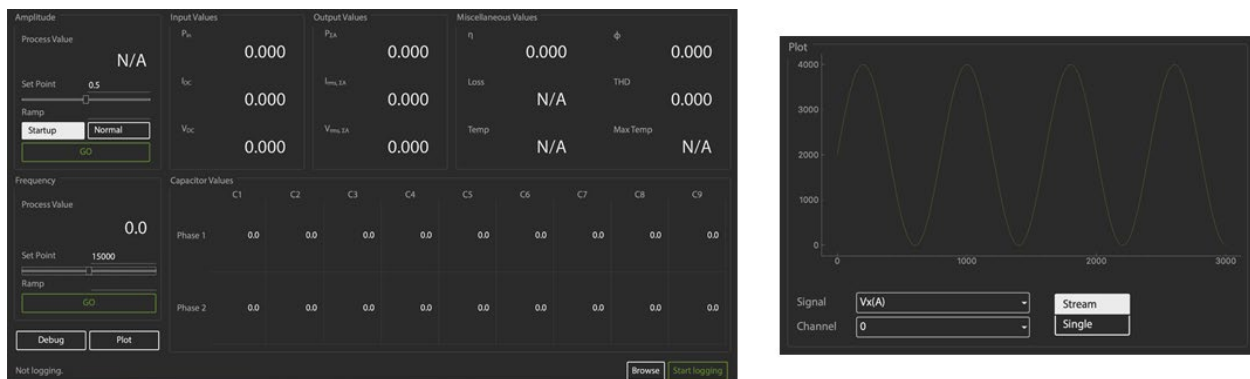


Figure 1.1.24.3 Data collection and parameter control set points shown in the left image. The right image shows an output voltage waveform being plotted in real time.

The thermal management design, already entirely unique, has made additional strides in both modelling and manufacturability. System-level CFD results indicate that the modular heat sinks see no great difference in cooling efficacy across the devices cooled, with device temperatures only varying by a few degrees Celsius. In order to achieve measurement results more closely matching simulation, prototypes of new heat sink mounting system, as well as a fixture for measuring contact pressure, have been printed.

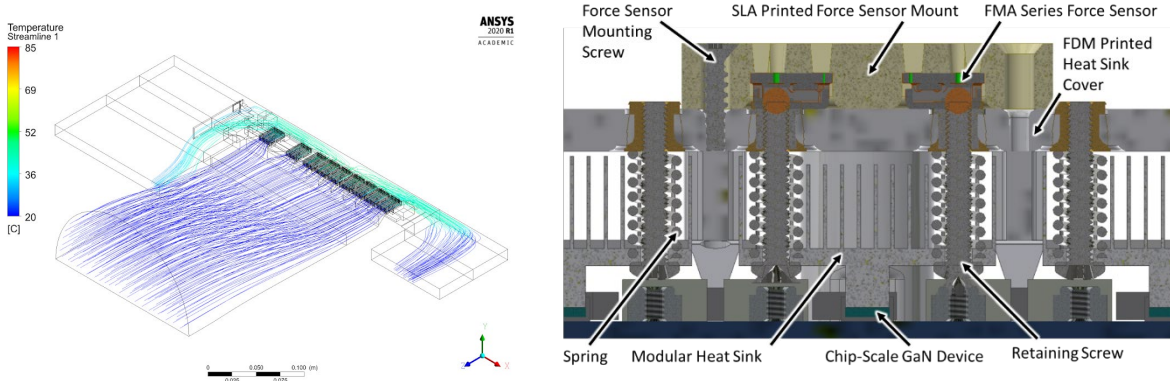


Figure I.1.24.4 CFD analysis of forced air flow shown in the left image. The right image shows a new modular heatsink mounting system.

The use of such a complex and novel design comes with new challenges in dealing with transient events such as short-circuit fault conditions as well as for lifetime reliability and reproducibility in the form of component variation concerns. Our team has worked diligently to model the converters and how they will respond to these situations. In addition, hardware tests have validated the efficacy of the design in these regimes. A Monte-Carlo study was performed in PLECS/MATLAB/Simulink to test how much component parameter variation (within the respective manufacturer tolerances and deratings) would influence matching between interleaved phases (and therefore current sharing). In addition, detailed functional models of the FCML converter were developed in both PLECS and MATLAB (using double Fourier technique [15]) and detailed simulation and experimental testing has been carried out with synchronized modules, indicating significant reductions in input and output harmonics, reducing the input and output filtering requirements.

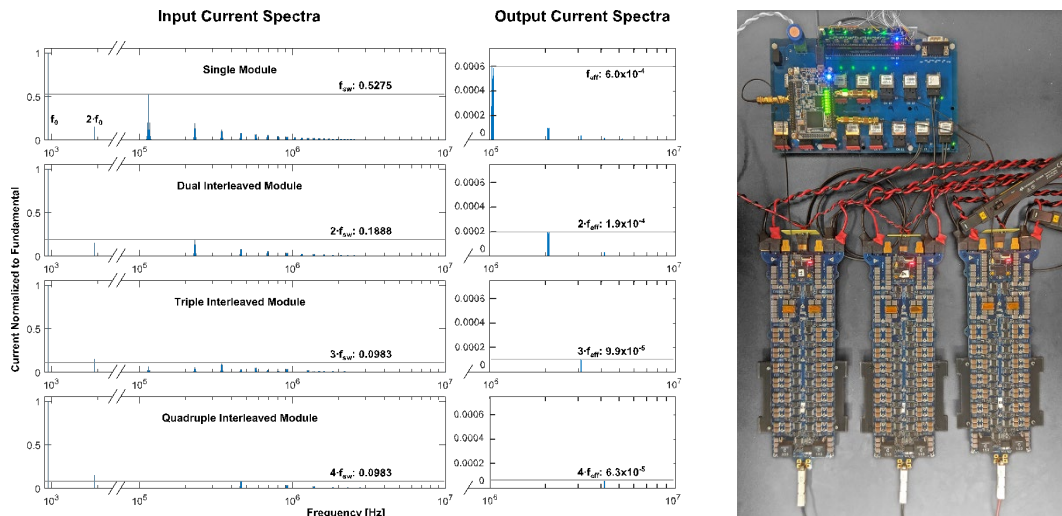


Figure I.1.24.5 EMI spectra for various converter configurations shown in the left image. The right image shows wiring connections for the experimental test setup verifying these simulations.

Parasitic inductances arising from the physical layout of the converter have a drastic impact on performance and reliability. A mathematical framework and corresponding program has been written in MATLAB to allow for the computation of these critical loop inductances without the need of finite-element analysis (FEA). This has been validated through simulation and experimental measurement and will be useful in both modelling and optimization routines for converter design.

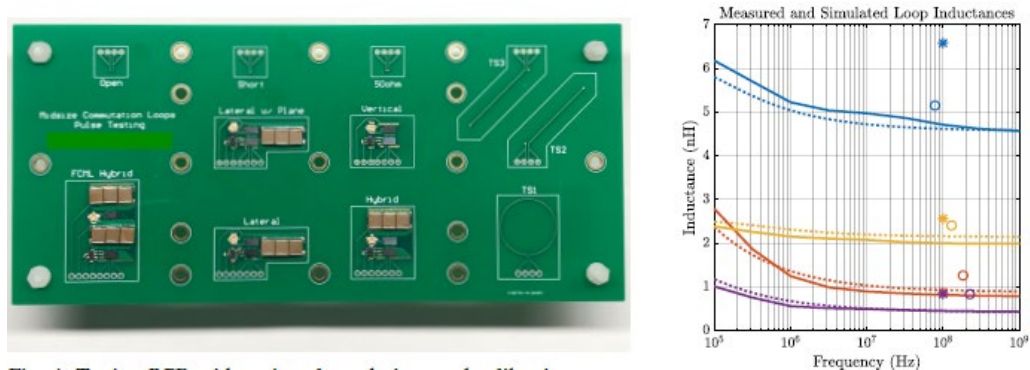


Figure I.1.24.6 Experimental printed circuit board (PCB) with various commutation loops and calibration structures shown in the left image. The right image shows comparative simulation and measured results for inductance across frequency.

Conclusions

Through an innovative circuit topology and advanced digital control, a high density, low-costs inverter prototype suitable for lightweight electric vehicle motors has been demonstrated. The high performance already demonstrated is likely to increase dramatically with the use of the new air-cooling test setup. Furthermore, the excellent results for the air-cooled indicates the move towards liquid cooling in the next phase of the project will provide the dramatic increase in volumetric power density required to meet or exceed the goals of the 2025 roadmap.

Key Publications

1. N. Pallo, S. Coday, J. Schaadt, P. Assem and R. C. N. Pilawa-Podgurski, "A 10-Level Flying Capacitor Multi-Level Dual-Interleaved Power Module for Scalable and Power-Dense Electric Drives," 2020 IEEE Applied Power Electronics Conference and Exposition (APEC), New Orleans, LA, USA, 2020, pp. 893-898, doi: 10.1109/APEC39645.2020.9124531.
2. S. Coday and R. C. N. Pilawa-Podgurski, "High Accuracy Calorimetric Measurements and Modeling of Ceramic Capacitor Losses Under Large Ripple Operation," 2020 IEEE Applied Power Electronics Conference and Exposition (APEC), New Orleans, LA, USA, 2020, pp. 188-194, doi: 10.1109/APEC39645.2020.9124490.
3. N. Pallo, M. G. Taul, A. Stillwell and R. C. N. Pilawa-Podgurski, "Short-Circuit Fault Ride-Through of Flying-Capacitor Multilevel Converters through Rapid Fault Detection and Idle-mode Operation," 2020 IEEE 21st Workshop on Control and Modeling for Power Electronics (COMPEL), Aalborg, Denmark, 2020, pp. 1-8, doi: 10.1109/COMPEL49091.2020.9265743.

References

1. Z. Yang, F. Shang, I. P. Brown and M. Krishnamurthy, "Comparative Study of Interior Permanent Magnet, Induction, and Switched Reluctance Motor Drives for EV and HEV Applications," IEEE Transactions on Transportation Electrification, vol. 1, no. 3, pp. 245-254, 2015.
2. X. Zhang, C. L. Bowman, T. C. O'Connell and K. S. Haran, "Large electric machines for aircraft electric propulsion," IET Electric Power Applications, pp. 767-779, 2018.

3. A. D. Anderson, N. J. Renner, Y. Wang, S. Argawal, S. Sirimanna, D. Lee, A. Banerjee, K. Haran, M. J. Starr and J. L. Felder, "System Weight Comparison of Electric Machine Topologies for Electric Aircraft Propulsion," in 2018 AIAA/IEEE Electric Aircraft Technologies Symposium (EATS), 2018.
4. E. Gurpınar and B. Ozpıneci, "Loss Analysis and Mapping of a SiC MOSFET Based Segmented Two-Level Three-Phase Inverter for EV Traction Systems," in 2018 IEEE Transportation Electrification Conference and Expo (ITEC), 2018.
5. J. Zhu, H. Kim, H. Chen, R. Erickson and D. Maksimović, "High efficiency SiC traction inverter for electric vehicle applications," in 2018 IEEE Applied Power Electronics Conference and Exposition (APEC), 2018.
6. A. Deshpande, Y. Chen, B. Narayanasamy, A. S. Sathyanarayanan and F. Luo, "A three-level, T-type, power electronics building block using Si-SiC hybrid switch for high-speed drives," in 2018 IEEE Applied Power Electronics Conference and Exposition (APEC), 2018.
7. R. Alizadeh, T. Adamson, J. C. Balda, Y. Zhao, M. Asheghi and K. E. Goodson, "A Compact 50-kW Traction Inverter Design Using Off-the-Shelf Components," in 2019 IEEE Applied Power Electronics Conference and Exposition (APEC), 2019.
8. N. Pallo, T. Foulkes, T. Modeer, S. Coday and R. C. N. Pilawa-Podgurski, "Power-dense multilevel inverter module using interleaved GaN-based phases for electric aircraft propulsion," in 2018 IEEE Applied Power Electronics Conference and Exposition (APEC), 2018.
9. T. Modeer, C. B. Barth, N. Pallo, W. H. Chung, T. Foulkes and R. C. N. Pilawa-Podgurski, "Design of a GaN-based, 9-level flying capacitor multilevel inverter with low inductance layout," in 2017 IEEE Applied Power Electronics Conference and Exposition (APEC), 2017.
10. Z. Ye, S. R. Sanders and R. C. N. Pilawa-Podgurski, "Modeling and Comparison of Passive Component Volume of Hybrid Resonant Switched-Capacitor Converters," in 2019 20th Workshop on Control and Modeling for Power Electronics (COMPEL), 2019.
11. S. Coday, C. B. Barth and R. C. N. Pilawa-Podgurski, "Characterization and Modeling of Ceramic Capacitor Losses under Large Signal Operating Conditions," in 2018 IEEE 19th Workshop on Control and Modeling for Power Electronics (COMPEL), 2018.
12. T. Foulkes, T. Modeer and R. C. N. Pilawa-Podgurski, "Developing a standardized method for measuring and quantifying dynamic on-state resistance via a survey of low voltage GaN HEMTs," in 2018 IEEE Applied Power Electronics Conference and Exposition (APEC), 2018.
13. N. Pallo, T. Modeer and R. C. N. Pilawa-Podgurski, "Electrically thin approach to switching cell design for flying capacitor multilevel converters," in 2017 IEEE 5th Workshop on Wide Bandgap Power Devices and Applications (WiPDA), 2017.
14. N. Pallo and e. al., "Modular heat sink for chip-scale GaN transistors in multilevel converters," in 2018 IEEE Applied Power Electronics Conference and Exposition (APEC), 2018.
15. B. P. McGrath and D. G. Holmes, "Analytical Modelling of Voltage Balance Dynamics Analytical Modelling of Voltage Balance Dynamics," IEEE Transactions on Power Electronics, vol. 23, no. 2, pp. 543-550, 2008.

Acknowledgements

The following graduate students at the University of California, Berkeley contributed to the content of this report: Nathan Pallo, Samantha Coday, Logan Horowitz, Joseph Schaadt and Pourya Assem. Amanda Jackson

and Avinash Jois, undergraduates at Berkeley, further assisted in the hierarchical control elements and user interface. Christopher Barth, formerly a graduate student at the University of Illinois, Urbana-Champaign and now with the NASA Glenn Research Center, contributed to the motor testing and hierarchical control. TDK Corporation provided applications and logistics support for the capacitors used in the demonstration hardware. Support for development of some of the hardware used in this project was also provided by the NASA Fixed Wing research program through the NASA cooperative agreement: NASA NNX14AL79A.

I.1.25 Device- and System-Level Thermal Packaging for Electric-Drive Technologies

Yogendra Joshi, Principal Investigator

Georgia Institute of Technology
771 Ferst Drive, Atlanta, GA 30332
Email: yogendra.joshi@me.gatech.edu

Samuel Graham, Co-PI

Georgia Institute of Technology
801 Ferst Drive, Atlanta, GA 30332
Email: sgraham@gatech.edu

Satish Kumar, Co-PI

Georgia Institute of Technology
771 Ferst Drive, Atlanta, GA 30332
Atlanta, GA 30332
Email: satish.kumar@me.gatech.edu

Susan Rogers, DOE Technology Development Manager

U.S. Department of Energy
Email: susan.rogers@ee.doe.gov

Start Date: April 1, 2019
Project Funding: \$1,500,000

End Date: Project continuation evaluated annually
DOE share: \$0 Non-DOE share: \$0

Project Introduction

This project aims to research, develop, and test Electric Traction Drive System Technology for use in vehicle applications capable of meeting the targets set by the Department of Energy Vehicle Technologies Office. The project is categorized into three major thrusts: Bonding interfaces for packaging, Thermal management of electric vehicles (EVs) power inverters, and Electric motor thermal management.

To improve the packaging of next-generation power electronic devices in EVs, a transient liquid phase bonding technique has been developed to directly bond copper substrates with AlSiC heatsinks for use in power electronic packages. AlSiC has been demonstrated to improve the lifetime of power packages by at least 16 times and overall significant performance enhancements can be achieved by eliminating the direct bonded copper (DBC) and integrating a streamlined substrate to cold plate assembly. Fabricated samples are found to have good interfacial adhesion, and resistance to applied shear stress.

To enable transition from silicon-based power inverter modules (PIM) to Wide Band Gap (WBG) ones, effective thermal management is required. To this end, experimental and numerical single/two-phase thermal management techniques using additively manufactured (AM) metal foams, jet impingement, and integrated vapor chamber technologies have been developed. In addition, micro pin fin array cooling technique was developed to remove 580 W/cm² heat flux at sub-100°C using single phase convection.

Electric motor thermal modeling is essential to enhance reliability and reduce size. To predict temperatures in electric motors at the early of the design phase, numerical modeling techniques using Finite Element Analysis (FEA), or Computational Fluid Dynamics/Heat Transfer (CFD/HT) are traditionally used to accurately predict temperatures inside a motor. These numerical models can have a high accuracy; however, they are known for having high computational time. Instead, a Lumped Parameter Thermal Network (LPTN) has much lower computational time than FEA or CFD/HT. However, LPTN cannot provide a full temperature map of each motor part. At the first stage of motor design process, this full temperature map is not necessarily needed. Nevertheless, hot spots need to be accurately predicted in each part of the machine. Here, we show that LPTN

can have this accuracy in the high temperature regions of the motor, and hence it can replace FEA or CFD models during the iterative design process.

Objectives

- Investigate the capability of the transient liquid phase bond (TLP) in bonding copper coupons to AlSiC heatsinks
- Study mechanical, elastic and physical properties of fabricated samples to determine bond quality, and model process temperature, bond pressure and composition of bond to decrease void fraction
- Investigate thermal management solutions for WBG EVs using single-phase and boiling flows in additive manufactured metal foams and jet impingement for system-level cooling of WBG device-based traction inverters
- Establish thermal management techniques to remove 500 W/cm² heat flux from power components.
- Validate Lumped Parameter Thermal Network (LPTN) against FEA and experimental data to derive its accuracy for each part of the motor.
- Perform sensitivity analysis of the main thermal resistances involved in the LPTN to identify the stator areas which impede efficient heat removal from the stator.

Approach

Bonding interface for packaging

The Cu-Al eutectic transient liquid phase bonding system has been shown effective in bonding AlN substrates to AlSiC. To further study the capabilities of the bond, the technique is applied to bond various highly conductive electronic materials, including copper, to AlSiC. The process involves the use of three Al foils between the layers. The foils are cleaned using 25% HCl solution, de-ionized water and acetone, sequentially. The TLP bonding technique of using Cu-Al hypoeutectic alloy for joining AlN with AlSiC has been described in detail by Pahinkar et al. [4]. In bonding Cu and AlSiC coupons, only Aluminum foils were placed in the interlayer, due to the abundance of Cu in the 2 mm pure copper coupon (Figure I.1.25.1). In contrast, the interlayer Al fraction for the AlN – AlSiC bond, that resulted in good adhesion strength was 80%.

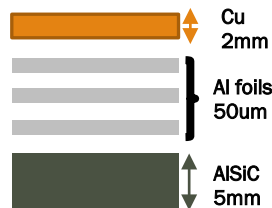


Figure I.1.25.1 Bonding stack for Cu – AlSiC layers

The combined stack is kept in a graphite rig and a pressure of 30 bar is applied. The rig is then kept in the furnace kept at pressure smaller than 2×10^{-2} Pa with special temperature profile.

Thermal management of electric vehicles (EVs) power inverters

Additive manufactured metal foams have been investigated as the thermal management solution. A combination of experimentation and computational methodology has been used to compute the performance of the metal foam structures. With direct printing, thermal interface materials and contact resistance were eliminated. Local control of parameters such as pores per inch (PPI), porosity (ϵ), elongation were enabled for localized hotspot cooling, thermal gradient management and vapor pathways. The two-phase work started with a simple geometry for learning the intricacies of two-phase simulations—specifically boiling flows. Simple rectangular microchannel geometries, with various passive pressure oscillation mitigation strategies, are being

used to facilitate future two-phase computational studies, while providing useful insight into the differences between the schemes. The prior work is being continued via the expansion of earlier additive manufactured metal foams into boiling flows. In addition, by using microscale pin fin array superior single-phase heat removal capability with the heat flux removal of 580 W/cm^2 were achieved during budget period 1.

To dissipate high-heat fluxes on the order of 1 kW/cm^2 , two ongoing projects, one with jet impingement and the other with vapor chamber are ongoing. The jet impingement project consists of a double-sided cooling approach using single phase and two-phase cooling for EV power inverters. This work will be conducted in two parts: part one with utilizing a resistive heater to simulate real SiC device, and part 2 two for testing with real SiC MOSFETs. Current focus is on part one in which a layer of Platinum on Silicon Carbide (SiC) is being used to simulate the heating, and a package for fluid delivery, and the fluidic loop are being designed. The design for the sub-mm vapor chamber includes an integrated condenser that can easily remove the system level heat using liquid cooling. The entire thermal management system is passive and as such highly reliable, resulting in enhanced thermal performance, while providing electrical compatibility. This project encompasses fabrication of capillary wick-based and patterned vapor chambers using different sizes of copper powders, thermal characterization of sub-millimeter size vapor chambers for integrated condenser design, optimal design of wicking structures for condensation using CFD/HT modeling to test the performance of vapor chambers.

Electric motor thermal management

The Nissan Leaf motor has been used as a reference in our study. To compare our LPTN model to experimental results, previous work from National Renewable Energy Lab (NREL) by Moreno [3] was used, where only the stator and the water-jacket were considered. The authors supplied the windings with DC current for a total heat generation of 567 W. The coolant (Water-Ethylene-Glycol mixture) flow rate in the water-jacket was 10 L/min. The FEA model uses the same geometry and boundary conditions as for the experiments conducted in [3]. Thermal conductivities and thermal contact conductance used in the FEA model are derived from previous experimental work performed by NREL [1], [2], [5]. The water-jacket heat-transfer coefficient (HTC) for 10 L/min flow rate is derived from a CFD/HT simulation results which are available in [3]. A section of one pole pitch was considered, instead of the full motor, due to tangential symmetries. The mesh for this section is shown in Figure I.1.25.2. The LPTN model was created with Motor-CAD software. The same thermal conductivities and thermal contact conductance as for the FEA were used to ensure consistency between the models. The windings were divided into ten cuboids to account for temperature gradient inside the slot.

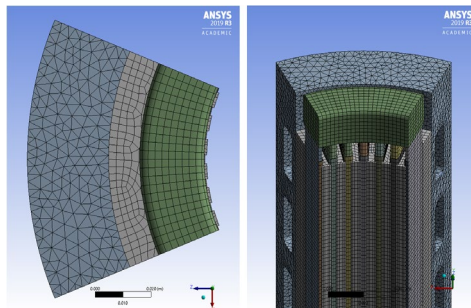


Figure I.1.25.2 Mesh for the FEA model (average size of 2.7 mm).

Results

Bonding interface for packaging

Bonded samples were cross-sectioned using electrical discharge machining (EDM) and finely polished to $0.05 \mu\text{m}$ using Silicon Carbide grit discs and Aluminum Oxide solution. Scanning Electron Microscope (SEM) imaging and Energy-dispersive X-ray spectroscopy (EDX) were conducted on cross-sectioned samples to examine the interface layer and microstructure of the resulting bond (Figure I.1.25.2 and Figure I.1.25.3). The

fabricated samples showed low bond line defects and high strength against shearing and tension (pending quantitative shear tests).

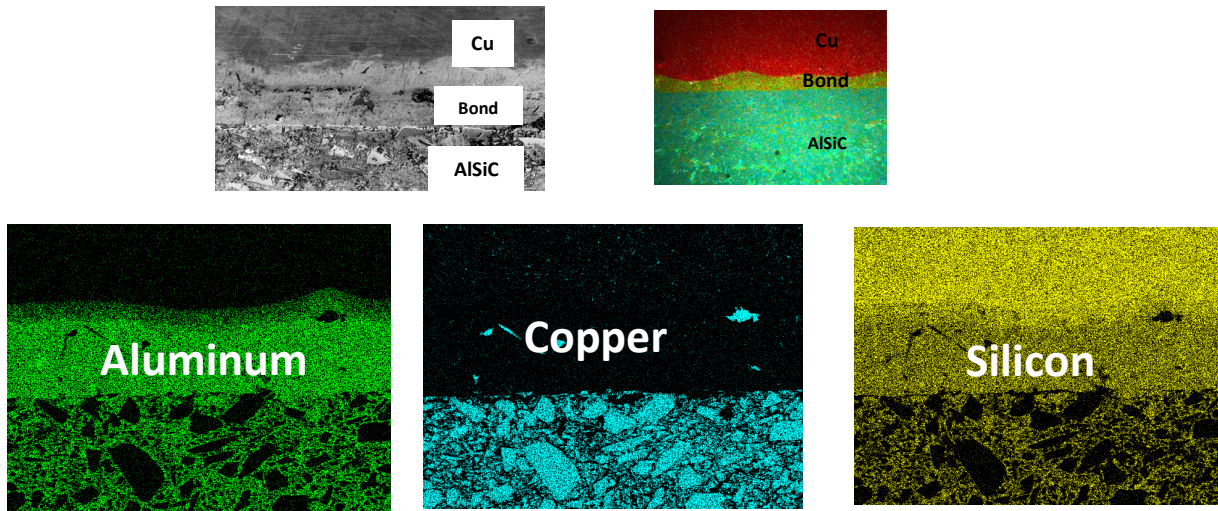


Figure I.1.25.3 EDX Images of Constituent Materials in Sample

As in the SEM image in Figure I.1.25.4, lateral cracks were observed below the bond line within the AlSiC layer unlike in AlN-AlSiC bonded assemblies. This phenomenon, occurring 0.7-1.5 mm beneath the Cu-Al bond, was examined to determine its root cause. It was determined that the presence of excess amounts of copper in the 2 mm coupon lowered the melt temperature of the Aluminum matrix in the AlSiC plate, resulting in formation of molten Cu-Al, thereby inducing residual stresses within the composite structure as it cooled. To mitigate this, a series of experiments are ongoing which vary the process parameters and material composition of the bond, to decrease the clamping pressure and increase bond and structural quality. Additionally, a diffusion model has been developed which simulates the phase change process between Cu and Al, as well as the transport of diluted Cu molecules through the ternary system.



Figure I.1.25.4 SEM Image Showing crack in AlSiC

Thermal management of electric vehicles (EVs) power inverters

CFD/HT modeling of cold plates with additive manufactured metal foam was conducted. Pore-scale models used to obtain thermohydraulic closure terms for volume-averaged simulations with two geometries with discrete heaters was tested: uniform structure and hotspot mitigating structure with spanwise densification at middle. Results showed noticeable decrease in maximum temperature (~14%). In parallel, the advantages of traditionally manufactured and AM metal foams for thermal management was demonstrated experimentally and validated CFD-HT models. It was showed that thermal performance of the AM sample was significantly

higher than that of the traditional metal foam. Moreover, tortuosity, Thermal Interface Material (TIM), thermal conductivity, and interfacial heat transfer coefficients were examined for the traditional versus AM structures.

The recent work primarily involved the CFD/HT simulations of boiling flows in microchannels. Four separate geometries representative of single microchannels were chosen to compare. One basic rectangular microchannel geometry, shown in Figure I.1.25.5a, is used for model validation and comparison with other cases. The height and width were 0.25 mm and 0.2 mm, respectively. The fin and substrate thickness were 0.1 mm. The total length investigated was 10.5 mm, with an adiabatic section of 0.5 mm at the inlet. The three mitigating geometries were constricted inlet, diverging, and auxiliary jetting microchannel. The diverging geometry is shown in Figure I.1.25.5 as an example case geometry. The working mechanism behind the first two (cases 2 and 3) is biasing bubble growth towards downwards direction/ restricting upward bubble expansion. Case 2 has the same dimensions as case 1 except for the adiabatic entrance section, which has the width decreased by a factor of ten. Case 3 has an expansion angle of 0.5 beginning at the heated section. Case 4 has an auxiliary jet that impinges normal to the microchannel flow at the midpoint of the heated section.

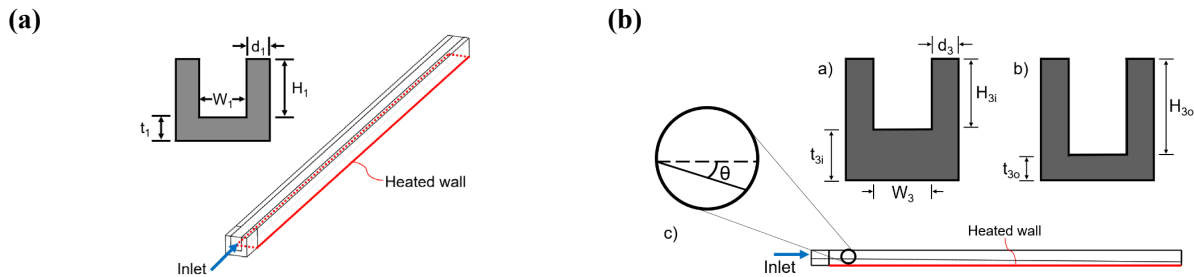


Figure I.1.25.5 (a) Computational geometry for baseline straight microchannel (b) Diverging microchannel geometry (case 3) with $\theta = 0.5^\circ$ showing inlet, outlet, and side profile

Water at a saturation temperature of 100 °C and copper at 100 °C were used for the simulations. A contact angle of 45° is obtained from reference. This contact angle gives moderate hydrophilicity and good wetting. They used a wide range of parameters to develop correlations for saturated flow boiling frictional pressure drop, which can be integrated along the channel for total frictional pressure drop. The acceleration pressure drop was added to the frictional pressure drop with the correlation of Zivi to account for void fraction. The total pressure drop along the channel was found to be 5,880 Pa, which is in reasonable agreement with 5,236 Pa, which was averaged over the 14 ms to 16 ms.

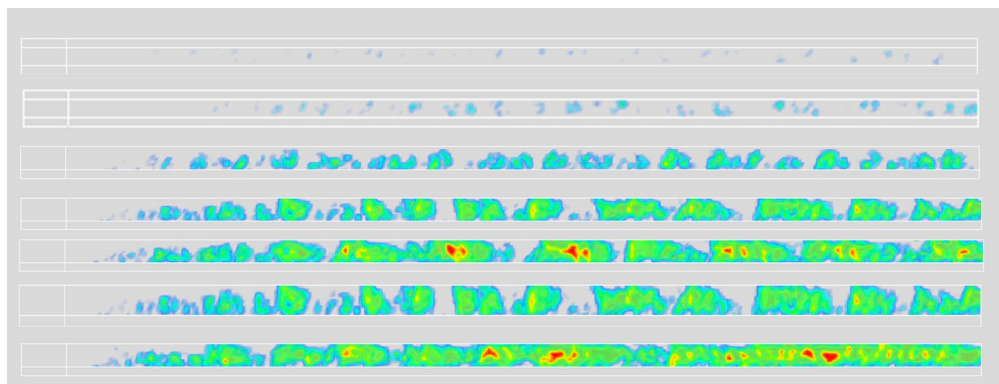


Figure I.1.25.6 Volume fraction of the vapor at different time steps.

The boiling number Bl , bond number Bo , and Reynolds number Re were used as nondimensional parameters, and calculating the x and y coordinates indicated the flow regime should be churn/confined annular. Figure

I.1.25.6 shows the vapor volume fraction at different time steps. The flow regime starts off with bubble nucleation, and then the bubbles grow and begin detaching. Eventually, the bubbles become confined to become confined bubbly flow. The bubbles further coalesce into slugs, and then the flow eventually becomes churn flow. In addition to temporal evolution of the flow, there is also spatial evolution, as the low-quality flow transitions from bubbly to churn along the flow direction. Although the flow regime comparison is qualitative, it nevertheless increases faith in model validity, and allows for further analysis.

Electric motor thermal management

First, we have compared the LPTN results with the experimental data. The results are shown in Figure I.1.25.7. The maximum relative error between LPTN and experimental data is 3.6%. Considering the low number of nodes in the LPTN, this is an excellent result. One can notice that the larger error is in the end-windings. Indeed, the end-windings are modeled as a single toroid, which is a significant simplification compared to real end-windings where end-turns are crossing each other and are inaccurately distributed along the tangential and radial directions. These high irregularities in the end-winding geometry explains this difference.

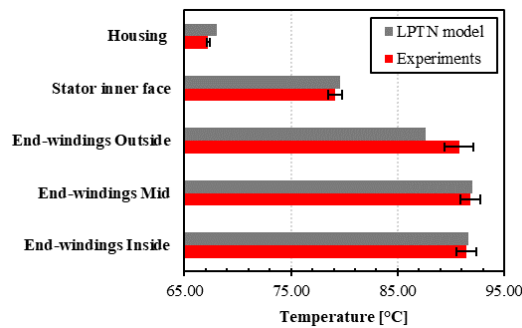


Figure I.1.25.7 Measured temperatures compared to LPTN output temperatures at 5 different points of the stator.

In order to have a detailed comparison of LPTN and FEA models, we considered 3 different paths in the motor instead of single temperature points as is usually done. As shown in Figure I.1.25.8, path (1) crosses radially the slot-windings until the water-jacket, path (2) crosses the stator tooth until the water-jacket and path (3) crosses radially the mid-plane of the end-windings.

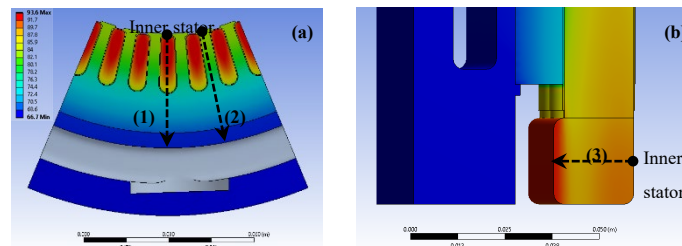


Figure I.1.25.8 Temperature profile paths: (a) path (1) (slot) and path (2) (tooth) | (b) path (3) (end-winding).

The results of the comparison for each path are provided in Figure I.1.25.9. The maximum relative error between LPTN and FEA is 2.08% in the end-windings. As for the LPTN vs. experimental data, the main relative error between LPTN and FEA occurs in end-windings. However, the reason for this error is different. For path (1) and (2), the relative error is below 1% which shows an excellent agreement between LPTN and FEA.

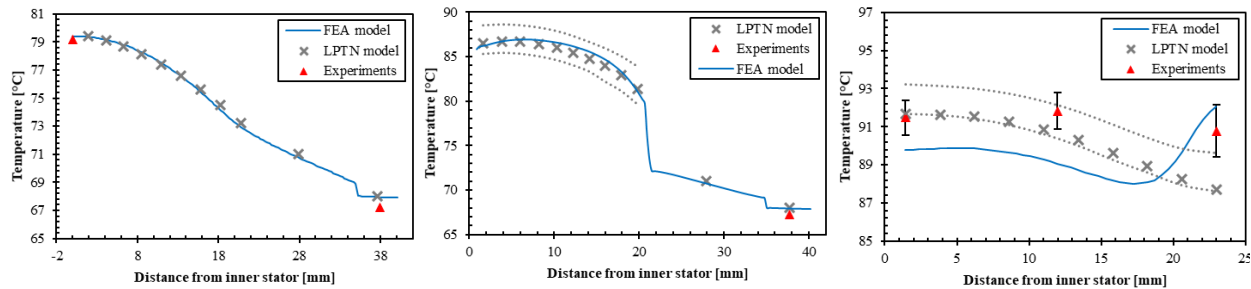


Figure I.1.25.9 Temperature profiles along path (1) (top-left), path (2) (top-right) and path (3) (bottom).

A sensitivity analysis was performed for six thermal resistances from the LPTN model (see y-axis of Figure I.1.25.10 for their name). Each of the resistance value was reduced by 20% and 50% with respect to their initial value. The sensitivity was assessed by computing the temperature difference ΔT between the winding maximum temperature with initial resistances and the winding maximum temperature with the new reduced resistance. The final results are shown in Figure I.1.25.6. According to this figure, the liner contact resistance has the highest sensitivity followed by the liner thermal resistance. Therefore, the liner region is critical and is the most responsible for temperature increase inside the windings. The high sensitivity of the liner contact resistance is due to its significantly low resistance value compared to other resistances which comes from air gaps at the liner surface created during the winding impregnation process.

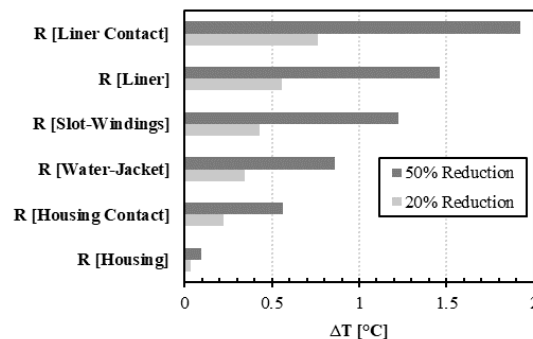


Figure I.1.25.10 Sensitivity analysis of the LPTN thermal resistances for 20 % and 50 % value reductions.

Conclusions

- A bond formed between two layers of Cu and AlSiC coupons showed strong adhesion and uniformity, but increased volume of Cu in the final bond resulted in development of a distinct melt-front in AlSiC unlike in an AlN-AlSiC bond. Future tests underway will vary the applied rig pressure, temperature profile and concentration of bond constituents according to diffusion model simulation. Final samples will undergo thermal cycling to assess thermomechanical properties.
- Thermal performance of the AM sample was significantly higher than that of the traditional metal foam. Tortuosity in ERG foam was shown to be $\sim 2.45x$ greater. Validated 1D resistor network showed diminishing benefits with improved TIM thermal conductivity. Interfacial heat transfer coefficient agrees with the correlations. The two-phase flow regime was qualitatively validated against a regime map.
- A detailed comparison of an LPTN model with experimental data for steady-state thermal analysis of the Nissan Leaf motor stator was proposed. End-windings were found to be a critical region in terms of modeling accuracy. The observed maximum relative errors are sufficiently low to claim that an LPTN can replace an FEA model for steady-state thermal analysis of an electric machine. A

sensitivity analysis was conducted for six thermal resistances involved in the LPTN model. Liner contact resistance had the highest influence. This analysis shows that improving heat transfer coefficient of a cooling system outside of the stator does not provide significant temperature reduction of the windings. Creating a very high-power-density electric motor will require having a cooling system inserted between the liner and the windings which means either inside the slots or on top of the end-windings.

Key Publications

1. Sequeira, Sebastien, Kevin Bennion, Emily Cousineau, Gilbert Moreno, Sreekant Nrumanchi, Satish Kumar, and Yogendra Joshi. 2020. "Validation and Parametric Investigations Using A Lumped Thermal Parameter Model of An Internal Permanent Magnet Motor." ASME InterPACK Conference. Virtual Online.
2. Justin Broughton and Yogendra Joshi. "Comparison of Single-Phase Convection in Additive Manufactured Versus Traditional Metal Foams." *Journal of Heat Transfer* 142, no. 8 (2020).

References

1. Cousineau, Emily, Kevin Bennion, Douglas DeVoto, and Sreekant Narumanchi. 2019. "Experimental characterization and modeling of thermal resistance of electric machine lamination stacks." *International Journal of Heat and Mass Transfer* 129: 152-159.
2. Cousineau, Emily, Kevin Bennion, Victor Chieduko, Rajiv Lall, and Alan Gilbert. 2018. "Experimental Characterization and Modeling of Thermal Contact Resistance of Electric Machine Stator-to-Cooling Jacket Interface Under Interference Fit Loading." *Journal of Thermal Science and Engineering Applications* 10 (4).
3. Moreno, Gilbert. 2016. *Thermal Performance Benchmarking*. Golden, CO: National Renewable Energy Lab. (NREL).
4. Pahinkar, Darshan, Waylon Puckett, Samuel Graham, Lauren Boteler, Dimeji Ibitayo, Narumanchi, Sreekant, Paul Paret, Douglas DeVoto, and Joshua Major. 2018. "Transient Liquid Phase Bonding of AlN to AlSiC for Durable Power Electronic Packages." *Adv. Eng. Mater* 20.
5. Wereszczak, Andrew A., J. Emily Cousineau, Kevin Bennion, Hsin Wang, Randy H. Wiles, Timothy B. Burrell, and Tong Wu. 2017. "Anisotropic Thermal Response of Packed Copper Wire." *Journal of Thermal Science and Engineering Applications*.

Acknowledgements

The principal investigators would like to thank Gilbert Moreno, Paul Paret, Kevin Bennion, Emily Cousineau, and Sreekant Narumanchi from NREL for their help and contribution to this project.

I.1.26 Heterogeneous Integration Technologies for High-temperature, High-density, Low-profile Power Modules of Wide Bandgap Devices in Electric Drive Applications

Guo-Quan Lu, Principal Investigator

Virginia Tech
Department of MSE and ECE - 0111
Blacksburg, VA 24060
Email: gqlu@vt.edu

Rolando Burgos, Co-Principal Investigator

Virginia Tech
Department of ECE, CPES - 0179
Blacksburg, VA 24060
Email: rolando@vt.edu

Khai D.T. Ngo, Co-Principal Investigator

Virginia Tech
Department of ECE, CPES - 0179
Blacksburg, VA 24060
Email: kdtng@vt.edu

Susan Rogers, DOE Technology Development Manager

U.S. Department of Energy
Email: susan.rogers@ee.doe.gov

Start Date: October 1, 2019

End Date: September 30, 2020

Project Funding: \$300,000

DOE share: \$300,000

Non-DOE share: \$0

Project Introduction

The goal of this project is to research, develop, and evaluate the integration and packaging technologies for making high-temperature, high-density, and low-profile wide-bandgap (WBG) power electronics modules. These modules are aimed at enabling the DOE VTO Electrification Technologies' University Consortium to reach its 2025 targets (listed below) for the cost, power density, and system peak power rating of automotive electric drive systems.

Table I.1.26.1 Power Electronics Requirements

Parameters	Measure
Cost (\$/Kw)	≤ 2.7
Power Density (kW/L)	≥ 100
System Peak Power Rating (kW)	100

Objectives

The overall objectives of this project are to:

- develop a low-cost sintered-silver interconnect technology for packaging power modules and gate drivers capable of working over 200°C;

- develop designs and fabrication processes of 3D, planar power modules with parasitic inductances < 5 nH, heat flux density > 400 W/cm², and working junction temperature $> 200^{\circ}\text{C}$; and
- design and prototype intelligent gate drivers with integrated current sensors and protection for the 200°C module.

A schematic of the hardware to be developed in this project is shown below in Figure I.1.26.1. Phase-leg modules capable of working at 200°C ambient will be designed and fabricated. Three of the phase-leg modules will be assembled on cooling plates (with or without double-side cooling) and interfaced to a bus bar and gate-driver boards. The gate driver boards will have integrated current sensors, power supplies, and other components that are capable of working at 200°C ambient.

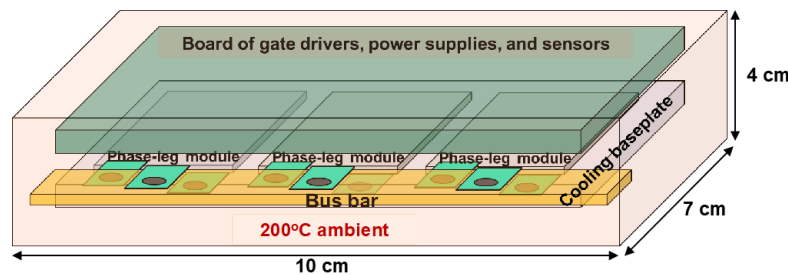


Figure I.1.26.1 Schematic of the hardware to be developed in this project.

For this reporting period, we focused on achieving the following specific objectives:

- Design two layouts of planar SiC phase-leg modules with double-side cooling for making segmented three-phase inverters developed at ORNL; fabricate and test double-side cooled phase-leg modules consisting of 1.2 kV and 149 A SiC MOSFETs;
- Evaluate die-attach on uncoated DBC by pressure-less silver-sintering in the air;
- Design integrated phase current sensors with short-circuit protection and current reconstruction based on module parasitics; verify the performances of the designed current sensor;
- Design a class-D based active EMI filter to contain all common-mode noise within the power modules; verify its performance with simulation results;
- Design a gate driver board with high-temperature driver IC from Cissoid;
- Design an air-core transformer with PCB winding for the class-E dc-dc converter with constant current output; test the dc-dc converter to verify the transformer design as well as to evaluate the converter performance.

Approach

To achieve the objectives for module design and fabrication, we conducted extensive electrical and thermal simulations to analyze the package parasitic inductances and thermal resistances of various layouts of the double-side cooled phase-leg module. In the first year of this project, we surveyed the literature for high-temperature packaging materials, and the results of the survey were used this year for assembling prototypes of the phase-leg modules. Modules having one of the layouts were fabricated and characterized for static performance. For the work on the current sensor based on module parasitics, theoretical analyses and simulations were carried out. A first version of the current sensor with the assumption of fixed parasitic wire bond resistance was designed, built, and characterized. Experiments were conducted to verify its improvement over the traditional open-loop method, as well as its sensitivity under a wide range of temperatures. Then, a new version of the current sensor accounting for the temperature factor was designed to improve the sensor's

performance. Also, many active EMI filter topologies for a three-phase inverter system were studied, and an effective class-D based active filter was designed with enhanced characteristics, such as high power density and high compensation bandwidth. Simulations of the designed active filter were run to verify the theoretical analysis. In the effort on power supplies for high-temperature gate driver development, designs of an air-core transformer with PCB winding were developed and analyzed by simulations for integration into a class-E dc-dc converter with constant current output. The converter was switched at 6.78 MHz to enable only 100 nH inductance thus small footprint. Zero voltage switching(ZVS) was designed for any load conditions. For the class-E dc-dc converter, the air-core transformer was specifically designed with the right mutual inductance to achieve a constant output current at 0.7 A and 180 nH leakage inductance so that the high-frequency harmonics do not influence the load-independent characteristics of the converter. To serve as the load of the converter for future testing, a gate driver board with high-temperature driver IC from Cissoid was designed and tested.

Results

1. Evaluation of silver-sintering on uncoated DBC in the air

It has been widely shown that a sintered-silver joint has 5 times better electrical conductivity, 3 times better thermal conductivity, and 5 times better reliability compared to a solder joint. However, a silver or gold surface finish is usually required on the DBC substrate to be compatible with silver-sintering. To avoid extra cost and complexity associated with coating the DBC substrate with silver or gold, we ran a parametric study on a modified silver paste for bonding in the air directly to the uncoated alumina DBC substrate. Figure I.1.26.2 shows the die-shear test results under the different sintering temperatures. Overall, strong bonding strengths were achieved in a wide range of sintering temperatures (220°C-262°C). To ensure good thermal, electrical, and reliability performance of the joint, a die-shear strength of over 30 MPa is recommended. We recommend sintering the new silver paste at 220°C for 75 minutes to minimize the extent of copper oxidation in the air. This study shows the feasibility of pressure-less silver-sintering on uncoated DBC in the air for bonding, e.g., chip-to-substrate, post-to-substrate, post-to-chip, etc. We will apply this study to fabricate our double-side cooled phase-leg modules to simplify the assembling process and reduce cost.

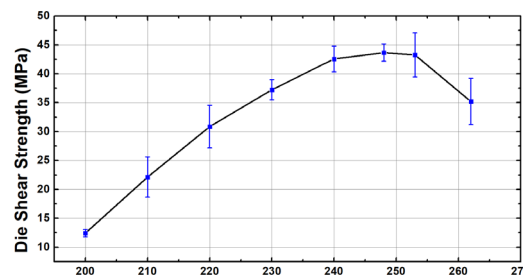


Figure I.1.26.2 Die-shear strength vs. sintering temperature of sintered-silver joints on a bare copper DBC substrate.

2. Phase-leg layout designs and simulations

We chose to start the high-temperature power-stage packaging effort by designing and fabricating packages of SiC MOSFET (1200 V, 13 mΩ, 149 A) from CREE. We have been in communication with Dr. Burak Ozpineci, Dr. Gui-Jia Su, and Dr. Emre Gurpinar at Oak Ridge National Laboratory to ensure that the designed switching cells once packaged can be inserted into a demo-inverter. Figure I.1.26.3 (a) and (b) show two layouts of the half-bridge power stages. The overall dimensions are 2.4 cm × 1.8 cm × 0.4 cm. The Layout #1 shown in Figure I.1.26.3 (a) has two SiC MOSFETs placed on the bottom substrate and six metal posts were used to interconnect the top substrate. All the terminals were designed on one side and the connectors for gate drivers and protections were on the other side. The parasitic inductance of this layout was simulated by ANSYS Q3D. The parasitic inductances of the power loop and drive loop were 4.67 and 3.44 nH, respectively. The Layout #2 shown in Figure I.1.26.3 (b) has one SiC MOSFET placed on the bottom substrate and the other

placed on the top substrate. The terminals and connectors were similar to Layout #1. Because of the shorter conduction path in the power loop, the parasitic inductance was reduced to 2.7 nH.

The thermal performances of the two layouts were simulated by ANSYS Workbench, and the results are shown in Figure I.1.26.3 (c). At 22°C ambient temperature, the relation between chip generated heat flux and the required convection coefficient to restrict junction temperature to 200°C was studied. For Layout #1, assuming a die heat flux of 400 W/cm² and a maximum junction temperature of 200°C, the required convection coefficient with double-side cooling is 46 % lower than that with single-side cooling. For Layout #2, because the chips are placed on two separate substrates, under the same heat flux and maximum junction temperature, the required convection coefficient with double-side cooling is further reduced by 19 % from that for Layout #1. These results confirm the advantage of the double-side cooling, meaning around a 50 % reduction in the required convection coefficient for cooling the module.

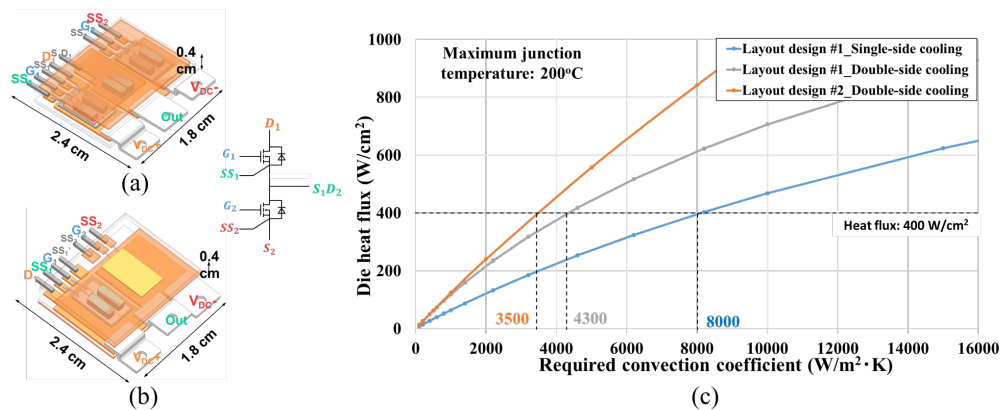


Figure I.1.26.3 Each double-side cooled phase-leg module consists of two 1.2 kV, 149 A SiC MOSFETs. (a) Layout #1 having both devices mounted on the bottom substrate; (b) Layout #2 having one MOSFET on the bottom substrate and the other on the top substrate; and (c) thermal simulation results of die heat-flux versus required convection coefficient for Layout #1 and Layout #2. Single-side cooling = convection applied on the bottom side; double-side cooling = convections applied on both sides).

3. Fabrication and testing of phase-leg modules

After designing the two layouts, we built a prototype of Layout #1 and tested the static characteristics of the packaged device. The bonded interfaces in this module were achieved by silver sintering. The prototype measured at 2.6 cm × 1.8 cm × 0.4 cm is shown in Figure I.1.26.4 (a). The static characteristics of the module were tested on an Agilent B1505A Curve Tracer. Figure I.1.26.4 (b) shows the zero-gate-voltage drain currents, and Figure I.1.26.4 (c) shows the on-state resistance of upper and lower SiC MOSFETs. The leakage currents of the SiC MOSFET before and after packaging are almost the same. The interconnect and terminals of the package added about 2 mohm on-resistance to the switch. Figure I.1.26.4 (d) shows the transfer characteristics of the packaged devices, which were similar to those of the bare die.

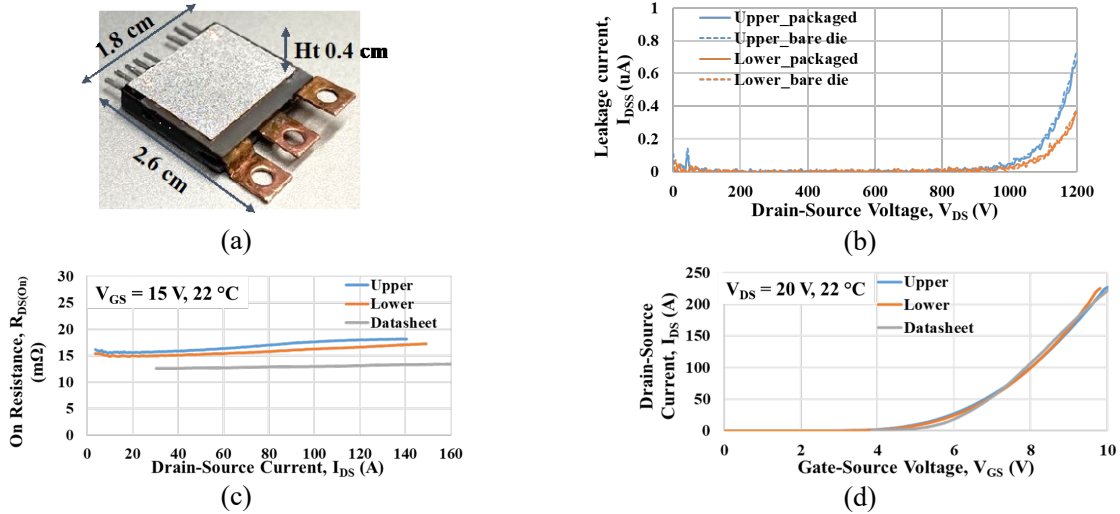


Figure I.1.26.4 (a) The prototype of module layout #1, (b) zero-gate-voltage drain current, (c) drain-source on-state resistance, and (d) transfer characteristics.

4. Gate driver board with high-temperature driver IC

A gate driver board was designed to test the chip from Cissoid and verify the function of gate driving circuits. Figure I.1.26.5 shows the gate driver board. Only top driver circuits are populated. The testing of the board was done with an 8 nF Capacitor as the load. Zoomed-in waveforms at turn-on and turn-off transient are shown in Figure I.1.26.6. The rising and falling time is equals to or less than 100 ns during switching transients.

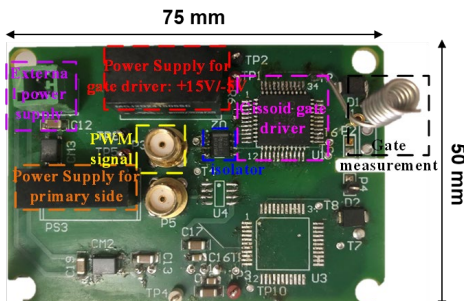


Figure I.1.26.5 Manufactured PCB of gate driver board with gate driver from Cissoid.



Figure I.1.26.6 (a) Zoomed-in waveforms at turn-on transient, and (b) zoomed-in waveforms at turn-off transient.

5. Design of power supply integrated with air-core transformer

5.1 Power supply circuit topology

To comply with the requirement for high temperature, an air-core transformer was designed with PCB winding. A class-E dc-dc converter integrated with the transformer was designed to validate the inductances of the transformer. The circuit topology of the converter is shown in Figure I.1.26.7. The converter operates at 6.78 MHz to enable inductors with hundreds of nH. By matching the inductances with C1 and C2, the output current is constant regardless of the load resistance. Zero voltage switching (ZVS) is maintained while the load varies.

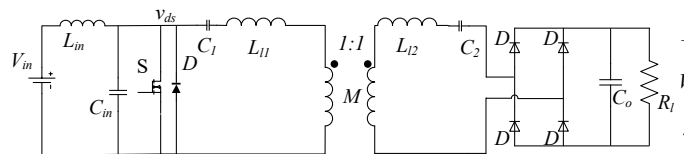


Figure I.1.26.7 Topology of the power supply.

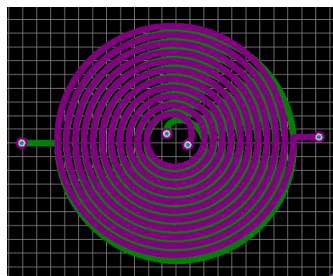
5.2 Air-core transformer design

The air-core transformer was designed with the specifications in Table I.1.26.2. L11 and L12 are designed to be the leakage inductors and M is designed as a magnetizing inductor. Figure I.1.26.8 (a) shows the drawing of the transformer on PCB. The primary and secondary sides are placed on the two middle layers to maximize M. Figure I.1.26.8 (b) shows the manufactured power supply. The Lin was made with Fair-Rite 67 core. The main switch is EPC2214 Enhancement-Mode GaN Power Transistor with only 15 m Ω on-resistance. Table I.1.26.2 also compares the designed and measured parameters of the transformer.

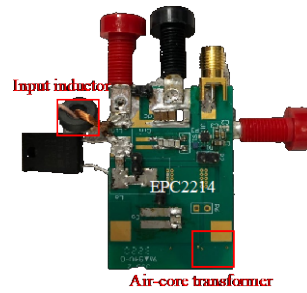
The class-E dc-dc converter has been tested with the transformer. The testing waveforms and output performance are shown in Figure I.1.26.9. Gate and Vds waveforms in Figure I.1.26.9 (a) show that ZVS is achieved. As shown in Figure I.1.26.9 (b), output voltage increases almost linearly with the load resistance, which verifies the constant-current-output characteristics of the converter.

Table I.1.26.2 Parameters of the Simulated Air-core Transformer

Parameters	Designed Value	Measured Value
L _{l1} , L _{l2}	246 nH	180 nH
M	360 nH	410 nH

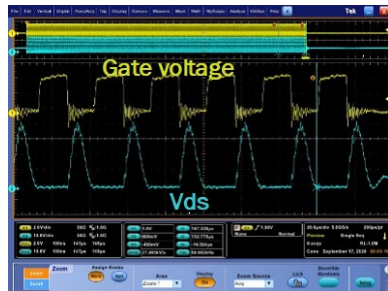


(a)

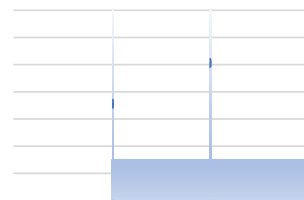


(b)

Figure I.1.26.8 (a) PCB drawing of the air-core transformer (windings are placed in the middle layers), and (b) class-E dc-dc converter with the integrated air-core transformer.



(a)



(b)

Figure I.1.26.9 Output performance of the power supply: (a) gate and Vds waveforms of the switch showing that ZVS is achieved, and (b) output voltage increases almost linearly with the load resistance. Constant-current output characteristics are verified.

6. Current sensing based on module parasitics

A current sensor based on module parasitics was designed. The proposed scheme 1 in Figure I.1.26.10 (a) includes an integral circuit and a feedback compensation circuit to eliminate the effect of the parasitic resistance. If the parameters are properly selected, the output of the current sensor scheme is obtained as:

$$v_o(s) = \frac{L_s}{mR'C'} \frac{\left(1 + \frac{r_s}{L_s s}\right)}{1 + \frac{1}{R'C'} \frac{R_{b3}}{R_{b1}} \frac{1}{s}} i_s(s) = \frac{L_s}{mR'C'} i_s(s) \quad (1)$$

The limit of this scheme is a fixed compensation under the change in the wire bond resistance due to temperature variation. Under the case, where the wire bond resistance is $r_s + \Delta r_s$, the transfer function from the switching current to the measurement current becomes:

$$H_i(s) = \frac{i_{s-meas}(s)}{i_s(s)} = \frac{\frac{mR'C'}{L_s} v_o(s)}{i_s(s)} = 1 + \frac{\Delta r_s}{1 + \frac{r_s}{L_s s}} \quad (2)$$

Since $H_i(s)$ consists of Δr_s , the accuracy of the measurement current using the scheme in Figure I.1.26.10 (a) is reduced under varied temperatures.

Figure I.1.26.10 (b) shows the experimental setup of the sensor scheme in Figure I.1.26.10 (a). The measurement current using the designed current sensor compared to that of a Rogowski coil are demonstrated in three cases: without feedback loop (Figure I.1.26.11 (a)), with feedback compensation at 25°C (Figure I.1.26.11 (b)), and with feedback compensation at 150°C (Figure I.1.26.11 (c)). It is seen that the performance of the current sensor is much improved with feedback compensation. Under 25°C, based on which the parameters of the feedback circuit are designed, the measurement current is the most accurate. However, under 150°C, there is a significant error between the measurement current and the actual one.

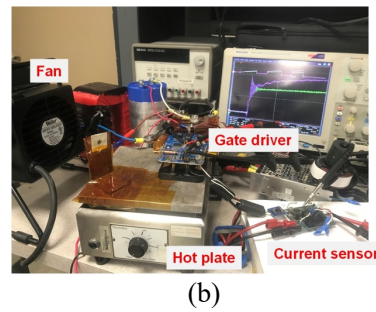
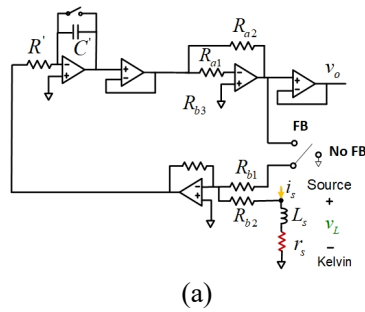


Figure I.1.26.10 (a) Proposed current sensor scheme 1, and (b) experimental setup of the current sensor scheme 1.

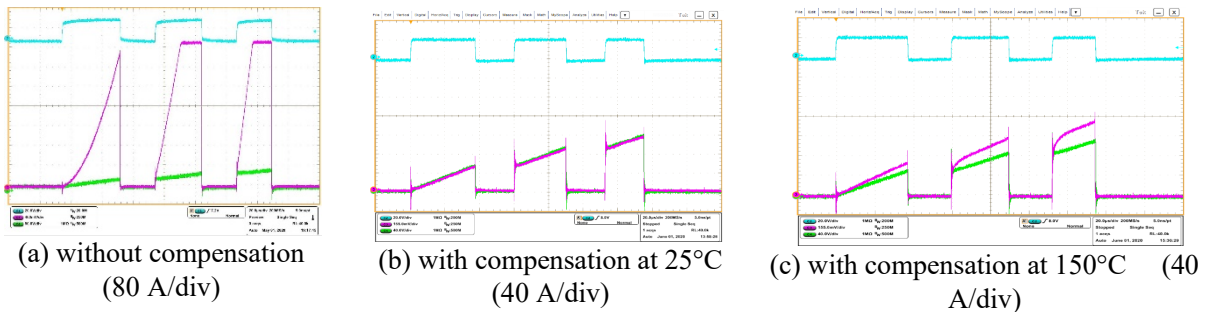


Figure I.1.26.11 Measurement current under different configurations.

To eliminate the effect of the operating temperature on the performance of the current sensor, a proposed current sensor with feedback compensation and resistance identification is presented in Figure I.1.26.12 (a). The resistance error is estimated and is continuously updated into the feedback loop. As compared to the proposed scheme in Figure I.1.26.10 (a), the scheme in Figure I.1.26.12 (a) has a similar feedback principle. However, the feedback signal is modified so that the wire bond resistance information can be kept track of, and

thus the error in the current sensor output is mitigated. Currently, an experiment setup of this proposed current sensor scheme is being built as shown in Figure I.1.26.12 (b), and its experimental results will be provided in future work.

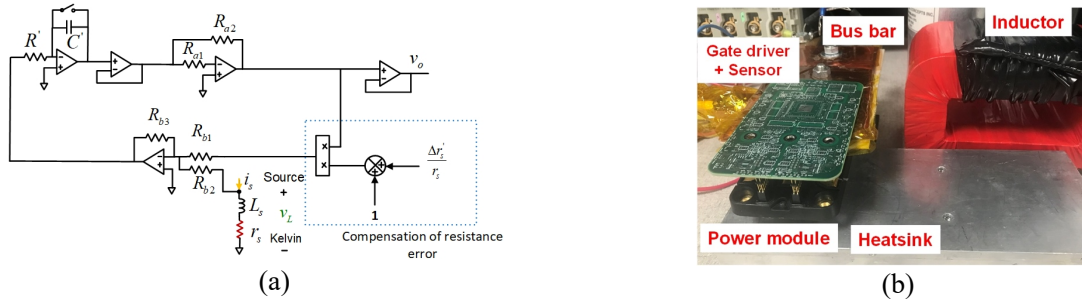


Figure I.1.26.12 (a) Proposed current sensor scheme 2, and (b) experimental setup of the current sensor scheme 2.

7. Class-D amplifier based active filter

An active filter, which is based on the class-D amplifier, was proposed to replace a conventional class AB amplifier in a hybrid passive-active electromagnetic interference (EMI) filter. The objectives are to contain all common-mode noise within the SiC MOSFET module, and to achieve a high efficiency, which is expected to be within 99 %. Also, the common-mode current information can be possibly derived from the proposed current sensor, which will help eliminate the need for the current transformer. The proposed active filter for a three-phase inverter system is illustrated in Figure I.1.26.13 (a). A significantly improved FFT of the output voltage of the LISNs in Figure I.1.26.13 (a), which is presented in Figure I.1.26.13 (b), indicates the effectiveness of the active filter. More theoretical analysis and simulation studies to further improve the performance of the class-D amplifier will be demonstrated in future work.

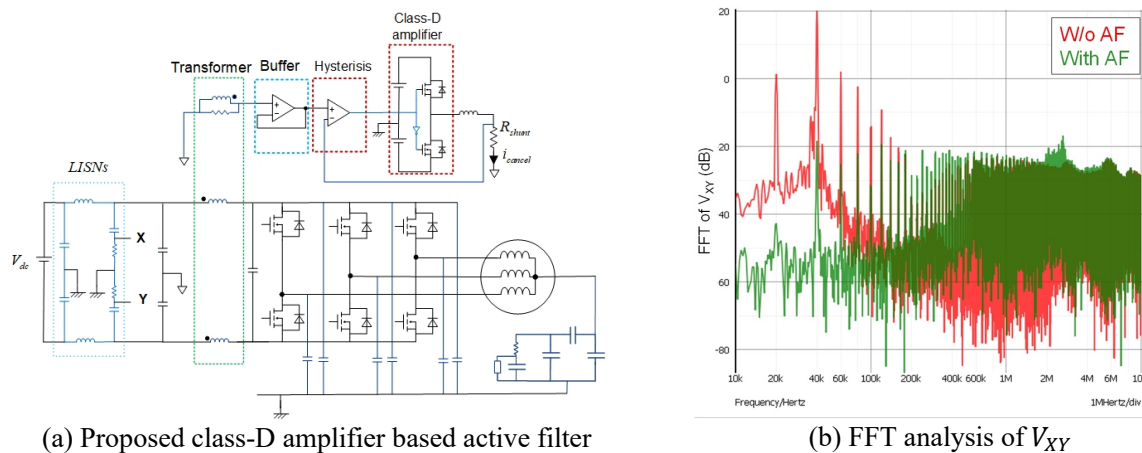


Figure I.1.26.13 Proposed class-D amplifier based active filter and FFT analysis of V_{XY} with and without the active filter.

Conclusions

Two geometric layouts of a SiC phase-leg module were designed and analyzed by computer simulations to determine parasitic inductances and thermal performance. The module layout with double-side cooling requires 46 % less convection coefficient compared to that with single-side cooling. We also varied the processing parameters for bonding on bare copper by silver-sintering in air. Power modules with one of the layout designs were fabricated and tested. The results showed that our module packaging process has no adverse impact on the characteristics of the devices.

A gate driver board with high-temperature driver IC was designed, and the switching performance with the capacitive load was verified. Measured mutual inductance of the air-core transformer showed a less than 10 %

difference with the design. This led to the expected 0.7 A constant output current with the help of the matching network design. The 180 nH leakage inductance reduced high-frequency harmonics to ensure load-independent ZVS characteristics of the class-E dc-dc converter.

A robust design of a current sensor based on module parasitics was completed. It has a feedback compensation scheme to eliminate the effect of changing wire-bond resistance from temperature variation. Experimental results of the current sensor with fixed compensation were provided, and an experiment on a newly designed current sensor with dynamic compensation is being conducted. Also, an effective class-D based active EMI filter was designed to contain all common-mode noise within the power modules. More advantageous features of the active filter and methods to further improve its performance are currently being investigated.

Key Publications

1. G-Q. Lu, C. Ding, “Double-side Cooled Power Module with Sintered-silver Interposers,” Invention Disclosure to Virginia Tech Intellectual Properties (VTIP); VTIP: 21-004, July 10, 2020.

Acknowledgements

We are grateful to Dr. Burak Ozpineci, Dr. Gui-Jia Su, and Dr. Emre Gurpinar of Oak Ridge National Laboratory (ORNL) for working with us to better design our SiC power modules to fit in their segmented three-phase inverter. They will also support us with the testing of our power modules in the testbed at ORNL.

I.1.27 Implementation of WBG devices in circuits, circuit topology, system integration as well as SiC devices (The Ohio State University)

Dr. Anant Agarwal, Principal Investigator

The Ohio State University
2015 Neil Avenue
Columbus, OH 43210
Email: agarwal.334@osu.edu

Dr. Jin Wang, CO-Principal Investigator

The Ohio State University
2015 Neil Avenue
Columbus, OH 43210
Email: wang.1248@osu.edu

Susan Rogers, DOE Technology Development Manager

U.S. Department of Energy
Email: susan.rogers@ee.doe.gov

Start Date April 1, 2020
Project Funding: \$300,000

End Date: March 31, 2021
DOE share: \$300,000

Non-DOE share: \$0

Project Introduction

All device vendors have compromised reliability/ruggedness of SiC MOSFETs to reduce cost. Short channel length is a good example which reduces device size and cost at the expense of reduced short-circuit time of 2 - 3 μ s. Another example is the gate oxide thickness which has been thinned to 30 - 40 nm without reducing the gate voltage in order to reduce device size and cost. This leads to gate oxide leakage issues and susceptibility to rupture during extreme events such as short-circuit and exposure to static electricity. Hence, commercial devices, available to-date, are not suitable for insertion into a vehicle power train for long operational life. A comprehensive reliability study is warranted for commercially available devices both as discrete devices and in an inverter to uncover failures such as threshold voltage instability, inadequate short circuit time, gate oxide failures due to gate voltage overshoot and high junction temperature, as well as body diode instability (Figure I.1.27.1). OSU is working collaboratively with Sandia National Labs and SUNY Poly on this project (Figure I.1.27.2).

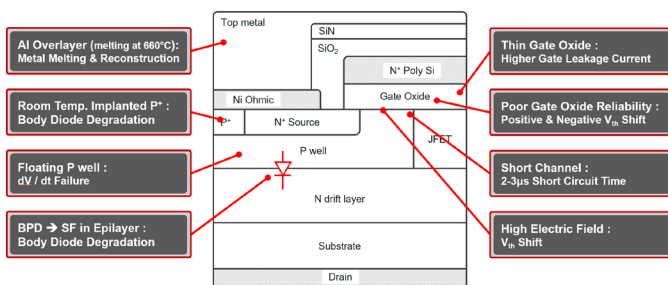


Figure I.1.27.1 SiC MOSFET Reliability Issues.

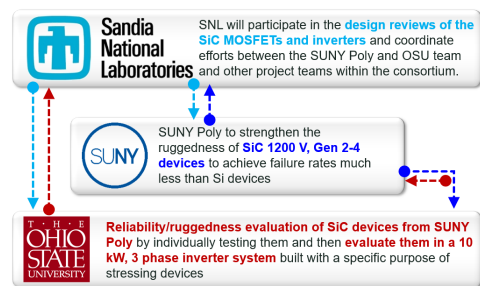


Figure I.1.27.2 Key Partnerships.

Objectives

The overall objective of the project is to ensure that SiC devices are reliable and rugged as required in automotive applications for operational life of 300,000 hrs and create new device designs to address various weaknesses in currently available commercial devices. OSU work will focus on reliability/ruggedness evaluation of SiC devices by individually testing them and then evaluating them in a 10 kW, 3 phase inverter system built with a specific purpose of stressing devices using realistic drive cycles such as a 10-minute hill climb. It should be noted that the primary purpose of the 10-kW inverter is to provide a platform for stressing the SiC devices under accelerated but realistic drive conditions and NOT to meet the 100-kW power and power density goals. The 100-kW inverter will be built by other team members. OSU will share the findings with SUNY Poly and collaborate with them to strengthen the existing device designs to overcome the specific weaknesses in the device. These devices will be fabricated in a state of the art commercial SiC Foundry. The new designs will be improved every year through extensive testing by OSU, re-design (in collaboration between OSU and SUNY Poly) and subsequent fabrication.

Objectives (FY2021):

- Ruggedness of commercial and Gen-1 SiC MOSFETs from SUNY Poly will be evaluated as stand-alone devices and in Inverter-1.
- A three phase Inverter-2 using commercial and Gen-1 MOSFETs from SUNY Poly will be designed and built.

Approach

Collaboration with National Laboratory:

OSU will coordinate and collaboratively conduct work with the Sandia National Laboratory (SNL) on selected tasks integral to the completion of the project. The results of this collaborative effort with the national laboratory will be included in all project reporting. SNL will participate in the design reviews of the SiC MOSFETs and inverters and coordinate efforts between the SUNY Poly and OSU team and other project teams within the consortium.

Results (Task 1.1 – Ruggedness of commercial SiC MOSFETs)

A. Gate leakage current behavior

The gate leakage currents for the packaged (TO-247) commercial SiC power MOSFETs manufactured by commercial vendor H are examined by applying constant voltage bias to the gate terminal while drain and source terminals are grounded. A source/measurement unit (Keysight B2901A) is used to apply the gate voltage and monitor the gate leakage current during the stress. The device under test (DUT) is put in an oven with the temperature set at 150°C. The stress is applied for up to 24 hours. The threshold voltage (V_T) variations during measurements are examined (Figure I.1.27.3) by interrupting the stress and measuring V_T of the DUT rapidly (< 10 seconds). V_T values are monitored throughout the stress for two distinct cases of $V_G = 38$ V, and 33 V (Figure I.1.27.3). A strong correlation between the threshold voltage variations and the gate leakage currents is observed. At $V_G = 38$ V, hole trapping dominates initially and the threshold voltage of the DUT decreases. Then the electron trapping overtakes, and the threshold voltage increases. At $V_G = 33$ V, only electron trapping exists so that the V_T trend shows a monotonic increase.

This research reveals insights of different failure mechanisms under different oxide electric fields and points out that Time Dependent Dielectric Breakdown (TDDB) measurements to predict useful life for gate oxides must be performed at lower electric fields to avoid the generation of holes in the oxide.

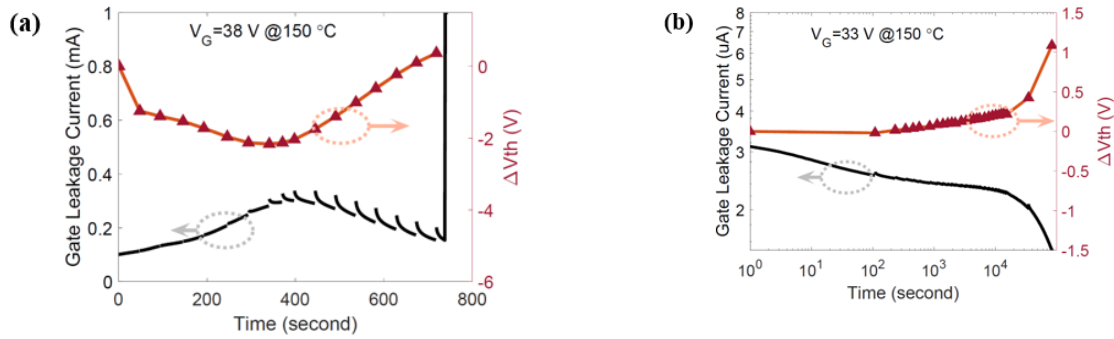


Figure I.1.27.3 Threshold voltage variations and gate leakage currents during stresses at $V_G=38, 33 \text{ V}$.

B. Time-Dependent Dielectric Breakdown (TDDB)

The failure times of constant voltage TDDB measurements are presented for vendor H as shown in Figure I.1.27.4. The results clearly show that the TDDB measurements should be performed at oxide fields below 9 MV/cm as pointed out in the previous section. Vendor C demonstrates notably wider variations of failure times for given gate biases. For all three gate biases, the results do not show any intrinsic region and seem to suggest different failure modes for each gate bias. These variations of the measured lifetime makes it impossible to predict the lifetime under a normal operating condition with any reasonable uncertainty level.

Lifetime variations for vendor C are linked to its threshold voltage variations since both are caused by non-uniform distribution of the high amount of interface traps and oxide defects and hence poor gate oxide quality.

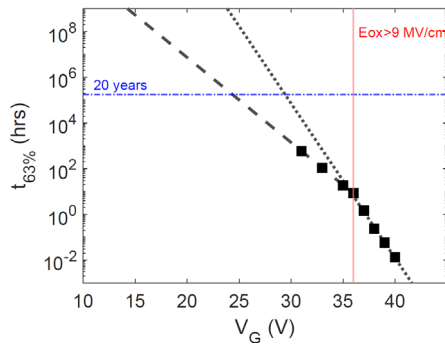


Figure I.1.27.4 63% failure times as a function of applied gate voltage for vendor H at 150°C .

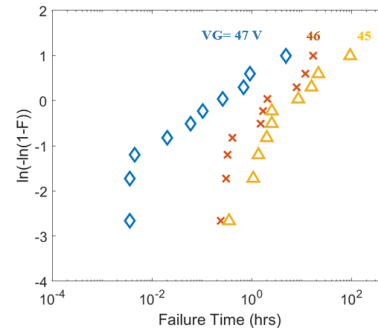


Figure I.1.27.5 Weibull distributions for vendor C at 28°C with gate biases of 45, 46, and 47 V.

C. Threshold voltage instability: PBTI and NBTI

The threshold voltage is affected by interface states since, in strong inversion, these states are negatively charged due to the capture of electrons. In addition to interface states, near-interfacial oxide traps (NIOTs), also known as border traps, give rise to threshold voltage instability. Under a high positive DC bias applied to the gate, electrons in the conduction band (CB) of SiC are injected into NIOTs by tunneling. In addition, holes back-tunnel from traps in the oxide to the valence band (VB) in SiC resulting in a net positive threshold voltage shift. Conversely, when a negative DC bias is applied, the threshold voltage shifts in the negative direction as electrons back-tunnel into the CB with hole injection from the VB. This may place devices into a normally-on state, especially in the devices with a low threshold voltage at elevated temperatures. Thus, it is important to study the threshold voltage instability in commercial devices to determine their robustness for automotive applications which require stringent reliability requirements.

Figure I.1.27.6 shows time-dependent threshold voltage shifts with various bias-stresses. Error bars at each point represent the variation in 5 devices. When a positive DC bias of $+20 \text{ V}$ is applied to the gate for 50 hours,

the threshold voltage shifts are 0.50 V, 0.35 V, 0.16 V, 0.06 V and 0.10 V for devices from vendor C, D, D', E', and I respectively (see Figure I.1.27.6 (a)). The largest threshold voltage shift was found in devices from vendor C (device C). The threshold voltage values are found to saturate in 20 hours in most cases. For the DC bias of +30 V, again devices from vendor C (device C) show the largest amount of shift about 0.74 V after 50 hours of stress. Conversely, when a negative bias of -10 V is applied to the gate for 50 hours, the threshold voltage shifts in the negative direction. The maximum shift of about -0.2 V is shown in device C while others show less than -0.1 V shift. Thus, for traps measured within the time scale of the measurements, we conclude that device C has the most number of NIOTs (see Figure I.1.27.6 (c)).

Considerable variance between devices from different vendors implies that some vendors have been able to significantly reduce the NIOTs in the gate oxide whereas the gate oxide quality poses a major reliability problem for many vendors.

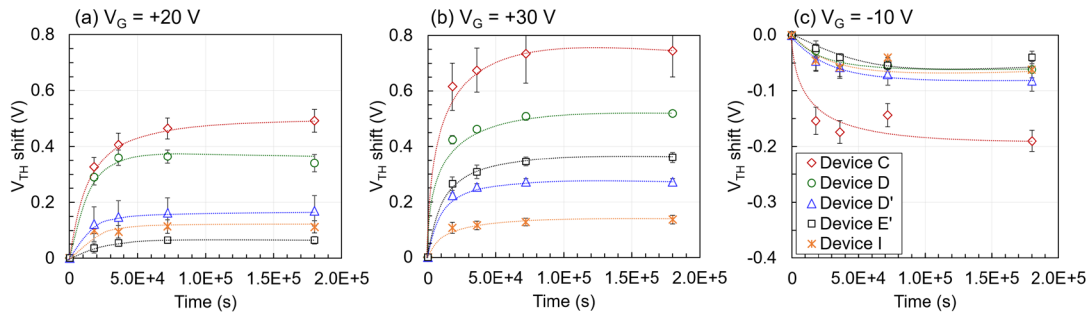


Figure I.1.27.6 Time-dependent threshold voltage shifts for (a) positive bias-stress of +20 V, (b) +30 V, and (c) negative bias-stress of -10 V for 50 hours. The error bars represent the spread of 5 devices measured for each vendor.

D. Short Circuit Withstand Time (SCWT)

SCWT is one of the major indicators for devices’ SC sustaining capabilities. Si IGBTs’ SCWTs are often higher than 7- μ s [1], [2] to ensure reliable and safe shutdown of the power converters. It is desirable for commercial SiC devices to also have sufficient SC sustaining capability. However, SiC devices show 4-to-8 times higher saturation current density as compared to a Si MOSFET, and 1.5-to-2.5 times higher as compared to a Si IGBT. This implies higher heat generation during a SC event. The internal temperature would rise quicker in SiC devices leading to shorter SCWTs. 1200-V rated devices D’, E’, and F’ were tested at a constant V_{ds} of 800 V with V_{gs} varying from 14 V to 20 V with a 2-V interval. The Si IGBT (device B) was also tested in the same condition with V_{gs} of 20 V as a comparison. For each gate voltage, tests started with a 1- μ s SC pulse, then 1 μ s was added in each follow-up SC pulses, until the device failed. The minimum interval between each pulse was 30 seconds. Figure I.1.27.7 shows SCWT for SiC MOSFETs ranges between 2.2-5 μ s at $V_{ds} = 800$ V and $V_{gs} = 20$ V. This means that automotive standards will need to be modified to accommodate much shorter SCWT as well as fast desat circuits will have to be used to protect devices during normal operation. A number of device design ideas to improve the SCWT in SiC devices are being pursued jointly by SUNY POLY and OSU teams.

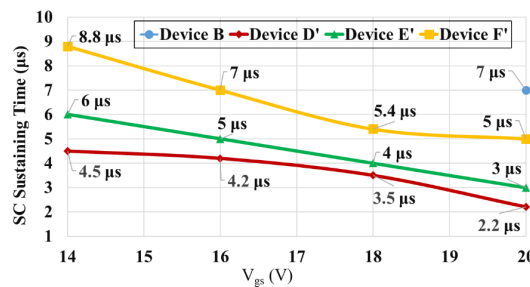


Figure I.1.27.7 SC sustaining time with different gate voltages with $V_{ds} = 800$ V. Devices D’ to F’ are SiC MOSFETs and device B is a Si IGBT.

Results (Task 2.1 – Ruggedness of Gen-1 devices)

Subtask 2.1.1: Gen-1 SiC MOSFETs will be packaged in metal packages

Another objective in this report is the reliability and ruggedness evaluations of Gen-1, 1200 V SiC MOSFETs from SUNY Poly. Fifty-two Gen-1 SiC MOSFETs from three different wafers are packaged. The process splits were discussed in the 1st year's report from SUNY Poly. Prior to the reliability evaluations, the preliminary electrical tests were performed. Following reliability tests are being performed on the 52 devices: (a) Body diode stability, (b) Threshold voltage instability, (c) Gate oxide leakage current behavior, (d) Short circuit withstand time, and (e) Avalanche energy.

Subtask 2.1.2: Comprehensive evaluation of Gen-1 packaged SiC MOSFETs for failures

A. Body Diode Stability

We previously reported the effect of body diode degradation on commercially available 1.2 kV 4H-SiC MOSFETs from three commercial vendors. Forward current stress on the body diode increased the forward voltage drop of the body diode in the MOSFET and degraded the majority carrier conduction by recombination-induced Stacking Faults (SFs). These results imply one of three reasons may be responsible for such a high degree of degradation. First, the device may be using room temperature (RT) ion implantation of Al to form p⁺ contacts which can create many Basal Plane Dislocations (BPDs) [3], [4]. Second, some other processes such as reactive ion etching may result in the creation of BPDs. Third, the starting epi-layer has many BPDs.

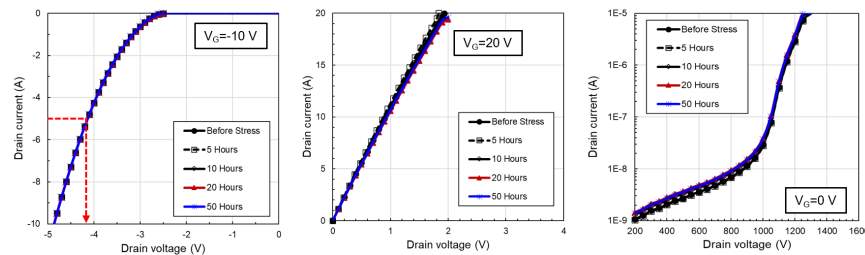


Figure I.1.27.8 Degradation of I-V curves for built-in body diode of Gen-1 DMOSFETs implanted at RT.

Our goal is to find out whether BPDs are introduced by the combination of the RT aluminum implantation and activation anneal. To apply forward-bias stress on the body diode, devices were connected in series. The body diodes were stressed at 10 A for 5 hours. During the forward bias stress on the body diode, the devices were mounted on a heat sink with a water chiller to maintain a case temperature of the MOSFET package below 50°C. Following this initial stress, all the measurements were repeated. After the stress, the devices were allowed to cool down to room temperature before the electrical tests. This process was repeated after 10 hours, 20 hours, and 50 hours. All the six MOSFETs of Gen-1 did not show any degradation after current stress of I_D=5 A, for 50 hours as shown in Figure I.1.27.8. **This indicates that ion implantation at room temperature for p⁺ contact does not cause process-induced Basal Plane Dislocations in 1200 V MOSFETs fabricated by SUNY POLY. This implies that tremendous cost reduction (up to 20%) can be achieved by using room temperature implants.**

Results (Task 1.2 – Inverter-1 build with commercial SiC MOSFETs)

A. A gate driver with comprehensive protection functions

The gate driver schematic diagram is shown in Figure I.1.27.9. This design is a compact, dual-channel, gate-driver solution for driving SiC MOSFETs in half bridge or two high sides configuration. This design provides 15 V and -5 V output voltage and 1 W output power for each channel. The current booster is capable of providing 14 A source and sink peak currents and up to 500 kHz switching frequency. The galvanic isolation supports 5.7 kV RMS isolation voltage. Active miller clamp is integrated for better switching performance. De-saturation protection and UVLO function protects the MOSFETs from unexpected faults. Each phase leg was designed on a four-layer PCB board with a 163 mm x 23 mm size. This design consists of three main parts

for each phase leg. The two isolated DC/DC converters provide 15 V, -5 V for the whole board. The interface functional element is isolated with the main power circuit. The input and output terminals for PWM signal and fault feedback are coaxial to provide better EMI immunity.

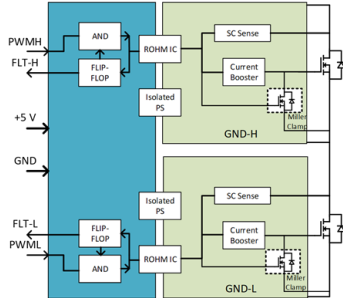


Figure I.1.27.9 Block diagram of gate drive circuit.

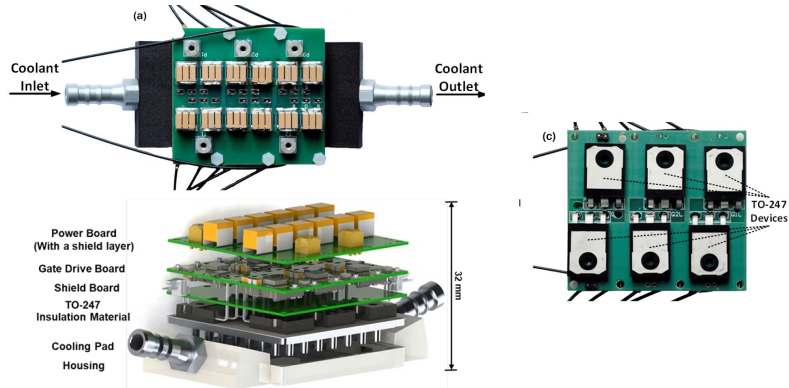


Figure I.1.27.10 Pin fins design liquid cooling system 3D model and TO-247 packaged power device board.

B. Thermal and mechanical designs of the Inverter-1

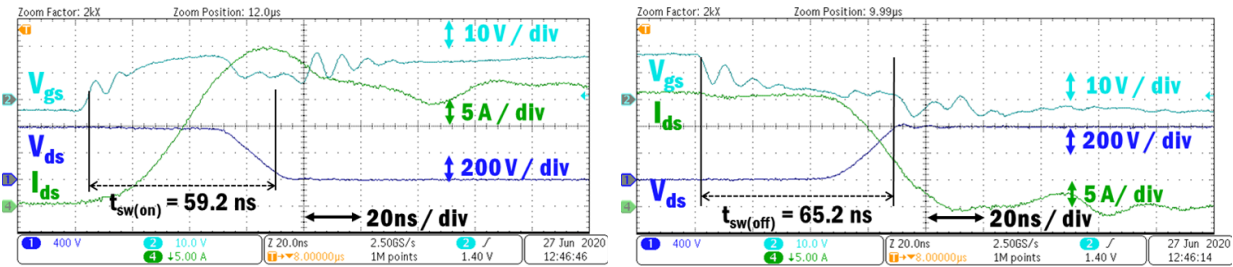
The liquid cooling is used to achieve higher power density and system reliability (Figure I.1.27.10). In the 10-kW high power density inverter, the expected heat dissipation is 120 W. The junction temperature is expected to be lower than 125°C. The thermal design is a cooling pad using aluminum pin fins and liquid tank. Insulation putty material serves as insulation layer and thermal layer to assure good contact between SiC MOSFETs and heatsink. To achieve high power density, the power board is stacked on top of the gate drivers. To avoid the interference produced by power loop switching, a shielding layer is placed between MOSFETs and gate drivers. The housing of the coolant is manufactured with 3D printed nylon material which is firm and waterproof. The detail of the structure is shown in Figure I.1.27.10. The thermal simulation is conducted to verify the cooling system capability. Ambient temperature is set at 85 degree C, coolant temperature is set at 70 degree C with 0.2 L/min flow rate. Under 120 W power dissipation condition, in FEA simulation, the highest temperature of junction temperature is lower than 100°C.

C. Double Pulse Test

In order to evaluate the performance of the gate driver, double pulse test with a proper gate resistor is conducted. Test waveforms are shown in Figure I.1.27.11. Gate resistor in the test is 15 Ω, which maintains relatively high switching speed and reduces the ringing. Based on the test, key parameters are extracted as shown in Table I.1.27.1.

Table I.1.27.1 Key parameters

Parameters	Value
$T_{\text{sw(on)}} (10\% V_{\text{gs}} \text{ to } 10\% V_{\text{ds}})$	59.2 ns
$T_{\text{sw(off)}} (90\% V_{\text{gs}} \text{ to } 90\% V_{\text{ds}})$	65.2 ns
Switch on dv/dt	33.9 kV/μs
Switch off dv/dt	34.7 kV/μs
$E_{\text{sw(on)}} (V_{\text{ds}} = 800 \text{ V}, I_{\text{ds}} = 20.0 \text{ A})$	562 μJ
$E_{\text{sw(off)}} (V_{\text{ds}} = 800 \text{ V}, I_{\text{ds}} = 20.0 \text{ A})$	147 μJ



(a) Device switch-on waveforms.

(b) Device switch-off waveforms.

Figure I.1.27.11 Double pulse test waveforms using the gate driver.

D. Three phase inverter test

Three phase inverter test is conducted to verify the function of the whole design. To assure the smooth operation of inverter, physical layout of the test setup is designed in a proper way. Input capacitor is placed as close as possible to the inverter to reduce stray inductance. To accurately measure the device temperature, a thermocouple is attached to the thermal pad of MOSFET device. The initial coolant temperature is 26°C, and coolant flow rate is 2.5 L/min. Test waveforms and data are shown as below (Figure I.1.27.12).

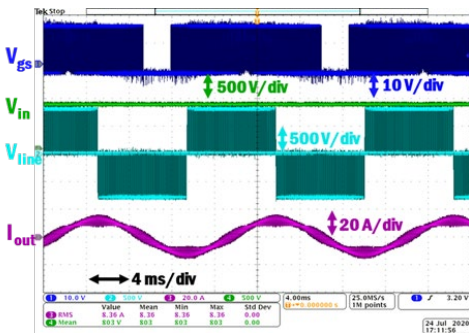


Figure I.1.27.12 Test Waveforms under 800 Vdc input.

V _{in} (V)	I _{in} (A)	I _{out, RMS} (A)	P _{in} (W)	P _{out} (W)	T _{measured} (°C)
200	2.24	2.12	448	446	28.9
400	4.46	4.23	1784	1771	31.7
600	6.68	6.31	4008	3954	34.7
800	8.89	8.40	7112	7007	40.1

Operation Condition	Total Device P _{loss}	Estimated T _{junction}	Efficiency η
Inverter Operation @ 4 kW, 30 kHz	54 W	44.6 °C	98.6%
Inverter Operation @ 7 kW, 30 kHz	95 W	57.5 °C	98.5%

Figure I.1.27.13 Inverter test data.

Based on the datasheet, thermal resistance between junction to case for power MOSFETs is 1.1°C/W. Switching losses, estimated junction temperature, and inverter efficiency can be calculated based on test data (Figure I.1.27.13). The calculated thermal resistance between case and coolant is 0.89°C/W. **Based on the test, inverter can reach the power density of 69 kVA/L with reactive load.**

Results (Task 2.2 – Inverter-1 build with Gen-1 SiC MOSFETs)

Subtask 2.2.1: Gen-1 SiC devices will be integrated into the Inverter-1 for realistic and accelerated operation at elevated temperature

A. Redesign of Inverter-1 with Gen-1 MOSFETs

The inverter-1 test platform delivered a power density of 69 kVA/L with reactive load and the maximum junction temperature of MOSFETs was lower than 60°C at 7 kW output power. However, there are some structural issues with inverter-1 design. Major issue is that the pins of Gen-1 device delivered by SUNY Poly are 5 mm shorter than commercial devices. The length is not enough for a bend-up design. Due to the placement of MOSFET switches and PCB layout, it is difficult for temperature measurement on each device. Space on PCBs for test points is also limited. A new design of inverter-2 will address these issues and will allow us to test Gen-1 devices. This work is in progress.

Conclusions

This report concludes that there are significant issues with commercial devices with respect to threshold voltage stability, short circuit withstand time not being adequate and stability of body diodes. Long term reliability tests using constant voltage TDDDB test indicate quite a bit of variability among different vendors implying significant differences in gate oxide quality and long-term prediction of useful life. The fabrication of Gen-1 devices by SUNY Poly indicates that some of these issues can be addressed by better design while gate oxide issues would have to be addressed by process improvement. Body-diode stability in Gen-1 devices with room temperature implants has been demonstrated implying future cost reduction by as much as 20%. A 10-kW inverter has been designed, built and successfully tested up to 7 kW. It shows that a power density of 69 kVA/L can be achieved with 98.5% efficiency. This inverter is being used to test commercial devices under realistic drive conditions and will be used to test Gen-1 devices as well.

Key Publications

1. (Published paper) Susanna Yu, Tianshi Liu, Shengnan Zhu, Diang Xing, Arash Salemi, Minseok Kang, Kristen Booth, Marvin H. White, Anant K. Agarwal, Threshold Voltage Instability of Commercial 1.2 kV SiC Power MOSFETs, 2020 IEEE International Reliability Physics Symposium (IRPS), Dallas, TX, USA, 2020, pp. 1-5
2. (Published paper) Tianshi Liu, Shengnan Zhu, Susanna Yu, Diang Xing, Arash Salemi, Minseok Kang, Kristen Booth, Marvin H. White, Anant K. Agarwal, Gate Oxide Reliability Studies of Commercial 1.2 kV 4H-SiC Power MOSFETs, 2020 IEEE International Reliability Physics Symposium (IRPS), Dallas, TX, USA, 2020, pp. 1-5
3. (Oral presentation) Minseok Kang, Susanna Yu, Diang Xing, Tianshi Liu, Shengnan Zhu, Kristen Booth, Marvin H. White, Anant K. Agarwal, Body Diode Reliability of Commercially Available 1.7 kV 4H-SiC MOSFETs, 62nd Electronic Materials Conference, 2020
4. (Oral presentation) Shengnan Zhu, Tianshi Liu, Susanna Yu, Diang Xing, Arash Salemi, Minseok Kang, Kristen Booth, Marvin H. White, and Anant K. Agarwal, An Investigation into Anomalous Time-Dependent Dielectric Breakdown Characteristics for 1.2 kV Commercial 4H-SiC Power MOSFETs, 62nd Electronic Materials Conference, 2020

References

1. Fairchild Semiconductor. IGBT Behavior under Short Circuit and Fault Protection. [Online]. Available: <https://www.yumpu.com/en/document/read/11384505/igbt-behavior-under-short-circuit-and-fault-protection>.
2. Analog Devices. IGBT Overcurrent and Short-Circuit Protection in Industrial Motor Drives. [Online]. Available: <https://www.analog.com/en/technical-articles/igbt-overcurrent-and-short-circuit-protection-in-industrial-motor-drives.html>
3. K. Konishi, R. Fujita, Y. Mori and A. Shima, "Inducing defects in 3.3kV SiC MOSFETs by annealing after ion implantation and evaluating their effect on bipolar degradation of the MOSFETs" Semicond. Sci. Technol. vol. 33, issue 12, 2018.
4. R. E. Stahlbush, K. N. A. Mahakik, A. J. Lelis, R. Green, "Effects of Basal Plane Dislocations on SiC Power Device Reliability", in Proc. 2018 IEEE International Electron Devices Meeting (IEDM), pp. 448-449, 2018.

I.2 Electric Drive Technologies Development

I.2.1 Amorphous Metal Ribbon (AMR) and Metal Amorphous Nanocomposite (MANC) Materials Enabled High Power Density Vehicle Motor Applications (Carnegie Mellon University)

Michael E. McHenry, Principal Investigator

Carnegie Mellon University
5000 Forbes Avenue
Pittsburgh PA 15213-3815
Email: mm7g@andrew.cmu.edu

Susan Rogers, DOE Technology Development Manager

U.S. Department of Energy
Email: susan.rogers@ee.doe.gov

Start Date: September 19, 2019

End Date: March 18, 2022

Project Funding: \$350,947

DOE share: \$350,947

Non-DOE share: \$0

Project Introduction

A collaborative team from *Carnegie Mellon Univ. (CMU)*, *North Carolina State Univ. (NCSU)* and *Metglas, South Carolina* proposes new high speed motors (HSMs) with high-power density for traction motors. These are enabled by hybrid designs exploiting permanent magnets without heavy rare earths and high induction/high resistivity soft magnetic materials allowing for high switching frequencies needed to increase power densities. Team members include Michael E. McHenry, Prof. Materials Science & Eng., CMU, with over 30 years experience in magnetic materials development; Subashish Bhattacharya, Prof. Electrical Eng. and Freedom Center Director at NCSU with over 30 years experience in development of power electronic components and systems and Eric Theisen, Director of Research at Metglas, the only US located supplier of AMR and MANC materials. The team offers a novel axial motor architecture [1] exploiting soft magnetic materials (SMMs) which switch with low loss at high frequencies [2] and heavy rare earth free permanent magnets that address issues of materials criticality, consequent supply chain risks, and high costs for traction motors.

Objectives

The project objective is to achieve an 8-fold increase in power density for a traction motor designed to showcase Amorphous Metal Ribbon (AMR) and Metal Amorphous Nanocomposites (MANCs). The motor is enabled by exploiting permanent magnets without heavy rare earths and high induction/high resistivity soft MANC allowing high switching frequencies needed to increase power densities.

Approach

Project Objectives are to be accomplished by tasks broken up into two budget periods:

Budget Period 1: Benchmark AMRs and MANC Alloys for Traction HSM Design: AMR materials will be benchmarked, in a Finite Element Analysis (FEA) model. Alloys will be cast at commercial scale and properties relevant to 5 kHz magnetic core losses and audible magnetostrictive noise will be measured and compiled. Sample ribbons will be provided to the DOE. A FEA model of a Traction High Speed Motor (HSM) will be designed, and performance evaluated.

Budget Period 2: Properties Optimization, Component Fabrication and Alloy Studies.: Properties of AMR materials will be optimized and benchmarked. Rotors and dual stators will be produced for testing and loss validation in the Flux Switching with Permanent Magnet (FSWPM) motor. Magnetic switching frequencies and mechanical properties will be evaluated. The measured properties will be incorporated into a

FEA model of a Traction HSM and used to finalize the design. This design will be used to benchmark new materials. Project Milestones are listed below in Table I.2.1.1:

Table I.2.1.1 DOE/VTO – DE-EE0008870 Program Milestones

Milestones	Description	Planned Competition Date	Actual Completion Date
Budget Period 1			
Design Traction Motor	Benchmark materials. Report FSWPM Motor Power Losses	6/15/20	6/22/20
AMR Loss at 5kHz Evaluation Complete	Compare wide cast AMR and MANC Ribbon evaluation at 5 kHz	12/15/20	
Evaluate Materials in Traction Motor Design	Complete Power Density Improvement Evaluation with AMRs and MANCs.	4/15/21	
Preliminary Design Validated to Achieve Performance Measures	FEA assessment of preliminary technology design has been completed, verifying an 8x increase in power density to be achievable.	6/15/21	
Budget Period 2			
Fabricate FeCo-based Dual Stators and Rotors.	Demonstrate Manufacturability of FeCo-based AMR motor.	12/15/21	
Evaluate Mechanical Properties of AMRs and MANCs Suitable for HSM	Use mechanical properties in FEA to verify that HSM is mechanically able to rotate at >20 krpm.	3/15/22	
Report Oxide properties for AMR and MANCs	Demonstrate resistance > coated laminates. Demonstrate Bulk resistivity > 150 mW-cm, surface resistivity > 500 mW-cm	6/15/22	
Test AMR and MANC Dual Stators and Rotors.	Report HSM power density for each material.	9/15/22	

Results

We experienced Covid19 delays and requested a 6 mo NCE. To date we have accomplished BP1 Tasks:

Task 0.0 –A Project Management Plan was submitted.

Task 0.1- project kickoff meeting was held with the DOE at Carnegie Mellon Univ. on Nov. 22, 2020.

Budget Period 1: Benchmark AMR and MANC Alloys for Traction HSM Designs.

Task 1.1 – Staff and train project personnel: **Complete**

Subtask 1.1.1 – We allocated staff for the Project. 100% **Complete**

Subtask 1.1.2 – CMU continued Comsol Multiphysics FEA Software licenses and maintains sufficient supplies of raw materials and casting expendables. **Complete**

Subtask 1.1.3 – Identified suppliers for permanent magnets. **Complete**

Task 1.2 – Begin FEM Motor Modeling, Alloy Development:

- Subtask 1.2.1** – Benchmark conductors, permanent magnets in prior FSWPM HSM Design. **Complete**
- Subtask 1.2.2** – Benchmark Metglas FeCo-based AMR in prior FSWPM HSM Design. **Complete**
- Subtask 1.2.3** – Begin Casting New FeNi-based MANC alloys. **Complete**
- Subtask 1.2.4** - Identify source of permanent magnets. **Complete**

Task 1.3– Begin FeCo AMR Casting Trials, Measure Properties:

- Subtask 1.3.1** – Identify FEM topology & 2-d grids for traction HSM > 5 kHz switching. **Complete**
- Subtask 1.3.2** – Cast Metglas FeCo-based AMR in 2-inch-wide ribbon for Evaluation. **Complete.**
- Subtask 1.3.3** - Measure Magnetostriction in Metglas FeCo-based AMR. **Complete.**
- Subtask 1.3.4** - Measure M(T), Bs, Tc, Crystallization temperatures and AC Losses. **Complete**

Task 1.4 – Screen Properties of MANC Alloys:

- Subtask 1.4.1** – Identify and Cast 2nd Generation FeNi MANC Alloy at Scale. **Complete**
- Subtask 1.4.2** – Measure Bs, Tc, Crystallization Temp. and AC Losses for MANC. **75% Complete**
- Subtask 1.4.3** – Measure Magnetostriction in FeNi-based MANC Alloys. (Underway)
- Subtask 1.4.4** – Initiate Thinning studies of FeNi MANC Alloys. (to be continued in NCE).

Future Work (BP1):

Task 1.5– Evaluate Materials in FEM Traction Motor Design:

- Subtask 1.5.1** – Benchmark conductors in Traction HSM Design.
- Subtask 1.5.2** – Benchmark Metglas FeCo-based AMR in Traction HSM Design.
- Subtask 1.5.3** – Benchmark Metglas FeNi-based MANC in Traction HSM Design.
- Subtask 1.5.4** – Report Power Density Improvement with AMRs and MANCs.

Subtask 1.2.2 addressed benchmarking to achieve BP1 Milestone. We completed building a 2.5 kW Flux Switching with Permanent Magnet (FSWPM) high speed motor (HSM) in DOE AMO Program DE-EE0007867. This motor is at NCSU for final power testing. Table I.2.1.2, below, details benchmarking of specific power improvements achievable in our FSWPM motor design.

Table I.2.1.2 DOE/VTO – DE-EE0008870 Benchmarking Enhancing Specific Power in a FSWPM axial motor design.

Enhancing specific power

Parameters	Initial (with verified material properties)	High power (with projected material properties)
Electrical Speed (at 6000 rpm)	1400 Hz	2100 Hz
Inner radius/outer radius	50 mm/80 mm	90 mm/115 mm
Flux density (peak)	0.60 T	1.53 T
Permanent magnet	Ferrite ($B_r = 0.4$ T)	NdFeB ($B_r = 1.2$ T)
Current density (peak)	6.0 A/mm ²	18.0 A/mm ²
Conductor filling factor	46 %	60 %
Torque	4.2 Nm	59 Nm
Power (at 6000 rpm)	2.6 kW	37 kW
Copper loss (DC)	34 W (1.3 %)	230 W (1.3 %)
Iron loss (at 6000 rpm)	7 W (0.3 %)	82 W (0.2 %)
Motor mass	5.8 kg	9.9 kg
Specific power	0.45 kW/kg	3.8 kW/kg

The Table summarizes key metrics for the materials as verified in our 2.5 kW AMO motor design. A higher power (20 kW) FSWPM motor design has been evaluated with projected materials properties to be achieved through the course of this project. On the basis of this benchmarking, we presented a FSWPM motor design, based on Comsol Multiphysics FE modeling, to satisfy Milestone 1 and presented this at the June 2020 DOE VTO Program Review.

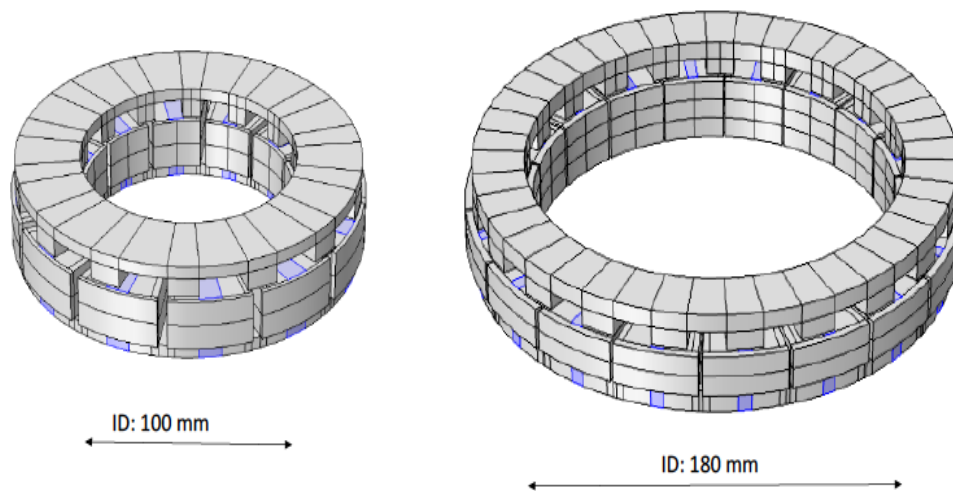


Figure I.2.1.1 (a) 2.5 kW dual stator FSWPM rare earth free permanent magnet HSM constructed as part of the DOE AMO Program DE-EE0007867; (b) 20 kW Dy-lean rare earth permanent magnet/MANC FSWPM design presented as Milestone 1 in our DOE VTO Project DE-EE0008870.

Conclusions

A 20 kW FSWPM motor design has been presented to the DOE VTO as part of deliverables for DOE VTO Project DE-EE0008870. We have benchmarked this HSM based on materials improvements and design modifications to a 2.5 kW FSWPM motor design of a motor built in DOE AMO Program DE-EE0007867. Permanent magnets have been machined for the new design and FeNi-based MANCs cast at commercial scale with partner Metglas.

Key Publications

1. Ohodnicki, P., Egbu, J., Yu, Y., Baltrus, J., Aronhime, N., Krimer, Y., Anand, P., Byerly, K., & McHenry, M. E. (2020) Surface Oxidation and Crystallization of FeNi-Based Soft Magnetic Nanocrystalline and Amorphous Nanocomposite Alloys. *J. Alloys Compds*, 155038. doi.org/10.1016/j.jallcom.2020.155038.

References

1. S. Simizu, P. R. Ohodnicki and M. E. McHenry; Metal Amorphous Nanocomposite (MANC) Soft Magnetic Material (SMM) Enabled High Power Density, Rare Earth Free Rotational Machines. *IEEE Trans. Mag.* **54(5)**, 1-5, (2018). [10.1109/TMAG.2018.2794390](https://doi.org/10.1109/TMAG.2018.2794390)
2. N. Aronhime, V. DeGeorge, V. Keylin, P. Ohodnicki, and M. E. McHenry, "The Effects of Strain-Annealing on Tuning Permeability and Lowering Losses in Fe-Ni-based Metal Amorphous Nanocomposites." *J. Materials* **69(11)**, 2164-70, (2017). [10.1007/s11837-017-2480-x](https://doi.org/10.1007/s11837-017-2480-x).

Acknowledgements

The team gratefully acknowledges many helpful discussions with P. R. Ohodnicki of the University of Pittsburgh and the continuing support of the DOE AMO and VTO teams.

I.2.2 Wound Field and Hybrid Synchronous Machines for EV Traction with Brushless Capacitive Rotor Field Excitation (Illinois Institute of Technology)

Ian P. Brown, Principal Investigator

Illinois Institute of Technology
3301 S Dearborn Street #103
Chicago, IL 60616
Email: ibrown1@iit.edu

Daniel C. Ludois, Principal Investigator

University of Wisconsin-Madison
1415 Engineering Drive
Madison, WI 53706
Email: ludois@wisc.edu

Steven Boyd, DOE Program Manager

U.S. Department of Energy
Email: steven.boyd@ee.doe.gov

Start Date: October 1, 2017
Project Funding: \$204,411

End Date: July 31, 2021
DOE share: \$999,752

Non-DOE share: \$112,995

Project Introduction

For mass adoption of electric vehicles (EVs), there is concern regarding the cost and materials supply chain for the vehicle's main traction motor. While DOE programs have been successful at lowering the cost of traction inverters and wide bandgap power electronics, the cost of traction electric motors has been resistant to change. Today interior permanent magnet synchronous machines (IPMSMs) and induction machines (IMs) are the commercially dominant traction motors. The rare-earth permanent magnets (PMs) used in IPMSMs have been subject to market volatility and are largely single sourced from a foreign power. The PMs are also a significant fraction of the cost of IPMSMs and impose temperature limits.

Additionally, the PMs provide a fixed flux level which is always, "on", leading to safety concerns during inverter faults and requiring additional current to be injected into the machine during field weakening to buck the magnetic flux. This additional current lowers the power factor of the machine, requiring that the traction inverter be oversized to supply the reactive current, leading to increased ohmic losses in the stator and inverter. Induction machines (IMs) must also draw reactive current from the traction inverter to magnetize the machine leading to a lower power factor.

Wound field synchronous machines (WFSMs) and hybrid excitation synchronous machines (HESMs) are potentially advantageous alternatives to the commercially dominant IPMSMs and IMs. WFSMs are PM free, and because of the DC field excitation is from the rotor side, the power factor of the machine is high, if not unity over most of the operating space. The complete control of the field excitation provides the potential for optimal field weakening and large constant power speed ranges with loss minimization. HESMs use a combination of PM and wound field excitation to combine the high efficiency of IPMSMs with the easy field weakening and high power factor of WFSMs while using considerably less PM. They also reduce the field power requirements.

EV traction applications require extremely high reliability and power density inhibiting the use of brushes and other classical field power transfer technologies such as brushless exciters. Brushless capacitive power transfer offers an attractive means of providing power transfer to the rotor field windings of WFSMs and HESMs.

Objectives

The objective of this project is to design, develop, and demonstrate wound field and hybrid excitation (permanent magnet and wound field) synchronous machines, with brushless power transfer to the rotor field winding, capable of achieving the performance metrics in Table I.2.2.1. A focus of this project is the cost target of 4.7 \$/kW. The brushless field power transfer will be accomplished using capacitive power transfer.

Table I.2.2.1 Prototype Wound Field and Hybrid Excitation Synchronous Machine Target Metrics

Parameter	Budget Period 2 Prototype	Final Prototype
Peak Power (kW)	≥55	≥55
Continuous Power (kW)	≥ 30	≥ 30
Specific Power Density (kW/kg)	1.5	1.6
Volumetric Power Density (kW/l)	5.0	5.7
Cost (\$/kW)	-	4.7

Approach

To meet the cost and power conversion targets, a number of approaches are being developed simultaneously in the context of wound field and hybrid excitation synchronous machines though many of the technologies will also apply to other electric machine types and applications.

- Die compressed windings to increase the slot fill of the stator and rotor windings for increased power density and efficiency.
 - Target slot fill of ~75% to 80% compared to 40 to 45% for random/mush distributed windings.
 - Single thermal mass with no air voids and improved heat transfer at the spray/end turn interface.
- Brushless power transfer to the rotor field winding using electric fields in a capacitive power coupler (CPC) excited by high frequency power electronics.
 - Reduce the mechanical complexity of the rotating capacitors. Three simpler rotating capacitor designs have been investigated: journal bearings, integrated LC coupler, and printed circuit board (PCB) capacitive plates with a tank circuit.
 - Increase the frequency of excitation to the megahertz regime to allow the use of a smaller capacitance, e.g., PCB based capacitors with a relatively large airgap.
 - Develop a wide bandgap (GaN or SiC) power converter with high efficiency which minimizes losses by operating in resonant soft switching.
- Reduce the punching scrap from the construction of the lamination stack. Typically 40% of the steel is scrapped when punching IPMSM laminations.
 - Leverage cut core and roll-up stator and rotor designs.
 - Segmented lamination structures allow for higher fill factors with needle or bobbin winding both rotor and stator windings and even higher slot fills with die compressed windings with the added benefit of reduced end turn length.
 - Develop low space harmonic content fractional slot concentrated windings, able to operate at high speeds, compatible with needle or die compressed windings.
- Hybrid excitation synchronous machines to lower the field power requirements.

- Bias the field flux for the most common operating point in a drive cycle with PMs.
- Extend the constant power speed range compared to pure permanent magnet machines.
- Develop high performance controls for WFSMs and HESMs.

Results

The major remaining tasks for this project were the construction of the final WFSM prototype and dynamometer testing of the prototype using brushes and slip rings and the CPC. The Covid-19 pandemic has delayed the construction of the final prototype and dynamometer testing. Both the Illinois Institute of Technology and University of Wisconsin-Madison campuses were shut down in March 2020 due to state “Shelter at Home” orders and only reopened this semester with restrictions on laboratory activities.

Dynamometer Generator Mode Testing of the CPC

The final CPC prototype was dynamometer tested to its full rated power with an older WFSM prototype, Figure I.2.2.1. The WFSM prototype was run as a generator to test the field excitation power transfer of the CPC. A three-phase resistive load bank was connected to the WFSM stator. The CPC tank current, WFSM load power, and WFSM stator line to line voltages were measured for a range of speeds and tank currents up to a rated WFSM speed of 4000 rpm and tank current of 4 A, Figure I.2.2.2. The load resistance was also reduced slightly at 4,000 RPM with a CPC tank current of 4 A to generate 30 kW of power. This power level is the required minimum power level for the DOE targets.

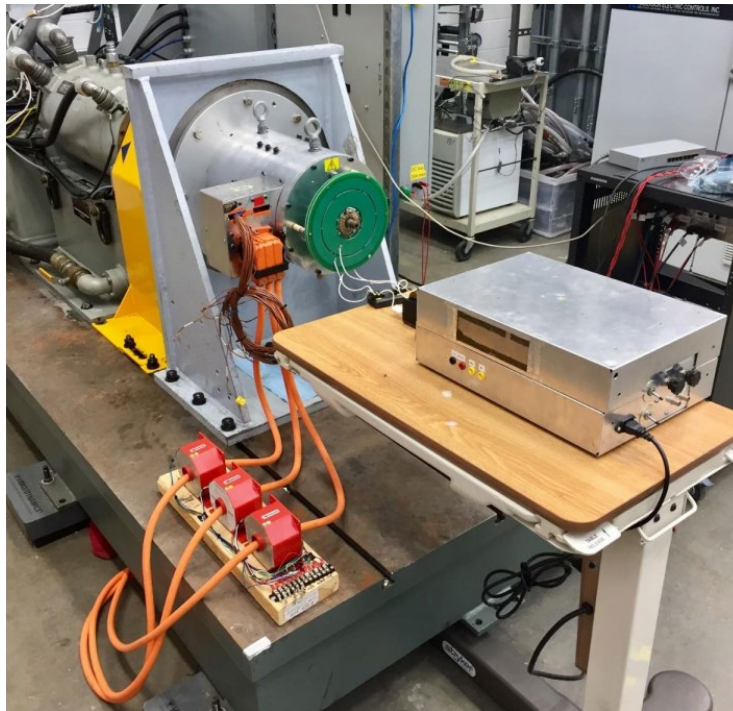


Figure I.2.2.1 Full load dynamometer testing of the CPC with an older WFSM prototype.

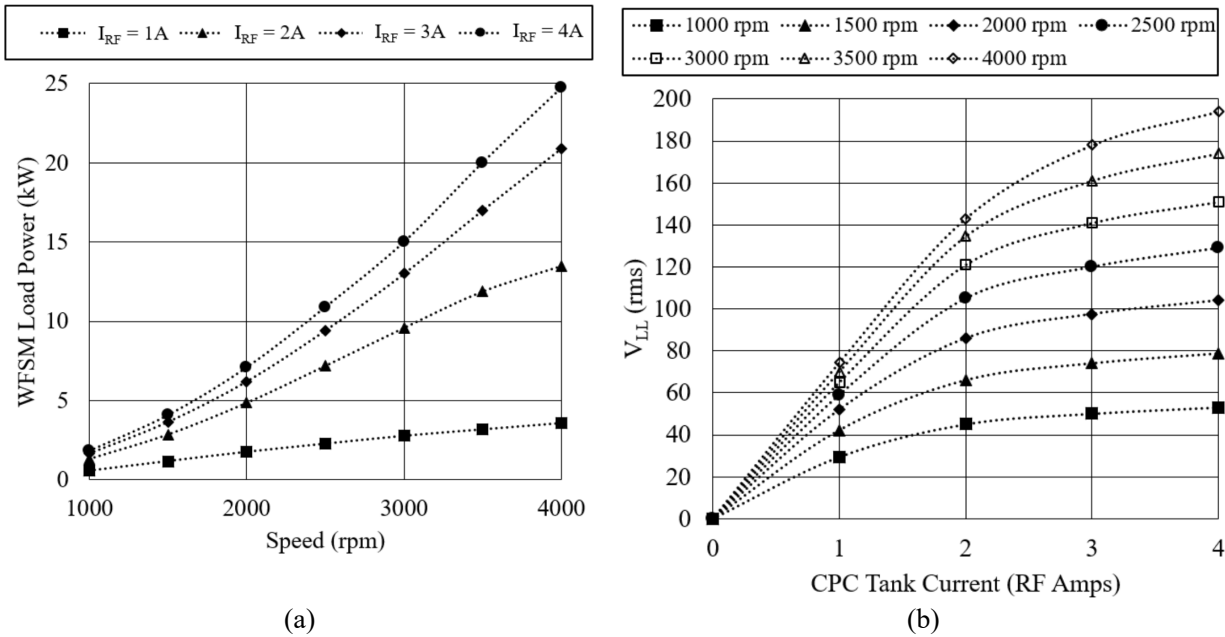
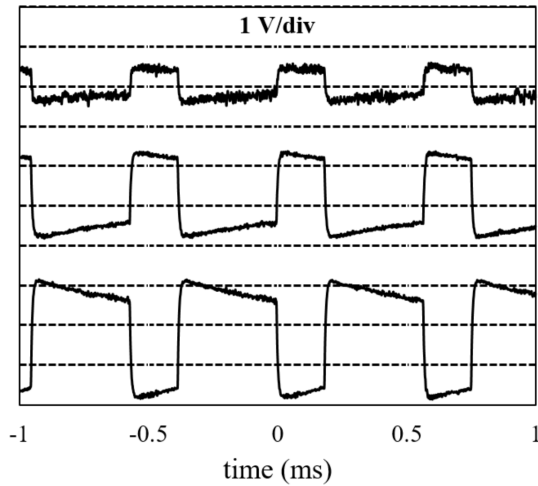


Figure I.2.2.2 WFSM generator mode with CPC field excitation load power and CPC tank current as a function of speed

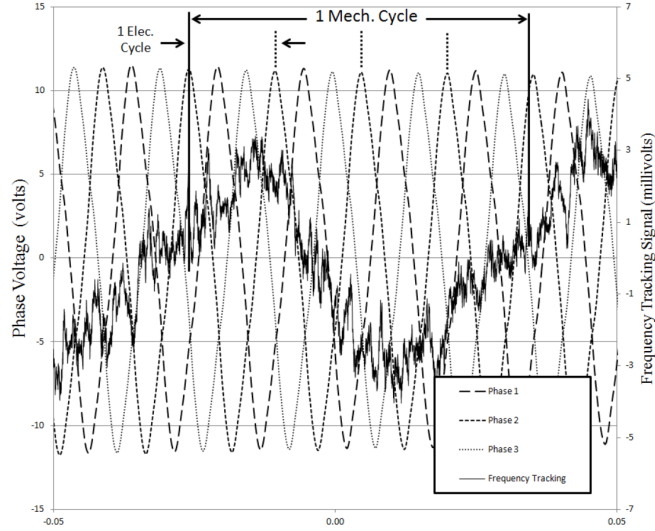
Initial Investigations of Using the CPC for Rotor Position Sensorless Control

Initial investigations were carried out to evaluate two potential methods for using the CPC for rotor position sensorless control of the WFSM. The first method would track variations in the stator three phase BEMF induced by the switching action of the rotor mounted buck converter. The voltages introduced in the stator winding are rotor position dependent. A back EMF tracking observer would then be used to extract the rotor position. Open circuit stator voltage measurements at a fixed rotor position with the with the rotor CPC buck converter switching, Figure I.2.2.3(a). The difference in voltage magnitude induced in the three phases is apparent.

To maintain resonance in the tank circuit, the CPC power electronics utilizes a phase locked loop. If the coupling capacitance and tank inductance were absolutely constant the resonant frequency of the converter would be constant. The tank inductance can be assumed to be essentially constant. However, the coupling capacitance in reality has some variation with rotor position. The variation of the coupling capacitance causes a variation in the PLL estimation of the resonant frequency. This variation of the resonant frequency can be tracked to estimate the rotor position. The variation of the PLL resonant frequency estimate with mechanical position is shown in Figure I.2.2.3(b) at a slow rotational speed. Because of the machine pole count, 1 mechanical cycle corresponds to 4 electrical cycles of the back-EMF.



(a)



(b)

Figure 1.2.2.3 Potential CPC related signals for rotor position sensorless control. (a) Stator back-emf voltages induced by switching of the buck regulator in the CPC. (b) CPC PLL resonant frequency estimate as a function of rotor position with 3 phase back-emf signals superimposed.

Construction of Final WFSM Prototype

Construction of the final WFSM prototype has been delayed because of Covid-19 pandemic related shutdown of the IIT campus. The final WFSM prototype design uses die compressed stator and rotor windings in a 12 slot 10 pole 2-layer topology with the stator winding connected in a star delta configuration. The planned stator and rotor die compressed windings have a non-rectangular profile to maximize the slot fills. Parametric die designs for the non-rectangular profile die compressed windings have been completed. The die for the rotor field coils is shown in Figure I.2.2.4.

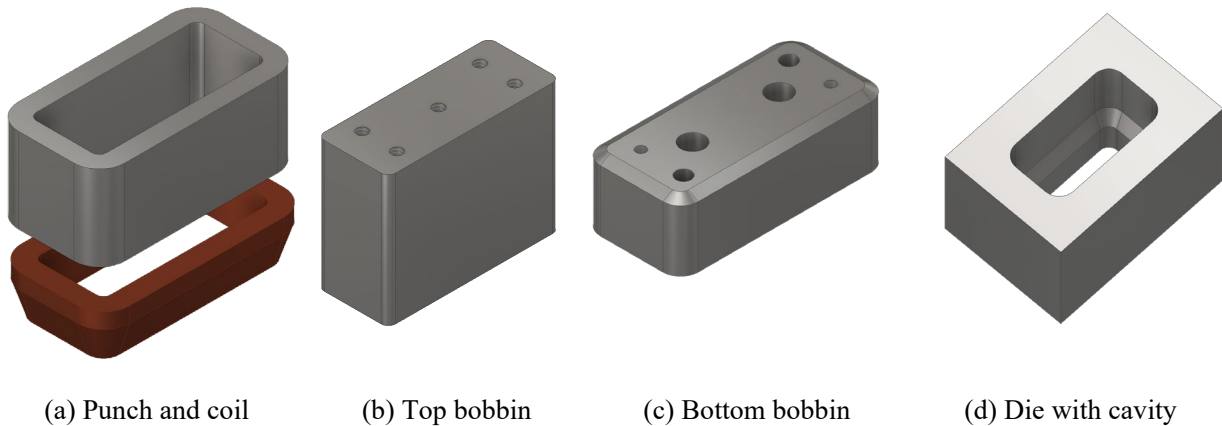


Figure I.2.2.4 Die components to produce non-rectangular profile rotor field coil.

The die compressed stator winding requires a number of strands in hand to be wound in parallel for each turn. The parallel strands in hand will ideally be laid out on the bobbin before compression in a single layer per turn orthocyclic pattern roughly matching the final compressed coil profile. This precompression layout minimizes the stress on the conductors and their insulation during the compression process. Keeping all the parallel strands in hand aligned to complete an orthocyclic winding is a major challenge. Further complicating the

precompression winding, two different number of turns and wire gauges are to be used for a star delta connection of the stator; eight turns for the star connected coils and 14 turns for the delta connected coils. To achieve maximized but approximately equal slot fills for a give slot area the number of choices of wire gauges and number of parallel strands in hand is restricted. For the star connected winding the wire in some cases becomes quite thick, leading to difficulties with work hardening as it is wound.

To facilitate winding multiple strands in hand simultaneously a number of improvements to a custom winding machine were added including a wire tensioner for up to 8 strands in parallel, multiple wire guides to align the strands, and multiple ramp inserts to assist the guiding and bending of all the parallel strands on the end turns of the top bobbin. The new tensioner and one of the new wire guides are shown in Figure I.2.2.6. The new tensioner allows for individual tension control on all the strands in parallel. Several iterations of 3D printed ramp guides were made for the ends of the bobbins to help all the parallel strands transition into the next turn. Examples of the end turn guides is shown in Figure I.2.2.5(a) and Figure I.2.2.5(b). Example multiple strands in hand orthocyclic windings with thick wire are shown in Figure I.2.2.5(c).

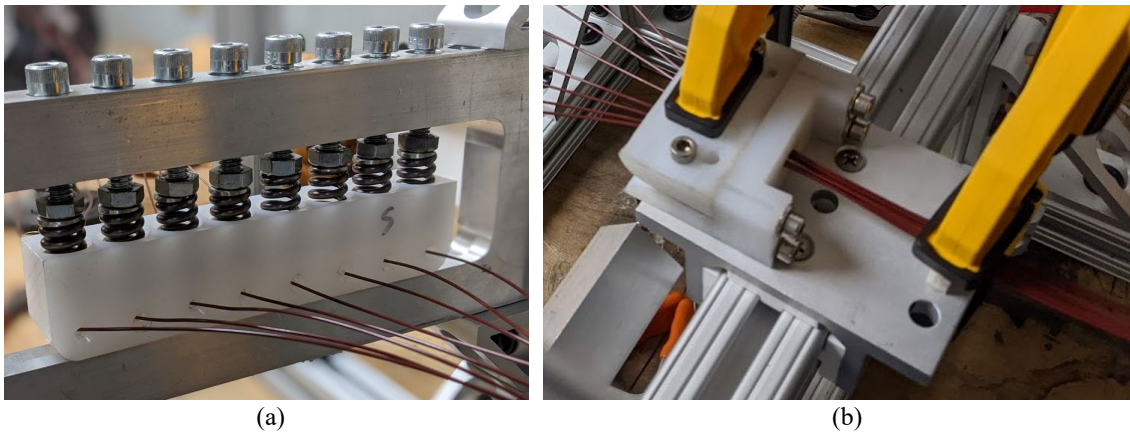


Figure I.2.2.5 Machine for orthocyclic winding of multiple wires simultaneously (a) tensioner, (b) wire guides.

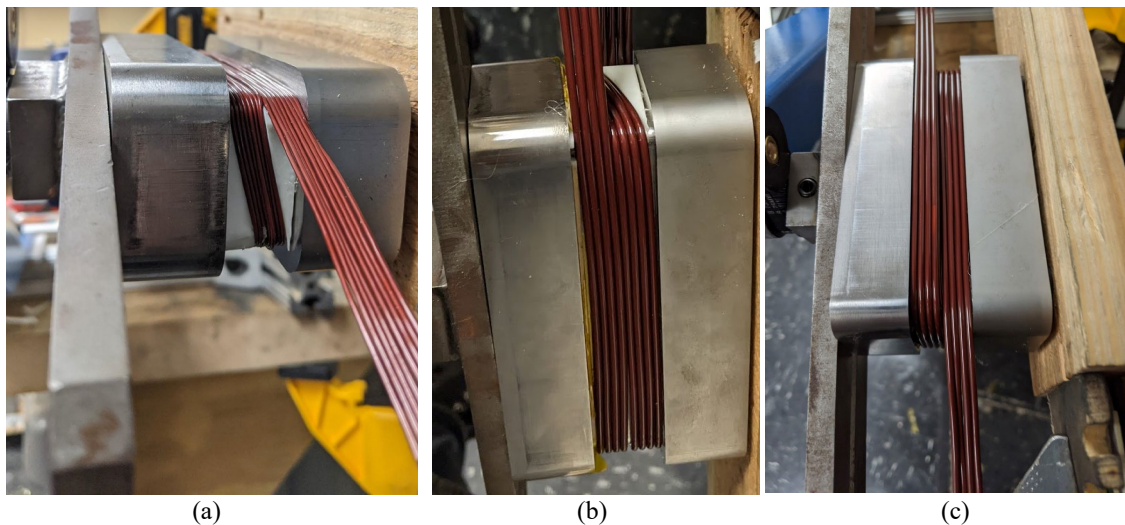


Figure I.2.2.6 Multistrand orthocyclic winding (a) and (b) end turn ramp guides and (c) example winding.

One of the remaining challenges is reducing a bump that forms on the end regions as the multiple strands in hand transition from one layer to another. This considerably complicates the design and manufacturing of the die.

As the die compressed windings are formed as an integral unit a segmented lamination structure must be used. While segmented laminations are relatively commonly used in the manufacture of servo motors using stamping dies with interlocking features there is relatively little public information about the tolerances required for assembly if a prototype is manufactured using laser cutting and stack bonding. A series of positive and negative dovetails with varying nominal gap distances were manufactured to gauge the impact of manufacturing tolerances on assembly, Figure I.2.2.7(a). A range of temperature differentials were tried for assembly including ovens for heating the negative dovetails, and dry ice and liquid nitrogen for the positive keys. An example of a shrink fit dovetail is shown in Figure I.2.2.7(b).

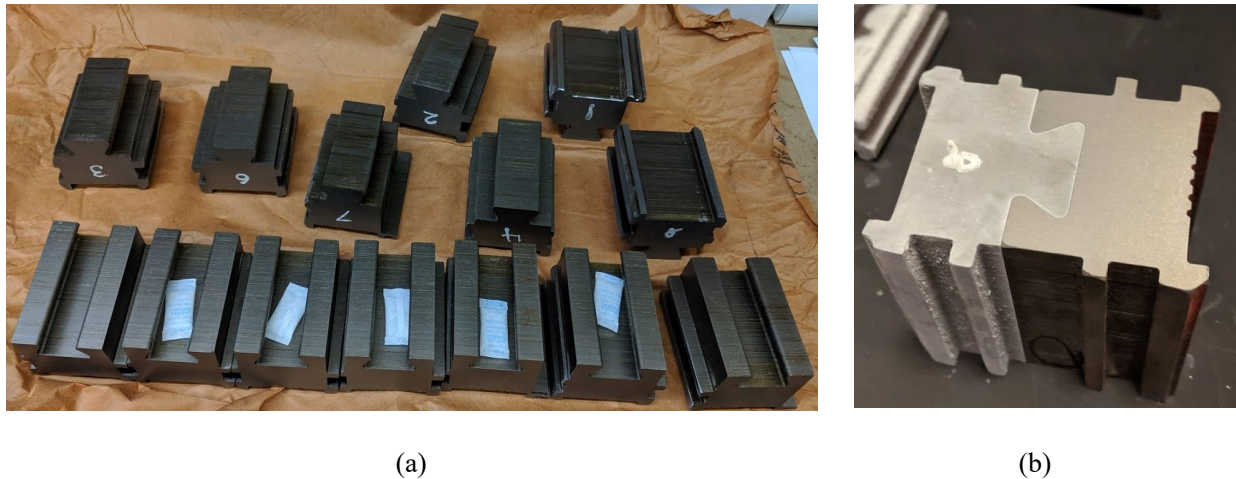


Figure I.2.2.7 Positive and negative stacked lamination dovetail (a) samples with varying nominal gaps and (b) example shrink fitting.

As a hedge against the possible failure of die compressed windings, square wire was investigated as a way to achieve slot fills slightly less than the die compressed windings. This type of winding potentially may also not require segmenting the lamination. If rotated 45 degrees, the square wire can be wound pseudo-orthocyclically, with each layer interlocking with the layer below. This requires a grooved support to position the first layer, and several such supports were tested, Figure I.2.2.8(a). An example square winding with a pseudo orthocyclic winding is shown in Figure I.2.2.8(b) and Figure I.2.2.8(c).

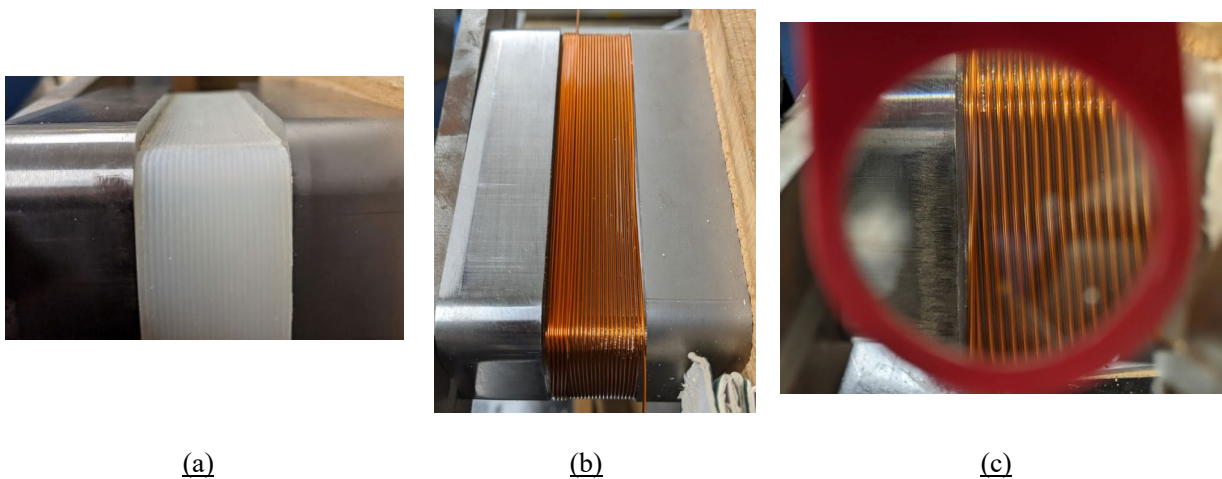


Figure I.2.2.8 Square wire (a) base layer winding guides, (b) wound bobbin, and (c) zoomed view of wound bobbin.

WFSM Current Regulators and Deadtime Compensation

Two new high performance discrete time WFSM current regulators were developed during this budget period. The first current regulator is based on speed dependent term decoupling and model matching concepts to improve the decoupling of the direct(d) and quadrature (q) and direct (d) and field (f) axes. In this current regulator, the speed dependent q-d flux voltage cross-coupling is decoupled using a flux observer in conjunction with a decoupling matrix. All the rotor speed dependent terms are contained in the decoupling matrix. This reduces the computational load of the controller. The d-f axis cross-coupling is not speed dependent and a model matching controller is used to achieve decoupling of these axes. In general, this current regulator has improved decoupling compared to the state-of-the-art complex vector current regulator for the q and d axis and separate PI regulator for the f axis. However, this controller appears to be sensitive to feedback noise.

A second current regulator was developed with good decoupling performance that does not suffer from feedback noise sensitivity was developed. The second current regulator based on accurate approximate discrete time modeling of the WFSM, modeling of the system latches in the correct frame, state feedback compensation of the discrete time system delays, and pole placement design. To reduce the computational complexity of the discrete time model, the speed dependent terms are approximated by regression based approximate models. An internal model control method is used to achieve the desired closed loop transfer function matrix. This second current regulator achieves better decoupling of the d, q, and f axes than the state-of-the-art d-q complex vector controller and separate PI regulator.

In addition to the two current regulators, an improved inverter nonlinearity compensation for WFSM was developed. Three inverter nonlinearities are compensated including deadtime, the switch's nonlinear characteristic, and zero current clamping.

Conclusions

WFSMs and HESMs with brushless capacitive rotor field power transfer are being developed as a high-performance, low cost, EV traction motor option. Work is underway to complete construction of the final WFSM prototype and dynamometer test it with the CPC to confirm that its performance exceeds the DOE 2020 power conversion targets. Cost evaluation of the final WFSM will also be carried out.

Key Publications

1. S. Hagen, M. Tisler, J.J. Dai, I.P. Brown, D.C. Ludois, "Use of the Rotating Rectifier Board as a Capacitive Power Coupler for Brushless Wound Field Synchronous Machines," accepted for publication in IEEE Journal of Emerging and Selected Topics in Power Electronics, 2020.
2. F. Guo, M. Salameh, M. Krishnamurthy, I.P. Brown, "Multi-Material Magneto-Structural Topology Optimization of Wound Field Synchronous Machine Rotors," IEEE Transactions on Industrial Applications, Vol. 56, No. 4, 2020, DOI: 10.1109/TIA.2020.2989682.

I.2.3 Cost Effective Rare-Earth-Free Flux Doubling, Torque Doubling, 8X Power Density Traction Motor with Near-Zero Open-Circuit Back- Electromotive Force (EMF) and No Cogging Torque (University of North Carolina at Charlotte)

Somasundaram Essakiappan, Principal Investigator

University of North Carolina at Charlotte
9201 University City Boulevard
Charlotte, NC 28223
Email: Somasundaram@uncc.edu

Susan Rogers, DOE Technology Development Manager

U.S. Department of Energy
Email: susan.rogers@ee.doe.gov

Start Date: October 1, 2019
Project Funding: \$354,848

End Date: March 31, 2022
DOE share: \$279,848

Non-DOE share: \$75,000

Project Introduction

This project proposes to develop a high-power density, high speed traction motor architecture called QMag, driven by a high-power density motor drive inverter using silicon carbide semiconductor devices. This new architecture will achieve the efficiency and power density targets by means of innovative winding and rotor structures, high bandwidth controls, and advanced thermal management solutions. The project team will pursue the goals of the project systematically, through Finite Element Analysis for machine design, through simulation and co-simulation techniques for power electronics and controls evaluation, by using design principles for prototyping, and finally laboratory testing and evaluation. If this project successfully achieves and demonstrates the DOE targets for power density, cost, and reliability, the technology has the potential to become a core enabler of the flagship higher power product portfolio in commercial traction businesses, which has so far been confined to DC, induction, Brush Less DC (BLDC), Permanent Magnet AC (PMAC), and reluctance machines.

Objectives

The U.S. DRIVE Electrical & Electronics Technical Team Roadmap (2017) [1] identified key challenges and R&D targets for Electric Traction Drive Systems in the year 2025 including: (1) cost reduction – achieving cost parity with ICE drivetrains at \$6/kW for 100 kW peak power rating; (2) power density improvement - addressing packaging challenges and achieving a motor power density of 50 kW/litre and power electronics density of 100 kW/litre, and an overall system figure of 33 kW/litre; (3) reliability improvement up to 300,000 miles (distance) or 15 years (lifetime); (4) reduction of reliance on rare-earths, with NdFeB –free/reduced, Dy-free/reduced designs. In order to achieve these targets, this project proposes to develop and demonstrate a novel 125kW motor architecture and SiC converter based electric traction drive system that can achieve 8X power density at half cost and 2X useful life, while applying the QMag principle to power conversion and motor design and advanced cooling. The project activities will focus on:

1. Feasibility evaluation, practical implementation and scaling of QMag principle
2. Design and implementation of power converter and motor drive system
3. Design and implementation of advanced cooling system
4. Overall system (motor + power converter) optimization for traction applications and testing

Approach

Traction motor: This project proposes to use the QMag topology to design the traction motor, which is based on the QMag technology, alternatively termed as the Parallel Path Magnetic Technology [2]:

- The QMag topology features permanent magnets placed in magnetically attracting manner (circumferentially vs radially) and inter-dispersed with control winding coils, enabling greater flexibility in flux path shaping, as shown in Figure I.2.3.1
- The castellated rotor has no interior or surface magnets, offering high-speed operation, reliability, and high-power density to achieve DOE targets
- Direct winding cooling techniques boost current density capability, hence the torque performance.

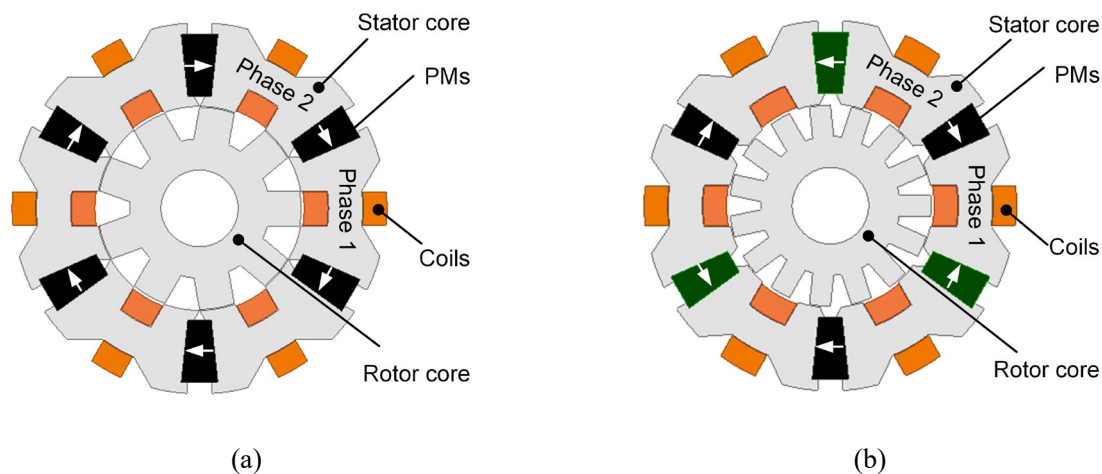


Figure I.2.3.1 QMag topology illustration, (a) type-C (all magnets are magnetized in the same direction), (b) type-A (adjacent magnets are magnetized in opposite directions to concentrate flux).

Motor drive inverter

This project will develop a motor drive inverter using half-bridge silicon carbide (SiC) modules. The inverter will operate at switching frequencies, thereby low distortion output current and reduced torque ripple. SiC power modules optimized for reduced conduction losses will be utilized, in order to handle high current drive requirements by the QMag motor. The switching frequency of the inverter will be optimized for all operating power ranges, high power quality, power density, and efficiency. Thermal management of the semiconductor devices will be achieved through liquid cooling, with a water – ethylene glycol mix being the coolant.

Integration of traction motor and drive inverter

The traction motor and drive inverter are being designed concurrently, with frequent coordination of operating conditions and performance specifications. Finite Element Analysis platforms (Ansys) are being used to design, optimize and validate the traction motor; power electronic simulation platforms (Powersim, Matlab) are used to design the drive inverter—the integrated traction system will be validated using co-simulation methods. The prototypes of traction motor and inverter drive will be integrated and tested on a dynamometer testbed.

Results

A survey of state-of-the-art designs for existing products and reported research studies was conducted in order to establish a basis of comparison for the electric machine performance and characteristics. The results provide the research team with a benchmark for evaluation of the QMag motor design under development and for substantiating relative merits and capabilities in terms of high-power density, high speed operation, simplified modular manufacturability, improved cooling, etc.

Parametric models for a number of motor topologies were developed following the principle of operation of QMag motors. Based on a parametric electromagnetic finite element analysis (FEA) model for the QMag topology with Gramme-type windings illustrated in Figure I.2.3.2 with 10 independent geometric and control variables, a large-scale design optimization was performed. The objective was to maximize the power density with a 50kW/L target, efficiency and power factor, assuming an equivalent electric loading, i.e., the product of current density and slot fill factor, equal to 9.75A/mm² can be achieved by the cooling design and advanced winding technology.

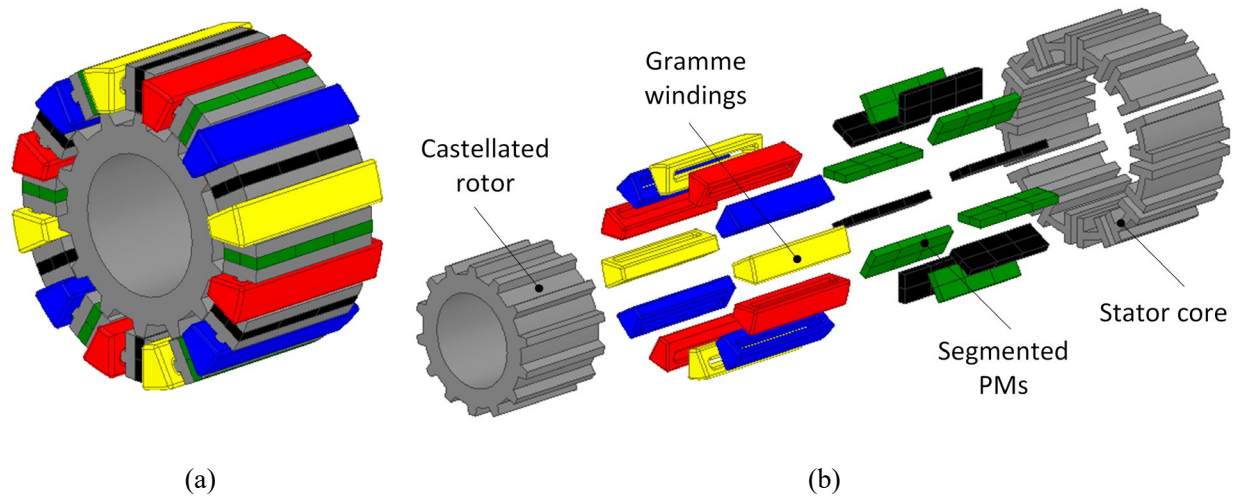


Figure I.2.3.2 One implementation of the QMag technology, (a) assembled view, (b) exploded view.

Multiple design generations of the adopted heuristic optimization yielded a satisfactory Pareto front. A number of candidate designs were identified, with estimated power density capable of meeting DOE targets, as shown in Figure I.2.3.3. The torque-speed and efficiency maps have also been calculated based on 2D electromagnetic FEA, showing that the optimally designed motor can operate with constant power 125kW at up to 3X the base speed 12,500r/min.

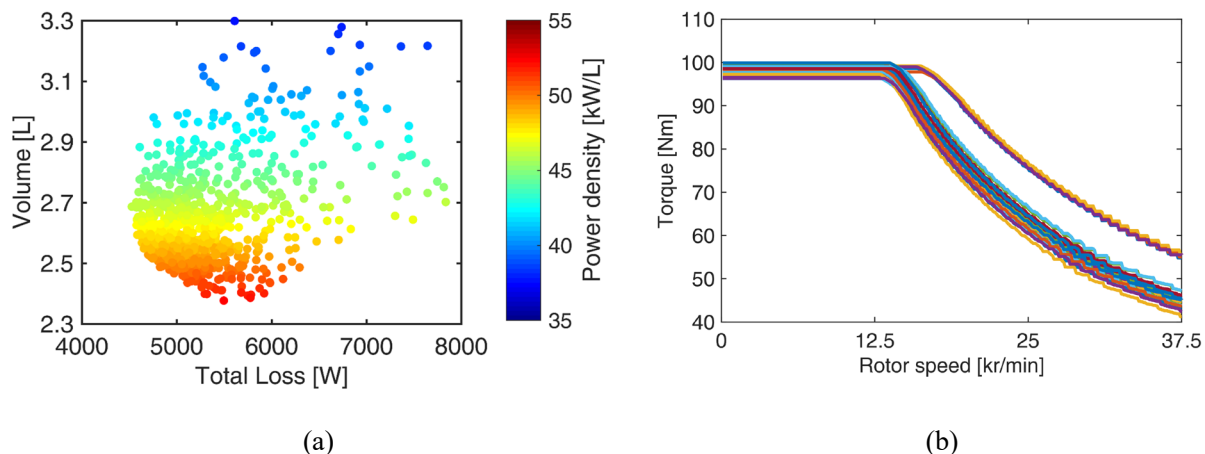


Figure I.2.3.3 Large-scale design optimization of one implementation of the QMag technology. (a) Designs evaluated by FEA, (b) Torque-speed envelopes of all the Pareto front designs in (a).

A systematic comparative study between two QMag motor topologies was also carried out based on multi-objective design optimizations, one with 10 rotor protrusions (10-P) and the other 14 rotor protrusions (14-P), as shown in Figure I.2.3.4. The three concurrent objectives were to maximize the power density, minimize the

total loss, and maximize the power factor. The computational results show that, optimal 14-P designs can achieve similar fundamental power factors as optimal 10-P designs. There are trade-offs between 10-P and 14-P designs in terms of the power density and total loss.

Advanced winding and cooling technologies for EV traction motors was surveyed, which served as the basis for the proposed winding manufacturing and cooling design of QMag motors. A concept design has been proposed using two stator cooling jackets, with the stator core, windings, and rotor immersed in oil or water coolants, in order to mitigate the heating effects of the large specific losses, which are typically high for high power density electric machines.

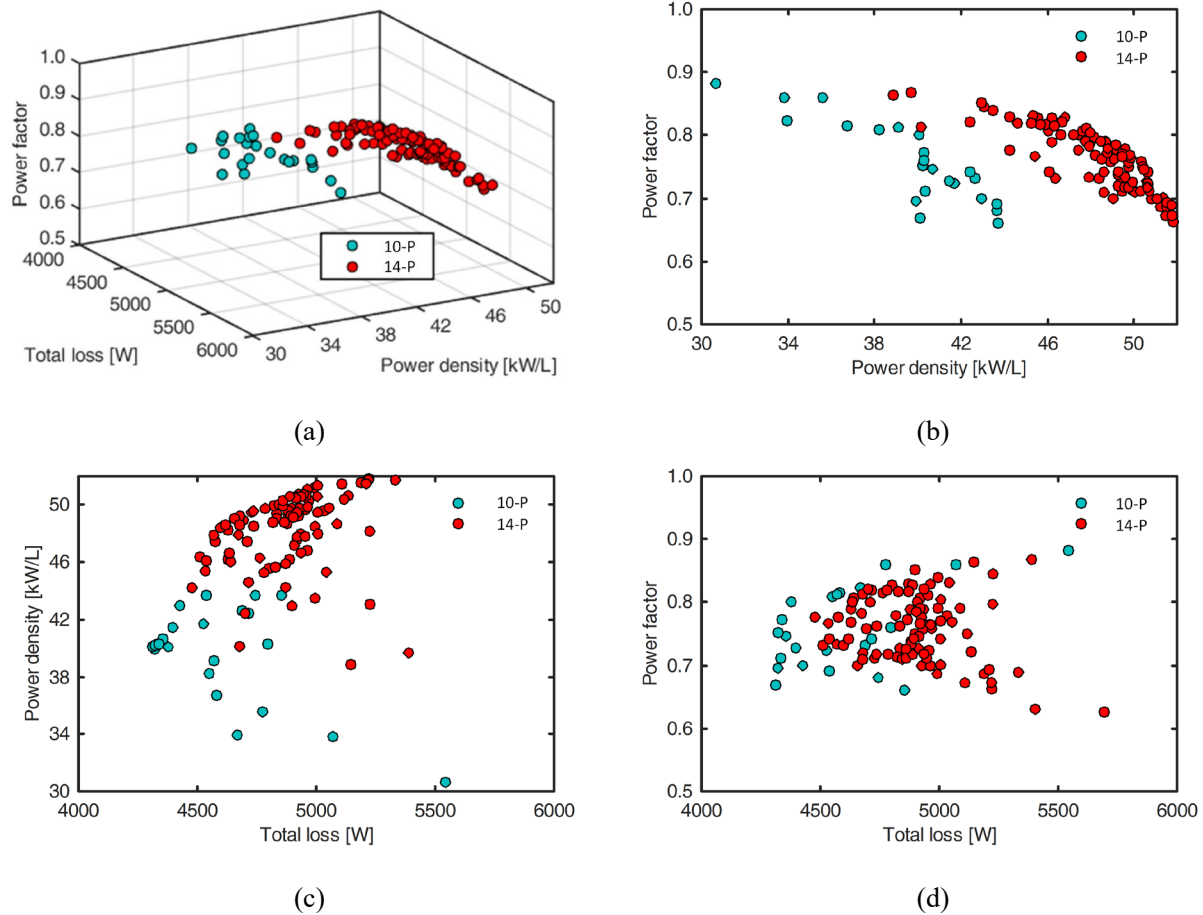


Figure I.2.3.4 Systematic comparison of two QMag motors with 10-P and 14-P, respectively. (a) 3D view of Pareto fronts, (b) projection in the power density-power factor plane, (c) projection in the total loss-power density plane, (d) projection in the total loss-power factor plane.

The SiC three phase motor drive and controller were developed and evaluated in simulation. The inverter was powered by a battery pack with voltage rated 800 V, and the power rating of the system was 125 kW. Non-ideal device models for the power semiconductor devices were used in the simulation analysis, which include on-state resistance and switching loss characteristics. The closed loop control algorithm includes speed and torque control loops to regulate inverter output (motor stator) currents in both motoring and regenerative braking modes – positive and negative torques application. A non-linear inductance model of the QMag motor

(direct and quadrature values) was created and this was used to represent the motor in the motor drive inverter closed loop controller design and simulation.

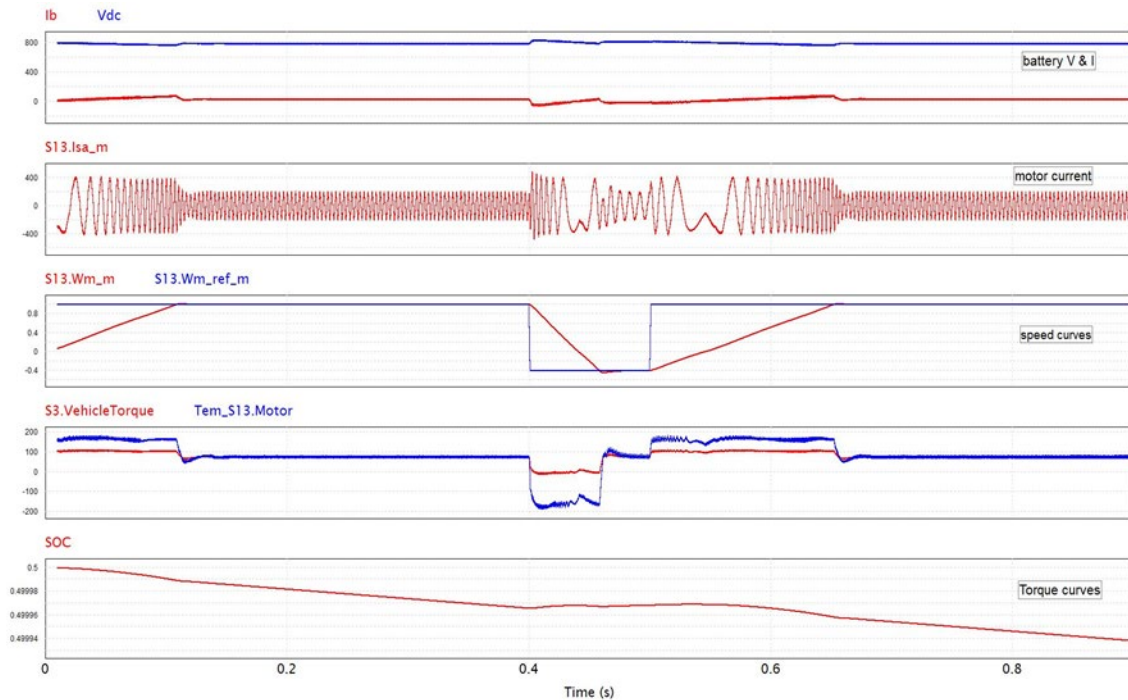


Figure I.2.3.5 Results of simulation analysis of motor drive inverter powering mathematical inductance model of the QMag motor

The results of the simulation of three phase inverter driving the machine model are given in Figure I.2.3.5. Plot 2 shows the stator current in one of the motor phases clearly exhibiting an increase in fundamental frequency as the speed increases. As the motor speed reaches the reference speed, as seen in plot 3, the stator current settles at a lower regulated amplitude and frequency, and the generated machine torque matches the load torque (plot 4) to provide constant speed operation. Regenerative braking operation is also demonstrated by the application of negative generated torque to drive the rotor speed to zero. The battery dc voltage and current can be seen in plot 1. It was observed that for high switching frequency operation of the inverter, in the range of 20 kHz to 100 kHz, provides low output current distortion, with a Total Harmonic Distortion (THDi) of less than 3%.

Loss budget analyses using estimated drive voltage and current requirements at rated power, junction temperatures, and switching frequencies were performed for candidate SiC modules. Based on the heat extraction needs, a thermal management system was designed, including identification of the liquid-cooled heat sink. A preliminary design for the inverter utilizing candidate SiC module Wolfspeed CAB450M12XM3 [3] is shown in Figure I.2.3.6. This design was found to have a power density in the range of 100 – 150 kW/litre, based on enclosure and ancillary component sizing, thereby able to meet DOE targets for power electronic power density.

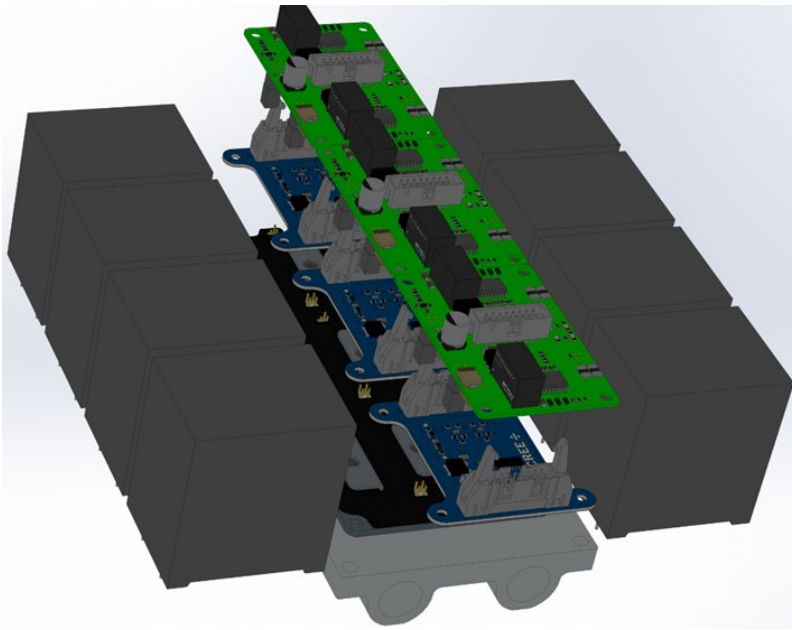


Figure I.2.3.6 Design of 125 kW motor drive inverter visualized, including semiconductor modules, gate drives and signal conditioning, DC bus capacitors and thermal management.

Conclusions

The proposed QMag architecture based electric drivetrain system under development promises to meet DOE EETT targets for power density improvement, cost reduction, and magnetics utilization. Motors based on QMag technology have been analyzed through large-scale design optimization studies and shown to be feasible candidates for traction applications with a maximized power density of over 50kW/litre, and additional merits of high-speed operation capability, a wide speed range of 3X base speed, simplified modular manufacturability, improved cooling, etc. The design and simulation of SiC inverter, control algorithm development, and loss analysis show operation in motoring and braking modes, and preliminary designs show that power densities at 100 – 150 kW/litre for the inverter, also meeting DOE targets. The project team is currently undertaking the design of thermal management system, and prototype manufacturing.

References

1. U.S. DRIVE Electrical and Electronics Technical Team Roadmap, October 2017
2. Charles J. Flynn, “Parallel Magnetic Circuit Motor”, US Patent US 2011/0089775A1
3. Cree Inc, CAB450M12XM3 datasheet, Available:
<https://www.wolfspeed.com/media/downloads/1493/CAB450M12XM3.pdf>

Acknowledgements

Contributions to the project were made by the following team members: Mr. Joe Flynn, Mr. Chandra Sekhar Goli, Dr. Peng Han, Dr. Hari Harikumar, Dr. Dan Ionel, Dr. Madhav Manjrekar, and Dr. Prasanth Kumar Sahu. The project team wishes to thank Mr. John Tabacchi, DOE NETL Program Officer.

I.2.4 Motor with Advanced Concepts for High power density and INtegrated cooling for Efficiency (MACHINE) – Raytheon Technologies Research Center

Dr. Jagadeesh Tangudu, Principal Investigator

Raytheon Technologies Research Center
411 Silver Lane
East Hartford, CT 06108
Email: tangudjk@rtx.com

Susan Rogers, DOE Technology Development Manager

U.S. Department of Energy
Email: susan.rogers@ee.doe.gov

Start Date: October 1, 2019

End Date: December 31, 2021

Project Funding: \$599,611

DOE share: \$479,689

Non-DOE share: \$119,922

Project Introduction

Raytheon Technologies Research Center (RTRC) is the central research and development (R&D) organization for Raytheon Technologies Corporation (RTX), and has extensive expertise in the design, modeling and analysis of high-performance electrical machines and thermal management for all of its business units. The proposing team consists of researchers from RTRC and John Deere (JD), will be referred as “Team”. Each organization has a long track record of successful R&D of materials, manufacturing, components, and systems for energy efficiency applications. Motor power density and efficiency are limited by fundamental physical trade-offs between electromagnetics, thermal management, and structural design considerations. The team is proposing to utilize novel technologies and multi-physics design methods to develop a Motor with Advanced Concepts for High power density and INtegrated cooling for Efficiency (MACHINE), demonstrating an 8X improvement in power density and 1% increase in efficiency.

Objectives

The objective of the project is to demonstrate a high speed (>20,000 RPM) electrical machine using non-heavy rare earth hard magnets, high Si soft magnetic steel, and embedded in-slot cooling. To achieve this goal, as part of this seedling effort, the proposed plan to address three key aspects with specific objectives towards meeting the target requirements, a) Motor design: Preliminary electromagnetic design meeting target performance metrics. This includes motor design studies to identify key machine parameters such as machine topology, operating speeds, material selection, number of poles, and current density. These parameters are optimized based on optimal magnetic loading, electric loading, airgap shear stress, and heat removal capacity of the select cooling mechanism; b) Thermal Management: The thermal management task includes identifying the appropriate materials, manufacturing methods and quantifies effective heat removal capacity for a select flow rate and pressure drop. This shall provide inputs to the motor design tasks in terms of maximum heat loads and achievable current density, and thereby contribute to the target power density; and c) Build a sectional prototype: Since this is a seedling effort, the team proposes to build a sectional prototype (3-4 slots) with concentrated winding and in-slot cooling. Heat load is generated by exciting the coils with current at a given current density and quantify the heat removal capacity of the thermal management solution by measuring the inlet and outlet temperatures.

Approach

Permanent magnet machines are proven to have high power density and efficiency. There are mainly two types of permanent magnet machines: concentrated windings and distributed, which will both be explored. State-of-the-art motor drives impose a frequency limit, which sets the allowable maximum speed the motor can possibly achieve. Thus, the maximum frequency limit of the drive is proposed to be used here. The main difference between the two topologies is that the windings are wound around a tooth for concentrated windings while the other

spans a certain number of teeth to make a return. The cooling channels are placed in the slot with the windings in order to effectively cool the copper in a slot. The two design approaches will be optimized so that their best achievable performance can be compared, and a final design will be down-selected from the optimization results.

Direct cooling of the stator windings provides temperature and power density benefits over conventional cooling with an outer jacket. To accomplish direct winding cooling, ceramic channels are inserted into slim rectangular openings between adjacent windings. These channels have multiple small openings for flowing cooling fluid. A conformal header distributes flow to the cooling channels and collects the flow at the opposite end of the stack. The header is designed using topology optimization to be low loss and achieve uniform distribution of the flow to each channel in a compact space.

Results

Team has performed electromagnetic design optimization and selected design candidates are presented in the design space as function of three design parameters: the core objective (power density), the stator outer diameter (OD), and the applied electric loading, i.e., a product of current density and a slot fill factor, depicted in Figure I.2.4.1. The volume of the machine takes the end winding, the shaft, and the frame of the motor into consideration as a buck volume. Based on the results, the power density can be improved by increasing the electric loading. However, if the electric loading is too high, the temperature will quickly go over the limit and efficiency will be degraded significantly simultaneously. Small OD designs tend to have a higher power density at high speed; however, they show relatively long stack length that leads to rotor dynamic problems. Whereas distributed winding topology-based results shows lower power density in general even at a higher speed, because this topology exhibits a lower slot fill factor and longer end winding overhang in the axial direction that results in higher volume. A final selected design should have an attractive power density within the thermal limit and a feasible rotor structure allowing the rotor to operate at the targeted speed.

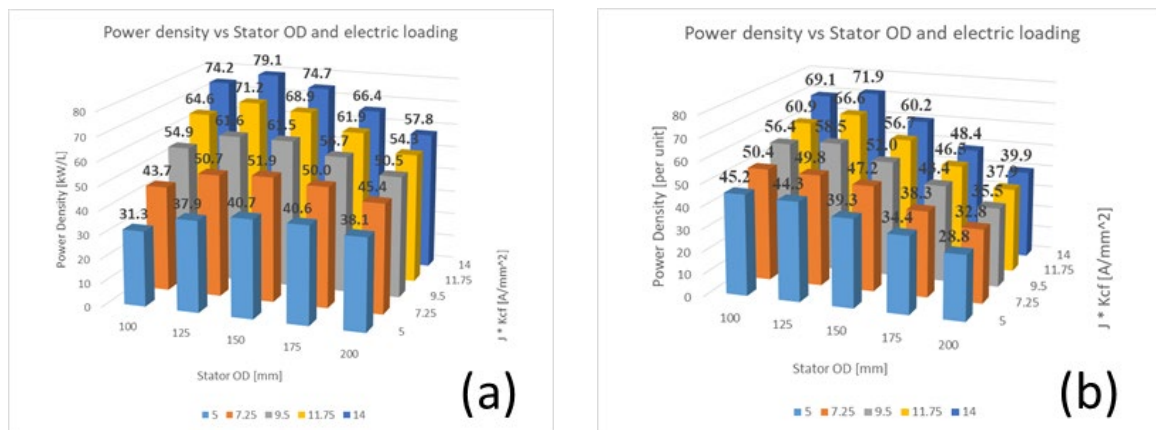


Figure I.2.4.1 Power density distribution in the design space for both topologies: (a) concentrated winding designs at 24000 rpm, (b) distributed winding designs at 30000 rpm.

Based on the performance of the two topologies, two designs were selected from the concentrated winding design topology. The cross section and the key geometric variables of the two selected designs are shown in Figure I.2.4.2. The magnets have <0.5% Dy content situated on the rotor. The aspect ratio (rotor OD to stack length) of the motor is selected to avoid rotor dynamic issues. Supercore materials are used in the stator to reduce the core loss at high frequency, improving the efficiency. The slot fill factor takes only the partial slot into consideration to account for the cooling channels and winding temperature was verified to stay under an acceptable temperature limit. An optimal thickness of carbon fiber wrap is included in the design wrapped around the magnets mounted on the rotor to retain them from flying due to centrifugal loads in the airgap. The second design (design-4) offers higher power density due to a higher electric loading.

Parameters	Design 3	Design 4
Power [kW]	125	125
Speed [rpm]	24000	24000
Torque [Nm]	49.7	49.7
Poles	10	10
Slots	12	12
Stator outer diameter [mm]	150	150
Stator inner diameter [mm]	91	90
Rotor outer diameter above magnet [mm]	87	86
Rotor outer diameter below magnet [mm]	70	69
Rotor inner diameter [mm]	50	48
Air gap	1	1
Wrap	1.1	1.1
Stack length [mm]	75.1	62.9
Back iron width [mm]	5.2	5.1
PM height [mm]	8.2	8.2
PM width [mm]	18	21
Tooth height [mm]	24	25
Tooth width [mm]	9	9
Slot opening [mm]	5	5
Stator steel	Supercore	Supercore
Rotor steel	M19	M19
Magnet	N55	N55

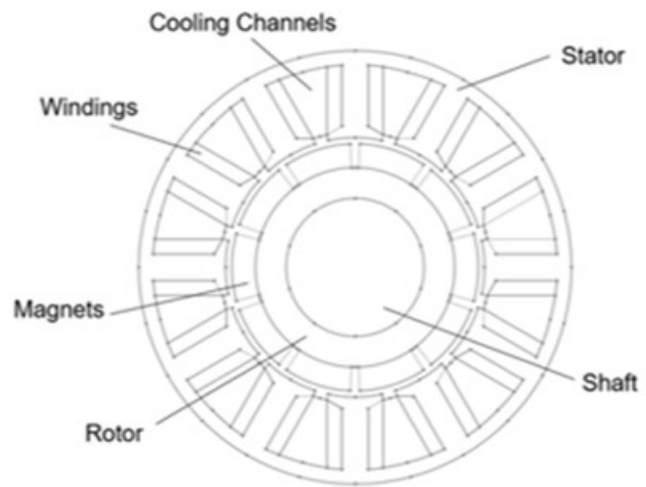


Figure I.2.4.2 Selected concentrated winding designs (Design 3 and Design 4) out of many designs considered.

Table I.2.4.1 Performance metric comparison against FOA

	FOA	Design 3	Design 4
Power Density [kW/L]	50	47.3	52.2
Cost [\$/kg]	6	6.09	6.04
Life	2x	TBD	TBD

The overall performance of both design metrics is summarized in Table I.2.4.1. So far, the volume includes the electromagnetic, the structural, and the thermal management system portions in the volume calculation. Design 3 has not reached the FOA design goal. Design 4 is just above the FOA target, and hence will be selected as a final design. The cost of the two designs are in a range of the FOA figure. The cost figure will be updated in the near future, as well as the life span, which can be determined by assessing the reliability of the materials at the rated operating temperature.

A 2D transient thermal simulation is implemented in COMSOL®. The domain is shown in Figure I.2.4.3. Ground insulation is implemented as an interface resistance between the winding and back iron as well as 3 mm long ‘tabs’ between the winding corners and cooling channel wall. A thermal interface material is modeled as an interface resistance on the remaining surfaces between the channel wall and winding and back iron. A convective boundary condition is applied to all internal surfaces of the cooling channel. The convective coefficient is computed from standard correlations for fully developed laminar flow in rectangular channels.

The cooling flow is 50/50 EGW flow at 60°C and 1.66 LPM/kW of heat loss at max rated load.

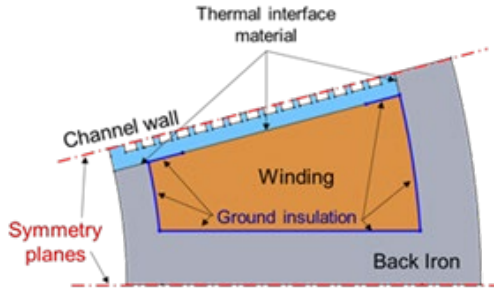


Figure I.2.4.3 Thermal model domain showing ground insulation and thermal interface material placement

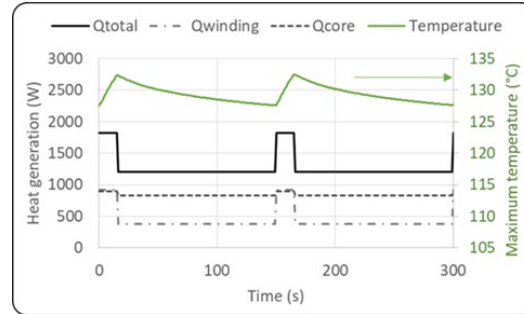


Figure I.2.4.4 Peak temperatures and contours in °C at: (a) max continuous load just before peak load applied; (b) after 15 s at peak load

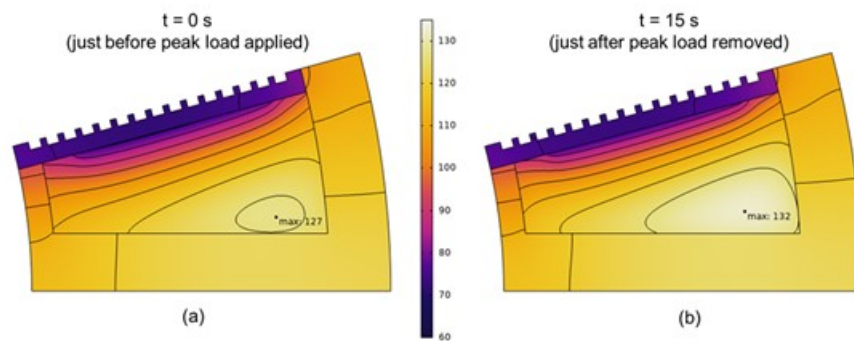


Figure I.2.4.5 Peak temperatures and contours in °C at: (a) max continuous load just before peak load applied; (b) after 15 s at peak load

Heat is generated in the winding and back iron, alternating between maximum continuous load for 135 seconds and peak load for 15 seconds. This loading condition is run over multiple cycles to ensure that the results are independent of initial conditions. The loading condition and resulting peak temperatures are shown in Figure I.2.4.4. The location of the peak temperatures and temperature contours are shown in Figure I.2.4.5. In order to implement direct embedded winding cooling, it is necessary to ensure that the appropriate amount of coolant flow is present in each of the flow channels in the stator slot. Therefore, properly designed supply and collection flow headers are needed to distribute the flow as evenly as possible by matching the impedance through each channel in the path from the central coolant supply source to the central coolant collection port. An optimally designed flow header can ensure maximal flow distribution and minimal pressure losses. This flow header will provide a 50/50 ethylene glycol water mixture at 50°C to the motor slots for direct winding cooling. The flow header is one portion of the integrated system. The design approach utilizes Raytheon Technologies' proprietary topology optimization tools to ensure uniform flow to the channels with minimal pressure drop.

In the first design, the design envelope features a radial inlet to facilitate compact geometry of the full system, as shown in Figure I.2.4.6. The primary location for the flow distribution is in the space located circumferentially on the outside of the motor package assembly. Two flow headers supply coolant to the inlet, therefore a symmetric section of the design space is used to bound the simulation. Two symmetric header halves distribute flow to the channels in a more uniform fashion and is also beneficial for manufacturability of the motor with integrated cooling system. Boundary conditions are applied at the inlet, outlets, and symmetric plane in the design space. The optimization objectives are to maximize flow uniformity and to minimize pressure drop in the flow header.

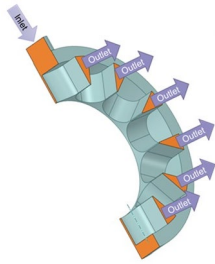


Figure I.2.4.6 Topology optimization: problem setup

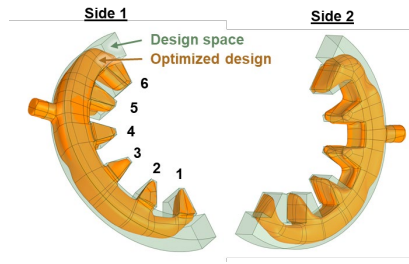


Figure I.2.4.7 Topology optimized flow header design

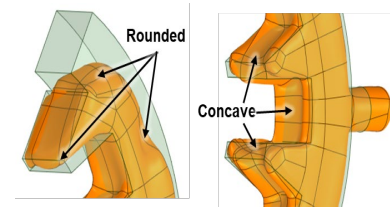


Figure I.2.4.8 Detailed features of topology optimized flow header

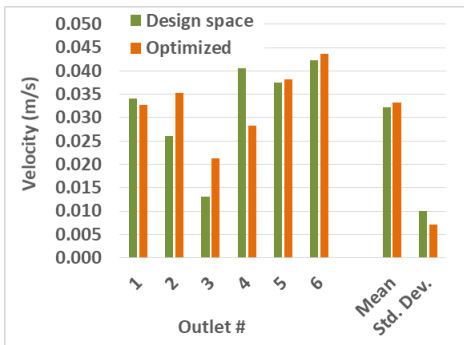


Figure I.2.4.9 Velocity distribution of optimized manifold

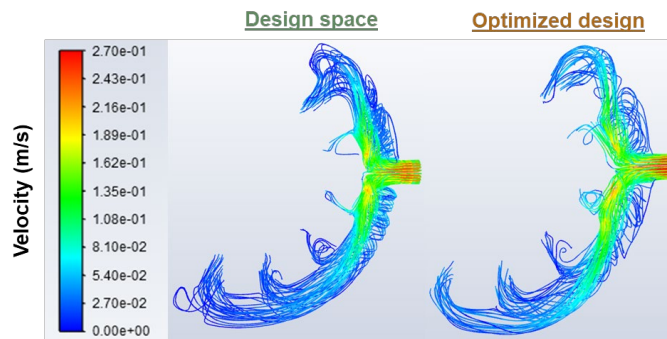


Figure I.2.4.10 Velocity streamlines of the design space compared with the optimized design

The optimized flow header design is shown in Figure I.2.4.7. As expected, the flow header takes on an organic shape to minimize flow resistance through the overall shape. Detailed features of the geometry are shown in Figure I.2.4.8. Header outlet channels (supplying flow to the channels embedded in the motor) closer to the header inlet have concave features that increase flow resistance, such as outlets #4 and #5 indicated in the figure. Header outlet channels further from the header inlet have rounded features that reduce the flow resistance, such as outlets #1 and #2. Together, these features balance out the flow impedance to provide uniform flow through the channels. The standard deviation of velocity at the outlet of each channel reduced by 29% during the optimization process, as shown in Figure I.2.4.9. CFD analysis indicates smoother streamline paths in the optimized design compared to the design space, as shown in Figure I.2.4.10. Analysis also indicated that gravity does not significantly influence the flow distribution in this design.

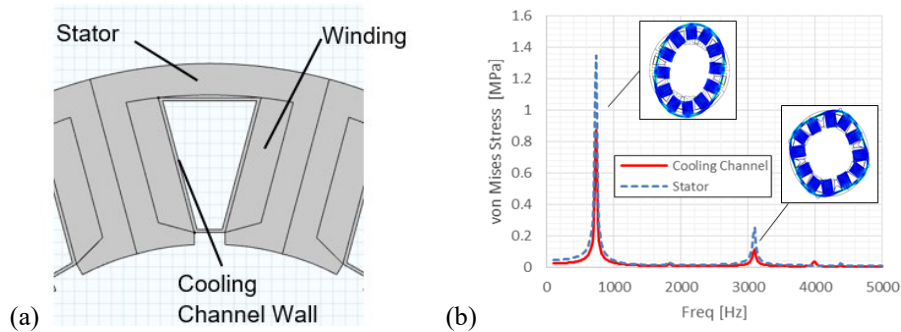


Figure I.2.4.11 COMSOL vibratory response analysis: (a) 2D COMSOL model (b) Stress response spectra (with excitation swept from 0 to 5000 Hz) with vibratory deformation shapes at two prominent resonant frequencies

Vibratory response characteristics of the proposed motor design with direct winding cooling channels were investigated for the purpose of assessing the potential risk of high cycle fatigue (HCF) failure in components due to electro-magnetic force induced vibrations. The focus was the vibratory stress on the thin-walled fluid channel structure. This was done by performing forced vibration analyses using COMSOL by creating a 2D motor model as shown in Figure I.2.4.11. The cooling channel walls were assumed to be made of CE221 polymer material. The actual cooling channel in operation would have the internal cavity filled with fluid. For this model, the cooling fluid was not modeled.

The electromagnetic excitation forces were calculated by a motor design software package (Infolytica) which provided forces acting on each of the twenty-four winding sections. The forces were calculated for the motor running at 24,000 RPM and subsequently converted into frequency spectra via Fourier transform. The spectra showed the fundamental frequency component of the excitation force at 4000 Hz. This fundamental force component was in turn imported into the COMSOL model and swept from 0 to 5000 Hz for frequency response analysis. As seen in the figure, the stress spectra for the stator and the cooling flow channel are characterized by discrete peaks associated with structural natural frequencies. The peak stress for the cooling channel component is 0.87 MPa which is associated with the resonance peak at 740 Hz. In terms of the risk of HCF failure, the fatigue strength (for 10^6 cycles) for plastics in general is said to range from 5 – 50 MPa. Considering that the peak stress value obtained for the analysis is less than 1 MPa, the risk of HCF failure appears to be small based on this current 2D model analysis.

Work is currently continuing to improve the accuracy of the prediction by extending the model from 2D to 3D, adding more detailed features, and refining the material property definitions.

Conclusions

This project is on its way to meet the proposed target metrics. Proposed design exceeds the power density of 52 kW/L (goal of > 50 kW/l), cost of 6.3 \$/kW (goal < 6 \$/kW). Cost target is slightly higher than goal but with further design refinements, this goal can be met. Team is also currently in the process of quantifying the life goal of 2X.

References

1. T. A. Lipo, Introduction to AC Machine Design, Wisconsin Power Electronics Research Center, Wisconsin, 2004

Acknowledgements

Acknowledgment: “This material is based upon work supported by the U.S. Department of Energy’s Office of Energy Efficiency and Renewable Energy (EERE) under the Vehicle Technologies Program Office Award Number DE-EE0008867.”

Disclaimer: “This report was prepared as an account of work sponsored by an agency of the United States Government. Neither the United States Government nor any agency thereof, nor any of their employees, makes any warranty, express or implied, or assumes any legal liability or responsibility for the accuracy, completeness, or usefulness of any information, apparatus, product, or process disclosed, or represents that its use would not infringe privately owned rights. Reference herein to any specific commercial product, process, or service by trade name, trademark, manufacturer, or otherwise does not necessarily constitute or imply its endorsement, recommendation, or favoring by the United States Government or any agency thereof. The views and opinions of authors expressed herein do not necessarily state or reflect those of the United States Government or any agency thereof.”

RTRC Team: Stephen Du, Kenji Homma, Kimberly Saviers, Artira Sur, Joe Turney, Jagadeesh Tangudu (PI), Brij Singh (John Deere)

NETL Manager: Nicholas Damico, Carla Winaught

I.2.5 Cost Effective 6.5% Silicon Steel Laminate for Electric Machines (Iowa State University)

Jun Cui, Principal Investigator

Iowa State University
2220 Hoover Hall
Materials Science and Engineering Department
Ames, IA 50011
Email: cuijun@iastate.edu

Steven Boyd, DOE Program Manager

U.S. Department of Energy
Email: steven.boyd@ee.doe.gov

Start Date: October 1, 2016
Project Funding: \$155,000

End Date: September 30, 2020
DOE share: \$140,000

Non-DOE share: \$15,500

Project Introduction

A rare earth magnet is the most expensive component in permanent magnet motor. Since 2000, the price of the rare earth NdFeB-Dy magnet has gone through a series of volatile rises and falls. As Europe and China are aggressively pursuing electric vehicle with higher efficiency, the demand for rare earth magnet is expected to be doubled by 2025. The rising demand and manufacturing cost make it difficult to meet the DOE 2025 cost target of \$6/kW for the 100-kW electric drive system.

MnBi permanent magnet is the only non-rare earth magnet holds a viable potential to meet the DOE cost target. The cost is expected be ~\$26/kg when mass produced. The price of MnBi magnet is expected to be stable over the next few decades due to the world-wide availability of the elements Mn and Bi. It is important to understand that criticality is defined by availability, not by abundance. The highest energy product that bulk MnBi permanent magnet can achieve using the current technology for mass production is about 8 MGOe at room temperature (theoretical limit is 20 MGOe). It is only about 20% of that of the Nd-Fe-B magnet. In order to meet the DOE 2022 power density targets of 1.6 kW/kg and 5.7 kW/L, the motor has to be operated at much higher excitation frequency, which in turn, demands advanced soft magnetic materials to make up the efficiency loss due to the rising eddy current.

Advanced soft magnetic materials, such as nanocrystalline and amorphous soft magnetic materials, possess high electric resistivity. They are more suitable for high frequency operation, but the materials and processing costs are high. High Si electrical steel has the potential to be both efficient and cost effective. Increasing Si content improves magnetic and electrical properties, with ~6.5 wt.% being optimum. However, at 6.5 wt.% Si, the steel is too brittle to be cold rolled or stamped. The current manufacturing method diffuses Si into the thin gauge 3.2 wt.% Si steel after chemical deposition. It is an elegant engineering solution but at great manufacturing cost (~5X of the price of 3.2 wt.% Si steel). Research showed that rapid solidification could bypass the formation of the embrittling ordered phases in 6.5% Si steel, greatly improve its ductility.

The overall project has three sequential tasks: 1) use non-rare earth magnet to lower motor's cost, 2) increase motor excitation frequency to improve motor power density, and 3) use advanced soft magnetic materials to improve motor efficiency at high frequency. The team comprises two universities (Iowa State University and Delaware University) specialized in magnetic materials and alloy development; one national lab (Ames Lab) specialized in predictive materials science, mid-scale (10 kg) alloy casting and processing, and magnetic materials development; and one company (United Technologies Research Center) specialized in motor design, construction and testing. In FY20, United Technologies merged with Raytheon Technology.

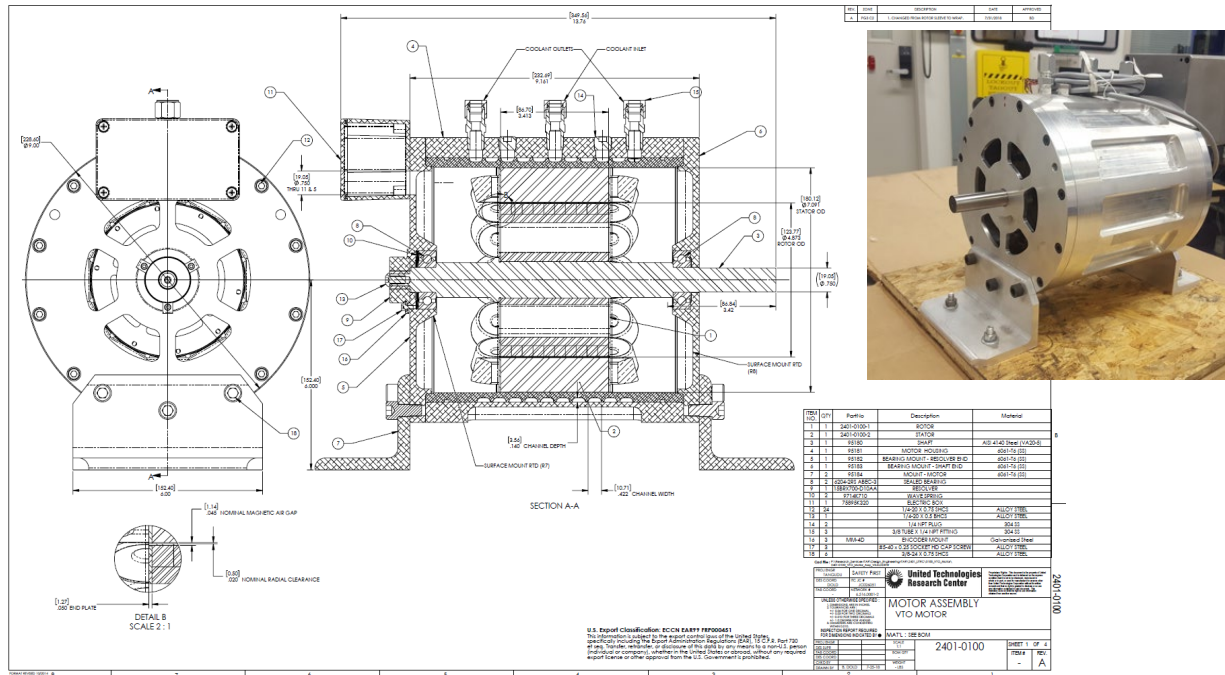


Figure I.2.5.1 Drawing motor assembly and picture of the actual motor built by Leppert-Nutmeg. This motor topology includes a Fractional Slot Concentrated Winding (FSCW) Surface Permanent Magnet (SPM) machine with a 10 poles and 12 slots combination using the equivalent MnBi magnets (SmCo) and the high silicon JFE steels (10JNEX900).

The UTRC team developed the design methodology using several complementary numerical programs. During the design optimization, UTRC team recorded a number of key design candidates shown in the design space spanned by the weight, the stator OD, and the operating current density. From the electromagnetics prospective, a large OD and a high current density can always improve the power density; however, the thermal and the structural prefer the stator OD and current density to be in the opposite direction because too large of these two figures can increase the stress and temperature due to the centrifugal force and copper losses, respectively. A final design was selected so that it features a high-power density while staying below the temperature and stress limits imposed by the thermal and structural physics. The drawing of the final design is shown in Figure I.2.5.1. Leppert-Nutmeg Inc., an electric motor turnkey service provider was selected to build the motor. The motor was built in July and delivered in August 2019.

From FY16 to FY19, the team has achieved 1) pilot production of MnBi bulk magnets with 8.5 MGOe (80 pieces, each weighs about 9 grams) and 2) designed and constructed a 400 Hz 10 kW motor using 6.5% Si steel and dummy magnets with energy product fixed at 8.5 MOe.

Objectives

The specific objective for FY20 is to complete the comprehensive testing of the motor built in FY19.

Approach

UTRC team has finished constructing the test-setup. The prototype motor was mechanically aligned to the dyne motor via a flexible coupler. The dyne motor is an inductor motor driven by a Siemens commercial drive operating under the speed mode; whereas the prototype motor is driven by a Phase-Motion drive operating at torque mode. Many RTD wiring connections and thermal couples were in place to monitor the winding temperature. In addition, cooling refrigerant, delivered by a cooler, is fed to the inlet and outlet of the cooling jacket. The torque meter is sitting between two motors in order to provide the actual speed and torque readings in real time during testing. A new encoder was attached to the end of the prototype machine. The encoder pulse readings are fed to the phase-motion drive as a source of the feedback signal for current regulation. Serial connection was established between the human interface, i.e., a Phase-Motion software program running on a computer, and the actual Phase-motion drive. The prototype motor was first test tested at no-load condition, then at full-load, then at 110% designed capacity. Key performance such as efficiency, torque, temperatures were measured.

Results

Electrical Measurements

The motor per phase resistance can be accurately measured using a micro-ohm meter. The phase inductance was measured using a sensitive multimeter. The resistance and the inductance measurements are given in Table I.2.5.1. against the predicted results. It can be seen that the measurements aligned to the prediction with minor discrepancy. This discrepancy in resistance is due to the connector as connector resistance is not included in the model predictions. The inductance discrepancy comes from the small numerical error in FE analysis. Nevertheless, the predicted results are very close to the actual measurements.

Table I.2.5.1 Per-phase resistance and inductance measurements.

	Predicted	Measured	Difference [%]
Ra [mW]	102	111.0	8.1
Rb [mW]	102	111.5	8.5
Rc [mW]	102	111.1	8.1
La [mH]	2.2	2.25	2.2

The back EMF testing was conducted. The rotor was able to change to different speeds by the Siemens drive. The three-phase back EMF was captured when the rotor is running at the rated speed, i.e., 2000 rpm. The per-phase back EMF was measured using three differential probes tapped between the neutral point of the machine and each motor winding input, shown in Figure I.2.5.2a. The predicted per-phase back EMF waveforms (Figure I.2.5.2b) are obtained using a transient solver in FE analysis. The comparison shows that the predicted waveform is very close to the measurement. The very small discrepancy comes from the actual magnet strength that is slightly different from specified. The back EMF magnitude versus speed is given in Figure I.2.5.2c. It can be seen that the back EMF is close to the predicted back EMF across all speeds.

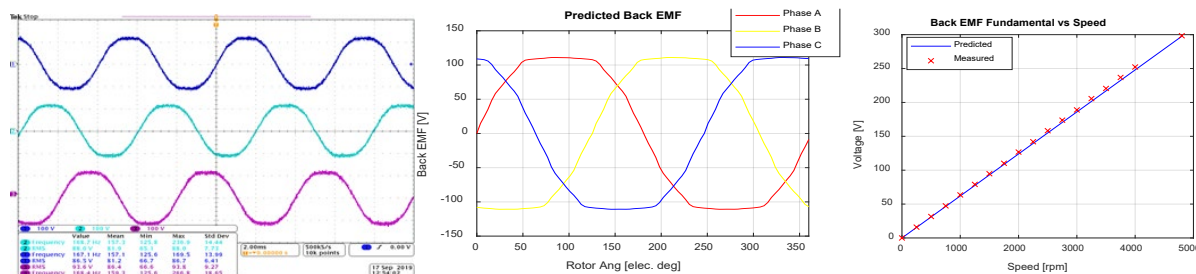


Figure I.2.5.2 Three phase back EMF at rated speed: (a) measurements, (b) predicted back EMF, (c) Measured and predicted back EMF versus different speeds

Different current loadings were applied in the load tests using the current regulator set up in the Phase-Motion drive based on the prototype motor characteristics. When the motor was at no-load condition, it still required a small amount of input power to overcome a certain amount of no-load mechanical losses (bearing and windage losses) associated within the motor rotating system. The no load mechanical losses are proportional to the rotor rotating speed. The no-load losses were identified by driving the test motor to various speed at no-load. The measured no-load losses are shown in Figure I.2.5.3. The core losses and the magnet loss are obtained using FE analysis. The remaining mechanical losses add onto the core losses and magnet loss to make up the total measured no-load loss in the system.

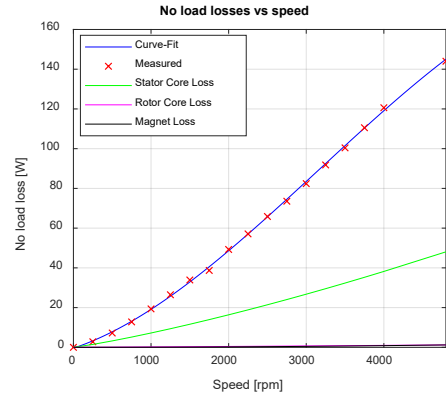


Figure I.2.5.3 Losses associated with the test motor at no-load.

The prototype motor was successfully driven to the required loads at the required maximum speed and frequency. The first load test was the torque/power per amp test running at the rated speed 2000 rpm. The torque and power for different current loadings is shown in Figure I.2.5.4 and Figure I.2.5.5. At light load, the experimental results match the prediction well, however, the magnitude of error increases at heavy load, especially in the overloading regime. The Error reaches 8% as shown in Figure I.2.5.4. This is due to the magnetic saturation in the iron, which is difficult to predict accurately in FE analysis. Nevertheless, the prototype is capable of delivering the rated load and the peak load according to the specifications with a very small amount of error, as shown in Figure I.2.5.5.

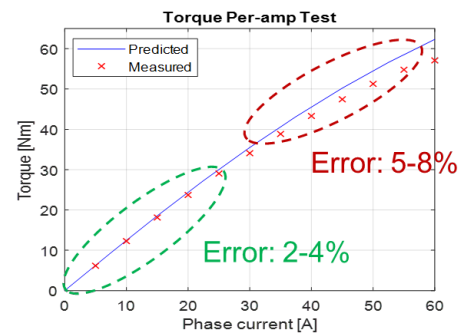


Figure I.2.5.4 Torque versus current loading test.

The efficiency was also recalled using a power analyzer, shown in Figure I.2.5.6. The prediction only accounts for the copper loss, the core loss, and the magnet loss, but not the mechanical losses and the stray-load losses. The efficiency is very high at light load, then it starts to drop at the rated and the overloading conditions, as predicted by FE analysis. The increased efficiency error is mainly due to the stray-load losses and other form of unpredicted losses due to iron saturation and mechanical coupling. However, the efficiency still shows a similar trend as does for the predicted results.

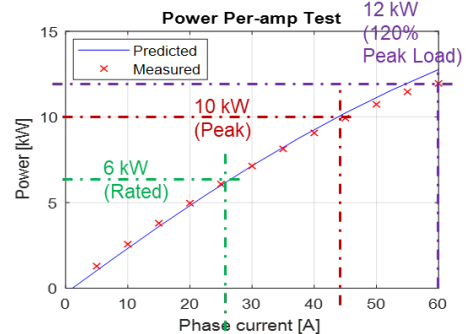


Figure I.2.5.5 Power versus current loading test.

The efficiency at different speeds for the same power delivery were measured and shown in Figure I.2.5.7. It matches the predictions at light field weakening conditions; however, the error increases as it approaches to deep field weakening conditions. This may be due to the actual magnet strength that is sensitive to the applied demagnetization force, resulting in a smaller magnetic loading in the deeper flux weakening regime. In summary, the field weakening performance of the prototype motor also matches the prediction reasonably well.

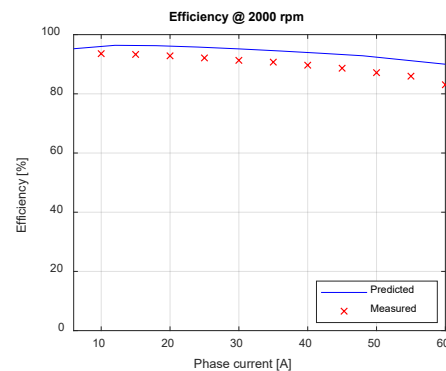


Figure I.2.5.6 Efficiency versus current loading.

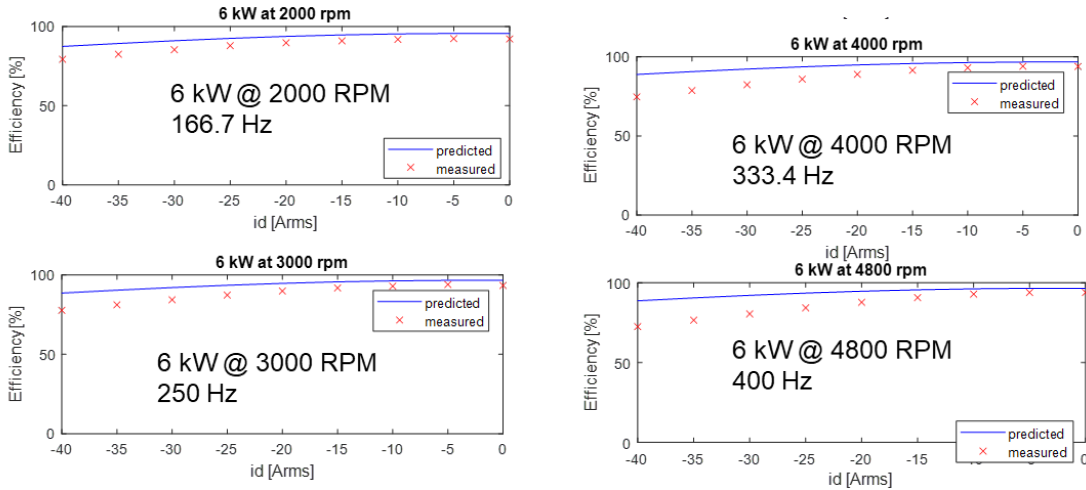


Figure I.2.5.7 Predicted and measured efficiency at different speeds and different field weakening conditions under rated load.

Thermal Measurements

Multiple operating points were tested to characterize the thermal performance of the assembled motor. Table I.2.5.2 provides details of the different test conditions. During the testing, the motor was connected to a cooling loop where water at 18°C is used as the coolant. The flow rate in the loop was 5 LPM. The coolant was maintained at 18°C using an external chiller. The temperature of the various components of the motor is measured using thermocouples (TCs) and RTD sensors which were embedded in the motor at the time of assembly. Both TC and RTD sensors are provided at the center of 3 stator coils. RTDs are also provided at the end windings of the same coils which have the embedded sensors in the middle of their axial length. During operation the TC readings appeared to be highly noisy which was attributed to EM interference as these TCs were not isolated. However, the RTD measurements did not suffer from EM interference and were considered for analysis.

Table I.2.5.2. Different test conditions used for assessing motor thermal performance

SI No.	Power output	Speed (RPM)	Type	Details
1	3 kW	1000	Steady	Steady
2	6 kW	4800	Steady	Steady
3	6 kW	4000	Steady	Steady
4	6 kW	2000	Steady	Steady
5	6 kW	3000	Steady	Steady @ 6 kW
6	1.2–10 kW	2000	Steady first (45 mins) and then cycling	Cycle between peak (10 s) and rated power (90 s) after achieving thermal steady state
7	6 – 10 kW	2000	Steady first (45 mins) and then cycling	Cycle between peak (10 s) and rated power (90 s) after achieving thermal steady state
8	3 – 5 kW	1000	Steady first (45 mins) and then cycling	Cycle between peak (10 s) and rated power (90 s) after achieving thermal steady state

From the measurements it is observed that the end winding temperature was higher than the temperature at the center of the coil in the axial section. This validates the thermal modeling concept used for temperature predictions in the electric motor. The measured coil center temperature (RTD1) and end coil temperature (RTD4) for temperature rise, steady state and temperature drop for the same coil are shown in Figure I.2.5.8.

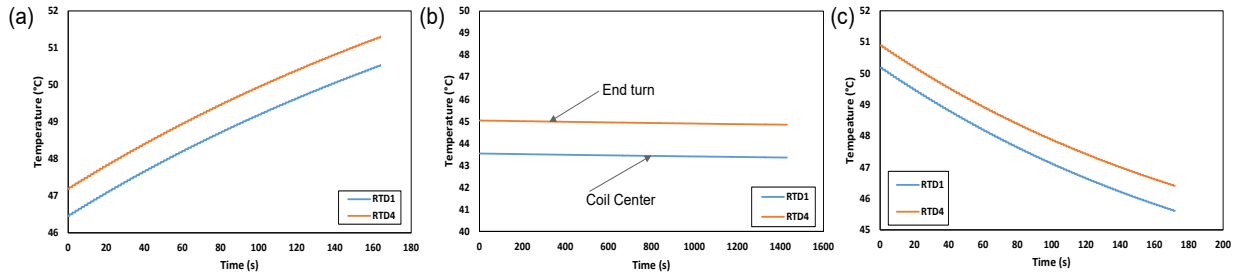


Figure I.2.5.8 Temperature measurements in end coils and coil center: (a) Rising temperature condition (b) Steady temperature and (c) Falling temperature.

The measured temperatures in the different coil end-turns exhibited variation. This variation can be attributed to uneven heat generation in the motor windings caused by factors such as variation in packing factors, assembly techniques and exact positioning of the RTDs. Figure I.2.5.9a shows the variation in the end coil temperatures at steady state for operation at 2000 RPM at the rated power output of 6 kW and a torque output of 28.5 Nm. The maximum steady state temperature was 60.6°C on one end turn which is ~ 5°C higher than the coldest end turn. Additionally, the temperature rise of 42.7°C is lower than the expected temperature rise of ~ 60°C from the steady state predictions using the thermal model. This can be explained due to the choice of the coolant and the coolant inlet temperature of 18°C. Water at this temperature has a much better thermal performance than the 60-40 EGW at 50°C which was used in the model predictions.

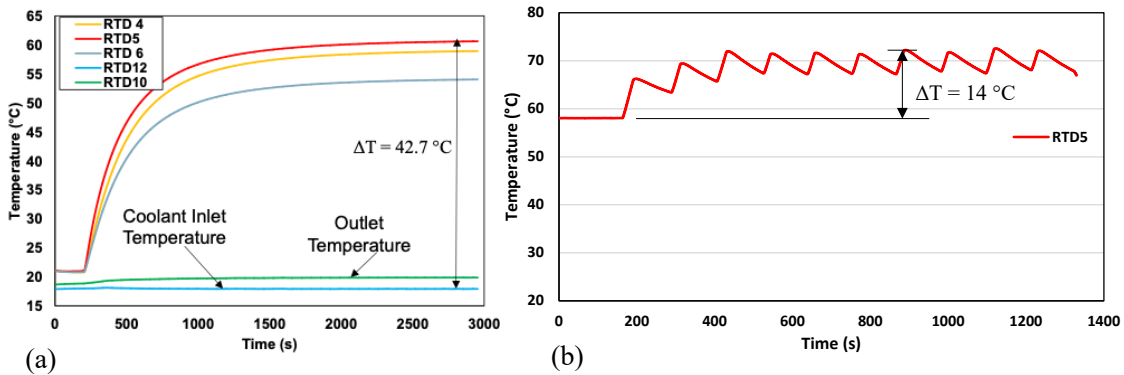


Figure I.2.5.9 (a) Temperature variation in different coil end turns for 2000 RPM, 6 kW and 28.5 Nm operation. (b) Temperature variation in end coil during transient testing at 2000 RPM cycling between 6 kW and 10 kW.

Transient tests were also conducted to assess the temperature rise in the motor windings. A 90% duty cycle was chosen for peak loading conditions at different speeds as indicated in Table I.2.5.1. Figure I.2.5.9b shows the temperature of the hottest end turn in the motor winding while operating at 2000 RPM. For this test the motor was allowed to achieve steady state at 6 kW output power while delivering 28.5 Nm torque. Thereafter, the motor was cycled to deliver 10 kW power and 48.375 Nm torque for 10 secs and then brought back to its steady operating point. The motor was driven through 10 such cycles and the temperatures recorded. The steady state temperature achieved by the motor was 58°C and during the power cycling, the end turn peak temperature increased to 72°C. This represents a 14°C rise in peak winding temperature. The different maximum temperature measurement for all the tests conducted on the motor are listed in Table I.2.5.3.

Table I.2.5.3 Thermal performance test summary.

SI No.	Power output Steady - Peak, (kW)	Speed, (RPM)	Torque Steady - Peak, (N-m)	Tmax Steady - Peak, (°C)
1	3	1000	28.9	50.9
2	6	4800	12.1	53.4
3	6	4000	14.5	47.4
4	6	2000	28.5	60.6
5	6	3000	19.39	43.6
6	1.2 - 10	2000	5.8 - 48.4	25.2 - 42.6
7	6 - 10	2000	25.8 - 48.4	58 - 72
8	3 - 5	1000	28.9 - 48.5	50.9 - 60.9

Cost modeling

The cost of a Brushless Permanent magnet (BPM) motor depends upon various factors including the material cost, vendor profit margins, labor cost, production volume etc. Typically, for achieving higher performance with a smaller and lighter motor designs, designers incline towards the use of rare-earth based permanent magnets. These magnets are three to five times stronger than the ferrite or ceramic permanent magnets and have a very high maximum energy product [1]. Though the rare earth magnets have a superior performance, historically price of these magnets have been uncertain.

In this project, non-rare earth magnets (MnBi) were used in the design of BPM motor and a cost model for varying production volume is generated. The cost of MnBi magnet is currently estimated at \$13.6/kg when mass produced (>20 kT/yr). This cost estimation is based on the same methodology used by IMARC group to study the feasibility of rare earth magnets manufacturing plant. It assumes the raw materials cost accounts ~80% of the final magnet price. In September 2020, the raw materials cost is \$5.3/kg (Mn accounts 20 wt.% at \$1.5/kg and Bi accounts 80 wt.% at \$6.2/kg); the manufacturing cost is about \$1.3/kg; the margin for manufacturer and supply chain is \$1.1/kg (~16% of the final price); and the final magnet price is about \$7.7/kg. In comparison, the price of Nd-Fe-B magnet (N45) is \$63/kg and that of the ferrite is \$7/kg. The corresponding price per energy product \$/kg/MGOe is 1.4, 1.5 and 0.9 for Nd-Fe-B, ferrite and MnBi, respectively. The price advantage of MnBi is obvious.

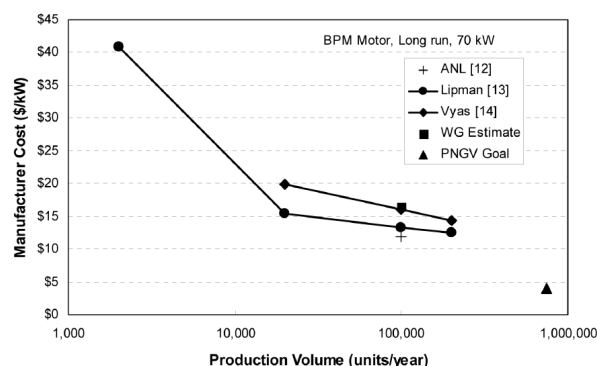


Figure I.2.5.10 BPM motor cost as a function of production volume.

As observed by Lipman in [2], the cost of BPM motor varies widely with its production volume. Graham et al. in their EPRI report [3] summarizes various motor cost models developed in early 2000's and came up with the cost formula of \$13.70/kW + \$190. Figure I.2.5.10 shows BPM motor costs per kW for various studies considering different production volumes. Estimates by ANL [4] for EV applications indicate that, for large production volumes BPM motors could be produced at \$10.50 per kW for a 70-kW motor. Lipman indicates that in quantities of 200,000 units per year, BPM motors of a similar size could be produced at \$12.50 per kW. Vyas [5] estimated that BPM motors in quantities of 100,000 will cost approximately \$16 per kW. Further In [6] Lipman et al. updated their cost model with the assistance of a major motor manufacturer and verified their

results by comparing the results with actual motor costs. The study was conducted for small (2000), medium (20000) and large (200000) volume productions.

Active material cost for 10 kW and 55 kW BPM motor using MnBi non-rare earth magnets and 6.5% Si steel for stator laminates are provided in Table I.2.5.4. Following [2] the active material cost is multiplied with a factor of 1.18 to account for 18% supplied profit margin and a factor of \$15/kW is added to the active material cost to account for the cost of adding value to the raw material. Since the production of motors with non-rare earth magnets can use the preexisting assembly and production lines, in this study the fixed cost of 660\$ is eliminated from the cost equations used by Lipman for small production volumes. Using the method described above, for a production volume of 2000/yr cost of 10kW and 55kW motors can be calculated as \$256.89 and \$1246.25.

Table I.2.5.4 Active material cost distribution for a 55 kW BPM motor using MnBi magnets.

Component	Weight (Kg)	Material	\$/kg	material Cost (\$)	% cost
Stator Laminates	13.68	6.5% steel	3.5	47.88	19.43
Copper	14.19	copper (C11000)	5.12	72.65	29.49
Cooling Jacket	23.40	6061-T6 Aluminum	1.5	35.10	14.25
Rotor Laminate	2.99	3.2%steel	2.2	6.57	2.67
Magnets	5.98	MnBi	13.6	81.32	33.01
Shaft	4.76	4140 steel	0.6	2.85	1.16
total cost				246.40	

Next, following the cost trends for different production volumes provided in [6], cost estimates for the designed MnBi magnet based 10kW and 55kW BPM motor are provided in Table I.2.5.5.

Table I.2.5.5 Cost estimates for MnBi Magnet based BPM motor for various production volumes.

Production Volume	10kW	55kW
2000/ yr	\$ 256.88	\$ 1264.25
20000/ yr	\$ 150.39	\$ 740.14
200000/ yr	\$ 84.36	\$ 415.16

Figure I.2.5.11 further outlines the variation in the motor cost (\$/kW) as a function of the cost of MnBi non-rare earth magnet and 6.5% Si steel cost for 55kW BPM motors. Currently the cost of MnBi magnet is predicted at 13.6\$/kg and 6.5% Si steel is predicted at 3.5\$/kg. For a production volume of 200,000 units/yr, this results in a cost figure of 7.54\$/kW for a 55kW motor. According to the report on the global EV outlook [7], if the annual growth of electrical mobility is predicted according to the existing government policies, by 2030 global electric vehicles are expected to reach nearly 140 million and account for 7% of the global vehicle fleet. This will further result in bringing down the production cost of BPM motors.

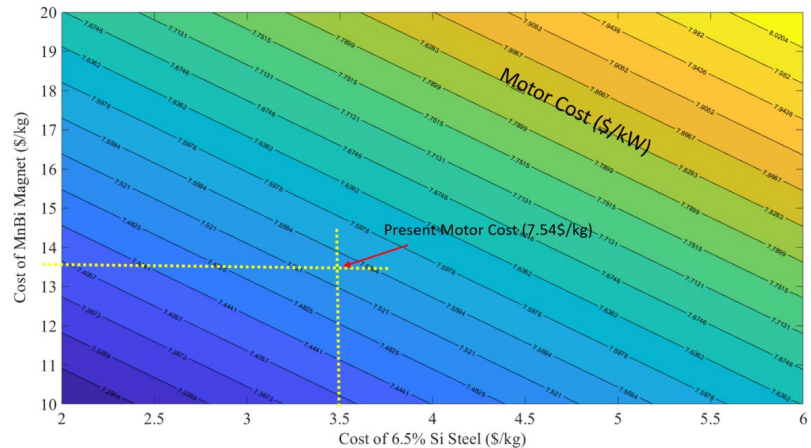


Figure I.2.5.11 Variation in motor cost (\$/kW) as a function of MnBi magnet and 6.5 % Si Steel cost for the manufacturing of 200000 units/yr for a 55 kW BPM motor.

Conclusions

The team has completed the build, experimental validation and final report, which includes, a) Completed first motor prototype build, b) Integrated the test motor with dyne setup, c) Completed testing of the motor at 20% over load at peak power (target: 10 kW) d) Completed flux weakening characterization up to 400 Hz (target frequency > 300 Hz) e) cost modeling. The prototype delivered 11 kW power at 400 Hz with 91% efficiency, exceeded the designed specification.

Key Publications

1. Ouyang, G., et. al., Near Net Shape Fabrication of Anisotropic Fe-6.5% Si Soft Magnetic Materials. *Acta Materialia*. (2020): 201, p.209-216.
2. Ouyang, G., et. al., "Characterization of ordering in Fe-6.5% Si alloy using X-ray, TEM, and magnetic TGA methods." *Materials Characterization* (2019): 109973
3. Gabay A, et. al., "Effect of Sb substitution on crystal structure, texture and hard magnetic properties of melt-spun MnBi alloys", *J. Alloy and Compound*, 2019, July 5; 792:77-86.
4. Ouyang, G., et al. "Review of Fe-6.5 wt% Si high silicon steel—A promising soft magnetic material for sub-kHz application." *Journal of Magnetism and Magnetic Materials* 481 (2019): 234-250.
5. Cui, S., et al. "Thermodynamic and kinetic analysis of the melt spinning process of Fe-6.5 wt.% Si alloy." *Journal of Alloys and Compounds* 771 (2019): 643-648.
6. Tangudu, J. et al. Trade Studies for a Manganese Bismuth based Surface Permanent Magnet Machine." In *2018 IEEE Transportation Electrification Conference and Expo (ITEC)*, pp. 600-605. IEEE, 2018.
7. Ouyang, G. et. al. "Effect of wheel speed on magnetic and mechanical properties of melt spun Fe-6.5 wt.% Si high silicon steel." *AIP Advances* 8, no. 5 (2018): 056111.
8. Gabay, A. et. al. "Preparation of highly pure α -MnBi phase via melt-spinning." *AIP Advances* 8, no. 5 (2018): 056702.

9. Cui, Jun, et al. "Current progress and future challenges in rare-earth-free permanent magnets." *Acta Materialia* 158 (2018): 118-137.
10. Ouyang, G. et. al. "Near net shape BULK laminated silicon iron electric steel for improved electric resistance and low high frequency loss", Provisional patent filed (2018)

References

1. Widmer JD, Martin R, Kimiabeigi M. Electric vehicle traction motors without rare earth magnets. *ustain Mater Technol* 2015;3:7–13. <http://dx.doi.org/10.1016/j.susmat.2015.02.001>
2. Lipman, Timothy, "The Cost of Manufacturing Electric Vehicle Drivetrains," "UCD Report Number UCD-ITS-RR-99-7," May 1999.
3. R. Graham, S. Unnasch, E. Kassoy, R. Counts, C. Powars, L. Browning, D. Taylor, J. Smith, et al., *Comparing the Benefits and Impacts of Hybrid Electric Vehicle Options*, Electric Power Research Institute (EPRI), 2001.
4. Cuenca, R.M., L.L. Gaines, and A.D. Vyas, "Evaluation of Electric Vehicle Production and Operating Costs," DOE Report Number ANL/ESD-41, November 1999.
5. Vyas, Anant and Dan Santini, "HEV Cost Analysis for the EPRI Working Group," presented July 2000.
6. Timothy E. Lipman, Mark A. Delucchi, A retail and lifecycle cost analysis of hybrid electric vehicles, *Transportation Research Part D: Transport and Environment*, Volume 11, Issue 2, 2006, Pages 115-132, ISSN 1361-9209, <https://doi.org/10.1016/j.trd.2005.10.002>.
7. <https://www.iea.org/reports/global-ev-outlook-2020>, as of 18th September 2020.

I.2.6 High Speed Hybrid Reluctance Motor Utilizing Anisotropic Materials (General Motors LLC)

Edwin Chang, Principal Investigator

General Motors Global Propulsion Systems
30003 Fisher Brothers Road
Warren, MI 48093
Email: edwin.chang@gm.com

Steven Boyd, DOE Program Manager

U.S. Department of Energy
Email: steven.boyd@ee.doe.gov

Start Date: October 2016

End Date: December 2020

Total Project Cost: \$7,081,060

DOE share: \$4,637,060

Non-DOE share: \$2,444,000

Project Introduction

The objective of this project is to design and verify motor designs without heavy rare earth (HRE) content capable of achieving DoE Motor Year 2020 performance and cost targets. These three motor variants are Variant 1: Heavy Rare Earth-free Permanent Magnet Motor (HRE-free PM motor), Variant 2: Synchronous Reluctance Motor (SyRM) with Small HRE-free Magnet Assist, and Variant 3: Hybrid Induction Motor with Insert Copper Bars and Cast Aluminum End-rings.

Objectives

The objective of the project is to research, develop, and demonstrate 3 new motor types for traction applications. Each design should be capable of achieving or exceeding the following technical targets, set by the DoE to be achieved by 2020:

- Cost (\$/kW) less than \$4.7
- Specific Power (kW/kg) greater than 1.6
- Power density (kW/L) greater than 5.7.

These motors are enabled by the following technologies, which are evaluated through the course of this project:

- HRE-free magnets must be developed to meet stringent coercivity and remanence performance criteria
- Copper – aluminum interfaces must be developed to be robust in a traction motor environment
- Motor electromagnetic and mechanical design techniques must be developed to ensure that these enabling technologies can be incorporated to meet motor performance requirements.

Each design should demonstrate advantages over conventional baseline designs in one or more of the following categories: cost, efficiency, and power density. Each design is also expected to have proven manufacturability and to undergo typical durability and performance testing by GM to ensure they meet market requirements.

Approach

Three motor design types will be studied to determine the feasibility of each approach. These three motor variants will be selected based on their expected ability to meet the technical targets. These design approaches

will take advantage of material advancements which will allow these motors to meet the performance requirements without heavy rare earth elements or rare earth elements altogether.

The project will concentrate on four major tasks:

Task 1: Material Evaluation and Selection

Task 2: Electromagnetic and Mechanical Machine Design

Task 3: Electric Motor Prototype Manufacturing

Task 4: Verification Testing and Performance Evaluation

Task 1: Material Evaluation and Selection

- Development of the requirements for Grain Oriented Electrical Steel (GOES)
- Survey of available grades of GOES
- Industry survey of GOES available grades and Selection for Electromagnetic Design Studies
- Execution of FEA-based design studies for Synchronous Reluctance Motor using GOES, and Hybrid Synchronous Reluctance Motor using Anisotropic HRE-free magnets and GOES
- Development of, working with suppliers, HRE-free anisotropic magnet material
- Evaluation of the developed anisotropic HRE-free magnets and Non-Oriented Electrical Steel (NOES) for use in the motor laminations.

Task 2: Electromagnetic and Mechanical Design of 3 Machines

- Detailed structural, thermal, and electromagnetic analysis of the machine concepts to ensure that the motors meet both the performance and reliability objectives required for use in General Motor's electrified vehicle portfolio
- Generation of an Indentured Bill of Materials (BoM).

Task 3: Electric Motor Prototype Manufacturing

- Prototype motors will be built to ensure that those meet all GM Production Bill of Process (BoP) requirements
- Production Manufacturing Equipment will be identified, and its associated costs will be documented
- Comprehensive test plan for machine verification will be defined and durability test plan for demonstration will be developed.

Task 4: Verification Testing and Performance Evaluation

- All three motor designs will be calibrated for peak torque and efficiency
- Machines will be tested for performance and efficiency verification
- Torque and power vs. speed curves will be generated
- Complete efficiency maps for both motoring and generating will be generated for operations at different voltage levels
- Measured performance maps will be compared to the predicted results for data correlation purposes

- Rotor durability testing will be executed on two variants (Synchronous Reluctance motor with HRE-free Magnet Assist and High Performance Hybrid Induction Motor using Inserted Copper Bars and Aluminum Die Cast End-rings) and will include rotor speed cycling at various RPM to induce fatigue failures in the rotor laminations
- HRE-free PM motor variant will be excluded from rotor durability testing due to its similarity to other production designs that have previously demonstrated superior reliability.

Oak Ridge National Laboratory, ORNL, a co-recipient of this project, is responsible for aspects of materials testing. The objectives are to characterize material properties of electrical steels and cast Al to Cu bar interfaces.

Results

Motor Design

Table I.2.6.1 summarizes the motor designs. The results are based on the test performance of each of the motor variants.

Table I.2.6.1 Summary of measured motor performance results for all three variants

	HRE-free PM Motor	Synchronous Reluctance Motor with HRE-free PM Assist	Hybrid Induction Motor with Insert Cu Bars and Cast Al End-rings
Stator Outer Diameter (mm)	208	190	190
Rotor Outer Diameter (mm)	139.5	139.1	139.1
Stator Core Length (mm)	200	100	100
Power (kW)	148	86	84
Torque (N-m)	372	249	310
Max RPM	12,000	16,500	14,000

Variant 1 – HRE-free Permanent Magnet motor

The efficiency of the Variant 1 motor, shown in Figure I.2.6.1, is high, consistent with other permanent magnet motors. Power is slightly below the predicted power of 148kW, but the requirements are still met for this motor.

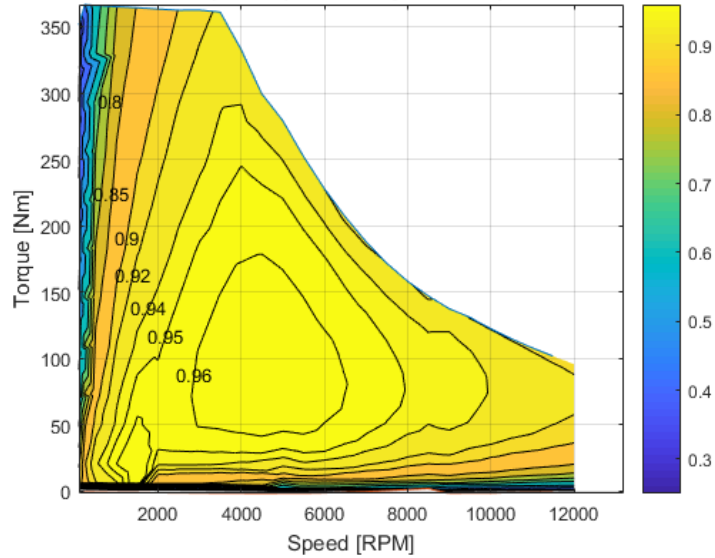


Figure I.2.6.1 Performance of Variant 1 motor, tested at 350V

Demagnetization testing was completed with the motor exposed to significantly higher temperatures than those expected during normal operation, and under adverse currents. These results provide good confidence that this motor, with HRE-free magnets, would be able to operate in vehicle conditions.

Overall, the motor meets the specific power, power density, and cost targets as defined by the **FOA 2019 AOI 5_1384-1599**

Table I.2.6.2 Performance to requirements of Variant 1 motor

Performance						
	Mass	Volume	Power	Specific Power	Power Density	Cost
Target				≥1.6 kW/kilogram	≥5.7 kW/Liter	\$4.7/kW
Variant 1	35.2 kg	6.6 L	146 kW	4.1 kW/kg	22.1 kW/L	Meets

Variant 2 - Synchronous Reluctance Motor with HRE-free PM Assist

The efficiency of the Variant 2 motor, shown in Table I.2.6.2, is high, with a maximum efficiency of 96%, and demonstrates overall higher efficiency than induction motors of similar sizes, and high-speed efficiency regions consistent with an intended usage as a secondary motor or e-axle operation.

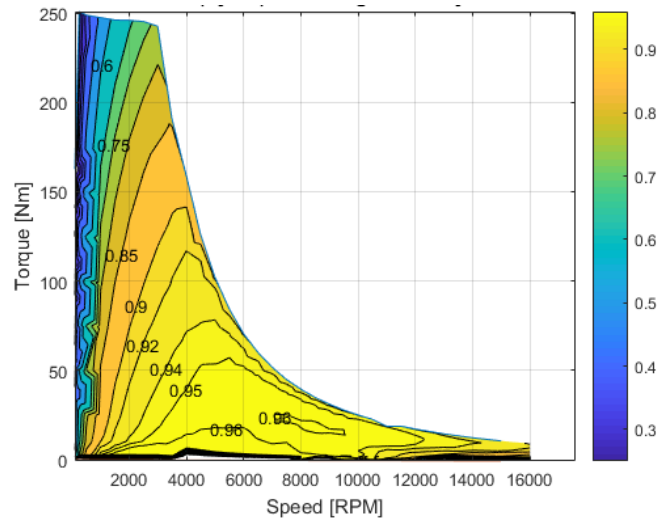


Figure I.2.6.2 Performance of Variant 2 motor, tested at 350V

During demagnetization testing, the motor was ramped to temperatures significantly above those predicted by multiple wide-open throttles, resulting in no significant demagnetization to the motor under adverse conditions. The rotor topology therefore shows significant protection to the magnets, enabling the use of lower coercivity magnets and no heavy rare earths.

High-speed fatigue testing was also completed for the Variant 2 motor. Although the scatter was relatively high for these rotors, this is perhaps due to the prototype stamping of these parts. The number of cycles to failure for these parts at the speed they were tested show promise for their potential application. Figure I.2.6.3 shows the failures of the motors after high-speed cycling.



Figure I.2.6.3 Variant 2 rotor after rotor endurance failure.

While the specific power and power density targets are met for this application by the rotor design, cost targets remained a challenge to meet, as shown in Table I.2.6.3. Cost is difficult to meet for this motor due to the lower peak power of the motor compared to the Variant 1 design.

Table I.2.6.3 Performance to requirements of Variant 2 motor

Performance						
	Mass	Volume	Power	Specific Power	Power Density	Cost
Target				≥1.6 kW/kilogram	≥5.7 kW/Liter	\$4.7/kW
Variant 2	24.1 kg	5.4 L	76 kW	3.15 kW/kg	14.1 kW/L	Does not meet

Variant 3 – Hybrid Induction Motor with Insert Cu bars and Cast Al End-rings

The efficiency of the Variant 3 is as predicted at 92% and shown below in Figure I.2.6.4. This higher efficiency is driven primarily by the copper bars improving the conduction losses of rotor. In addition, the high efficiency region is notable in the high-speed regions, consistent with one of the possible applications of the motor.

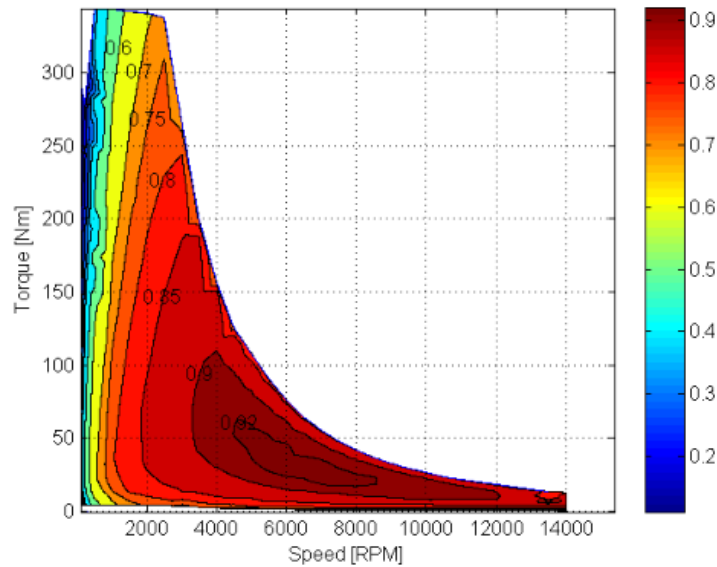


Figure I.2.6.4 Performance of Variant 3 motor

The motor was run at repeated cycles at high speed until failure. Cracking occurred at the end-rings, likely initiating at the interface between the cast aluminum and the copper bars as shown in Figure I.2.6.5.



Figure I.2.6.5 Variant 3 rotor after rotor endurance failure

Like the Variant 2 motor, while the specific power and power density targets were met by this motor design, the cost remained a challenge, driven primarily by the cost of the copper bars and the lower power of the induction machine.

Table I.2.6.4 Performance to requirements of Variant 3 motor

Performance						
	Mass	Volume	Power	Specific Power	Power Density	Cost
Target				≥1.6 kW/kilogram	≥5.7 kW/Liter	\$4.7/kW
Variant 3	27.3 kg	5.4 L	84 kW	3.2 kW/kg	16.3 kW/L	Does not meet

Oak Ridge National Lab (ORNL) testing

Rotor bar tensile and fatigue testing

Based on guidance from GM, a custom test fixture was designed and fabricated to grip rotor bar test specimen for tensile and fatigue testing. Tensile test data is shown in Figure I.2.6.7 and it is shown that the average maximum loading is quite close between the two variants (3,610.6 N and 3,586.6 N for Batch #1 and #2, respectively), but the average displacement is considerably different, with an average of 19.69 mm and 14.23 mm for Batch #1 and #2, respectively. Inspection of the failed tensile specimens indicates that all Batch #1 specimens failed near the center of the copper bar, while all Batch #2 specimens failed in the copper bar near the cast interface.



Figure I.2.6.6 Custom test fixture made for testing rotor bars.

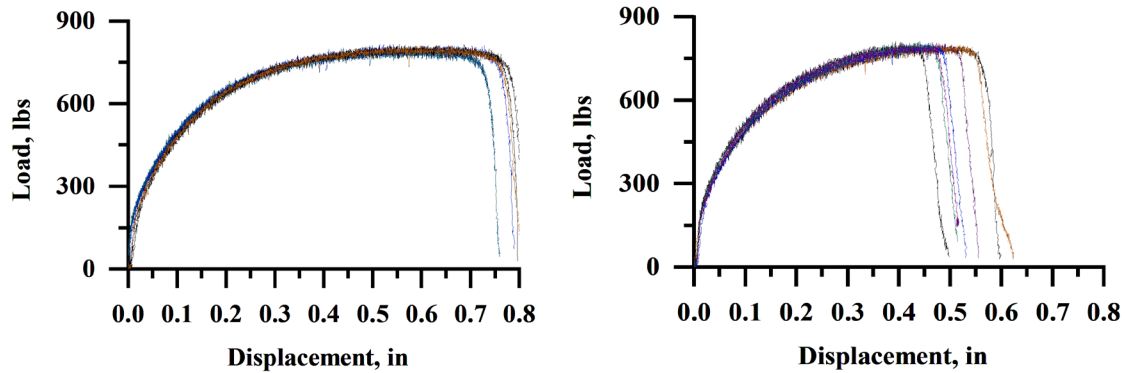


Figure I.2.6.7 Rotor bar tensile test results, Batch #1 (left) and Batch #2 (right).

Edge Microscopy

Edge microscopy of the stamped edge was performed on the gauge section indicated by red lines in Figure I.2.6.4, as two samples for each material were inspected. Scanning electron microscopy (SEM) with secondary electron image (SEI) was used to obtain more detailed topographical information. Observations were made to identify rollover, shear, tear/fracture zones, and burr. Measurements for the first sample of material A (“A1”), are shown in Figure I.2.6.8.

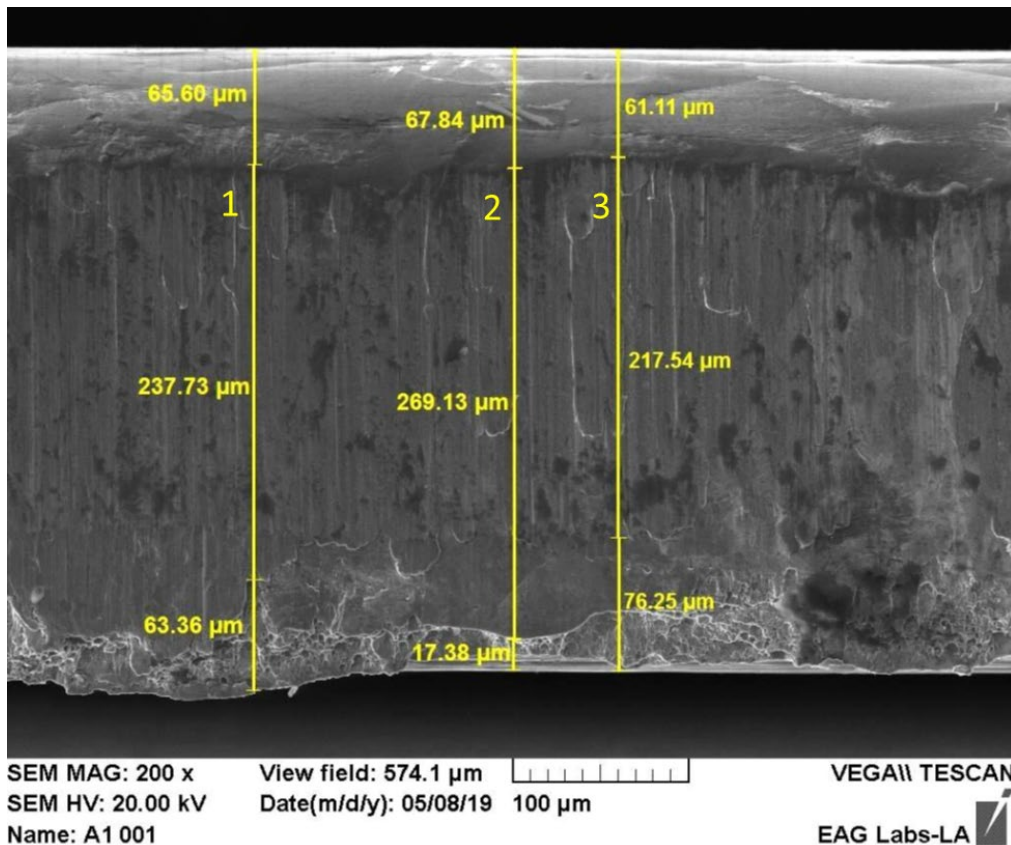


Figure I.2.6.8 SEM SEI image showing Sample A1 measurement sets 1-3 at 200X magnification.

Magnetic steel testing

GM provided Epstein and single sheet tester (SST) lamination steel samples for electromagnetic testing. The Epstein test frame is shown in Figure I.2.6.9. Testing was performed in accordance with ASTM A343, as

masses and other measurements of the specimen were made prior to testing. The key purpose of these tests is to provide a comparison of magnetic properties between materials and to compare magnetic properties between the same materials that have and have not been subjected to stress-relief annealing (SRA).

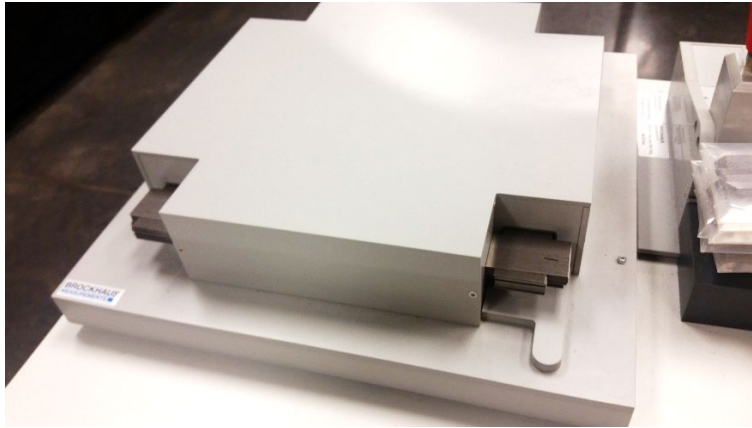


Figure I.2.6.9 Epstein test frame.

The SST (single strip tester) frame, shown in Figure I.2.6.10, offers much faster setup time and a wider testing range due to the smaller sample size and much less volume required to magnetize. The method was used for both stress-relief annealed (SRA) and not-SRA (NSRA) variants. A comparison of test results with strip quantities provides insight into the impact of residual stresses from punching action, as it is typical for residual stresses to negatively impact the magnetic characteristics of lamination steel. Furthermore, these tests provide insight into the effectiveness of the SRA process to restore magnetic properties by mitigating residual stresses.

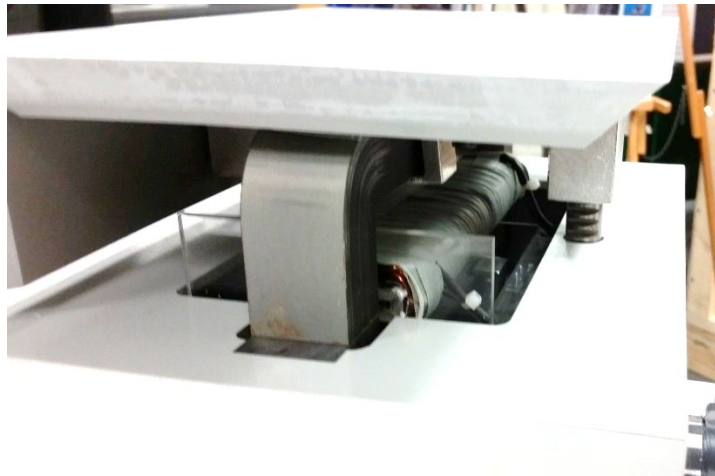


Figure I.2.6.10 SST Frame

Conclusions

GM completed the testing of the three motor variants, which all resulted in close results to the predicted power and efficiency values. Motor variants 1 and 2 show good resistance to demagnetization using HRE-free magnets, a key objective of the project. In addition, mechanical sacrifices necessary to improve power in the Variant 2 and efficiency in the Variant 3 motors were found to be acceptable from the perspective of rotor efficiency, but cost remained a challenge for these motors.

Acknowledgements

ORNL testing managed by Tim Burress, who also contributed text and images for the Oakridge National Lab testing portion of this report. Motor testing and calibration activity coordinated by Edgar Oviedo Monsivais, with calibrations performed by Cristian Lopez-Martinez, Mehdi Rexha, and Michael Rios. GM electric drive engineering, research and development, motor manufacturing, and development/validation teams contributed design, manufacturing, and testing expertise to this project. GM contract management performed by Sean Campbell.

I.2.7 Highly Integrated Wide Bandgap Power Module for Next Generation Plug-In Vehicles (General Motors)

Mohammed Khorshed Alam, Principal Investigator

General Motors
777 Joslyn Avenue
Pontiac, MI 48340
Email: mohammed.k.alam@gm.com

Steven Boyd, DOE Program Manager

U.S. Department of Energy
Email: steven.boyd@ee.doe.gov

Start Date: January 1, 2016	End Date: December 31, 2020	
Project Funding: \$1,136,690	DOE share: \$755,899	Non-DOE share: \$380,791

Project Introduction

This project aims to develop a highly integrated wide bandgap (WBG) power module and a three-phase voltage source inverter that will exceed DoE's specific targets. Developed power module will be functionally and mechanically optimized for next generation electric vehicles. This inverter will be tested to quantify efficiency at e-drive dynamometer. Operation at increased efficiencies will enable range improvements in electric vehicles.

Objectives

The goal of this project is to develop a highly integrated and optimized SiC power module that targets GM's next generation plug-in and electric vehicles. Requirements for the power module will be derived from the projected specifications of vehicles launching over the next few years. The power module will be functionally, electrically and mechanically optimized for GM's traction inverter architecture.

The resulting voltage source inverter will achieve or exceed DOE's specific targets of

- power density above 14.1 kW/kg
- power volumetric density above 13.4 kW/L
- cost below \$3.3/kW.

In addition to achieving DoE targets, the inverter shall operate more efficiently, providing increased power throughput, and increased electric vehicle range. Each design should demonstrate technical advantages over conventional Si traction inverter baseline designs in one or more of the following categories: cost, efficiency, and power density.

Approach

In order to achieve DoE targets, latest generation and most efficient SiC die was selected to develop the power module. It is critical to optimize power module layout to enable fast switching of WBG devices by lowering total power loop inductance. GM has explored improvement of the following components and features: gate drive circuitry, high bandwidth phase leg current measurement, fast and reliable over current protection, gate drive IC's with high common mode transient immunity (CMTI) - ideally greater than 100V/ns, distributed DC link capacitors with a portion of DC link capacitors integrated with the power module, low inductance gate control interface, and potential for on-die sensing.

The targeted maximum junction temperature of the power module is 200 C. To achieve this goal, GM has evaluated new technologies for bonding and joining. GM has also investigated new thermal management technologies that can further reduce overall thermal impedance of the power module and improve high temperature reliability. Efficiency of the traction drive is an important design target, and a trade-off study is being conducted to determine if it is better to set maximum temperature below 175°C to achieve larger vehicle range. Operating at high temperatures results in high conduction losses in SiC MOSFETs, reducing overall drive efficiency. Therefore, it is desired to set maximum temperature limit that will not severely affect drive efficiency.

To achieve the aggressive power density targets for the power module with high reliability requires:

- Evaluate performance of SiC die to eliminate parallel Schottky SiC die
- Use 900V and 1200V SiC MOSFET die that are being developed by our partners
- Customize die topside metallization to provide manufacturability and good thermal and electrical conductivity
- Use double side sintering and copper wirebonding
- Optimize power module layout to achieve low stray inductance
- Use high performance Si₃N₄ substrate for better thermal performance and optimize SiC die size
- Design power module with low thermal resistance
- Evaluate die characteristics at high junction temperatures (>150°C) to properly design power module protection.

SiC MOSFET's body diode can be used for commutation with other SiC MOSFET in the same phase leg, thereby reducing or eliminating the need for separate anti-parallel Schottky Barrier Diodes (SBD). GM studied the effects of SBD elimination on switching characteristics, losses, and thermal management without the anti-parallel Schottky Diodes and concluded that newly developed 900V and 1200V SiC die have body diodes that meet inverter specifications. Hence the SBD are not necessary to be used in the power module, simplifying module design, reducing cost, and saving space. Internal body diode has low reverse recovery losses and can commute fast with the SiC switch. It has higher conduction losses, but the body diode will conduct only during dead-time, increasing the overall switch losses by only few tens of watts.

GM will verify the performance of the resulting power module and fully packaged inverter prototypes using a selected set of GM production validation tests, including inverter level testing with inductive loads and active load emulators. Finally, the inverter will be tested with GM developed motors in the dynamometer to optimize e-drive operating conditions and quantify e-drive efficiency. This will ensure that both inverter and motor are operating with synergy to achieve highest possible efficiency.

Results

The GM team, its subrecipients and suppliers have developed a functional power module based on 1200 V Cree die. This design is based on the 900V rated power module developed last year. This module has been welded to polymer multilayer (PML) capacitor from Polycharge featuring high capacitance density and low stray inductance (~8 nH). A new gate driver board is designed to interface the power module and tested successfully. In order to test the inverter on e-drive dynamometer, motor characterization has been completed with an off-the-shelf SiC inverter purchased from a GM supplier.

In addition, a novel on-die temperature estimation technique has been developed and tested in collaboration with Virginia Polytechnic Institute and State University (Virginia Tech). It is important to understand impact

of high voltage and dv/dt on the motor insulation over the life of the vehicle. A project with The Ohio State University on modeling and testing impact of HV SiC inverters on motor insulation is on-going. Below is a summary of the accomplishments for each area.

1200 V SiC Power Module Design and Characterization

Power modules for automotive applications need to meet several important characteristics such as high efficiency power conversion, wide range of temperature variation, robustness to environmental and electrical stresses (i.e., humidity, vibration, electrical transient peaks, etc.), and compliance with electro-magnetic interference (EMI) standards. It also needs to meet the overall volume, mass and interface requirement to achieve required power density at inverter level. In addition, the SiC power module needs optimized packaging to achieve high switching speed while keeping the voltage stress across the devices within safe operating area and suppress excessive ringing resulting from parasitic components.

The power module build has been completed with an emphasis on making new samples with 1200V SiC die that have an improved metallization stack-up. The improved metallization stack-up is necessary to ensure sinterability of the 1200V SiC die to the direct bonded aluminum (DBA) substrates. Copper wirebonds are placed on top of the die to connect them to aluminum substrates. In order to improve switching performance and achieving strong decoupling between the control and power loops, a flexible PCB circuit is soldered perpendicular to the power loop. Finally, wire-bonds are used for connecting gate and source pads of the die to the flex PCB. This approach helps easy integration of the PCB flex into the power module and can be used to control, protect and characterize the SiC MOSFETs. Figure I.2.7.1 shows an open frame photograph of the developed power module.



Figure I.2.7.1 Open frame 1200V SiC power module

Complete static characterization of the power module was performed in the GM lab at different junction temperatures. Figure I.2.7.2 shows typical I-V characteristic and on-state switch resistance (R_{ds_ON}) at different gate voltages. Device output characteristic becomes more linear with increase in gate voltage and switch on-state resistance decreases accordingly. Switch resistance increased around 65% from 2.92 m Ω with temperature increase from 25 C to 150 C. Thermal resistance of the power modules was measured with body diode characteristics with zero or negative gate bias voltages ($V_{gs}=0V$, $V_{gs}=-5V$ and $V_{gs}=-8V$). This method

increases accuracy of the measurement due to higher voltage drop across drain and source. Average thermal impedance of the power module was 0.15 C/W.

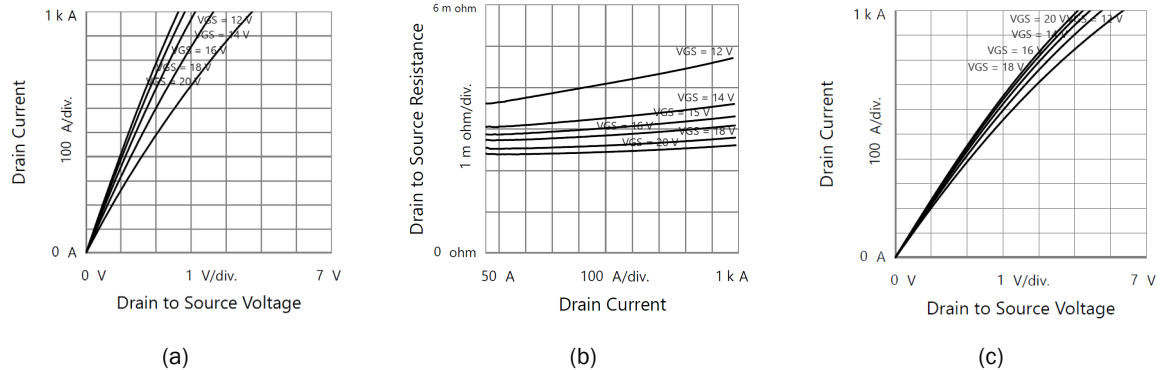


Figure I.2.7.2 (a) (b) Output characteristics and on-state resistance of the power module at 25 °C, (c) output characteristics of the power module at 150 °C

Shipment of the PML capacitors was delayed due to COVID-19. This delayed power module dynamic characterization, inverter build and dynamometer testing. Two capacitors were received and welded successfully to the power module for inverter build. The new gate driver board was fully characterized at different temperatures before integrating to the power stage and tuned for high voltage dynamometer testing. The gate bias supply is designed to provide a very reliable gate voltage (+/-150mV) across all temperatures from -40 to 150°C. This tight voltage regulation enables implementation of precise gate bias voltages, improving performance and efficiency. A new motor was procured and characterized for high voltage dynamometer test. This motor will be used for efficiency and performance characterization of the inverter.

Online Junction Temperature Estimation

A junction temperature estimation algorithm was developed with Virginia Tech. The developed method was verified using Cree 1200 V SiC power module (CAS300M12BM2). Current through the power module switch was measured during on-state along with the drain to source voltage measurement using the gate driver interface. By adjusting the time delay between two signals, it is possible to measure on-state resistance. The SiC power module's on-state resistance is a thermally sensitive electrical parameter (TSEP) and it was used for developing the algorithm to predict the junction temperature of the device.

The power module was characterized at different temperatures for every 5 C interval. Figure I.2.7.3 (a) shows device on-state resistance versus temperature for both first and third quadrant operation as a function of current. The first quadrant operation shows a quadratic behavior. Device resistance varies as a function of temperature more widely at higher current. At very low currents close to 0 A, the measurements are not very accurate as the device voltage drop is very low. Figure I.2.7.3 (b) shows more details of the third quadrant behavior of the power module. It is necessary to understand external diode's knee characteristic with change of temperature. The first zone is where the MOSFET is still the dominant conductor. The second zone is where the external diode is the dominant conductor. The 3rd and 4th regions fall below and above the diode knee characteristic, respectively, with the MOSFET and the external diode are both dominant conductors, respectively. An advanced algorithm was developed to determine device junction temperature based on this device on-state resistance measurement and tested on the bench with approximately 96% or higher accuracy.

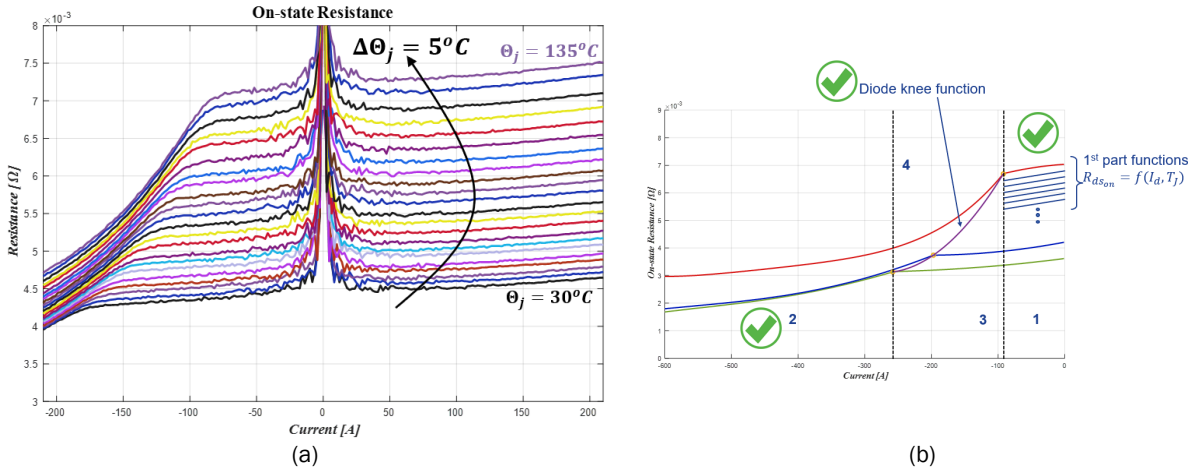


Figure I.2.7.3 (a) (b) Curve tracer characterization results for on-state resistance at different temperatures (C) detailed characterization of third quadrant operation

Electric Drive System Level Characterization with High Voltage Motor and SiC Inverter

GM has collaborated with The Ohio State University to understand the impact of high voltage and high dv/dt on the motor insulation. ANSYS Maxwell was used for constructing and simulating a 2D finite element model of the motor stator. Square wave voltage waveform was produced by the SiC inverter and characterized to use in the simulation. Two solvers were used in the simulation process: the electrostatic solver and the magnetic transient solver. Simulation results were analyzed and compared with the test data by measuring waveforms at the motor terminal. Parameters in the 2D FEA model were adjusted, and additional assembly components were incorporated to improve the simulation model. Figure I.2.7.4 (a) and (b) show the test setup and measured waveforms over one fundamental electrical frequency. Test results showed close correlation with the measured waveforms.

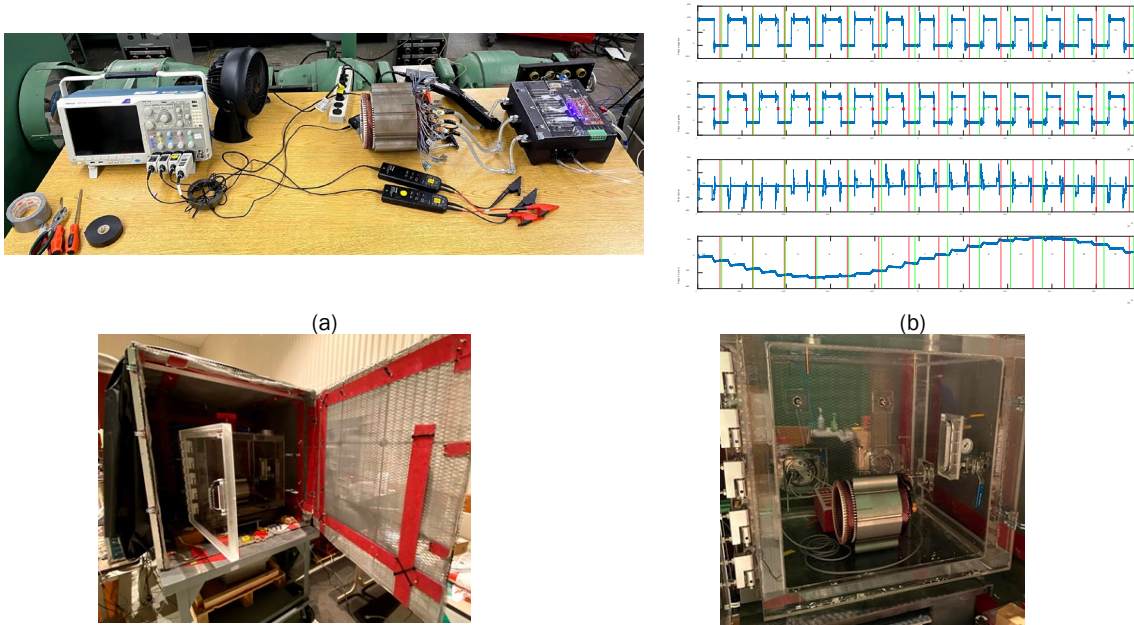


Figure I.2.7.4 (a) Test setup to measure voltage waveform at the motor terminals along with SiC inverter, (b) waveforms measured at the motor terminals, (c) partial discharge-measuring pressure chamber inside Faraday cage (left); stator assembly inside pressure chamber (right).

Partial discharge inception voltage (PDIV) was measured under different operating conditions to understand the effect of three different variables: air pressure, winding temperature, and insulation thickness on the hairpin weld points. General procedure in PDIV testing includes increasing the applied voltage between each phase lead of the stator windings and the stator core until significant high-frequency noise (an indicator of partial discharge events) is received by monitoring equipment. The measurement devices and the test sample contained within a Faraday cage which prevents external noise interrupting PDIV measurements. A high frequency current transformer (HFCT) was used for measuring the applied voltage, and an ultra-high frequency antenna was utilized to detect PD emissions. A barometer, humidity sensor and thermometer were used in every test to monitor ambient conditions inside the test chamber. Figure I.2.7.4 (c) shows the pressure chamber contained within the Faraday cage, and the bar-wound stator inside the pressure chamber.

The air pressure inside the test chamber was set to sea level (760 Torr) in one test case, and 8000 feet (580 Torr) in another. 8000 feet of elevation corresponds to a 25% reduction in air pressure. For the winding temperature tests, PDIV was first measured at room temperature (25 C), and then the stator assembly was heated to 80 C for the other test case. A final test will be performed to evaluate the impact of additional insulating varnish on the hairpin weld points in the stator windings after the planned PDIV tests are completed.

Conclusions

This project is in phase three and planned to be completed by the end of 2020. Power module development with 1200 V SiC die is complete and fully characterized. The module is welded to the capacitor and successfully tested with the developed gate driver board. In addition, motor characterization, software development and calibration are completed for dynamometer testing. The next step is testing the inverter at dynamometer to quantify both inverter and complete e-drive efficiency.

Key Publications

1. G. Watt et al., “Design of a Compact, Low Inductance 1200 V, 6.5 mΩ SiC Half-Bridge Power Module with Flexible PCB Gate Loop Connection,” 2019 IEEE Applied Power Electronics Conference and Exposition (APEC), Anaheim, CA, USA, 2019, pp. 2786-2793.
2. Mocevic et al., “Phase Current Reconstruction based on Rogowski Coils Integrated on Gate Driver of SiC MOSFET Half-Bridge Module for Continuous and Discontinuous PWM Inverter Applications,” 2019 IEEE Applied Power Electronics Conference and Exposition (APEC), Anaheim, CA, USA, 2019, pp. 1029-1036.
3. G. Watt, S. Mocevic, R. Burgos, A. Romero, M. Jaksic, and M. Teimor, “Current Sharing Behavior and Characterization of a 1200 V, 6.5 mΩ SiC Half-Bridge Power Module with Flexible PCB Gate Loop Connection”, ECCE 2019, Baltimore, MD.
4. M. Jaksic et al., “Novel SiC Power Module for Traction Power Inverters with Low Parasitic Inductances”, ECCE 2019, Baltimore, MD
5. M. Jaksic, M. Teimorzadeh, “High Density WBG Traction Inverter for Automotive Applications”, presentation at PowerAmerica special session at ECCE 2019, Baltimore, MD.
6. Invention “Low Inductance Package for Traction Power Modules” (P045682), was reviewed internally in GM and decided to proceed with filing.
7. Invention “High frequency dc bulk capacitor design with interleaved busbar structure” (P044918), was reviewed internally in GM and decided to proceed with filing.

I.2.8 Mapping the North American Rare Earth Magnets Supply Chain: Assessment of Suppliers, Technology Developments and Gaps. (Synthesis Partners, LLC)

Christopher L. Whaling, Principal Investigator

Synthesis Partners, LLC
11250 Roger Bacon Drive, Suite 2
Reston, VA 20190
Email: cwhaling@synthesispartners.com

Steven Boyd, DOE Program Manager

U.S. Department of Energy
Email: Steven.Boyd@ee.doe.gov

Start Date: October 1, 2019

End Date: September 30, 2020

Project Funding: \$219,958

DOE share: \$219,958

Non-DOE share: \$0

Project Introduction

This project covers original research on the North American (NA) supply chain for rare earths (RE) and RE permanent magnets employed in traction drive motors. This work addresses the need for an up-to-date, independent assessment of the NA RE mine-to-magnet supply chain including key players, revenue rankings, technology developments, business model issues and VTO-relevant gaps. The gap intelligence is based on 100s of customized primary source inputs, extensive market data and a supply chain database that includes 193 RE mine-to-magnet organizations with information on their collaborations, technologies, suppliers, supplier and business relationships. The collection cut-off date was July 31, 2020. More information is available in a forthcoming public report provided by Synthesis Partners, LLC (SP).

Objectives

The objective of this work is to provide EERE with quantitative and qualitative information on markets, trends and technologies relevant to the mission of increasing technology options for energy affordability, efficiency and resiliency with regard to EV manufacturing in NA. This work identified and characterized NA RE mine-to-magnet R&D gaps and capabilities in the supply chain that can impede or accelerate the transition of R&D into NA supply chain entities. By collecting, analyzing and reporting on vetted, multi-sourced data regarding the NA RE mine-to-magnet supply chain, this project provides EERE with actionable intelligence relevant to R&D and technology transition planning.

Approach

This research is based on a 2019-2020 assessment of thousands of secondary sources alongside hundreds of anonymized, primary industry sources that exchanged information with SP directly. Quantitative data on the supply chain, including gaps, is ordered, ranked and analyzed according to a RE mine-to-magnet domain model developed by SP. Qualitative information is assessed through multi-source vetting, which includes running insights by several sources, quantitative information filters and secondary source confirmation. Each primary source is hereby acknowledged by SP and thanked for their time and contributions to this effort. All errors and omissions remain the sole responsibility of SP.

Results

SP identified 193 companies and organization as active in the NA RE mine-to-magnet supply chain. These companies are characterized in an internal database according to the products or services they provide, their size (by revenue and employees), their JV and partnership relationships, their business model type and links to technical product specification information. The following provides an overview of selected public findings.

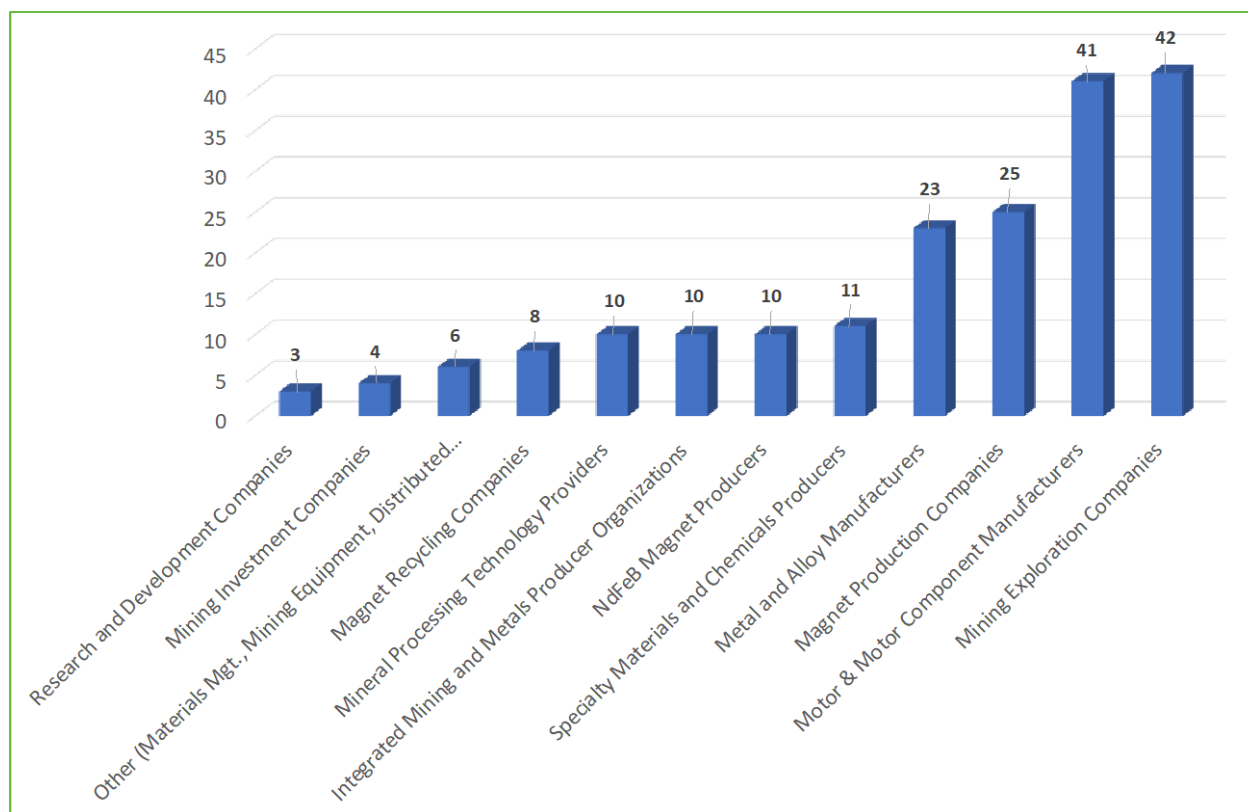


Figure I.2.8.1 NA RE Mine-to-Magnet Supply Chain Overview

The following key points are drawn from the NA RE mine-to-magnet database and SP's analysis of the relevant, associated primary and secondary source data (collection cut-off date: July 31st, 2020).

- SP identified 23 beyond- or outside-of-China RE exploration and mining development activities that are relevant to the NA supply chain. Each of these 23 projects is assessed in detail (in terms of its' geographic location, public-source investor relationships, types of RE elements that can be mined and produced, and status as of August 2020) in an upcoming public report.
- Of the 23 RE mining and exploration entities identified, which are all seeking to develop the building blocks for a beyond-China RE mine-to-magnet supply chain that can serve NA EV needs, nineteen (19) are cumulatively seeking approximately \$3.6 billion in CAPEX investment funding as of July 2020.
- Of the 23 RE mining and exploration entities identified, four (4) have secured approximately \$1.7 billion in CAPEX investment as of July 2020.
- By way of comparison, more than ten-times (10x) the CAPEX that is estimated to be needed for nineteen (19) beyond-China RE mining and exploration entities seeking funding is spent by Amazon on R&D in one year; and more than 4x is spent by VW on R&D in one year; and more than 2x is spent by Toyota on R&D in one year.
- Even if the above SP RE project investment estimates are doubled or tripled, the total investment required to transform the NA RE mine-to-magnet supply chain does not appear large when compared to the size of automotive OEM investments in R&D. In short, relatively modest global investments can transform the NA RE mine-to-magnet supply chain.

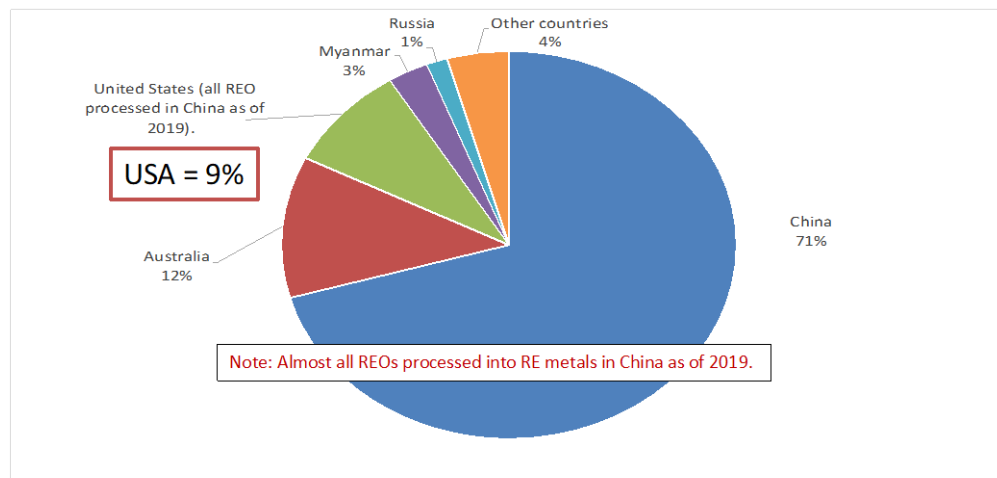
- Links between NA automotive EV magnet buyers and RE metal producers are increasingly important. However, the following categories of entities within the NA RE supply chain are found to have relatively few links to the automotive sector: namely – Magnet recycling organizations; Mining investment organizations; Mineral processing technology organizations; and Other (Materials Mgt; Mining Equipment; Distributed Energy Services).
- RE magnets for all applications (not just EVs) account for the largest share of total RE metals demand. RE magnets are projected to account for 28% of RE metals demand in 2021. EVs take up the majority of that RE magnet demand, and are increasing their share, underscoring the importance of automotive OEM and RE magnet manufacturer supply chain relationships.
- Magnet recycling is increasingly important in general and end-of-life-permanent magnet recycling is a growing sector every year. However, this project identified only eight (8) organizations whose primary mission is magnet recycling in the NA mine-to-magnet supply chain. This is a sector that deserves attention because it is expected to grow significantly in the near future.
- To-date, almost all RE ores are refined into RE metals in China, and this bottleneck is one that is larger than R&D and requires strategic long-term policy to redress. Many of the 193 entities in the NA RE mine-to-magnet supply chain can be part of plans to effectively counterbalance monopoly pricing in the RE PM supply chain.
- To develop RE processing and refining outside of China to serve the NA EV market will require a new level of networking, collaboration and commitment across the supply chain with automotive EV customers. Economically-viable NA-based, RE element processing and PM production can be accelerated by higher level OEM engagement.

Market Projections Regarding RE Elements Employed in Traction Drive Motors

A key finding from SP's review of the market research is that the main question is less about who is mining what REs where, and more about who understands how to support a fully integrated RE mine-to-magnet supply chain in order to establish a NA RE mine-to-magnet supply chain with long-term viability.

China is the only country that has a fully integrated, scaled RE mine to RE PM motor supply chain. Further, China has deployed billions of dollars down the value chain to enable China's "Made in China" 2025 EV strategy and this investment will impact availability of rare earth oxide and metal supplies going forward. In this context we provide just two charts with associated key findings here. Additional market data will be available in the public report.

Distribution of Rare Earth Element Production: 2018.



Synthesis Partners, LLC ©

Figure I.2.8.2 Distribution of Rare Earth Element Production, by Country: 2018
Source: Synthesis Partners, LLC. Data is from US Geological Survey (November 2019).

SP reviewed 15 market research demand forecasts for RE metals and oxides covering the period 2020 through 2030. The market research reports are grouped as follow:

- Three (3) market research reports with REE demand projections through 2024;
- Six (6) with REE demand projections through 2025;
- Nine (9) with REE demand projections through 2026; and
- Two (2) with REE demand projections beyond 2026.

Across these 15 market research reports, the average projected compound annual growth rate (CAGR) in global RE metal and oxide demand (in tonnes) is 8.4%, from 2024 to 2030. This represents the middle view of a wide selection of data on the global REE market. The forecasts range from a low of 6% to a high of 10.8% CAGR in REE demand growth. Based on the middle view, SP has high confidence in relatively strong growth in REE demand from 2020 through 2030. Also, the impacts of COVID-19 are not expected to be extreme by these market research reports (on average) in REE markets. This is due in part to the strong underlying trend around the world toward electrification across all levels and types of transportation, mobility and logistics.

China dominates the production of both RE oxides and RE metals. China controls not just the mining of RE ores but also the production of magnets from these ores. The expanding number of options for mining of RE ores outside of China provides strong evidence that the level of Chinese dominance *in mining* will fade over time. The key issue that remains for US policymakers is how RE *oxide processing* and RE *metal production*, and subsequently, RE PM *R&D and innovation*, can be returned to NA as a core capability that enables next-generation EV motors. Break-through RE magnet metallurgical developments, RE metal processing innovation and related technology, craft and IP developments in magnet systems benefits from a full spectrum understanding of how RE ores are transformed into magnets. The fact that this knowledge is still dominated by China is the crux of the challenge facing a revival of the NA RE supply chain for traction drive motor magnets.

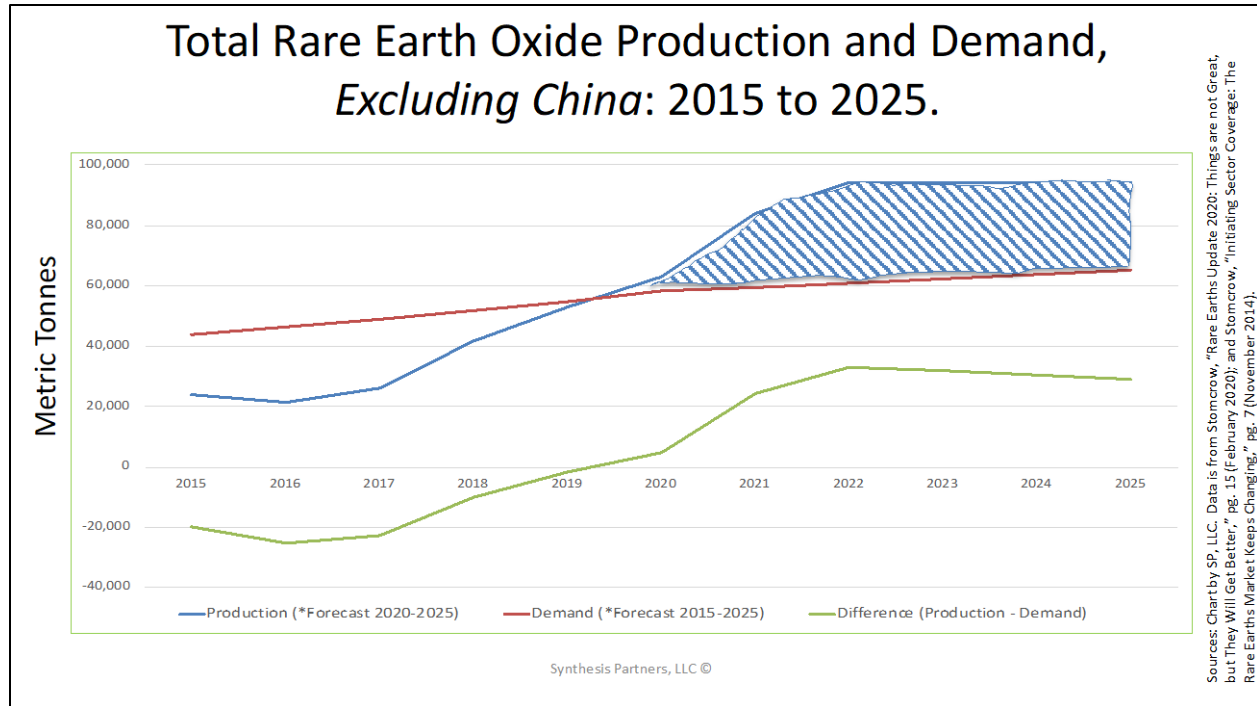


Figure I.2.8.3 Total Rare Earth Oxide Production and Demand (incl. Nd & Pr), Excluding China

Source: Synthesis Partners, LLC (August 2020).

Within the context of the increased decoupling of global supply chains from China, SP further assesses that market projections should take the following (esp. post-COVID-19) findings into account:

1. RE ores, concentrates and oxides produced by China will be less reactive to world demand going forward (due to increased domestic use of and control of REs within China), and therefore potentially less accessible at globally competitive prices, which will impact the costs of OEM EV magnet technology choices downstream.
2. The time-frame for building alternatives to Chinese sources for RE magnets is shrinking fast with COVID-19 accelerating the supply chain decoupling process and changes happening both within and outside China. It has been reduced from a decade (pre-COVID-19) to a few years in SP's estimate.
3. As China moves to use more domestic materials for domestic needs, there is also evidence that China is seeking more RE concentrates outside of China. Assuming past is prologue and China seeks large strategic purchases of such RE concentrates it is expected that control of key RE concentrates and oxides produced outside China will be an area of competition and potential trade leverage (in that countries with the RE supplies will seek to attract investors with long-term beneficial trade agreement policies).
4. Increased awareness of the level of environmental damage that has occurred inside China from the past decades' nearly unconstrained rate of RE ore mining and metal production is leading to two significant realizations: 1) Recognition that a beyond-China based RE mining and processing industry will be developed with a dramatically more environmentally sound approach in NA and elsewhere, and; 2) Recognition that such a different approach can cause a shift in the core economics of RE metals production that can impact OEM buyers globally. In other words, the upcoming fundamental shift in the manner of sourcing RE metals is a strategic development that is both necessary for national security, the environment and a likely driver of significant new costs for RE metals globally. All

(legal) beyond-China RE sources are expected to cost more because they will be required to manage life-cycle environmental management issues in the mining, processing and metal production stages in a way that has not been the case to-date (with a few rare exceptions).

- It takes years to build the craft-based RE mining, processing and magnet metal manufacturing capabilities that are needed for an electrified world, and therefore decisions to re-energize the NA RE mine-to-magnet technology supply chains need to be comprehensive (i.e., focusing on R&D as well as stockpiles, re-shoring and alternative material-science approaches), need to take place rapidly and yet also carry the expectation they will take years to achieve measurable results.

As the Chart above shows, beyond-China production of RE oxides needed for traction drive motors, Nd and Pr metals specifically, is not expected to be in shortage in the near-term. This underscores the point made above that RE oxides are not the main issue. The RE oxides needed outside of China can be produced outside of China. The Chart above and the twenty-three (23) RE mining and exploration entities that this study identified provide cumulative evidence of this fact. However, the costly, highly regulated and environmentally challenging process of refining these oxides into RE metals is still a major challenge outside of China. It is this specific area that needs attention for any future NA RE mine-to-magnet supply chain to achieve global competitiveness in terms of cost of production, sustainable growth to match rapidly increasing electric motor demand, and predictable regulatory frameworks.

Selected Findings Regarding Ten-Year Forward-Looking Gap Analysis and Potential R&D Topics

SP executed 100s of primary source contacts during the January through July 2020 time-period to produce 41 in-depth interviews with SMEs regarding NA RE supply chain gaps. Each gap statement is complemented by secondary source information. The following data provides summary results of the quantitative assessment by SP of the gap statements. All interviews were open-ended, sources were encouraged to provide their perspectives from the context within which they operate and were not asked to agree or disagree with narrowly framed survey questions. The interview information is therefore qualitative, is designed to “get behind” the data and trends, and is not designed to report purely statistical, randomized-survey results.

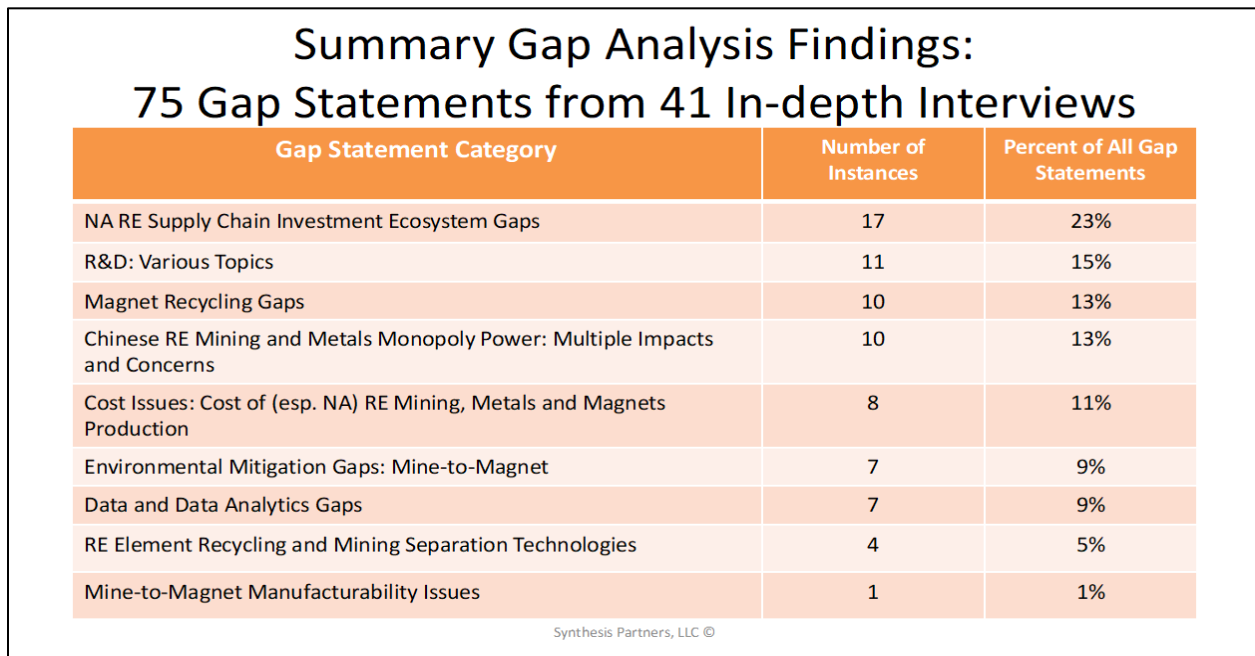


Figure I.2.8.4 Priority Gap Areas, by Frequency of Gap Statements
 Source: Synthesis Partners, LLC NA RE Mine-to-Magnet Supply Chain Database (August 2020).

The top five categories of sources accessed for the gap analysis, by source's organizational type, are:

- RE Explorers: Acquire, develop and explore RE mining properties (21% of interviews);
- Other (RE Associations, Consultancies, Market Research Companies, SMEs) (20% of interviews);
- RE Processing Technology Organizations (15% of interviews);
- Motor Manufacturers and Motor RDT&E (12% of interviews);
- Specialty Metals and Alloy Manufacturers (7% of interviews).

The Chart above shows that the largest short-term (within 5-year time horizon) gap identified is the complex set of constraints that have limited investment flow into NA RE mining, exploring, processing and metal production. According to this finding, the main issue in NA RE supply chain development is a non-optimized, investment ecosystem. This has many facets, however, sources with this viewpoint are in general agreement that China's monopoly control of the RE mining, processing and metal production has constrained investments in NA and elsewhere (because it is difficult to attract investment if the global price of REs and RE metals can be manipulated by one player at any time). The key finding is that most issues or gaps can be resolved with proper investment flowing into NA RE mining and processing activities.

The next set of short-term gaps are specific R&D topics raised by sources, and each one represents a productive area for drill-down inquiry. They include:

1. Cooling of copper rotors and windings.
2. Improved manufacturing technologies for better efficiency and effectiveness using near net-shape production technologies, including using powder-metallurgy, sintering and backward extrusion. This, as well as 3D printing or additive manufacturing, is a potential pathway to achieving 2-3x higher power density in traction drive motors.
3. Corrosion protection for Ce-based magnet phases.
4. Research and development of applied soft magnet powder composites (SMC) plus laminations, e.g., SMC powder parts in traction drive motors to allow for the reduction of rare earths and combining SMC with laminations to achieve required cost and coercivity targets.
5. RE recycling and mining separation technologies and the training of engineers in these areas. Magnet and RE element recycling are significant issues in the evolving supply chain. For example, end-of-life-permanent magnet recycling is growing every year though this project has also found that monopoly control of magnet waste-streams is an increasing issue, esp. in Europe. It is reportedly difficult to get access to sufficient numbers of magnets to scale recycling at cost-competitive rates according to several sources. That fact and the issue that only eight (8) organizations have as their primary mission magnet recycling in the NA mine-to-magnet supply chain suggests that this is a sector that deserves particular attention.

Lastly, the following are a few examples of the longer-term (approximately 10-year time-horizon) R&D gaps discovered through the gap analysis research. These are examples of long-term bets uncovered through both primary source and secondary literature reviews. The near-term work is considered the first priority to catalyze the NA RE mining-to-magnet supply chain; the longer-term work shows pathways to accelerate and expand on shorter-term R&D action and benchmarks.

1. Relocatable, Containerized RE Mining, Refining and Transport Logistics: To include using container-based mining and processing technologies, which can be shipped via low-cost air (e.g., airships), rail

or marine, to enable low-cost, environmentally transformative, resilient mine-to-metal mining, processing and shipping of materials. This is especially relevant in austere, undeveloped regions and permafrost-Arctic regions where traditional road construction is both expensive, unrealistic and environmentally challenging.

2. Clean Water Risk Mitigation near to RE Mining: Pathways, including using more recycling, processing of existing mining tailings (already mined and above ground) and better approaches to mining to establish new baselines for sustainable RE mining-to-magnet supply chains are called for. Environmental mitigation and environmental planning represent a significant, underlying gap area highlighting the need for new approaches and larger investments to reduce environmental risks in RE mining, from mine-to-magnets.
3. Lifecycle Materials Management: Technology and business model development to support “blue check” RE mineral governance systems, to include R&D to enable tracing of the source of all RE magnets to approved mine and metal processing sites.
4. Deep Sea RE Mining: Japanese researchers have found that deep sea ocean mud in the eastern-southern and central-northern Pacific Ocean contains significant amounts of HREEs and Yttrium (Y) and the grade of HREEs. In some fields the concentration is reportedly higher than that found in the southern ion-absorbed clay deposits in China, suggesting this is an area for consideration.

Conclusion

This project’s FY20 research on the current state and gaps in the NA RE mine-to-magnet supply chain provides the basis for the selected conclusions and recommendations raised above. Additional findings and data will be incorporated in the upcoming public report.

Key Publications

Most recent publications or presentations based on EERE sponsored work:

1. Synthesis Partners, LLC, North American (NA) Light Duty Electric Vehicle (LDEV) Supplier Equipment Market and Supply Chain Gap Intelligence, April 2020.
2. Synthesis Partners, LLC, Traction Drive RE Magnet NA Supply Chain Assessment: Trends, Gaps and Anticipated Strategic Moves of Interest to VTO R&D Planners, Presentation by C. Whaling on June 2, 2020 to VTO Annual Merit Review (AMR) meeting.

References

This research is built on an extensive list of prior written studies and work. A selected list of approximately 500 bookmarks, grouped by content category, will be made available at <https://sp-supplychainresearch.com/>. For further information please contact the PI, Christopher Whaling at cwhaling@synthesispartners.com. Thank you.

Acknowledgements

Special thanks to Mr. Steven Boyd, Program Manager, Batteries and Electrification for his technical guidance and management, and to Mr. Nicholas Damico, Contracting Officer at the National Energy Technology Laboratory (NETL) for his ongoing oversight of this effort. SP acknowledges the entire EERE-VTO team for their active interest and support of this work. SP team members are: Ryan Bunch, Research Analyst; Richard Holcomb, Managing Partner; Steve Johnson, Senior Researcher; and Michael Willis, Senior Policy Analyst.

I.2.9 Wound Field Synchronous Machine System Integration towards 8x Power Density and Commercialization (Magna Services of America, Inc.)

Lakshmi Varaha Iyer, Principal Investigator

Magna Services of America, Inc.
750 Tower Drive
Troy, MI 48098
Email: LakshmiVaraha.Iyer@Magna.com

Susan Rogers, DOE Technology Development Manager

U.S. Department of Energy
Email: susan.rogers@ee.doe.gov

Start Date: October 1, 2019	End Date: December 31, 2022	
Project Funding: \$875,000	DOE share: \$700,000	Non-DOE share: \$175,000

Project Introduction

In support of VTO's Electric Drive R&D activity, the Electric Drive Technologies (EDT) Consortium, a multi-disciplinary team of national labs and universities, coordinates and conducts a portfolio of research to advance the state-of-the-art in electric drive technologies. The Consortium has established the following strategic goal listed in the table below:

EDT Research Consortium Strategic Goal (compared to 2015 baseline)

A 125kW electric traction drive system:

- 8X power density improvement, or 1/10 the volume (33 kW/L)
- ½ the cost (\$6/kW)
- 2X useful life (300,000 miles)
- 1000 kW/L inverter and a <20,000 rpm, 50kW/L electric motor.

Objective

The objective is to demonstrate a 125kW Wound Field Synchronous Machine (WFSM) with 8X power density improvement and cost below \$3.3/kW.

Approach

The approach includes the development of Wound Field Synchronous Machine (WFSM) and Capacitive Power Coupling (CPC) technology. The project is divided into three phases outlined below. This report presents tasks pursued and results obtained in one part of Phase 1.

- Phase 1 – Simulation to determine feasibility of achieving goal and concept design
- Phase 2 – Design and build of prototype motors for test/evaluation
- Phase 3 – Test and evaluation of motor relative to project goals.

Phase 1 includes tasks such as:

- Investigation of novel stator and rotor cooling systems
- Comparative analysis of cooling systems

- Development of magneto-structural WFSM design optimization tools
- Initial high-power density WFSM electromagnetic and structural design
- Design of the MHz frequency wireless power transfer inverter
- Design of the rotating rectifier board with integrated coupling structure.

This project aims to focus on five areas to achieve the 8X power density improvement objective:

1. Magneto-structural Optimization - The use of high yield strength electrical steel in the rotor will be investigated to increase the base and maximum speeds of the WFSM. Optimization will include:
 - Structural finite element analysis tool, integrated into the WFSM magnetic and thermal design optimization suite
 - Multi-material magneto-structural topological optimization
2. High Slot Fill Windings - High slot fill windings constructed from either rectangular cross-section conductors or die compressed coil technology allows for increased ampere turn loadings and reduced Ohmic loss through the almost doubling of the slot fill compared to traditional random mush windings. For the stator windings increased slot fill random mush windings, bar/hairpin windings, and die compressed fractional slot concentrated windings will be investigated both from an electromagnetic design and manufacturing perspective. For the rotor field winding wound rectangular or wound on corner rectangular conductors along with die compressed windings will be investigated. Specific manufacturing issues that will be considered include minimizing the number of coil end junctions/brazing points.
3. Reinforced Rotor End Turns - With increased rotor speeds, the end turns of the field winding are subject to substantial centripetal forces. Low-cost structural bracing techniques need to be developed. Techniques that will be investigated but are not limited to non-magnetic steel retention rings, loaded plastic over-molds, and low-cost banding.
4. Excitation System Refinement - Increasing the wireless power transfer frequency to excite the rotor from 2 MHz to > 3 and ≤ 6.7 MHz, minimizing the printed circuit board (PCB) capacitive power coupler's (CPC's) mechanical footprint while bringing the frequency into compliance with the established industrial scientific and medical (ISM) bands. The frequency increase will be achieved by enhancing the GaN inverter layout. Minimizing parasitic capacitances and inductances are the primary concern at these frequencies (for soft switching) and ensuring compatibility with the DC bus of the traction drive. Signal injection in the kHz range to the rotor will be utilized for resolver functionality, combining the exciter and resolver functionality into a single component.
5. Integrated Stator and Rotor Cooling – Stator and rotor cooling is required to increase current density on the rotor: Various cooling techniques involving spray, jets, direct cooling, two-phase, pulsating and rotating heat pipes technologies will be investigated. Various fluid flow and rotary seal technologies will be investigated.

Results

The following tasks were pursued:

1. Magneto-structural Optimization
 - Established motor structural design targets and input, output and performance specifications

- WFSM design tool for large scale evolutionary optimization to determine Pareto fronts was used. Conducted multi-objective optimization to maximize the electromagnetic torque and minimize the machine losses subject to constraints.
- The model variables include stator and rotor slot fills; variable and fixed current densities, current density levels, stator and rotor ohmic and core losses; fixed and incremental constraints, slot/pole combinations, etc.
- Various stator and rotor core materials were also investigated.
- The number of designs evaluated during optimization runs up to >50,000 designs. Example representative designs are provided in Figure I.2.9.1. Figure I.2.9.2 shows a representative pareto map generated as a result of analyzing various WFSM machine designs against the specified power rating targets.

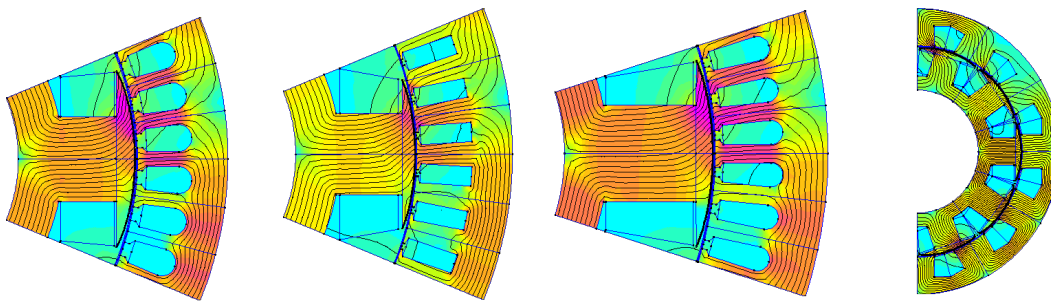


Figure I.2.9.1 Sample representative WFSM designs from large-scale optimization study

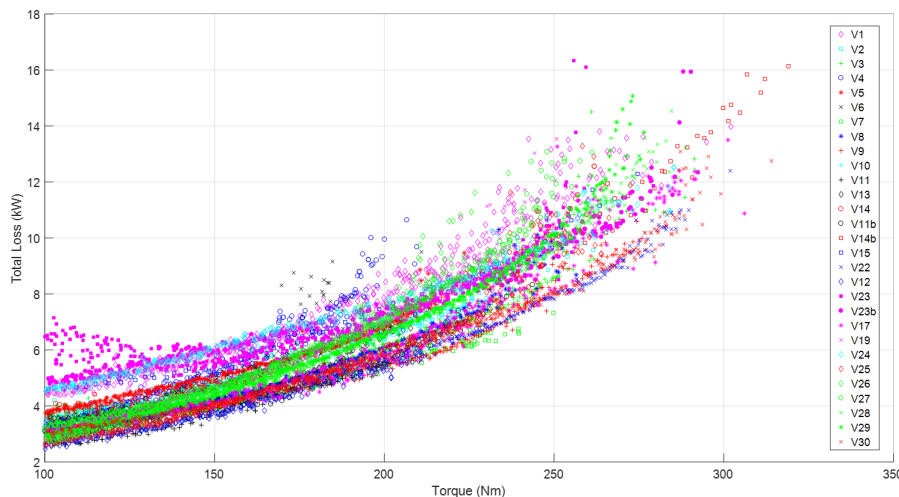


Figure I.2.9.2 Summary of optimization pareto fronts

1. High Slot Fill Windings - High slot fill windings enables increased ampere turn loadings and reduced Ohmic losses.
 - For the stator windings increased slot fill random mush windings, bar/hairpin windings, and die compressed fractional slot concentrated windings were investigated from an electromagnetic design perspective.
 - For the rotor field winding, wound rectangular or wound on corner rectangular conductors along with die compressed windings were also investigated from an electromagnetic design perspective.

- Examined many distributed/fractional slot concentrated winding slot pole configurations and winding technologies including ~15 stator and rotor geometric variables.

2. Excitation System Refinement –

- Influence of the wireless power transfer frequency on the dimensions and power rating of the of the capacitive power transfer system was studied. Rotor electronics architecture was defined. The capacitive power coupler is designed to output 2.5kW power. Simulated efficiency is more than 90%. Capacitive power coupling PCB's were designed against the WFSM shaft dimensions. Figure I.2.9.3 show a representative picture of PCBs arranged on the shaft of the motor.
- Single phase GaN inverter with high power density and efficiency was designed and fabricated to excite the coupler system. Initial rendering of the rotor electronics board to excite the capacitive coupler is shown in Figure I.2.9.4. The prototype has a 4" x 6" footprint and used GaN FETs. The GaN FETs are switched at 6.78MHz.
- Minimizing parasitic capacitances and inductances were the primary concern at very high frequencies (for soft switching) and ensuring compatibility with the DC bus of the traction drive.

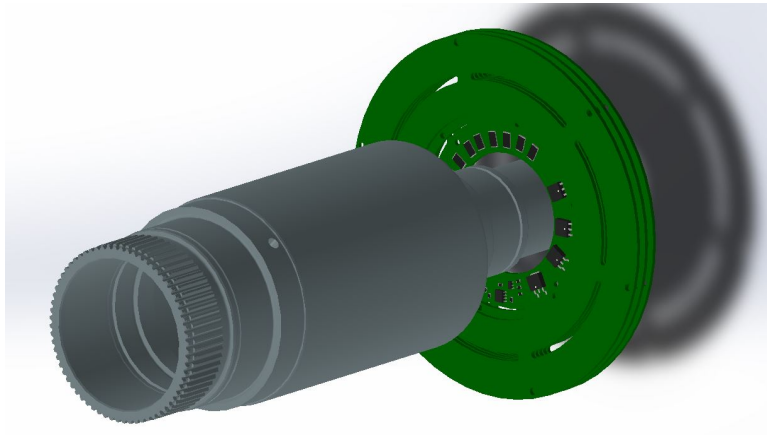


Figure I.2.9.3 Capacitive power coupling stack on WFSM Shaft

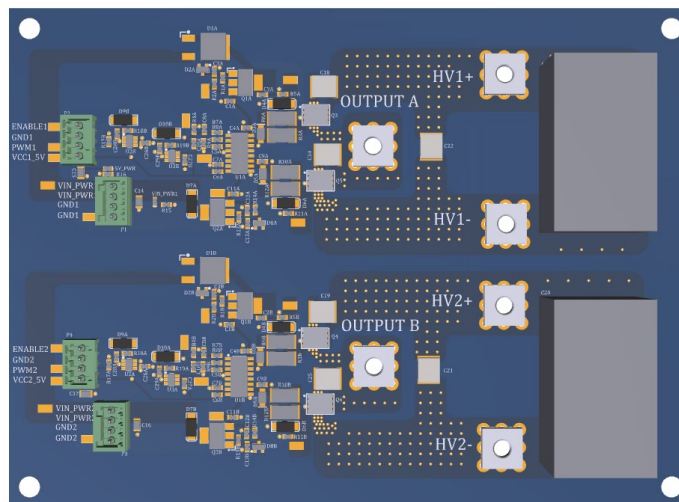


Figure I.2.9.4 Initial rendering of 6.78 MHz Rotor Inverter

3. Stator and Rotor Cooling –

- Various motor package dimensions; coolant types; inputs for flow rate, coolant temperature and pressure drop, etc. were established for both stator and rotor cooling
- Geometry and meshing for CFD analysis were setup for baseline case and flow path, temperatures and velocities were verified.
- Various stator jackets designs were analyzed using CFD software. Flow rate was varied between 4 and 12L/min, coolant inlet temperatures were varied between 45 and 85 deg C. Designs were compared based on heat transfer capability, pressure drop and temperatures throughout the axial length of the jacket. Sample jacket design is provided in Figure I.2.9.5 and sample results obtained from analysis is provided in Figure I.2.9.6. The objective is to find an optimal design with respect to pressure drop, temperature symmetry and heat transfer capability while maintaining cost targets.
- Multiple integrated stator and rotor cooling system architectures were investigated including a variation of different inputs and design parameters such as jacket type, flow channels, coolant type, spray type, inlet temperature, flow rate, etc.
- Few architectures are chosen for further thermal design optimization along with electromagnetic design optimization.

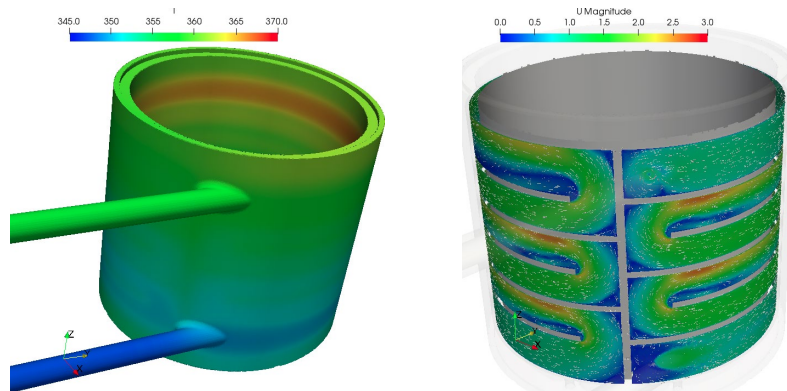


Figure I.2.9.5 Temperature and velocity analyzed on a sample design of the stator jacket for the WFSM.

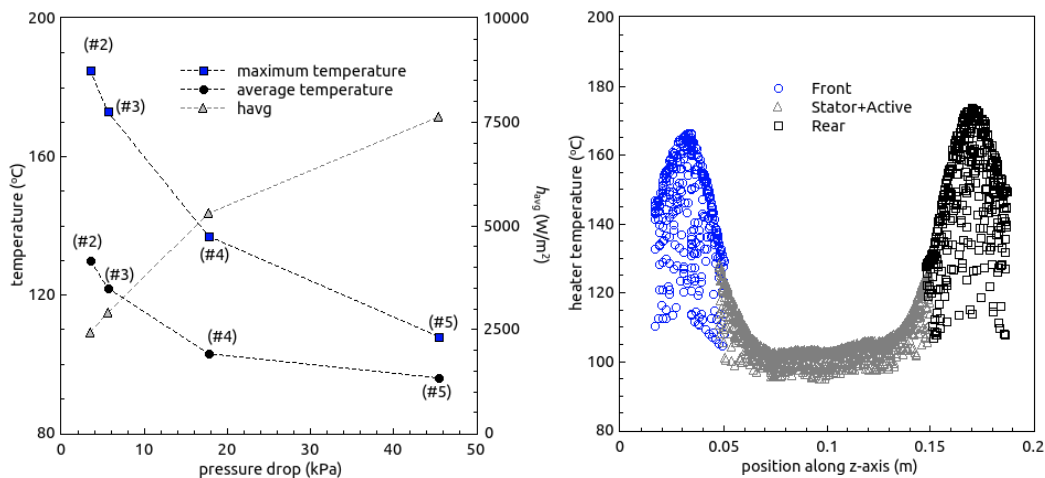


Figure I.2.9.6 Sample temperature and pressure drop profiles for various jacket designs investigated for the WFSM.

Conclusions

- Simulation results show WFSM could meet the targets of 8X power density improvement and cost < \$3.3/kW

II Grid and Infrastructure

II.1 Industry Awards

II.1.1 SCAQMD ZECT-SanPedro FCCEV and HEV Demo (South Coast Air Quality Management District)

Seungbum Ha, Principal Investigator

South Coast Air Quality Management District
21865 Copley Drive
Diamond Bar, CA 91765
Email: sha@aqmd.gov

Adrienne Riggi, NETL Program manager

U.S. Department of Energy
Email: Adrienne.Riggi@NETL.DOE.GOV

Lee Slezak, DOE Technology Manager

U.S. Department of Energy
Email: Lee.Sezak@ee.doe.gov

Start Date: October 1, 2014

End Date: September 30, 2021

Project Funding: \$20,410,075

DOE share: \$9,725,000

Non-DOE share: \$10,685,075

Project Introduction

The proposed project area is known as the Los Angeles Goods Movement and Industrial Corridor. This area is adjacent to the Ports of Long Beach and Los Angeles, the busiest port complex in North America. The area is in an industrial setting with diesel truck activity mingled with a variety of uses including residences, schools, daycares and senior centers. The area is also a known Environmental Justice Community made up of predominantly low-income and minority populations that are adversely impacted by vehicle emissions.

The proposed technologies, fuel cell range extenders and hybrid electric trucks, face many challenges in the process of commercialization: proper sizing of the fuel cell stack, battery and fueling system; system integration and packaging of power train components and systems for safe, efficient and economical deployment of the technologies are just a few of the challenges. Many options exist in sizing the energy systems for these type of vehicle architectures – making the battery, engine or fuel cell dominate in size; plug in charging versus operation in charge sustaining mode and sizing of the energy storage system. Considerations for the power requirements of vehicle under load and providing enough onboard energy to attain the range requirements for the drayage operation and duty cycles all come into play in the design of the energy storage and power systems. Another challenge is to design the energy and power train systems described above and then integrate them into a vehicle for safe and efficient operation that can be made economical in volume and series production.

Objectives

- Reduce criteria pollutants and GHG's in South Coast Air Basin by reducing diesel emissions from transportation and movement of goods
- Accelerate introduction and penetration of zero and near-zero emission fuel cell and hybrid technologies in cargo transport sector

- Execute a joint project with the Port of Los Angeles and Long Beach consisting of demonstration, data collection and analysis of seven fuel cell and hybrid trucks on five different vehicle architectures.

Approach

ZECT 2 Projects



Figure II.1.1.1 CTE/Kenworth Fuel Cell Truck



Figure II.1.1.2 TransPower Fuel Cell Truck in Foreground & CNG Truck in Background

CTE/BAE Systems and Kenworth have developed a battery electric truck with a hydrogen fuel cell range extender. The vehicle will operate in electric mode at all times and all speeds until the battery energy system reaches a lower operating state of charge level, at which point the hydrogen range extender would be activated to supplement power.

TransPower has developed two battery electric trucks with hydrogen fuel cell range extenders. These trucks will employ a small fuel cell and stored hydrogen. One truck will be equipped with a 30-kW fuel cell and one with a 60-kW fuel cell, enabling a direct comparison of both variants.

U.S. Hybrid has developed two equivalent battery electric trucks with an on-board hydrogen fuel cell generator. Each truck is estimated to have 20 kg of hydrogen storage at 350 BAR with an estimated fueling time under 10 minutes.

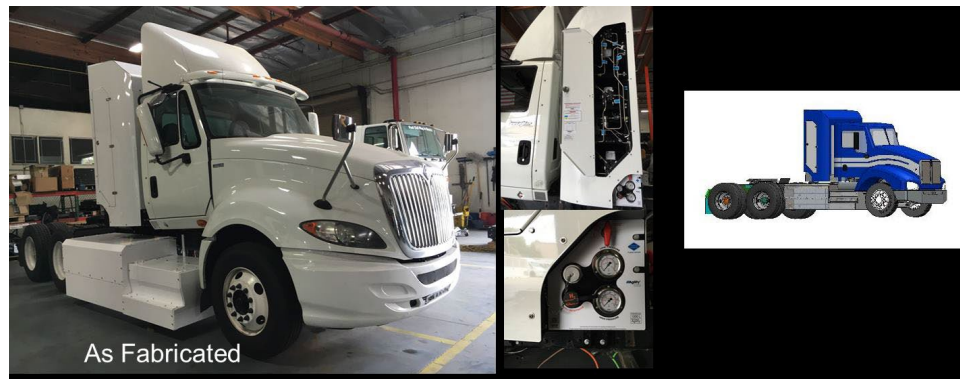


Figure II.1.1.3 U.S. Hybrid Truck: Design to Fabrication

GTI/BAE Systems and Kenworth have developed one hybrid battery electric truck with CNG range extender. The proposed technical concept provides an all-electric mode, and in a conventional hybrid mode using CNG. The truck will have an on-board battery charger to fully charge the batteries in daily use.

Hydrogenics has replaced International Rectifier in the ZECT 2 San Pedro Bay project, and they will be developing and demonstrating a fuel cell range extended Class 8 truck. Hydrogenics working with Daimler’s VVG dealership group developing a fuel cell range extended truck under a California Energy Commission (CEC) project.

Table II.1.1.1 Hydrogenics Vehicle Systems Specifications

Item	Target Specification
Chassis	Daimler Freightliner Cascadia Day Cab
GVWR	80,000 lbs
Fuel Cell Power System	Hydrogenics CelerityPlus
Electric Drive	Siemens ELFA PM Motor
Battery	ACTIA100 kWh
System Voltage	650 V
Hydrogen Storage	30 kg @ 350 bar
Refuel Time	10-15 minutes
Expected Range	150-200 mi



Figure II.1.1.4 Kenworth/BAE - CNG Hybrid System Architecture

Results

TransPower

Fourth Quarter 2019

The first fuel cell truck had been returned to Transpower’s integration facility due to several issues which impacted its use as a reliable carrier.

- TransPower removed the YHKAM battery string and replace with Nissan batteries, such that the two trucks will have batteries of identical design.
- After repairing the leak, Hydrogenics noted several cells were below expected voltage. Rebuilding with new cells was negotiated with Hydrogenics considering the very limited use of the fuel cell (50 hours), to cover entire cost of rebuilding to new specs.

The second fuel cell truck (FC2) has been in regular service since April 2019

- FC2 has been reliable and has seen increasing use in service as the truck continued to provide reliable drayage towing. The end of September mileage of FC2 was 4791 miles, with 1456 miles added in Q3, followed by an additional 1806 miles in Q4.
- The first two weeks of December the truck was driven 534 miles, until service was interrupted due to an electrical failure in an air conditioning circuit which caused enough concern to remove the truck from service, it is now at the TransPower Escondido integration facility where there is investigation into the cause of the failure and replacement of the failed parts. Following the truck will be recommissioned and returned to service.

First Quarter 2020

The first fuel cell truck had been returned to Transpower’s integration facility due to several issues which impacted its use as a reliable carrier.

- TransPower removed the YHKAM battery string and replace with Nissan batteries, such that the two trucks now have batteries of identical design. The battery system replacement is complete, along with major changes in the high current wiring and the addition of the high voltage junction box.
- Once fuel cell stack has been re-installed, it has been observed that the fuel cell system has power variability which detracts from average power. Hence the validation process has been expanded to include software improvement and validation.

The second fuel cell truck (FC2) has been in regular service since April 2019

- The truck was repaired for electrical failure in an air conditioning circuit and returned to service in January.
- Subsequent to returning FC2 to TTSI the combination of the impact of tariffs and the COVID-19 has led to a near shutdown of the port shipping traffic. Hence the truck logged only 516 miles in Q1, for a closing odometer reading of 7116.

Second Quarter 2020

Fuel cell truck #1

- Since fuel cell stack has been re-installed, it has been observed that the fuel cell system has power variability which detracts from average power. Hence the validation process has been expanded to include software improvement and validation.
- The commissioning and validation has been initiated, the truck drives well but for the aforementioned power issues which are the current focus. The truck was driven 79 miles the past month, current mileage is 3305 miles.

Fuel cell truck #2

- Due to impact of COVID-19, TTSI has suspended the demonstration and the truck has been parked at TTSI without operation. The technician at TTSI and TransPower engineer have checked vehicle status and condition regularly.

Third Quarter 2020

Fuel cell truck #1

Recommissioning of the prototype truck, FC1 continues. The limited availability of the test driver has slowed this testing, and on one occasion refueling at Del Mar was not available. Discussion with First Element resulted in assurances that they would support 350 bar fueling. An additional driver has been hired, the driver started the last day of August. This truck registers 3434 miles, with 53 miles driven this past month. Software limitations reducing fuel cell power was cured by reinstalling the SCM software used in FC2, bypassing the innovations that had imposed limits. A single issue remains a fault resulting in a flashing amber wrench on the dashboard. Engineers have done datalogging to trace this issue and await a response from the TransPower software group. The truck will be more tested with trailer replicating typical deliveries including full load.

Fuel cell truck #2

FC2 has a failed fuel cell, hydrogenics' engineer team has investigated the issue. The team recognized blower issue and the part has been ordered. Once the part arrives, the failed blower will be replaced immediately, and the truck will be redeployed.

Current mileage is 7150.

US Hybrid**Fourth Quarter 2019**

TTSI continues to operate fuel cell truck #1 in regular service. While the truck has been demonstrated, minor technical issues such as software upgrade, replacement of fuses and sensors were addressed.

Fuel cell Truck #2 has been in US Hybrid's facility to replace failed hydrogen tank valve. The part has been replaced and the trucks is under test for recommissioning.

To address TTSI's feedback on the fuel cell demo trucks with regards to longer range requirement, US Hybrid decided increasing H2 tank capacity from 25kg to 35kg to fulfill up to 280miles range per fill. Once the tank is upgraded, the truck will go through final test followed by deploy to TTSI.

First Quarter 2020

During the beginning of Q1 2020, Truck #2 was redeployed to TTSI in Mid-January. Due to seasonal downturn of activities, the vehicles were not being used. In addition, due to the COVID-19 pandemic, TTSI suspended all Alternative Fuel Vehicle Programs until business returned to normal. US Hybrid will be waiting until business returns back to normal and will continue operation support and data collection on both vehicles.

Second Quarter 2020

Due to the continuing COVID-19, TTSI continued to suspend/limit all Alternative Fuel Vehicle Programs until business returned to "somewhat normal" as stated above. Truck #2 was last operated in March 2020. As business slowly begins to return back to normal, TTSI will gradually prepare to reintroduce AFV Programs back into rotation at the port. Additionally, US hybrid has been waiting for the DMV, which has been extremely backed up due to the pandemic, to give the registration to operate the vehicle again. It is expected to receive the up-to-date registration by Mid-August 2020.

Third Quarter 2020

As business slowly begins to return back to normal, TTSI has resumed demonstration. The fuel cell truck #2 has been registered at end of the quarter and will be deployed to TTSI.

The fuel cell truck #1 has completed demonstration at TTSI and now the truck is out of registration. US Hybrid is seeking for new fleet operator to demonstrate this truck for other fleets experienced with fuel cell technology. Once alternative fleet is selected, SCAQMD will report to the DOE and request an approval.

CTE/BAE and Kenworth Fuel Cell Truck**Fourth Quarter 2019**

The truck returned to service and faced several issues including limited fuel cell power, dead LV batteries, and a blown power steering HV fuse. The vehicle experienced a fuel cell fault occurring when the main hydrogen low-pressure valve drops out and cuts off the fuel cell's hydrogen supply. Ballard addressed issue and resolved it by replacing the old relay board with a new board that features Ballard's most up-to-date software which resolves the start-up and low-pressure valve faults. Kenworth replaced the failed LV battery and power steering HV fuse, validated vehicle functionality, and returned the truck to TTSI to resume service operation.

The truck ran without fault for the rest of October on approximately 20–25 mile routes up to four times a day with freight varying between 10,000-39,000 lbs.

At the end of November, an operator experienced a boot up issue and intermittent power steering failure on bumpy roads. The Kenworth team came on site to investigate and determined the root cause of the issue was the internal motor wiring. The technicians replaced a HV fuse and the faulty wiring and the vehicle returned to service shortly after the repair.

The vehicle operated without technical fault for the rest of the reporting period. The truck has accumulated over 10,000 miles at the end of the reporting period.

First Quarter 2020

Since the truck has re-entered operation with TTSI, it ran without fault for a week before indicating low fluid on the fuel cell system. The root cause of the leak was originally thought to be the deterioration of the sight glass used to measure the current fluid level. The fuel cell fluid was topped off, the sight glass was replaced, and the truck re-entered operation with TTSI for the rest of January. The truck operated without issue for most of February. TTSI reported low fuel cell coolant again towards the end of February. The Project Team attempted to diagnose root cause of the coolant leak again and suspected it was due to one or a combination of an improper coolant cap, improper coolant reservoir gasket, and/or an inappropriately routed coolant return line to the reservoir. The vehicle remained operational by regularly topping off with coolant or DI water.

The truck was operated in limited hours in March due to COVID-19 impacting the freight volume. During that time, TTSI worked with Air Products to swap out one of the hydrogen refueling trailers for re-certification. Towards the end of the reporting period, TTSI reported the truck was also having intermittent power steering issues that Kenworth was working to resolve. However, Kenworth was unaware that this issue had resurfaced and planned to send a team onsite. This diagnosis has been delayed due to COVID-19 restrictions.

Second Quarter 2020

In June, TTSI's freight volume began to pick back up to ~1100 containers a week on

average or about 35% below their average before COVID-19. This led TTSI to begin hiring and training drivers again. TTSI resumed the alternative fuel vehicle program from end-June. Towards the end of the reporting period, TTSI coordinated with Air Products to switch out the mobile H2 mobile refuelers for scheduled maintenance and re-certification. The trailer swap was successfully completed, and the refueling station is fully operational.

Kenworth worked with TTSI to complete diagnostics on the power steering. After additional testing, it was determined that intermittent power steering issues reported were not indicative of any mechanical failure.

During the reporting period, Kenworth was able to complete manufacturing and installation of the custom coolant reservoir cap that is designed to block coolant flow through the cap's vent.

Third Quarter 2020

Due to COVID-19, registration has been delayed. After TTSI received the new tags, it was intended to immediately return the truck to service. However, the truck had issues with the 24v battery when the truck started. Kenworth engineers are working with TTSI to investigate remotely.

The fuel cell reservoir sight glass is cracked, but it does not prevent the ZECT from re-entering service. Although the sight glass is not leaking, it will be replaced to ensure further cracking does not create a leak. This work will be completed at the Kenworth facility which has been affected by COVID-19 shutdowns. This item will be resolved once the return-to-work authorization is given.

TTSI is back up to ~ 1400 containers a week and working a full seven days every week. TTSI is looking to hire and train an additional 40 drivers. Additionally, TTSI executed the contract with the customer looking to use exclusively zero emission trucks.

Once the truck is redeployed to TTSI, it will be actively operated in regular service, especially for the customer requiring zero emission trucks.

GTI/BAE and Kenworth CNG Hybrid Truck**Fourth Quarter 2019**

The truck completed the 200-mile roundtrip final test with no issues and was shipped to TTSI on Oct 5th. Kenworth team has visited TTSI and trained the local personnel in the key aspects of the vehicle safety and operation. TTSI has reported difficulties in registering and licensing the vehicle in CA DMV due to the electronic systems not recognizing the vehicle type. After a couple-week delay TTSI resorted to hiring a 3rd party that assisted with vehicle licensing and the license plates have been received in the first week of November.

Calstart has coordinated with TTSI and telematics equipment provider to instrument the baseline vehicles (diesel and CNG) and began the data collection

The HECT truck accumulated 1,264.2 miles in November and December of 2019. The data from the vehicle has been shared with NREL and Calstart for analysis.

First Quarter 2020

The vehicle has accumulated 2055 miles in January and 1200 miles in February revenue service with no issues reported. The fleet operator, TTSI has reported a slowdown in cargo traffic at the Port of LA, at first due to the Chinese New Year, followed by coronavirus outbreak in China and finally by the outbreak in the US. Lower cargo volume may reduce opportunities for in-service operation of the HECT truck. Anecdotal reports indicate daily container volume of 50 (the typical volume is 1700 per day). CALSTART has performed the PEMS testing with support from Sensors Inc., Kenworth and TTSI in the first week of March. After completing the PEMS testing, the truck was reported to have developed an issue with CNG pressure sensor that forced the truck out of service. The vehicle was moved to the local Kenworth dealer and is waiting for the technician to troubleshoot the wiring. CALSTART is working with Sensors, Inc. on analysis and interpretation of the PEMS testing results. Data collection for the baseline diesel and CNG vehicles is still in progress due to Viriciti data acquisition equipment issues.

Second Quarter 2020

After completing the PEMS testing in March, the truck was reported to have developed an issue with CNG pressure sensor that forced the truck out of service. The failed fuel gauge was resolved by replacing a standard fuse, after extensive troubleshooting effort. Primary cause of engine fuse failure is likely from the emissions test equipment which overloaded the engine circuit. Once the fuse was replaced, the engine started without any issue and no further issues were found. The vehicle was returned to service on May 19th.

While in service, a routine inspection identified two fluid leaks on the truck. The dealer performed initial maintenance, however the leaks proved persistent, and the truck is still in the shop. The total accumulated miles of commercial service in SoCal is now at 5495 miles.

Data collection for the baseline diesel vehicle is still in progress due to Viriciti data acquisition equipment communication issues with Mack truck. Some data has been collected and will be analyzed by CALSTART.

Third Quarter 2020

During a routine inspection in June the technician identified fluid leaks on the truck. The truck leaks were addressed at the dealership and the truck returned to service. With the increased freight volumes, the HECT truck ran as needed in the first half of July, then daily between 07/17 and 07/31. During routine inspection in August the truck was reported to have lost a low voltage fuse box cover. The cover was replaced after the fuse panel and fuse connections were cleaned and tested. All the fuses and relays were fine, but the truck experienced a high voltage interlock loop (HVIL) failure that caused an emergency shutdown condition and prevented the vehicle engine from starting. After a couple of weeks of tests on different sections of the harness, on multiple component connectors and a careful review of the collected data prior to the HVIL fault it was

determined that the in-dash emergency stop switch was tripped. Once this was reset, the engine restarted and was prepped for return to service.

The HV fuse for the chassis air compressor failed during system initialization and without full pressure. The chassis air compressor fuse was replaced, operational air-pressure was achieved, and the vehicle was ready for commercial service.

The truck has accumulated 2048 in-service miles in July and 34 miles in August/September due to electrical issues.

CALSTART continued working on Task 9 (Data Collection and Vehicle Performance Evaluation) and Task 10 (Commercialization Roadmap and Scenario Analysis).

Hydrogenics

Fourth Quarter 2019

Hydrogenics has informed delayed progress due to delayed delivery of long-lead items.

- In regular update meeting with South Coast AQMD, Hydrogenics requested to delay the delivery to the end of February 2020. South Coast AQMD required Hydrogenics to prepare and submit a letter of justification for the delay to support the request. Hydrogenics submitted letter of justification with updated schedule and confidence level in the schedule.
- On November 7, 2019 South Coast AQMD issued stop work order for all work under the contract.
- Cummins/Hydrogenics provided South Coast AQMD with the latest confirmed schedule with Cummins commitment after evaluating the resources availability.
- Cummins committed to support this project for a successful delivery of the truck and successful demonstration.

First Quarter 2020:

- Cummins engineering and project management resources have been brought in to complete the project
- CEC Truck build complete and commissioning in progress (250 mi. accumulated)
- System design in final stage and all major components have been ordered
- Design improvements from CEC truck include:
 - Adapting layout and packaging to MY 2020 chassis (front hood interferes with radiator and fuel cell cradle placement, firewall interferes with fuel cell, frame requires different motor mounts)
 - Battery upgrade from prototype to production pack. Different battery chemistry (from LTO to NMC) and cooling needs require update to thermal management system.
 - Improving power steering pump compatibility issues with motor to solve pump stalling.
 - Improved packaging of thermal management system and power electronics rack for better manufacturability (move junction boxes to reduce cabling, easier installation of components).
 - Different motor inverter for better performance and lower weight.
- Cummins engineering and project management resources have been brought in to complete the project

- Truck build and commissioning scheduled in Q3 2020. Vehicle hand-off to customer and operator training completion planned November 2020.
- COVID-19 impact on project schedule:
 - Shelter-in-place orders in CA preventing access to facilities
 - Longer supplier lead time for major components, Cummins companywide reduction in working hours (80% in Q2 & Q3)

Second Quarter 2020:

- CEC Truck project is experiencing delays and necessitates redesign / rework that will impact ZECT II.
 - H2 PRD Ports: current H2 pressure relieving device ports location was deemed not safe, and valves need to be relocated to safely vent H2 out in the atmosphere.
 - Celerity Fuel Cell: H2 leak between stack cells. FC unit shipped back to Mississauga for diagnostic and repair. Waiting on diagnosis to understand impact on schedule.
 - Cabin AC: cabin AC system was removed and needs to be rebuilt and commissioned. Currently assessing parts requirement and needs for control logic development and system commissioning.
- Project schedule updates
 - Company-wide furloughs at Cummins reduced engineering work hours by 20% in Q2 and Q3.
 - Rise in new COVID-19 cases will limit travel to CCW and interaction with CCW staff (risk of additional delays).
 - Truck is expected to be completed in Q4 2020. Field demonstration will begin in Q1 2021.

Third Quarter 2020

Cummins continued design and modeling work for major powertrain components and cooperated with CCW for truck assembly.

- Completed design modifications of the power electronics rack to improve the fit on the truck, reduce high and low voltage cable lengths and enhance manufacturability.
- Completed the high voltage battery chiller installation design.
- Evaluated and finalized the thermal management system for the new XMP76P battery pack from XALT Energy.
- Completed the design upgrades specific to the MY 2020 Freightliner Cascadia chassis (power steering, air-compressor and other components).
- Improved the control system based on feedback from the California Energy Commission truck (grant agreement ARV-15-002).
- Planned to outsource the vehicle build to Complete Coach Works (CCW) to mitigate project delays due to COVID-19 and internal resource constraints.
- Received approval from the SCAQMD and U.S. DOE to use CCW as a vendor to perform the vehicle build.

- Reviewed the current fuel cell truck design with CCW and established preliminary plan for collaboration between Cummins and CCW.

Cummins proposed to the U.S. DOE and SCAQMD to pursue this project using Cummins' most up-to-date heavy-duty fuel cell powertrain architecture and design. This fuel cell powertrain is designed for regional haul and port drayage duty cycles and builds on the learnings from several previous Hydrogenics and Cummins projects, including the California Energy Commission grant agreement ARV-15-002.

II.1.2 Cummins Electric Truck with Range-Extending Engine (ETREE) (Cummins, Inc.)

Jesse Dalton, Principal Investigator

Cummins, Inc.
1900 McKinley Avenue
Columbus, Indiana 47201
Email: jesse.dalton@cummins.com

Lee Slezak, DOE Technology Development Manager

U.S. Department of Energy
Email: lee.slezak@ee.doe.gov

Start Date: July 1, 2016	End Date: September 30, 2020	
Project Funding: \$9,808,542	DOE share: \$4,126,570	Non-DOE share: \$5,681,972

Project Introduction

Many medium duty commercial vehicles (classes 5 - 7) have daily duty cycles with energy requirements that may lend themselves to the use of a plug-in electrified powertrain. However, often the duty cycle energy requirements are near, or over, the limits that can be served by a pure battery electric vehicle (BEV). A range extending electric vehicle (REEV) architecture may enable the fleet operator's needs to be met using a substantial amount of grid energy, while also allowing the vehicle to complete any number of more challenging duty cycles typically completed by conventionally powered vehicles.

The Cummins Electric Truck with Range Extending Engine (ETREE) project makes use of grid energy to offset fuel consumption used by medium duty commercial vehicles and, specifically, those that are used for class 6 urban/suburban pickup and delivery.

The ETREE project aims to develop a class 6 (GVW 26k lb.) box truck, with equivalent performance to conventional diesel-powered trucks, that reduces fuel consumption by at least 50% over a wide range of urban/suburban pickup and delivery applications.

Objectives

In the target vehicle (a Kenworth K270 equipped with a 24' van body), the electrified powertrain will achieve at least a 50% fuel consumption reduction for a wide range of pickup and delivery workday drive cycles compared to the baseline powertrain (a Cummins 6.7L ISB diesel engine and automatic transmission).

The Kenworth K270 with the ETREE powertrain will be demonstrated in simulation, in a powertrain test cell, on a test track (SAE J1526 testing), and in fleet operation.

Approach

ETREE is a Cummins-led project with assistance from the following partners:

- PACCAR, Inc.,
- Argonne National Laboratory (ANL),
- National Renewable Energy Laboratory (NREL), and
- The Ohio State University (OSU)

The project will:

- Develop target entire workday duty cycles by employing NREL's FleetDNA and DRIVE Analysis Tools.
- Rely on simulation (by ANL, Cummins and OSU) to determine component requirements for a plug-in series hybrid.
- Build test vehicles which include:
 - The use of applicable electrified vehicle accessories,
 - Appropriate thermal management systems, and
- Employ a "test heavy" project schedule (simulation, powertrain test cell located at Cummins Technical Center, test tracks, and fleet operators) to confirm predicted results.
- Identify & deploy test vehicle(s) to fleet operators that would likely use these vehicles in production.

Results

Previously, the ETREE project developed the target workday duty cycles which are used to measure the project against its objectives. These workday duty cycles, denoted NREL 80 and NREL 100, are 80 and 100-mile duty cycles, respectively, applicable for use for class 6 pickup and delivery. Their required duty cycle energies are in the 80th and 95th percentile of all measured duty cycles available in NREL's FleetDNA database.

In FY2017, simulation against the workday duty cycles, and against typical class 6 performance metrics, ANL, Cummins and OSU identified the components as summarized in Table II.1.2.1. This component selection assured the fuel consumption reduction targets will be met on the workday duty cycles. Also, in FY2017, the simulation results were validated in a powertrain test cell, equipped with a battery emulator at the Cummins Technical Center as shown in Figure II.1.2.1.

Table II.1.2.1: Summary of ETREE Powertrain Components

Component	Description
Traction Motor	160 kW permanent magnet traction motor
Transmission	Allison 3000 ETREE transmission with transmission input stop-start system
Nominal DC bus voltage	700 VDC
Energy Storage	112 kW-h NMC Li-ion battery
Range Extender – Generator	130 kW permanent magnet generator
Range Extender – Engine	155 kW ISB4.5 w/ full complement of aftertreatment components (diesel particular filter, selective catalytic reduction, diesel oxidation catalyst)
Final Drive Ratio	5.29

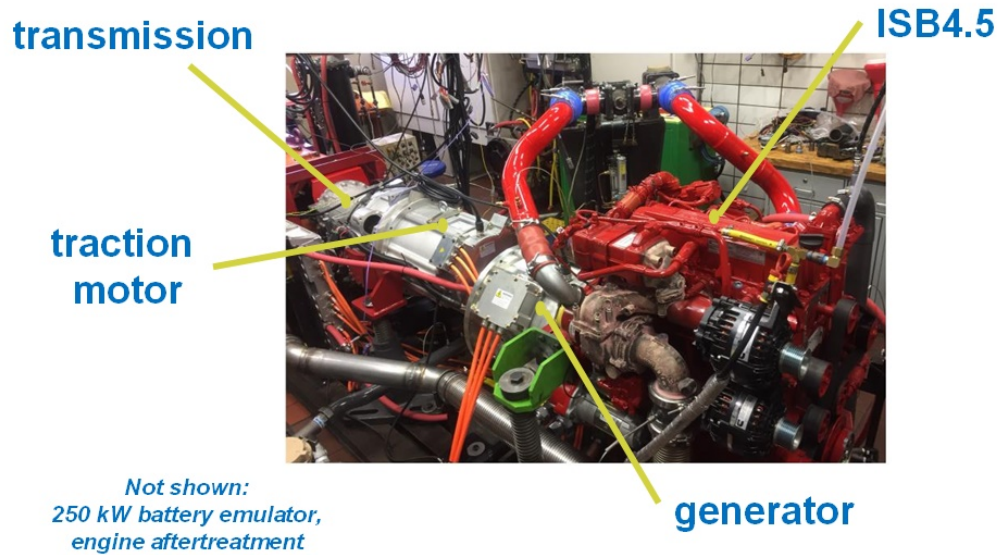


Figure II.1.2.1 ETREE powertrain test cell located at Cummins Technical Center, Columbus, Indiana

In FY2018, two test trucks were built based on the Kenworth K270 / Peterbilt Model 220 chassis. These trucks underwent validation testing where it was found that the original 112 kw-h NMC li-ion batteries did not exhibit the desired robustness for a demonstration project to be used at a customer location. Due to this reliability concern, the decision was made to create alternate batteries.

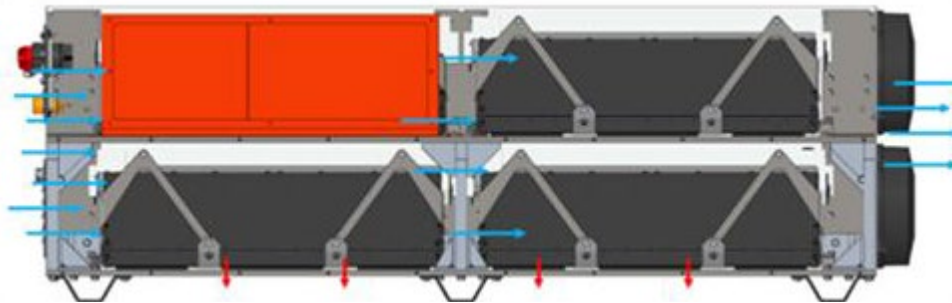


Figure II.1.2.2 ETREE alternate battery – drivers side enclosure (shown without cover)

An alternate battery (drivers side enclosure shown in Figure II.1.2.2), consisting of a nominal total energy capacity of 123 kw-h, was designed to fit the space-claim of the original batteries. This battery, consisting of 14 44V/200A-h production Li-ion battery modules—or 7 on each vehicle side—connected in series, was developed in less than four months. After construction, the battery underwent extensive testing at the Battery Innovation Center (BIC) in Newberry, Indiana. The full suite of tests was completed as scheduled, and the batteries were put into use on both ETREE trucks.

In FY2019, the two test trucks were subjected to an extensive verification and validation plan to ensure they meet performance, reliability, and robustness expectations necessary to operate in a public fleet. This included static tests, dynamic tests, closed course testing, and accumulated mileage on public roads.

Also, in FY2019, a key technical objective of the project was to demonstrate on a test track, during a J1526 test (employing a baseline and ETREE truck), the project fuel consumption targets are met. This included the modification of the target NREL 80 drive cycle, by NREL and Cummins, so that it is more appropriate to operation on a test track while still containing similar energy requirements and drive cycle metrics. This testing was conducted in conjunction with Southwest Research Institute, who administered the testing at a test track in Uvalde, Texas. A semi-autonomous drive system consisting of accelerator position and brake control was installed on both the ETREE and baseline trucks to ensure cycle to cycle repeatability during each run of testing. As well as the ETREE truck and the baseline vehicle were operated simultaneous for each of 3 runs of the cycle, spaced 5 minutes apart. The ETREE truck demonstrated **65%** fuel reduction with 1.8% confidence interval over the modified NREL80 cycle, which was better than the project goal of 50% and in line with simulation prediction. Testing results for the 3 NREL80 test runs are summarized in Table II.1.2.2 below.

Table II.1.2.2: Summary J1526 Testing Results

ETREE Compared to Baseline Truck on Modified NREL80 Cycle	
Average Difference in Fuel Quantity (lbs.)	46.46 ± 1.27
% Less Fuel Consumed by ETREE	65.3% ± 1.8%

In FY2020, one of the ETREE trucks was deployed temporarily in service at a fleet in Indianapolis, IN in January. Figure II.1.2.3 below depicts the truck charging after a workday. During this deployment a gap in the prototype battery management system was discovered that could potentially prevent the truck from starting after it had sat for long periods of time without a charger, such as an extended delivery stop of 4 hrs. Because of this the deployment was paused until weather conditions improved in spring.



Figure II.1.2.3 ETREE vehicle at fleet site charging

In spring as the weather turned favorable to restart the fleet trial the COVID-19 pandemic also became a major challenge for society and businesses to navigate through. After much thought and discussion with the original fleet as well as other local fleets it was determined that deploying a prototype vehicle into service during this time posed additional unnecessary risk to fleet operators considering COVID-19.

In order to demonstrate the ETREE vehicle’s viability in service and complete the final project milestone an independent company was utilized to operate the ETREE truck on daily routes locally for 2 months. Both day

and night routes were conducted on the truck during this period with daily route mileage varying between 40 – 175 miles. The truck was able to accumulate an additional 3300 miles of service during this time and continue to demonstrate the architecture’s ability to complete a range of workday missions comparable to a conventional powertrain.

Additional in late FY2019 & early FY2020 the ETREE vehicles participated in the SAE COMVEC Technology Demo at the Indianapolis Motor Speedway (Figure II.1.2.4) and the Work Truck Show respectively. Both events were great opportunities to educate the public and commercial fleets on range extended electric vehicle technology and its value to commercial fleets. During the Work Truck Show in addition to participating in the ride and drive the project partnered with Greater Indiana Clean Cities Coalition to host a lunch and learn session with local fleet owners and industry representatives to highlight the commercial and environmental value of a medium duty range extended electric vehicle architecture.



Figure II.1.2.4 ETREE vehicle at IMS for SAE COMVEC Technology Demo

Conclusions

The ETREE program team has developed an EV powertrain and related systems to meet the project goals. The team has validated the powertrain in a powertrain test cell. The ETREE architecture installed in vehicle was put through a verification and validation process to demonstrate robustness in line with expectations from a fleet operator. Including more than 10,000 miles of on road use spanning multiple states and weather conditions.

Additionally, the ETREE project completed J1526 fuel consumption testing operated by Southwest Research Institute at a test track located in Uvalde, Texas. This testing demonstrated 65% reduction in fuel consumption on a modified NREL80 cycle over a baseline vehicle, which exceeded the project goal of 50%.

Lastly the ETREE project completed a short fleet trial as well as 3,300 miles of daily routes between 40 and 175 miles by an independent driving company demonstrating real world architecture practicability. As well as continue to promote the commercialization of range extended electric vehicle architectures through public outreach and industry trade shows.

Key Publications

1. The following technical paper, based on ETREE project work, was published as an SAE Technical Paper in 2020: Title: Development and demonstration of a class 6 range- extended electric vehicle for commercial pickup and delivery operation, SAE Technical Paper 2020-01-0848, 2020, Primary Author: Matthew Jeffers of NREL
2. The following technical paper, based on ETREE project work, was presented at the 2019 Innovations in Mobility Conference: Title: Opportunities and Challenges of Internal Combustion Engine Range Extenders in Commercial Vehicles, Primary Author: Ke Li
3. The following technical paper, based on ETREE project work, was presented at the 2018 SAE World Congress: Title: Development of 80- and 100-Mile Workday Cycles Representative of Commercial Pickup and Delivery Operation, Primary Author: Adam Duran of NREL, Additional Authors: Ke Li and John Kresse of Cummins, Ram Vijayagopal of ANL
4. The following technical paper, also based on ETREE project work, was presented at the 2018 ASME Dynamic Systems and Controls conference: Title: Battery Discharge Strategies for Energy Management in Electrified Truck for Pick-up and Delivery Application, Primary Author: Mukilan Arasu, Additional Authors: Qadeer Ahmed and Giorgio Rizzoni

II.1.3 Development and Commercialization of Heavy-Duty Battery Electric Trucks Under Diverse Climate Conditions (DTNA)

Marcus Malinosky, Principal Investigator

Daimler Trucks North America LLC
4555 North Channel Avenue
Portland, OR 97217
Email: marcus.malinosky@daimler.com

Lee Slezak, DOE Technology Manager

U.S. Department of Energy
Email: lee.slezak@ee.doe.gov

Start Date: October 1, 2019

End Date: December 31, 2022

Project Funding: \$3,897,603

DOE share: \$1,880,970

Non-DOE share: \$2,016,633

Project Introduction

Daimler Trucks North America (DTNA) will develop and demonstrate electric Innovation Fleet eCascadia 2.0 to improve cost, reliability, and performance over DTNA's recently completed heavy-duty electric truck. Improving cost and performance characteristics will address immediate barriers to adoption and support growth for zero-emission truck technologies in freight applications. Range and performance factors can prevent heavy-duty fleets from adopting zero emission technologies. Support from the Department of Energy will allow DTNA to overcome this barrier developing, and demonstrating a more fully integrated and capable, commercialized 116" day-cab electric tractor to serve freight and goods movement sectors having a daily travel profile of up to 250 miles.

Meijer and United Parcel Service (UPS) have both committed to participate as co-creation fleet partners and South Coast Air Quality Management District (SCAQMD) will provide guidance and expertise on incentives, regulations and policies as they relate to the market potential for heavy-duty electric trucks. This project will advance state-of-the-art heavy-duty electric truck technologies to full commercialization, and in doing so provide a platform for the market to reduce fleet operating costs, diesel consumption and energy costs, as well as significant NOx, PM, and carbon emissions.

Objectives

The objective of the DTNA E-Mobility Group (EMG) Innovation eCascadia 2.0 project is to research, develop, and demonstrate a fully commercialized Class 7/8 electric tractor with range and durability sufficient to meet the needs of 70% of freight movement in the United States. DTNA has recently completed the design of the prototype eCascadia 1.0 test units, which will be operated by Penske Truck Leasing and NFI Industries throughout Southern California in 2019 and 2020. Leveraging the significant investment, experience and learning from eCascadia 1.0, this proposed project will develop the next generation of this electric truck technology: the eCascadia 2.0, a commercialized electric truck product with significantly improved cost and operational performance capabilities.

Overall Technical Targets

- Develop and bring to market a fully commercialized, all-electric Class 7/8 day cab tractor
- Increase range capabilities to 250 miles per charge and improve efficiency to achieve 2.0 kWh/mile through a redesigned 500-550 kWh battery back system and ultra-efficient integrated e-axles.
- Provide a life-cycle cost-effective and zero-emission freight movement solution for more than 70% of use cases

Approach

The project involves three (3) phases. During Phase 1 the vehicles were developed for real world conditions expected of a Class 7/8 tractor. Vehicle designs were approved by co-creation fleet partners and the B-Sample vehicle assembly was completed during this phase. Performance tests were conducted to validate vehicle design and operational capabilities. These tests will conclude with a 'market readiness' demonstration event. In Phase 2, the finalized vehicles will be delivered to fleets for initial deployment and the customer trials will begin. Performance data and records will be continuously captured to assess vehicle performance and durability. Upon receiving certification demonstrating vehicle readiness DTNA EMG will work with co-creation fleets to develop case-study and other promotional materials.

Project Phases

- Phase 1a: Research, Design Building and Commissioning: Vehicle Design and Specification
- Phase 1b: Research, Design Building and Commissioning: Commercial Scale Production Model
- Phase 2 Deployment and Demonstration

DTNA EMG is leveraging global design, engineering, sourcing and vertically integrated production capabilities to quickly achieve economies of scale and reduce product costs. Through a 'co-creation' approach with fleet partners, DTNA EMG will collect operator feedback and determine best practices for continuous improvement. In order to ensure a successful program, we will review and track the status of the program at the end of each phase. Based on the go/no go decision points, we will evaluate the progress using the success criteria as show in the table below. These are general success criteria that are associated with the Milestones as listed in the Milestone Log. In addition, the TRL status of the overall program will be reviewed for progressing from one TRL to the next level.

Technical Strategies

- Reengineer battery structure and develop proprietary design
- Develop proprietary e-Axle integration
- Simplify vehicle components and reduce the number of electric motors
- Consolidate vehicle components and maximize assembly efficiency
- Develop proprietary control software to improve overall power and enable peak performance
- Vertically integrate design, development and in-house production of batteries, transmission and telematics systems

Results

DTNA EMG has completed all Phase 1a milestones and technical targets during Budget Period 1. Testing on the B-sample build vehicles achieved target metrics in performance, efficiency, range, and cost effectiveness for the production process. C-sample vehicle design/integration is complete and vehicle simulation is ongoing. The project team has also initiated procurement processes for both the C and D sample builds.

Table II.1.3.1 Project Milestones

PHASE	DESCRIPTION	STATUS/COMPLETION DATE*
Phase 1a	100% Finalization of Component Specifications	COMPLETE (July 2019)
	Feasibility Analysis of Series Development Confirmed (Go/No-Go)	COMPLETE (April 2020)
	Project Implementation Specifications Confirmed	COMPLETE (April 2020)
	Supplier Pre-Selection Confirmed	COMPLETE (June 2020)
	B-Sample Vehicle Specification Targets Achieved (Go/No-Go)	COMPLETE (September 2020)
Phase 1b	Target Vehicle Metrics Achieved	COMPLETE (September 2020)
	Final Assembly of Test Vehicles Complete	June 2021
	Finalization of Data List to be Collected and Analyzed	June 2021
	Finalization of Design Elements	June 2021
	C-Sample Vehicle Specification Targets Achieved (Go/No-Go)	June 2021
Phase 2	Start of Production Tests/ 100% of Parts are Customer Ready	November 2021
	Start of Commercial Series Production	January 2022
	Vehicle Delivery and Demonstration Initiation	June 2022
	Data Evaluation, Measurement and Verification	December 2022

The DTNA EMG initiated this project at Technology Readiness Level (TRL) 4 and will progress to TRL 8 by the end of the project period. The project team characterized the initial technology readiness at TRL 4 because the prototype vehicle was currently on the test bench undergoing validation of high-voltage components on both the battery and eAxle. The project team also conducted functionality testing in a prototype environment with early B-sample supplier parts as well as validity and concept design testing of vehicle systems. The project team advanced to TRL 5 upon the successful build of a B-sample truck with knowledge of functionality in a real-world environment. Commissioning of the vehicle prototype in a real-world environment will include charging functionality testing, safety requirement testing and integration of the electric powertrain into the chassis design

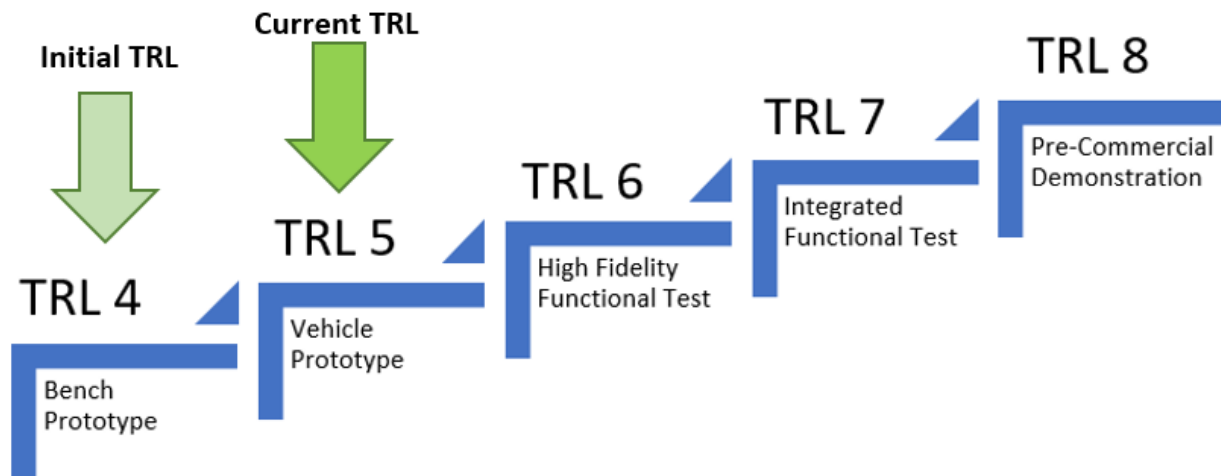


Figure II.1.3.1 Technology Development Level Progression of the Work

Conclusions

The project team has made significant progress and achieved critical project milestones for Phase 1a: Research, Design, Building and Commissioning – Vehicle Design and Specifications, including completing the B-sample build and achieving critical go/no-go milestones including demonstrating an average efficiency of 2.1 kWh/mile to realize 250-mile daily range capabilities.

The advanced heavy-duty transportation technologies supplied by DTNA through this project will result in a heavy-duty vehicle platform that provides added flexibility, operational performance, efficiency and maintenance cost savings to the end user. The most direct outcome will be a commercial production capable zero emission heavy duty option with a 250-mile range and sufficient payload for regional haul duty cycles (Table 1). The larger outcome will be an acceleration of the market transformation away from petroleum-based fuels. DTNA's comprehensive sales team, dealer network, customer network and maintenance and support teams will ensure that this is not a standalone zero-emission truck, but rather one that can be produced, marketed and operated at scale to realize vast greenhouse gas and criteria pollutant emissions reductions, while also bringing zero emission vehicles closer to cost parity. Via DTNA's "co-creation" approach with its fleet partners, DTNA will continue to collect operator feedback and best practice information for continuous improvement activities and the development of best practice case studies for other future commercial vehicle operators.

Key Publications

1. DTNA EMG and the Freightliner Electric Vehicle Council presented at the 2019 North American Commercial Vehicle (NACV) Show in Atlanta in October. The objectives of the presentation were to share lessons learned, review progress on DTNA's electric vehicle deployment and discuss the path towards commercialization and series production.
2. DTNA EMG presented at the Electric Vehicle Council in June 2020; all presentation materials are protected and provided in a separate attachment during regular project reporting.

II.1.4 Development and Demonstration of Medium-Heavy Duty PHEV Work Trucks (Odyne Systems)

John R. Petras, Principal Investigator

Organization: Odyne Systems LLC
 W237 N2878 Woodgate Road, Suite 2
 Pewaukee, WI 53072
 Email: John.Petras@Odyne.com

Ken Kelly, Principal Investigator

National Renewable Energy Laboratory (NREL)
 15013 Denver West Parkway
 Golden, CO 80401
 Email: Kennith.Kelly@nrel.gov

David Smith, Principal Investigator

Oak Ridge National Laboratory (ORNL)
 2370 Cherahala Boulevard
 Knoxville, TN 37932
 Email: Smithde@ornl.gov

Steven Boyd, DOE Program Manager

U.S. Department of Energy
 Email: Steven.Boyd@ee.doe.gov

Start Date: January 19, 2017

End Date: January 31, 2021

Project Funding: \$6,172,732

DOE share: \$2,149,644

Non-DOE share: \$4,023,088

Project Introduction

The heavy-duty vehicle market (Class 6-8) has been a difficult segment for the introduction of plug-in vehicles due to the large energy storage requirement (with corresponding cost), challenging duty cycles, and the diversity of vehicle configurations. The Work Truck market represents a significant opportunity for Heavy-Duty PHEV adoption. Odyne proposes development of a new class of PHEV Work Truck which will be modularized and customized to provide optimal ROI across multiple customers and applications. The proposed project will first demonstrate this technology as a Utility Work Truck variant:

- The usage cycle includes driving and stationary/worksite power requirements, ensuring full daily usage of the grid-charged battery (battery size: 25-40kWhr). Though daily driving can often be short (an average of 26 miles per day), worksite power includes substantial demand (hydraulics, exportable 110/220V power, 12V support, HVAC).
- Worksite power demands for conventional vehicles require continuous loaded engine operation, resulting in significant emissions, fuel consumption and noise impacts.
- These trucks serve an industry that is strongly incentivized to promote vehicle electrification, and which has publicly committed to spending a portion of their annual vehicle purchase budget on electrified vehicles (EEI press release of 11/18/14).

This project will develop and demonstrate a medium/heavy duty plug-in hybrid solution capable of meeting the needs of the work truck market while delivering fuel and emissions reductions of 50% when evaluated against the full-day work truck duty cycle.

Objectives

The project goal is to design, develop, and demonstrate a new generation of medium/heavy-duty plug-in hybrid electric work truck that achieves a 50% reduction in fuel consumption versus a conventional vehicle baseline when evaluated across a full day work cycle representative of the vocational work truck. The primary objectives are:

- To simulate, design and develop unique and innovative integrated powertrain, software, and calibrations which will optimize the complete diesel/transmission/hybrid powertrain and demonstrate the potential for driving fuel efficiency improvements greater than 40% with commensurate reductions in GHG emissions.
- To develop and validate a modular Lithium-Ion battery system based on high volume lower cost cells and modules that are utilized in the light-duty sector which will meet the power, energy, and duty cycle requirements of the MD-HD vocational truck market at a cost approaching half that of currently available low volume solutions.
- To integrate fully electrified worksite functions and a daily duty cycle optimization function with the powertrain and battery solutions on an OEM class 6-7 chassis and demonstrate the capability of 50% reduction in total fuel used when measured against a full day duty cycle's and real-world performance.
- To demonstrate ten optimized PHEV work trucks and validate the vehicle's operating performance, emissions and full work cycle fuel reduction capability in excess of 50%.

Approach

The proposed solution incorporates a simple, parallel hybrid system that allows the torque of the electric motor to augment the torque output of the diesel engine, thus saving fuel. The motor speed is synchronized with the engine speed through the existing power take-off (PTO) unit. The traction motor drives the PTO, adding torque to the rear axle, or converts torque from the PTO into power to charge the PHEV batteries (see Figure II.1.4.1). Six patents have been granted, and other patents are pending prior to initiation of this project.

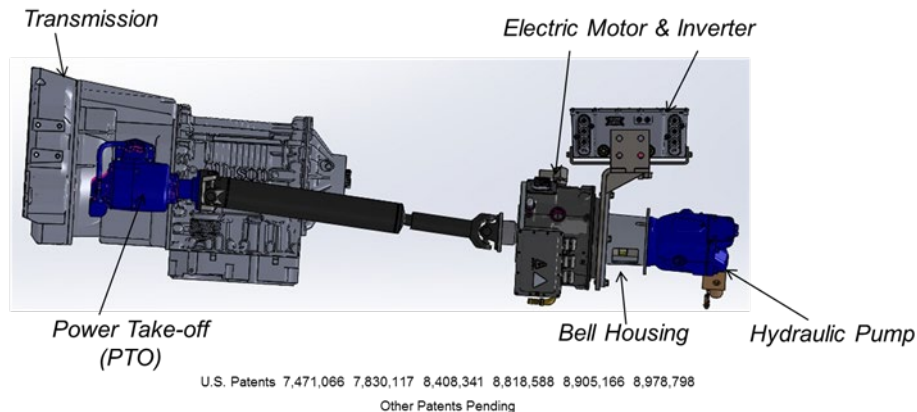


Figure II.1.4.1 Odyne powertrain configuration

The system is also designed to provide full jobsite engine off electrification utilizing power from the lithium-ion battery system to provide 120/240 V exportable power, 12V chassis systems support, high efficiency electric heating and air conditioning along with the power to drive the primary work equipment (Figure II.1.4.2).

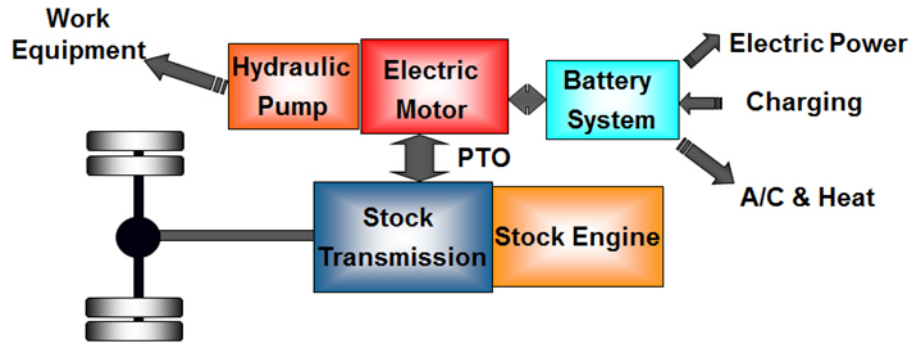


Figure II.1.4.2 Odyne hybrid architecture

The project will be conducted in three periods:

Period 1: System Design and Analysis: Analysis of existing fleet data will be performed and will be used for the establishment of baseline driving and full day usages cycles and current vehicle performance for system simulation, development and test. The project will create designs and systems which, when integrated, will produce a Medium-Heavy duty work truck capable of achieving requirements under real world conditions. The period will conclude with an analytical simulation verifying this performance improvement.

Period 2: System and Vehicle Verification: The subsystems will be verified and refined using prototype hardware and the full vehicle will undergo final development, functional and performance test. The prototype phase will conclude with test results confirming that the final design will provide a $\geq 50\%$ reduction in fuel use under real world conditions. Approximately ten vehicles will be built to support field test and evaluation.

Period 3: Prototype Vehicle Demonstration: Ten vehicles will be put in regular service with telematics to measure performance. The Recipient will analyze the data along with customer feedback and will report the calculated real-world reduction in fuel use and customer acceptance of the technology.

The project will integrate three development streams into a final Prototype vehicle solution and 10 vehicle field demonstrations:

Powertrain Development and Optimization

- Odyne – Lead, Hybrid Powertrain development and design, Hybrid optimization and control strategies
- NREL – Duty cycle analysis, Dynamometer test, Full-year fuel use simulation and analysis
- Oak Ridge National Laboratory – Powertrain simulation and optimization, HIL Test
- Allison Transmission – Transmission control and optimization strategies

Battery Development

- Odyne – System Specifications and integration requirements, system integration test
- Odyne, Ricardo Strategic Consulting – Battery System supply chain evaluation
- Enerdel – Lithium-Ion Module and BMS Supplier, Component System integration requirements

Chassis Development & Integration

- Odyne – System design, control, cost, and integration lead, Systems Efficiency & Sizing, System build
- Freightliner – OEM Chassis Integration improvements, Prototype chassis supplier.

Results

In FY20, the project completed development and test of the drive optimization strategies on the Oak Ridge National Laboratory Hardware-in-Loop (HIL) powertrain dynamometer, baseline and hybrid fuel and emissions testing on the National Renewable Energies Lab ReFUEL Chassis dynamometer, integration and validation of the primary path battery system, and released final designs for the system to be integrated into the demonstration vehicles.

Powertrain Development and Optimization

Odyne worked with Oak Ridge National Laboratory (ORNL) to finalize the driving strategies utilizing the ORNL Hardware-in-Loop (HIL) powertrain dynamometer (Figure II.1.4.3). The testing was based on strategies developed in CY19 using full vehicle simulation. During dynamometer testing it was noted that the fuel economy improvements on the HIL (CD-HIL) did not match achieve the levels of improvement predicted by the model (CD-Model) in three of four duty cycles (Table II.1.4.1). After investigation, it was determined that there was significant interaction between the hybrid drive strategy and the powertrain SCR strategies. It was not known at the time of testing whether this interaction was a laboratory phenomenon or a real-world interaction. Although the HIL testing did not achieve the targeted 40% fuel economy improvement target, the 25 – 38% improvement was determined to acceptable at this stage of development. The project team devised an “SCR mitigation” strategy to be available for evaluation during full vehicle testing at NREL.

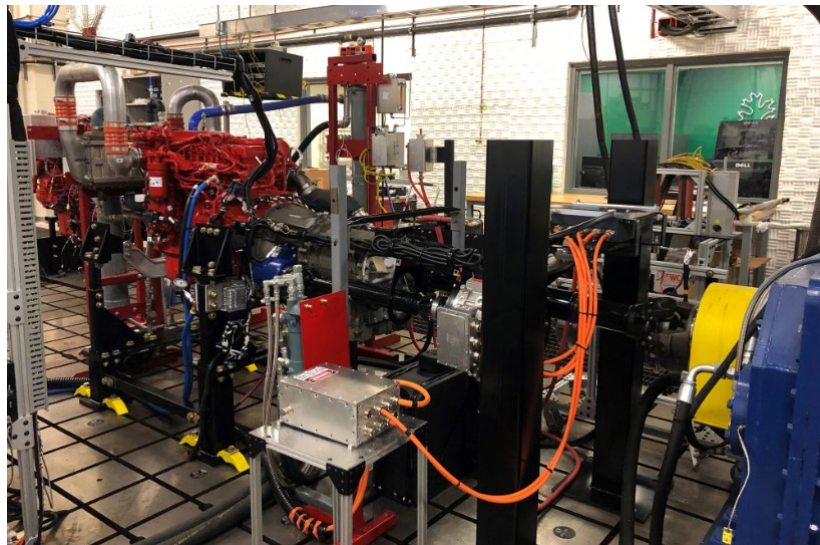


Figure II.1.4.3 Odyne / Oak Ridge HIL powertrain test stand

Table II.1.4.1 Oak Ridge Driving Simulation vs HIL Test Fuel Economy Improvement Summary

Cycle	CD - Model	CD - HIL
UDDS	29%	36%
HHDDT	48%	38%
NREL Med	44%	35%
NREL Low	57%	29%

The prototype hybrid drive software was installed in the project test vehicle and the test vehicle was shipped to the NREL ReFuel chassis dynamometer in February 2020. The scheduled testing was delayed due to the shutdown of the facility. Testing began in July 2020 and was completed in late August under a reduced number of duty cycles due to laboratory backlog. In this testing the project team tested both a low energy strategy (Mild) and the previously developed CD strategy, now termed “Aggressive” against three duty cycles, eliminating the HHDDT cycle which

was considered to have similar characteristics to the NREL Med cycle developed for this project. During chassis testing, the impact of the SCR system did not appear to interact as significantly as on the ORNL testing. The SCR mitigation strategy was also utilized. Preliminary fuel economy improvement results for Chassis dynamometer testing ranged from 69 – 75%, far exceeding the project target of 40% improvement (Table II.1.4.2).

Table II.1.4.2 NREL ReFUEL Chassis Dynamometer Fuel Economy Improvement

Cycle	Mild	Aggressive
UDDS	9.5%	69.4%
NREL Med	16.7%	75.4%
NREL Low	23.1%	70.0%

These results will be utilized to develop a blended strategy for the demonstration vehicles considering the energy needs for stationary work to achieve an optimized hybrid and electrification strategy for the full day work truck duty cycle.

Battery and Chassis System Development

During FY20, the design team developed the packaging, subsystem and component layouts and drawings to efficiently install the hybrid electrification system on a wide range of work trucks. Because of the compact size of the Enerdel battery, most of the freestanding power and control components were able to be attached within the footprint of the previous battery bracket, greatly reducing the system package space, number of sub-assemblies, and wiring complexity. Figure II.1.4.5 illustrates the prior design configuration with hybrid components represented in green, Figure II.1.4.4 represents the new configuration.

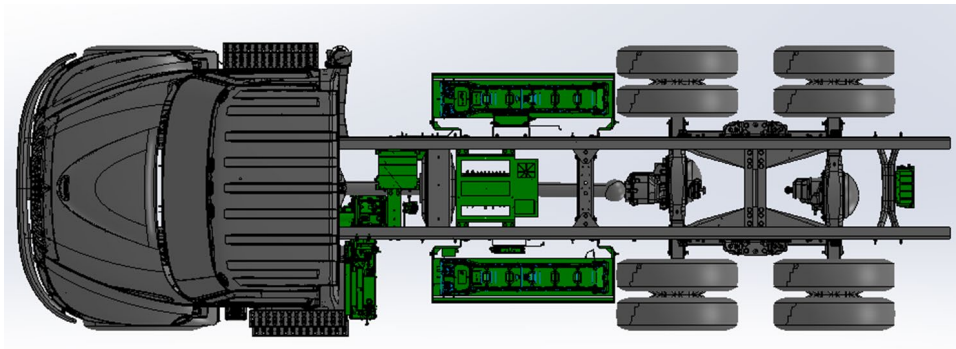


Figure II.1.4.4 Odyne Current Production Layout

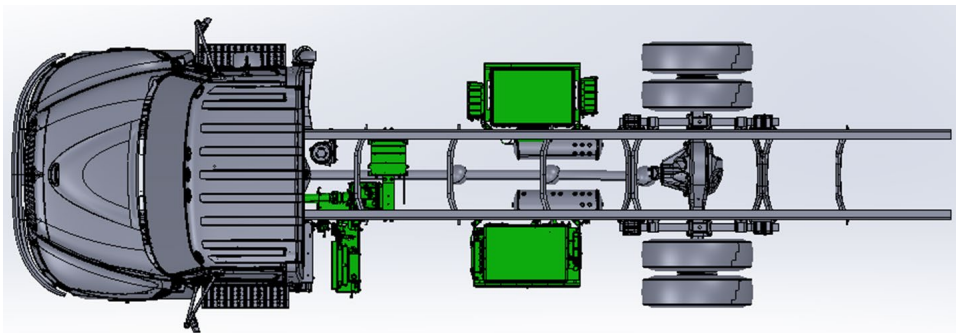


Figure II.1.4.5 Odyne Project System Layout

Conclusions

In FY20, the project completed the development and test of the hybrid drive strategies and completed the system integration, layout and design to be utilized for the demonstration vehicles as well as future Odyne production. The drive testing demonstrated that the system is capable of delivering up to 75% fuel economy improvement, depending on duty cycle, although a lessor driving strategy will ultimately be utilized when considering battery cost and size, stationary energy needs, and the real-world duty cycle of the Medium/Heavy Duty work truck. The final goal of the project is to demonstrate the capability to reduce the full day fuel use of a Medium/Heavy Duty work truck by over 50%.

Acknowledgements

Odyne wishes to acknowledge the substantial contributions of John (Jason) Conley, Michael Ursic (NETL), Eric Miller, Peter Sindler, Jonathan Burton, Matt Thornton, Kevin Walkowicz (NREL), Adian Cook, Dean Deter (Oak Ridge National Laboratory), Greg Mann, Brent Maurer (Allison Transmission), Dan Purdy (Freightliner Trucks), and Mark Kuhn, Alan Munday (Ricardo Strategic Consulting).

II.1.5 Medium-Duty Urban Range Extended Connected Powertrain (MURECP), Robert Bosch LLC

Matt Thorington, Principal Investigator

38000 Hills Tech Drive
Farmington Hills, MI 48331

Email: Matt.Thorington@us.bosch.com

Lee Slezak, DOE Program Manager

U.S. Department of Energy

Email: Lee.Slezak@ee.doe.gov

Start Date: August 18, 2016

End Date: September 30, 2020

Original Project Cost: \$6,716,791

DOE share: \$4,318,834

Non-DOE share: \$2,682,138

Project Introduction

The purpose of this project is to develop and demonstrate a commercially viable PHEV powertrain for MD vehicles that reduces fuel consumption by 50% on a real-world drive cycle by utilizing an advanced dual-planetary gear transmission with multiple clutches, coupled with cost-optimized electric machines. Such an improved powertrain efficiency will translate to a reduced fuel consumption of approximately 26 million diesel gallons per year, based on an average use of 22,000 miles per year at 8.3 mpg and a 30% market penetration for Class 4 delivery trucks.

The proposed design approach optimizes the usage of all powertrain components, particularly the internal combustion engine [ICE], the electric powertrain, and the battery pack to result in an incremental price and economic payback required for widespread commercial fleets' purchase without requiring financial incentives. Future developments are planned to explore the suitability of the MURECP powertrain for Class 2b – 8a delivery trucks.

Objectives

Key objectives:

- Dual Planetary Gear Transmission with multiple clutches, enabling the use of cost-optimized electric motors (PC/LD separated motor generators, high speed/ power dense design)
- Development of a multi-mode control strategy that ensures system optimal efficiency under a wide range of operating conditions, especially with the flexibility of powersplit operation
- Efficient downsizing of the ICE for further reductions in fuel consumption.
- Electronic Horizon forward-looking input to HEV and EV driving modes, maximizing real-world fuel consumption reduction
- Provide a >35-mile all-electric range, achievable with existing battery packs on the CSHVC cycle.

Approach

The project will be conducted in 3 budget periods:

Budget Period 1 (Aug '16 – Nov '17): Powertrain Development: Hybrid-electric vehicle topologies will be investigated through simulation and evaluation of each configuration on a real-world drive cycle to define the technical requirements and most promising architecture for the powertrain system.

Budget Period 2 (Dec '17 – Oct '19): Powertrain Integration: The supervisory control algorithms, battery management system, thermal energy management, and vehicle control strategy will be integrated with the conventional powertrain controller and further refined. The mechanical design and assembly of the hybrid drive system will also be completed along with the manufacturing of the prototype transmission. All PHEV solution components and a downsized diesel engine will be integrated onto the prototype vehicle.

Budget Period 3 (Oct '19 – Sept '20): Powertrain Demonstration: The prototype vehicle will be tested and deployed, including chassis dynamometer testing and demonstrations on closed courses to quantify the achievable benefits and help finalize the control algorithms.

Results

Task 6 – Validate Supervisory Control Algorithms

Simulation results evaluating the impact of various strategies show that the new rule-based strategy closely follows the overall system optimal results (figure 1) and represents a rather small software change effort. For these reasons, the new rule-based strategy was implemented into the project. While Equivalent Consumption Minimization Strategy (ECMS) showed favorable results, ECMS was not included in this demonstrator project due to effort and timing involved.

Optimization results (simulation)

Power strategy:

SOC	Min power	Power offset
Mid, high	26.8 kW	20.5 kW
Low	74.5 kW	34.5 kW

- ▶ New rule-based strategy comes close to online system optimal strategy
- ▶ No big SW changes required

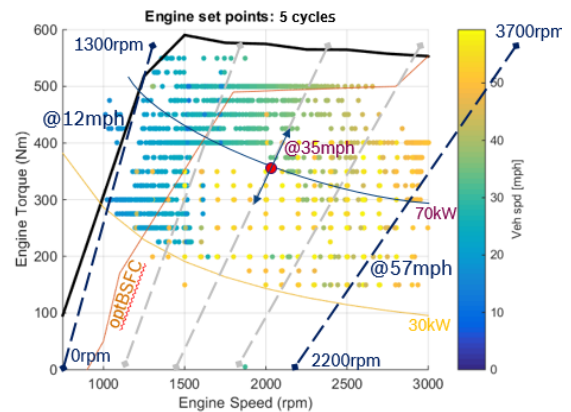
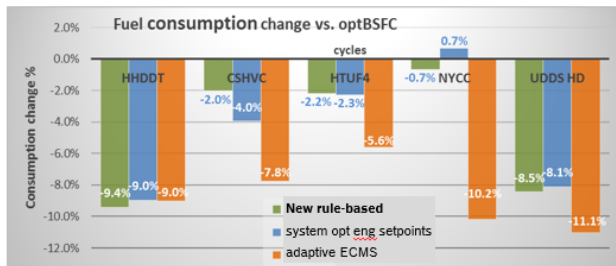


Figure II.1.5.1 New rule-based strategy shows close alignment with system optimal strategy

Subtask 7.1 – Develop Power Prediction Algorithm

Multi-pack coordinator (MPC) implementation with parallel battery packs was unsuccessful. The team reconfigured the SW, thereby reducing the complexity for implementation, calibration, and troubleshooting. The truck operated with only one battery pack. Decision was made to complete the demonstration project with this limitation. The battery state of single pack used was communicated directly to the VCU (with MPC removed).

Subtask 10.1 – Downsized Engine Calibration

Minor modifications incorporated into the production engine calibration to accommodate the hybrid powertrain for use in chassis dyno.

Subtask 10.2 – Aftertreatment System Verification

Following the installation of the exhaust line with aftertreatment components on the powertrain dyno, temperature measurements were collected during running of a City Suburban Heavy Vehicle Cycle (CSHVC). Measurements were collected for both a cold and a warm engine. From the temperature measurements collected (Figure II.1.5.2 (cold) & Figure II.1.5.4 (warm engine)), simulation results for both configurations of underfloor SCR and close-coupled SCR are displayed in Figure II.1.5.3 (cold) & Figure II.1.5.5 (warm engine results). Simulated tailpipe emissions compared favorably with the baseline measurement using the 6.7l engine. The exhaust temperatures did not climb substantially until well into the second half of the 1700 second duration CSHVC cycle. An investigation was conducted to determine if a faster heat-up was possible. The results of the investigation, confirm that the operating points for the MURECP powertrain during the CSHVC are already in an optimal range for fast heat-up with minimum NOx creation.

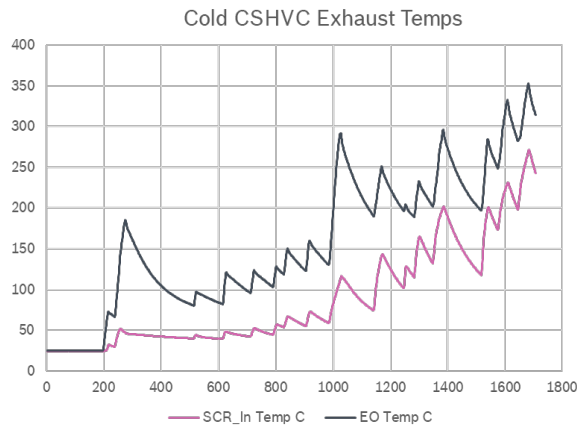


Figure II.1.5.2 SCR Inlet & Engine Out
Temperatures for Cold Engine

Cold Engine compared to baseline measurement

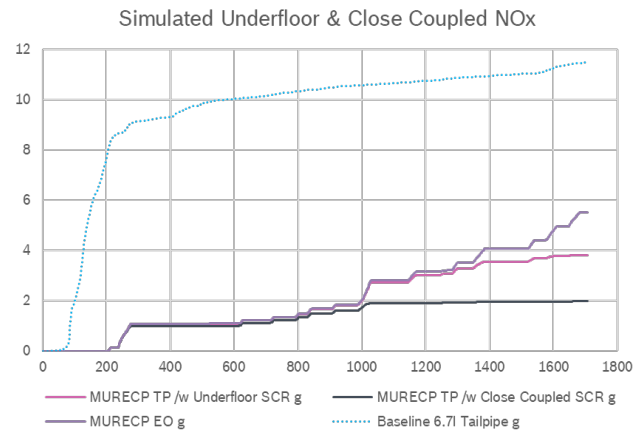


Figure II.1.5.3 Simulated Underfloor & Close
Coupled SCR Results for MURECP

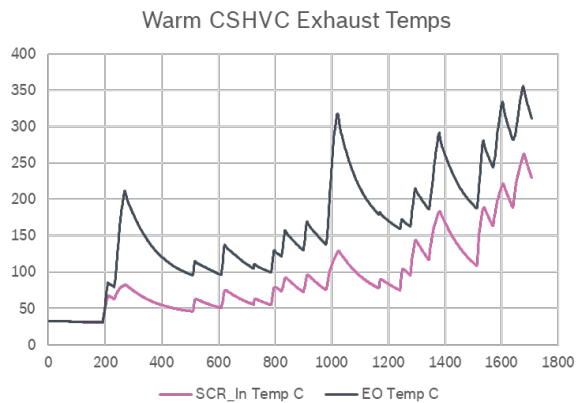


Figure II.1.5.4 SCR Inlet & Engine Out
Temperatures for Warm Engine

Warm Engine compared to baseline measurement

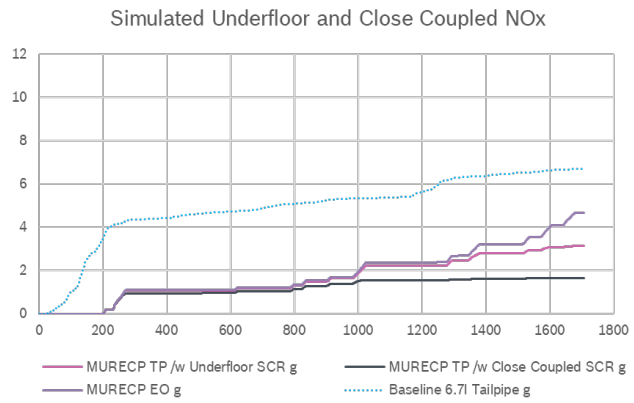


Figure II.1.5.5 Simulated Underfloor & Close
Coupled SCR Results for MURECP

Subtask 10.3 – VCU & ECU Software Implementation

On the powertrain dyno, testing of alternative commercial vehicle cycles commenced. Testing of New York City Cycle (NYCC), Urban Dynamometer Driving Schedule (UDDS), Hybrid Truck Users Forum Cl 4 (HTUF4), and Heavy Heavy-Duty Truck (HHDDT) were initiated. Several additional software updates were incorporated allowing the system to operate on various maps as the battery charge state reduced. Shown in Figure II.1.5.6-Figure II.1.5.9 are the results from the alternative cycles mentioned above indicating the time spent in each mode, the number of switches and the average switch times. The nomenclature used in the figures are as follows. 1MEV represents time operating using one electric motor to drive the dyno. 2MEV represents two electric motors and PS represents the Powersplit mode during which both electric motors as well as the internal combustion engine are operating. During mode switches, 1MEV remains connected to the final drive providing torque at all times and is represented by 1MEV MS. Mode switching occurrence is plotted for each of the six changes. In addition, the average time for each of the six changes measured over all the mode switches is plotted. Lastly, the diesel fuel consumption alone (% reduction) and in total including that of the electrical energy consumed (total equivalent fuel % reduction and mass consumed, MPGe) are plotted. Here a conversion factor of 244g Diesel represents 1kWh was developed via simulation models.

MURECP Engine Dyno
2020-01-16_SN002_SWB649_NYCC.dat

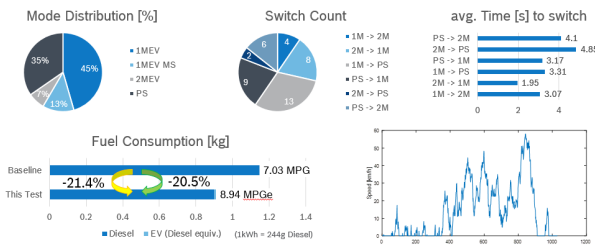


Figure II.1.5.6 Operation summary during NYCC

MURECP Engine Dyno
2020-01-16_SN002_SWB649_UDDS.dat

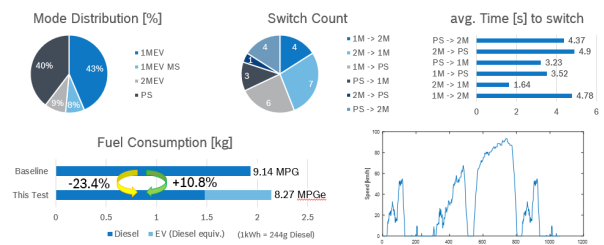


Figure II.1.5.7 Operation summary during UDDS

MURECP Engine Dyno
2020-01-20_SN002_SWB649_HTUF4.dat

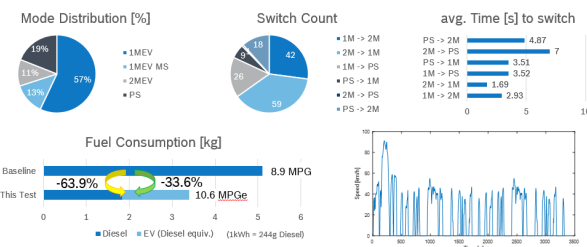


Figure II.1.5.8 Operation summary during HTUF4

MURECP Engine Dyno
2020-01-21_SN002_SWB649_HHDDT.dat

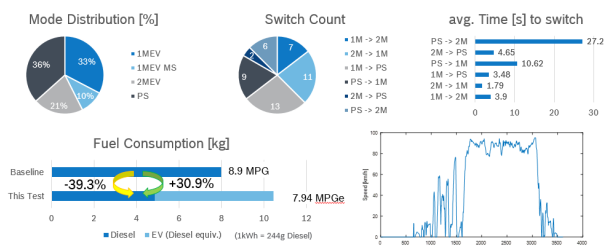


Figure II.1.5.9 Operation summary during HHDDT

Subtask 10.4 – Integrated Powertrain Calibration Optimization

Improvements demonstrated on the powertrain dyno transferred to the vehicle via a dataset merge. Minimal additional powertrain calibration efforts were integrated onto the demonstrator vehicle.

Subtask 11.2 – Sub-System Integration

Based upon a number of setbacks experienced during 3Q the team decided to bypass the Multi-Pack Coordinator (MPC) along with the second High Voltage Battery Pack (HVBP) and the On-Board Charging Module (OBCM). The project moved forward using one HVBP and updated VCU CAN messages sending required communications to the HVBP. Further sub-system integration was not pursued at this time. The existing condition of the demonstrator vehicle was sufficient to conduct chassis dyno testing for the duration of the project while demonstrating the main project objective.

Subtask 12.1 – Powertrain On-Road Calibration

No additional on-road calibration required as vehicle will be operated only in a chassis dyno setting for the duration of this project

Subtask 12.2 – Vehicle Safety and Monitoring Concept Development

No additional functional and safety monitoring functions need be incorporated for vehicle operation limited to chassis dyno utilizing one battery pack. On-road testing is restricted for the duration of this project.

Task 13 – Fuel Economy Testing

Upon achieving a transient cycle capable demonstrator vehicle, multiple runs of the CSHVC cycle were conducted on the chassis dyno. Starting with a battery pack at maximum charge, cycles were repeated until a charge sustaining result was achieved. Summary results for each of the four runs are shown in Figure II.1.5.10- Figure II.1.5.13 with contents similar to that described in subtask 10.3. The dashed line appearing in the fuel consumption section represents overall project target. In addition, the battery pack state of charge SOC was included. Overall, the four runs demonstrated an average fuel economy improvement of 52%. As the battery pack state of charge is depleted, more operation in the powersplit mode is observed.

► Chassis Dyno Testing: CSHVC in EV Mode only (High SOC)

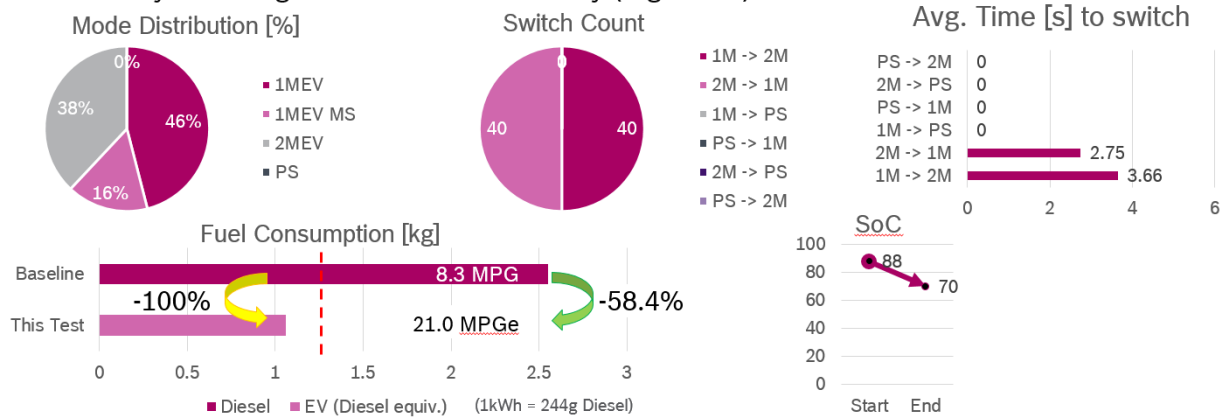


Figure II.1.5.10 Operation summary during CHSVC starting with full battery charge

► Chassis Dyno Testing: CSHVC in HEV Mode (High to Med SOC)

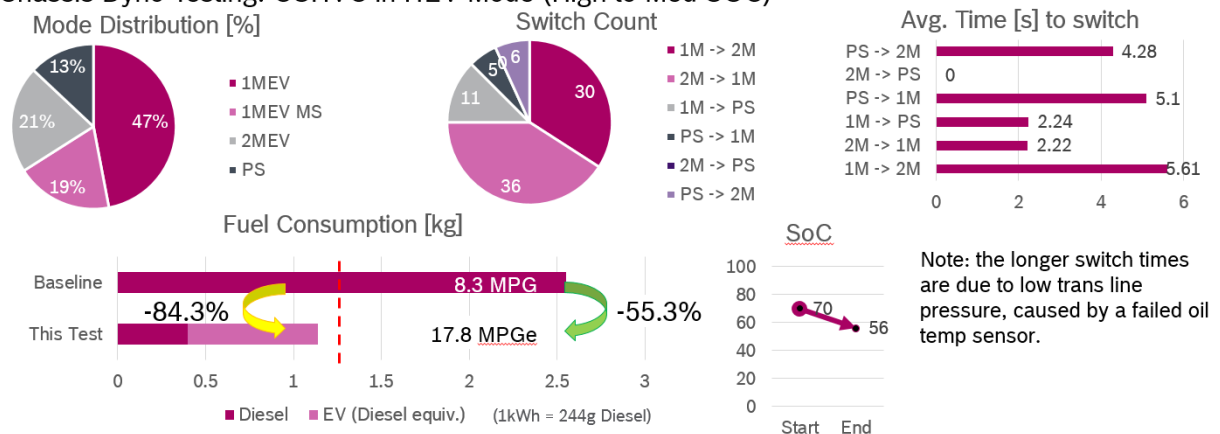


Figure II.1.5.11 Operation summary during CHSVC with High-Medium battery charge

► Chassis Dyno Testing: CSHVC in HEV Mode (Med SOC)

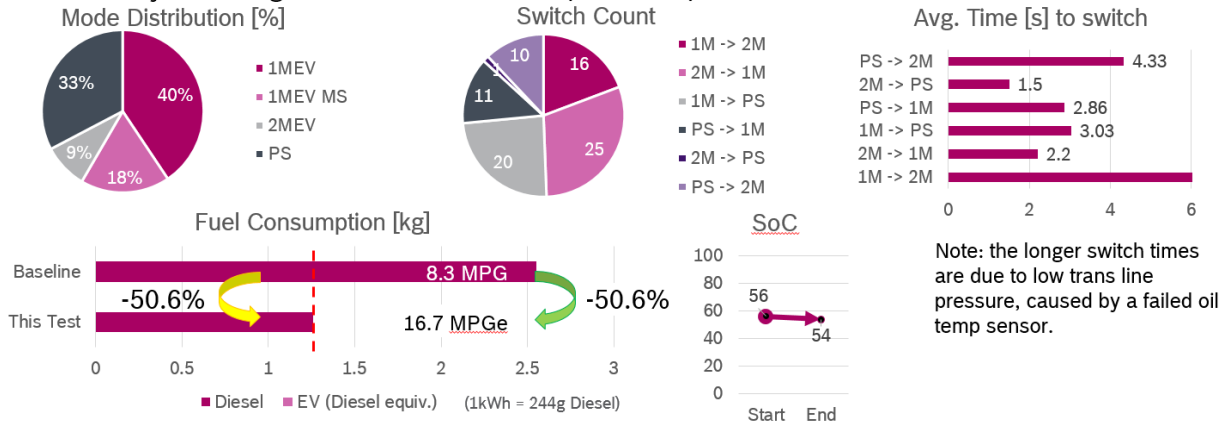


Figure II.1.5.12 Operation summary during CSHVC with Medium battery charge

► Chassis Dyno Testing: CSHVC in HEV Mode (Med - Low SOC)

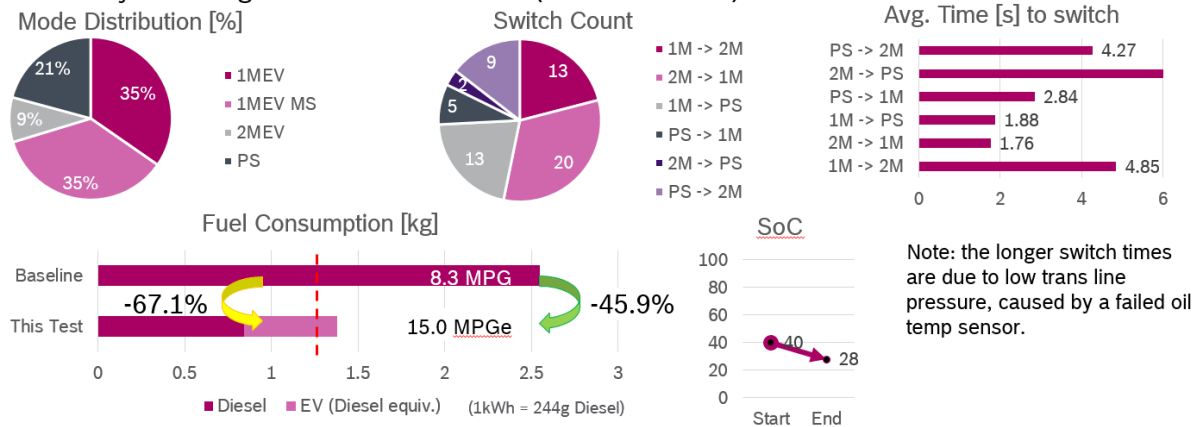


Figure II.1.5.13 Operation summary during CSHVC with Medium-Low battery charge

Conclusions

Due to delays and additional spending by BOSCH during BP2, along with the current business situation resulting from COVID-19, BP3 was rescoped to stop after chassis dyno testing (modified GNG#3 milestone). The project successfully demonstrated the fuel economy savings target while operating the CSHVC on a Bosch chassis dyno.

Key Publications

1. Thorington, Matt, U.S. Department of Energy Vehicle Technologies Office 2020 Annual Merit Review and Peer Evaluation Meeting, June 3, 2020, Virtual. Project ID-elt190, MURECP: Medium-duty Urban Range Extended Connected Powertrain
2. Thorington, Matt, 21CTP Powertrain Tech Team, September 22, 2020, Virtual. Presentation of MURECP project overview

II.1.6 Long-Range, Heavy-Duty Battery-Electric Vehicle with Megawatt Wireless Charging

Brian Lindgren, Principal Investigator

Kenworth Truck Company
485 Houser Way North
Renton, WA 98057

Email: brian.lindgren@paccar.com

Lee Slezak, DOE Technology Manager

U.S. Department of Energy

Email: Lee.Slezak@EE.DOE.GOV

Start Date: October 1, 2019

End Date: December 31, 2022

Project Funding: \$8,620,126

DOE share: \$4,989,299

Non-DOE share: \$3,630,838

Project Introduction

Most heavy-duty battery-electric trucks in operation today are designed for one shift per day and 100 miles or less operation, such as port drayage, due to the existing technology barriers of battery energy density and charging power capability. However, most truck operators prefer trucks that can achieve longer range without interrupting the daily delivery schedule to cover both intercity and regional hauling routes and to facilitate their dispatch efforts. For fleets where the diesel-powered trucks typically have a range of 350 to 500 miles, introducing trucks with shorter range presents a significant impact on operating cost, productivity, and schedule planning.

This project aims to demonstrate that 400 miles or more per day across two shifts can be achieved with little impact on a fleet's operations by developing a megawatt wireless charging technology that is capable of fully charging the battery pack during a driver's 30-minute required break. By applying the megawatt wireless charging technology, the daily operating range of the battery-electric truck-tractor can be extended without disrupting the delivery schedule and while keeping the required battery pack mass to a minimum.

Objectives

- Design and build a Class 8 Battery Electric Truck-Tractor with sufficient range to run from Seattle to Portland at 80,000 lbs Gross Combination Weight.
- Design and build a wireless charging system capable of megawatt power transfer rate.
- Demonstrate the vehicle and charging system in commercial operations of at least 400 miles per day with a major shipping company.
- Collect and analyze data from commercial use over a period of up to three months, which will provide real-world feedback on how a large, electrified tractor-trailer might be used in freight operations.

Approach

During the project, Kenworth will leverage previously-tested electric powertrain technology, and will design and build a Long-Range Battery-Electric Tractor (LRBET) specifically tailored for this application. Technical challenges that will be overcome during this project include mounting this quantity of battery capacity without adversely impacting the tractor's durability or vehicle dynamics, selecting appropriate battery chemistry and pack design to achieve high C-rate charging, providing adequate cooling for the batteries and power electronics during vehicle operations and the extreme fast charging, and developing the controls code to manage the vehicle during vehicle operations and during charging.

Utah State University (USU) will leverage its core expertise in high C-rate battery charging, high power density grid-tied power electronics and wireless charging systems to design the megawatt inductive charging equipment circuitry and topology. The planned inductive wireless charging system will allow power to be transferred wirelessly between a primary (charging) pad embedded in the ground and a secondary (receiving) pad mounted on the bottom of the vehicle by using high frequency AC magnetic fields. Inductive charging is a mature and proven technology; however, it is seeing wider adoption today due to the availability of high-performance semiconductor devices, capacitors and cables. The technology is able to operate in varying environmental conditions, including rain and snow, requires no operator interaction, and maximizes effective use of land with no above ground obstacles or components.

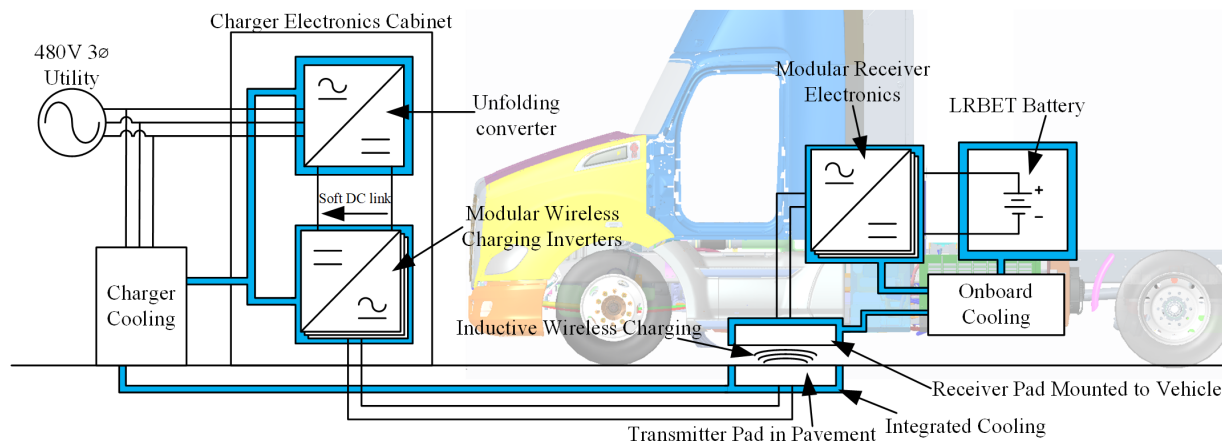


Figure II.1.6.1 System block diagram

WAVE has commercialized wireless charging systems capable of transferring up to 250 kW over an air gap of 10 inch and has obtained UL Field Certification. The maximum power that can be transferred with a wireless charging system is typically limited by the leakage magnetic fields that are generated since international standard bodies such as the International Commission on Non-Ionizing Radiation Protection (ICNIRP) regulate the maximum allowable leakage fields. USU has developed a charging pad configuration that utilizes multiple field shaping strategies as well as newly developed techniques to facilitate charging at power levels of one megawatt while maintaining leakage fields below ICNIRP regulations. USU's system has also considered other aspects of the system such as the power electronics design, thermal management and tolerances.

Local electric utilities Seattle City Light and Portland General Electric will participate by providing installations of electrical grid connections and transformers to power the ground-based vehicle chargers at each location.

Results

Fourth Quarter 2019: Project team meetings began, and the responsibilities of each partner were defined. Communication paths were established, including secure file transfer between parties.

First Quarter 2020:

Route data for the Seattle-to-Portland trip was acquired using an existing range-extended battery-electric truck. This activity satisfies Milestone 1.1 to obtain data of the proposed route. High-level details include:

- CNG range-extended battery-electric tractor, chassis #359051
- Gross Combination Weight (GCW) 76,300 lbs
- Total trip length 340 miles (170 miles each way)

- Nearly all at highway speeds
- 2 trips completed, one in rain and one in dry conditions
- Overall electrical consumption was 2.65 kW-hr/mile on wet roads, 2.55 kW-hr/mile on dry roads.

The energy consumption profile was added to the simulation model and the optimum battery capacity was determined to be 650 kW-hours.

Battery specifications were developed, an RFQ released to four potential suppliers, and the responses were studied to find the best fit. A battery system was selected:

- Manufacturer: Romeo Power
- 660 kW-hours in six parallel 110-kW-hr sub-packs
- NMC chemistry
- Capable of recharging 462 kW-hrs in 30 minutes daily for at least a year.

Utah State University conducted investigation and analysis to determine appropriate topology and magnetic design to meet vehicle parameters and charging requirement. Results from many ANSYS simulations were reviewed to identify most appropriate path forward for a scaled prototype pad and shield development and testing.

Initial weight and space estimates for the batteries, charger and power electronics were completed for coordination between project partners.

Second Quarter 2020

Directional effort on the design of the LRBET chassis layout:

- Preliminary definition of the Romeo Power battery packs was determined to be:
 - 4 tower packs of 110 kW-h each mounted above the frame rails back-of-cab
 - 2 saddle-mounted packs of 110 kW-h attached to the sides of the rails left and right, ahead of the drive tires
- Major focus was on the back of cab battery assemblies, and the team developed a plan to leverage most of the inner components from these back of cab assemblies for the side of rail pack assemblies, albeit in a different packaging arrangement.
- Kenworth submitted to WAVE a directional shape of the charge plate shield for analysis and consideration in their charger design. This plate is intended for use and installation on the vehicle.
- The team completed directional packaging studies of vehicle-side charger equipment and interface contact points.
- Kenworth generated a vehicle integration checklist for team and suppliers.

Utah State University worked toward on building and validating a 250-kW prototype:

- Conducted a trade study: megawatt wireless charger magnetics and electronics design and simulation. Various circuit topologies were investigated for the charging system to achieve higher efficiency, smoother power control, lower semiconductor device stresses, and a compact system.

- With the tradeoffs from the investigation, the topology for the charger was finalized. FEM simulations of the wireless charging pads were conducted. Further simulations are considered to account for the physical realization of the structure.
- With the design parameters obtained from the trade study, a full-scale system from grid to battery was simulated and validated in PLECS simulation software.
- A small-scale prototype rated at 1 kW was built and tested to determine the efficacy of the selected charger topology. A scaled down model of a wireless charging pad was built to verify leakage fields between physical measurements and FEM-simulations
- The loss estimation of the truck-side components which include the receiver and power electronics was done to determine the specifications for the cooling system. A heat rejection limit of 30 kW was specified by USU. A higher-level cooling architecture was finalized based on the discussion with Kenworth. The full-scale design of the cooling system is ongoing.
- The design of the wireless charger components is in progress. The truck-side power electronics were designed, and the components were selected. The battery charging profile was determined with the inputs from the battery vendor Romeo Power Technology.

Third Quarter 2020

The Project Design Review was presented to the DOE team on July 29th, 2020.

Kenworth continued design of the LRBET chassis layout:

- The KW team has selected the electric powertrain is working with the supplier to finalize design.

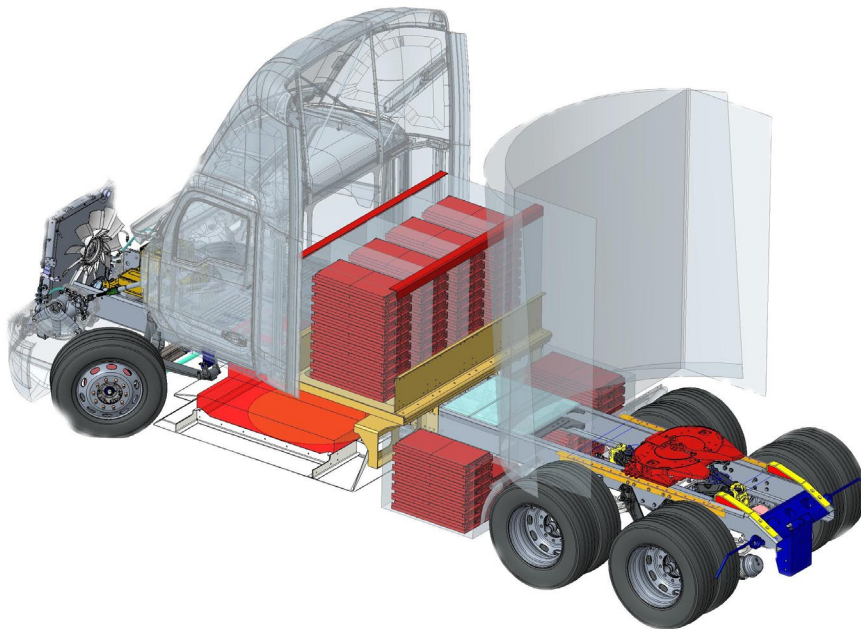


Figure II.1.6.2 Chassis Layout

- KW has also selected HV auxiliary suppliers and is soliciting quotes with delivery commitments that meet project schedule.

- Kenworth continued chassis design with solid representation of the WAVE charger and shield plate, HV battery tower and side pack designs, intended power train components and initial placement of auxiliary and power management accessories placed on the chassis.
- The HV battery designs are iteratively approaching design and installation intent. Unfortunately, the battery supplier's design review presented an unacceptable charge profile, not reaching the agreed energy content within the specified time. The KW team rejected the proposed charge profile and halted their product development cycle. KW initiated work with the supplier to mitigate this issue and to hold as close as possible to the intended drive cycle.
- Kenworth electrical, physical and control models for power distribution continued and were continually updated to match vehicle and subsystem state conditions.
- Kenworth maintained the vehicle integration checklist for the team and suppliers.

Utah State University completed Milestone 1.3 establishing design parameters for the AC-AC converter:

The block diagram of the AC-AC conversion system driving a wireless power transfer (WPT) is shown in Figure II.1.6.1 above. The system consists of a 1 MW unfold module which provides a soft DC-link. A modular structure of the T-type converter is used to achieve a wide range of power control with module shedding. The inputs of the T-type converter modules are connected to the soft DC-link voltage derived from the unfolder as shown in Figure II.1.6.3. The outputs of the T-type converter are paralleled for high current and for achieving modularity. An LCCL-LCCL compensation is used considering the optimal voltage and current stresses on the coils and the inverter. The primary and secondary coils of the WPT system are made of bifilar windings with current sharing chokes in series with them.

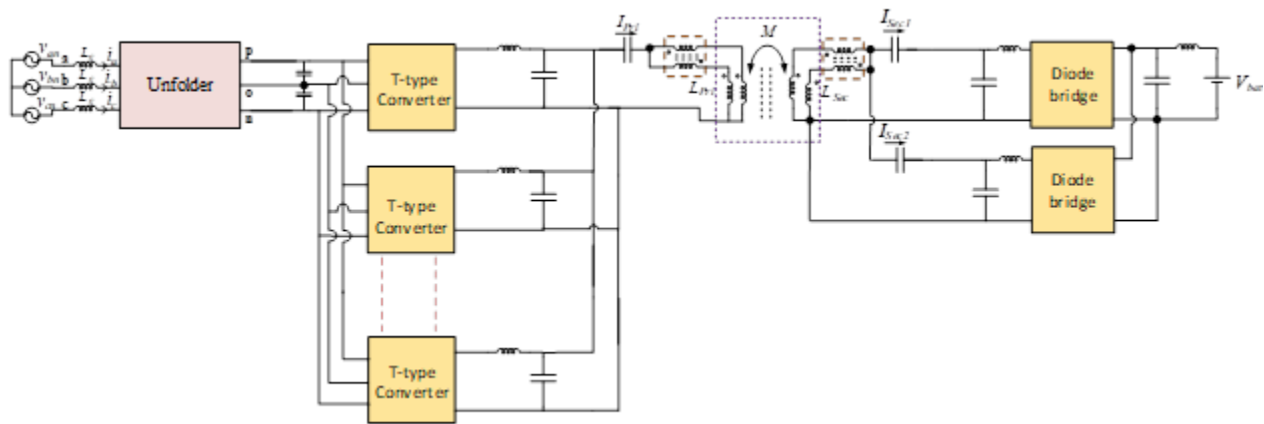


Figure II.1.6.3 Configuration of the designed WPT system

To achieve higher efficiency and higher power density an unfold + T-type topology shown in Figure II.1.6.3 is employed. The soft DC-link approach requires lower grid-side filtering, thus achieving higher power density. The proposed system acts as a buck-type PFC. The maximum RMS voltage at the output of the T-type converter is $1.1\sqrt{2} \cdot V_{dc}$ (529 V). This report consists of the design of AC-AC stage parameters, which are the components involved in the conversion of 60 Hz utility voltage into an 85 kHz voltage. Parameters of the 1 MW wireless charging system lumped into the circuit diagram of Figure II.1.6.4 are given in Table II.1.6.1. To achieve power control, 8 modules of T-type converter each rated for 125 kW are being considered. To get reduced power, some of the modules will be disabled. Disabling of modules results in detuning of the resonant tank. However, the system operation is not significantly affected. The characteristics of the system with some modules disabled are given in Table II.1.6.2. Due to the hard switching in the T-type converter at lower modulation indexes (M), a 10% variation of modulation index from $M=0.9$ to $M=1$ is considered for each

module to keep the system efficiency high. This results in a smoother control of power for a limited range within those discrete steps in power resulted in disabling of modules.

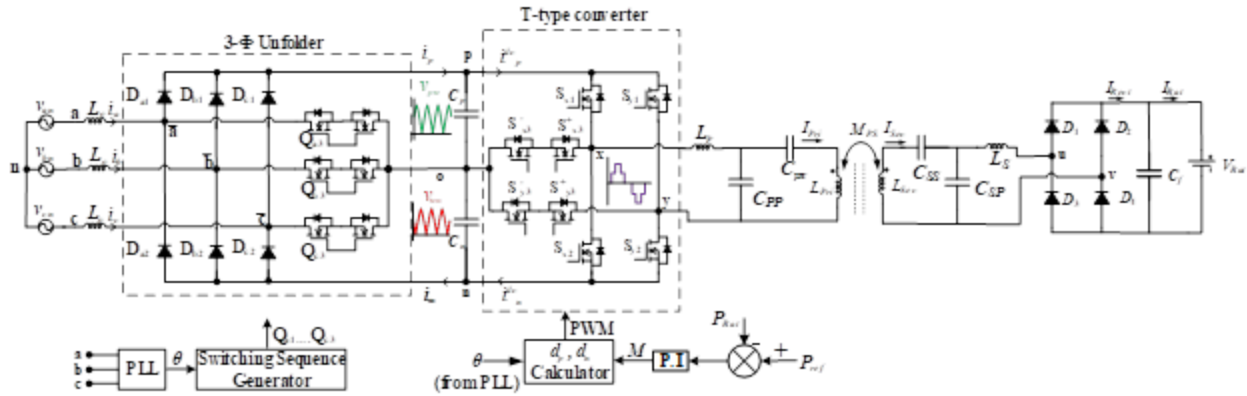


Figure II.1.6.4 Circuit diagram of an AC-AC conversion system

Table II.1.6.1 Parameters of the 1 MW wireless charging system given in Figure II.1.6.4

Parameter	Value	Parameter	Value
Input voltage	480 V, 3-Ø, 60 Hz, AC	T-type converter operating frequency (f_s)	85 kHz
Output voltage	649-750 V, DC	Mutual inductance (M)	2.17 μH
Peak output power	1 MW	Coupling coefficient (k)	0.3
Power per T-type module	125 kW (8 modules)	Primary parallel capacitance (C_{pp})	3.71 μF
Grid inductance (L_g)	5 μH	Primary series Inductance (L_p)	0.94 μH
Soft DC-link capacitance (C_p and C_n)	30 μF	Secondary series capacitance (C_{ss})	0.5 μF
Maximum primary voltage ($V_{x_{rms(max)}}$)	529 V	Secondary parallel capacitance (C_{sp})	2.62 μF
Primary coil inductance (L_{Pr1})	6.26 μH	Primary series capacitance (C_{ps})	0.59 μF
Secondary coil inductance (L_{Sec})	8.34 μH	Secondary series Inductance (L_s)	1.33 μH

Table II.1.6.2 Charging characteristics with varying number of modules

No of active modules	Output power (kW) at $M=1$	Output power (kW) at $M=0.9$	Battery Current (A)	Current in the active modules (A)	Current in the disabled modules (A)
8/8	1043	939	1605	271.87	
7/8	912	821	1403.2	269.63	308.07
6/8	782	704	1204.2	268.03	300.75
5/8	649	584	999.22	266.72	294.25
4/8	518	466	797.69	265.7	289.01
3/8	384	346	591.08	262.68	284.78
2/8	252	227	388.8	260.01	278.8
1/8	121	109	186.2	268.29	263.24

Site visits at UPS terminals in Seattle and Portland were conducted, attended by personnel from UPS, Kenworth, WAVE, Seattle City Light (Seattle terminal) and Portland General Electric (Portland terminal). Lists of preliminary components requirements was made for each location.

Conclusions

At the end of FY2020, the conclusions of this program to date are:

- The basic design and layout of the LRBET is complete, with all major components having been identified and ordered. Battery charge profile predictions, while not meeting the desired energy in the specified time to eliminate range anxiety through end-of-life, appear to show sufficient energy transfer to complete the intended route profiles. Detailed design of mounting hardware and wiring harnesses has commenced. Vehicle build is planned to begin in the first quarter of 2021.
- Similarly, the basic design and parameters for the charging equipment was defined, and detailed design of the ground-based and vehicle-based systems has commenced.

Site plans for both the Seattle and Portland locations have been initiated.

II.1.7 Medium-Duty Vehicle Powertrain Electrification and Demonstration (McLaren Engineering)

Mr. Wiley McCoy, Principal Investigator

McLaren Engineering Division of Linamar
32233 West Eight Mile Road
Livonia, MI 48152
Email: Wiley.Mccoy@Linamar.com

Lee Slezak, DOE Technology Manager

U.S. Department of Energy
Email: lee.slezak@ee.doe.gov

Start Date: June 1, 2016

End Date: June 2021

Project Funding: \$3,650,000

DOE share: \$2,640,000

Non-DOE share: \$2,559,000

Project Introduction

This project is intended to address a number of technical barriers regarding use of electric / hybrid drive systems in the medium duty marketplace as described in the Vehicle Technologies Multi-Year Program Plan. Specifically, the technical barriers are:

- Acceptance of electric drive as Medium Duty vehicle choice.
- Reduce the carbon footprint of transportation (FE Improvement)
- Cost of hybridization (medium duty TCO)

A team consisting of industry leading engineering, production and user companies was formed to specify, design, build and test a commercially viable medium duty drive system that would reduce fossil fuel use by a minimum of 50% in real world drive cycles. McLaren Linamar, AVL, & UPS were partnered to achieve the program objectives.

Objectives

The Project Objective and expected outcome have altered as the time frame has extended due to development issues and COVID. The goal of 100% improvement in Fuel Economy over real-world drive cycles was met in both simulation and bench testing. The 2nd objective to achieve a project conclusion of a commercially viable system in both reliability and 2nd cost of ownership expected in this medium duty arena has not been reached.

Approach

Project Approach – Team has developed the hybrid system specifications in simulation and completed the first milestone by showing a 100% fuel economy improvement over real-world drive cycles measured over UPS delivery routes. This completed the first phase of the program.

The second phase, which has been to develop the unique eAxle system that meets the fuel economy goal and is commercially viable has developed many issues over the past year, both in complexity, failed durability goals and cost targets. The project approach has shifted to a compare program to study the ability to meet performance goals with the original 2 motor / 2 speed systems vs. a Gen 2.0 system now in process. The Gen 2 system is funded outside DOE and is a single motor / single speed system. The approach is now focusing on running the 2 projects in parallel to collect the data required. The Gen 2.0 system also has the design and material specifications to enable commercial goals to be achieved.

Results

In the 2020 FY, the entire time was used to continue development of the original Gen 1.0 unit as a 2 speed/2 motor package. End result is that the Gen 1.0 package will not meet targets of a commercially viable cost-effective system. Valuable data was developed in parallel to the Gen 2.0 program that helps justify the decision to repurpose the Gen 1.0 system to a multi-speed development program. No intention to commercialize. Covid 19 interrupted the available time frame to a very condensed program.

In the 2020FY, the time was severely truncated by COVID19. The actual task completion was limited by several months of minimum work schedules. Once completed vehicle was used in Q4 2019 to test under real world driving conditions in the Orange County/San Diego area with simulated UPS drive routes. Various problems arose with the 2-speed axle system and the Re-gen hybrid system. Work began to find solutions in Q1 2020, then shut down due to COVID. Back to work capabilities in late Q2 into Q3 allowed the 2 speed solutions to be implemented and bench tested. As of end of Q3, the on-road testing has not started due to COVID.

The solutions to the 2 speed problems revolved around the shifting mechanism combined with software calibration adjustments. Some redesign and remanufacture of parts was required and took up most of the time in Q2 and Q3 that was available.

Attached are a series of photos showing the Gen 2.0 single speed / single motor system in early build and bench testing configuration.

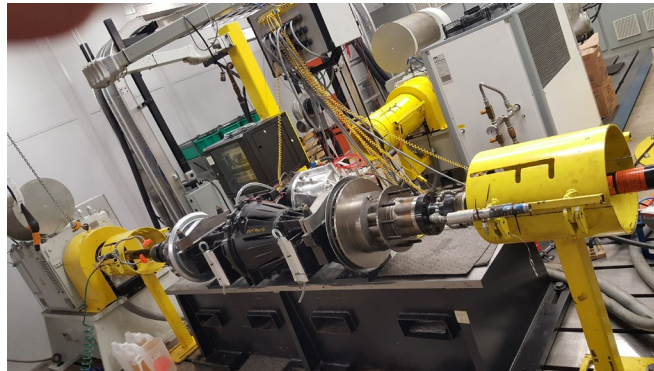


Figure II.1.7.1 Gen 2.0 single speed/single motor system in early build and bench test configuration

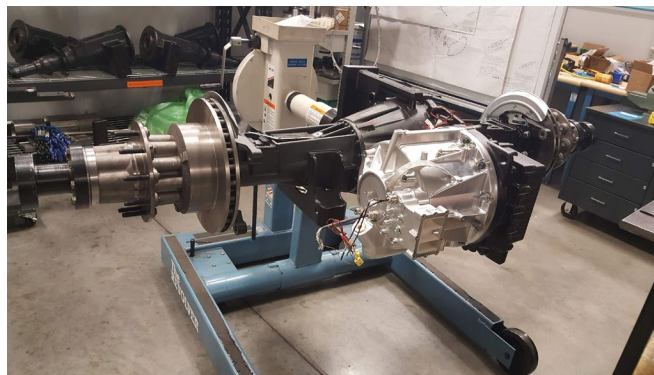


Figure II.1.7.2 Gen 2.0 single speed/single motor system in early build and bench test configuration

Conclusions

As of the end of FY 2020, the conclusions of this program to date are:

1. A system can be designed and manufactured using advanced modeling and simulation tools that demonstrate an electrified medium duty powertrain system that will achieve overall program objectives.
2. With proper real-world testing in addition to bench testing provides the collaboration accuracy required to validate the simulation and modeling.
3. The commercial viability goals can be met with the ability of the team to create a different system to overcome the cost challenge that appeared as the Gen 1.0 system was developed.

II.1.8 Improving the Freight Productivity of a Heavy-Duty, Battery Electric Truck by Intelligent Energy Management

Teresa Taylor, Principal Investigator

Volvo Group North America
7825 National Service Road
Greensboro, NC 27409
Email: teresa.taylor@volvo.com

William F. Northrop, Principal Investigator

University of Minnesota
200 Oak Street SE
Minneapolis, MN 55455
Email: wnorthro@umn.edu

Lee Slezak, DOE Technology Development Manager

U.S. Department of Energy
Email: lee.slezak@ee.doe.gov

Start Date: October 1, 2019
Project Funding: \$1,895,180

End Date: December 31, 2020
DOE share: \$1,348,442

Non-DOE share: \$546,738

Project Introduction

The project will develop an intelligent Energy Management System (i-EMS) for use with Volvo's electric heavy-duty tractors for use on regional haul freight movement routes that operate at least 250 miles a day. The developed i-EMS technologies will decrease the cost and time required for on-route charging, recommend energy efficient routing, and provide eco-driving recommendations to the operator. The developed i-EMS will be integrated onto two early production Volvo Electric Class 8 tractors and demonstrated in-service at the two partner fleets (winter in Minnesota and summer in Texas) to determine the performance and optimize the system. The full suite of vehicle analysis in the i-EMS will extend the vehicle's battery driving range by 20-30%. When combined with utility service cost savings, Volvo is projecting a vehicle operating cost efficiency improvement of 50%.

Objectives

The objective of the project is to research, develop, and demonstrate life cycle cost-effective Class 8 battery electric vehicles equipped with an intelligent Energy Management System (i-EMS) capable of commercial operations of ≥ 250 miles per day as well as increased efficiency and productivity when compared to baseline 2019 Mack and 2015-2020 Volvo heavy duty battery electric vehicle fleet performance.

Approach

Our approach is to first understand our fleet partner's, (HEB Companies and Murphy Logistics), baseline operations to be able to establish project duty cycles. In addition, we will combine physics-based truck model, battery information, utility demand charges and database parameters as inputs to a machine learning algorithm that will predict energy use, operational energy cost, and battery performance. The resulting i-EMS will be implemented on 2 Volvo VNR Battery Electric Vehicles, (BEVs), using a low-distraction screen to display charging and routing recommendations to the operators. Charging stations will be installed at HEB Companies and Murphy Logistics. Finally, we will demonstrate i-EMS in daily operations with HEB Companies in hot weather conditions and Murphy Logistics in cold-weather conditions.

Results

Task 1: REQUIREMENTS & PLANNING

Task 1.2: Collect and analyze fleet customers baseline duty cycles

During this phase of the project in order to collect the baseline data, we installed 10 UniCANs on our fleet partners existing trucks, 5 were installed at Murphy Logistics by a Volvo technician and 5 were installed at HEB Companies, by an HEB technician. The installations occurred in late July and early August. Therefore, the collection of the baseline data is in process and will run for 3-4 months, ending in Nov/Dec timeframe.

UMN and Volvo have agreed to share a secured synchronized Google Drive folder for short-term data transfer. Using sample trip files, scripts have been developed by the UMN team to aid in data visualization and analysis once received.

Task 1.3: Create a baseline database using all collected parameters for chosen duty cycles and decide representative duty cycle for the project

Data is being received by Volvo to review and then shared with University of Minnesota during this phase.

Collected baseline vehicle data will be stored in a secure spatial database to determine the representative project duty cycles.

Once data is received from Volvo, the data will be organized and stored in the UMN database managed by UMN U-Spatial. UMN U-Spatial has prepared a database using PostgreSQL/PostGIS servers that will be accessed by the UMN team via SQL using verified U-Spatial accounts. Server management is done by UMN OIT, U Services, and U-Spatial. UMN systems comply with [University of Minnesota Information Security Standards and Guidelines](#) which include standards for authentication and access management.

Task 2: TECHNOLOGY & ALGORITHM DEVELOPMENT

Task 2.1: Create physics-based, battery electric truck model

The UMN team has developed three separate vehicle models to use in conjunction with machine learning algorithms in the i-EMS. All three models, which include baseline models for HEB and Murphy trucks as well as the Volvo BEVs, will require parameter tuning using the practical driving cycles to validate their accuracy. Each model estimates the power required throughout a drive cycle based upon the vehicle velocity and acceleration as well as the road inclination. Vehicle parameters include the rolling resistance and drag coefficients, wheel radius and inertia, and the overall efficiency from engine or battery to wheels. The mass of the vehicle and auxiliary energy (i.e., from HVAC) may vary over the course of a trip. Finally, the Volvo BEV model includes an extra regenerative braking efficiency term incorporated in the friction loss calculation. The equations for the model power computations are shown below. The engine power is discounted for parasitic losses, and the battery power is a function of the current, internal resistance, and open-circuit voltage.

Baseline: $P_d(v, a, m, \theta) = P_{accel} + P_{ascent} + P_{drag} + P_{rr} + P_{inertia} + P_{fric} = P_{eng}\eta_{eng-to-wheels}$

$$P_{eng} = \tau_{brake}\omega_{eng} = (\tau_{eng} - \tau_{loss})\omega_{eng}$$

Electric: $P_d(v, a, m, \theta) = P_{accel} + P_{ascent} + P_{drag} + P_{rr} + P_{inertia} + P_{fric} = P_{bat}\eta_{bat-to-wheels}$

$$P_{bat} = V_{oc}I - R_{int}I^2$$

Task 2.2: Create initial machine learning

Combine the low-order physics model, battery information, utility demand charges and database parameters as inputs to a machine learning algorithm that will be used to predict energy use, operational energy cost, and battery performance for each duty cycle.

Code for three machine learning models has been developed and tested by the UMN team using data from a former project while awaiting data from Volvo. The first two models use the same feedforward neural network

(FNN) structure with different loss functions leading to different model outputs. Both FNN models output statistical values that help predict the probability of a vehicle needing to charge during a trip and the amount of charge needed to complete a trip. The first FNN model uses the negative log likelihood (NLL) loss function and outputs the mean and variance of the predicted total energy needed to complete a trip, while the second FNN model uses lower upper bound estimation (LUBE) loss function and outputs the expected lower and upper bounds of the energy usage needed to complete a trip with a certain interval coverage probability. Finally, a recurrent neural network (RNN) model using the rectified linear (ReLU) activation function was built that takes advantage of the temporal autocorrelation of the vehicle state of charge and predicts the expected energy needed to complete a trip much like the FNN NLL model. Model training inputs for all three NN models include time, velocity, state of charge, and GPS data from previous trips. Although NN models take a significant amount of time and data to train, the trained models make predictions extremely quickly and can be used for online range prediction.

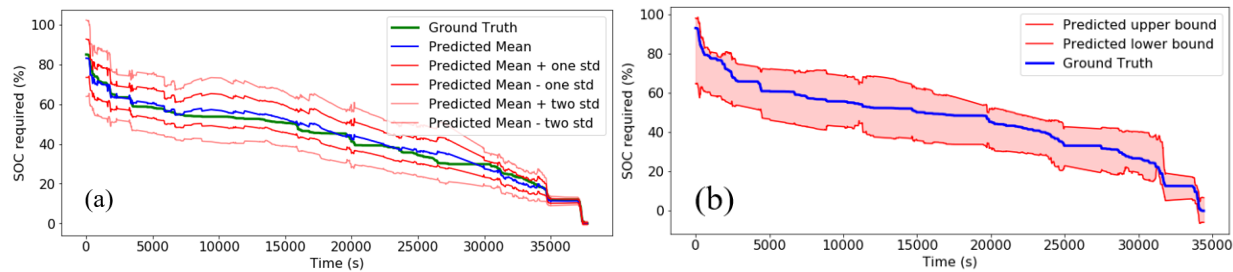


Figure II.1.8.1 FNN model trip predictions with (a) NLL loss function (b) LUBE loss function. Both models predict the amount of energy needed to complete a given route. The prediction uncertainty decreases at the end of trips as the vehicle data used to train the model has a consistent return trip energy usage pattern when vehicles return to a depot.

In addition to the above models, the UMN team is working on developing deep neural network (DNN) and reinforcement learning (RL) models which rely more heavily on the physical vehicle model to make predictions. Any combination of these models could be used by the i-EMS to help predict the on-route energy use and charging needs of electric vehicles. Following the introduction of Volvo driving data, the UMN team will likely alter the model inputs, but otherwise maintain the general model structure.

Formal methods of quantifying and classifying battery performance and operational energy cost have not yet been defined. Operational energy cost may depend on the time of day, which could influence the choice of when and how much to charge. Battery performance may be assessed for each driving cycle based upon how the ground truth energy consumption compares with the predicted value.

Task 2.3: Define locations for on-route charging

Subtask 2.3: - Develop energy-efficient routing and driving algorithms for use in demonstrator

The UMN team has received 27 trips worth of previous Volvo LIGHTS project data from a single vehicle that will be used to develop energy-efficient routing algorithms. The data was collected at 1Hz resolution, and each record contains 44 fields, including vehicle statuses, spatial location, as well as a timestamp. Figure II.1.8.2 shows a route traveled by the vehicle in one trip. Much of the route is composed of highway driving. By observing the maps of the routes of all 27 trips, the team found that the vehicle typically traveled along the shown route with minimal alterations.

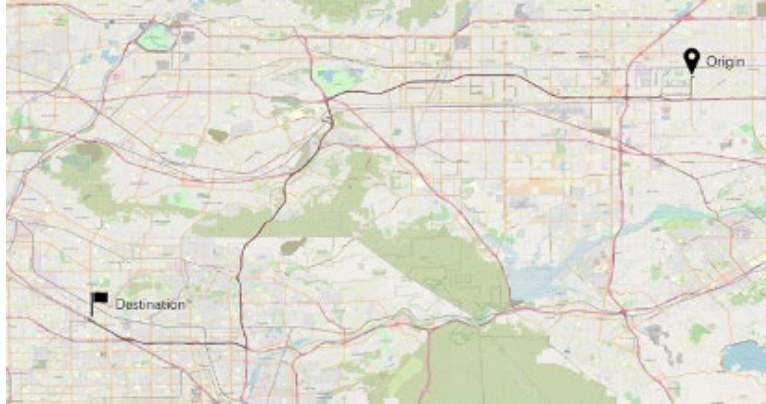


Figure II.1.8.2 A trip of the vehicle from which collected data.

The UMN team also explored the potential of predicting energy consumption as well as velocity profile in the future using historical data, which is a core component of the intended energy-efficient routing method. Figure II.1.8.3 shows the remaining vehicle energy for each round trip, with the vehicle charging at the origin each time. The energy consumption of each round trip was similar. Taking the first-round trip as an example, it is possible to split each trip into its two driving segments and a charge segment. In the first 4000 seconds, the truck traveled from the origin to the destination, and the energy reduced to about 160 kWh. Then, from 4000 to 10000 seconds, the vehicle returns to the origin and charges at the origin before repeating the cycle.

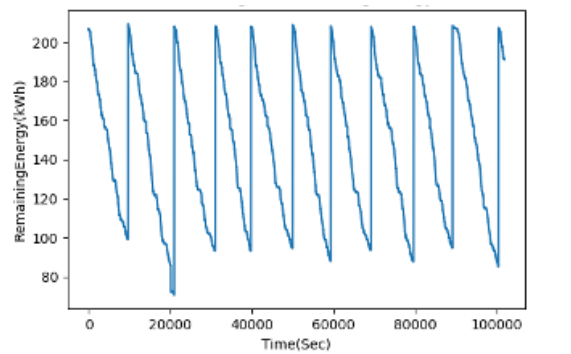


Figure II.1.8.3 Remaining energy of the vehicle along trips

The UMN team mapped the velocity profile of the first 2 round trips (Figure II.1.8.4 and Figure II.1.8.5). It was found when analyzing the data that most vehicle speed changes were due to infrequent but predictable traffic at highway on-ramps and intersections (highlighted by red circles). For a vast majority of road sections (e.g., highway sections), the vehicle speed tends to be stable. The results show that both energy consumption and velocity profile are potentially predictable.

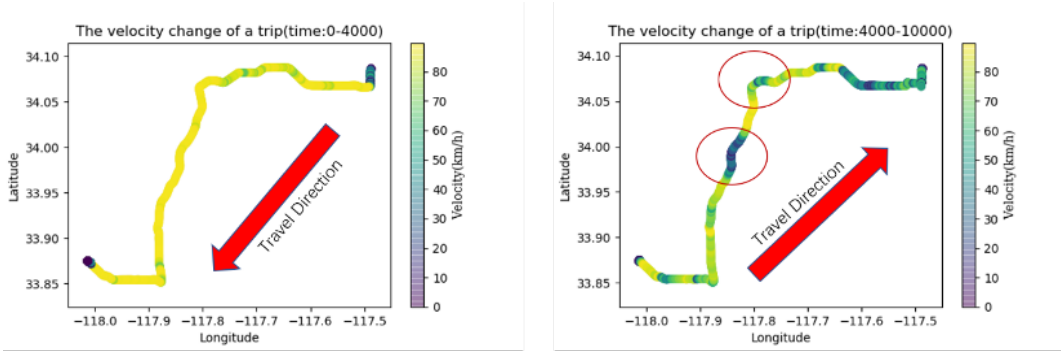


Figure II.1.8.4 The velocity profile of the first round trip

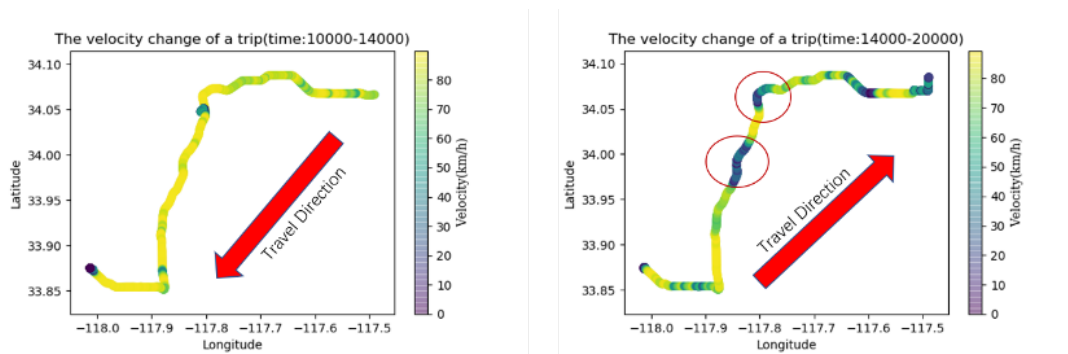


Figure II.1.8.5 The velocity profile of the second round trip

Task 2.4: Determine optimal on-route charging locations for fleets

Subtask 2.4 – Define on-route charging locations for demonstration: Define on-route charging locations for demonstration. The established routes at each operator, and other information from Task 1.2 will be analyzed to determine demonstration phase charging locations.

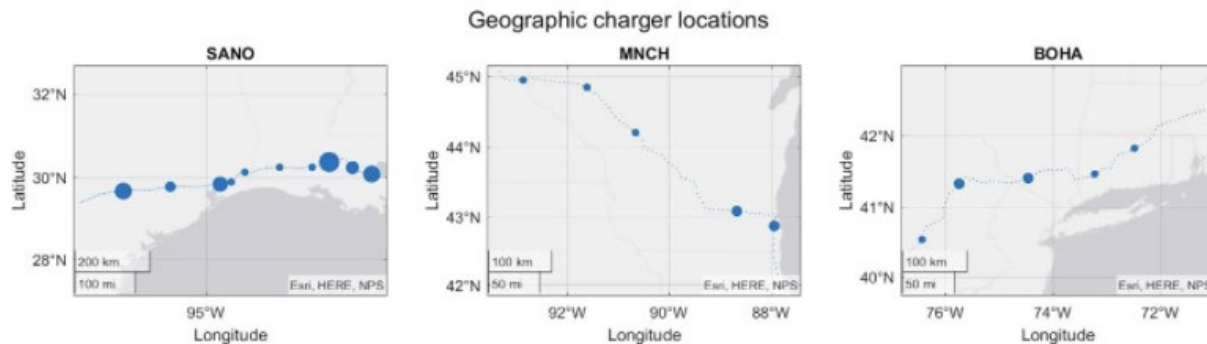


Figure II.1.8.6 Example optimal charger station placement output from genetic algorithm optimization. Locations and number of chargers were chosen along three common trucking corridors: (1) San Antonio, TX to/from New Orleans, LA, (2) Minneapolis, MN to/from Chicago, IL, (3) Boston, MA to/from Harrisburg, PA. The objective function considered local property costs, inter-charger distance, corridor trucking traffic, and expected charging wait times.

To optimize charger station locations for fleets of vehicles, the UMN team has developed a plan for simulating trucks on the road network according to driving data from the baseline vehicles. The formulation for optimization is as follows: Given the vehicle GPS data, the road network is discretized into an undirected graph structure with edges denoting parts of road segments. Road segments are assigned time and state of charge weights according to the driving data and charging stations can be placed at a constrainable subset of

nodes. In the simulation step, trucks are generated as agents on the road network according to historical driving data and navigate the same road segments according to the Volvo BEV model developed in Task 2.1. As the simulated trucks navigate the road network graph according to their routes, their states of charge are updated and the nodes in the road network at which trucks need to charge are monitored. When a truck needs to charge in the initial simulation, it is assumed that charging stations could be placed at any available node. The initial simulation then outputs the expected charging demand serviced by placing a charging station at each node on the road network, and the choice of charging stations is then formulated as a MIP optimization problem. The number of chargers to place is iteratively increased until all vehicles are expected to be able to complete their routes with minimal delays and/or budgetary constraints are exceeded.

Conclusions

Despite many challenges during the first phase of the project due to COVID-19, including delay of data-loggers, restricted travel, and loss of key personnel, this project has been able to move forward. The project team has protocols in place for the exchange of data. Progress is reviewed on a monthly basis with the project team and DOE.

II.1.9 Intelligent, Grid-Friendly, Modular Extreme Fast Charging System with Solid-State DC Protection (North Carolina State University)

Srdjan Lukic, Principal Investigator

North Carolina State University
1791 Varsity Drive
Raleigh, NC 27695
Email: smlukic@ncsu.edu

Steven Boyd, DOE Program Manager

U.S. Department of Energy
Email: steven.boyd@ee.doe.gov

Start Date: October 1, 2018

End Date: July 31, 2022

Project Funding: \$4,519,074

DOE share: \$2,008,326

Non-DOE share: \$2,510,748

Project Introduction

With the wider adoption of electric vehicles, there is an urgent need for an electric vehicle (EV) charging infrastructure that will parallel the refueling capabilities of existing gasoline stations, particularly in regions where long-distance trips are common. However, designing and deploying such an EV charging infrastructure is complex, and must consider competing industry standards, available technologies, grid impacts, and other technical and policy issues. With higher penetration of the EVs in the near future, the EV charging infrastructure will present itself as a substantial load and its impact on the power grid could be significant. Specifically, the additional load at a single point of interconnection can lead to feeder overload and voltage variations beyond the allowable limits along the feeder. Thus, any large extreme fast charger (XFC) installations should control their power factor to help mitigate the voltage deviations and should be able to curtail their loads in case of a contingency on the grid. Another issue is the availability of utility service at a selected XFC installation location. Feeding loads at hundreds of kilowatts requires new electrical service and significant infrastructure for the grid tie capacity, including step down transformers and metering. Co-locating multiple chargers allows for the costs associated with new service to be spread over multiple stalls and allows the station owners to take advantage of lower energy rates that may be available from the utility for large power consumers. This project aims to develop a framework for designing compact and efficient medium voltage (MV) XFC stations for electric vehicles that minimize the negative effect on the power grid, while also minimizing installation and operating costs of the system and providing design flexibility for the installers and system integrators.

Objectives

Our proposed solution is to design a novel XFC infrastructure that addresses many of the challenges associated with high-power charging requirements. The team will design a 1 MVA charger that connects directly to the MV distribution line. The system will consist of a solid-state transformer (SST) that delivers power to a shared DC bus, to which multiple vehicles and storage units connect (see Figure II.1.9.1). The system will be protected using novel intelligent solid-state DC circuit breakers. Each vehicle will interface to the DC bus through a DC/DC converter, allowing charging in the 50 kW to 350 kW range at the vehicle battery voltage. The innovations of the proposed concept includes an SST that connects directly to the MV line, a DC distribution network feeding multiple DC nodes, and an integrated energy management platform. Each component is described in detail below.

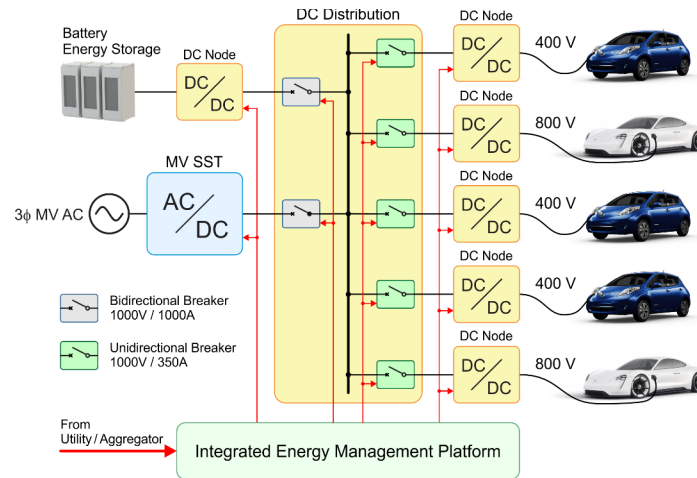


Figure II.1.9.1 System Layout showing the key components: MV SST, DC distribution network, and DC node that contains the DC/DC converter and vehicle interface

An SST that connects directly to the medium voltage (MV) line, without use of a step-down transformer, significantly reduces the system footprint and power conversion losses compared to the state of the art. The smaller footprint allows system installation in space-constrained areas, while significantly reducing installation costs. Higher power conversion efficiency reduces operating costs by delivering more of the input power to the vehicle. The MV SST allows bidirectional power flow and connects directly to the MV distribution grid, eliminating the need for a bulky and inefficient step-down transformer. The MV SST provides ancillary services to the grid to help mitigate power quality issues on its feeder. Key capabilities of the SST are its ability to control the power factor and provide for bi-directional power flow in response to a command from the utility. By controlling the power factor of the station, the MV fast charger not only compensates for its effect on the feeder, but also can help maintain a flat voltage profile along the feeder, resembling a capacitor bank's characteristics.

A **DC distribution network** allows for efficient, low-cost integration of storage with minimal number of conversion stages between the storage system and the vehicle battery. A key innovation of the proposed approach is the use of a shared DC bus and solid-state protection to supply multiple chargers from a single MV SST. Conventional solutions do not have the ability to share the same power electronics and route the power processing capacity to different stalls. A shared DC bus, on the other hand, naturally allows power sharing between all nodes. Furthermore, the shared DC bus allows for simple integration of storage or renewables directly to the DC bus, thus eliminating the costs and losses associated with the AC/DC conversion stage and simplifying the interconnection to the utility, since no separate utility-grade metering infrastructure is necessary.

DC Nodes using DC/DC converters enable optimal sharing of the available 1 MVA power between multiple vehicles, while reducing the number of power conversion stages. The system will efficiently serve state-of-the-art EVs at voltages below 500 V, at power levels up to 175 kW, while also delivering power to next-generation vehicles following emerging standards, where the vehicle battery operates at voltages up to 1,000 V, at power levels up to 350 kW.

The integrated energy management platform will allow the utility to take control actions including (1) curtailing power delivered to the station; (2) controlling the power ramp rates; and (3) controlling the XFC power factor or the reactive power injection into the grid. Further, the platform will optimally dispatch the available storage resources to satisfy vehicle-charging requirements. The team will deliver a centralized, integrated energy management platform that will communicate with the local storage, EVs, and the utility substation. The integrated solution will use commercial off-the-shelf products and microgrid controller

platforms that communicate with the utility substations. The integrated solution will allow for the optimal use of the available resources, dispatched by the charging station operator or directly by the utility.

Approach

The scope of this project is to demonstrate operation of the proposed MV fast charger in the field. The system will consist of a medium voltage (MV) solid-state transformer (SST) that delivers power to a shared DC bus, to which multiple vehicles and storage units are connected through DC/DC converters. The DC bus will be protected using novel intelligent solid-state circuit breakers. Each vehicle will interface to the DC bus through a DC node, which contains a correctly sized DC/DC converter, allowing charging at the vehicle battery voltage. The project will be conducted in three budget periods:

Budget Period 1 – Sub-system Development: This effort will evaluate the SST, DC node, and DC distribution network designs to optimize for reliability and maintenance simplicity, while keeping system initial cost low. The team will design, prototype and individually test the SST and the DC nodes that make up the 1 MVA XFC station. The team will prototype the DC circuit breaker and demonstrate its operation in the laboratory. The team will select a site and complete engineering drawings for the system deployment. The team will also develop a detailed use case and fault case test plan.

Budget Period 2 – System Integration: The team will finalize, package, and test the SST, DC node, DC distribution network and protection, and integrated energy management system. The systems will be fully tested in the lab prior to deployment to ensure that the system operates as expected. The site preparations will be completed to prepare the site for system deployment.

Budget Period 3 – System Deployment and Demonstration: The integrated 1 MVA XFC will be shipped to the site and commissioned. The team will demonstrate the use case scenarios and fault scenarios outlined in the test plan and develop a comprehensive operations and maintenance manual.

Results

The focus in FY2020 has been on the design, development and initial prototyping of the solid-state transformer and the solid-state DC breakers. In addition, the team completed the site engineering drawings based on which a site construction bid package can be issued. The team faced significant setbacks due to the covid-19 outbreak, and subsequent shutdowns of facilities throughout North Carolina and New York. At NC State University, the university was shut down on March 15, and no researchers were allowed to enter the laboratory until June, when restrictions were gradually lifted. Currently, the state of North Carolina is still in a “Phase 3” of reopening, and the impacts on the work progress have been significantly reduced. The team is working around these restrictions to keep the project timeline on track, and current projections are that no additional time delays will occur.

Solid state transformer (SST) design, development and construction

A key deliverable for FY2020 was to demonstrate the viability of the medium voltage (MV) solid state transformer (SST) implementation proposed in the project plan. The team has made significant steps toward reaching this goal. The team finalized the SST topology and has selected the suppliers for all key long-lead-time components, including the isolation transformer and the silicon carbide switching devices.

The selected SST topology is modular and consists of six *levels* which are stacked in input-series output-parallel (ISOP) configuration (see Figure II.1.9.2). The series connection on the input allows for the connection of the system directly to the medium voltage line at 13.2kV ac line-to-line. Each *Level* is made up of three identical *modules*, where each *module* connects to one of the lines of the three-phase system. Each module consists of an active front end (AFE) and an isolated DC/DC stage. The MV ac side forms the well-known cascaded H-bridge topology (implemented by a 5-level flying capacitor topology), while the isolation stage uses the dual active bridge topology (DAB). To minimize the number of modules on the high voltage side, we use the full-bridge neutral-point clamped (NPC) topology for the DAB on the high-voltage (HV) side while we

use a standard bridge on the low voltage (LV) side of the converter. A centralized controller coordinates the AFEs in all modules.

Decentralized control of DAB stage uses only local measurements, thus simplifying the overall system control and coordination. Input line filter and output capacitor size is significantly reduced by using an interleaved modulation of AFEs (six interleaved AFEs in each phase of U, V, and W), and interleaved modulation of low-voltage side bridges of DABs. As mentioned earlier, the DABs are designed to for sinusoidal power flow: three DAB outputs (phases U, V, W) in each level generate DC power. This results in minimized energy storage requirements on MVDC (2kV) bus, reducing the size of the medium voltage capacitors. Our approach is to control the DAB to act as a DC transformer meaning the voltage on the LV side of the DAB will always be proportional to the voltage on the HV side of the DAB. Since all DABs are connected in parallel on the output, they share a common output dc voltage which can be measured by all DABs. As a result, if each DAB maintains the MV DC bus voltage to be proportional to the LV DC bus voltage, all 18 MV DC bus voltages will be balanced. This approach is different from the state of the art, where the central controller regulates the MV bus voltages, requiring high bandwidth measurement of the 18 voltages by the central controller.

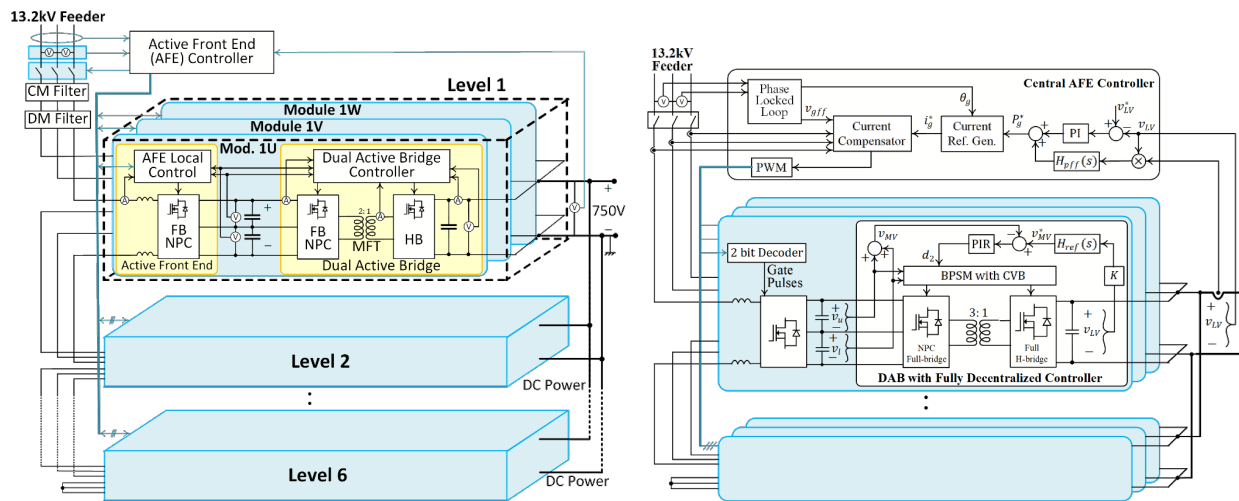


Figure II.1.9.2 MV SST Converter topology. The SST is made up of 6 Levels connected in input-series output-parallel configuration. The figure on the left shows the design of a single module with the active front end, followed by the dual active bridge topology. The figure on the right shows the details of the control approach. Each DAB is controlled using a fully decentralized controller that acts as a “DC transformer” mirroring the voltage measured on the low voltage side onto the high voltage bus. A central controller coordinates all 18 front ends to maintain a stable DC bus on the output

The central controller design is also shown in Figure II.1.9.2. As noted, due to the proposed design, there is no need for the central controller to regulate the MV bus capacitor voltages, thus reducing the communication requirements. Rather, the central controller regulates the output DC voltage using a proportional-integral (PI) controller and a feedforward term. A current compensator delivers a PWM signal to each active front end. Each active front end is treated as an H-bridge, allowing the state encoding with only two signals. In turn each AFE has its own local protection and decoding scheme.

Early in the project, the team designed a low-power prototype of three modules that make up one level of the SST. Following the validation at low power, the team completed the design and construction of the full-scale SST module prototype shown in Figure II.1.9.3. The system in Figure II.1.9.3 was designed to deliver 95kW continuously, which is 115% of the module rated power. The unit consists of an active front end (AFE), and the dual active bridge (DAB) which is made up of three components: the DAB medium voltage (MV) side, the high frequency transformer, and the DAB low voltage (LV) side. Each sub-system is described in more detail in what follows.

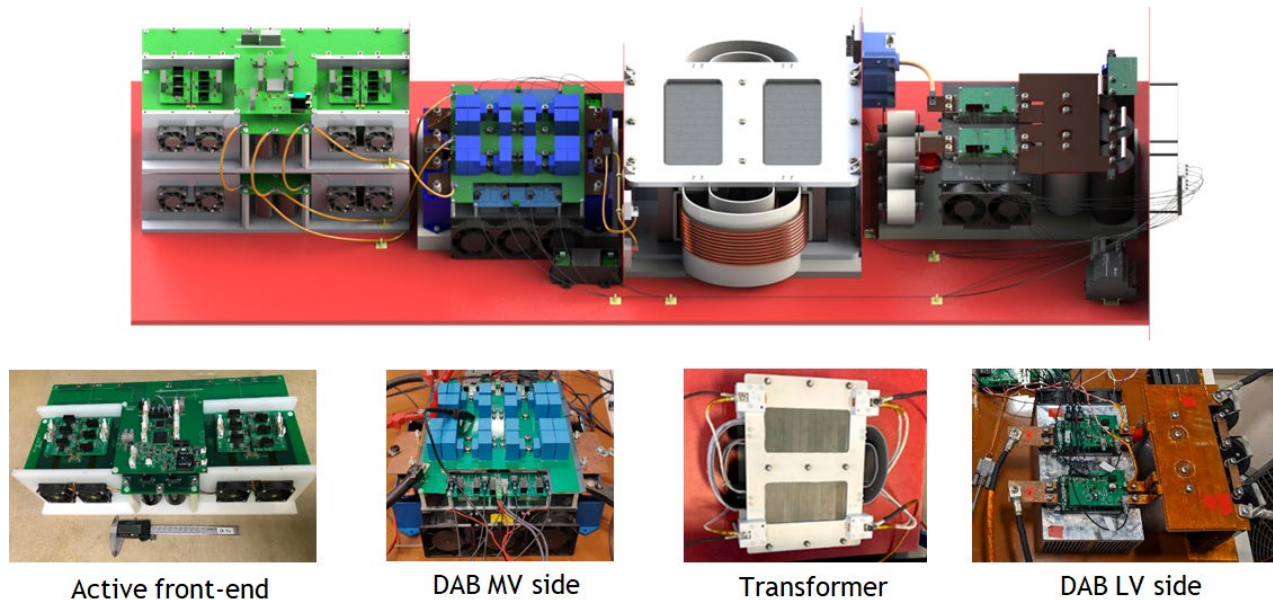


Figure II.1.9.3 Design and implementation of a single module of the solid-state transformer

The AFE stage is constructed out of a 5-level flying capacitor topology. The converter uses lower cost 1.2kV SiC devices in TO-247 package and connects to the 2.15kV MVDC bus. As noted, the six levels that make up the SST are connected in series on the input and in parallel on the output. As a result, the six AFEs in a single phase are connected in series. The AFE uses a hybrid solution to balancing the capacitors of the flying capacitor topology. Compared to the passive solution, the proposed hybrid solution has no requirement to fully charge and discharge for flying capacitors and exhibits reduced power loss and size on clamping circuits significantly. Compared to the active solution, the proposed hybrid solution significantly simplifies the gating sequence and eliminates the need of voltage sensing; therefore, a standard gate driver meets the requirements.

The DAB topology uses an all SiC solution with 1700V modules on MV and 1200V modules on LV side. The switching frequency is 20kHz, and the module outputs are interleaved to on the LV bus to minimize the storage requirements. A proportional-integral-resonant (PIR) compensator eliminates second harmonic power oscillations on the MV DC bus. A bidirectional phase-shift modulator (BPSM) with capacitor voltage balancing (CVB) generates the gate pulses for the primary and secondary bridges of the DAB.

The transformer designed at NCSU is shown in Figure II.1.9.3. To meet the challenging design requirements the design approach relies on winding separation in air to meet isolation requirements, and reinforced isolation between windings and core. Further the design is compatible with transformer insertion in oil and uses relatively low flux in ferrite to minimize and distribute the produced heat and to ensure operation in linear range. The thermal performance of the transformer was validated in ANSYS, and in hardware, while the partial discharge performance was tested in simulation; the partial discharge testing in the laboratory is now ongoing. In addition, the team is also looking for external supplies for the transformer.

To test out the possible fault scenarios and fault isolation strategies, the team has done comprehensive system level simulations to test out various fault conditions. The simulations consider system startup and system shutoff as well as various fault conditions. In addition to the step load change simulations, the team has done comprehensive simulations of the system startup and loss of load performance. Further, the system level controller has been designed to monitor and report a number of faults at the component level up to the system level for coordinated action (i.e., shutdown) and for easy debugging.

The team fully validated the performance of the SST DAB module in closed loop. Figure II.1.9.4 shows the dual active bridge under testing in the lab at 95 kW (115% of rated load). As noted, all components are thermally stable, and the peak temperature measured on the setup was below 70 degrees Celsius. The system efficiency is measured at 98.9%, which agrees well with the simulations.

Next steps involve the design of six such modules to build and demonstrate a 500kVA system in the lab. Following successful demonstration of the system at half power, the team plans to develop a second prototype rated at the full 1,000kVA with emphasis on system packaging for eventual field testing. We note that future work is contingent on funding availability.

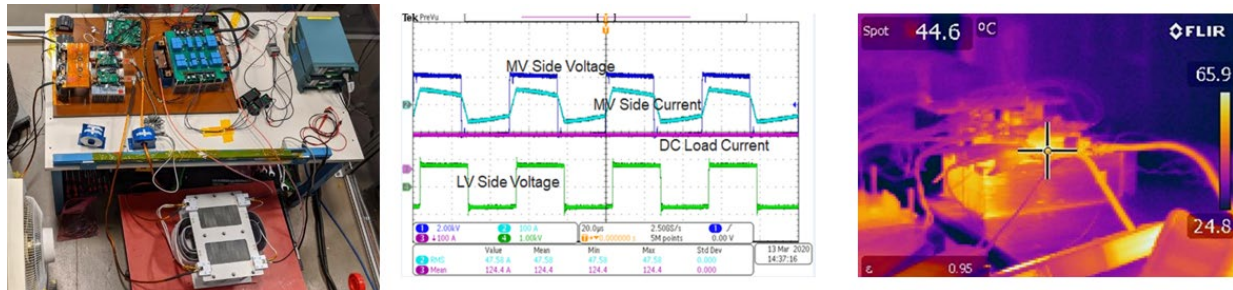


Figure II.1.9.4 (Left) Dual active bridge under test in the lab (middle) waveforms captured showing the MV and LV side voltages and currents. The waveforms show a small voltage overshoot on device drain-to-source voltage (Right) Thermal image of the setup while in operation. The peak temperature measured on the setup was below 70 degrees Celsius.

Development of solid-state breakers

The team worked on specifying the protection system requirements for the solid-state switchgear design. ABB has completed the topology and design on the DC circuit breakers that are needed for the protection and coordination of the DC distribution system for the XFC. ABB has completed the prototyping phase and has partially validated the design of each single breaker design. The team completed tests on both breaker poles for short circuit current interruption and nominal current temperature rise. Moreover, ABB completed the first stage of the system and protection simulation study that helped defining the requirements for the circuit breakers design and fault protection and coordination electronics. The next steps will involve comprehensive prototype testing.

The team started developing the DC switchgear and two Solid State DC Circuit Breaker (SS DCCB) sizes (one rated at a nominal current of 1500 A and one rated at 500 A). The 1500 A class SS DCCB will be used as main circuit breakers, one connecting the power from the main power source (SST) and another connecting the battery energy storage system. The 500 A class SS DCCB is a unidirectional breaker that will be used as branch circuit breaker for the protection of the cables transferring power to the SST to the DC/DC converters and protect against short circuit and grounding faults.

The team has identified the system-level requirements and has defined the technical requirements for the two types of circuit breakers to be designed. Further, the team completed the initial system protection and coordination simulation; made progress on designing the control board platform for the detection of high di/dt short circuit faults and protection coordination. Fault scenarios under investigation listed below and correspond to locations in Figure II.1.9.5:

- (1) Fault at the output of the SST
- (2) Fault at the output of the BESS DC-DC converter
- (3) Fault at the DC bus (within the switchgear cabinet)
- (4) Fault on one of the charger branch, just after B2 breaker (high di/dt fault)

- (5) Fault on one of the charger branch, near the input of the charger DC-DC converter (lower di/dt fault compared to 4)

The fault cases will consider system variances to include different output/input filter capacitances, unidirectional vs bidirectional B2 breakers and different cable impedances.

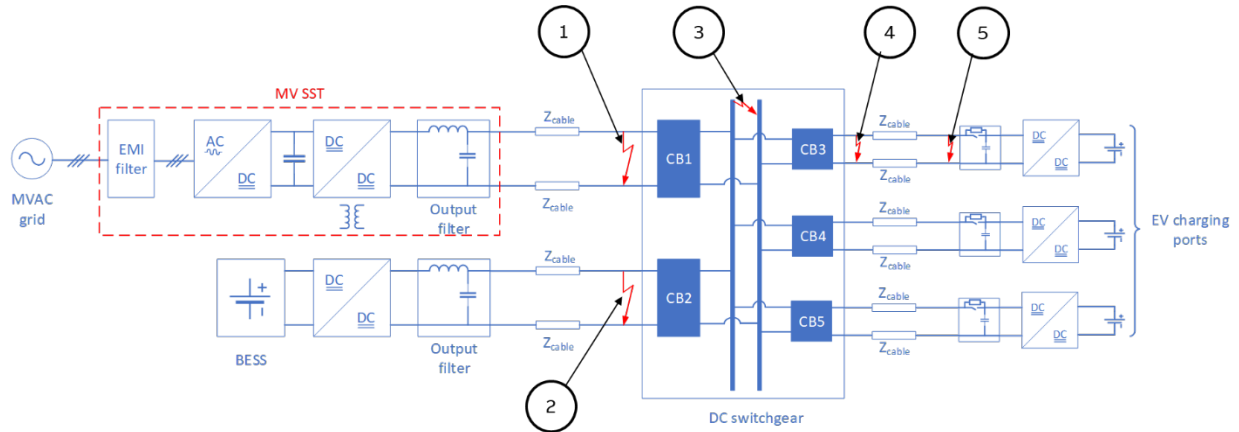


Figure II.1.9.5 Fault scenarios under investigation.

The team developed two types of cooling systems that were optimized for the two circuit breaker classes. One of the cooling systems is based on an advanced thermosyphon, a two-phase cooling method dissipates large amounts of heat making it well-suited for the 1500 A class and enables high power density. The main benefits of the advanced thermosyphon design include (1) High Power Density (-60% volume reduction, -50% weight reduction compared to air heatsink) (2) Simplicity of Air-cooled solution and (3) Performance similar to liquid cooling but with less auxiliaries and maintenance. The cooling elements were designed for following requirements (1) Thermal loads up to 750 W per cooler, design target $R_{th} = 0.067$ K/W, with $\Delta T < 50$ K, at 40°C intake temperature and (2) Heat flux up to 20 W/cm². Figure 6 shows the assembled prototype of 1500 A solid state DC circuit breaker, including the thermosyphon cooling design. The cooling system performance has been experimentally validated on a full-scale prototype.

The other cooling system is based on forced-air heat sinks designed for double side cooling of the power semiconductors. This cooling system is robust and economical, and it fits well the requirements of the 500 A class SS DCCB. Advantages of forced air-cooling for 500 A include the simplicity and low cost of air-cooled solution and the ability to reduce the footprint for 500 A breaker (<50% volume compared to 1500A breaker). The cooling elements were designed for following requirements: (1) air flow validation for 500 A and overload conditions; (2) Thermal loads up to 250 W per heat sink, design target $R_{th} = 0.2$ K/W, with $\Delta T < 50$ K, at 40°C intake temperature; and (3) Heat flux up to 10 W/cm². Figure II.1.9.6 shows the assembled prototype of 500 A solid state DC circuit breaker, including the forced-air heat sink cooling design. The cooling system performance has been experimentally validated on a full-scale prototype.

The team designed, simulated, and manufactured a mixed signal electronic circuit for fast detection circuit of high di/dt faults and for protection coordination. The control circuit was designed for fault detection in less than 10 μ s for up to 500A/ μ s. The mixed signal solution has the robustness of digital filters and logic and the speed of analogue circuits. The fast short circuit detection will enable protection coordination for systems with high power converters penetration, like EV charging infrastructures.

The team manufactured the cooling system for SS DCCB B1 and the mechanical design of the internal bus bar connections, the custom 40kN mechanical clamp for the bidirectional stack, and the mechanical support structures. The team also designed and manufactured the samples of power stack for the SS DCCB B2 based on the selected and validated cooling elements. The team designed the mechanical support structures and bus

bar connections for the galvanic isolation switch and the metal oxide varistors for SS DCCB B2. Figure II.1.9.6 shows the inside view of the first assembled prototype for the 1500 A SS DCCB B1 and the 500 A SSDCCB B2 breakers.

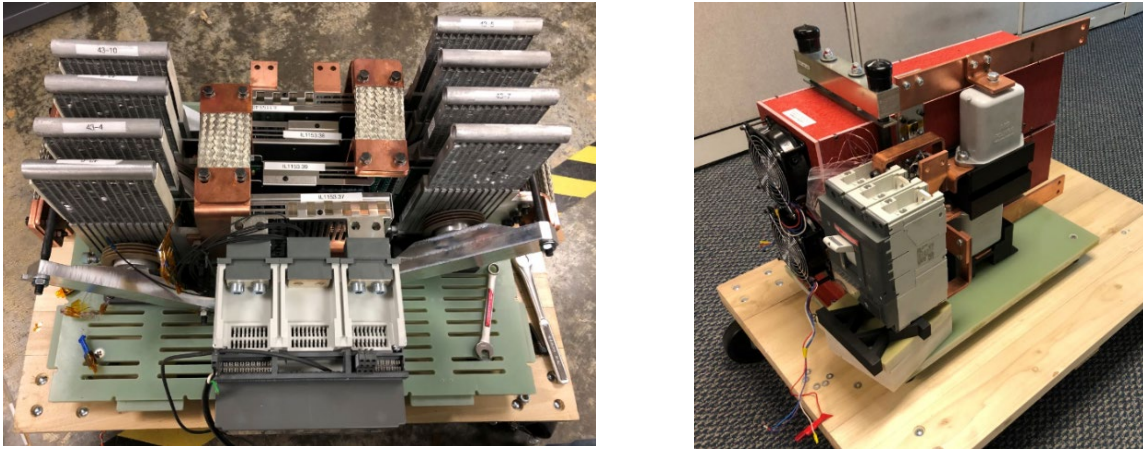


Figure II.1.9.6 (Left) Assembled prototype of 1500 A SS DCCB B1 (inside view); (Right) Assembled prototype of unidirectional 500 A SS DCCB B2 (inside view).

The team also proposed the initial mechanical and thermal design of the enclosure for the DC switchgear that will house the SS DCCBs. Input on the high-level design and footprint of the DC switchgear was provided for the first assessment of the demo site identified by the team.

The team at ABB has started testing the protection coordination between the assembled prototypes (SS DCCB B1 and B2). This is important, to validate that in the case of a fault event, only the breaker in the fault branch is selectively tripped and the rest of the system can continue operation, ensuring a high system availability. As part of the initial tests, faults at locations 3, 4 and 5 (from Figure II.1.9.5) have been emulated in the lab with higher levels of system inductances ($L_{\text{sys}} \sim 300\mu\text{H}$) and breaker coordination has been successfully verified. In the next steps, tests at other fault locations will be conducted and the system inductances will be progressively lowered to validate the settings and performance of the control electronics.

Site selection and site preparation for deployment

Working with NYPA, the team identified the feeder that will supply the proposed charging station at a location at the Clark Energy Center in Marcy, New York. The selected deployment site meets the project requirements, since the location has a dedicated space for the installation of the medium voltage extreme fast charger and medium voltage service to the location. The NYPA team and their subcontractors have completed detailed engineering drawings by taking input from all stakeholders including NCSU, ABB, and the site engineers at the deployment site. The bid package was completed at the end of Q4 of 2020, and the site preparation is expected to be completed in early 2021. The site preparation will consist of installing MV switchgear that will allow for the entire XFC site to be energized or isolated from the grid. In addition, the contractors will install Trenwa trenches that will route power to the SST and the individual charging ports and insert the appropriate cabling into the trenches. Once this work is complete, the site will be ready for the equipment to be delivered, at which point the contractors will make the necessary connections to the power supply at the site.

Conclusions

In FY20, the project team has made significant progress in all key aspects of the XFC station design. The team has constructed a full-scale module prototype of the solid-state transformer and has validated the control approach both in simulation and in hardware. The team has made significant progress in developing the DC solid-state breaker and has completed the initial prototype of both the 1500A and 500A breaker prototypes. In addition, the team completed a number of system-level protection coordination studies, which will drive the

design of the DC distribution system. Finally, the team has completed the detailed engineering drawings for the system site and has issued a bid package for the site preparation work to begin in early 2021.

Key Publications

1. H. Tu, H. Feng, S. Srdic and S. Lukic, "Extreme Fast Charging of Electric Vehicles: A Technology Overview," in *IEEE Transactions on Transportation Electrification*, vol. 5, no. 4, pp. 861-878, Dec. 2019.
2. M.A. Awal, I Husain, Md R. H. Bipu, O. Montes, F. Teng, H. Feng, M. Khan, S. Lukic "Modular Medium Voltage AC to Low Voltage DC Converter for Extreme Fast Charging Applications", arXiv preprint, submitted June 2020, arXiv:2007.04369
3. M.A. Awal, Md. Bipu, O. Montes, H. Feng, I. Husain, W. Yu and S. M. Lukic, "Capacitor Voltage Balancing for Neutral Point Clamped Dual Active Bridge Converters", in *IEEE Transactions on Power Electronics*, vol. 35, no. 10, pp. 11267-11276, Oct. 2020.
4. L. Qi, P. Cairoli, Z. Pan, C. Tschida, Z. Wang, V. R. Ramanan, L. Raciti, A. Antoniazzi, "Solid-State Circuit Breaker Protection for DC Shipboard Power Systems: Breaker Design, Protection Scheme, Validation Testing" in *IEEE Transactions on Industry Applications*, Vol. 56, No. 2, March-April 2020
5. Dakai Wang and Wensong Yu, "Series Connection of SiC MOSFETs with Hybrid Active and Passive Clamping for Solid State Transformer Applications," presented at *2019 IEEE 7th Workshop on Wide Bandgap Power Devices and Applications (WiPDA)*, Raleigh, NC, October 2019.
6. S. Chen, M. Bipu, D. Wang and W. Yu, "Analysis and Solution of the Unbalanced Device Voltage Issue for SiC MOSFET Based Diode Neutral Point Clamped Converter," presented at *2020 IEEE Applied Power Electronics Conference and Exposition (APEC)*, New Orleans, LA, USA, March 2020
7. MA Awal, Iqbal Husain, Md Rashed Hassan Bipu, Oscar Andreas Montes, Fei Teng, Hao Feng, Mehnaz Khan, Srdjan Lukic, "Modular Medium Voltage AC to Low Voltage DC Converter for Extreme Fast Charging Applications" *arXiv preprint* arXiv:2007.04369

II.1.10 Enabling Extreme Fast Charging with Energy Storage (Missouri S&T)

Jonathan Kimball, Principal Investigator

Missouri University of Science and Technology
301 West 16th Street
Rolla, MO 65409
Email: kimballjw@mst.edu

Sam Gillard, DOE Technology Manager

U.S. Department of Energy
Email: samuel.gillard@ee.doe.gov

Start Date: October 1, 2018	End Date: September 30, 2022	
Project Funding: \$963,100.98	DOE share: \$382,422.88	Non-DOE share: \$580,678.10

Project Introduction

This project aims to advance electric vehicle (EV) adoption by enabling widespread deployment of charging stations that can re-charge an EV in a time similar to refueling a conventional vehicle. The proposed work will create and demonstrate an extreme fast charging (XFC) station that operates at a combined scale exceeding 1 MW while mitigating grid impact with smart charging algorithms and local energy storage. An active front-end (AFE) will connect directly to a distribution feeder and provide reactive power support and harmonic compensation.

The station will incorporate high-frequency transformers instead of conventional low-frequency transformers for isolation, thereby reducing size. A stationary battery will be used to buffer power transients due to charge initiation and termination. The complete station will be coordinated by a high-level controller that uses information gleaned from distribution network analysis to ensure grid compatibility.

There are three basic challenges: power conversion at 1 MW from a medium-voltage (12.47 kV) source; grid compatibility between this large, dynamic load and a wide range of possible distribution networks; and battery charging at high rates (beyond 5C) with minimal degradation. Battery charging algorithm development must account for the internal construction of the cells, modules, and pack, and also requires innovation in the pack design.

Objectives

The high-level objective of this project is to demonstrate a complete XFC station, capable of charging three vehicles at 350 kW each, with local energy storage to mitigate active power transients and station control to ensure grid compatibility. The station will connect to a 15-kV-class network (e.g., 12.47 kV three-phase). The objective for the budget period that began in FY 2019 and continued through FY 2020 is to develop a sub-scale version of the station.

For the power conversion aspect, the objectives are to develop a laboratory-scale power converter, with 1/10th voltage, 1/10th current, and 1/100th power ratings (1247 V input, 10 kW); to develop a converter control system that coordinates the grid input (AFE) and high-frequency isolated dc-dc converter; and to explore alternative topologies, components, and construction methods.

For the grid compatibility aspect, the objectives are to obtain network data for the demonstration site; to analyze static and transient requirements considering only local impacts; to construct a simulation of the distribution network; and to derive specifications for the XFC station, considering grid compatibility.

For the battery aspect, the objectives are to create a single-particle model of the target lithium-ion cells that incorporates degradation models; to derive optimal charging algorithms; to validate the algorithms experimentally; and to design and document a complete vehicle pack for later testing.

In future budget periods, contingent on funding, these separate aspects will be integrated, the power and voltage level will be scaled up, and the system will ultimately be demonstrated at a field site.

Approach

The overall XFC station architecture is illustrated in Figure II.1.10.1. The station comprises a multi-level AFE, a multi-phase dc-dc converter with isolation, multiple non-isolated dc-dc converters to provide charging ports, and a bidirectional dc-dc converter that connects to a fixed battery (energy storage system, or ESS).

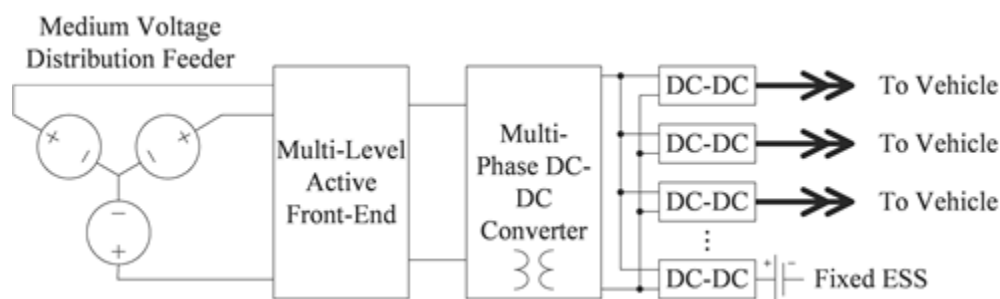


Figure II.1.10.1 Block-diagram schematic of the XFC station.

The project has three main thrusts: grid interaction optimization; power conversion; and battery charging algorithms. In FY 2020, grid interaction optimization has included both control algorithm development for voltage regulation and constrained economic optimization (mixed integer nonlinear programming) for longer time-scale control. The power conversion thrust has developed low-power, low-voltage subsystems in hardware and explored multiple control algorithms to manage the multiple stages and time-scales in operation. The battery charging algorithm thrust has developed control-oriented degradation models and two qualitatively different algorithms, with experimental validation on coin cells.

Results

Grid Interaction Optimization

The XFC station must ensure that the local distribution network voltage stays within specifications. An algorithm has been derived that combines reactive power control and active power buffering to accommodate a wide range of operating conditions. Figure II.1.10.2 illustrates the impact of the proposed algorithm as three vehicles arrive and are charged. Case 1 has no voltage control. Case 2a has reactive power control. Case 2b has both reactive power control and active power buffering and is the method that will be used in the final demonstration station. This control method is appropriate over intermediate time scales, on the order of seconds.

The XFC's ESS provides additional flexibility over longer time scales, on the order of hours. The ESS will have a certain power (kW) and energy (kWh) rating. Depending on the time-varying price of electricity, the cost of the ESS, and the vehicle charging load, there may be an opportunity for price arbitrage (charging the ESS during low-cost times, discharging during high-cost times). When ESS degradation is incorporated, a mixed integer nonlinear programming model must be solved. S&T researchers used CONOPT in AIMMS to solve the problem and perform sensitivity analysis.

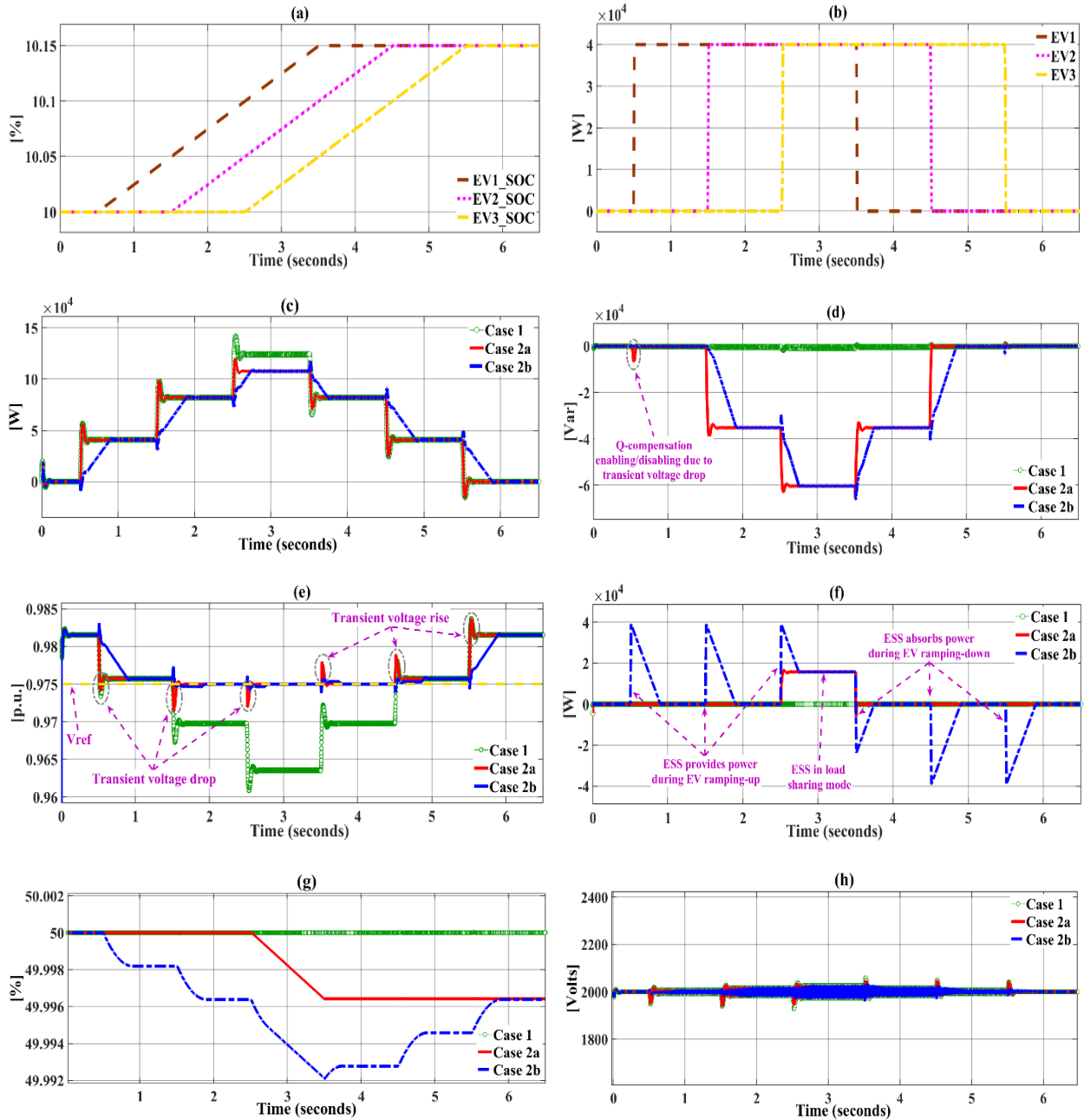


Figure II.1.10.2 Case study results: (a) EVs SOC variation, (b) EVs load, (c) measured active power at PCC (d) measured reactive power at PCC (e) PCC voltage, (f) ESS power, (g) ESS SOC variation, (h) DC link voltage.

Missouri S&T researchers performed a case study to obtain the optimal ESS power and energy sizing and optimal energy management for the XFC station. The input parameters to run the simulations are presented in Table II.1.10.1

Table II.1.10.1 Simulation parameters for ESS optimization.

Parameter	Value	Parameter	Value
ESS technology	Li-ion	ESS Efficiency	0.98
ESS power rating cost [\$/kW]	300	AC/DC Conversion efficiency	0.95
ESS annual O&M cost [\$/kW]	-	Project Lifetime [years]	10
ESS energy rating cost [\$/kWh]	695	Optimization horizon [years]	1
ESS installation cost [\$/kWh]	3.6	interest rate [%]	4
ESS Energy to Power ratio γ^{\min} , γ^{\max}	1, 8	Simulation time step [h]	1/60

The power demand for the charging station under study is taken from literature and modified for a charging station with 5 charging ports, each rated at 200 kW. In addition, the calculated daily average charging station demand and hourly electricity prices are assumed to be the same for each day of the year. Figure II.1.10.3(a) presents the hourly electricity prices and energy demand of the station for a typical weekday and weekend day. The hourly electricity price signal and ESS parameters are taken from literature. Figure II.1.10.3(b) presents the optimal energy management of the charging station and the SoC variations of the ESS. When the electricity prices are lower, for approximately the first 240 minutes, the ESS stores energy and later discharges it to satisfy the charging station demand for the peak price periods, between 12:00 and 17:00 hours.

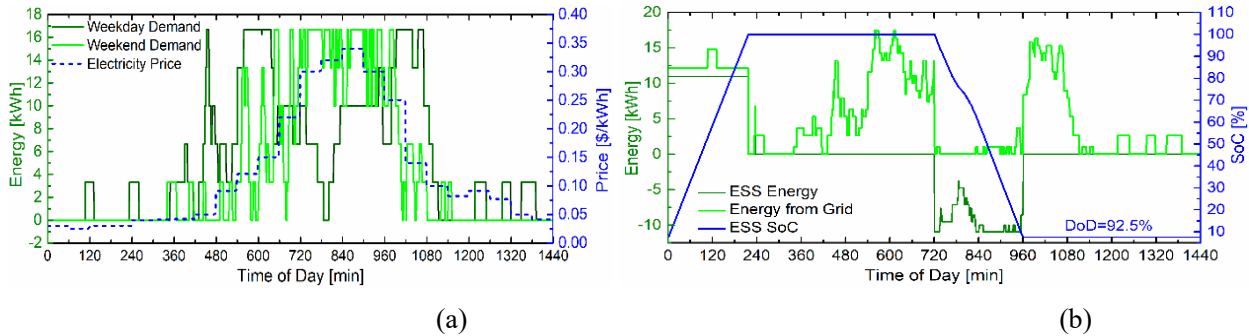


Figure II.1.10.3 (a) Charging station demand and electricity price. (b) Energy from distribution grid, ESS charging and discharging energy, and ESS SoC.

Given the aforementioned parameters, the optimal power and energy ratings of the ESS are 657 kW and 2511 kWh, respectively. Moreover, the optimal DoD and ESS cycles are 92.5% and 338 cycles per year, respectively. Therefore, SoC of the ESS is limited between 7.5-100%. With the consideration of ESS degradation, the optimized results make sure the ESS does not reach End of Life (EOL) in 10 years and therefore does not need to be replaced within the project lifetime. Furthermore, a simulation is also run for the case without considering the ESS degradation, which results in optimal power and energy sizing of the ESS to be 714 kW and 2800 kWh, respectively, with an optimal DoD of 100% and ESS cycle rate of 375 cycles per year. However, in this case the ESS will reach its EOL after ~7.2 years and will need to be replaced, thus incurring extra cost.

Next, sensitivity analyses were performed as many factors affect the optimal operation and cost-effectiveness of the ESS. The key parameters that were explored were the allowed number of ESS cycles per year, the cost of electricity, and the capital cost of the ESS. Results are shown in Figure II.1.10.4.

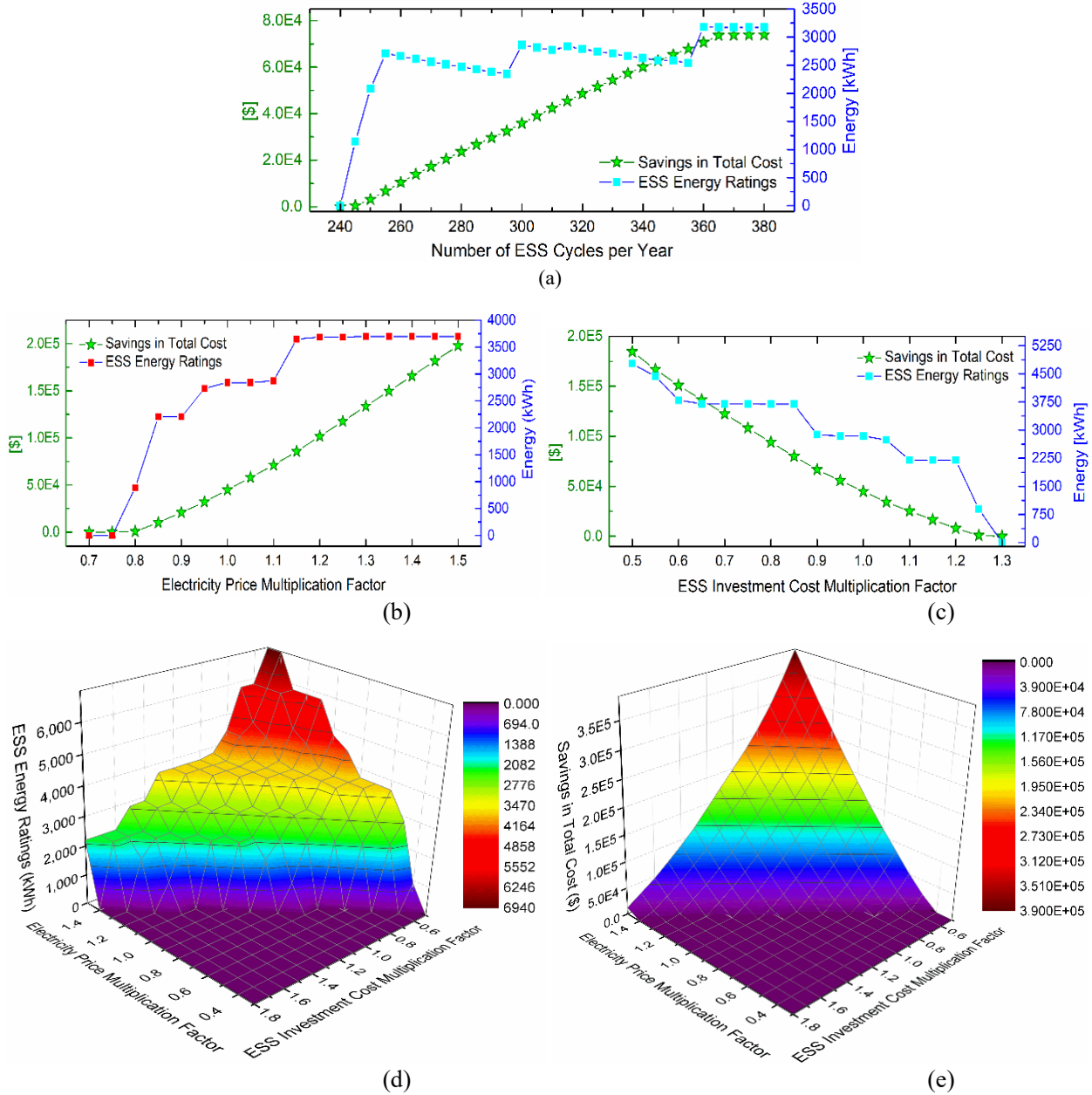


Figure II.1.10.4 Sensitivity analyses on ESS energy sizing and the savings in total cost; (a) Impact of varying the allowed No. of ESS cycles; (b) Impact of varying electricity price; (c) Impact of varying the ESS investment cost; (d-e) impact of both electricity price and investment cost on ESS energy sizing and the savings in total cost respectively

Power Conversion Subsystem

The overall structure of the system is shown in Figure II.1.10.5. The high-side board for modular HF isolation converters was designed and developed earlier. This board consists of 4 IGBTs operating as a part of the cascaded H-bridge inverter. Each of these IGBTs are rated at 1200V, 30A. On the output, there are 4 more IGBTs to drive the HF transformer. Gate signals are delivered using 8 optic fibers. The module DC link consists of 4 electrolytic capacitors in 2-parallel-2-series configuration as well as a film capacitor to achieve a rating of 1200 Vdc. An isolated 12 V dc input is needed to power this board. The hardware prototype is shown in Figure II.1.10.6. Design specifications are given in Table II.1.10.2.

Table II.1.10.2 Low-power hardware parameters.

	Project's goal	Extended goal
Overall Rating	1/10 th Current	1/5 th Current
	1/10 th Voltage	1/2 nd Voltage
	1/100 th Power	1/10 th Power
	With respect to the full system	With respect to the full system
Switching Frequency	4 kHz	40 kHz
Number of Cascaded-H-bridges per Phase	7	7
Input Voltage	1250 Vac RMS	6,250 Vac RMS
Output Voltage	100 Vdc	550 Vdc
HF DC Link Voltage	180 Vdc	900 Vdc

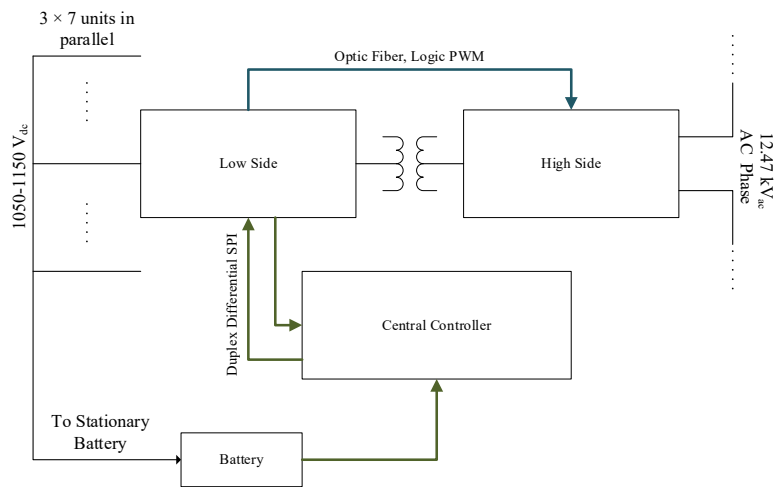


Figure II.1.10.5 Overall structure of the system.



Figure II.1.10.6 Low-power hardware prototype.

Output of this PCB is connected to a 2:1 transformer being developed by MPS magnetics in Texas as a planar transformer structure with $\frac{1}{2}$ secondary – primary – $\frac{1}{2}$ secondary configuration on a split core filled with resin rated for 15 kV isolation between the windings. This forms an 800:400 transformer at 15 A RMS at the primary.

The low-side controller has been designed and populated (shown in Figure II.1.10.7). This controller has the 4 low-side switched on the output of the transformer rated at 1200V, 50A. Also, a TI DSP handles the local control, driving the low/high-side signals, and communication. Additionally, an isolated voltage measurement circuitry to measure the floating high-side voltage is implemented on this board.

A partially-assembled low-voltage prototype system is illustrated in Figure II.1.10.8. The central phase controller controls all of the modules in a single phase of the three-phase system.



Figure II.1.10.7 PCB board of the low-side controller.

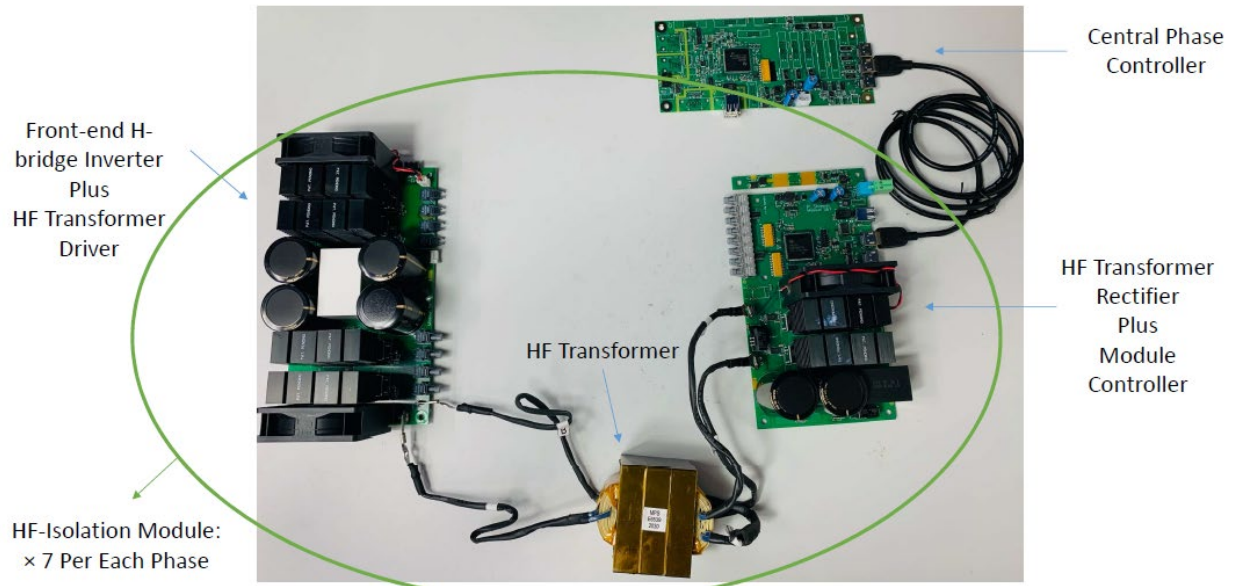


Figure II.1.10.8 Overall connection of the system.

A heuristic dynamic programming (HDP) had been implemented in the previous phase of the project. The main advantage of the HDP technique, as a reinforcement approach, is its ability to adjust its parameters based on various operating conditions. Conventional HDPs include two subnetworks: (i) action network and (ii) critic network. The action neural network (NN) generates a set of control signals, and a critic NN evaluates the performance of the action network. To accurately model the relation between the performance of the system and the control signal generated by the action network, the system model is required. In the previous approach, the model of the system had been used to utilize the effect of the system dynamics. However, in this approach, a neural network was developed to perform as the system model. The implementation of the system's neural network overcomes the drawbacks regarding the unknown system or inaccurate system's parameters.

The MDHDP-based, grid-connected, virtual inertia-based inverter is illustrated in Figure II.1.10.9. As shown, there are three neural networks performing as action, critic, and model networks. The model NN predicts the state variables for the next time step to train the critic neural network. Experimental results given in Figure II.1.10.10 demonstrate the superior behavior of the HDP-based approach over a traditional synchronverter controller in response to active power step commands.

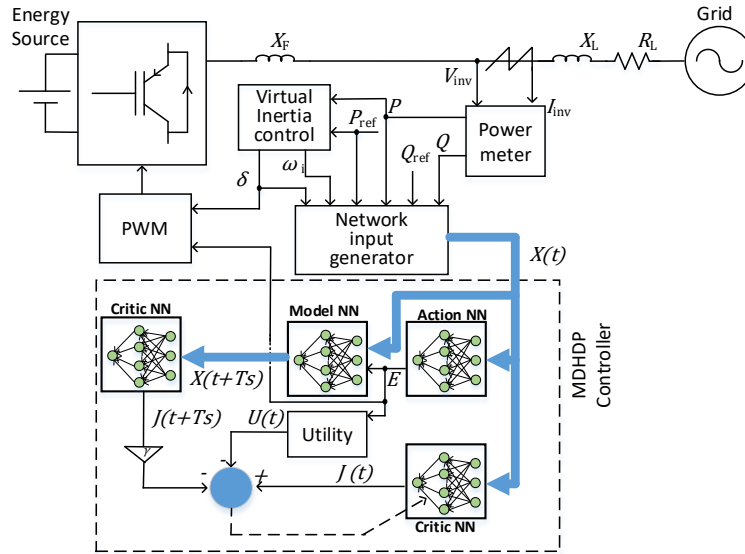


Figure II.1.10.9 Block diagram of the proposed MDHDP for VSG.

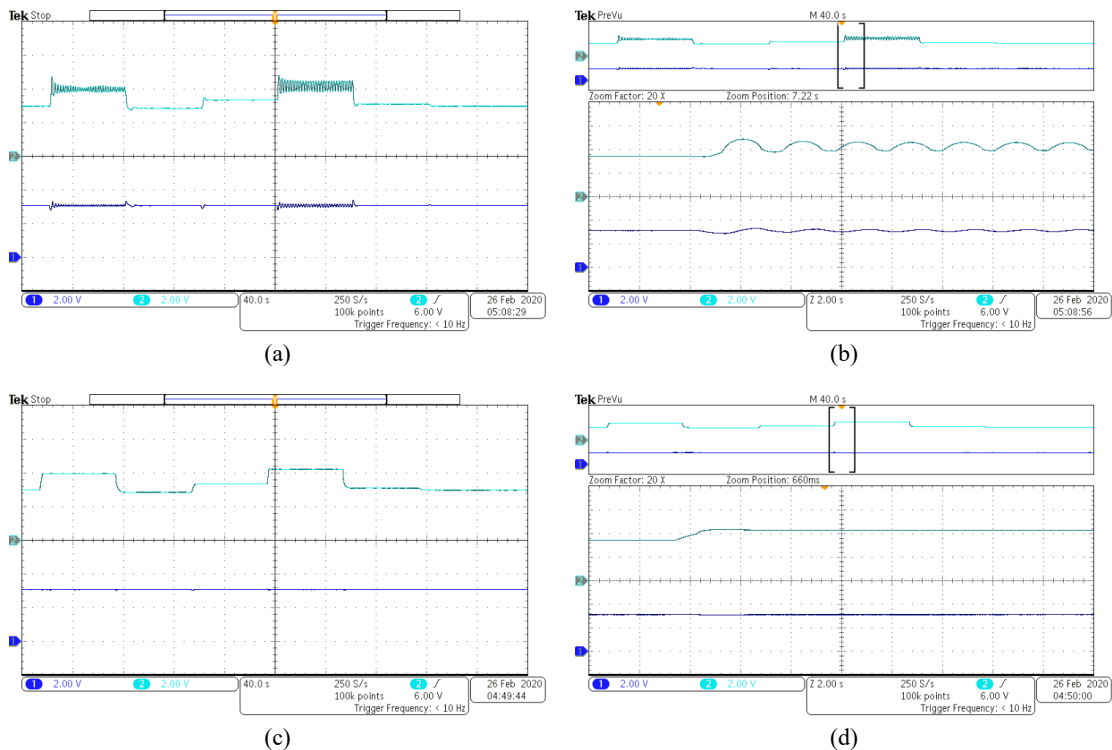


Figure II.1.10.10 Injected active and reactive power from a three-phase grid connected synchronverter facing active power reference changes (a) traditional VSG, (b) magnified response for traditional VSG, (c) HDP-based VSG (d) magnified output waveform of HDP-based VSG

Battery Modeling and Algorithm Development

The first new charging approach is termed CQtCV: constant lithium plating reaction current, $(\frac{dQ_{Li}}{dt})$ rather than conventional constant terminal current, followed by constant voltage charging. This approach reduces lithium plating, a key degradation mechanism in extreme fast charging systems. A comparison between the new method and conventional CCCV is illustrated in Figure II.1.10.11.

The conventional charging protocol (CCCV) and the new protocol (CQtCV) are conducted on the test cells. The current and voltage of first 3 cycles are presented in Figure II.1.10.12. As shown in Figure II.1.10.12(a), instead of a constant 3C charging current, the charging current of CQtCV varies from 5.5C to 2.7C before entering the CV region. Due to the varying charging current, the cell voltage of CQtCV reaches the upper voltage limit (4.2 V) later than CCCV (Figure II.1.10.12(b)), which means a shorter CV process. Since the charging efficiency in CV region is very low, the new charge protocol CQtCV successfully makes the total charge time for cells to charge to 80% capacity much shorter than CCCV.

The average charging time of CCCV is around 2 h while it only takes about 20 min in CQtCV. The charging capacities of test cells are summarized in Figure II.1.10.13(a). Comparing the charging capacity of two charging protocols, although the charging time in CQtCV is much less than CCCV, its charging capacity is even higher in the first 15 cycles. Figure II.1.10.13(b) shows the discharging capacity of CCCV and CQtCV as a function of cycle number. As shown, the capacity fade rate of CQtCV in first 20 cycles are really fast. After 20 cycles, the capacity fade rate decreases and becomes stable. However, it is still larger than that in CCCV. This may be caused by the gap between experimental cells and simulations since the experimental cells have gone through lots of characterization before cycling test, while the simulations are conducted based on a fresh cell.

Considering the charging current C_{rate} of CQtCV ranges from 0 to 5.5C, additional CCCV cycling tests with 4C and 5C are conducted for comparison. As shown in Figure II.1.10.13(c)-(d), in the first 8 cycles, the charge capacity of 4C and 5C CCCV cycling drops about 25% and 20%, respectively, much larger than 8% in CQtCV. Meantime, the charging time of 4C and 5C CCCV cycling test ranges from 2 h to 5 h, indicating that CQtCV is capable to achieve less degradation and short charge time than 4C and 5C CCCV cycling test. Therefore, the new charging protocol demonstrates its huge potential as an efficient XFC charging protocol.

The second innovative charging approach uses a single-particle (SP) model of the cell and direct optimization of charge time and degradation (Li et al. 2020). Two algorithms have resulted: CQO (constant capacity fade optimization, where the time is reduced but degradation is the same as in CCCV) and CTO (constant time optimization, where the degradation is reduced but the charging time is the same as in CCCV). Simulation results are illustrated in Figure II.1.10.14 and Figure II.1.10.15. Experimental validation is ongoing.

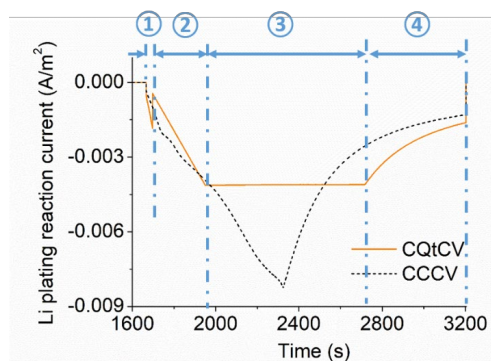


Figure II.1.10.11 Li plating current as a function of time in CCCV and CQtCV in charging process.

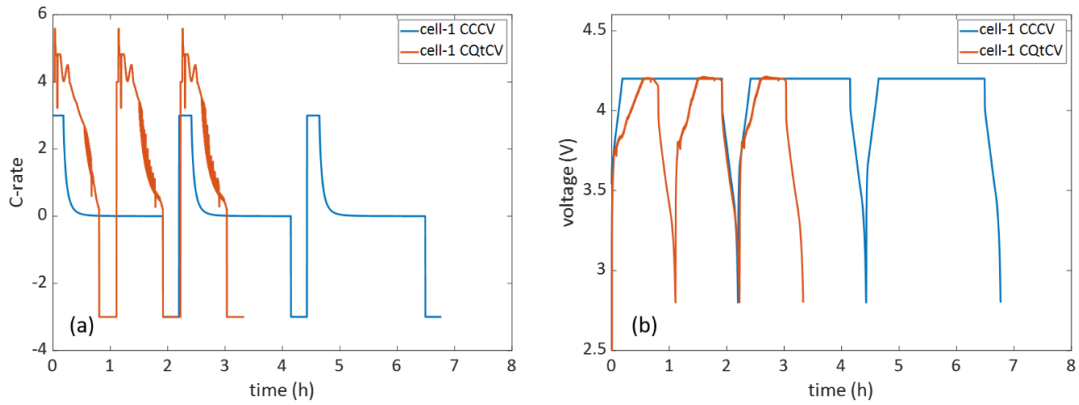


Figure II.1.10.12 (a) Input current C-rate profile (b) cell voltage of CCCV and CQtCV.

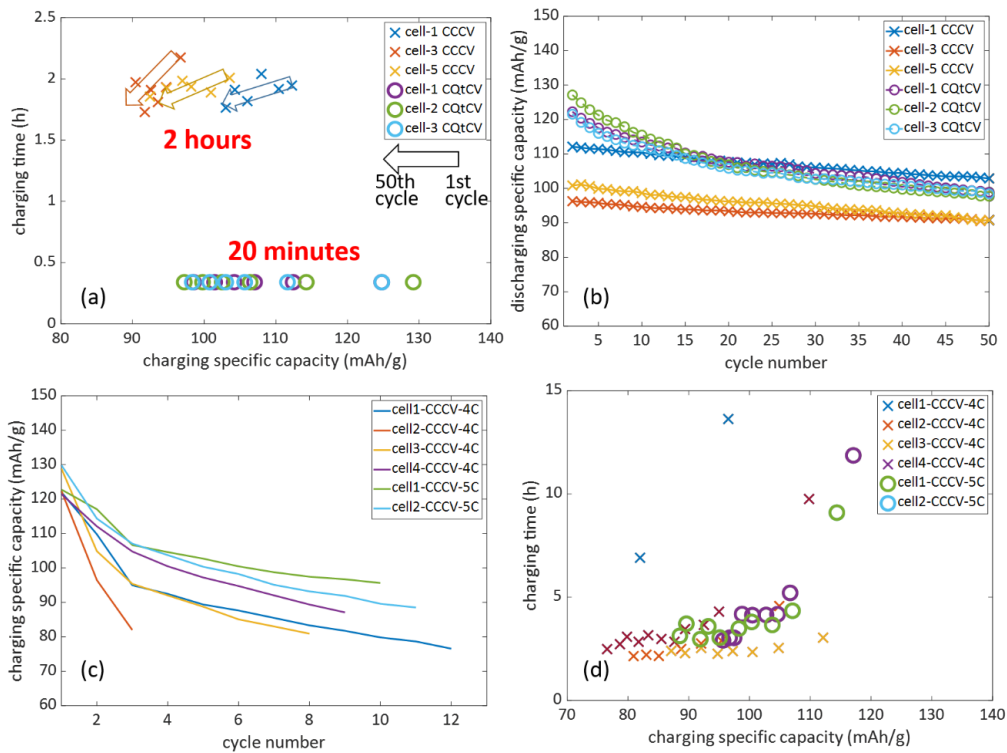


Figure II.1.10.13 (a) Charge time vs. charge specific capacity (b) discharge specific capacity of 3C CCCV and CQtCV cycling test, (c) charge specific capacity (d) charge time of 4C and 5C CCCV cycling test.

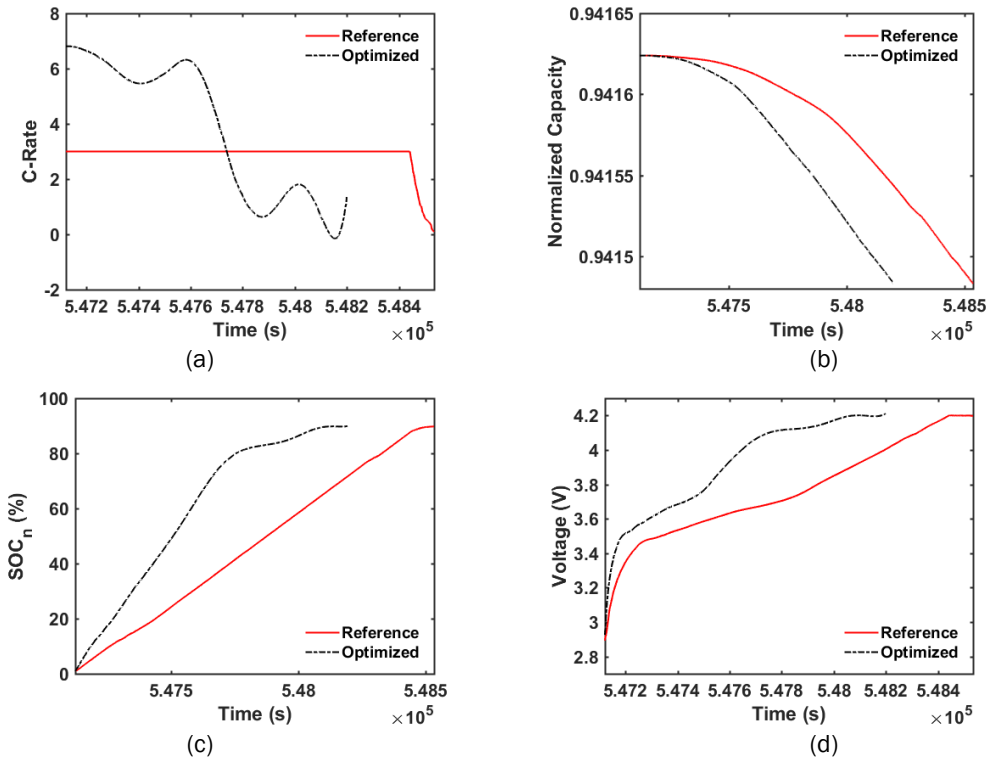


Figure II.1.10.14 (a) C-rate, (b) normalized capacity, (c) anode state of charge, and (d) terminal voltage for CQO and 3CCCV.

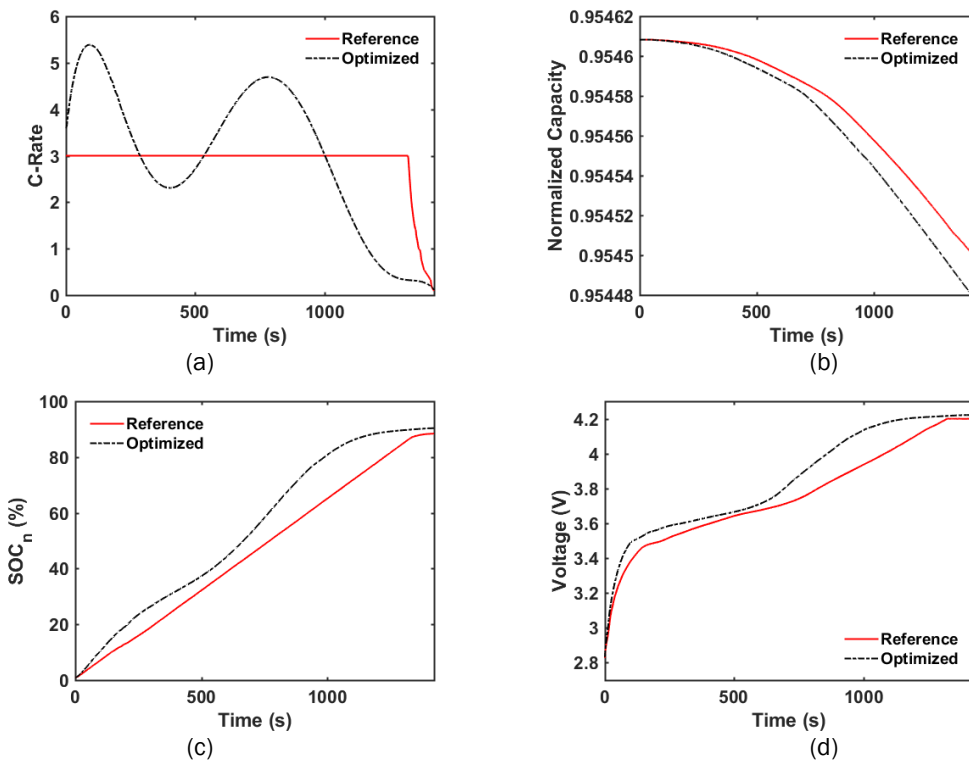


Figure II.1.10.15 (a) C-rate, (b) normalized capacity, (c) anode state of charge, and (d) terminal voltage for CTO and 3CCCV charging.

Conclusions

This project has achieved the planned objectives for the first budget period: subsystem and lab-scale validation of the various key technologies. Grid analysis is complete for local behavior on the scale of seconds; long time-scale behavior has been studied for optimal system design and for price arbitrage. Power conversion hardware subsystems have been evaluated, as well as key control algorithms. Battery charging algorithms have been selected; all have been simulated and experimental validation is ongoing.

Key Publications

1. S. Saadatmand, M. S. S. Nia, P. Shamsi and M. Ferdowsi, "Dual heuristic dynamic programming control of grid-connected synchronverters," *2019 North American Power Symposium (NAPS)*, Wichita, KS, USA, 2019.
2. S. Saadatmand, M. S. S. Nia, P. Shamsi, M. Ferdowsi and D. C. Wunsch, "Heuristic Dynamic Programming for Adaptive Virtual Synchronous Generators," *2019 North American Power Symposium (NAPS)*, Wichita, KS, USA, 2019.
3. S. Saadatmand, M. S. S. Nia, P. Shamsi, M. Ferdowsi and D. C. Wunsch, "Neural Network Predictive Controller for Grid-Connected Virtual Synchronous Generator," *2019 North American Power Symposium (NAPS)*, Wichita, KS, USA, 2019.
4. M.S. Sanjari Nia, S. Saadatmand, M. Altimania, P. Shamsi and M. Ferdowsi, "Analysis of Various Transformer Structures for High Frequency Isolation Applications", *2019 North American Power Symposium (NAPS)*, 2019.
5. M.S. Sanjari Nia, S. Saadatmand, M. Altimania, P. Shamsi, and M. Ferdowsi, "Analysis of Skin Effect in High Frequency Isolation Transformers", *2019 North American Power Symposium (NAPS)*, 2019.
6. K. J. P. Veeramraju, J. w. Kimball, "An improved method for the practical determination of core and copper losses in high frequency switchmode transformers," in *Proc. 2019 North American Power Symposium (NAPS)*, 2019.
7. M. S. Sanjari Nia, P. Shamsi and M. Ferdowsi, "Investigation of Various Transformer Topologies for HF Isolation Applications," in *IEEE Transactions on Plasma Science*, vol. 48, no. 2, pp. 512-521, Feb. 2020.
8. M.S. Sanjari Nia, M. Altimania, P. Shamsi, and M. Ferdowsi, "Comprehensive Analysis for Electric Field and Potential for Polymeric and Ceramic Insulators," *American Journal of Electrical and Electronic Engineering*, Volume 8, No. 1, pp. 26-34, 2020.
9. S. Saadatmand, H. Alharkan, P. Shamsi, and M. Ferdowsi, "Value gradient learning approach in power and frequency regulation of grid-connected synchronverters," in *Proc. IEEE Power & Energy Conf. at Illinois (PECI)*, 2020.
10. S. Saadatmand, P. Shamsi and M. Ferdowsi, "The Voltage Regulation of a Buck Converter Using a Neural Network Predictive Controller," *2020 IEEE Texas Power and Energy Conference (TPEC)*, College Station, TX, USA, 2020.
11. S. Saadatmand, P. Shamsi and M. Ferdowsi, "The Heuristic Dynamic Programming Approach in Boost Converters," *2020 IEEE Texas Power and Energy Conference (TPEC)*, College Station, TX, USA, 2020.

12. M.S. Sanjari Nia, M. Altimania, P. Shamsi, and M. Ferdowsi, "Magnetic field analysis for HF transformers with coaxial winding," in *Proc. IEEE Kansas Power & Energy Conference (KPEC)*, Manhattan, KS, July 2020.
13. M.S. Sanjari Nia, M. Altimania, P. Shamsi, and M. Ferdowsi, "Electric field and parasitic capacitance analysis for HF transformers with coaxial winding arrangements," in *Proc. IEEE Kansas Power & Energy Conference (KPEC)*, Manhattan, KS, July 2020.

References

1. J. Li, R. G. Landers, and J. Park, "A comprehensive single-particle-degradation model for battery state-of-health prediction," *J. Power Sources*, vol. 456, article 227950, 30 April 2020.

Acknowledgements

At Missouri S&T, other faculty on the project are Rui Bo, Mehdi Ferdowsi, Robert Landers, Jonghyun Park, and Pourya Shamsi. Subawardees are Ameren (Jason Wibbenmeyer, Technology Transfer Manager); Bitrode Corporation (Elaine Raterman, Engineering Director); and LG Chem Michigan (Mohamed Alamgir, Director of Research).

II.1.11 High-Efficiency, Medium-Voltage-Input, Solid-State-Transformer-Based 400-kW/1000-V/400-A Extreme Fast Charger for Electric Vehicles (Delta Electronics (Americas) Ltd)

Charles Zhu, Principal Investigator

Delta Electronics (Americas) Ltd
46101 Fremont Boulevard
Fremont, CA 94538
Email: charles.zhu@deltaww.com

Steven Boyd, DOE Program Manager

U.S. Department of Energy
Email: steven.boyd@ee.doe.gov

Start Date: July 20, 2018

End Date: November 30, 2021

Project Funding: \$2,120,588

DOE share: \$1,060,294

Non-DOE share: \$1,060,294

Project Introduction

Range anxiety and long battery charging time continue to be critical challenges to mass adaptation of EVs. A major identified gap to wider adoption of BEVs is the ability and availability to refuel quickly or to fast charge. Studies have shown that in areas where drivers have access to 50-kW or 120-kW fast charge stations, annual electric vehicle (EV) miles traveled (i.e., eVMT) increased by over 25%, even in cases where fast charging was used for 1% to 5% of total charging events [1]. Charge stations of higher power not only alleviate the “range anxiety” and reduce the driver’s waiting time, but also requires less investment. Michigan Energy Office completed a study in early 2019 titled “Electric Vehicle Charger Placement Optimization in Michigan: Phase I – Highways”. This study finds a system with 150kW chargers, though more expensive individually, actually has lower total system cost when compared to a 50kW charging system when serving the same battery size EV [2]. To be truly competitive to the ICEV refueling experience, even higher power stations are necessary. However, high power charge stations would create large power draws from the grid. If this occurs during peak demand periods, grid capacity could be overloaded. This problem needs to be addressed to reduce the impact on the electric utility infrastructure.

The main goal of this project is to develop a 400-kW/400-A XFC system targeting total efficiency of 96.5 percent from the MVAC grid to a vehicle. The novel SST power cell topology, combined with a new silicon carbide (SiC) MOSFET device, enables a 3.5 percent improvement in system efficiency, a 50-percent smaller equipment footprint, and four times less weight than today’s DCFC systems. The SST technology would directly utilize MVAC at 4.8-kV or 13.2-kV. This would eliminate the line frequency transformer (LFT), which steps down medium-voltage AC to 3-Phase 480-V line-to-line voltage in current DCFC systems. Activities in this fiscal year includes specification development, advanced circuit development and 1-phase series SST and Buck cell Integrated test.

Objectives

The objectives of the program are:

To design and test a high-efficiency, medium-voltage-input, solid-state-transformer-based 400-kW Extreme Fast Charger (XFC) for electric vehicles, achieving better than 96.5 percent efficiency.

To demonstrate extreme fast charging with a retrofitted General Motors’ light-duty battery electric vehicle at 3C or higher charging rate for at least 50 percent increase of SOC.

To achieve a 180-mile charge within 10 minutes.

Approach

The XFC system consists of a Solid-State Transformer (SST), a Charge Controller (in power cabinet), a Charge Dispenser (A.K.A. User Unit) and an optional Energy Storage System (ESS). The system block diagram is illustrated in Figure II.1.11.1.

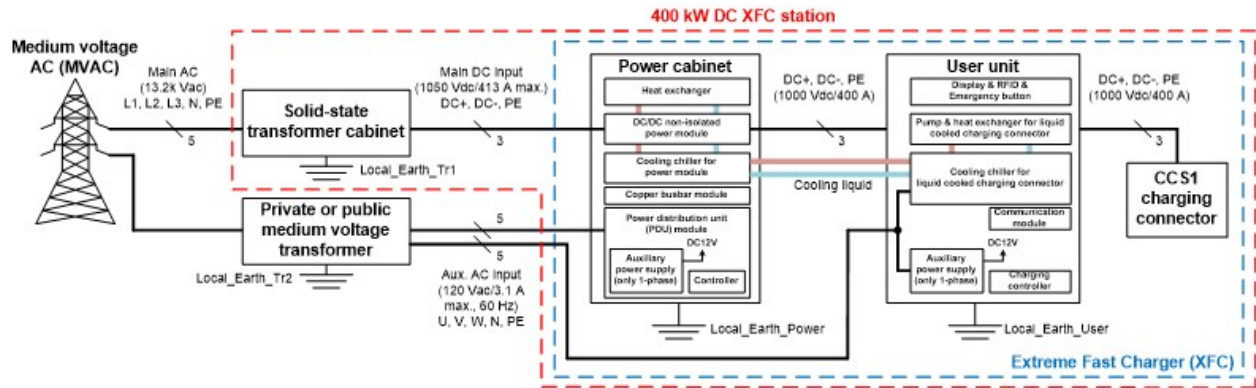


Figure II.1.11.1 XFC System Architecture

The SST is the key component in the whole system because it has multiple functions such as voltage step-down, AC/DC conversion, MV insulation, and grid interface. The team selected modularized architecture to accommodate the various voltages. Each SST module is rated at 15-kW, which is optimized for the transformer thermal dissipation. Cascaded H-bridge (CHB) topology is used in system level, which lowers the voltage stress on semiconductor devices, reduces the filter size with more voltage level, and improves the power quality and electromagnetic interference (EMI) performance on grid side. The power module’s circuit diagram is illustrated in Figure II.1.11.2.

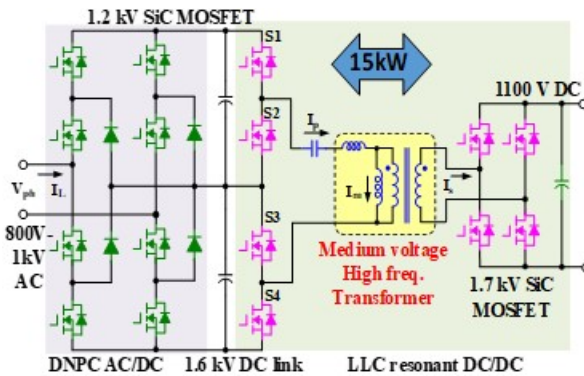


Figure II.1.11.2 Circuit Diagram of Power Module

The charging controller has a modularized design as well. Each power module is capable of outputting 200-A 135kW, are connected in parallel. The charging controller module is based on Buck topology, thus also called Buck module. The buck converter runs at continuous conduction mode (CCM) with 50-kHz switching frequency. A full-bridge SiC MOSFET module with 1.2-kV, 50-A rating is used as the switching device. The picture of charging controller module is shown in the right half of Figure II.1.11.3.



Figure II.1.11.3 Picture of an SST Module at left, and Charging Controller (Buck) Module at right

For a 13.2-kV medium-voltage application, nine SST power cells in each phase are connected in series for the higher voltage. The outputs of all the power cells in three phases are connected in parallel to provide total 400-kW power to the 1050-V intermediate DC bus. Total 27 cells are installed in three cabinets. The SST also includes an AC input cabinet and a control/DC cabinet. The dimensions of the SST are 3100x1300x2100mm. The weight is approximately 3000 -kG. It is cooled by forced air. The cabinet is rated for NEMA 3R outdoor usage. Figure II.1.11.4 shows the complete 13.2-kV 400-kW SST.



Figure II.1.11.4 Front View of 13.2kV/400kW SST Design

Three Buck power modules are connected in parallel to handle 500-A 400-kW charging power. The supporting plant includes a control module and a chiller. The dimensions of the power cabinet are 1318 x 1280 x 1432 mm. The weight is 800-kG. It is cooled by forced air with an internal chiller. Figure II.1.11.5 shows the complete 400-kW charger power cabinet.



Figure II.1.11.5 3-D View of the 400-kW Charger Power Cabinet

The dispenser features a 500A CCS1 vehicle charging interface, an LCD user interface and a charging cable chiller. The dimensions of the power cabinet are 600 x 400 x 2400 mm. The weight is 800-kG. It is cooled by forced air with an internal chiller. Figure II.1.11.6 shows the dispenser design.



Figure II.1.11.6 3-D View of the Charging Dispenser

The 400kW power system and supporting infrastructure has been installed at NextEnergy's Microgrid Power Pavilion. This includes a step-up transformer, a 15kV switch, power distribution panels, contactor, surge suppression equipment, and all cabling. Final inspection of the XFC test setup was conducted on September 28, 2020. Figure II.1.11.7 and Figure II.1.11.8 are the pictures of the 400kW XFC setup at NextEnergy.



Figure II.1.11.7 400kW XFC Setup Front View (SST, Charger Power Cabinet, Dispenser, and DCE from left to right)



Figure II.1.11.8 400kW XFC Setup Rear View (DCE Cooling System, Buck charger, SST from Left to Right)

In parallel to the XFC development, General Motor has been developing the vehicle Rechargeable Energy Storage System (RESS), Charge Inlet, and Vehicle Integration Control Module (VICM).

Testing of the four battery subpacks was completed in order to verify temperature rise is within thermal limits after occurrence of the current profile based on fast charging event. Since the test is primarily intended to evaluate joule heating induced temperature rise in cables, busbars, and contactors (not heat generated internally in the cells), a discharge current vs. time profile was used with current equal in magnitude to the charging current profile as determined from simulation with 500A total current.

Vehicle retrofit is 75% complete. The preparation of rear compartment is completed to make room for the battery pack. Cables and coolant lines have been routed. A bracketry has been fabricated to support the front part of RESS frame. Emergency shutdown mechanization and circuit interfaces has been developed. The vehicle body has been modified and the DC charge inlet has been installed on the right side of vehicle to the rear of the rear passenger door. Figure II.1.11.9 shows the retrofit vehicle with partially assembled RESS tray loaded.



Figure II.1.11.9 Retrofit Vehicle with Partially Assembled RESS Tray Loaded

Results

XFC Full System Efficiency Test Result

The function and efficiency of 400kW XFC system was tested at full voltage and power range at total 44 points. The test result matches the design calculation very well. It meets and exceeds the specification. The peak efficiency is 97.6%. Figure II.1.11.10 shows the whole system efficiency curves. Figure II.1.11.11 shows the SST efficiency curves. Figure II.1.11.12 shows the Buck charger efficiency curves.

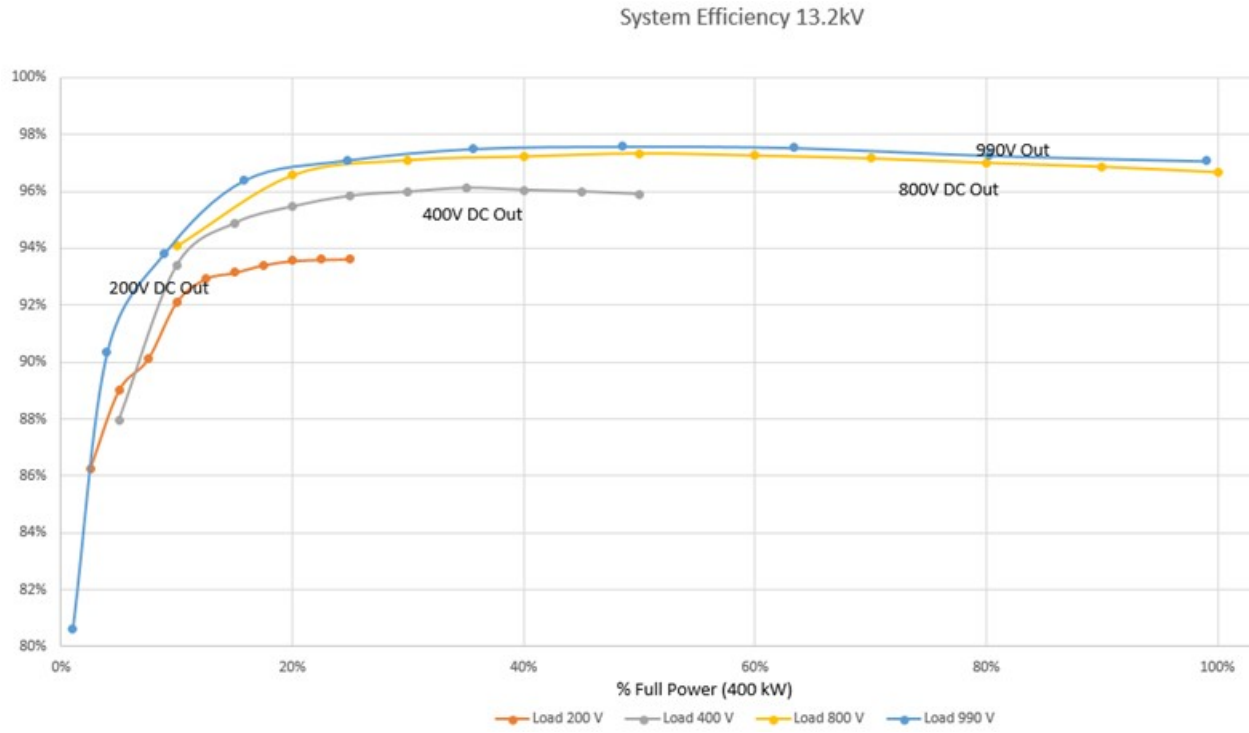


Figure II.1.11.10 13.2-kV 400-kW XFC System Efficiency Curves

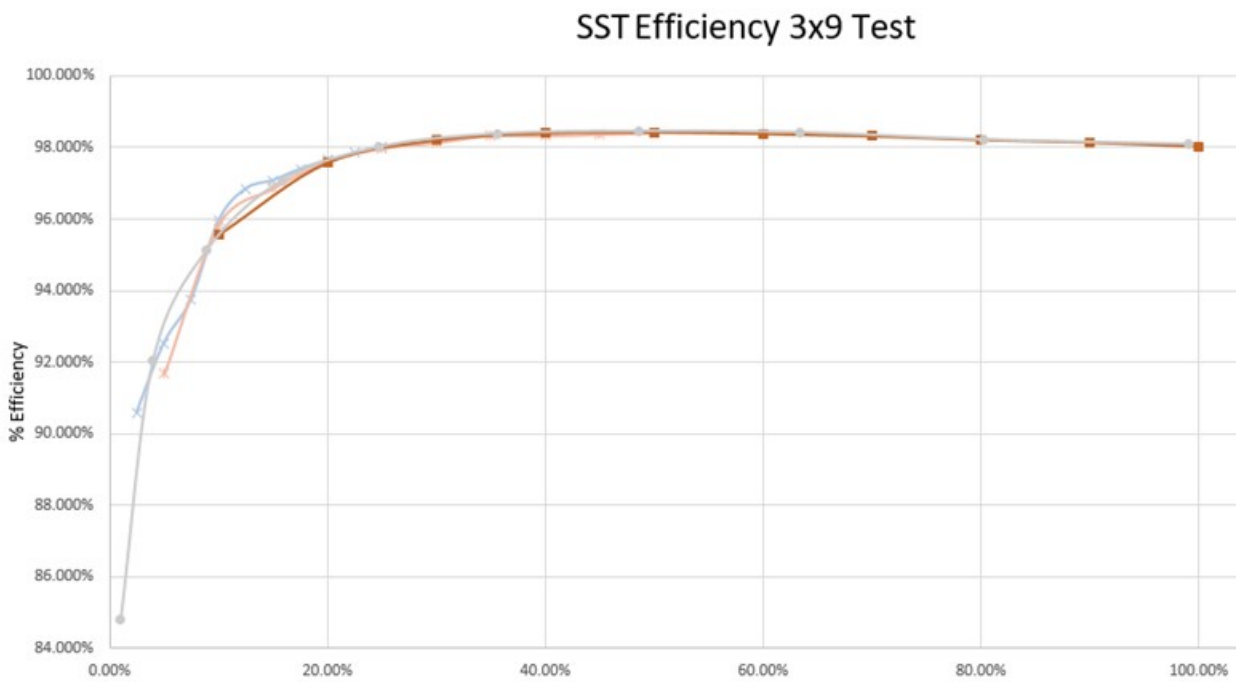


Figure II.1.11.11 13.2-kV 400-kW SST Efficiency Curves

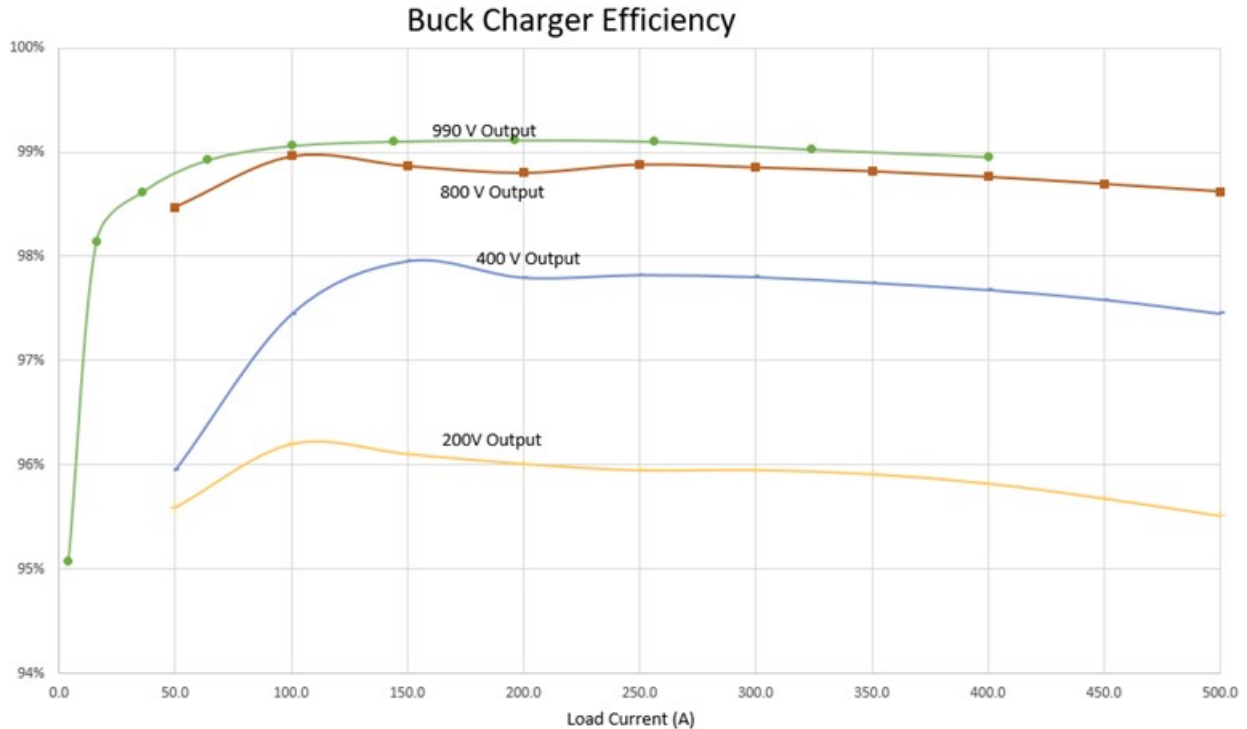


Figure II.1.11.12 400-kW Buck Charger Efficiency Curves

Vehicle RESS Test Result

The vehicle RESS system was tested with liquid cooling, 25C coolant temperature and was stabilized before the test. The measured temperatures are within expected limits, consequently fast charging rate is not expected to be limited by heating in RESS components other than cells.

In the lab test setup, contactors were controlled via test controllers that did not include an economizer function. Contactor temperatures continued to rise moderately after current tapering rather than leveling off or falling as expected, and it was found that this was due to heat generation in the contactor coil. When the system is integrated with the intended vehicle controllers currently in bench verification testing, the system will use an economizer function to reduce heat generation while the contactors are closed.

After a rest time of 15-20 minutes, RESS component and cell temperatures have been cooled substantially and approach pre-test values.

Figure II.1.11.13 and Figure II.1.11.14 show the measured temperatures of the key components in the RESS.

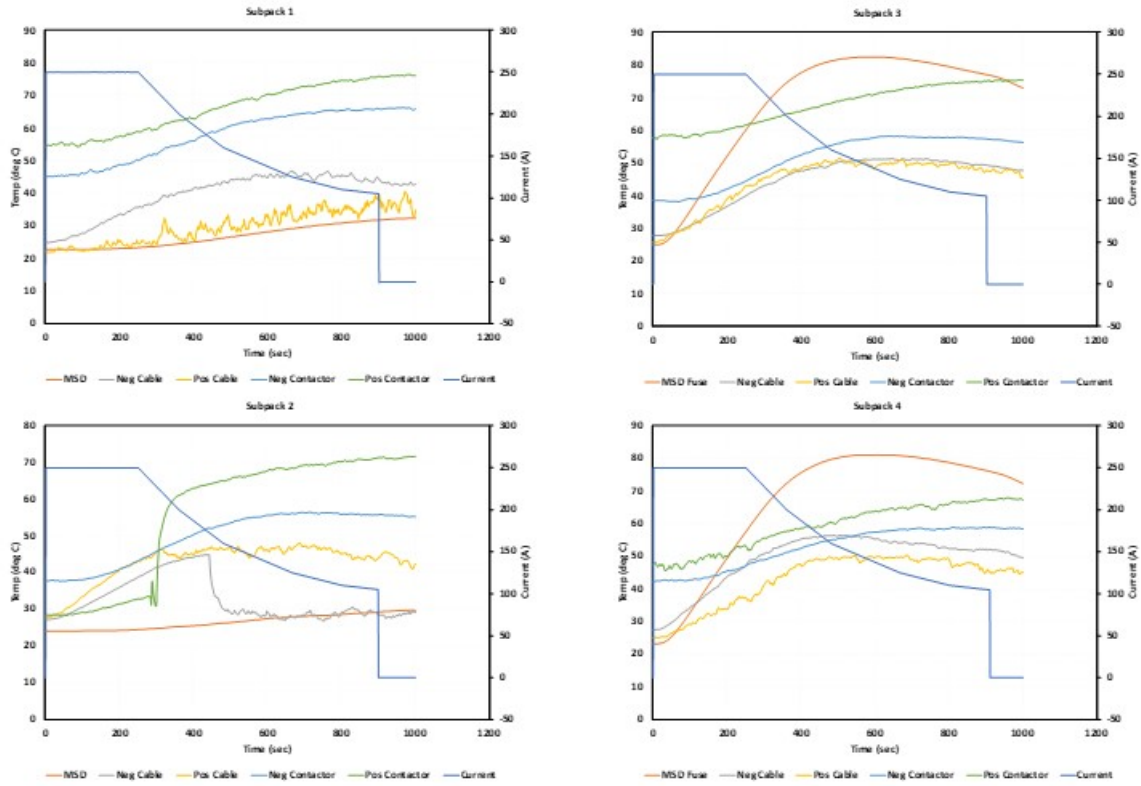


Figure II.1.11.13 Temperature Rise in the RESS Components during Current Profile

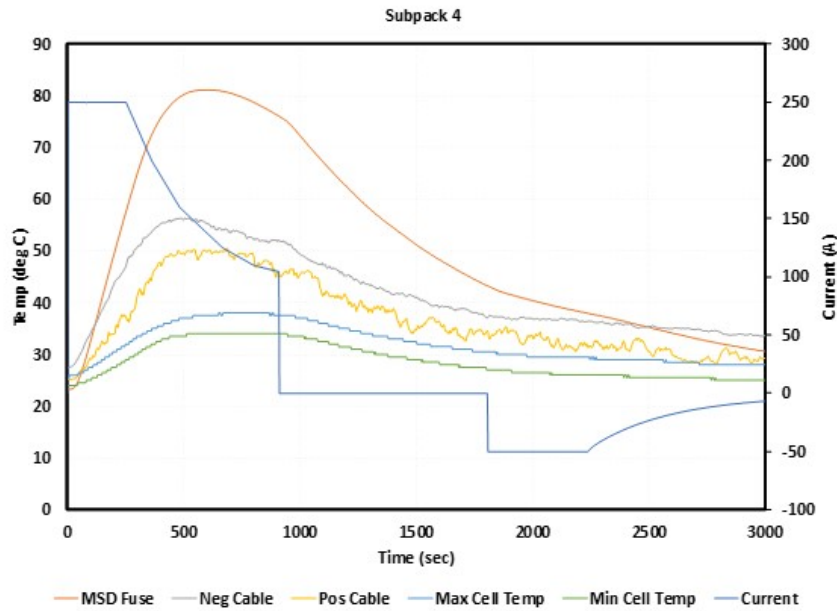


Figure II.1.11.14 Subpack 4 Component Cool-Down after End of High Current Event

Conclusions

The test result shows that the 13.2kV 400kW SST, the 400kW Buck charger power cabinet and the dispenser meet the specification. The integration of the 13.2kV 400kW XFC system is successful and the performance of

simulated load meets and exceeds the target specification. The program objects of FY 2020 is completely met. The next step is to install an XFC system at DTE site and test full power charging with GM's retrofit vehicle.

Key Publications

1. Charles Zhu, "Medium Voltage Input 400-kW Extreme Fast Charger by Utilizing Solid-State-Transformer Technology," presentation in IEEE Energy Conversion Congress and Exposition, October 2019, Detroit, MI.

References

1. D. Howel, S. Body, B. Cunningham, S. Gillard, and L. Slezak, "Enabling Fast Charging: A Technology Gap Assessment," U.S. Department of Energy, October 2017. [Online]. Available: <https://energy.gov/sites/prod/files/2017/10/f38/XFCn%20Technologyn%20Gapn%20Assessmentn%20Reportn%20FINALn%2010202017.pdf>
2. Mehrnaz Ghamami, Ali Zockaie, Joy Wang, Steven Miller, "Electric Vehicle Charger Placement Optimization in Michigan: Phase I – Highways", Michigan Energy Office, February 2019. [Online]. Available: https://www.michigan.gov/documents/energy/EV-Charger-Placement-Opt-PhaseI-Final-Report-021319_646220_7.pdf
3. L. D. Stevanovic, K. S. Matocha, P. A. Losee, J. S. Glaser, J. J. Nasadoski, and S. D. Arthur, "Recent Advances in Silicon Carbide MOSFET Power Devices," 2010 Twenty-Fifth Annual IEEE Applied Power Electronics Conference and Exposition (APEC), Palm Springs, CA, 2010, pp. 401-407.
4. J. S. Glaser, J. J. Nasadoski, P. A. Losee, A. S. Kashyap, K. S. Matocha, J. L. Garrett, and L. D. Stevanovic, "Direct Comparison of Silicon and Silicon Carbide Power Transistors in High-frequency Hard-switched Applications," 2011 Twenty-Sixth Annual IEEE Applied Power Electronics Conference and Exposition (APEC), Fort Worth, TX, 2011, pp. 1049-1056.
5. T. Daranagama, N. Udugampola, R. McMahon, and F. Udrea, "Comparative Analysis of Static and Switching Performance of 1.2 kV Commercial SiC Transistors for High Power Density Applications," The 1st IEEE Workshop on Wide Bandgap Power Devices and Applications, Columbus, OH, 2013, pp. 48-51.

Acknowledgements

This work is supported by the DOE Office of Energy Efficiency and Renewable Energy, Vehicle Technologies Office, and administrated by National Energy Technology Laboratory, under contract number DE-EE0008361. The author wishes to thank project team members:

Steven Boyd and Lee Slezak of VTO and Michael Ursic and John Jason Conley of NETL for their contributions.

II.1.12 High Efficiency Powertrain for Heavy Duty Trucks using Silicon Carbide (SiC) Inverter - DE-EE0008806 (Ricardo)]

Ben Marquart, Principal Investigator

Ricardo Inc
40000 Ricardo Drive
Van Buren, MI 48111-1641
Email: ben.marquart@ricardo.com

Lee Slezak, DOE Technology Manager

U.S. Department of Energy
Email: Lee.Slezak@ee.doe.gov

John J. Conley, NETL Project Manager

U.S. Department of Energy
Email: John.Conley@netl.doe.gov

Start Date: October 1, 2019
Project Funding: \$1,711,263

End Date: June 30, 2023
DOE share: \$4,605,398

Non-DOE share: \$2,785,513

Project Introduction

The Ricardo led High Efficiency Propulsion (HEP) project will develop a high efficiency and compact 250kW continuous power SiC inverter designed to support the high continuous loads and challenging shock/vibration environment of heavy-duty trucks with an electrified axle specifically designed for high performance and efficiency in battery-electric Class 8 trucks used in medium range (~250 mile) distribution. The project is split into 3 budget periods, with the first two being design and development focused and the final one is a demonstration phase.

The HEP team is comprised of Ricardo as the prime and Transpower and NCSU as the subs with the primary project objective of developing a 250kW SiC continuous power inverter. An electrified axle with integrated 3-speed gearbox developed under Meritor's "eAxle" product line will be utilized. These components will be integrated with a variant of the TransPower efficient EV architecture, which has been successfully utilized in numerous Class 8 truck and tractor models. This combination will provide an extremely compact, lightweight, robust and easy to integrate drive system for electric Class 8 trucks. It is expected that performance of the 250kW continuous power operation on an eAxle integrated into a vehicle with actual in-field use will be verified during the demonstration period.

Objectives

Budget Period 1: Development of Controls and Design of the Inverter

- Task 1.1 – Inverter Concept Design:
 - The initial inverter design concept will be developed to support the required continuous power. The mechanical design concept including integration into the eAxle packaging a chassis mounted design will be defined.
- Task 1.2 – A-Sample Electronic Design:
 - The A-sample inverter electronic design will be refined, and modeling of key components such as the DC link capacitors, bus bars, current sensors, etc. will be performed. Design of custom components will kick-off.
- Task 1.3 – Mechanical Design:

- The mechanical design of the inverter enclosure will be initiated and prepared for A-Sample build and test.
- Task 1.4 – Software Design:
 - Embedded software development will include embedded OS selection, driver development, and porting and/or development of necessary protocol stacks to the selected processor target.
- Task 1.5 – Prototype Build:
 - A-sample prototype build will be initiated.
- Task 1.6 – Functional and Performance Test:
 - The various electrical and mechanical parts will be assembled and tested first for basic electrical operation, then for functional performance. Low voltage testing will be completed to ensure basic operation and safety before applying high voltage supply.
- Task 1.7 – Hardware / Software Integration Testing:
 - Hardware/software testing to confirm continuous operation will be performed.
- Task 1.8 – System Integration Testing:
 - Controls required on the eAxle will be tested with discrete modules.
- Task 1.9 – Preliminary Design Validation Performance Testing Complete:
 - Acceptance tests will be performed.
- Task 1.10 – eAxle Subsystem Design:
 - The eAxle subsystem will be completed and will consist of the electrified axle assembly comprised of a tandem axle configuration with two drive motors (one in each axle).
- Task 1.11 – Integrated Drive System Design:
 - The Integrated Drive System Design will be combined with the eAxle subsystem and assembled into the ZANZEFF Peterbilt 579 trucks.
- Task 1.12 – Validation Truck Assembly and Testing:
 - Five Peterbilt 579 trucks will be built using the drive system design developed with the Meritor 14Xe axle using a two-speed gearbox as POC.

Budget Period 2: System Integration and Evaluation of the Proposed Design

- Task 2.1 – B-Sample Design:
 - Results of testing from A-sample build will be reviewed and updates to the specification, electrical and mechanical design and testing methodology will be applied as learnings to the B-sample development effort. An updated system specification will be drafted based on the outcome of the reviews with all team members.
- Task 2.2 – Mechanical Design:

- Thermal and detailed design will be updated along with drawings. FMEA review of mechanical design to ensure improvements include design for manufacturing and assembly (DFM/A), and the lower cost solution.
- Task 2.3 – Electronic Design:
 - Updates will be made to the HW requirements spec and design will commence. Schematic design, custom component calculations, specifications and quotation, and PCB design updates will all be performed. FMEA review of electronic design to ensure improvements include design for manufacturing and assembly (DFM/A), and the lower cost solution. Manufacturing data will be generated and checked.
- Task 2.4 – Software Update:
 - Software will be updated as required to optimize the design.
- Task 2.5 – Prototype Build:
 - Electronics manufacturing will be initiated, and mechanical components procured.
- Task 2.6 – Hardware Test:
 - The various electrical and mechanical parts will be assembled and tested first for basic electrical operation, then for functional performance. Additional controls work will be performed to test system functional operation, including early vehicle control interface debugging. Functional testing will be performed until desired specification levels are reached. Simulated load cycles will be performed to test for thermal and mechanical performance.
- Task 2.7 – Hardware / Software Integration & Functional Testing:
 - Motor-inverter characterization of hardware/software testing on back-to-back dyno testing continuous operation will be performed.
- Task 2.8 – System Integration Testing:
 - Testing of SiC inverter on early drive systems as well as communication testing with the Meritor eAxle and discrete control modules will begin.
- Task 2.9 – Hardware Design Documentation Update:
 - Results of testing from B-sample build will be reviewed and updates to the specification, electrical and mechanical design and testing methodology will be applied as learnings to the final development effort. The data pack will be compiled, and production recommendations provided.
- Task 2.10 – Mechanical Design:
 - The mechanical design will be updated, and the 3D design work will be readied for prototype manufacturing quotation and review.
- Task 2.11 – Production-Ready Design Validation Performance Testing Complete:
 - Acceptance testing will be completed.
- Task 2.13 – eAxle Prototype Fabrication and Testing:

- Prototypes will be manufactured for in-house testing and for installation into the two demonstration trucks. The axle will be installed into one of the trucks. Powertrain Control Module (PCM) software will be developed to optimize performance of the tandem eAxle system using the new 3-speed gearbox.
- Task 2.14 – Drive System Component Development:
 - Assemble the subsystems required to equip the Class 8 demonstration trucks with the upgraded EV architecture featuring the 3-speed eAxle and SiC inverter.

Budget Period 3: Demonstration Vehicle Development

- Task 3.1 – Demonstration Vehicle Development:
 - The subsystems will be integrated and assembled into the two Class 8 demonstration trucks. Two Peterbilt 579 gliders will be acquired and drive system components and all high and low voltage wiring, and integration hardware will be installed.
- Task 3.2 – Demonstration:
 - The two demonstration trucks will be entered into operational service to demonstrate the performance of the integrated drive systems in Class 8 trucks under real-world operating conditions. Remote telematics will be used to continuously gather information on the performance of the trucks.

Approach

- Year 1: Design and Prototype Testing with the aim to demonstrate >92.5% SiC inverter efficiency
 - SiC inverter concept design (Ricardo with NCSU support)
 - Requirements/specifications development
 - Gate driver simulations with soft switching
 - Component architecture and device options investigation
 - Initial firmware development
 - Complete system simulation (Ricardo with NCSU support)
 - SiC inverter design (Ricardo with NCSU support)
 - Topology confirmation and thermal management development
 - Finalize block diagram, schematic and layout
 - Design release and component procurement
 - A-sample inverter testing and simulation verification → go/no-go decision based on meeting 92.5% efficiency (Ricardo)
 - Packaging and system component design and controls development (Transpower)
- Year 2: Inverter B-sample Development and Drive System Component Development

- B-sample SiC inverter design and development → go/no-go decision based on inverter design validation efficiency of 98.5% (Ricardo with NCSU support)
- Subsystem and system testing (Transpower with Ricardo support)
- System integration development and vehicle build (Transpower)
- Year 3: Vehicle Integration and Demonstration of 2 class 8 Trucks (Transpower with Ricardo support).

Results

No results are available yet since the a-sample development phase is not complete. A-sample boards are undergoing testing in January 2021, with inverter build and testing expected in February/March 2021.

A summary highlighting completed activities follows:

Inverter Hardware Architecture Design

The inverter hardware architecture was reassessed and redefined per input from proof-of-concept design discussions, simulation results and feedback from power device manufacturers.

Key electronic component selection

- Power Module: Danfoss DCM 1000 Series Half Bridge
- MCU: SPC5744P
- Gate driver: GD3100 (Optimized for 1200V SiC MOSFET)
- Power Management: SBC MC33FS6512C
- CAN transceiver: TJA1051
- Resolver-to-Digital IC: AD2S1210-12bit
- SPI communication between MCU / SBC and MCU / Gate driver.

The blurred hardware architecture system diagram is shown in Figure II.1.12.1 below.

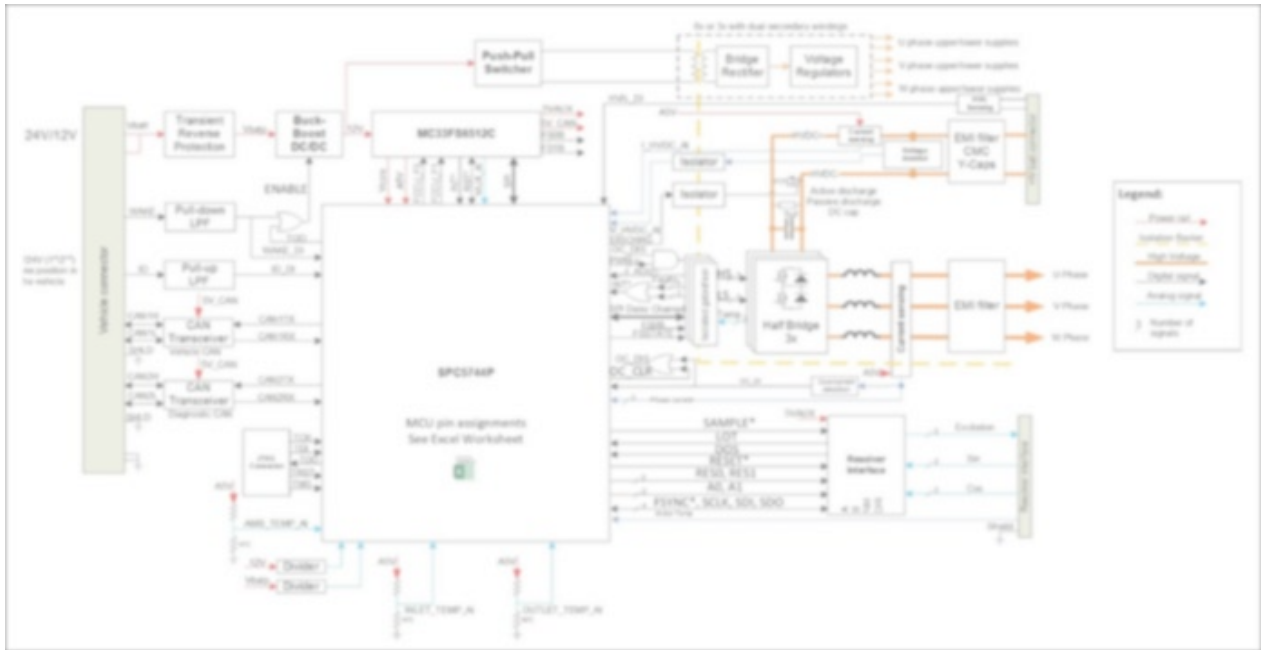


Figure II.1.12.1 Hardware architecture system diagram (blurred purposely)

Completed gate driver and control board design shown in Figure II.1.12.2 and received H/W for initial bring up.

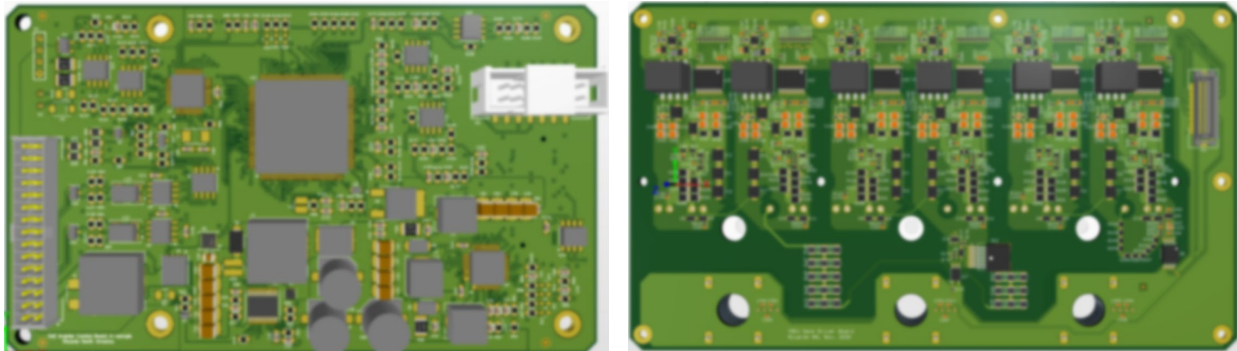


Figure II.1.12.2 Control board and Gate Driver board

CAD Development and Mechanical Design

The inverter mechanical design is complete (components are defined, placed, packaged and thermal analysis complete), with the final BOM now in RFQ. Figure II.1.12.3 provides an isometric view of the design.

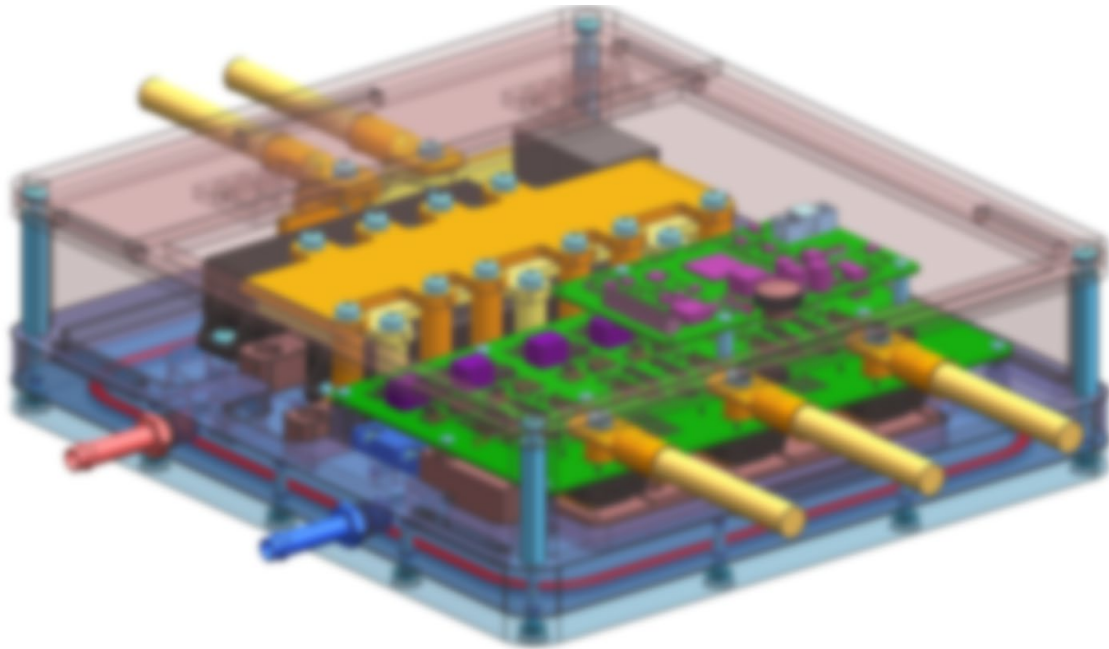


Figure II.1.12.3 Inverter design

Software Development

Base software development for board bring up is complete (Release 1.5), with application software ongoing to meet A-sample completion target of end of February 2021 in time for inverter builds and testing. The software development plan emphasizes software feature implementation based on Software Requirements and High-level Software Design.

NCSU Status

NCSU has supported the inverter development by providing simulation analysis, supporting component selection, and developing the current sensor.

TransPower Status

TransPower has been actively involved in the ZANZEFF BEV truck design all year which is the platform that the Ricardo inverter will eventually be installed into. First vehicle build has commenced.

Conclusions

The Ricardo led High Efficiency Propulsion (HEP) project will develop a high efficiency and compact 250kW continuous power SIC inverter designed to support the high continuous loads and challenging shock/vibration environment of heavy-duty trucks with an electrified axle specifically designed for high performance and efficiency in battery-electric Class 8 trucks used in medium range (~250 mile) distribution. The project is split into 3 budget periods, with the first two being design and development focused and the final one is a demonstration phase.

The project completed its first year of work during FY20.

Acknowledgements

NCSU's Dr. Iqbal Husain and Dhruvo Rahman have been instrumental in supporting and progressing the inverter design.

II.1.13 Enabling Secure and Resilient XFC: A Software/Hardware Security Co-Design Approach (Virginia Tech)

Ryan Gerdes, Principal Investigator

Virginia Tech
900 North Glebe Road
Arlington, VA 22203
Email: rgerdes@vt.edu

Jason Conley, Project Manager

U.S. Department of Energy NETL
Email: John.Conley@NETL.DOE.GOV

Lee Slezak, DOE Technology Manager

U.S. Department of Energy
Email: Lee.Slezak@ee.doe.gov

Start Date: October 1, 2018
Project Funding: \$1,714,458

End Date: October 31, 2020
DOE share: \$1,368,879

Non-DOE share: \$345,579

Project Introduction

Extremely fast charging (XFC) has the potential to reduce the charging time of battery electric vehicles (BEV) to be equivalent to the filling time of internal combustion engine vehicles (ICEV), thus eliminating one of the few advantages ICEV still poses for light- and heavy-duty vehicles. Enabling XFC will, however, require coordination and cooperation between the grid, charging stations, and the vehicles themselves, which leads to an inevitable increase in the attack surface for all systems combined. In securing the overall system, we must not only embrace traditional cybersecurity, which is chiefly concerned with communications and the operation of digital systems, but also cyber-physical systems security as the proper operation of XFC is critically dependent on systems' abilities to know about (sense) and interact with (actuate) the physical world. The project team consists of academic and industry researchers with backgrounds in cybersecurity, cyber-physical systems security, learning in adversarial environments, transportation security, grid security and resilience, wireless power transfer, converter design, and battery management systems.

The goal of the proposed work is to enable the decrease in battery charge time in a secure and efficient manner. Charging will occur under situations in which electric vehicle service equipment (EVSE) and the BEV themselves are untrustworthy (or at least not trusted by each other or the grid). While we will adopt strategies and designs to produce secure EVSE and BEV, it is inevitable that successful compromises of either BEV or EVSE will take place. It is thus necessary that a resilient (and not just secure) system be put in place: one that is able to detect compromises, minimize their effects, and prevent them from spreading. Given the inherently, and necessarily, dispersed nature of charging infrastructure and the possible disruption resulting from widespread inoperable EVSE for even a short time, operators should also be able to remotely address compromises (e.g., through over-the-air updates (OTAU)) in a secure manner. Finally, as XFC is expected to lead to increased demands on the electrical grid, it will be necessary to securely coordinate the actions of charging networks so as to prevent EVSE from being used to undermine the operation of the grid. Fully preventing the latter will require deployment of grid-side monitoring and response technologies to counter compromised EVSE/BEV.

Objectives

The objective of this project is to develop security-hardened controllers, converters, and monitoring systems for a fast charging infrastructure that maintains user privacy by using secure sensing and actuation techniques and learning-enabled moving-target defense while providing successful remediation of vulnerabilities through

remote updates. The feasibility of the technologies developed will be demonstrated on a real-world testbed that includes an extreme fast charge (XFC) unit and Electric Vehicle (EV) situated in a microgrid.

Approach

To achieve our goal of secure and efficient charging, we propose a hardware/software-security (HW/SW- Sec) co-design approach that will: 1) provide resilient operation of BEV/EVSE/grid through the use of security-hardened controllers, converters, and monitoring systems that leverage secure sensing/actuation techniques, moving-target based detection and mitigation strategies, and 2) the ability to guarantee successful remediation of vulnerabilities in EVSE/BEV through remote updates, all while 3) respecting end-user privacy.

Our work will be carried out on a real-world testbed that includes the Bronzeville Community Microgrid (a neighborhood in Chicago, IL), a charger capable of 350 kW, and a Ford Focus EV. The specific tasks and points of focus include: T1) undertaking a cyber-physical threat and vulnerability assessment of EVSE/BEV/grid systems using a game-theoretic risk analysis and an automatic attack graph generator; T2) performing experimentally-validated, grid-side modeling of XFC loading on a microgrid and using a reachability analysis to determine the safety of a given charge request; T3) development of a moving-target defense for sensor and actuator attacks against EVSE/BEV/grid controllers; T4) designing AC-DC (for EVSE) and DC-DC (for BEV) converters and battery management systems (for BEV) capable of resisting false data and false actuation attacks by leveraging redundancy, diversity, and watermarking; T5) using device fingerprinting to determine whether an actual EV is connected to the EVSE and, for the case of inductive charging, building a secure ranging system with spoofing detection to ensure that a vehicle is properly and safely aligned with the charging pad; T6) leveraging a trusted-computing base to guarantee that a formally verified, remote firmware update procedure takes place, even in the case of unreliable primary communications; and T7) extending the ISO/IEC 15118 protocol to ensure user privacy even in the case of untrustworthy agents or when communication has been impaired. It is anticipated that some tasks will span multiple domains (e.g., be undertaken for both EVSE and BEV). All work will be evaluated through modeling, simulation, and experimentation in the testbed (or on/in components thereof).

Results

Budget period one had 15 tasks. The team has made progress on Tasks 2–4, 6–13 during FY 20. Tasks 1 and 5 were completed in FY 19 and Tasks 14 and 15 have been moved to budget period two.

Task 2: Vulnerability Assessment of BEV

In FY 19 selected two high impact attacks for validation on the vehicle. Specifically, in order to cause permanent damage to the vehicle, we are attempting to overheat the main battery pack by either under-cooling the pack or over-charging it. The internal modules controlling cooling and charging have been identified and the team is has worked to understand their interactions and how fail-safes might be bypassed. A failsafe hardware injector with a communication interface capable of substituting arbitrary CAN messages in a timely fashion and impersonating legitimate sensor readings, which will be made available to other researchers, has been under development by undergraduate researchers at Virginia Tech. We also received a second vehicle for which a vulnerability assessment of the SAE J2847-2 communication interface is planned, thus emulating an EVSE attempting to compromise a BEV.

Task 3: Trust Models

For automatic threat assessment and attack graph generation, we have focused on CPS-centric attacks (i.e., delay, jamming, false-data injection, false-actuation injection) against the inputs and outputs of an AC/DC converter and DC/DC converter in a BMS. As both approaches require a model of the system under consideration, initial work has focused on a linearized model of the converters (Figure II.1.13.1). A cost-benefit analysis, based on a linear-quadratic differential game, was used to examine the effects of false-data injection (FDI), sensor jamming, and false-data actuation (FDA) against the team's proposed BMS design. The results show that most vulnerable components of the system lie primarily with the current and voltage sensor and that efforts should be expended on hardening these attack points from false-data injection and jamming, the

latter of which was found to be the most cost effective. To mitigate these attacks our hardened converter designs will have to rely on sensor/actuator redundancy and sensor diversity and the moving target defense.

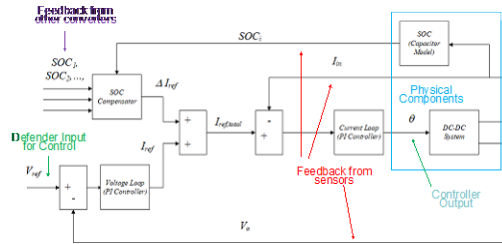


Figure II.1.13.1 BMS Model; Feedback Susceptible: FDI or Jamming; Controller Output Susceptible: FDA

For the threat assessment we have continued work to place constraints on attacker input and defender response. We have determined a new game formulations to enable stability and controllability analysis. Analysis indicates that jamming is the cheapest and most effective attack vector (Figure II.1.13.2); a new game formulation was devised to allow us to study the cost effectiveness of sensor redundancy for reducing the impact of the jamming attack, which is informing new hardware designs for the project. For automatic attack graph generation, we completed a formulation that accommodates FDI and FDI in a computationally efficient and tractable manner, with feasible paths forward for jamming/delay of actuation/sensor signals. Given the new formulation it is possible to state definitely whether an attacker could cause the system to enter an unsafe state. Based on this work, we have been able to unify the two problems (i.e., solving the jamming problem for will solve the cost-effective problem, too, as they are both optimization problems using linear-time invariant state-space models).

Sensors Jammed	$ \hat{v}_i $	$ \hat{v}_o $	$ S\hat{O}C $	$ \hat{x}_i $	$ \hat{x}_v $
2	0.047	2.9	0.04	0.047	0.00066
3	0.052	0.75	0.04	0.013	0.00035
4	0.041	0.7	0.04	0.017	0.0005

Figure II.1.13.2 Jamming effectiveness: perturbation leading to violation of small signal approximation. Sensor List: 2 - Current (Output perturbation > 5%, violation), 3 - Voltage sensor (Output perturbation > 5% if FDI is used in combination) 4-5 - SOC sensors (other converters)

Task 4: Vulnerability Assessment of EVSE

The team acquired a high-power charger (350 kW) from our new charging partner in Q2 0202 (Figure II.1.13.3). The high-power charger lacks UL certification but was delivered to partner ComEd’s research laboratory and will be integrated to it in Q1 2021.



CONNECTORS	CHAdEMO and CCS (Type 1 or 2)
POWER	Up to 50kW
SUPPLY INPUT	380 - 480 V AC 3ø
SUPPLY FREQUENCY	50-60 Hz
IP RATING	IP65
EFFICIENCY	>92%
POWER FACTOR	0.99
OPERATING TEMPERATURE	-35°C to 50°C
NETWORK CONNECTION	3G and Gigabit Ethernet
RFID	MIFARE ISO/IEC14443A/B, ISO/IEC15693, ISO/IEC18000-3, FeliCa, NFC, EMV 2.0
COMMUNICATION PROTOCOL	OCPP 1.5 and 1.6J
WEIGHT	165 kg
ELECTRICAL PROTECTION	Short circuit; Over voltage; RCD
DIMENSIONS	2000(H) x 750(W) x 330(D) mm
FREIGHT	24 units per 20' container
CERTIFICATION	CE, UL, CHAdEMO, RCM, FCC, IC

Figure II.1.13.3 A 350 kW XFC acquired from Tritium for project use.

Task 6: Develop a simulation circuit of the Bronzeville Community Microgrid

A one-line diagram of the Bronzeville Community Microgrid (~5,000 nodes) was used to create the microgrid network in OPAL-RT and RTDS simulators. In addition to the one-line diagram, necessary electrical characteristics of the microgrid have been gathered from ComEd, including feeder characteristics (i.e., length, R and X values, as well as existing protection and monitoring devices), operating characteristics of existing generating sources (i.e., solar PV, battery, diesel generator) and loads at each node of the microgrid were used by the team to develop a detailed circuit model of the Bronzeville Community Microgrid in Cyme. ComEd also developed a detailed RSCAD model that will be utilized for Hardware in the loop simulations (Task 7) on their RTDS system.

Task 7: Create BEV charging profiles using Monte Carlo simulation and insert BEV charging units with variation of charging profiles into the microgrid

The team has developed an initial draft of the XFC test plan; specifically, initial integration and test architecture was developed for testing of XFC in ComEd Grid Integration and Testing lab in Maywood (Figure II.1.13.4). ComEd have reached out to six vendors for the design and development of a 350kW EV simulator which is to be placed in an outdoor container capable of testing and validating the XFC from Tritium.



Figure II.1.13.4 ComEd’s Integration and Technology lab

Since we have not obtained actual XFC performance data, we have used publicly available EV charge/discharge data to study the impact of EV operation on the power network. CYME software, as well as a state-space approach, was used to study the network performance. Loading effects due to increased EV usage appeared to scale non-linearly (Figure II.1.13.5).

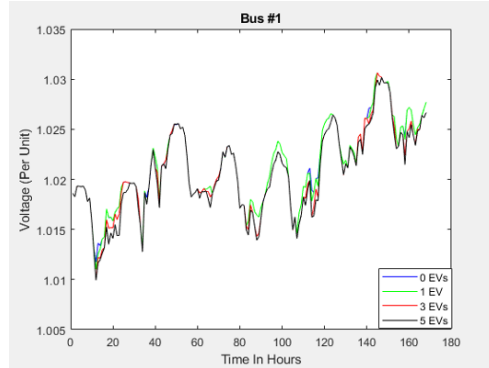


Figure II.1.13.5 Variation of bus voltage with time for varying number of EVs during charging.

Task 8: Combined proactive and reactive defense mechanism

Security in CPS often relies on detectors that require models of the system, to compare what the readings are versus the expected value, to find malicious activity. Due to measurement and process noise, it is possible that an adversary may perpetrate undetectable attacks. To provide motivation for our MTD, which does not require a model, we examined the sensitivity of model-based attack detectors to measurement and modeling uncertainty, ultimately showing the weaknesses in relying solely on model-based detectors for attack detection.

To address this, we developed a model-free framework for optimal output feedback control by stochastic approximate dynamic programming (ADP) for DC-DC converters with enhanced security capabilities. We consider systems with actuator and sensor redundancy with parallel layout of same DC-DC converter structure but different component values. Proactive defense mechanism is realized by a moving target defense (MTD, Figure II.1.13.6) strategy to dynamically switch amongst different modes. Reactive defense mechanism utilizes the Bellman error to detect attacks for the actuators and sensors compromised by additional false data. Switching rules with proactive defense and reactive defense mechanism are proposed to guarantee the asymptotical stability of the switched system. Finally, simulation results of a real DC-DC converter show the effectiveness, the cost, and the computational capabilities of the MTD defense mechanism and Bellman error detection approach.

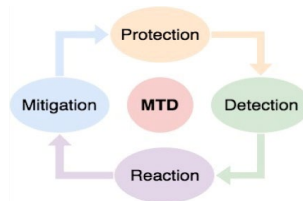


Fig. MTD framework with detection and mitigation

Figure II.1.13.6 The components of a moving target defense.

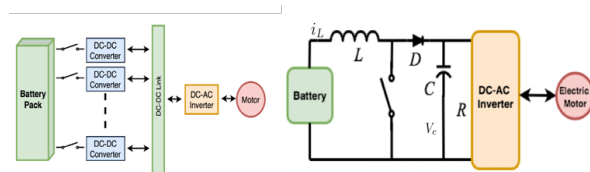


Fig. DC-DC converter topology and set-up

Figure II.1.13.7 DC-DC Converter topology enabling MTD.

We have also extended this framework by introducing adversaries with bounded rationality into cyber-physical security, leading to non-equilibrium games. A sequential procedure is presented, that allows for the formulation of policies chosen by adversaries with different levels of intelligence. It is shown that, under appropriate conditions, the infinite thinking step coincides with the Nash equilibrium, thus allowing for an optimum defense. A model-free framework is modified to facilitate learning of defense policies with arbitrary levels. A cognitive hierarchy approach is considered, where the levels are assumed to follow a Poisson distribution. An algorithmic framework is constructed, that allows the defender to learn the value of the distribution by interacting with the adversaries in a sequential manner (thus enabling the defense).

In order to strengthen our MTD we have also developed a data-based, learning framework for the detection and mitigation of replay attacks against actuators. In our approach optimal watermarking signals are added to actuator signals and we then use a data-based technique to learn the best defending strategy in the presence of worst-case disturbances, stochastic noises, and replay attacks. A data-based Neyman-Pearson detector design was proposed to identifying replay attacks (Figure II.1.13.8).

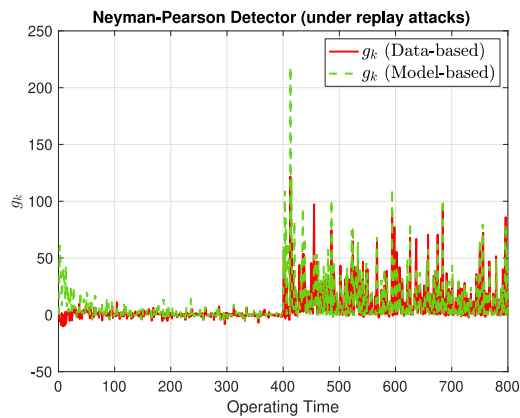


Figure II.1.13.8 A data-driven framework for detection of replay attacks is able to detect attacks more accurately than traditional model-based detectors.

Task 3: Iterative design of 300 kW AC-DC converter and 5 kW integrated active BMS plus DC-DC converter

The team has identified vulnerabilities in the AC-DC and DC-DC converter after performing cyber-physical attacks in hardware using intentional electromagnetic interference (IEMI) attacks. As part of that the process the team performed intentional electromagnetic interference attacks on the AC-DC 2 kW prototype and DC-DC converter hardware to identify the vulnerabilities. The experimental results show that both the voltage and current sensing feedback signals and the PWM signals of the AC-DC converter could potentially be manipulated (Figure II.1.13.9). Based on the assessment results, the team has proposed several hardware hardening approaches to increase the cyber-physical security. A publication detailing our analysis, showing the first ever attacks against power switches, has been produced (Figure II.1.13.10). Prototype boards containing the proposed countermeasures have been developed and manufactured and the countermeasures proposed therein are being evaluated by the team. Efficacious countermeasures will be incorporated into the final converter designs.

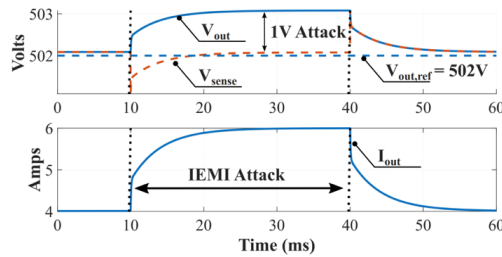


Figure II.1.13.9 A linear scaling of voltage sensor output from an intentional electromagnetic interference attack leads to an exponential increase in output current in a prototype AC-DC converter.

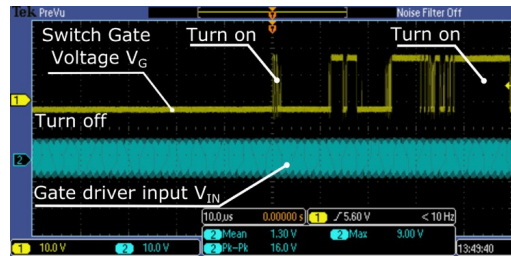


Figure II.1.13.10 Intentional electromagnetic interference forces a switch closed in an AC-DC converter, resulting in a short circuit.

The evaluation boards were designed so that different hardening techniques could be evaluated reliably in the presence of an IEMI attack. From the previous attacks on the hardware, it was hard to tell whether the IEMI attack was effectively coupled to the signal traces or just the scope probes due to the lack of quality test points on the signal traces. The evaluation boards were designed to have a multitude of test points which can accommodate a probe ground spring which helps reduce the loop area of the probe resulting in a cleaner measurement in the presence of IEMI.

The system level iterative design of the full power AC-DC converter (480 V 3-phase AC input, 350 kW rated power AC-DC converter, consisting of five modules with 70 kW rated power each) and the 5-kW integrated active battery management system has been completed (Figure II.1.13.11) and components finalized. In the first phase of development, the topology and control design of the converter module had minimal consideration of cyber-physical security hardening, which were enhanced in later design iterations.

The AC-DC converter consists of one Unfolder feeding multiple DC-DC modules. The DC-DC modules will all be connected in parallel at the input side which is connected to the Unfolder's Soft DC-Link. The output of the 20 DC-DC modules are connected by stacking 5 sets of 4 paralleled modules as shown in Figure II.1.13.12. The modular structure of the AC-DC system allows for the DC-DC converter to be designed considering a narrower range of output voltage and current which increases the efficiency at all operating conditions. The modular design also provides more flexibility in implementing the moving target defense for the full power AC-DC converter. Each DC-DC module is rated for 18 kW. The chosen topology for the DC-DC module is the 3-Level Asymmetrical Dual Active Bridge (3LADAB).

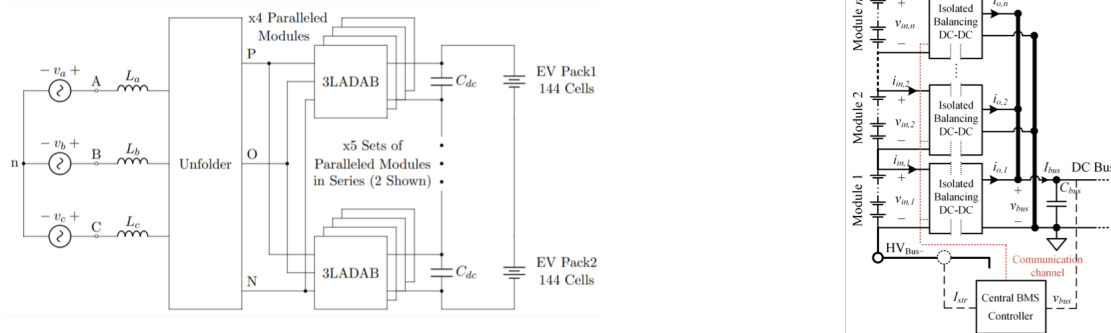


Figure II.1.13.11 (left) 350 kW AC-DC System Architecture and (right) 5 kW BMS System Architecture

Task 10: Hardware construction of BMS with integrated 5 kW DC-DC for vehicle LV loads

The team has completed another iteration of the DC-DC converter layout design with the lessons learned from the tests and the integration of cyber-physical hardened designs. The lessons learned from the second iteration of the DC-DC converter layout have been integrated into a final revision that has been sent out for manufacture. A scaled battery pack for battery pack cooling design validation has been assembled and thermal testing is underway. Testing open-loop bi-direction up to full power (300 W) for the DC-DC converter and thermal performance of the DC-DC converter. The efficiency of the DC-DC converter module has been measured for both forward and reverse power operation.

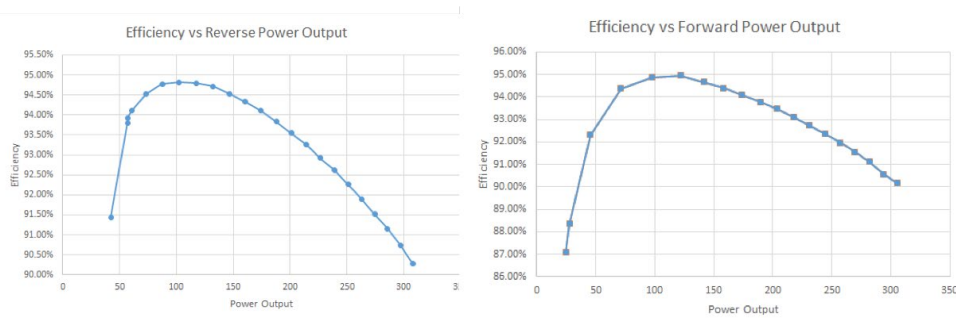


Figure II.1.13.12 Efficiency of reverse and forward power output of BMS design.

Task 11: Hardware construction of 60 kW module prototype for AC-DC converter

The team has worked on the testing and closed-loop implementation of the 2-kW prototype, full power AC-DC converter specification, and hardware construction of the 18 kW (previously identified as 60 kW) module prototype for this task. AC-DC closed-loop testing has been completed on the developed 2 kW prototype. The lessons learned and control strategies validated from the low power prototype have been applied to the hardware construction and control implementation of the 18-kW module prototype for the AC-DC converter. The PCBs for the 18-kW module prototype were sent out for fabrication. Hardware construction and testing of the first high-power Unfolder module has been completed and verified with a resistive load.

Task 12: Devising device fingerprinting methodologies for conductive and inductive chargers

A loop detector architecture was devised to allow for the extraction of a rich feature set for vehicle identification. Current fingerprinting approaches based on loop detectors make use of a small set of features that are only able to differentiate between classes of vehicles. Over the last reporting period the team evaluated, via simulation, three proposed fingerprinting architectures: 1) using traditional inductive-loop oscillators with time-varying components; 2) extracting additional features from traditional loop systems; and 3) generating and transmitting complex, high bandwidth waveforms examining the signal returned by the vehicle through coupling. The primary evaluation criteria was the extent to which information-rich waveforms

could be extracted from vehicle interactions, based on the theory that identifying individual vehicle models will require greater information content than existing inductive-loop detectors possess. The team finalized the design of, and purchased components for, a fingerprinting architecture capable of driving a highly inductive load over a 16-octave bandwidth at sufficiently high current (3 A nominal) to couple to a vehicle (Figure II.1.13.13).

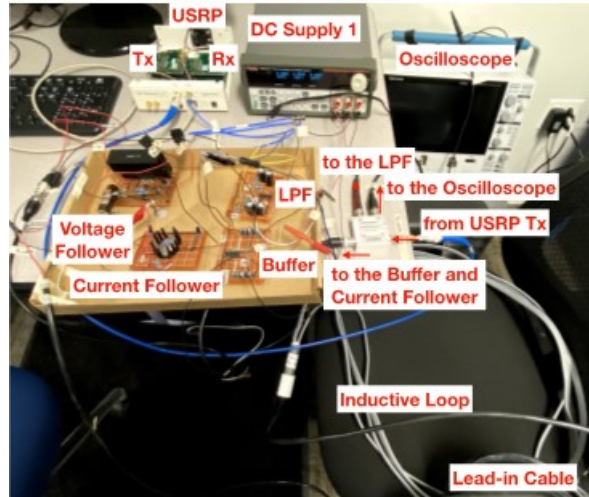


Figure II.1.13.13 Transmitter and receiver components for inductive-loop fingerprinting of vehicles.

Task 13: Creation of formally verified update procedure

Leveraging ARM's trusted execution model, we proposed a design model for improving the security of over the air updates (OTA) for EVSE/BEV. Our approach wraps a standard OTA verification framework (UPTANE) inside a trusted execution environment (TEE) to guarantee execution of the update framework. A C implementation of the client side of the UPTANE framework has been completed, which includes wrapper functions for encoders, JSON/DERR processing, and general functionality for verifying updates after they've been downloaded and for sending feedback to the central repository was completed. We leveraged the SAW tool to formally verify our proposed framework, while checking for any software vulnerability in our implementation. A working implementation was demonstrated on a Raspberry Pi 3B using ARM TrustZone and OP-TEE.

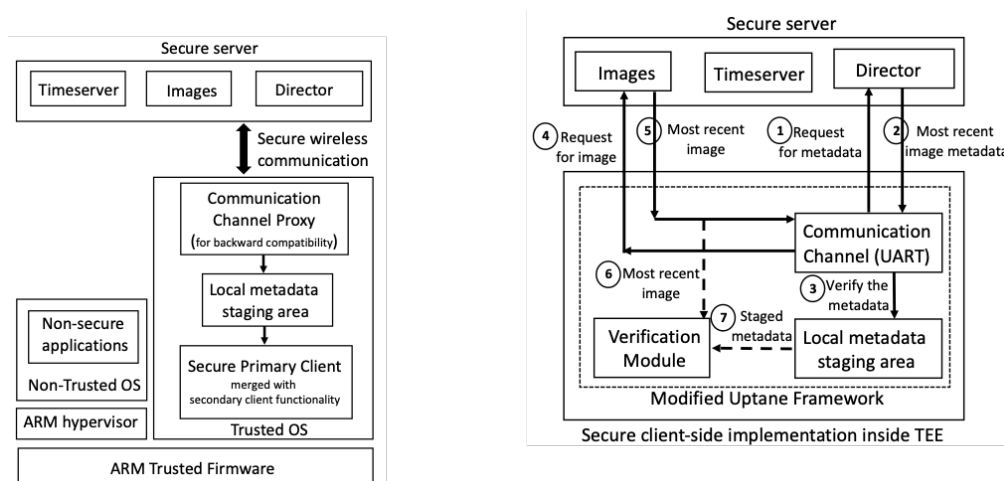


Figure II.1.13.14 (left) Update architecture and (right) formally verified update procedure for input data correctness/parsing

Conclusions

Extremely fast charging (XFC) has the potential to reduce the charging time of battery electric vehicles (BEV) to be equivalent to the filling time of internal combustion engine vehicles (ICEV), thus eliminating one of the few advantages ICEV still possess for light- and heavy-duty vehicles. Enabling XFC will, however, require coordination and cooperation between the grid, charging stations, and the vehicles themselves, which leads to an inevitable increase in the attack surface for all systems combined. In securing the overall system, we must not only embrace traditional cybersecurity, which is chiefly concerned with communications and the operation of digital systems, but also cyber-physical systems security as the proper operation of XFC is critically dependent on systems' abilities to know about (sense) and interact with (actuate) the physical world.

Key Publications

1. Gu, Patrick, and Ryan M. Gerdes. "Linear-Quadratic Game Theoretic Analysis for Securing Battery Management Power Converter Systems." In Proceedings of the Second ACM Workshop on Automotive and Aerial Vehicle Security, pp. 15-22. 2020.
2. Dayanikli, Gokcen Y., Rees R. Hatch, Ryan M. Gerdes, Hongjie Wang, and Regan Zane. "Electromagnetic Sensor and Actuator Attacks on Power Converters for Electric Vehicles." In Proceedings of IEEE Workshop on the Internet of Safe Things (SafeThings), 2020.
3. Garrett, Ian Y., and Ryan M. Gerdes. "On the Efficacy of Model-Based Attack Detectors for Unmanned Aerial Systems." In Proceedings of the Second ACM Workshop on Automotive and Aerial Vehicle Security, pp. 11-14. 2020.
4. Zhai, Lijing, and Kyriakos G. Vamvoudakis. "A data-based private learning framework for enhanced security against replay attacks in cyber-physical systems." *International Journal of Robust and Nonlinear Control* (2020).
5. Kanellopoulos, Aris, and Kyriakos G. Vamvoudakis. "A moving target defense control framework for cyber-physical systems." *IEEE Transactions on Automatic Control* 65, no. 3 (2019): 1029-1043.

Acknowledgements

The team is grateful for the input provided by, and insights of, Jonathan Petit and his team at Qualcomm Technologies, Inc.

II.1.14 Cybersecurity for Grid Connected eXtreme Fast Charging (XFC) Station (ABB)

David Coats, Principal Investigator

ABB Inc.
1021 Main Campus Drive, Suite 100
Raleigh, NC 27606
Email: David.coats@us.abb.com

Don Scoffield, Principal Investigator

Idaho National Laboratory
1955 North Fremont Avenue
Idaho Falls, ID 83415
Email: don.scoffield@inl.gov

Karl Heimer, Principal Investigator

APS Global
3001 Gazebo Court
Silver Spring, MD 20904
Email: karl.heimer.pro@gmail.com

Austin Benzinger, Principal Investigator

XOS Trucks
11347 Vanowen Street
North Hollywood, CA 91605

Lee Slezak, DOE Program Manager

U.S. Department of Energy
Email: Lee.Slezak@ee.doe.gov

Start Date: October 1, 2018
Project Funding: \$1,300,000

End Date: June 30, 2021
DOE share: \$1,047,000

Non-DOE share: \$253,000

Project Introduction

Deployment of electric vehicle supply equipment (EVSE) requires widespread infrastructure to meet market demand at the different places where cars travel, such as homes, public/private establishments, or the highway corridor. The impact of extreme fast chargers (XFCs) on the distribution system may be neglected for small charging stations with only a few chargers, however, when many EVs are charging simultaneously at an EVSE installation site, the aggregate energy demand may provide a significant grid impact to a distribution or other energy delivery system. As charging power levels and charging speeds increase over time with newly manufactured EVSEs, EVs, and battery storage, this cumulative EV charging load becomes a greater issue. The synchronous charging of multiple battery EV type vehicles at an XFC station may cause potential adverse impacts to the distribution system (e.g., distribution network and protection). Through this funded project, these grid impact events are first modeled and then categorized with threat analysis, detected using a Coordinated Anomaly Detection System (CADS), and incorporated into a secure XFC Management system (XMS) for resilient control.

Objectives

ABB (Prime Contractor), in collaboration with its partners at Idaho National Laboratory, APS Global and XOS Trucks, will perform research, development, and demonstration of a security domain layer that enables an XFC station to detect and defend against cyber-attacks. The project members will develop algorithms hosted at the EVSE level that defend against cyber-attacks, including a State Estimation (SE) method for measurement

verification and CADs for improving SE based on operation over time or extensive generation of simulated data. These algorithms together form a secure XMS which aims to protect against disruption to electric power service and/or charging station operation while allowing new device integration such as Battery Energy Storage Systems (BESS).

Approach

ABB and the project team will design and test an alerting defense system to improve cyber-security situational awareness in electric vehicle supply equipment (EVSE) as part of a connected eXtreme Fast Charging (XFC) Management System (XMS). The project team aims to achieve robust performance capability with component-level validation in a laboratory setting with power hardware-in-the-loop simulators. In some cases, new functionality such as BESS integration and optimization will be prototyped to demonstrate new use cases that more fully display potential grid impact and the importance of secure communications in the face of increasing demands for connected utility services at the XFC station level. The project will demonstrate the system in a testbed environment and validate the timing and security aspects. The outcome of this project will enhance XFC station management systems (XMS) and other devices with new hardware and firmware/ software function(s) to support detection and defense mechanisms.

Results

Within the second fiscal year of the Cybersecurity for Grid Connected XFC Station project (CyberX), the project team has used a versatile XFC station model to create a hardware in the loop testbed in real-time, incorporated high fidelity Personal Electric Vehicle (PEV) charging and load forecasting PEV models, developed an adversarial attack tree and five most likely threat paths to general EVSE, and a prototype XMS integration controller for measurement monitoring and anomaly detection algorithms with real and simulated EVSE devices. Primary accomplishments and supporting tasks related to key milestones of (1) XFC management system steady state validation and (2) Hardware integration with HIL co-simulation platform were completed and started respectively and will be outlined in the following results and figures. Some aspects of hardware integration and software testing have been delayed due to COVID-19.

XFC Station Modeling and Real-time Simulation

In the first fiscal year of the project, a representative XFC station and its feeder system were modeled within MATLAB/Simulink and Opal-RT systems for several XFC station operation conditions supporting site management and interconnection. The initial modeled power distribution system is shown in Figure II.1.14.1.

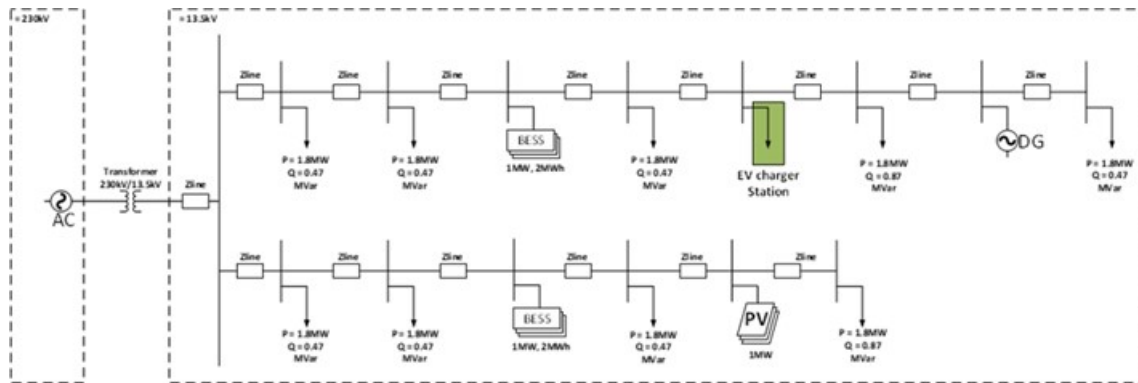


Figure II.1.14.1 Single line diagram of the modeled power distribution system with XFC Station

In the second fiscal year, this modeling work was improved with a focus on greater accuracy of modeled components and modeling of control and communication capabilities in real-time. A three-phase rectifier as a power interface connects the battery DC voltage to the grid AC voltage. The corresponding power and voltage controller was designed and is shown here in Figure II.1.14.2. Energy storage battery and renewable energy generation solar power are modeled in MATLAB/Simulink and integrated with the CyberX HIL simulation in

Opal-RT. Control commands and setpoints can be sent from the XMS platform to the BESS model over Modbus and OPC-UA protocols according to an optimal scheduling while adversarial input commands can also be simulated. Connections to protection devices are enabled by using IEC61850 protocols and status of devices is available within modeled scenarios such as steady state operations or adversarial conditions.

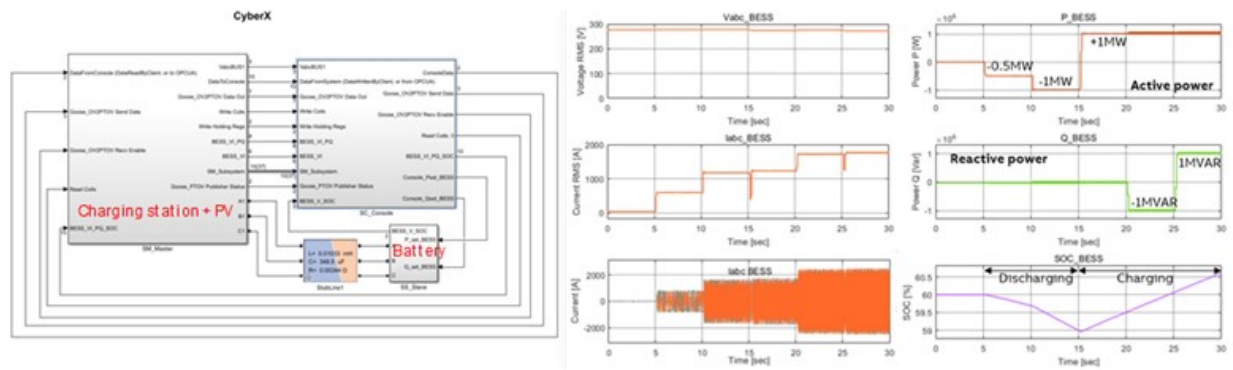


Figure II.1.14.2 Real-time model developed in Opal-RT with communications and simulated BESS

XFC and Management System Threat Analysis

ABB with partner APS Global analyzed 3,982 exploit kill-chains modeled for XFC, BESS, and Remote Operators of charging station and provided the top fourteen impactful events within DoE project Milestone report 2. Most likely attack methods for EVSE were found to be (1) exploitation of cellular technology in XFC, (2) exploitation of the physical state of the charging cable to cause a cyber physical effect, and (3) exploitation of the charging unit human machine interface (HMI). Five most likely exploit kill-chains were determined and ABB with APS Global created a test plan to explore these cases further within the project. Three demonstration attack vectors were determined for demonstration within the project with intended cyber physical effect was determined. These scenarios include (1) spoofing of EV state of charge and EVSE metering, (2) artificial reduction of reported charging aggregate current from multiple chargers, and (3) tampering with BESS control to cause improper charge and discharge cycles for reduced economic performance. Mitigations were planned for each potential threat and testing of these mitigations is in process at ABB facilities delayed by COVID-19 and reduced laboratory access time. APS Global subject matter experts have set up a remote testbed connected to an EVSE, EV charging emulator, and XMS control equipment to verify planned demonstration scenarios.

Resilient Control Architecture Design

The resilient control architecture for integration of local energy resources (e.g., DER or BESS) and XFC charging station site equipment consists of two main concepts currently in development with significant year 2 results. The first concept is an XFC management system (XMS) consisting of a hardware gateway and modular local interface modules (LIM). These LIMs may be software-based or hardware devices placed within EVSE charging station cabinets designed to provide measurements to the XMS hardware through on-site connections. The XMS has been designed to host a battery optimizer application, communication and measurement interfaces, State Estimation method, and communications monitoring feeding into a Coordinated Anomaly Detection System (CADS). The prototype XMS provides several communications protocols currently featuring Modbus and OPC-UA for BESS integration, IEC61850 GOOSE communication for protection device integration, Open Charge Point Protocol (OCPP) for monitoring EVSE metering and transaction information, and Control Area Network (CAN) for more granular monitoring of EVSE.

Battery Optimizer and XMS Integration

The use case of focus in this effort is a public XFC depot that includes a stationary BESS that is used to shift load to manage power constraints and save energy costs. In order to get the best performance out of the BESS, an optimizer module has been developed for the XMS. The optimizer finds a schedule of charging and

discharging commands for the BESS that minimizes total costs, given input forecasts of energy price and EV load developed by INL. By using load and price forecasts, the optimizer manages the BESS state of charge, ensuring that it is neither fully charged nor discharged when it is needed. A model-predictive-control approach is used, where the optimizer solves the problem periodically, applying the first element from the BESS command schedule then updating the schedule as the load forecast changes. This mitigates forecast inaccuracy. Figure II.1.14.3 shows the results of an offline test of the optimizer using EV load data generated with Caldera. The BESS is controlled to minimize the total cost to supply the EV load which, it is assumed, cannot be adjusted. The energy price varies over time; Figure II.1.14.3 shows that the BESS charges right before the price increases and discharges while the price is high.

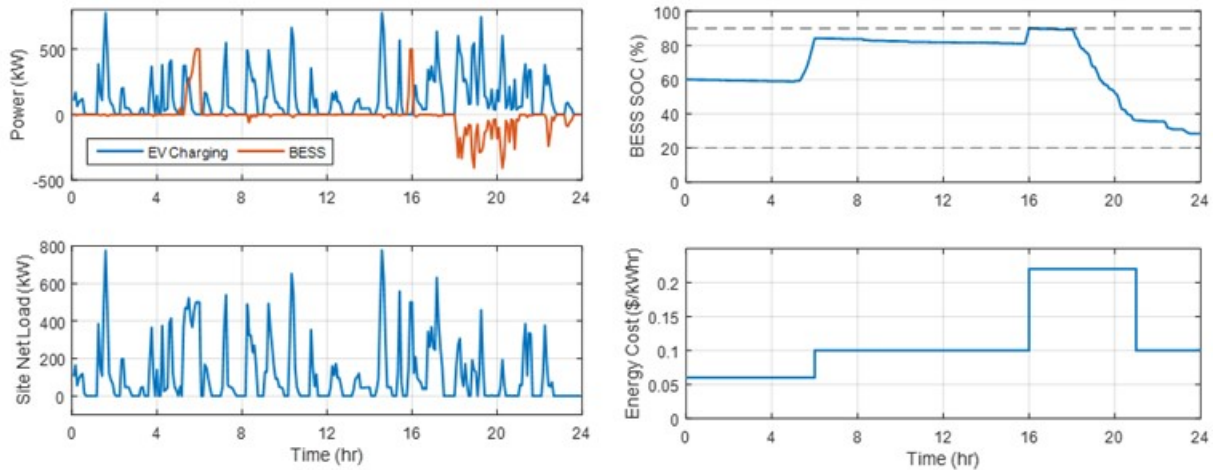


Figure II.1.14.3 Actual EV load and optimized BESS results (top left); optimized BESS SOC (top right); net station load (bottom left); and input energy price profile (bottom right)

The optimizer module has been integrated into an XMS environment based on the ABB Zenon electrical system management platform. This prototype XMS solution provides a user interface that monitors energy flows and charging status, which can be read from field devices over a variety of communication protocols. The XMS runs the optimizer every 30 seconds using updated EV charging data, then issues the BESS charge/discharge command over Modbus.

Coordinated Anomaly Detection System

The Coordinated Anomaly Detection System (CADS) takes input measurements, status information from multiple communications sources, historical data and trends of these inputs, and provides rule-based determinations of emergent anomalous operational states. Separate algorithms contribute to the combined CADS including state estimation-based measurement validation and recurrent neural network parameter estimation. The state estimation algorithm detects faulty sensors or false data injection attacks in the EV charging station by forming a weighted estimation matrix of the electrical system. The matrix is formed based on the Kirchhoff's Current Law physical parameters of the system, topology, circuit breaker status, and redundant measurements allowing a SE error percentage metric to be determined for each measurement. Based on this error percentage as an indicator of potential tampering with measurements and spoofing of data, an alert is sent to the XMS and action can be taken by an operator ranging from isolating devices from the charging network or sending maintenance staff to verify system conditions.

In order to detect abnormal operation, redundant measurements and system topology of EV charging station are taken into account in the estimation matrix. The performance of the state estimator can be improved by factoring in chargers with a two-channel "Dynamic DC Charging" feature. This allows three current measurements to be obtained for single EVSE unit. The added current measurements and topological complexity improve the state estimator's ability to detect and identify abnormal measurements. This charging

site configuration is shown in Figure II.1.14.4 with abstracted measurements feeding into the state estimation matrix and subsequent machine learning parameter estimation. The state estimation is then used to provide.

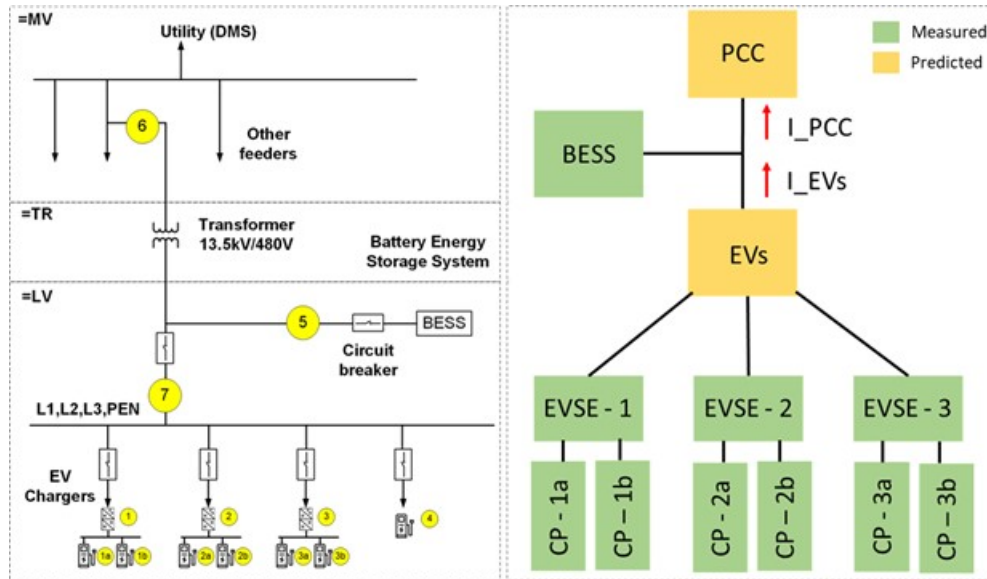


Figure II.1.14.4 Figure Physical and abstracted measurements for Coordinated Anomaly Detection System

Sensor data spoofing has been identified by APS Global as one of the critical cyber-security risks and planned for in adversarial testing. The BESS charging optimizer also uses sensor measurements from various parts of the EV charging station for its control actions and provides a good case study for the types of EV charging applications of growing importance to charging station operators. Thus, checking that the sensor data for BESS and EV metering has not been spoofed is of highest importance. This is the goal of the Coordinated Anomaly Detection System (CADS) and the recurrent neural network parameter estimation subsystem. Multiple LSTM (Long-Short Term Memory) recurrent neural networks are trained to predict the RMS current at the point of common coupling (PCC) to utility distribution system and the RMS current at the aggregation of EV chargers. Each neural network ignores a subset of sensor measurements from one EV charger. If a consensus can be reached between the multiple predictions of these trained LSTMs and also the actual measurements, then the sensor data has been verified to be secure. If there is an anomaly, then the appropriate charger can be flagged. A total of 55 features or measurements are available including charging status information.

The data for training is obtained from simulations of the EV charging station. Caldera models from Idaho National Labs are used to obtain realistic charging profiles. The EV charging stations is simulated in SIMULINK with randomized charging events. The sensor data is sampled at 1 Hz. The LSTM training is done in Python. LSTMs are known to work well for time-series predictions. The plot shown in Figure II.1.14.5 provides a prediction of the normalized current at the point of common coupling (PCC) when RMS current data from EV charger EV1a is ignored. The LSTMs are currently being tuned and the dataset is being expanded for better training results. The prediction results are promising. This approach is easy to deploy for any EV charging station electrical architecture – as long as the training data can be collected.

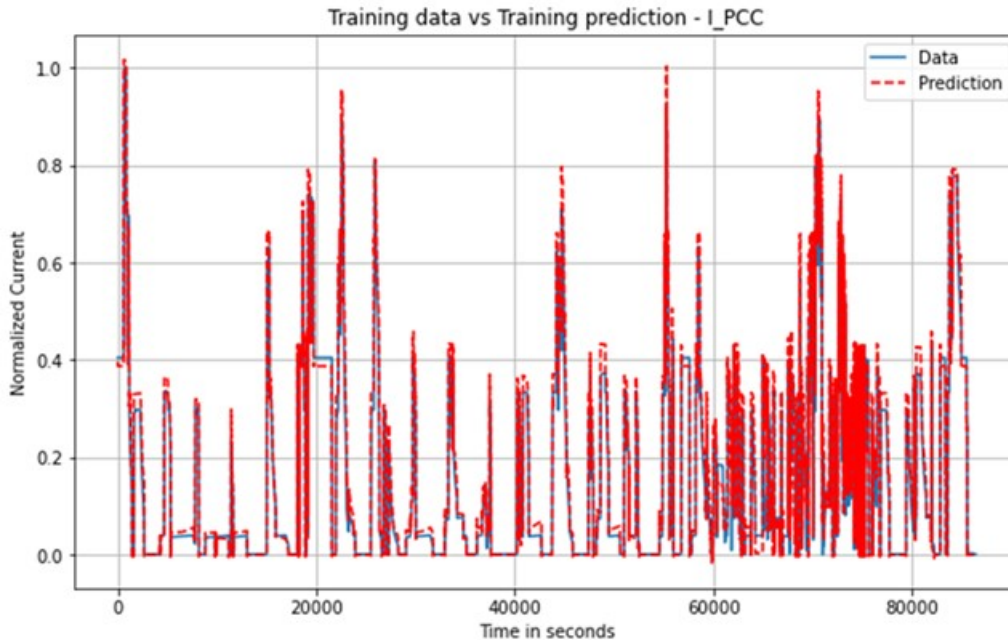


Figure II.1.14.5 Prediction results for normalized charging site current based on Long-Short Term Memory

Testbed and Demonstration Platform

Combining the distribution grid model, high fidelity PEV charging models, existing ABB EV charging station, the prototyped XMS platform, and novel CADs algorithms, ABB and team have built a preliminary resilient control steady state test platform. This existing intermediate HIL testbed is outlined in Figure II.1.14.6. The Medium Voltage (MV) utility distribution grid, the XFC station transformer, and Low Voltage (LV) protection equipment and BESS are all simulated in the Opal-RT platform in real-time. Several XFC with connected PEV are modeled on a Linux host device and integrated with the Opal-RT over ethernet internet protocol (IP) connection. A physical EVSE is also provided with a connected resistive vehicle charging emulator capable of charging over Combined Charging system (CCS) connector. These simulated devices also provide measurement information to the XMS control platform over OCPP and OPC-UA secure protocol implementations. The XMS acts as an OCPP central system emulator and provides control signals to BESS over Modbus or OPC-UA communications. The XMS also communicates with a real ABB charger by means of a hardware Local Interface Module, and inputs from all chargers can be provided as inputs to the CADs algorithm along with circuit breaker status and transaction commands sent over OCPP. These measurements additively contribute to the anomaly detection algorithms prototyped to detect abnormal measurements. The XMS, LIMs, and Opal-RT form part of a mobile testbed and are planned for transfer to the INL EVIL testbed by the end of the CyberX project for full demonstration and further validation of XMS hosted algorithms with prototype medium duty trucks provided by XOS trucks.

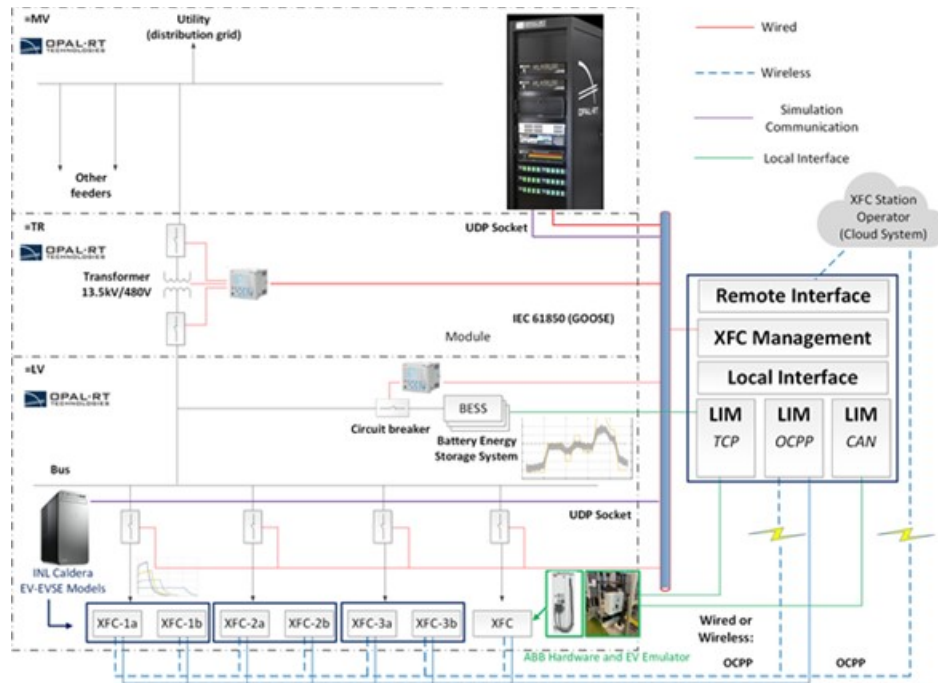


Figure II.1.14.6 Extreme Fast Charger Management System (XMS) Incorporated in HIL Testbed

Conclusions

A resilient architecture with security-focused communications monitoring has been determined for the XFC management systems and demonstrated using HIL modeling for initial results. This management system includes several component systems that additively provide a resilient operating platform for an XFC station. This includes Battery Energy Storage Systems (BESS) and other renewable sources integration and optimization along with measurement inputs from protection and control systems at an EV charging site. A steady state operation and battery optimization method was developed as a baseline for resilient control of the XFC station. A secure communication monitoring and analytics method was demonstrated to support layered control operations and a coordinated anomaly detection system (CADS).

This CADS is demonstrated by monitoring key communication protocols locally and developing algorithms to detect abnormal charging durations and measurement based on system measurement. State estimation-based measurement validation and recurrent neural network parameter estimation subsystems of the CADS algorithm were prototyped and tested. Initial test scenarios were prototype to demonstration (1) spoofing of EV state of charge and EVSE metering, (2) artificial reduction of reported charging aggregate current from multiple chargers, and (3) tampering with BESS control to cause improper charge and discharge cycles for reduced economic performance.

Key Publications

1. D. Coats, H. J. Lee, A. Brissette, J. Wang, "Resilient Control Architecture Report - Cybersecurity for Grid Connected eXtreme Fast Charging (XFC) Station (CyberX)," Jan. 2020
2. D. Woodbury, R. Hansen, "Threat Analysis Report - Cybersecurity for Grid Connected eXtreme Fast Charging (XFC) Station (CyberX)," Jan. 2020

References

1. J. C. Gomez and M. M. Morcos, "Impact of EV Battery Chargers on the Power Quality of Distribution Systems," in IEEE Transactions on Power Delivery, vol. 18, no. 3, pp. 975-981, July 2003.

2. T. Yang, H. Sun and A. Bose, "Transition to a Two-Level Linear State Estimator—Part II: Algorithm," in IEEE Transactions on Power Systems, vol. 26, no. 1, pp. 54-62, Feb. 2011.
3. E. Chemali, P. J. Kollmeyer, M. Preindl, R. Ahmed and A. Emadi, "Long Short-Term Memory Networks for Accurate State-of-Charge Estimation of Li-ion Batteries," in IEEE Transactions on Industrial Electronics, vol. 65, no. 8, pp. 6730-6739, Aug. 2018, doi: 10.1109/TIE.2017.2787586.

Acknowledgements

The author would like to thank the ABB project team (V.R. Ramanan, Alex Brissette, Zhenyuan Wang, Yuzhi Zhang, and Harish Suryanarayana), former team members (Junho Hong, HyoJong Lee, Joseph Carr, and Alok Kucheria) the APS Global and partners project team (Rick Hansen and Duncan Woodbury), and the Idaho National Laboratories team (Yusheng Luo and others).

II.1.15 Bidirectional Wireless Power Flow for Medium-Duty Vehicle-to-Grid Connectivity

Steven Sokolsky, Principal Investigator

CALSTART
1509 Wendy Lane
Madison, WI 53716
Email: ssokolsky@calstart.org

Omer C. Onar, Technical Lead

Oak Ridge National Laboratory, Vehicle Power Electronics Research Group,
National Transportation Research Center, 2360 Cherahala Boulevard
Knoxville, TN 37932
Email: onaroc@ornl.gov

Burak Ozpineci, Section Head and ORNL Program Manager

Oak Ridge National Laboratory, Vehicle and Mobility Systems Research Section
National Transportation Research Center, 2360 Cherahala Boulevard
Knoxville, TN 37932
Email: burak@ornl.gov

Lee Slezak, DOE Program Manager

U.S. Department of Energy
Email: Lee.Slezak@ee.doe.gov

Start Date: October 2016

End Date: June 2021

Project Funding: \$2,631,321

DOE share: \$1,949,007

Non-DOE share: \$712,314

Project Introduction

Wireless power transfer (WPT) is a paradigm shift in electric-vehicle (EV) charging that offers the consumer an autonomous, safe, and convenient option to conductive charging and its attendant need for cables. With WPT, charging process can be fully automated due to the vehicle and grid-side wireless communication systems, and is non-contacting and inherently isolated; therefore, issues with leakage currents, ground faults, and touch potentials do not exist. It also eliminates the need for touching the heavy, bulky, dirty cables and plugs. It eliminates the fear of forgetting to plug-in and running out of charge the following day and eliminates the tripping hazards in public parking lots and in highly populated areas such as shopping malls, warehouse loading areas, recreational areas, parking buildings, etc. Furthermore, the high-frequency (HF) magnetic fields employed in power transfer across a large air gap are focused and shielded, so that fringe fields (i.e., magnetic leakage/stray fields) attenuate rapidly over a transition region to levels well below limits set by international guidelines for the public zone. With the bidirectional wireless power transfer, not only vehicles can be wirelessly charged, but also the vehicles can wirelessly provide power back to the grid or the facility. With bidirectional power flow, vehicles can be enabled to provide microgrid or grid support or ancillary services. Grid support may include peak shaving, renewable energy firming/integration, time of use energy management, power quality improvement, voltage regulation, reactive power compensation, etc. Grid ancillary services to be provided might include spinning and non-spinning reserves, area/frequency regulation, load following, scheduling and dispatch, etc. if a number of vehicles are aggregated to provide such services. In the case of an outage, vehicle batteries can also serve as an emergency backup power for a period of time.

In this project, CALSTART, ORNL, UPS, Workhorse Group, and Cisco Systems proposed to model, research, analyze, design, develop, integrate, and demonstrate a bi-directional wireless power transfer system (BWPT) suitable for Class 5 and Class 6 medium-duty plug-in hybrid delivery trucks. The project team designs, develops, integrates, and tests a bi-directional wireless charging system capable of meeting the 11-inch ground

clearance needed for UPS delivery trucks. After integrating to a Workhorse manufactured plug-in hybrid electric vehicle (PHEV), the system performance will be demonstrated at the deployment site. Within the first budget period of the project (May 2017-May 2018), team has completed the modeling, simulations, design, and analysis of the system power conversion stages including the 3-phase active front-end rectifier with power factor correction (also grid interface inverter), primary-side HF inverter (also primary-side rectifier), primary and secondary-side resonant tuning components, primary and secondary-side electromagnetic coupling coils, vehicle-side HF rectifier (also the vehicle-side HF inverter). As of submission time of this report, hardware both the primary and secondary sides have been completed and the power conversions stages have been successfully tested. All of the subsystems and components have been validated based on their parameters and performance metrics. Now the team is starting the vehicle integrations and system will be deployed with full vehicle integrations for the testing, demonstrations, and data collection purposes.

Objectives

The overall project objectives can be summarized as follows:

1. Provide an automated, high power, interoperable, high-efficiency wireless charging for a plug-in hybrid electric medium duty delivery truck with a nominal ground clearance of approximately eleven (11) inches.
2. Optimize the add-on vehicle-side wireless charging components through integration and utilization of already existing vehicle-side components while implementing grid-side controls and regulations to reduce the vehicle-side cost, size, volume, and complexity.
3. Utilize bi-directional wireless charging systems when trucks are parked in the yard for staging to provide grid support applications or ancillary or grid support services such as frequency regulation, load leveling/peak shaving/load factor improvement/reactive power support/demand charge management, and spinning/non-spinning reserves.
4. Provide an integrated > 20kW wireless charging system (grid to vehicle) with high efficiency (85%) while meeting the international guidelines on electromagnetic and electric field emissions during charging and include all other appropriate safety features.
5. In vehicle-to-grid mode, achieve 6.6kW wireless power transfer to building or grid loads.

Approach

Starting from the AC grid to the vehicle battery terminals, the system power converters must be well-designed and operated in order to achieve high efficiency. In addition, power flow control to the pick-up system should be resolved where the control parameters (DC link voltage, frequency, duty cycle, phase-shift, etc.) are actively controlled to improve efficiency while meeting the vehicle-side target voltage, current, and/or power. Simultaneously, vehicle-side DC link or battery voltage, current, temperature, and the state-of-charge (SOC) should be carefully monitored and fed-back to the primary side for controls. Moreover, the battery management system (BMS) or other vehicle-side functions (i.e., contactors and liquid cooling system) should be monitored for safety. The bidirectional wireless charging system that will be used in this project is shown in Figure II.1.15.1. This is the overall system architecture that is determined and agreed upon by the technical team. For this architecture, the baseline performance metrics have been defined, system specifications have been determined, and the hardware including the power stages and passive components have been designed and developed in ORNL PEEM laboratory. As shown in Figure II.1.15.1, system utilizes a three-phase rectifier/inverter system that interfaces the wireless charging system to the grid. During charging, the active-front end rectifier with power factor correction (PFC), delivers power from the grid with high power factor to the HF power inverter's input. The input (grid) current is controlled in order to regulate the inverter input voltage, depending on the amount of power to be transferred to the vehicle-side battery. The HF power inverter generates the HF current for the primary coupling coil. On both primary and secondary, LCC type resonant tuning configuration was utilized for operational symmetry since the bidirectional power flow is needed.

Additionally, LCC type resonant tuning circuitry provides load and coupling factor independent constant current on primary coil which simplifies the communication requirements and the control systems. On the vehicle side, there is a receive coil with a rectifier/inverter, and a filter capacitor. During discharging or vehicle battery powering the AC grid/building loads, the vehicle-side converter is operated in an inverter mode and delivers HF current to the vehicle coil. The vehicle-side coil generates a magnetic field that is linked to the ground coil. The ground coil induces a high frequency voltage that is rectified and inverted to 60Hz to power the building loads or to the AC grid.

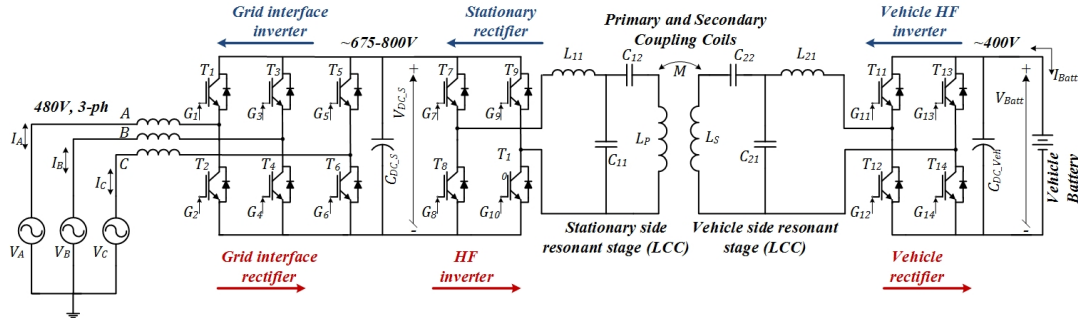


Figure II.1.15.1 System level diagram of the proposed architecture for the bidirectional wireless charging system.

This FY team continued the benchtop laboratory tests of the system for verifying the design parameters and the functionalities. This included testing and validating the parameters of each power conversion stage both at component and subsystem levels using grid and battery emulators. Later, the whole system integrated together, and the operation of the entire system is validated in both power flow directions including the communications link for the closed loop operation. Finally, the vehicle integrations are completed and the whole system is validated on the vehicle. The vehicle integration efforts are visualized in Figure II.1.15.2.

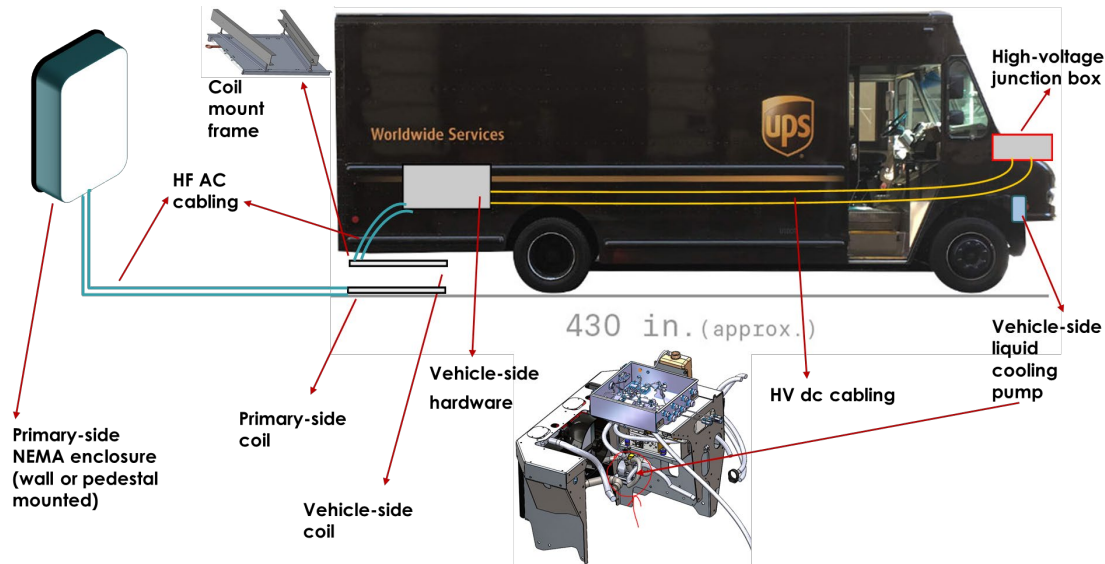
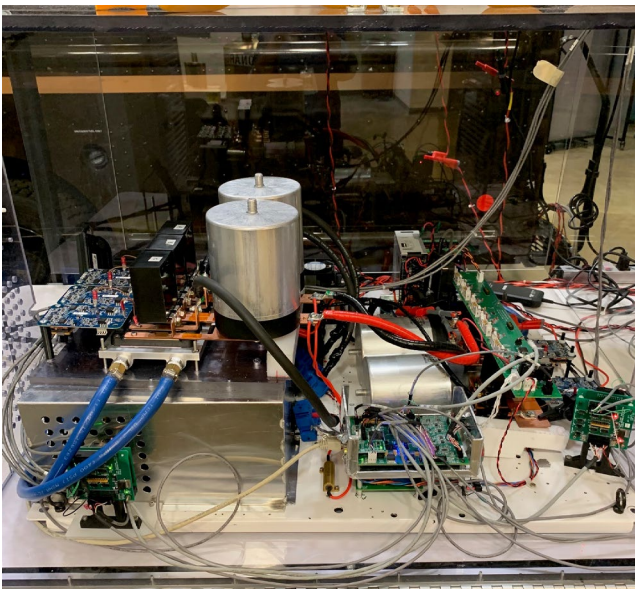


Figure II.1.15.2 System level diagram of the proposed architecture for the bidirectional wireless charging system.

The back of the vehicle is used for the vehicle-side coupler installation for two main reasons. The first reason is that these trucks back up at the docks; and the coil at the front of the vehicle would have larger misalignments if the vehicle was parked even with a small angle when backing up. The other reason is that a receiver coil at the front of the vehicle would require much longer high-frequency AC cabling from primary-side unit to the transmit pad. Similarly, a decision had to be made for the location of the vehicle side unit which could be either at the back closer to the receiver coil or at the front closer to the high-voltage junction

box that houses the battery connection terminals. Team decided to mount the vehicle side unit closer to the vehicle-side coil in order to minimize the high-frequency cabling length from coil to the vehicle side unit. If mounted at the front, the high-frequency cabling around 30 feet would cause a considerable amount of losses in addition the stray fields generated along the cabling. High-voltage dc cabling on the other hand, is a lot more efficient than high-frequency ac cabling with no issues on field emissions. For the vehicle side coupler, ORNL developed a custom design coil mount frame that was installed on truck's crossmember rails. For the cooling of the vehicle-side power electronics, the initial wish was to utilize the existing liquid cooling system of the on-board charger. However, the 12V pump of the liquid cooling system was tightly surrounded by other engine related components and it was very difficult to access to the output hoses as well as to the pump 12V input to activate it when charging. In addition, since this pump is at the front of the vehicle while the vehicle-side unit is at the back, that 30 feet of length would cause considerable drop of the pressure in the cooling lines. Therefore, team decided to use a separate dedicated thermal management system for the vehicle-side unit of the wireless charging system.

In Figure II.1.15.3 (a), the primary-side hardware is shown which includes the input LC filter stage, 480V 3-phase connection to the front-end rectifier/inverter, high-frequency inverter/rectifier, and the inverter output LCC resonant tuning tank before the primary coupler. Primary-side also includes a main 3-phase contactor that connects and disconnects the system from/to grid which is followed by a pre-charge circuitry that uses a series resistor to charge the dc bus capacitors without a surge current which bypassed by another 3-phase contactor during normal operation. The input connection is also fused. Primary side also utilizes a DSP based controller and gate driver boards. 3-phase phase-to-neutral voltage sensors and 3-phase line current sensors at the input to properly control the input current. There is also a dc bus voltage sensor which is a direct indication of power transfer level. There is also a 480V 3-phase ac to 24V dc converter which is then converted to +/- 15V and 5V levels for low power controls, fans, sensors, DSP, gate drivers, and other electronics. Figure 3 (b) shows the vehicle-side unit that consists of connection to the secondary coil, vehicle-side LCC resonant tank, high-frequency rectifier/inverter, power modules with gate drivers, DSP board, a main contactor to the battery along with a pre-charge circuitry with pre-charge resistor and bypass contactor, an output fuse, and an output filter inductor to reduce battery current ripples. This unit also includes 12V to +/- 15V and 5V converters for the operation of controllers, sensors, contactors, gate drivers, fans, and all other low power electronics etc.



(a)



(b)

Figure II.1.15.3 Primary-side (a) and the secondary-side hardware of the system.

In Figure II.1.15.4 (a), the coil mounting rail frames are shown that are bolted to the vertically running vehicle crossmember rails with adjustable height. While the average vehicle ground clearance is about 11 inches, the lowest point under the vehicle is 8 inches above the ground which is the frontal subframe and the coupling rod or differential between the rear wheels. As required by the project, 11 inches magnetic airgap is used from the surface of the secondary coil to the ground level as shown in Figure II.1.15.4 (b).

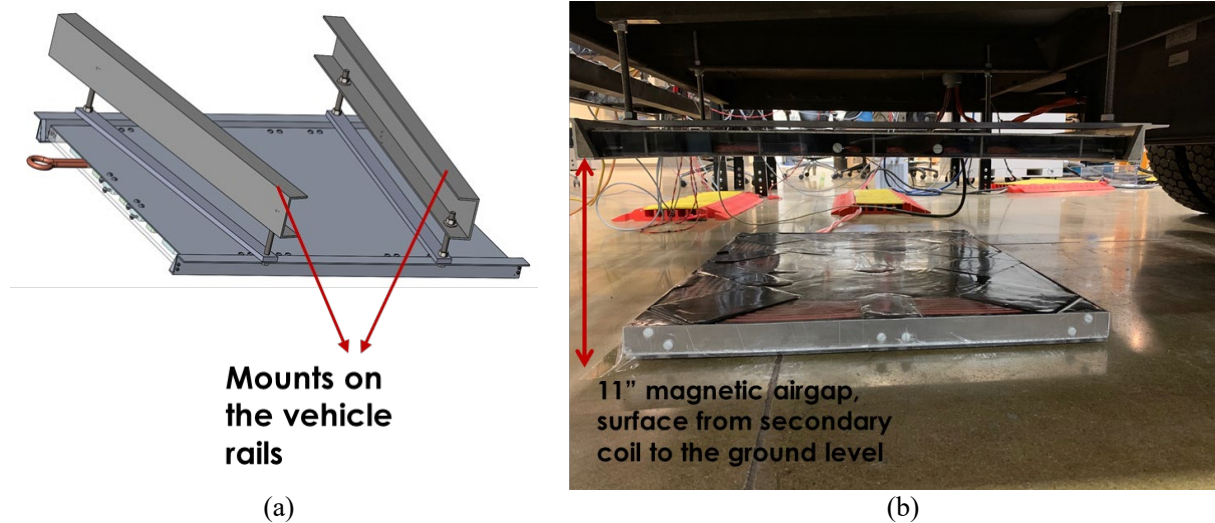


Figure II.1.15.4 Vehicle-side coil mount assembly (a) and the primary and secondary couplers with 11 inches magnetic airgap (b).

Results

After extensive laboratory testing, the UPS truck and the wireless charging hardware are deployed at the Grid Research Integration and Deployment Center (GRID-C) of ORN as shown in Figure II.1.15.5 for the project demonstration event that was hold on February 27, 2020.



Figure II.1.15.5 Resonant voltage gain of the system using the analytical model (a) and the experimental validation (b).

The instrumentation setup for the demonstration is shown in Figure II.1.15.6 where a power analyzer was set to read the voltage, current, power, and efficiency of all the power conversion stages, an oscilloscope was used to capture some of the selected input and output voltage and current waveforms of the system. Finally, a laptop PC was connected to the vehicle battery management system (BMS) to display the battery voltage, current, and state-of-charge to the users.



Figure II.1.15.6 Instrumentation setup for the project demonstration.

Demonstration of the system included displaying and recording the system performance in both power flow directions where G2V indicates power flow from grid-to-vehicle (charging or drawing power from the grid) and V2G indicates power flow from vehicle-to-grid (discharging or injecting power back to the grid). In Figure II.1.15.7, the power analyzer test results are displayed where the vehicle battery receives 20.36 kW of power. The combined efficiency of the grid interface converter (rectifier) and the high-frequency inverter is recorded 97.30%, coil-to-coil efficiency is 96.96% which includes the efficiency of the primary and secondary-side LCC resonant tuning components, and the vehicle-side rectifier efficiency is 98.59%. This results in an overall end-to-end efficiency of 93% for G2V (charge mode) operation (>85% was the project requirement). Also as shown in Figure II.1.15.7, input power factor on the grid side was 0.999 (0.95 was the project requirement) for all the input phases while the total harmonic distortion on the input current was <0.8-0.95 on all phases (<5% was the project requirement). These performance results indicate that the system operation exceeds all the project requirements in terms of overall efficiency, power level, power factor, and total harmonic distortions.

Similar test results for the V2G (discharge mode) are displayed in Figure II.1.15.8 where 12.8 kW (>6.6 kW was the project requirement) was transferred from vehicle battery to the 480V 3-phase power grid. In this operating mode, vehicle-side inverter's efficiency was 99.38%, coil-to-coil efficiency was 92.8% including the losses across the resonant tuning components, and primary-side high-frequency rectifier and grid interface inverter's combined efficiency was recorded 96.61%. This results in an overall end-to-end efficiency of 89.09% (>85% was the project requirement) from vehicle battery to the power grid. In this mode of operation, the power factor was maintained >0.99 (0.95 was the project target) across all the grid phases while the total harmonic distortion on grid current was about 1-1.5% (<5% was the project target) across the grid phase currents. This mode of operation also met all the project requirements in terms of power level, power transfer efficiency, grid power factor, and the grid current total harmonic distortions. The main reason for less efficient operation in V2G mode is that most power converters and coupling coils are less efficient in light load operations, i.e., with some margin added, the overall system is designed for 30-35 kW; therefore, 12 kW is

about 30% of the power rating. 20 kW power transfer to the grid would be a lot more efficient and comparable to the G2V efficiency.



Figure II.1.15.7 G2V operation test results.



Figure II.1.15.8 V2G operation test results.

Conclusions

During the first budget period of the project, the team worked on modeling, simulations, analysis, and design of the system power conversion stages and control systems. Upon the successful design review meeting in May 2018 which concluded the first budget period of the project, team started building the hardware of all the system power conversion stages along with the control systems. During the second budget period, team built all the power electronic converter hardware and fabricated all the passive components including the 3-phase grid-connected inductors, capacitor systems, resonant tuning circuit components, coupling coils, and the vehicle-side filter components. Team also designed and developed two DSP interface boards for the primary and secondary sides. Team has successfully tested the operation of the power conversion stages. Then the whole system tested together with the vehicle integrations. According to the results, G2V operation was 20.36 kW with 93% end-to-end efficiency over 11 inches of magnetic airgap with asymmetric voltage gain (~ 0.5) on the resonant stage with high power quality on the grid side. Similarly, V2G operation was demonstrated with 12.8 kW power transfer, 11 inches of airgap, 89.1% end-to-end efficiency, and asymmetric voltage gain (~ 2) on the resonant stage with high power quality on the grid side.

Future work includes packaging the primary-side components, performing several long-duration tests for full charge/discharge cycles, and adding some operational functionalities prior to the deployment at the UPS' Sandy Creek facility near Atlanta where they have the Smart Hub. After the final deployment, UPS will use the system for 6 months. Data will be collected during this period to demonstrate the repeatability of the performance and analysis of the use cases.

Key Publications

1. "Secondary Active Rectifier Control Scheme for a Wireless Power Transfer System with Double-Sided LCC Compensation Topology," in Proc., 44th Annual Conference of the IEEE Industrial Electronics Society (IECON), October 2018, Washington, D.C.
2. "Sensitivity of an LCC-LCC Compensated 20-kW Bidirectional Wireless Charging System for Medium-Duty Vehicles," in Proc., IEEE Transportation Electrification Conference and Expo (ITEC), June 2019, Novi, MI.
3. "Bidirectional LCC-LCC Compensated 20-kW Wireless Power Transfer System for Medium-Duty Vehicle Applications," under review, submitted to the IEEE Transactions on Transportation Electrification.

Acknowledgements

Project team would like to thank Manish Mohanpurkar from the U. S. Department of Energy and Jason Conley from National Energy Technology Laboratory for their continued guidance and support on this project. We would also like to thank Dr. David Smith (ORNL) for his guidance and support which is greatly appreciated.

II.1.16 Wireless Extreme Fast Charging for Electric Trucks

Michael Masqueller, Principal Investigator

WAVE
4752 West California Avenue, Suite B400
Salt Lake City, UT 84104
Email: michael@waveipt.com

Steven Boyd, DOE Program Manager

U.S. Department of Energy
Email: Steven.Boyd@ee.doe.gov

Start Date: August 1, 2018

End Date: October 31, 2021

Project Funding: \$2,709,098

DOE share: \$1,215,238

Non-DOE share: \$1,493,860

Project Introduction

The purpose of the wireless extreme fast charging (WXFC) truck project is to significantly accelerate electrification of heavy-duty trucks, starting with shipping ports and expanding to regional delivery operations across the US. Charging time and range anxiety are major barriers to electric vehicle adoption, particularly for truck applications. Therefore, the major goal of this project is to demonstrate high efficiency, WXFC as applied to Class-8 trucks that have a typically higher gap and lower available space than, for example, transit buses.

Objectives

The objective of this project is to develop and integrate a new 500kW WXFC system developed by WAVE into a Class 8 electric drayage truck developed by Cummins so that it can automatically and wirelessly charge at a high charging rate (c-rate) during their dwell times. The proposed wireless charger features a direct connection to the Medium Voltage (MV) 3-phase grid developed by Utah State University and Schneider Electric and the final prototype will be deployed at Total Transportation Services Inc. (TTSI), which is a truck operator at the Port of Los Angeles (POLA).

Approach

WAVE has assembled a strong and diverse team to develop, deploy, and operate two all-electric Class-8 drayage trucks with WXFC at the Port of Los Angeles

(POLA). The WXFC truck project leverages active involvement of key partners on six major project tasks, as shown in Figure I.1.16.1. Project tasks include:

- Evaluation of a 250-kW wireless fast charging system in a Class 8 Truck field deployment
- New development of 500 kW wireless power transmitter and receiver modules
- New battery pack and Class 8 truck powertrain development to support high C-rate charging
- New development of an MV grid-tied converter to improve safety and simplify grid integration of WXFC stations
- WXFC grid and vehicle side system integration
- WXFC system deployment and evaluation at POLA

WXFC for electric trucks is a WAVE-led project with assistance from the following partners:

- The Port of Los Angeles – Deployment partner
- Los Angeles Department of Water and Power – Deployment partner
- Total Transportation Services Inc. – Port trucks partner
- Cummins – Truck integration and electric drivetrain partner
- Utah State University – Research partner
- Schneider Electric – Electrical supplier, industrialization partner

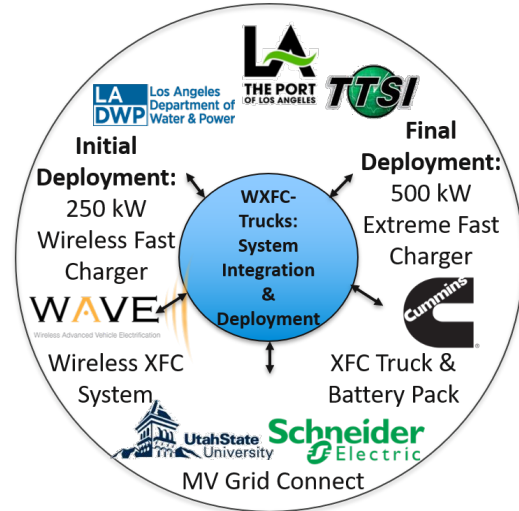


Figure II.1.16.1 WXFC project activities.

The general project approach for the MV AC-DC Converter, wireless charger, and the high c-rate Class 8 drayage truck development is outlined in Figure II.1.16.2

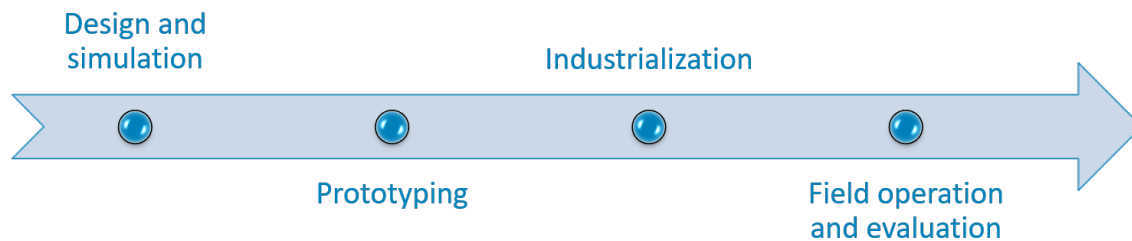


Figure II.1.16.2 Project design and implementation approach.

The USU approach to the MV, grid connected, AC/DC supply is:

- 3-phase unfolder with a soft DC bus two-level output
- Develop the 3-phase unfolder to achieve direct MV grid connection with switches commutating at the line frequency
- Design the series stacked isolated DC/DC converters to achieve the voltage step down function from MV naturally with near unity conversion ratio to obtain high efficiency

The WAVE approach to the 500kW wireless charger is:

- Develop and simulate new magnetics design for the higher power density required at 500kW
- Build and characterize a 250kW prototype pad set based on the new design
- Leverage deployment experience with 250kW charger to feed into design updates of the 500kW charger

The Cummins approach to the extreme fast charging capable electric truck is:

- Investigate appropriate battery chemistry (LTO cells or NMC cells)
- Design custom thermal management for the cell to facilitate charging at 3C
- Select appropriate battery pack capacity and cell chemistry to integrate with electric powertrain applicable to Class 8 drayage applications

Results

The project team has worked together to define the requirements for the MV AC/DC supply, wireless charger, and Class 8 truck to deliver a solution that meets the needs of TTSI. A block diagram for the system is shown in Figure II.1.16.3.

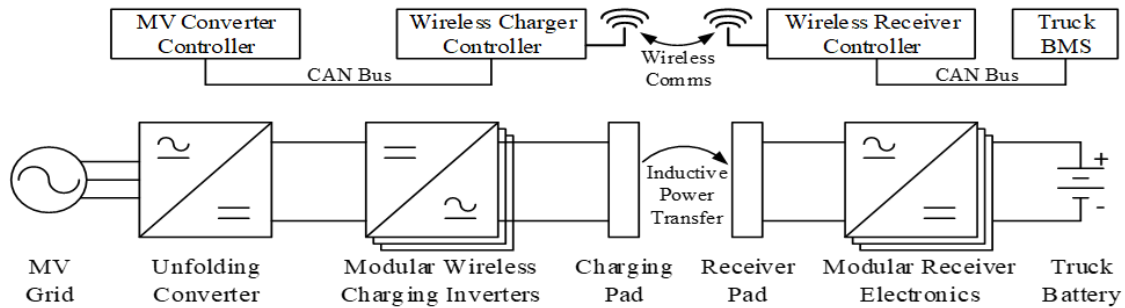


Figure II.1.16.3 System block diagram.

While there has been some project impacts due to COVID-19 restrictions, work continues to move forward as allowed, and significant progress was made in all project areas. A full power, 80kW DC-DC module for the MV supply has been built along with the unfolder and testing is underway. WAVE has selected a pad topology and will deploy 2 x 250kW pads. A prototype 250kW pad set has been built and will be characterized in the coming months. WAVE component models have been integrated into the Cummins truck design and the build of truck 1 is progressing well.

Schneider Electric is continuing to support the MV supply with their expertise and facilities for cabinet design and regulatory compliance and testing as well as working on site planning and grid connection requests. TTSI and Cummins continue to work together to make sure the truck is prepared to meet the real-world requirements.

Challenges have been seen in determining what will be an acceptable installation site for TTSI along with service application to the utility. It has been decided that the charger will be installed back at the original TTSI location and a service application has been submitted to LADWP. The team has continued project execution as summarized in the following project summary tables.

Table II.1.16.1 Budget Period 1 (BP1) – Project Plan Summary

Task 1: Deploy 250kW wireless fast charger	Task Description & Deliverable	Estimated Percent Complete	Original Estimated Completion Date	New Estimated Completion Date
1.1.1	Evaluate deployment of the 250kW unit in field operation	100%	12/31/2019	Complete

Task 2: Wireless XFC system design	Task Description & Deliverable	Estimated Percent Complete	Original Estimated Completion Date	New Estimated Completion Date
2.1.1	Magnetics study and optimization	100%	4/15/2019	Complete
2.1.2	Electronics study and optimization	100%	5/15/2019	Complete
2.1.3	Initiate system hardware design	100%	9/30/2019	Complete
Task 3: XFC electric truck simulation & design	Task Description & Deliverable	Estimated Percent Complete	Original Estimated Completion Date	New Estimated Completion Date
3.1.1	Vehicle performance and efficiency simulation	100%	5/30/2019	Complete
3.1.2	Battery pack simulation and selection	100%	1/8/2019	Complete
3.1.3	Thermal management system design	100%	8/15/2019	Complete
3.1.4	Vehicle controls design (design in BP1, implemented with truck in BP2)	80%	10/31/2020*	NA
3.1.5	Battery pack and wireless charging integration (design in BP1, implemented with truck in BP2)	95%	7/30/2020*	NA
3.1.6	Final BOM development (<i>aerodynamic improvements originally considered in this task - no longer in scope</i>)	100%	10/15/2019	Complete
3.1.7	Truck 1 construction (w/o WAVE components)	90%	1/15/2020*	3/31/2021*
Task 4: MV grid connected converter prototype	Task Description & Deliverable	Estimated Percent Complete	Original Estimated Completion Date	New Estimated Completion Date
4.1.1	Grid side converter modelling (LV migrated to MV) Includes LV prototype to validate modeling	100%	6/15/2019	Complete
4.1.2	Converter design and component selection (MV)	100%	4/30/2019	Complete
4.1.3	Construct MV unfold & full power DC/DC converter module prototypes	100%	10/31/2019	Complete
4.1.4	EMC testing of prototypes (initial functionality verification) at USU (industrialization EMC test at Schneider in Budget Period 2)	100%	10/31/2019	Complete
Task 5: Full System Design & Simulation	Task Description & Deliverable	Estimated Percent Complete	Original Estimated Completion Date	New Estimated Completion Date
5.1.1	Decide on the ratings and interfaces between subsystems	100%	3/30/2019	Complete
5.1.2	Create complete system simulation	100%	3/30/2019	Complete
5.1.3	Refine system simulation based on prototype hardware results	60%	10/31/2019	BP2

Task 6: WXFC System Site Planning	Task Description & Deliverable	Estimated Percent Complete	Original Estimated Completion Date	New Estimated Completion Date
6.1.1	Identify extra hardware required for XFC system deployment (transformers, switchgear, etc.)	100%	12/31/2018	Complete
Task 7: Initial 500kW Prototype Development	Task Description & Deliverable	Estimated Percent Complete	Original Estimated Completion Date	New Estimated Completion Date
7.1.1	Determine specifications for 500kW prototype charger	100%	2/15/2020	Complete
7.1.2	Complete design of 500kW prototype	100%	5/20/2020	Complete
7.1.3	Order parts for 500kW prototype	100%	6/30/2020	Complete

Table II.1.16.2 Budget Period 2 (BP2) – Project Plan Summary

Task 1: Build and Test 500kW Prototype System	Task Description & Deliverable	Estimated Percent Complete	Estimated Completion Date
1.2.1	Build system	0%	3/31/21
1.2.2	Initial development and 500kW power transfer	0%	4/15/21
1.2.3	Test and validate operation	0%	4/30/21
Task 2: Develop prototype WXFC	Task Description & Deliverable	Estimated Percent Complete	Estimated Completion Date
2.2.1	Construct new charging coils	100%	Complete
2.2.2	Develop higher power modules	30%	11/30/20
2.2.3	Test and validate operation of controls and hardware	0%	12/31/20
Task 3: Extreme fast charged electric truck construction and testing	Task Description & Deliverable	Estimated Percent Complete	Estimated Completion Date
3.2.1	Truck 1 construction and validation	70%	3/31/21
3.2.2	Truck 2 construction and validation	15%	6/1/21
3.2.3	Trucks delivered to WAVE for hardware integration	0%	6/10/21
Task 4: Industrialize and construct MV unfolding converter	Task Description & Deliverable	Estimated Percent Complete	Estimated Completion Date
4.2.1	Unfolder and module industrialization	40%	12/31/20
4.2.2	Vendor negotiation	10%	12/31/20
4.2.3	Full converter construction	0%	3/31/21
4.2.4	Converter and enclosure integration and testing	0%	5/31/21
4.2.5	Ship converter to WAVE	0%	6/30/21
Task 5: Full system controller simulation	Task Description & Deliverable	Estimated Percent Complete	Estimated Completion Date
5.2.1	Simulate fault conditions to inform hardware protection design	25%	2/28/21
5.2.2	Verify system stability and adjust controller as required	15%	5/31/21

Task 6: Carry out system compatibility testing	Task Description & Deliverable	Estimated Percent Complete	Estimated Completion Date
6.2.1	Test systems operation with each other	0%	6/30/21
6.2.2	Integrate systems into truck	0%	4/30/21
6.2.3	Carry out safety and stability tests*	0%	BP3
6.2.4	Final revisions of hardware and controllers*	0%	BP3
Task 7: WXFC site design	Task Description & Deliverable	Estimated Percent Complete	Estimated Completion Date
7.2.1	Design the layout for the MV utility connection	100%	Complete
7.2.2	Prepare appropriate plans for documentation to apply for permits	90%	12/31/20
7.2.3	Prepare plan for operation of deployment test site	0%	4/15/20

WXFC System Design Progress

WAVE has continued work on the extreme fast charger at 500kW with a particular focus on the magnetics. The pad topology has been selected and refined. WAVE will use a modular design for secondary pads deploying 2x 250kW assemblies. The physical dimensions and mounting scheme have been finalized with Cummins and the vehicle pad model shown below has been provided to Cummins to be included on the truck model.

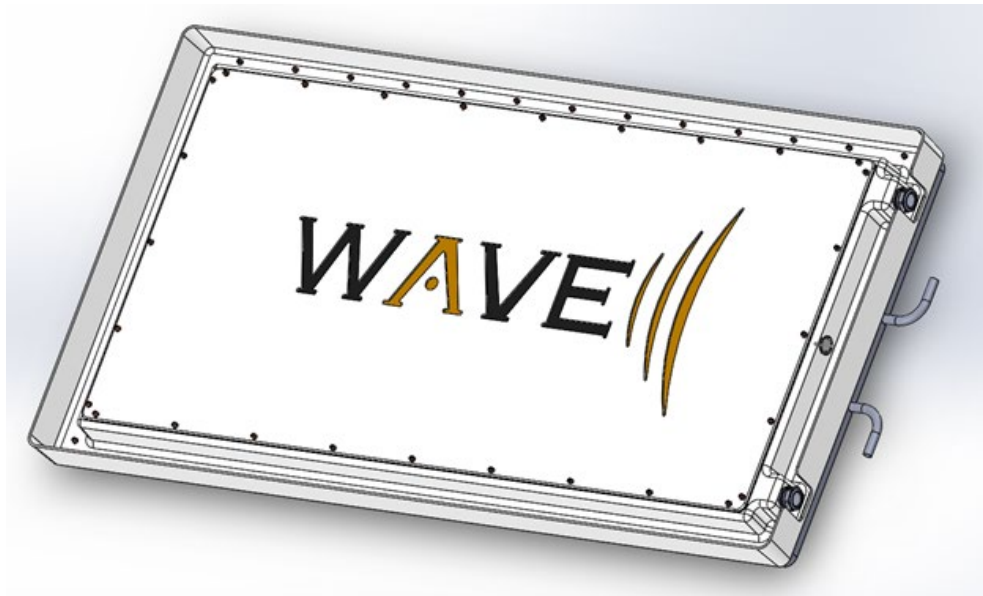


Figure II.1.16.4 250kW Secondary Pad Model Provided to Cummins

The details for the primary pad and tub have also been refined for use in preliminary site plan drawings. The primary pad model is shown below.

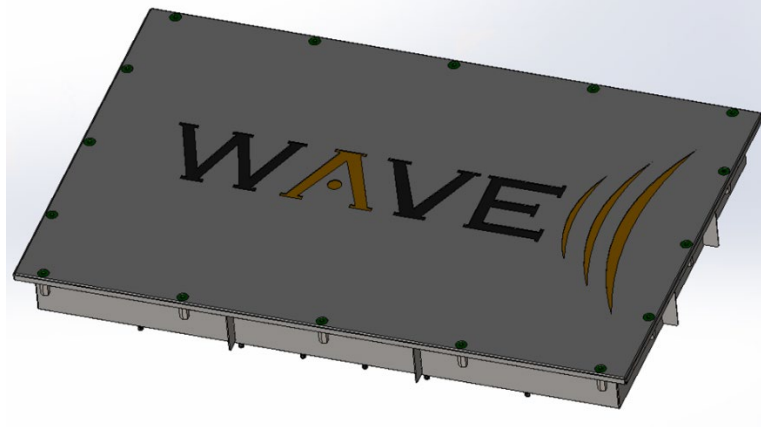


Figure II.1.16.5 250kW Rectifier Assembly

For space and weight savings the two WAVE 250kW rectifiers have been combined into a single assembly with modular pieces and active cooling. This single watertight enclosure is capable of handling 500kW and the electrical and cooling interfaces have been agreed upon with Cummins.

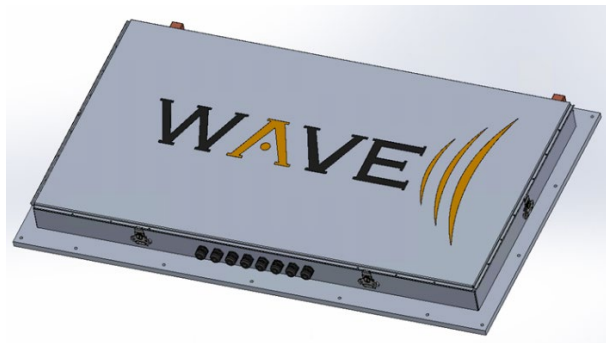


Figure II.1.16.6 500kW Rectifier Assembly

The prototype full power pad set design build has been completed and is pictured below. Characterization and full power testing will be completed in 2020.



Figure II.1.16.7 Prototype Full Power Pad Set

In order to achieve a highly-efficient design of WPT charger, the possible deployment of wide-bandgap semiconductor switches is being investigated. The latest, most-efficient SiC switch options for this application available at the market have been reviewed. Among those, a suitable SiC MOSFET is chosen as a possible replacement for the existing Si IGBT switches at the charger transmitter side. Similarly, a SiC diode module is picked as the replacement of the existing Si diodes. As a beginning step, drop-in replacements with sufficiently higher estimated efficiency compared to the previous switches are being considered as the selection criteria. Initial testing on SiC diode indicate a 30% reduction in losses in the rectifier. WAVE has also received another SiC diode option to test as well as a SiC MOSFET along with the gate driver and adapter board required to test in our current inverters. Those evaluations will take place next quarter.

MV Grid Connected AC/DC Supply Progress

MV Supply Progress Summary

The USU team has made progress in each of the six core task areas (Tasks 4.1.1-4.1.4 and tasks 5.1.1-5.1.2). Tasks 4.1.3, 4.1.4 and 5.1.2 have been completed. For Task 5.1.3, significant efforts have been made to complete fabrication on the full power DC-DC converter module and conduct full power tests. Likewise, with task 4.1.4, USU was able to design and build two FCC Part 15 50 mH LISNs and signal splitter to distinguish common-mode and differential mode emissions. These pieces of equipment, along a spectrum analyzer, were used to obtain initial emissions results. Tasks 5.1.2 and 5.1.3 were not progressed meaningfully, as focus was directed towards fabrication of the DC-DC modules for testing and input to the system simulation. Collaboration continues with project partners, WAVE and Schneider, on how to integrate the AC-DC converter into a cabinet with minimized overall footprint size and meet cooling requirements of the converters.

Task 4 MV grid connected converter prototype

Construction of the MV unfold is complete. All components for the unfold have been specified and procured. There were delays with the bus bar in vendor fabrication and discovered manufacturing limitations to meet the upper 12 kV requirements. To address these limitations, design reviews with the manufacturer have been conducted to align design to requirements and fabrication is continuing. In order to progress project, and meet budget period objectives, an earlier procured bus bar was assembled to the unfold to allow for processing of full current.

Additionally, the 85 kW DC-DC converter design was fabricated and tested. Below are explanations and results from those evaluations.

85 kW Triple Active Bridge Testing

The testing of the DC-DC converter in Triple Active Bridge (TAB) configuration at rated power is complete. To test the converter at rated output power of 80 kW a recirculating test setup was developed. The output of the converter is fed back to the input ports which are connected in series. The power supplies only provide for the losses in the converter. This allows for accurate loss measurements in the converter. Each input voltage is set to 400 V. Since the output is connected to the series connection of input voltages, it is set to 800 V. The transformer winding currents are close to sinusoidal which helps in reducing radiated EMI. The switching instant current are in the direction to help zero-voltage switch all the semiconductor devices reducing the switching losses of the devices to be zero. This results in very high efficiency of the converter. A measured peak efficiency of 99.16% has been achieved at 40% load and an efficiency of 98.64% has been achieved at full load output (80 kW).

Task 4.1.4 EMC testing of prototypes

[COMPLETE] – USU has completed initial EMI testing. Further evaluation will take place as the system layout and design is complete for cabinet integration. This testing will be done with support from project partners. USU has constructed the means to evaluate conductive emissions for the module, through two LISNs developed by the team. The objective of conducted tests was to better understand what type of filtering would be required and are to be used as an input to the design of EMI filtering. Out test setup can be viewed schematically in Figure 10. As our testing was completed with recirculating power, we anticipate that the results will differ when the LISNs are connected to the completed cabinet with the unfolders and the full set of converters. However, for the intent of this milestone, our goal was to obtain a baseline measurement of the noise signals for one DC-DC converter.

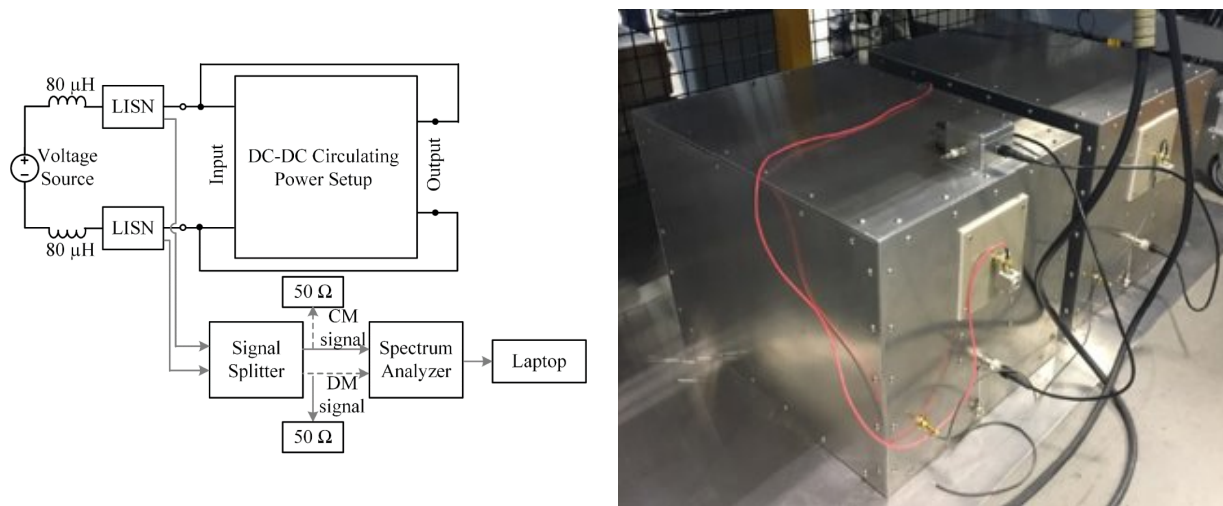


Figure II.1.16.8 EMI Test Setup

BP2 Task 4.2.1 Unfolder and module industrialization

[IN PROGRESS] – This task of the unfolders and module industrialization marks the beginning of BP2 for the USU team. Thermal design of the power converter is being done digitally using ANSYS Icepak software. The airflow requirements and hot spots for each subcomponent will be simulated. Loss break-down at sub-component level is necessary. Almost all these losses are temperature dependent and analytical understanding of these losses as a function of temperature improve the fidelity of simulation models. These simulation models will also be useful to understand the trade-offs between cooling power and system efficiency.

UL Field Certification Requirements

The project partners, WAVE, SE, and USU, have had multiple discussions with UL field technicians regarding the standards associated with the project. Currently it is likely the main standard that will be applied is UL

347A. However, there may be additional aspects of other standards such as UL 2877 that could be considered by UL for the field certification requirements. Ongoing discussion is pending with UL, including quotation for field certification process, and technical review of design.

System Control for Stable Operation

The main challenge for the converter control is to regulate the 60 Hz grid current to be sinusoidal while remaining stable for practical line impedances seen when connected to a Utility grid. This stability requirements generally leads to an upper limit for the allowable bandwidth of the control loop. In this section a novel approach is discussed that can remain stable for high line impedance yet maintaining good PFC action.

AC-DC Module Controller

- Proposed Controller

Given the nature of the topology as a quasi-single stage approach, the complexity of the control design lies in the DC-DC converter shown in Figure II.1.16.9

The two major control requirements done in the DC-DC converter are power factor correction and output power regulation. The proposed control strategy uses two control loops to achieve the aforementioned control requirements. For the PFC action, the control loop is actively regulating the ratio of input currents i_p/i_n using the ratio of duty cycles for the primary bridges $d_{p/n}$. The output current i_{out} is regulated using the quadrature component of the two primary voltages V_{pq} . A feedforward calculation is then used to estimate the primary duty cycles d_p and d_n , and the secondary bridge phase shift d_{edge} .

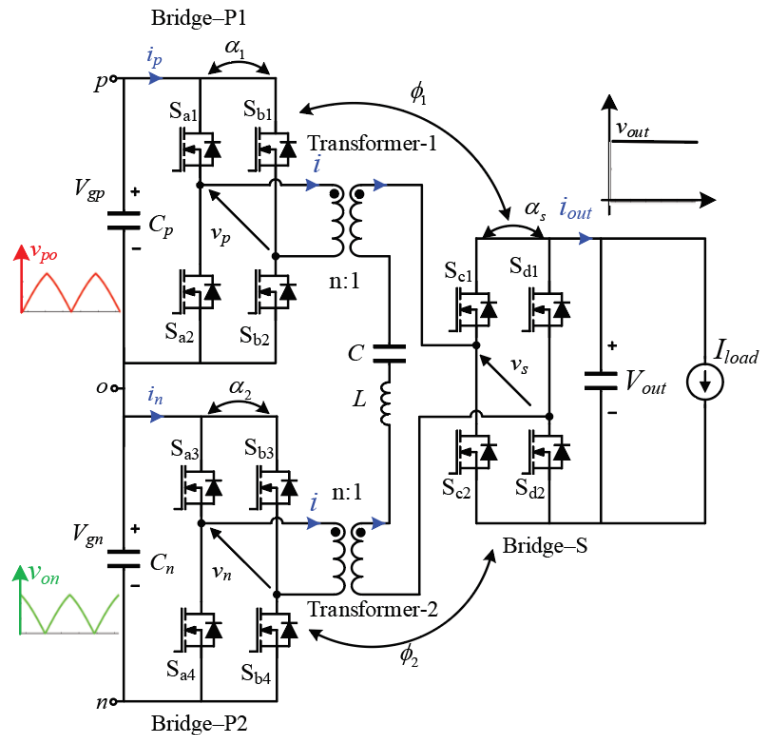


Figure II.1.16.9 TABSRC Schematic

- Small Signal Modeling

Control parameters and control loops were selected such that they are decoupled in nature. The small signal analysis has been performed to validate the decoupling and stability of the selected control loops. Four transfer functions have been derived for low frequency gains of the regulated values i_p/i_n and i_{out} with respect to the control variables $d_{p/n}$ and V_{pq} .

For the output power loop, which is controlled by $I_{out}-V_{pq}$ transfer function, it is clearly seen how very small the $I_{out}-d_{p/n}$ transfer gain is with respect to the $I_{out}-V_{pq}$ signal. Hence, we can see that the output power regulation is stable and decoupled from the PFC controller.

For the PFC loop, controlled by $I_p/I_n-d_{p/n}$ transfer function, the transfer function I_p/I_n-V_{pq} is relatively small with respect to $I_p/I_n-d_{p/n}$. Also, during normal operation, the output power controller is running at a much lower bandwidth than the PFC loop. Hence, the PFC loop is stable and decoupled from the output power controller.

- Simulation Validation

The presented control strategy was validated in simulation with the full AC-DC converter with one DC-DC module for the 2kW system. The simulation results validate the stability of the two loops regulating i_p/i_n for PFC and i_{out} for output power. The results also show the controller remains stable during a transient presented as a step in the output current reference I_{out_ref} . The PFC loop is operating with a 1 kHz bandwidth, while the output power is regulated at 10 Hz. The selected bandwidths allow for stable operation, even with practical input line impedance considered.

- Hardware Validation

Hardware validation is currently ongoing on the 2kW prototype to test and validate the full AC-DC closed loop system.

Task 4.2.2 Vendor Negotiation

[IN PROGRESS] – USU has engaged with a local power electronics fabrication company that has experience with high-voltage power supplies to review the design of the 80-kW transformer and quote on building it. They would like to build one first before quoting on building all of them. They plan to see whether one of their existing isolated power supply designs can be adapted to supply power to the gate drive circuits. They also have experience building current transformers, so they will be looking at the current transformer we need for the H-Bridge controllers to see if they can make them for us.

Electric Truck Development Progress

As a subrecipient to WAVE on project **DOE DE-EE0008360**, Cummins will deliver two class 8 day-cab battery electric trucks, suitable for demonstration by TTSI, utilizing:

- High C rate battery & associated thermal management
- Wireless charging components provided and installed by WAVE

For Q2 2020, Cummins work focused on:

- Finalizing build of truck 1
- Continuing to develop controls
- Building up a single string, of nominal voltage of 630 VDC and total capacity of 53 kW-h

For Q3 2020, Cummins work focused on:

- Finalizing build of truck 1
- Continuing to develop controls
- Testing a single string (630 VDC / 53 KW-h nominal) to verify it will support up to 3C charge and 2C discharge as required by the project

Truck requirements

Previous discussions with TTSI indicated the need for a class 8 tractor (GCVW of 80k lbs.) that could consistently accomplish 30-mile round-trip drayage routes in the Los Angeles basin. Further discussions revealed that routes are an additional 10-15 miles longer due to trailer placements (drop-off and/or pick-up); therefore, the trucks must be designed to meet a **range requirement of 45 miles**. Also, as previously discussed, the trucks must maintain a vehicle speed of at least 30 mph, at full load, on the 5-6% grades encountered on the Vincent Thomas Bridge that connects POLA to the mainland.

The performance requirements of the truck (startability, gradeability esp. at 6%, acceleration and top speed) will be satisfied using an electric powertrain currently in development, on-schedule, at Cummins. Details of this powertrain are currently considered business confidential, but they include an internal permanent magnet traction motor with continuous power capability of at least 330 kW to ensure the minimum vehicle speed on the bridge grade is achieved. The powertrain development (which is outside the scope of this project) is progressing and is continuing to be developed in a test cell.



Figure II.1.16.10 Kenworth T680 Class 8 Truck with Day Cab

An important consideration when building an electric truck is its curb weight. As batteries for a class 8 truck can be upwards of several tons, the truck must be designed so that its curb weight is not a limiting factor in delivering freight. A new California law (AB 2061) was enacted in January 2019 providing an additional 2,000 lbs. of allowable weight allowance for alternate fueled class 8 trucks (including those for this project). So, the truck's total weight, including trailer, container and container load (maximum possible of over 43k lbs.), must not exceed 82k lbs. Accounting for the tare weight of the container and trailer, the final, not-to-exceed tractor curb weight target for this project is 23,000 lbs., which is nearly best-in-class for a class 8 EV tractor. After implementing various options to reduce traction weight and with recent updates from WAVE for the rectifier and secondary charging pad weight, the tractor is now estimated to weight **23,070 lbs**; this has been recently verified by measuring the truck as it's being built.

Recent powertrain testing (funding of which is outside the scope of this project) has proven the performance and durability of the EV powertrain (motor, inverter and transmission) in a powertrain test cell at Cummins. This includes validating predicted efficiency on the target duty cycle for the project.

Battery Requirements

The battery requirements have been modified to account for the additional distance discussed above and are as summarized in Table II.1.16.3.

This was the result of a simulation analysis, using a five-hour round trip duty cycle (as previously discussed in Q4). Based on the workday duty cycle, *along with an additional five miles to account for additional possible trailer movement revealed during recent discussions with TTSI* (and assuming a fully loaded truck for the outbound route and a partially loaded truck for the return trip), one round-trip at this newly identified maximum route length (including allowances for traffic and accessory load) requires **140 kW-h** to achieve its mission. Assuming a 10% expected battery life degradation over a maximum possible one-year demonstration phase¹⁹, the minimum useable energy for the truck's battery shall be 156 kW-h. Assuming a typical useable range (to ensure battery life) of 80%, the minimum battery shall be sized at 195 kW-h.

It should be noted that full power charging is only possible to ~80% SOC. Assuming the need to maintain at least 10% SOC during typical operation for battery life, the typical useable battery energy is roughly **148 kW-h**. This is still acceptable to meet the maximum mission (described above as 140 kW-h). If an extra-long mission is required, charging to 90% is possible, but the last 10% SOC will need to be made at lower power levels. While the charge profile is automatically determined, the driver's normal 15–20 minute charge event, may be noticeably longer (30 minutes) if attempting to charge to this charge state-of-charge. *So, this will be an important of the program: when is a 50% longer charge event worth it?*

¹⁹ Though the project is committed to two trucks each running six months during the demonstration phase, the trucks should be designed to achieve a minimum one-year life to account for the validation phase.

Table II.1.16.3 Battery Requirements Summary

Battery useable energy (kW-h)	Battery useable energy (kW-h) for extreme fast charging	Battery total energy (kW-h)	Battery charge power [kW] minimum of 20 minutes for (20 - 80%) SOC	Battery VDC range [VDC]
170	148	212	500	520 - 700

Cummins has worked with the battery manufacturer and the battery is now fully capable, for testing and customer deployment, to support 3C charging.

Beginning in August and continuing into early October, single string (640 VDC / 53 kW-h nominal) battery testing was completed at Battery Innovation Center in Newberry, Indiana. These tests allowed for validation of the full range of intended battery operation: 3C charging and 2C discharging. Tests also used representative duty cycles for the TTSI routes including simulating the high current draw due to the Vincent Thomas bridge grade.

The figure below shows test results of both a 3C charge event (from 20-90% SOC and a similar discharge event). The data was logged at 6 samples per second. At about 3000 samples, the charge control transitioned from a constant current (of ~3C) to approximate constant voltage (to ensure the cell voltage limits were not exceeded).

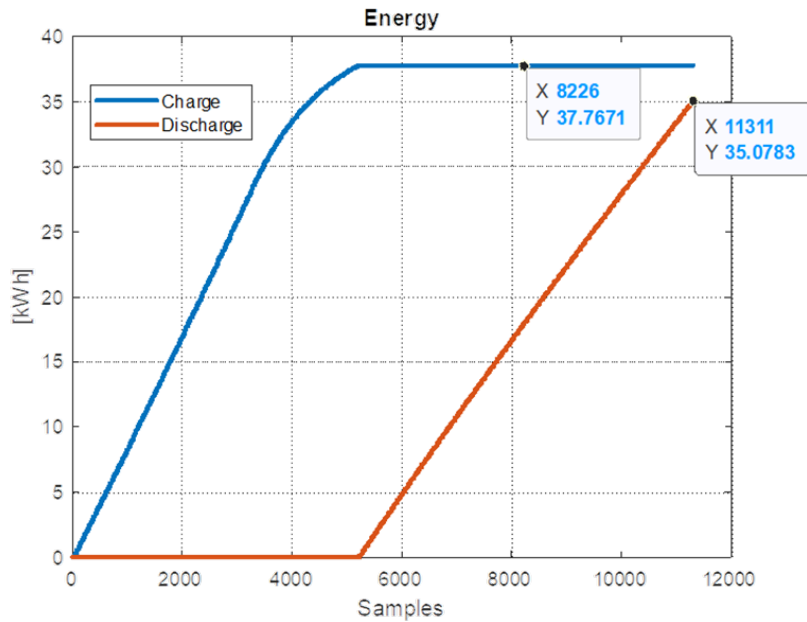


Figure II.1.16.11 Single String Battery Testing Results

(blue line: 3C charge, red line: 2C discharge)

Challenges

While COVID-19 impacted the vehicle build and battery testing in Q2-Q3, it currently has limited impact on the project. Parts are being received, technicians and engineers are working on the truck, and the project is following a normal trajectory.

Future travel, at least for the next six months, will, however, continue to be impacted by COVID-19. It is preferable, for example, to have Cummins personnel at WAVE in Q1 2021 for the integration of the secondary charging pads and rectifier on Truck 1. It is likely this support will need to be handled remotely which adds integration risk.

Conclusions

It is important to consider the entire workday duty cycle based on customer requirements and to have a good understanding of port operations. Initial discussions indicated a 30-mile range requirement which did not account for 10-15 miles of trailer movement in addition to the typical drayage route. Based on this information the truck battery requirements were adjusted accordingly to provide a 45-mile range needed for TTSI operation.

This project is well positioned with the correct technical requirements to address the range anxiety and charging time restrictions, which are the key barriers to electric vehicle operation at the Port of Los Angeles. With all project partners involved in hardware builds and prototype testing we are on track to launch the demonstration next year.

Key Publications

1. M. Masquelier, "Wireless Extreme Fast Charging for Electric Trucks." 2019 DOE VTO Annual Merit Review, Washington, DC, June 2019.

II.1.17 High-Power Inductive Charging System Development and Integration for Mobility (ORNL)

Omer C. Onar, Principal Investigator

Oak Ridge National Laboratory, Power Electronics and Electric Machinery (PEEM) Group
National Transportation Research Center, 2360 Cherahala Boulevard
Knoxville, TN 37932
Email: onaroc@ornl.gov

Burak Ozpineci, Section Head and ORNL Program Manager

Oak Ridge National Laboratory, Vehicle and Mobility Systems Research Section
National Transportation Research Center, 2360 Cherahala Boulevard
Knoxville, TN 37932
Email: burak@ornl.gov

Lee Slezak, DOE Program Manager

U.S. Department of Energy
Email: Lee.Slezak@ee.doe.gov

Start Date: October 2018

End Date: December 2021

Project Funding: \$4,707,901

DOE share: \$2,207,901

Non-DOE share: \$2,500,000

Project Introduction

Extreme fast charging (XFC) is considered one of the most important research topics in the field of electromobility with the potential to significantly reduce charging times. With extreme fast charging, i.e., charge rates higher than or equal to 3C, it is possible to reduce EV charging times to 10 minutes for 50% increase in the battery state-of-charge (SOC). However, there are several challenges for establishing XFC systems, such as logistics and infrastructure requirements, design and deployment of the grid interface converters, grid power quality (power factor and harmonic distortions), availability of the power (integration with renewable energy or energy storage systems if needed), isolation requirements, distribution voltage level at the point of grid connection, hardware connectivity, power electronic semiconductor and architecture limitations, thermal management systems, and the vehicle side power delivery architectures.

High-power wireless power transfer (WPT) is an attractive option for fast charging because the user is not required to handle any heavy and bulky high-power equipment. WPT is also a key enabling technology for autonomous vehicles. However, power transfer capability of WPT systems is closely linked to the size and mass of the transmitter and receiver pads. The feasibility of high-power WPT systems greatly depend on the ability to improve the power density and specific power of wireless charging systems.

The difficulties of high-power wireless charging are exacerbated by the need to meet the same practical constraints associated with vehicle integration as lower power systems. Therefore, more advanced techniques are necessary to improve power density and specific power of wireless charging systems for high-power applications. This paper proposes three-phase inductive WPT systems with bipolar phase windings with significantly increased surface and volumetric power density of the couplers.

The primary objective of this project is to address the challenges of XFC charging systems for electric vehicles that increases their utilization factors, improves the total electric miles travelled, and improves their return on investment that results in industry and consumer acceptance. The project will also reduce the technology costs through a modular and reconfigurable power electronics architecture and by leveraging the current DOE research activities in power electronics, wide bandgap device-based power electronic converters, vehicle systems, wireless charging systems, and modernization of grid infrastructures in order to meet the project

goals. This project will also generate DOE-owned intellectual property on high-frequency / high-power inverters, high-frequency AC links, novel integrated and polyphase magnetic structures, and thermal management systems to be used in extreme fast charging of EVs. Technology developed in this project will be transferable to other vehicle classes such as medium-duty and heavy-duty vehicles.

Objectives

This project is the first research effort that will showcase an inductive XFC charging system with all the outlined functionalities such as using a poly-phase electromagnetic coupling coils and a modular, scalable, reconfigurable grid-interface power electronic converter architecture. The overall goals of the project to address the challenges of XFC charging systems are:

1. Provide a high-technology, fully automated, high-power, modular, scalable, interoperable, high-efficiency plug-less extreme fast charging system;
2. Design an inductive coupling system that supports a variety of vehicle ground clearances that is designed for 100 kW and 300 kW nominal power levels;
3. Have minimal grid level disruptions with <5% harmonic distortions on the grid current and >95% grid power factor;
4. Design and develop a poly-phase electromagnetic coupling coils with optimal geometry for the highest utilization of the coupler surface area,
5. Achieve end-to-end high charging efficiencies greater than 90%,
6. Integrate vehicle to infrastructure charging communications, and
7. Understand and address vehicle integration issues of XFC technology, including energy storage impacts and thermal management considerations.

Approach

Starting from the AC grid to the vehicle battery terminals, the system power converters must be well-designed and operated in order to achieve high efficiency. In addition, power flow control to the secondary system should be resolved where the control parameters (DC link voltage, frequency, duty cycle, phase-shift, etc.) are actively controlled to improve efficiency while meeting the vehicle-side target voltage, current, and/or power. In this project, team used iterative design and utilized finite element analysis (FEA) based modeling for the design optimization of the electromagnetic coupling coils. Vehicle battery and grid voltage and power levels are used for the proper system design and cascaded down to the appropriate subsystems and components. Furthermore, research team modeled and simulated the grid interface (front-end) power blocks based on the DC link voltage requirements of the proposed system and the grid infrastructure parameters. Also, the system power conversion stages are designed in an integrated approach for an optimal system design in terms of complexity and compactness. Regarding the system tests, all the power conversion stages are being tested and validated individually before the full system integration (for functionality and performance) which is followed by the entire system tests using grid and battery emulators before vehicle integrations. Although it was not required, team also designed and developed a prototype for proof of concept before designing and developing the high power scaled couplers and converters. The system level circuit diagram of the proposed system is given in Figure II.1.17.1. At the input of the system, a number of parallel connected grid interface converters are used to provide controllable and regulated voltage to the primary-side high-frequency power inverters. In order to achieve high-power at the high-frequency inverter level, the drive system uses open-ended winding dual-inverter design using two inverters sharing the same DC bus. This can also be interpreted as using 3 H-bridge inverters with each inverter feeding one phase of the primary coupler. Using a single three-phase inverter was not possible with 325 kW output power due to current rating and thermal constraints of the semiconductor power devices. Although a second inverter increases number of components and the

complexity, the total power rating and the power density of the drive system is significantly increased as this inverter assembly can provide up to 500 kW at the input. This approach doubles the effective output voltage while maintaining DC-link capacitor size reduction compared to a single 3-phase inverter. Our earlier studies showed that a single three-phase inverter using CREE SiC module CAS325M12HM2 or ROHM SiC module BSM600D12P3G001 would result in 150°C or 140°C junction temperatures which would be very close to their maximum thermal limits and it would be very risky not to have sufficient operational thermal margin. The other approach would be to use a conventional 6-phase (2 three-phase inverters paralleled), or a series cascaded multilevel inverter. Table I summarizes the comparisons between a single three-phase inverter, a conventional six-phase inverter, series cascaded multilevel inverter, and the proposed open-ended winding dual inverter architectures. As seen from Table I, the proposed architecture reduces most of the voltage and current stress levels in the semiconductor devices and the windings.

Table II.1.17.1 Comparisons of High-frequency Power Inverter Architectures

Inverter type	Phase current [A _{rms}]	FET current [A _{rms}]	Primary coil current [A _{rms}]	Secondary coil current [A _{rms}]	Secondary diode voltage [V _{rms}]	Secondary diode current [A _{rms}]
Single 3-phase inverter	294.4	204.8	289.3	553.6	288.24	394.6
6-phase inverter	144.3	100.4	144.2	277.6	285.6	196.2
Series cascaded multilevel inverter	71.8	101.4	71.7	277.7	285.4	197.1
Open-ended winding dual-inverter (proposed)	155.2	109.9	63.1	108.2	255.8	72.1

Also shown in Figure II.1.17.1 is the double-sided LCC resonant tuning configuration implemented both for primary and secondary side with each phase having a dedicated compensation circuitry. In this extreme fast inductive charging system, primary-side power electronics, resonant tuning components, and the primary coupler are interoperable both with the 100-kW receiver and 300 kW receiver systems.

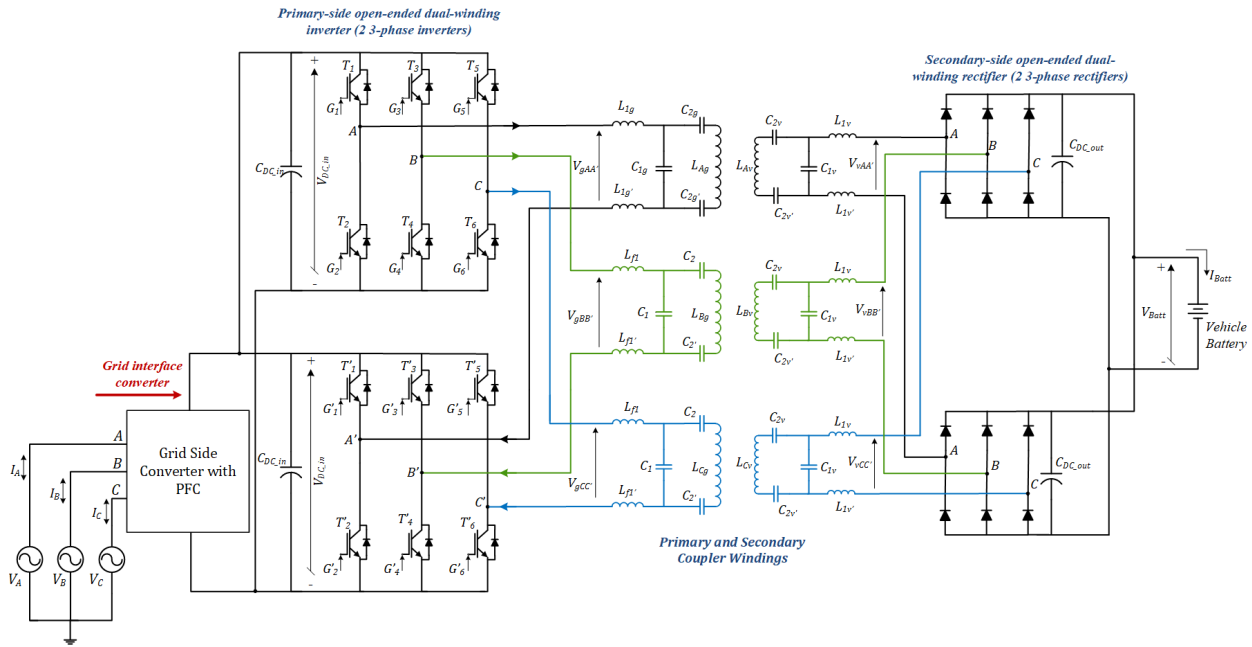


Figure II.1.17.1 System level diagram of the proposed XFC inductive charging system.

The inverters shown in Figure II.1.17.1 uses 1200 V / 356 A rated CREE CAS325M12HM2 SiC MOSFET power modules with an on-resistance of $R_{dson} = 3.7 \text{ m}\Omega$ and stray inductance of $L_{stray} = 5 \text{ nH}$. Detailed loss models are developed for this module based on the device characteristics considering the turn-on and turn-off times, deadtime, reverse recovery time, and the internal on resistance. Thermal performance is analyzed to evaluate the devices in a 3-phase inverter arrangement. Accordingly, each three-phase inverter shown in the primary-side in Figure 1 is expected to operate up to 250 kW continuously which results in a total of 500 kW power capability of the primary-side power electronics. The engineering CAD drawing of the inverter system and its actual physical hardware realization are shown in Figure II.1.17.2 (a) and (b), respectively.

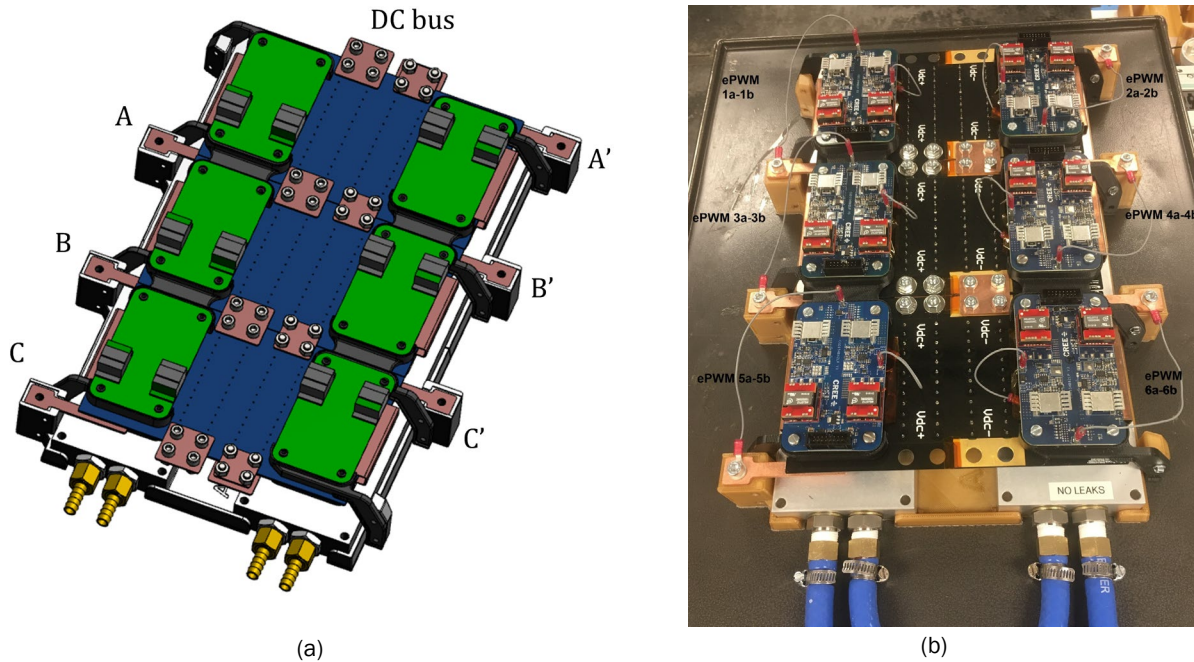


Figure II.1.17.2 3D engineering CAD design of the 300-kW primary-side open-ended dual-winding high-frequency, high-power inverter (a) and physical hardware development of the inverter.

In Figure II.1.17.2, DC bus is distributed across the left hand-side and right hand-side 3-phase inverters. While the first inverter's AC terminals are phase A, B, and C for the phase outs to the couplers and the second 3-phase inverters' outputs are labeled A', B', and C' which are the return windings from the couplers. The other way to analyze and operate this inverter is that this structure is composed of 3 H-bridge inverters such that terminals A-A', B-B', and C-C' each form an H-bridge inverter while each H-bridge inverter powers one phase of the transmitter windings. This inverter is based on ORNL custom designed printed circuit board (PCB) based DC bus bars instead of conventional machined copper dc bus bars. The reason for this change was that a typical film capacitor on the dc bus usually ineffective for the high-frequency harmonic components of the dc bus voltages and the dc bus current ripples due to the self-resonant frequency of those capacitors and the relatively large internal equivalent series inductances (ESI) at those frequencies. Therefore, a decision was made to use the B58033I9505M001 Ceralink capacitors on the dc bus that requires a custom designed PCB with advanced wave soldering. These capacitors introduced an extremely low parasitic inductance of 4 nH. The physical hardware development of this inverter is shown in Figure II.1.17.2 (b) with the ePWM signal sequencing labeled on the phase-leg power modules. As shown in this image, the custom designed PCB bus bar has three pieces with each serving as a building block of one H-bridge inverter. With this building block approach, this inverter structure is expandable for higher power applications by adding additional modules. The approximate dimensions of this development are $300 \times 420 \times 70 \text{ mm}$ (W×L×H) which corresponds to 8.82 ℓ volume. This volume and 0.5 MW power rating provides a power density of 56.7 kW/ℓ.

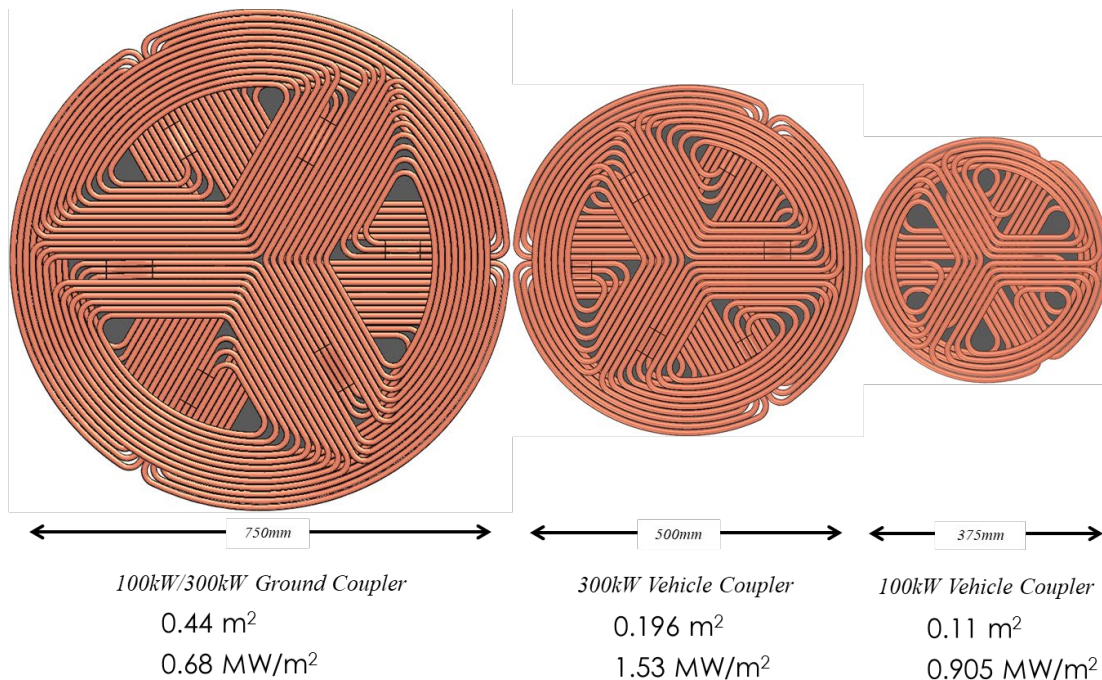
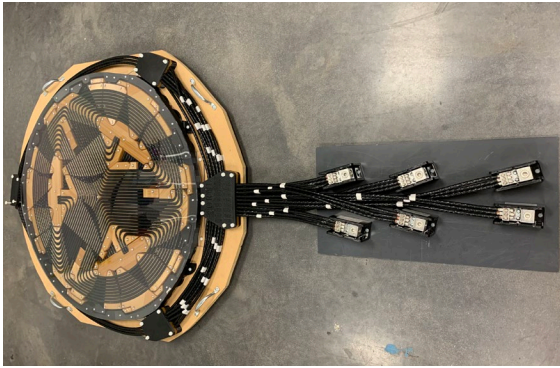


Figure II.1.17.3 Engineering CAD designs of the 100/300 kW transmitter and the 100- and 300-kW receiver pads.

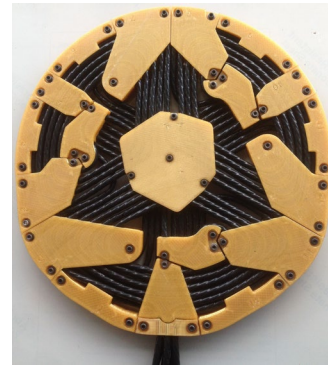
The primary and secondary side couplers designed for this project are shown in Figure II.1.17.3 along with some of the key specifications. The transmitter is common and can perform both the 100- and 300-kW power transfer and it has a diameter of 750 mm which corresponds to 0.68 MW/m² surface power density. The 300-kW receiver has a diameter of 500 mm with a surface power density of 1.53 MW/m² while the 100-kW receiver has a diameter of 375 mm with 0.905 MW/m². Some other key parameters of the couplers are provided in Table II.1.17.2. Each of the couplers has 3 phases and for the 300-kW receiver and 300 kW transmitter there are 3 windings for each phase. It should also be noted that these couplers are designed for up to 125 mm misalignment tolerance in any direction. The completed laboratory development of 100/300 kW ground coupler and the 100-kW vehicle coupler are given in Figure II.1.17.4.

Table II.1.17.2 Primary and Secondary Side Coupler Specifications

	Interoperable Transmitter	100 kW Receiver	300 kW Receiver
Diameter	750 mm	375 mm	500 mm
Litz Wire / Wiring	3×4 AWG/phase	1×4 AWG/phase	3×4 AWG/phase
Litz + Ferrite Thickness	33.6 mm (18.6+15)	28.6 mm (18.6+10)	33.6 mm (18.6 + 15)
Litz + Wire Mass	42.2 kg (9.9+32.3)	8.8 kg (2.4+6.4)	19.4 kg (4.7+14.7)
Worst Case Losses	2362 W (697+1665)	596 W (169+311)	1343 W (331+1012)
Surface Area	0.44 m ²	0.196 m ²	0.11 m ²
Surface Power Density	0.68 MW/m ²	1.53 MW/m ²	0.905 MW/m ²
Coil-to-Coil Efficiency		97.4%	98.8%



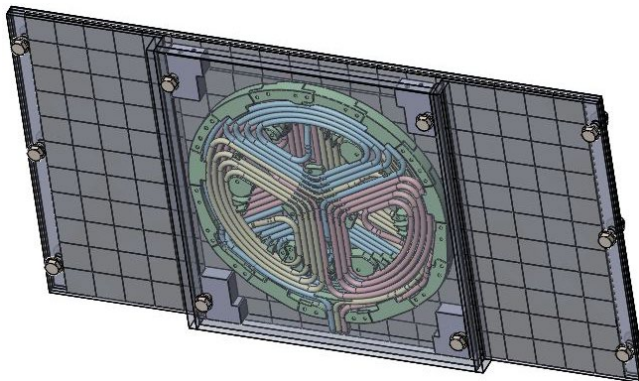
(a)



(b)

Figure II.1.17.4 Engineering CAD designs of the 100/300 kW transmitter and the 100- and 300-kW receiver pads.

For the 100-kW receiver coupler, ferrites added in simulations only under the area covered by the coil. In order to reduce the magnetic field emissions below ICNIRP 2010 requirements and to reduce the possible eddy current losses and temperature rise on the vehicle body, a vehicle-side shield was designed and developed. This shield design is shown in Figure II.1.17.5 (a) whereas the physical laboratory development is given in Figure II.1.17.5(b).



(a)



(b)

Figure II.1.17.5 Engineering CAD designs of the 100/300 kW transmitter and the 100- and 300-kW receiver pads.

Team also received the Hyundai KONA EV from the Hyundai-Kia North America Technical Center (HATCI) which is shown in Figure II.1.17.7 (a) at the parking lot of the National Transportation Research Center at ORNL and in Figure II.1.17.7 (b) on the vehicle lift. The structural design of the coil mount apparatus was also completed, and it is currently being fabricated at the ORNL machine shop as shown in Figure II.1.17.6. Upon the completion of the laboratory benchtop tests, vehicle integrations will be performed which will be followed by the vehicle tests.

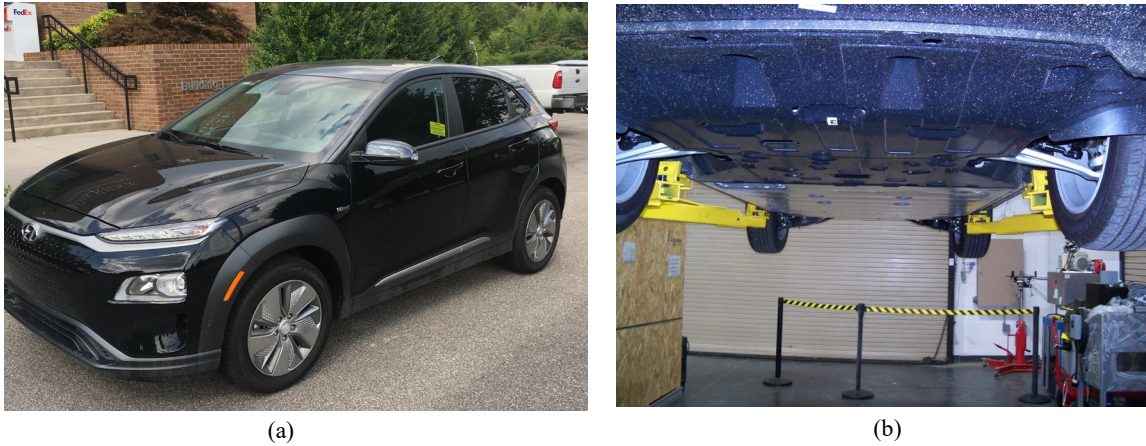


Figure II.1.17.6 Hyundai KONA EV research vehicle at the parking lot (a) and on the vehicle lift (b).

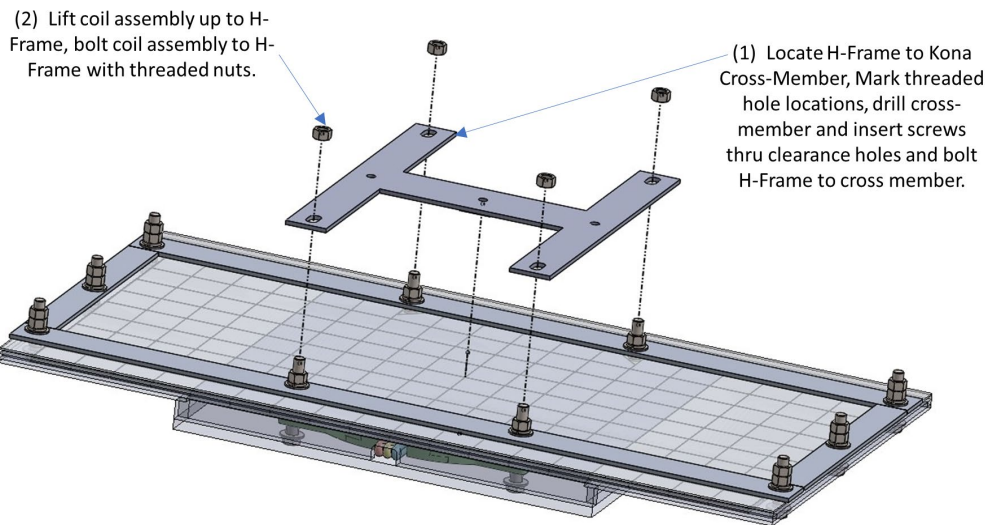


Figure II.1.17.7 100-kW receiver coil and the shielding system mounting platform designed for Hyundai KONA EV research vehicle integration.

For the resonant tuning network, both LCC-series and LCC-LCC tuning configurations were considered, and the component stresses were analyzed for both of these resonant tuning circuitries. These findings are summarized in Table II.1.17.3.

Table II.1.17.3 Component Stress Analysis Results for Secondary-Side Series and LCC Tuning Options

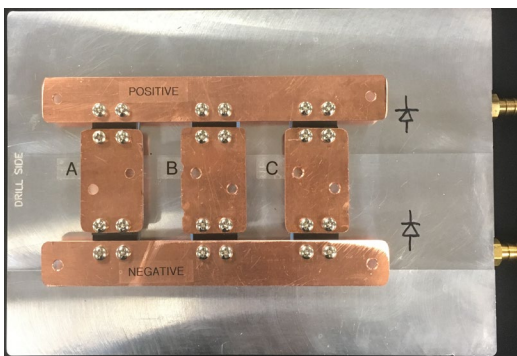
Comparison	Component Ratings & Ripples	Secondary-Side Resonant Tuning	
		Series	LCC
dc-link current ripple	Capacitor size (<10 V _{pp} ripple)	39 μF	15 μF
	Current ripple	155 A _{rms}	79 A _{rms}
Inverter output current [A]	Current rating	183 A _{rms} , 171 A _{avg}	159 A _{rms} , 140 A _{avg}
	Turn-off current	129 A _{rms} , 229 A _{avg}	18 A _{rms} , 110 A _{avg}
Primary coupler current [A]	Current rating	86 A _{rms}	88 A _{rms}

Secondary coupler current [A]	Current rating	142 A_{rms}	110 A_{rms}
Rectifier input current [A]	Current rating	381 A_{rms} , 344 A_{avg}	402 A_{rms} , 351 A_{avg}
Rectifier output current [A]	Capacitor size (<10 V_{pp} ripple)	175 μF	74 μF
	Current ripple	240 A_{rms}	100 rms

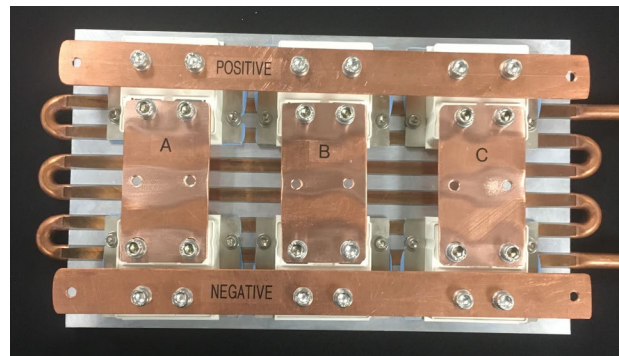
For the vehicle-side rectifiers, two different options are considered including the GB2X100MPS12-227 SiC Schottky diode module manufactured by GeneSiC and the APTDF400U120G Si p-n junction diode module manufactured by Microsemi. The comparisons of these two options are provided in Table II.1.17.4. Due to the lower losses, higher efficiency, and reduced thermal management requirements, the decision was made to use the GeneSiC SiC diode modules in vehicle side rectifiers. For comparisons and experimentally validating their performances, 50 kW rectifiers are assembled as shown in Figure II.1.17.8. As of today, the GeneSiC three-phase rectifier has been successfully tested up to 50 kW, rectifying 90 kHz voltage, with an efficiency of 99.3%.

Table II.1.17.4 Vehicle-side Rectifier Design Considerations for 300-kW Receiver

	GB2X100MPS12-227 SiC Schottky diode module T_j at 125°C	APTDF400U120G Si p-n junction module T_j at 100°C
Number of diodes	36 (12 for 100-kW system)	12 (same for the 100-kW system)
Total rectifier area	66.96 sq.in	284.76 sq.in
Losses	2686 W (0.89% of P_{out})	3060 W (1.02% of P_{out})
Cold plate requirements	<0.032 °C/W for all 18 modules on a single cold plate	<0.0156 °C/W for all 12 modules on a single cold plate
Cost	\$135 /module	\$65 /module
Maximum current	300 A @ 75 °C T_c	400 A @ 80 °C T_c
Forward voltage drop	1.9 V @175 °C T_j	2V @150 °C T_j
Maximum junction temperature	175 °C	150 °C
Reverse recovery current	0 A	120 A @ 100 °C T_j
Maximum reverse leakage current	108 μA @ 1200 V, $T_j=175^\circ C$	5000 μA @ 1200 V, $T_j=125^\circ C$



(a)

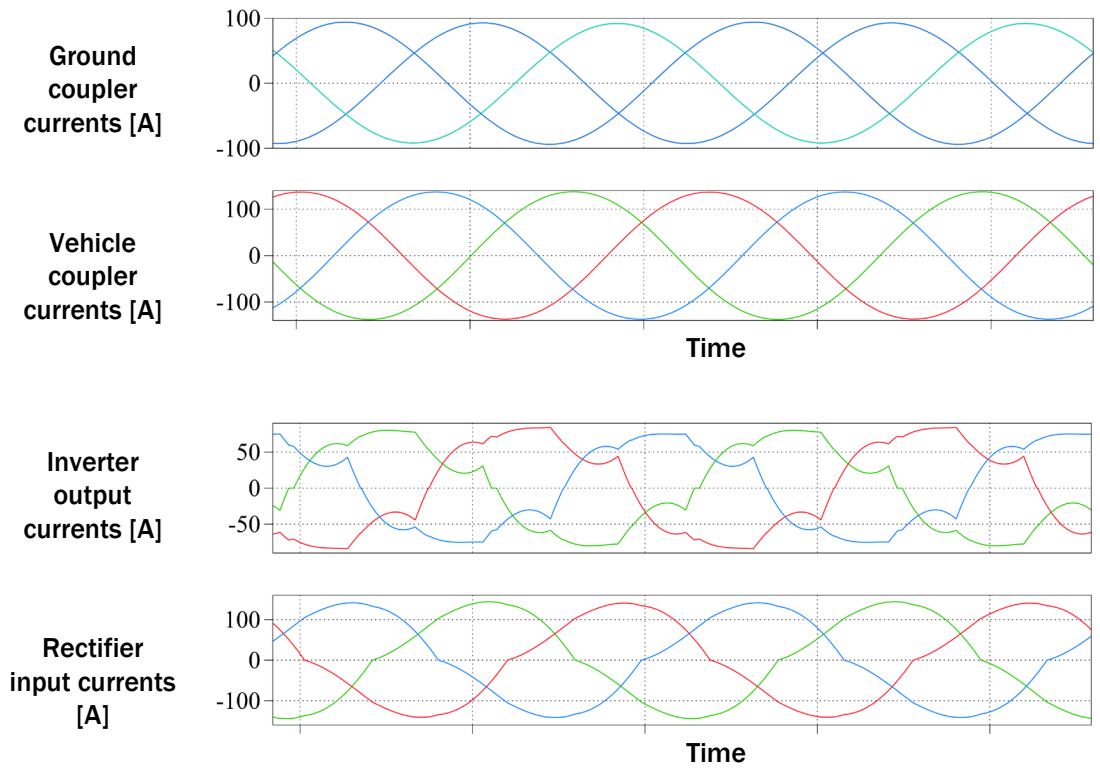


(b)

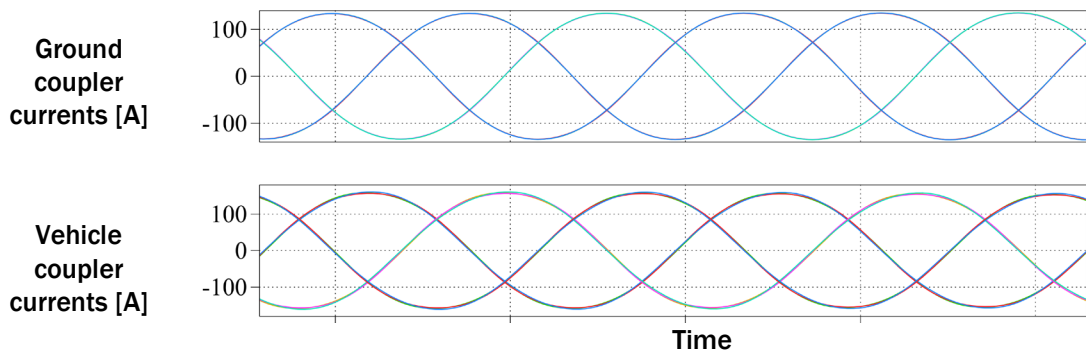
Figure II.1.17.8 Laboratory prototypes of the 50 kW rectifier blocks assembled using the GeneSiC SiC diode modules (a) and MicroSemi Si diode modules (b).

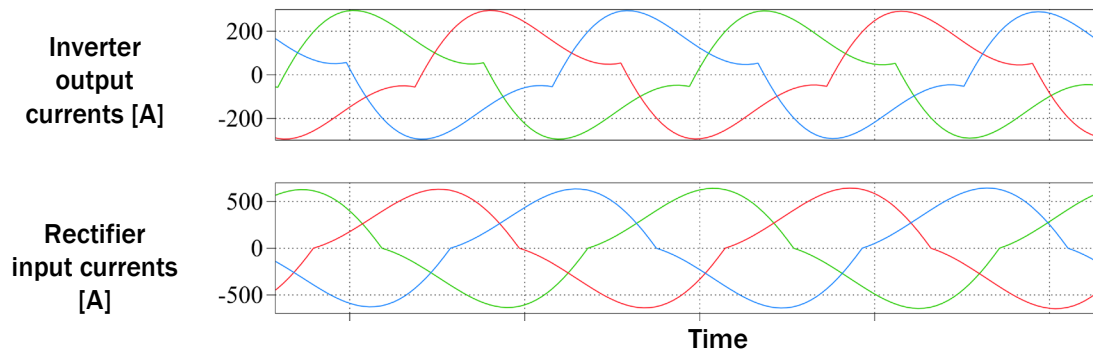
Results

Research team have completed the simulations for the 100 kW and 300 kW operations with the inverter, resonant network and transmitter coil, and two different receivers. These simulation results are provided in Figure II.1.17.9 showing the ground coupler currents, vehicle coupler currents, inverter output currents and rectifier input currents. These simulation results indicate that that the currents are balanced among nine individual phase windings (300 kW transmitter and 300 kW receiver have three parallel wires for each phase winding). The other observation we made is that we might need to adjust the frequency or modify the tuning slightly to improve efficiency at lower power to maintain the zero-voltage-switching on the inverter. However, these results confidently show that the 100 kW and 300 kW receivers can be powered by the same transmitter with interoperability.



(a)





(b)

Figure II.1.17.9 100-kW receiver coil and the shielding system mounting platform designed for Hyundai KONA EV research vehicle integration.

In terms of the experimental results, the very first step was to characterize the inverter’s voltage overshoot characteristics while turning off relatively high current. In the experiments, it was observed that the turn-off took 50 ns while turning off 221 A while the voltage overshoot was only 87 V above the 600 V dc bus voltage which is very low and ensures the safe operation of the inverter power MOSFETs (rated for 1200V) and the dc bus bar capacitors (rated for 900V continuous maximum). The experimental result of the turn-off characteristics with voltage overshoot observation is provided in Figure II.1.17.10.

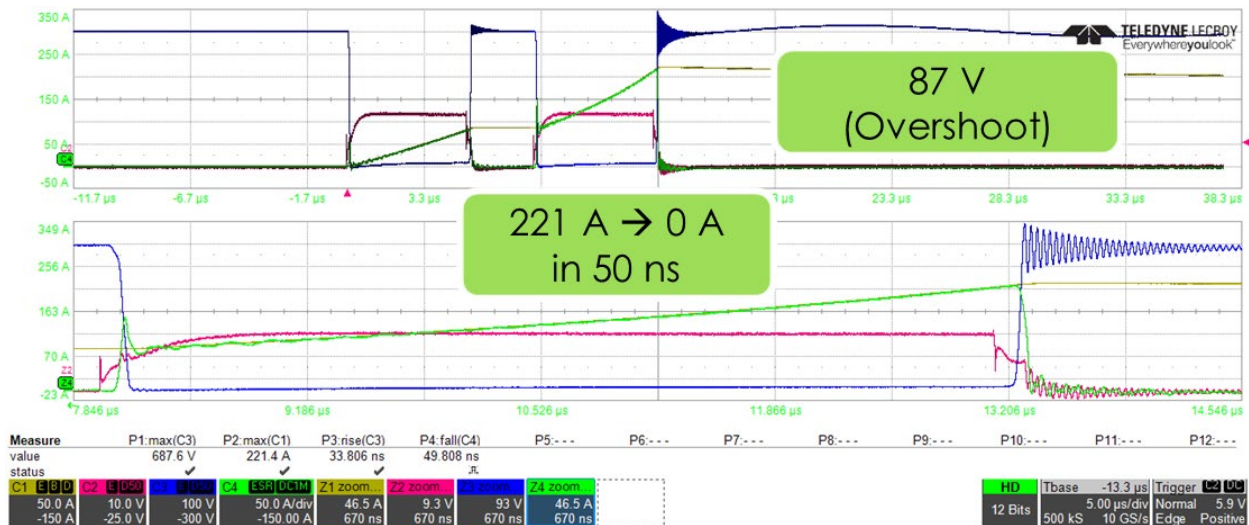


Figure II.1.17.10 Experimental voltage overshoot analysis of the inverter for turning of 221 A in 50 ns.

While the resonant stage compensation network components are under development, we have also tested the inverter and rectifier with the resonant state (coupling coils and resonant tuning components) are represented with an RLC network. In other words, in between the inverter output and the rectifier, an RLC circuitry was formed to emulate the resonant stage of the WPT system. The combined efficiency of the inverter, RLC circuit, and the rectifier was measured 98.6% (dc in to dc out) at 85 kHz switching frequency with a load power of 85.22 kW. The experimental results on the power analyzer is provided in Figure II.1.17.11.

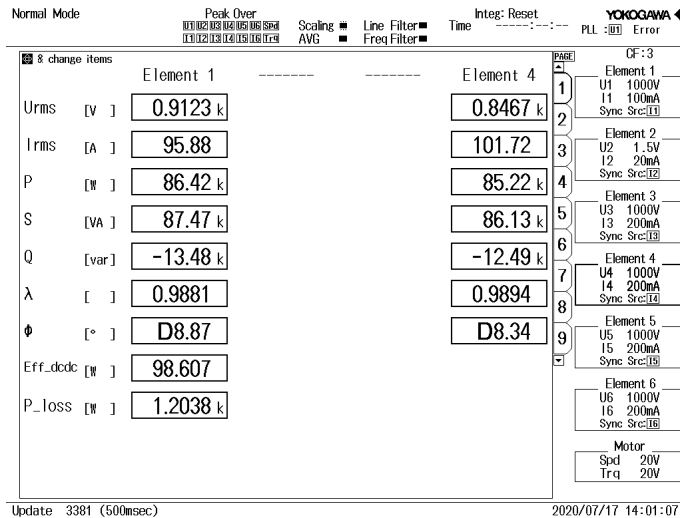


Figure II.1.17.11 Experimental results of the inverter and rectifier operating at 85 kHz with 85.22 kW output.

Conclusions

During the first budget period of the project, the team worked on modeling, simulations, analysis, and design of the system power conversion stages and control systems and completed the design and simulations of the polyphase inductive charging system with an 300-kW interoperable transmitter and primary-side power electronics that can operate with 100- and 300-kW receiver systems. Since proposed concept is new, a relatively low-power, scaled-down version of the couplers was developed and tested to validate the concept and the operation. The prototype was tested with ~95% dc-to-dc efficiency with ~50 kW output. Simulation results agreed with the experimental results for improved confidence for the 100- and 300-kW systems. During the second budget period of the project, team worked on the hardware development. So far, building block H-bridge of the open-ended winding dual inverter was tested up to 85 kW of power with a combined inverter and rectifier efficiency of 98.6%. The vehicle-side building block of the rectifier, which is rated at 50 kW, is also tested up to 50 kW. The future steps include the completion of the resonant tuning network hardware for the 300-kW transmitter and the 100- and 300-kW receiver systems. Completion of the benchtop 100 kW tests will be followed by the vehicle integration efforts for the Hyundai KONA EV. Successful testing of 100 kW power transfer to Hyundai KONA EV will be followed by demonstrations of the technology.

Key Publications

1. "A 50 kW Three-Phase Wireless Power Transfer System Using Bipolar Windings and Series Resonant Networks for Rotating Magnetic Fields," IEEE Transactions on Power Electronics, vol. 35, no. 5, pp. 4500-4517, May 2020.
2. "Shield Design for 50 kW Three-Phase Wireless Charging System," in Proc., IEEE Energy Conversion Congress and Exposition (ECCE), October 2020, Detroit, MD.
3. "Advances in High-Power Wireless Charging Systems: Overview and Design Considerations," IEEE Transactions on Transportation Electrification, vol. 6, no. 3, pp. 886-919, July 2020.
4. "Comparison of Magnetic Field Emission from Unipolar and Bipolar Coil-Based Wireless Charging Systems," in Proc., IEEE Transportation Electrification Conference and Expo (ITEC), June 2020, Chicago, IL.

5. "Review of Safety and Exposure Limits of Electromagnetic Fields (EMF) in Wireless Electric Vehicle Charging (WEVC) Applications," in Proc., IEEE Transportation Electrification Conference and Expo (ITEC), June 2020, Chicago, IL.
6. "A Tradeoff Analysis of Series/Parallel Three-Phase Converter Topologies for Wireless Extreme Chargers," in Proc., IEEE Transportation Electrification Conference and Expo (ITEC), June 2020, Chicago, IL.
7. "A 50-kW Three-Phase Wireless Power Transfer System using Bipolar Windings and Series Resonant Networks for Rotating Magnetic Field," IEEE Transactions on Power Electronics, vol. 35, no. 5, pp. 4500-4517, October 2019.
8. "Variable Duty Control of Three-Phase Voltage Source Inverter for Wireless Power Transfer Systems," in Proc., IEEE Energy Conversion Congress and Exposition (ECCE), Sept.-Oct. 2019, Baltimore, MD.
9. "Comparison of Leakage Magnetic Field from Matched and Mismatched Double-D Coil based Wireless Charging System for Electric Vehicles," in Proc., IEEE Energy Conversion Congress and Exposition (ECCE), Sept.-Oct. 2019, Baltimore, MD.
10. "Design of an EMF Suppressing Magnetic Shield for a 100-kW DD-coil Wireless Charging System for Electric Vehicles," in Proc., IEEE Applied Power Electronics Conference and Exposition (APEC), March 2019, Anaheim, CA.

Acknowledgements

Project team would like to thank Manish Mohanpurkar from the U. S. Department of Energy and Jason Conley from National Energy Technology Laboratory for their continued guidance and support on this project. We would also like to thank Dr. David Smith (ORNL) for his guidance and support which is greatly appreciated.

II.1.18 Direct Current Conversion Equipment Connected to the Medium-Voltage Grid for XFC Utilizing a Modular and Interoperable Architecture (EPRI) [DE-EE0008448]

Watson Collins, Principal Investigator

Electric Power Research Institute (EPRI)
3420 Hillview Avenue
Palo Alto, CA 94304-1338
Email: wcollins@epri.com

John J. Conley, NETL Project Manager

U.S. Department of Energy/ NETL
Email: john.conley@netldoe.gov

Steven Boyd, DOE Program Manager

U.S. Department of Energy
Email: steven.boyd@ee.doe.gov

Start Date: Oct 1, 2018
Project Funding: \$5,803,000

End Date: Jul 31, 2022
DOE share: \$2,601,500

Non-DOE share: \$3,201,500

Project Introduction

Preparation for vehicle charging at 150 kW and above is underway at multiple vehicle manufacturers, in the automotive, truck, and bus segments. The Society of Automotive Engineers (SAE) vehicle connector standards (SAE J-1772) have been evolving to accommodate these higher power levels. Connector standards also are being developed for conductive, automatic charging at power levels up to 1,200 kW (1,200 Amps at 1,000 Volts DC) by the SAE (SAE J-3105) to serve medium- and heavy-duty vehicles. In addition, the CharIN association is advocating for connector standards capable of delivering greater than 1MW power levels utilizing DC power supply. An industry consensus has emerged that DC power is the preferable means of delivering higher power to vehicles. The U.S. Department of Energy has recently coined the term Extreme Fast Charging (XFC) for 350 kW and above DC charging. For utilities, the current practice in serving DC fast charging sites involves the provision of a 480 Volt AC service fed from the medium voltage grid and converting to DC power for charging. For higher power levels and for simultaneous charging of many vehicles, this approach can create a large hardware footprint rendering it expensive to scale. To address this challenge, medium voltage Silicon Carbide (SiC) based AC to DC conversion solutions provide viable solutions. The SiC based conversion solutions eliminate the intermediate 480 Volt AC stage and convert utility's medium voltage to DC for vehicle charging. Additionally, such Direct Current technologies when integrated with a DC common bus could facilitate the integration of distributed energy resources (DER) to minimize the impact on the grid. This approach could help mitigate electric grid impacts, enable new integration approaches, reduce the impacts brought by demand charges, and reduce XFC related infrastructure costs. This DOE project addresses the design, development, implementation, and performance verification of a medium voltage SiC based conversion solution enabled for DER connectivity. Performance will be verified through laboratory testing and field installation to assess XFC with 350 kW capable vehicles. The project team will work with automakers, charging hardware manufacturers, utilities, and demonstration site hosts to address interoperability and commercialization pathways.

Objectives

The objective of the program is to develop and demonstrate prototype hardware for use in extreme fast charging (XFC) equipment capable of simultaneously charging multiple light duty plug-in electric vehicles (PEV)s at rates of ≥ 350 kW and a combined power level of ≥ 1 MW while minimizing the impact on the grid and operational costs. The hardware being developed includes medium voltage Silicon Carbide (SiC) -based AC to DC conversion equipment, DC Distribution bus and DC-to-DC head-end charging units.

The project goals are:

- Develop the design, performance guideline and specifications for the medium voltage (MV) connected Direct Current (DC) EV-charging architecture
- Test the MV-connected DC technology for Extreme Fast Charging (XFC) and document functional, performance characteristics
- Demonstrate the MV-connected DC technology at a viable field site available to charge XFC compatible vehicles, acquire performance data and document results.

Approach

To meet the project objectives, EPRI along with the project team will develop prototype hardware with upstream interfacing capabilities to the utility grid and downstream configuration for DC load distribution along with complete system engineering design. The overall system architecture is shown in Figure II.1.18.1. The system comprises of a medium-voltage AC-to-DC converter or the Solid-State Transformer, the DC distribution bus, and the head unit DC-to-DC converter units.

A Utility interconnection interface (not shown in Figure II.1.18.1) provides single point connectivity to the utility medium voltage Grid. The XFC hardware using DC technologies will serve to minimize adverse load impacts to the grid by facilitating EV Grid Integration and Services. DER such as PV, Energy Storage and microgrids can be connected to the hardware and maintain single point interconnectivity to the utility Grid. The Research effort could also serve to identify new opportunities for interoperability, flexible operation, and technical transfer activities. The project team will investigate potential impacts such as total cost of ownership including demand charges for XFC site hosts and utilities, efficiency improvements and reducing system losses, new capabilities for grid support (power factor correction, VAR compensation, disturbance isolation etc.) and optimization of equipment sizing for upstream Grid assets that serve the XFC equipment. The project will ultimately lead to a fully tested prototype system capable of charging multiple light-duty plug-in electric vehicles (EVs) at a combined power level of ≥ 1 MW. The system will be installed and demonstrated at a utility site to showcase extreme fast charging infrastructure.

Project Teaming Strategy

The project team is uniquely qualified to conduct research and demonstration tasks for the successful accomplishments of project objectives. EPRI is the project lead with equipment manufacturers, university and national lab partners supporting various tasks within the project.

- Power Electronics - System specifications determined collaboratively, while the development of the two major power electronics pieces are designed by two leading manufacturers of power equipment:
 - Eaton is leading the work on the Medium Voltage AC to DC converters
 - Tritium is leading the work on the DC to DC head-end chargers

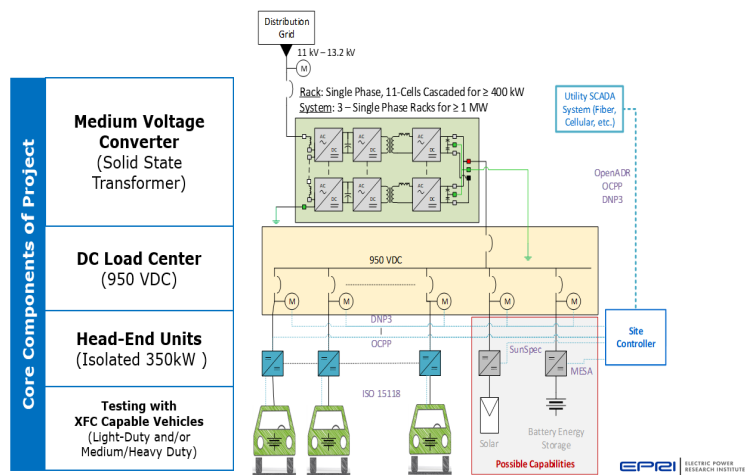


Figure II.1.18.1 Architecture and Core Components

- Testing - Three levels of testing are included in the project:
 - Component level testing and end-of-line production testing performed by respective manufacturer
 - System testing to occur at NREL laboratory with simulated and actual vehicles
 - Demonstration site testing in collaboration with host utility with actual vehicles
- Vehicles - Supporting automakers (Hyundai America Technical Center and Fiat Chrysler Automobiles) are included in the project to support testing. If vehicles capable of charging at 350kW and above are unavailable for testing from supporting automakers, EPRI will identify and obtain vehicles from other vehicle manufacturers.
- Demonstration Site - EPRI has more the three supporting utilities interested in hosting the demonstration site. The decision on the actual demonstration site will be based on specific site characteristics identified by the utilities, anticipated vehicle charging to occur at site and the site development budget.

Unique Aspects and Collaboration

The project serves unique aspects which contribute to the accomplishment of project objectives:

- Pathway to Commercialization- Seeking to develop equipment, standards and techniques that exhibit possible pathways to commercialization.
- Interoperability – Seeking to develop a system capable of operating with power conversion equipment and head end units from multiple manufacturers.
- Technology Transfer –collaborating with industry participants throughout the project process.
- Diverse Project Team – including project partners from various perspectives (utilities, hardware manufactures, automotive manufacturers, national laboratories, and university)

EPRI is collaborating with multiple utilities and organizations as shown in Figure II.1.18.2. These efforts enable the project team improve industry engagement, assess interconnection and integration challenges, identify potential sites, and define demonstration requirements. The hardware design, manufacturing and testing of the XFC system is the first of its kind in many ways. Project partners and stakeholders have various perspectives based on use cases and their specific role and as a result the technical specifications to build a system versatile enough to accommodate various interconnection standards/best practices, protection requirements, loads and site requirements are quite broad.

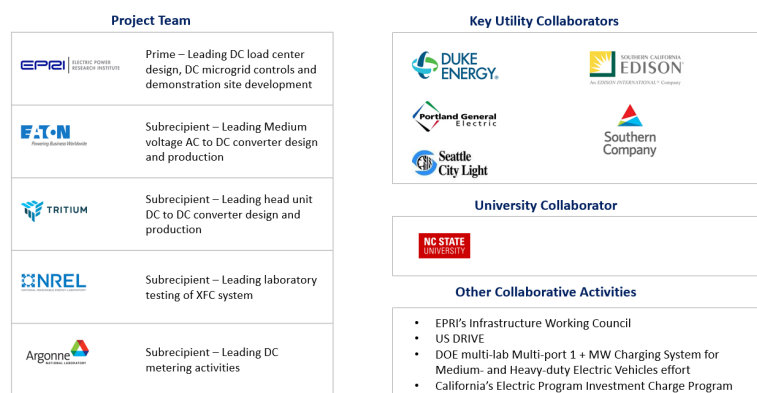


Figure II.1.18.2 Collaboration and Coordination

Challenges and Barriers

The project team has identified the following challenges and barriers that can potentially impact the project. Mitigation plans for some key ones have been identified to ensure project objectives are met in a timely manner and within budget.

- Performance of the initial cell and module testing at Eaton’s facility may not meet modeled results or other criteria (Low probability, Medium Impact)
- Development of an isolated XFC dispenser with a 950V DC supply may encounter integration challenges (Low probability, Medium Impact)
- y-capacitance issues may be problematic for stable operations, protection, and safety of system (Low probability, Medium Impact)
- Unexpected problems may be discovered during testing at NREL’s laboratory (Medium probability, Medium Impact)
- Lack of consensus of interoperability approaches, common understanding of DC topologies, equipment options and communications systems for the DC bus (Medium probability, Low Impact)
- Implementation of communication protocols. Which ones are appropriate, which ones are implemented vs standard being defined (Medium probability, Low Impact)
- Covid-9 related impacts on supply chain, key resources, or organizations (Medium probability, Medium Impact).
- Key longer-term risks based on the current state of the industry are:
 - Lack of equipment and system standards
 - Proprietary components and control/communications architecture
 - Lack of standardized system design approaches
 - Site-driven parametric dependencies that impact design.

The project team is seeking to develop equipment, standards and techniques that exhibit possible pathways to standardization and commercialization. The team is also exploring ways to develop design criterion focused on interoperability to support ways to operate with power conversion equipment and head end units from multiple manufacturers.

Project Status

Eaton Corporation is a multinational power management equipment manufacturing company with industry leading products for electric, aerospace, hydraulic and vehicle applications. Eaton has established expertise and knowledge in power electronics engineering and manufacturing. EPRI, Eaton, NREL and electric utilities have established the design for the XFC system and are collaborating on the design and fabrication of the Medium Voltage Converter System also known as the Solid State Transformer (SST). The SST converts utility AC medium voltage at 11-13.2kV to 950-1000V DC. Eaton is manufacturing three (3) single-phase SST modules that constitutes the Medium Voltage Converter System. Each single-phase SST module consists of two (2) medium voltage converter racks, each rack composed of eleven (11) cells in cascaded H-bridge with dual-active-bridge configuration for a total power rating of $\geq 400\text{kW}$. The 11-cell single-phase cascade design bridges the 7.6/13.2kV utility medium voltage connection. Each cell has a power rating of 40kW and are connected in parallel on the DC side of the converter.

Tritium are world leaders in DC-DC charging equipment with high power dispensing capabilities. Tritium has multiple commercially available EV chargers ranging from 75kW to 350kW. These chargers have been installed and operating in Europe and North America. This project will utilize Tritium’s new, next generation 350kW isolated DC-to-DC Head-End technology delivered in an IP65 sealed enclosure with liquid cooled technology. The 350kW Tritium charger comprises of fourteen (14), 25kW isolated DC-to-DC modules. The

25kW modules have been fully factory-tested with multiple module combinations running synchronized and in parallel. Tritium is anticipated to supply two (2) 150kW and four (4) 350kW isolated DC-to-DC Head-End chargers for this project for comprehensive testing at NREL prior to site installation. The two (2) 150kW units and one (1) 350kW unit will be used as test units and will stay at NREL for ongoing testing and performance verification. Three 350kW after testing at NREL will be shipped to the demonstration site. A significant accomplishment for the project team was changing the DC-to-DC head-end unit from the originally scoped non-isolated design to isolated. This had to be done to accommodate the revised design of the DC distribution (DC Load Center), which Tritium took upon as a challenge and completed the design and initial testing. The originally planned Tritium's 350kW non-isolated head unit had a switched matrix DC distribution.

EPRI has developed a design specification for the DC Load Center (DC distribution Bus) to be used for soliciting quotes from equipment vendors to build. The solid-state transformer (SST) feeds DC power to the DC Load Center, which then enables powering the galvanically isolated EV chargers to charge electric vehicles. Various UL and IEC standards require galvanic isolation between the grid and the vehicles, and from vehicle to vehicle. The use of a charging head with a 'buck' topology has been assessed. The Project Team selected a voltage of nominally 950V for the SST output to the DC distribution bus, as this gives adequate headroom above the 920V maximum required by the vehicle. The load on the DC distribution bus will come from the charging head units as planned within the project. Future enhancements to this project could be to add DER such as Photovoltaic (PV), Energy storage, and V2G vehicles, all of which can connect easily to the DC Bus. The team also decided on a mid-point grounded DC output from the SST to reduce the size of the DC gear and cable requirements.

Special facilities access and planned utilization:

- ANL: Argonne National Lab's efforts have been directed towards enabling harmonized EV charging device specifications and common test procedures. ANL has developed prototypes of accurate, stable, and easy to install low-cost compact DC submeters for high power EV charging (1000Vdc/500 Adc). One of these prototypes has been commercialized by Riedon. Meter development, connection architecture, and test plans for DC metering on this project will be coordinated with ANL.
- NREL: Lab testing and verification of the XFC charging system with 3 installations of Tritium's DC-to-DC Head-End chargers, Eaton's Medium Voltage Converter System with three SST modules, the DC Load Center and 350kW charge capable vehicles will be hosted and administered at NREL's Energy Systems Integration Facility (ESIF). The 182,500-square-foot (17,190-square-meter) facility is a first-of-its-kind design with a unique merging of three distinct and very specialized components: an ultra-green workplace, a high-performance computing data center, and a highly sophisticated high-bay laboratory. NREL is working with the project team to define the test procedures and acquire test equipment for system testing, operational and performance verification.

Results

The following results were accomplished during the first year (Y2020) of the project:

Development of system architecture, technical performance specification and interoperability parameters for the medium-voltage AC-to-DC converter and the head unit DC-to-DC converter completed. Selection of a system topology, requirements and design trade-offs have been assessed. Converter design and control approach, input, and output ratings along with control functions have been defined. Trade-off analyses between various commercially available SiC power modules was completed, and the most commercially ready devices chosen. Similarly, the high frequency transformer design was reviewed with respect to switching frequency and type of core material. Based on the analysis and the efficiency needed the design was completed with off-the-shelf cores.

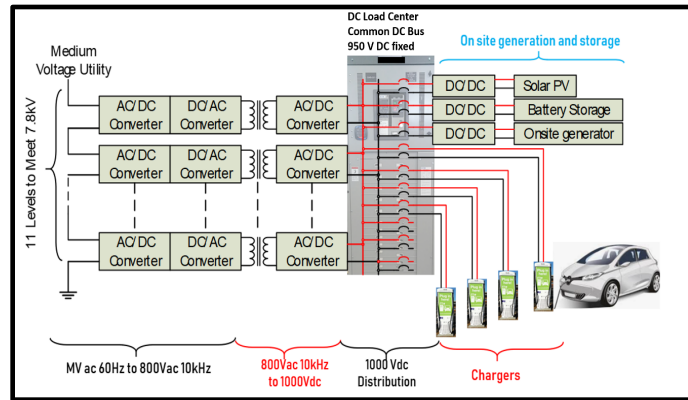


Figure II.1.18.3 System Overview

- DC Load Center design specification as shown in Figure II.1.18.4 has been reviewed by AHJ for the test site (NREL). The DCLC design will be used to manufacture the DCLC by an equipment manufacturer. The DCLC is custom equipment currently with a PLC incorporated for decision-making for protection and coordination. It is anticipated that the DCLC design will enable pathways for interoperable designs and commercialization.
- Medium-Voltage Converter module design, system topology and architecture are complete. Prototype modules have been assembled and are undergoing tests at Eaton’s lab. Key simulation results for the converter module performance with utility interconnection and high-side DC bus voltage control are shown in Figure II.1.18.5. Controls and Protection design has been completed. Testing, simulation, and physical realization of advanced control systems for the converters is in progress.
- The electric design of the controller is determined. The PLC side is the focus of review and finalization to define overall control for switching HMI / SCADA control, handling faults, and updating values.

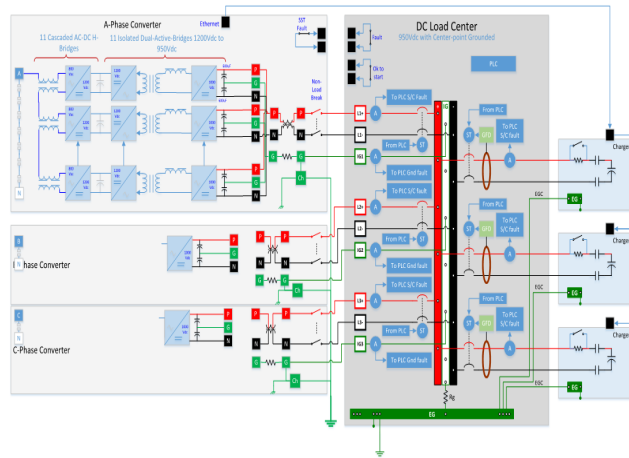


Figure II.1.18.4 DC Load Center Specification Design

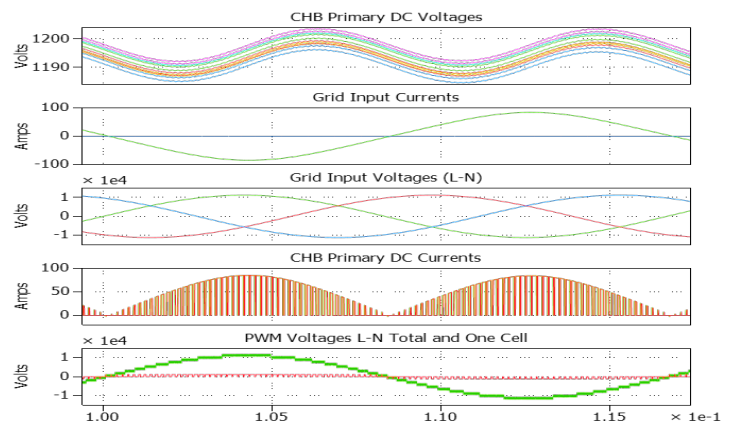


Figure II.1.18.5 Medium Voltage Converter Module performance simulations

- A comprehensive grounding design developed to help define and specify ground connectivity from the MV overhead line through the Utility Interconnection Interface, SST, DCLC, Charger, and ending at the EV.
- The XFC system will be a containerized package with air cooling. The three converter modules of the SST – A, B, C would be housed inside a standard 20 ft container (20x8x8 ft). The utility connection interface and the DC Load Center will be cabled to the container either through overhead tray cabling or underground trenches.

Conclusions

The primary conclusions to date are derived from the XFC MV converter and DC Load Center design and development. Prototypes of the power cells in the Medium Voltage Converter and modules in the Head-End Unit are at advanced stages. Simulation testing of the hardware shows control performance of the converter system is within limits. The DC Load Center design specification enables protection and relaying designs that vary by site requirement. With the design and performance assessment of the system in progress, testing of the system at NREL is desired to be comprehensive to the extent budget and scope allow. Multiple sites are currently under consideration, from the listed utility collaborators involved in the project. Several of the potential demonstration sites also include vehicle collaborators.

High level interest in DC distribution for DC fast charging exists within the utility industry and with other organizations associated with vehicle electrification.

II.1.19 Comprehensive Assessment of On-and Off-Board Vehicle-to-Grid Technology Performance and Impacts on Battery and the Grid (EPRI)

Sunil Chhaya, PhD, Principal Investigator

Electric Power Research Institute (EPRI)
3420 Hillview Avenue
Palo Alto, CA 94304
Email: schhaya@epri.com

Lee Slezak, DOE Program Manager

U.S. Department of Energy
Email: Lee.Slezak@ee.doe.gov

Start Date: October 1, 2016	End Date: June 30, 2021	
Total Project Funding: \$2,786,278	DOE share: \$1,547,678	Non-DOE share: \$1,238,600

Project Introduction

There is heightened interest in the value for Vehicle-to-Grid (V2G) applications to provide energy management services to support grid reliability and resiliency. The research community is seeking to maximize the total value of a vehicle by exploring other services beyond transportation, but the automotive manufacturing and transportation battery communities remain reluctant to embrace V2G applications because of uncertainties associated with the exposure to grid applications and concerns about potential degradation of the transportation battery. Also, there are the challenges for enabling V2G technology development of bidirectional power electronics with the functionality, communications, and controls that are compliant with applicable regulatory and safety requirements, and standards. This proposal is to address the automotive industry concerns and the regulatory challenges to V2G technology.

The requirements for grid interconnected bidirectional inverters impose significant challenges to the automakers for on-vehicle inverter V2G functionality. Automakers self-certify their vehicles to Society of Automotive Engineers (SAE) and Federal Motor Vehicle Safety Standards (FMVSS) requirements, and do not submit vehicles to National Recognized Test Laboratories (NRTL) such as UL. SAE is addressing this by developing SAE J3072 "Interconnection Requirements for On Board Utility Interactive Inverter Systems" providing communications and process requirements for validating the on-vehicle inverter certification. It incorporates the test certifications required by UL 1741 and requirements of IEEE1547. Acceptance by utilities of a J3072 compliant vehicle inverter certification is an open issue. As a part of a collaborative California Energy Commission program the team evaluated and verified these requirements for on-vehicle bidirectional inverters.

In contrast, off-vehicle inverter enabled V2G using DC charging avoids the issues and challenges relative to on-vehicle V2G inverters. DC chargers contain the charge control electronics and are a location fixed asset that is hard wire connected to the grid. Because DC chargers are a fixed standalone product, they can easily be UL tested, certified, and site permitted. No vehicle UL certification would be required. The vehicle is only required to be DC charge capable with embedded J2847/2 communications software and J2931/1 power line communications (PLC) compliant connectivity with the DC charger which is standard with all DC charge capable Electric Vehicles.

The DC charger integrated off-vehicle bidirectional inverter is the most viable strategy and less challenging method for automakers to engage in commercialization of V2G as a distributed resource. However, there are still the automaker concerns with battery capacity degradation from V2G cycling and impacts on warranty services. This DOE project is to address the development, implementation, and verification of DC charging integrated off-vehicle bidirectional inverter enabled V2G; and to assess the impact of V2G cycling on battery

durability. Also, will be working with the SAE J2847/2 task force in the development and testing of the control messaging requirements and protocol for V2G communications that is presently ongoing.

Objectives

The objective of the program is to test and evaluate grid DER management / integration use cases using V2G bidirectional power flow (charging and discharging) integrated with solar and stationary energy distributed resources in the AC (on-vehicle) and DC (off-vehicle) domains. The outcome is data to be analyzed and evaluated for performance, durability, and usage characteristics of the V2G technology, and impacts on battery life and vehicle components. As such, the proposal involves evaluation of Vehicle to Grid (V2G) technologies for on-vehicle (AC) and off vehicle (DC) bi-directional inverters thereby providing the best research value for the DOE.

The project goals are:

- Provide experimental and analytical basis to V2G technology as a key enabler in improving the value of owning a Plug-in Electric Vehicle.
- Demonstrate the usefulness of off-vehicle Smart Power Integrated Node (SPIN) system to further enhance the value of V2G by enabling increased renewable generation on the grid and providing Vehicle to Home type services in conjunction with on-vehicle and off-vehicle storage.
- Provide experimental and analytical basis for assessing effect on EV batteries from their application to grid services
- Provide key metrics for evaluation of performance and value of an off-vehicle V2G system in comparison to an on-vehicle V2G system
- Assess the effect of transformer constraints on grid service implementation
- Provide analytical framework and research results on the valuation of V2G services for high-impact (high-stress) regions of the distribution grid.

Approach

The project is the comprehensive development, testing, and evaluation of Vehicle to Grid (V2G) and energy management technologies for on-vehicle bidirectional inverters, through a companion cost share project and for off-vehicle bidirectional inverters, through this DOE funding request. Figure II.1.19.1 provides a representative overview of the two V2G projects. The cost share funded project focuses on the effects of V2G energy management on the distribution system using on-vehicle inverter enabled bi-directional power flow to balance solar output for improved grid reliability and stability, including an economic evaluation of V2G services.

The focus of this DOE project is to develop, test, and demonstrate off-vehicle inverter enabled bidirectional power flow (V2G) utilizing a DC charging bi-directional converter integrated into a Smart Power Integrated Node (SPIN) system. The communications, control, and interface functionality for the SPIN system will be based on SAE standards (SAE J2847/2, J2931/1, J2931/4). The intent is to demonstrate a fully functional, grid-compatible DC charging based V2G end-to-end system that provides secure, interoperable communications and information processing.

The uniqueness is the SPIN system capability to control and process power flow between PEVs (charging/discharging), the grid, local solar and backup energy storage with a single multifunctional modular unit. The SPIN system will synchronize these energy sources to act as dispatchable DER. Innovation lies within the development of V2G with DC bi-directional charging, and support of local Distributed Energy

Resource (DER) integration use cases that will accelerate the deployment of V2G as a part of an integrated DER ecosystem.

The project is to achieve the objectives through accomplishment of the following activities:

- Development/fabrication of the Smart Power Integrated Node System hardware integrating a bidirectional dual active bridge converter using Wide Band Gap SiC power module technology with DC charging functionality (6.7kW to 10kW).
- Development/integration of the system control and communications software utilizing standards-based protocols with interoperability between the SPIN system, utility or Energy Service Provider, and the PEV. This includes the development/integration of Energy Management System (EMS) control algorithms and functionality in the SPIN hardware for integrating V2G with solar and back up energy storage as coordinated distributed energy resources. Expectation is to extrapolate data on customer value and utility benefits for V2G DER integration.
- Develop/test determined cycle plan based on selected grid service use cases in both a lab environment and subsequently in a vehicle field demonstration.
- Evaluate battery life and conduct battery durability impact testing and analyses at NREL
- Conduct a field or in-lab demonstration of the V2G grid service use cases utilizing Fiat City EV and fully developed SPIN systems. The systems will be connected to a single transformer to allow evaluation of the grid impact from clustered EV charging and discharging.

The design, component technical specification, and simulation of the SPIN bidirectional converter has been completed by Flex Power Control (FPC) under a Technology Innovation contract from EPRI. ORNL has had specific experience in the development and integration of Wide Band Gap Silicon Carbide (SiC) power module devices in inverter systems for electric drive propulsion systems, and will provide engineering expertise to evaluate, test and verify the SPIN system design. Hardware fabricator Current Ways has established expertise and knowledge in power electronics manufacturing engineering and in UL certification processes. FPC, ORNL, and Current Ways have an established interaction on the design for the SPIN system and are collaborating on the design and fabrication of the FPC-designed SPIN technology.

The SAE J2847/2 and J2847/3 standards incorporating the required PEV/charger communications for PEV reverse power flow are in progress. EPRI is a working member of the SAE Task Force and is engaged in the development of these standards. This project will correlate with the development of the standards and provide a basis for verification of the determined communications requirements.

Kitu Systems is presently developing the IEEE 2030.5 software into the AeroVironment EVSE for the CEC V2G project, which will be leveraged to successfully implement the software for the SPIN system. Additionally, EPRI will work with Fiat Chrysler to implement the required J2847/2 communications for V2G, which are based on the DIN 70121 protocol, into the Pacifica Mini Van PHEVs for the field demonstration.

EPRI developed and deployed residential community DER management control algorithms in another project in Southern California around a community of Zero Net Energy homes, and these control algorithms will utilize the underlying stack developed by Kitu Systems that creates open standards-based communications. This experience integrating DER as well as the code-base will be leveraged to develop and implement the SPIN EMS control algorithms for coordinated DER management of V2G, solar, and back up energy storage, establishing the capability for micro grid operations at the local facility or residential level. EPRI's ongoing work with NREL on the INTEGRATE projects will inform the open DERMS and DRMS integration. In addition, EPRI will develop the grid models and provide the simulated utility DR and ISO regulation command/request signals for activating V2G during the lab testing and field demonstration phases.

LG Chem are the world leaders in electric mobility and grid-scale Lithium-ion batteries and will be an active participant in this project to lend both battery application, testing and data interpretation expertise, with battery hardware and test services to create data sets that can be analyzed.

Stellantis is making available CCS-equipped Model Year 2022 Fiat City EVs (Fiat 500) for this pilot for which the software will be modified to add off-vehicle V2G services related control algorithms. Modified Chrysler Pacifica PHEVs have been utilized and outfitted with on-vehicle V2G bidirectional charger as well as charger to EVSE communications utilizing J2847/3 and SAE J3072 standard application based on IEEE2030.5 protocol will be developed by EPRI and Kitu Systems. EPRI is developing the IEEE2030.5 translation to the vehicle CAN to ensure interoperability of the protocols for V2G functionality and control. The key use cases of the on-vehicle V2G part of the project, along with valuation of the V2G services and considerations for the V2G capable

Special facilities access and planned utilization

- ORNL: Characterization and system integration testing of the Spin System will be accomplished at the ORNL Power Electronics and Electric Machinery Laboratory is in the National Transportation Research Center (NTRC), which has more than 9,000 square feet of space for developing, fabricating, and testing the next-generation power electronics and electric machine technologies. Lab testing of the complete V2G system with the SPIN system and LG battery packs will be accomplished at the Distributed Energy Communications and Control (DECC) Laboratory at ORNL which focuses on distribution system control and operation, grid interconnection and control of distributed energy resources including energy storage and electric vehicles, as well as smart grid, and communication applications.
- The University of California, San Diego, also known as UCSD, is a public research university located in the La Jolla neighborhood of San Diego California in the United States. The university occupies 2,141 acres near the coast of the Pacific Ocean with the main campus resting on approximately 1,152 acres. UC San Diego is the seventh oldest of the 10 University of California campuses. UCSD is the host and testing site for multiple California Energy Commission funded EV Infrastructure projects with a comprehensive installation of DC Fast Chargers and AC Level 2 EVSEs from multiple manufacturers and EV service providers.



Figure II.1.19.1 Project Footprint for Concurrent Engineering

- Fiat Chrysler Automobiles Group: Stellantis' Auburn Hills engineering center has world-class facilities and engineering staff that will be leveraged to do vehicle software and CAN bus integration of the grid communications hardware and software, as well as system commissioning and integration with SPIN module available for functional testing and performance assessment. One Pacifica PHEV will remain with Chrysler to validate any software or hardware changes in the lab before making them in the field.
- Rhombus Technology Solutions: Rhombus are the SPIN system build partners, with facilities in Dearborn, MI and in San Diego, CA. Rhombus' San Diego, CA lab space will be used for end-to-end system integration and testing with Stellantis Fiat City EV.
- National Renewable Energy Lab Energy System Integration Facility (ESIF): NREL ESIF primary role is to set up and assess the incremental impact of grid services on PEV batteries, to identify the opportunity for grid services as well as its economic potential for the EV owner.
- The remainder of the facilities (GridScape, Fremont CA, IoTecha in NJ and EPRI in Knoxville, TN as well as Palo Alto, CA) are primarily the software and system engineering staff.

Results

For BP3 related scope, the team began the work with the intent to get the build different parts of the system together for integration with the EV in 3Q 2020. The work during this phase was progressing at five locations simultaneously, as shown in the map in Figure II.1.19.1 above, until COVID19-related stay-at-home orders disrupted this plan. The major impact of this was on the rate of progress of on-vehicle software verification, as well as battery performance impact testing at NREL.

The following Table II.1.19.1 describes the revised timeline for BP3 completion that was agreed in early 2020 and approved, based on the tasks remaining and the time that would be required to complete them.

Table II.1.19.1 Revised BP3 Milestones Factoring in COVID19 Delays

Description	Type	Planned Task Detail
Complete OEM Vehicle / SPIN DC V2G Communications Implementation and Verification	March 2020	Development, implementation and testing of SPIN DC Communications Control Module (CCM): DC V2G based on SAE standards (J2847/3, DIN Spec harmonized, IEEE2030.5) Interoperability DSO Server/SPIN/Vehicle (FCA Pacifica Van PHEV) communications
Complete V2G Lab Demonstration	April 2021	Perform Vehicle/SPIN integrated DC V2G demonstration.
Complete Demonstration Report	Aug 2021	Report will be generated covering the demonstration and data from characterization and use case functional testing.
Complete Battery Pack Durability Test Report	April 2021	Assessment and evaluation of impact from 6 month V2G cycle operations. Pack impedance/capacity will be evaluated before and after the testing.

This timeline was further revised to push the Complete V2G Lab Demonstration to 2021 after COVID19 shutdowns. The team has managed to maintain this revised timeline.

Hardware Development / Readiness / Acceptance Testing

The project team continued to work at their respective locations, and the design-intent hardware build commenced in 1Q of 2020 for the SPIN system and completed in the third quarter of 2020. The fully-built prototype inside view and the outside view is shown along-side the original CAD layout. The SPIN system

includes the core SPIN hardware – the PV inverter, the Grid interface, the switching matrix that routes the power from the PV to either the local stationary storage or to the EV charging, or from the storage and/or EV to the grid or local premise, under the control of the built-in Energy Management System.

SPIN System Hardware Layout in Productized Concept

Flex Power Controls-led team won yet another DoE SETO award (DE-EE-0008352) to productize the SPIN technology, under FOA 1740. This project is underway currently and will embody all of the learnings from the various contributing projects to-date, to create an integrated DC-coupled multi-port DER ecosystem that is grid-interactive and resiliency-enabling, replete with the necessary customer interface, open standards-based communications and an ability to operate standalone or in a legacy environment with existing smart inverters with PV and storage while allowing EVs to provide V2G services. Figure II.1.19.2 below shows a conceptual layout of this integrated SPIN system.

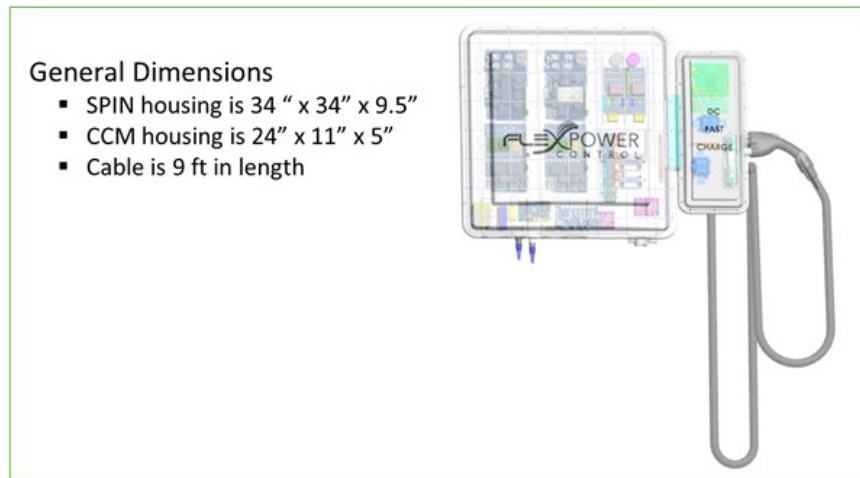


Figure II.1.19.2 SPIN Product Concept 3D-Layout including DC CCM and Charging Cable

SPIN Prototype Build

During BP3, and for BP1 of SETO project, the Flex Power and Rhombus teams worked to design and assemble as well as validate the control functionality of the first-ever prototype of the SPIN unit. The component subassemblies of this system are shown in the Figure II.1.19.3 below.

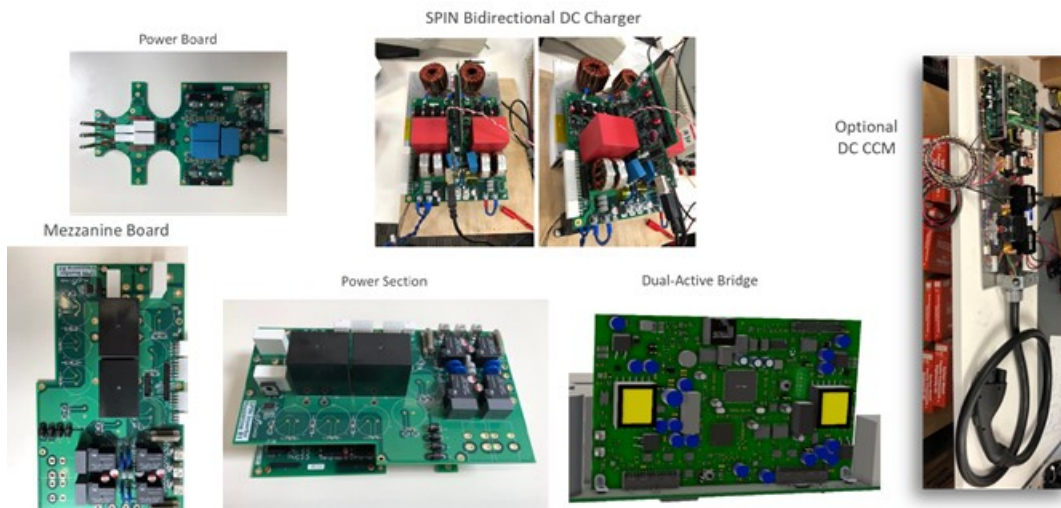


Figure II.1.19.3 SPIN System Component Subassemblies

Under the funding from SETO EE0008352 project, SPIN project team comprising of Flex Power Controls and Rhombus Technology Solutions assembled these to create the first-ever SPIN prototype, as seen in Figure II.1.19.4 (open lid) and Figure II.1.19.5 (closed lid) below.

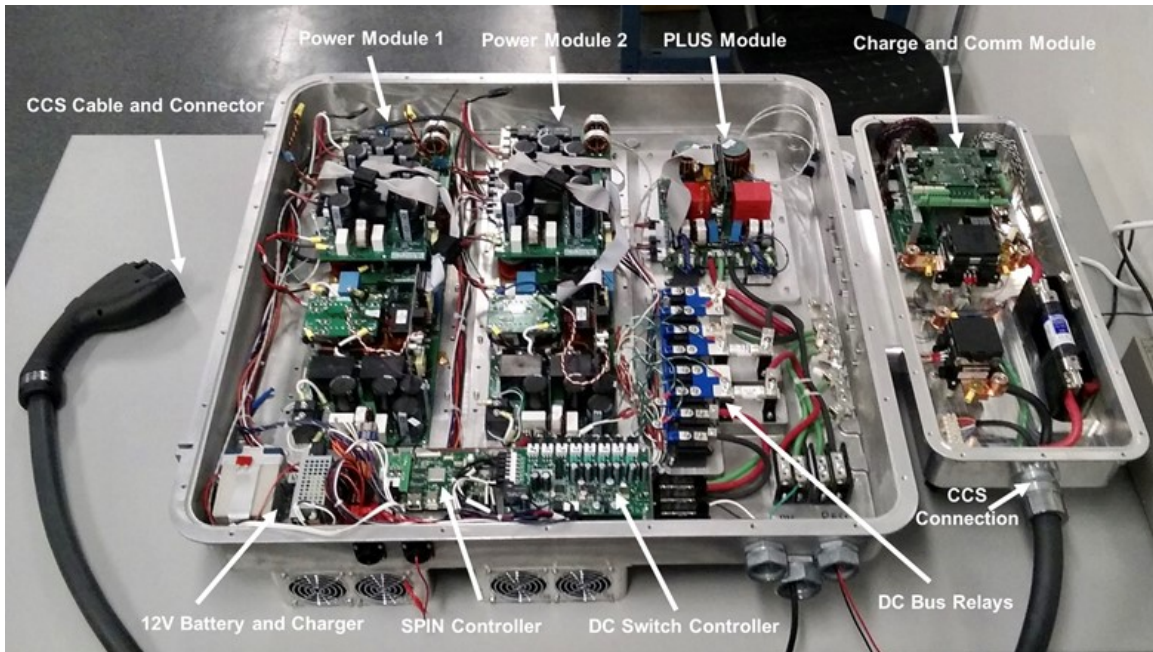


Figure II.1.19.4 First-Ever SPIN Design Intent System, Open Lid, with CCS Cable and DC Charge Interface



Figure II.1.19.5 SPIN System with DC Fast Charge Module and CCS Interface, with Closed Lid

SPIN System Software: Use Cases, Architecture, Design:

Through a companion CEC project, the team is implementing applying SPIN module to three distinct scenarios:

1. Standalone, managing residential DERs including V2G capable EV
2. In a grid-interactive building environment, interfacing with the Building Management System (in this case, the BMS resides inside the SPIN itself),

3. In a microgrid interfacing with the DERMS and integrating V2G capable EV.

SPIN also has external interfaces to interact with the grid directly in response to grid signals, as communicated by the DSO (Distribution System Operator) over IEEE2030.5 and to its own proprietary backhaul in the cloud to perform analytics and forecasting functions to enable predictive control algorithms. Figure II.1.19.6 shows these scenarios in more detail.

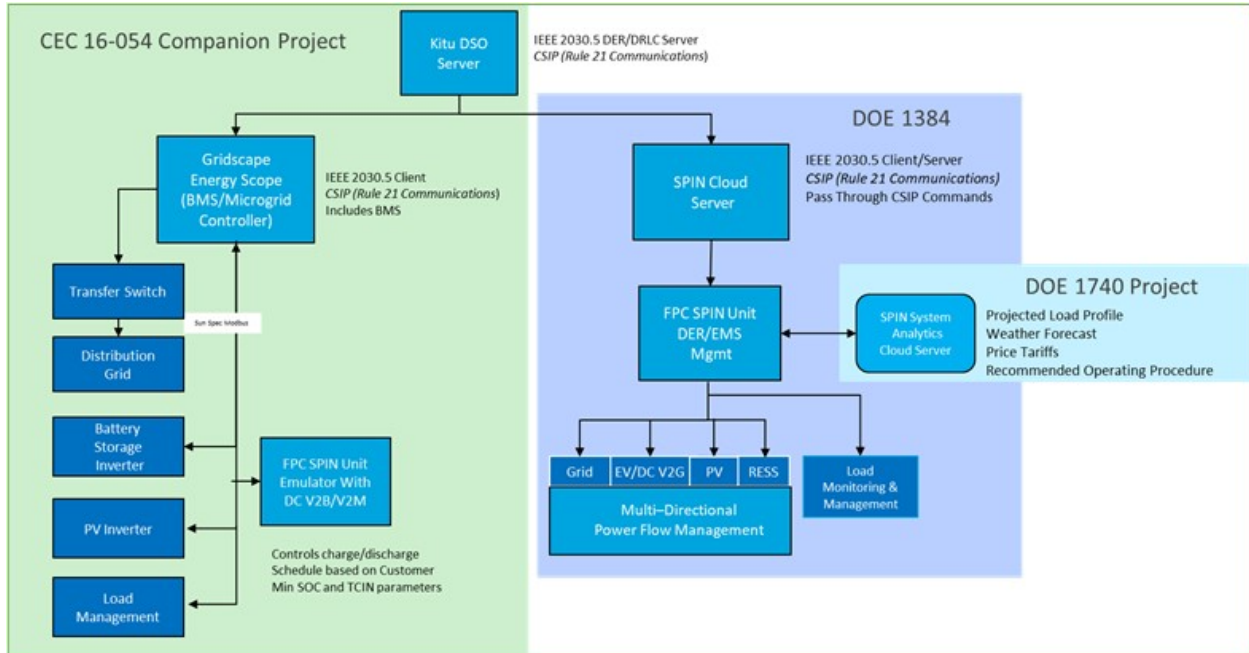


Figure II.1.19.6 SPIN Application Scenarios being Designed for Verification

SPIN Controls / Communications Architecture

Flex Power Controls, EPRI, Stellantis and IoTecha as well as GridScope (microgrid operator with DERMS) collaborated to create an all-encompassing software architecture that serves the entire ecosystem in which SPIN resides. This is depicted in Figure II.1.19.7 below.

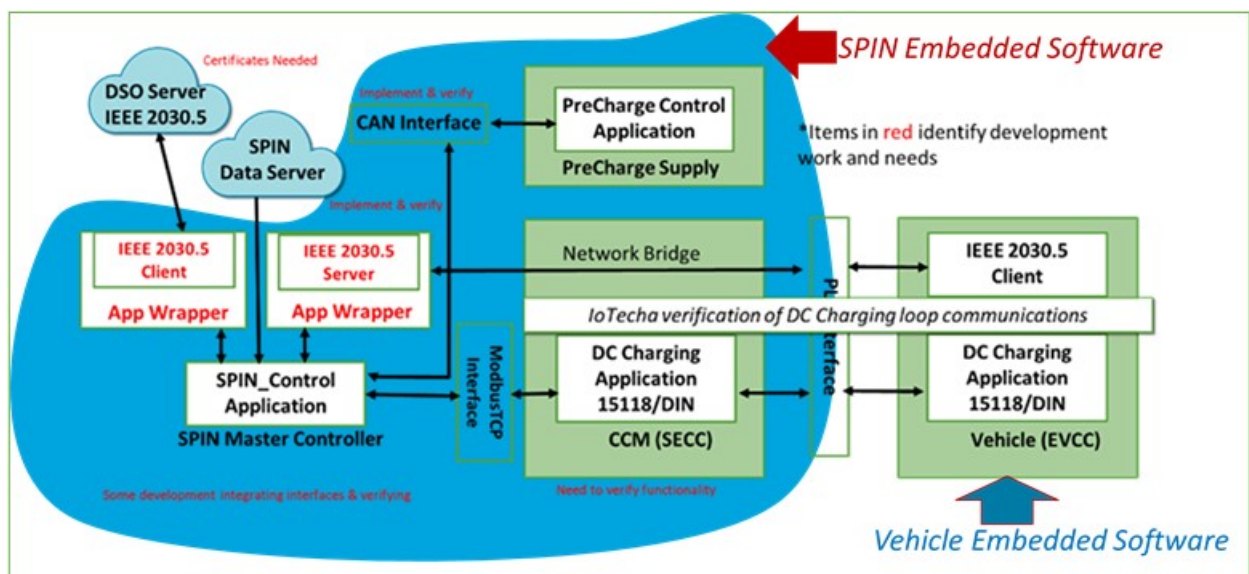


Figure II.1.19.7 SPIN Integrated Ecosystem Software Architecture: In-Cloud, On-Vehicle and On-SPIN

- A description of the key software components is as follows:

In-Cloud

- DSO Server – this server is DSO-resident wide-area DERMS that dispatches DERs across the DSO or in specific segments. The communications to these DERs are over IEEE2030.5-2018 version. A server resides in the cloud

On SPIN

- IEEE 2030.5 client resides on the SPIN. An App wrapper translates the IEEE2030.5 signals to local parameters (and vice versa). This IEEE2030.5 client has a mirror image IEEE2030.5 server that communicates to the IEEE2030.5 client residing in the EV over PLC link facilitated by the IoTecha control card.
- SPIN Master Controller: This is the central, orchestration piece that coordinates operation of each of the DERs (PV, EV, Storage) according to the real-time and forecasted conditions while complying with the grid and local energy needs using the information from the vehicle, the DERs and the grid.
- SECC – this is the Supply Equipment Communications Controller that enables J2847/2 DIN 70121 communications to enable DC charging and acts as a pass-through for the IEEE2030.5 messages. Figure II.1.19.8 shows the sequence diagram that explains the coordinated communications between SECC and EVCC and orchestration of DER messages via IEEE2030.5 and DC charging comms via the DIN spec. The reverse power flow is facilitated simply by reversing the current sign (positive to negative).

On-Vehicle

- IEEE2030.5 Client communicates with the IEEE2030.5 server residing on SPIN. Here, On-vehicle V2G project based IEEE2030.5-2013 version client/server pair is leveraged as-is. IEEE2030.5 provides the smart inverter related messages.
- DIN70121 client – this enables the vehicle to request negative or positive current from the SPIN, allowing the batteries to either send or receive power from the grid. DIN 70121 client resides on the EV Communications Controller (EVCC) that facilitates the IEEE2030.5 and DIN message communications over PLC link and these messages are locally translated to CAN messages that the vehicle can process.

Most of the year 2020 was spent implementing these control algorithms at the microgrid controller level (GridScape), SPIN Master Controller (Flex Power), On-vehicle bidirectional power management control (Stellantis, with assistance from IoTecha), and DSO to SPIN Communications (Kitu Systems). EPRI served as the software integration lead to ensure each connecting party had the right requirements and created tools to test communications in a pairwise manner (one pair at a time), followed by the entire integrated system via software emulators. Even when the COVID19 related stay-at-home orders were in effect, EPRI continued to lead the software integration, especially between SPIN and EV including SPIN master controller, actively debugging and troubleshooting issues, engaging engineers from Stellantis, IoTecha and Rhombus.

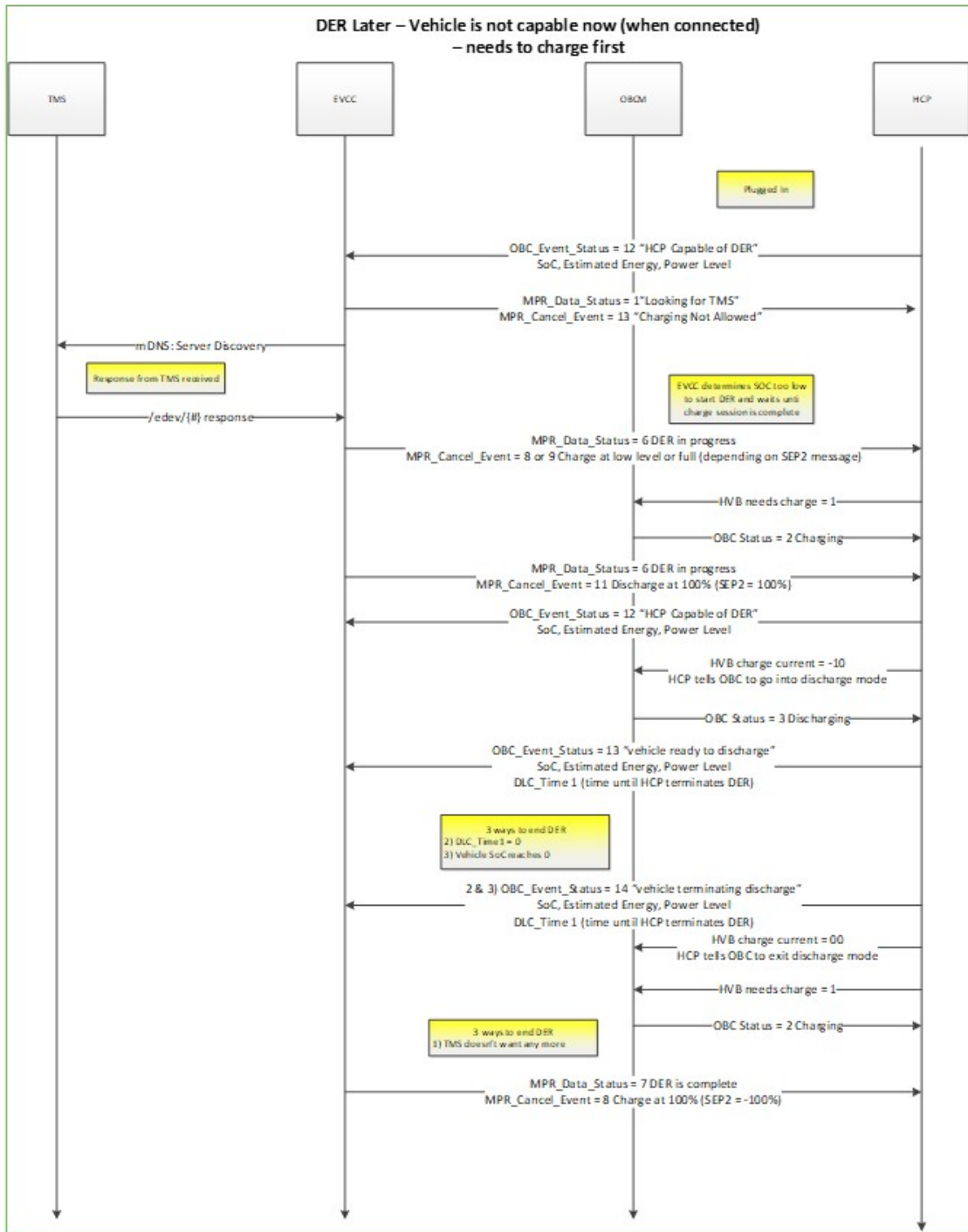


Figure II.1.19.8 Combined IEEE2030.5 and DIN 70121 Communications Sequence Diagram

Also, the team discovered that extended shutdowns and stay-at-home orders in Tennessee would disallow any visitors, including EPRI and Flex Power Controls staff to visit ORNL. This meant that the venue for final system integration with SPIN and EV was required to be moved away from ORNL. This required funding shift from ORNL to Rhombus in San Diego, CA. Through ORNL management cooperation and DoE VTO guidance, this funding transfer was completed in 3Q2020, so that the stage was set for the entire system to be integrated and tested in San Diego at Rhombus facility.

Battery Impact Assessment

Planning: FCA has shipped two Chrysler Pacifica PHEV battery packs to NREL ESIF for performance and impact evaluation. NREL is tasked with testing the two battery packs – one on the regular PHEV mobility-only duty cycle and another on a mobility and grid services combined duty cycle, to assess the impact of grid services on the battery life and performance. FCA and NREL agreed to a test protocol that is considered reasonable and more realistic. below shows the energy consumption estimates related to this protocol.

Table II.1.19.2 Pacifica PHEV Battery Impact Energy Consumption for Test Protocol (Source: FCA, NREL)

Cycle Discharge ~ 15 mi.					
	Cycle	Time (hr)	Distance (mi)	Energy Throughput (kWh)	Net Energy (kWh)
CD	CD1 City	0.3811	7.44	3.96	2.24
	CD US06	0.1667	8.01	5.27	2.81
CD total		0.5478	15.45	9.22	5.05
Total pack kW					11.8
Usable energy after both drive cycles (kW)					6.75
Proposed discharge power (kW) - available for DER					2
DER Duration (Hrs)					3.375

Table II.1.19.3 below shows how each of the two packs will be tested. The plan is to exercise the batteries with two cycles run per day, so as to assess one year-worth of battery impacts in six-month testing window. In addition, there will be one full deep-discharge cycle at C/3 rate + HPPC (High Power Pulse Characterization) Cycle.

Table II.1.19.3 Battery Test Cycle for Grid Services Impact Evaluation

	Cycle Time (Hours)	
	Pack 1 (Reference)	Pack 2 (Test Pack)
At work		
Drive home	0.5	0.5
discharge at home (10kW)	1	0
charge to 100%	2	1
Wait (key cycle – Contactor open)	1	3
drive to work	0.5	0.5
Charge (50% to 100%)	1	1
Total time/cycle	6	6

The battery cycling took about a year to begin. So, instead of beginning in mid-2019, it began in mid-2020. The primary cause for this delay was the setting up of NREL ESIF battery testing, especially the battery test system software interface with the Battery Management System. It took NREL and Stellantis teams two quarters to debug, and another quarter for the system to be fully operational. The following Figure II.1.19.9 shows the battery test setup at NREL ESIF with a test pack and a baseline pack being subjected to the same operating conditions except for the duty cycle as described earlier.

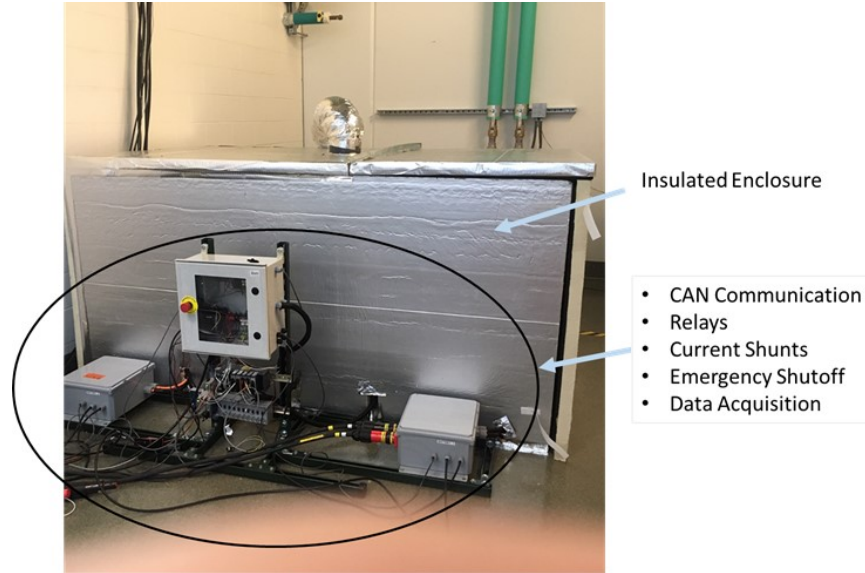


Figure II.1.19.9 NREL ESIF Battery Packs in the Insulated Enclosure for Performance Testing

By August of 2020, the testing at ESIF for the battery packs had begun, with three cycles per day, meaning one month of testing generated three month-worth of test data. This was further automated in September after initial debugging of the parameters being recorded. The testing of the battery performance impact from grid services has continued uninterrupted even when the visitor and on-site work restrictions have lifted gradually. This allowed the team to continue testing and collecting data on batter performance throughout COVID shutdowns and stay-at-home orders in Colorado. One representative sample of early test data from October 2020 is shown in the charts below, in Figure II.1.19.10, Figure II.1.19.11 and Figure II.1.19.12. The testing will continue through the first half of 2021 as the team has been able to receive a No-Cost Time Extension until June 2021 to finish the work scope for BP3.

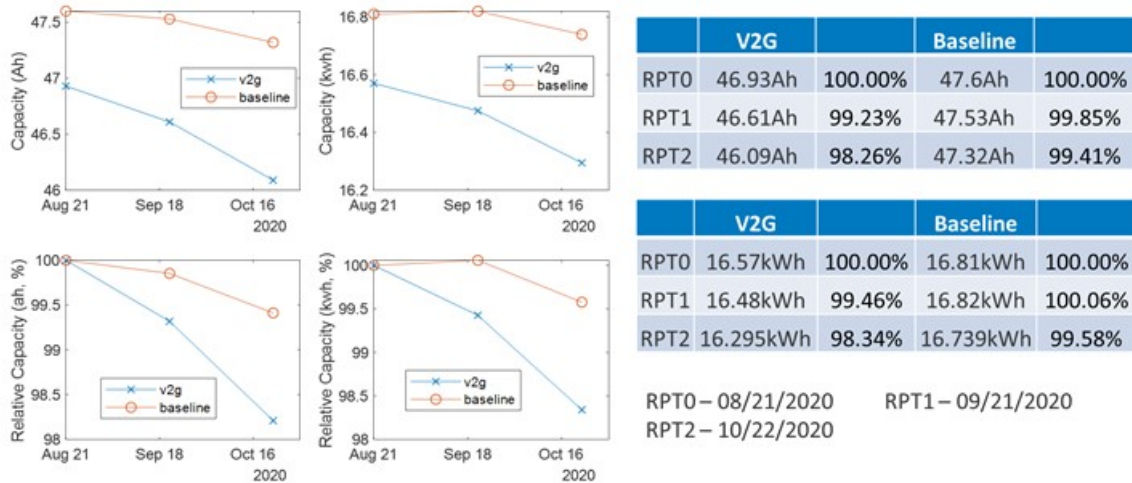


Figure II.1.19.10 Reference Performance Test Data for 9-month Effective Period

The Reference Performance Test (RPT) date clearly shows that the V2G pack is degrading at a faster pace than the baseline (non-V2G, mobility-only) pack. This is to be expected. The question is how much degradation is acceptable while still maintaining all the throughput for mobility and not compromising electric mobility.

Figure II.1.19.11 shows the same RPT in a time-series fashion, showing Current and Power draw from the baseline and V2G packs.

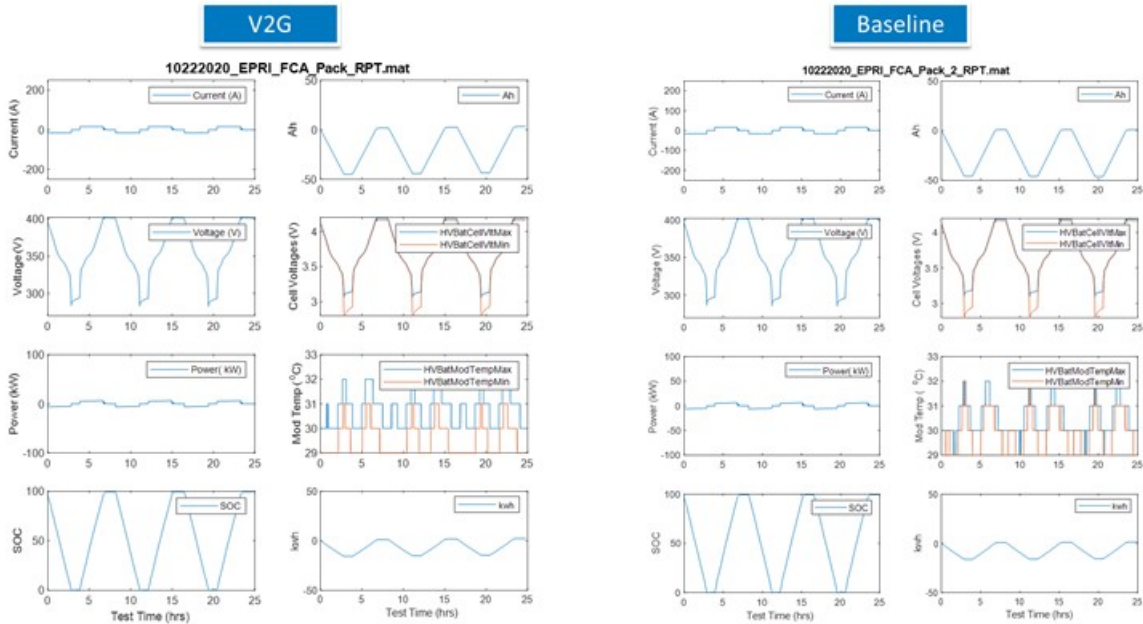


Figure II.1.19.11 RPT for V2G and Baseline Packs showing SOC, Power, Current and Voltages vs. time

The following graphs show the artifact of the performance degradation in terms of internal resistance (Figure II.1.19.12), that increases, thereby reducing the peak (10 second) power capability of the batteries without violating the minimum Voltage requirement.

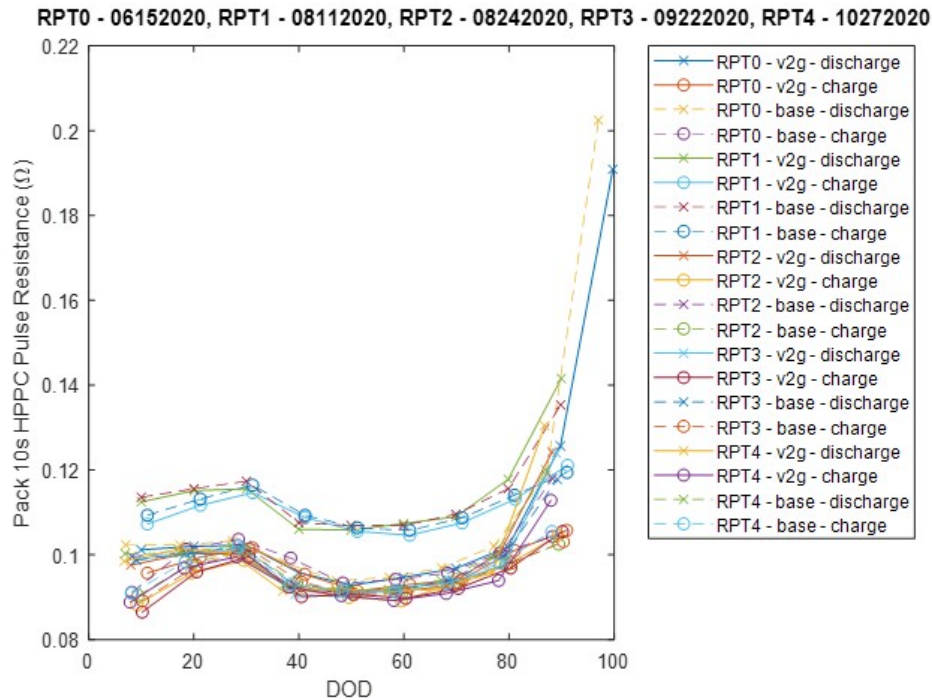


Figure II.1.19.12 High Power Performance Characterization (HPPC) Test Profiles, Baseline vs. V2G Packs

Conclusions

2020, in spite of the COVID19 shutdown, was the ‘show-me’ year for this project. The hardware design for design-intent prototype was completed, the system was assembled, and the software was integrated after going through rigorous component, subsystem and system integration test through the extensive use of emulators.

The hardware prototype for SPIN was built and integrated with the functional software. All of its basic functionality has been verified equivalent to the proof-of-concept rack system that was tested at ORNL.

At Stellantis engineering center at Auburn Hills, MI, the team developed the V2G software functionality without having a bidirectional charger at location, by implementing the DIN 70121 DC charging communications software on a CCS-capable Fiat 500 City EV and testing this in conjunction with a production DC EVSE that could only provide power from the charger to the EV. The expectation is that a V2G capable charger will be able to absorb reverse power flow from the EV.

The key learnings were in the area of software integration between DSO and SPIN master controller, as well as SPIN Master Controller and SECC (the board that communicates bidirectional DIN 70121 DC charging process signaling). Further, switching from Pacifica to Stellantis City EV required the EVCC control system integration and DC EVSE integration at Stellantis Technical Center in Auburn Hills.

Lastly, significant unforeseen effort was expended in deciphering the signaling between Battery Controller Module and the NREL ESIF Labview based Instrumentation System so that automated battery cycling can be synthesized. The good news is that in each of the case, the team emerged successful through persistence and ingenuity.

Key Publications

On-Board V2G part of the project resulted in the following publications:

1. https://www.academia.edu/38676029/Distribution_System_Constrained_Vehicle-to-Grid_Services_for_Improved_Grid_Stability_and_Reliability
2. Open Standards-Based Vehicle-to-Grid: Technology Development, EPRI, 3002014770, 2018, <https://membercenter.epri.com/abstracts/Pages/ProductAbstract.aspx?ProductId=00000003002014770>
3. Open Standards-Based Vehicle-to-Grid: Integrated Resource Planning Considerations, EPRI, 3002014801, <https://membercenter.epri.com/abstracts/Pages/ProductAbstract.aspx?ProductId=00000003002014801>
4. Open Standards-Based Vehicle-to-Grid: Value Assessment, EPRI, 3002014771, 2019, <https://membercenter.epri.com/abstracts/Pages/ProductAbstract.aspx?ProductId=00000003002014771>

Acknowledgements

The project team would like to recognize continued encouragement, support and understanding of DoE VTO program managers, John Conley and Lee Slezak, without whose patient guidance, this project would have failed after Budget Period 1!

The Principal Investigator would also like to express his profound gratitude to the entire team including EPRI staff, Flex Power Controls, Rhombus Technology Solutions, Stellantis Group, NREL and ORNL scientists and engineers, who formed the backbone of this project. The project success belongs to the team.

II.1.20 Cybersecurity Platform and Certification Framework Development for eXtreme Fast Charging (XFC): (EPRI)

Sunil Chhaya, PhD, Principal Investigator

Electric Power Research Institute (EPRI)
3420 Hillview Avenue
Palo Alto, CA 94304
Email: schhaya@epri.com

Rish Ghatikar, Co-Principal Investigator

Electric Power Research Institute (EPRI)
3420 Hillview Avenue
Palo Alto, CA 94304
Email: GGhatikar@epri.com

Lee Slezak, DOE Technology Manager

U.S. Department of Energy
Email: Lee.Slezak@ee.doe.gov

Start Date: October 1, 2018 End Date: March 31, 2021
Total Project Funding: \$2,786,278 DOE share: \$1,547,678 Non-DOE share: \$1,238,600

Project Introduction

In support of this paradigm shift to electric transportation, the EV charging infrastructure including the charging stations (also known as Electric Vehicle Supply Equipment, or EVSE), DC Fast Charging (DCFC) equipment and eXtreme Fast Charging (XFC, with charge rates above 200kW) is being deployed at a fast pace. Studies estimate that 12-million residential charging points and 1.2-million public charging points will be installed in North America by 2030 [1]. In 2020, the United States (U.S.) has 25,000 alternating current (AC) Level 2 (AC-L2) EVSEs and over 4,000 direct current (DC) fast chargers (DCFC) installed [1]. AC Level 2 EVSEs are limited to 19.2 kilowatt (kW) peak power levels, and typical DCFCs can charge at up to 350 kW [2] peak power levels. To meet EV drivers' increasing desire for faster charging times than AC-L2 or typical DCFC XFCs with power levels of > 200 kW are being deployed at strategic locations such as along highways. For example, the Electrify America initiative in the U.S. has deployed high-powered charging stations at levels up to 350 kW. These high peak power levels mean that a malicious actor can cause a fleet of XFCs to pose larger impact on the grid, especially when multiple EVs are made to charge simultaneously [3]. Furthermore, given that the EVs, the charging networks, the payment networks, utility back office and the smart metering systems, as well as the charging network aggregators are all connected, cyber-intrusion at any point in the ecosystem could create risks in the other parts of the system, if the system is not properly designed.

To address this challenge, the Electric Power Research Institute (EPRI), electric utility partners, EV original equipment manufacturers (OEMs), charging station manufacturers, charging network operators, and research partners, which included U.S. DOE national laboratories, National Renewable Energy Laboratory (NREL) and Argonne National Laboratory (ANL), conducted research, development, and demonstration (RD&D) project titled, "Cybersecurity Platform and Certification Framework Development for XFC-Integrated Charging Infrastructure Ecosystem (*Secure Grid-XEV*)." Deriving from an earlier EPRI study [4], the *XFC ecosystem* can be defined as the network of all involved players (organizations), systems, and sub-systems that are responsible for monitoring the grid-impacting data with an ability to send or receive control signals to alter the power usage of an XFC, using a diversity of communication technologies, and standards and protocols. With an emphasis on addressing the grid impacts resulting from potential cybersecurity compromises, the goal of the *Secure Grid-XEV* project is to develop and test technologies and approaches that identify, minimize, or

eliminate critical cybersecurity vulnerabilities that result from the transition of EV charging to power levels above 200 kW, i.e., the *XFC ecosystem*.

At the forefront of cybersecurity research, EPRI has held a prominent role in Smart Grid Cybersecurity [5] by addressing the emerging threats to an interconnected electric sector through multidisciplinary, collaborative research on cyber security technologies, standards and business processes with a broad focus on enabling technologies, standards, demonstrations and technology transfer. EPRI has one of the longest-running Electric Transportation [6] research programs, spanning over 3 decades and representing a global footprint of stakeholders engaged in collaborative RD&D focusing on EV and infrastructure technologies, vehicle-grid integration into distributed energy resources (DER) ecosystems, techno-economic and environmental analysis, and technology transfer for utilities and practitioners. Likewise, EPRI leads the electric industry in Information and Communications Technologies (ICT) [7] for electric sector by defining, formulating and implementing communication technologies and open, interoperable standards and protocols. Figure II.1.20.1 shows the project's focus on XFC infrastructure with the goal of strengthening the cybersecurity of EVs, EV charging infrastructure and the electric grid that intersects the three EPRI research portfolios of cybersecurity, electric transportation and ICT. All the three research portfolios were leveraged to enable secure interoperability among the electric grid, markets, and operations, and its integration across the EVs, and charging infrastructure

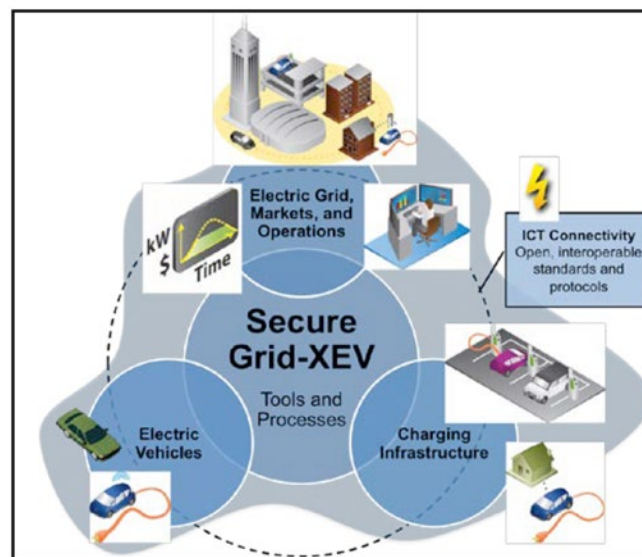


Figure II.1.20.1 Research scope of Cybersecurity Platform and Certification Framework Development for XFC-Integrated Charging Infrastructure Ecosystem (Secure Grid-XEV)

The EV ecosystem is extremely diverse, technologically advanced, and connected. This includes players such as EVSE and EV OEMs, grid operators, third-party network operators and service providers with each offering unique and diverse connected subsystem. Each subsystem and its component in the EV ecosystem are designed to operate standalone with direct interfaces to a connected subsystem. *The study defines a subsystem, as any standalone system that an XFC interfaces with. A component is a functional part of a subsystem such as a payment module.*

Goals and Objectives

The project goals are to: (1) Equip the EV and electric grid stakeholders with reference tools and processes that can be leveraged to support baseline security functional requirements; and (2) to accelerate the secure deployment and grid integration of EV charging infrastructure.

The core project objectives are to:

- Evaluate and assess cybersecurity risks to develop a reference network architecture of connected systems, sub-systems, and communications for an XFC ecosystem.
- Conduct cybersecurity threat and vulnerability assessment to identify and classify assets for XFC sub-systems.
- Recommend cybersecurity controls, system architecture, and a reference design for a *Secure Network Interface Card (S-NIC)* for XFCs.
- Assess and develop sub-system and component-level XFC ecosystem testing for verification of the requirements.
- Develop Integrated Grid Security Risk Management (IGSRM) tool for wider dissemination of research recommendations to the industry.
- Proactively engage diverse industry stakeholders for perform research analysis and conduct technology transfer through EV Infrastructure Cybersecurity Working Group (EVICWG).

Approach

Addressing cybersecurity for the XFC ecosystem requires a review of multifaceted technical and non-technical barriers, systems-centric requirements that involve all the EV ecosystem players, and engagement of the stakeholders to ensure that project findings are robust. Considering this approach, the project will be executed in two phases:

- **Phase 1 (October 2018–December 2019): Develop Reference Architecture.** The study to assess cybersecurity risks, threats and vulnerabilities to analyze the functional cybersecurity requirements and a reference architecture for each of the subsystems and components within the XFC ecosystem.
- **Phase 2 (January 2020–March 2021): Combined Test Results and Assessment.** Develop test plans, conduct laboratory tests to review the collated results to create a final set of cybersecurity requirements, and vulnerabilities and mitigation strategies.

The focus of this report is on the Phase 2 activities for the year 2020.

Phase 1 Summary

To summarize the Phase 1, the activities focused on the four core areas: 1) assess cybersecurity requirements; 2) conduct risk, threat, and vulnerability assessment; 3) mainstream the research; and 4) recommend cybersecurity controls, XFC ecosystem reference architecture, and S-NIC reference design. The Phase 2 final cybersecurity reference architecture and reference standards, test protocols and guiding principles for certification process will be developed based on the Phase 1 results so that stakeholders can effectively implement the architecture-specific modular security controls and standards for the XFC ecosystem.

As illustrated in figure below, the Phase 1 research and approach included three core and interrelated activities for XFC components, systems, and sub-systems, and communication technologies: (1) develop framework for analyzing risks across the EV ecosystem; (2) assess threats and vulnerabilities based on functional requirements; and (3) recommendations with security controls and standards, and next steps. The project approach focused on identification of cybersecurity solutions.

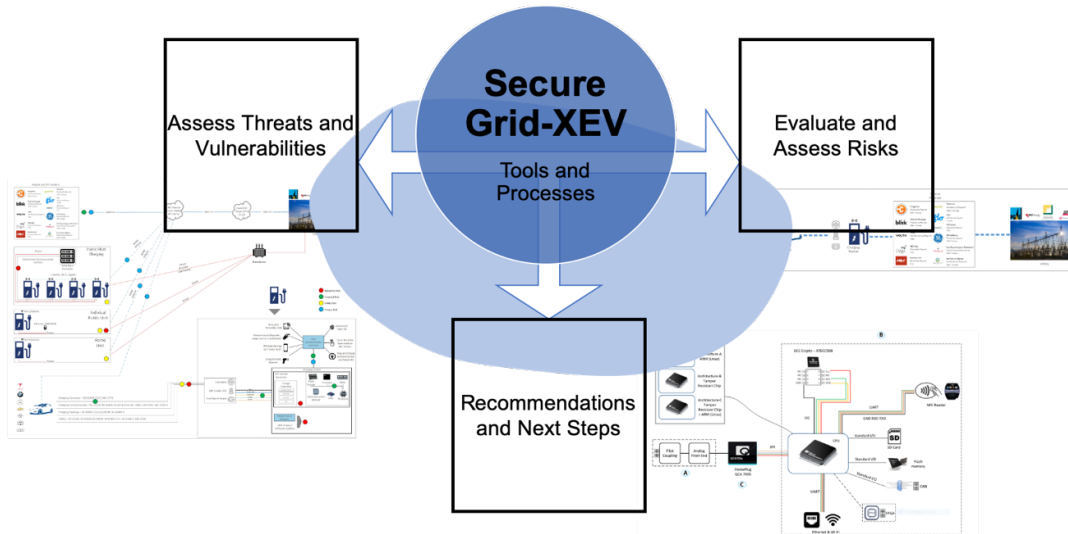


Figure II.1.20.2 Project Approach and Activities for Phase 1 Research

Each of these interrelated activities are reported in the 2019 report and include a classification and evaluation of cybersecurity risks for XFC infrastructure and its interrelated systems and sub-systems such as EVs, third-party operators, utilities, buildings, etc. This risk framework and XFC deployment architecture and communication technologies considerations were used for a comprehensive cybersecurity threat and vulnerability assessment. The risk mitigation techniques addressed the financial data, privacy of customer information and grid reliability controls. EV ecosystem-related communications standards based on open standards such as Level 2 AC, DCFC, XFC, and other EV charging standards will be assessed. As a result, recommended security controls and a reference design for secure network interface card (S-NIC) were proposed – all of which will become the basis for the Phase 2 research.

Phase 2 Summary

Phase 2 efforts focused on using Phase 1 findings and recommendations to:

Conduct Combined Test and Verify Results: The study conducted experiments and assessed results to create cybersecurity requirements, test protocols, results, vulnerabilities and mitigation schemes or strategies in close association with the cybersecurity reference architecture. An Integrated Grid Security Risk Management (IGSRM) tool was designed in support of the reference architecture.

Test and Verify Reference Architecture: The cybersecurity reference architecture, related technologies using various threat and vulnerability assessment techniques were tested and verified. These tests included network security for data-in-motion or transit, system and application-layer cybersecurity for interfaces and data-at-rest, physical security for components, and end-to-end security integration.

Develop an Integrated Grid Security Risk Management (IGSRM) Tool: The IGSRM design was used to develop a web evaluation tool prototype to help vendors, service providers and utilities to navigate through the various cybersecurity standards. All applicable network, system, application and physical security controls, communication standards were included in the tool. The tool development shall be completed in 2021.

Mainstream and Standardize Interoperable Cyber Secure Ecosystem: Continuing from the Phase 1 efforts, the project engaged the EV Infrastructure Cybersecurity Working Group (EVICWG) to review project outcomes and obtain feedback to engage the industry in the market transformation of cybersecure XFC infrastructure. The final recommendations shall be transferred to a standard enforcement or interoperability certification process to ensure that the reference architecture is effectively applied to all XFC stakeholders and is industry-approved for implementation through deployments and regulatory framework.

To ensure adequate stakeholder coordination, and technology and knowledge transfer, the project leveraged the capabilities of partner U.S. DOE national laboratories: Argonne National Laboratory (ANL) and National Renewable Energy Laboratory (NREL) that comprise DOE’s SMART Mobility Consortium [8]. This project also set up an “EV Infrastructure Cybersecurity Working Group (EVICWG)” to review project outcomes, obtain feedback, and to engage the industry in the market transformation of cybersecure XFC infrastructure.

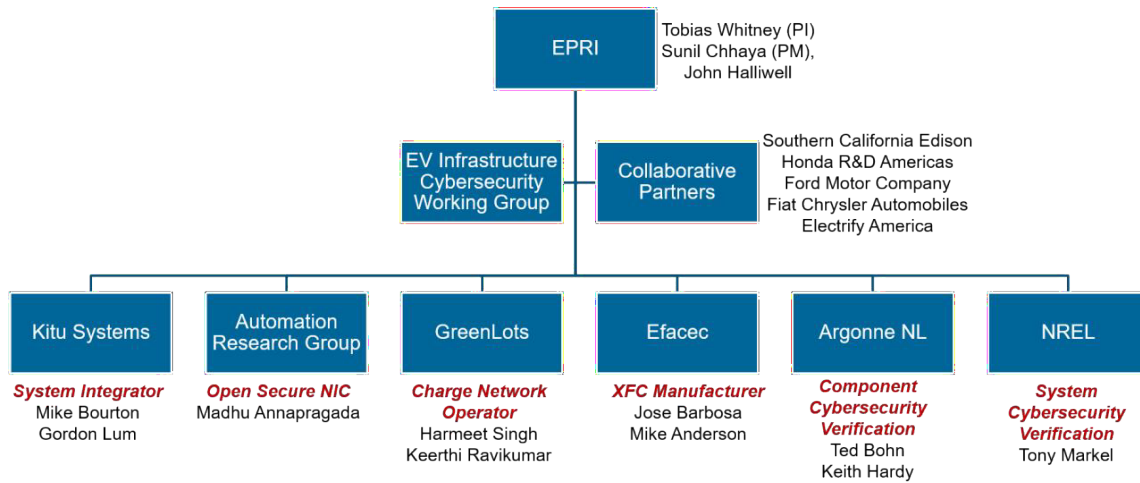


Figure II.1.20.3 Participants & Other Collaborating Organizations

Results

The following table summarizes the activities for 2020 for which the results are described.

Table II.1.20.1 2020 Activities

Milestone	Type	Description and Status	Delivery Date
End-to-End Security Test Plan	Technical	Cybersecurity testing plans.	Q1 2020 → Draft submitted to DOE.
Integrated Grid Security Risk Management (IGSRM) Tool Finalized	Technical	Tool prototype developed and updated based on testing results.	Q2-Q3 2020 → completed by Q2 2020.
Cybersecurity Testing and Results	Technical	Testing completed by EPRI and NREL with results documented. ANL testing and results are pending.	Q3 2020 Q1 2021 → Due to COVID-19 Challenges, recommend completion by Q3 2021.
Integrated Grid Security Risk Management Tool Published	Technical	Reference architecture is market-ready for implementation through industry deployments and regulatory framework.	Q3 2020 Q1 2021 → Due to rescheduling of testing and process, scheduled completion by Q3 2021.

The XFC infrastructure is large and has variety of actors in each subsystem. The labs have developed the test plans to best of their ability. The Cybersecurity Research Lab (CSRL) is primarily focused on the EVSE (Charge Station) and its interfaces. National Renewable Energy Lab (NREL) is focused on the communication link between EVSE and the backend/cloud. Lastly Argonne National Lab (ANL) is focused on communications between EVSE, Site Controller and Energy Storage. Overall test plans cover majority of areas

in the XFC infrastructure needed to be tested. EPRI will continue to coordinate and prioritize areas to be tested with respect to key recommendations. The working group meetings have facilitated the laboratories to present their test plans and get valuable feedback on their approach and identify any potential gaps or missing areas. The table below summarizes the testing conducted by each of the laboratories.

Table II.1.20.2 Summary of the Test Cases by Partner Laboratories and Relation to Phase 1 Activities.

Laboratories and Test Cases	Relation to Key Recommendations
<p>EPRI Cybersecurity Research Laboratory (CSRL)</p> <ol style="list-style-type: none"> 1. Spoof Payment / Authentication System – SNIC 2. Evaluation of attack surface of UI 3. Evaluating functional behavior of EVSE in absence of network or un-responsive Charging service provider 4. EVSE Communications channel vulnerability assessment 5. Maliciously exploit EVSE API 6. Theft of Credentials or Keys 	<ul style="list-style-type: none"> • PKI for end devices and their clouds. • Encryption of PII, data at rest and in motion • Secure NIC • 2-way communication between EVSE and cloud (Bi-directional) with defined alert stack.
<p>National Renewable Energy Laboratory (NREL)</p> <ol style="list-style-type: none"> 1. Man in the middle attack 2. Denial of Service attack 3. Communication chain EVSE to Cloud 	<ul style="list-style-type: none"> • PKI for end devices and their clouds. • Encryption of PII, data at rest and in motion • Secure NIC
<p>Argonne National Laboratory (ANL)</p> <ol style="list-style-type: none"> 1. Network Level Site Controller: Evaluate dependencies of EVSE-EVSE interactions in clusters and the site controller. 2. Evaluate security of EVSE communications within a facility. 3. Test integrated energy storage, DC as a service with an EVSE. 4. Evaluate Confidentiality, Integrity and Availability (CIA) for communication between cloud/back-end and the EVSE. 	<ul style="list-style-type: none"> • PKI for end devices and their clouds. • Encryption of PII, data at rest and in motion • Secure NIC • Load Smoothing by deploying power dense storage solutions.

Below is a consolidated list of test cases that each of the laboratory is testing. The key recommendations that are addressed have been elaborated for each test case.

Cyber Security Research Lab, Electric Power Research Institute – Knoxville TN (CSRL)

- A. Behavior and Response evaluation for Network issues, Unavailability of payment interfaces, Tampered Chips/Components/Cabinets.

This test case provides insight on how well the 2-way communication is implemented and handling of alerts (alert stack) during network unavailability and any physical attacks or tampering. The key recommendations evaluated are #1 and #3.

- B. Perform vulnerability assessment for EVSE physical interfaces.

This test is to understand the security and resiliency of interfaces on an EVSE. Physical interfaces like USB ports, Serial Ports and inputs are the gateways to access data on the EVSE. Encryption or anonymization of any data accessible via these interfaces is important. The key recommendation evaluated is #7.

- C. Evaluate attacks on user interfaces (Touchscreen, buttons and other means of input).

This test case is a subset of case B.

- D. Spoof/Phish different authentication and payment methods and analyze functionality of the EVSE.

This test case involves SNIC, which will help identify any tampering done to the packets on their way to payment gateway or the authentication server. PKI will play a major role in authentication process. This test will evaluate key recommendation #2.

- E. Evaluate access controls and their implementation for the applications used.

This test case aims to test how well the access controls are implemented. This applies to any interaction from users, maintenance personnel and any remote access. Key recommendations evaluated are #1 and #3. The EVSE should be able to communicate back with alerts and error messages to the operator or the site owner and to the user in certain cases.

- F. Identify data flows for an active charge session and security aspects of it.

This test case is to evaluate security between backend system and the EVSE during an active charge session. The key recommendation being evaluated is #2, since most of communication between EVSE and backend/cloud will utilize PKI to authenticate and secure the messages.

National renewable Energy Laboratory, Golden, CO. (NREL)

- A. Evaluate attack scenarios for PLC communications (Broadcast of MAC-ID, pings and handshake). What part of the process can be exploited?

This test case evaluates security of communications between electric vehicle and the EVSE. PKI (#2) is one of the key recommendations that is being evaluated between the two subsystems. SNIC will be used in this test case.

- B. Man-in-the-middle, replay and fuzzing attacks on communication between EVSE and the backend (Charging Service Provider).

This test case will evaluate key recommendations #2 and #7 - PKI and encryption of PII.

- C. Pen-testing in a realistic environment with EVSE and the cloud portion of service provider.

This test monitors the communication chain between EVSE and the cloud to identify which parts of messages are suspected to modification. Key recommendations evaluated are #1 and #3. The EVSE should be able to initiate communication in case of any issues and not wait for the cloud/master to poll.

Argonne National Laboratory, Lemont IL (ANL)

- A. Test behavior/response when modifying/adding a signal tap on the charging cord (Different cases for Can and PLC). Testing with an adapter would be ideal too.
- B. Evaluate dependencies of an EVSE with other EVSEs in a facility. This test case will evaluate key recommendation #1 and #3. In case of any cyber-attacks or functional issues, the EVSEs should be able to operate individually and isolate themselves from the infected EVSEs. 2-way communication and alert stack will ensure EVSEs in a region are aware of any compromises and

alert the responsible entity. This test expands by including a site controller and testing the dependencies again.

- C. Evaluate security of communications between EVSEs in a facility (If they communicate – Bluetooth, Wi-Fi or RF)
- D. Test integrated energy storage, DC as a service with an EVSE.

This test case provides insight on security implications by having DC storage as a service to EVSEs. The key recommendation being evaluated is #4.

- E. Evaluate Confidentiality, Integrity and Availability (CIA) for communication between cloud/back-end and the EVSE.
- F. Evaluate PKI implementation and behavior of end-nodes in various cases like expired/revoked/fake certificates.
- G. Test functionality and behavior of EVSE when the cloud/service provider is down or unavailable.

Part of the cybersecurity development included the development of Secure Network Interface Card (SNIC), which was designed and described in the Phase 1 report.

The SNIC was successfully moved from design phase to prototype development. The prototype is open source, and the schematics were made available to working group members and the laboratories participating in testing.

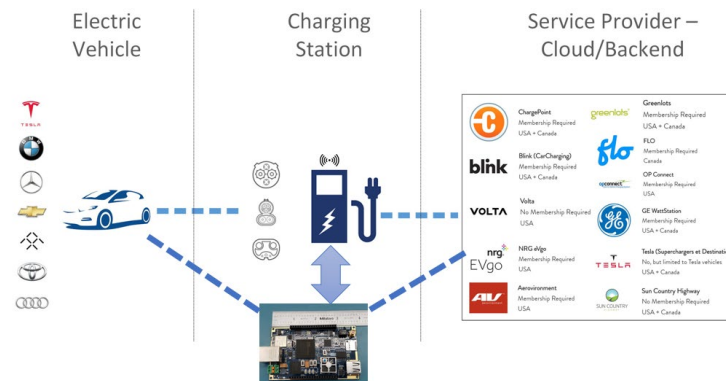


Figure II.1.20.4 Secure Network Interface Card Role in the XFC Infrastructure

The SNIC will play a key role in testing communication security. Below diagram shows the position of SNIC in the XFC infrastructure. The SNIC will act as a wrapper to all communications originating from any of the subsystems shown below. Apart from securing the communications, it will provide protection to hardware from tampering and also verify changes to firmware and boot operations.

The major components of the system to support the requirements would fall into the following major categories:

- **Central Processing Unit/System:** This is the core of the system and the “brains” that will ensure proper elucidation of protocols and keep track of security issues. It also supports all required authentication mechanisms.
- **Vehicle Communication:** Capability of being able to communicate to the vehicle to support secure protocols for charge (and optionally discharge) in various deployment scenarios.

- **Cloud Communication:** Most of the current authentication methods require custom / open-source protocols travelling all the way to the cloud servers using the internet. So, to be able to utilize the benefits of these methods of authentication, the system(s) needs to have a way of communicating with the servers in the internet.

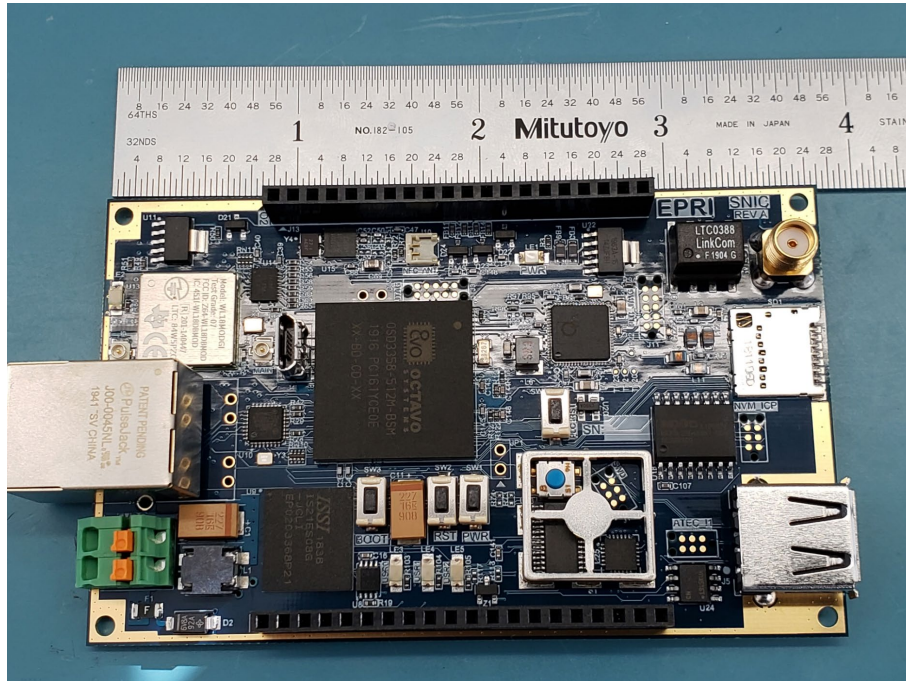


Figure II.1.20.5 Secure Network Interface Card prototype board

The prototype for SNIC has arrived and will play a major role in testing activities conducted by the laboratories. Below is an image showing the prototype board with all the components in place.

Integrated Grid Security Risk Management (IGSRM) Tool Finalized

To ensure modular development of the XFC ecosystem and assignment of cybersecurity risks and recommendations for the industry to use, the project team's activities resulted in the following:

- a. Conducted design and development of the Integrated Grid Security Risk Management (IGSRM) tool. The tool is a security architecture tool (web-based) to help vendors, service providers and utilities navigate the various security considerations for the XFC ecosystem. The IGSRM tool provides a baseline for subsystem and end-to-end security controls. The team developed IGSRM functional specification and requirements and reviewed them with the EVICWG.
- b. The team finalized the use of a well-known and industry-wide enterprise architecture modeling tool, Enterprise Architecture (EA). The EA tool provides scalable and modular features to develop the back-end library of XFC ecosystem and the related cybersecurity requirements or recommended controls.
- c. The project team working on a scope for the subcontractor to develop the web-based tool that will provide the EV industry with the XFC subsystem-specific controls. The EVICWG members assisted

in defining the requirements for the IGSRM tool. The web-based tool provides an easy to access tool across the industry stakeholders to motivate them to use the tool and cybersecurity practices.

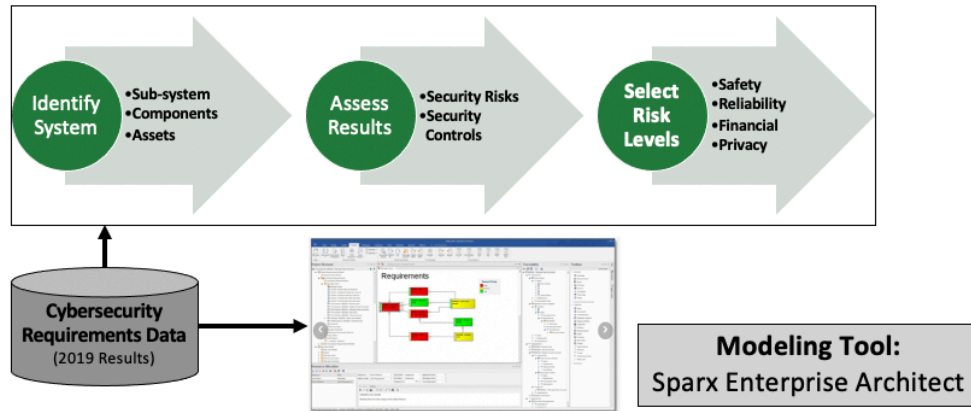


Figure II.1.20.6 Conceptual Representation of the IGSRM Tool

The guiding principles for the development of the tool included:

- Architectures should be recognizable representations of smart grid systems, sub-systems, and components (e.g., distribution, sub-station, grid-edge, DER).
- Tool* should be easy to navigate from high-level system architecture to define cybersecurity requirements for its sub-systems and components.
- Tool* should be easy to maintain and modular in design to include new architecture patterns and cybersecurity requirements.
- Tool* should be scalable and allow efficient design, reuse, and editing of architecture patterns and cybersecurity requirements for multiple architectures.
- Target audience:
- Utility and industry members deploying grid systems, sub-systems, and components.
- Cybersecurity practitioners familiar with the represented systems.

Cybersecurity Testing and Results

The test plans described earlier by each of the laboratories, EPRI CSRL, NREL, and ANL were used to conduct tests, the following is the summary of the results from EPRI CSRL and NREL. The test results from ANL are still awaited.

Cyber Security Research Lab, Electric Power Research Institute – Knoxville TN (CSRL)

The objective of testing was to assess the cybersecurity posture of an Electric Vehicle Supply Equipment (EVSE) system representative of the available systems on the market. A test plan was developed from the results of risk analysis performed at the inception of the working group. The focus of the test plan was to test and evaluate the EVSE subsystems susceptibility to exploitation and manipulation theft of information, theft of service, and disruption of service.

The testing approach was to perform a survey of the system for likely points of attack, and further, to probe those attack points to verify their susceptibility to exploitation as an attacker would. Therefore, attempts to

implement Man In The Middle attacks, spoof commands, or steal credentials were within scope of the objectives.

The CSRL is housed within EPRI's test facilities in Knoxville, TN. This facility includes 20,000 sq. ft of indoor and 400 sq ft of outdoor electric facilities. Smart inverters up to 100-kVA, three-phase can be tested with variable DC and AC interface. Lab equipment includes PV and grid simulators, R-L-C load banks, power quality meters, wave shape recorders, and controller hardware-in-loop (C-HIL) testbed. Programmable DC and AC power sources allow engineers to test DER under different environmental conditions (sunny, cloudy, highly variable, etc.) and grid disturbances (over/under voltage and frequency, faults including sags/swells, interruptions, etc.).



Figure II.1.20.7 CSRL Testing Hardware

For CSRL's testing, a 7.2 KW Level 2 charger was installed in the lab. The charger system was comprised of two primary components:

- EVSE Payment Module - payment processing, C&C, network routing
- EVSE Charging Module - power electronics for the charging system

An engineering workstation hosting a virtual instance of Kali Linux was used to facilitate the regular operation, profiling, and attempted exploitation of the charger.

National renewable Energy Laboratory, Golden, CO. (NREL)

Testing and analysis of components within the EV charging ecosystem was conducted in collaboration with a team of researchers led by the Electric Power Research Institute (EPRI). This report summarizes the test plans and outcomes focusing on the communication between the electric vehicle supply equipment (EVSE) and the control network operator or the charging service provider backend. The focus of these tests was to identify potential vulnerabilities associated with the use of Open Charge Point Protocol (OCPP), which is an open standard protocol supporting EVSE interoperability. The work was led by EPRI and sponsored by the US Department of Energy (DOE). The NREL research team conducted a portion of the overall testing with other portions being contributed by EPRI and ANL.

The EV ecosystem will include multiple components and entities that must communicate and coordinate securely. Within this testing project the primary components of interest were broken down into Vehicle, EVSE, and Systems Control/Backend. As shown in Figure II.1.20.8, both the components and the interfaces between these systems present potential targets.



Figure II.1.20.8 Simplified EV Systems Architecture

The tests performed included both physical and virtual components for replicating the environment with EVSE, communications, and the service provider/backend represented. This report summarizes the test setup, the procedures, and the outcomes. Information gleaned from testing is provided. Note that our specific implementation is not inclusive of the breadth of fielded systems and thus should be repeated in the case of implementation variations. Recommendations for additional testing and system enhancements are offered.

The testing objective was to better understand and evaluate scenarios in which the communications between the EVSE and the service provider could be manipulated and as such disrupt a charging process or cause damage to components or the system. A risk assessment completed by the project team during the early phases of this project identified this communications linkage as one of the many components within the EV charging architecture to evaluate.

The test strategy for this project focused on the communications between the charge network operator's server and the client (charger) to emulate vehicle charging infrastructure. Both local and remote server representations were used in addition to a virtual client and physical client to implement end-to-end OCPP communications. Outcomes of testing can characterize potential consequences of a malicious agent listening to the request/response sequences and injecting fake messages after capturing the details of the communication.

Conclusions

In the development of the IGSRM tool, the EA tool and database provided a scalable architecture to develop new sub-systems, components, and cybersecurity risks and recommendations. The tool shall be used to develop a web-based IGSRM tool that reflect the reference cybersecurity architecture of a connected XFC ecosystem, recommended controls and their associated risk profiles.

For the cybersecurity testing at the laboratories, The EPRI CSRL team focused on the EVSE charging infrastructure in fulfillment of its evaluation objectives. That focus primarily being the data flows into and out of the EVSE that could be exploited for theft of credentials, theft of service, or other malicious exploitation of the system via MITM, replay attacks or DOS. The utilization of standard cyber security controls to mitigate risk could provide great benefit in mitigating the risks associated with implementing this type of system. Encrypted channels for communication, message authentication methodologies, along with intrusion detection technologies would all aid in creating a secure, layered defense against a multitude of threats.

The NREL team completed laboratory testing of several cybersecurity aspects of the EV charging ecosystem using hardware, software emulation, and cloud interfaces. The tests performed focused on aspects of the OCPP communications between EVSE and a charge network operator server. The outcomes contribute to improving our understanding of the tools and test methods available for security testing of EVSE infrastructure in addition to identifying potential gaps and enhancements to the cybersecurity posture. The cyberattacks conducted through testing used MITM, replay, and denial of service methods toward the communications between the EVSE and the backend networks. The implementation options within the OCPP interoperability standards for EVSE allow for security configuration flexibility that can either provide more or less secure operating environments depending on network operator approach. Within a scenario with network access and un-encrypted communications, there is a clear ability to impact operations of the EV ecosystem. The use of

encryption and authentication methods in current and future OCPP implementations is highly recommended based on these tests. The observations and recommendations provided from testing offer ways of improving the security and reliability of XFC infrastructure. These steps may be beneficial near-term actions while more overarching security solutions like a secure network interface card handling all communications with encryption can be developed and deployed broadly.

References

1. U.S. Department of Energy, Office of Energy Efficiency and Renewable Energy, Alternate Fuels Data Center Website, Accessible at <https://afdc.energy.gov/stations/#/find/nearest?fuel=ELEC>
2. Green Car Reports, Electrify America turns on first 350-kW fast charger in California. Accessible at https://www.greencarreports.com/news/1120372_electrify-america-turn-on-first-350-kw-fast-charger-in-california
3. Department of Energy (DOE), Office of Energy Efficiency and Renewable Energy (EERE). Fiscal Year 2018 Advanced Vehicle Technologies Research Funding Opportunity Announcement (FOA). 2018. DE-FOA-0001919.
4. Grid Security of Connected Devices: Final Report. EPRI, Palo Alto, CA: 2019. 3002016154.
5. EPRI's Cybersecurity Portfolio: https://www.epri.com/#/portfolio/2019/research_areas/2/072143
6. EPRI's ET Portfolio: https://www.epri.com/#/portfolio/2019/research_areas/2/053122
7. EPRI's ICT Portfolio: https://www.epri.com/#/portfolio/2019/research_areas/2/062333
8. The Systems and Modeling for Accelerated Research in Transportation (SMART) Mobility Consortium "aims to deliver new EEMS data, analysis, and modeling tools, and create new knowledge to support smarter mobility systems." <https://www.energy.gov/eere/vehicles/energy-efficient-mobility-systems>

Acknowledgements

The project team would like to recognize continued encouragement, support and understanding of DOE VTO program managers, John Conley and Lee Slezak.

The Principal Investigators would also like to express his profound gratitude to the entire team including EPRI staff, NREL and ANL scientists and engineers, industry partners comprising of automotive OEMs, utilities, vendors and integrators (Greenlots, EVSE, LLC, Kitu Systems, etc.), and the EVICWG members who formed the backbone of this project. The project success belongs to the team.

II.2 Grid Interoperability and Control

II.2.1 Smart Vehicle-Grid Integration (Argonne National Laboratory)

Keith Hardy, Principal Investigator

Argonne National Laboratory
9700 South Cass Avenue
Lemont, IL 60439
Email: khardy@anl.gov

Lee Slezak, DOE Program Manager

U.S. Department of Energy
Email: Lee.Slezak@ee.doe.gov

Start Date: October 1, 2018
Project Funding: \$1,700,000

End Date: September 30, 2021
DOE share: \$1,700,000

Non-DOE share: \$0

Project Introduction

Problem Statement – The charging of grid connected vehicles must be managed and controlled or else the impacts of EVs at scale on the grid will be extremely disruptive, expensive, and will lead to the need for increased generating capacity. EVs at scale can contribute to grid resilience and reliability if charged intelligently. This will require controlled charge management that is coordinated with building and distribution network loads and requirements. Grid services previously identified in VTO-sponsored projects must be integrated into Smart Charge Management to maximize the potential benefit of EVs at scale to vehicle owners, building managers, charging network operators, grid services aggregators, and utilities.

Benefits of plug-in vehicles will be fully realized when the automotive, EVSE and utility industries cooperate, technically and programmatically, to ensure an integrated grid perspective and an implementation approach that supports sustainable business. This project takes a step in that direction by partnering with the Global Grid Integration Program, whose members are from US and European automotive, utilities, energy companies and research organizations. The intent is to collaborate on use cases/requirements for vehicle-grid integration and interim technology demonstrations, leading to a ‘public’ demonstration of smart energy management, where vehicles, buildings, renewable energy sources and energy storage are linked to meet the needs of customers as well as the electric power grid. This project will result in a managed network of devices at Argonne’s Smart Energy Plaza capable of demonstrating the use cases/grid services specified by the GMLC and our industry partners.

Objectives

Primary goals – Demonstrate how smart charge management can be integrated with a network of building systems, renewables and energy storage, using an open-source approach to:

- Respond to grid conditions/signals with minimal impact on local operations
- Identify potential benefits/impacts of EVs @ scale (controlled v. uncontrolled charging)
- Maximize the benefits of VGI on the customer-side of the meter
- Develop monetization scenarios of VGI for owners, utilities and aggregators

Achieving this goal necessitates several technical achievements: incorporating protocols for High-Level Communication (HLC) to enable ‘smart’ charging; control strategies that balance the needs on the customer-

side of the meter with grid conditions; and enabling technologies (i.e., digital communication, tools to verify interoperability and perform diagnostics). This project's yearly objectives:

Year 1 – Establish expectations and requirements for vehicle integration in the home and workplace (with automotive and utility industry partners); demonstrate GMLC use cases using Smart Charge Management. Demonstrate key enabling technologies (e.g., sub-meter system and beta version of DEVA). Define HIL methodology and design of experiments.

Year 2 – Demonstrate use cases to meet utility/grid demands (e.g., price signals; grid services or emergency power); integrate enabling technologies in the Smart Energy Plaza and develop field test plan with industry partners.

Year 3 – Demonstrate a fully integrated 'Grid of Things' system concept, illustrating the benefits of controlled versus uncontrolled charging using the energy plaza and a simulated grid. Initiate field testing, technology transfer and commercialization studies; plan public demonstration projects with industry partners.

Approach

Argonne utilizes its integrated network of devices at the Smart Energy Plaza to develop integrated control strategies for EV charging, building power demands, utilizing solar photovoltaic power and interacting with the Argonne grid. This includes demonstrating the flexibility/agility to manage loads and supply power from the customer side of the meter ... considering actual conditions on the grid side of the meter as well as characteristics of a simulated distribution network.

In addition, the plaza is used to demonstrate enabling technologies that support smart energy management, including the Common Integration Platform (CIP.io), Smart Charge Adapter (SCA), the Diagnostic Electric Vehicle Adapter (DEVA), SpEC communication control modules, sub-metering and test equipment to verify interoperability.

Task 1: Quantify benefits of smart charging (w/GMLC use cases)

Barriers:

- Lack of consensus on 'smart' VGI communication protocols (i.e., ISO 15118 or SEP2.0)
- Use cases demonstrated in the GMLC 062 project were implemented without the 'smart' protocols due to lack of commercially available compliant hardware (EVs and EVSE).

Solution:

Collaborate with GGIP to refine use case definitions from an industry perspective, facilitate interim technology demonstrations and help source EVs/EVSE with HLC capability. Acquire EVs and EVSE with HLC, link to CIP.io and demonstrate the GMLC-defined use cases using 'smart' communication and control (FY 2019 milestones listed):

- Acquire ISO 15118-compliant EVs and EVSE (Q1)
- Adapt ISO 15118 EVSE to CIP.io (Q1)
- Demonstrate demand response and charge mitigation use cases (Q3)
- Demonstrate frequency regulation and charge capacity deferral use cases (Q4)

Task 2. Develop and demonstrate control strategies for grid integration (GMLC+)

Barrier:

- Lack of use cases with DC charging and grid integration based on economics

Solution:

Demonstrate additional uses cases identified by technical advisors to the project “to adequately assess the potential benefits of smart charging and its role in providing grid services”. GMLC use cases were limited to AC conductive charging and did not consider the smart charging capabilities of ISO 15118. All the recommended use cases require smart communication; the two cases planned for FY 2019 are listed.

- Demonstrate Plug’n Charge (Q4)
- Transactive energy trading with cryptocurrency(Q4)

Task 3. Optimized control for grid resiliency/reliability; Impact of EVs @ scale**Barriers:**

- Unknown ability of Smart Charge Management to respond to grid conditions
- Lack of control strategies that consider the customer and the grid simultaneously
- Unknown impact of EVs @ scale.

Solutions:

Characterize the ability of a network of controlled devices on the customer side of the meter to respond to grid conditions utilizing control strategies that support the customer and/or the grid. Translate the network responses to node characteristics (i.e., behaviors) in the distributed network model to allow studies of the impact of EV penetration and use patterns at the distribution level. The knowledge from distribution level studies will be translated to INL grid models to identify potential impacts of controlled versus uncontrolled charging on local, regional and national grids.

Since this task must follow the implementation of smart communication with EVs and EVSE, only one task was defined for FY 2019, ‘Requirements and interfaces of Argonne and INL grid models defined’ (Q4).

Task 4. Early-stage R&D; Interoperability/grid integration components**Barriers:**

- Equipment to verify interoperability and identify communication faults.
- Compact sub-meters for multi-unit EVSE installations.
- VGI solution for OEMs.

Solutions:

- Develop and demonstrate the Diagnostic Electric Vehicle Adapter (DEVA) (Q4) – Based on the refined SCA, this device will enable digital communication for smart charge management, assess EV-EVSE interoperability and identify faults. Note that development of the SCA is separately funded by the Technology Commercialization Fund and its status is reported separately.
- Compact, low-cost sub-meters (Q4) – Power panel configuration to monitor and report from multiple EVSE plus PV/battery inverter buffer and net load on the main feed to the load center.
- Develop the Smart Inlet (TBD) – This device was proposed as a possible solution to VGI following discussions with an OEM in FY 2018. A derivative of the SCA, it would be designed for the inlet space of an EV (roughly half the size of the SCA). In contrast to the SCA or DEVA, this component would need to meet the harsher requirements of a vehicle environment.

Results

Quantifying the benefits of smart charging (Task 1) and developing control strategies for grid integration (Task 2) depend on integrating EVs and EVSE with HLC capability to implement smart energy management. Few EVs and EVSE are available globally with this capability, and none in the US so far. Though some compliant hardware was acquired from Europe, the EVSE were not ‘open’ to allow direct communication and control via CIP.io. The access issues are being resolved with the EVSE OEMs, but the demonstrations of use cases defined in Tasks 1 and 2 have been shifted to FY 2020. Despite the inability to complete the milestones, preparations have been underway to integrate the compliant hardware when the access issues are resolved.

Note: All the tasks depend primarily on access to the facilities and equipment at the laboratory; their performance schedules were substantially impacted by COVID-related restrictions at Argonne and project partners’ sites.

Task 1. Quantify benefits of smart charging (w/GMLC use cases)

Milestone 1.1 – Acquisition of ISO 15118-compliant EVs and EVSE

- The GMLC use cases were previously demonstrated with emulated smart charging using simulated vehicle charging patterns and recharge energy requirements.
- To support demonstration of GMLC use cases with smart charging, one compliant EV and two EVSE were acquired from European manufacturers, however neither had open access to implement smart communication and control.
- The ‘compliant’ EV required a further software update by the manufacturer (Daimler) in order to establish high level communication with the EVSE and CIP.io, but COVID-related restrictions delayed the update until the end of Q4 FY 2020.
- Argonne attempted to establish a non-disclosure agreement (NDA) with one EVSE supplier to gain access to their Application Programming Interface (API) and worked with a software supplier (and the EVSE OEM) to acquire an interface to the other EVSE. Though these issues were expected to be resolved in Q1 FY 2020, they were not successful. Argonne had established a Go/No Go decision to deal with this potential result. Therefore, Argonne developed its own ISO 15118-compliant EVSE to communicate with the Daimler ISO 15118-compliant EV, thus developing a test platform for the development of control strategies and software for the GMLC use cases with ‘smart’ charging. Development of these use cases has slipped to begin in Q1 FY 2021.
- Argonne acquired a Porsche 15118-compliant EVSE with an EEBUS interface. ANL engineers worked with a vendor to deploy their EEBUS energy management system at the Smart Energy Plaza. The system was evaluated and, unfortunately at the time of testing, charge scheduling via ISO 15118 was not supported.

Milestone 1.2 – Integrate ISO 15118-compliant EVSE in CIP.io (originally Q1 2019).

- Developed ISO 15118 EV Charge Scheduler with User Interface in CIP.io. Since acquiring the EVSE API was not successful and Argonne developed its own compliant EVSE, the integration of the EVSE in CIP.io was delayed until the end of FY 2020. Hence, scheduling charge sessions at the Energy Plaza can begin in FY 2021.

Milestones 1.3-1.6 – Demonstration of Demand Response, Demand Charge Mitigation, Frequency Regulation and Charge Capacity Deferral (originally Q3/Q4 FY 2019)

These milestones were delayed until the ISO 15118-compliant EV and EVSE are integrated with CIP.io; this is now expected to be accomplished in Q1/Q2 FY 2021, essentially a one-year slip due to the need to develop a compliant EVSE and the COVID-related delays.

Task 2. Develop and demonstrate control strategies for grid integration (GMLC+)

Milestone 2.1 – Demonstrate Plug’n Charge (originally Q4 FY 2019)

Due to the one-year slip of Task 1, these task milestones have also slipped.

Milestone 2.2 – Demonstrate Transactive Energy w/Cryptocurrency (originally Q4 FY 2019)

The need to accomplish this milestone is being reconsidered. Argonne will await developments from the recently announced program by Honda and General Motors (<https://www.crypto-news-flash.com/iota-honda-and-general-motors-to-develop-global-blockchain-standard-for-ev-grid-integration/>) to determine if further research is warranted.

Task 3. Optimized control for grid resiliency/reliability; Impact of EVs @ scale

This hardware-in-the-loop (HIL) task links a grid distribution system model with the integrated network of devices at the Energy Plaza via a real-time simulator. This was accomplished in FY 2020 and nodes representing commercial/residential EV charging areas and fast charging stations were added. Enhancements included additional programmable nodes to evaluate the impact of fast charging stations, with EVSE ranging from 50 kW to 300 kW; energy storage systems and photovoltaics were integrated as well to minimize dynamic loads and mitigate the impacts of managed EV fast charging (Figure II.2.1.1).

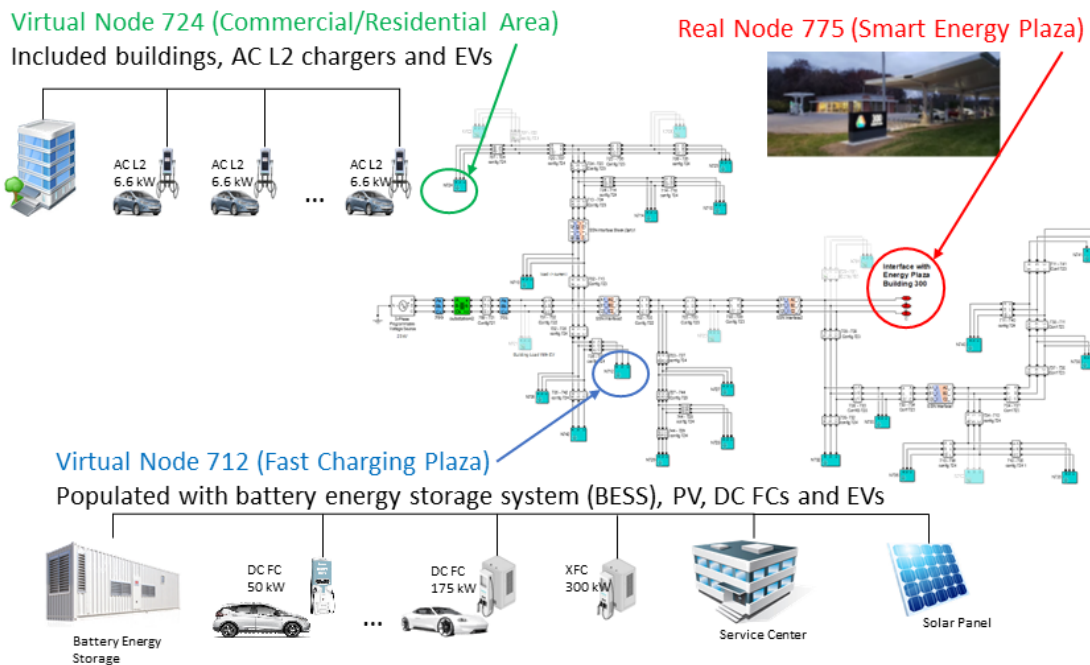


Figure II.2.1.1 Structure of the distribution network model

The ability of EVs to support grid services, such as frequency regulation, is being addressed in this task with modeling, simulation and demonstration. The analytical so far have demonstrated the potential for EVs to decrease frequency deviation of the system, while simultaneously meeting the demands of EV charging, via appropriate charge control. Though the ability to meet the prescribed response requirements for frequency regulation was previously demonstrated by using the Smart Charge Adaptor, the use of HIL enables the assessment of additional grid services and conditions in FY 2021.

Task 4. Early-stage R&D; Interoperability/grid integration components

Milestone 4.1 – Diagnostic Electric Vehicle Adapter (originally Q4 FY 2019)

Refinement of the DEVA (shown in Figure II.2.1.2) continued, including implementation and testing of a HomePlug Green PHY (HPGP) driver in Q3 FY 2020. Work began on a TCP/IPv6 stack as well. However, due to COVID-related delays, implementation of High-Level Communication (HLC, e.g., ISO 15118 protocol) via Power Line Communication (PLC) in DEVA has slipped to Q2 of FY21.



Figure II.2.1.2 DEVA prototype in use and refined design for production

Smart Grid PEV Communication (SpEC) Module 2.0

Completed debugging of the Alpha boards (Figure II.2.1.3) and created list of updates. Delays in development occurred due to licensing constraints with potential licensee. However, the lab is moving forward to optimize the design of the board and move forward with using SpEC module 2.0 as an R&D EVSE platform for our research in VGI and EV communication protocols in FY 2021.



Figure II.2.1.3 SpEC module 2.0 alpha board

Milestone 4.3 – Compact, low-cost sub-meters (originally Q4 FY 2019)

This activity was directly impacted by the schedule/limitations of the EVSE partner, who is considering the technology for their next generation high power EVSE. Certification for this application is the responsibility of the partner and this has not been accomplished to date. In addition, there were plans to install a multi-unit sub-meter in the Energy Plaza to support smart charge management studies, but this was delayed due to COVID restrictions at the lab; this is now expected in FY 2021.

Milestone 4.2 – Smart Inlet (Go/No Go FY 2020)

This device was proposed as a possible solution to VGI following discussions with an OEM in FY 2018. It would be a derivative of the SCA, with a new enclosure designed for the existing inlet space of an EV (roughly half the size of the SCA). However, a ‘No Go’ decision was made by Argonne based on a lack of vehicle OEM commitment and the perceived need to adapt the SCA/DEVA technology to DC charging applications.

Conclusions

Progress has been made toward incorporating EVs and EVSE with ‘smart’ communication capabilities in the network at the Smart Energy Plaza. Argonne developed its own ISO 15118-compliant EVSE to enable development of GMLC use cases with smart charging; this development was required to complete the smart charging studies despite the lack of smart EVSE with open communication. The time required for this

development, plus the COVID-related delays in updating the ISO 15118-compliant EV, has resulted in slipping the control strategy and software development for ‘smart’ use cases to FY 2021.

Notwithstanding COVID-related delays, progress has been made in developing the enabling technologies. PLC drivers were implemented and tested for the Diagnostic Electric Vehicle Adapter (DEVA). Alpha boards for the SpEC 2.0 communication module have been tested and further development is underway. Completion of the sub-meter package has been delayed, but integration in the Smart Energy Plaza is expected in FY 2021. In summary, delays at Argonne, development partners and vendors will cause the Smart VGI project to be extended into FY 2022.

Future Work – FY 2021 will prioritize the ‘smart’ GMLC use cases that were postponed due to COVID; specifically, demonstration of use cases using HLC using the Argonne-developed ISO 15118-compliant EVSE and the compliant EV. In addition, Argonne-developed technology will be applied to campus-level SCM and refined for more universal applications as described below.

SCM Integration in Workplace Systems – Leverage the work done on the Qmulus Cloud Platform in the SCA TCF to design and implement a campus-wide EV registration system with a mobile app and integrated communication (in cooperation with Argonne Sustainability, subcontractor Farshore and Qmulus). Utilize predictive analytics and machine learning to predict charging needs (e.g., power and time) and provide these analytics via 3rd party API for mitigation in the universal SCM/EMS. Provide a campus-wide visualization and SCM capability from the platform. Features include an EV driver mobile app will allow reservation and enabling of adapters/stations as well as a web app for a station operator that will include the ability to change station availability. The activity will develop a baseline EV charge forecast machine learning model for integration into Universal SCM/EMS (described below).

Universal SCM/EMS – Based on many inquiries regarding an energy management system that can utilize the open-source technology Argonne developed to enable communication using popular protocols (e.g., Modbus, OCPP, Open ADR, etc.), a campus, building and/or fleet EV charge controller will be initiated in FY 2021. The first “use-case” would focus on a single point of common coupling (building premise meter, campus meter, etc.) and provide the “user” a simple-to-use interface that connects their premise meter and OCPP stations to CIP.io. This is envisioned as a single board computer in an ANL enclosure with the application and a simple web-based user interface, i.e., docker-ized communication components for Modbus, OCPP, etc. supporting a central means of communication via MQTT with configuration via a basic web interface and database storage component. This capability will be the building block for other use cases.

Key Publications

1. D. Dobrzynski, J. D. Harper, ANL-IN-19-053 - US Utility Application - Transactive Framework for Electric Vehicle Charging Capacity Distribution (patent application #16/863,958)

Acknowledgements

The work in this report was conducted by researchers in the Advanced Mobility and Grid Integration Technology Section of the Energy Systems Division of Argonne National Laboratory: Jason Harper, Dan Dobrzynski, Bryan Nystrom, Nick Lau and Zhouquan Wu (grid integration, communication, diagnostic technologies and hardware-in-the-loop) supported by subcontractors PDT Astronics; Ted Bohn (sub-metering) supported by subcontractors 2G Engineering and Amzur Technologies.

II.2.2 Demand Charge Mitigation Technologies (NREL)

Andrew Meintz, Principal Investigator

National Renewable Energy Laboratory
15013 Denver West Parkway
Golden, CO 80401
Email: Andrew.Meintz@nrel.gov

Lee Slezak, DOE Program Manager

U.S. Department of Energy
Email: Lee.Slezak@ee.doe.gov

Start Date: October 1, 2017
Project Funding: \$250,000

End Date: September 30, 2020
DOE share: \$250,000

Non-DOE share: \$0

Project Introduction

Most commercial buildings or facilities pay for their electricity bills with two types of charges—energy charge and demand charge. Energy charge is the cost for the total energy consumption for the month and demand charge is the charge for the peak power demand of the month. The peak power demand of the month for billing is usually calculated as an average demand in 15-minute time frames. NREL has a contract with the utility at \$0.04/kWh for energy charge and at \$16.79/kW for demand charge in 2017. With this price rate, even 50 kW peak reduction can result in saving more than \$800. Therefore, electricity cost can be lowered not only by using energy efficient products but also by reducing peak demand by distributing power demand throughout the day for flexible devices, specifically plug-in electric vehicles (PEV) charging.

Objectives

One of main issues with demand charge mitigation and load control is integration of heterogeneous components and scalability of the existing structure as the number of controllable load devices increases. Distributed control without information on the other devices such as controllable water heater, HVAC, etc. can make the whole system unstable because each device can compete with each other due to lack of information on the other devices. Suppose that load control of individual devices is dependent on the total load and are distributed (each control system does not have information on other control systems). Then, if a controller of a device reduces its load during the peak, it will lower the total load. Then, a controller of another device may try to increase its load because total load is reduced, which increases total load again and can make the whole system unstable. Centralized control algorithms [1] can resolve this problem by coordinating each controller together but become complicated and inefficient if the size of the system becomes large. Further, addition of new resources to the system must be scalable to eliminate integration issues.

As an alternative to centralized methods, algorithms using a game theoretic approach were proposed for demand side management [2],[3]. They use real-time pricing information in solving the problem, which is not available in every territory and the conditions for the Nash equilibrium are not always satisfied in real-world conditions. Different from the abovementioned techniques, this project aims to develop a control algorithm combining centralized and distributed methods with the hierarchical and distributed control structure.

Approach

Prior work for this project presented a method to resolve the issue described in the previous section through distributed control with hierarchical structure and utilization of energy constraints as described in [4]. Figure II.2.2.1 illustrates the approach used in this project. The goal of this scheme is to find an optimal energy use first at each time step given a total energy forecast and then allocate the obtained energy amount to each device depending on its energy need priority. The inclusion of PEVs complicated the problem because they require a specific amount of energy at departure.

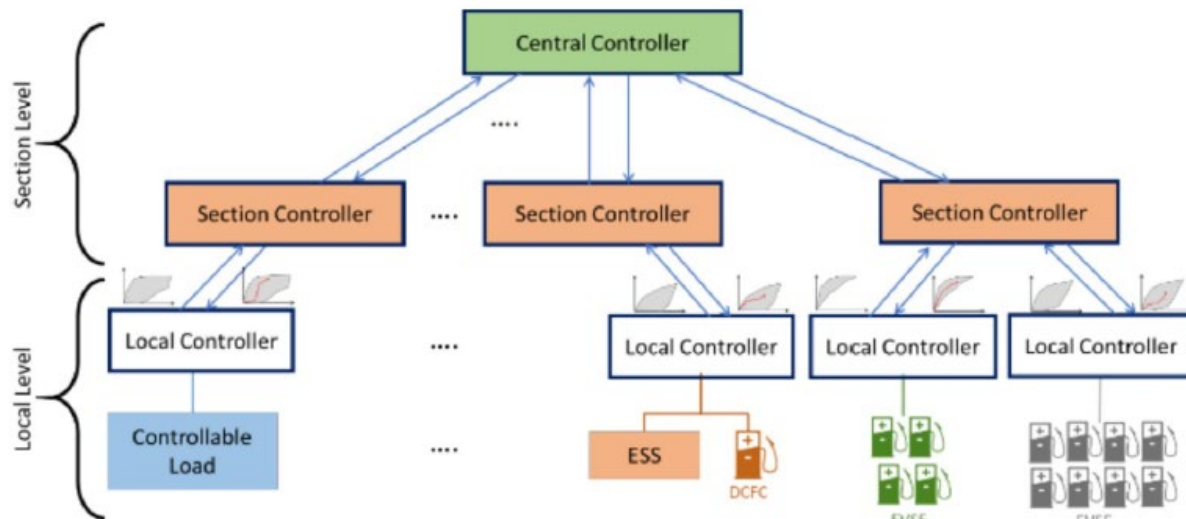


Figure II.2.2.1 Structure of distributed control with hierarchy

DC fast charging has changed rapidly with the integration of every higher power levels and the introduction of new vehicles that charge at higher voltages and with markedly different power profiles. As power levels grow to include extreme fast chargers (XFC) it became apparent that a hardware system was required to do power-hardware-in-the-loop (PHIL) evaluation of the XFCs in the lab. These changes necessitated the development of the charge control box (CCB) which emulates a vehicle by performing all the necessary communication with the fast charger and other laboratory equipment to facilitate a fully powered charge cycle. Replacing a vehicle in the charging loop with an emulator allows for more experimentation flexibility because the CCB can be programmed with any charging profile and it does not require the vehicle be discharged before another experiment can be run. Further, through multiple CCBs and bidirectional supplies it alleviates the need to acquire vehicles of various type to perform an experiment, but instead virtualize the vehicle responses.

Results

Extreme fast charging equipment was integrated into new supporting electrical infrastructure as the new Electric Vehicle Research Infrastructure (EVRI) evaluation platform in at the Energy Systems Integration Facility (ESIF). This space also includes the new Commercial Buildings Research Infrastructure (CBRI) to facilitate high-powered extreme fast charger evaluation with commercial building loads to build on the integration challenges discussed in the previous sections as seen in Figure II.2.2.2.

The electrical infrastructure of the EVRI has been designed to support two independent research electrical systems at 480V one with a 208/120V secondary and the other with a 240/120V split-phase system. Each of the electrical systems can be tied directly to the grid emulation capabilities at ESIF to allow for AC PHIL experiments for the charging. Additionally, these electrical systems can be tied directly with the CBRI to allow for demand charge experiments with advanced commercial building equipment that allow for load flexibility or simply integrating with non-flexible loads for experiments with charging flexibility. This work included construction of four CCBs to allow for experimentation with chargers from different manufacturers and the

integration of the Tritium charger and Samsung energy storage system that was being used for previous experiments in a different lab space.



Figure II.2.2.2 Electric Vehicle Research Infrastructure (EVRI) on right with four vehicle parking bays each with both DC and AC charging and Commercial Building Research Infrastructure (CBRI) on the left with building loads and emulation

Charge Control Box Construction

The vehicle charging emulation capability is available at each parking bay with four identical CCBs that consist of the following major components. A completed CCB is shown in Figure II.2.2.3 which is located behind each of the charging dispenser in Figure II.2.2.2 with the charging inlet visible next to first dispenser.

1. Vehicle charge control unit (VCCU)
2. Vehicle charging inlet
3. Real-time computer (RTC)
4. DC contactors and fuses
5. Current and voltage sensors.

The VCCU is manufactured by Vector (bottom right image in Figure II.2.2.3) and is responsible for handling the communication with the charger which is done through power-line communication (PLC). This communication is connected to the Electric Vehicle Supply Equipment (EVSE), or charging dispenser, through the SAE J1772 standard charging inlet or Combined Charging System (CCS) connector. The VCCU communicates charging data such as the energy required by the vehicle in addition to monitoring charger diagnostics like the status of the charger handle (e.g., plugged or unplugged) and handle temperature.

All this information is transmitted to the OPAL OP-4200 RTC (top right image in Figure II.2.2.3) which packages it and sends it to another supervisory RTC which houses system models and controls. The other responsibilities of the RTC include controlling the DC contactor that connects the charger to the battery emulator, recording data from the voltage and current sensors, and finally controlling the status lights through its digital outputs.



Figure II.2.2.3 Completed CCB cabinet

Lab Architecture

Each CCB is a part of a larger system, illustrated in Figure II.2.2.4, that is controlled by another RTC the OPAL OP-5707. The OP-5707 is responsible for running the battery models for each CCB along with any vehicle emulation tasks or logistic control required by the VCCU in each CCB. Each OP-4200 communicates with the OP-5707 through fiber optic connection and acts as remote analog and digital I/O. Housing the models on the OP-5707 allows for greater battery model complexity as it has several CPU cores devoted to the task.

Battery emulation will be accomplished using an Anderson bidirectional DC supply whose voltage is controlled by the analog output of a local OP-4200 which communicates with the OP-5707 via fiber optic connection. The bidirectional DC supply is connected via the black and red ports visible in the bottom of the CCB shown in Figure II.2.2.3. Through this electrical connection the power supply to emulate any battery voltage in the range of the 200 to 1000V CCS standard and essentially an infinite capacity since the DC supply energy will be returned to the grid. The battery models on the OP 5707 can be used to emulate cold or hot battery conditions through the voltage command to the DC supply and through battery management system models that send current limits through the VCCU to the charging hardware.

The software architecture that will run on the OP-5707 is shown in Figure II.2.2.5 and consists four independent copies of the same control structure, one for each CCB. First, the battery model is responsible for reading current from the bidirectional DC supply and setting the supply's voltage set point. Second, the charging logic portion will be responsible for all handshaking and communication with the VCCU to walk it through the DC charging process. Next, the status light control will run status lights to provide visual feedback to the user. Finally, the contactor control will determine the status of the high voltage DC contactors which

connect the charger to the battery emulator. All of this is programmed with Matlab/Simulink which allows for quick turnaround time from simulation to hardware implementation.

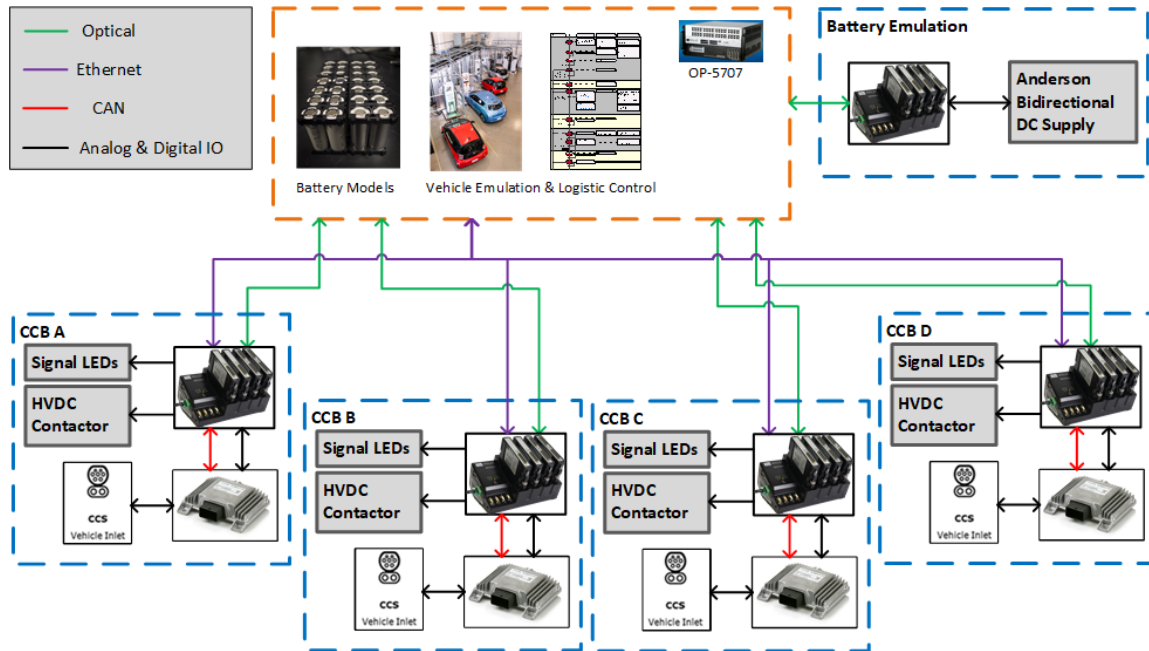


Figure II.2.2.4 Control hardware structure

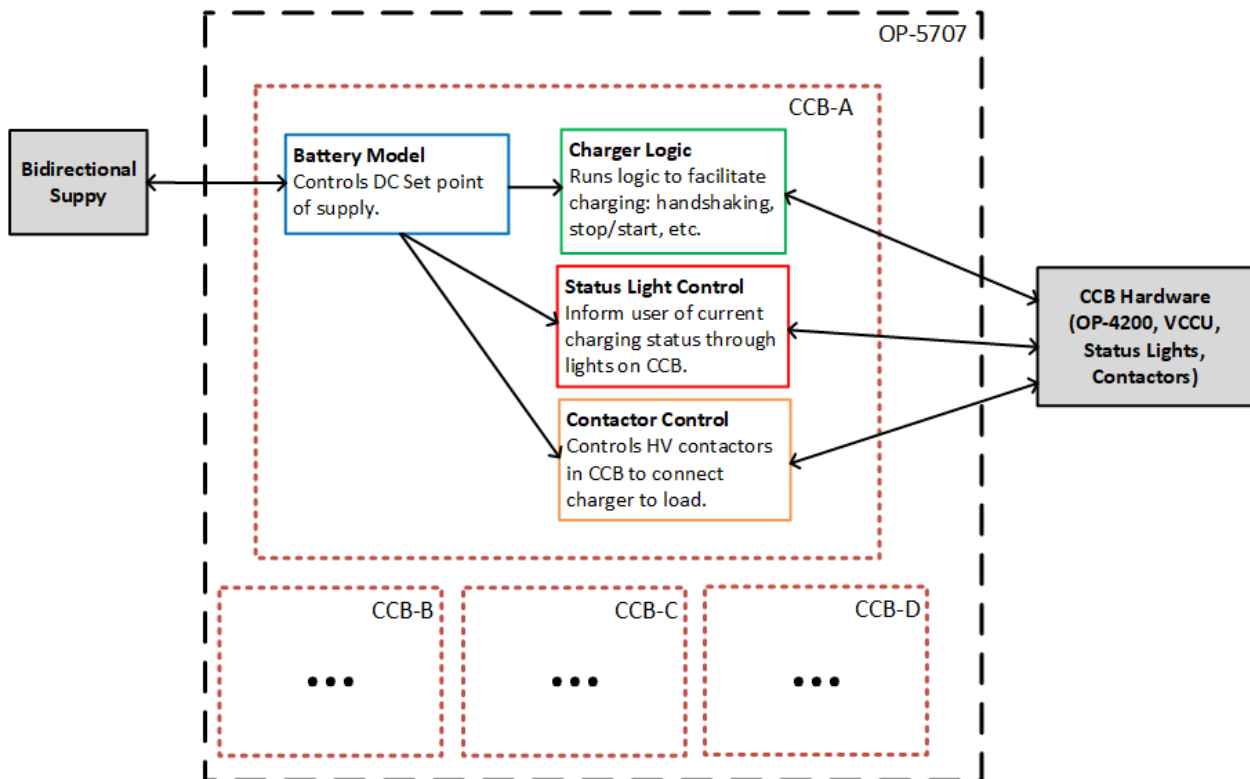


Figure II.2.2.5 OP-5707 software diagram

Hardware Installation in EVRI

In addition to the hardware discussed previously, two pieces of equipment which were used for prior work on this project were moved into the EVRI lab to integrate them into the XFC system. These pieces include a Tritium fast charger and a Samsung energy storage system shown in Figure II.2.2.6. Also shown in the foreground of Figure II.2.2.6 is the server rack that houses the OP-5707 as well as a computer that houses the network switch for control of the EVSEs through the distributed control hierarchy in Figure II.2.2.1.



Figure II.2.2.6 Tritium fast charger (on left) and Samsung energy storage system with OPAL 5707 server rack (on right)

Conclusions

Through the course of this project, NREL has developed a charge management system which integrates many different types of controllable loads for demand charge mitigation. The local controllers are connected to the controllable loads with different interfaces. They translate messages in different communication protocols into MQTT messages through which the central controller communicates with the local controllers. This structure facilitates addition of new types of controllable loads without modifying the interface of the central controller. The central controller only needs to add a list of MQTT message topics that are required for the new controllable loads and aggregate the forecasted energy needs of them into the optimization.

NREL has also performed tests on a testbed consisting of level 2 EVSE's, a DC fast charger, and a stationary ESS. The level 2 EVSE's are used by NREL employees without a pre-coordinated test scenario. The drivers use the chargers based on their own schedules. Experiments show that each local controller commanded to reduce power to each controllable load when campus load or forecasted campus load is high and each controllable load decreased load accordingly to not contribute to peak load. Experiments also show that the central controller successfully integrates each local controller through a common communication interface and that it provides an optimal power setpoint value based on expected energy needs and forecasted load.

As work on this project progressed and power levels for demand charge mitigation of extreme fast chargers grew, the need to build a system which could allow charging hardware to run a charging cycle without a vehicle in the loop became apparent. This year NREL completed the construction of this system which included building CCB hardware along with the integration of previously used charging hardware and energy storage. This hardware and new emulation capability will support the on-going DirectXFC project.

References

1. T. Logenthiran, D. Srinivasan, and T. Z. Shun, “Demand side management in smart grid using heuristic optimization,” *IEEE Trans. Smart Grid*, vol. 3, no. 3, pp.1244-1252, 2012.
2. Z. Ma, D. S. Callaway, and I. A. Hiskens, “Decentralized charging control of large populations of plug-in electric vehicles,” *IEEE Trans. Control Systems Technology*, vol. 21, no. 1, pp.67-78, 2013.
3. M. H. K. Tushar, C. Assi, and M. Maier, “Distributed real-time electricity allocation mechanism for large residential microgrid,” *IEEE Trans. Smart Grid*, vol. 6, no. 3, pp. 1353–1363, 2015.
4. S. Vandael, B. Claessens, M. Hommelberg, T. Holvoet, and G. Deconinck, “A scalable three-step approach for demand side management of plug-in hybrid vehicles,” *IEEE Trans. Smart Grid*, vol. 4, no. 2, pp.720-728, 2013.

Acknowledgements

The Demand Charge Mitigation project principal investigator acknowledges the contributions of team members: Keith Davidson, Don Finley, Shivam Gupta, Myungsoo Jun, Darren Paschedag, and Darin Smith. The project team also acknowledges the support of Lee Slezak (DOE HQ) and Manish Mohanpurkar (INL).

II.2.3 Adapter for Smart EV Charging to Improve Grid Integration and Interoperability (Argonne National Laboratory)

Jason D. Harper, Principal Investigator

Argonne National Laboratory
9700 South Cass Avenue
Lemont, IL 60439
Email: jharper@anl.gov

Lee Slezak, DOE Program Manager

U.S. Department of Energy
Email: Lee.Slezak@ee.doe.gov

Start Date: October 1, 2018
Project Funding: \$1,180,698

End Date: May 30, 2021
DOE share: \$590,349

Non-DOE share: \$590,349

Project Introduction

Argonne National Laboratory (ANL) has invented and patented a universal smart charge adapter (SCA) that is connected between any AC charge station and plug-in electric vehicle. The smart charge adapter integrates legacy non-networked AC charge stations into a managed charging network that allows communication with grid operators. The smart charge adapter enables metering, monitoring and management control of charge sessions in response to local supply/demand levels. Qmulus, LLC (Chicago, IL) has an agreement with Argonne regarding the issued US patent and the EU patent application and is commercializing the technology.

The availability of the smart charge adapter will support the integration of EV charging as an additional grid resource, enabling grid operators to maintain supply/demand grid balance in part by controlling networked EV charging sessions as needed. As more EVs come under this level of control, it will support a reduction in the potential for brownouts, outages and voltage/frequency fluctuations that are caused by excess demand within a local or regional grid. Currently available charge stations (EVSE) are either not connected to the developing smart grid or are connected only through proprietary, insular platforms making it extremely difficult to interface charge sessions from large networks of diverse EVSE to monitor and control EV charging demand.

Qmulus is the primary partner working with ANL. Final development of the Beta prototype and commercial smart charge adapter is underway on a contract basis with a contract-engineering firm. Zen Ecosystems (Newport Beach, CA) is providing access to its customer base for the full field trial. California Energy Commission (CEC) is providing advisory services for engagement with California utilities and for regional market and EV user information.

The primary goal of the project is to create a commercial SCA design that includes hardware, firmware, and software applications. The Beta prototypes will be tested at ANL in a controlled use setting and with end-users in Zen Ecosystems' coverage areas in California. Feedback from the current Beta device and our Beta pilot programs will lead to a commercial SCA design. An additional pilot(s) are targeted for California utilities (and/or another regional utility) in cooperation with Zen and the California Energy Commission (CEC).



Figure II.2.3.1 The SCA is an in-line adapter for SAE J1772™ PEV charging

Objectives

Qmulus' commercial strategy initially focuses on public and semi-public owners of EVSE who are interested in a low cost, single interface for their networked and non-networked EVSE. These users will be able to network all their AC EVSE, regardless of brand, under a single interface via the SCA's Wi-Fi communications and cloud platform. Qmulus' longer-term strategy will target utilities to support their grid management needs. Residential users are also considered in their planning, particularly to support the various utility energy savings programs in which an EV driver may enroll. The initial markets are guiding the development plan, since larger scale users desire a more rigorously tested and certified solution. Ultimately, Qmulus hopes to support utility-sponsored energy programs for both home and workplace charging, enabling utilities to realize increased potential for smart grid management.

Development of the Beta version of the SCA was not complete by the start of the TCF award period thus the TCF funds were used, in part, towards final development and testing at ANL during Phase 1 of the TCF project. Testing and conformance to the specifications has been performed by ANL. The SCA will meet all design and conformance tests before being deployed in pilot programs. A successful Phase 1 will result in beta HW and software ready for pilot program deployment as well as the design of the commercial SCA.

In Phase 2, the Beta prototypes will be field tested in two separate pilot programs. Phase 2 will provide critical data and feedback on the Beta SCA that will guide the development of the commercial version. User surveys will be conducted throughout the pilot programs to understand users' perceptions of the device, applications and controlling software. The surveys will be revised and updated as new information is obtained. Qmulus will work with CEC to understand and target the needs of California consumers and utilities for a smart grid enabled SCA. Root cause failure analysis (RCFA) will be used to examine any devices that have failed in the field to identify the causes behind the failure. These findings will support any changes to the design package for a commercial SCA.

In Phase 3, the partnership will continue its ongoing efforts with CEC to engage one or more utilities to plan an EV Smart Charging Pilot. In addition, further collaborations with Zen will be developed. This will parallel Qmulus' commercial roll-out for public and semi-public users. Working independently of the TCF project, Qmulus will have completed all business development and marketing steps required for the short-term launch goals. Engagement with a utility and planning for a demonstration pilot will be important for the intermediate and long-term business strategy. A successful Phase 3 will result in identifying proactive utilities looking to implement EV smart charging programs and engaging them.

Approach

Phase 1: Finalize SCA Development and Testing

This phase began prior to TCF funding; however, it has carried into the TCF period. This phase involves finalizing all hardware (mechanical/electrical), software, firmware, and cloud platform. Design will focus first on a Beta SCA and web platform that are as close to commercial production as possible. Twenty Beta SCAs will be built for testing in the Phase 2 field trial. A user friendly, secure and reliable Beta web platform will be developed. Testing in the laboratory and at ANL's IOC will be performed.

Phase 2: Beta Pilot Programs

Qmulus, Zen and CEC would implement two small-scale EV Demand Response pilot projects, utilizing Zen's OpenADR 2.0a/b certified cloud which would enable the SCA to act as a Virtual End Node (VEN), providing automated Demand Response dispatch from utility Demand Response Automation Servers (DRAS). The first pilot (Pilot A) would be performed at ANL and deploy ~10 SCAs onto ANL workplace charge stations resulting in ~72 kW of controllable load. Pilot A would focus on the integration of the ZEN's OpenADR cloud interface into the Qmulus Cloud Platform to add EV charging into an OpenADR demand response program. Successful completion of Pilot A would result in the integration of the SCA/QCP into Zen's OpenADR system for 2 weeks with simulated DR events.

Working with Zen, Enersponse and CEC, the second pilot (Pilot B) will focus on deploying SCAs (20 - 100) onto EVSE in territories in which Enersponse has established Demand Response programs and is actively participating in DR markets. The SCAs would then become a part of Enersponse's DR portfolio that will be used, in combination with Zen's smart thermostat and other controllable load under management, to deliver DR to a range of existing demand response programs. In addition to the monitoring and management enabled by the SCA/QCP, Pilot B participants (EVSE owners) may be compensated for allowing their charge stations to be enrolled in the DR markets. A successful Pilot B will result in a demonstration of utilizing the SCA EV load to provide demand side management of the grid.

Phase 3: Utility Pilot Planning

Qmulus is partnering with Zen and the California Energy Commission (CEC) to identify California utilities willing to participate in an EV Smart Charging pilot. Prior to the TCF award, Qmulus and CEC will use their established contacts to engage partners and plan the pilot in California. Qmulus is also currently looking for potential partners in the Chicago, Denver, and Minneapolis metropolitan areas. Given the long planning periods of utilities, it is not expected that this Phase will be completed during the TCF project period, only that the engagement of partners, planning and development of the pilot will occur. If successful, the TCF project will lead to the EV Smart Charging pilot project, which will also support Qmulus' goal of identifying utilities that are potential customers for the SCA. Results of the EV Smart Charging Pilot may lead to further revisions to the design of the device, its software or firmware (if needed) or to a utility production package that ensures a reliable, rugged device and software that can be integrated into utility management systems or easily exchanged for utility-developed software.

Results

The project saw great strides in the area of hardware and software development in FY20. Beta firmware development for the adapters continued through FY20. Commercial development began on the hardware design with five (5) commercial Alpha units (Figure II.2.3.2) being delivered in FY20. An additional phase of work commenced on the Qmulus Cloud platform as well. Unfortunately, the Beta pilot programs were delayed due to the COVID-19 pandemic.

Smart Charge Adapter Hardware

Further lab testing was performed on the beta adapters during Q1/Q2 of FY 20. Multiple iterations of firmware resulted in fixing bugs and issues with the original firmware. ANL engineers implemented firmware to optimize power consumption in Q1/Q2 of FY20 as well.

Working with our engineering team at PDT, a more robust mechanical design was implemented (Figure II.2.3.3). Changes from the beta design include redesigning the gaskets to achieve an IP65 ingress protection rating. The decision was made to switch from using a COTS EVSE connector and PEV inlet. The new commercial alpha design will utilize a custom molded EVSE connector and PEV inlet, with custom socket/pin assemblies. Other mechanical changes include swapping the location of the AC/DC power module and battery from the bottom of the unit to the top, necessitating a redesign of the main and rear housings. Another significant change was the SCA latch. The latch was completely redesigned to optimize ruggedness and ergonomics. The EVSE locking mechanism was also changed in this iteration of hardware. An LED light pipe was also added to this version of the hardware to provide a visual indication of the SCA status. The entire design was optimized for manufacturability to reduce the time to assemble the units on the factory floor.

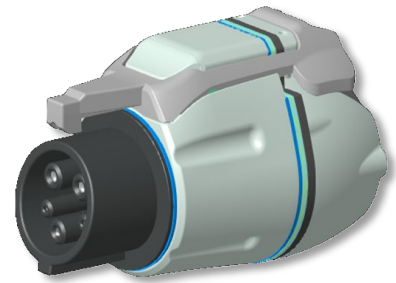


Figure II.2.3.2 Commercial Alpha Smart Charge Adapter: Portable, Robust and Easy to Use.

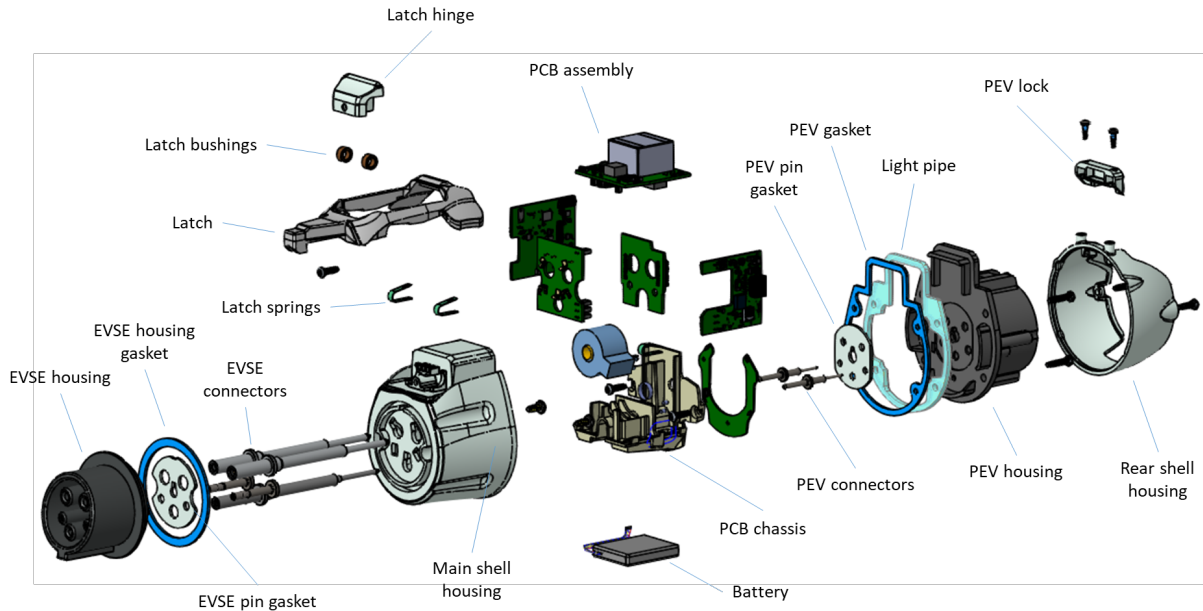


Figure II.2.3.3 Exploded View of Commercial Alpha Smart Charge Adapter

From an electrical perspective, the battery capacity utilized in the new design has doubled from the previous battery capacity, utilizing the same footprint. The circuits' stand-by power has also been optimized to extend the life of the SCA between charges. It is estimated the new SCA design can maintain 4 weeks of life between EV charge cycles when disconnected from the EVSE and PEV. Even if the SCA battery dies, it will be unknown to the end-user because the SCA instantly wakes up when an active EV charge session occurs. Additional circuits were added to the SCA design to wake the SCA up from trigger events.

Qmulus Cloud Platform and Mobile App Development

The first phase of the Qmulus Cloud Platform (QCP) was finished in FY20. Features of the cloud platform include management, monitoring and control of Smart Charge Adapters as well as Open Charge Point Protocol EVSE. The second phase of work was kicked off in Q4 of FY20. The development work will focus on implementing a third-party API to integrate Qmulus devices into third party applications including the Zen HQ™ platform for demand response applications. Additional features to be implemented include charge scheduling, authorization/access control, group power management, and enhanced notifications in this second phase of work.

The QCP has been developed for single SCA owners (PEV drivers) and commercial EVSE owners representing the semi-public and public charging markets. The QCP allows for easy management, monitoring and control of EV charging from any EVSE utilizing a single interface. Designed with ease-of-use in mind, the Qmulus Cloud Platform allows station and adapter owners the insights and controls to manage their stations and EV charging sessions. Both Android and iOS mobile apps were developed and delivered in FY20. The

mobile apps allow single device SCA owners to monitor and control their EV charging sessions and access historical charge session data.

Through the web or mobile apps, individual SCA owners have three options to control their EV charging (Figure II.2.3.4). The first method of control is manual control. SCA owners can apply a current or power set point to limit the amount of current/power in real time. This method of control is convenient to limit a circuit breaker or premise to a predefined limit. Once the third-party API is finished in the next phase of development, dynamic control is possible and would allow EV charging control via the SCA to be integrated into home or building energy management systems. The second option for EV charging control is based on EV mileage accumulation. SCA owners can add multiple EV's to their account and given the specific make and model, the platform estimates EV mileage accumulation via charging and stops the charge session when the limit is reached. This type of control is often utilized when a full charge is not needed, and the driver wants to limit the consumption of the vehicle to a specific number of electric miles. The third method of EV charging control is timer-based control. The EV driver can set a specific duration of charging and once the timer expires, charging is stopped.

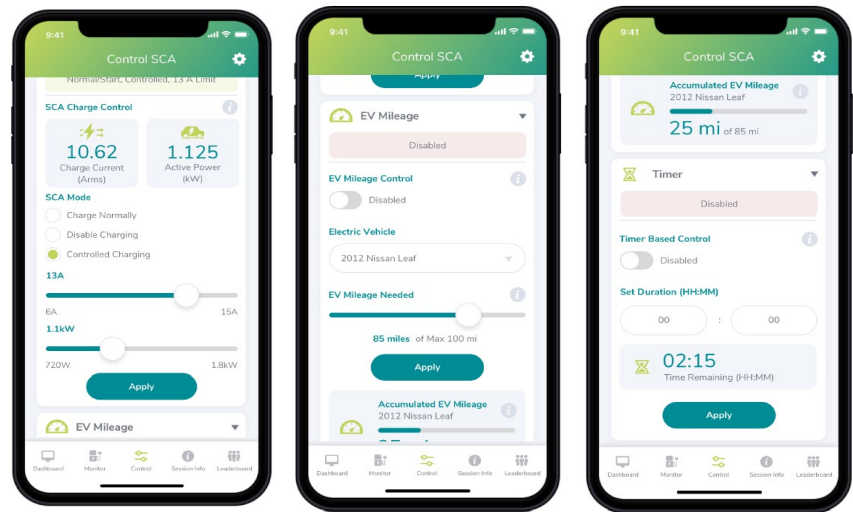


Figure II.2.3.4 SCA Control Options: (L) Manual Control, (M) EV Mileage Control, (R) Timer Control

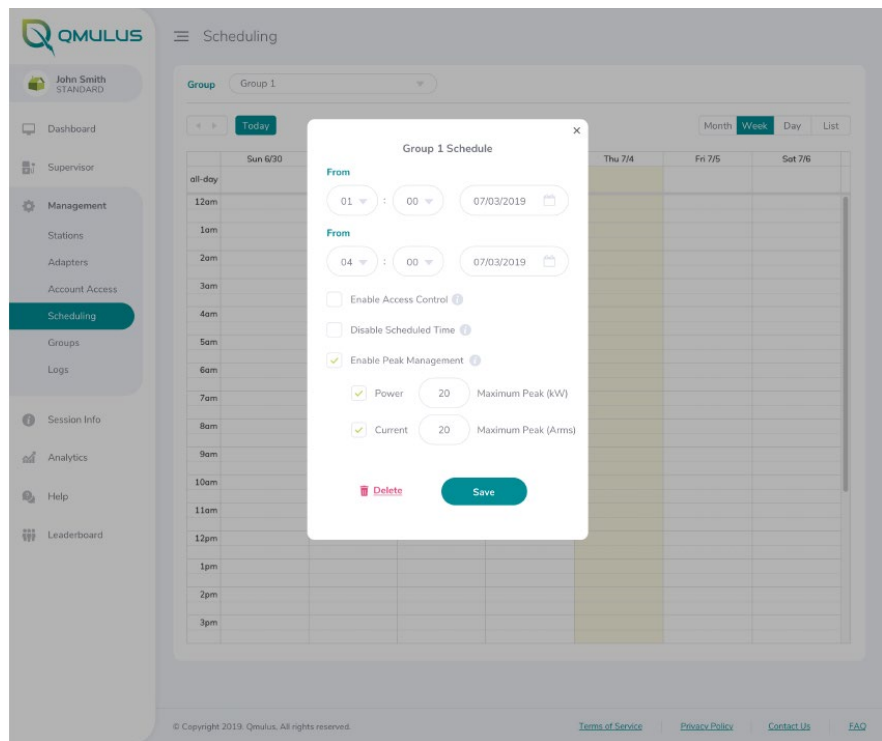


Figure II.2.3.5 Screenshot of setting up charge schedule through the web app.

In the next phase of work in FY21, charge-scheduling control (Figure II.2.3.5) will be implemented from the web app. This feature will allow EV drivers to setup a reoccurring schedule to start and stop charging. This is particularly useful for EV drivers on a time-of-use (TOU) tariff with their local utility. Once a charge schedule

is setup, EV drivers will be able to plug in their SCA/EVSE into their PEV and charging will begin/end based on the setup schedule.

Pilot Programs

Due to the COVID-19 pandemic, the pilot programs were put on hold in FY20. However, given this delay the cloud platform and mobile apps will now be deployed during the pilot program. This will allow for private residential users to be a part of the pilots. In late FY20, the team began to gather beta testers and deploy units to individual Argonne employees for use in their private residences. In addition to residential users, beta SCA units have been locked to AC L2 stations around the Argonne campus. The principal investigator has been using an adapter with the cloud platform at his residence and at ANL to charge his EV since Q2 of FY20 and has dispensed almost 200 kWh of energy through the adapter (Figure II.2.3.6).

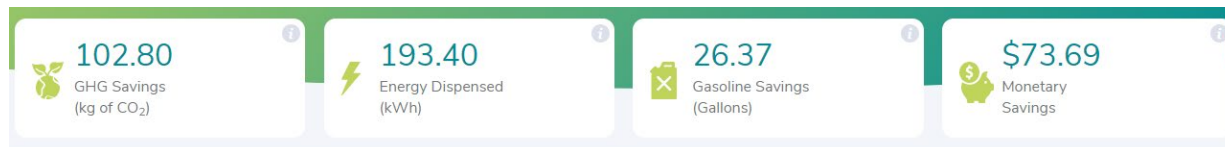


Figure II.2.3.6 Principal Investigator's charging data overview since Q2 FY20.

We continue discussions with our partner Zen Ecosystems with respect to a California pilot in Q3 of FY21. We will continue to monitor the pandemic and assess the viability of moving forward with a California pilot in the early spring of FY21.

Conclusions

The SCA beta hardware and firmware was fully developed and tested in FY20. Unfortunately, the Beta pilot programs were delayed due to the COVID-19 pandemic. In late Q4 of FY20, SCA units were deployed as part of the ANL pilot program. We continue discussions with Zen Ecosystems with respect to a California pilot slated for Q3 of FY21. The design of the commercial Alpha was completed in FY20. Five (5) units were manufactured and tested. Feedback from this testing will guide the next phase of development leading into commercially tooled parts and twenty-five (25) commercial units ready for UL testing in FY21. Significant progress has been made on the Qmulus Cloud Platform including a fully functional web app and mobile apps ready for pilot testing. Qmulus has engaged multiple utilities for beta testing and qualification and is in contract negotiation or initial discussions with five interested North American utilities. This includes an engagement with Exelon and their DOE-sponsored in Maryland.

II.2.4 Scalable Electric Vehicle Smart Charging Using Collaborative Autonomy (LLNL)

Steve Chapin, Principal Investigator

Lawrence Livermore National Laboratory
7000 East Avenue
Livermore, CA 94550
Email: chapin8@llnl.gov

Jovana Helms, Principal Investigator

Lawrence Livermore National Laboratory
7000 East Avenue
Livermore, CA 94550
Email: helms7@llnl.gov

Lee Slezak, DOE Program Manager

U.S. Department of Energy
Email: Lee.Slezak@ee.doe.gov

Start Date: October 1, 2018
Project Funding: \$1,570,000

End Date: June 30, 2021
DOE share: \$1,570,000

Non-DOE share: \$0

Project Introduction

Since 2011 the number of plug-in electric vehicles (PEVs) has grown exponentially, both in the U.S. and across the world, and this number is expected to continue to grow [2]. Along with these new vehicles, coupled with increases in vehicle battery sizes, comes a large demand for electric vehicle charging stations. The expected increase in electricity demand from PEV charging presents a challenge to reliable power grid operation, as many PEV owners are likely to plug in their vehicles immediately after the morning and afternoon commutes, times of day that are already high-demand periods for the power grid. In this way, unregulated charging would lead to higher demand peaks, increasing the need for controllable generation and thus making reliable power grid operation more difficult.

To illustrate the scale of the problem imposed by widespread EV adoption, consider the Riverside Public Utilities, which has approximately 110,000 metered customers spread across 14 distribution feeders. At the California average of 4% of households having PEV, that means that approximately 4,400 RPU customers have EVs, which is of a scale handled by traditional centralized mechanisms. California had approximately 500,000 PEV as of November 2018 [3], and is expected to grow to 5,000,000-11,000,000 EV by 2030, a 10- to 22-fold increase¹, and also representing 33-70% of the total vehicles on the road in California. This means that RPU would be supplying charging for 45,000-97,000 vehicles in 2030.

In contrast, if properly managed, the widespread adoption of PEVs presents a mechanism for demand response through vehicle charging. While today most charging stations simply provide power to connected vehicles until the charge capacity is reached, there has been a great deal of interest in developing “smart charging” technology, that is, charging stations with the ability to respond to market signals to control vehicle charging. Smart charging stations have the potential to communicate with the power grid to implement demand response, i.e., intelligently charge PEVs in order to improve charging economics, and to improve the resilience and reliability of the power grid [4],[5],[6],[7],[8],[9]. With these methods, typically a PEV owner specifies some

¹ A 25% growth rate, which the state has exceeded in 6 of 8 years since 2011, yields 5,000,000 PEV in CA in mid-2026, and almost 11,000,000 EV by 2030.

willingness to have vehicle charging delayed in exchange for a lower price. Given that flexibility, smart charging can be used to shift demand from peak hours to off-peak hours.

Smart charging could also be used to improve power grid stability and protect equipment such as transformers from overloading. Some prior work has considered using PEVs for voltage and frequency regulation in the power grid. In this application, if there is a disturbance in the power grid, e.g., a failure at a major power plant, the smart charging stations can respond by increasing or decreasing the power draw to help regulate voltage or frequency on the power grid [10],[11]. Due to the strain on batteries, most charging customers are unlikely to agree to have their PEVs discharged regularly, but PEV owners may be incentivized to allow their vehicles to be leveraged in this way on the rare occasion that it is necessary to prevent a power outage event or other grid instability.

To the authors' knowledge, no prior work on voltage and frequency regulation with smart chargers has considered the challenges associated with effectively scaling to hundreds of thousands or even millions of PEVs in the system. Most prior work on this topic requires PEVs "register" with a central control system, which sends charge/discharge commands to the connected charging stations. This approach is problematic when the system scales to large numbers of devices, as the control center often must perform some nontrivial calculation (such as the optimization problem solved in [11]) and communicate the results to many smart chargers. Broadcasting messages to a large number of chargers is in itself a nontrivial communication task that takes enough time to hinder the system's ability to respond to voltage and frequency fluctuations in a timely manner.

One approach to the scalability problem is to develop hierarchical systems, in which clusters of smart chargers are governed by individual control computers; clusters of control computers are, in turn, governed by higher-level control computers, and so on until a central controller is reached. This approach is scalable, but brittle: if any point in the control hierarchy fails, an entire branch of smart chargers will be disabled. Such problems have been observed in hierarchical road networks; in 2016, for instance, the Nipigon River Bridge in Canada sustained a partial failure, completely severing traffic between eastern and western Canada for several days. Because the Nipigon River Bridge was a key component in a road hierarchy, its failure caused a widespread problem.

Having a single or a small number of control centers for such a large system also presents a security vulnerability to the power grid. A malicious actor who gained access to the control center could send malicious control commands to the smart charging stations in order to destabilize the power grid, for example, by commanding all charging stations to immediately draw maximum power.

A solution to these issues arises from the field of *collaborative autonomy* (CA), also called collaborative intelligence. Collaborative autonomy comprises of techniques for distributed, networked, multi-agent systems to work together to solve problems autonomously. One can use collaborative autonomy to enable, for example, a group of autonomous vehicles to work together to travel safely at highway speeds; a group of search-and-rescue drones to collectively search for people trapped after natural disasters; or a group of computers to work together to watch for signs of cyber intrusions. Collaborative autonomy is particularly useful when no central controlling computer exists or communication with the central computer is slow or unreliable.

In our system, we will use the computational capabilities of the Electric Vehicle Supply Equipment (EVSE) that supply charging to PEVs to form the basis of our collaborative autonomy network. The EVSE will work together to find a feasible charging schedule for the PEVs attached to them.

Objectives

The primary objectives for FY 20 (Year 2) were to increase the flexibility and reliability of the computation while allowing cost minimization through enabling ancillary services. Both objectives build on our initial proposed alternating direction method of multipliers (ADMM) framework, completed in Year 1.

Our objective for reliability was to incorporate node failure, either through malice or misfortune, allowing the EVSE be removed from the system during computation of a schedule. This required modifications to the framework that are described in the Approach and Results sections. These modifications will also form the basis for further work in Year 3 to introduce redundant computation to counter malicious activity by individual nodes.

Our objective for enabling ancillary services was based on the introduction of having multiple administrative authorities, each managing a subset of the EVSE on the grid. The original framework allowed calculations to be done in a decentralized manner but assumed that charging stations were working together to converge on a solution for a single universal objective. In reality, since charging stations are owned by different entities, each entity will be motivated to control its charging stations in a way that minimizes costs for itself. Decisions must still be made in a way that ensures grid reliability. This problem can be thought of us a simultaneous multiplayer game, in which each player (set of charging stations controlled by a single entity) makes decisions to minimize its costs and ensure its vehicle customers are satisfied while working with its neighbors to ensure grid stability.

We will extend our ADMM framework to solve the multi-player vehicle charging station problem by iterating until a solution is found in which the grid is stable, and the players are content. Such a modification would be a contribution not only to the specific application of electric vehicle charging but to the study of solution algorithms for simultaneous games in general, as multi-player simultaneous games are known to be hard to solve, especially when an overarching social welfare objective is included, and would thus benefit from parallelization.

Approach

Our approach was to extend the work from Year 1 into a fully-decentralized algorithm for solving convex optimization problems with global coupling constraints. Specifically, our algorithm can solve problems of the form

$$\begin{aligned} \min_{x_i \in \mathcal{X}_i} \quad & \sum_{i=1}^I f_i(x_i) + \sum_{k=1}^K \max_{j \in \mathcal{J}(k)} \left(\sum_{i \in \mathcal{I}^g(k)} g_{i,j}(x_i) \right) \\ \text{s.t.} \quad & \sum_{i \in \mathcal{I}^h(l)} h_{i,l}(x_i) \leq B_l \quad l = 1, \dots, L, \end{aligned}$$

where x_i is the variable block associated with agent i ; \mathcal{X}_i , $i = 1, \dots, I$ is a closed convex set; f_i , $g_{i,j}$ and $h_{i,l}$ are convex functions; $\mathcal{J}(k)$, $k = 1, \dots, K$ is a partition of $\{1, \dots, I\}$; and $\mathcal{I}^g(k) \subseteq \{1, \dots, I\}$, $k = 1, \dots, K$ and $\mathcal{I}^h(l) \subseteq \{1, \dots, I\}$, $l = 1, \dots, L$. This problem structure is not particular to our formulation of the optimal EV charging problem. It arises in several variants of optimal EV charging.

Three key features of our approach are:

- It is failure tolerant; if agent i fails, or it is removed from the system due to security/cybersecurity considerations, the algorithm will find the solution to the problem without agent i , as long as the underlying communication network between continuing agents remains connected.
- Our algorithm is based on ADMM and it is mathematically equivalent, in terms of iterations, to the distributed approach of. Therefore, it finds the exact solution of the optimal EV charging problem.
- We incorporate reserve groups that combine multiple charging stations managed by a single administrative authority (such as a charge network operator (CNO)) into a resource that can provide Demand Response (DR), thus minimizing cost and helping to stabilize the distribution grid.

Our approach models the optimal EV charging problem from the perspective of charging station owners or operators, that is, we minimize the total electricity bill of all charging stations. The model assumes that when an EV arrives at a charging station, the EV tells the EVSE how long it plans to be connected and what its desired state of charge (SOC) is at the end of the connection period. At this time, we only assume one-way power flows in charging (V1G), although there are no assumptions in our model to prevent future extension to allow vehicle-to-grid (V2G) power flows. The implications of this are that EV cannot truly act as generators, but rather can only balance increases in demand elsewhere in the distribution grid by decreasing their own demand for a period of time. This is still sufficient to provide Demand Response (DR) services, as we shall see.

Figure II.2.4.1 presents a schematic of the charging infrastructure considered in this work.² Each *charging station* $s \in S$ is behind a certain *meter* $m(s) \in M$ (the point of connection with the distribution network), which in turn is connected to a certain *distribution feeder* $f \in F : s \in S(f)$. Charging station s buys electricity from the distribution network at the energy price at its corresponding meter, $\Pi^{\text{energy}}_{m(s)}$. The peak power drawn from the grid at meter m (by all stations in $S(m)$) over the horizon $T = \{1, \dots, T\}$ is priced at $\Pi_m^{\text{peak}} > 0$ and billed to the charging stations in $S(m)$. At the same time, each charging station s participates in a *reserve group* $g \in G : s \in S(g)$ which provides aggregated ancillary services to the grid. We focus only on spinning reserve, which is sold to the system by each reserve group at $\Pi_{g,t}^{\text{spin}}$ for intervals in $\{T^{\text{spin}} + 1, \dots, T\}$, where T^{spin} is the number of intervals between the last spinning reserve market clearing and realtime operation. For intervals in $\{1, \dots, T^{\text{spin}}\}$, the amount of spinning reserve to be provided has already been determined in previous runs of the scheduling process, and a penalty of $\Pi^{\text{fail}} > 0$ is billed to charging stations per unit of reserves they fail to provide.

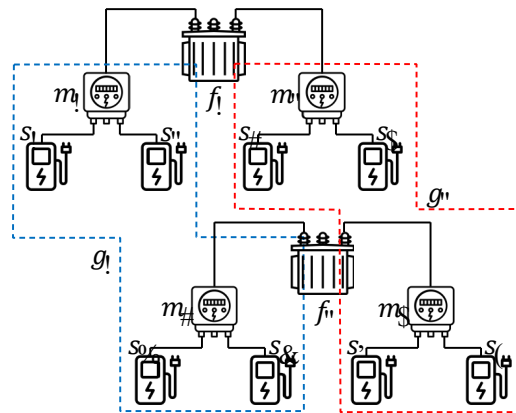


Figure II.2.4.1 Example topology of the charging infrastructure considered in this work. Here $S(m_1) = \{s_1, s_2\}$, $S(f_1) = \{s_1, s_2, s_3, s_4\}$, $S(g_1) = \{s_1, s_2, s_5, s_6\}$. Stations in different feeders can be part of the same reserve group.

Our approach computes schedules for each reserve group allowing it to decrease demand for a set period of time, and therefore to provide DR. For each interval t until the time horizon T , the spinning reserve for the group can be activated. This activation requires charging operations in later intervals to be adjusted to meet the target SOC of each EV before its scheduled disconnection time. Our charging schedules assume a worst-case approach, ensuring that no matter when a reserve group is activated, there will always be a feasible charging schedule to meet the target SOC for each EV connected to a charging station that is a member of the group.

The full details of the algorithm are described in our key publication [1], and an outline of the approach is as follows:

1. Each charging station solves a quadratic problem with linear constraints for its own load.

² Station, meter and transformer illustrations sourced from *Noun Project*, <https://thenounproject.com/>.

2. Do distributed sums
 - a. Capacity usage of stations under each feeder
 - b. Estimated peak power for all stations under each meter
 - c. Provision spinning reserve over all EVSE in the reserve group
3. Compute agreement subproblems
 - d. Solve capacity subproblem for each distribution feeder ($O(n)$)
 - e. Solve peak-power subproblem for each meter ($O(n \log n)$)
 - f. Solve reserve commitment for each reserve group ($O(n)$)
4. Update dual multipliers. If convergence is not yet reached, loop back to step 1.

Step 1, solving the charging station problem, is performed first. Steps 2 and 3 solve three subproblems in parallel. The first subproblem is determining the capacity usage of stations under a distribution feeder. The second subproblem is for peak power usage for all the stations behind a single meter. The third subproblem is computing a schedule for each reserve group's spinning reserve.³ Each subproblem has two steps: a distributed sum of values from each EVSE's individual computations in Step 1, followed by an agreement computation. If the resulting values are within the required global constraints, then the computation terminates; otherwise, another round of iteration ensues using values computed in step 4 to adjust each EVSE's planned charge level.

Results

We implemented our approach in C++ using Ipopt [12] and HSL [13] for solving the station-level subproblem (Step 1), and MPI [14] for communication in our experiments. We conducted our experiments on the Quartz cluster at LLNL, with 2 Intel Xeon E5 processors, with 36 cores and 128 GB of RAM per node. Our experiments used a symmetric topology (each feeder had an identical number of meters, and each meter had the same number of charging stations). Our charging stations had 4 EV charging ports, with 7 kW/port maximum capacity, with a station maximum of 18kW. Our charging schedules are computed for the next 24 hours, broken down into 64 total intervals: 24 5-minute periods (two hours), 24 15-minute periods (6 hours), and 16 1-hour periods. Vehicle arrivals, storage capacity (40 kWh to 70 kWh), maximum charge capability (5 kW to 7 kW), charge efficiency (90% to 100%) current SOC (15% to 45% of capacity), desired SOC (between current SOC and storage capacity, capped by maximum possible delivered charge over the charge duration), and charging duration (20 minutes to 8 hours) are randomly generated. EVSE are randomly assigned to spinning reserve groups. Using these parameters, we generated 10 instances each experiments with 36, 72, 144, 288, 576 and 1152 charging stations.

Our solution times are shown in Figure II.2.4.2. The times-to-solution remain within the 5-minute hard constraint imposed by real-time electricity market operations. Figure II.2.4.3 shows the parallel overhead. We tested the failure tolerance of our solution by simulating random failures of stations. Figure II.2.4.4 graphs the primal and dual residuals for runs of 288 stations with random failures. To maintain the same relative accuracy as the original tests after we lose a charging station, we recompute the primal and dual tolerances after each

³ All participating EVSE solve the meter and feeder-level problems; only a reserve group's EVSE solve the provisioning and commitment subproblems for the group.

iteration. Charging station failures appear in Figure II.2.4.4 as sharp increases in the primary and dual residuals. Our tests showed little increase in iteration count under station failure.

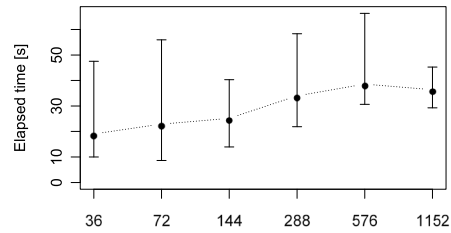


Figure II.2.4.2 Whiskers plot for solution times (wall clock) of our algorithm on all synthetic instances. Dots indicate median times over 10 instances for every charging station count.

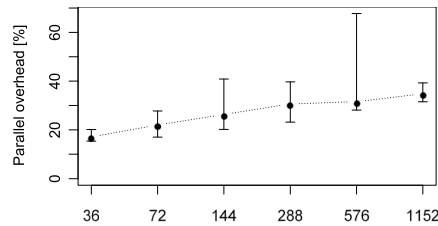


Figure II.2.4.3 Whiskers plot for parallel overhead of our algorithm on all synthetic instances. Dots indicate median overheads over 10 instances for every charging station count.

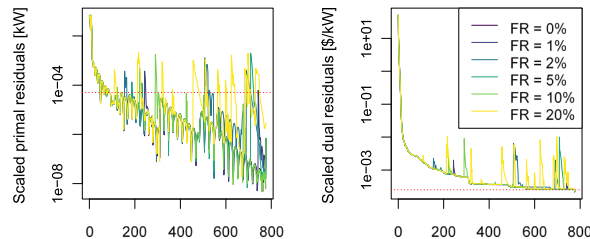


Figure II.2.4.4 Primal and dual residuals at each iteration for 288 stations, while simulating random failures with different failure rates (FR). Residuals scaled by $p|S| \times (2T + T_{\text{spin}})$. Tolerances indicated with a dashed red line.

Conclusions

Our work in FY 20 achieved our objectives of extending our ADMM-based, decentralized solution for managing charging of fleets of vehicles to include failure tolerance and support for cost minimization through the use of spinning reserve groups administered by competing charge network operators. This sets the stage for continued improvement in reliability through adding redundancy and the development of prototypes of smart EVSE running our software to facilitate grid integration in FY 21.

Key Publications

1. Ignacio Aravenas, Steve J. Chapin, and Colin Ponce. "Decentralized Failure-Tolerant Optimization of Electrical Vehicle Charging." Submitted to *IEEE Transactions on the Smart Grid*, 2020.

References

1. Agency, International Energy, "Global EV Outlook," 2017. [Online]. Available: <https://www.iea.org/publications/freepublications/publication/GlobalEVOutlook2017.pdf>.

2. J. Szczesny, "Sales of Electric Vehicles Growing Steadily in California," The Detroit Bureau, 11 Dec 2018. [Online]. Available: <https://www.thedetroitbureau.com/2018/12/sales-of-electric-vehicles-growing-steadily-in-california/>.
3. S. Deilami, A. S. Masoum, P. S. Moses and M. A. S. Masoum, "Real-Time Coordination of Plug-In Electric Vehicle Charging in Smart Grids to Minimize Power Losses and Improve Voltage Profile," Transactions on Smart Grid, vol. 2, no. 3, pp. 456-467, Sep 2011.
4. Z. Fan, "A Distributed Demand Response Algorithm and Its Application to PHEV Smart Charging in Smart Grids," Transactions on Smart Grids, vol. 3, no. 3, pp. 1280-1290, Sep 2012.
5. P. Zhang, K. Qian, C. Zhou, B. G. Stewart and D. M. Hepburn, "A Methodology for Optimization of Power Systems Demand Due to Electric Vehicle Charging Load," Transactions on Power Systems, vol. 27, no. 3, pp. 1628-1636, Aug 2012.
6. S. Shao, M. Pipattanasomporn and S. Rahman, "Demand Response as a Load Shaping Tool in an Intelligent Grid with Electric Vehicles," Transactions on Smart Grid, vol. 2, no. 4, pp. 624-631, Dec 2011.
7. P. Finn, C. Fitzpatrick and D. Conolly, "Demand-side Management of Electric Car Charging: Benefits for Consumer and Grid," Energy, vol. 42, no. 1, pp. 358-363, 2012.
8. R. Abousleiman and R. Scholer, "Smart Charging: System Design and Implementation for Interaction Between Plug-In Electric Vehicles and the Power Grid," Transactions on Transportation, vol. 1, no. 1, pp. 18-25, Jun 2015.
9. C. Wu, H. Mohsenian-Rad, J. Huang and J. Jatskevich, "PEV-Based Combined Frequency and Voltage Regulation for Smart Grid," in PES Innovative Smart Grid Technologies (ISGT), Washington, DC, 2012.
10. A. Y. S. Lam, K. C. Leung and V. O. K. Li, "Capacity Estimation for Vehicle-to-Grid Frequency Regulation Services with Smart Charging Mechanism," Transactions on Smart Grid, vol. 7, no. 1, pp. 156-166, Jan 2016.
11. A. Wachter and L. T. Biegler, "On the implementation of an interior-point filter line-search algorithm for large-scale nonlinear programming," Mathematical Prog., vol. 106, no. 1, pp. 25-57, 2006.
12. HSL, "A collection of fortran codes for large scale scientific computation," 2015. [Online]. Available: <http://www.hsl.rl.ac.uk/>
13. Message Passing Interface Forum, "MPI: a message-passing interface standard," June 2015, version 3.1. [Online]. Available: <https://www.mpiforum.org/docs/mpi-3.1/mpi31-report.pdf>
14. M. G. Vaya, G. Andersson, and S. Boyd, "Decentralized control of plug-in electric vehicles under driving uncertainty," in IEEE PES Innovative Smart Grid Technologies, Europe, 2014, pp. 1-6.

Acknowledgements

Thanks to Jon Donadee and Amy Musselman for developing the original solution in Year 1, to Colin Ponce for continued development of the underlying Skynet ADMM platform, and to Jovana Helms for assistance in project administration.

II.3 High Power Charging (HPC) Enabling Technologies

II.3.1 Fast Charging: Interoperability and Integration Technologies (Argonne National Laboratory)

Daniel Dobrzynski, Principal Investigator

Argonne National Laboratory
9700 South Cass Avenue
Lemont, IL 60439
ddobrzynski@anl.gov

Lee Slezak, DOE Program Manager

U.S. Department of Energy
Email: Lee.Slezak@ee.doe.gov

Start Date: October 1, 2018
Project Funding: \$800,000

End Date: September 30, 2020
DOE share: \$800,000

Non-DOE share: \$0

Project Introduction

This project addresses key enablers for fast charging, i.e., DC EVSE capable of delivering 150-350 kW, often referred to as extreme fast charging, or xFC. Argonne's areas of interest are testing and evaluation, focusing on EV-EVSE-network connectivity, interoperability and backward compatibility (i.e., the requirement to charge vehicles with a lower battery voltage and 50 kW maximum charge rate).

This is a cooperative project with industry; participation ranges from providing technical support for purchased EVSE to providing complete EVSE system(s) and supporting the testing. Argonne provides infrastructure modifications, hardware installation and testing at the Smart Energy Plaza. The project will provide data and insight to support standards and technology development for xFC implementation in the public domain and enable studies related to grid impacts, energy management and mitigation of peak power demands.

As part of the cooperative agreement between DoE and the European Commission's Joint Research Center (JRC) xFC EVSE systems are being tested at JRC and Argonne, utilizing specific capabilities of each lab, e.g., electromagnetic compatibility and network connectivity/communication, respectively.

Objectives

The objective is to identify issues associated with EV-EVSE-network connectivity, interoperability and backward compatibility. The project will also develop/verify interoperability test procedures for xFC in cooperation with JRC. Since xFC will be deployed in the public domain in support of DOE's objectives for vehicle fleet electrification, it is necessary to develop procedures to evaluate the functionality and interoperability of the systems.

ANL, in cooperation with industry, developed the requirements, procedures and test equipment for AC interoperability testing (i.e., the SAE J2953 standard). That knowledge was transferred to the joint activity with the Global InterOP team (the precursor of the Global Grid Integration Program) to develop a set of universal AC/DC requirements for verification testing in the US and Europe. This program will utilize that equipment and develop any new procedures deemed necessary.

Approach

The primary issue is to understand the ramifications of implementing xFC, with peak charging rates of 5 to 50 times current Level 2 AC EVSE. Considerations include the requirements of and implications for the infrastructure, communication/control requirements and standards for the EV-EVSE connection as well as the

grid interface. In addition, xFC must be incorporated in energy management strategies and integrated control schemes with other grid-connected devices (e.g., building energy management systems and battery storage).

The primary technical challenge is to assemble test hardware and implement a test program that covers the range of the vehicles that will utilize xFC systems, i.e., ranging from 50 kW @ ~400Vdc to 350 kW @ ~1000Vdc. Vehicles with 800-900-volt systems (i.e., due to battery charge current limitations) will not be readily available until at least MY 2020, necessitating the use of vehicle emulators for testing.

Additional challenges are the necessary infrastructure modifications and the installation of new dual 350 kW charging equipment due to the failure of the previously installed system to function according to the specifications, including electrical code violations and lack of certification in the US. The delivery and installation have been delayed further due to COVID-related delays at the equipment vendors.

Argonne proposed a phased testing program that aligns with the expected capabilities of vehicles over life of the project. Prior to high voltage EVs being available, Argonne will utilize its in-house emulator, a programmable source/sink that is capable of 170 kW and explore the benefits of incorporating available vehicles with 800-900 Vdc batteries (e.g., medium-duty trucks or buses).

The development and adoption of DC interoperability standards are still in process. However, since Argonne and its automotive partners participated in Global InterOP, which led the development of requirements for an AC/DC interoperability test tools for the US and Europe, the requirements and tools will be incorporated in this program.

The Global InterOP collaboration led to a series of testing requirements and procedures that were developed into testing libraries used by ScienLab and Keysight Technologies in the Keysight Charge Discovery System (CDS). ANL acquired the Keysight CDS system (Figure II.3.1.1), using laboratory funds, to complement the capabilities of the Comemso testing tool used in previous projects.

There were some issues with the Comemso tool due to its state of development and the detailed knowledge of the system required, resulting time-consuming testing with some inconclusive results. The Comemso test libraries were still under development, test cases were not automated, and instant test results were not provided. Despite these issues, the Comemso is an excellent tool for detailed diagnostics and will continue to be used in future projects.



Figure II.3.1.1 Keysight Charge Discovery System (CDS) Hardware

Results

200kW Charge System

The 200kW charge system was evaluated for connectivity, control and interoperability in FY 2019 and was documented in the FY 2019 annual report. Additional interoperability and conformance testing were carried out in FY 2020 using the Keysight CDS.

The BTC Power (BTCP) 200kW charging system was tested using Keysight's CDS SAE J2953/2 EVSE and DIN 70121 test libraries. Most of the automated test cases were completed successfully, while some were not executed due to errors in the DC emulation equipment software (which was still under Beta development). The results from the CDS corroborated results from 2019 using the Comemso testing tool. SLAC and non-SLAC communication was executed by the BTCP station in correct formats and within timing limits.



Figure II.3.1.2 Keysight CDS connected to BMW i3

When analyzing the EVSE in interoperability tests with multiple EVs in a man-in-the-middle testing mode the BTCP station had mixed results. There were some issues with various EVs when coupled with the Keysight CDS system. The BTCP station control pilot signal was vulnerable to noise as power increased in CCS cable and EV capacitance added to the charging system. The man-in-the-middle mode was successful using one CCS EV but did not work with another CCS EV.

Figure II.3.1.2 shows the BTCP station coupled to a CCS EV through the CDS in man-in-the-middle mode and Figure II.3.1.4 characterizes the noise on the Control Pilot signal (depicted by the green trace). This signal is extremely clean prior to the rise in current (red trace) and power (blue trace). The power transfer correlates with noise that begins to couple onto the Control Pilot signal and eventually the EV thresholds are exceeded, and the EV initiates a shutdown of the charge. In this example the EV and EVSE charge normally when the Keysight is de-coupled from the charge session; the assumption is that the extra cable length on the Keysight CDS is a factor when it is coming to Control Pilot noise coupling. However, when the Keysight CDS and EV are tested with other DCFC stations at ANL the issue is not apparent, and the control pilot signal remains clean. This could imply that the BTCP control pilot signal is particularly susceptible to coupled noise.

In the previous testing the EVs under test were limited to 50kW charging capability. The expectation is that as EVs with higher power capabilities enter the market there is heightened chance for control pilot noise to become an issue even when the Keysight CDS or some other Man-in-the-middle device is not inserted, especially for those EVSE that are showing noise susceptibility currently.

At these higher power levels test equipment like the Keysight CDS may not adequately find these issues since its addition would make session power transfer difficult. This would suggest an adapter-based analysis tool, such as DEVA, which is implemented in line without adding cable length, could be an elegant solution to eliminate the noise coupling factor.

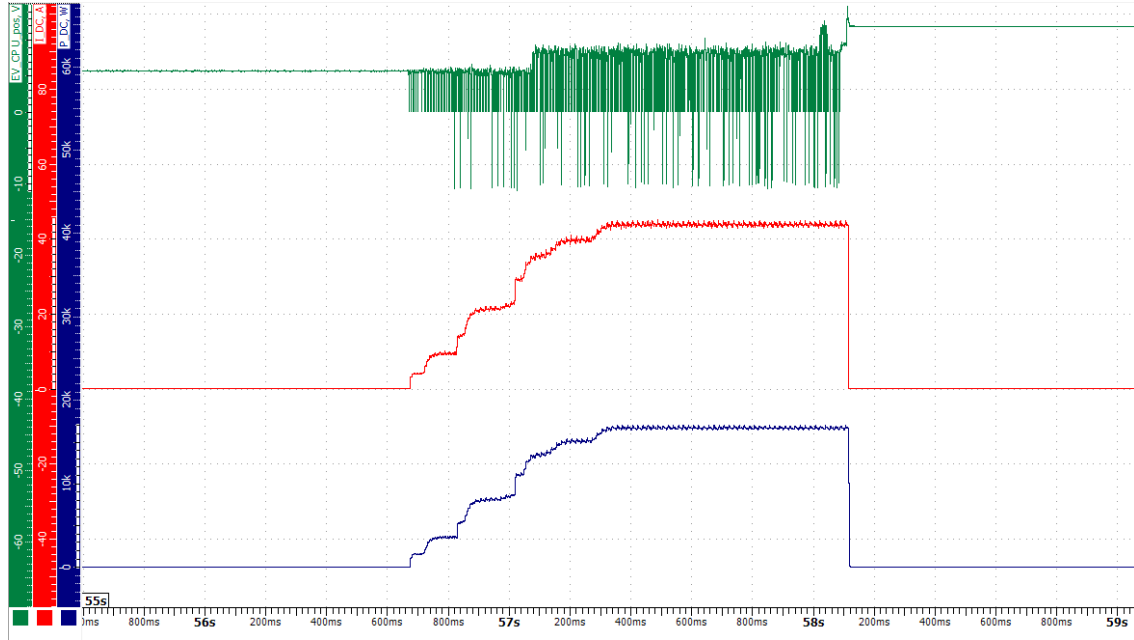


Figure II.3.1.3 BTCP 200kW - Keysight CDS Control Pilot Noise

Finally, the Keysight CDS did capture some SLAC PLC attenuation metrics. Figure II.3.1.4 depicts the normal attenuation levels of the various carriers within the PLC signal. It is important to note that these attenuation levels were captured before the power transfer phase of the session, so they are in normal range. There is no indication that power transfer interrupted PLC-based communication between the EVSE and CDS, however it would be reasonable to explore the PLC-based communication results when higher power levels are achieved in man-in-the-middle modes.



Figure II.3.1.4 BTCP 200kW - Keysight CDS PLC SLAC Attenuation

Dual350kWCharging System

The Porsche transformer and enclosure were removed in early FY 2020; this was complicated and time-consuming, requiring extensive interaction with Porsche Engineering management, Argonne Legal and Facilities Management.

A replacement system (dual 350 kW) was procured in FY 2019, requiring infrastructure modifications including a 2.5 MW transformer and switchgear. Delivery was expected in early FY 2020, but due to COVID-related delays at the vendors, the installation and commissioning have slipped to Q2 and Q3 FY 2021.

- The system will be paired with a Battery Energy Storage System (BESS) and integrated with CIP.io to support grid integration and peak power mitigation studies. A candidate BESS solution was identified that meets power (1 MW), energy (660 kWh) and communication requirements to support the Plaza and local grid. Argonne has initiated a lease agreement to allow for advances in battery technology and avoid issues of disposition after the project is complete.

Test Procedures and Equipment

Argonne has aligned its interoperability test procedures with those of our global testing partners. A significant portion of these procedures and test cases were developed in the Global Interop activity (the precursor to the Global Grid Integration Program (GGIP) that included OEM partners in the US and Germany, JRC (Ispra, IT location) and Argonne. This activity led to three companies in Germany developing interoperability test equipment. Both JRC and ANL currently use the Comemso EV Charging Analyzer (EVCA) and have developed proficiency in its use and capabilities.

The Keysight Charge Discovery System (CDS) was procured with Argonne funds and it was received in Q4 FY 2020; it adds SAE J2953 testing libraries, DC emulation, and insulation resistance monitoring features (TBD), complementing the capabilities of the Comemso system.

The CDS system is an automated conformance and interoperability test device for R&D as well as End-of-Line applications. It utilizes time synchronous measurements to decode communication and power signals. The CDS does have an extensive test case library that span various worldwide standards including SAE 2953(1/2), IEC 61851, DIN SPEC 70122, ISO 15118. These standards include TLS/Plug-n-Charge for AC and DC. The CDS custom testing software interface allows for easy setup and automation so that tests can be run and deciphered seamlessly. Test results and signal traces can be packages and output of the system to be deciphered in alternative formats such as .csv making the capture system agnostic to various software licenses.

Conclusions

Experience in Argonne's Fast Charging Enabling Technologies project indicates that high power charging systems and test equipment require further development to be considered (reliable) commodities. Argonne's lab partner, JRC, has found this to be the case as well. Argonne and JRC agree that one role of the labs is to uncover 'childhood diseases' in new technology and inform the manufacturer accordingly. But the global demand for high power charging is growing at a rapid pace ... charging technology and associated test equipment is expected to mature at a similar rate by necessity.

Argonne's xFC testing observations are based on experience with only two systems, one of which was not placed in operation. The 200 kW xFC system had a few technical issues early on, but when these issues were addressed by the manufacturer it was found to communicate according to the standards using an industry-standard interoperability test tool. And the results showed the EVSE to be backward compatible with EVs below 50 kW charge levels; the DC communication analysis showed consistent messaging and timing. The results also imply that integration of higher power charging stations in communication networks via OCPP should be accomplished with no more effort than lower power EVSE that communicate using OCPP.

- The project also demonstrated the need to continue efforts to formalize testing procedures and processes, e.g., implementation of (globally agreed upon) test libraries. The project has developed a

baseline for testing and evaluation that will be enhanced with the additional test libraries. The project will lead to a more comprehensive process as Argonne expands testing capabilities, further aligns procedures with JRC and gains access to additional xFC EVSE.

- **Future Work:**
- The procedures developed and testing equipment acquired for fast charging will support VTO projects for FY 2021 and beyond, including the ANL-led Lab Call ‘Assessment and Validation of Next Generation EVs HPC Profiles’ and the Exelon-led project ‘Demonstration of Utility Managed Smart Charging for Multiple Benefit Streams’.
- The ANL HPC Profiles project will require development of procedures to capture charge profiles that will include various EV and EVSE combinations. Working with the next generation of HPC capable EV and EVSE will likely result in some interoperability issues that warrant diagnostic and interoperability testing with the Comemso and/or Keysight CDS systems.
- The Exelon smart charging project will rely the ISO 15118 communication standard, so it will be critical to have the Keysight CDS ISO library to ensure that grid service messages are communicated and executed properly. Enabling technologies, including the ANL-developed Smart Charge Adapter, will be used in the project and the Comemso diagnostic suite will be critical in identifying issues encountered with various EV and EVSE.

II.3.2 High Power and Dynamic Wireless Charging of EVs (ORNL, INL, NREL)

Veda Prakash Galigekere, Principal Investigator

Oak Ridge National Laboratory
2360, Cherahala Boulevard
Knoxville, TN 37932
Email: galigekerevn@ornl.gov

Richard Carlson, Principal Investigator

Idaho National Laboratory
2525 North Fremont Avenue
Idaho Falls, ID 83415
Email: richard.carlson@in.gov

Andrew Meintz, Principal Investigator

National Renewable Energy Laboratory
15013 Denver West Parkway
Golden, CO 80401
Email: andrew.meintz@nrel.gov

Burak Ozpineci, Vehicle and Mobility Systems Research Section, Section Head and ORNL Program Manager

Oak Ridge National Laboratory, Vehicle Systems Research Group
National Transportation Research Center, 2360 Cherahala Boulevard
Knoxville, TN 37932
Email: burak@ornl.gov

Lee Slezak, DOE Technology Manager

U.S. Department of Energy
Email: Lee.Slezak@ee.doe.gov

Start Date: October 1, 2019
Project Funding: \$4,000,000

End Date: September 30, 2021

DOE share: \$4,000,000 Non-DOE share: \$0

Project Introduction

Dynamic charging of electric vehicles (EVs) can significantly alleviate or eliminate range anxiety while concurrently reducing the required on-board battery capacity. Current state-of-the-art light duty dynamic wireless EV charging prototypes are limited in power level to approximately 20 kW. This leads to significant portion of the roadway to be electrified to achieve charge balanced mode of operation. It was previously determined that for light-duty (LD) vehicles to achieve charge balancing mode of operation on primary roadways (between cities) with minimal infrastructure cost, power transfer levels in the range of 200 kW are required. The study is extended to include intracity travel, and the optimal form for range extension for LD EVs is analyzed.

For a nominal dynamic power transfer level of 200 kW, optimal system architecture including power electronics and power transfer couplers are identified to enable efficient transfer and accurate control of power for speeds indicative of real-world usage. The implications of embedding couplers in the roadway are analyzed and a suitable coupler system and power electronics are designed, developed, and laboratory characterization is carried out. Electromagnetic emissions and the required shielding solutions to ensure a safe high power dynamic wireless charging system are also developed. Necessary enabling technologies such as alignment,

data acquisition, and communication systems are being developed to realize a practicable vehicle integrated 200 kW dynamic EV charging system.

Objectives

The overall goals and objectives are

1. Design, develop and perform preliminary benchtop characterization of 200 kW+ dynamic wireless EV charging system suitable for vehicle integration
 - a. Identify optimal architecture to enable 200 kW vehicle integrated high power dynamic wireless charging
 - b. Design, develop, and assemble optimized power electronics and couplers suitable for 200 kW+ vehicle integrated dynamic wireless EV charging system.
 - c. Perform benchtop characterization of the coupler and power electronics to serve as preliminary validation for 200 kW power transfer capability.
2. Analyze the benefits of high-power dynamic wireless charging on LD EVs as applied to intercity travel
 - d. Develop a tool to evaluate the large-scale deployment of DWPT systems using real road network and real-world vehicle travel data
 - e. Explore the feasibility of large-scale deployment of DWPT systems on primary roadways in Atlanta for LD vehicles using real road network from TomTom database and real-world travel data from TSDC database, considering
 - Different DWPT system designs,
 - Different system placements techniques (uniform and optimized), and
 - Different vehicle models.
3. Develop novel shielding and data acquisition techniques necessary for safe and optimal deployment of vehicle integrated 200 kW high power dynamic wireless EV charging system.

Approach

Optimal Architecture Selection, and Design and Development of Power Electronics

Overall power electronics architecture capable of transferring 200 kW+ dynamically is identified with the objective of enabling optimal power density, and fast and accurate control necessary for regulated EV charging at speeds greater than 55 mph. For a given power transfer level, the dimension and mass of the receiver coil is inversely proportional to operation frequency, consequently 85 kHz was selected (over 22 kHz or 40 kHz) [1]. This also leads to reduced filter capacitor requirements thereby further improving the power density [2]. A high-level depiction of the proposed 200 kW dynamic wireless EV charging system is shown in Figure II.3.2.1, It consists of two primary side parallel high-frequency (HF) inverters, LCC primary resonant network, transmitter coil, vehicle coil, secondary series resonant capacitor, secondary HF rectifier, DC-DC buck converter, output filter and the vehicle battery.

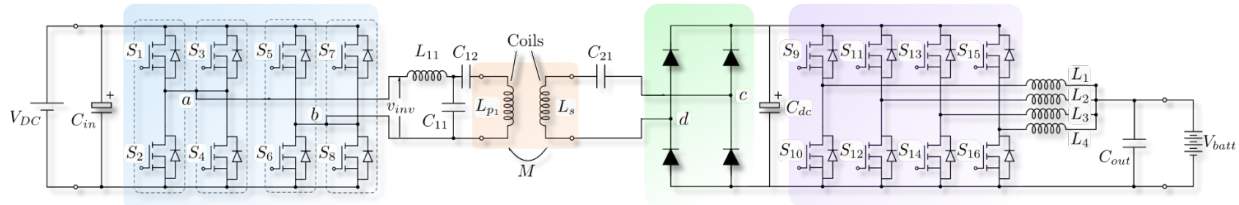


Figure II.3.2.1 Proposed optimized architecture to enable 200 kW+ dynamic wireless EV charging.

Based on the identified architecture, the power electronics inverter, rectifier, and dc-dc converter are set a design target to operate at 800 V and up to 85 kHz. For the specified operating conditions, three possible Silicon carbide (SiC) SiC phase leg modules were identified: CAB450M12XM3 (1200 V 450 A), CAB400M12XM3 (1200 V 400 A), CAS325M12HM2 (1200 V 325 A). Based on simulation and analytical studies it was identified that the primary side HF inverter has the worst-case operating conditions, hence loss analysis was performed for the three modules for single module per leg and two paralleled modules per leg approach. The summary of the loss analyses is shown in Table II.3.2.1. Figure II.3.2.2

Table II.3.2.1 Summary of loss analysis of power semiconductor modules for 200 kW+ operation at 85 kHz.

	CAB450M12XM3		CAB400M12XM3		CAS325M12HM2	
Modules in parallel	1	2	1	2	1	2
Total Loss (kW)	4.144	3.879	2.571	2.025	2.299	1.821
Inverter Efficiency	0.983	0.984	0.989	0.991	0.990	0.992

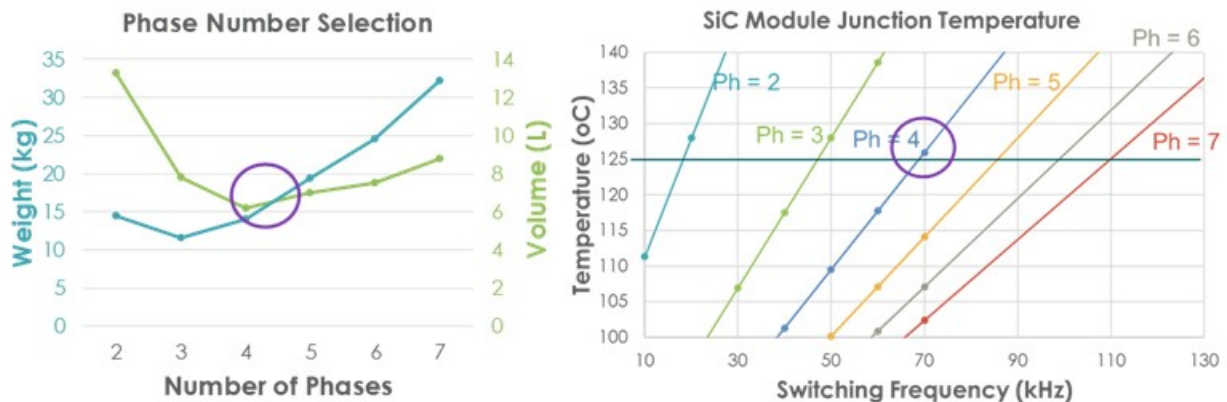


Figure II.3.2.2 Weight and volume of secondary side DC-DC converter including the power electronics and the filter components as a function of number of phases and Junction temperature as a function of switching frequency and number of phases for secondary side dc-dc converter.

High performance decoupling capacitor should be optimally selected and placed as near to the module as possible with minimal impedance in between the capacitor and the module to supply the energy required for the HF switching (85 kHz) with short switching transitions (< 50 ns). A detailed simulation study was conducted to estimate the magnitude and frequency component of the current ripple that the decoupling capacitor should be able to supply to realize efficient and safe 85 kHz operation. It was found from the simulation studies that there is a considerably higher frequency component to the inverter input current (~ 5 A at 1 MHz). CAS325M12HM2, 1200 V, 5 nH package Wolfspeed SiC phase leg module and B5803319505M001 5 μ F, 1300 V CeraLink Capacitor is selected for the power electronics building block

(phase leg module) for the primary side HF inverter, secondary side HF rectifier, and the secondary side DC-DC converter. An optimization study was conducted to identify the optimal number of parallel phases of the DC-DC converter and the switching frequency leading to an overall minimal mass and volume without compromising efficiency. Figure II.3.2.3

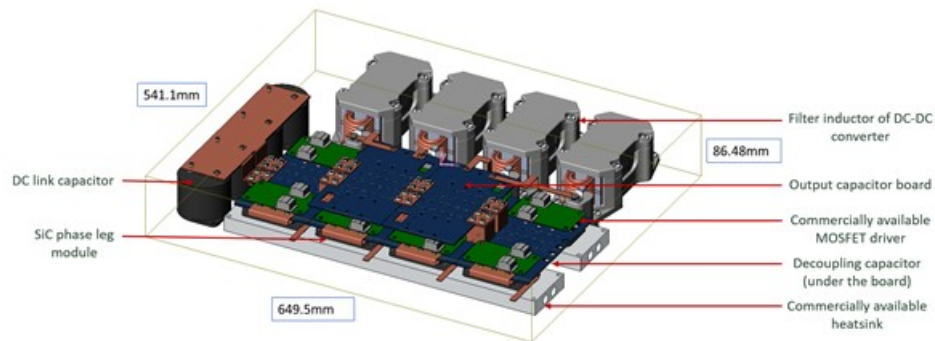


Figure II.3.2.3 CAD model of the vehicle side high frequency rectifier and secondary side dc-dc converter.

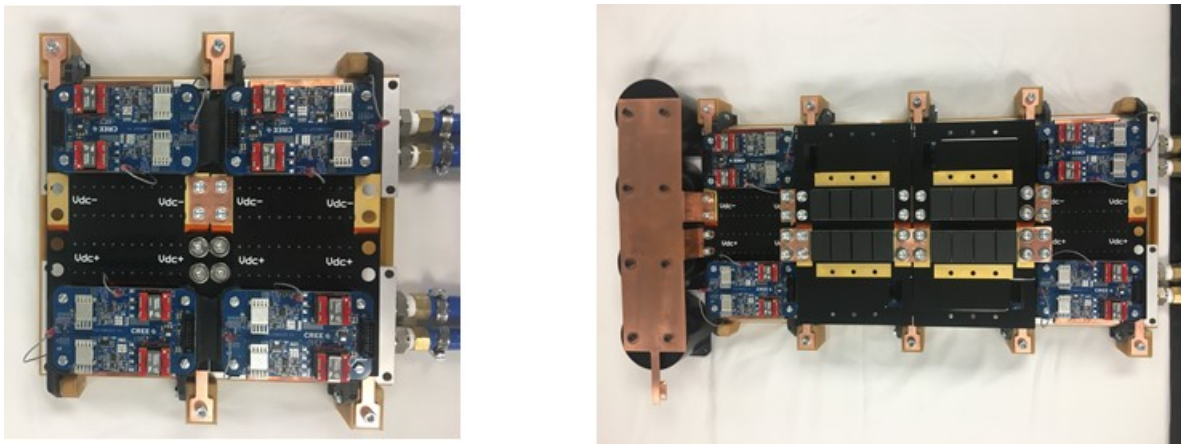


Figure II.3.2.4 Prototypes of optimized primary side SiC based high frequency (85 kHz) inverter and optimized vehicle side high frequency rectifier and dc-dc converter.

Figure II.3.2.3 depicts the CAD model of the vehicle side rectifier and dc-dc converter. Figure II.3.2.4 shows the prototypes of SiC module based 200 kW+ primary side HF inverter (left) and the optimized SiC based vehicle side rectifier and dc-dc converter (right).

Design and Development of Optimized Couplers for 200 kW+ Dynamic Wireless EV Charging

The development of couplers envisaged a long transmitter coil comparable to the length of a LD EV and a 200-kW vehicle receiver optimized to fit under a LD EV. The width of the transmitters was limited to 12' to match the assumed lane width. This allows for deploying the DWPT by square precast concrete blocks or provides accommodation for expansion joints if the couplers were directly buried. The target vehicle is a Hyundai Kona having a wheelbase of 102.4" and trackwidth of 62". All ground and vehicle electromagnetic coupler designs were constrained to fit within the smallest area bounded by the tires of the vehicle. We also assume that the surface of the ground couplers are buried 4" beneath the surface of the pavement. Assuming a minimum ground clearance of 6" for the vehicle couplers, the total coupler surface-to-surface airgap is 10". The couplers are designed to transfer 230 kW with ground side and vehicle DC-link voltages of 800 V and primary side LCC and secondary side series tuning. Specific design constraints on the ground coupler force the vehicle coupler to be larger than for an equivalent power stationary WPT system. Horizontal gaps between the ground coupler ferrites and windings provide enough space for ½" diameter fiberglass rebar embedded vertically to assist in transferring shear loads from the pavement surface to below the ferrite. Vertical spacing between the

ferrite and coils allows enough space for horizontal rebar for additional reinforcement and load transfer between pavement sections.

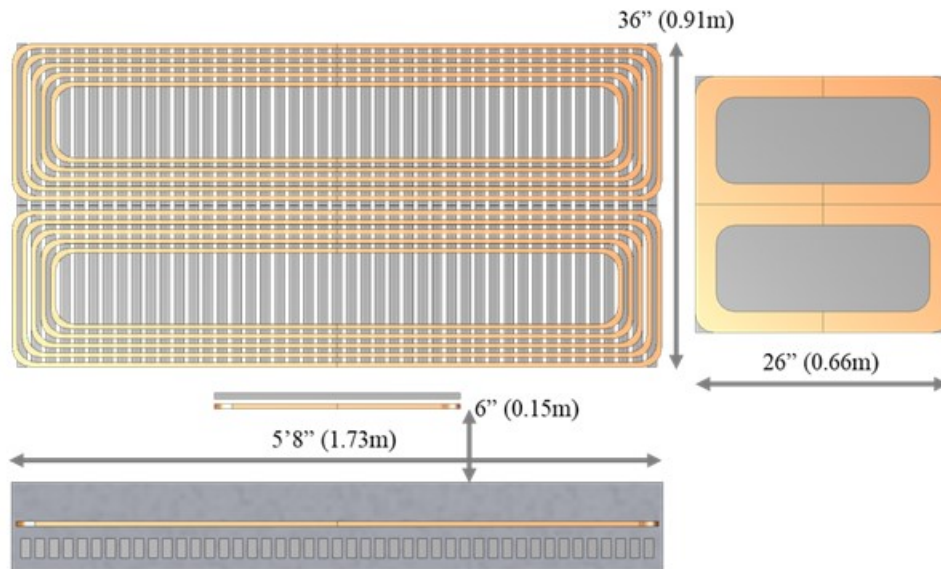


Figure II.3.2.5 Top view of the ground coupler (top left) and vehicle coupler (top right); images are to scale. Side view of the ground coupler showing the surrounding concrete and vehicle ground clearance (bottom).

Thermal constraints also limit the number of amp-turns on the ground coupler and maximum flux density in the ferrites. Figure II.3.2.6 shows the simulated steady-state temperature distribution on the pavement surface and through the roadway cross section assuming an ambient temperature of 55C. The design was constrained to limit the maximum hot-spot temperature to 100C. It is important to note that this simulation assumes 100% up-time for the ground coupler.

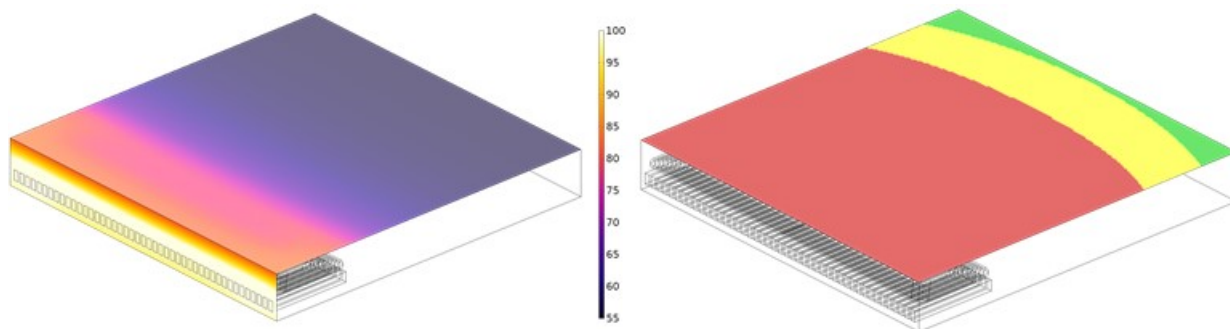


Figure II.3.2.6 Thermal analysis of DWPT system embedded in concrete with ambient temperature of 55C for half lane of 6' width (left), Map of critical electromagnetic field emission regions on the surface of the roadway; Green – below 15uTrms, Yellow – between 15uTrms and 27uTrms; Red – Above 27uTrms (right).

Figure II.3.2.6 also shows a map of the critical regions for electromagnetic field emissions just above the surface of the pavement. Half of the 12' wide lane is depicted. The transmitter meets the ICNIRP and SAEJ2954 specifications for pacemaker safety of 15uTrms at the lane boundary. This indicates that high-power DWPT systems can be safely implemented in HOV lanes without causing safety concerns for adjacent vehicles.

Finite-element analysis of a system with four ground-side transmitters and one vehicle side receiver was analyzed in COMSOL to derive the position dependent inductances and losses of the system. A particularly important aspect of this model was the inclusion of a model of the vehicle (based on approximate dimensions

of the Hyundai Kona) to estimate the losses due to the presence of ferromagnetic material in the chassis. A cross section of the model is shown in Figure II.3.2.7.

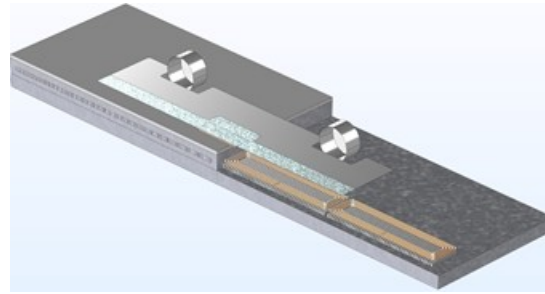


Figure II.3.2.7 Cross section of the DWPT system model with four transmitters, one receiver, and vehicle chassis and wheel model. The vehicle chassis and wheels are assumed to be a standard structural steel. A thin aluminum strip runs down the center of the vehicle frame to reduce the losses in the most prone regions.

This model has a small aluminum strip running down the center of the vehicle chassis. Assuming that the undercarriage is a flat plate of steel and no shielding – the worst-case scenario – this model predicts chassis losses of 20kW or about 10% of rated system power. The thin aluminum strip reduces the losses to a more manageable 2kW. The assumption on the geometry of the vehicle undercarriage is rather coarse, but it indicates the importance of shielding to system efficiency.

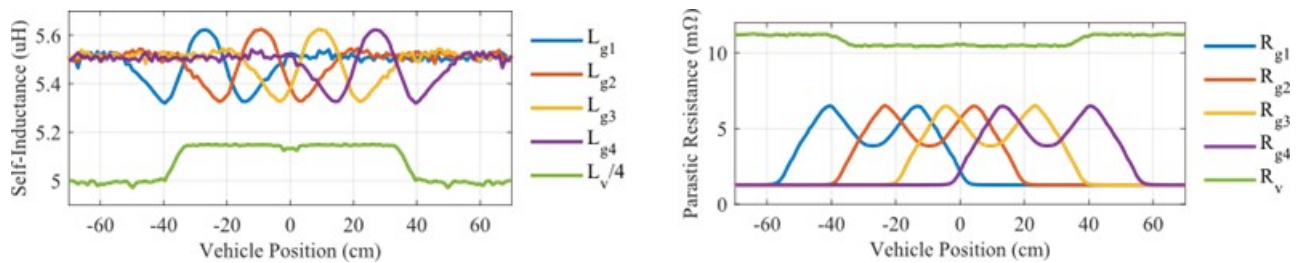


Figure II.3.2.8 (Left) Ground and vehicle coil self-inductances, (right) ground and vehicle coupler parasitic resistances.

The position dependent parameters are shown in Figure II.3.2.8. Movement of the vehicle causes the transmitter self-inductances to oscillate above and below the inductance value when the vehicle is far away. The decrease in inductance is caused by interference of the vehicle chassis with the magnetic fields created by the transmitter. The increase is caused by the reduced reluctance of the magnetic circuit when the receiver ferrite is aligned with a given transmitter. The receiver self-inductance increases for the same reason. The resonant network analysis was carried out including the effects of variation of self-inductance and parasitic resistance as a function of vehicle position. Figure II.3.2.9. shows the CAD model of the ground side and vehicle coupler designed for 200 kW dynamic EV charging.

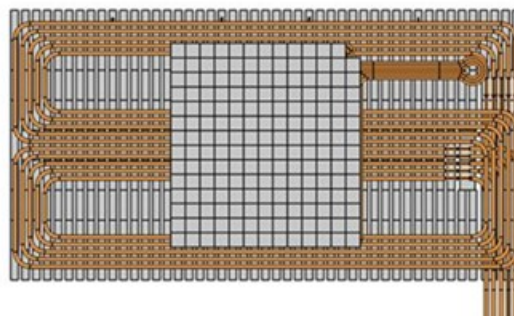


Figure II.3.2.9 CAD model of designed 200 kW ground-side and vehicle-side couplers with 11' separation (top view).

Analysis of Impact of High-Power Dynamic Wireless Charging on Intracity Travel

A unique test platform for analyzing the large-scale deployment of DWPT system on roadways is developed, as depicted in Figure II.3.2.10. The goal is to use the tool to understand the contribution of a DWPT system on primary roadways toward the driving range of LD EVs intracity travels. In addition, it helps to identify the best placement for the system that enables charge-sustaining operation for the entire fleet and enhances the range contribution to the intracity travel for each vehicle. The tool incorporates real road network, real-world travel data, a vehicle powertrain model, a DWPT charger power model, and a management algorithm.

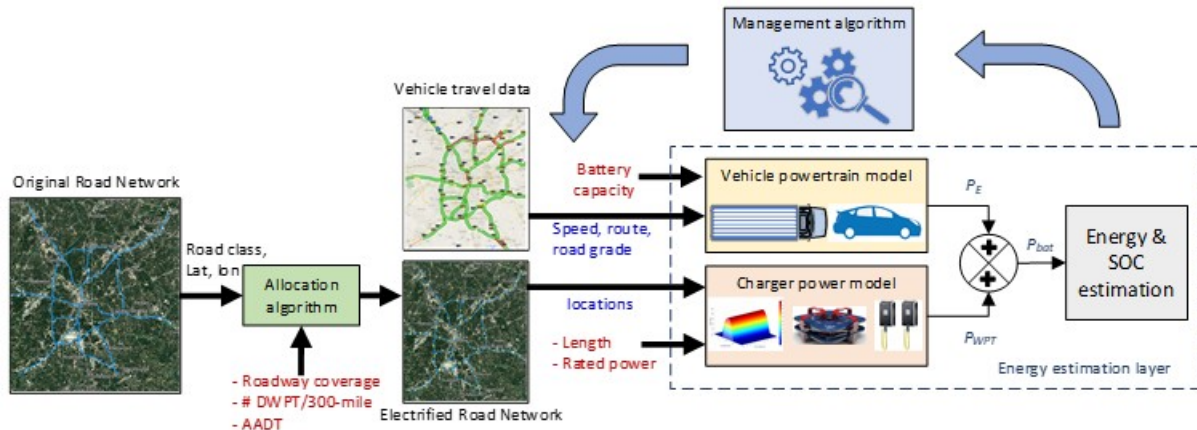


Figure II.3.2.10 Block diagram of test platform for large-scale deployment of DWPT system on roadways.

The actual primary road network in Atlanta as represented in the TomTom database by classes 0 and 1 is considered for this study. In this study, around 285 miles of primary roadway around Atlanta are considered for electrification with DWPT system. In addition, NREL's team incorporates real-world travel data in Atlanta for LD vehicles from NREL's TSDC database [7]. The data includes around 26 million data points in Atlanta, which represents around 1,585 vehicles (6,749 24-h tours) and over 251,000 miles traveled. Uncertainty in the vehicle efficiency is considered by developing two LD vehicle powertrain models using NREL's FASTSim tool [8], to represent a compact vehicle (high efficiency) and a heavy SUV-type vehicle (low efficiency).

Three DWPT system designs from FY19 work are evaluated in this analysis, which are indicated in Table II.3.2.2. For each design, placement of DWPT system on roadways is explored using two approaches: a) *Uniform placement*, in which DWPT segments are placed at equal distances with the same length at each location, and the number of positions per 300-mile of the road is swept from 20 to 100, and b) *Optimized placement*, in which the locations and length of DWPT segments vary based on the annual average daily traffic (AADT) data published by the federal highway administration (FHWA) [9].

Table II.3.2.2 DWPT system designs under test based on FY19 feasibility analysis.

	DWPT1	DWPT2	DWPT3
Approach	- CS on primary roadways, - minimum road coverage, - low travel requirements (65 mph, 270 Wh/mile)	- CS on primary roadways, - min overall system cost, - high travel requirements (86 mph, 350 Wh/mile)	- CS on primary roadways, - min overall system cost, - medium travel requirements (74 mph, 310 Wh/mile)
Battery size (kWh)	59	30	30
Charging power, P_c, (kW)	235	225	200
Road coverage (%)	8.2	16.6	14.56
Min. # DWPT/300 miles	7	15	13

Shielding and Data Acquisition Techniques for High Power Dynamic Wireless EV Charging

Using advanced magnetics 3-D finite element modeling tools, new EM-field mitigation solutions and designs can be designed and evaluated for performance and effectiveness. Additionally, laboratory hardware testing and evaluation are used to validate the modeling results therefore providing high levels of confidence in the effectiveness of future designs developed via modeling and simulation methods. Data acquisition requirements and methodologies are developed using the anticipated electrical parameters and performance design considerations. Due to the vehicle speed during power transfer for in-motion dWPT, i.e., 70mph vehicle speed, the data acquisition system must have very high sampling rate capabilities to accurately capture the electrical, magnetic, and power transfer performance of the dWPT system. The design approach in this task includes using commercially available sensors, meters, and data acquisition tools to minimize costs and accelerate development time.

Results

Validation of High Frequency Power Electronics

Primary-side inverter, secondary-side rectifier, and dc-dc converter are all assembled by paralleling individual H Bridge modules, which are obtained by paralleling the DC+ and DC- outputs of two modules and extracting the output from the midpoints of the phase leg modules. One H bridge configuration or the power electronics building block is configured and experimentally verified for voltage withstanding capability, switching behavior, power conversion efficiency, and evaluated for the existence of any temperature hot spots. The assembled power electronics building for the power electronic systems of high power and dynamic wireless EV charging system is shown in Figure II.3.2.11.

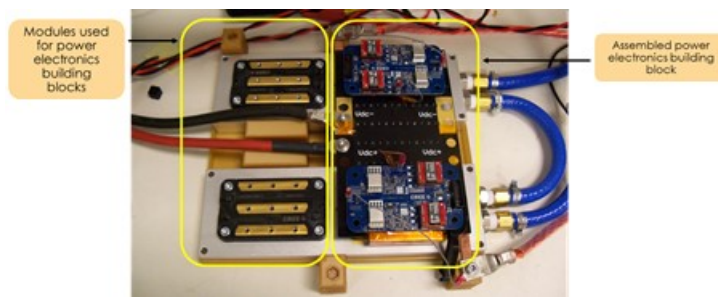


Figure II.3.2.11 Assembled power electronics building block of 200 kW+ dynamic wireless charging system.

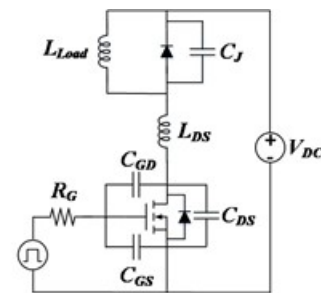


Figure II.3.2.12 Standard double pulse test setup wherein the device under test is the bottom MOSFET.

Power electronics hardware validation of the building block is carried out in the following steps:

- Double-pulse test – this is a standard test conducted to evaluate important parameters associated with switching behavior such as current turn-off time and voltage overshoot caused by the resonance of MOSFET output capacitance and package parasitic inductance. The schematic for the double-pulse test is shown in Figure II.3.2.12.
- Continuous power test – power electronic building block will be tested in a resonant inverter mode at rated voltage (800 V) and 85 kHz to measure efficiency and temperature rise to ensure safe and efficient operation when implemented with WPT couplers.

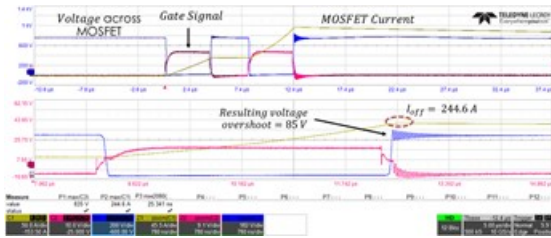


Figure II.3.2.13 Standard double pulse test setup wherein the device under test is the bottom MOSFET.

Double-pulse Test: In this test, two switching pulses are given at the required voltage to recreate the operating conditions of the designed system at the rated operating voltage and current. This gives a way to evaluate the switching behavior at the rated conditions before subjecting it to actual high-power validation. Per the envisaged operating condition, the upper bound of the MOSFET DC voltage is ~ 750 V, and turn-off current is ~ 250 A. The L_{Load} inductor value and the duty-cycle of the bottom MOSFET (device under test) were varied to practically realize a turn-off current of 244 A at 750 V DC. The

resulting voltage overshoot was measured to be 85 V over the 750 V DC link. This gives ample margin to the maximum device rating of 1200 V. The experimental results are shown in Figure II.3.2.13.

Continuous power test: the objective is to validate the building block power electronics as a HF inverter. High frequency polypropylene capacitors available in the lab were configured to obtain a resonant capacitance of 1 μ F, and Litz wire-based air core inductor was included to obtain a resonant frequency of ~ 85 kHz. The inverter and the LC resonant network were connected to a previously validated HF rectifier, and a resistive load bank in parallel with an NHR 9300 1200 V/100kW electronic load. Experimentally obtained input voltage, output voltage, output current, and MOSFET terminal voltage (drain-to-source) at 80 kW continuous operation is shown in Figure II.3.2.15. From Figure II.3.2.15, the measured overall system efficiency at 85.22 kW output is 98.6 %. This includes the losses in the resonant capacitor, wires and terminations, and the HF rectifier. It is plausible that the inverter efficiency is > 99 %.

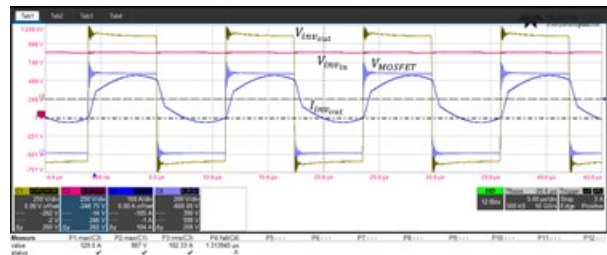


Figure II.3.2.14 Experimentally obtained input voltage, output voltage, output current, and MOSFET terminal voltage (drain-to-source) at 80 kW continuous operation.

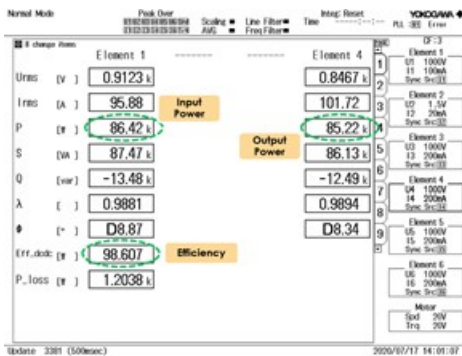


Figure II.3.2.15 Measured input and output voltage, current, power, and overall efficiency of HF power electronics resonant inverter-rectifier assembly at 85.2 kW output power.

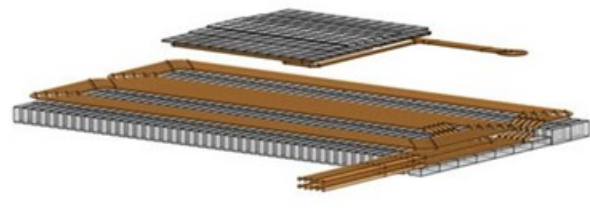


Figure II.3.2.16 FEA Simulation model of 200 kW+ dynamic wireless EV charging system.

Characterization of High Power Dynamic EV Charging Couplers by Simulation and Measurement

The FEA simulation model shown in Figure II.3.2.16 was setup to recreate the vehicle movement and the receiver coil traversed the length of the coil at a coil-to-coil distance of 11 inches. The receiver coil is envisaged to travel from left to right, and the coupler inductances and coupling coefficient is obtained at several points along the span of 2.43 m, thereby generating a profile of mutual inductance. The mutual inductance profile is used in PLECS circuit simulation platform to verify the power transfer capability for a baseline speed of 55 mph. Figure II.3.2.17 shows the inter coupler mutual inductance M , input power, and

output power as a function of the vehicle position. It can be seen from Figure II.3.2.3 that the output power smoothly ramps up and reaches 240 kW when the receiver coil is over the transmitter. The circuit simulation indicates power transfer capability up to 240 kW. Power transfer level beyond 200 kW is not evaluated as the current density in the receiver coil is anticipated to reach a maximum allowed value at ~ 200 kW. This gives considerable buffer for intended continuous operation at 200 kW.

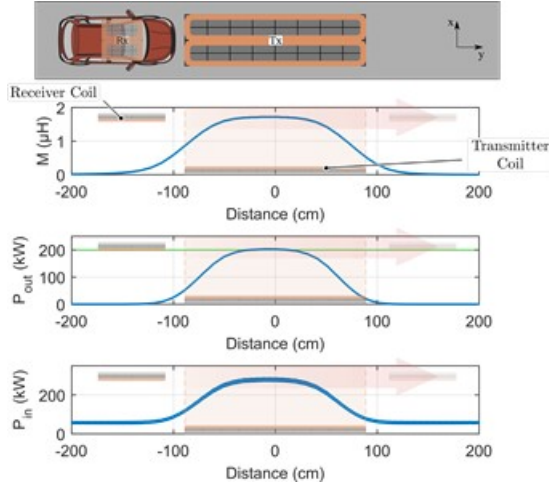


Figure II.3.2.17 Mutual inductance obtained by FEA simulation, input power and output power of the dynamic wireless EV charging system obtained by circuit simulation.



Figure II.3.2.18 Experimental setup for characterization of 200 kW+ dynamic charging transmitter and receiver coils with 11-inch spacers.

Figure II.3.2.18 shows the receiver coil placed over the transmitter coil with spacers for ~ 11 inches. The ground coil, vehicle coil, and mutual inductances (M) were measured using LCR meter Agilent E480A. The characterization was performed at 85 kHz. Table II.3.2.3. presents the coil and mutual inductances obtained by FEA simulation and measurement. From Table II.3.2.3. it can be observed that the measured GA coil and mutual inductances are less than the corresponding values obtained by FEA simulation. This can be attributed to the fact that the leads from the primary side transmitter is approximately 5 m in length. This is to enable the connection of transmitter to the ground side power electronics placed in the roadside unit. This lead is not accounted for in the FEA simulation model.

Table II.3.2.3 Coupler parameters obtained by FEA simulation and laboratory characterization for the centrally aligned case

Parameter	Text	Text
Ground Coil Inductance (μH)	5.5	8.2
Vehicle Coil Inductance (μH)	21.8	20.6
Mutual Inductance (μH)	1.4	1.7

Impact of High-Power Dynamic Wireless Charging on Intracity Travel

Sample results of analyzing 5 cases of uniform placement of DWPT charging locations at {20, 40, ..., 100} DWPT/300-mi distributions on primary roadways in Atlanta are presented in Figure II.3.2.19–Figure II.3.2.24. and Table II.3.2.4. Figure II.3.2.19. and Figure II.3.2.20. show the distribution of driving ranges of light and heavy LD vehicle models considering DWPT2, as an example. As noted, the 40 DWPT/300-mi distribution shows the best performance for both light and heavy vehicle models by providing the highest contribution driving range extension.

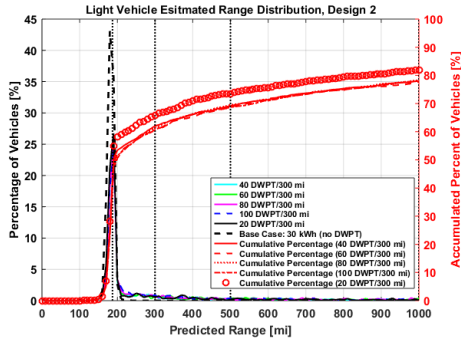


Figure II.3.2.19 Distribution of driving range of light vehicle model with and without DWPT2.

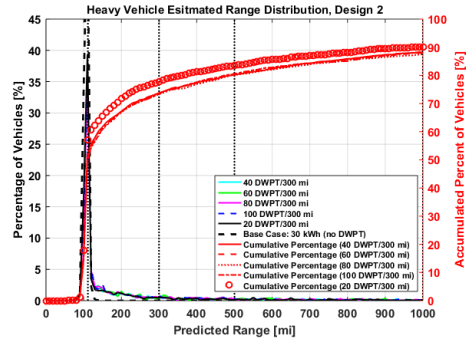


Figure II.3.2.20 Distribution of driving range of heavy vehicle model with and without DWPT2.

Range extension ratio (RER), which is the new range relative to the original range, is estimated for all designs with 40 DWPT/300-mi case and compared in Figure II.3.2.21. and Figure II.3.2.22. and Table II.3.2.4. As shown, with DWPT2, more vehicles realize high range extension followed by DWPT3 and DWPT1. The results show that in addition to the ability of DWPT2 system to provides near 100% charge-sustaining for inter-city travels, it has the potential to contribute significantly to intracity travels by allowing around 25% of vehicles to realize more than a 500-mile range compared to a 150-mile range without the system and approximately 17% exceeds a 1000-mile range. Average power and energy profiles for all DWPT system designs with a 40 DWPT/300-mi distribution are presented in Figure II.3.2.23. and Figure II.3.2.24. The figures show power profiles that match with a traffic-flow profile with peak demand in the morning and evening. Heavy vehicle models consume more energy and show higher power demand. Designs with higher roadway coverage show higher power and energy demand due to serving more travel.

Table II.3.2.4 Driving range evaluation for different designs with 40 DWPT/300-mi.

Design	Light vehicle			Heavy vehicle			Average		
	DWPT1	DWPT2	DWPT3	DWPT1	DWPT2	DWPT3	DWPT1	DWPT2	DWPT3
Average base range (mile)	347	187	187	211.5	111.3	111.3	279.25	149.2	149.2
Vehicles > 500 mi (%)	34.86	30.42	29.48	16.01	19.43	15.96	25.44	24.93	22.72
Vehicles > 1000 mi (%)	21.06	21.98	19.91	7.03	11.68	8.67	14	16.83	14.29
Vehicles > 2 base range (%)	29.55	35.24	33.31	19.59	30.72	28.33	24.57	32.98	30.82
Vehicles > 4 base range (%)	17.38	26	24.22	8.85	21.4	17.24	13.115	23.7	20.73
Vehicles > 6 base range (%)	12.04	20.85	19.13	5	16.61	12.1	8.52	18.73	15.62

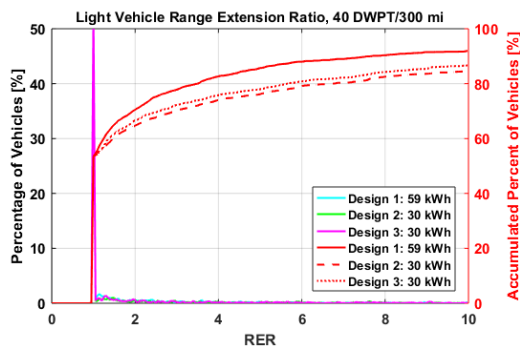


Figure II.3.2.21 RER for light vehicle model with all designs

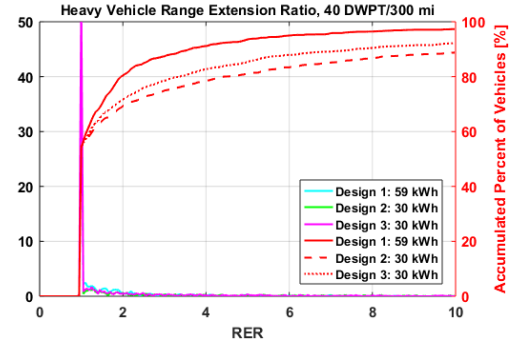


Figure II.3.2.22 RER for heavy vehicle model with all designs

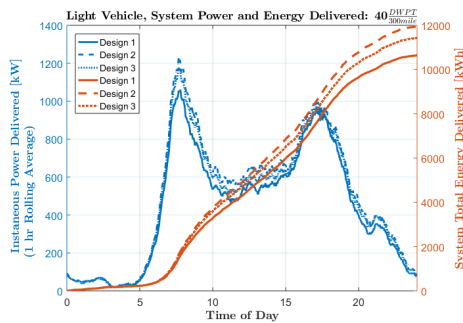


Figure II.3.2.23 24-h average power and energy profiles for the entire DWPT system for all designs with 40 DWPT/300-mi, and light vehicle model

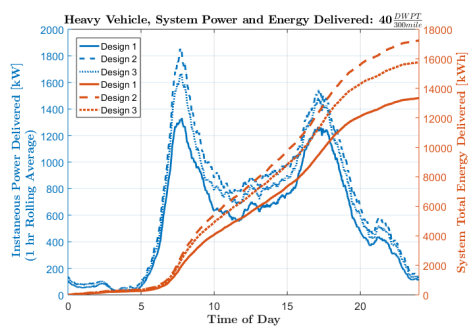


Figure II.3.2.24 24-h average power and energy profiles for the entire DWPT system for all designs with 40 DWPT/300-mi, and heavy vehicle model

EM-field Shaping and Shielding Solutions

FEA based software tools were utilized in developing models and advanced shielding solutions to ensure compliance to industry standard of 15 μ T in the vicinity of the couplers for various misalignment conditions. Figure II.3.2.25 shows the baseline WPT design and the WPT system with the final proposed EM field shielding design. The baseline is 120 kW WPT system with parameters based on ORNL’s WPT design [1]. The new shielding solution accentuates the magnetic field along the central axis and reduces stray emissions by utilizing ferrite teeth placed on the edges of both ground and vehicle side backing ferrites. Additionally, to ensure EM safety during misalignment, up to 100mm as defined by SAE J2954 safety criteria, backing ferrites are extended in the y-direction only due to the anisotropy field distribution created by DD coils.

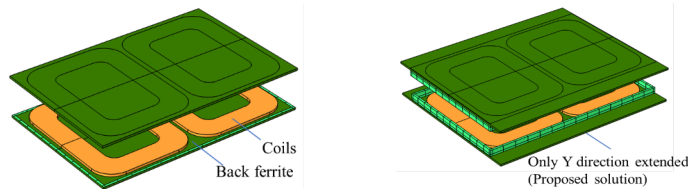


Figure II.3.2.25 Baseline WPT System and Final WPT System and Proposed shielding design for High-Power WPT applications.

Passive EM safety design for dynamic WPT

Based on EM field shielding design for high-power static dWPT, INL designed an EM shielding solution for the dynamic wireless charging system shown in Figure II.3.2.26(a). The overall charging process and

simulation strategy can be divided into two scenarios, as shown in Figure II.3.2.26(b) First, the vehicle side coil is over a ground side coil. Second, the vehicle-side coil is between two ground side coils.

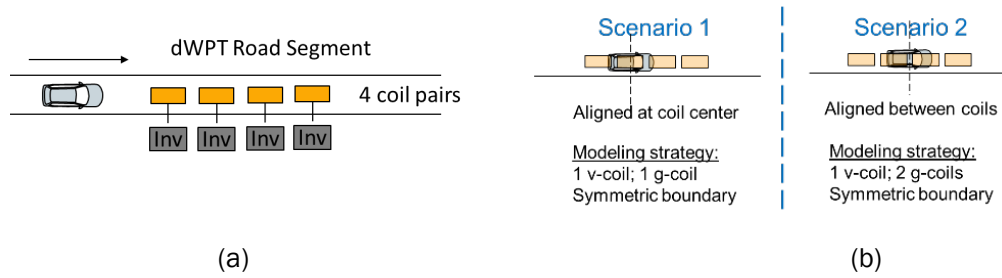


Figure II.3.2.26 dWPT Roadway Segment and Two Scenarios for dWPT EM Safety Design and Evaluation

Scenario #1 is defined as the vehicle coil being centered in the x-direction over the ground side coil. For this scenario, a dWPT finite element model has been developed, as shown in Figure II.3.2.27(a), to evaluate the EM field surrounding the dWPT system during various y-misalignment conditions. Symmetric boundaries are utilized at the leading and trailing ends of the ground side coil to mimic multiple ground side coils. To further study the EM field emissions, the finite element model has been further updated, as shown in Figure II.3.2.27(b) during scenario #2, when vehicle coil is between two ground coils.

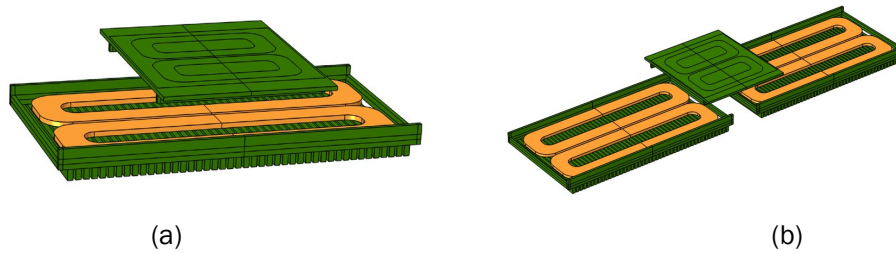


Figure II.3.2.27 dWPT Finite-element Model of (a) Scenario #1 and (b) Scenario #2 for EM Field Safety Design

The final shielding design incorporates many elements used for the static WPT shielding design such as the wrap-around vertical tooth extension ferrite and y-extension backing ferrite. However, this new design does not utilize the vertical tooth ferrite ends in the x-direction in order to not impede the magnetic field coupling duration in-motion charging. The scenario 1 and scenario 2 modeling and analysis of the final shielding design indicates 200 kW operation is safe for the general public at the roadway lane's edge (at least 1.35m away from dWPT center). The stray field is less than 15 mT across a wide range of misalignment conditions and scenarios. The final EM field shielding design dimensions are presented in Figure II.3.2.28 Note that dWPT coil design and original backing ferrites dimensions are based on ORNL's 200kW dWPT design specifications.

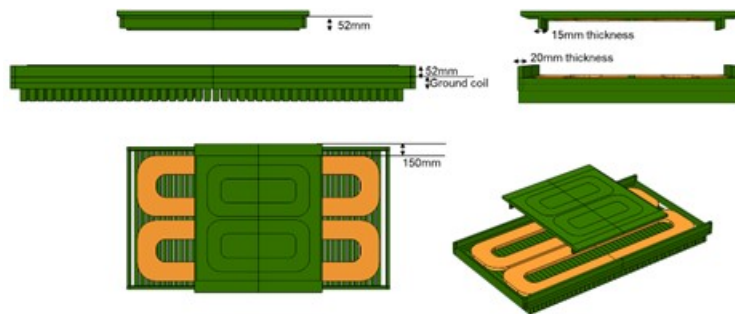


Figure II.3.2.28 Designed dimension of passive EM shield for dWPT.

dWPT Data Acquisition Requirements and Methodology

INL has completed the development of the data acquisition requirements as well as verified the operational functionality of the measurement components used to evaluate the high power dWPT operational performance and safety. The data acquisition system consists of ground-based and vehicle-based measurement and data collection systems. The measurement parameters include electrical, dWPT coil position, and EM-field of the dWPT during a wide range of operation (speed, misalignment, power, etc.). Since measurements are acquired both on vehicle-side and ground-side components during operation, a synchronization trigger is used to initiate and synchronize the LabVIEW data collection for both the vehicle and ground side collection. Upon testing completion, the two data sets are merged and analyzed to provide dWPT system operation results.

Component evaluation was conducted to verify the response dynamics of the non-contact distance sensors utilized to measure the y-alignment of the dWPT during operation. Due to COVID “work from home” safety requirements, lab testing was not possible for many months. Instead, creative evaluation methods were conducted at “EVIL-R”, the remote Electric Vehicle Infrastructure Lab (a.k.a. home office). A box fan was utilized to determine the analog output response dynamics of the non-contact distance sensors. This evaluation shows in Figure II.3.2.29, the sensors are capable of measuring distance for vehicle speeds in excess of 70 mph.

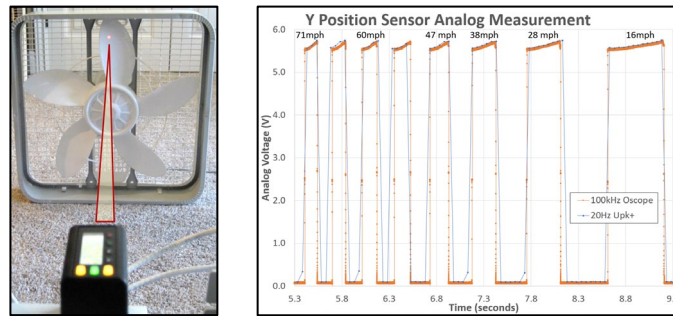


Figure II.3.2.29 Dynamic Response Verification of Non-contact Position Sensor for dWPT Y-alignment Measurement

The setup and positioning of several measurement components for dWPT testing is very important. Figure II.3.2.30 shows the relative position for the critical measurement components height and distance from the dWPT center line. The ground-side EM-field probe will be positioned at the roadway’s lane edge at a height centered in the dWPT magnetic coil gap. In the U.S., the standard interstate driving lane is 12’ wide (3.685m). The EM-field probe center will be positioned at 1829mm from the dWPT centerline (1/2 of lane width). The distance between the EM-field probe and the vehicle will vary between 791.5mm and 1191.5mm during +/- 200mm y-misalignment testing. This is acceptable in avoiding unintentional collision of the vehicle and the ground-side EM-field probe during in-motion power transfer testing. Each of the six non-contact Y-alignment distance sensors will each be positioned near the roadway lane’s edge 2787.5mm from the dWPT center line. Each sensor will be in-line with the coil center of each dWPT ground-side coil perpendicular to the direction of travel. The measured distance to the side of the vehicle will vary between 1800mm and 2200mm during dWPT misalignment testing. This is a good balance between a high sensor resolution of +/-1.5mm and minimum sensor disruption from the air turbulence created by the high-speed vehicle passing across the dWPT.

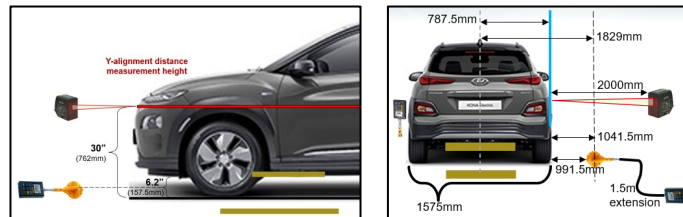


Figure II.3.2.30 Position of Measurement Probes (EM-field and Y-alignment) with Respect to Vehicle Chassis

Conclusions

- The 100 kW power electronics building block was optimized for high voltage (800 V) high-frequency operation (85 kHz) using state-of-the-art SiC phase leg modules and CeraLink capacitors in conjunction with ORNL custom-designed high current PCB.
- Double pulse test was carried out to validate the high-performance switching behavior of the assembled power electronic block. The results indicated 85 V overshoot while turning off over 244 A. This indicates safe operation even up to 900 V of DC link, thereby giving additional flexibility for control.
- The 100-kW block was subject to rated power test using resonant LC network which recreated the behavior of WPT system. The measured inverter efficiency was over 98.5 % indicating satisfactory operation. Temperature of the system was also monitored and a maximum temperature of 40.7° C was measured indicating satisfactory and safe operation.
- Prototype ground transmitter and vehicle couplers were assembled in the laboratory after the design targets (200 kW power transfer capability) were verified for power transfer capability by simulation.
- Laboratory characterization was performed, and the coupler inductances were noted for different positions along the intended power transmission zone.
- The FEA simulation-based value of transmitter self-inductance (5.5 μH) is less than the measured value of 8.2 μH . This can be attributed to the 5 m long leads in the actual coil, which is not accounted for in the FEA model. This can be compensated by slightly modifying the resonant inductor and/or varying the operation frequency around the nominal 85 kHz.
- The optimized dynamic coil system indicated peak coil-to-coil efficiency of 98.85 %, and the emissions were less than 15 μT (pacemaker limit) at the lane boundary distance (6' from the center of the coil).
- Conducted a feasibility analysis to evaluate the contribution of DWPT systems on primary roadways toward extending the driving range for intracity LD EV travel considering: 3 different DWPT system designs, 2 different vehicle models (high and low efficiency), 5 different uniform allocations (20–100 segments/300-miles road), and an optimized placement for the system based on AADT.
- Developed a dynamic visualization tool for DWPT system in Atlanta (placement and operation).
- Key findings:
 - Increasing the number of locations for the same roadway coverage at uniform placement does not always improve the contribution of the system toward driving range extension but likely increases the system cost.
 - 40 DWPT/300-mi of road shows a good balance between performance and cost in all designs and vehicles.
 - DWPT system design with higher roadway coverage (e.g., DWPT2) shows higher contribution toward increasing the driving range when compared to the lower coverage design (e.g., DWPT1).
 - With uniform placement of DWPT2, 19.43%–30.42% of vehicles experience more than a 500-mile range and 11.68%–21.06% of vehicles realize more than a 1000-mile driving range compared with an average 150-mile range without DWPT system.

- INL has successfully completed the annual milestone in support of the dynamic and high-power wireless power transfer project. This milestone involved the completion of an EM-field shielding design for the 200kW dWPT to enable safe operation with stray fields below the safety limits of 15 μ T.

Key Publications

Oak Ridge National Laboratory

1. Subhajyoti Mukherjee, Veda P. Galigekere, Omer C. Onar, Burak Ozpineci, Jason Pries, Rong Zeng, and Gui-Jia Su, "Control of Output Power in primary Side LCC and Secondary Side Series Tuned Wireless Power Transfer System without Secondary Side Sensors," 2020 IEEE Energy Conversion Congress and Exposition (ECCE), Detroit, Michigan, October 2020.
2. Tarak Saha, Subhajyoti Mukherjee, Veda P. Galigekere, and Omer C. Onar, "Design of Auxiliary Circuit Elements for Achieving Zero Voltage Switching in a Wireless Power Transfer System," 2020 IEEE Energy Conversion Congress and Exposition (ECCE), Detroit, Michigan, October 2020.
3. Utkarsh D. Kavimandan, Veda P. Galigekere, Burak Ozpineci, Jason Pries, Omer Onar, and Satish M. Mahajan, "A Sensorless Coil Detection Scheme based on Dead-Time Effect in Dynamic Wireless Power Transfer Systems", 2020 IEEE Energy Conversion Congress and Exposition (ECCE), Detroit, Michigan, October 2020.
4. U. D. Kavimandan, V. P. Galigekere, O. Onar, B. Ozpineci and S. M. Mahajan, "Comparison of Dead-Time Effects in a WPT System Inverter for Different Fixed-Frequency Modulation Techniques," 2020 IEEE Transportation Electrification Conference & Expo (ITEC), Chicago, IL, USA, 2020, pp. 277-283, doi: 10.1109/ITEC48692.2020.9161646.
5. J. Haruna, U. D. Kavimandan, O. Onar, V. P. Galigekere and J. Pries, "Sensitivity Analysis of Compensation Topologies for Dynamic WPT System," 2020 IEEE Transportation Electrification Conference & Expo (ITEC), Chicago, IL, USA, 2020, pp. 284-289, doi: 10.1109/ITEC48692.2020.9161465.
6. S. Mukherjee, V. P. Galigekere, O. Onar and B. Ozpineci, "DC Link Capacitor Reduction with Feedforward Control in Series-Series Compensated Wireless Power Transfer Systems," 2020 IEEE Applied Power Electronics Conference and Exposition (APEC), New Orleans, LA, USA, 2020, pp. 3540-3546, doi: 10.1109/APEC39645.2020.9124336.
7. S. Mukherjee, V. P. Galigekere and O. Onar, "Methods to Synchronize and Control the Secondary Side Active Rectifier in Wireless Power Transfer Systems," 2020 IEEE Transportation Electrification Conference & Expo (ITEC), Chicago, IL, USA, 2020, pp. 955-960, doi: 10.1109/ITEC48692.2020.9161711.
8. U. D. Kavimandan, V. P. Galigekere, O. Onar, B. Ozpineci and S. M. Mahajan, "A Control Scheme to Mitigate the Dead-Time Effects in a Wireless Power Transfer System," 2020 IEEE Applied Power Electronics Conference and Exposition (APEC), New Orleans, LA, USA, 2020, pp. 3172-3179, doi: 10.1109/APEC39645.2020.9124590.
9. V. P. Galigekere, R. Zeng, J. Pries, O. Onar and G. Sui, "Direct Envelope Modeling of Load-Resonant Inverter for Wireless Power Transfer Applications," 2020 IEEE Applied Power Electronics Conference and Exposition (APEC), New Orleans, LA, USA, 2020, pp. 3195-3199, doi: 10.1109/APEC39645.2020.9124589.
10. R. Wojda, V. P. Galigekere, J. Pries and O. Onar, "Copper-Clad Aluminum Windings as an Alternative Conductor for High-Power Electric Vehicle Wireless Charging," 2020 IEEE

Transportation Electrification Conference & Expo (ITEC), Chicago, IL, USA, 2020, pp. 1197-1200, doi: 10.1109/ITEC48692.2020.9161643.

11. R. Wojda, V. P. Galigekere, J. Pries and O. Onar, "Thermal Analysis of Wireless Power Transfer Coils for Dynamic Wireless Electric Vehicle Charging," 2020 IEEE Transportation Electrification Conference & Expo (ITEC), Chicago, IL, USA, 2020, pp. 835-838, doi: 10.1109/ITEC48692.2020.9161453.

Idaho National Laboratory

1. B. Zhang, Richard B. Carlson, Veda Galigekere, Omer C. Onar, and Jason Pries, "Electromagnetic Shielding Design for 200 kW Stationary Wireless Charging of Light-Duty EV," 2020 IEEE ECCE, Detroit, Michigan, October 2020.
2. Zhang, Bo; et. al.; "Challenges of Future High Power Wireless Power Transfer for Light-Duty Electric Vehicles----Technology and Risk Management"; eTransportation Elsevier; 2019.

References

1. V. P. Galigekere et al., "Design and Implementation of an Optimized 100 kW Stationary Wireless Charging System for EV Battery Recharging," in 2018 IEEE Energy Conversion Congress and Exposition (ECCE), 23-27 Sept. 2018, pp. 3587-3592.
2. J. Pries et al., "Coil Power Density Optimization and Trade-off Study for a 100kW Electric Vehicle IPT Wireless Charging System," in 2018 IEEE Energy Conversion Congress and Exposition (ECCE), 23-27 Sept. 2018, pp. 1196-1201.
3. B. Zhang, R. B. Carlson, J. G. Smart, E. J. Dufek, and B. Liaw, "Challenges of Future High Power Wireless Power Transfer for Light-duty Electric Vehicles—Technology and Risk Management," eTransportation, vol. 2, p. 100012, 2019.
4. SAEJ2954, Wireless Power Transfer for Light-Duty Plug-In/Electric Vehicles and Alignment Methodology. [online] available: https://www.sae.org/standards/content/j2954_201904/, April 23, 2019.
5. I. C. Non-Ionizing, "ICNIRP Statement-Guidelines for limiting exposure to time-varying electric and magnetic fields (1 Hz to 100 kHz)," Health Physics, Article vol. 99, no. 6, pp. 818-836, DEC 2010.
6. ICNIRP_2010; <https://www.icnirp.org/cms/upload/publications/ICNIRPLFgdl.pdf>
7. "About the Transportation Secure Data Center | Transportation Secure Data Center | NREL." [Online]. Available: <https://www.nrel.gov/transportation/secure-transportation-data/tsdc-about.html>.
8. Brooker, A., Gonder, J., Wang, L., Wood, E., Lopp, S. and Ramroth, L., 2015. FASTSim: A model to estimate vehicle efficiency, cost and performance (No. 2015-01-0973). SAE Technical Paper.
9. "Annual Vehicle Distance Traveled in Miles and Related Data - 2000" <https://highways.dot.gov/>

Acknowledgements

Project team would like to thank Lee Slezak and Manish Mohanpurkar from the U. S. Department of Energy and Jason Conley from National Energy Technology Laboratory for their continued guidance and support on this project.

II.3.3 Fast Charging Grid Impacts and Cybersecurity 1.3.2.111 (INL)

Timothy Pennington, Principal Investigator

Idaho National Laboratory
 P.O. Box 1625
 Idaho Falls, ID 83415-2209
 Email: timothy.pennington@inl.gov

Lee Slezak, DOE Program Manager

U.S. Department of Energy
 Email: Lee.Slezak@ee.doe.gov

Start Date: October 1, 2018	End Date: December 31, 2020	
Project Funding (all Carryover into FY20): \$425,000	DOE share: \$425,000	Non-DOE share: \$0

Project Introduction

As the market for electric vehicles (EVs) matures, the charging infrastructure required for an electrified national fleet must be reliable, safe, and secure. Technology and engineering advancements must ensure the charging infrastructure provides benefit to, or at least does not negatively impact, the electric grid. Additionally, the charging infrastructure network must be robust to cyber manipulation to ensure safe, reliable, and secure charging operation for the electrified fleet.

Objectives

The Fast Charging: Grid Impacts and Cyber Security project objective is to investigate and assess the interaction of fast charging with the grid, based on the power demanded during normal EV charging and also during abnormal operation resulting from a malicious cyber-attack.

Approach

As EV charging energy and power requirements increase, the grid impacts and cybersecurity vulnerabilities of fast charging infrastructure must be understood, in order for researchers and product developers to take steps to ensure security and grid stability. During fiscal year 20, this project completed important foundational tasks necessary to achieve this understanding. First, INL installed and characterized the operation of a commercial-off-the-shelf extreme fast charger (XFC) through testing. The purpose of this characterization was to understand how power flows from the grid, through the XFC, to a vehicle during charging. Testing was conducted using a production light-duty EV and a production electric transit bus. A sophisticated data acquisition system was configured to characterize XFC operation with high fidelity. Second, the project also produced a vehicle emulator that is capable of mimicking vehicles with different charge power capacities. This was necessary to allow charging characterization across a range of power levels, including what may be experienced when vehicles with 350-kW charging capability come to market in the future. This vehicle emulator is an important component of INL's power-hardware-in-the-loop platform that will be used many future projects to simulate fast charging on the grid in real time. The largest (monetary) accomplishment of the project during FY20 was completing the long-term project goal of connecting the 540 kVa Ametek grid emulators to the ABB Terra HP XFC charger and then completing an end-to-end test validating the capability to provide grid power through the grid emulators, to the charger and consume that power with the vehicle emulator; and then manipulate the grid conditions and assess the response of the entire system.

Results

High Power Electric Vehicle CCS Charging Emulator

A high value, high power electric vehicle CCS charging emulator was assembled and operation was verified at high charge power in INL's Electric Vehicle Infrastructure Laboratory (EVIL).

This consists of high value, high power DC load bank capable of up to 900V and 500A, CCS communications module from COMEMSO, and interface connection including the high current CCS inlet port.



Figure II.3.3.1 Overview of high-power CCS charging emulator w/ 350kW XFC and grid emulator for variable input supply

With a vehicle charging emulator, multiple vehicle classes can be emulated with the XFC to determine the operation characteristics of the XFC over a wide range of conditions. For light duty EVs, there appears to be three categories of EV charging capability. First is the legacy EVs designed for charging up to 50 kW and typically have battery voltages below 400VDC. Second, a new generation of EVs with higher charging power capability also with battery voltage typically below 400VDC but with significantly higher charge current capability resulting in charge power up to 150kW. Lastly a few new EVs will have XFC charging capabilities up to 350kW. This is possible by both high charge current capability as well as higher battery voltage of roughly 800VDC or more.

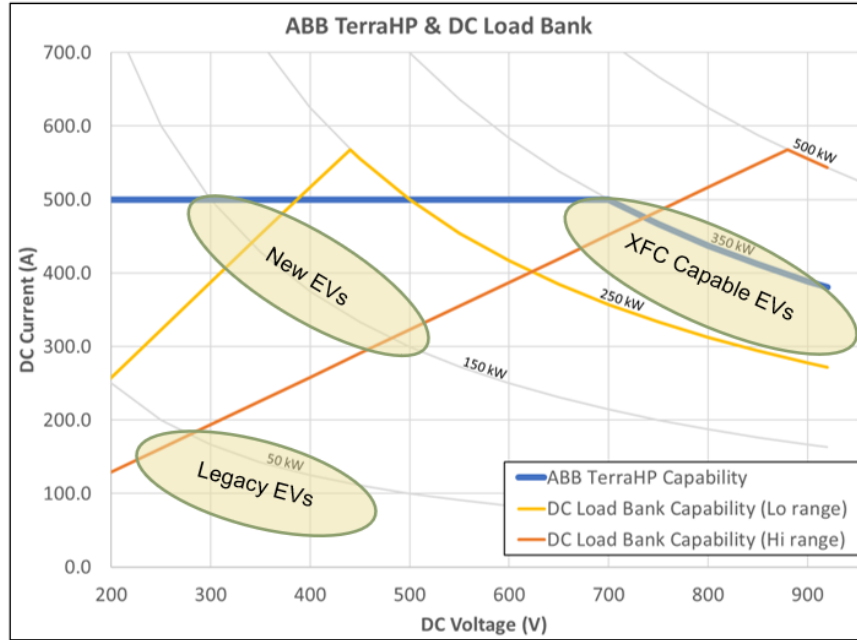


Figure II.3.3.2 Design objective and capability goal of the high-power CCS charging emulator with the ABB XFC

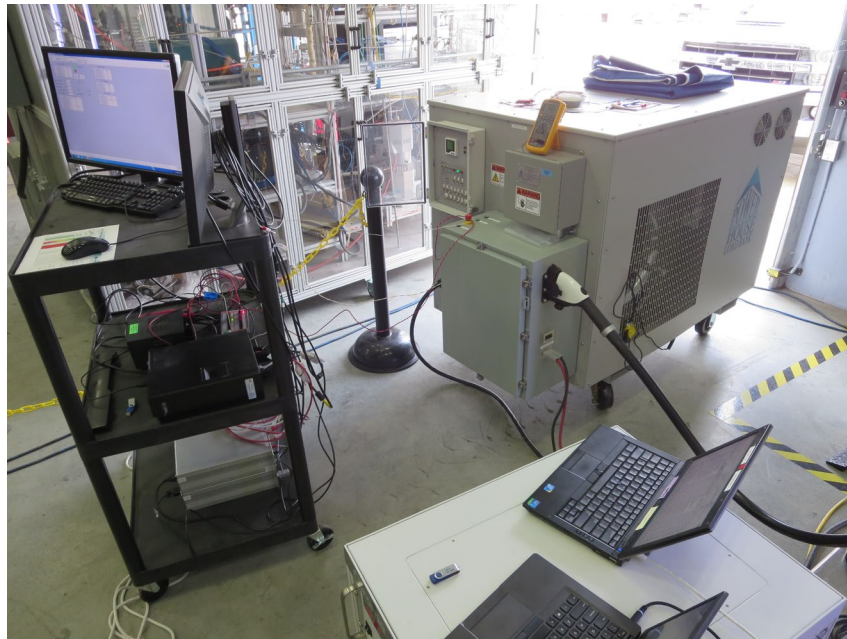


Figure II.3.3.3 High power electric vehicle CCS charging emulator in INL's Electric Vehicle Infrastructure Lab



Figure II.3.3.4 ABB TerraHP (350 kW) XFC charging the CCS vehicle charging emulator in INL's EVIL

With the utilization of the CCS charging vehicle emulator, the ABB TerraHP XFC was operated across a wide range of output current, voltage, and power, which were not previously possible. From this operation preliminary results show the characteristics for efficiency and power quality.

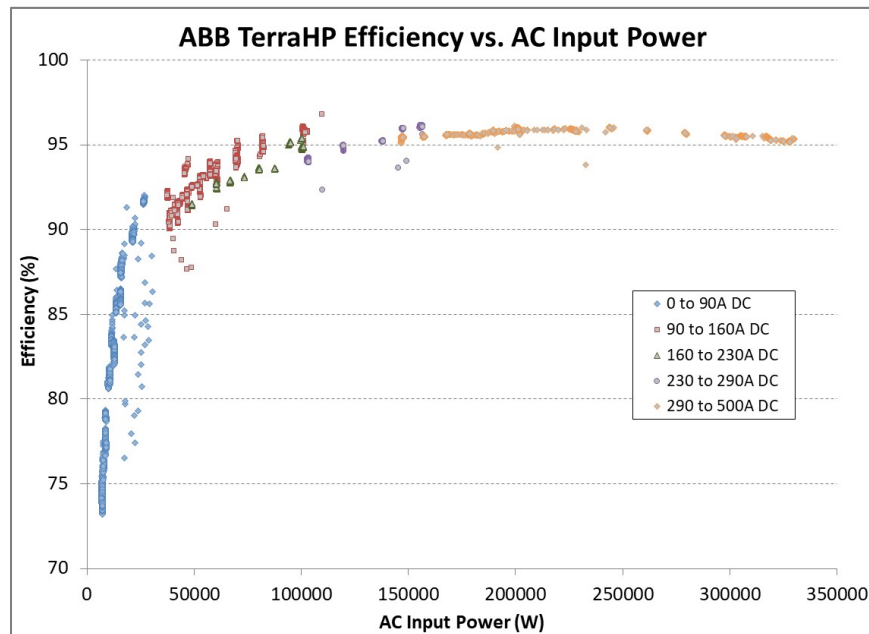


Figure II.3.3.5 Efficiency versus power of the 350-kW ABB TerraHP XFC

The charging equipment specifically designed for XFC, shows peak efficiency around 200kW with very good efficiency (95% or >) from 100kW to >325kW, with slight variation depending upon voltage at a given power.

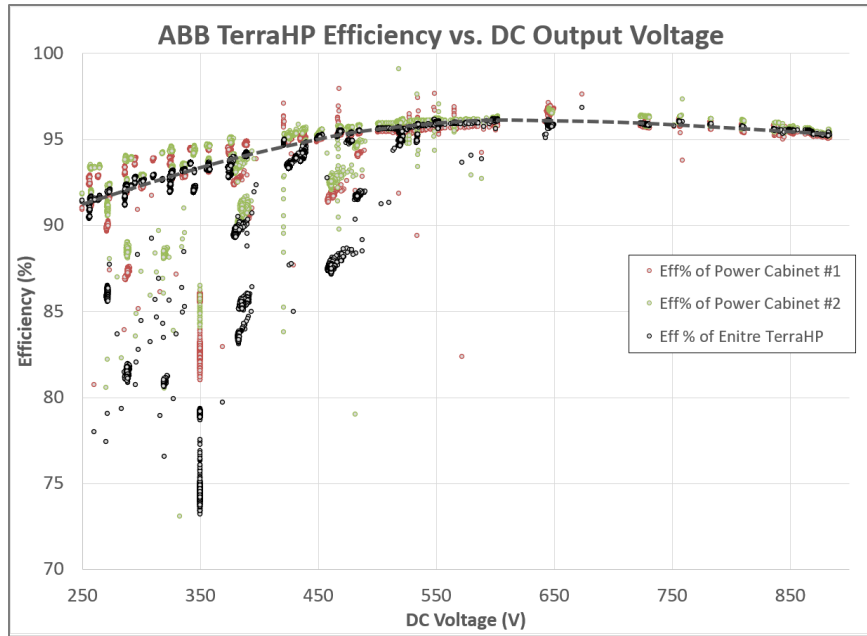


Figure II.3.3.6 Efficiency versus DC output voltage of the 350-kW ABB TerraHP XFC

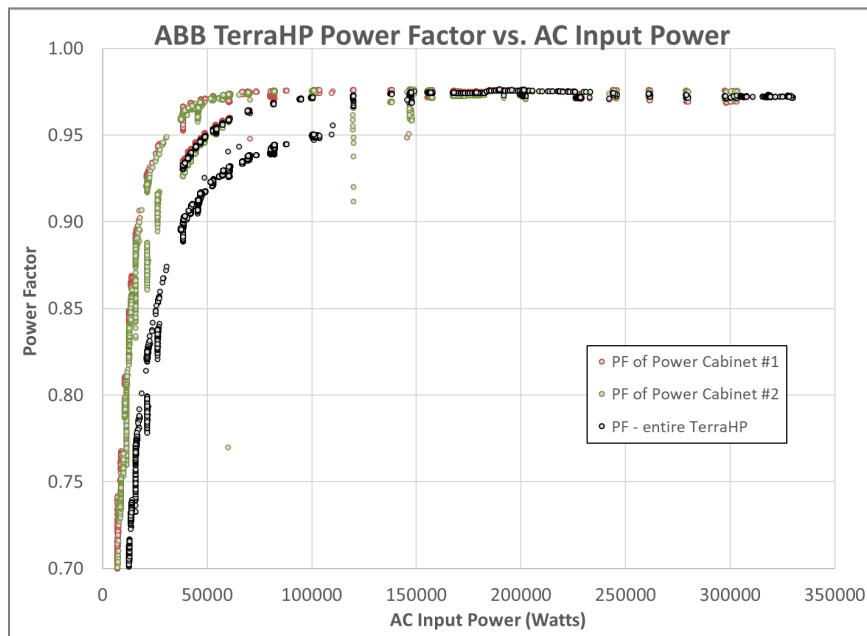


Figure II.3.3.7 Power Factor versus power of the 350-kW ABB TerraHP XFC

The power factor is also greater than 0.95 for the majority of likely charge powers that it will be used for (50-350kW).

Grid Emulator Integration with the XFC

A 540 kVA grid emulator was integrated with the ABB TerraHP XFC to enable the further testing of the XFC unit with various grid conditions and emulations which are not possible with the rigid external grid connection used otherwise.



Figure II.3.3.8 Overview schematic of complete high-power charging lab research capability

The electrical connection from the grid emulator output to the XFC input is accomplished by routing electrical cabling in over-head cable trays to reduce trip hazards and enable more floor space for research activities. Additionally, a “tap box” is utilized for easy reconfiguration of connections between multiple systems. As shown on Figure II.3.3.8 the grid emulator is now connected to the ABB TerraHP XFC in the Electric Vehicle Infrastructure lab at INL. The impacts of the COVID-19 pandemic did cause delays in the construction projects required to create these lab capabilities and as such a no-cost extension has been requested and granted to continue this project into FY21 Q1. The current project end date is 31 December 2020.



Figure II.3.3.9 Electrical connection between grid emulator and XFC in ESL

To verify proper operation of the lab capability, the XFC was utilized to charge a production vehicle while input power was provided by the grid emulator. As seen in figure below the input voltage was changed from 480VAC to 461VAC during charging, and then returned to 480VAC a few seconds later. During this input voltage deviation, the charger continued to charge the vehicle, as expected. This capability will enable future valuable investigation into grid dynamics interactions with high power EV charging infrastructure.

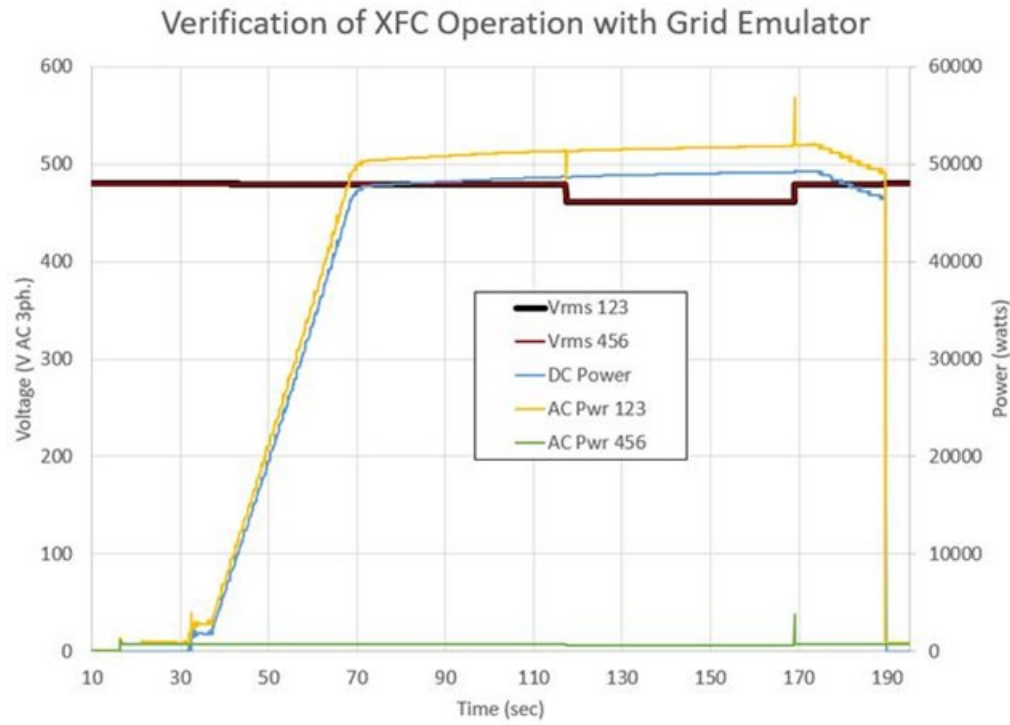


Figure II.3.3.10 350-kW ABB TerraHP XFC operation with grid emulator 480V variable input

Conclusions

This project completed the primary objective of building and exercising the lab capability to investigate the critical details of XFC hardware characterization, and high-fidelity real time impacts on the grid. With a reliable connection between the recently purchased grid emulators and the XFC station it will be possible to study a variety of grid conditions in which an XFC might operate. With the development of the vehicle emulator, it is possible to load the XFC in a large variety of ways that today's vehicles do, and tomorrow's vehicles are likely to charge – without having the vehicles themselves. It will also be possible to manipulate the charging more easily with this internally developed system as opposed to OEM vehicles to emulate compromised vehicle software or other anomalous hardware/charge events. Lastly the entire lab arrangement produces a system capable of detailed study on grid impacts of the new and growing XFC hardware.

References

ABB High Power Charging Products and Downloads, <https://new.abb.com/ev-charging/products/car-charging/high-power-charging>.

II.3.4 Development of a Multiport 1+Megawatt Charging System for Medium and Heavy-Duty Electric Vehicles (NREL)

Andrew Meintz, Principal Investigator

National Renewable Energy Laboratory
15013 Denver West Parkway
Golden, CO 80401
Email: Andrew.Meintz@nrel.gov

Madhu Chinthavali, Principal Investigator

Oak Ridge National Laboratory
2360, Cherahala Boulevard
Knoxville, TN 37932
Email: chinthavalim@ornl.gov

Theodore Bohn, Principal Investigator

Argonne National Laboratory
9700 South Cass Avenue
Lemont, IL 60439
Email: tbohn@anl.gov

Lee Slezak, DOE Program Manager

U.S. Department of Energy
Email: Lee.Slezak@ee.doe.gov

Start Date: October 1, 2018
Project Funding: \$2,000,000

End Date: December 31, 2021
DOE share: \$2,000,000

Non-DOE share: \$0

Project Introduction

Medium-duty (MD) and heavy-duty (HD) electric vehicles (EVs) are being manufactured today and will soon necessitate the use of megawatt (MW)-scale charging systems that can quickly charge large capacity (~800 kWh) battery packs in less than ~30 minutes at an attractive charging cost (\$/kWh). This fast charging time is needed to maximize the revenue-generating operations of commercial MD/HD vehicles. The integration of renewable energy and grid-tied energy storage, coupled with these large and semi-variable high-power vehicle charge events, will require an integrated system which has minimum impact on the grid. Many challenges must be met to realize this integrated system, including 1) optimizing power demand and management requirements, 2) configuring local infrastructure requirements, 3) designing grid interface converters, 4) managing impacts on grid power quality, 5) developing distribution voltage-level hardware for grid connection, 6) developing safe and robust hardware connections, 7) overcoming power electronics semiconductor and architecture limitations, 8) developing robust thermal management systems, and 9) developing vehicle-side power delivery architectures.

This project, led by the National Renewable Energy Laboratory (NREL) in coordination with Oak Ridge National Laboratory (ORNL) and Argonne National Laboratory (ANL), will create models of the system and components, control methods for power and charging, and hardware to address MW-scale charging infrastructure challenges for MD/HD EVs. The primary objective of this project is to develop solutions which enable 1+ MW charging systems for MD/HD EVs of various vocations to maximize utilization and the all-electric miles travelled and improve the return on investment, ensuring industry and consumer acceptance. The project will design and develop a cost-efficient, modular, and reconfigurable power electronics architecture, leveraging current DOE research activities and team members' world-class experience, wide bandgap device-based power electronic converters, vehicle charging and energy storage systems, automated wireless charging

systems, and grid modernization. The work will generate DOE-owned intellectual property on high-frequency/hi-power inverters, high-frequency AC links, novel integrated magnetic structures and planar transformers, vehicle battery pack thermal management, and connecting mechanisms. In 2020, the project made significant advancements toward these goals as work continues into the project's third year. These advancements include power electronic hardware design and control, industry engagement, power grid impact analysis, and system control simulation and hardware implementation.

This project will ensure that the United States remains a leader in innovative transportation systems by accelerating adoption of MD/HD EVs and assuring the convenient, flexible, and safe integration of 'beyond' extreme fast-charging (XFC) technology with our nation's grid infrastructure.

Objectives

Power Electronics, Host Controller, CAD design (ORNL)

The second-year project objectives include the development of the power electronics parametric design and hardware component selection based on an assessment of current supply equipment in the MD/HD charging space and topology selection from year one work. This parametric design supports CAD modeling to develop power electronics building blocks including magnetics design, thermal performance, and integration for improved power density. For the selected power electronics design, host controllers for each power stage to support a single multiport MW charging system will be developed.

Grid Impacts (NREL)

Heavy-duty EVs will require extremely fast charging rates to reduce charging time and will induce very high charging loads (at the multiple-megawatt scale) if several vehicles charge at the same time. Therefore, unlike other types of charging stations, the multiple-megawatt scale charging load of the heavy-duty charging station may induce adverse impact on the grid if there are no effective mitigation strategies. Therefore, the grid analysis task is designed to comprehensively understand the impact which the heavy-duty EV charging station will bring and deliver effective solutions.

Advanced Battery Management Systems (NREL)

This task will deploy: (i) an electric vehicle (EV) battery model and a battery management system (BMS) algorithm for power hardware-in-the-loop (PHIL) simulations, (ii) a communication framework to periodically send EV/BMS status to the site controller, and (iii) capabilities to emulate multiple EVs arriving and charging at the station based on an arrival schedule.

Site Controller (NREL)

To integrate these multi-megawatt sites with the grid a smart control for overall site management is needed. This control system must incorporate grid constraints, minimizes charging time and cost, and support multiport charging stations with onsite distributed energy resources (DER).

Connector Evaluation (NREL)

A new multi-megawatt charging standard is needed for the electrification of medium- and heavy-duty vehicles as existing charging standards are not capable at these power levels. This project is supporting the Charging Interface Initiative, CharIN, an association of specialists from various industries which promotes the standardization and interoperability of battery charging systems for electrified vehicles through the Megawatt Charging System (MCS) Task Force. NREL hosted a CharIN MCS evaluation event to evaluate proprietary prototype designs from multiple manufacturers with the objective of providing feedback that improves interoperability, reliability, efficiency, and cost-effectiveness of high-speed medium- and heavy-duty electric vehicle charging systems.

Industry Engagement (ANL)

Building an ‘information nexus’ on megawatt level charging system requirements which can be discussed with industry stakeholders. Address control/safety functions for MW+ multiport charging of ‘commercial electric vehicles at scale’. The scope of the requirements study and resulting report covers:

- Class 8 Heavy Duty Electric Trucks (depot and on-road/truck stop)
- Electric Buses (depot and on-route)
- DC as a Service central power conversion and DC distribution to isolated dispensers at each vehicle.

The objectives for the industry engagement effort in year 1 established an industry work group to discuss and capture MW+ Multiport charging system requirements for MD and HD electric vehicles. Hosted monthly web based interactive meetings and several in person meetings to gather input and feedback for content of the charging requirements report.

In year 2, this effort leveraged year 1 requirements document to create a technology testbed capabilities matrix. Use matrix to specify capabilities allowing the goal of the testbed is to serve as a method to evaluate standards gap and collect data.

Approach***Power Electronics, Host Controller, CAD design (ORNL)***

With a focus on the medium voltage dc coupled architecture, suitable power electronics components were evaluated at the switching devices first to compare the performance of medium voltage silicon IGBTs versus medium voltage silicon carbide MOSFETs in the selected topology for electrical losses, thermal auxiliary impacts, and system level power density impacts. A detailed CAD design of the proposed power converters was created to include the switching devices, magnetics, and thermal management sizing to compare proposed power density in comparison with existing solutions. With a suitable switching device and magnetics design identified, the system was modeled for operational modes to ensure grid and load side support and stability. This system simulation was utilized to develop the control strategy and controller hardware requirements for both the source and load side converters. Both switching and average models were developed to be used in the next phase of implementation for controller hardware in the loop (CHIL) simulations.

Grid Impacts (NREL)

To analyze the impact and provide corresponding resolutions, we select four representative distribution systems including different single-feeder cases and multi-feeder cases, and design thorough test metrics to perform the impact analysis. The charging load profiles used in the analysis are modeled using NREL developed direct current (DC) fast-charging station modelling tool EV-EnSite, short for Electric Vehicle Energy Storage and Site Optimization tool. Charging stations are placed in three different representative locations on each distribution system including best-, good-, and worst-locations. Mitigation strategies using different size combinations among smart charger, onsite solar generation, and onsite battery energy storage, are proposed, and evaluated.

Advanced Battery Management Systems (NREL)

A reduced-order electrochemical model for the EV battery and a model-based control approach are used to develop the EV/BMS model. The cell-level reduced-order electrochemical model is scaled to different EV battery pack sizes and used to calculate state-of-charge (SOC), voltage response, and heat generation at different states of charge (SOCs). Combined with a lumped-capacitance thermal model, it provides all the necessary response signals to develop a model-based BMS (flowchart in Figure II.3.4.1). The EV model can be calibrated to different battery chemistries. At present, we have calibrated model parameters representing lithium cobalt oxide (LCO) and lithium nickel manganese cobalt oxide (NMC) cathodes. This underlying battery model is further used in conjunction with a model predictive control (MPC) framework to develop a

BMS algorithm that can (i) control the charging current given the state of the battery, (ii) account for external charging limits such as site controller allocated power, and (iii) communicate present/predictive battery information externally. The BMS algorithm solves an optimal control problem (*OCP*) online (using a pseudo-spectral optimization approach to reduce the computational burden) every 10 seconds such that the EV battery is charged as fast as possible while satisfying constraints on voltage, current, temperature rise, and site controller allocated reference power. Once an optimal solution is found over a time horizon, the first control input is communicated to the EV model and the optimization problem is solved in the next sampling time.

In the CHIL simulation, the EV battery model will run in an Opal-RT system while the BMS algorithm will be deployed to a DSP (digital signal processor) board as shown in the communication interface in Figure II.3.4.2. The voltage, current, SOC, and temperature values of the EV battery model are transmitted to the BMS through an analog signal interface. The optimal charge acceptance values from the BMS are transferred to the energy management system (EMS) through CAN communication.

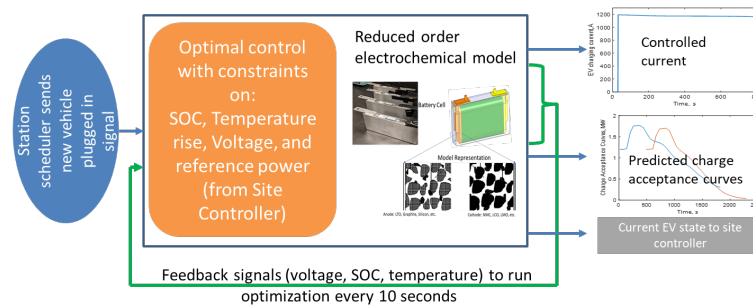


Figure II.3.4.1 Flowchart of the BMS algorithm and its input/output and feedback signals

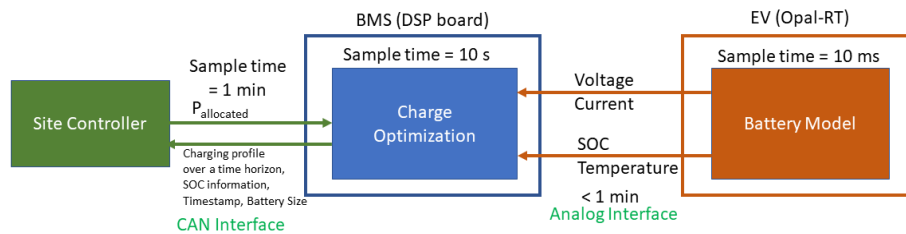


Figure II.3.4.2 Communication interface between the BMS, the EV battery model, and the Energy Management System (a part of the Site Controller)

Site Controller (NREL)

Site controller is a bi-level real-time energy management system, which monitors the entire system in real-time, including distributed energy resources (DERs), EV loads, and grid, and manages EV charging, power dispatch for ESSs, and PV operation. It incorporates (see Figure II.3.4.3):

- Energy Management Optimization (EMO), which optimizes the overall station performance in real-time considering limitations for grid, EV, BMS, and converters.
- Real-time Energy Management System (RT-EMS), which coordinates between the optimal set point from EMO and real-time variability of EV load and DERs, and performs voltage regulation on the AC side using volt-var.

EMO solves a multi-objective linear optimization problem every minute to estimate the charging power, and energy storage system dispatch, considering predicted solar radiation, real-time electricity price, real-time station schedule, real-time EV battery acceptance power, and real-time distribution feeder capacity. RT-EMS

compares between optimum set point and real-time measurements and adjust the set point to compensate for fast disturbances in EV load and DERs.

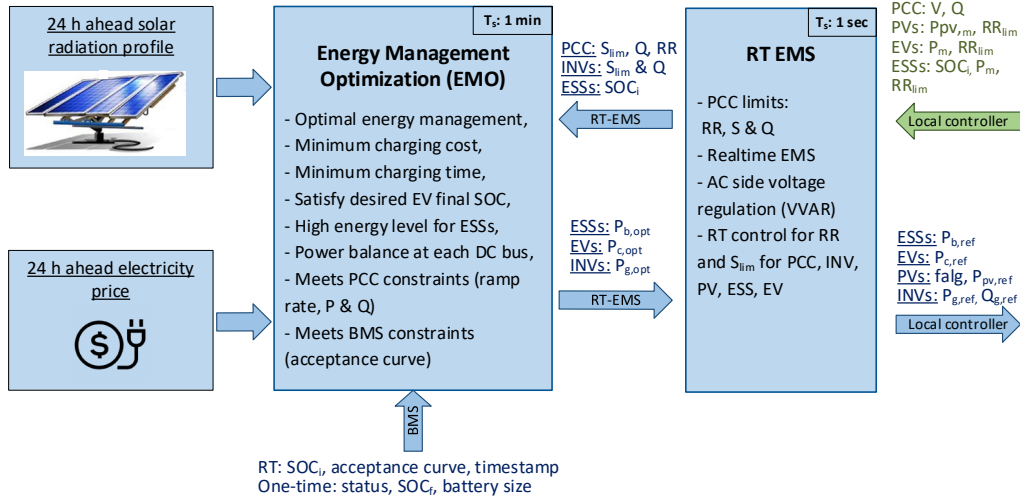


Figure II.3.4.3 Block diagram of the site controller (EMO and RT-EMS)

Connector Evaluation (NREL)

The connector evaluation event evaluated manufacturer-provided equipment using three distinct tests. Level 0 tests included fit and ergonomic evaluations of participant manufacturer’s charging equipment. Level 1 tests used a test bench set up to record instrumentation of participant manufacturer’s charging equipment thermal performance up to 350A with only passive cooling. Level 2 and 3 tests used a test bench set up to record instrumentation of participant manufacturer’s charging equipment thermal performance up to 3000A with active cooling.

Industry Engagement (ANL)

The diverse set of topics covered in the requirements study for these charging use cases, and interactions of technical systems are illustrated in the Venn diagram in Figure II.3.4.4. The center circle focuses on charging systems and functions at the 1 MW and above level. The tangential circles (outside the central purple circle) address technologies that can be leveraged for ‘high power’ charging systems that are under 1MW but not directly applicable for MD and HD electric vehicle charging. These represent depot charging where vehicles are stationary overnight or while out of service during low vehicle usage/demand during the day. These represent the counterargument that more power is always beneficial. Slower charging rates when possible, including battery swapping are often a better solution for cost/benefit tradeoffs, if sufficient charging dwell time for these vehicles are available. The aggregate of multiple sub-MW charging adds up to multi-MW loads.

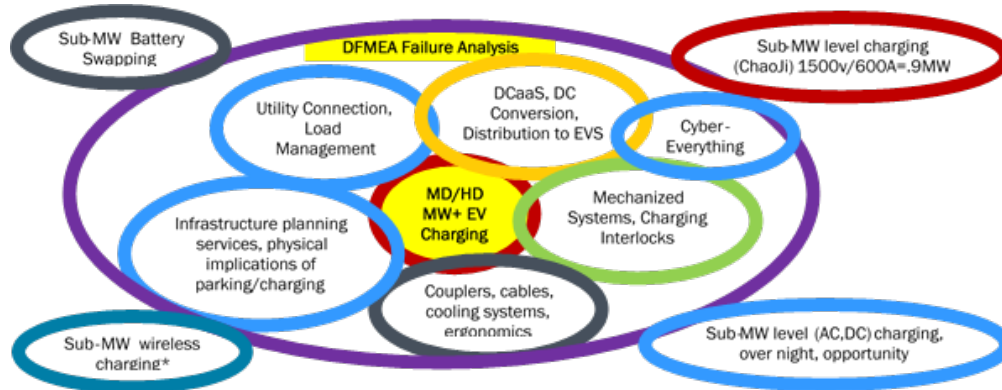


Figure II.3.4.4 Industry Engagement Use Cases and Interactions

The scope of the charging requirements report spans energy delivered from utility interconnection at the sub-transmission level, to the on-site conversion of medium voltage AC to ~ 1000 V dc to distribution of the DC (DC as a Service) power to isolated dispensers at each vehicle to active/passively cooled cables that deliver power to the vehicle battery via standardized MW level couplers. The scope includes connection equipment such as cord handling/cord retriever systems to handle heavy charging cables to mechanized charging systems for both SAE J3105 and CharIN MCS couplers with robotic actuators to insert/remove up to 3000A contacts reliably.

Results

Power Electronics, Host Controller, CAD design (ORNL)

The proposed architecture of Extreme Fast Charger (xFC) for medium duty and heavy-duty vehicles is shown in Figure II.3.4.5. Three isolated DC ports are created by the power electronics converters fed through 13.8 kV MV distribution grid. The load power is also supported by renewable resources (Photovoltaic System (PV) and Energy Storage System (ESS)) located at the common 2 kV DC bus. The architecture is split into 2 parts to facilitate system development efforts:

Source Side: The source side converter module is a combination of Cascaded H-Bridge (CHB) rectifier and a Dual Active Bridge (DAB) DC-DC converter. The CHB rectifies the medium voltage AC grid voltage and creates an intermediate 3 kV DC-link. The DAB converts the 3 kV to a common 2 kV DC bus where the output side of all source DAB's are tied together. The source side contains a stack of four module packs (1 CHB + 1 DAB) per phase for a total of 12 module packs for the entire topology. Each of these module packs was evaluated for a minimum of 100kW to 300kW by leveraging the power module building blocks to support a minimum 1.2MW single station or a common three port 3.6MW station.

Load Side: The load side contains the PV system, ESS system and Load DAB string (3 x 400 kW to support 1.2 MW vehicle charging power). The load side converters are tied together on the 2 kV DC bus along with the renewable PV and ESS resources which work in the current control mode to inject current into the bus. The voltage is still maintained by the source side converter. The Load DAB also works in current control mode and is responsible to provide the controlled charging current to the EV battery while providing galvanic isolation between the vehicle and the rest of the system. The interaction between the converters tied on the 2 kV bus will be optimized by the EV BMS, ESS BMS and PV and Grid dispatch commands coming from the supervisory control layer.

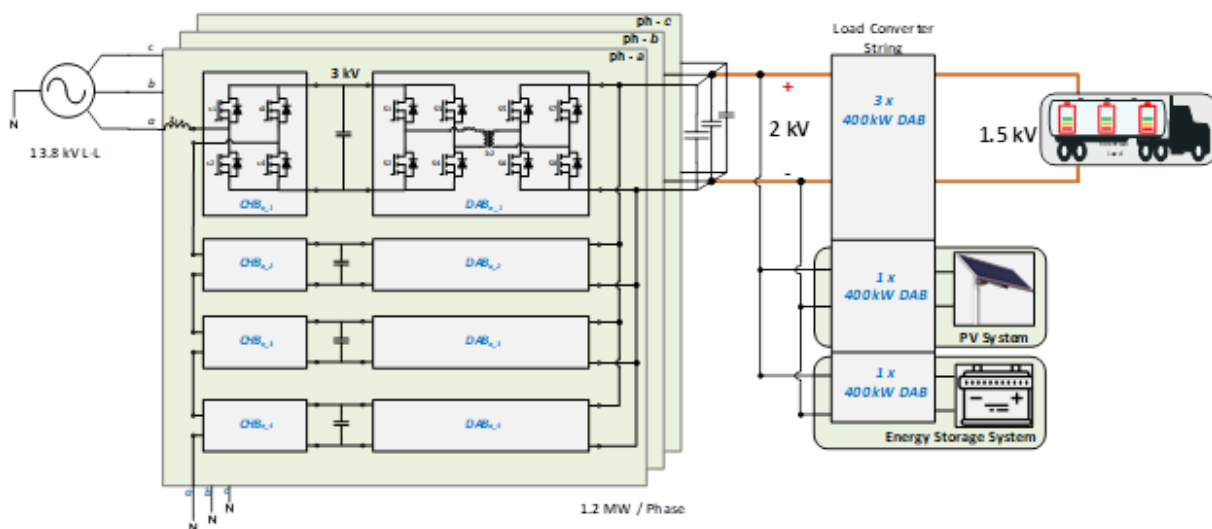


Figure II.3.4.5 Proposed xFC Topology

Power Electronics Design

To support these power electronics requirements, power module technologies for both silicon and silicon carbide were reviewed in the 3.3kV to 6.5kV range to compare switching frequencies, power losses, and current range availability. Based on the proposed topology, base wave forms and available datasheets, an estimation of the conduction and switching losses for the switch and diode or body diode, assuming ZVS-on for all eight switches in the DAB topology, was performed for several device vendors at 1kHz maximum for the silicon and extended to 10kHz for the silicon carbide. For the same power module sizing, the silicon carbide demonstrated 50% reduction of losses while switching at ten times the frequency. A 6.5kV SiC Power module based on a high voltage industrial standard footprint, which utilizes a low inductance bus structure to support high frequency switching, was selected as the building block for all stages of the converters on the load and source side. For the estimated semiconductor losses, the heat sink air flow requirements were designed to operate at maximum semiconductor junction temperature of 150°C, minimize the overall pressure drop of the system, and decrease the parasitic losses from the fan. With the selection of the switching frequency and power module sizing, the design of the magnetics required for the DAB structure was initiated. To optimize the high frequency transformer and provide a tailored leakage inductance for the DAB control, the transformer and leakage inductor were independently designed to improve the overall power density of the system. All magnetics were designed to be air cooled with minimal air flow of 2 m/s at 50°C to support cabinet operation. The power electronics were packaged in building block enclosures as shown Figure II.3.4.6 for the source CHB-DAB module pack supporting up to 300kW with an estimated efficiency of 97% and the load DAB converter enclosure supporting up to 400kW with an estimated efficiency of 98%. Comparing this topology to current 480V charging infrastructure, it was estimated that the power electronics efficiency will be similar or improved by as much as 3% while the power density was increased by 2-3X thus consuming less physical area at the station. This information is being supplemented by the smaller balance of system for the grid interface and isolation required for direct 13.8kV medium voltage switchgear.

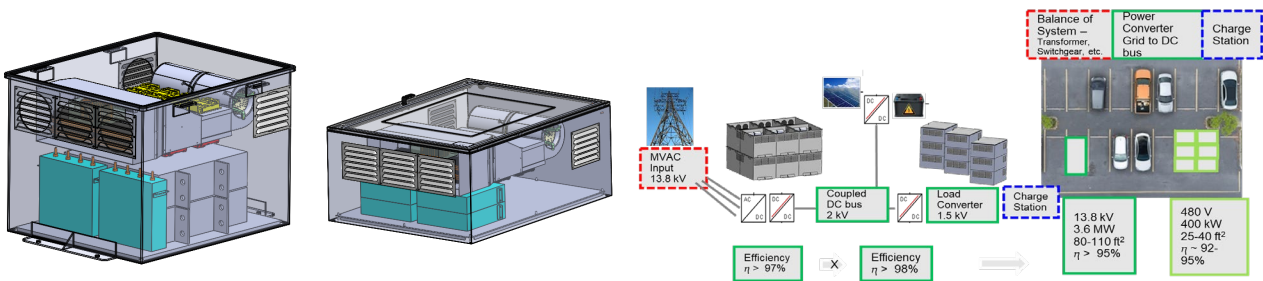


Figure II.3.4.6 Power electronics CAD design (a) Source CHB-DAB Module Pack, (b) Load DAB Converter, and System comparison to 480V charging equipment

Simulation Results: Combining the Source and Load DAB's

A benefit of the proposed topology is the isolation provided by the DAB structure on both the load and source sides, but this does raise some concerns for system stability for both parallel DAB operation for each side and the series combination of source-load DABs. A simulation model was created by combining the Source and Load DAB's together with the ESS. The simulation model is shown in Figure II.3.4.7(a). The source side stability was verified using this simulation model, and simultaneous charging of EV and ESS battery was also demonstrated. To fully reap the benefits of PV in use cases when generation can be higher than xFC load, the ESS system was strategically located on the 2 kV bus to enable simultaneous charging of both EV and ESS batteries in times of lite or no load. A simulation case is presented in Figure II.3.4.7(b) where the grid side and ESS current is kept constant, and the PV converter is operated in MPPT condition. The steps shown in the third plot with orange line was the MPPT algorithm compensating for the drop in irradiation. The bottom plot showed the Load (EV) DAB currents. They are changing with the MPPT steps because the simulation is run in a balanced condition where $P_{EV} = P_{Grid} + P_{ESS} + P_{EV}$. The grid and ESS power were constant in this case.

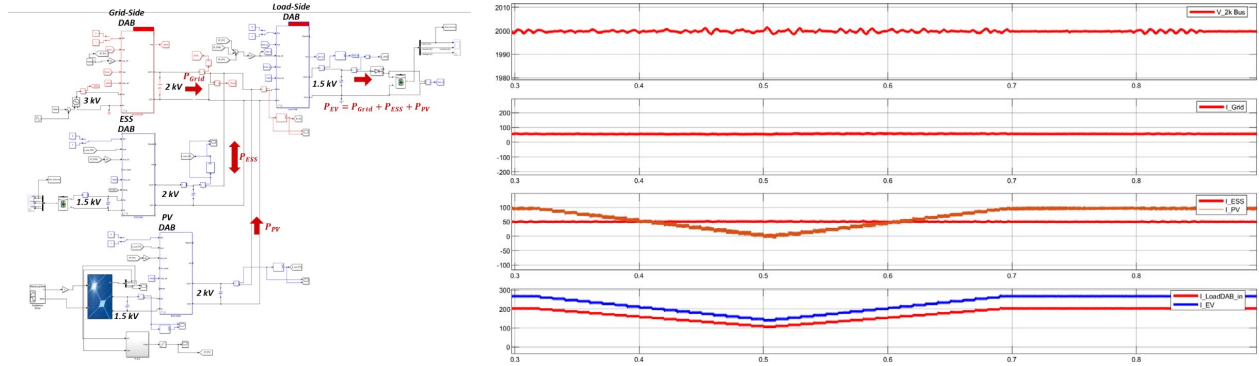


Figure II.3.4.7 Simulation Setup with Grid, 1 Source DAB, 1 Load DAB, ESS and PV

CHIL Architecture Development

To validate the complete control of the xFC station, a Controller Hardware in the Loop (CHIL) testbed is planned with the power electronics power stage simulated inside the OPAL-RT and real TI DSP based converter controller hardware outside the simulation talking to the realistic converter simulation via hardwired Raspberry-pi enabled communication layer. As an initial step toward the complete CHIL test, a test plan was developed where the master controller layer of the power electronics control will be developed and evaluated with the averaged models of the converters inside OPAL-RT simulator as shown in Figure II.3.4.8. This intermediate step simplified the number of controller hardware components needed to demonstrate the communications by eliminating the slave controller layer where PWM gating signals are generated for switching models. This approach reduced the development time for the simulation models while still providing necessary analog measurement signals for the master controller layer. No modifications will be required in the Master Controller Layer for moving to switching models because the averaged OPAL-RT models are set up in such a way that it accepts the same control variable that will be communicated to the Slave Controller Layer in Full Demo and performs the averaged calculations inside.

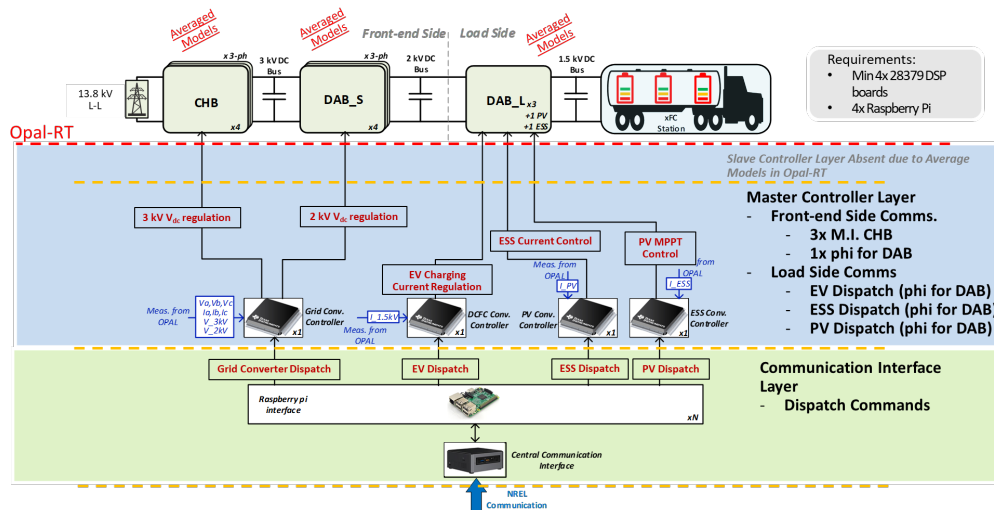


Figure II.3.4.8 Intermediate CHIL Architecture

Grid Impacts (NREL)

Two sets of simulations were conducted for the best/good/worst locations of the four representative feeders, including one set of placing the charging station in the system without any mitigation strategies, and one set with a simplified power factor (PF) control method to let smart charger provide reactive power support to the grid connection point when the EVs are pulling power from the grid. Under these conditions the maximum ramping rates and charging loads each location can host are determined. Figure II.3.4.9 shows a bar plot of the

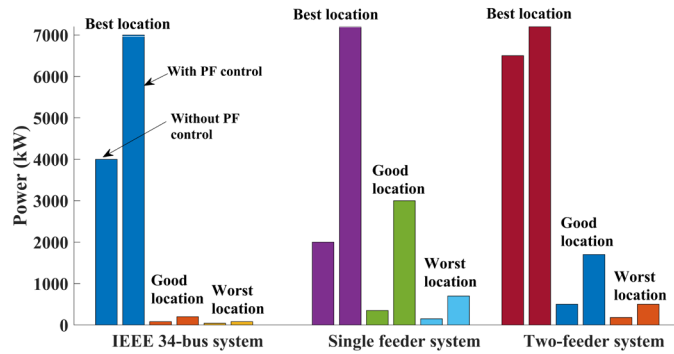


Figure II.3.4.9 Charging station hosting capacity analysis results

maximum hosting charging loads of each location on the feeders. Table II.3.4.1 summarizes the ramping rates and maximum load requirements for best locations of each feeder. It can be observed that the best locations on the feeders can host large travel centers such as 6-port charging stations with some mitigations and even with very limited mitigations. The good and worst locations can barely host a 3-port or even 1-port charging stations with mitigations. If we advance the mitigation setups to include onsite generation like PV or energy storage (ESS) rather than only reactive power support, the good/worst locations can host larger charging stations. Table II.3.4.2 shows sample onsite PV-ES-Inverter solutions for hosting a 3-port charging station that will be used in year 3 to analyze the effectiveness of the site controller.

Table II.3.4.1 Feeder Requirement

Distribution Systems: Best Location		Ramping Rate		Peak Charging Load	
		Without mitigation (MW/min)	With mitigation (MW/min)	Without mitigation (MW)	With mitigation (MW)
IEEE standardized test case: IEEE 34-bus system	Nominal	2.00	5.00	3.50	6.50
	Maximum	2.50	5.50	4.00	7.00
Single feeder case: California feeder	Nominal	1.80	2.50	1.80	30.00 *
	Maximum	2.00	3.00	2.00	31.50 *
Two feeder case: Hawaii feeder M1&M2	Nominal	2.16	6.50	5.50	70.00 *
	Maximum	2.20	7.00	6.50	75.00 *
Dedicated feeder case: derived from California feeder	Nominal	2.17	5.22	19.50*	47.00 *
	Maximum	2.22	5.33	20.00*	48.00 *

* Total capacity will be limited by substation transformer and sub-transmission limitations, usually 10MVA

Table II.3.4.2 Onsite PV-ES-Inverter Solutions

Distribution System	Site System	Best Location	Good Location			Worst Location		
			Low PV size	Medium PV size	High PV size	Low PV size	Medium PV size	High PV size
Single feeder case: California feeder	Grid Inverter	3.6 MVA	3.8 MVA	3.7 MVA	3.65 MVA	4.5 MVA	4 MVA	3.8 MVA
	PV	0	0.077MW	0.4MW	0.7 MW	0	0.6MW	1 MW
	ESS	0	0.33MWh /0.077MW	1.88MWh /0.4MW	7.7MWh /0.7MW	0	3.5 MWh /0.6MW	8.5MWh /1MW

Advanced Battery Management Systems (NREL)

In a case study, the EV/BMS model is used to simulate the charging of four EVs arriving at the station with different initial SOC, temperature, and different battery capacities (three with 600 kWh batteries and one with a 1200 kWh battery pack). At the points “A”, a new vehicle plugs in and the EV/BMS model is reset to control the charging of that vehicle. The vehicle charges between either points “A” and “B” (if it has enough time to reach a target SOC) or “A” and “C” (if the next vehicle shows up before the present vehicle charges to a target SOC), since waiting mechanisms are dealt by the station and not by the EV/BMS model. The underlying optimal control problem (OCP) is solved repeatedly to obtain an optimal current such that the vehicles charge within given constraints, e.g., the site controller or the energy management optimization (EMO) based reference power. Similarly, stricter thermal constraints can be implemented to get a different optimal charging profile depending on the battery chemistry and design.

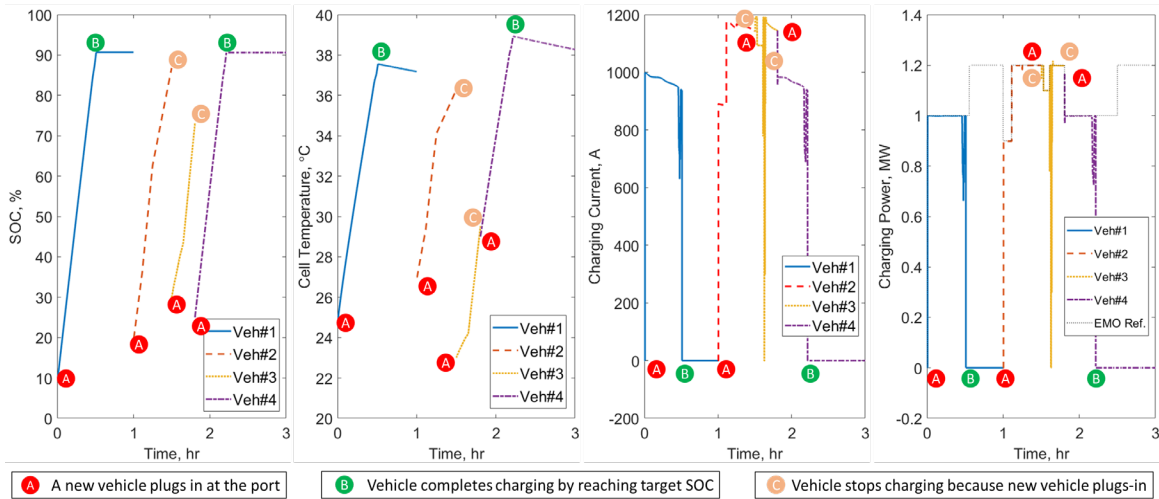


Figure II.3.4.10 Charging of four vehicles using the MPC-based BMS algorithm

Site Controller (NREL)

Site controller including EMO and RE-EMS are implemented in a MATLAB environment and preliminary performance is indicated in and Figure II.3.4.12. Figure II.3.4.11 shows optimum set point for a single DC bus over a 24 h operating time as function of electricity price. Figure II.3.4.12 shows the interaction among EMO, real-time measurements, and RT-EMS.

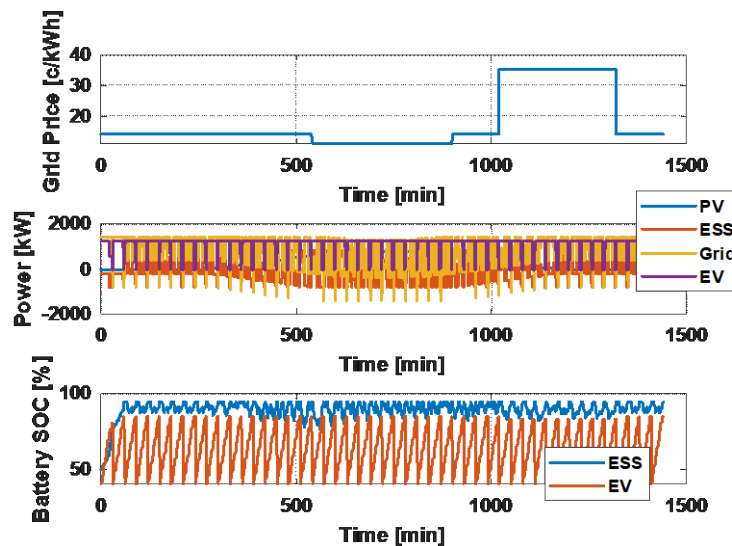


Figure II.3.4.11 Interaction among RT-EMS and EMO over 2 minutes

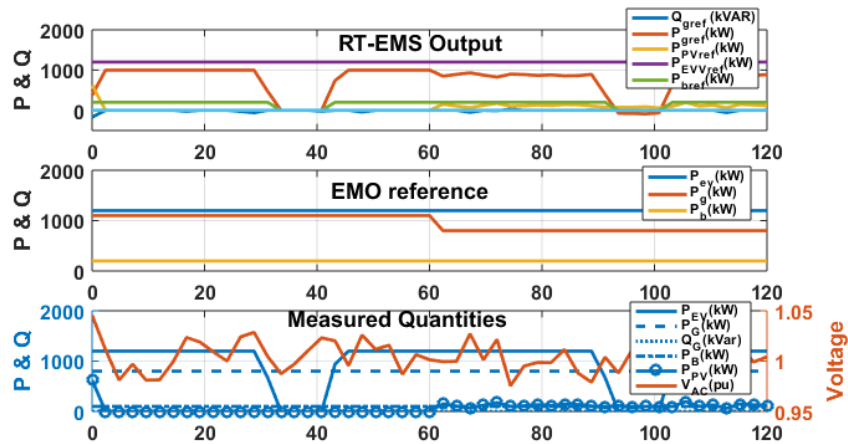


Figure II.3.4.12 EMO over 24 h operating period.

Connector Evaluation (NREL)

The event included a fit and ergonomics evaluation (Figure II.3.4.13), and event takeaways were compiled for the MCS Task Force. The functional evaluation data of the thermal performance of the connectors and inlets was also collected to share with the hardware developers.



Figure II.3.4.13 Fit and ergonomics evaluation of the MCS connector and inlet at NREL

Industry Engagement (ANL)

Industry engagement for MW+ Multi-port EV charging technology gap assessment started in FY19 by holding monthly web-based meetings culminated by an end of year workshop hosted at ANL. The initial draft report on charging system requirements was peer reviewed and new material was added to the report before it was submitted for release in Q2-FY20.

A total of 24 monthly web meetings and two workshops were held by the end of FY20. Each of the web meetings was recorded and archived for review by any stakeholders that could not attend meetings in real-time. Slide materials from guest speakers on technical topics and perspectives on needed solutions were also distributed to the ~300 industry stakeholder mailing list.

Industry stakeholders include a diverse group that covers the span of charging energy flow from utility interconnection to power conversion/dispenser to vehicle couplers to vehicle battery terminals. These groups include manufacturers of EVSE electronics, couplers, charging cables, MD/HD electric vehicles, energy storage systems and protection system components. The groups also include 22 utilities, 21 site operators, and 14 planning services agencies.

Progress continued in year 2 of the MW+ Multi-port EV charging system industry engagement activities with interactive discussions about gaps and needed testing/research topics. The top five charging process gaps are described as the following:

- **Sub-transmission Interconnection:** Gaps exist for charging installations that go beyond a standard low voltage (480vac) utility-owned pad-mounted transformer limitation of ~3000A. For advanced charging systems that may include local PV generation and storage able to export available (and/or) surplus power for the regulation services market, the interconnection agreement can be complicated, expensive, and have a long lead time. Medium voltage (MV) systems require space for MV rated load centers with circuit protection and must meet the associated arc flash hazard mitigation requirements.
- **Low/Medium Voltage AC-DC Power Conversion:** Following the pad-mounted transformer limitation for larger capacity charging installations gap, there are two paths for AC-DC power conversion at the Low Voltage (LV) and Medium Voltage (MV) levels. A MV connected power converter is sometimes referred to as a ‘solid state transformer’ (SST) using switch mode semiconductors above 1000v (AC and DC sections). Semiconductors with appropriate ratings for MW+ power levels are a gap, as are robust gate drive circuits to control the semiconductors at these voltage levels. The ability to connect smaller power converters in parallel to reach MW+ charging levels in a safe, highly stable manner is a readiness gap as well. Few standards exist for MV AC-DC power conversion electronics. Supervisory control can be handled by SCADA which lacks clarity.
- **DC-DC Power Conversion to Decouple Loads/Sources on Common DC Bus:** MW+ multi-port charging systems that incorporate local PV/other generation and storage need to decouple these sources from a common DC bus. There is a lack of standards on mechanical connections and modular packaging that could allow (more) scalable charging systems with multiple parallel modules on each energy node. DC-DC converters for multi-port systems need to communicate with a site controller to manage resources as well as coordinate usage of charging nodes for the multiple vehicles vying for the same set of finite charging power resources over the window of available charging time per vehicle.
- **MW+ Rated Output Charging Cables/Couplers:** There is a gap in standards-based vehicle charging couplers at the MW+ level (such as the work-in-progress CharIN HPCCV coupler). Liquid cooling of high current conductors has not been validated. Non-cooled charging cables can be prohibitively heavy, placing strain on the charging coupler/vehicle inlet leading to increased contact resistance that in turn can increase heat dissipation in the coupler to a level too hazardous to touch. Cord handling systems have a gap in terms of the span required to reach trucks that are far from the dispenser or access from overhead.
- **Vehicle Side Components:** MD/HD electric trucks and buses do not have a standardized charging inlet location that could facilitate best practices on floorplan design for charging facilities. Cooling of charging inlet pins and conductors inside the vehicle are a challenge where conductors have finite space to connect the inlet power to circuit protection devices, batteries and traction system electronics. Vehicle-to-charging station communication via powerline communication on the pilot signal to verify robust operation while scaling from 200A up to 3000A is a technology gap.

Conclusions

The use of medium voltage silicon carbide devices and low inductance power modules provides a key enabler to minimize the number of series stack stages required for medium voltage grid connection and to increase the switching frequency for the DAB topologies. The increased switching frequency allowed for significant reduction of the magnetics sizing while still reducing the overall semiconductor losses compared to the silicon equivalents. The detailed CAD design for the power converter stages highlighted the ability to scale to 1+MW systems and improve power density over current 480V charging solutions. The DAB source-load topology provided needed

isolation on both sides of the system to support multiple EV loads from the common grid interface in addition to integration of the distributed energy resources on the DC bus to help offset grid requirements.

The DAB source control was demonstrated to maintain a steady 2kV DC bus voltage with a current balancing feature to ensure uniform power distribution between the paralleled DAB converters and subsequently the output power of the CHB rectifiers. This stability and control were verified in detailed source, load and coupled source-load simulations for the full power range including stability under step load changes. The interaction of the source and load DABs was simulated in conjunction with the PV and ESS on the 2kV bus to demonstrate the source side stability and simultaneous charging of EV and ESS battery. These controls were implemented in TI DSP controllers and are being refined to support the CHIL Architecture development which will be coupled with the average and switching models developed in the power electronics hardware section. The detailed communication structure for the power electronics interface to the central communication and the individual controllers has been outlined and will be implemented with the CHIL interface and NREL supported BMS and Grid optimization.

The grid impact analysis has shown the ramping rate limits and peak charging power for across a few feeders at good locations showing the impact of reactive power to improve these limits. Additional analysis has shown for a feeder the relative size of the grid-tied inverter, photovoltaics, and energy storage systems at a three-port site. A battery management system and site controller have been developed to allow for the CHIL evaluation of a site that can manage the charger rate of multiple vehicles with the distributed energy resources and grid constraints. These control systems will be implemented in embedded hardware for the demonstration.

This project has undertaken a significant industry engagement and support effort. The interaction with the CharIN MCS task force to support the development of multi-megawatt connectors is providing key insights in thermal, fit and function, and communications. The monthly web meetings are ensuring that the results of this project are shared with industry for feedback and that the approaches undertaken are ground.

Key Publications

1. Xiangqi Zhu, Barry Mather, and Partha Mishra, “Grid Impact Analysis of Heavy-Duty Electric Vehicle Charging Stations”. Proc. of 2020 IEEE Power & Energy Society Innovative Smart Grid Technologies Conference (ISGT). IEEE
2. Xiangqi Zhu, Rasel Mahmud, Barry Mather, Partha Mishra, and Andrew Meintz, “Voltage Control Analysis for Heavy Duty Electric Vehicle Charging Station”, submitted to 2021 IEEE Power & Energy Society Innovative Smart Grid Technologies Conference (ISGT). IEEE
3. Mingzhi Zhang, Xiangqi Zhu, Barry Mather, and Andrew Meintz, “Location Selection of Fast Charging Station for Heavy Duty EVs using GIS and Grid Analysis”, submitted to 2021 IEEE Power & Energy Society Innovative Smart Grid Technologies Conference (ISGT). IEEE
4. Xiangqi Zhu, Barry Mather, Partha Mishra, Mingzhi Zhang, and Andrew Meintz, “Grid Impact Mitigation of Heavy-Duty Electric Vehicle Charging Stations”, under internal review, prepare to submit to IEEE Transactions on Smart Grid.
5. Xiangqi Zhu, Barry Mather, Mingzhi Zhang, Partha Mishra, and Andrew Meintz, “Grid Impact Analysis and Mitigation of Heavy-Duty Electric Vehicle Charging Stations”, technical report, under review

Acknowledgements

The 1+MW Charging System for MD/HD Principal Investigators acknowledge the contributions of team members: Aswad Adib, Rachit Agarwal, Kevin Bennion, Mike Coop, Keith Davidson, Myungsoo Jun, Shilpa Marti, Eric Miller, Partha Mishra, Ahmed Mohamed, Brian Rowden, Darren Paschedag, Shriram Santhanagopalan, Michael Starke, and Xiangqi Zhu. The project team also acknowledges the support and guidance of Lee Slezak (DOE HQ) and Manish Mohanpurkar (INL).

II.3.5 Smart Electric Vehicle Charging for a Reliable and Resilient Grid (Recharge)

Andrew Meintz, Principal Investigator

National Renewable Energy Laboratory
15013 Denver West Parkway
Golden, CO 80401
Email: Andrew.Meintz@nrel.gov

Matthew Lave, Principal Investigator

Sandia National Laboratories
7011 East Avenue
Livermore, CA 9455
E- mail: mlave@sandia.gov

Don Scoffield, Principal Investigator

Idaho National Laboratory
775 MK Simpson Boulevard
Idaho Falls, ID 83415
Email: Don.Scoffield@inl.gov

Lee Slezak, DOE Program Manager

U.S. Department of Energy
Email: Lee.Slezak@ee.doe.gov

Start Date: October 1, 2018
Project Funding: \$2,000,000

End Date: December 31, 2021
DOE share: \$2,000,000

Non-DOE share: \$0

Project Introduction

Adoption of plug-in electric vehicles (PEVs) has expanded over the last few years and the light duty market share of these vehicles will increase as the diversity of models continues to grow. On a national scale, the transportation sector was one of the largest consumers of energy in 2019, second only to electricity. The growing trend of electric transportation will shift this energy consumption to rely on the national electric grid more heavily. This project plans to assess the new load that will arise from PEVs and electric vehicle supply equipment (EVSE) to determine possible challenges, as well as opportunities that may arise during this transition.

The National Renewable Energy Laboratory (NREL) is leading this three-year project, which also includes Sandia National Laboratories (SNL) and Idaho National Laboratory (INL). During the first year of this project The Recharge team analyzed PEV adoption rates for medium and high scenarios throughout the next decade, in which PEVs could account for as much as 13% of the total fleet in the United States by 2030. The team then assembled real world travel data for vehicles in the Minneapolis and Atlanta metro regions to assess possible charging needs using EVI-Pro. Using this technique, multiple charging scenarios were developed for varying adoption levels as well as charging preferences for home or workplace charging.

The second year of this project has expanded on these efforts and provided more detailed analysis on the potential grid impacts. Under a co-simulation environment between INL's Caldera software and OpenDSS [1], the NREL and Sandia grid teams assessed the impacts this charging will have on each region's primary distribution networks. The teams performed their analysis for uncontrolled charging to act as a baseline level of impact. These results were then compared to the grid performance using smart charge management controls developed within the Caldera framework. Comparing the level of impact before and after the implementation

of these control strategies helps to determine the value they offer: PEV owners, building managers, charge network operators, grid services aggregators, and utilities.

The final year of this project will result in the development of more sophisticated control strategies and a broader scope of the grid impact analysis. Additional control strategies will be developed outside of Caldera, accounting for DER predictions and real-time feedback from OpenDSS. The grid impact analysis will also be expanded to include secondary analysis of the Minneapolis region and the bulk electric supply along transmission grids in the Atlanta region. A better understanding of the development work required for these controls, as well as a wider scope of analysis will wrap up the project by providing stakeholders with the information required to determine the value smart charge management controls provide as PEV adoption continues to grow.

Objectives

Modeling Smart Charge Control Strategies (INL)

This effort focuses on developing Caldera which is a charging infrastructure simulation platform developed for this project to support detailed analysis of different charging strategies. Caldera which is used by the Sandia and NREL grid groups. The Caldera simulation platform consists of 2 components:

1. Library of high-fidelity vehicle charging models for a wide range of vehicles and charging technology (Level 2, DCFC, XFC)
2. Smart charging strategies that have been developed in multiple VTO Grid & Infrastructure projects

Minneapolis Distribution System Results (NREL)

The objective of the work is to estimate the impact of future EV charging loads on the distribution grid, using a set of 11 representative feeders from the Minneapolis-St. Paul metropolitan area (cold-weather region). The 11 feeders were selected based on their high potential for hosting home, workplace and public charging for future EV adoption scenarios, and represent a cross-section of feeders in the metro area.

Atlanta Distribution System Results (SNL)

The intent of this work is to estimate the potential impact of Electric Vehicle (EV) on distribution systems. The effort examined 10 feeders in the Atlanta, Georgia region comprised of various levels of residential, commercial, and industrial loads.

Development of Secondary Models (NREL)

Partnering with Xcel Energy to study the impacts of EVs on the distribution feeders in the Minneapolis-St. Paul area, an important area of concern for Xcel Energy (and other electric utilities) is the EV impact on the secondary networks. These networks include utility assets from the service transformers to the customer energy meters. Not only do the secondary networks represent a big unknown to the utilities, but the high current draw from EV charging could adversely impact voltages at the customer-end and the utilities may not be aware of these until the problems become ubiquitous. Thus, the NREL team focused on developing secondary networks for its EV impact analysis.

Beyond Hosting Capacity Analysis (SNL)

In the analysis efforts partnering with Georgia Power for the analysis of the distribution feeders in the Atlanta area, the Sandia team thought it was important to understand if an approach similar to photovoltaic hosting capacity analysis could be better adopted for analysis of EV charging on feeders. These efforts encompassed two approaches:

- Stochastic Hosting Capacity of Electric Vehicle Grid Integration
A system-wide hosting capacity analysis to understand an electric feeder's voltage response to various levels of electric vehicle (EV) integration levels and the need for control.

- Estimation of Feeder’s Voltage Response to EV Charging using X/R Ratios
Explore the potential to classify a feeder’s response to new EV charging using only the X/R ratios.

Demand Charge Mitigation Control for Workplace Charging (NREL)

The objectives of the demand-charge mitigation control for workplace charging effort are to: (i) development of a building load prediction algorithm with weather forecast input data, (ii) development of a charge management system integrating building load prediction, real-time building load, and users energy needs, and (iii) evaluation and demonstration of the system on the NREL testbed.

Approach

Modeling Smart Charge Control Strategies (INL)

This task will study the potential of multiple control approaches, through the Caldera tool developed as part of this project, to mitigate negative impacts of PEV charging at scale and provide grid services. New functionality will be added to control PEVs across multiple distribution feeders and to include bulk grid impacts in the objective function. A series of simulations will be run to compare the efficacy of each control’s approach in delivering multiple grid services in various future scenarios. The value of implementing smart charging will be quantified by comparing the increase in PEV charging capacity will be compared against the “cost” of smart charging to determine the value and tradeoff of smart charging.

Minneapolis and Atlanta Distribution System Results (NREL, SNL)

To estimate the impact on the electric grid in both the Minneapolis St-Paul and Atlanta regions, the research included OpenDSS time-series simulations that used electric vehicle driving patterns (generated by EVIPro) and EV charging needs (provided by Caldera). Simulation of the 11 feeders in Minneapolis and 10 feeders in Atlanta provide a realistic representation of system operations using home and work dominant EV charging scenarios. The outputs from the model included load profiles, geographic maps of the system and loads, and the feeder’s performance (i.e line overloading and minimum voltage).

Development of Secondary Models (NREL)

The team used information from Xcel Energy to develop secondary networks and realistic load profiles for the individual customers on the selected feeders. The utilities typically do not include the secondary networks for purposes of planning and operations due to the sheer network size and lack of high-fidelity data. This is demonstrated in Figure II.3.5.1 below for the different feeders.

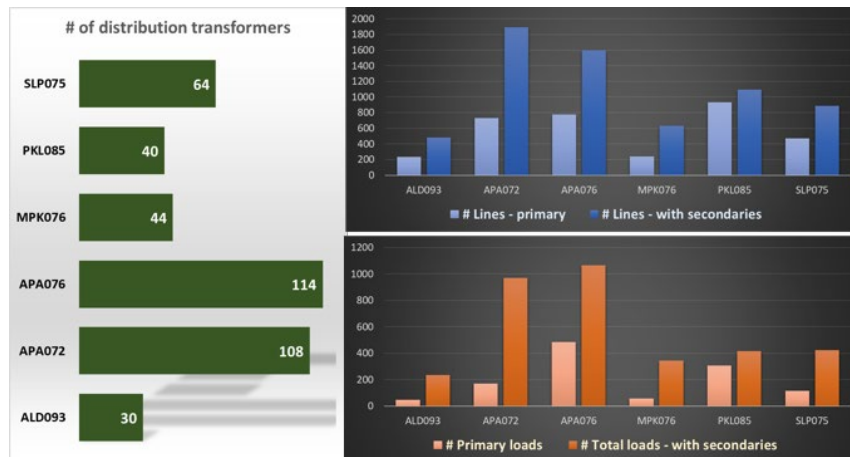


Figure II.3.5.1 Increase in model complexity from adding secondary networks for grid analysis

The team has developed an open-source software record for developing secondary networks titled, Secondary network model development for distributed resources integration (SPROUT), available at <https://github.nrel.gov/sghosh/RECHARGE-modeling>. Utilizing SPROUT would require a secondary database

that the utility maintains where topological information is gathered for consumers connected at the peripheries (low-voltage customers). The database need not contain any identifiable data on consumers. (such as addresses or names), only electrical connection information would suffice. SPROUT would work with the utility planning models in a plug-n-play manner where the circuit is expanded to populate the secondaries with appropriate parameters. The code base primarily uses Python.

In case a utility-maintained secondary database is not available, SPROUT will take statistical distribution on necessary parameters as inputs (such as typical number of customers, length of service lines etc.) and create the secondary topology. The network model output can be a generic graph representation, however, for practical purposes, OpenDSS models are formed at the end of model development cycle. Indices are available that creates an overview of the model created – such as distribution of secondary customers connected per transformer, line lengths, voltage drops etc. This process for developing the secondary networks is presented in the Figure II.3.5.2.

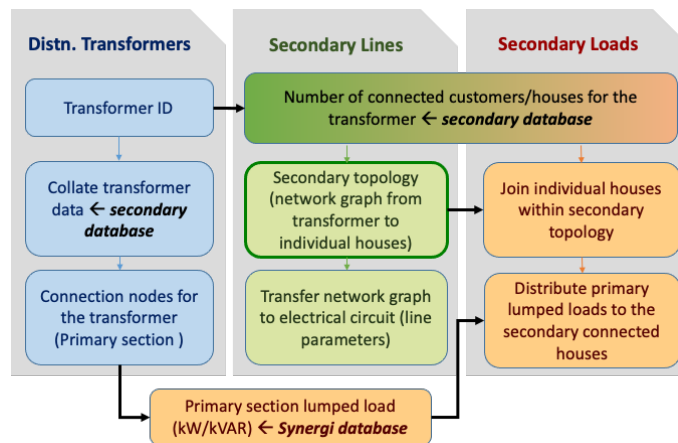


Figure II.3.5.2 Process for developing secondary distribution networks

Beyond Hosting Capacity Analysis (SNL)

Stochastic Hosting Capacity of Electric Vehicle Grid Integration

The experiment involved the simulation (using OpenDSS) of the rated feeder demand and various levels of EV charging loads distributed stochastically throughout each system. In addition to the no control case, two control approaches were implemented and included local and global Volt-Var Curve schemes. Local control used the voltage measurement at the point of common coupling and global used the lowest value measured on the feeder.

Estimation of Feeder's Voltage Response to EV Charging using X/R Ratios

The X/R ratio defines the general characteristics of the lines within a distribution feeder. The ratio explains the relationship between reactance (X) and resistance (R); the magnitude of the ratio impacts the performance of the system. These ratios provide a critical information that potentially define the feeder's voltage response to increased loads. This worked used a Principal Component Analysis (PCA) algorithm to group each feeder's X/R ratios. The X/R ratio groups were then compared with the stochastic hosting capacity voltage response results to see if any correlations exist.

Demand Charge Mitigation Control for Workplace Charging (NREL)

The charge management system consists of three modules; weather forecast data retrieval module, campus load forecast module, and EVSE controller module as shown in Figure II.3.5.3. The 6-hour weather forecast data is retrieved from the high-resolution rapid refresh (HRRR) National Oceanic and Atmospheric

Administration (NOAA) operational weather prediction system and is stored in a Structured Query Language (SQL) database server.

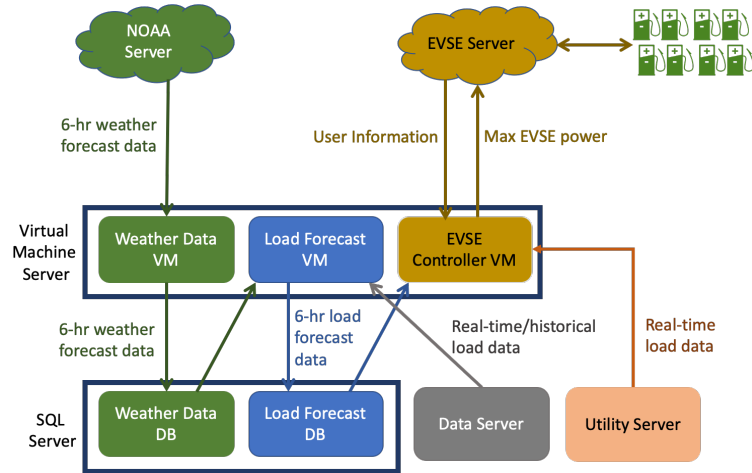


Figure II.3.5.3 Architecture of NREL charge management system

The building load forecast module uses the weather forecast data from the SQL server, generates a 6-hour building load forecast, and uploads the forecast data to the SQL server. The building load forecast model is based on the long short-term memory (LSTM) model, a type of machine learning algorithm, using historical building load data and weather training data and produces a net building load forecast. that is specialized for time series modeling.

The EVSE controller module solves an optimization problem to set a maximum allowed EVSE load [2],[3]. The optimization problem considers the building load forecasts and user information (energy needs and departure time).

$$\min_{P_{EVSE}(t)} \max (P_{forecast}(t) + P_{EVSE}(t))$$

subject to

$$P^{lower_limit} \leq P_{EVSE}(t) \leq P^{upper_limit} \quad \forall t \in \{0, \dots, t_{end}\}$$

$$E^{min}(t) \leq E(t) \leq E^{max}(t) \quad \forall t \in \{0, \dots, t_{end}\}$$

$$E(t+1) = E(t) + P_{EVSE}(t)\Delta t \quad \forall t \in \{0, \dots, t_{end}\}$$

Here, t_{end} is the end of the time horizon (6-hour time horizon was used in the experiments), P^{upper_limit} and P^{lower_limit} are the physical limits of maximum and minimum EVSE power, respectively. The optimization problem tries to find the optimal total EVSE power value, $P_{EVSE}(t)$, for $\forall t \in \{0, \dots, t_{end}\}$ that minimizes the peak of the total campus load. The EVSE controller adjusts the maximum EVSE power value every 5 minutes.

Results

Modeling Smart Charge Control Strategies (INL)

In this project PEV charging and PEV charging control strategies is enabled by Caldera. The foundation of Caldera is a library of high-fidelity EV charging models derived from extensive charging and battery testing data that INL has collected over the past decade. Caldera's charging models accurately estimate charge power profiles, efficiency, and power factors for a wide variety of vehicles and charging technologies under varying grid conditions. This capability is critical for predicting charging impact on the grid.

In addition to the high-fidelity EV charging models implemented in Caldera, four charging control strategies for Level 2 charging have also been fully implemented into Caldera and have been used by the NREL and SNL grid teams to investigate the benefit of these control strategies. These four strategies are each described below.

- **TOU (Time of Use)**- The TOU strategy corresponds likely PEV charging in response to standard time of use rates used by many utilities. In the Electric Vehicle project, utilities that employed time of use rates (with reduced energy costs during the nighttime hours) observed that many PEV owners programmed their EVSE/PEVs to begin charging at the beginning of the time of use rate period. The TOU control strategy models this behavior by waiting to begin charging until the beginning of the time of use period. This strategy shifts PEV charging energy from peak hours to off peak hours, but it causes a step change in load at the beginning of the time of use rate period which may be problematic, see Figure II.3.5.4.
- **Random TOU**- The Random TOU strategy builds on the TOU strategy by randomizing the PEV charge start time within the time of use rate period. The charge start time is selected in a way to ensure that each PEVs charging needs are met and maximum charge energy is consumed during the time of use rate period. The Random TOU strategy is able to shift PEV charge energy to off peak hours but eliminates the step change in load that is present in the TOU strategy, see Figure II.3.5.4.
- **Random Dwell**- The Random Dwell control strategy selects each PEVs charge start time randomly during the park. The charge start time is selected in a way to ensure that each PEVs charging needs are met. This strategy is most effective when the time required to charge is a lot smaller than the park time. The Random Dwell strategy shifts most PEV charge energy to off peak hours and effectively flattens and smooths the load profile, see Figure II.3.5.4.
- **Centralized**- The Centralized control strategy is more complex than the other three control strategies, but it can achieve the global optimal outcome. All PEV charging decisions are made by a centralized aggregator that requires bidirectional communication with each PEV. This control strategy can shift all PEV charge energy to off peak hours and minimizes the amount of variation in the load profile, see Figure II.3.5.4.

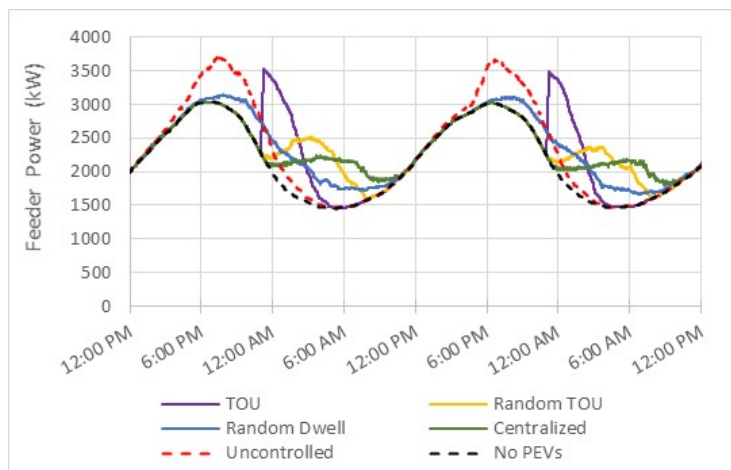


Figure II.3.5.4 Feeder power for test system that demonstrates the functionality of the control strategies implemented in Caldera

Minneapolis Distribution System Results (NREL)

The Home-dominant charging scenario impacts the residential feeders the most, due to the significant increase in EV charging loads. Given that an EV charging load is on par or higher than an average peak power consumed by a home, that the residential feeders may not have excess capacity and that the evening peak coincides with EV charging peak, home-dominant charging for high EV adoption has a significant impact of

residential feeders in the study. However, the commercial and industrial feeders in the study have additional spare capacity to accommodate increase in loading from EV charging. Total power for these feeders is shown in Figure II.3.5.5 in relationship to the base load for the home-dominant and work-dominant charging

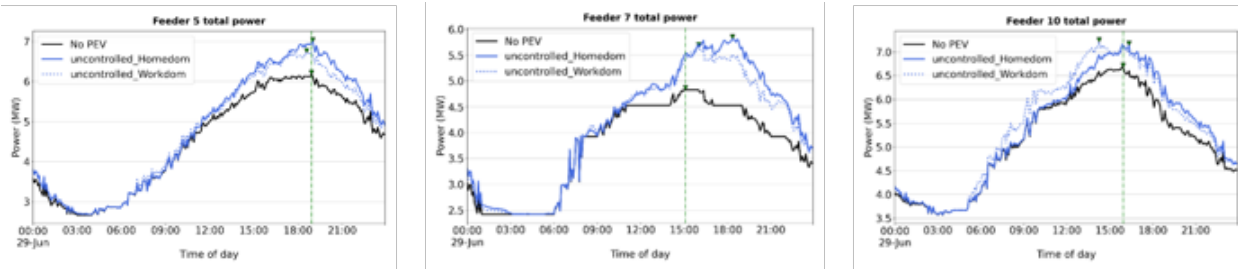


Figure II.3.5.5 Feeder Total Power for three scenarios: No PEV (baseline), Uncontrolled (Home), Uncontrolled (Work) for Residential (Feeder 5), Industrial (Feeder 7) and Commercial (Feeder 10) feeders

scenarios.

The impact of the three different control strategies for the different feeder types are presented in Figure II.3.5.6. Many utilities across the country currently use Time of Use (TOU) pricing for managing EV charging. When we assume that a large number of vehicles start charging at the start of TOU, this strategy has a significant adverse impact on the feeders due to the high peak load, and thus, this strategy may not be feasible for future high EV adoption rates. The other control strategies show acceptable impacts on the loading.

The grid impacts of EV charging is presented in Table II.3.5.1. The two metrics presented here are maximum line loading and minimum voltage across the feeder. The feeder sections that see high line-loading would need to be upgraded to accommodate the increased load. Similarly, when the voltages go below 0.95, the utility would need to upgrade the section or add additional equipment (capacitor banks, voltage regulators) to ensure the voltages are within acceptable limits (between 0.95 and 1.05pu). The residential feeders see the highest impact in terms of both metrics, while commercial feeders have sufficient spare capacity to accommodate additional loading from EV charging. Addition of Workplace charging relieves some of the overloads by shifting these vehicles from residential locations.

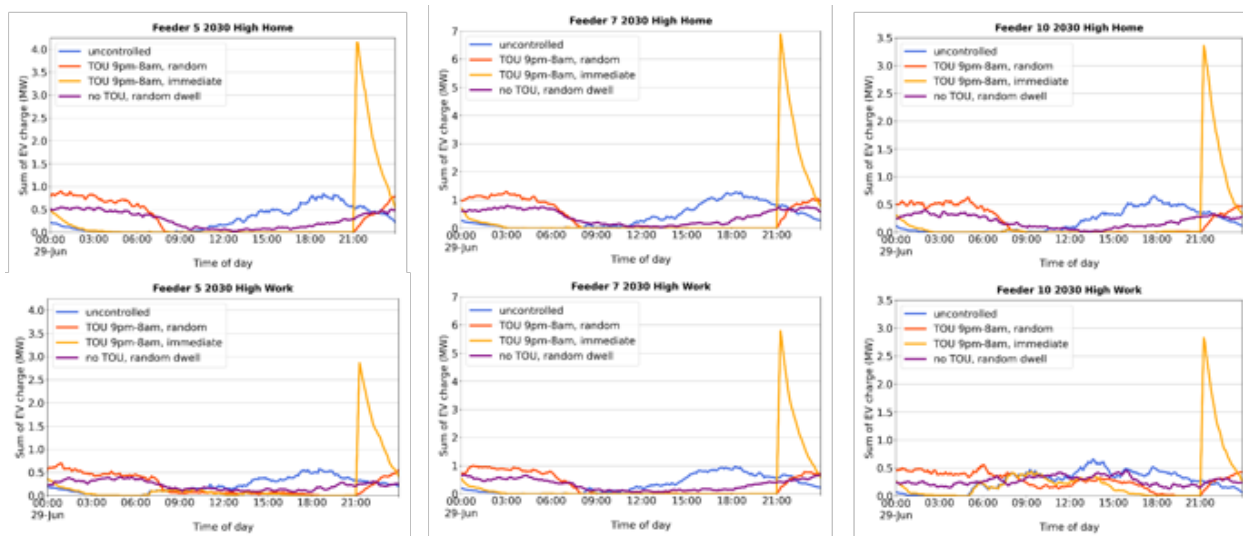


Figure II.3.5.6 EV Charging Load for four control scenarios: Uncontrolled (baseline), Time of Use - random start, Time of Use - Immediate and Random Dwell without TOU for Residential (Feeder 5), Industrial (Feeder 7) and Commercial (Feeder 10) feeders

Table II.3.5.1 Minneapolis Summary of EV Charge Control Impacts on Feeder Performance

Feeder	Scenario	Maximum Line Loading (%)					Minimum Voltage (pu)				
		No EVs	No Ctrl.	TOU Rand.	TOU Imm.	Rand. Start	No EVs	No Ctrl.	TOU Rand.	TOU Imm.	Rand. Start
5 Res	Home	83	86	83	121	84	1.014	1.012	1.015	0.994	1.014
	Work	83	85	83	102	84	1.014	1.011	1.015	1.001	1.014
7 Ind	Home	70	74	70	94	71	1.032	1.03	1.032	1.021	1.031
	Work	70	73	70	89	71	1.032	1.030	1.032	1.022	1.032
10 Comm	Home	89	90	89	94	89	1.032	1.032	1.033	1.028	1.032
	Work	89	90	90	93	90	1.032	1.031	1.032	1.029	1.031

Atlanta Distribution System Results (SNL)

This report documents the results from three systems that represent feeders with mostly residential (Feeder 1), mix of residential and commercial (Feeder 8), and mostly commercial (Feeder 9). Figure II.3.5.7 (a), (b), and (c) describes each of the three feeder’s profile without EVs and the integration of EV’s without control. Feeders 1 and 8 experienced an increase in the original peak for both the home and work dominant scenarios. In contrast, Feeder 9’s peak remained around the same time form the home dominant case but shifted to around hour 9 in the work dominant scenario.

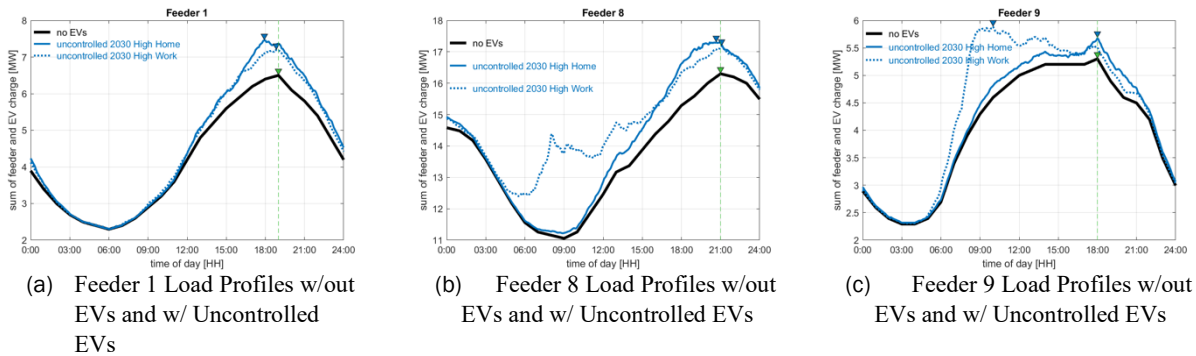


Figure II.3.5.7 Load profiles with and without the Electric Vehicle charging results varied depending on the feeder type. Feeders with a significant number of residential loads (Feeders 1 and 8) experienced an increase in the original peak under both home and work dominant integration strategies. The commercial feeder’s peak changed under the work dominant case but remained the same with the home dominant charging.

The control of the EV charging could improve the overall feeder’s performance. To examine the impact of controls, the simulation effort included typical control approaches, such as random time of use (TOU), immediate TOU, and random charging start times. The results, described in Figure II.3.5.8, provide an overview of how the EV charging throughout the day changed using the three control approaches under the different charging scenarios within each of the feeders. The feeder with a majority of residential load experienced a shift in the EV load that was very similar for the work and home dominant scenarios. Feeders 8 and 9 results resembled Feeder 1’s home dominant scenario outcomes and shifted the load away from the feeder’s peak. The work dominant results were different from Feeder 1 however, since the uncontrolled charging load was largest during the day. The random TOU and random start control did reduce the EV load at the feeder’s peak. The immediate TOU, that increased the cost of electricity between the hours of 19 to 12, exhibited an extreme surge in EV charging demand at hour 19.

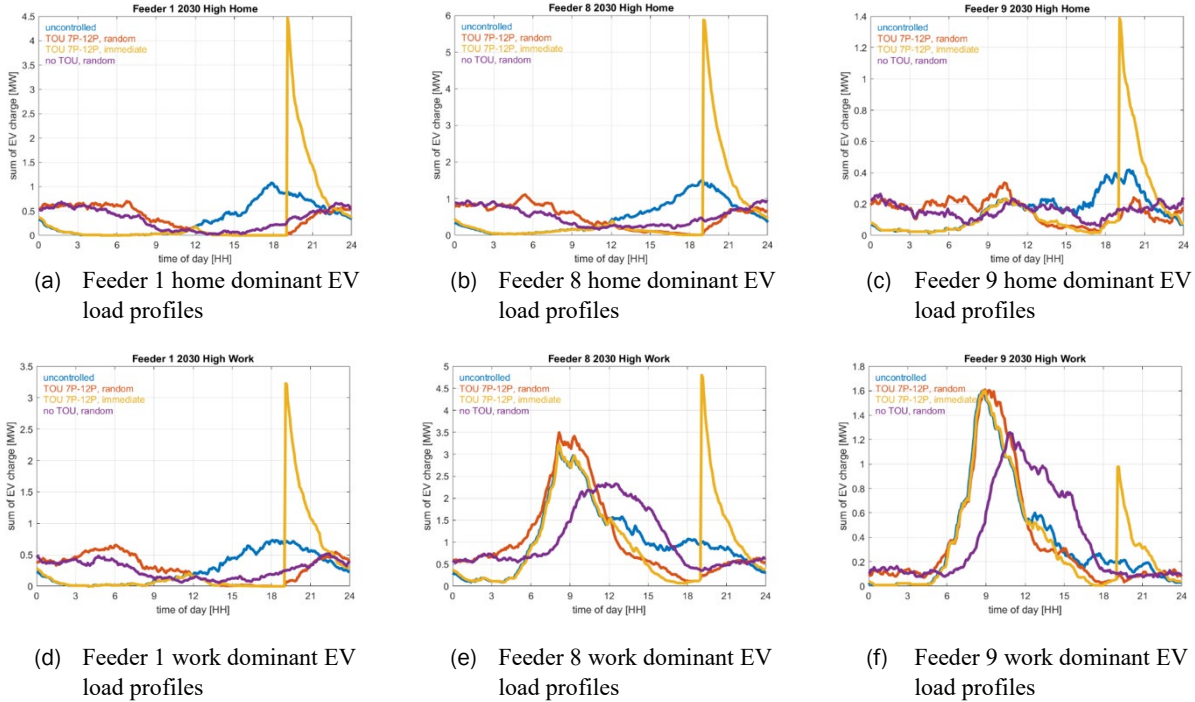


Figure II.3.5.8 The Electric Vehicle (EV) profiles varied depending on the control type and the integration scenario (i.e., home or work dominant). Feeder 1's uncontrolled and controlled profiles had similar results for the home and work dominant scenarios. Feeders 8 and 9, that had considerable commercial loads, exhibited different outcomes depending on the integration strategy. Under each integration scenario the controls shifted the peak from the late evening to the middle of the day with the exception of one. The immediate Time of Use control caused an extreme surge in power demand at hour 19 for all of the cases.

The inclusion of EV charging controls provided some performance benefits for each of the feeders. The results, described in Table II.3.5.2, showed that the minimum voltage response to the addition of EVs was insignificant; the incorporation of EV controls did not improve system voltage, nor did produce a negative result. The line loading did increase on all the feeders after the EVs were added. Not all the control approaches improved the line loading: the TOU immediate caused a significant increase in the line loading. The TOU random and random start produced similar results that decrease line loading below the no control case for each feeder under the two integration scenarios.

Table II.3.5.2 Atlanta Summary of EV Charge Control Impacts on Feeder Performance

Feeder	Scenario	Maximum Line Loading (%)					Minimum Voltage (pu)				
		No EVs	No Ctrl.	TOU Rand.	TOU Imm.	Rand. Start	No EVs	No Ctrl.	TOU Rand.	TOU Imm.	Rand. Start
1 Res	Home	42	50	74	42	44	1.006	1.006	1.007	1.007	1.007
	Work	42	46	65	43	44	1.006	1.006	1.007	1.006	1.007
8 Res-Com	Home	82	90	122	87	87	0.998	0.996	0.996	0.99	0.997
	Work	82	89	114	85	86	0.998	0.996	0.997	0.993	0.997
9 Comm	Home	27	30	37	27	27	1.004	1.002	1.004	0.998	1.004
	Work	27	42	42	42	37	1.004	0.994	0.994	0.994	0.996

Development of Secondary Models (NREL)

A key outcome from modeling the secondary distribution networks is that the utilities will see adverse effects on the secondary networks before the impacts become apparent on the primary networks. The EV smart charging strategies should account for local voltage issues on the secondary networks to reduce the impacts of EV charging loads.

The distribution grid analysis results on the impact of EVs is presented through a few metrics, feeder peak load, minimum voltage, maximum voltage, and average change in line load. The difference in these results can be seen in Figure II.3.5.9 – EV impacts on distribution grid for 2030 High adoption scenario for four different control scenarios (top table) without secondary networks (bottom table) with secondary networks. Figure II.3.5.9 where the data on the top represents distribution grids without the secondary networks, while the data

Metric name	No EVs	2030 High Home				2030 High Work			
		No	TOU	TOU	Random	No	TOU	TOU	Random
		Control	random	imm.	dwell	Control	random	imm.	dwell
Feeder peak load (MW)	10.62	13.1632	11.141	24.12	11.3714	12.348	10.9011	20.66	11.0958
Minimum voltage (pu)	1.008	0.9973	1.0067	0.953	1.0043	1.0005	1.0043	0.964	1.0024
Maximum voltage (pu)	1.05	1.0500	1.0496	1.0500	1.0498	1.0502	1.0497	1.05	1.0500
Avg. line loading change (%)	0	5.88	3.52	28.05	2.81	4.84	2.24	21.1	2.46

Metric name	No EVs	2030 High Home				2030 High Work			
		No	TOU	TOU	Random	No	TOU	TOU	Random
		Control	random	imm.	dwell	Control	random	imm.	dwell
Feeder peak load (MW)	10.79	13.42	11.306	25.67	11.5892	12.587	11.05	21.79	11.34
Minimum voltage (pu)	0.95	0.8324	0.8601	0.612	0.88384	0.817	0.8405	0.63	0.84722
Maximum voltage (pu)	1.050	1.0504	1.0495	1.05	1.04944	1.0504	1.0495	1.05	1.04985
Avg. line loading change (%)	0	14.50	13.57	10.75	10.41	15.21	11.25	16.28	13.44

Figure II.3.5.9 EV impacts on distribution grid for 2030 High adoption scenario for four different control scenarios (top table) without secondary networks (bottom table) with secondary networks

on the bottom represents the impacts with the secondary network modeled for a selected feeder.

Beyond Hosting Capacity Analysis (SNL)

Stochastic Hosting Capacity of Electric Vehicle Grid Integration

The uncontrolled capacity for each feeder varied depending on the baseline voltage and the general response to an increase in EV loads as shown in Figure II.3.5.10 (a). Five out of the six feeders reach the minimum voltage threshold of 0.975 pu on the primary lines, which allows for a buffer of 2.5% for the secondary system so that the feeder will not violate the ANSI standard of 0.95 pu. Feeder 1 exhibited a high rate of change as the number of EV increased, whereas Feeder 4's voltage changed at a very slow rate. The rate of change decreased when the simulation incorporated a volt-var control.

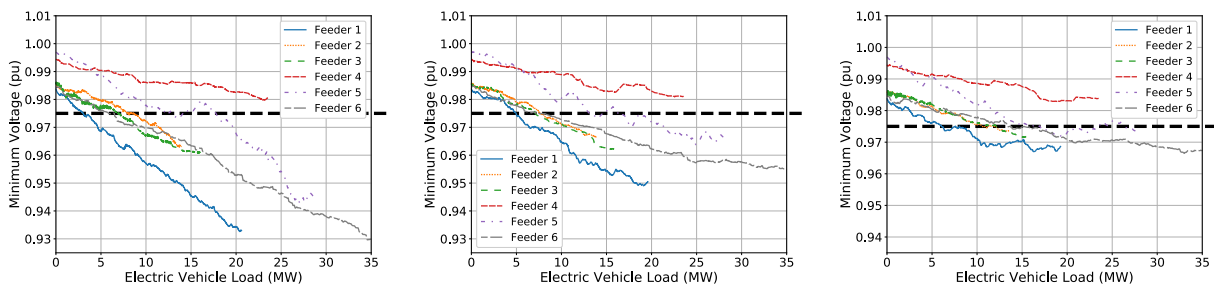


Figure II.3.5.10 Five of the six feeders experienced minimum voltage violations on the primary system in the uncontrolled case.

The two control approaches increased the capacity of each of the feeders by injecting reactive power. The VVC control that used the local voltage measurement as a reference did not prevent violations from occurring but did extend the capacity considerably for Feeder 1 and very little for the other feeders as shown in Figure II.3.5.10 (b). The uncontrolled scenario simulations indicated that the feeders could support the adoption of 15%, 55%, 43%, 100%, 44%, and 14% of the assumed total, where each customer charged two vehicles at the same time. The number of potential EVs increased by 64%, 0%, 3%, 2%, and 32% for feeders 1, 2, 3, 5, and 6 respectively. The control scenario that used the global voltage as a reference showed significant improvements in the overall capacity from the uncontrolled baseline (Figure II.3.5.10 (c)). The increased capacity allowed for the number of EVs to increase by 100%, 53%, 75%, 30%, and 129% for feeders 1, 2, 3, 5, and 6 respectively.

Estimation of Feeder's Voltage Response to EV Charging using X/R Ratios

The classification of X/R ratios for each of the feeders corresponded to the change in minimum voltage with respect to the increase in the EV load. The least-squares regression line slopes determined using minimum feeder voltage as the dependent variable and the EV load as the independent variable qualified the feeder groups. Feeders 2, 3, and 5 had similar slopes and feeders 1 and 5 were each different as shown in Figure II.3.5.11 (a) that compared the normalized voltages to one at the EV load equal to zero. The groups corresponded well with the principal component analysis results.

The first two components of the PCA, which captured over 60% of the variance, for each of the feeders grouped similar to the slopes of the minimum voltage versus load lines. The principal components for Feeders 1 and 4 exhibited differences that set them apart from the other four feeders as shown in Figure II.3.5.11 (b). Feeders 2, 3, 5, and 6 all had similar principal components and thus could be grouped together as shown on the bottom left of Figure II.3.5.11(b). These groups corresponded well with the calculated slopes where Feeder 1 had a slope of -0.0024, Feeder 4's slope was -0.00051, and the remaining feeders had an average slope of -0.00158 with a very small standard deviation of 7.34e-05.

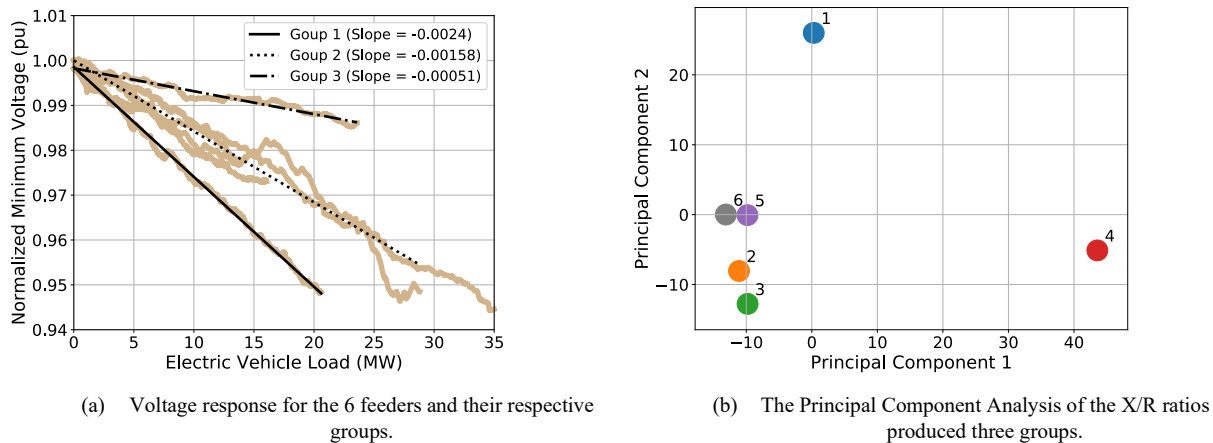


Figure II.3.5.11 The voltage response for the six feeders ended up in three groups and corresponded with the principal component analysis results that used the X/R ratio from each of the feeders.

Demand Charge Mitigation Control for Workplace Charging (NREL)

The load forecast model uses irradiance, temperature, cloud cover, humidity, snow depth, and other parameters to predict the net load on campus. The predicted load (green line in Figure II.3.5.12(a)), is compared to the actual load (yellow line), and the irradiance (blue line), where the predicted and actual power reduce when the irradiance increases due to photovoltaics on campus.

The charge management system was deployed starting March 16, 2020 for tests and evaluation. The test results for March 23, 2020 is shown in Figure II.3.5.12 (b). Tests showed that the total EVSE power (solid orange

line) stays below the commanded EVSE power set point value (dashed black line). The EVSE setpoint value does not completely sync with campus load (solid blue line) but has relatively lower values when campus load is high because the EVSE setpoint values are derived based on load forecasts and user information (energy need and departure time) at the current time.

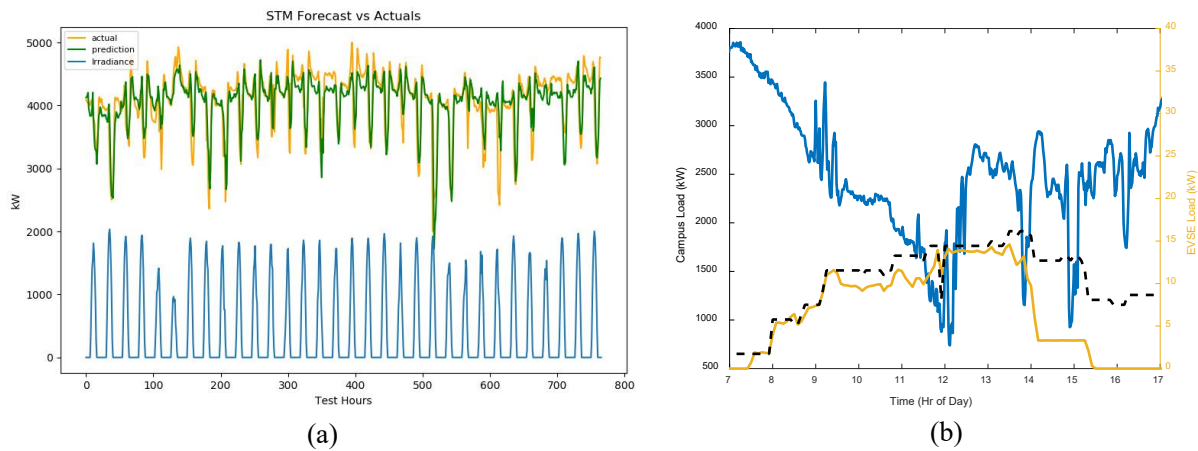


Figure II.3.5.12 (a) Campus net load forecast compared to actual load for December 2019, (b) Test results of charge management performed for the NREL parking garage EVSE's

Conclusions

This project has provided more detailed analysis on the potential grid impacts of PEVs at Scale. Through the co-simulation environment between INL's Caldera software and OpenDSS, the NREL and Sandia grid teams assessed the impacts this charging will have on each region's primary distribution networks. In order to quantify the effects of uncontrolled charging to understand how increased PEV adoption may negatively impact the grid, and to analyze the effectiveness of multiple control strategies in mitigating negative grid impacts introduced by PEVs at scale, it is essential to have high fidelity models of PEVs and effective PEV charging control strategies.

To this end high fidelity charging models have been integrated into Caldera as well as four control strategies of various complexity and performance. The work to analyze the benefits of each of these PEV charging control strategies on real feeder systems in Minneapolis and Atlanta has been started by the NREL and SNL grid teams, respectively. These efforts have shown the impact of various smart charge strategies to the line-loading and voltage across the feeders. The analysis of the potential benefits of each of these strategies compared against the cost of implementing each of these control strategies will help to inform industry of the true value of controlling PEV charging.

References

1. Open Distribution System Simulator™. Available: <http://sourceforge.net/projects/electricdss/>. Accessed October 11, 2019.
2. S. Vandael, B. Claessens, M. Hommelberg, T. Holvoet, and G. Deconinck, "A scalable three-step approach for demand side management of plug-in hybrid vehicles," *IEEE Trans. Smart Grid*, vol. 4, no. 2, pp.720-728, 2013
3. Z. Yi, D. Scofield, J. Smart, A. Meintz, M. Jun, M. Mohanpurkar, and A. Medam, "A highly efficient control framework for centralized residential charging coordination of large electric vehicle populations," *International Journal of Electrical Power & Energy Systems*, Vol. 117, 2020

Acknowledgements

The Recharge Principal Investigators acknowledge the contributions of team members: Jesse Bennett, Kalpesh Chaudhari, Brooke Garcia, Shibani Ghosh, Birk Jones, Myungsoo Jun, Chris Neuman, Priti Paudyal, Manoj Sundarajan and Santosh Veda. The project team also acknowledges the support and guidance of Lee Slezak (DOE HQ) and Manish Mohanpurkar (INL).

II.3.6 Directed Electric Charging of Transportation using xFC (DirectXFC)

Timothy Pennington, Principal Investigator

Idaho National Laboratory
P.O. Box 1625
Idaho Falls, ID 83415-2209
Email: timothy.pennington@inl.gov

Andrew Meintz, Principal Investigator

National Renewable Energy Laboratory
15013 Denver West Parkway
Golden, CO 80401
Email: Andrew.Meintz@nrel.gov

Daniel Dobrzynski, Principal Investigator

Argonne National Laboratory
9700 South Cass Avenue
Lemont, IL 60439
Email: ddobrzynski@anl.gov

Lee Slezak, DOE Program Manager

U.S. Department of Energy
Email: Lee.Slezak@ee.doe.gov

Start Date: December 1, 2019
Project Funding: \$1,500,000

End Date: March 31, 2021
DOE share: \$1,500,000

Non-DOE share: \$0

Project Introduction

Consumer demand for faster charging has prompted charging infrastructure providers to introduce extreme fast charging (xFC). With charge power of over 150 kW, xFC offers numerous benefits for plug-in electric vehicles (PEVs); however, xFC systems must be intelligently managed and integrated with the grid and distributed energy resources (DER) to mitigate negative grid impacts, control system costs, and enable grid services. DirectXFC will explore, simulate, emulate and then assess the value of site and system control strategies for improved grid impacts of xFC charging.

Objectives

Simulation of Multiple Possible Future xFC Charging Scenarios (INL)

The first task of DirectXFC is to simulate future xFC charging scenarios. That simulation must be conducted in a detailed fashion to produce specific load profiles at each charging station so that the detailed impact on the distribution feeders can be assessed. To achieve these simulations INL's Caldera simulation platform requires expansion and additional software functionality. The platform must be capable of not simply modeling the charging needs of the vehicles but rather based on the travel itinerary of each individual vehicle and the topology and known condition of the charging infrastructure landscape—where and when will each vehicle choose to charge. Uncontrolled cases may achieve this simply by simulating the vehicle's use, state of charge and likely recharge point. However, the controlled cases will require the vehicles be aware of availability, and cost of charging, and also their own future travel plans and timing. To facilitate the control strategies within the infrastructure Caldera must represent the charging station's ability to maintain a schedule and accept reservations, communicate variable pricing, and execute station level controls including dispatch of battery energy storage systems (BESS).

Travel Scenarios for Uncontrolled xFC Charging at scale (NREL)

To understand how EVs will charge it is necessary to generate travel data to support xFC simulations via the Caldera tool. This is the first step in the control, optimization, and incentive methods that will be applied to reduce any negative impacts of xFC PEV charging. In order to represent real world vehicle usage a full week of travel data was required to account for daily variations in both driving and charging. Real-world measured driving segments were used as a basis for vehicle travel and charge sessions were determined by the dwell periods associated with the destination land use at each location. The energy requirements for these charge sessions were determined by actual measured driving segments and the performance metrics for a wide range of current and future EV models. The trips were also required to preserve the overall location and time properties of the original population dataset, this means that once simulated the travel patterns would reflect the total population real world use.

Electric Vehicle Adoption Scenarios (NREL)

The travel scenarios are a result of real-world measured driving segments and reflect the mobility requirements for the population dataset. However, a better understanding of the EV fleet makeup was needed to determine specific energy requirements. Therefore, it was necessary to model electric vehicle adoption for a wide range of vehicle types to more precisely model the energy required for each charge session and the power level the vehicle would be capable of. This process began by setting overall fleet adoption trends, outlined in Table II.3.6.1, which were informed by considering prediction models from the Electric Power Research Institute (EPRI), Energy Information Administration (EIA) Annual Energy Outlook (AEO), NREL’s Automotive Deployment Options Projection Tool (ADOPT), and ORNL’s Market Acceptance of Advanced Automotive Technologies (MA3T) model. These predictions detail the adoption percentage as a share of all PEVs for the following vehicle types; battery electric vehicles (BEV), battery electric vehicles with a range exceeding 200 miles (BEV200+), PEV sedans (Sedan), and PEVs with ability to charge at a rate exceeding 150 kW (xFC).

Table II.3.6.1 Fleet Adoption Trends as a Share of PEV

Vehicle Type	2025	2030	2035	2040	2045
BEV	72%	75%	77%	79%	80%
BEV200+	59%	63%	68%	69%	71%
Sedan	67%	58%	57%	57%	56%
xFC	53%	64%	72%	79%	80%

Implementation of xFC station management (NREL)

Demonstration of station control of xFC and the other site devices (e.g., DERs, stationary energy storage) for real-time control implementation will utilize a power hardware in the loop (PHIL) setup at NREL. This setup allows for the team to verify the performance of the INL-developed load profiles and demonstrate operational scenarios from the simulation activities in this project.

Implementation of xFC station management (ANL)

The ANL contribution to the Direct XFC project is based on hardware-based research, i.e., integration of high-power DC charging equipment and a battery system to support peak power mitigation studies in FY 2020.

The hardware includes two (2) 400kW capable CCS EVSE and a ~600kWh Battery Energy Storage System (BESS). The BTCP EVSE have been delivered; each EVSE includes two power cabinets capable of 200kW each and a single dispenser unit.

Distribution Network Interfaces design and Control Hardware in the Loop Testing (ANL)

One of Argonne’s tasks is to determine the communication and control requirements to mitigate potential negative impacts of high-power charging on the local grid and to demonstrate the ability to control the net power demand at the interface to the Energy Plaza.

Approach***Simulation of Multiple Possible Future xFC Charging Scenarios (INL)***

To achieve the objective of a detailed simulation of charging behavior and evaluation of associated grid impacts the approach taken in this research project is the employment and expansion of the agent-based modeling tool—Caldera. Through this type of modeling each vehicle is represented as an agent moving through the simulation and maintaining an accurate state of charge during its itinerary. Caldera is already capable of computing the station load curves generated with high fidelity charging profiles. However, the agent-based framework must be expanded to allow for the objectives of vehicle agents that make independent selections of charging times and locations, and a charging infrastructure capable of communicating to vehicles, being aware of availability and cost of charging and capable of accepting reservations. Finally, station level control of BESS must also be simulated.

To achieve the necessary vehicle agent charging behaviors a new functional unit of software was created and added to Caldera called the Charge Decision Module (CDM). The CDM applies serves to represent the vehicle owner in selecting where and when to charge. In the uncontrolled scenario these decisions can be made based on rather simple criteria such as charging during the trip when the end SOC is expected to fall below a threshold the driver is comfortable with and at the xFC station which is most proximal to the path of that trip. In order to respond appropriately to incentives that will be employed by advanced control strategies the CDM is also capable of calculating optimal charge events based on minimizing total cost of the reasonably available options given the vehicle’s other itinerary. The algorithm developed to assess the cost of various charge options considers many forms of cost including the fees, additional miles driven to the station, and the cost of the driver’s time spent on achieving the charge. To facilitate both uncontrolled and controlled charging decisions it is necessary to integrate a vehicle routing engine capable of calculating driving routes to various stations and the associated time and energy to reach them. The CDM must also execute the communications required to receive the cost and availability data from the charging infrastructure as well as the ability to place and maintain a reservation.

The approach used to achieve the necessary expansions of Caldera with respect to the infrastructure system was the development of the Infrastructure Agent. The Infrastructure Agent possesses several features, but the fundamental capabilities are to maintain a schedule which is able to inform a vehicle if a specific charge point is available at any given time, and what the fees associated with charging at that location, time, power rate, and duration will be. Building the tool in this way allows for the ability to accept and maintain reservations, temporarily close a charge point if the station manager deems it necessary to control total station energy and thus demand charges and provide dynamic pricing as part of a larger control strategy.

To prepare for simulating station level control strategies (which will eventually be tested through HIL) the approach taken was to integrate an existing INL reduced order electro-chemical battery model into Caldera’s model library and then develop a control platform and optimization algorithms. This BESS simulation dispatches energy from the stationary battery to reduce the load applied to the grid during peak charging events at the station. It also charges the stationary battery from the grid at opportune times when station demand is low and grid capacity exists. This control method can be used to avoid demand charges on the station but with increased inputs could also be used to respond to grid conditions upon request and aggregate infrastructure system demand.

Travel Scenarios for Uncontrolled xFC Charging at scale (NREL)

The approach for this task was to use the Zone Entity Probabilities (ZEP) tool to generate weeklong travel data. The ZEP tool was created for the RECHARGE project and further developed through this project. The

tool is a multistep approach that takes millions of real world independent recorded trips and creates multiday travel itineraries. This is done by using the independent trips in conjunction with multiple probability matrices to guide behavior in a stochastic manner to reflect real world chained driving patterns. This approach allows for the known arrival times and departures for a vehicle and determines how to exploit these for greatest charging utility.

Development work specific to DirectXFC were as follows:

- Moving all probability matrices from the California Household Travel Survey (CHTS) to the National Household Travel Survey (NHTS)
- Breaking out behavior by weekdays and weekends
- Exporting the specific land use of trip destinations
- Reconciliation of work vs recreation (i.e., Determining who is going to a commercial zone for shopping vs employment)
- Multiprocessing architecture to allow create of trips at 10x speeds
- Creation of a weekday to weekend user stitching logic to run the ZEP algorithm on weekday-based probabilities and then join them with weekend for the same vehicle.

Electric Vehicle Adoption Scenarios (NREL)

The overall light-duty fleet adoption trends were used to create electric vehicle adoption scenarios to precisely understand the energy requirements and charging power capabilities for specific vehicles. These scenarios included several generic vehicle models to represent the different PEVs available in each scenario year and are simplified by combining all SUV and pickup variants under the truck classification. The key performance metrics outlined for each model were range, efficiency, and fast charging power. These metrics, as well as each vehicle model's share of all PEVs are displayed in Table II.3.6.2. This table also outlines the state of EV adoption in 2020 by mapping the national fleet makeup of current vehicle options from ANL's e-drive data to their representative model in this project. These adoption scenarios were developed in conjunction with the RECHARGE, BTMS and XCEL projects and are a crucial element in developing the energy needs for each charging session. They also are intended to represent a growing industry through the development of more advanced generations of many vehicles that correspond to the transition from older technology to newer options with increased range and charging capabilities.

Table II.3.6.2 Electric Vehicle Adoption Scenarios as a Share of PEV

Vehicle Model	2020 (%)	2025 (%)	2030 (%)	2035 (%)	2040 (%)	2045 (%)	EV Range (miles)	Efficiency (wh/mile) ¹	Fast Charging (kW)
Sports Car (Gen 2)				0.5	0.8	1.1	250	350	400
Sports Car (Gen 1)		1	1	0.5	0.2	0.05	250	350	300
XFC 300 Truck (Gen 3)				6	8	14	300	475	575
XFC 300 Car (Gen 3)				4	15	24.9	300	325	400
XFC 250 Truck (Gen 2)			7	11	10	8	250	475	350
XFC 300 Car (Gen 2)			4	12	16	14	300	325	300
XFC 200 Truck (Gen 1)	7	25	24	13	9	4	200	475	150
XFC 275 Car (Gen 1)	32	27	23	19	10	5	275	300	150
BEV 250 Car	4	6	4	2			250	300	75
XFC 150 Car (Gen 2)			5	6	10	9	150	300	150
BEV 150 Car	18	13	7	3			150	300	50
PHEV 50 Truck	5	8	11	13	16	18	50	475	n/a
PHEV 50 Car	14	13	9	8	5	2	50	310	n/a
PHEV 20 Car	20	7	5	2			20	250	n/a

Implementation of xFC station management (NREL)

Part of the xFC station management effort for DirectxFC will be evaluated at NREL using the Electric Vehicle Research Infrastructure (EVRI) evaluation platform described in Figure II.3.6.1. This platform will have xFC units from three different suppliers (ABB, BTC Power, and Efacec) all connected to a common AC electrical infrastructure. This enables emulation of the hardware diversity seen in field installations. A site controller will be used to implement the xFC station management approaches developed in the Caldera effort. An energy storage system in the lab will be used in some of the scenarios to buffer the load of the entire site. To emulate multiple vehicles arriving to the site to charge a vehicle emulator tied to a bidirectional DC supply will act as the vehicle battery of multiple vehicles through their charging session.

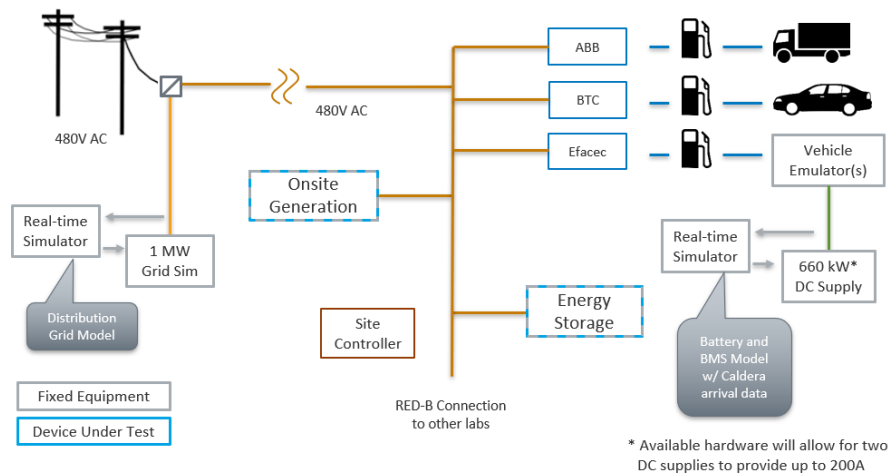


Figure II.3.6.1 xFC Station Management Implementation for PHIL Evaluation

Implementation of xFC station management (ANL)

However, COVID-related delays at the hardware vendors and Argonne resulted in an expected slip to Q3 FY 2021 to have fully operational hardware, i.e., commissioned and integrated with the energy management system, CIP.io.

The BTCP EVSE have been delivered; each EVSE includes two power cabinets capable of 200kW each and a single dispenser unit. The dispenser unit, shown in Figure II.3.6.2 at right, is outfitted with the ANL-licensed SpEC module, i.e., the BTCP Supply Equipment Charge Controller (SECC). The equipment will be installed after site preparations and transformer installation are complete.

ANL is expecting delivery of the BESS from Aggreko in spring of 2021; the ‘Y.Cube’ is capable of sinking or sourcing 1MW for 30 minutes. The system is a single self-contained unit that includes requisite energy storage modules, inverters, HVAC system, power management system, and all safety/alarm systems (as shown in Figure II.3.6.3 below).



Figure II.3.6.2 BTCP 400kW Dispenser unit

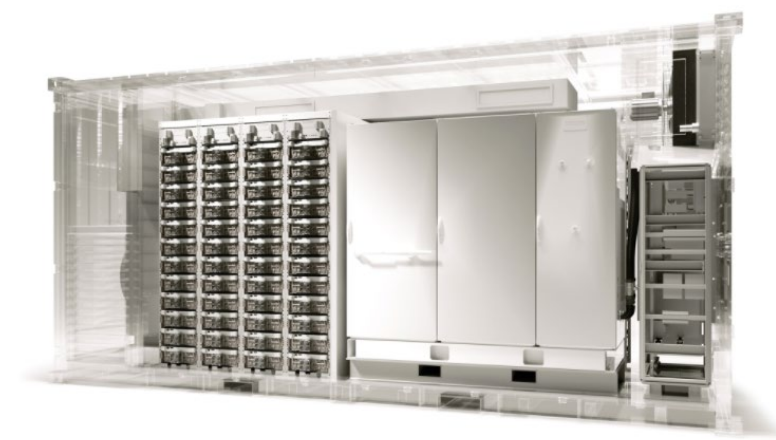


Figure II.3.6.3 Y.Cube Battery Energy Storage System by Aggreko

Distribution Network Interfaces design and Control Hardware in the Loop Testing (ANL)

The task includes grid modeling and simulation, connected to the network of devices at the Plaza via a real-time simulator, to enable hardware-in-the-loop testing. Though installation of the high-power EVSE and BESS have been delayed, the grid distribution network model has been enhanced in FY 2020 with nodes representing commercial/residential EV charging areas and fast charging stations.

Results

Simulation of Multiple Possible Future xFC Charging Scenarios (INL)

The results of this task during FY20 have been substantial amounts of development within the Caldera simulation framework. The development has prepared the team for large scale xFC simulations during early FY21. Some internal demonstrations have proven the functionality of the CDM and Infrastructure Agent. The charging station level controller and stationary battery model have been used to produce some initial results studying the power profiles of a busy urban xFC station with various classes of vehicles using the station and BESS being deployed to reduce the peak power of the charging station. Figure II.3.6.4 below shows the results of these simulations and the initial success of the controller at reducing peak power.

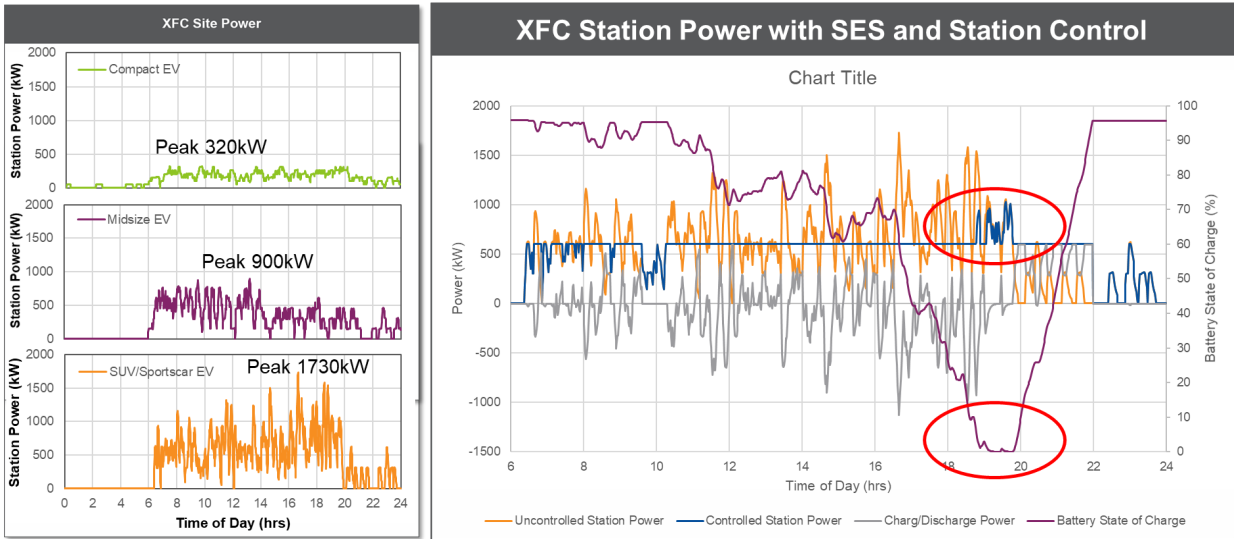


Figure II.3.6.4 (Left)XFC Site Power (Right)XFC Station Power

Travel Scenarios for Uncontrolled xFC Charging at scale (NREL)

The result of this task's effort was the creation of 24 million vehicle trips, representing the year 2045 High PEV population of 975K vehicles. There were 8 different validation metrics governing the success of this approach, these validation metrics included:

- Vehicle initialization - How well could the vehicle home locations be assigned according to registration probabilities.
- Start Time – Evaluates the distribution of vehicle initial start times as compared to the 2017 NHTS.
- Return Time – Evaluates the distribution of vehicle return times as compared to the 2017 NHTS.
- Vehicle Miles Traveled (VMT) – Evaluates the distribution of the vehicle VMT Cumulative Distribution Function (CDF) as compared to the 2017 NHTS.
- City Wide Vehicle Activity – Evaluates the shape of the vehicle activity as compared to the 2017 NHTS and compares when people are active vs idle.
- Zone Arrival Error by Hour of Day – In each hour there is an expected number of arriving vehicles in each city zone; this evaluates the error of vehicles expected vs vehicles existing.
- City Wide Zone Arrival Validation – Similar to the last, this validation metric evaluates the number of vehicles existing in a zone vs expected for the whole city.
- Mean Average Percent Error as a Function of Zone Size – Evaluates how the error is affected by the magnitude of expected vehicles in each area.

One of the validation metrics Vehicle Miles Traveled (VMT) is displayed below in Figure II.3.6.5. The VMT is an important metric since it correlates to the distribution of energy usage of a vehicle population.

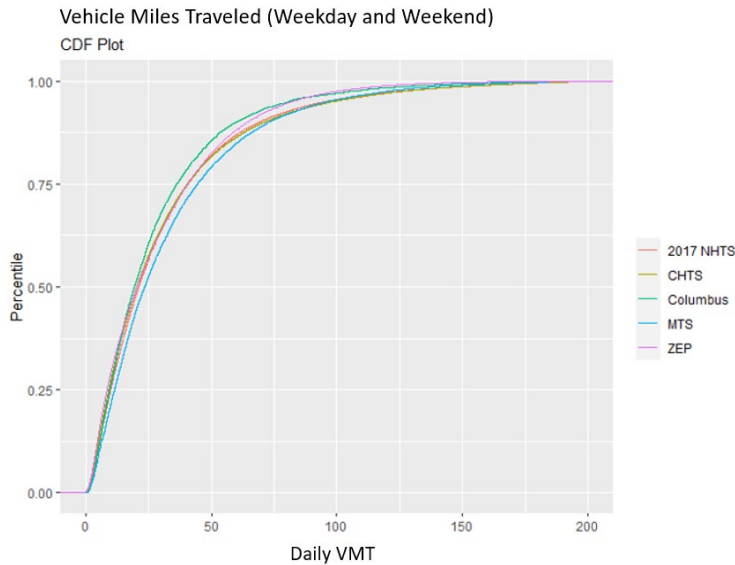


Figure II.3.6.5 ZEP Generated Vehicle VMT

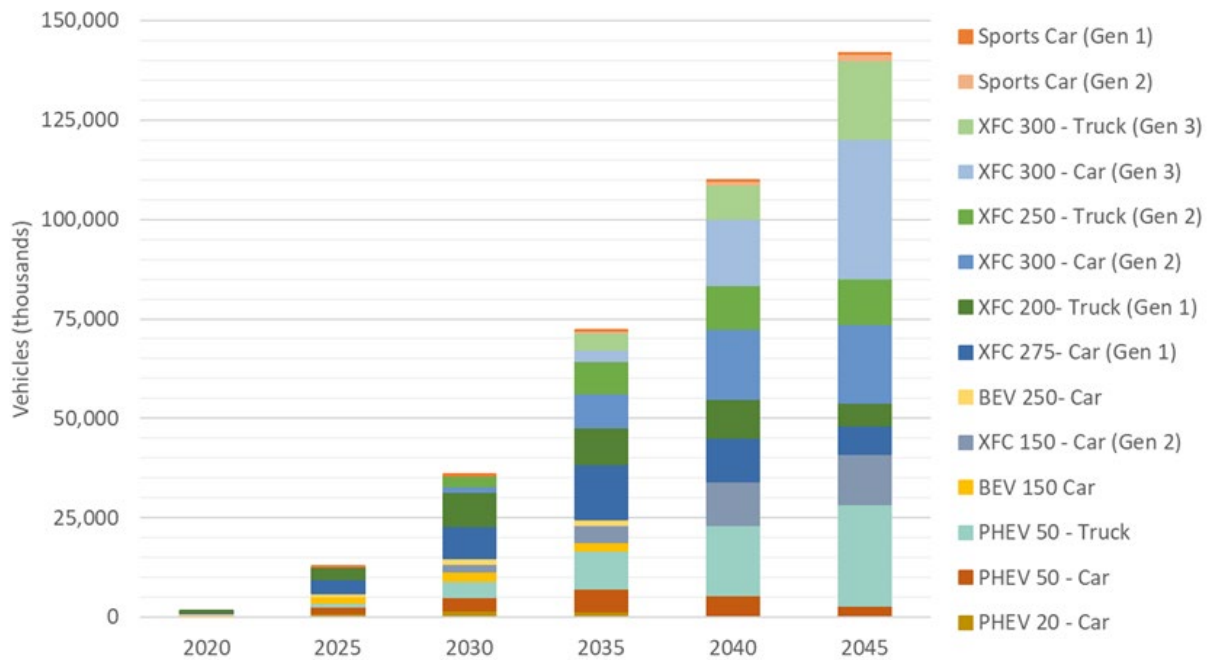


Figure II.3.6.6 PEV Stock by Model (US Total)

Electric Vehicle Adoption Scenarios (NREL)

The result of this effort was the development of 5 possible EV adoption scenarios from 2025 through 2045 that are comprised of 14 different vehicle models. Each of these models is intended to represent one possible scenario for the future of EV adoption in the United States. Therefore, it was important to also consider how reasonable this transition would be from a market perspective. Figure II.3.6.6 outlines the total PEV stock across each year after applying the adoption scenarios to the total light duty vehicle fleet in each subsequent year. These fleet numbers were established using EIA’s AEO 2019 reference case ranges from 71.3 to 77.9 million car and truck sales for the 5-year intervals from 2025-2029 and 2045-2049. This figure also displays the advent of the second generation XFC Car and Truck models in 2025, followed by the arrival of the third

generation of these vehicles in 2030. It also should be noted that the PHEV20 Car, as well as the BEV150, and BEV250 are completely phased out of the fleet by 2040.

This represents the overall growth in PEV adoption for each scenario year, but it was also important to consider how quickly the market share of each vehicle type would increase. Figure II.3.6.7 outlines the net change in PEV stock by model in 5-year intervals accounting for new sales and retired vehicles. This table displays the largest 5-year net-growth coming from the XFC300 Car (Gen 3) with an increase of over 18 million vehicles from 2040 to 2045.

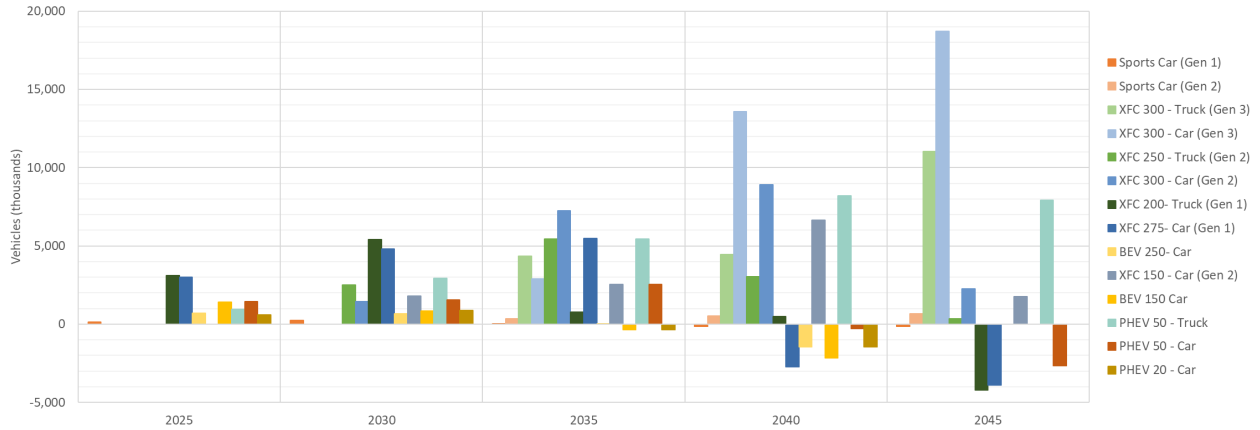


Figure II.3.6.7 Net Change in PEV Stock by Model

Implementation of xFC station management (NREL):

The team has received, installed, commissioned, and evaluated charging equipment from ABB and BTC Power this year in the EVRI lab. Initial evaluation of the charging units was completed using a Nissan Leaf to verify the installation hardware setup. To achieve xFC charging power at up to 200 kW the team will utilize the vehicle emulation hardware to emulate the response of many different vehicle charging profiles. See Figure II.3.6.8 for photos of the EVSE installations.



Figure II.3.6.8 BTC Power 350 kW charger connected to Nissan LEAF (left) and ABB Terra HP 350 kW charger connected to vehicle emulation hardware (right)

Implementation of xFC station management (ANL)

A 2MW transformer is required to power the Y.Cube and co-located XFC stations. This transformer package will be comprised of medium voltage switchgear, an enclosed transformer and switching house with low-voltage switchgear. Substantial ANL directorate level funding was acquired for the procurement and installation of the transformer equipment package since it will be a laboratory resource and can be utilized for other projects as well.

ANL has also completed the formal design phase of the project with the aid of a contract design firm to complete the electrical infrastructure design and transformer bid specification as the transformer is the critical point of common coupling for the project.

Figure II.3.6.9 depicts the site layout of the eXtreme Fast Charge site expansion at ANL. The purple indicator highlights the point of common coupling for the expansion, the medium voltage switchgear and transformer. The red section indicates the location of the switch-house which will include all low-voltage switchgear that feeds the XFC stations, Y.Cube BESS, and any auxiliary loads required. The blue section indicates the location of the four (4) XFC power cabinets and two (2) dispensing units. Finally, the green section indicates the Y.Cube BESS location.

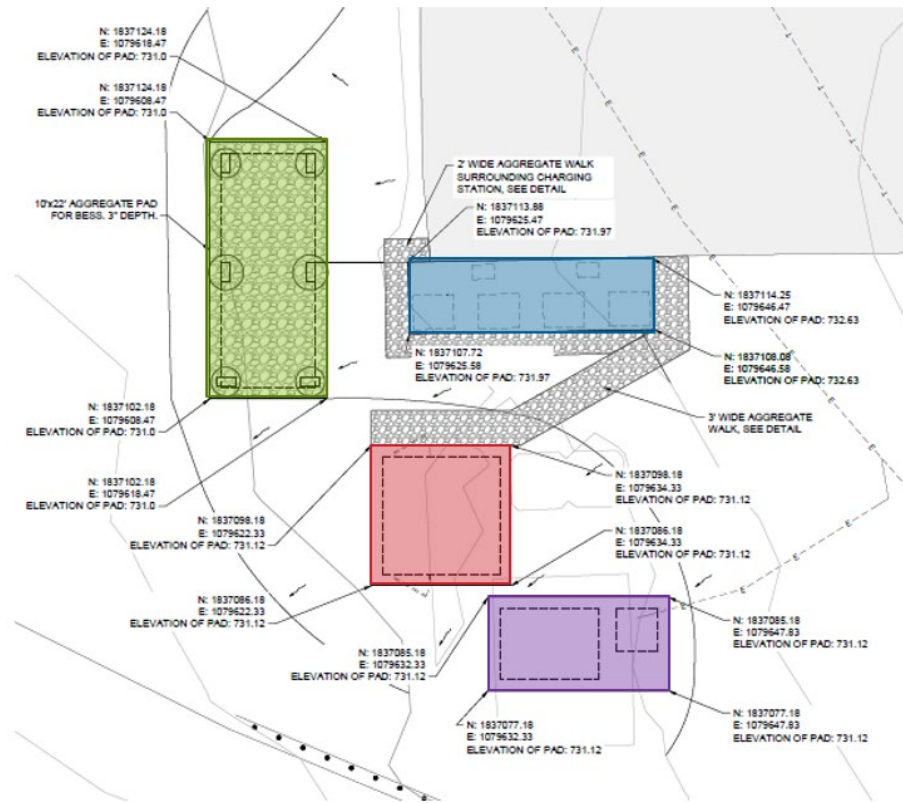


Figure II.3.6.9 Site Layout Plan for eXtreme Fast Charging Station on the Smart Energy Plaza

Distribution Network Interfaces design and Control Hardware in the Loop Testing (ANL)

Programmable nodes were added to evaluate the impact of fast charging stations with EVSE ranging from 50 kW to 300 kW, energy storage systems and photovoltaics were integrated as well. In addition, the interface between distributed network model and CIP.io, the common integration platform for the devices at the Plaza, has been established.

Conclusions

The groundwork has been successfully laid for detailed xFC impact assessment simulations to be carried out and control strategies to be developed and evaluated. With the vehicle adoption quantities and models agreed upon by the team (in collaboration with several other project teams) the agents which will participate in the simulation have been established.

The travel scenarios were developed using the ZEP tool which was a good fit for generating the data required for the DirectXFC project. This method created millions of viable vehicle itineraries from a disparate database of non-chained trips. Joining the independent trips based on multiple stochastic methods allowed for the creation of a much more valuable database for researchers to evaluate their control methods.

The simulation platform, Caldera, has been enhanced to enable the vehicle agents to make decisions about when and where to charge in the absence of or in response to control strategy incentives and reservations. Caldera has been enhanced with an Infrastructure Agent capable of scheduling and pricing charges as well as booking reservations. The site level controller has also been developed and successfully produced simulation results including BESS control at the xFC station. The evaluation of xFC station management approaches are progressing with the installation of xFC hardware at NREL, and planning and procurement occurring at ANL.

References

1. E. Wood, C. Rames, M. Muratori, S. Raghavan, and S. Young, "Charging electric vehicles in smart cities: An EVI-Pro analysis of Columbus, Ohio." Nat. Renewable Energy Lab. (NREL), Golden, CO, Tech. Rep. NREL/TP-5400-70367, 2017
2. Cantelmo, G. Qurashi, M. Prakash, A. Antoniou, C. Viti, F. (2020). Incorporating trip chaining within online demand estimation. *Transportation Research Part B: Methodological*, Volume 132, pp 171-187. <https://doi.org/10.1016/j.trb.2019.05.010>.
3. U.S. Department of Transportation, Federal Highway Administration, 2017 National Household Travel Survey. URL: <http://nhts.ornl.gov>.
4. Electric Power Research Institute, "Plug-in Electric Vehicle Market Projections: Scenarios and Impacts," EPRI Report #3002011613, <https://www.epri.com/#/pages/product/3002011613/>, 2017
5. E. Kontou, C.Z. Liu, F. Xie, X. Wu, Z.H. Lin. Understanding the linkage between electric vehicle charging network coverage and charging opportunity using GPS travel data *Transp. Res. C Emerg. Technol.*, 98 (2019), pp. 1-13
6. Primerano, F., Taylor, M.A.P., Pitaksringkarn, L. et al. Defining and understanding trip chaining behaviour. *Transportation* 35, 55–72 (2008). <https://doi.org/10.1007/s11116-007-9134-8>
7. Miller, H. J., & Shaw, S. L. (2001). *Geographic information systems for transportation: principles and applications*. Oxford University Press on Demand.
8. City of Atlanta - Department of City Planning. (2019). Zoning Map [GIS Shapefile]. Retrieved from <https://dcp-coaplangis.opendata.arcgis.com/datasets/zoning-map>

Acknowledgements

The following investigators have worked on this project: Don Scoffield, Zonggen Yi, Manoj Kumar Cebol Sundarrajan, Paden Rumsey, Jesse Bennet, Keith Davidson, Chris Neuman, and Darren Paschedag, Daniel Dobrzynski.

II.3.7 Grid-Enhanced Mobility-Integrated Network Infrastructures for Extreme Fast Charging [GEMINI-xFC] (NREL, LBNL)

Matteo Muratori, Principal Investigator

National Renewable Energy Laboratory
15013 Denver West Parkway
Golden, CO 80401
Email: matteo.muratori@nrel.gov

Timothy Lipman, Principal Investigator

Lawrence Berkeley National Laboratory
2150 Allston Way, #280
Berkeley, CA 94720
Email: tlipman@lbl.gov

Lee Slezak, DOE Technology Manager

U.S. Department of Energy
Email: lee.slezak@ee.doe.gov

Start Date: December 1, 2019
Project Funding: \$1,000,000

End Date: December 1, 2022
DOE share: \$1,000,000

Non-DOE share: \$0

Project Introduction

The Grid Enhanced Mobility-Integrated Network Infrastructures - Extreme Fast Charging (GEMINI-XFC) project is exploring the grid impacts of future electric transportation scenarios and the ability of coordinated grid and mobility control to help manage resulting challenges. The project focuses on the demands of extreme fast charging (XFC) for the light duty fleet on the electric distribution system. GEMINI-XFC is creating a novel joint grid-transportation co-simulation framework that captures mobility and electric interactions at the individual level for millions of customer/agents covering an entire large metropolitan region to provide unprecedented resolution and scale for evaluating controllers and analyzing impacts and synergies across transportation and the power system.

Increasing vehicle electrification will significantly alter the transportation sector over the coming decades. These changes will likely include extensive use of extreme fast charging (XFC), especially for larger vehicles, to enable long-distance travel, convenience, and to support consumers that cannot reliably charge at home/work. Simultaneously, the continued growth of mobility-as-a-service will likely demand fast charging solutions to support greater vehicle utilization and avoid expensive downtime. Furthermore, self-driving vehicles will require high rates of utilization that will make XFC a potential key to cost-recovery.

However, uncoordinated XFC can create grid challenges, particularly at the distribution level (Muratori 2018; Masoum et al. 2010). Two strategies can support widespread XFC: gold-plate the grid (i.e., upgrade all systems to enable worst-case, fully coincident loads) or use integrated planning and coordinated operations to enable a smart system based on advanced controls that leverage load flexibility and distributed energy resources (DERs). With the right design, operating practices, and control; XFC can simultaneously support both mobility and grid operations, but fully realizing the potential of XFC will require unprecedented coordination among the charging infrastructure, grid, and vehicles.

The future demand for XFC and the optimal control strategy to mitigate grid challenges will depend on the evolution of both the transportation and power systems. Transportation scenarios with varying levels of electric vehicle (EV) adoption and penetration of advanced mobility options (e.g., ride-hailing and automation)

as well as grid scenarios differing in variable renewable energy generation and prevalence of DERs are being explored in this project to assess the resulting impacts of XFC.

Objectives

The GEMINI-XFC project combines high-fidelity grid and transport modeling at an unprecedented level of resolution to both co-design and simulate operations of a smart system based on advanced controls that leverage load flexibility and DERs to optimize the integration of XFC across a full regional scale.¹ A key goal of the project is to conceive, develop, implement, and evaluate a smart controller to mitigate possible negative effects of EV XFC on electric distribution systems.

To do so, GEMINI-XFC uses first-of-a-kind integrated high-fidelity grid and transport modeling to identify effective pathways for widespread electrification by leveraging control to minimize the impact of XFC on distribution systems at a full regional scale with individual customer resolution. The focus of GEMINI-XFC is on-road passenger mobility in the entire San Francisco Bay Area looking at transportation options and grid systems in a long-term future (~2040) characterized by significant changes compared to today's systems.

Approach

Broadly, the project has three parallel and interacting efforts:

1. Mobility-grid controller design for XFC integration
2. Transportation scenario development and demand-side modeling
3. Large-scale transportation-grid co-simulation for performance evaluation and impact analysis.

Controller Design

The overall controller aims to co-optimize mobility and power systems operations: minimize outages, travel and charging times, voltage excursions, and excessive operation of legacy voltage control devices. The different control objectives are weighted such that critical objectives, like avoiding outages are prioritized first, while desirable outcomes that are not critical are weighted less. For the grid aspects, most of the considerations have three categories: 1) an absolute limit that should not be violated for reliable operations, 2) an acceptable operating range, where operation should be limited to shorter durations, and 3) a desired operating range where operations can be conducted indefinitely. For instance, above a certain power threshold (often well over the nominal rating) distribution line and transformer overloads, have a high likelihood of leading to outages.

As a result, these are minimized first because not only would these outages prevent charging but would also adversely affect other customers on the same feeder. Similarly, for extreme voltage violations. The next priority is to focus on mobility objectives by minimizing travel and charging times so that travelers maintain easy access to mobility. The controller would then attempt to minimize the extent of “acceptable for a limited time” grid operations. Voltage excursions are minimized next because they are tolerable to a small degree for short periods of time; however, they can be problematic if they occur for longer durations or extreme excursions. Voltage excursions as discussed here are any bus voltages outside ANSI range A, which is defined as being from $\pm 5\%$ or 0.95 to 1.05 per unit. ANSI range B of -8.3% to $+5.8\%$ is considered acceptable for short periods of time, while violations outside of range B are considered unacceptable and are minimized in the same category as outages. Transformer tap changes and capacitor switches are the last objective, because while tap changes are not inherently harmful, many changes in a short period may indicate an instability and large increases over time cause excessive wear.

The smart controller is structured and implemented in two distinct levels: planning and operation levels. The planning level determines charging station levels and locations as exogenous input to the operations

¹ XFC in this project is defined with a grid perspective: any EV charge point (or station) with a charger (or plug) capable of charging at 250 kW or more, or at least 1 MW of total site load from several chargers of least 50 kW each.

simulation. The operational level uses inputs from the planning level and several transportation and grid scenarios to control EV charging and distributed storage assets and simulates responses of passenger vehicle movement and charging of EVs, and distribution system stability.

Co-simulation for evaluation and analysis

To evaluate the performance of the controller and analyze the impacts on the mobility and grid systems, a center piece of the project is the development and use of a co-simulation that involves mobility and grid models, as illustrated in Figure II.3.7.1. The Hierarchical Engine for Large-scale Infrastructure Co-Simulation (HELICS) will coordinate execution timing and data flows among all participating sub-models (Palmintier et al. 2017). The Behavior, Energy, Autonomy, and Mobility (BEAM) model is used to model mobility (Sheppard and Waraich 2019) and the PyDSS extensions (Latif 2020) to OpenDSS is used to model the electric distribution systems. Data for electric distribution system is taken from the Smart-DS project's synthetic San Francisco dataset (Palmintier et al. 2021).

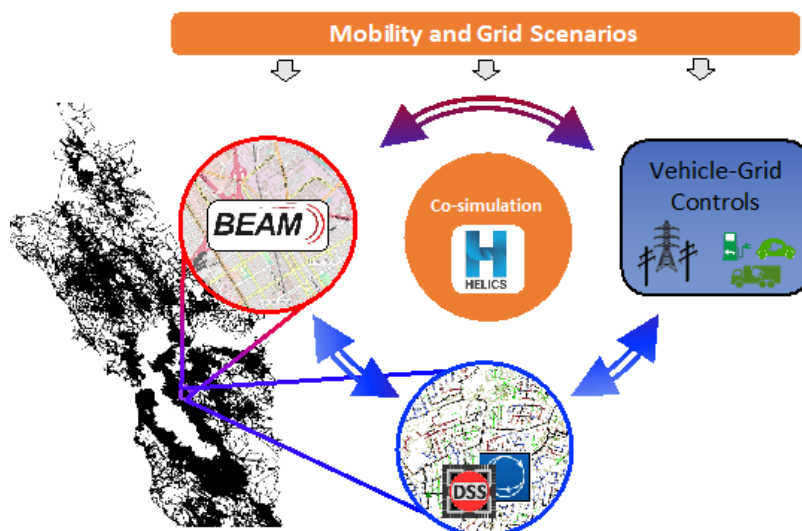


Figure II.3.7.1 HELICS Co-Simulation Framework Overview

The BEAM model is used in the HELICS framework to simulate the transportation network and EV charging demands both geographically and temporally for a sample analysis day. BEAM is an agent-based transportation system model designed for analyzing future large-scale transportation network scenarios. BEAM interacts with infrastructure planning modules such as LBNL's FCSPan and NREL's EVI-Pro to simulate large networks of privately and fleet-owned EVs with a combination of human drivers and automated operation.

BEAM, the distribution model, and the distribution controller, interface via the HELICS co-simulation platform. This co-simulation will allow each simulation to maintain high fidelity modeling by avoiding the need for a single computationally demanding model that captures all assets and behaviors. The transportation system will be modeled down to individual vehicles at a 5-minute resolution and the distribution system down to individual customers at a 15-minute resolution. These high-fidelity model interactions will allow increased flexibility of control and better representation of charging effects on the grid.

Scenario Development

Work recently completed for the DOE Smart Mobility consortium used a combination of these infrastructure planning tools and the capabilities of BEAM to develop a scenario analysis looking across several dimensions (charging system power levels, EV battery sizes/driving ranges, and ride-hailing fleet sizes) to find points of diminishing return in for example investments in the extent of XFC charging infrastructure (Zhang et al. 2019; Zhang et al. 2020). In the iterative process of defining recharging networks and converging on a solution for

each scenario (including layout of infrastructure, size of EV fleet, driving range/battery capacity, and spatially and temporally resolved charging loads), the detailed operations of a ride-hailing fleet consisting of both ICEVs and EVs along with privately owned-vehicles is simulated.

Privately owned EVs charge at home (if residential charging is available) and at other locations, including workplace and public charging. Automated electric ride-hailing vehicles are assumed to charge at a set of charging depots that can be accessed only by automated ride-hailing vehicles. Human-driven electric ride-hailing vehicles compete with non-ride hail vehicles on the public charging network. The optimal depot charging network is defined by FCSPlan (Zhang et al. 2020) and the public charging network is defined by EVI-Pro (Wood et al 2018), both with an iterative process. In the first iteration of this process, vehicles are simulated as having access to XFC or lower power direct current fast charging (DCFC) levels at all potential parking spots. Using initial outputs from BEAM, based on nodal demands in this scenario with unconstrained charging infrastructure, the FCSPlan model then chooses optimal locations for a limited amount of DCFC stations to support the operation of the automated electric ride-hailing vehicles. See Figure II.3.7.2 for an example of DCFC location planning for the San Francisco Bay Area for future fleets of automated electric vehicles (AEVs).



Figure II.3.7.2 Example of Charging Infrastructure Planning Integration with BEAM

EVI-Pro uses the methodology described above to site charging infrastructure to meet charging demand from human driven ride-hailing and personal-use vehicles. The constrained charging networks generated by FCSPlan and EVI-Pro are used in BEAM for subsequent runs with the same vehicle fleet, and system performance metrics are produced using this more detailed fleet simulation.

Results

Progress has been made on all three aspects of the project. Initial results at this stage of the project include establishing an initial set of scenarios, progress with BEAM development including identification and tracking of XFC events as defined in GEMINI, considerable progress with design and implementation of an integrated set of system controllers and prototyping the co-simulation framework for a significant sub region of the bay area electric system.

Progress towards definition of future mobility/power scenarios requirements and format

GEMINI-XFC will use a combination of the Transportation Energy & Mobility Pathway Options (TEMPO) and BEAM models to establish future transportation scenarios. During this first phase, the project focused on identifying the potential data linkages between TEMPO and BEAM, so they can be effectively exercised during the project. Table II.3.7.1 shows a summary comparing the scenario capabilities of both models

Table II.3.7.1 Summary Capabilities of TEMPO and BEAM

	TEMPO	BEAM
Geography	National with implicit geographic representation (e.g., urban, suburban, etc.)	Large Metropolitan Areas
Time	Multi-annual simulations with two-hour resolution of a representative week	Daily Simulations
Transportation Technologies	Generic powertrains covering entire sector	Complex Fleet Mixes Including Personally-Owned and Ridehail Vehicles Operating as Gasoline ICEs and Battery EVs
Mobility Demand	Household mobility and freight demand	Derived From Evolution of MATSim Programming
Endogenous Model Decisions	Mode choice, technology adoption, and vehicle ownership	Driver and Transit/TNC Customer Behavior in Response to Transportation Network Conditions

The following TEMPO inputs will be coordinated with BEAM inputs:

- LDV size class distributions (e.g., midsize, SUV, etc.);
- LDV technology assumptions (e.g., battery capacity, fuel economy, etc.); and
- Electricity and other fuel costs.

In addition, the following TEMPO outputs will be provided as BEAM inputs:

- LDV powertrain mix for personally owned and Mobility as a Service (MaaS) LDVs;
- Household LDV ownership; and
- Adoption of automation for personally owned and MaaS LDVs.

To do so, TEMPO data will be disaggregated from an implicit geographic and household composition resolution to match BEAM households modeled for the San Francisco Bay Area. This will result in the following transportation scenario dimensions:

- Adoption of PEVs for both fleets and personally-owned LDVs, including BEVs and PHEVs at various all-electric ranges;
- Personal LDV vehicle ownership (as a result of increased penetration MaaS);
- Recharging opportunities for personally-owned and MaaS LDVs, including charging power levels and the availability of home, workplace, and public charging; and
- Automation of personally-owned and MaaS vehicles, with automation as a variable (0-100%) for personally owned and MaaS LDVs and other vehicles (e.g., buses).

The BEAM model helps to identify transportation system charging demands for different types of EVs (privately and fleet owned) at specific locations defined in a framework of transportation analysis zones (TAZ). The planning of the charging station infrastructure is based on the workflow that had been developed during the U.S. DOE SMART Mobility project for San Francisco Bay Area (Smart et al. 2020). Both residential and public charging network designs were provided using the National Renewable Energy

Laboratory's (NREL's) EVI-Pro (Wood, Rames, and Muratori 2018). EVI-Pro uses data on vehicle travel patterns, EV attributes, and charging station characteristics in bottom-up simulations to estimate the quantity and type and location of public charging infrastructure necessary to support regional adoption of EVs, and their resulting charging load profiles.

The SMART Mobility workflow has adopted an iterative multi-step process. For each simulation scenario, BEAM determines which households across San Francisco will be simulated as owning a BEV based on vehicle adoption distributions. These distributions are conditioned on the household income of each home. For each household that owns a BEV, BEAM uses housing stock characteristics from UrbanSim (i.e., tenure, residency type) in order to make on-the-fly estimates of residential charging availability based on EVI-Pro residential charging assumptions. Household-level residential charging availability estimates are used within BEAM to simulate utilization of an unconstrained public charging network. EVI-Pro uses public charging demand placed on the unconstrained network to design a public network of Level 2 and direct current fast-charging stations to meet driver demand realistically. A final round of BEAM simulations is conducted using the constrained public charging network supplied by EVI-Pro. A similar approach is taken by FCSPlan—a tool developed under the SMART Mobility Alternative Fueling Infrastructure pillar—to design a dedicated network of fast-charging stations for automated ride-hail fleets simulated in BEAM (Zhang et al. 2020).

For the power system scenarios, the project will largely leverage existing defined scenarios. For the distribution system, which is the core focus for GEMINI-XFC, this includes using the randomized scenarios included with the Smart-DS datasets for DER Technology adoption (e.g., solar PV, energy storage) with customer-level resolution. Bulk electric system data will be taken exogenously from NREL Standard Scenarios for regional generation mix and wholesale prices.

Initial XFC Simulations in BEAM

Initial simulations for this project show the capability of BEAM to identify XFC events for the grid at different locations and times. Presented below are the results of an initial set of BEAM runs, as well as some sensitivity analysis related to assumptions that are relevant for the scenarios such as the details of charging system availability and overall levels of private vehicle ownership. These results are intended to illustrate the model capabilities, help fully characterize the spatiotemporal XFC demand, and provide useful sensitivities to inform final scenarios for the project.

Table II.3.7.2 shows some key parameters for these initial central and sensitivity scenarios. Residential Charging indicates the share of EV drivers that have access to a dedicated residential plug. Vehicle Ownership is the overall level (percentage of the fleet) of private vehicle ownership. Ride-Hail Fleet is the share of ride-hail vehicles in the fleet. Note that the ride-hail vehicles perform more daily VMT than personal vehicles, so they have a larger share of VMT and energy use in the results presented below than they do in terms of share of vehicles. Fast Chargers represents the shares of different nominal power-level chargers from 50kW to 250kW. EV Range is the assumed vehicle range: 200 miles for all EVs in these scenarios. Future simulations will include varying the EV driving ranges and potentially including heterogenous fleets, for example 200-mile range vehicles in the private fleet and 300-mile vehicles for the automated ride-hail fleet. Household L1/L2 is the ration of L1 to L2 residential plugs. CAVs is the share of connected and automated vehicle (used for ride-hailing). Personal and Ride-hail EVs are respectively the shares of personal and ride-hail electric light-duty vehicle fleet, which consist mostly of battery electric and a small fraction of plug-in hybrid vehicles.

Table II.3.7.2 Summary of the Scenarios Explored – Fleet and Charger Composition

Scenarios	Residential Charging	Vehicle Ownership	Ride-Hail Fleet	Fast Chargers			EVs Range (miles)
				50 kW	150 kW	250 kW	
Baseline	0.6	0.6	0.08	0	0.9	0.1	200
Low Vehicle Ownership	0.9	0.4	0.11	-	-	-	-
High Vehicle Ownership	0.3	0.8	0.03	-	-	-	-
Low Residential Charging	0.3	-	-	-	-	-	-
High Residential Charging	0.9	-	-	-	-	-	-
High Fast Charger	-	-	-	0	0	1	-

Table II.3.7.3 Summary of the Scenarios Explored – Fleet Composition

Scenarios	Household L1/L2	Personal EVs	Ride-hail EVs	CAVs
Baseline	0.6	0.36	0.03	0.05
Low Vehicle Ownership	1.2	0.24	0.05	-
High Vehicle Ownership	0.27	0.41	0.02	-
Low Residential Charging	0.3	-	-	-
High Residential Charging	0.9	-	-	-
High Fast Charger	-	-	-	-

The Central Scenario includes 108,000 personally owned EVs, 23,400 human-driven ride-hailing vehicles, and 9,000 automated electric ride-hail vehicles. These vehicles are supported by 347 public DCFC stations and 20 depots for automated ride-hailing vehicles. In post-processing, the personally owned EVs are scaled up by 31x to account for both population size and discretionary activities. Likewise, the ride-hail fleet is scaled up to match the portion of 8% of personally owned vehicles. For this initial set of scenarios, both personally and fleet owned (ride-hail) vehicles are considered, but note that, as mentioned above, only commute trips are included in this initial set of BEAM model runs (impacting travel needs and behavior). In the near future and as the project progresses, additional light-duty vehicle travel will be included to account for daytime shopping trips, etc., and that will add additional charging demands throughout the day. The resulting overall estimated charging demands are expected to then be somewhat larger overall and less “peaky” than the ones depicted here.

In the Baseline case, all the EVs in the simulation have a 200-mile driving range for both personal and ride-hail vehicles. Previous BEAM simulations have included calibrated scenarios with different range EVs, and with some next-step refinements in the model these will be repeated for the GEMINI-XFC project in a subsequent round of model runs. This will be considered in future project work along with more complex (heterogenous) charge power networks.

Figure II.3.7.3 shows the hourly distribution of charging for a simulation day in the central scenario, composed of the five different charger types. There is a moderate morning peak but then a pronounced evening peak in these basic simulations that consider only commute travel and uncoordinated vehicle charging (without any application of “managed charging” through for example time-of-use electricity rates or demand response programs). Simulated DCFC loads occur fairly consistently from early in the morning to late evening but peaking in the early evening hours.

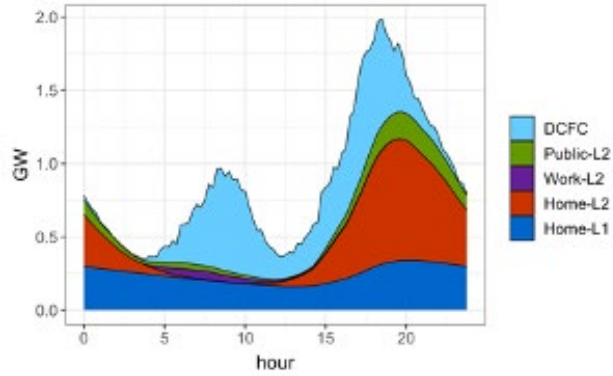


Figure II.3.7.3 Hourly EV Charging Load by Charger Type and Location for the Central Scenario.

As shown in Figure II.3.7.4, about two thirds of total EV charging occurs at home locations, nearly evenly split between Level 1 and Level 2. Level 2 workplace charging makes up about 2% of total charging. Public Level 2 contributes about 10%, and DCFC contributes about 15%, of total charging in the central scenario.

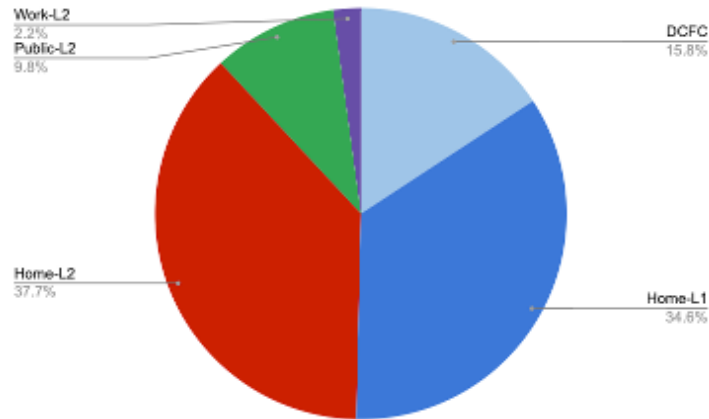


Figure II.3.7.4 Percentage Breakdown of Projected EV Charging Demands by Charger Type and Location.

As mentioned earlier, ride-hailing fleets of automated electric ride-hailing vehicles charge at dedicated depots. Presented in Figure II.3.7.5 below is the split between depot-based charging for these fleets and the general public charging that can be used by drivers of personally owned vehicles as well as human driven ride-hail vehicles. The graphs are differentiated based on site level power consumption of less than 1 MW, between 1 MW and 5MW, and greater than 5 MW (that are expected to require greater distribution systems upgrades). Charging load at public charging locations is much higher than depot charging. However, most of the depot charging requires 5 MW or more, while public DCFC stations are often operated at lower power levels.²

² Some of the charging load at <1MW qualifies as XFC as defined in this project due to individual chargers rated at 250+ kW, something that will be further investigated as the project progresses

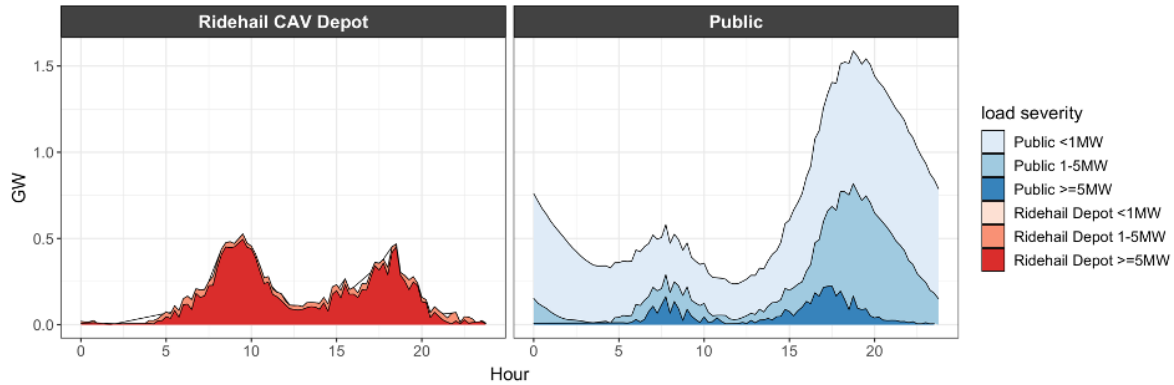


Figure II.3.7.5 Hourly EV Charging Load by Charging Location Type and Peak Site Power

Figure II.3.7.3 and Figure II.3.7.5 illustrate the temporal variability in the aggregate EV charging load and the role of DCFC, and XFC in particular. The BEAM model also locates all individual charging events making up these aggregate loads spatially. Figure II.3.7.6 shows four static snapshots from the daily simulation to illustrate the geographic and temporal variability in the overall EV charging and XFC charging demands. As shown the charging demand peaks in the mid-morning and early evening in terms of the severity of the load at individual sites around the San Francisco Bay Area. The charging events are distributed unevenly in the San Francisco Bay area as a result of different travel and location of charging stations. In particular, XFC charging appears concentrated in certain areas. As expected, the highest load severity concentrates around the late-afternoon and early evening. Very little XFC happens in the nighttime hours in these scenarios.

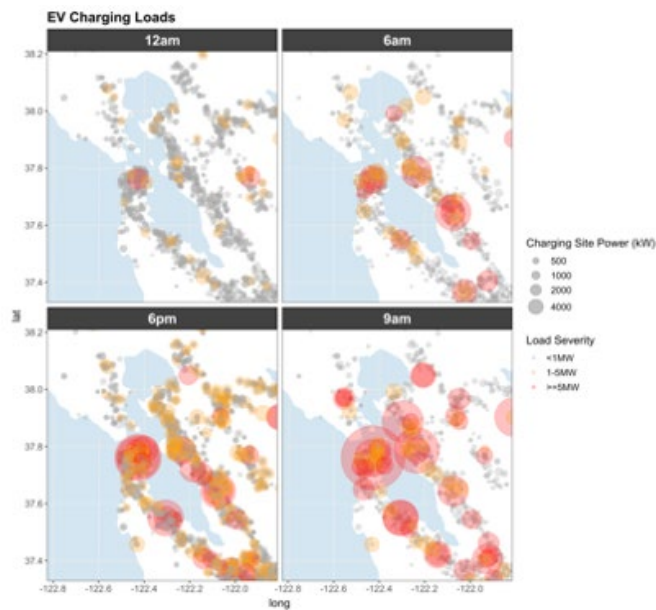


Figure II.3.7.6 Forecast of Temporal and Spatial Variation in EV Charging Loads

Progress on Controller Development

The controller development this year looked the controller structures, and how these will be evaluated within the co-simulation for both the planning level and the operational level. The full scheme of both planning and operational levels are shown in Figure II.3.7.7, which presents the overall scheme for modeling and controller interactions in the GEMINI project.

Distribution Controller Approaches

The Distribution Controller sends load limits and, if necessary, may expand to include localized incentives for charging at one station at a particular time versus another. These load limits are expected to be sent at two levels: 1) hard “unacceptable” levels which include both interconnection point, and power-flow derived limits to prevent unacceptable loading; and 2) guidance limits which attempt to improve grid operations, but if exceeded would only result in “acceptable for a limited time” conditions.

There are three potential optimization methods that will be explored for the Distribution Controller: a heuristic method, a load sensitivity matrix method, and a reinforcement learning method. Each subsequent method is more complex and will have higher memory and computational requirements, so the control methods will be tested sequentially for each scenario to determine the simplest sufficient implementation and avoid unnecessary complexity and testing time. Additional optimization approaches may be needed if additional optimization terms for overloads, reactive power dispatch, or voltage control operation counts are required or if it becomes necessary to send control signals out to legacy utility equipment. Of particular interest in these cases are recent efforts around the hierarchical, cell-based controls schemes pioneered by the Autonomous Energy Systems LDRD at NREL (Kroposki 2020).

Co-simulation Prototype

Rather than initially extending to the entire Bay Area, we started with a proof-of-concept simulation that combines a portion of one of the 40 regions from the distribution grid data, “p1uhs1,” with a simplified “Beamville” tutorial model for mobility. The “p1uhs1” region includes 9025 buses of the roughly 3 million in the bay area and is a portion of the “p1u” region located in downtown San Francisco, South of the Bay Bridge, shown in Figure II.3.7.8 for both the Base and High DER grid scenarios (see (Muratori et al. 2020) for details). Distribution system Distribution scenarios are taken from the Smart-DS datasets.

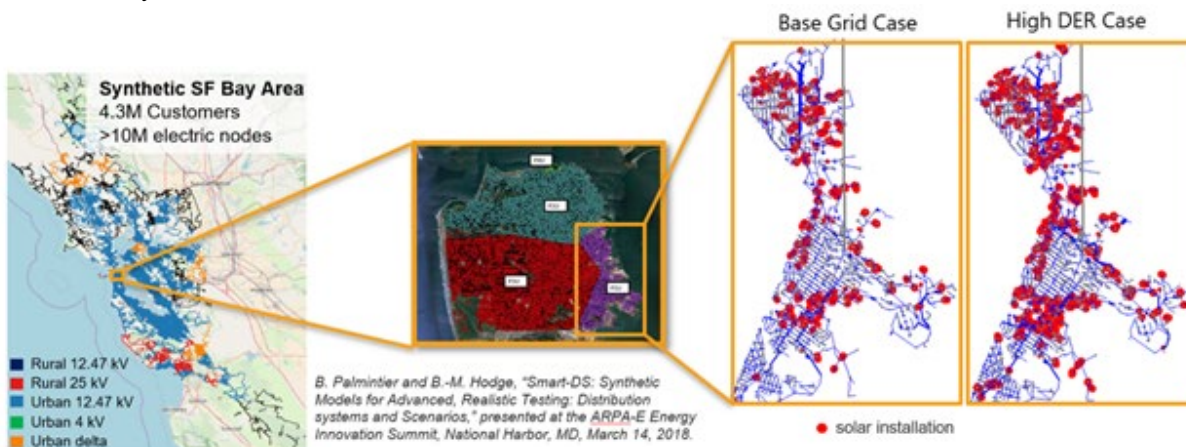


Figure II.3.7.8 Grid Modeling at High Resolution and With Base and High DER Cases for SF Bay Area

PyDSS is used to simulate the “p1u” region for both cases in a hierarchical manner to allow distribution of the computational load. PyDSS is a tool which leverages OpenDSS to allow interfacing with HELICS and easy application of control setpoints to distributed energy resources.

Conclusions

In conclusion, the GEMINI project is well on track to complete its objectives. The project team has demonstrated the ability of BEAM to model XFC events in time and space across a modeling day of the SF Bay Area, a controller design and implementation strategy, and work on defining EV and grid scenarios to model in the next project steps. The project team will work next to further implement these control strategies into progressively larger co-simulation scenarios with BEAM and PyDSS and envisions no significant obstacles to completing the project objectives.

References

1. Kroposki, Benjamin. 2020. "Autonomous Energy Systems." Workshop, August. <https://www.nrel.gov/grid/assets/pdfs/aes-kroposki.pdf>.
2. Masoum, Amir S., Sara Deilami, Paul S. Moses, and Ahmed Abu-Siada. 2010. "Impacts of Battery Charging Rates of Plug-in Electric Vehicle on Smart Grid Distribution Systems." In 2010 IEEE PES Innovative Smart Grid Tech. Conference Europe (ISGT Europe), 1–6. <https://doi.org/10.1109/ISGTEUROPE.2010.5638981>.
3. Muratori, Matteo. 2018. "Impact of Uncoordinated Plug-in Electric Vehicle Charging on Residential Power Demand." *Nature Energy* 3 (3): 193–201. <https://doi.org/10.1038/s41560-017-0074-z>
4. Muratori, Matteo, Colin Sheppard, Tim Lipman, Bryan Palmintier, Nadia Panossian, Haitam Laarabi, R. Waraich, A. Desai, and Paige Jadun. 2020. "Grid-Enhanced, Mobility-Integrated Network Infrastructures for Extreme Fast Charging (GEMINI-XFC)." AMR Annual Review. Department of Energy. <https://www.nrel.gov/docs/fy20osti/76718.pdf>
5. Palmintier, Bryan, Tarek Elgindy, Carlos Mateo, Fernando Postigo, Tomás Gómez, Fernando de Cuadra, and Pablo Duenas Martinez. 2021. "Experiences Developing Large-Scale Synthetic U.S.-Style Distribution Test Systems." *Electric Power Systems Research* 190 (January): 106665. <https://doi.org/10.1016/j.epsr.2020.106665>
6. Palmintier, Bryan, Dheepak Krishnamurthy, Philip Top, Steve Smith, Jeff Daily, and Jason Fuller. 2017. "Design of the HELICS High-Performance Transmission-Distribution-Communication-Market Co-Simulation Framework." In Proc. of the 2017 Workshop on Modeling and Simulation of Cyber-Physical Energy Systems. Pittsburgh, PA. <https://doi.org/10.1109/MSCPES.2017.8064542>
7. C. Sheppard, R. Waraich, A. Campbell, A. Pozdnuikov, A. R. Gopal, Modeling plug-in electric vehicle charging demand with BEAM: The framework for behavior energy autonomy mobility, Tech. Rep., Lawrence Berkeley National Lab. (LBNL), Berkeley, CA (United States) (2017).
8. Smart, John et al. 2020. "SMART Mobility Advanced Fueling Infrastructure Capstone Report." DOE Capstone. US DOE Office of Energy Efficiency and Renewable Energy. https://www.energy.gov/sites/prod/files/2020/08/f77/SMART-AFI%20_Capstone_7.22.20_0.pdf
9. Wood, Eric W., Clement L. Rames, and Matteo Muratori. New EVSE Analytical Tools/Models: Electric Vehicle Infrastructure Projection Tool (EVI-Pro). No. NREL/PR-5400-70831. National Renewable Energy Laboratory (NREL), Golden, CO (United States), 2018. <https://www.nrel.gov/docs/fy18osti/70831.pdf>
10. Zhang, Hongcai, Colin J.R. Sheppard, Timothy E. Lipman, Teng Zeng, and Scott J. Moura (2020). Charging Infrastructure Demands of Shared-use Autonomous Electric Vehicles in Urban Areas. *Transportation Research Part D: Transport and Environment* 78: 102210. 10.1016/j.trd.2019.102210.
11. Zhang, Hongcai, Colin J.R. Sheppard, Timothy E. Lipman, and Scott J. Moura (2019), "Joint Fleet Sizing and Charging System Planning for Autonomous Electric Vehicles," *IEEE Intelligent Transportation Systems Transactions*, 10.1109/TITS.2019.2946152.

Acknowledgements

The GEMINI project Principal Investigators acknowledge the contributions of team members Andrew Meintz, Bryan Palmintier, Nadia Panossian, Paige Jadun, Ranjit Desai (NREL), Haitam Laarabi, Colin Sheppard, Zachary Needell, and Keith Moffat (LBNL), as well as those of project advisor Alexandra von Meier (UC Berkeley). The project team also acknowledges the support of Lee Slezak (DOE HQ), Manish Mohanpurkar (INL), John Farrell (NREL), and Tom Kirchstetter and Mike Mills (LBNL).

II.4 Cybersecurity

II.4.1 Consequence-Driven Cybersecurity for High Power EV Charging Infrastructure (Idaho National Lab, Oak Ridge National Lab, National Renewable Energy Lab)

Richard “Barney” Carlson and Kenneth Rohde, Principal Investigators

Idaho National Lab
2525 North Fremont Avenue
Idaho Falls, ID 83415
Email: richard.carlson@in.gov; kenneth.rohde@inl.gov

Tony Markel and Anuj Sanghvi, Principal Investigators

National Renewable Energy Laboratory
15013 Denver West Parkway
Golden, CO 80401
Email: tony.markel@nrel.gov; anuj.sanghvi@nrel.gov

Michael D. Iannacone and Omer Onar, Principal Investigators

Oak Ridge National Laboratory
1 Bethel Valley Road
Oak Ridge, TN 37830
Email: Iannaconemd@ornl.gov; onaroc@ornl.gov

Lee Slezak, DOE Program Manager

U.S. Department of Energy
Email: Lee.Slezak@ee.doe.gov

Start Date: October 1, 2019
Project Funding: \$985,000

End Date: September 30, 2020
DOE share: \$985,000

Non-DOE share: \$0

Project Introduction

With the emergence of electrified transportation, there is a desire for faster recharge times and integrated energy management for charging infrastructure. The development and deployment of extreme fast charging (XFC) and wireless power transfer (WPT) emphasizes the need for cybersecurity of these high-power EV charging systems. The use of high voltage, high current, and high magnetic fields for high power charging systems presents potential public safety hazards if not controlled properly. Additionally, many advanced control systems and communication networks are utilized to maximize the efficiency of this high-power EV charging infrastructure. With these safety and energy management controls systems, cybersecurity vulnerabilities may be present.

This cybersecurity project includes the analysis and evaluation of cybersecurity of high power conductive and wireless charging infrastructure. INL is leading this project in collaboration with ORNL, NREL, ABB, Tritium, and Electrify America focused on prioritizing and securing cybersecurity vulnerabilities and threats for high power EV charging infrastructure. The purpose of this research project is to first conceptualize possible disruptive events caused by cyber means related to XFC and WPT systems, secondly evaluate the impact severity potential of these events, and thirdly develop mitigation solutions to secure the infrastructure. The impact-based framework methodology used prioritizes disruptive events based on severity of impact and cyber manipulation complexity, leading to defined high consequence events (HCEs). In later stages of the project, preliminary mitigation strategies and solutions will be identified and investigated to defend, identify, and resolve cyberattacks.

Charging infrastructure is designed to meet EV energy transfer requirements with safe, high efficiency operation at a low cost, but often cybersecurity is not at the forefront of the design process when engineering such systems. By identifying and prioritizing potential disruptive cybersecurity events into a list of HCEs, cybersecurity research efforts can be focused on the highest priority events. Using input from industry manufacturing, engineering, cybersecurity, and electric sector subject matter experts, a comprehensive list of HCEs has been developed for high-power EV charging infrastructure.

In addition to the XFC challenges discussed above, chargers using wireless power transfer (WPT) are also emerging from the research environment into the early stages of commercial products; pilot sites for these systems have already reached 200kW. It is critically important to protect these devices themselves and their supporting information networks, and to do this at the earliest stage possible as these products are being developed.

This task area uses an approach to managing cybersecurity risks adapted from a proven process used by INL to secure power plants and other critical infrastructure. It goes beyond generic “good hygiene” cybersecurity recommendations and instead presents a consequence-driven approach to holistically assess, prioritize, and manage a broad range of risks, from privacy concerns and denial of service to destruction of property and disruption of the electric grid. We examine the impact and feasibility of these risks, and we make specific recommendations to stakeholders for how these can be mitigated.

Objectives

Charging infrastructure is a system of systems, including physical, communication, and control layers. Physical systems include vehicles, charging equipment, supporting electrical equipment at the charging site (e.g., power converters, transformers, etc.), distributed energy resources (DERs) such as stationary energy storage and solar photovoltaic (PV) arrays that support XFC charging stations, and the distribution feeder electrical equipment that services charging sites. The objective of this project is to develop solutions and recommendation for the highest prioritized events to secure vulnerabilities, means to detect attacks, and methodologies to respond and restore from an HCE. The outcome of the project will be actionable information that industry can immediately apply to their WPT product development efforts, including recommendations on High Consequence Event (HCEs) mitigation strategies, allowing them to engineer cybersecurity into their products before market introduction. This project will identify the highest priority risks and recommend mitigation strategies, providing industry and government leaders the means to focus their finite resources.

Approach

The impact and consequence-based cybersecurity analysis framework used in this project will first prioritize high consequence events caused by cybersecurity manipulation that can cause physical adverse effects to the EV charging infrastructure. This prioritization is accomplished using an internally developed scoring matrix based on impact severity and cyber manipulation complexity. Secondly, the impact severity and cybersecurity complexity of these potential events will be evaluated using laboratory equipment to validate the prioritization and to investigate the vulnerabilities and attack pathways leading to the high consequence events. Third, mitigation solutions and strategies will be developed to secure vulnerabilities and threats. Recommended response strategies and methodologies based on the analysis done will also be developed. Lastly, publication of recommendations, project findings, and a stakeholder action plan will be published to inform industry of the solutions developed to secure high power charging infrastructure.

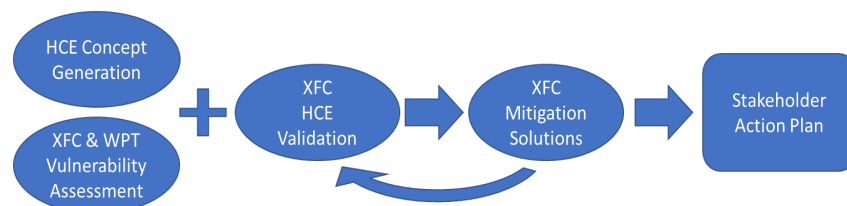


Figure II.4.1.1 Project tasks flow chart

Cybersecurity vulnerability and cyber-attack path assessment in this project will be focused on device-level and supervisory control systems and the sophisticated communication they require within and between vehicles, EVSE, DERs, building and other third-party controllers, utilities, and/or other entities. Assessment of the electric grid’s cybersecurity vulnerabilities is addressed by other programs and is therefore out of the scope of this project. However, this project will assess threats to the local distribution network and broader grid stability caused by compromised high power charging infrastructure.

The effort required for the success of this three-year project led by Idaho National Lab involves the collaboration of two other national labs (National Renewable Energy Lab, Oak Ridge National Lab) and three collaborative industry partners (ABB, Tritium, Electrify America). Together the expertise and capabilities of these partners will enable the successful outcome for this project.

Results

The impact and consequence-based analysis framework used during this project draws on elements of the Consequence-driven Cyber-informed Engineering (CCE) methodology developed by Idaho National Laboratory (Freeman et al. 2019). The CCE methodology was developed to assist private and public organizations examine their own operational technology environment, identify and prioritize potential HCEs, enumerate possible methods by which an adversary could affect a physical process via cyber means, and implement mitigation strategies via engineering to minimize the risk of cyber-attack. A foundational assumption of the CCE methodology is if an entity is targeted by an advanced cyber adversary, it will be compromised; the only question is when. Drawing from this established CCE analysis framework, researchers created a comprehensive list of potential HCEs for the XFC and WPT charging infrastructure. Results of these efforts will be shared with the appropriate XFC and WPT control system manufacturers to develop engineering strategies to mitigate the potential consequence. XFC vulnerability assessment, impact severity evaluation, and cybersecurity complexity evaluation were conducted this year.

XFC Vulnerability Assessment

A vulnerability assessment of the high-power EV charging infrastructure was performed in the Idaho National Laboratory (INL) Electric Vehicle Infrastructure Laboratory (EVIL). This environment as shown in allows multiple charging stations to be connected on a research network and integrated with charge management systems. The charging stations are powered by a grid emulator system which enables power-hardware-in-the-loop operation for grid modeling and system simulation for further analysis.

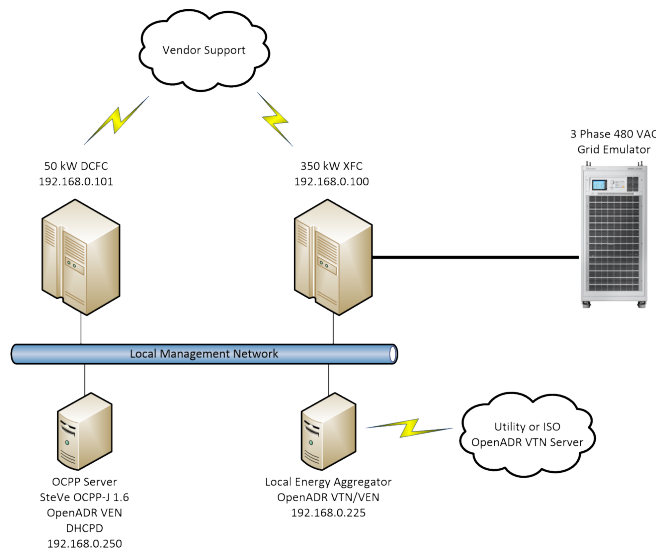


Figure II.4.1.2 Laboratory Network Diagram

The primary target of the vulnerability research is the ABB TerraHP 350 kW XFC station, its integration with, and impact to, the electric grid. Also located in the lab is an older ABB Terra53 CJ 50 kW DCFC. An OCPP server is running the open-source SteVe OCPP-J version 1.6. The OCPP server is also configured as an OpenADR Virtual End Node (VEN) with a Local Energy Aggregator. The Local Energy Aggregator is running the EPRI open-source OpenADR Virtual Top Node (VTN) software and acts as an intermediary server for collecting ADR messages from a utility company.

The local management network is a basic managed Ethernet switch connecting all of these resources together on a single flat network. This basic network is used for simplicity but is representative of a much larger and complex network created by a Charge Network Operator (CNO), like Electrify America, for remotely managing their charging stations.

The assessment activities focus on identifying vulnerabilities in the XFC as well as the connected energy management systems and how the XFC interacts with these systems. The assessments primary goal is to identify nefarious cyber methods that allow any of the identified High Consequence Events (HCEs) to be executed.

Laboratory HCE Severity Impact and Cybersecurity Complexity Evaluation

The following table lists the top 15 HCEs based upon their initial scoring and ranking performed in year one of this project. Table II.4.1.1 is a brief summary of the research status of select HCEs evaluated during year two.

Table II.4.1.1 Top Fifteen Prioritized High Consequence Events

Rank	Event
1	Power Outage(s) Due to Sudden Load Shed from XFCs.
2	Injury or loss of life due to electrocution, electrical shock, or burns from exposed conductors of the XFC cord set cable.
3	Power outage(s) due to sudden load shed or increase from on-site energy storage system manipulation.
4	(WPT Only) Medical device failure or injury caused by exposure of high electromagnetic field to implanted medical devices
5	Damage to equipment within the feeder distribution area (transformers, switch gear, harmonics, overload capacitor bank, high reactive power).
6	The XFC and Distributed Energy Resource (DER) at the site are not able to provide grid services (ex. curtailment) when needed causing decreased stability/reliability of the grid.
7	System shutdown (XFC or charging site) due to creation of software error state.
8	Users are burned by hot cord set without electrical insulation failure.
9	System shutdown due to network outage (WiFi, cellular, or other communications outage).
10	Hardware damage to the charger over very long duration of elevated temperature.
11	(WPT Only) Induced voltage (high V/m) on vehicle components or electrical harnesses may damage harness or electrical components not associated with WPT system. Vehicle components that are not rated or shielded from high magnetic field levels may heat up.
12	Theft or alteration of Personally Identifiable Information (PII) data transmitted between vehicle, XFC, EV driver, network operator, etc.
13	Vehicle fire due to vehicle battery overcharge.
14	(WPT Only) Vehicle electrical component damage due to over-voltage condition of the vehicle side WPT components.
15	Hardware damage to the XFC(s).

During the cyber evaluation of each HCE, the cyber complexity multiplier (or manipulation likelihood) has been updated for five of the HCE. The complexity multiplier is a reflection of the effort required by the

assessment team to identify and exploit the vulnerability(ies) necessary to execute the HCE. Table II.4.1.2 describes the basic factors used to determine the complexity multiplier score for an HCE.

Table II.4.1.2 Definition of Cybersecurity Complexity Multiplier for High Consequence Events

Multiplier	Description
5	Extremely Low Complexity - Only a single system requires modification. System is easily reachable by the adversary (physical or virtual). No preconditions required.
4	Low Complexity - Only a single system requires modification. System not easily reachable, but compromise of the system is trivial once access is available. No preconditions required.
3	Medium Complexity - One or more than one system requires modification. System(s) are reachable with effort, but compromise is generally successful. Preconditions may be required.
2	Difficult Complexity - More than one system requires modification. Systems are difficult to reach. Compromise requires specialized skills. Preconditions are required for successful exploit.
1	Extremely Difficult Complexity - More than one system requires modification. Systems are very difficult to reach. Compromise is not always successful. Preconditions are required for successful exploit, and these conditions are rare.

HCE #1 – Power Outage(s) due to sudden load shed from XFCs.

Two methods to accomplish this HCE were identified. Each method leads to the immediate stop of a charge event by the XFC. The evaluation has resulted in a change in the cyber complexity multiplier to 4 – *Low Complexity*. Further testing is planned to determine how quickly and concurrently multiple XFC respond to these methods being triggered by a remote adversary. During the additional testing, grid impact data from the event will be collected and used in future modeling efforts. *Method 1:* XFC compromised using a custom exploit. The HMI panel of the XFC is compromised and has access to the control network. Control messages transmitted by the HMI stop the current charge event with the same effect as a user depressing the emergency stop button located on the front panel of the XFC. *Method 2:* The OCPP server uses OCPP v1.6 and the messages are not encrypted or authenticated. The attacker can generate arbitrary OCPP messages including the stop charge method.

HCE #2 – Injury or loss of life due to electrocution, electrical shock, or burns from exposed conductors of the XFC cord set cable. HCE #8 – Users are burned by hot cord set without electrical insulation failure.

From published standards, ISO 17409 and IEC 61851-23 ed.2 the vehicle inlet port should include temperature sensing. In the occurrence of an exploit that is able to manipulate the XFC cable cooling system, the vehicle will sense any unacceptable temperature rise at the vehicle inlet port and respond by reducing charge current request. Therefore, for either of these HCEs to be possible, both the vehicle inlet port temperature sensing and the XFC thermal management system must be manipulated. This result concluded with a change in the cyber complexity multiplier to 2 – *Difficult Complexity*.

HCE #7 – System shutdown (XFC or charging site) due to creation of software error state.

Two methods to accomplish this HCE were identified. Each method leads to the immediate shutdown of the XFC, and the XFC remains inoperable for the duration of the cyber-attack. *Method 1:* OCPP 1.6 is vulnerable to message injection on the local network. Arbitrary OCPP *ChangeAvailability* messages are easily crafted and sent to all XFC placing them in an “*Out of Order*” state. *Method 2:* The XFC HMI is compromised and can arbitrarily inject control protocol messages or cause a Denial of Service (DoS) on the control message bus. The evaluation has resulted in a change in the cyber complexity multiplier to 4 – *Low Complexity*.

HCE #12 – Theft or Alteration of Personally Identifiable Information (PII) data transmitted between XFC, EV or Driver.

Using the published methods and software from Oxford University, the assessment team replicated the ability to passively monitor CCS communications using a Software Defined Radio (SDR). The assessment team confirmed theft of the CCS data is possible, even on the liquid cooled cord set of the XFC. Future testing is

cyber analytics and defense tools. We expanded the modeled scenarios to include EV charging infrastructure (three vehicles in lower left of Figure II.4.1.4 interacting with the grid as well as DERs. The networking and power controls (floating dots and gray lines, Figure II.4.1.4) of each device can be exposed for cyber manipulation and consequence evaluation. Identification and mitigation strategies could be evaluated in the future within this architecture.

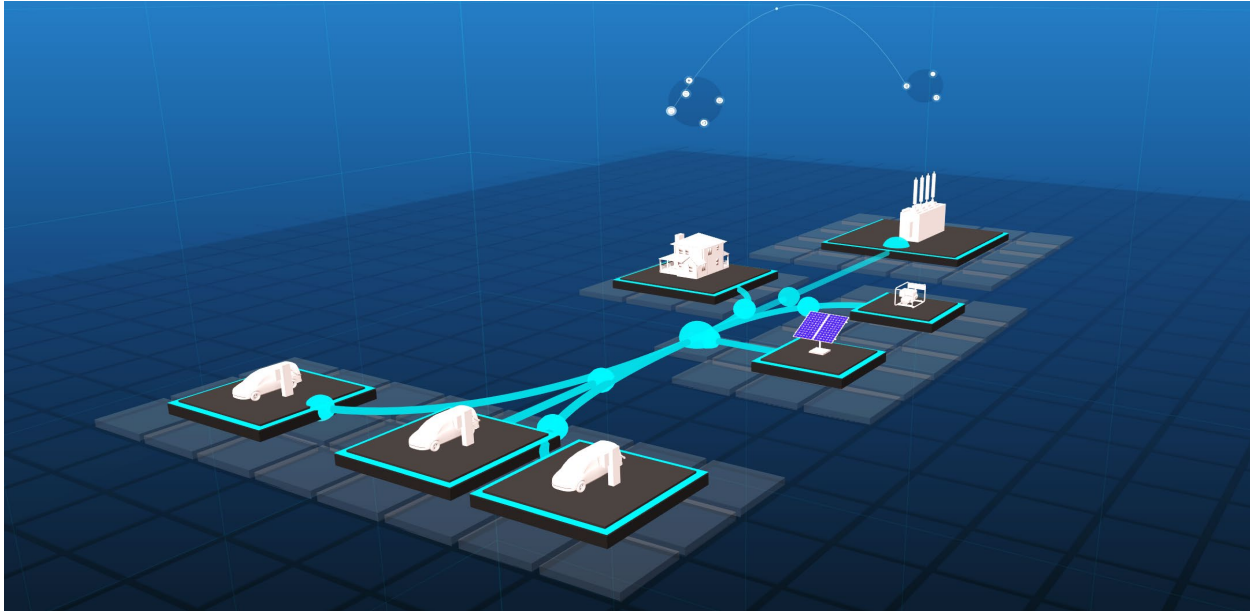


Figure II.4.1.4 EV Fueling Station Power and Network Representation in Cyber Energy Emulation Platform

The digital representation described above was also tied to physical devices within ESIF's Optimization and Controls Laboratory (OCL). The power system is represented using OpenDSS while all network communications is emulated with virtualized nodes. In addition to the fast charge station with multiple EVSE, the representation includes energy storage, PV, and the distribution grid shown in Figure II.4.1.4. As mentioned, CEE Platform is also hosting a virtual OCPP server and clients to represent the network communications taking place between the fast chargers and the station operator.

Hardware in the Loop (HIL) System Implementation

For the HIL integration, a Tritium 50kW fast charger with Nissan Leaf located in OCL was tied to CEE Platform. This physical/virtual linkage enables monitoring and response to both real and virtual malicious network traffic under a variety of scenarios. A message replay attack toward the EVSE and a denial-of-service attack toward the OCPP server have been tested. This initial work sets the stage for being able to develop and test mitigations to the high consequence cyber events (HCE's) previously identified.

The work completed now enables researchers to safely explore high-consequence cyber threats and mitigation methods. The team continued work to identify high-consequence cyber events for electric vehicle (EV) fast chargers that are integrated with distributed fueling stations. By leveraging ESIF's hardware-in-the-loop simulation capabilities, the Cyber-Energy Emulation Platform is now capable of communicating with a fast charger located within the facility, allowing the analysis of real and virtual network traffic in both normal and cyberattack scenarios. The accomplishment is significant as it is the first step toward using a unique emulation tool to develop a better understanding of attacks and mitigation strategies for a fast-charge fueling stations. The research efforts will impact the security of the 50,000+ fast charge stations expected to be in operation by 2025.

Analysis of Wireless Power Transfer Vulnerabilities

In FY20, the team built on our earlier work by analyzing the architecture of several WPT systems, including existing early, low power commercial systems, commercial pilot systems, and research systems. We use this architectural knowledge to analyze potential vulnerabilities, create attack paths for all HCEs, and we consider the feasibility and risk of these attack paths.

To validate the complexity multiplier scores discussed above, and to begin making specific recommendations to EVSE manufacturers, operators, and regulators, we have reviewed several current and future WPT charging systems. The first of these systems is an early commercial WPT system, operating at <10kW, using a commercial off-the-shelf (COTS) short-range 2.4GHz radio control channel between the charger and the vehicle. Next, we evaluated several research prototypes, operating at 100s of kW, using a different COTS radio system as its control channel. Finally, we have evaluated a commercial pilot system, operating at 50-200kW. This system is currently using a similar COTS radio control channel as the research systems, with future plans to use a custom short-range inductive control channel.

As a result of studying these systems, we identified several potential vulnerabilities in these architectures. We then considered a representative architecture which closely corresponded to these above systems, and which would demonstrate the same vulnerabilities and failure modes. This is shown in Figure II.4.1.5, and an abstracted view of this system is shown in Figure II.4.1.6.

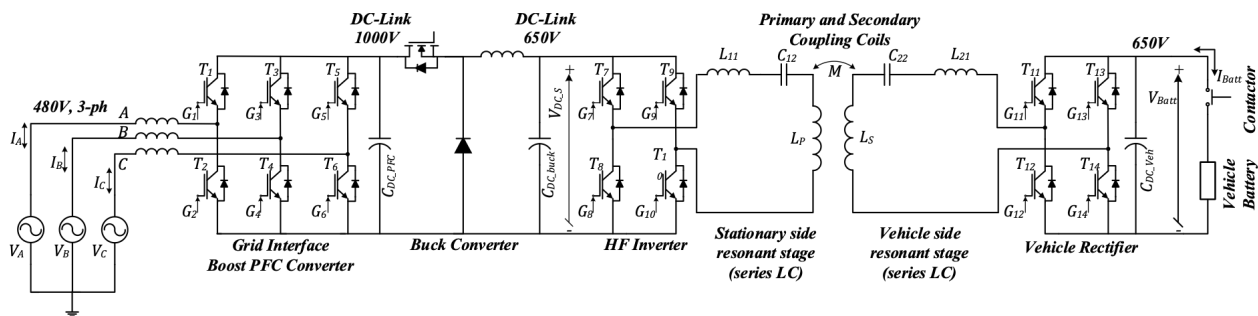


Figure II.4.1.5 Architecture of a Representative WPT System

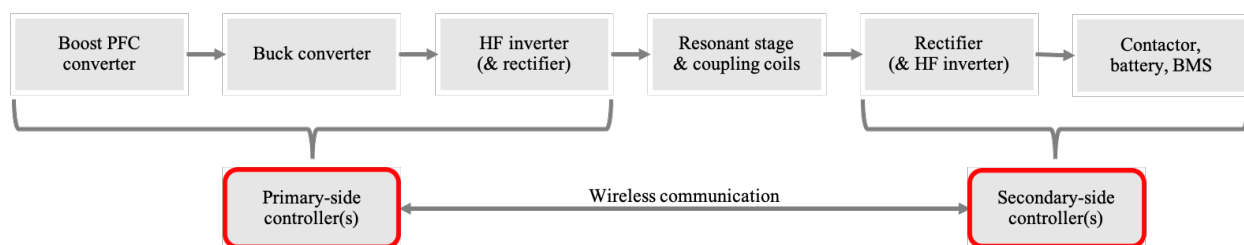


Figure II.4.1.6 Abstracted Architectural Diagram

WPT Cyber Attack Path and Risk Analysis

Using the generalized, representative architecture in Figure II.4.1.5, we considered the potential vulnerabilities, and grouped the HCEs which would require the same/similar vulnerabilities and attack paths. These groups were:

1. Manipulating Active Rectifier or Buck Converter
2. Manipulating HF Inverter Operation

3. Tampering with Vehicle Control Systems or Control Channel
4. Tampering with Pairing Process
5. Interfering with Foreign Object Detection
6. Tampering with or Intercepting Other Communications

We observed that these first two groups contain the highest severity HCEs and represent the most direct paths for an attacker to achieve these HCEs. We then performed simulations to model the failure modes and the impact an attacker could have using these methods. We considered manipulating the active rectifier (group 1) to create a phase-to-phase short circuit, and we considered manipulating the HF Inverter (group 2) to create a short across the (650V) DC bus. Both of these cases result in sudden, unstable, and high reactive loads on the grid interface, as well as damage to charging equipment.

We also considered an example of the third group, manipulating the vehicle to cause a sudden, unexpected drop in load. In this case, unexpected large voltages (in the 1 to 8 KV range) can be generated across several internal components, likely damaging equipment; this can also generate large reactive loads at the grid interface. For further details and simulation results, see “key publications” below.

Conclusions

Multiple HCEs were evaluated to investigate the magnitude of impact severity and cybersecurity complexity. Based on the findings of these evaluations, several HCE complexity multiplier scores were adjusted. The list of HCE were reprioritized using the adjusted total prioritization scores.

A vulnerability assessment was completed on the 350kW XFC. This assessment identified vulnerabilities in the XFC as well as the connected energy management systems and how the XFC interacts with these systems. The assessment’s primary goal was to identify nefarious cyber methods that allow any of the identified High Consequence Events (HCEs) to be executed.

The team successfully completed a hardware in the loop integration of a physical fast charger and the Cyber Energy Emulation Platform in FY20 such that future cyber impact and mitigation scenarios could be more fully understood. The first steps toward enhancing this research system with local energy storage system (both physical and virtual) was also completed. Future efforts using these new testing capabilities will enhance knowledge of cyber risk and strategies to improve overall EV fast charge fueling system response to be resilient to potential cyber consequences.

As wireless EV charging infrastructure is beginning to appear, and as power levels increase, the need for cybersecurity is vital for safety, robustness, and consumer confidence. Research efforts for this project are focused on trying to prevent high consequence manipulation and misuse of EV charging infrastructure.

In order to achieve this, researchers first conceptualized events that could be brought about by cyber manipulation to create a physically adverse effect on high-powered charging infrastructure, EVs, and/or the electric grid. Researchers then quantitatively scored the events using an impact severity scoring matrix and complexity multiplier. The high consequence events were scored and prioritized based upon this quantitative method. Vulnerabilities and attack paths which could lead to these HCEs were described and studied.

In our upcoming work, mitigation strategies and solutions will be developed that can detect, mitigate, or even prevent these cyber threats. The findings and solutions developed in this project will be published to advise industry on methods to improve cybersecurity for high power EV charging infrastructure.

Key Publications

1. Sanghvi, A., Markel, T., “Cybersecurity for Electric Vehicle Fast-Charging Infrastructure.” IEEE Innovative Smart Grid Technologies Conference. February 15-18, 2021.

2. Park, Yongwan, Omer C. Onar, and Burak Ozpineci. "Potential Cybersecurity Issues of Fast Charging Stations with Quantitative Severity Analysis." In *2019 IEEE CyberPELS (CyberPELS)*, pp. 1-7. IEEE, 2019.

References

1. Freeman, Sarah G., Curtis St Michel, Robert Smith, and Michael Assante. 2019. *Consequence-driven cyber-informed engineering (CCE)*. October 18. Accessed February 18, 2019. doi:doi:10.2172/1341416
2. Richard Baker, Ivan Martinovic; "Losing the Car Keys: Wireless PHY-Layer Insecurity in EV Charging", University of Oxford, 28th USENIX Security Symposium, 978-1-939133-06-9, 2019.
3. Adarsh Hasandka; Joshua Rivera; Joshua Van Natta. 2020. *NREL's Cyber-Energy Emulation Platform for Research and System Visualization*. NREL/TP-5R00-74142. <https://www.nrel.gov/docs/fy20osti/74142.pdf>.

Acknowledgements

We would like to acknowledge the rest of our INL, NREL, and ORNL team members, especially Laura Anderson, Ronald Salesky, and Rob Gillen for their significant contributions and expertise.

II.4.2 Securing Vehicle Charging Infrastructure

Jay Johnson, Principal Investigator

Sandia National Laboratories
 P.O. Box 5800 MS1033
 Albuquerque, NM 87185-1033
 Email: jjohns2@sandia.gov

Lee Slezak, DOE Program Manager

U.S. Department of Energy
 Email: Lee.Slezak@ee.doe.gov

Start Date: October 1, 2018
 Project Funding: \$1,000,000

End Date: September 30, 2021
 DOE share: \$1,000,000

Non-DOE share: \$0

Project Introduction

As the US electrifies the transportation sector, cyber-attacks targeting vehicle charging could bring consequences to electrical system infrastructure. This is a growing area of concern as charging stations increase power delivery and must communicate to a range of entities to authorize charging, sequence the charging process, and manage load (grid operators, vehicles, OEM vendors, charging network operators, etc.). The research challenges are numerous and are complicated because there are many end users, stakeholders, and software and equipment vendors interests involved. Poorly implemented electric vehicle supply equipment (EVSE), electric vehicle (EV), or grid communication system cybersecurity could be a significant risk to EV adoption because the political, social, and financial impact of cyberattacks—or public perception of such—ripples across the industry and has lasting and devastating effects. Unfortunately, there is no comprehensive EVSE cybersecurity approach and limited best practices have been adopted by the EV/EVSE industry. There is an incomplete industry understanding of the attack surface, interconnected assets, and unsecured interfaces. Thus, comprehensive cybersecurity recommendations founded on sound research are necessary to secure EV charging infrastructure. This project is providing the power, security, and automotive industry with a strong technical basis for securing this infrastructure by developing threat models, determining technology gaps, and identifying or developing effective countermeasures. Specifically, the team is creating a cybersecurity threat model and performing a technical risk assessment of EVSE assets, so that automotive, charging, and utility stakeholders can better protect customers, vehicles, and power systems in the face of new cyber threats.

Objectives

The goal of this project is to protect US critical infrastructure and improve energy security through technical analysis of the risk landscape presented by the anticipated massive deployment of interoperable EV chargers. To improve the vehicle industry's cybersecurity posture, this project is:

- conducting adversary-based assessments of charging equipment,
- creating a threat model of EV charging, and
- analyzing power system impact for different attack scenarios.

This will provide DOE and automotive, EVSE vendors, and utility stakeholders with:

- clear documentation of gaps in EVSE cybersecurity and the path forward to address those weaknesses,
- a threat model for EVSEs and associated infrastructure and services,
- recommendations for the automotive industry based on EVSE penetration testing, and

- cyber-attack impact analyses of the power system with remediation recommendations.

Approach

The team is executing on the following integrated cybersecurity R&D tasks:

1. Conduct threat modelling to understand what potential cyber hazards exist with EVSE communications;
2. Assess the current state-of-the-art cybersecurity posture of EVSE equipment using authorized, adversary-based assessment techniques (penetration testing and red teaming);
3. Establish credible attack vectors based on the cybersecurity assessments and threat model;
4. Determine the impact of current and potential vulnerabilities on distribution and transmission power systems; and
5. Create a risk matrix to prioritize mitigations that reduce the number of high-consequence/low-threat level attacks.

The task structure of this project is shown in Figure II.4.2.1, wherein the left side (blue) estimates the probability of different attack scenarios and the right side (green) estimates the consequence of attack scenarios. The cybersecurity risk of a particular attack is the combination of the likelihood and impact of the attack. By studying a range of attack scenarios, optimal mitigations can be determined to prevent attacks at specific points in the attack kill chain (i.e., the steps to accomplish adversary goals).

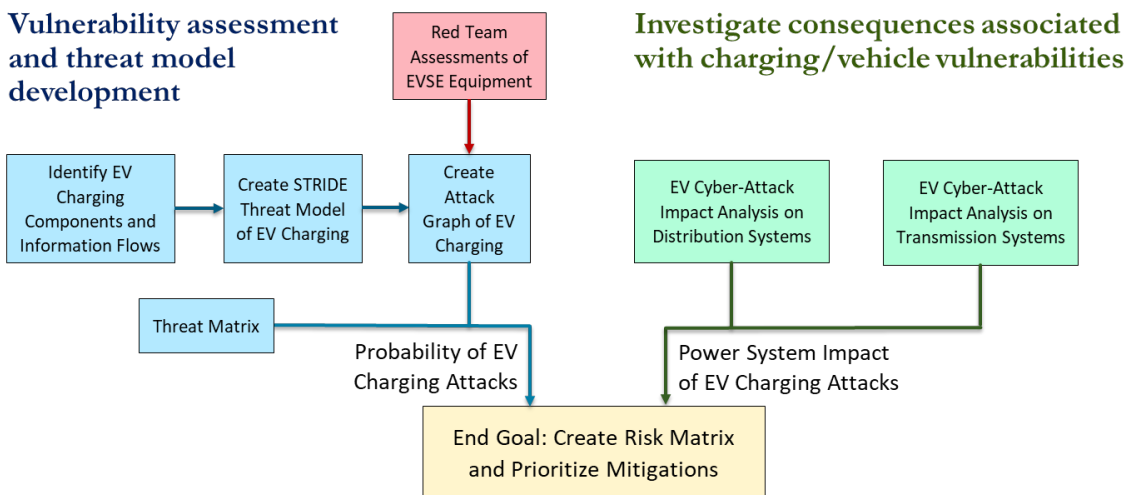


Figure II.4.2.1 Project tasking.

Results

The project team has evaluated probable attacks based on hands-on cybersecurity assessments with partner organizations and evaluated the probability of success against the skill level required to conduct the attack. A detailed threat model was created for different EVSE chargers with connections to external entities. Attack graphs were developed and then revised based on penetration testing of multiple EVSEs. A distribution simulation of EVSE charging with and without vehicle-to-grid (V2G) functionality was conducted to determine if malicious control of EVSEs could cause high or low voltages on feeder circuits. Transmission simulations of coordinated charging control was modeled for the Western Electricity Coordinating Council (WECC) were also performed to understand bulk system impact from coordinated cyber-attacks.

EVSE Penetration Testing

Since year one, the team has worked closely with multiple EVSE vendors to better understand the vulnerabilities presented by EVSE equipment and associated networks. The project’s second year focused on further understanding vulnerabilities that affect supporting IT systems. This included assessing remote access controls, use of insecure protocols, and the ability to fingerprint devices from their online presence. This involved working with the threat models and attack graphs from year one and validating some of the approaches. Findings from network traffic analysis, forensic analysis, and open-source information gathering have led to vulnerability enumeration in both the EVSE as well as their supporting infrastructure. Use of insecure protocols, such as OCPP 1.6 and MQTT, on the globally routable Internet have resulted in several findings that were disseminated back to EVSE manufacturers for remediation. Additionally, the team was able to use their findings to create a generalized "fingerprint" for EVSE deployments, allowing the team to search for and enumerate similar systems that were Internet connected. From these similar systems, specific characteristics such as open ports, software versions, or reports of vulnerabilities were used to identify other instances of EVSE deployments. The hands-on assessments for EVSE equipment found many areas for improvement, e.g., failure to physically secure EVSE enclosures; default passwords for internal systems, or credentials posted inside enclosure; data not encrypted at rest and only financial data is encrypted in transit; unnecessary ports and services are enabled. A list of best practices was generated from these assessments [1], shown in Figure II.4.2.2. In the final year of the project, an anonymized set of findings will be published. The assessment team also provided EVSE partners with the findings and potential mitigations for identified vulnerabilities. Some recommendations are included in Figure II.4.2.3.



Figure II.4.2.2 EVSE Best Practices [1].

Attack Graphs

Attack graphs show the steps an attacker must take to move from a system/network access point to a consequence or objective. The use of attack graphs simplifies the identification of key steps an attacker must take to achieve their objectives, allowing those actions to be detected or prevented. Figure II.4.2.4 illustrates access points, staging areas, and consequences of concern related to a generic EV charger network. In this figure, one of the attack paths involves an attacker using an initial compromise of an EVSE provider’s business network to impact the bulk power system. By analyzing the steps in this attack path, detective or preventive

controls – such as monitoring for unusual Network Time Protocol traffic or requiring code signing of EVSE updates – can be implemented. The team used the information gathered from their assessments, publicly available information regarding vulnerabilities, and knowledge regarding the tactics, techniques, and procedures used by attackers to advise the attack graph. In the case of coordinated EVSE attacks that disrupt the power system, there were two major questions:

- Can the attacker “pivot” between the components, systems, and networks in the EV/EVSE ecosystem to compromise the necessary information flows?
- Can an attacker synchronize their attack to affect large portions of the grid simultaneously?

From the assessment activities, it appears both are possible so an attacker *could* manipulate large networks of EVSEs and cause distribution and transmission impacts.



Figure II.4.2.3 EVSE vendor recommendations based on penetration tests of EVSE equipment and networks [1].

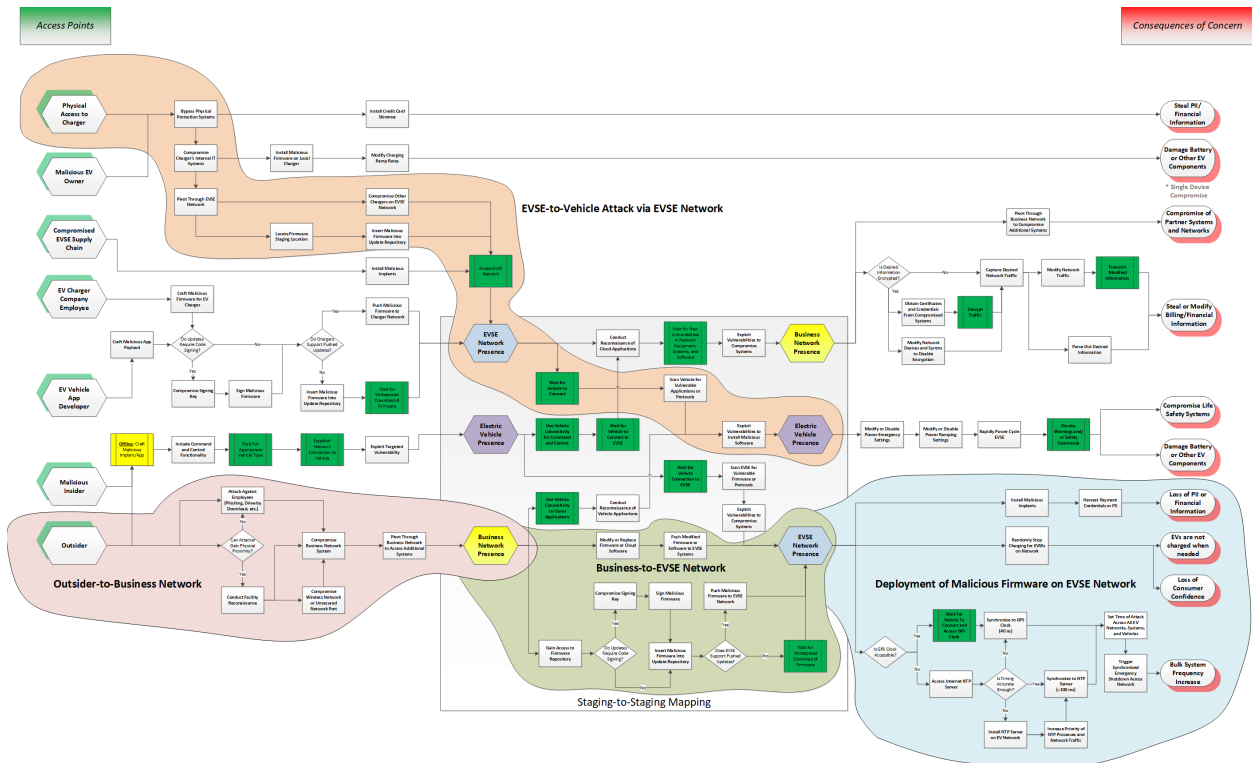


Figure II.4.2.4 Complete graph. Details presented in [2].

Threat Model Development

PNNL led the task to develop a threat model of high-power electric vehicle charging infrastructure and systemically analyze it for threats that have the potential to bring wide-ranging consequences to the electric grid and transportation systems. PNNL derived a novel consequence-centric variant of the STRIDE threat modeling methodology to: (i) discover consequences that potentially impact vehicles, the electric supply, and transportation; and (ii) focus subsequent modeling and analysis on threats that may precipitate the consequence. STRIDE is an industry-accepted approach to threat modeling, first made popular for its application at Microsoft. Examples of the system models used for the threat modeling are depicted in Figure II.4.2.5, which show decomposition of chargers and vehicle into components, how data flows between components, and the relationships of components to external entities. After the threats are enumerated, safeguards and countermeasures are identified to mitigate the vulnerabilities. By focusing on consequences, insights into the security and resiliency of the EV charging ecosystem is gained. Importantly, the threat model analysis suggests that no single entity (for example, charging station vendor or charging network operator) is ideally situated to secure the ecosystem, but instead, requires the concerted effort of the ecosystem. The threat model, analysis, and results are detailed in [3].

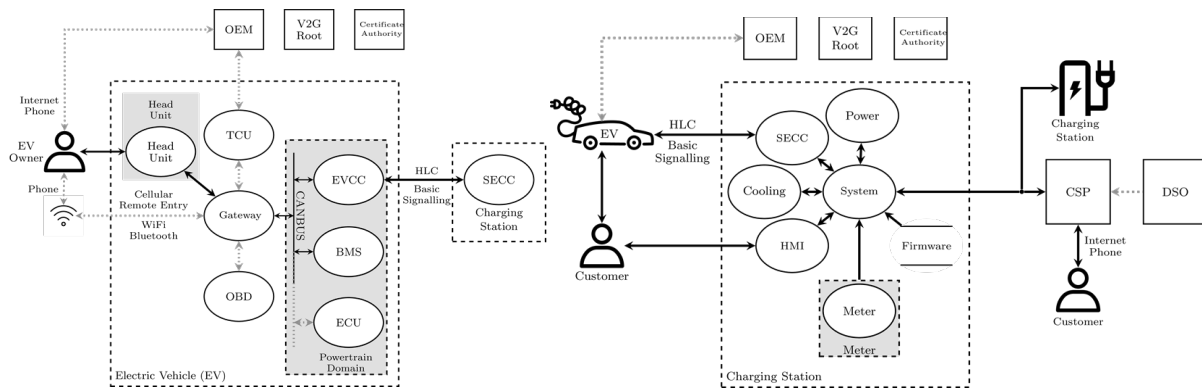


Figure II.4.2.5 The vehicle system model (left) depicts the components of the vehicle and their relationship to the charger. The charger system model (right) illustrates the relationship of the components and information flows.

Transmission System Consequence Analysis Simulations

PNNL's Consequence Analysis results indicate that for the specific events studied in this work, the impact on the WECC system is minimal. Two different types of studies were simulated: a large discrete WECC-wide EV load drop across the region intended to raise frequency, and several smaller EV load modulation events intended to excite system inter-area oscillations along the California Oregon Intertie (COI). Figure II.4.2.6 illustrates this procedure. Here the green and blue dots indicate a distributed load to modulate on either side of the COI. The graph above the map shows that the loads are 180 degrees out of phase. Conceptually, if loads in the north are high and loads in the south are low, this will create a flow north along the COI. Similarly, when loads are low in the north and high in the south, this will tend to generate flows south along the COI. No significant adverse effects were observed in either set of simulations, however, COI flows of up to 3 times the oscillating load size were observed in the load modulation studies. Inter-area oscillations are of concern in that they put the grid in elevated state of risk during system events as well as making it difficult to achieve ideal transfer capacities and optimal power flows. Further details are presented in [4]-[7].

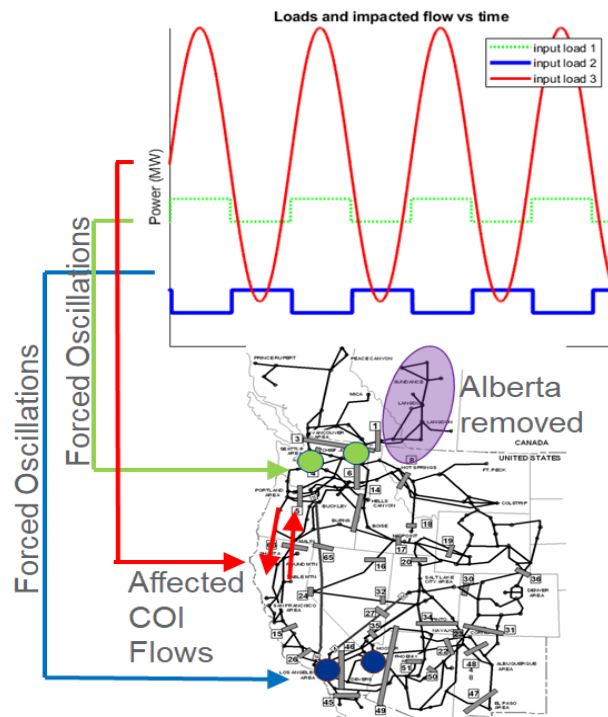


Figure II.4.2.6 Load oscillation simulation

Conclusions

This project is helping identify potential EV charger vulnerabilities and quantify the risk to critical infrastructure when vehicle chargers are maliciously controlled. This risk assessment is only an initial step in a continuous process of hardening charging infrastructure against cyber-attacks. There is much more work to secure charging infrastructure from cyber-attacks, including:

- Developing standardized policies for managing chargers and other assets in the charging ecosystem.

- Designing effective perimeter defenses to protect the assets including firewalls, access control mechanisms, data-in-flight requirements (encryption, authentication), etc.
- Creating situational awareness systems and intrusion detection/prevention systems in an ecosystem of diverse communication networks and systems.
- Researching response mechanisms to prevent further adversary actions on the system, nonrepudiation technologies, and dynamic responses.
- Creating hardware- and software-based fallback and contingency operating modes.

References

1. J. Johnson, B. Anderson, B. Wright, J. Daley, R. Varriale, "Recommended Cybersecurity Practices for EV Charging Systems," Sandia National Laboratories, SAND2020-11401 D, doi.org/10.13140/RG.2.2.11141.37602.
2. B. Anderson, "Securing Vehicle Charging Infrastructure Against Cybersecurity Threats," 2020 SAE Hybrid and Electric Vehicle Symposium, Pasadena, CA, 28-30 Jan 2020.
3. T.E. Carroll, G.B. Dindlebeck, R.M. Pratt, L.R. O'Neil, "A Threat Model of High-Power Electric Vehicle Charging Infrastructure," Journal of Information Warfare (forthcoming).
4. J. G. O'Brien, P. R. Maloney, U. Agrawal, T. E. Carroll, and R. M. Pratt, "Electric Vehicle Infrastructure Consequence Assessment," Pacific Northwest National Laboratory, Technical Report PNNL-29121, 2019.
5. Pratt R.M., T.E. Carroll, G.B. Dindlebeck, P.R. Maloney, and J.G. O'Brien. 06/02/2020. "Cybersecurity: Securing Vehicle Charging Infrastructure - Consequence Analysis and Threat Assessment.", United States. PNNL-SA-152801.
6. J.G. O'Brien, P.R. Maloney, U. Agrawal, T.E. Carroll, R.M. Pratt, "Electric vehicle infrastructure consequence assessment," Pacific Northwest National Laboratory Technical Report PNNL-29514, 2019.
7. Pratt R.M., T.E. Carroll, J.G. O'Brien, P.R. Maloney, L. O'Neil, and U. Agrawal. 2019. PNNL Cyber VTO Annual Progress Report. PNNL-29374. Richland, WA: Pacific Northwest National Laboratory.

Acknowledgements

DOE and the PI wish to thank the multi-laboratory team for this work: SNL (Ben Anderson, Brian Wright, Josh Daley, Jimmy Quiroz), PNNL (Rick Pratt, Tom Carroll, Lori Ross O'Neil, Brian Dindlebeck, Patrick Maloney, James O'Brien) and ANL (Roland Varriale, Ted Bohn, and Keith Hardy).

Sandia National Laboratories is a multimission laboratory managed and operated by National Technology & Engineering Solutions of Sandia, LLC, a wholly owned subsidiary of Honeywell International Inc., for the U.S. Department of Energy's National Nuclear Security Administration under contract DE-NA0003525.

(This page intentionally left blank)

U.S. DEPARTMENT OF
ENERGY

Office of
**ENERGY EFFICIENCY &
RENEWABLE ENERGY**

For more information, visit:
energy.gov/eere/vehicles

DOE/EE-2334 • June 2021